Development of A Tabulated Thermo-Viscoplastic Material Model with Regularized Failure for Dynamic Ductile Failure Prediction of Structures under Impact Loading

by Murat Buyuk

B.Sc. in Mechanical Engineering, May 1999, Yıldız Technical University
M.Sc. in Design and Manufacturing Engineering, May 2003, Gebze Institute of Technology

A Dissertation submitted to

The Faculty of
The School of Engineering and Applied Science
of The George Washington University
in partial fulfillment of the requirements
for the degree of Doctor of Philosophy

May 19, 2013

Dissertation directed by

Cing-Dao (Steve) Kan
Research Professor of Civil Engineering
and
Azim Eskandarian
Professor of Engineering and Applied Science

The School of Engineering and Applied Science of The George Washington University certifies that Murat Buyuk has passed the Final Examination for the degree of Doctor of Philosophy as of March 25, 2011. This is the final and approved form of the dissertation.

Development of A Tabulated Thermo-Viscoplastic Material Model with Regularized Failure for Dynamic Ductile Failure Prediction of Structures under Impact Loading

Murat Buyuk

Dissertation Research Committee:

Azim Eskandarian, Professor of Engineering and Applied Science,
Dissertation Co-Director

Cing-Dao (Steve) Kan, Research Professor of Civil Engineering,
Dissertation Co-Director

Pedro F. Silva, Professor of Civil and Environmental Engineering,
Committee Member

Samer H. Hamdar, Professor of Civil and Environmental Engineering,
Committee Member

Dhafer Marzougui, Research Professor of Civil Engineering,
Committee Member

Gilbert K. Queitzsch, Chief Scientist and Technical Advisor for Engine System Dynamics, Federal Aviation Administration
Committee Member

Paul A. Du Bois, Senior Scientist, Livermore Software Technology Corporation
Committee Member

Dedication

To my parents, Fatma Sevinc and Zeki

Acknowledgments

I would like to thank Prof. Azim Eskandarian for his academic supervision, personal support and constant inspiration throughout my studies in graduate school.

I would like to express my sincere gratitude to Prof. Cing-Dao (Steve) Kan, who has been my research advisor and supervisor during my doctoral research. I also would like to acknowledge the financial, academic and technical support he provided me as the Director of the National Crash Analysis Center (NCAC).

I would like to express my sincere appreciations to Prof. Dhafer Marzougui, who has always guided and supported me with his broad knowledge in computational mechanics. I cannot thank him enough for being such a great mentor, a friend and a reason for motivation during my doctoral studies.

I would like to acknowledge Prof. W. M. Kim Roddis and Prof. Majid T. Manzari, as chairs of the Civil & Environmental Engineering Department of the George Washington University for their invaluable support during my doctoral studies.

My keen appreciation goes to Prof. Pedro F. Silva and Prof. Samer H. Hamdar for taking the time from their busy schedules and serve as my committee members.

I also would like to take this opportunity to extend my gratitude to Dr. Gilbert (Chip) Queitzsch for bringing the invaluable industrial and governmental insight to my research and acting as a member of my committee. His guidance has been very influential for me to comprehend the scientific contribution of a doctoral research on potential applications. His input while perfecting this dissertation is greatly appreciated.

It has been a privilege having the opportunity to work with Mr. Paul A. Du Bois, who is an internationally known expert in computational mechanics, during the course of my research. His scientific approach to a problem has shown me the admirable ways of being a true scholar.

This research was funded by the Federal Aviation Administration. I would like to acknowledge Mr. William Emmerling and Mr. Donald Altobelli of the Federal Aviation Administration's Aircraft Catastrophic Failure Prevention Research Program, and Hughes Technical Center, Atlantic City, N.J., for their technical and financial support throughout this research.

I would like to acknowledge Dr. John O. Hallquist of Livermore Software Technology Corp. (LSTC) for providing me the required tools during the implementation of the material model into LS-DYNA.

I would like to acknowledge Prof. Amos Gilat and Dr. Jeremy Seidt of Ohio State University (OSU) for their cooperation within the framework on uncontained aircraft engine failure research program and providing the material test data.

Special thanks to Dr. Kelly S. Carney, Dr. J. Mike Pereira, Dr. Duane M. Revilock, Dr. Chuck Ruggeri and Dr. Brad Lerch of NASA Glenn Research Center for their support on the research program and providing ballistic impact test results.

I would like to acknowledge Prof. Tarek Zohdi, Prof. George Johnson and Dr. David Powell of University of California, Berkeley (UCB) for their cooperation within the framework on uncontained aircraft engine failure research program and providing ballistic impact test results.

Thanks to Dr. Qing (Jeanne) He from Forming Simulation Technology LLC. for bringing the metal forming insight into this research.

Sincere thanks are due to fellow students, all my colleagues, friends and staff at the Department of Civil & Environmental Engineering of the George Washington University and National Crash Analysis Center. Special thanks to Kivanc Sengoz for his friendship.

Finally, heartfelt thanks to my parents Fatma Sevinc and Zeki, who have shown constant support throughout my studies. I don’t know what it would be like without your devotion.

Abstract

Development of A Tabulated Thermo-Viscoplastic Material Model with Regularized Failure for Dynamic Ductile Failure Prediction of Structures under Impact Loading

It is important to understand the dynamic failure behavior of structures subjected to impact loading in order to improve the survivability. Materials under impact are utterly affected by large deformations, high strain-rates, temperature softening and varying stress-states, which finally may lead to failure. It is shown that the impact characteristics are prone to change with several independent factors such as; impact speed, material thickness, and shape and orientation of the impacting object. Validated numerical simulations of impact tests reveal that the failure on ductile metals occur at certain locations of the failure locus that is constructed on a space as a function of all three stress invariants, which indicates that the failure depends profoundly on the state-of-stress. It is shown that existing material models are not always successful enough to cover the whole range of the failure locus and predict the failure. Therefore, it is a common practice to use different sets of material model parameters tuned or calibrated to cover a specific region of the failure loci in an ad hoc manner for practical reasons to match particular test results. Even in that case, specially tuned material properties are not capable of predicting these limited cases if differences in the mesh size and pattern need to be considered.

In this dissertation a new, generic, thermo-elastic/viscoplastic material model with regularized failure is introduced. The new material model is implemented into a non-linear, explicit dynamics finite element code, LS-DYNA. A von Mises type isotropic, isochoric plasticity is utilized, where isotropic hardening, strain-rate hardening and temperature softening is considered. The model takes adiabatic heating and softening into

account due to the plastic work. The constitutive relation is coupled with a new regularized accumulated failure law that is specifically developed to cover a large extent of the failure locus as a function of state-of-stress, strain-rate and temperature. Regularization treatment is implemented to reduce mesh size dependency especially for the problems where softening and failure is involved for the failure prediction.

Ductile deformation and failure mechanism of 2024-T3/T351 aluminum alloy is investigated experimentally and numerically for quasi-static and dynamic conditions at various temperatures and stress-states. An intelligently contrived test matrix is developed by designing specific test specimens with different geometries that can construct a failure locus as a function of state-of-stress, strain-rate and temperature. An inverse material characterization algorithm is then introduced to generate input data for the new material model. Tabulated inputs of characterized material test results are directly used for both the constitutive and failure treatment of the new material model. Component based specimen tests that are used to characterize the material input properties and full-scale impact tests that are performed at different target thicknesses and impact speeds are used to validate and show the robustness, accuracy and efficiency of the new material model.

It is shown that the new material model is capable of predicting ballistic limit and failure modes accurately for structures under impact even if the failure mode changes drastically. It is also shown that the new regularization model provides less mesh size dependency. These associated features of the model suggest that the new material model can be used as a promising generic tool for diverse applications of dynamic ductile deformation and failure phenomenon.

Table of Contents

Pages

Dedication ..... **iii**

Acknowledgments ..... **iv**

Abstract ..... **vii**

Table of Contents ..... **ix**

List of Figures ..... **xviii**

List of Tables ..... **xlviii**

List of Symbols ..... **liv**

List of Acronyms ..... **lix**

CHAPTER 1 - Introduction **1**

1.1 Introduction **1**

1.2 Background and Motivation **3**

1.3 Research Objectives and scope **13**

1.4 Original Contributions **15**

1.5 Outline of the Dissertation **16**

CHAPTER 2 - Literature review **18**

2.1 Introduction **18**

2.2 Review on the ductile failure of metals **18**

2.3 Summary **27**

CHAPTER 3 - Problem definition **28**

3.1 Introduction 28

3.2 An examination of the state-of-the-arts: Explicit FE analysis of ballistic impact 29

3.2.1 Ballistic impact testing of 2024-T3/T351 aluminum material 29

3.2.2 Numerical modeling 31

3.2.2.1 Finite Element Models 31

3.2.2.2 Material Models 34

3.2.2.3 Johnson-Cook Material Model 35

3.2.3 Ballistic impact simulation results 45

3.2.3.1 Results for target thickness 1.5875mm 45

3.2.3.2 Results for target thickness 3.175mm 47

3.2.3.3 Results for target thickness 6.35mm 48

3.2.4 Ballistic impact simulation summaries and discussion 50

3.3 Summary 53

CHAPTER 4 - Methodology 54

4.1 Introduction 54

4.2 Development and implementation of a new material model, TRAUM 62

4.2.1 Constitutive relation 63

4.2.2 Time integration and numerical implementation 68

4.2.3 Accumulated failure algorithm 73

4.3 Development of a generic failure locus for ductile materials based on multiple states-of-stress 74

4.3.1 Identification of the stress-states 79

4.3.1.1 Uni-axial state 79

4.3.1.2 Plane-stress state-of-stress 80

4.3.1.3 Axi-symmetric state-of-stress 82

4.3.1.4 Plane-strain state-of-stress 84

4.3.2 Notable points on the stress-state space 85

4.3.3 Identification of the stress-states for structures under impact loading 87

4.4 Devising a testing program to characterize a generic failure locus 90

4.4.1 Construction of a failure locus for multiple states-of-stress 91

4.4.2 Construction of a failure locus for strain rate and temperature dependency 101

4.4.3 Key aspects of iterative specimen design algorithm for specific states-of-stress 107

4.4.3.1 Dependency on the material properties 115

4.4.3.2 Dependency on the location of the FE calculation 116

4.4.3.3 Dependency on the mesh size and the significance of mesh regularization 118

4.4.4 Initial specimen geometries to characterize a failure locus depending on multiple states-of-stress 131

4.4.4.1 Specimens for plane-stress tension 131

4.4.4.2 Specimens for axi-symmetric tension 135

4.4.4.3 Specimens for plane-strain tension 139

4.4.4.4 Specimens for uni-axial compression 144

4.4.4.5 Specimen for torsion / shear 146

4.4.4.6 Specimens for combined tension - shear 150

4.4.4.7 Specimens for punch tests 155

4.4.5 Collection of specimens for the characterization of a failure locus depending on multiple states-of-stress 164

4.5 Single element verification analysis for the new material model 166

4.5.1 Single element analysis and verification of TRAUM with J-C material model for loading path dependency considering different values of stress-triaxiality 166

4.5.1.1 Benchmark-problem definition 166

4.5.1.2 Benchmark-problem results 174

4.5.2 Single element analysis and verification of TRAUM with J-C material model for mesh size dependency on the prediction of failure 178

4.5.2.1 Benchmark-problem definition 178

4.5.2.2 Benchmark-problem results 179

4.5.3 Single element analysis and verification of TRAUM with J-C material model for a non-monotonic representation of the failure locus 181

4.5.3.1 Benchmark-problem definition 181

4.5.3.2 Benchmark-problem results 184

4.5.4 Single element analysis and verification of TRAUM for a Lode-angle-dependent failure surface 185

4.5.4.1 Benchmark-problem definition 185

4.5.4.2 Benchmark-problem results 191

4.6 Summary 192

CHAPTER 5 - Experimental program 194

5.1 Introduction 194

5.2 Material of interest 194

5.3 Methodology 197

5.4 Digital Image Correlation (DIC) 200

5.5 Characterization of the quasi-static hardening curve at room temperature 202

5.5.1 Dynamic strain aging and Portevin–Le Châtelier effect 206

5.5.2 Iterative methodology for the characterization of the hardening curve 209

5.5.3 Verification of the quasi-static hardening curves for axi-symmetric tension at room temperature 228

5.5.4 Verification of the quasi-static hardening curves for uni-axial compression at room temperature 231

5.5.5 Verification of the quasi-static hardening curves for torsion at room temperature..... 235

5.6 Characterization of the temperature dependent quasi static hardening curves 238

5.6.1 Determination of the testing range for temperature dependent behavior..... 239

5.6.2 Temperature dependent Young's modulus, Poisson's ratio and specific heat... 241

5.6.3 Apparatus for temperature dependent testing 244

5.6.4 Assessment of the quasi-static testing conditions considering the deformation heating and the isothermal assumption..... 255

5.6.5 A multi-case automated material characterization methodology by using AO algorithm based on SRSM..... 271

5.6.6 Characterization of the temperature dependent hardening curves at quasi-static conditions by using automated AO with SRSM 302

5.7 Characterization of the strain-rate dependent hardening curves at room temperature 313

5.7.1 Determination of the testing range for strain-rate dependent behavior 313

5.7.2 Apparatus for strain-rate dependent testing 316

5.7.2.1 Compression Split Hopkinson Bar (CSHB) apparatus 317

5.7.2.2 Tension Split Hopkinson Bar (TSHB) apparatus 325

5.7.2.3 Shear Split Hopkinson Bar (SSHB) apparatus 330

5.7.3 Modifications on the automated material characterization methodology considering high strain-rate testing, adiabatic heating and dynamic force equilibrium 336

5.7.4 Characterization of the strain-rate dependent hardening curves at room temperature by using automated AO with SRSM 338

5.7.4.1 Characterization of the high strain-rate rate dependent flow in tension 338

5.7.4.2 Characterization of the high strain-rate dependent flow in compression 340

5.7.4.3 Characterization of the high strain-rate dependent flow in shear 343

5.8 Adiabatic and isothermal flow surface for Al2024-T351 346

5.9 Determination of the regularization curve 351

5.9.1 Localized tensile instability 359

5.10 Characterization of the failure locus 368

5.10.1 Plane-stress tension specimens 369

5.10.2 Axi-symmetric tension specimens 378
5.10.3 Plane-strain tension specimens 389
5.10.4 Uni-axial compression specimen 397
5.10.5 Shear/torsion specimen 399
5.10.6 Combined tension/torsion specimens 402
5.10.7 Punch test specimens 409

5.11 Construction of the failure surface for quasi-static conditions and room temperature 415

5.12 Characterization of the strain-rate dependent scaling curve for the failure surface 427

5.13 Characterization of the temperature dependent scaling curve for the failure surface 430

5.14 Summary and conclusions 433

CHAPTER 6 - Validation of the material test results 435

6.1 Introduction 435

6.2 Plane-stress tension specimens 436

6.3 Axi-symmetric tension specimens 441

6.4 Plane-strain tension specimens 448

6.5 Uni-axial compression specimen 452

6.6 Shear/torsion specimen 453

6.7 Combined tension/torsion specimens 454

6.8 Punch test specimens 456

6.9 Summary and conclusions 457

CHAPTER 7 - Impact loading applications 459

7.1 Introduction 459

7.2 Ballistic impact with spherical projectiles 459

7.3 Ballistic impact with cylindrical projectiles 465

7.3.1 Target geometries 466

7.3.2 Projectile geometries 466

7.3.3 Ballistic impact test apparatus 467

7.3.4 Ballistic impact test results 468

7.3.5 Numerical models of the ballistic impact with cylindrical projectiles 469

7.3.6 TRAUM predictions for 3.175mm targets under ballistic impact with cylindrical projectiles 472

7.3.7 TRAUM predictions for 6.35mm targets under ballistic impact with cylindrical projectiles 474

7.3.8 TRAUM predictions for 12.7mm targets under ballistic impact with cylindrical projectiles 477

7.4 Summary 478

CHAPTER 8 - Summary, Conclusions and Recommendations 480

8.1 Summary and contributions 480

8.2 Conclusions 481

8.2.1 Ballistic impact simulations on aluminum plates 481

8.2.2 Development of an elastic/viscoplastic material model with a regularized failure, TRAUM 481

8.2.3 Material characterization for Al2024-T351 482

8.2.4 Validation and verification of material tests 483

8.2.5 Validation and verification of impact tests 483

8.3 Recommendations for future research 483

References 485

Appendix - A: Preliminaries of the stress tensor and invariants 503

Appendix - B: Specimen geometries and FE models 507

Appendix - C: Details of the test results that are used for the characterization of the material input data 528

Appendix - D: List of tests for characterization of the input data for TRAUM 576

Appendix - E: Mesh patterns that are used for regularization 578

Appendix - F: Verification of the input values for TRAUM simulations 582

Appendix - G: Mesh dependency of the prediction of localized necking 597

Appendix - H: Characterization of the ductile failure based on the state-of-stress for the corresponding tests and the specimens 600

List of Figures

Pages

Figure 1-1: Applications of dynamic failure for different structures; (a) offset frontal crash of a passenger car (http://www.iihs.org), (b) uncontained aircraft engine failure (http://www.ntsb.gov), (c) rupture after hydroforming on pipes (http://www.uscar.org) and (d) different failure modes after ballistic impact of projectiles with different nose shapes, adapted from [14]. 2
Figure 1-2: Failure modes in impacted plates, after [12] [77]. 5
Figure 1-3: Comparison of viscoplastic flow functions, adapted from [79]. 6
Figure 1-4: Transition of the failure modes and comparison of the failure loci for Al2024-T351. 9
Figure 1-5: 3D adaptations of the failure models on the space described by stress-triaxiality and Lode-angle-parameter for Al2024-T351; (a) J-C model with Set-1 [85], (b) model by Bao [99], (c) model by Xue with Lode-angle-parameter dependency introduced [103]. 11
Figure 1-6: Asymmetric failure surface incorporating the effects of stress-triaxiality and Lode-angle-parameter [104]. 12
Figure 1-7: Material behavior with changing strain rate and load duration, adapted after [111]. 14
Figure 1-8: Comparison of yield surfaces for different materials under combined loading; (a) after [109] and (b) after [110]. 15
Figure 2-1: A schematic representation of the ductile failure in metals, adapted after [5]. 19
Figure 2-2: SEM images from a uni-axial test for ‘cup’ (a) and ‘cone’ (b) regions of the failure zone, adapted after [5]. 19
Figure 3-1: Experimental setup for ballistic impact testing for Al2024-T3/T351 plates. 30
Figure 3-2: Ballistic limit for findings three different thickness 2024-T3/T351 target plates. 30
Figure 3-3: Mesh patterns for 1.5875mm thickness target. 32

Figure 3-4: Mesh patterns for 3.175mm thickness target. 33
Figure 3-5: Mesh patterns for 6.35mm thickness target. 33
Figure 3-6: Differences in flow surfaces depending on the sets of material model parameters; hardening for (a) Set-1 and (b) Set-2, 3 and 4; softening for (c) Set-1 and (d) Set-2, 3 and 4. 40
Figure 3-7: Strain rate dependent hardening curves defining different flow surfaces for 2024-T3/T351 resulting from different J-C parameter sets at room temperature. 41
Figure 3-8: Temperature dependent hardening curves defining different flow surfaces for 2024-T3/T351 resulting from different J-C parameter sets at a nominal strain rate of 1 s^{-1} 41
Figure 3-9: Differences in the failure loci for 2024-T3/T351 resulting from different J-C parameter calibration from different tests. 43
Figure 3-10: Strain rate dependent failure loci comparing different sets of J-C parameters. 44
Figure 3-11: Temperature dependent failure loci comparing different sets of J-C parameters. 44
Figure 3-12: Penetration through 1.5875mm target and petal formation; (a) Simulation, (b) Test-Front Face, (c) Test-Rear Face. 45
Figure 3-13: Ballistic limit predictions for 1.5875mm targets. 46
Figure 3-14: Penetration through 3.175mm target and mixed-mode failure formation; (a) Simulation, (b) Test-Front Face, (c) Test-Rear Face. 47
Figure 3-15: Ballistic limit predictions for 3.175mm targets. 48
Figure 3-16: Penetration through 6.35mm target and plug formation; (a) Simulation, (b) Test-Front Face, (c) Test-Rear Face. 49
Figure 3-17: Ballistic limit predictions for 6.35mm targets. 49
Figure 3-18: Ballistic limit predictions due to the transition of the failure modes with respect to target thickness. 51
Figure 3-19: Transition of the failure modes depending on the state-of-stress based on target thickness. 52
Figure 4-1: Failure surface for Al2024-T351 constructed by J-C equation and projection of the meridians on to the plane of stress-state. 56

Figure 4-2: Failure surface for Al2024-T351 with three different branches depending on stress-triaxiality. 57
Figure 4-3: Symmetric failure surface for Al2024-T351 with a dependency on stress-triaxiality and Lode-angle-parameter. 58
Figure 4-4: Asymmetric failure surface for Al2024-T351 with a dependency on stress-triaxiality and Lode-angle-parameter. 59
Figure 4-5: Projection of the 3D failure locus on to the stress-space defined by stress-triaxiality vs. Lode-angle-parameter. 60
Figure 4-6: Methodology flow diagram. 61
Figure 4-7: The role of elasto-plastic return-mapping algorithms. 68
Figure 4-8: Geometric interpretation of the radial-return in principle stress space. 69
Figure 4-9: Geometric interpretation of the radial-return in deviatoric stress space. 70
Figure 4-10: Geometric interpretation of the radial-return on the invariant plane. 71
Figure 4-11: Successive secant iterations. 72
Figure 4-12: Stress-state envelope in the stress-triaxiality vs. product-triaxiality space. 76
Figure 4-13: Representation of a three dimensional failure surface; (a) J-C relation, (b) projection on to the plane of stress-state defined by stress-triaxiality vs. Lode-angle-parameter and (c) projection on to the plane of stress-state defined by stress-triaxiality vs. product-triaxiality. 78
Figure 4-14: Plane-stress state conditions on the stress-space. 82
Figure 4-15: Axi-symmetric stress-state conditions on the compression meridian of the stress-space. 83
Figure 4-16: Axi-symmetric stress-state conditions on the tension meridian of the stress-space. 84
Figure 4-17: Plane-strain stress-state conditions on the plane-strain meridian of the stress-space. 85
Figure 4-18: Notable points on stress-triaxiality versus product-triaxiality space. 86
Figure 4-19: Transition of the failure modes with target thickness under impact loading due to the state-of-stress. 88
Figure 4-20: Selected elements for state-of-stress identification. 88

Figure 4-21: States-of-stress for the selected finite elements under the impact region as a function of stress-triaxiality and product-triaxiality. 90
Figure 4-22: Representation of the J-C failure surface; (a) with test points suggested later in this Chapter, (b) projection on to the plane of stress-triaxiality vs. effective plastic strain at failure, showing no Lode-angle-parameter dependency and (c) projection on to the plane of stress-state defined by stress-triaxiality vs. Lode-angle-parameter showing the paths suggested for bridging the stress-states. 94
Figure 4-23: Representation of a Lode-angle-parameter dependent failure surface; (a) failure surface defined by surface fitting over the test points defined in [104], (b) projection on to the plane of stress-triaxiality vs. effective plastic strain at failure showing Lode-angle-parameter dependency with different stress meridians and (c) projection on to the plane of stress-state defined by stress-triaxiality vs. Lode-angle-parameter showing the paths suggested for bridging the stress-states. 95
Figure 4-24: Outline of determining the stress-states while constructing the failure locus by bridging. 97
Figure 4-25: Identifying the bridging paths while constructing the failure locus through stress meridians and notable values of the stress-states considering the zone of interest suggested for ductile materials under impact loading; (a) representation of bridging on the plane of stress-state defined by stress-triaxiality vs. Lode-angle-parameter and (b) representation of bridging on the plane of stress-state defined by stress-triaxiality vs. product-triaxiality. 98
Figure 4-26: (a) Representation of a Lode-angle-parameter dependent ruled failure surface defined by stress meridians as splines swept from the test points defined later in this Chapter; (b) three-dimensional representation of the splines in stress space, (c) stress meridians projected on to the plane of stress-triaxiality vs. effective plastic strain at failure showing Lode-angle-parameter dependency and (d) representation of paths used for bridging stress-states. 100
Figure 4-27: Strain rate dependent failure locus constructed by offsetting the initial failure surface. 103
Figure 4-28: Strain rate dependent scaling factor (curve) and the scaled stress meridians of the failure surface. 104

Figure 4-29: Temperature dependent failure locus constructed by offsetting the initial failure surface. 105
Figure 4-30: Temperature dependent scaling factor (curve) and the scaled stress meridians of the failure surface. 106
Figure 4-31: Specimen geometries and loading conditions categorically associated with certain stress meridians; (a) plane-stress, (b) axi-symmetric tension, (c) plane-strain, (d) punch, (e) compression, (f) shear (torsion) and (g) combined tension - shear (torsion) specimens. 108
Figure 4-32: Flowchart for iterative specimen design procedure for desired states-of-stress. 109
Figure 4-33: Determination of the targeted state-of-stress and the corresponding specimen geometry; (a) on the plane of stress-state defined by stress-triaxiality vs. Lode-angle-parameter, (b) on the plane of stress-state defined by stress-triaxiality vs. product-triaxiality. 112
Figure 4-34: Axi-symmetric notched specimen geometry in tension for Bridgman's analysis. 113
Figure 4-35: Single finite element in the center of the specimen gauge region for stress-state calculations. 113
Figure 4-36: Bridgman's analysis utilized for the first iteration of an initial design procedure. 114
Figure 4-37: Dependency of the stress-triaxiality on the material properties. 116
Figure 4-38: Dependency of the stress-triaxiality on the location of the calculation point within the gauge cross-section of the specimen. 117
Figure 4-39: Cross-section of the FE model with different characteristic element lengths for the initial specimen geometry. 118
Figure 4-40: Evolution of stress-triaxiality with effective plastic strain when J-C material model is utilized for the simulations with different characteristic element lengths. 119
Figure 4-41: Effect of mesh size dependency on the prediction of end displacements. 121

Figure 4-42: Effect of mesh size dependency on the prediction of end displacements. 123
Figure 4-43: Effect of mesh regularization on the prediction of end displacements. 124
Figure 4-44: Mesh size dependent failure locus constructed by offsetting the initial failure surface. 125
Figure 4-45: Mesh size dependent scaling factor (curve) and the scaled stress meridians of the failure surface. 126
Figure 4-46: Averaged stress-triaxiality for the first iteration of the initial design. 127
Figure 4-47: Averaged stress-triaxiality for the second iteration of the initial design. .. 128
Figure 4-48: Modified Bridgman relation to find the initial specimen geometry for the targeted stress-triaxiality value. 129
Figure 4-49: Averaged stress-triaxiality for the third iteration of the initial design. 130
Figure 4-50: Determination of the targeted states-of-stress and the corresponding plane-stress specimen geometries on the planes defined by; (a) stress-triaxiality vs. Lode-angle-parameter and (b) stress-triaxiality vs. product-triaxiality. 133
Figure 4-51: Comparison of the initially targeted and calculated states-of-stress for plane-stress specimens. 134
Figure 4-52: Determination of the targeted states-of-stress and the corresponding axi-symmetric specimen geometries on the plane defined by; (a) stress-triaxiality vs. Lode-angle-parameter and (b) stress-triaxiality vs. product-triaxiality. 137
Figure 4-53: Comparison of the initially targeted and calculated states-of-stress for axi-symmetric specimens. 138
Figure 4-54: Determination of the best thickness for the plane-strain specimens considering the predictions on the states-of-stress. 140
Figure 4-55: Determination of the best thickness for the plane-strain specimens considering the load carrying capacity of the test apparatus. 141
Figure 4-56: Determination of the targeted states-of-stress and the corresponding plane-strain specimen geometries on the plane defined by; (a) stress-triaxiality vs. Lode-angle-parameter and (b) stress-triaxiality vs. product-triaxiality. 143
Figure 4-57: Comparison of the initially targeted and calculated states-of-stress for plane-strain specimens. 144

Figure 4-58: Effects of the diameter to height ratio and the coefficient of friction on the state-of-stress predictions. 146
Figure 4-59: Determination of the targeted states-of-stress and the corresponding compression and torsion specimen geometries on the plane defined by; (a) stress-triaxiality vs. Lode-angle-parameter and (b) stress-triaxiality vs. product-triaxiality. ... 147
Figure 4-60: Alternative positions for calculating state-of-stress on shear specimen. ... 148
Figure 4-61: Position of the failure and the stress-state calculation for shear specimen. 149
Figure 4-62: Comparison of the initially targeted and calculated states-of-stress for shear specimen. 150
Figure 4-63: Determination of the targeted states-of-stress and the corresponding combined loading cases sharing the same Lode-angle-parameters with the plane-stress specimens on the plane defined by; (a) stress-triaxiality vs. Lode-angle-parameter and (b) stress-triaxiality vs. product-triaxiality. 152
Figure 4-64: Combined loading under tension and torsion. 153
Figure 4-65: Comparison of the stress-states against proportion of combined loading. 154
Figure 4-66: Comparison of the initially targeted and calculated states-of-stress for combined tension - shear specimens. 156
Figure 4-67: Punch test requirements for (a) Nakazima and Hasek test with different specimen geometries, (b) Keeler test with different punch radii, adapted after [216]. 157
Figure 4-68: Characterization properties of different test methods and punch tests illustrated on a FLD, adapted after [216]. 157
Figure 4-69: Effects of nose shape on the failure mode, adapted after [14]. 158
Figure 4-70: (a) Test assembly for punch Specimen #18 and (b) location of the failure initiation point, where the state-of-stress is calculated for specimen design. 160
Figure 4-71: (a) Test assembly for punch Specimen #19 and (b) location of the failure initiation point, where the state-of-stress is calculated for specimen design. 160
Figure 4-72: (a) Test assembly for punch Specimen #20 and (b) location of the failure initiation point, where the state-of-stress is calculated for specimen design. 161

Figure 4-73: Comparison of the initially targeted and calculated states-of-stress for punch test specimens..... 162
Figure 4-74: Determination of the targeted states-of-stress and the corresponding punch specimen geometries on the plane defined by; (a) stress-triaxiality vs. Lode-angle-parameter and (b) stress-triaxiality vs. product-triaxiality..... 163
Figure 4-75: Overview of the test program and initially targeted states-of-stress for each specimen on the plane defined by; (a) stress-triaxiality vs. Lode-angle-parameter and (b) stress-triaxiality vs. product-triaxiality..... 165
Figure 4-76: Single element models with the boundary conditions representing proportional and non-proportional loading conditions. 166
Figure 4-77: Applied displacement on the single finite element models..... 167
Figure 4-78: States-of-stress for each finite element on the plane defined by; (a) stress-triaxiality vs. Lode-angle-parameter and (b) stress-triaxiality vs. product-triaxiality. 169
Figure 4-79: Stain-rate dependent flow surface at room temperature representing; (a) Set-4 of the J-C material model parameters and (b) tabulated format of the J-C flow surface for TRAUM..... 170
Figure 4-80: Temperature dependent flow surface at a nominal strain rate of $1.0s^{-1}$ representing; (a) Set-4 of the J-C material model parameters and (b) tabulated format of the J-C flow surface for TRAUM. 171
Figure 4-81: Failure surface at room temperature and a nominal strain rate of $1.0s^{-1}$ representing; (a) tabulated format of the J-C failure locus for TRAUM and (b) TRAUM's three dimensional representation for Set-4 of the J-C material model parameters. 172
Figure 4-82: Scaling factors for TRAUM offsetting the failure locus with; (a) strain-rate dependent scaling curve normalized for a nominal-strain rate of $1.0s^{-1}$ (b) temperature dependent scaling curve normalized for room temperature..... 173
Figure 4-83: Scaling factor for TRAUM offsetting the failure locus with element size dependent scaling curve..... 174
Figure 4-84: Comparison of the displacements for different boundary conditions on single elements..... 175

Figure 4-85: Evolution of the effective plastic strain to failure paths as a function of stress-triaxiality for proportional and non-proportional loading indicating identical J-C and TRAUM results. 176
Figure 4-86: Comparison of effective stress and effective plastic strain response for different boundary conditions. 177
Figure 4-87: Comparison of the stress-strain response for J-C and TRAUM with different boundary conditions. 178
Figure 4-88: Single element models for regularization. 179
Figure 4-89: Evolution of the effective plastic strains to failure with different element lengths for J-C. 180
Figure 4-90: Evolution of the effective plastic strain to failure with different element lengths for TRAUM. 181
Figure 4-91: Single element models representing notable stress-triaxialities. 182
Figure 4-92: States-of-stress for each finite element on the plane defined by; (a) stress-triaxiality vs. Lode-angle-parameter and (b) stress-triaxiality vs. product-triaxiality. 183
Figure 4-93: Failure surface at room temperature and a nominal strain rate of $1.0s^{-1}$ representing; (a) tabulated format of the Bao's failure locus for TRAUM and (b) Bao failure locus in three dimensional representation with constant Lode-angle-parameter dependency. 184
Figure 4-94: Comparison of the failure predictions for different states-of-stress when a non-monotonic failure locus is utilized by TRAUM. 185
Figure 4-95: Single element models representing notable Lode-angle-parameters. 186
Figure 4-96: Single element models representing notable Lode-angle-parameters. 188
Figure 4-97: Applied pressure on the single finite element models without the scaling factors. 188
Figure 4-98: States-of-stress for each finite element on the plane defined by; (a) stress-triaxiality vs. Lode-angle-parameter and (b) stress-triaxiality vs. product-triaxiality. 189

Figure 4-99: Failure surface at room temperature and a nominal strain rate of 1 s^{-1} representing (a) tabulated format of the Xue's failure surface for TRAUM and (b) Xue's failure surface. 190
Figure 4-100: Comparison of the failure predictions for different states-of-stress when a Lode-angle-dependent failure surface is utilized by TRAUM. 191
Figure 5-1: Principle Aluminum alloys and Al2024, adapted after [228]. 196
Figure 5-2: Orthogonal directions of the rolled plate and specimen orientations..... 197
Figure 5-3: Steps for material characterization. 199
Figure 5-4: Binocular stereovision technique; (a) calculation of image point by triangulation, (b) temporal calculation of 3D displacement field and (c) temporal calculation of 3-D strain field, after [248]. 201
Figure 5-5: Binocular stereovision camera systems for; (a) quasi-static testing and (b) dynamic testing, after [108]. 202
Figure 5-6: Servo-hydraulic Load Frame, after [108]. 203
Figure 5-7: Numbering scheme for test results. 204
Figure 5-8: Flow and failure behavior of Al2024-T351 for quasi-static uni-axial tension at room temperature..... 205
Figure 5-9: DSA and PLC effect for Al2024-T351. 207
Figure 5-10: Stability maps for PLC effect; (a) Generic N-shaped stability map, adapted after [253], (b) stability map for Al2024 based on critical stress, digitized and adapted after [254], (c) stability map for Al2024 based on critical strain, digitized and adapted after [254] and (d) stability map for Al2024 based on critical strain, digitized and adapted after [261]. 209
Figure 5-11: Illustration of the strain field with a given DIC extensometer. 210
Figure 5-12: Methodology to obtain true plastic strain vs. stress raw data; (a) Force vs. displacement curve, (b) engineering stress vs. strain curve, (c) true stress vs. strain curve and (d) true plastic strain vs. stress curve. 212
Figure 5-13: Smoothed true stress vs. true strain curve and the onset on necking. 214
Figure 5-14: Yield, necking and failure points on the hardening curves. 215
Figure 5-15: Bridgman's correction for diffuse necking on axi-symmetric cylindrical specimen geometry in tension. 216

Figure 5-16: Schematic illustration of the necking mechanisms developing during the progressive deformation of a rectangular bar under uni-axial tension up to failure. 217
Figure 5-17: Determination of the hardening curve beyond the necking point. 221
Figure 5-18: Hardening curves for different number of rows in the neck area beyond necking point. 224
Figure 5-19: Comparison of the prediction performance of the extrapolated hardening curves. 225
Figure 5-20: Comparison of the quasi-static hardening curves for Al2024-T351 by other researchers. 226
Figure 5-21: Characterized quasi-static hardening curve at room temperature for Al2024-T351 and predicted force vs. displacement curves with different characteristic element lengths. 228
Figure 5-22: Strain-rate dependent quasi-static hardening curves at room temperature. 229
Figure 5-23: Verification of the hardening curves for plane-stress and axi-symmetric specimens sharing the same stress-triaxiality. 230
Figure 5-24: Quasi-static compression test setup with LVDT fixture, after [108]. 234
Figure 5-25: Flow and failure behavior of Al2024-T351 for quasi-static uni-axial compression at room temperature. 234
Figure 5-26: Calculation of the shear strains with respect to DIC measurements. 237
Figure 5-27: Comparison of the flow behavior for specimens with different states-of-stress. 238
Figure 5-28: Temperature increase due to the plastic work for 1.5875mm thick targets under impact. 240
Figure 5-29: Temperature increase due to the plastic work for 3.75mm thick targets under impact. 240
Figure 5-30: Temperature increase due to the plastic work for 6.35mm thick targets under impact. 240
Figure 5-31: Temperature dependent Young’s modulus and Poisson’s ratio for Al2024. 243

Figure 5-32: Evolution of tabulated Young's modulus and constant Poisson's ratio for Al2024-T351. 243
Figure 5-33: Servo-hydraulic Load Frame with ATS 3620 furnace, after [108]. 245
Figure 5-34: Servo-hydraulic Load Frame with Research, Inc., E4-2 IR furnace, after [108]..... 245
Figure 5-35: Servo-hydraulic Load Frame with cryogenic chamber, after [108]. 246
Figure 5-36: Instrumentation of the tension specimens with thermocouples for (a) high temperature and (b) low temperature testing, after [108]. 247
Figure 5-37: Evolution of temperatures within the testing apparatus for quasi-static uni-axial tension at targeted values of; (a) 423K, (b) 573K, (c) 723K and (d) 223K. 248
Figure 5-38: Temperature profiles of the tension specimens until the targeted testing temperatures. 249
Figure 5-39: Instrumentation of the compression specimens with thermocouples for (a) high temperature and (b) low temperature testing, after [108]. 250
Figure 5-40: Evolution of temperatures within the testing apparatus for quasi-static uni-axial compression at targeted values of; (a) 423K, (b) 573K, (c) 723K and (d) 223K. 251
Figure 5-41: Temperature profiles of the compression specimens until the targeted testing temperatures. 252
Figure 5-42: Servo-hydraulic Load Frame with torsion grips, after [108]. 253
Figure 5-43: Instrumentation of the torsion specimens with thermocouples for (a) high temperature and (b) low temperature testing, after [108]. 255
Figure 5-44: Evolution of temperatures within the testing apparatus for quasi-static torsion at targeted values of; (a) 423K, (b) 573K, (c) 723K and (d) 223K. 257
Figure 5-45: Temperature profiles of the torsion specimens until the targeted testing temperatures. 258
Figure 5-46: Evolution of temperature with respect to strain at quasi-static testing and the amount of plastic work converted into heat. 260
Figure 5-47: Evolution of temperature at quasi-static testing due to the plastic work; (a) initial conditions and (b) before failure. 261

Figure 5-48: Evolution of temperatures at the selected points along the specimen with respect to deformation. 262
Figure 5-49: Thermo-mechanical problem for uni-axial tension. 264
Figure 5-50: Evolution of temperatures with respect to deformation for coupled thermo-mechanical problem. 265
Figure 5-51: Temperature distribution within the specimen based on the formulation of the thermo-mechanical problem. 266
Figure 5-52: Heat flux within the specimen due to the thermo-mechanical problem. ... 267
Figure 5-53: The amount of plastic work converted into heat and the corresponding total temperature increase. 268
Figure 5-54: Calculating isothermal hardening curves from adiabatic hardening curves. 270
Figure 5-55: Flow diagram of the automated parameter identification process for material characterization by using SRSM for temperature dependent tests. 272
Figure 5-56: First stage of the automated parameter identification process for material characterization by using SRSM for temperature dependent tests. 273
Figure 5-57: Features of OCM methodology. 277
Figure 5-58: Features of PCM methodology, adapted from [327]. 278
Figure 5-59: Adjustment of the successive sub-regions in SRSM by using; (a) pure panning, (b) pure zooming and (c) a combination of panning and zooming, adapted from [321]. 285
Figure 5-60: Initial conditions: (a) initial design space and inputs for TRAUM and (b) initial response functions compared with the targeted response. 288
Figure 5-61: History of optimization: evolution of combined objective functions for each discrete variable. 289
Figure 5-62: History of optimization: evolution of design variables for Hollomon Model. 290
Figure 5-63: History of optimization: evolution of design variables for Ludwik Model. 290
Figure 5-64: History of optimization: evolution of design variables for Swift Model. .. 290
Figure 5-65: History of optimization: evolution of design variables for Voce Model. .. 291

Figure 5-66: History of optimization: evolution of design variables for Hockett/Sherby Model. 291
Figure 5-67: History of optimization: evolution of design variables for Ghosh Model. 291
Figure 5-68: History of optimization: evolution of design space and sub-regions for H Model. 292
Figure 5-69: History of optimization: evolution of design space and sub-regions for H/S Model with different combinations of variables showing; (a) $C1, C2, C3$ and (b) $C1, C3, C4$. 293
Figure 5-70: History of optimization: evolution of design space and sub-regions for H/S Model on a plane with different combinations of variables showing; (a) $C1, C2$, (b) $C1, C3$ and (c) $C1, C4$. 294
Figure 5-71: History of optimization: evolution of design space and sub-regions for H/S Model on a plane with different combinations of variables showing; (a) $C2, C3$, (b) $C2, C4$ and (c) $C3, C4$. 295
Figure 5-72: History of optimization: selection of design points and the corresponding responses for the iterations; (a) 1st, (b) 2nd, (c) 3rd and (d) 4th. 297
Figure 5-73: History of optimization: selection of design points and the corresponding responses for the iterations; (a) 5th, (b) 6th, (c) 7th, (d) 8th, (e) 9th, (f) 10th and (g) 11th. 298
Figure 5-74: History of optimization: selection of design points and the corresponding responses for the iterations; (a) 12th, (b) 13th, (c) 14th and (d) 15th. 299
Figure 5-75: Optimum conditions; (a) optimum design space and inputs for TRAUM and (b) optimum response functions compared with the targeted response. ... 301
Figure 5-76: Temperature dependent, quasi-static flow surface that is characterized from uni-axial tension tests. 304
Figure 5-77: Temperature dependent, quasi-static flow surface that is characterized from uni-axial compression tests. 305
Figure 5-78: Thermo-mechanical problem for uni-axial compression. 306
Figure 5-79: Temperature distribution within the specimen for the thermo-mechanical problem with uni-axial compression. 307

Figure 5-80: Heat flux within the specimen due to the thermo-mechanical problem with uni-axial compression. 308
Figure 5-81: Temperature dependent, quasi-static flow surface that is characterized from torsion tests. 309
Figure 5-82: Thermo-mechanical problem for torsion. 310
Figure 5-83: Temperature distribution for the thermo-mechanical problem with torsion. 311
Figure 5-84: Heat flux within the specimen due to the thermo-mechanical problem with torsion. 311
Figure 5-85: Comparison of the flow behavior for specimens with different orientation and states-of-stress. 312
Figure 5-86: Strain-rates achieved for 1.5875mm thick targets under impact. 314
Figure 5-87: Strain-rates achieved for 3.75mm thick targets under impact. 314
Figure 5-88: Strain-rates achieved for 6.35mm thick targets under impact. 314
Figure 5-89: CSHB apparatus, after [108]. 317
Figure 5-90: Schematic CSHB apparatus and the Lagrangian diagram for wave propagation, modified after [108]. 318
Figure 5-91: Evolution of the wave forms on incident and transmitter bars for Test #26.1e on CSHB apparatus. 319
Figure 5-92: History of the specimen for Test #26.1e on CSHB apparatus. 321
Figure 5-93: Boundary of dynamic equilibrium for Test #26.1e on CSHB apparatus; (a) wave analyses for nominal stress measurements and (b) determination of the boundary for equilibrium based on the wave analyses. 324
Figure 5-94: TSHB apparatus, after [108]. 326
Figure 5-95: Schematic TSHB apparatus and the Lagrangian diagram for wave propagation, modified after [108]. 327
Figure 5-96: Evolution of the wave forms on incident and transmitter bars for Test #XX on TSHB apparatus. 328
Figure 5-97: History of the specimen for Test #24.1e on TSHB apparatus. 329
Figure 5-98: Flow behavior for Test #24.1e on TSHB apparatus. 330
Figure 5-99: SSHB apparatus, after [108]. 332

Figure 5-100: Schematic SSHB apparatus and the Lagrangian diagram for wave propagation, modified after [108]. 333
Figure 5-101: Evolution of the wave forms on incident and transmitter bars for Test #31.1e on SSHB apparatus. 334
Figure 5-102: History of the specimen for Test #31.1e on SSHB apparatus. 335
Figure 5-103: Flow behavior for Test #31.1e on SSHB apparatus. 336
Figure 5-104: Flow diagram of the automated parameter identification process for material characterization by using SRSM for rate dependent tests. 337
Figure 5-105: First stage of the automated parameter identification process for material characterization by using SRSM for rate dependent tests. 338
Figure 5-106: Flow behavior of Al2024-T351 for uni-axial tension at room temperature. 340
Figure 5-107: Strain-rate dependent flow surface that is characterized from TSHB tests at room temperature. 341
Figure 5-108: Flow behavior of Al2024-T351 for uni-axial compression at room temperature. 342
Figure 5-109: Strain-rate dependent flow surface that is characterized from CSHB tests at room temperature. 343
Figure 5-110: Flow behavior of Al2024-T351 for torsion at room temperature. 345
Figure 5-111: Strain-rate dependent flow surface that is characterized from SSHB tests at room temperature. 345
Figure 5-112: Strain-rate dependent flow surfaces that are characterized from uni-axial tension tests; (a) adiabatic and (b) isothermal. 346
Figure 5-113: Strain-rate dependent flow surfaces that are characterized from uni-axial compression tests; (a) adiabatic and (b) isothermal. 347
Figure 5-114: Strain-rate dependent flow surfaces that are characterized from torsion tests; (a) adiabatic and (b) isothermal. 348
Figure 5-115: Temperature dependent flow surfaces that are characterized from uni-axial tension tests; (a) adiabatic and (b) isothermal. 349
Figure 5-116: Temperature dependent flow surfaces that are characterized from uni-axial compression tests; (a) adiabatic and (b) isothermal. 350

Figure 5-117: Temperature dependent flow surfaces that are characterized from torsion tests; (a) adiabatic and (b) isothermal. 351
Figure 5-118: Iterative, 'trial and error' failure strain characterization. 352
Figure 5-119: Force vs. displacement predictions for different characteristic element lengths before regularization for the same failure strain. 353
Figure 5-120: Plastic strains at failure for the corresponding characteristic element lengths. 354
Figure 5-121: Geometrical representation of a neck and material properties for the empirical determination of the regularization boundaries. 355
Figure 5-122: Regularization curve for six different characteristic element lengths. 358
Figure 5-123: Regularization curve for TRAUM. 359
Figure 5-124: Force vs. displacement predictions for different mesh sizes after regularization. 361
Figure 5-125: Analysis of an oblique necking of an anisotropic strip in tension, adapted after [94]. 361
Figure 5-126: Discontinuities of relative velocity, adapted after [377]. 362
Figure 5-127: Crack initiation in tension, after [145]. 363
Figure 5-128: Uni-axial tension experiment on SHLF apparatus with Specimen #1; (a) pristine specimen and (b) post-test specimen with localized necking, after [108]. 365
Figure 5-129: Formation of the localized necking instability; (a) FE deformation and (b) localization of the effective plastic strain at necking. 365
Figure 5-130: Evolution of deformation and failure; (a) fringe plot of plastic strains and (b) iso-surface plot of plastic strains. 366
Figure 5-131: Randomness of the localized neck depending on the characteristic element length; (a) for [t/5] model and (b) for [t/10] model. 367
Figure 5-132: Plane-stress tension specimens, after [108]. 370
Figure 5-133: Positions of the DIC gauge lengths for plane-stress tension specimens. 371
Figure 5-134: Characterization of the stress-states and failure strain for Specimen #1 372
Figure 5-135: Force vs. displacement results for plane-stress specimens. 372

Figure 5-136: Evolution of the stress-state dependent failure in three dimensional failure space for plane-stress specimens represented by; (a) the space defined by stress-triaxiality vs. Lode-angle-parameter and (b) the space defined by stress-triaxiality vs. product-triaxiality. 374
Figure 5-137: Evolution of the stress-state dependent failure for plane-stress specimens projected on; (a) the plane defined by stress-triaxiality vs. Lode-angle-parameter and (b) the plane defined by stress-triaxiality vs. product-triaxiality. 375
Figure 5-138: Evolution of plastic strain and states-of-stress for plane-stress specimens with averaged values as a function of; (a) stress-triaxiality, (b) Lode-angle-parameter and (c) product-triaxiality. 377
Figure 5-139: Evolution of the state-of-stress for the central and root elements in the notch geometry. 378
Figure 5-140: Axi-symmetric tension specimens, after [108]. 379
Figure 5-141: Positions of the DIC gauge lengths for axi-symmetric tension specimens. 381
Figure 5-142: Force vs. displacement results for axi-symmetric specimens. 382
Figure 5-143: Characterization of the stress-states and failure strain for Specimen #5 382
Figure 5-144: Evolution of the stress-state dependent failure in three dimensional failure space for axi-symmetric specimens represented by; (a) the space defined by stress-triaxiality vs. Lode-angle-parameter and (b) the space defined by stress-triaxiality vs. product-triaxiality. 384
Figure 5-145: Evolution of the stress-state dependent failure for axi-symmetric specimens projected on; (a) the plane defined by stress-triaxiality vs. Lode-angle-parameter and (b) the plane defined by stress-triaxiality vs. product-triaxiality. 386
Figure 5-146: Evolution of plastic strain and states-of-stress for axi-symmetric specimens with averaged values as a function of; (a) stress-triaxiality, (b) Lode-angle-parameter and (c) product-triaxiality. 387
Figure 5-147: Morphology of the PLC bands propagating along the smooth gauge section of the axi-symmetric specimen in tension, after [380]. 388
Figure 5-148: Plane-strain tension specimens, after [108]. 389

Figure 5-149: Positions of the DIC gauge lengths for plane-strain tension specimens. 390
Figure 5-150: Force vs. displacement results for plane-strain specimens. 391
Figure 5-151: Characterization of the stress-states and failure strain for Specimen #11..... 392
Figure 5-152: Evolution of the stress-state dependent failure in three dimensional failure space for plane-strain specimens represented by; (a) the space defined by stress-triaxiality vs. Lode-angle-parameter and (b) the space defined by stress-triaxiality vs. product-triaxiality. 394
Figure 5-153: Evolution of the stress-state dependent failure for plane-strain specimens projected on; (a) the plane defined by stress-triaxiality vs. Lode-angle-parameter and (b) the plane defined by stress-triaxiality vs. product-triaxiality. 395
Figure 5-154: Evolution of plastic strain and states-of-stress for plane-strain specimens with averaged values as a function of; (a) stress-triaxiality, (b) Lode-angle-parameter and (c) product-triaxiality. 396
Figure 5-155: Uni-axial compression specimen, after [108]. 397
Figure 5-156: Characterization of the stress-states and failure strain for Specimen#14. 398
Figure 5-157: Torsion specimen; (a) spools shaped specimen geometry for torsion and (b) position of the DIC gauge length for torsion specimen, after [108]. 400
Figure 5-158: Characterization of the stress-states and failure strain for Specimen #15..... 401
Figure 5-159: Combined tension/torsion specimen; (a) spools shaped specimen geometry and (b) position of the initial DIC gauge length for combined tension/torsion specimen, after [108]. 403
Figure 5-160: Characterization of the stress-states and failure strain for Specimen #16..... 405
Figure 5-161: Characterization of the stress-states and failure strain for Specimen #17..... 405
Figure 5-162: Evolution of the stress-state dependent failure in three dimensional failure space for uni-axial compression, torsion and combined tension/torsion

specimens represented by; (a) the space defined by stress-triaxiality vs. Lode-angle-parameter and (b) the space defined by stress-triaxiality vs. product-triaxiality. 406
Figure 5-163: Evolution of the stress-state dependent failure for uni-axial compression, torsion and combined tension/torsion specimens projected on; (a) the plane defined by stress-triaxiality vs. Lode-angle-parameter and (b) the plane defined by stress-triaxiality vs. product-triaxiality. 407
Figure 5-164: Evolution of plastic strain and states-of-stress for uni-axial compression, torsion and combined tension/torsion specimens with averaged values as a function of; (a) stress-triaxiality, (b) Lode-angle-parameter and (c) product-triaxiality. 408
Figure 5-165: Quasi-static punch testing apparatus by SHLF and DIC set-up, modified after [384]. 409
Figure 5-166: Characterization of the stress-states and failure strain for Specimen #18..... 411
Figure 5-167: Characterization of the stress-states and failure strain for Specimen #18; (a) just before failure and (b) after the initial failure. 412
Figure 5-168: Evolution of the stress-state dependent failure for punch test specimens projected on; (a) the plane defined by stress-triaxiality vs. Lode-angle-parameter and (b) the plane defined by stress-triaxiality vs. product-triaxiality. 414
Figure 5-169: Overview of the test program after characterized flow surface is attained for the calculation of the targeted states-of-stress for each specimen on the plane defined by; (a) stress-triaxiality vs. Lode-angle-parameter and (b) stress-triaxiality vs. product-triaxiality. 416
Figure 5-170: Stress-state dependent failure strains and their limits on the plane defined by stress-triaxiality vs. plastic strain at failure..... 417
Figure 5-171: Stress-state dependent failure strains and their limits on the plane defined by Lode-angle-parameter vs. plastic strain at failure..... 417
Figure 5-172: stress-state dependent failure strains and their limits on the plane defined by product-triaxiality vs. plastic strain at failure. 418
Figure 5-173: Three dimensional representation of the characterized failure points for each state-of-stress based on the averaged values and mean failure strain on the

plane defined by; (a) stress-triaxiality vs. Lode-angle-parameter and (b) stress-triaxiality vs. product-triaxiality. 419
Figure 5-174: Three dimensional B-splines that are used to construct the boundaries of the ruled failure surface from the corresponding stress meridians. 420
Figure 5-175: B-spline approximations in the direction of Lode-angle-parameter that are used to construct the three dimensional failure surface with bivariate splines. 423
Figure 5-176: Bivariate spline approximation to the original test data or the failure strain for quasi-static conditions and room temperature for TRAUM. 424
Figure 5-177: Relative error for the B-spline approximation of the failure space. 425
Figure 5-178: Failure surface for quasi-static conditions and room temperature with; (a) the bounding stress-meridians and (b) with the corresponding specimens representing the failure characteristics. 426
Figure 5-179: Comparison of the test results with the predicted failure that is found by TRAUM simulations by using the characterized values of the failure strains for the corresponding strain-rates showing; (a)-(e) the comparison of the failure point for each strain-rate and the mean of the TRAUM simulations and (f) the comparison of the mean values of the plastic strain at failure for TRAUM simulations at each strain-rate. 428
Figure 5-180: Strain-rate dependent scaling curve for the failure surface for TRAUM. 429
Figure 5-181: Strain-rate dependent failure surfaces for TRAUM. 430
Figure 5-182: Comparison of the test results with the predicted failure that is found by TRAUM simulations by using the characterized values of the failure strains for the corresponding temperatures showing; (a)-(e) the comparison of the failure point for each temperature and the mean of the TRAUM simulations and (f) the comparison of the mean values of the plastic strain at failure for TRAUM simulations at each temperature. 431
Figure 5-183: Temperature dependent scaling curve for the failure surface for TRAUM. 432
Figure 5-184: Temperature dependent failure surfaces for TRAUM. 433

Figure 6-1: Characterized material input data for TRAUM and the path towards validation..... 436
Figure 6-2: Quasi-static test results for Specimen #1; (a) DIC strain field measurement, (b) Test #2 surface strain prediction with TRAUM and (c) force vs. displacement comparison between Test #2 and Test #3 results and TRAUM predictions..... 437
Figure 6-3: Quasi-static test results for Specimen #2; (a) DIC strain field measurement, (b) Test #33 surface strain prediction with TRAUM and (c) force vs. displacement comparison between Test #33 results and TRAUM predictions. 438
Figure 6-4: Quasi-static test results for Specimen #3; (a) DIC strain field measurement, (b) Test #34 surface strain prediction with TRAUM and (c) force vs. displacement comparison between Test #34 results and TRAUM predictions. 439
Figure 6-5: Quasi-static test results for Specimen #4; (a) DIC strain field measurement, (b) Test #35 surface strain prediction with TRAUM and (c) force vs. displacement comparison between Test #35 results and TRAUM predictions. 440
Figure 6-6: Quasi-static test results for Specimen #5; (a) DIC strain field measurement, (b) Test #4 surface strain prediction with TRAUM and (c) force vs. displacement comparison between Test #4 results and TRAUM predictions. 442
Figure 6-7: Quasi-static test results for Specimen #6; (a) DIC strain field measurement, (b) Test #36 surface strain prediction with TRAUM and (c) force vs. displacement comparison between Test #36 results and TRAUM predictions. 443
Figure 6-8: Quasi-static test results for Specimen #7; (a) DIC strain field measurement, (b) Test #37 surface strain prediction with TRAUM and (c) force vs. displacement comparison between Test #37 results and TRAUM predictions. 444
Figure 6-9: Quasi-static test results for Specimen #8; (a) DIC strain field measurement, (b) Test #38 surface strain prediction with TRAUM and (c) force vs. displacement comparison between Test #38 results and TRAUM predictions. 445
Figure 6-10: Quasi-static test results for Specimen #9; (a) DIC strain field measurement, (b) Test #39 surface strain prediction with TRAUM and (c) force vs. displacement comparison between Test #39 results and TRAUM predictions. 446

Figure 6-11: Quasi-static test results for Specimen #10; (a) DIC strain field measurement, (b) Test #40 surface strain prediction with TRAUM and (c) force vs. displacement comparison between Test #40 results and TRAUM predictions. 447
Figure 6-12: Quasi-static test results for Specimen #11; (a) DIC strain field measurement, (b) Test #41 surface strain prediction with TRAUM and (c) force vs. displacement comparison between Test #41 results and TRAUM predictions. 449
Figure 6-13: Quasi-static test results for Specimen #12; (a) DIC strain field measurement, (b) Test #42 surface strain prediction with TRAUM and (c) force vs. displacement comparison between Test #42 results and TRAUM predictions. 450
Figure 6-14: Quasi-static test results for Specimen #13; (a) DIC strain field measurement, (b) Test #43 surface strain prediction with TRAUM and (c) force vs. displacement comparison between Test #43 results and TRAUM predictions. 451
Figure 6-15: Quasi-static test results for Specimen #14; (a) Test #6 surface strain prediction with TRAUM and (b) force vs. displacement comparison between Test #6 results and TRAUM predictions. 452
Figure 6-16: Quasi-static test results for Specimen #15; (a) DIC strain field measurement, (b) Test #8 surface strain prediction with TRAUM and (c) force vs. displacement comparison between Test #8 results and TRAUM predictions. 453
Figure 6-17: Quasi-static test results for Specimen #16; (a) DIC strain field measurement, (b) Test #44 surface strain prediction with TRAUM and (c) force vs. displacement comparison between Test #44 results and TRAUM predictions. 454
Figure 6-18: Quasi-static test results for Specimen #17; (a) DIC strain field measurement, (b) Test #45 surface strain prediction with TRAUM and (c) force vs. displacement comparison between Test #45 results and TRAUM predictions. 455
Figure 6-19: Quasi-static test results for Specimen #18; (a) corresponding punch nose shape and (b) force vs. displacement comparison between Test #46 results and TRAUM predictions..... 456
Figure 6-20: Quasi-static test results for Specimen #19; (a) corresponding punch nose shape and (b) force vs. displacement comparison between Test #47 results and TRAUM predictions..... 457

Figure 6-21: Quasi-static test results for Specimen #20; (a) corresponding punch nose shape and (b) force vs. displacement comparison between Test #48 results and TRAUM predictions..... 458
Figure 7-1: Ballistic limit predictions for 1.5875mm targets with TRAUM. 460
Figure 7-2: Penetration through 1.5875mm target and petalling; (a) quarter of the full model, (b) simulation with TRAUM and (c) rear face of the test, after [57]. 461
Figure 7-3: Ballistic limit predictions for 3.175mm targets with TRAUM. 462
Figure 7-4: Penetration through 3.175mm target and mixed-mode failure formation; (a) quarter of the full model, (b) simulation with TRAUM and (c) front face of the test with the plug, after [57]. 463
Figure 7-5: Ballistic limit predictions for 6.35 mm targets with TRAUM. 464
Figure 7-6: Penetration through 6.35mm target and plug formation; (a) quarter of the full model, (b) simulation with TRAUM and (c) front face of the test with the plug, after [57]. 465
Figure 7-7: Specimen and fixture geometry that was used during the ballistic impact tests with three different target thicknesses, after [388]. 466
Figure 7-8: Cylindrical projectile with a round nose shape. 467
Figure 7-9: Ballistic impact apparatus, after [388]. 468
Figure 7-10: Ballistic impact test results, after [388]. 469
Figure 7-11: Quarter of the finite element model for 3.175mm thick targets with Projectile #1 showing; (a) quarter model, (b) close-up to the impact zone, (c) FE details of the concentric zoning, (d) FE details of the impact zone and (f) FE details of the cross-section of the projectile and the target for the quarter model. 470
Figure 7-12: Ballistic limit predictions for 3.175mm targets with TRAUM. 472
Figure 7-12: Incremental solution steps of the plug formation for 3.175mm target with TRAUM. 473
Figure 7-14: Ballistic limit predictions for 6.35mm targets with TRAUM. 474
Figure 7-15: Incremental solution steps of the plug formation for 6.35mm target with TRAUM. 475
Figure 7-16: Incremental solution steps of the plug formation and projectile stuck for 6.35mm target with TRAUM. 476

Figure 7-17: Ballistic limit predictions for 12.7mm targets with TRAUM. 477
Figure 7-18: Incremental solution steps of the plug formation and projectile stuck for 12.7mm target with TRAUM. 479
Figure A-1: Normal and shear stresses. 503
Figure A-2: Haigh–Westergaard space. 506
Figure B-1: Plane-stress smooth specimen, Specimen #1. 508
Figure B-2: Plane-stress notched, Specimen #2. 509
Figure B-3: Plane-stress notched, Specimen #3. 510
Figure B-4: Plane-stress notched, Specimen #4. 511
Figure B-5: Axisymmetric smooth specimen, Specimen #5. 512
Figure B-6: Axisymmetric notched specimen, Specimen #6. 513
Figure B-7: Axisymmetric notched specimen, Specimen #7. 514
Figure B-8: Axisymmetric notched specimen, Specimen #8. 515
Figure B-9: Axisymmetric notched specimen, Specimen #9. 516
Figure B-10: Axisymmetric notched specimen, Specimen #10. 517
Figure B-11: Plane-strain smooth specimen, Specimen #11. 518
Figure B-12: Plane-strain notched specimen, Specimen #12. 519
Figure B-13: Plane-strain notched specimen, Specimen #13. 520
Figure B-14: Compression specimen, Specimen #14. 521
Figure B-15: Shear and combined tension-shear specimens, Specimen #15, Specimen #16 & Specimen #17. 523
Figure B-16: Punch specimen, Specimen #18. 524
Figure B-17: Punch specimen, Specimen #19. 525
Figure B-18: Punch specimen, Specimen #20. 526
Figure B-19: Torsion specimen, Specimen #21. 527
Figure C-1: Test #1 results and repeatability. 529
Figure C-2: Test #2 results and repeatability. 530
Figure C-3: Test #3 results and repeatability. 531
Figure C-4: Test #4 results and repeatability. 532
Figure C-5: Test #5 results and repeatability. 533
Figure C-6: Test #6 results and repeatability. 534

Figure C-7: Test #7 results and repeatability. 535
Figure C-8: Test #8 results and repeatability. 536
Figure C-9: Test #9 results and repeatability. 537
Figure C-10: Test #10 results and repeatability. 538
Figure C-11: Test #11 results and repeatability. 539
Figure C-12: Test #12 results and repeatability. 540
Figure C-13: Test #13 results and repeatability. 541
Figure C-14: Test #14 results and repeatability. 542
Figure C-15: Test #15 results and repeatability. 543
Figure C-16: Test #16 results and repeatability. 544
Figure C-17: Test #17 results and repeatability. 545
Figure C-18: Test #18 results and repeatability. 546
Figure C-19: Test #19 results and repeatability. 547
Figure C-20: Test #20 results and repeatability. 548
Figure C-21: Test #21 results and repeatability. 549
Figure C-22: Test #22 results and repeatability. 550
Figure C-23: Test #23 results and repeatability. 551
Figure C-24: Test #24 results and repeatability. 552
Figure C-25: Test #25 results and repeatability. 553
Figure C-26: Test #26 results and repeatability. 554
Figure C-27: Test #27 results and repeatability. 555
Figure C-28: Test #28, #29 and #30 results. 556
Figure C-29: Test #31 results and repeatability. 557
Figure C-30: Test #32 results and repeatability. 558
Figure C-31: Test #33 results and repeatability. 560
Figure C-32: Test #34 results and repeatability. 561
Figure C-33: Test #35 results and repeatability. 562
Figure C-34: Test #36 results and repeatability. 564
Figure C-35: Test #37 results and repeatability. 565
Figure C-36: Test #38 results and repeatability. 566
Figure C-37: Test #39 results and repeatability. 567

Figure C-38: Test #40 results and repeatability. 568
Figure C-39: Test #41 results and repeatability. 569
Figure C-40: Test #42 results and repeatability. 570
Figure C-41: Test #43 results and repeatability. 571
Figure C-42: Test #44 results and repeatability. 573
Figure C-43: Test #45 results and repeatability. 574
Figure C-44: Test #46, #47 and #48 results. 575
Figure E-1: Plane-stress specimen with smooth section (Specimen #1), 1 element through the thickness [t/1]. 578
Figure E-2: Plane-stress specimen with smooth section (Specimen #1), 2 elements through the thickness [t/2]. 579
Figure E-3: Plane-stress specimen with smooth section (Specimen #1), 3 elements through the thickness [t/3]. 579
Figure E-4: Plane-stress specimen with smooth section (Specimen #1), 4 elements through the thickness [t/4]. 580
Figure E-5: Plane-stress specimen with smooth section (Specimen #1), 5 elements through the thickness [t/5]. 580
Figure E-6: Plane-stress specimen with smooth section (Specimen #1), 10 elements through the thickness [t/10]. 581
Figure E-7: Plane-stress specimen with smooth section (Specimen #1), 20 elements through the thickness [t/20]. 581
Figure F-1: Verification of the hardening curve for Test #1 at a strain-rate of $1.0x10^{-4}s^{-1}$ and RT. 582
Figure F-2: Verification of the hardening curve for Test #2 at a strain-rate of $1.0x10^{-2}s^{-1}$ and RT. 582
Figure F-3: Verification of the hardening curve for Test #3 at a strain-rate of $1.0s^{-1}$ and RT. 583
Figure F-4: Verification of the hardening curves for Test #4 at a strain-rate of $1.0x10^{-2}s^{-1}$ and RT. 583
Figure F-5: Verification of the hardening curves for Test #5 at a strain-rate of $1.0x10^{-4}s^{-1}$ and RT. 584

Figure F-6: Verification of the hardening curves for Test #6 at a strain-rate of $1.0x10^{-2}s^{-1}$ and RT. 584
Figure F-7: Verification of the hardening curves for Test #7 at a strain-rate of $1.0s^{-1}$ and RT. 585
Figure F-8: Verification of the hardening curves for Test #8 at a strain-rate of $1.0s^{-1}$ and RT. 585
Figure F-9: Verification of the hardening curves for Test #9 at a strain-rate of $1.0s^{-1}$ and 443K. 586
Figure F-10: Verification of the hardening curves for Test #10 at a strain-rate of $1.0s^{-1}$ and 573K. 586
Figure F-11: Verification of the hardening curves for Test #11 at a strain-rate of $1.0s^{-1}$ and 723K. 587
Figure F-12: Verification of the hardening curves for Test #12 at a strain-rate of $1.0s^{-1}$ and 223K. 587
Figure F-13: Verification of the hardening curves for Test #13 at a strain-rate of $1.0s^{-1}$ and 423K. 588
Figure F-14: Verification of the hardening curves for Test #14 at a strain-rate of $1.0s^{-1}$ and 573K. 588
Figure F-15: Verification of the hardening curves for Test #15 at a strain-rate of $1.0s^{-1}$ and 723K. 589
Figure F-16: Verification of the hardening curves for Test #16 at a strain-rate of $1.0s^{-1}$ and 223K. 589
Figure F-17: Verification of the hardening curves for Test #17 at a strain-rate of $1.0x10^{-4}s^{-1}$ and RT. 590
Figure F-18: Verification of the hardening curves for Test #18 at a strain-rate of $1.0x10^{-2}s^{-1}$ and RT. 590
Figure F-19: Verification of the hardening curves for Test #19 at a strain-rate of $1.0s^{-1}$ and RT. 591
Figure F-20: Verification of the hardening curves for Test #20 at a strain-rate of $1.0s^{-1}$ and 423K. 591

Figure F-21: Verification of the hardening curves for Test #21 at a strain-rate of $1.0s^{-1}$ and 573K. 592
Figure F-22: Verification of the hardening curves for Test #22 at a strain-rate of $1.0s^{-1}$ and 723K. 592
Figure F-23: Verification of the hardening curves for Test #23 at a strain-rate of $1.0s^{-1}$ and 223K. 593
Figure F-24: Verification of the hardening curves for Test #24 at a strain-rate of $500s^{-1}$ and RT. 593
Figure F-25: Verification of the hardening curves for Test #25 at a strain-rate of $1800s^{-1}$ and RT. 594
Figure F-26: Verification of the hardening curves for Test #26 at a strain-rate of $1400s^{-1}$ and RT. 594
Figure F-27: Verification of the hardening curves for Test #27 at a strain-rate of $5000s^{-1}$ and RT. 595
Figure F-28: Verification of the hardening curves for Tests #28, #29 and #30 at RT and strain-rates of $8100s^{-1}$, $9800s^{-1}$ and $11000s^{-1}$, respectively. 595
Figure F-29: Verification of the hardening curves for Test #31 at a shear strain-rate of $866s^{-1}$ and RT 596
Figure F-30: Verification of the hardening curves for Test #32 at a shear strain-rate of $5000s^{-1}$ and RT 596
Figure G-1: Tensile instability and the effects of mesh size; (a) by using [t/4] model and (b) by using [t/20] model. 597
Figure G-2: Tensile instability and the effects of mesh size; (a) by using [t/3] model and (b) by using [t/2] model. 598
Figure G-3: Tensile instability and the effects of mesh size by using [t/1] model. 599
Figure H-1: Characterization of the stress-states and failure strain for Specimen #2. ... 600
Figure H-2: Characterization of the stress-states and failure strain for Specimen #3. ... 601
Figure H-3: Characterization of the stress-states and failure strain for Specimen #4. ... 601
Figure H-4: Characterization of the stress-states and failure strain for Specimen #6. ... 602
Figure H-5: Characterization of the stress-states and failure strain for Specimen #7. ... 602
Figure H-6: Characterization of the stress-states and failure strain for Specimen #8. ... 603

Figure H-7: Characterization of the stress-states and failure strain for Specimen #9. ... 603
Figure H-8: Characterization of the stress-states and failure strain for Specimen #10 ... 604
Figure H-9: Characterization of the stress-states and failure strain for Specimen #12 ... 604
Figure H-10: Characterization of the stress-states and failure strain for Specimen #13 ... 605
Figure H-11: Characterization of the stress-states and failure strain for Specimen #19 ... 605
Figure H-12: Characterization of the stress-states and failure strain for Specimen #20 ... 606

List of Tables

Pages

Table 2-1: Commonly used empirical failure criterion. 23
Table 3-1: Details of the finite element mesh. 32
Table 3-2: Sets of J-C material model parameters. 38
Table 4-1: Notable points and their stress-state parameters. 86
Table 4-2: Set-1 and Set-4; J-C material model input data for the iterative specimen design procedure and successive FE simulations. 115
Table 4-3: Plane-stress specimens in tension associated with the targeted stress-states. 132
Table 4-4: Axi-symmetric specimens in tension associated with the targeted stress-states. 136
Table 4-5: Plane-strain specimens in tension associated with the targeted stress-states. 142
Table 4-6: Model dimensions and friction coefficients for uni-axial compression simulations. 145
Table 4-7: Compression specimen with stress-state design parameters. 145
Table 4-8: Shear specimen with stress-state design parameters. 148
Table 4-9: Combined tension - shear specimen with corresponding loading ratios and stress-state design parameters. 155
Table 4-10: Punch test specimens and test assembly with stress-state design parameters. 161
Table 4-11: Summary of specimens with initially targeted stress-state design parameters. 164
Table 4-12: Evolution of the corresponding states-of-stress for different loading conditions. 168
Table 4-13: J-C material model input data used for single element simulations [58]. ... 168
Table 5-1: Material specifications for Al2024-T351. 195
Table 5-2: The chemical composition of aluminum alloy Al2024-T351. 195

Table 5-3: Test cases that are used to characterize quasi-static hardening curve at room temperature. 204
Table 5-4: Notable points on hardening curves. 214
Table 5-5: Predicted failure parameters for number of elements in the neck area. 222
Table 5-6: Predicted failure parameters for different row of elements in the neck area. 222
Table 5-7: Predicted coefficients for the power law plasticity for different row of elements at the necking area. 223
Table 5-8: Amount of error between the test and the simulation results for different hardening characteristics. 225
Table 5-9: Mesh patterns that are used to test the mesh dependency of the flow behavior for the characterized quasi-static hardening curve. 227
Table 5-10: Test cases that are used to verify quasi-static hardening curve at room temperature. 230
Table 5-11: Test cases that are used to verify quasi-static hardening curves for uni-axial compression at room temperature. 233
Table 5-12: Test cases that are used to verify quasi-static hardening curves for torsion at room temperature. 235
Table 5-13: Test cases that are used to characterize temperature dependent quasi-static hardening curves for uni-axial tension. 247
Table 5-14: Test cases that are used to characterize temperature dependent quasi-static hardening curves for uni-axial compression. 250
Table 5-15: Test cases that are used to characterize quasi-static hardening curves for torsion. 254
Table 5-16: Test cases that are used to characterize quasi-static hardening curves for torsion. 264
Table 5-17: List of hardening models. 275
Table 5-18: List of hardening models. 284
Table 5-19: List of the values for the initial design variables and the bounds for the corresponding hardening models. 287

Table 5-20: Test cases that are used to characterize dynamic hardening curves with TSHB at room temperature. 339
Table 5-21: Test cases that are used to characterize dynamic hardening curves with CSHB at room temperature. 341
Table 5-22: Test cases that are used to characterize dynamic hardening curves with SSHB at room temperature. 344
Table 5-23: Characteristic element lengths used for the regularization models. 354
Table 5-24: Test cases for characterization of the quasi-static failure strains at room temperature for plane-stress tension specimens. 370
Table 5-25: Characterized plastic strains at failure and corresponding stress-states for plane-stress specimens in tension. 373
Table 5-26: Test cases for characterization of the quasi-static failure strains at room temperature for axi-symmetric tension specimens. 380
Table 5-27: Characterized plastic strains at failure and corresponding stress-states for axi-symmetric specimens in tension. 383
Table 5-28: Test cases for characterization of the quasi-static failure strains at room temperature for plane-strain tension specimens. 390
Table 5-29: Characterized plastic strains at failure and corresponding stress-states for plane-strain specimens in tension. 393
Table 5-30: Test cases for characterization of the quasi-static failure strains at room temperature for uni-axial compression specimens. 397
Table 5-31: Characterized plastic strains at failure and corresponding stress-states for plane-strain specimens in tension. 399
Table 5-32: Test cases for characterization of the quasi-static failure strains at room temperature for torsion specimens. 400
Table 5-33: Characterized plastic strains at failure and corresponding stress-states for torsion specimens. 402
Table 5-34: Test cases for characterization of the quasi-static failure strains at room temperature for combined tension/torsion specimens. 403
Table 5-35: Characterized plastic strains at failure and corresponding stress-states for torsion specimens. 404

Table 5-36: Test cases for characterization of the quasi-static failure strains at room temperature for punch test specimens. 410
Table 5-37: Characterized plastic strains at failure and corresponding stress-states for punch test specimens. 413
Table 5-38: Matrix of coefficients for the bivariate spline approximations of the failure surface. 427
Table 7-1: Projectiles that were used during the ballistic testing of Al2024, after [388]. 467
Table B-1: Specimen geometries and corresponding cross-references in the dissertation. 507
Table C-1: Test #1 parameters for the characterization of the flow surface. 529
Table C-2: Test #2 parameters for the characterization of the flow surface. 530
Table C-3: Test #3 parameters for the characterization of the flow surface. 531
Table C-4: Test #4 parameters for the characterization of the flow surface. 532
Table C-5: Test #5 parameters for the characterization of the flow surface. 533
Table C-6: Test #6 parameters for the characterization of the flow surface. 534
Table C-7: Test #7 parameters for the characterization of the flow surface. 535
Table C-8: Test #8 parameters for the characterization of the flow surface. 536
Table C-9: Test #9 parameters for the characterization of the flow surface. 537
Table C-10: Test #10 parameters for the characterization of the flow surface. 538
Table C-11: Test #11 parameters for the characterization of the flow surface. 539
Table C-12: Test #12 parameters for the characterization of the flow surface. 540
Table C-13: Test #13 parameters for the characterization of the flow surface. 541
Table C-14: Test #14 parameters for the characterization of the flow surface. 542
Table C-15: Test #15 parameters for the characterization of the flow surface. 543
Table C-16: Test #16 parameters for the characterization of the flow surface. 544
Table C-17: Test #17 parameters for the characterization of the flow surface. 545
Table C-18: Test #18 parameters for the characterization of the flow surface. 546
Table C-19: Test #19 parameters for the characterization of the flow surface. 547
Table C-20: Test #20 parameters for the characterization of the flow surface. 548
Table C-21: Test #21 parameters for the characterization of the flow surface. 549

Table C-22: Test #22 parameters for the characterization of the flow surface. 550
Table C-23: Test #23 parameters for the characterization of the flow surface. 551
Table C-24: Test #24 parameters for the characterization of the flow surface. 552
Table C-25: Test #25 parameters for the characterization of the flow surface. 553
Table C-26: Test #26 parameters for the characterization of the flow surface. 554
Table C-27: Test #27 parameters for the characterization of the flow surface. 555
Table C-28: Test #28, #29 and #30 parameters for the characterization of the flow surface. 556
Table C-29: Test #31 parameters for the characterization of the flow surface. 557
Table C-30: Test #32 parameters for the characterization of the flow surface. 558
Table C-31: Test #2 and #3 parameters for the characterization of the failure surface. 559
Table C-32: Test #33 parameters. 560
Table C-33: Test #34 parameters. 561
Table C-34: Test #35 parameters. 562
Table C-35: Test #4 parameters for the characterization of the failure surface. 563
Table C-36: Test #36 parameters. 564
Table C-37: Test #37 parameters. 565
Table C-38: Test #38 parameters. 566
Table C-39: Test #39 parameters. 567
Table C-40: Test #40 parameters. 568
Table C-41: Test #41 parameters. 569
Table C-42: Test #42 parameters. 570
Table C-43: Test #43 parameters. 571
Table C-44: Test #6 parameters for the characterization of the failure surface. 572
Table C-45: Test #8 parameters for the characterization of the failure surface. 572
Table C-46: Test #44 parameters for the characterization of the failure surface. 573
Table C-47: Test #45 parameters for the characterization of the failure surface. 574
Table C-48: Test #46, #47 and #48 parameters for the characterization of the failure surface. 575
Table D-1: List of tests that are used to characterize the flow surface. 576

Table D-2: List of tests that are used to characterize the failure surface. 577

List of Symbols

Roman Symbols

a	Mie-Gruneisen EOS first order volume correction
$\mathbf{a}, a_l$	Coefficients of the basis functions for AO
a, a', a''	Curves that are used for matching
A	J-C static yield limit
A, A_0	Current and initial areas
B	J-C strain hardening modulus
$\mathbf{B}_i$	Constraint functions during curve matching
$\widetilde{\mathbf{B}}_i^{(k)}$	Constraint functions for the *k*-th sub-problem
C	J-C strain rate coefficient
$\mathbf{C}$	Vector of material parameters during curve matching
$\boldsymbol{C}$	Fourth order positive definite isotropic stiffness tensor
$C_1,\ C_2,\ C_3,\ C_4$	Hardening model parameters
C_{ijkl}	Elastic tensor in the component form
C_{sp}	Mie-Gruneisen EOS intercept of the vs-vp curve
C_p	Specific heat
$\boldsymbol{C}_p$	Set of discrete design variables during curve matching
$\mathbf{C}^{\text{approximate}}$	Vector of approximate material parameters during curve matching
$\mathbf{C}^{\text{real}}$	Vector of known material parameters during curve matching
C_j^{Lower}, C_j^{Upper}	Lower and upper bounds of the continuous design variables
$C_j^{Lower^{(k)}}, C_j^{Upper^{(k)}}$	Bounds for the *k*-th sub-problem
$\boldsymbol{C}_p^{(k)}$	Set of discrete design variables for the *k*-th sub-problem
d_i	Distances between the point pairs during curve matching
D	Damage parameter
D, D_0	Current and initial diameters
D_1, D_2, D_3, D_4, D_5	J-C failure parameters
D_{cr}	Critical failure value
$\dot{\boldsymbol{e}}$	Deviatoric strain rates
e_n	Error during curve matching
$\dot{\boldsymbol{e}}_{\boldsymbol{p}}$	Plastic deviatoric strain rate
E	Modulus of elasticity
$\min E, \mathbf{E}$	Combined error during curve matching, objective function
E_1	MSE during curve matching
E_2	Error of sum of volumes during curve matching

E_{int}	Mie-Gruneisen EOS internal energy
E_t	Tangent or hardening modulus
$\tilde{\mathbf{E}}^{(k)}$	Objective function for the *k*-th sub-problem
$f(variables)$	Function of the variables
g	Experimental curve
g_n	Experimental points
G	Shear modulus
H, H_0	Current and initial heights
$\mathbf{I}$	Second-order unit tensor
$\mathbb{I}$	Fourth-order, symmetric unit tensor
I_1, I_2, I_3	Mie-Gruneisen EOS stress invariants
J	Polar moment of inertia
J_1, J_2, J_3	Deviatoric stress invariants
K	Bulk modulus
l_x, l_y, l_z	Characteristic element lengths
L	Current length
L_0	Initial length, gauge length
m	J-C thermal softening exponent
M	Moment
n	J-C strain hardening exponent
$\boldsymbol{n}$	Number of independent variables
N	Normal force
N	Number of response surfaces
$\mathbf{N}$	Prandtl-Reuss normal outward flow vector
p	Pressure
$\dot{p}$	Pressure rate
p^{n+1}	Updated pressure
p_e^{n+1}	Trial pressure
P	Load
r	Order of the approximation
r_m	Mean gage radius
r_o	Outer radius
s	total polygon length for curve a
$\dot{\mathbf{s}}$	Deviatoric stress rates
s_1, s_2, s_3	Deviatoric principle stresses
s_n	Scale factors during curve matching
s_{ij}	Deviatoric stress tensor
$\dot{\boldsymbol{s}}_{\mathrm{e}}$	Elastic trial stress
$S_1 - S_3$	Mie-Gruneisen EOS coefficients of the slope of the vs-vp curve
t	total polygon length for curve a'

$t, t_{n+1/2}, t_{n+1}$	Time increments
T	Temperature
T	Torque
T_{melt}	Melting temperature
T^*	Homologous temperature
T^n	Current temperature
T_{room}	Room temperature
tr	Trace of a tensor or matrix
w	Width
W_n	Weighting factors during curve matching
$\dot{W}$	Plastic dissipation work

Greek symbols

β	Taylor–Quinney coefficient
γ	Shear strain
γ_0	Gruneisen gamma
δ_{ij}	Kronecker delta
$\Delta\varepsilon_p$	Plastic strain increment
ε	Strain tensor
$\boldsymbol{\varepsilon}$	Operational strain vector during curve matching
$\dot{\varepsilon}$	Strain rate (rate-of-deformation) tensor
ε_i	Error between the curves for the *i*-th design point during AO
ε^0	Engineering strain
$\varepsilon_p, \bar{\varepsilon}_p$	Effective plastic strain
$\dot{\varepsilon}^*$	Normalized effective plastic strain rate
$\dot{\varepsilon}^e$	Elastic components of the rate of the strain tensor
$\dot{\varepsilon}^p$	Plastic components of the rate of the strain tensor
$\dot{\varepsilon}^V$	Volumetric strain rate
$\dot{\varepsilon}_p^V$	Plastic volumetric strain rate
$\varepsilon_p^f, \bar{\varepsilon}_p^f$	Effective plastic strain at failure
η	Stress-triaxiality
$\eta_i, \eta_i', \eta_i''$	Vertices of mapped curves
θ_L	Lode-angle-parameter
λ	Plastic multiplier
$\dot{\lambda}$	Rate of plastic multiplier
λ^e	One of the Lamé constants
μ	One of the Lamé constants ($\mu = G$)

$\boldsymbol{\mu}$	Lode parameter
ν	Poisson's ratio
ξ_i, ξ_i', ξ_i''	Vertices of mapped curves
π	The number Pi
ρ	Density
ρ_0	Initial density
$\boldsymbol{\sigma}$	Cauchy stress tensor
$\bar{\sigma}$	Equivalent stress
$\sigma_1, \sigma_2, \sigma_3$	Principle stresses
σ_{ij}	Second-order stress tensor
σ_H	Hydrostatic stress
σ_{kk}	Trace of the stress tensor
σ_m	Mean stress
σ_V	Viscoplastic stress
σ_{vm}	von Mises stress
σ_y	Yield, flow stress
σ^0	Engineering stress
$\boldsymbol{\sigma}^{\text{real}}$	Targeted stresses during curve matching
σ^*	Stress-triaxiality
$\widetilde{\boldsymbol{\sigma}}^{(\mathbf{k})}$	Targeted stresses for the *k*-th sub-problem
σ_p^*	Product-triaxiality
σ_{Target}^*	Targeted stress-triaxiality
σ_{vm}^n	Initial von Mises stress
σ_{vm}^{n+1}	Updated von Mises stress
$\sigma_{vm,e}^{n+1}$	Trial von Mises stress
σ_y^n	Initial Yield stress
σ_y^{n+1}	Updated Yield stress
$\sigma_{y,e}^{n+1}$	Trial yield stress
τ	Shear stress
φ_l	Basis functions for approximation for AO
ϕ	Twist angle

Subscript/superscript

i, j, k, l, m, p	Indices
x, y, z	Cartesian coordinate indices
$1,2,3 \ldots, n$	Indices
e	Elastic, elastic trial

k	*k*-th sub-problem durin AO or sub-region during SRSM
$n, n+1$	Time increments
H	Hydrostatic
p	Plastic
vm	von Mises
y	Yield

List of Acronyms

AHSS	Advanced High Strength Steels
AO	Approximate Optimization
bcc	Body-Centered-Cubic
CDM	Continuum Damage Mechanics
CTOA	Crack-Tip-Opening-Angle
CSHB	Compression split Hopkinson bar
DIC	Digital Image Correlation
DSA	Dynamic Strain Aging
DSP	Digital Speckle Photography
EOS	Equation of State
FAA	The Federal Aviation Administration
FAR	Federal Aviation Regulation
FBO	Fan Blade Out
fcc	Face-Centered-Cubic
FE	Finite Element
FEA	Finite Element Analysis
FEM	Finite Element Model
GA	Genetic Algorithm
H,L,S,V,S/H,G	Hollomon, Ludwik, Swift, Voce, Hockett/Sherby, Ghosh Hardening Models
J-C	Johnson-Cook Material Model
LVDT	Linear Variable Differential Transformer
LSE	Mean Squared Error
MSE	Mean Squared Error
NCAC	National Crash Analysis Center
OCM	Ordinate-based Curve-Matching
PCM	Partial Curve Mapping
PLC	Portevin–Le Chatelier
RT	Room temperature
RVDT	Rotary Variable Differential Transformer
SEM	Scanning Electron Microscope
SHLF	Servo-Hydraulic Loading Frame
SHPB	Split Hopkinson Pressure Bar
SRSM	Successive Response Surface Methodology
SSHB	Shear split Hopkinson bar
SQRT(x)	Square root of (x)
TSHB	Tension split Hopkinson bar

TRAUM	**T**abulated failure and viscoplasticity - **R**egularized failure - **A**diabatic heating - **U**ser defined material **M**odel
Tri	Triaxiality

CHAPTER 1 - **Introduction**

1.1 **Introduction**

It is vital to understand the dynamic deformation and failure characteristics of structures to design better engineered products. Designing lighter and cost effective structures under impact loading without any compromise from structural performance, safety and integrity has been one of the most important areas of research in mechanics for several decades [1].

Structures can deform and fail either by a brittle or ductile mechanism, or a combination of both, depending on the type of material, geometry, loading conditions and constraints. This study is focused primarily on the ductile deformation and failure under impact loading that can be substantially distinguished from brittle failure by the type of crack initiation, growth and propagation patterns both at the micro and macro-mechanical levels [2] [3] [4] [5].

Rosakis and Ravichandran [6] infer that the use of dynamic failure analysis will be applicable to a much wider spectrum of very diverse applications. They imply that with the development of verifiable computational methodologies, dynamic failure analysis can be applied to accident prevention, manufacturing processes, and reliability in design is not limited to the previously recognized applications of rupture and catastrophic failure of pressure vessels or military ballistic applications. They suggest that the dynamic failure applications can be extended to 'aircraft hardening', 'spacecraft/satellite shielding', 'high speed machining' and 'armor penetration.' Some of the potential applications of ductile dynamic failure are illustrated in Figure 1-1 for automotive-crashworthiness, aerospace-uncontained engine debris protection, metal forming-pressurized pipes and defense-armor penetration. The circumstances that are illustrated in Figure 1-1 prove the importance of successfully predicting the dynamic failure for engineering practice, where an unsuccessful prediction may put the engineering structure in jeopardy.

Zukas suggests four approaches to the solution of nonlinear problems if fast, transient loading is involved, which are experimental, semi-empirical data fits, engineering models, and numerical models [7]. Experimental approaches are limited to the number of

different scenarios that can be tested, instrumentation, constraints on cost and time, and repeatability. Semi-empirical data fits are typically limited by the experimental data distribution and variety. Engineering models are limited by nonlinearities. Therefore, depending on the application, use of numerical models is found to be the most general approach with the fewest limitations on the geometry and scope of a problem, and most promise for being able to include complex nonlinearities. For computational modeling of impact loading on metallic materials subjected to ductile failure that occurs after a significant amount of plastic deformation followed by material instability that leads to necking or shear localization, adequate models and data exist to model large deformation effects quite accurately; however, failure models range from inadequate to impractical and the available data for existing models is very limited [8] [9] [10] [11] [12] [13].

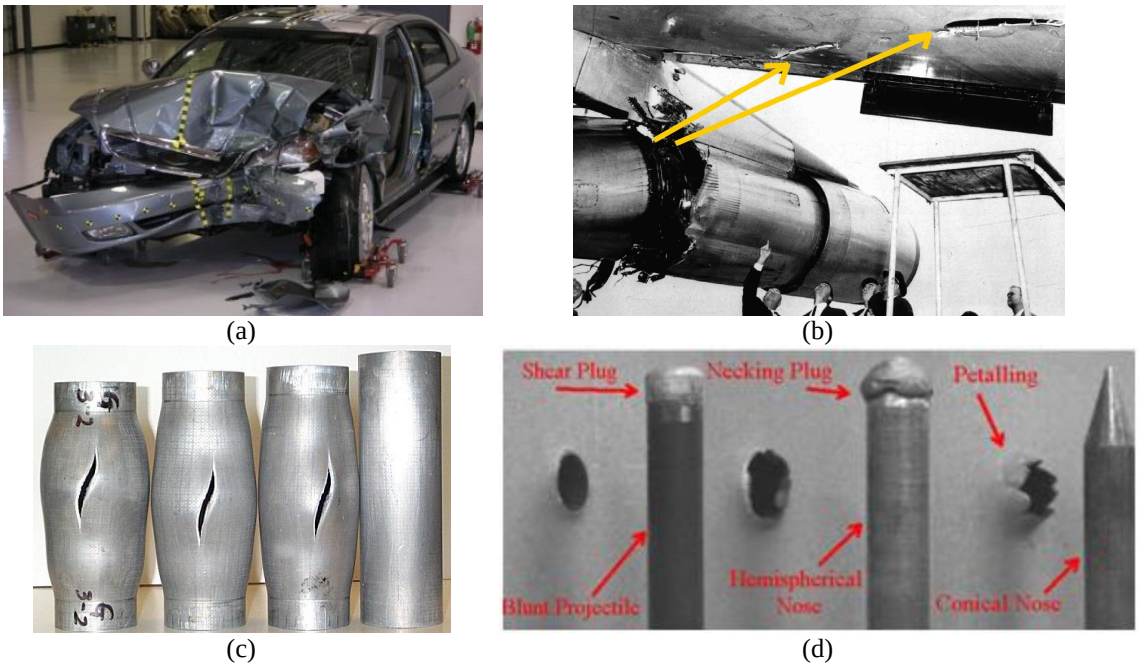

(a) (b) (c) (d)

Figure 1-1: Applications of dynamic failure for different structures; (a) offset frontal crash of a passenger car (http://www.iihs.org), (b) uncontained aircraft engine failure (http://www.ntsb.gov), (c) rupture after hydroforming on pipes (http://www.uscar.org) and (d) different failure modes after ballistic impact of projectiles with different nose shapes, adapted from [14].

Moreover, numerical models require a complete description of the material behavior, where all states of elastic-plastic response, yielding, flow and failure are needed, and histories of stress, strain-rate, and temperature effects should be accounted for [9] [10]

[11] [12] [13]. Considering the effects of softening and failure, having accurate plasticity models does not always solve the problems in non-linear FE analyses without a mesh regularization algorithm. Unlike linear FE analysis, increasing the number of elements does not guarantee a convergence with non-linear problems. Besides, softening and failure challenge uniqueness of the solution and mesh sensitivity of these problems rise as the ellipticity is lost [15]. Therefore, regularization and non-local methods are utilized to overcome mesh sensitivity issues of the FE models. Despite its fundamental importance in engineering design practice, dynamic failure of ductile materials is a phenomenon that remains practically unexplored and is not understood completely. Therefore, developing more accurate, efficient and robust numerical failure models for ductile materials is an important area of research in nonlinear mechanics and is still required [2] [6] [16].

To address this requirement, in this dissertation, a new thermo-elastic/viscoplastic material model is developed, coupled with a regularized failure model that incorporates state-of-stress, temperature, and strain rate effects to predict ductile failure. The new model is supported by an experimental program to characterize the material properties for the model input. Ballistic impact experiments are performed within a parallel experimental program to validate the accuracy and robustness of the model.

1.2 **Background and Motivation**

Uncontained turbine engine debris presents risks to an aircraft where high energy fragments impacting the aircraft need to be considered. Damage from an engine rotor burst can be catastrophic because the events may compromise structural integrity, initiate a fire, endanger critical systems or put lives in danger [17] [18] [19]. The Federal Aviation Airworthiness Regulations require aircraft be designed to minimize and mitigate these risks. FAR 25.903(d) (1) states: ‘Design precautions must be taken to minimize the hazards to the airplane in the event of an engine rotor failure.’ Therefore, there is significant interest in methods that can be applied to better understand events and improve aircraft designs. Following a catastrophic uncontained fan disk failure in commercial passenger service in 1989 [18], The Federal Aviation Administration (FAA) initiated a research program called Uncontained Engine Debris Mitigation Program, part of the Aircraft Catastrophic Failure Prevention Program, to investigate methods for

analyzing and designing for uncontained engine debris mitigation. Different methods were suggested to minimize the hazards, although it was understood that absolute containment is unlikely and consequently, the minimization of fragment energies and developing mitigation strategies in the aircraft were the reasonable methods of compliance [20].

Civil aviation authorities also require that turbine engines in civil service be designed to contain the release of any single compressor or turbine blade. To demonstrate compliance, FAR 33.94 requires every new civil engine design be tested to prove that the highest energy blade will be contained [21]. After successful demonstration of the highest energy blade, the other stages in the engine are allowed to be shown to comply by analysis. Considering the cost, difficulty and time demands of performing such tests, the engine manufacturers want to be sure that their engine will pass the first time it is tested. Therefore predictive numerical models and analysis of the containment structures is used during the design process to reduce the risk of having to repeat the blade containment test. Computational mechanics has evolved to a level that performance of structures under impact loading can efficiently and effectively be predicted by employing numerical techniques with high accuracy if accurate material models are used [12] [22] [23]. Therefore, there is a significant amount of literature about the assessment of dynamic behavior and impact performance evaluation of major aerospace materials along with their capability to mitigate hazards from uncontained engine debris [24] [25] [26] [27] [28] [29] [30] [31] [32] [33] [34] [35] [36] [37] [38] [39] [40] [41] [42] [43] [44] [45] [46] [47] [48] [49] [50] [51] [52] [53] [54] [55] [56] [57] [58] [59] [60] [61] [62] [63] [64] [65] [66] [67] [68] [69] [70] [71] [72].

Ballistic impact tests using similar projectiles for targets at different thicknesses or by using fragments of different shape and size for similar targets reveal that different modes of failure exist depending on the target material characteristics and thickness, impact velocity and orientation of the projectile [12] [20] [22] [23] [30] [32] [73] [74] [75] [14]. Common failure mechanisms under impact loading were summarized by Backman [76] and Backman and Goldsmith [23] and an illustration of these failure modes are categorized by Zukas as shown in Figure 1-2 [12] [77]. However, no failure mode solely exists and ballistic impact tests often exhibits a combination and transition of the failure

modes that are illustrated in Figure 1-2 [20] [30] [32]. Accurate prediction of these failure modes by numerical simulations is achievable only if a material model is used that utilizes explicitly defined deformation and failure characteristics, which should incorporate strain-rate, temperature and stress-state effects as addressed by Perzyna [78].

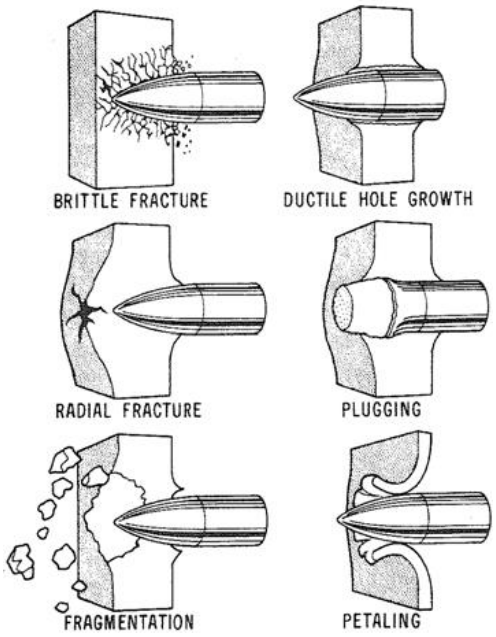

Figure 1-2: Failure modes in impacted plates, after [12] [77].

Several different thermo-viscoplastic models were suggested in the literature where a good comparison is provided by Chaboche [79] for their viscoplastic flow functions. Figure 1-3 illustrates the comparison between the viscoplastics models by Krempl [80], Miller [81], Delobelle [82], Bodner [83], Johnson-Cook (J-C) [84] [85] and Kocks [86]. In this figure, viscoplastic stress σ_V vs. plastic strain-rate was compared in a logarithmic scale. Even though some of the models were specifically suggested for creep applications, it is seen that a phenomenological model that was suggested by Johnson-Cook (J-C) [84] [85] can predict quasi-static and dynamic ranges reasonably well and stays within the distribution of the other viscoplastic models. Several other viscoplastic models were suggested for high-strain rate deformation by Steinberg, et al. [87] Clifton [88], Follansbee [89], Zerilli and Armstrong [90], Follansbee and Kocks [91], and Kocks

[92]. Among the other models, the unique characteristics of being able to predict lower and higher strain rates, makes J-C a good candidate for modeling viscoplastic behavior. Moreover, J-C provides a convenient-straightforward programming methodology that can be vectorized for fast solutions. Therefore J-C is accepted as one of the most commonly used material models in impact dynamics applications [93]. Consequently, in this study, J-C is selected as the reference model that the new material model will be compared to.

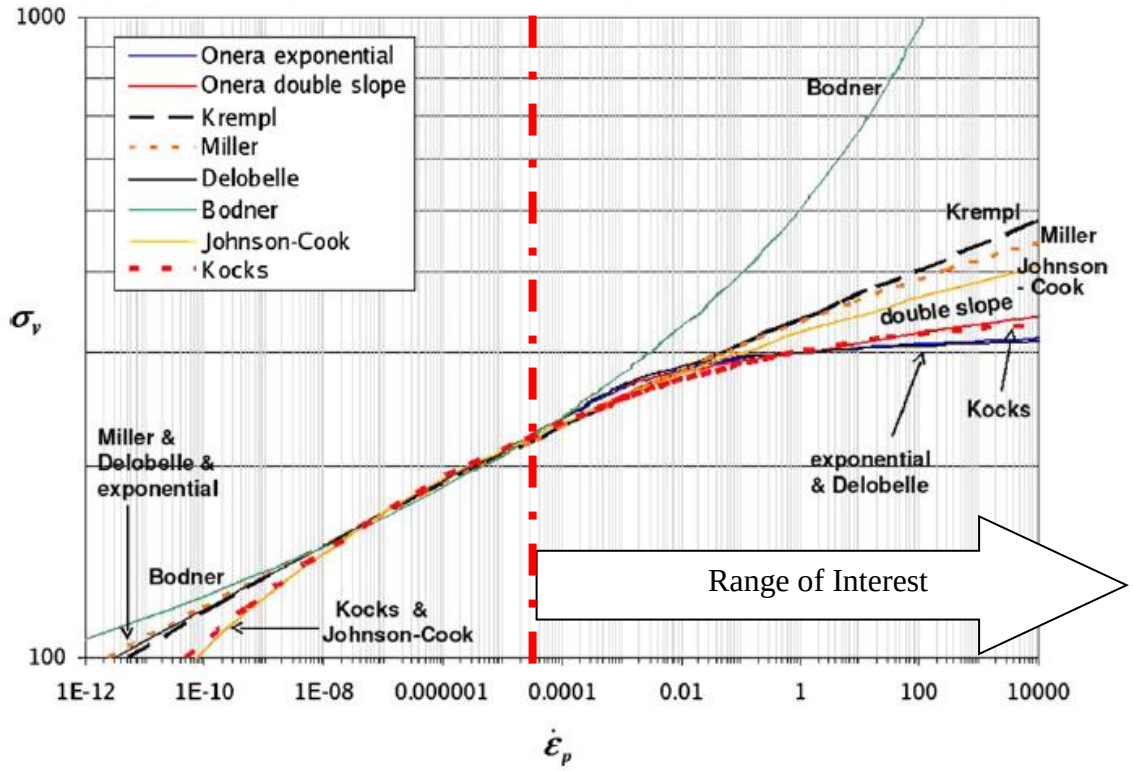

Figure 1-3: Comparison of viscoplastic flow functions, adapted from [79].

J-C phenomenological constitutive and failure model utilizes a multiplicative decomposition for the definition of the flow stress as:

$$\sigma_y = \left(A + B\left(\varepsilon_p\right)^n\right)(1 + C\ln\dot{\varepsilon}^*)(1 - T^{*m}) \tag{1.1}$$

where, $A,\ B, n, C$ and m are material constants that are characterized from temperature and strain rate dependent tests, ε_p is the effective plastic strain, $\dot{\varepsilon}^*$ is the normalized

effective plastic strain rate (typically normalized to a strain rate of 1.0 s^{-1}). T^* is the homologous temperature defined as:

$$T^* = \frac{T - T_{room}}{T_{melt} - T_{room}} \tag{1.2}$$

This material model is coupled with an accumulated damage model, where the failure is controlled by a damage parameter defined by Equation (1.3) and accumulates in time until failure occurs as the ratio of plastic strain ε_p to failure strain ε_p^f reaches unity.

$$D = \int_0^{\varepsilon_p^f} \frac{d\varepsilon_p}{\varepsilon_p^f} \tag{1.3}$$

Effective failure strain is defined as:

$$\varepsilon_p^f = [D_1 + D_2 \exp(D_3 \sigma^*)][1 + D_4 \ln\dot{\varepsilon}^*][1 + D_5 T^*] \tag{1.4}$$

where, D_1, D_2, D_3, D_4 and D_5 are the material constants related to failure that are characterized from temperature and strain rate dependent tests, σ^* is the stress-triaxiality defined by Equation (1.5) as the ratio of hydrostatic stress σ_H to the equivalent stress $\bar{\sigma}$ [94] [95].

$$\sigma^* = \frac{\sigma_H}{\bar{\sigma}} \tag{1.5}$$

Hydrostatic stress can be formulated as:

$$\sigma_H = \frac{1}{3}\sigma_{kk} \text{ or } \sigma_{H=}\sigma_m \Longrightarrow \frac{(\sigma_1 + \sigma_2 + \sigma_3)}{3} = -\frac{p}{3} \tag{1.6}$$

and the equivalent stress as von Mises stress:

$$\bar{\sigma} = \sigma_{vm} = \sqrt{\frac{3}{2} S_{ij} S_{ij}} \tag{1.7}$$

where, σ_m is the mean stress, p is the pressure and $S_{ij} = \sigma_{ij} - \sigma_m \delta_{ij}$ is the deviatoric stress tensor (see Appendix–A).

Due to the convenience in numerical implementation and programming, in this study, pressure p is utilized for calculating stress-triaxiality [7] [96] [13], where the definition of stress-triaxiality given by Equation (1.5) becomes:

$$\sigma^* = \frac{p}{\sigma_{vm}} \tag{1.8}$$

The sign associated with triaxiality reverses depending on whether one uses the definition convention in Equation (1.5) or (1.8). Both conventions appear in the literature and this author has elected to use the convention defined by Equation (1.8) (i.e., hydrostatic compression is positive, hydrostatic tension is negative).

Despite the implementation advantages of the J-C model, it is limited to an exponential curve fitting of triaxiality to represent the behavior of stress-state dependent failures. Hence, J-C is not always capable of predicting the whole range of the failure locus accurately based on stress-triaxiality [60] [97] [98]. Therefore, there is a need to address the effects of stress-triaxiality on the failure behavior of materials. A new ductile failure criterion that covers a wider range of triaxiality is suggested by Bao [99] and Bao and Wierzbicki [100] by defining three distinct branches on the failure locus as illustrated in Figure 1-4 for Al2024-T351 Aluminum alloy. Consequently, it is shown in Figure 1-4 that J-C models from assorted sources in the literature are only covering the failure space by single smooth monotonic functions (i.e., Set-1, Set-2, Set-3 and Set-4), whereas, experimental findings by Bao [99] imply that there are at least three distinct branches of failure modes on the same failure locus that will require a more complex function. In practice, J-C model is tuned or calibrated for a specific test point (e.g., uni-axial tension was preferred and torsion was ignored to have a smooth function [85]), and therefore are only able to match that one particular test condition and cannot be expected to accurately

predict other test conditions [101]. Figure 1-4 illustrates the complexity of the failure locus of a typical ductile material and illustrates why such materials cannot be represented by a single exponential function. It can also be noticed that even partitioning the failure locus into three distinct branches can generate problems related to the continuity or objectivity of the failure curve since the boundaries of the curves might cause overlapping or jump conditions.

Different J-C material model failure loci that are illustrated in Figure 1-4 will be discussed in Chapter 3 for a comparison on their performance in predicting ballistic impact tests with varying thickness and impact speed.

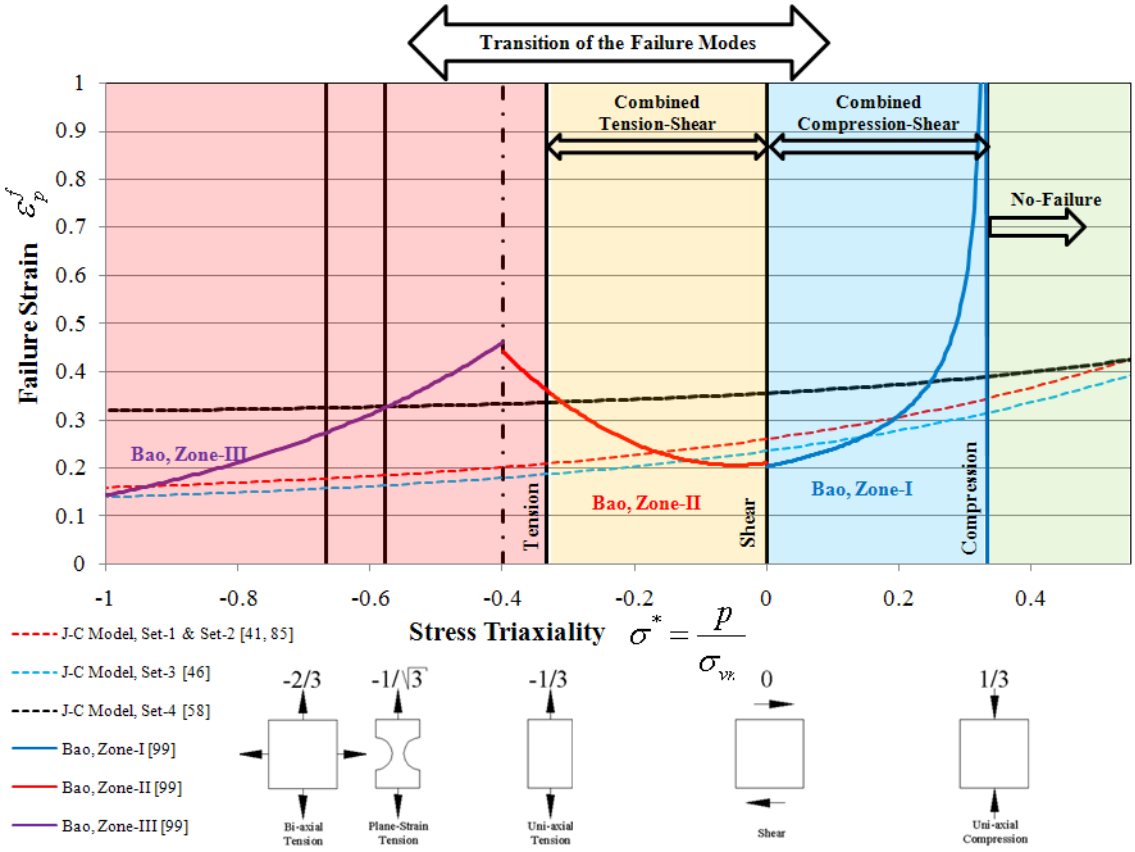

Figure 1-4: Transition of the failure modes and comparison of the failure loci for Al2024-T351.

J-C model [85] and the model suggested by Bao [99] with three distinct branches do not incorporate the effects of Lode-angle-parameter and therefore are insensitive to the effects of the third stress invariant on failure. Recently, Barsoum and Faleskog [102] and

Xue [103] extended the two dimensional failure locus to construct a three dimensional failure surface by incorporating the effects of Lode-angle-parameter $\left(\theta_L = \frac{27}{2}\frac{J_3}{\sigma_{vm}^3}\right)$, which is associated with the third deviatoric stress invariant $(J_3 = s_1 s_2 s_3)$ (see Appendix–A). In this postulation, the failure surface was still assumed as a phenomenological decaying function that is symmetric around the $\theta_L = 0$ meridian, which corresponds to a state of plane-strain [103]. Three dimensional failure loci were constructed by surface fitting through the available test results for the available values of stress-triaxiality and Lode-angle-parameters.

The differences between these three approaches can be observed in Figure 1-5. The failure surfaces, which were suggested by J-C model [85] and by Bao [99], remain unchanged along the Lode-angle-parameter axis. Figure 1-5(a) represents the surface form of the first J-C curve that is illustrated as Set-1 in Figure 1-4. Independent of the Lode-angle-parameter, J-C surface shows a monotonically increasing smooth exponential form. Figure 1-5(b) represents the surface form of the three distinct branches that is illustrated as in Figure 1-4 and still shows no dependency on the Lode-angle-parameter. Bao's model was recognized due to its three branches that show a higher representation capability on the stress-triaxiality compared to J-C. Figure 1-5(c) represents the Lode-angle-parameter dependent failure surface that was constructed through surface fitting on the experimental data given by Bao [99] while forcing the surface as a decaying symmetric function. It can be concluded that even as the same test data was used for both Figures 1-5(b) and 1-5(c), based on the surface fitting methodology and Lode-angle-parameter dependency, failure surfaces can drastically differ in shape. Stress-state dependency of the failure locus is further discussed in Chapter 4.

Nevertheless, additional test results (i.e., especially around the biaxial tension stress-state) revealed that the failure locus was not symmetric about the $\theta_L = 0$ meridian and a higher order surface fitting is necessary to represent the failure surface more accurately [104]. Therefore, more recently, an asymmetric failure locus was proposed that was constructed through the test points by implying a functional convexity by Bai [104] and Bai and Wierzbicki [105]. A geometrical representation of the asymmetric failure locus in 3D space is shown in Figure 1-6.

(a)

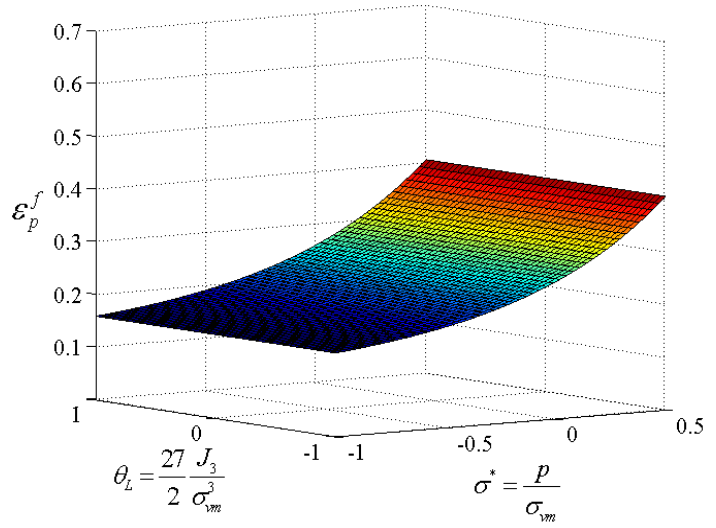

(b)

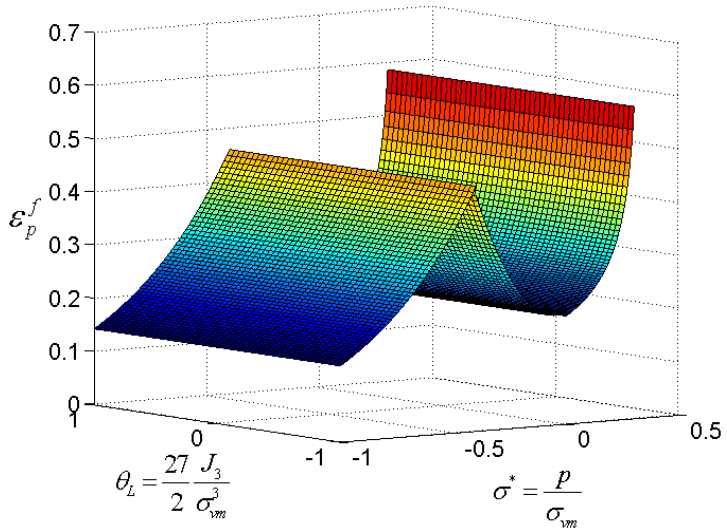

(c)

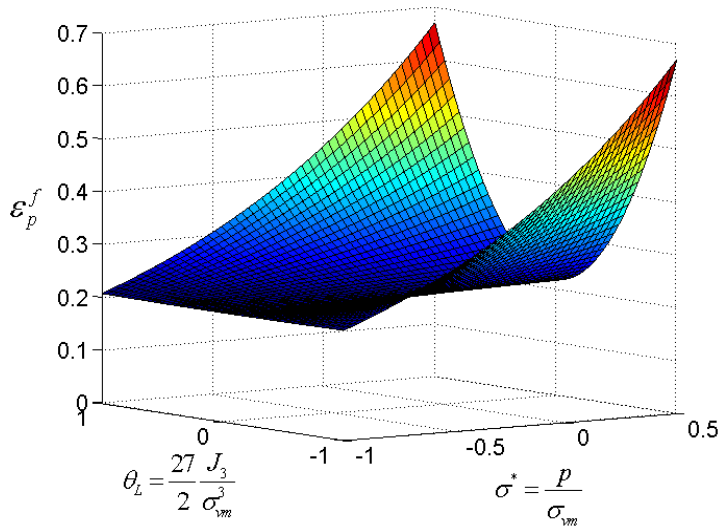

Figure 1-5: 3D adaptations of the failure models on the space described by stress-triaxiality and Lode-angle-parameter for Al2024-T351; (a) J-C model with Set-1 [85], (b) model by Bao [99], (c) model by Xue with Lode-angle-parameter dependency introduced [103].

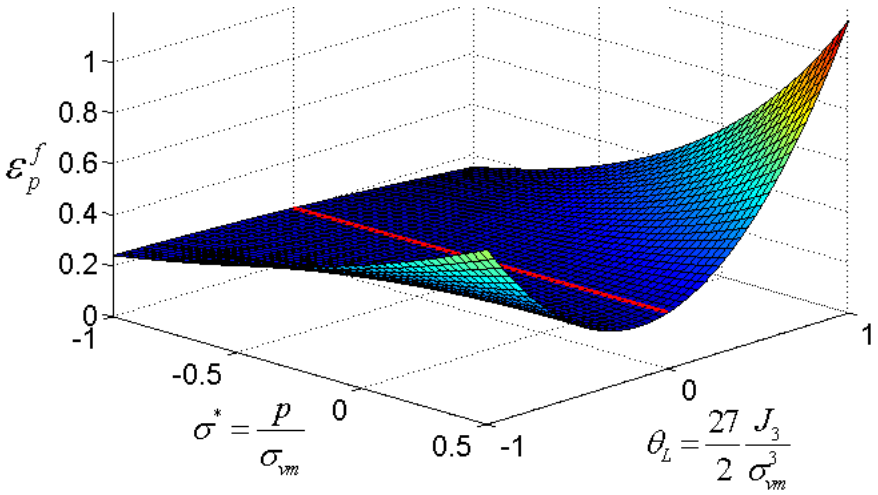

Figure 1-6: Asymmetric failure surface incorporating the effects of stress-triaxiality and Lode-angle-parameter [104].

These approaches imply that the shape and quality of the failure surface directly depends on the number and distribution of the available test points and there is a need to construct the failure surface in a more generic way. The Lode-angle-parameter, which changes between plus and minus unity $(-1 \leq \theta_L \leq +1)$, provides a good boundary for the definition of the failure surface. However, physical boundaries of the failure surface have to be identified more explicitly on the stress-triaxiality axis. Although, it is found that there is a cutoff pressure when $\sigma^* = +\frac{1}{3}$ corresponding to the uni-axial compression case, stress-triaxiality can change between plus and minus infinity $(-\infty \leq \sigma^* \leq +\infty)$ [99] [106]. Consequently, it is required to analytically determine the reasonable boundaries for stress-triaxiality [107].

Therefore, there is still a need to develop a new material model that can be used as a generic tool to simulate dynamic ductile deformation and failure behavior of materials under impact loading. This material model should incorporate state-of-stress, temperature and strain-rate dependency and should be coupled with a regularized failure model. The failure surface should explicitly be constructed through experimentally obtained, stress-state dependent failure points. A parallel material testing program should be performed to characterize the material behavior and generate input data for the numerical model.

1.3 **Research Objectives and scope**

Given the motivation and background, the ultimate aspiration of this research is to further understand the thermo-viscoplastic behavior of ductile materials under impact loading and contribute to the common knowledge about the impact performance evaluation phenomenon.

The main goal of this dissertation is to develop a new thermo-elastic/viscoplastic material model coupled with an accumulated regularized failure criterion that can incorporate high strain rate and temperature effects. The new material model is implemented into an explicit dynamics finite element (FE) code, LS-DYNA, as a user defined material subroutine. This model is expected to be used as a generic tool to simulate any ductile metal under impact loading.

In order to meet the objectives, first; the applicability and effectiveness of the existing ductile failure criteria is reviewed and evaluated.

A new failure locus is then proposed in the equivalent failure strain and the stress-triaxiality space over the entire range of states-of-stress, where conventional compression, torsion, tension tests, and also newly developed shear combined loading tests and biaxial punching/bulging tests are designed and performed within the framework of a parallel material testing program [108]. The failure locus is obtained for Al2024-T351 aluminum alloy, which is a commonly used material in aerospace industry.

An inverse approach by using coupled FE simulations and force-displacement curves is introduced to characterize and model the strain rate and temperature dependency of the material of interest.

A regularization method is also developed to solve mesh size dependency of the material model. The prediction capability of the new model with the regularization algorithm is discussed for different failure modes.

Ballistic impact tests, using specimens fabricated from a single stock of material, are also used to test the prediction capability of the new model. Application of the newly developed ductile failure criterion to high velocity impact events is used to demonstrate the validity of the approach and illustrate the drawbacks of existing failure models available in the literature.

The range of strain-rate effects targeted in this research covers a large spectrum from quasi-static to highly dynamic as illustrated in Figure 1-7. Intended engineering applications can be seen in Figure 1-1, most of which are often classified as being in the sub-ordnance range [9] [12] [23]. Based on the validation work performed, the model is shown to accommodate high strain rate dependency on material strength but it has not been expanded to investigate material phase transformations.

A von Mises (J_2) type of plasticity is considered in the course of this dissertation while modeling the flow surface of the material model. This assumption is justified based on the experimental finding by Lode [109] and Taylor and Quinney [110]. Both studies have tested samples under combined loading and have checked the yield surfaces of the materials of interest. Lode tested steel, copper and nickel and Taylor and Quinney have tested copper, aluminum and mild steel. The results of their findings are illustrated in Figure 1-8(a) for Lode and Figure 1-8(b) for Taylor and Quinney, where it is shown that the materials of interest behave closer to the von Mises yield surface than to Tresca theory. Therefore, the new material model is formulated according to the (J_2) flow theory to be able to provide a generic simulation tool for a wide range of materials.

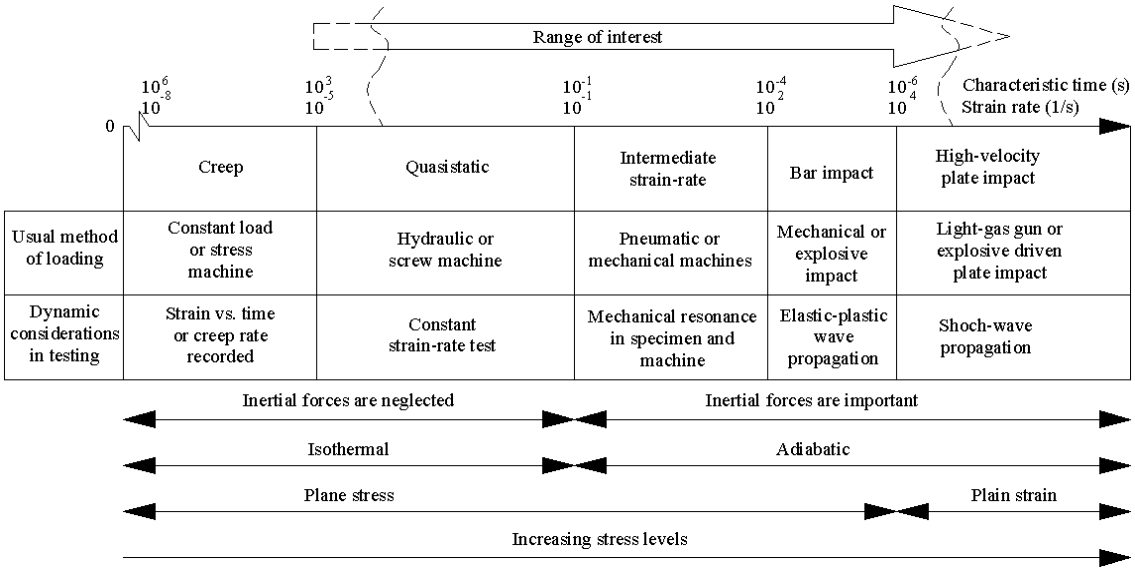

Figure 1-7: Material behavior with changing strain rate and load duration, adapted after [111].

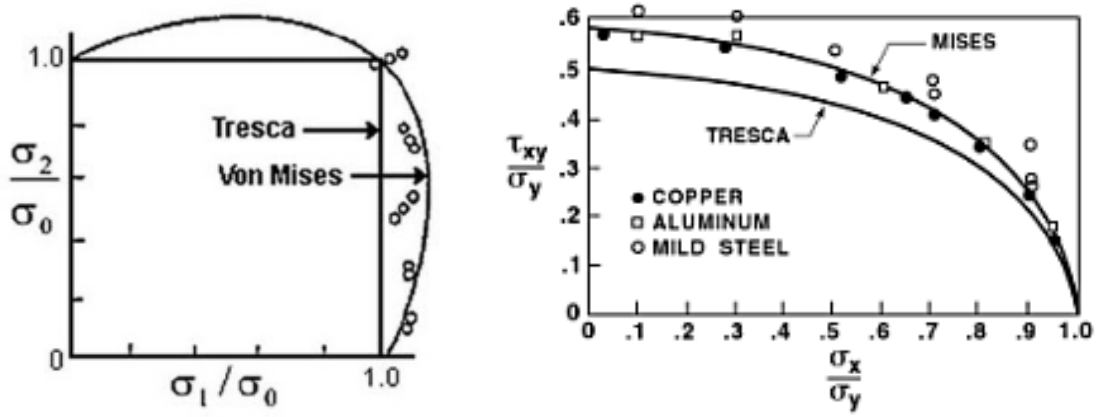

(a) (b)

Figure 1-8: Comparison of yield surfaces for different materials under combined loading; (a) after [109] and (b) after [110].

1.4 **Original Contributions**

The original contributions accomplished within the course of this Dissertation can be summarized as:

Development and implementation of a thermo-elastic/viscoplastic material model coupled with an accumulated regularized failure model. A new viscoplastic material model is developed, which employs tabulated inputs of stress-strain curves to construct the flow surface as a function of strain-rate and temperature. A new accumulated failure model is developed and implemented which also employs tabulated inputs of plastic strains at failure depending on the state-of-stress, strain rate, temperature and element size for regularization. An alternative variable called product-triaxiality, which is a function of the third stress invariant, is utilized on defining the state-of-stress space with respect to stress-triaxiality. Failure strains from the 3D failure locus are projected on a space represented by stress-triaxiality vs. product-triaxiality. Failure of ductile materials under impact loading is shown to occur within the envelope defined between this space defined by product-triaxiality and stress-triaxiality.

Dynamic behavior of Al2024-T351 is investigated. A new experimental program is designed to characterize quasi-static and dynamic deformation and failure properties of ductile materials.

Flow surface of Al2024-T351 is explicitly constructed through hardening curves at different strain rates and temperatures. Failure surface of Al2024-T351 is constructed through tabulated inputs of plastic strains at failure depending on the state-of-stress, strain rate, temperature and element size.

Impact performance of Al2024-T351 is investigated experimentally and numerically under different loading conditions. It is successfully shown that the state-of-stress has a significant role in the dynamic failure behavior of ductile materials under impact loading. It is also shown that the new material model can be utilized as a promising tool to evaluate the dynamic failure prediction of structures.

1.5 **Outline of the Dissertation**

The dissertation consists of 8 interrelated chapters.

Chapter 1 provides background information and motivation, defines objectives and scope, and presents an overview of the thesis.

Chapter 2 presents an overview of ductile failure in structural metals. This chapter presents a review of the common approaches currently used to model material failure including void growth models, porous plasticity laws, continuum damage mechanics (CDM), cohesion zone models and empirical criteria. The general procedures used to implement these approaches are briefly described and an assessment of the shortcomings associated with each approach is discussed.

Chapter 3 provides an extensive analysis of a series of controlled impact tests using FEA models that implement one of the most commonly used material models. It is shown that material model tuned to a single set of test parameters in an ad hoc manner may not necessarily predict the ballistic impact performance of a material if there is a significant change and transition in the deformation mode and that traditional FEA predictions are highly mesh dependent. Therefore, it is elaborated in this chapter that in addition to the need of a more general material model, there is a need for a new regularized material model capable of covering the whole fracture locus and potential states-of-stress.

Chapter 4 describes the methodology of newly proposed tabulated thermo-elastic/viscoplastic material model with regularized failure. Details of the constitutive model and its numerical implementation are delineated first and a detailed description of

the effects of state-of-stress on the ductile failure of metals under impact loading is provided. A testing program is devised to generate the proposed failure locus. Different specimens are designed for the proposed testing program for targeted states-of-stress. The proposed material model is compared and benchmarked with an existing material model by utilizing single element tests. Numerical stability, accuracy and robustness of the new model is benchmarked with an existing model, where various failure modes are compared by using proportional and non-proportional loading at different states-of-stress.

Chapter 5 describes the details of the experimental program and the specimens that are used to generate input data for the newly proposed material model. Compression, shear, tension and combined loading cases are considered to obtain data covering the whole state-of-stress space. Furthermore, depending on the shape of the specimens, plane-stress, plane-strain, axi-symmetric and biaxial punch tests are performed. A test matrix is designed to generate input data for strain rate and temperature dependency. Test results are used for characterizing the material properties for the new material model. Temperature and strain rate dependent stress-strain curves are generated for the material model input. Also failure strains are characterized for a wide range of state-of-stress. Failure locus of Al2024-T351 aluminum alloy is obtained for validation purposes.

Chapter 6 presents the validation procedures for the material model, where component based test specimens are simulated and compared with the test results. Digital image correlation (DIC) technique is used to compare the strain field of the experiments with FE calculations.

Chapter 7 presents the validation procedures of the proposed material model, where full scale impact tests are simulated and compared with the test results. This chapter also benchmarks the predictive capability of the new model for full scale tests against an existing material model. The material models are tested for whether they can predict the changes in the deformation and failure modes upon impact with respect to a qualitative comparison as well as a quantitative comparison of the residual velocities.

Finally, a summary of the main results is presented in Chapter 8. A list of contributions to the philosophy of engineering science and recommendations for future research and potential applications are also provided.

CHAPTER 2 - **Literature review**

2.1 **Introduction**

Although it has been more than 100 years since Mohr-Coulomb strength theory was established [112] and despite its fundamental importance in engineering design practice, dynamic failure of ductile materials is a phenomenon that remains virtually unexplored and is still not fully understood [2] [6] [16]. In this Chapter, only a small part of the Century old existing literature that is directly relevant to the topic guided and motivated by the evolution of the computational mechanics is addressed. Readers are encouraged to consider excellent review papers about the topic from Curran, et al. [2], Garrison and Moody [3] and Yu [112].

2.2 **Review on the ductile failure of metals**

Ductility, which is often defined by a measure of deformation to failure, is not only a unique property of the material; it also combines the geometrical dependencies of localized conditions of stress, strain, and temperature, where complicated plastic deformation such as necking and shear localization may occur prior to failure [113]. Physically, it is accepted that ductile failure is mostly driven by microscopic voids, where initiation of nucleation followed by void growth with increasing deformation and finally coalescence of micro-cracks lead to failure [2] [3] [4] [5]. A schematic representation of the complete ductile failure process is illustrated in Figure 2-1 with the following steps; (a) the un-deformed state, (b) the micro-void nucleation state, (c) the micro-void growth state and three stages of failure surface formation involving (d) incipient micro-void coalescence, (e) internal microscopic necking, and (f) knife-edge separation [5].

All engineering metals and alloys contain imperfections to some degree, which leads to ‘cup and cone’ type of failure under uni-axial tension due to localized internal necking of the inter-void matrix across a sheet of micro-voids. Figure 2-2(a) illustrates SEM photographs of the central region of the failure surface at various magnification factors. At a lower magnification factor, ‘cup’ formation can be seen with a ‘fibrous’ appearance and, at higher magnifications, ‘dimpled rupture’ is observed verifying complete necking

of the inter-void matrix and finally ‘knife-edge’ separation with equi-axed dimples caused by void growth and coalescence [5].

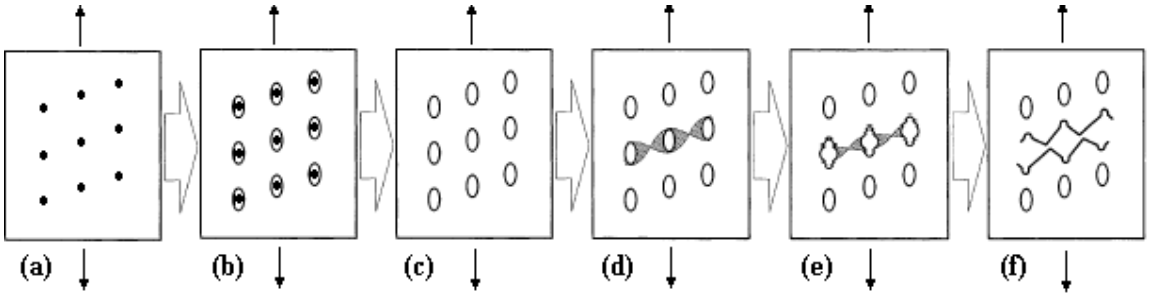

Figure 2-1: A schematic representation of the ductile failure in metals, adapted after [5].

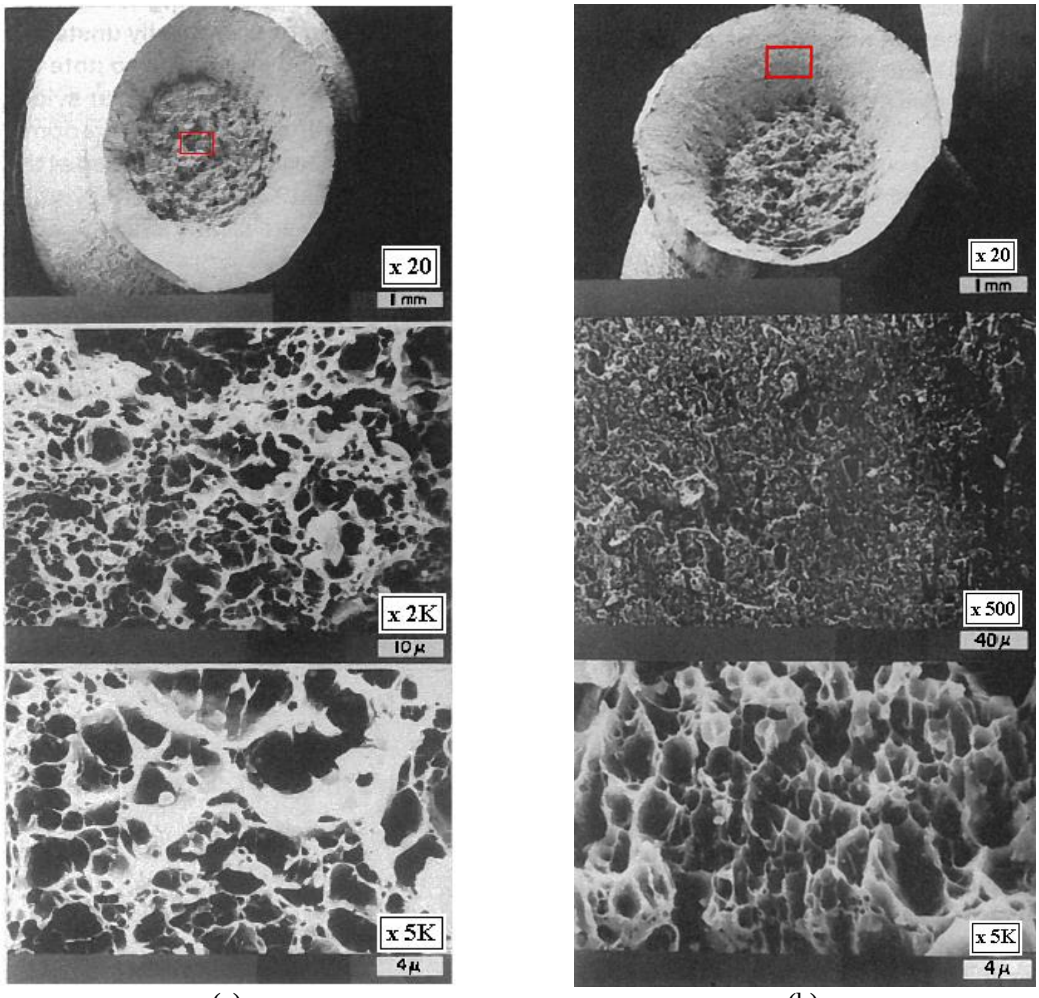

(a) (b)

Figure 2-2: SEM images from a uni-axial test for ‘cup’ (a) and ‘cone’ (b) regions of the failure zone, adapted after [5].

‘Shear lips’ or the conical region of the failure surface that is illustrated with the SEM photographs in Figure 2-2(b) represents a much smoother appearance at lower magnifications. However, at higher magnifications, a fibrous nature is clearly observed that also leads to ‘dimpled rupture’ with elongated dimples formed by void coalescence during shear lip formation. Therefore, ‘shear lips’ are secondary failure effects in uni-axial tension tests and should be treated as tensile failure on an inclined surface rather than a ‘shear’ failure considering that the failure mechanism is also similar at the micro-mechanical level [5]. Several different approaches have been suggested for the prediction of ductile failure in the literature considering these complex and combined failure mechanisms. Atkins [114], while combining the fields of metal forming and fracture mechanics, mentions five major different approaches: void growth models, porous plasticity laws, continuum damage mechanics (CDM), cohesion zone models and empirical criteria.

Studies on the micro-mechanics of void nucleation, growth and coalescence for simple stress and strain states are proposed in the literature, where cylindrical and spherical hole growth models are suggested beginning with the pioneering work of McClintock [115] and studied further by Cockcroft and Latham [116] and Rice and Tracey [117] in that respect. More detailed investigations of the stress and strain fields are performed by Brozzo, et al. [118], Hancock and Mackenzie [119], LeRoy, et al. [120], Oh, et al. [121] and Clift, et al. [122].

Gurson [123] [124] suggested a porous plasticity model, where interaction between internal damage and flow behavior of the material is taken into account by a porous sensitivity yield function while Tvergaard [125] [126] [127], Needleman and Tvergaard [128], Tvergaard and Needleman [129] [130], and Rousselier [131] have also contributed to this model. However, inadequate calibration of such models with many model parameters, which are strongly coupled, forced the methodology to evolve to the unit cell approach. Xia, et al. [132], Xia and Shih [133] [134] [135], Faleskog, et al. [136], Gao, et al. [137] and Jun [138] corroborated the observations that ductile failure is governed by void growth while calibrating model parameters with unit cells and inversely fitting numerical models to experimental data. However, these methods also required extensive

modeling and calibration effort that makes them infeasible for modeling failure process effectively and efficiently. Moreover, difficulties during testing microstructure for calibration purposes have caused inaccuracies for some of the models at certain loading conditions, where testing was not even viable. Furthermore, in the case of shear localization, the model is unable to predict failure since the failure occurs without any void growth observed. Therefore, modifications to the Gurson model are suggested to predict localized shear and shear bands more accurately [139] [140].

An alternative approach to simulate ductile failure is by utilizing the CDM concept, which follows the damage parameter introduced by Kachanov [141]. Lemaitre [142] [143] [144] [145] also introduced a scalar damage variable and proposed an evolution equation for failure, where a thermodynamic potential and a potential of dissipation were proposed to obtain the relation between damage strain energy release rate and stress-strain states. Various CDM models that have different damage evolution laws were also proposed by Wang [146] [147], Horstemeyer, et al. [148], Dhar, et al. [149], and Rosa, et al. [150] assuming different dissipation potentials since the shape of the potential of dissipation has not been well established in the literature. The coupling of the damage variable and constitutive relation makes the calibration of the material constants and damage law difficult to carry out, where the damage variable generally cannot be obtained from direct output of the test.

Another innovative way of analyzing crack formation and propagation is by using cohesive zone and interface elements, which depend on the concepts suggested by Barenblatt [151] and Hillerborg, et al. [152] initially for brittle materials. Given that the cohesive zone modeling methodology employs special interface elements at the failure region, a traction-separation law is used to simulate the behavior of the material. Therefore, adaptations of this method for different materials under different loading and constraint conditions also required utilization of various traction-separation laws [153] [154] [155] [156] [157]. Tvergaard [158] [159] [160] suggested a modified version of this traction law and multi-axial separation became possible. However, it is shown that separation work per unit area and the peak stress required for separation are not constant for different states-of-stress during the entire process and they need to be calibrated with special attention [161]. Furthermore, modeling failure with cohesive zone elements and

interfaces requires prior knowledge about where the crack initiates and how it propagates. Moreover, the methodology is strictly mesh-dependent.

For practical reasons, a number of empirical failure criteria have also been proposed to simulate ductile failure more effectively and efficiently. Although it is commonly assumed that hydrostatic stress has no effect on plastic yield [94], earlier experimental and theoretical [162] [95] [163] [164] [165] [166] studies indicated that when voids are present in ductile materials, the hydrostatic component of stress can cause macroscopic dilatation through the mechanism of void growth. Since the pioneering work by Bridgman [162] [95], most empirical criteria derived from the void growth models usually suggest that the failure occurs at a critical value D_{cr} depending on the equivalent plastic strain $\bar{\varepsilon}_p$, which is accumulated in the body and depending often on the state-of-stress that can be represented by Equation (2.1) in general terms as:

$$D_{cr} = \int_0^{\bar{\varepsilon}_p^f} f(\text{state} - \text{of} - \text{stress}) d\bar{\varepsilon}_p \tag{2.1}$$

Table (2.1) summarizes some of the most commonly used empirical criteria proposed in the literature, where the simplest case is called equivalent failure strain criterion and the state-of-stress is assumed to have no effect (i.e., $f(\text{state} - \text{of} - \text{stress}) = 1$). In quantitative investigations of ductile failure by void growth; stress-triaxiality that is defined by Equation (1.8) is found to have a strong dependency on the void growth rate. Therefore in many cases the effective plastic strain at failure can be written as a function of stress-triaxiality as shown in Equation (2.2).

$$\bar{\varepsilon}_p^f = f(\sigma^*) = f\left(\frac{p}{\bar{\sigma}}\right) \tag{2.2}$$

Experimental results by Bridgman [162] [95], Hancock and Mackenzie [119] and Mackenzie, et al. [167] also supports that ductility is governed by the degree of triaxiality and material failure can be expressed by a failure envelope that is described by Equation (2.1).

Table 2-1: Commonly used empirical failure criterion.

Criterion	Description	
Equivalent failure strain	$\bar{\varepsilon}_p^f = \bar{\varepsilon}_p$	(2.3)
McClintock [115]	$D_{cr} = \int_0^{\bar{\varepsilon}_p^f} \left[\frac{\sqrt{3}}{2(1-n)}\sinh\left(\frac{\sqrt{3}}{2(1-n)}\frac{\sigma_1+\sigma_2}{\bar{\sigma}}\right)+\frac{3}{4}\frac{\sigma_1-\sigma_2}{\bar{\sigma}}\right] d\bar{\varepsilon}_p$	(2.4)
Cockcroft and Latham [116]	$D_{cr} = \int_0^{\bar{\varepsilon}_p^f} \left(\frac{\sigma_1}{\bar{\sigma}}\right) d\bar{\varepsilon}_p$	(2.5)
Rice and Tracey [117]	$D_{cr} = \int_0^{\bar{\varepsilon}_p^f} \exp\left(\frac{3}{2}\frac{\sigma_H}{\bar{\sigma}}\right) d\bar{\varepsilon}_p$	(2.6)
Brozzo, et al. [118]	$D_{cr} = \int_0^{\bar{\varepsilon}_p^f} \left(\frac{2\sigma_1}{3(\sigma_1-\sigma_H)}\right) d\bar{\varepsilon}_p$	(2.7)
Hancock and Mackenzie [119]	$D_{cr} = \int_0^{\bar{\varepsilon}_p^f} \exp\left(\frac{3\sigma_H}{2\bar{\sigma}}\right) d\bar{\varepsilon}_p$	(2.8)
Oh, et al. [121]	$D_{cr} = \int_0^{\bar{\varepsilon}_p^f} \left(\frac{\sigma_1}{\bar{\sigma}}\right) d\bar{\varepsilon}_p$	(2.9)
LeRoy, et al. [120]	$D_{cr} = \int_0^{\bar{\varepsilon}_p^f} (\sigma_1-\sigma_H)\, d\bar{\varepsilon}_p$	(2.10)
Clift, et al. [122]	$D_{cr} = \int_0^{\bar{\varepsilon}_p^f} \bar{\sigma}\, d\bar{\varepsilon}_p$	(2.11)
Norris, et al. [163]	$D_{cr} = \int_0^{\bar{\varepsilon}_p^f} \left(\frac{1}{(1-D_1\sigma_H)}\right) d\bar{\varepsilon}_p$	(2.12)
Oyane, et al. [164]	$D_{cr} = \int_0^{\bar{\varepsilon}_p^f} \left(1+\frac{\sigma_H}{D_1\bar{\sigma}}\right) d\bar{\varepsilon}_p$	(2.13)
Atkins [165]	$D_{cr} = \int_0^{\bar{\varepsilon}_p^f} \left(\frac{1+\frac{1}{2}\frac{d\varepsilon_2}{d\varepsilon_1}}{1-D_1\sigma_H}\right) d\bar{\varepsilon}_p$	(2.14
Johnson and Cook (J-C) * [85]	$\int_0^{\bar{\varepsilon}_p^f} \left(\frac{1}{D_1+D_2\exp\left(D_3\frac{\sigma_H}{\bar{\sigma}}\right)}\right) d\bar{\varepsilon}_p = 1$	(2.15)
Wilkins, et al. [166]	$D_{cr} = \int_0^{\bar{\varepsilon}_p^f} \left(\frac{1}{1-D_1\sigma_H}\right)^{D_2} \left(2-\mathrm{Max}\left(\frac{s_2}{s_3},\frac{s_2}{s_1}\right)\right)^{D_3} d\bar{\varepsilon}_p$	(2.16)

*Strain rate and temperature dependent terms are ignored from Equation (1.4)

Rice and Tracey [117] postulated a general form of a stress-triaxiality function to describe the growth of a spherical void. However, this model was developed to predict failure that was under hydrostatic tension and was not meant to model compression or shear accurately. Therefore, the failure models were capable of covering only a small segment of the failure locus as a function of state-of-stress. Many adaptations have been made to extend the failure locus by extrapolation to cover failure zones at different stress-states, where usually a monotonic function was utilized (e.g., Wilkins, et al. [166], Oyane [164], Rice and Tracey [117], Johnson and Cook [85], Johnson and Holmquist [168], Hancock and Mackenzie [119], Ganser, et al. [169], Borvik, et al. [170] [171]).

Moreover, while characterizing the failure locus as a function of state-of-stress, it is a common practice to use either axi-symmetric dog bones with smooth and notched geometries under tension for negative stress-triaxiality values or cylinders under compression for positive stress-triaxiality values without knowing the characteristics of the material for other values of the triaxial stress-state [85] [119] [16]. Therefore, using a single monotonic function is often not enough to represent the overall characteristics of the failure locus with different states-of-stress without testing many specimens with different geometries.

Likewise, experimental findings that were shown during the last decade by Bao [99], Bao and Wierzbicki [100] suggest that for Al2024-T351, the failure cannot be represented by a single smooth monotonic function as shown and compared with a Johnson and Cook criterion in Figure 1-4. Instead, a partitioned failure locus was proposed, where a transition region was suggested between negative and positive stress-triaxiality values of the stress-state.

The applicability of the several failure criteria (e.g., Tresca, Wilkins [166], Marciniak-Kuczynski [172], Gurson [123] [124], Johnson-Cook [85], CrachFEM [173]) was further investigated and compared by Bao and Wierzbicki [101], Wierzbicki, et al. [97], Tenh, et al. [98], and Zadpoor, et al. [174], in terms of the ability to predict the failure locus over stress space depending on a number of available calibration points, which were characterized through several different tests. It was shown that some of the models could successfully predict the failure loci as a function of triaxiality when the

required number of calibration points was employed. However, if the number of calibration points was small, over-fitting may occur, which can then lead to an inaccurate prediction of the failure loci. Moreover, even though some of the models were found to successfully predict a certain range of the triaxiality space with a given number of calibration points, these models were still limited to the given triaxiality range and were unable to represent the rest of the space effectively. Therefore, there is a need to construct the failure envelope in a more flexible and generic way so that each failure point can explicitly be defined in a tabulated manner as a function of strain, state-of-stress, strain rate and temperature for the required ranges, where failure loci can be generated without being dependent on a pre-accepted curve shape.

Developments in damage plasticity theory during the last decade have shown that the critical plastic strain at failure for ductile solids not only depends on stress-triaxiality but also on the Lode-angle-parameter θ_L, which can be related to the third deviatoric stress invariant since $\theta_L = \frac{27}{2}\frac{J_3}{\sigma_{vm}^3}$. Therefore, ductile failure of metals can easily be described and characterized by combinations of all three principal stresses or the three stress invariants, where they can be incorporated by combinations of hydrostatic stress, von Mises stress and Lode-angle-parameter as illustrated in Figure 1-5 and represented by Equation (2.17) [103] [140] [175] [176] [177].

$$\varepsilon_p^f = f(\sigma^*, \theta_L) = f\left(\frac{p}{\sigma_{vm}}, \frac{27}{2}\frac{J_3}{\sigma_{vm}^3}\right) \tag{2.17}$$

In this research, a new representation of the failure locus is proposed as a function of stress-triaxiality and a newly defined product-triaxiality parameter σ_p^* [107]. Product-triaxiality is defined by normalizing the product of all principle stress components or third stress invariant I_3 with von Mises stress as:

$$\sigma_p^* = \frac{I_3}{\sigma_{vm}^3} \tag{2.18}$$

The new definition generates a well-defined failure locus within an envelope of third stress invariant as represented by Equation (2.19).

$$\varepsilon_p^f = f\left(\sigma^*, \sigma_p^*\right) = f\left(\frac{p}{\sigma_{vm}}, \frac{I_3}{\sigma_{vm}^3}\right) \tag{2.19}$$

It is shown in this dissertation that ductile failure under impact loading occur within an envelope defined by stress-triaxiality vs. product-triaxiality. Then, a 3D failure surface is constructed through characterization of the failure strains for specifically designed test specimens for specific values of the stress-triaxiality, product-triaxiality and Lode-angle-parameter.

However, determining the failure locus experimentally and characterizing the material parameters for a large range of stress-states, strain rate and temperature is still a challenging task. This is due to the high complexity of the process of failure, the absence of adequate computational methodologies capable of modeling the formation and propagation of failure with reasonable computational times, high accuracy and the lack of well-established calibration procedures. Moreover, determination of the failure initialization and growth while capturing the stress and temperature fields in the vicinity of the failure using currently available instruments is not any easy task. Advances in computing as well as measurement instrumentation have recently allowed for the investigation of dynamic failure phenomena in a more detailed way than previously possible [6]. In this dissertation a coupled experimental and numerical framework is proposed with well-defined calibration procedures and a joint effort will be presented towards the development of a macroscopic failure criterion that can be used as a generic tool for modeling failure characteristics of several engineering materials. These calibration procedures require determination of the strains to failure ε_p^f, where it is shown that the failure strains are not constant and change under different loading conditions depending on the state-of-stress, strain rate, and temperature.

Although the effects of temperature and strain rate was reported to have minor contribution on the failure strain compared to the effects of state-of-stress, most of these studies were performed either for lower ranges of strain rates, or performed for a limited

number of stress-triaxiality values and temperatures. It is also common to assume that the sensitivities can be diverse for different materials. Weldox 460E steel was tested by Hopperstad, et al. [178] for negative stress-triaxiality values and it was found that for a strain-rate hardening material, ductility considerably depends on the effects of stress-triaxiality, where no significant effects of increasing strain-rate were found. Borvik [171] and Borvik, et al. [179] also reported that the temperature dependency of the failure strain is not as significant as the dependency on the stress-triaxiality for Weldox 460E. Therefore, the new material model incorporates the effect of stress-state on the failure strain by considering all three stress invariants. The effects of temperature and strain rate are also taken into account.

One of the major concerns in non-linear mechanics is the stress and strain concentrations that often happen when there are geometric and material discontinuities, which may lead to plastic instability. Under these circumstances it is difficult to predict stress, strain fields, and particularly failure at the correct location accurately. Consequently, the problem becomes explicitly sensitive to the mesh pattern and size. Needleman and Tvergaard [180], Skallerud and Zhang [181], and Wilsius, et al. [182] have reported the influence of mesh size on predicting ductile failure. Therefore it is important to utilize a mesh regularization rule that can help predict failure independent of the mesh size. The new material model developed in this research also incorporates a mesh regularization scheme to help solve mesh size dependency of the failure.

2.3 **Summary**

In this Chapter, a brief literature review was given about the dynamic ductile failure of materials. Literature suggests five major approaches for investigating the ductile failure: void growth models, porous plasticity laws, CDM, cohesion zone models and empirical criteria [114]. A brief introduction of the proposed failure model was given by listing some of the most commonly used phenomenological models. Different approaches for constructing a stress-state dependent 3D failure surface as a function of the stress-triaxiality and Lode angle were introduced.

CHAPTER 3 - **Problem definition**

3.1 **Introduction**

In this Chapter, ballistic impact simulations of tests conducted on Al2024-T351 targets are performed by utilizing the Johnson-Cook (J-C) material model. J-C material model is selected for the analysis since it is predominantly used for ballistic impact analysis and commonly used as comparison or benchmark standard while developing new material models [183]. As described in Section 1.2, J-C is a phenomenological model providing a thermo/visco-plastic formulation coupled with a failure criterion. J-C provides a straightforward formulation for the flow and failure surfaces, which bestow convenient coding solutions for the finite element (FE) programming. Impact simulations usually need large FE models and require extensive computational resources, where simplicity becomes an advantage since it will lower the computational cost substantially [184]. Moreover, characterization of the high strain rate tests often requires extensive efforts. J-C provides well defined calibration procedures for the material constants that are used to construct flow and failure characteristics [84] [85]. Therefore, it is preferred for large scale FE analysis of high strain rate phenomena.

However; as it was mentioned in Section 1.2 before, phenomenological models are often tuned or calibrated for a specific test (e.g., uni-axial tension, shear or compression) to be able to match a particular test condition by utilizing single monotonic functions and it is assumed that the model will adequately predict different test conditions. Additionally, as illustrated in Figure 1-4, the failure locus of ductile materials can be very complex and cannot be represented by a single monotonic function. Therefore, when using J-C, there is a need to identify the experimental data set that the model was calibrated for. Depending on the details of the calibration, the data sets can affect the predictive performance of the FE analyses depending on target thickness, projectile impact speed and model mesh size.

In this section, ballistic impact predictive performance of four different sets of J-C material model parameters (i.e., Set-1, Set-2, Set-3 and Set-4) is compared. The four material model parameter sets were characterized for Al2024-T351 at different test conditions [41] [46] [58] [84] [85]. Therefore, it is expected to obtain different flow and

failure surface definitions for each set of material parameters that will lead to different ballistic limit predictions as the material thickness, impact speed and FE mesh size changes. The results of this section will be used as a justification of the requirement for a new material model that can provide a more generic flow and failure definition for the material independent of the mesh size.

3.2 **An examination of the state-of-the-arts: Explicit FE analysis of ballistic impact**

In this section, the methodology that is used to simulate ballistic impact tests is introduced. Details and sensitivities of the numerical models are discussed. Prediction capabilities of the ballistic impact tests by using FE simulations are presented

3.2.1 **Ballistic impact testing of 2024-T3/T351 aluminum material**

Numerous researchers have investigated the ballistic capabilities of aluminum alloys [22] [185] [186] [187] [188] [189] [190]. Data for this work is taken from experiments performed by Kelly and Johnson [57], who performed impact tests on 1.5875mm (1/16″), 3.175mm (1/8″) and 6.35mm (1/4″) thick plates. The 304.8mm (12″) by 304.8mm (12″) targets were supported in a steel target frame that was 50.8mm (2″) wide to ensure target rigidity. A 12.7mm (0.5″) diameter spherical projectile made of 52100 alloy tool steel was used for the impacts. Figure 3-1 illustrates the test setup for the ballistic impact tests.

Ballistic limits of Al2024-T3/T351 plates for three different thicknesses are summarized by Figure 3-2 by plotting input versus residual velocities of the projectiles. Typically, after the ballistic limit, the residual velocity rises sharply and later follows a 45 degree reference line, which is a characteristic property for many ductile materials [9] [184]. The ballistic limit for 1.5875mm plate was found to be about 122 m/s, for 3.175mm it was about 213 m/s and for 6.35mm it was about 411 m/s. It was shown that the aluminum plates failed by dishing and petalling with slight plugging for the thinnest targets. As the thickness increased, the amount of dishing and petalling decreased and the failure mode moved towards plugging. Consequently, the ballistic tests exhibited the transition of the failure mode with the change in thickness and impact velocity.

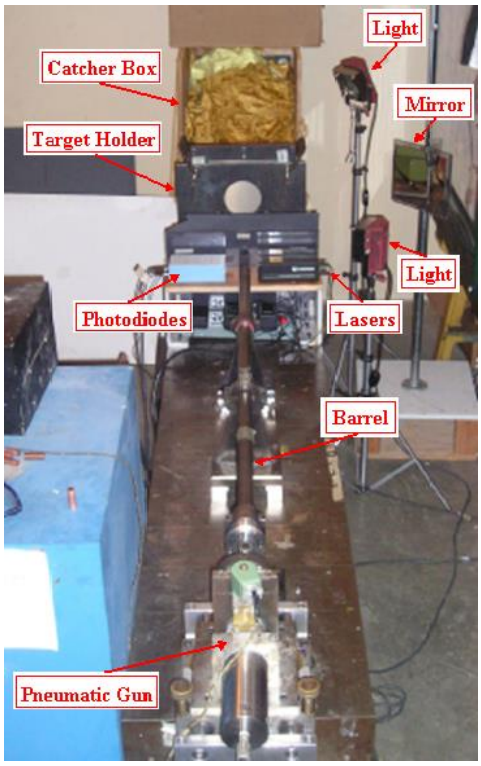

Figure 3-1: Experimental setup for ballistic impact testing for Al2024-T3/T351 plates.

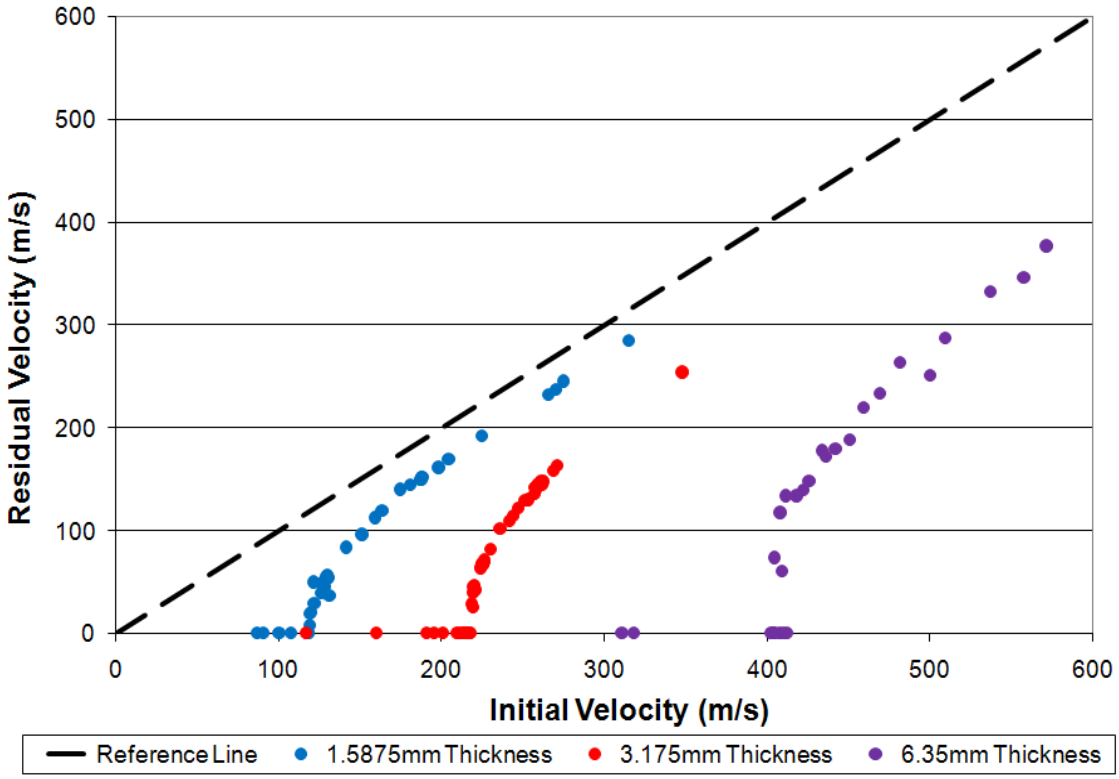

Figure 3-2: Ballistic limit for findings three different thickness 2024-T3/T351 target plates.

3.2.2 **Numerical modeling**

In order to predict the ballistic limits for Al2024-T351, FE models are developed. All numerical models in this study are developed to be used with LS-DYNA [191] [96] [192] as a non-linear explicit dynamics FE solver.

3.2.2.1 Finite Element Models

In non-linear FE analysis, simply refining the mesh does not necessarily improve the accuracy [15] [193] [194]. Moreover, there are no clear theoretical guidelines on the required mesh density for the range of impacts covered in this Chapter and the FE modeling process is user dependent [195]. Considering the effects of thermal softening, failure and plastic instabilities such as localization due to necking, FE models suffer from mesh dependency [196]. Moreover, it is a common practice to calibrate the material model parameters for a specific mesh size often by utilizing only a single test condition (e.g., uni-axial tension or simple shear) [41] [46] [85]. However, the calibrated mesh size, which is found by an ad-hoc manner, may not necessarily provide the optimum solution for an impact simulation considering several non-linear effects that were not taken into account during the calibration. Therefore, the only reasonable method to determine the most appropriate mesh size is 'trial-and-error' while comparing the results against a controlled test data. Subsequently, it is possible to arrive to an optimum mesh option after experimenting with different alternatives and draw some guidelines for a particular test case. Consequently, in this section, three different quarter symmetric FE models are developed to investigate their predictive performance. Each target thickness is modeled with three mesh densities. The mesh pattern and size dependency are examined to find an optimized mesh for stability, accuracy and efficiency of the impact analysis. These models are cost effective 3D models, where a nearly perfect hit with non-oblique projectile orientation can be modeled successfully. Since the target and the projectile are symmetric about both the horizontal and vertical axes, only one quarter models of the test target and the projectile are developed. Both the target and projectile are modeled with 8-node under-integrated hexagonal solid elements. Fully fixed boundary conditions are imposed on the outer boundary and the symmetry boundary conditions are imposed at the

other free surfaces. The mesh just under the projectile is chosen to be cylindrical to assure that the failure occurs along the element boundaries. Mesh patterns and model set-ups can be seen in Figures 3-3, 3-4 and 3-5 for three different thicknesses.

The mesh density under the impact zone is modeled with finer elements than the plate surrounding the impact zone. The in-plane mesh pattern is kept the same for all models while the element size through the thickness is varied. So, the number of elements is doubled with the increase in thickness. FE model information and corresponding element sizes are summarized in Table 3-1.

Table 3-1: Details of the finite element mesh.

Mesh type	Mesh-I			Mesh-II			Mesh-III		
Target thickness (mm)	1.5875	3.175	6.35	1.5875	3.175	6.35	1.5875	3.175	6.35
Total number of elements	1674	3348	6696	3348	6696	13392	6975	13950	27900
Number of elements; through the thickness	2	4	8	4	8	16	3	6	12
Number of elements; in-plane	837			837			2325		
Mesh size; through the thickness (mm/element)	0.79375			0.396875			0.529167		

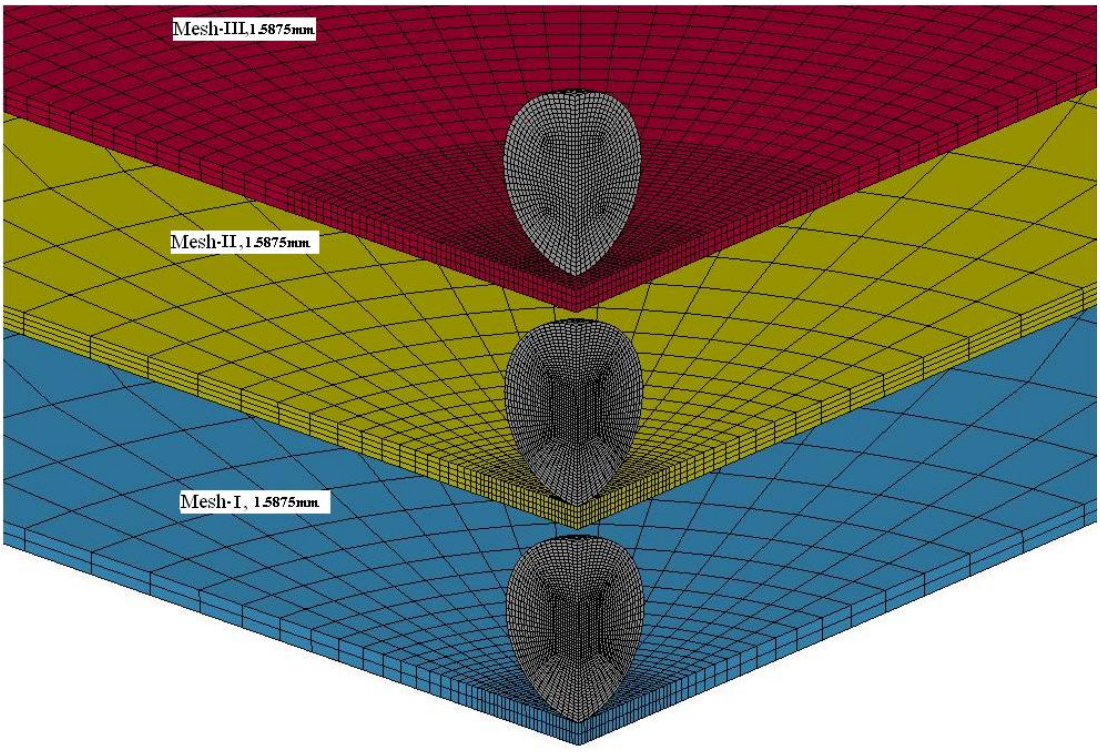

Figure 3-3: Mesh patterns for 1.5875mm thickness target.

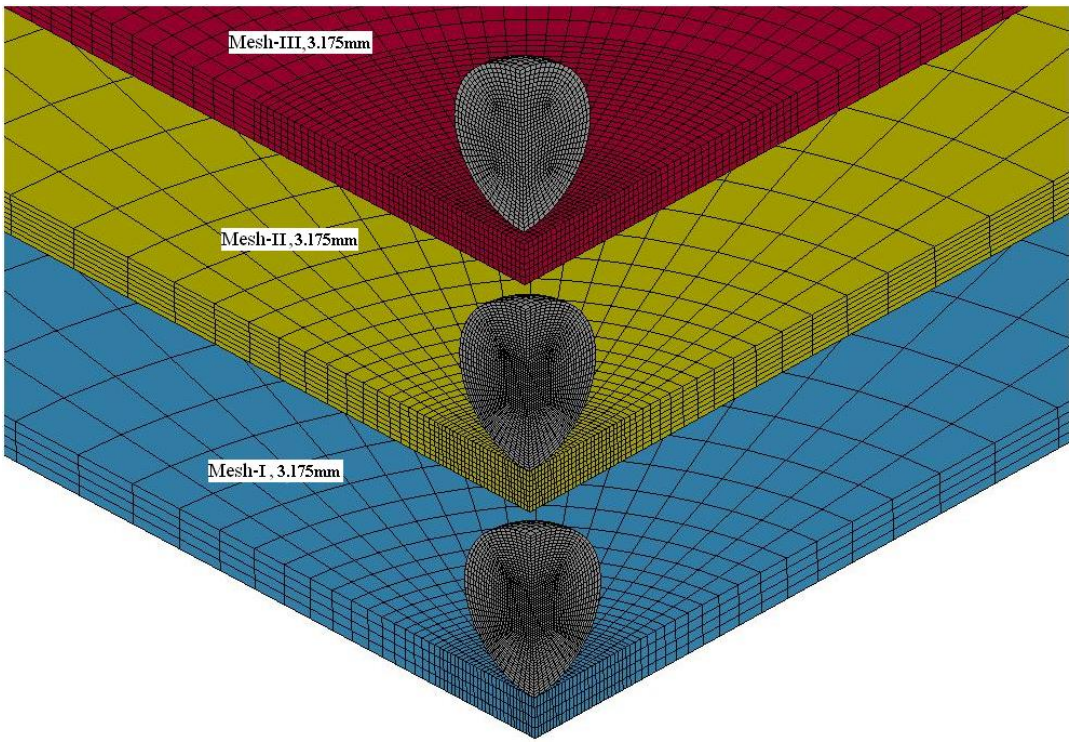

Figure 3-4: Mesh patterns for 3.175mm thickness target.

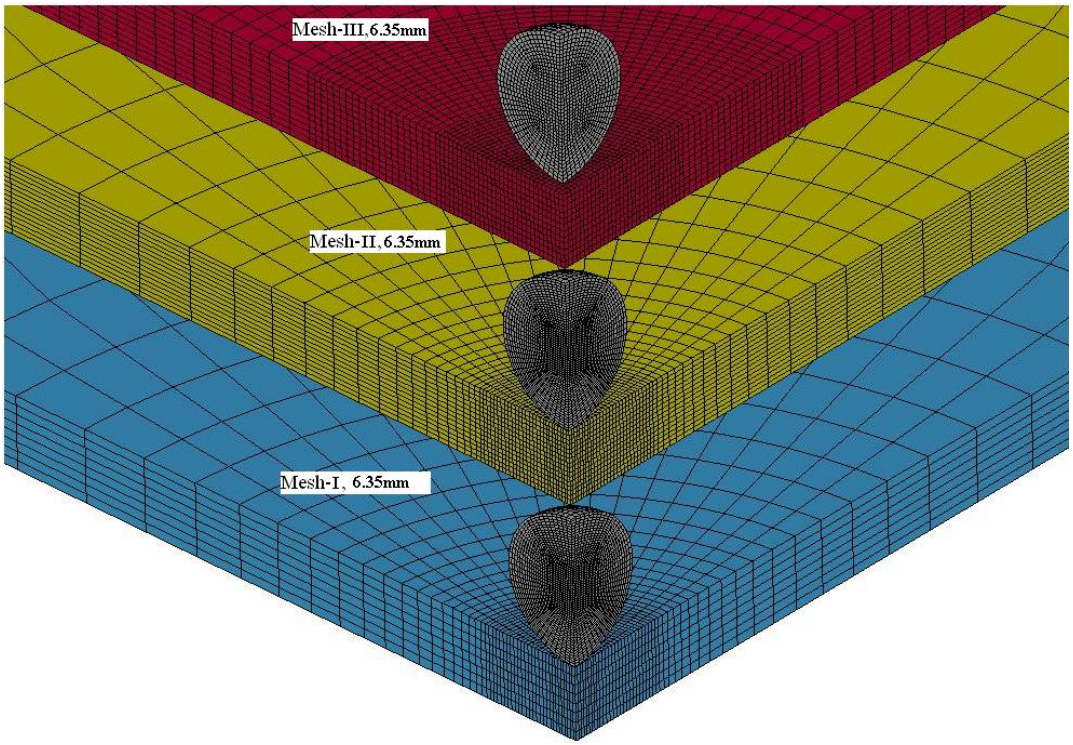

Figure 3-5: Mesh patterns for 6.35mm thickness target.

For Mesh-I and Mesh-II, as mesh patterns, 1.5875mm targets are modeled with 2 and 4 elements through the thickness respectively, where 3.175mm plate is modeled with 4 and 8 elements through the thickness and the 6.35mm plate is modeled with 8 and 16 elements through the thickness correspondingly. For Mesh-III, as mesh pattern, concentric circular layers of the target are divided into three regions in radial direction and the mesh density is gradually coarsening from inner region, which is the potential impact region, to the outer region. Mesh transition between regions are arranged to give less than 5:1 ratio to prevent stress wave reflections from the boundaries of successive regions [197] [198]. Three elements are used to model the through the thickness for the 1.5875mm target as a baseline since implementation of reduced integration solid elements requires at least three elements through the thickness to be able to capture accurate bending deformation modes.

Figures 3-3, 3-4 and 3-5 illustrate the close-ups of the 1.5875mm, 3.175mm and 6.35mm targets with the corresponding mesh patterns of Mesh-I, Mesh-II and Mesh-III, respectively.

Using under integrated elements can cause zero energy modes or hourglass modes in the analysis [15] [96] [192]. Especially at high speed impact simulations these modes can be excited and cause numerical instability. Therefore, a viscous based stabilization method is used during the simulations to prevent hourglass modes of the reduced integration elements. The amount of artificial energy is kept below 10% of the kinetic energy throughout the simulation.

Contact behavior between the projectile and the target is attained by using a penalty based single surface type contact algorithm that utilizes a nodal constraint formulation with an element erosion scheme [96] [192].

3.2.2.2 Material Models

The steel projectile is modeled by using linear elastic material model. The model does not allow plastic yielding but can have large deformations. Plasticity is unnecessary for this component, because neither the tests nor early runs showed any signs of yielding in the projectile [57]. A more sophisticated material model is necessary and is introduced in the next section for the targets to simulate ballistic impact response.

3.2.2.3 Johnson-Cook Material Model

The J-C strength model is an empirical equation and is widely used in practical impact simulations for its broad consideration of strain hardening, strain rate sensitivity and temperature weakening [93].

J-C phenomenological constitutive and failure model utilizes a multiplicative decomposition for the definition of the flow stress as:

$$\sigma_y = \left(A + B\left(\varepsilon_p\right)^n\right)(1 + C\ln\dot{\varepsilon}^*)(1 - T^{*m}) \tag{3.1}$$

where, $A,\ B,\ n, C$ and m are material constants that are characterized from temperature and strain rate dependent tests, ε_p is the effective plastic strain, $\dot{\varepsilon}^*$ is the normalized effective plastic strain rate that is typically normalized to a strain rate of $1.0s^{-1}$, T^* is the homologous temperature defined as:

$$T^* = \frac{T - T_{room}}{T_{melt} - T_{room}} \tag{3.2}$$

This material model is coupled with an accumulated damage model, where the failure is controlled by a damage parameter as:

$$D = \int_0^{\varepsilon_p^f} \frac{d\varepsilon_p}{\varepsilon_p^f} \tag{3.3}$$

The damage parameter accumulates in time until failure occurs when D reaches unity. The failure strain is defined as:

$$\varepsilon_p^f = [D_1 + D_2\exp(D_3\sigma^*)][1 + D_4\ln\dot{\varepsilon}^*][1 + D_5T^*] \tag{3.4}$$

where, D_1, D_2, D_3, D_4 and D_5 are material constants specific to failure that are characterized from temperature and strain rate dependent tests, σ^* is the stress-triaxiality defined as:

$$\sigma^* = \frac{p}{\sigma_{vm}} \tag{3.5}$$

where, p is the pressure and σ_{vm} is the von Mises stress defined as:

$$\sigma_{vm} = \sqrt{\frac{3}{2} S_{ij} S_{ij}} \tag{3.6}$$

where, S_{ij} is the deviatoric stress tensor defined as: $S_{ij} = \sigma_{ij} - \sigma_m \delta_{ij}$.

In this analysis, J-C is used in conjunction with Mie-Gruneisen Equation of State (EOS) model, which defines the pressure volume relationship in one of two ways, depending on whether the material is compressed or expanded. The Mie-Gruneisen EOS with cubic shock velocity-particle velocity defines pressure for compressed materials as:

$$p = \frac{\rho_0 C_{sp}^2 \mu \left[1 + \left(1 - \frac{\gamma_0}{2}\right)\mu - \frac{a}{2}\mu^2\right]}{\left[1 - (S_1 - 1)\mu - S_2 \frac{\mu^2}{\mu + 1} - S_3 \frac{\mu^3}{(\mu + 1)^2}\right]} + (\gamma_0 + a\mu) E_{int} \tag{3.7}$$

and for expanded materials as:

$$p = \rho_0 C_{sp}^2 \mu + (\gamma_0 + a\mu) E_{int} \tag{3.8}$$

where, E_{int} is internal energy, C_{sp} is the intercept of the particle velocity, shock velocity (vs-vp) curve; $S_1 - S_3$ are the coefficients of the slope of the vs-vp curve, γ_0 is the Gruneisen gamma, a is the first order volume correction to γ_0, and $\mu = \frac{\rho}{\rho_0} - 1$.

Different J-C material model parameters are found in literature for Al2024-T351 depending on the range of application and characterization methodologies. These

differences can be found both on the flow surface and failure curves. The differences on the flow surface are mainly due to the type of characterization tests, where shear and tensile tests are utilized for different ranges of strain rates. The differences on the failure curves are mainly due to length scales, where materials at different thicknesses are utilized for the calibration of the failure parameters. Four different sets of material model parameters [41] [46] [58] [84] [85] that are listed in Table 3-2 for Al2024-T351 are used in this Chapter. These sets of material model parameters are utilized to evaluate their predictive performance on the ballistic limit prediction while the material thickness changes along with the impact speed and element size as described in Section 3.2.2.1.

The first set of material model parameters, which is named as Set-1, is taken from the two papers by Johnson and Cook [84] [85] for Al2024-T351. These two papers are the initial papers where the J-C material model was introduced with parameters characterized for several different materials. Quasi-static and dynamic torsion tests were used to characterize the flow surface for Set-1, where the range of the strain rates was from quasi-static to $400s^{-1}$. The model was extrapolated beyond this range [84].

The second set of material model parameters, which is named as Set-2, suggests a different flow surface with different material parameters characterized from different tests [41] while adapting the same failure curve parameters from the paper by Johnson and Cook [85]. The flow surface for Set-2 was characterized through quasi-static and Split Hopkinson Bar (SHB) experiments on tension and compression samples [41]. The compression rates were conducted at rates up to $4000s^{-1}$ and tension rates were conducted at rates up to $8000s^{-1}$. Set-3 and Set-4 use the same flow surface suggested by Set-2.

The differences between the two flow surfaces are illustrated in Figure 3-6 for both strain rate hardening (at room temperature) and temperature softening (at a nominal strain rate of $1s^{-1}$) behaviors. These flow surfaces are constructed by plugging in the material model parameters from Set-1 [84] and Set-2 [41] (also Set-3 and Set-4), which are listed in Table 3-2, into Equation (3.1). Figures 3-6(a) and 3-6(b) illustrates the hardening characteristics of the flow surfaces at room temperature through the logarithmic strain rate axis. For illustration purposes, upper limit of the strain rates for both sets of parameters (i.e., Set-1 and Set-2) are plotted up to $5000s^{-1}$. Under the condition that a

finite element might experience higher strain rates during the simulation, J-C model calculates and utilizes any strain rate based on Equation (3.1).

Table 3-2: Sets of J-C material model parameters.

Parameters	Notation	Set-1 [84] [85]	Set-2 [41]	Set-3 [46]	Set-4 [58]
Strength Parameters					
Density [kg/m^3]	ρ	2770	2770	2770	2770
Poisson Ratio	ν	0.33	0.33	0.33	0.33
Modulus of Elasticity [MPa]	E	73084	73084	73084	73084
Static Yield Limit [MPa]	A	265	369	369	369
Strain Hardening Modulus [MPa]	B	426	684	684	684
Strain Hardening Exponent	n	0.34	0.73	0.73	0.73
Strain Rate Coefficient	C	0.015	0.0083	0.0083	0.0083
Thermal Softening Exponent	m	1.0	1.7	1.7	1.7
Reference Temperature [K]	T_{room}	294	294	294	294
Melting Temperature [K]	T_{melt}	775	775	775	775
Specific Heat [J/kg-K]	c_P	875	875	875	875
Failure Parameters					
D_1		0.13	0.13	0.112	0.31
D_2		0.13	0.13	0.123	0.045
D_3		1.5	1.5	1.5	1.7
D_4		0.011	0.011	0.007	0.005
D_5		0	0	0	0
Mie-Grunesien EOS Parameters					
S_1		1.338	1.338	1.338	1.338
S_2		0	0	0	0
S_3		0	0	0	0
γ_0		2	2	2	2

Specific strain rates are highlighted in Figures 3-6(a) and 3-6(b) for better illustration of the flow. These highlighted hardening curves are projected on to the flow stress versus effective plastic strain plane as illustrated in Figure 3-7 for a better comparison of the two surfaces. Figures 3-6(c) and 3-6(d) illustrates the softening characteristics of the flow surfaces at a nominal strain rate of 1 s^{-1} beginning with room temperature (i.e., 294K), up to the melting temperature (i.e., 775K). Set-1 and Set-2 material parameters from Table

3-2 are utilized and Equation (3.1) is employed to construct the flow surfaces. Hardening curves at specific temperatures are also highlighted for better illustration of the flow. Highlighted curves are projected on to the flow stress versus effective plastic strain plane as illustrated in Figure 3-8 for a better comparison of the two surfaces. The effects of the flow surface on the ballistic impact response during the finite element simulations are discussed in this Chapter through the proceeding sections.

The third set of material model parameters, which is named as Set-3 in Table 3-2, suggests a different failure curve with different material model parameters [46] while adapting the same flow surface parameters from the report by Lesuer [41]. The significance of this failure curve was the characterization procedure. Ballistic impact tests were utilized to characterize the failure curve for relatively thinner targets.

The fourth set of material model parameters, which is named as Set-4 in Table 3-2, also suggests a different failure curve characterization with different material parameters [58] while adapting the same flow surface parameters from the report by Lesuer [41]. Set-4 differs from Set-3 in failure curve parameters that were calibrated for thicker samples.

It is reported that the type of failure mode is subjected to change from petaling to plugging due to the change in thickness and impact velocity, where the state-of-stress is found to be a major concern [57]. Therefore, the same set of failure parameters may not necessarily be appropriate for the whole range of material thicknesses and impact velocities [42] [58]. Consequently, calibration of the failure parameters is necessary to find the best set of parameters that can work reasonably well for the rest of the stress-states and predict the failure strain appropriately.

Three different sets of failure model parameters are listed in Table 3-2 for Set-1, Set-3 and Set-4 (Set-2 uses the same failure parameters with Set-1). The failure locus can be obtained by utilizing Equation (3.4) and plugging in the failure parameters.

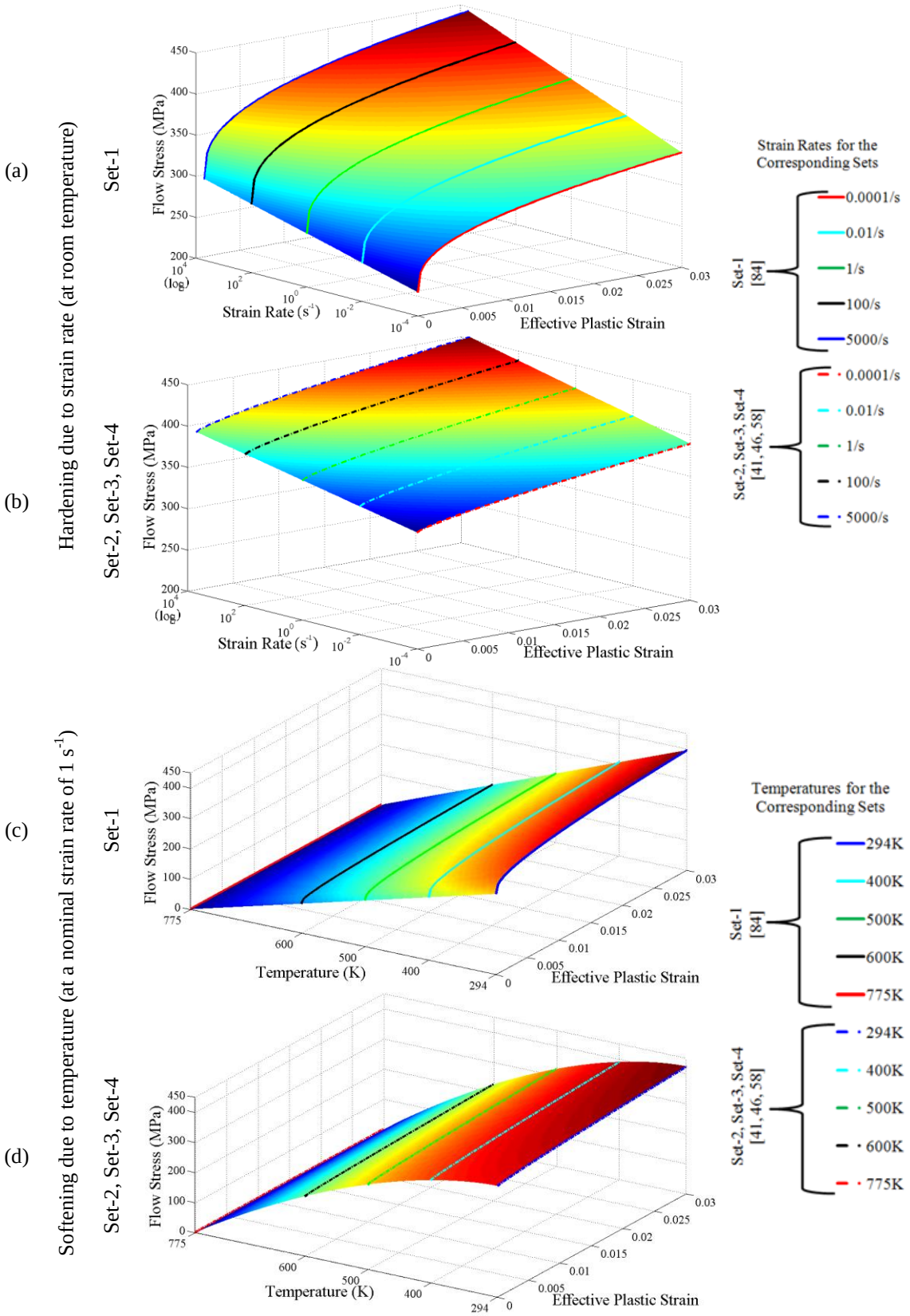

Figure 3-6: Differences in flow surfaces depending on the sets of material model parameters; hardening for (a) Set-1 and (b) Set-2, 3 and 4; softening for (c) Set-1 and (d) Set-2, 3 and 4.

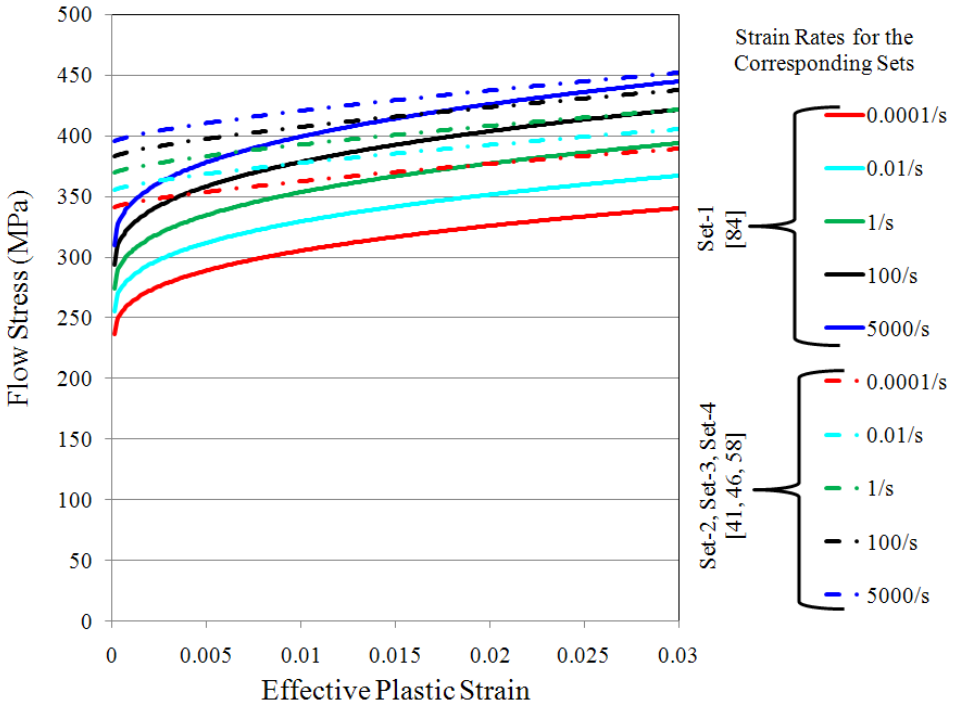

Figure 3-7: Strain rate dependent hardening curves defining different flow surfaces for 2024-T3/T351 resulting from different J-C parameter sets at room temperature.

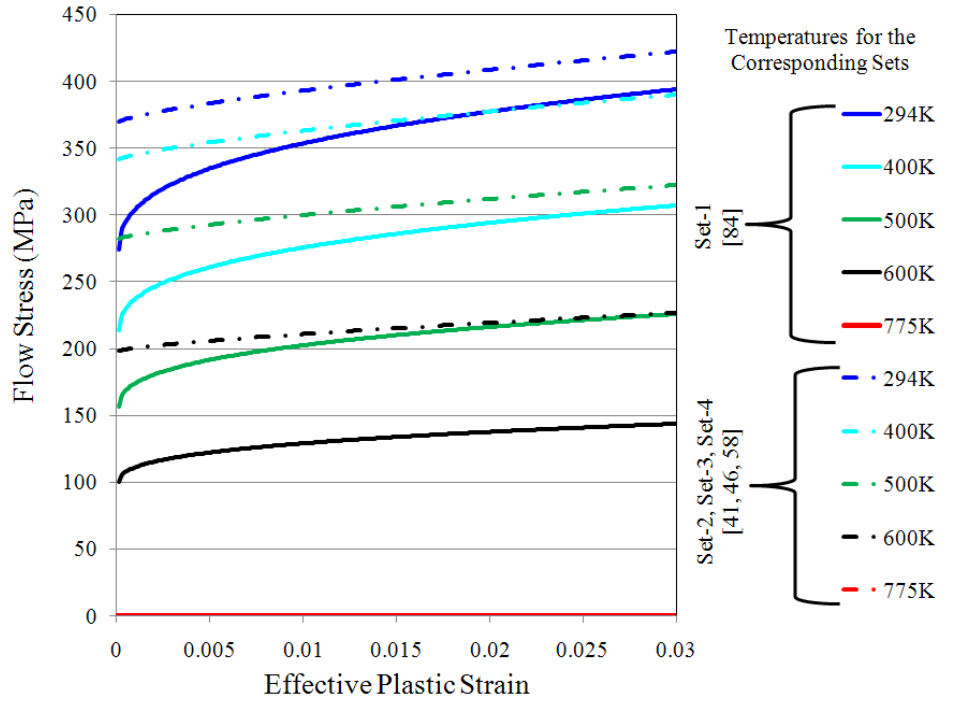

Figure 3-8: Temperature dependent hardening curves defining different flow surfaces for 2024-T3/T351 resulting from different J-C parameter sets at a nominal strain rate of 1 s^{-1}.

The differences in fracture loci are illustrated in Figure 3-9 with respect to stress-triaxiality $\sigma^* = \frac{p}{\sigma_{vm}}$ at a nominal strain rate of 1.0 s^{-1} at room temperature. Set-3 and Set-4 differ from the rest by considering a recalibration of the parameters with the ballistic impact test results [46] [58]. It is shown by Equation (3.4) that the failure model fits an exponential monotonic curve for the calibration purposes and expected to behave differently under different states-of-stress. A single FE element can experience different states-of-stress during the impact. Depending on the set of parameters used for the simulation, the element may fail early if the state is in tension or shear when Sets-1, 2 and 3 is used compared to Set-4. For instance, if a uni-axial tension case is considered for a single element with a triaxiality of $\sigma^* = -\frac{1}{3}$ and a nominal strain rate of 1.0 s^{-1} at room temperature, the corresponding failure strain values will be calculated by utilizing Equation (3.4) for different sets in Table 3-2 as:

$$
\begin{aligned}
&\Longrightarrow \sigma^* = -\frac{1}{3}, \dot{\varepsilon}^* = 1s^{-1} \\
&\Longrightarrow \varepsilon_p^f = [D_1 + D_2 \exp(D_3 \sigma^*)][1 + D_4 \ln \dot{\varepsilon}^*][1 + D_5 T^*] \\
&\Longrightarrow \text{Table } 3-2 \text{ for } D_1, D_2, D_3, D_4 \text{ and } D_5 \\
&\text{Set} - 1 \Longrightarrow \varepsilon_p^f = \left[0.13 + 0.13 \exp\left((1.5)\left(-\frac{1}{3}\right)\right)\right] \approx 0.2088 \\
&\text{Set} - 2 = \text{Set} - 1 \Longrightarrow \varepsilon_p^f \approx 0.2088 \\
&\text{Set} - 3 \Longrightarrow \varepsilon_p^f = \left[0.112 + 0.123 \exp\left((1.5)\left(-\frac{1}{3}\right)\right)\right] \approx 0.1866 \\
&\text{Set} - 4 \Longrightarrow \varepsilon_p^f = \left[0.31 + 0.045 \exp\left((1.7)\left(-\frac{1}{3}\right)\right)\right] \approx 0.3355
\end{aligned}
\tag{3.9}
$$

As it is demonstrated in Equation (3.9), even for a simple uni-axial tension case, the failure strains for a single element may change drastically depending on the set of material parameters.

Equation (3.4) also comprises a strain rate and temperature dependent term, where the failure locus is offset according to the amount of strain rate and temperature. Figure 3-10

illustrates strain rate dependency on the failure loci for three different sets of failure parameters. As it can be observed from the figure, the amount of effective plastic strain that is required to fail a finite element increases with the strain rate. For demonstration purposes, Figure 3-10 is plotted up to a strain rate of 5000 s^{-1}, where for higher strain rates J-C model calculates the corresponding offset distance according to Equation (3.4).

None of the references, where the material model parameter sets were cited from, have conducted failure tests depending on the temperature. Therefore, no temperature dependent term was suggested for the failure parameters in Table 3-2. However, assuming that effective plastic strain at failure is fully dependent on the homologous temperature (i.e., $D_5 = 1$), Figure 3-11 illustrates how Equation (3.4) can offset the failure loci up to the melting temperature.

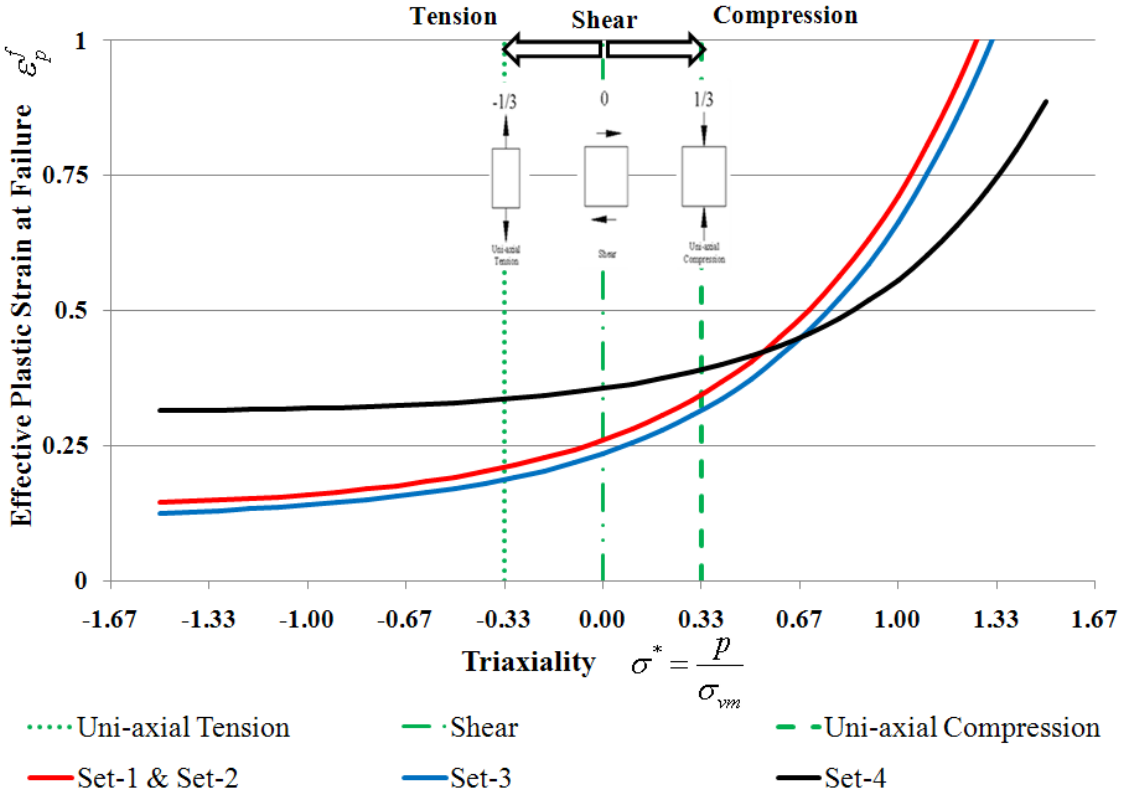

Figure 3-9: Differences in the failure loci for 2024-T3/T351 resulting from different J-C parameter calibration from different tests.

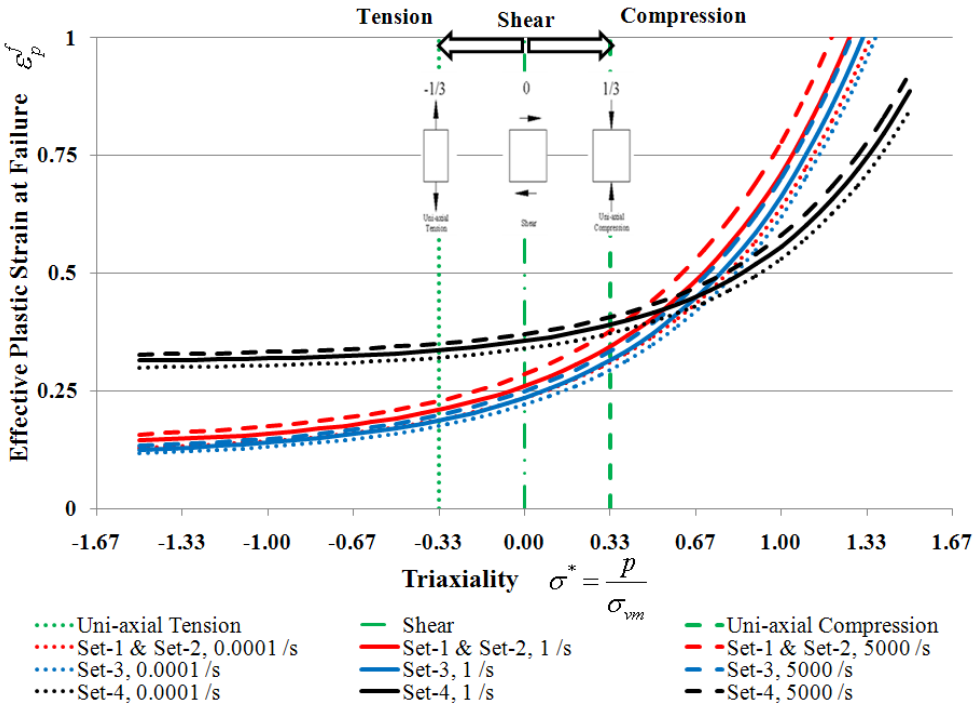

Figure 3-10: Strain rate dependent failure loci comparing different sets of J-C parameters.

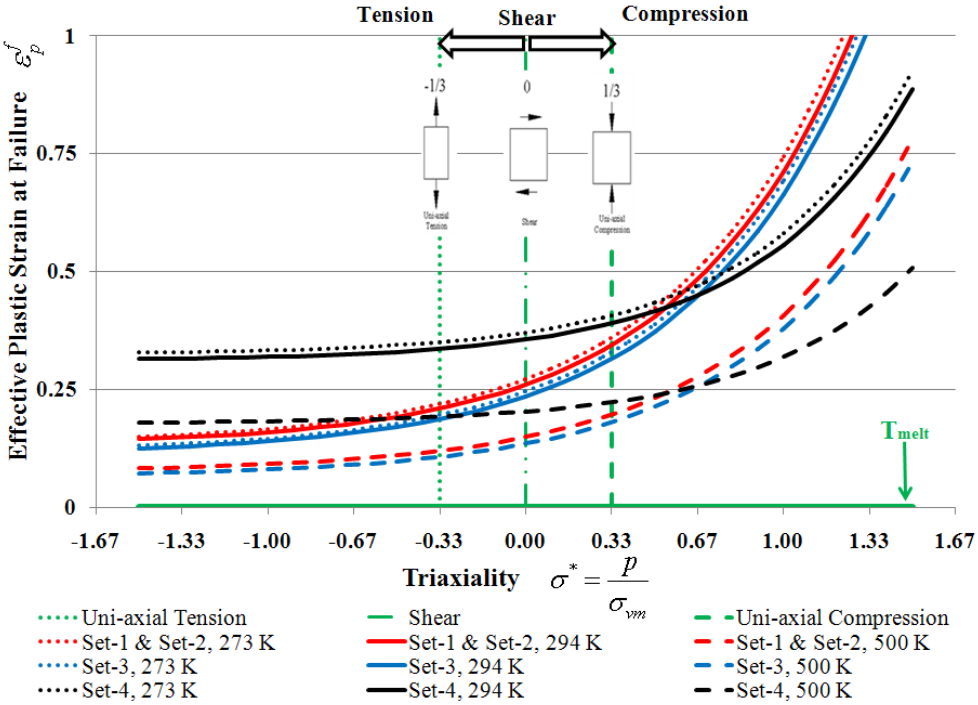

Figure 3-11: Temperature dependent failure loci comparing different sets of J-C parameters.

3.2.3 **Ballistic impact simulation results**

Ballistic impact response for three different material thicknesses is examined with different meshing options and by employing four different material model parameters from Table 3-2 representing two flow surfaces and three failure loci. The responses are illustrated by generating initial velocity versus residual velocity graphs, where they can be compared to the ballistic test data. The "Reference" line that is overlaid in each graph represents the condition if impact and exit velocities are the same, which indicates no loss in the initial kinetic energy. Therefore, the distance between the reference line and the data line can be accepted as the velocity or energy lost during the penetration [77] [12] [9].

3.2.3.1 Results for target thickness 1.5875mm

The penetration through 1.5875mm aluminum target is illustrated in Figure 3-12. A petaling type of deformation mode is observed. There is significant local bending in the target and material fails mostly in tension. It should be noted that the plug is pushed out in front of the sphere, and there are four radial cracks in the target. The failure mode, the plug formation and the radial cracks all correspond well with the test results.



(a) (b) (c)

Figure 3-12: Penetration through 1.5875mm target and petal formation; (a) Simulation, (b) Test-Front Face, (c) Test-Rear Face.

The comparison between the measurements and computations is shown in Figure 3-13 for the entire ballistic limit test matrix. It can be observed that the Set-3 material data

gives excellent correlation, where the rest of the material model parameters with different flow surface and failure parameters do not agree as well with the test results and demonstrate mesh sensitivity.

Set-4 material model parameters over predicts the ballistic limit. This can be explained by the fact that the failure parameters were adjusted for thicker targets [58] and may not necessarily be appropriate for thinner samples.

A better correlation is seen with Set-2 material model parameters compared to Set-1 material model parameters when using the same mesh pattern. This can simply be explained by the differences in the flow surface since both sets utilize the same failure locus. The range of strain rates observed during a high speed impact exceeds the ranges used during the material characterization of Set-1 [84]. Set-2 material model parameters were characterized for higher ranges of strain rates [41]. Therefore, Set-2 and Set-3 surface is found to be more accurate in simulating high speed impact tests for this target thickness.

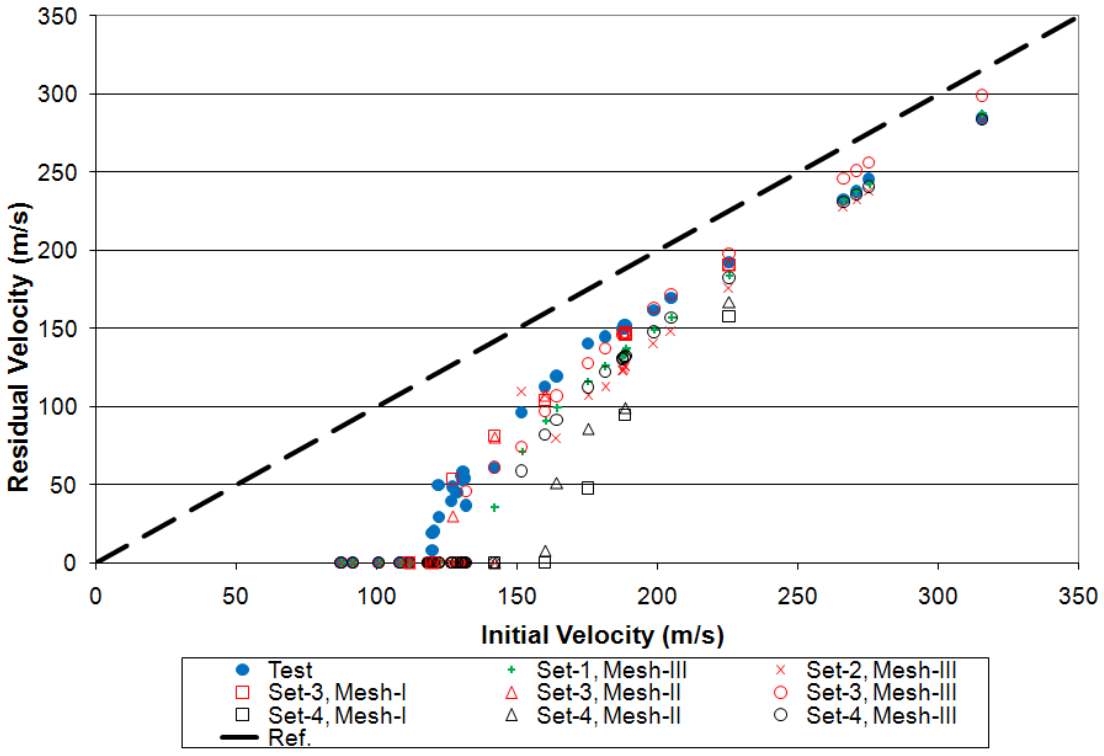

Figure 3-13: Ballistic limit predictions for 1.5875mm targets.

Even though, the effects of material model parameters are found to be more significant than the effects of mesh size, Mesh-III is found to provide the best results and Mesh-I is found to be the least successful overall. This can be explained by the fact that using two reduced integration elements through the thickness is not enough in predicting bending behavior. Moreover, Mesh-III has more in plane elements that can provide better representation of the petalling than Mesh-II.

3.2.3.2 Results for target thickness 3.175mm

The penetration through 3.175mm aluminum target is shown in Figure 3-14. The projectile penetrates through the target in a mixed failure mode: partly petaling and partly plugging. There is some local bending and some local shearing in the target, where the material fails partially in shear and partially in tension. Note that a plug is pushed out in front of the sphere and the size of the radial cracks in the target gets smaller. The failure mode and plug formation correspond with the test results.

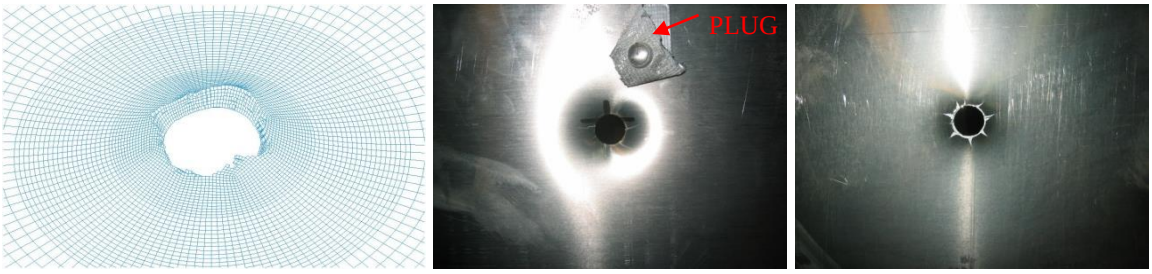

(a) (b) (c)

Figure 3-14: Penetration through 3.175mm target and mixed-mode failure formation; (a) Simulation, (b) Test-Front Face, (c) Test-Rear Face.

The comparison between the measurements and computations is shown in Figure 3-15 for the entire ballistic limit test matrix. Simulations with Set-1, Set-2 and Set-3 material model parameters show a poor correlation with the test data for all three mesh patterns. Since the failure parameters were tuned for thinner samples, these three sets of material model parameters under-predict the ballistic limit. Set-4 material model parameters, with failure parameters for thicker plates, agree better with the test results.

Set-4 material model parameters with Mesh-I and Mesh-II over-predict the ballistic limit, where Mesh-III with more in-plane elements provides better correlation. Set-2, Set-3 and Set-4 show relatively better results compared to Set-1 due to better high strain rate characterization.

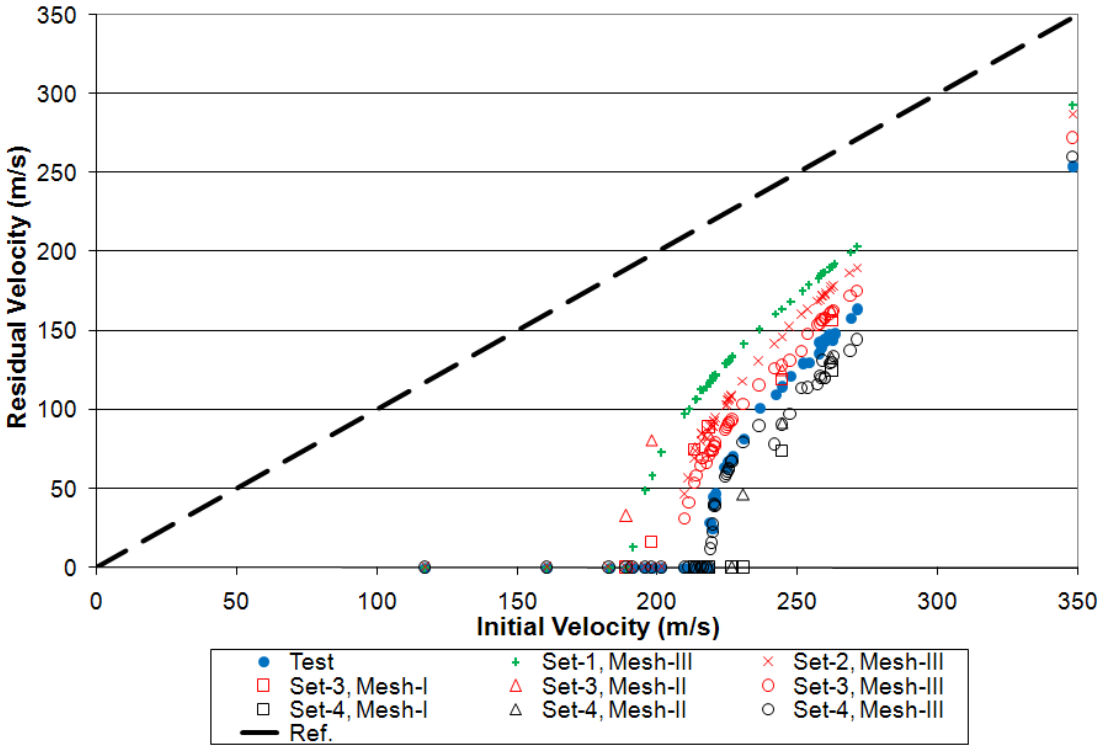

Figure 3-15: Ballistic limit predictions for 3.175mm targets.

3.2.3.3 Results for target thickness 6.35mm

The penetration through 6.35mm aluminum target is illustrated in Figure 3-16. The projectile penetrates through the target in plugging mode. The material fails entirely in shear. It is noted that a plug is pushed out in front of the sphere, and there are no radial cracks in the target. The failure mode and the plug formation correspond with the test results.

The comparison between the measurements and computations is shown in Figure 3-17 for the entire ballistic limit test matrix. Simulation results with Set-1, Set-2 and Set-3 material model parameters give a poor match with the test. However, results with Set-4

material model parameters are much better due to the failure model calibration for thicker targets.

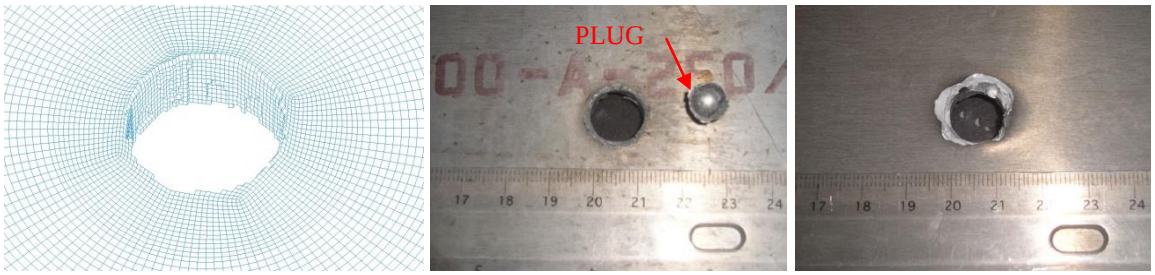

(a) (b) (c)

Figure 3-16: Penetration through 6.35mm target and plug formation; (a) Simulation, (b) Test-Front Face, (c) Test-Rear Face.

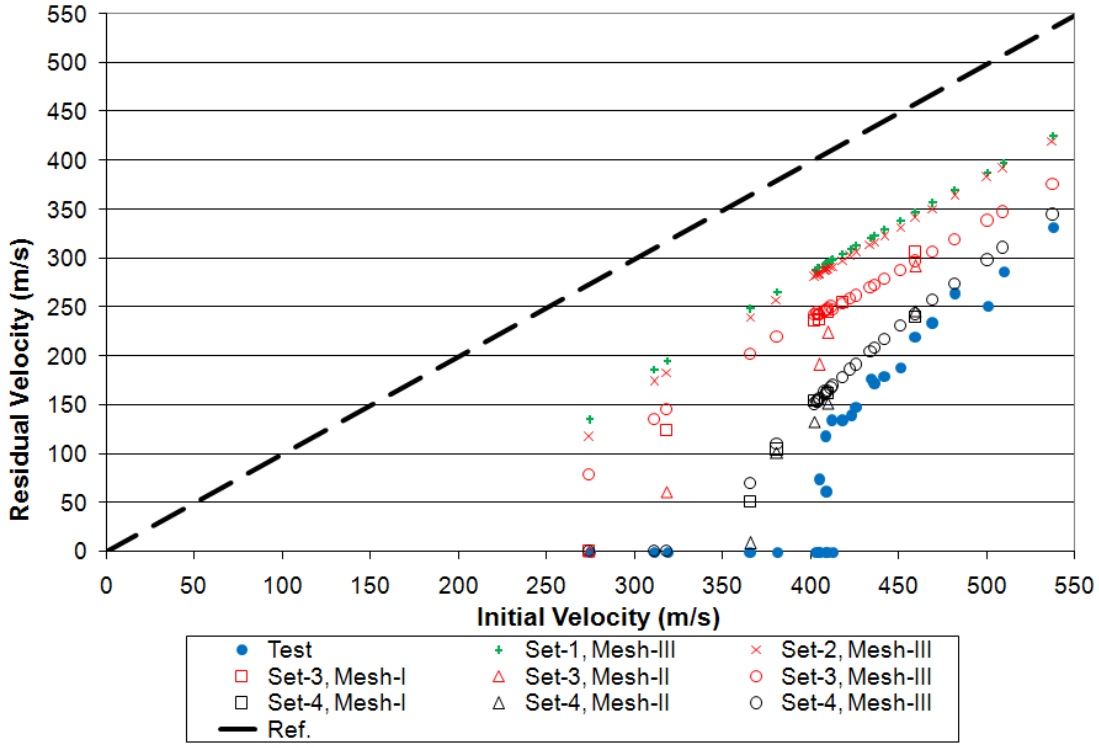

Figure 3-17: Ballistic limit predictions for 6.35mm targets.

3.2.4 **Ballistic impact simulation summaries and discussion**

Predictive performance of the ballistic limit for four different sets of material model parameters and three different mesh patterns are assessed. A summary of the ballistic limit predictions can be seen in Figure 3-18 for the best mesh pattern options of Set-1 and Set-2 (i.e., Mesh-I and Mesh-III, respectively), and all mesh patterns for Set-3 and Set-4. The predictive performance of the simulations for 1.5875 mm target thickness is found promising for all parameters except for the Set-4, which is expected since this particular set was tuned for the thicker targets. However, when the material thickness increases, the accuracy is no longer satisfactory compared to the experimental results. All sets of material model parameters, independent of the mesh pattern, under predict the ballistic limit for 6.35 mm target thickness. Overall prediction performance of Set-2, Set-3 and Set-4 are found to be more than Set-1 considering that the flow surface of these sets was calibrated for higher strain rates. It is observed in Figure 3-18 that, as the failure mode changes from petalling to plugging, none of the failure loci were able to predict this transition accurately.

Figure 3-19 illustrates the change in the failure mode from petalling (tension) into plugging (shear) by plotting the history of effective plastic strain at failure as a function of triaxial state-of-stress for three representative finite elements from the failure zone of each target thickness. Failure loci that were characterized through exponential curve fitting for J-C failure model and illustrated in Figure 3-9 are also plotted in Figure 3-19 for a comparison of the stress-state histories of these three representative finite elements that have failed. It is found for plates under impact loading that with varying target thickness and impact speed, failure profoundly depends on multi-axial state-of-stress.

For a target thickness of 1.5875 mm, three representative elements show that the average history of triaxiality stays principally below uni-axial tension point (i.e., $\sigma^* < -\frac{1}{3}$). For thicker targets (i.e., 3.175 mm and 6.35 mm) the average history of triaxiality approaches and exceeds the shear point (i.e., $\sigma^* \Longrightarrow 0$). It can be concluded that, as the thickness changes (also with the increase in ballistic limit), the type of failure changes drastically from petalling (bending and necking) to plugging (shearing).

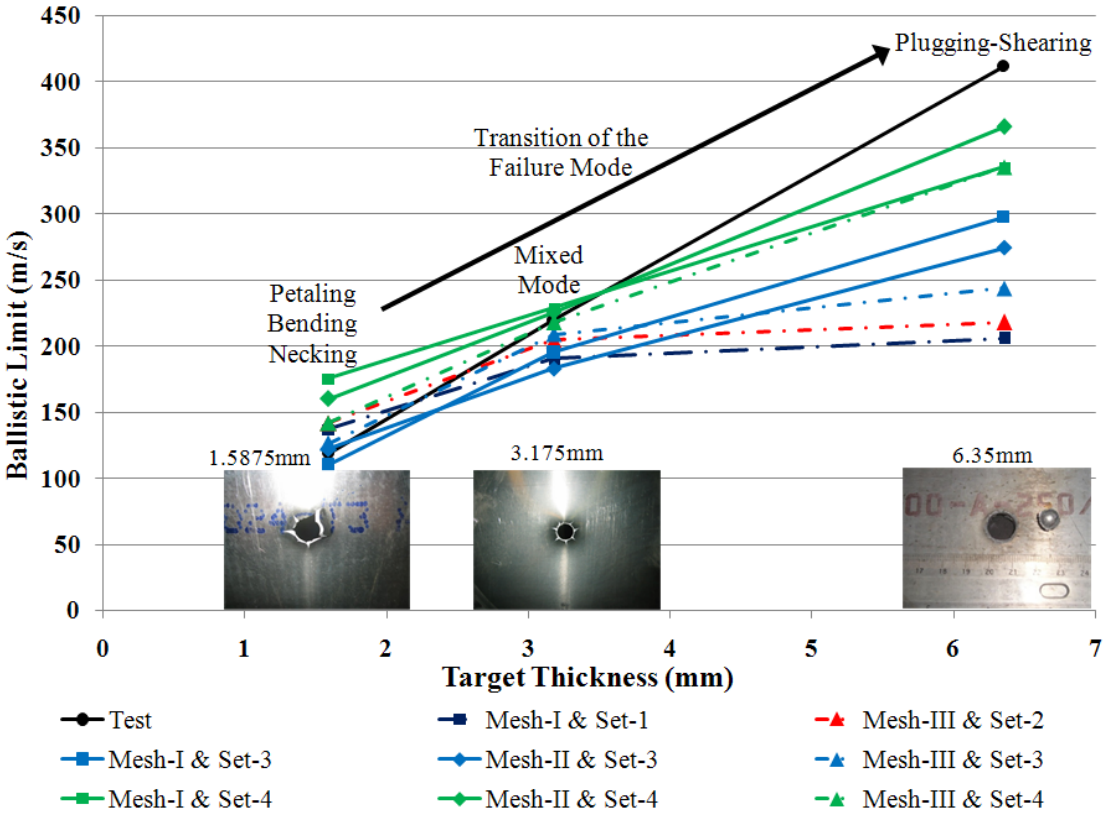

Figure 3-18: Ballistic limit predictions due to the transition of the failure modes with respect to target thickness.

It should be noted that the failure loci, which are illustrated in Figure 3-19, are plotted for a nominal strain rate of 1 s^{-1} and the finite elements that are chosen from the impact zone and failing are clearly experiencing higher strain rates. Therefore, the accumulated plastic strains at failure are shown to be exceeding (i.e., above the failure curve) the illustrated failure loci with an offset distance depending on the actual strain rate that an individual finite element experiences. Figure 3-10 illustrates how J-C relation is used to offset the failure loci depending on the strain rate.

It can be seen from these comparisons that the oscillatory evolution of the histories of the state-of-stress and transition of the failure mode may not necessarily be represented by a single monotonic function, which is often calibrated only for a single stress-state.

Thickness (mm)	Failure Mechanism	Illustration of the Failure Modes and the Corresponding States-of-Stress for the Elements at Failure
1.5875	Petalling Bending Necking	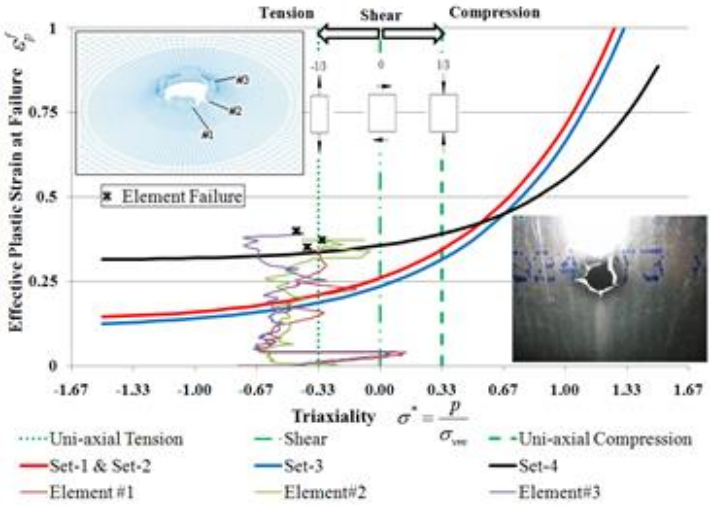
3.175	Mixed-mode	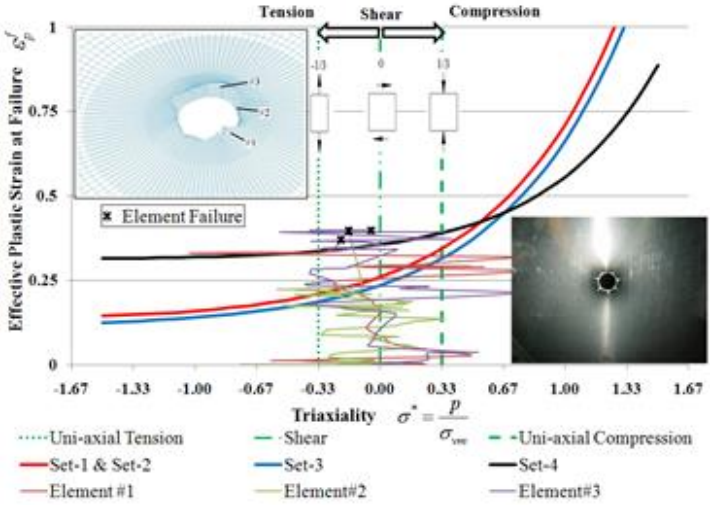
6.35	Plugging Shearing	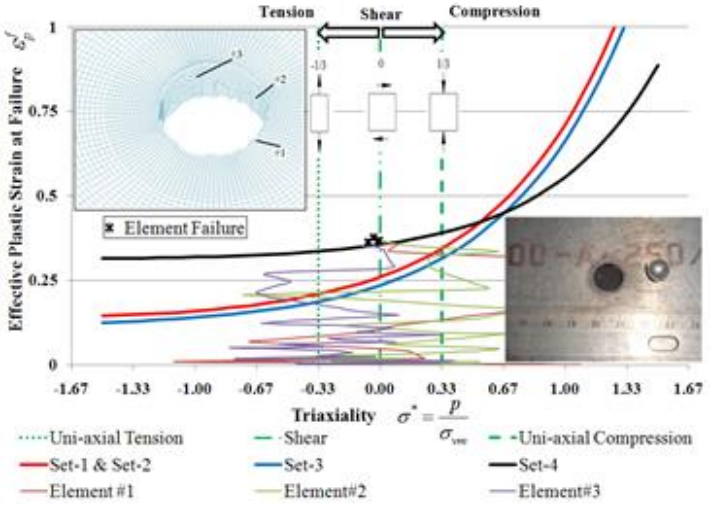

Figure 3-19: Transition of the failure modes depending on the state-of-stress based on target thickness.

3.3 **Summary**

In this Chapter, ballistic impact simulations of Al2024-T351 are carried out by utilizing J-C model since it is almost always used as a comparison or benchmark standard for new material model development. It is shown that J-C failure model, which uses an exponential function to construct the failure locus based on stress-triaxiality, is not always successful in predicting strains at failure accurately.

Material model parameters for J-C are calibrated for a particular material gauge length and for a particular test condition, which gives a particular stress-state. These parameters cannot be adjusted or tuned according to the changes and transitions in deformation and failure. Consequently, it is expected to have some compromise in the predictive performance if the transition happens by an alteration in the test condition and the stress-state changes. These alterations can be in the form of a change in material thickness, impact speed and orientation or the shape of the impacting object.

It is also shown that the in-plane or through the thickness mesh sensitivities are depending on the material model parameters. It is found that the set of material model parameters that are tuned for a specific element size gives better accuracy. Consequently, increasing the element density does not improve the performance significantly. Therefore, it is necessary to recalibrate the J-C damage parameters for a given element size in order to attain a better consistency between simulations and the ballistic limit measurements. However, even if the parameter sets are recalibrated, transition of the failure mode makes it difficult to capture the change in deformation and failure by using a single set of parameters as illustrated in Figure 3-19.

The phenomenological models and J-C in particular, with predetermined functions for flow and failure cannot provide a generic solution for a wide range of deformation and failure behavior. Therefore, it is justified that a regularized (mesh size independent) material model is needed with generic tabulated inputs of flow surface as functions of strain rate and temperature dependent hardening curves coupled with a failure locus that can cover a wider range of state-of-stress, strain rate and temperature. The following Chapter describes the details of the proposed material model.

CHAPTER 4 - **Methodology**

4.1 **Introduction**

The predictive capability of material models for ductile metals under impact loading predominantly depends on accurate representation of flow and failure surfaces and mesh regularization as depicted in the previous Chapter. Figures 3-14 and 3-15 represents the drawbacks of a commonly used material model. Like all phenomenological models that utilize predetermined functions to define flow and failure characteristics, J-C is also limited to the space characterized through a set of parameters with an exponential curve fitting. However, as it can be seen from Figures 3-14 and 3-15, one unique set of J-C parameters can only predict failure either in a single state of tension, shear or compression and cannot cover all. Therefore, with a set of parameters that is characterized through simple uni-axial tests, which is usually the general practice, a single FE that experiences different states-of-stress other than tension (e.g., shear or compression) will not be able to predict failure accurately. Moreover, the parameters that are incorporated for the material model are subject to mesh dependency, especially under softening and failure.

Therefore, a new material model is formulated in this Chapter that will address the shortcomings of existing technology and provide a generic tool for predicting failure under impact loading for ductile materials. A clear description of the preliminaries of stress tensor and its invariants is presented in Appendix-A to help the derivation of the material model in the proceeding section.

Most phenomenological strength models formulate flow rules as a function of several state and history variables as:

$$\sigma_y = f\left(\varepsilon_p\ , \dot{\varepsilon}_p, T\right) \tag{4.1}$$

where, ε_p is the plastic strain, $\dot{\varepsilon}_p$ is the plastic strain rate and T is the temperature.

These models are preferred due to their convenient way of programming, requiring only a limited number of material characterization variables and their computational efficiency. On the other hand, it is assumed that an adequate precision in material

characterization can be achieved [199]. Characterization of fully coupled thermo/mechanical plasticity can be very challenging. Most of the models do not use directly tabulated test results due to the concerns about computational cost. Therefore, often material model parameters are ignored, extrapolated or even guessed. However, with the progression in computational mechanics and as the cost of high performance computational resources becomes affordable and widely accessible, implementation of fully tabulated material input data can be achievable. In this Chapter, a multiplicative decomposition of the flow surface is adopted.

Most of the existing failure models utilize simple monotonic functions based on limited test data to fit a failure locus for the material. Bao [99] and Bao and Wierzbicki [100] postulated a new approach to solve the monotonic curve fitting problem by employing three different zones for curve fitting and characterizing failure points of specimens with different geometries that revealed good information about the stress-states on the stress-triaxiality space. Based on Bao's experiments, it is clearly seen in Figure 4-1 that the failure of Al2024-T351 can only be modeled by utilizing different curve fitting methods for different ranges of the stress-triaxiality. That method may not be applicable to other materials when different numbers of zones are encountered and shapes of the curves may not necessarily be compatible. Moreover, these former approaches utilize only stress-triaxiality for characterization of the failure locus, where J-C model also considers strain rate and temperature effects. Therefore, plastic strain at failure can generally be represented in the form of:

$$\varepsilon_p^f = f\left(\sigma^*, \dot{\varepsilon}_p, T\right) \tag{4.2}$$

where, σ^* is the stress-triaxiality $\dot{\varepsilon}_p$ is the plastic strain rate and T is the temperature.

However, the two-dimensional failure locus that is suggested and employed by J-C model cannot provide a solution for the cases where the same stress-triaxiality exists but the state-of-stress can in fact be different. Equation (4.3) represents the stress invariants involved in the determination of the stress-triaxiality factor while constructing the failure surface. Clearly, Equation (4.3) only uses the first and the second invariants to calculate the stress states and that is not sufficient to characterize multiple failure points having the

same stress-triaxiality. To illustrate, consider axi-symmetric tension ($\sigma^* = -\frac{1}{3}, \theta_L = +1$), it is possible to be on the axi-symmetric compression ($\sigma^* = -\frac{1}{3}, \theta_L = -1$), plane-strain ($\sigma^* = -\frac{1}{3}, \theta_L = 0$) and plane-stress ($\sigma^* = -\frac{1}{3}, \theta_L = +1$) meridians as depicted in Figure 4-1. It is also shown in Figure 4-1 that projection of the stress meridians on to the plane defined by stress-states is used to describe particular stress-states. Similarly the failure surface that was suggested by Bao [99] with three different branches of stress-triaxiality values can be illustrated as in Figure 4-2. Bao has constructed this surface through stress-state dependent tests; however did not consider the effects of the third stress invariant and the failure strains for each stress-triaxiality value reside as constant.

$$\varepsilon_p^f = f(\sigma^*) = f\left(\frac{p}{\sigma_{vm}}\right) = f\left(\frac{-\frac{1}{3}I_1}{\sqrt{I_1^2 + I_2}}\right) \tag{4.3}$$

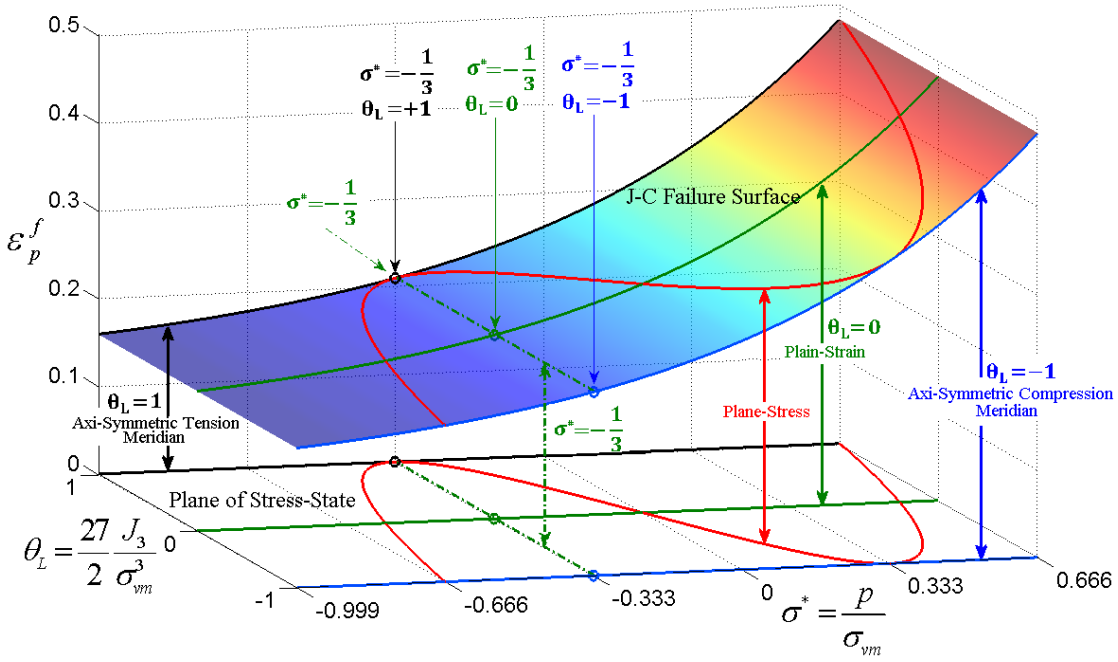

Figure 4-1: Failure surface for Al2024-T351 constructed by J-C equation and projection of the meridians on to the plane of stress-state.

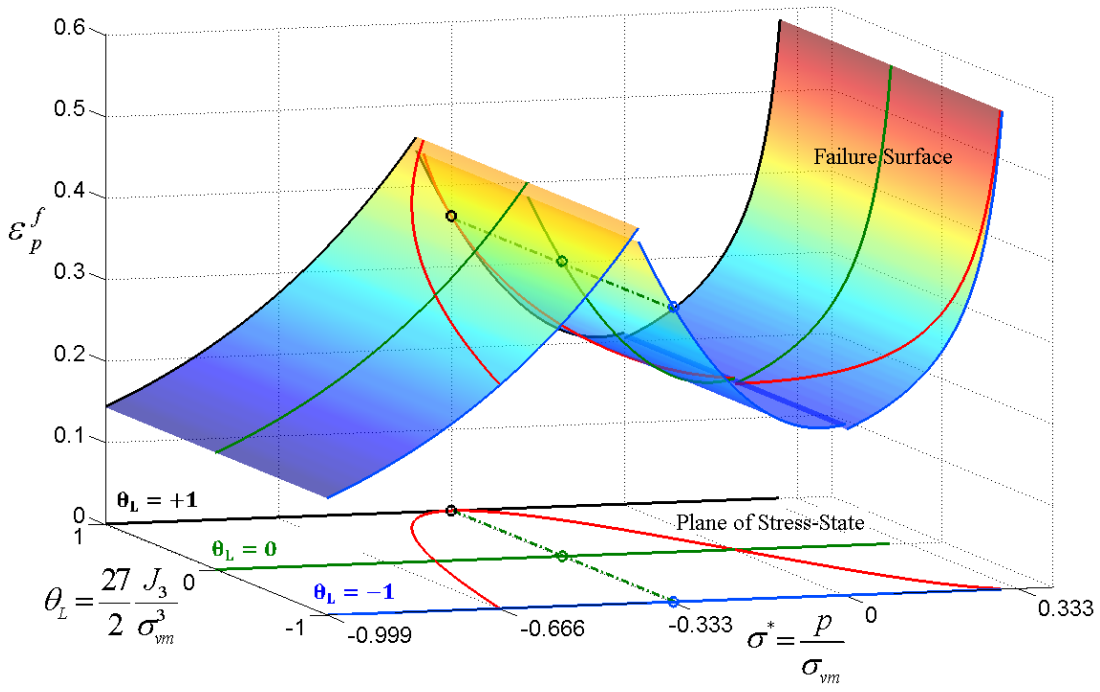

Figure 4-2: Failure surface for Al2024-T351 with three different branches depending on stress-triaxiality.

Bao's experiments prove that the failure strains strongly depend on the stress-triaxiality and a single monotonic function may not necessarily be sufficient to represent the failure locus of Al2024-T351. More recently, Xue [103] and Bai [104] also used the same experiments and postulated new failure surfaces. The third deviatoric stress invariant J_3 has been proposed to be an alternative way to construct a three-dimensional failure surface [102] [103] [104] [105]. The Lode-angle-parameter, which is defined by Equation (4.4), is employed to be the third dimension on the three-dimensional failure locus after effective plastic strain at failure and stress-triaxiality.

$$\theta_L = \frac{27}{2}\frac{J_3}{\sigma_{vm}^3} \tag{4.4}$$

where, Lode angle is defined for the range $-1 \leq \theta_L \leq +1$. By ignoring the temperature and strain rate effects, Equation (4.2) can be rewritten with the newly defined parameter as in Equation (4.5), to include all three stress invariants in defining the failure locus.

$$\varepsilon_p^f = f(\sigma^*, \theta_L) = f\left(\frac{p}{\sigma_{vm}}, \frac{27J_3}{2\sigma_{vm}^3}\right) = f\left(\frac{-\frac{1}{3}I_1}{\sqrt{I_1^2 + I_2}}, \frac{I_1^3 + \frac{9}{2}I_1I_2 + I_3}{(I_1^2 + I_2)^{\frac{3}{2}}}\right) \tag{4.5}$$

Figure 4-3 and Figure 4-4 illustrate such three-dimensional failure loci constructed by surface fitting from test data considering the effects of stress-triaxiality and Lode-angle on the failure strain. The assumption of having a symmetric surface around the plane-strain meridian (i.e., $\theta_L = 0$) is shown to be inaccurate as the number and variety of the test cases become more available [104] [105]. Figure 4-4 illustrates a higher order surface fitting for the same experimental data used by Bao [99] and Xue [103]. These surface fitting approaches require an extensive, coupled experimental program in which the failure points are characterized inversely using numerical methods, like FE calculations.

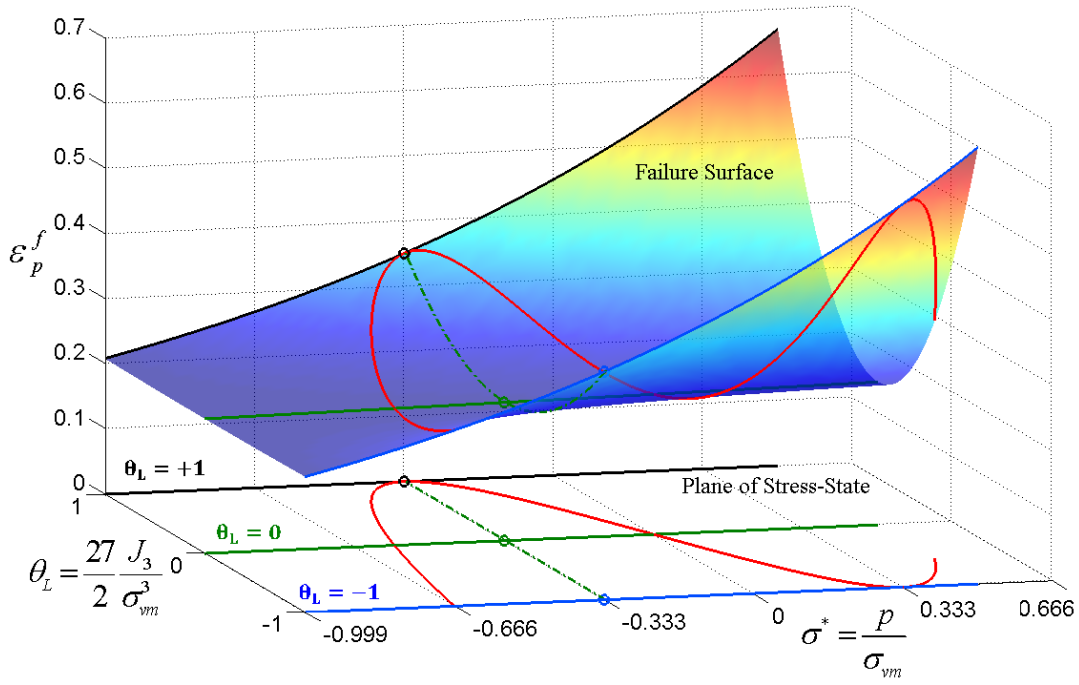

Figure 4-3: Symmetric failure surface for Al2024-T351 with a dependency on stress-triaxiality and Lode-angle-parameter.

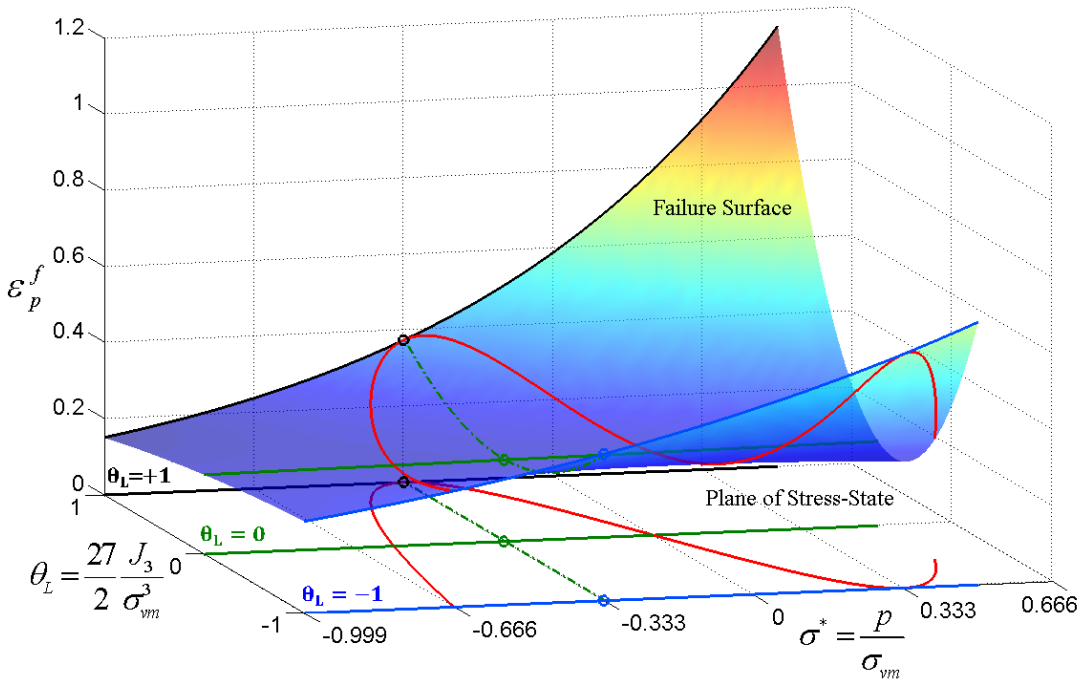

Figure 4-4: Asymmetric failure surface for Al2024-T351 with a dependency on stress-triaxiality and Lode-angle-parameter.

However, implementation of the third deviatoric stress invariant does not directly solve the problems about determining the boundaries of the failure locus especially for ductile metals. It is utmost important to choose enough number of testing points with good resolution at required stress-states to construct a representative surface successfully. Therefore, there is a need to identify the critical stress-states with a selection methodology that can be justified by pointing out the area of interest within the failure space.

Figure 4-5 illustrates a projection of the three-dimensional failure surface on to the two-dimensional stress-space, which is spanned by stress-triaxiality and Lode-angle-parameter. Similar projections are shown in Figures 4-1, 4-2, 4-3 and 4-4. Using the projected stress–states is a convenient way of positioning and illustrating the states-of-stress that are investigated or tested. It is seen that the boundaries of the three-dimensional failure locus is defined by introducing Lode-angle-parameter as it is deviating in between ± 1 (i.e., $-1 \leq \theta_L \leq +1$). However, in the three-dimensional stress space, stress-triaxiality theoretically can vary in between $\pm$ infinity (i.e., $-\infty \leq \sigma^* \leq$

$+\infty$), which clearly can lead to expectable limitations in testing and may have unrealistic consequences (i.e., negative failure strains) on the failure surface as the missing points on the boundaries are often filled by extrapolation. Therefore, the boundaries for the stress-triaxiality need to be defined precisely especially for negative triaxiality values [106]. It was experimentally found for ductile metals that there is a cut-off pressure value exists at the stress-triaxiality of $\sigma^* = +\frac{1}{3}$ and no failure is assumed beyond that stress-state as shown on the projected stress-space in Figure 4-5 [95] [99]. However, no similar experimental limit is postulated for negative stress-triaxiality values and a justification for that limit is required for practical reasons.

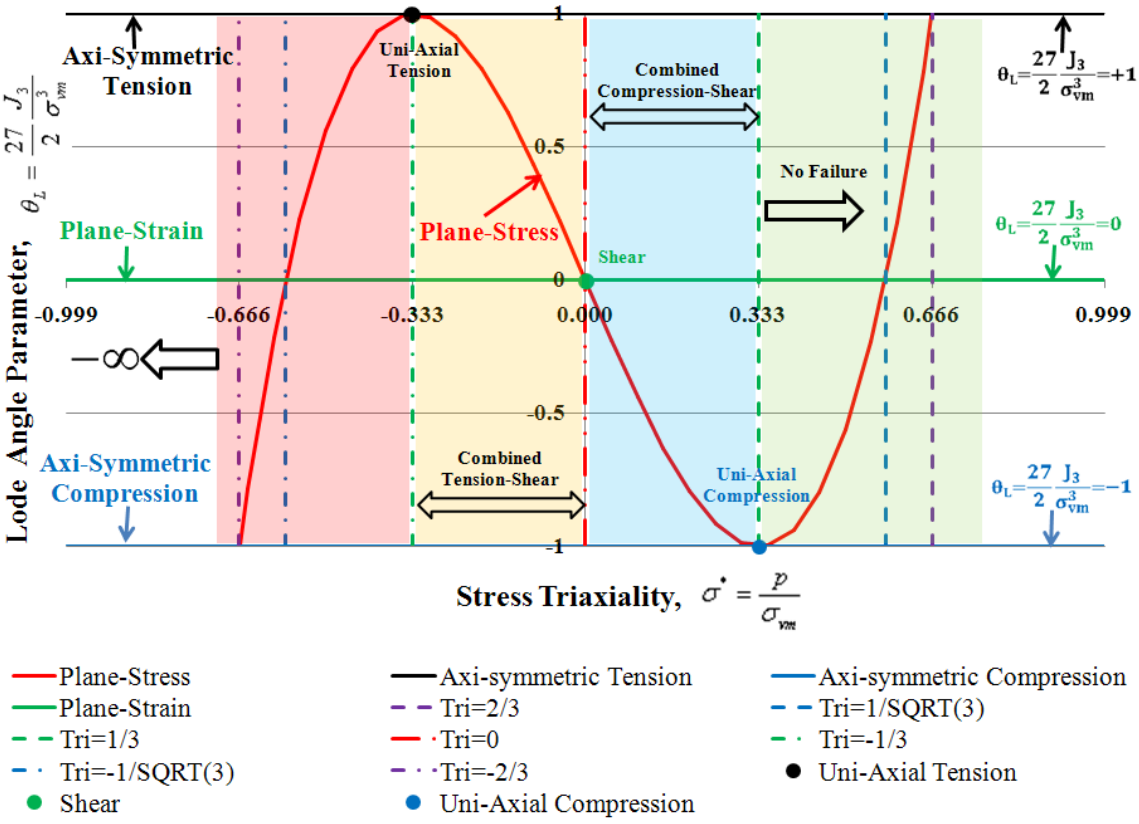

Figure 4-5: Projection of the 3D failure locus on to the stress-space defined by stress-triaxiality vs. Lode-angle-parameter.

Consequently, a justification is required to define the stress-states and help illustrating them with adequate boundaries as a function of state-of-stress. Therefore, a new

parameter, ‘product-triaxiality’, is analytically determined and newly introduced to identify the boundaries of the failure surface projected on a stress-state diagram in Section 4.3 [107]. This new state variable will be used to adequately illustrate the states-of-stress between the meridians spanned by functions of the stress invariants and will lead to a clear visualization of the state-of-stress range for ductile metals under impact loading. Figure 4-6 illustrates the steps of the methodology that will be followed during the implementation of the new material model.

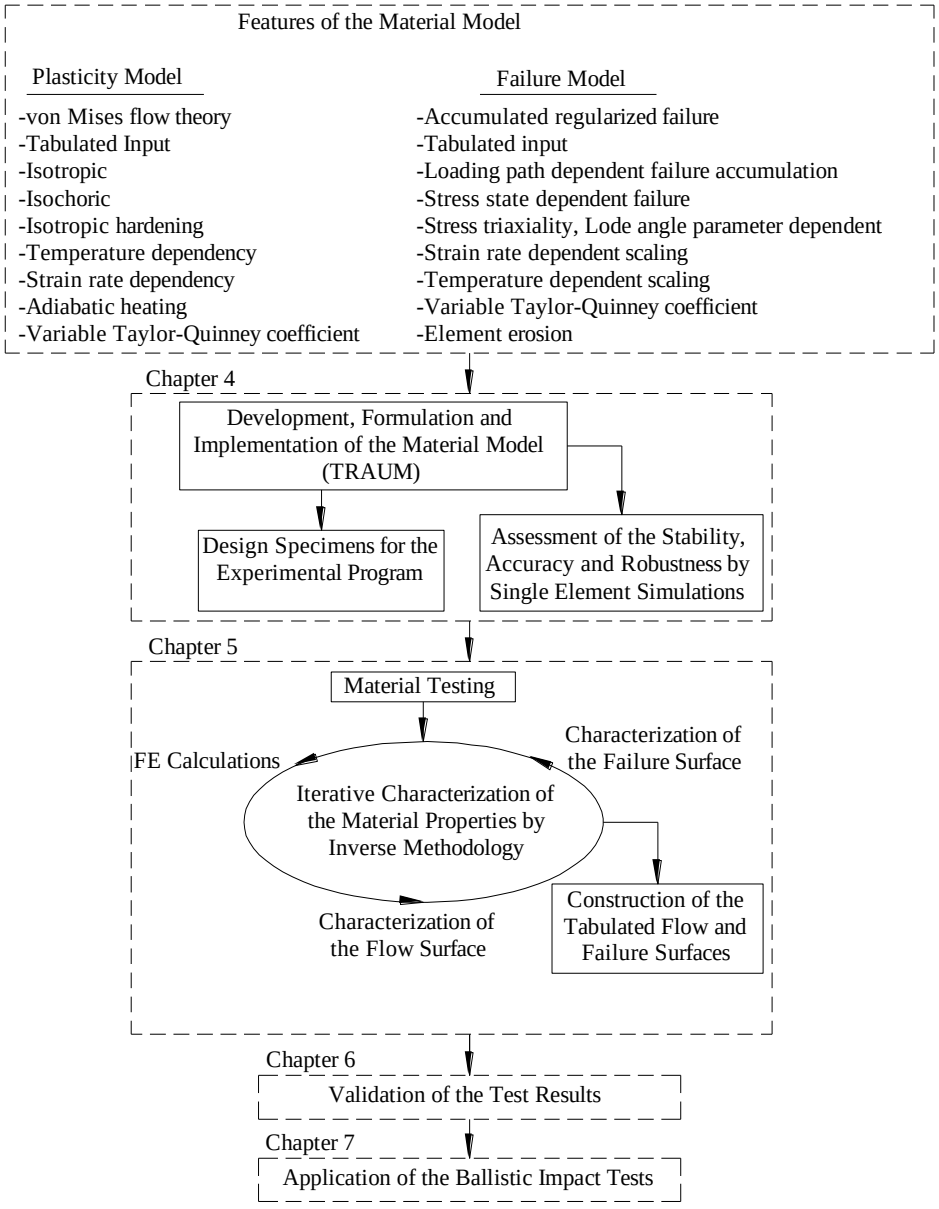

Figure 4-6: Methodology flow diagram.

A thermo-elastic/viscoplastic algorithm and a coupled regularized failure model is formulated and implemented in this Chapter. In Chapter 4, specimen design procedures are also described and corresponding specimen geometries are introduced for the required stress-states. Single element simulations are utilized to compare the stability, accuracy and robustness of the new model against an existing material model. The results of the material testing program are provided in Chapter 5, where an inverse methodology is incorporated to characterize the material test data and the steps for generating the required input for the new material model are described. Tabulated flow and failure surfaces are also constructed for Al2024-T351 in Chapter 5. Validation of the material model with characterized material properties is attained by comparing the test results with the calculations from FE simulations in Chapter 6. In Chapter 7 further validations are presented for ballistic impact applications.

4.2 **Development and implementation of a new material model, TRAUM**

A new macro-mechanical material model is developed and implemented into a non-linear explicit dynamics FE code, LS-DYNA [96] [192]. A user defined material subroutine (UMAT) is developed to address the problems mentioned regarding the necessity to build well defined flow and failure surfaces for ductile materials. An abbreviation is suggested addressing the capabilities of the model and will be used from this point forward to address the new material model as: **T**abulated failure and viscoplasticity - **R**egularized failure - **A**diabatic heating - implemented as a **U**ser defined material **M**odel (TRAUM).

TRAUM is developed to solve the problems described due to curve fitting monotonic functions to a number of test results. Explicitly characterized tabulated surface definitions within the space constructed through the flow characteristics and failure components such as; plastic strain, strain rate, temperature, stress-triaxiality, Lode-angle-parameter, and product-triaxiality are employed for the new model. Therefore, TRAUM is formulated to have a thermo-elastic/viscoplastic algorithm for the flow generalization and will be coupled with an accumulated failure rule. One of the most important features of the newly proposed model will be the mesh size regularization of failure. It is mentioned that, especially numerical models that incorporate softening and failure are extremely mesh

dependent [15] [200] [201] [194] [193] [202]. Therefore, the proposed failure algorithm will also consider mesh size effects. Moreover, loading history/path dependency on the failure accumulation is also considered, where the accumulation of failure strain will be sensitive to non-proportional loading or different loading paths and sequences.

4.2.1 **Constitutive relation**

An isotropic von Mises plasticity algorithm is utilized with isotropic strain hardening, stain rate hardening, and temperature softening features, where adiabatic heating due to the plastic work is considered. The model can be formulated as a multiplicative decomposition of flow stress as:

$$\sigma_y = k1(\varepsilon_p, \dot{\varepsilon}_p) kt(\varepsilon_p, T) \tag{4.6}$$

where, ε_p is the plastic strain, $\dot{\varepsilon}_p$ is the equivalent plastic strain rate and T is the temperature.

The model resembles J-C in terms of the decomposition; however, the new model utilized tabulated inputs of strain rate dependent isothermal hardening curves at room temperature given by $k1(\varepsilon_p, \dot{\varepsilon}_p)$ and temperature depended quasi-static hardening curves by $kt(\varepsilon_p, T)$ (e.g., often at a nominal strain rate of 1.0 s^{-1}). Instead of using effective strain rate, plastic strain and plastic strain rate are specifically utilized to overcome oscillation problems due to the elastic component [203].

Adiabatic heating occurs due to plastic work and the temperature is calculated as:

$$T = T_{room} + \frac{\beta}{C_p \rho} \int_0^{\varepsilon_p} \sigma_y d\bar{\varepsilon}_p \tag{4.7}$$

where, T_{room} is the room/current temperature, β is the Taylor–Quinney coefficient that represents the proportion of plastic work converted into heat. Here β is taken to be 0.9,

which is assumed to be a proper value for metals [204]. C_p is the specific heat at constant pressure, ρ is the density, σ_y is the flow stress and ε_p is the plastic strain.

An elastic predictor, plastic corrector scheme is used to map the stresses to the next time step by utilizing a radial return algorithm [205] [206]. A hypo-elastic [207] [208] prediction is computed first, and then corrected back to the yield surface if the yield condition is exceeded. This technique is known to work efficiently and accurately for the J_2 yield condition and flow rule, provided that the time increment is sufficiently small. Considering that an explicit dynamic code is utilized for the analysis, this conditional stability is satisfied within the numerical integration scheme and the time step size is limited by Courant-Friedrichs-Levy criterion [209].

The plastic deformation is assumed as isochoric (i.e., volume preserving); therefore, plastic deformation is assumed to happen at constant volume and exhibit no volumetric strain. In shell elements a co-rotational formulation is adopted in order to simplify the formulation of plasticity, where the local coordinate system constructed at each integration point.

The kinematics of the deformation can be defined by decomposing strain rate (rate-of-deformation) tensor as [15]:

$$\dot{\varepsilon} = \dot{\varepsilon}^e + \dot{\varepsilon}^p \tag{4.8}$$

where, $\dot{\varepsilon}^e$ and $\dot{\varepsilon}^p$ are the elastic and plastic components of the strain rate tensor, respectively. Clearly, as the volume stays constant during the plastic deformation, the plastic strain rate designates only deviatoric components as the trace of the plastic strain rate is equal to zero:

$$\mathrm{tr}\dot{\varepsilon}^p = 0 \tag{4.9}$$

Assuming that the elastic response of the material is isotropic, the governing constitutive law can be formulated by using Hooke's law and relating the strain rate tensor to an objective rate of the Cauchy stress tensor as:

$$\dot{\boldsymbol{\sigma}} = \mathbf{C}\colon \dot{\varepsilon}^{e} = \mathbf{C}\colon (\dot{\varepsilon} - \dot{\varepsilon}^{p}) \tag{4.10}$$

where, $\mathbf{C}$ is the fourth order positive definite isotropic stiffness tensor and can be described as:

$$\mathbf{C} = K\mathbf{I} \otimes \mathbf{I} + 2G\left(\mathbb{I} - \frac{1}{3}\mathbf{I} \otimes \mathbf{I}\right) \tag{4.11}$$

where, $\mathbf{I}$ is the second-order unit tensor and $\mathbb{I}$ is the fourth-order, symmetric unit tensor, $K = \frac{E}{3(1-2\nu)}$ is the bulk modulus and $G = \frac{E}{2(1+\nu)}$ is the shear modulus.

The elastic tangent modulus tensor can also be represented in the component form with respect to a Cartesian basis as:

$$C_{ijkl} = \lambda^{e}\delta_{ij}\delta_{kl} + \mu\left(\delta_{ik}\delta_{jl} + \delta_{il}\delta_{jk}\right) \tag{4.12}$$

where, $\lambda^{e} = K - \frac{2}{3G}$ and $\mu = G$ are the Lamé constants given as functions of elastic constants.

Poisson's ratio ν is assumed to stay constant during the overall deformation and failure process. Elastic modulus $E = E(T)$ is assumed to be a function of current temperature and the plastic part of the deformation is treated by strain rate and temperature dependent tabulated hardening curves.

Rate of the Cauchy stresses can be decomposed into deviatoric and volumetric parts by using deviatoric stress rates ($\dot{\mathbf{s}}$), and pressure rate ($\dot{\boldsymbol{p}} = \frac{1}{3}tr\dot{\boldsymbol{\sigma}}$) as:

$$\dot{\boldsymbol{\sigma}} = \dot{\mathbf{s}} - \dot{\boldsymbol{p}}\delta \tag{4.13}$$

Similarly, strain rate tensor can be decomposed into deviatoric and volumetric parts by using deviatoric strain rates $\dot{\mathbf{e}}$, and volumetric strain rate $\dot{\varepsilon}^{V}$ as:

$$\dot{\varepsilon} = \dot{\mathbf{e}} + \frac{\dot{\varepsilon}^{V}}{3}\boldsymbol{\delta} \tag{4.14}$$

And plastic strain rate is decomposed as:

$$\dot{\varepsilon_p} = \dot{\mathbf{e}}_p + \frac{\dot{\varepsilon}_p^V}{3}\boldsymbol{\delta} \tag{4.15}$$

where, $\dot{\mathbf{e}}_p$ is the plastic deviatoric strain rate and $\dot{\varepsilon}_p^V$ is the plastic volumetric strain rate.

Rate of the Cauchy stresses can then be written as:

$$\dot{\boldsymbol{\sigma}} = 2G\left(\dot{\mathbf{e}} - \dot{\mathbf{e}}_p\right) + K\left(\dot{\varepsilon}^V - \dot{\varepsilon}_p^V\right)\boldsymbol{\delta} \tag{4.16}$$

Hypo-elastic pressure term reduces the material law further since volumetric plastic strain rate is zero ($\dot{\varepsilon}_p^V \equiv 0$) and plastic strain rate is equal to its own derivative ($\dot{\mathbf{e}}_p = \dot{\varepsilon_p}$):

$$\dot{\boldsymbol{\sigma}} = \underbrace{2G\left(\dot{\mathbf{e}} - \dot{\varepsilon_p}\right)}_{\text{Deviatoric Part}} + K\dot{\varepsilon}^V\boldsymbol{\delta} \tag{4.17}$$

Therefore, the deviatoric stress rates can be written as:

$$\dot{\mathbf{s}} = 2G\left(\dot{\mathbf{e}} - \dot{\varepsilon}_p\right) \tag{4.18}$$

The yield criterion f, which is defined as a convex function in stress space, determines the limit of the elastic range and due to the inelastic nature of the plastic deformation, it is expected to be a function of deviatoric stresses only and can be written as:

$$f\left(\boldsymbol{\sigma}, \sigma_y\right) \leq 0 \Rightarrow f\left(\mathbf{s}, \sigma_y\right) \leq 0 \tag{4.19}$$

where, $\sigma_y = \sigma_y\left(\varepsilon_p, \dot{\varepsilon}_p, T\right)$ is the yield stress as a function of plastic strain, plastic strain rate and temperature. The yield function can be written more explicitly as:

$$f(\boldsymbol{\sigma}, \sigma_y) = \sigma_{vm} - \sigma_y = \sqrt{\frac{3}{2}\mathbf{s}:\mathbf{s}} - \sigma_y \leq 0 \tag{4.20}$$

The associative flow rule is adopted, and plastic strain rate is defined by introducing a rate of plastic multiplier ($\dot{\lambda}$) as [210]:

$$\dot{\varepsilon}_p = \dot{\lambda}\frac{\partial f}{\partial \boldsymbol{\sigma}} \Rightarrow \dot{\varepsilon}_p = \dot{\lambda}\frac{\partial f}{\partial \mathbf{s}} \Rightarrow \dot{\varepsilon}_p = \dot{\lambda}\frac{3}{2\sigma_{vm}}\mathbf{s} = \dot{\lambda}\mathbf{N} \tag{4.21}$$

where, **N** is explicitly given as the Prandtl-Reuss normal outward flow vector to the yield surface [211].

Plastic rate parameter $\dot{\lambda}$ is found by defining the rate of work due to plastic dissipation ($\dot{\boldsymbol{W}}$) and defining the rule for plastic strain rate as a work conjugate quantity to von Mises stress:

$$\dot{\boldsymbol{W}} = \sigma_{vm}\dot{\varepsilon}_p \Rightarrow \dot{\varepsilon}_p = \sqrt{\frac{2}{3}\dot{\varepsilon}_p:\dot{\varepsilon}_p} = \sqrt{\frac{2}{3}\dot{\lambda}^2\left(\frac{3}{2\sigma_{vm}}\right)^2\mathbf{s}:\mathbf{s}} = \dot{\lambda} \tag{4.22}$$

Rate of plastic multiplier is used to obtain the evolution equation of the hardening parameter as:

$$\dot{\boldsymbol{\sigma}}_y = \dot{\lambda}\frac{\partial \boldsymbol{\sigma}_y}{\partial \lambda} \Rightarrow \dot{\boldsymbol{\sigma}}_y = \frac{\partial \boldsymbol{\sigma}_y}{\partial \varepsilon_p}\dot{\varepsilon}_p \tag{4.23}$$

The plastic strain rate is expected to satisfy the complementary conditions or the loading–unloading conditions that are stated in Kuhn–Tucker form as [208]:

$$f(\boldsymbol{\sigma}, \sigma_y) \leq 0, \qquad \dot{\lambda} \leq 0, \qquad \dot{\lambda} f(\boldsymbol{\sigma}, \sigma_y) = 0 \tag{4.24}$$

Rewriting the material law for deviatoric stresses and introducing the elastic trial stress ($\dot{\mathbf{s}}_e = 2G\dot{\mathbf{e}}$), a system of six equations with seven unknowns obtained and that can be solved from the complementary conditions with an additional equation as:

$$\begin{aligned}
&\dot{\mathbf{s}} = 2G\left(\dot{\mathbf{e}} - \dot{\varepsilon}_p\right) = 2G\left(\dot{\mathbf{e}} - \dot{\lambda}\frac{3}{2\sigma_{vm}}\mathbf{s}\right) = \dot{\mathbf{s}}_\mathbf{e} - \dot{\lambda}\frac{3G}{\sigma_{vm}}\mathbf{s} = \dot{\mathbf{s}}_\mathbf{e} - \dot{\varepsilon}_p\frac{3G}{\sigma_{vm}}\mathbf{s} \\
&\Rightarrow \text{if } f\left(\boldsymbol{\sigma}, \sigma_y\right) < 0 \Rightarrow \dot{\lambda} = 0 \Rightarrow \dot{\lambda}\dot{f}\left(\boldsymbol{\sigma}, \sigma_y\right) = 0 \\
&\text{or} \\
&\Rightarrow \text{if } f\left(\boldsymbol{\sigma}, \sigma_y\right) = 0 \Rightarrow \dot{\lambda} > 0
\end{aligned} \tag{4.25}$$

4.2.2 **Time integration and numerical implementation**

A forward Euler radial return algorithm that is suggested by Wilkins [205] and further investigated by Krieg and Krieg [212] is implemented for a von Mises type plasticity algorithm with isotropic hardening. A schematic representation of the return mapping algorithm is illustrated in Figure 4-7 [208].

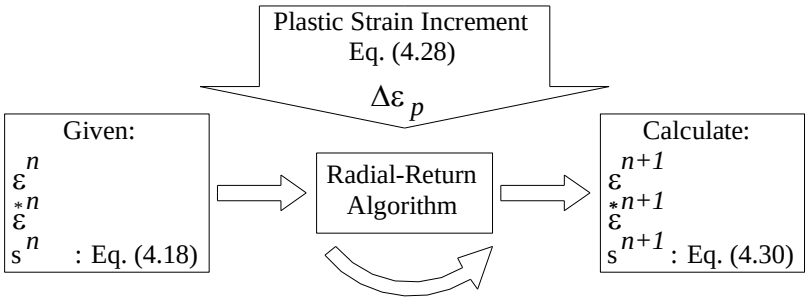

Figure 4-7: The role of elasto-plastic return-mapping algorithms.

Discretization of the stresses in the material law by using elastic trial stress leads to a radial return in deviatoric stress space as shown by Equation (4.26). The time increment is achieved through a central difference scheme.

$$\begin{aligned}
&\dot{\mathbf{s}} = \dot{\mathbf{s}}_\mathbf{e} - \dot{\varepsilon}_p\frac{3G}{\sigma_{vm}}\mathbf{s} \Rightarrow \mathbf{s^{n+1}} - \mathbf{s^n} - \dot{\varepsilon}_p\Delta t\frac{3G}{\sigma_{vm,e}^{n+1}}\mathbf{s}_e^{n+1} \\
&\Rightarrow \mathbf{s^{n+1}} = \mathbf{s}_e^{n+1}\left(1 - \Delta\varepsilon_p\frac{3G}{\sigma_{vm,e}^{n+1}}\right)
\end{aligned} \tag{4.26}$$

where, $\sigma_{vm,e}^{n+1}$ is the trial von Mises stress of the expanded yield surface at time $t = t_{n+1}$.

The elastic trial and von Mises stresses are solved by multiplying the equations by itself as:

$$\Rightarrow \sqrt{\frac{3}{2}\mathbf{s}^{\mathbf{n+1}}:\mathbf{s}^{\mathbf{n+1}}} = \sqrt{\frac{3}{2}\mathbf{s}_e^{\mathbf{n+1}}\left(\mathbf{1} - \Delta\varepsilon_p \frac{3G}{\sigma_{vm,e}^{n+1}}\right):\mathbf{s}_e^{\mathbf{n+1}}\left(\mathbf{1} - \Delta\varepsilon_p \frac{3G}{\sigma_{vm,e}^{n+1}}\right)} \tag{4.27}$$

$$\Rightarrow \sigma_{vm}^{n+1} = \sigma_{vm,e}^{n+1} - 3G\Delta\varepsilon_p$$

Figure 4-8 illustrates the geometric interpretation of the elastic predictor-return-mapping / radial-return in principle stress space.

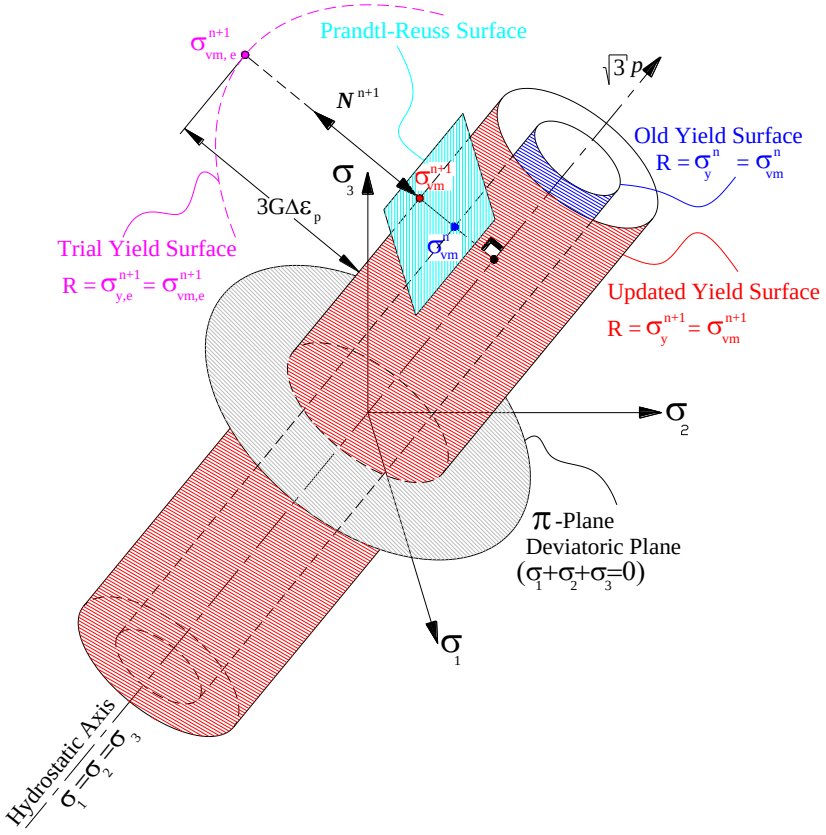

Figure 4-8: Geometric interpretation of the radial-return in principle stress space.

An orthogonal trial stress prediction is calculated first and scaled back to the yield surface at time $t = t_{n+1}$, the same path is used for the projection. This method is particularly efficient for von Mises type of yield surfaces since the surface is convex at all

points and an orthogonal plane (e.g., Prandtl-Reuss) can be found easily [208]. Another geometric interpretation of the algorithm can be illustrated in deviatoric stress space or π–plane as shown in Figure 4-9 when the yield surfaces are concentric spheres and the resulting stress return path is parallel to the deviatoric stress vectors suggested by the constitutive law.

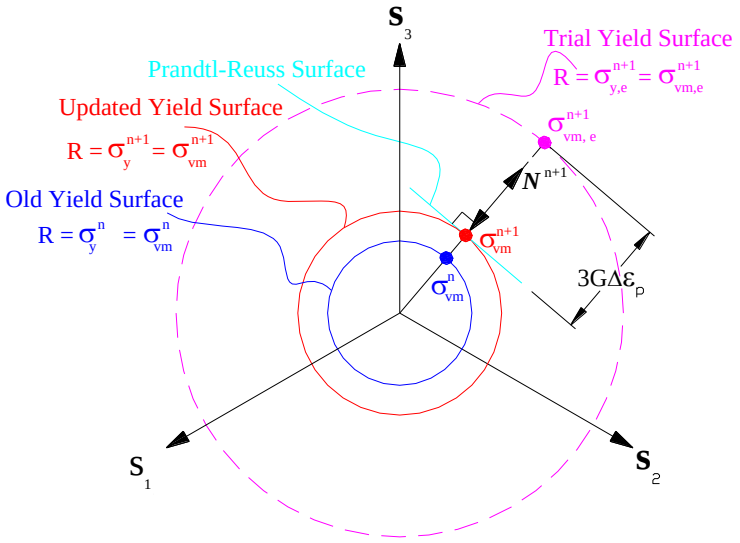

Figure 4-9: Geometric interpretation of the radial-return in deviatoric stress space.

Figure 4-10 also suggests a clear interpretation of the radial-return algorithm on invariant plane of von Mises stress versus pressure, where it is shown how the pressure remains unaffected by the plasticity. High accuracy and efficiency of the selected radial-return method lies within its simplicity. Solving for the yield function at time $t = t_{n+1}$ a non-linear equation is derived to be solved for the plastic strain increment $\Delta\varepsilon_p$ as:

$$
\begin{aligned}
&f^{n+1} = \sigma_{vm}^{n+1} - \sigma_y^{n+1} = 0 \\
&f^{n+1} = \sigma_{vm,e}^{n+1} - 3G\Delta\varepsilon_p - \sigma_y^{n+1} = 0 \\
&f^{n+1} = \sigma_{vm,e}^{n+1} - 3G\Delta\varepsilon_p - \sigma_y\left(\varepsilon_p^{n+1}, \dot{\varepsilon}_p^{n+1}, T^{n+1}\right) = 0 \\
&f^{n+1} = \sigma_{vm,e}^{n+1} - 3G\Delta\varepsilon_p - \sigma_y\left(\varepsilon^n + \Delta\varepsilon_p, \frac{\Delta\varepsilon_p}{\Delta t}, T^n + \frac{\beta}{\rho C_p}\Delta\varepsilon_p \frac{\sigma_{vm}^n + \sigma_{vm}^{n+1}}{2}\right) = 0 \\
&\Rightarrow \sigma_{vm,e}^{n+1} - 3G\Delta\varepsilon_p = \sigma_y\left(\varepsilon^n + \Delta\varepsilon_p, \frac{\Delta\varepsilon_p}{\Delta t}, T^n + \frac{\beta}{\rho C_p}\Delta\varepsilon_p \frac{\sigma_{vm}^n + \sigma_{vm}^{n+1}}{2}\right)
\end{aligned}
\tag{4.28}
$$

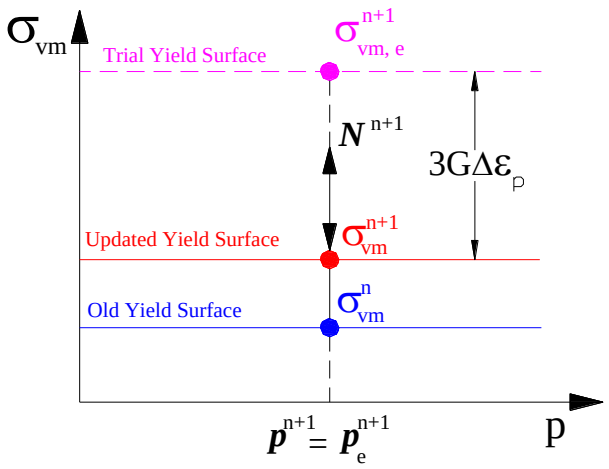

Figure 4-10: Geometric interpretation of the radial-return on the invariant plane.

Solving for the yield function at time $t = t_{n+1}$ a non-linear equation is derived to be solved for the plastic strain increment $\Delta\varepsilon_p$ as:

$$
\begin{aligned}
f^{n+1} &= \sigma_{vm}^{n+1} - \sigma_y^{n+1} = 0 \\
f^{n+1} &= \sigma_{vm,e}^{n+1} - 3G\Delta\varepsilon_p - \sigma_y^{n+1} = 0 \\
f^{n+1} &= \sigma_{vm,e}^{n+1} - 3G\Delta\varepsilon_p - \sigma_y\left(\varepsilon_p^{n+1}, \dot{\varepsilon}_p^{n+1}, T^{n+1}\right) = 0 \\
f^{n+1} &= \sigma_{vm,e}^{n+1} - 3G\Delta\varepsilon_p - \sigma_y\left(\varepsilon^n + \Delta\varepsilon_p, \frac{\Delta\varepsilon_p}{\Delta t}, T^n + \frac{\beta}{\rho C_p}\Delta\varepsilon_p \frac{\sigma_{vm}^n + \sigma_{vm}^{n+1}}{2}\right) = 0 \\
\Rightarrow \sigma_{vm,e}^{n+1} - 3G\Delta\varepsilon_p &= \sigma_y\left(\varepsilon^n + \Delta\varepsilon_p, \frac{\Delta\varepsilon_p}{\Delta t}, T^n + \frac{\beta}{\rho C_p}\Delta\varepsilon_p \frac{\sigma_{vm}^n + \sigma_{vm}^{n+1}}{2}\right)
\end{aligned}
\tag{4.28}
$$

where, T^n is the current temperature, C_p is the specific heat at constant pressure (assumed constant during the numerical simulation), β is the Taylor–Quinney coefficient that represents the proportion of plastic work converted into heat, which is taken to be 0.9 in the current study. The incremental temperature increase caused by dissipation of plastic work due to adiabatic heating is calculated to incorporate temperature softening.

The plastic strain increment in Equation (4.28d) is solved through a secant method by using the following initial values and iterative scheme [194] [203]:

$$\Rightarrow f^{n+1} = \sigma_{vm,e}^{n+1} - 3G\Delta\varepsilon_p - \sigma_y^{n+1} = 0$$

$$\left.\begin{aligned} \Delta\varepsilon_p^0 &= 0 \\ \Delta\varepsilon_p^1 &= 2\frac{\sigma_{vm,e}^{n+1} - \sigma_y^n}{3G} \end{aligned}\right\} \text{Initial guess for solution interval}$$

$$\Delta\varepsilon_p^2 = \Delta\varepsilon_p^1 - f\left(\Delta\varepsilon_p^1\right)\frac{\Delta\varepsilon_p^1 - \Delta\varepsilon_p^0}{f\left(\Delta\varepsilon_p^1\right) - f\left(\Delta\varepsilon_p^0\right)} \tag{4.29}$$

$$\vdots$$

$$\Delta\varepsilon_p^{k+1} = \Delta\varepsilon_p^k - f\left(\Delta\varepsilon_p^k\right)\frac{\Delta\varepsilon_p^k - \Delta\varepsilon_p^{k-1}}{f\left(\Delta\varepsilon_p^k\right) - f\left(\Delta\varepsilon_p^{k-1}\right)}$$

$$\text{check if } \left|f\left(\Delta\varepsilon_p^{k+1}\right) - f\left(\Delta\varepsilon_p^k\right)\right| \leq tolerance = 10^{-6} \Rightarrow STOP$$

The algorithmic setup is illustrated in Figure 4-11 for the secant iterations.

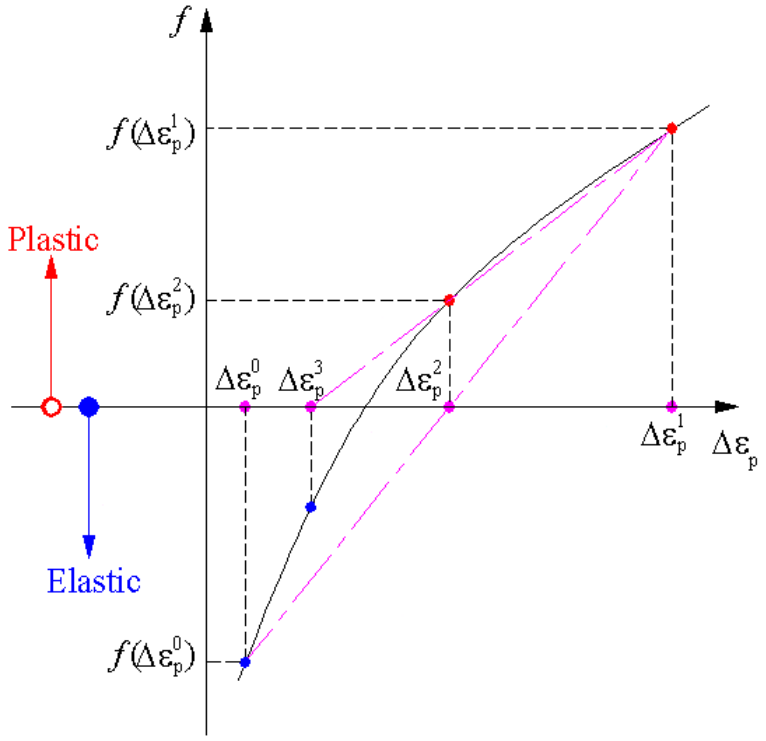

Figure 4-11: Successive secant iterations.

After finding the plastic increment, final stresses are computed as:

$$\Rightarrow \mathbf{s^{n+1}} = \mathbf{s}_e^{n+1}\left(1 - \Delta\varepsilon_p \frac{3G}{\sigma_{vm,e}^{n+1}}\right) = \mathbf{s}_e^{n+1}\frac{\sigma_y^{n+1}}{\sigma_{vm,e}^{n+1}} \tag{4.30}$$

The trial stresses are scaled back to the yield surface as illustrated in Figures 4-8, 4-9 and 4-10.

4.2.3 **Accumulated failure algorithm**

Failure is assumed when damage variable of a finite element reaches a critical limit described by a failure surface that is constructed through multiplicative decomposition of tabulated inputs of stress-triaxiality, Lode-angle-parameter, strain rate, temperature, and a regularization term within a critical element size as formulated in Equation (4.31). As the damage variable reaches unity (i.e., reaches the scaled failure surface), finite element is failed by an element erosion technique [96].

$$\begin{aligned} \varepsilon_p^f &= f\left(\frac{p}{\underbrace{\sigma_{vm}}_{\sigma^*}}, \underbrace{\frac{27}{2}\frac{J_3}{\sigma_{vm}^3}}_{\theta_L}\right) g\left(\dot{\varepsilon}_p\right) h(T) i(l_{cr}) \\ D_{cr} &= \int_0^{\varepsilon_p^f} \frac{d\varepsilon_p}{\varepsilon_p^f} \geq 1 \Rightarrow \text{failure} \end{aligned} \tag{4.31}$$

where, $f\left(\frac{p}{\underbrace{\sigma_{vm}}_{\sigma^*}}, \underbrace{\frac{27}{2}\frac{J_3}{\sigma_{vm}^3}}_{\theta_L}\right)$ represents a failure locus specific to a material, which can be used as a generic way of constructing failure loci for ductile materials based on multiple states-of-stress. Stress-triaxiality and Lode-angle-parameter dependent failure surfaces were also described by Equation (4.5) and illustrated by Figures 4-3 and 4-4. In Equation (4.31), $g\left(\dot{\varepsilon}_p\right)$ represents the strain rate dependent term/curve that scales the failure strain, $h(T)$ is the temperature dependent failure term/curve that scales the failure strain and $i(l_{cr})$ is the regularization term/curve that scales the failure strain according to the initial

element size. Failure is assumed when the accumulated failure strain reaches a critical value that is defined by D_{cr}.

The numerical implementation of the algorithm can be represented by Equation (4.32) considering the central difference time integration scheme as:

$$\varepsilon_p^{f,n+1} = f\left(\underbrace{\frac{p^{n+1}}{\sigma_{vm}^{n+1}}}_{\sigma_{n+1}^*}, \underbrace{\frac{27}{2}\frac{J_3^{n+1}}{(\sigma_{vm}^{n+1})^3}}_{\theta_L^{n+1}}\right) g\left(\dot{\varepsilon}_p^{n+1/2}\right) h(T^{n+1}) i(l_{cr}^0)$$
$$D_{cr}^{n+1} = D_{cr}^n + \frac{\Delta\varepsilon_p}{\varepsilon_p^{f,n+1}} \tag{4.32}$$
$$D_{cr}^{n+1} \geq 1 \Rightarrow \text{failure}$$

4.3 **Development of a generic failure locus for ductile materials based on multiple states-of-stress**

In order to generalize the definition of failure in three-dimensional space by defining the domain constituted by all possible states-of-stress, the third stress invariant is selected to help define the boundaries of the failure locus especially towards the negative values of the stress-triaxiality as illustrated in Figure 4-5. Therefore, an alternative triaxiality parameter is utilized to incorporate the third stress invariant while defining the plane of stress-space as a projection of the three-dimensional failure surface. The new parameter is called as 'product-triaxiality' (σ^*) [107] and is defined as:

$$\sigma_p^* = \frac{I_3}{\sigma_{vm}^3} = \left(\frac{\sigma_1\sigma_2\sigma_3}{\sigma_{vm}^3}\right) \tag{4.33}$$

Therefore, by incorporating all stress invariants the expression can be expanded and the new failure locus (i.e., plane of stress-space as a projection of the three-dimensional failure surface) will be in the form of:

$$\varepsilon_p^f = f\left(\sigma^*, \sigma_p^*\right) = f\left(\frac{p}{\sigma_{vm}}, \frac{I_3}{\sigma_{vm}^3}\right) = f\left(\frac{-\frac{1}{3}I_1}{\sqrt{I_1^2 + I_2}}, \frac{I_3}{\left(I_1^2 + I_2\right)^{3/2}}\right) \tag{4.34}$$

In the general state-of-stress, the principle stresses σ_2 and σ_3 can be written as linear functions of σ_1, except for the case of σ_1 being exactly zero or negative (i.e., compressive), where in that case if the first principal stress is compressive then all three principle stresses are compressive and no failure will occur. Therefore, the principle stress parameters are defined by $\sigma_2 = a\sigma_1$ and $\sigma_3 = b\sigma_1$ if $\sigma_1 \neq 0$ as:

$$\begin{bmatrix} \sigma_1 & 0 & 0 \\ 0 & \sigma_2 & 0 \\ 0 & 0 & \sigma_3 \end{bmatrix} = \begin{bmatrix} \sigma_1 & 0 & 0 \\ 0 & a\sigma_2 & 0 \\ 0 & 0 & b\sigma_3 \end{bmatrix} \tag{4.35}$$

When $\sigma_1 = 0$, σ_2 and σ_3 can be written directly without substitution. Since, by definition $\sigma_1 \geq \sigma_2 \geq \sigma_3$, the bounds $1 \geq a \geq -\infty$ and $a \geq b \geq -\infty$ exist for a and b. Pressure term, von Mises stress and the third stress invariant can then be written as:

$$\begin{aligned} p &= -\frac{\sigma_1(1 + a + b)}{3} \\ \sigma_{vm} &= \sigma_1\sqrt{1 + a^2 + b^2 - ab - a - b} \\ I_3 &= \sigma_1^3 ab \end{aligned} \tag{4.36}$$

Consequently, stress-triaxiality and product-triaxiality terms can be rewritten as in Equations (4.37) and (4.38), respectively.

$$\frac{p}{\sigma_{vm}} = -\frac{1}{3}\frac{\sigma_1}{|\sigma_1|}\frac{1 + a + b}{\sqrt{1 + a^2 + b^2 - ab - a - b}} \tag{4.37}$$

$$\frac{\sigma_1\sigma_2\sigma_3}{\sigma_{vm}^3} = \frac{\sigma_1^3}{|\sigma_1^3|}\frac{ab}{\sqrt[3]{1 + a^2 + b^2 - ab - a - b}} \tag{4.38}$$

Considering the bounds $1 \geq a \geq -\infty$ and $a \geq b \geq -\infty$ exist for a and b, Equations 4.37 and 4.38 can be redefined on the boundaries to specify an envelope of solutions as:

$$\text{if } a = 1 \Rightarrow \begin{cases} \dfrac{p}{\sigma_{vm}} = -\dfrac{1}{3}\dfrac{b+2}{-(b-1)} \text{ and } \dfrac{\sigma_1\sigma_2\sigma_3}{\sigma_{vm}^3} = \dfrac{b}{-(b-1)^3} \\ \dfrac{p}{\sigma_{vm}} = -\dfrac{1}{3}\dfrac{b+2}{+(b-1)} \text{and } \dfrac{\sigma_1\sigma_2\sigma_3}{\sigma_{vm}^3} = \dfrac{b}{+(b-1)^3} \end{cases} \tag{4.39}$$

$$\text{if } a = b \Rightarrow \begin{cases} \dfrac{p}{\sigma_{vm}} = -\dfrac{1}{3}\dfrac{1+2a}{-(1-a)} \text{ and } \dfrac{\sigma_1\sigma_2\sigma_3}{\sigma_{vm}^3} = \dfrac{a^2}{-(1-a)^3} \\ \dfrac{p}{\sigma_{vm}} = -\dfrac{1}{3}\dfrac{1+2a}{+(1-a)} \text{and } \dfrac{\sigma_1\sigma_2\sigma_3}{\sigma_{vm}^3} = \dfrac{a^2}{+(1-a)^3} \end{cases} \tag{4.40}$$

Equations (4.39) and (4.40) are plotted in Figure 4-12, where they represent the lower (negative) and upper (positive) bounds for the solution envelope. As it can be observed from this figure, multiple product-triaxiality solutions exist for a given stress-triaxiality value and the $\left(\frac{p}{\sigma_{vm}}, \frac{I_3}{\sigma_{vm}^3}\right)$ value pair overlaps at certain regions. For the value pairs of $\left(\pm\frac{1}{3}, 0\right)$ for the $a = 1 \Rightarrow (\sigma_1 = \sigma_2)$ curves and $\left(\pm\frac{2}{3}, 0\right)$ for the $a = b \Rightarrow (\sigma_2 = \sigma_3)$ curves, the limit curves overlap.

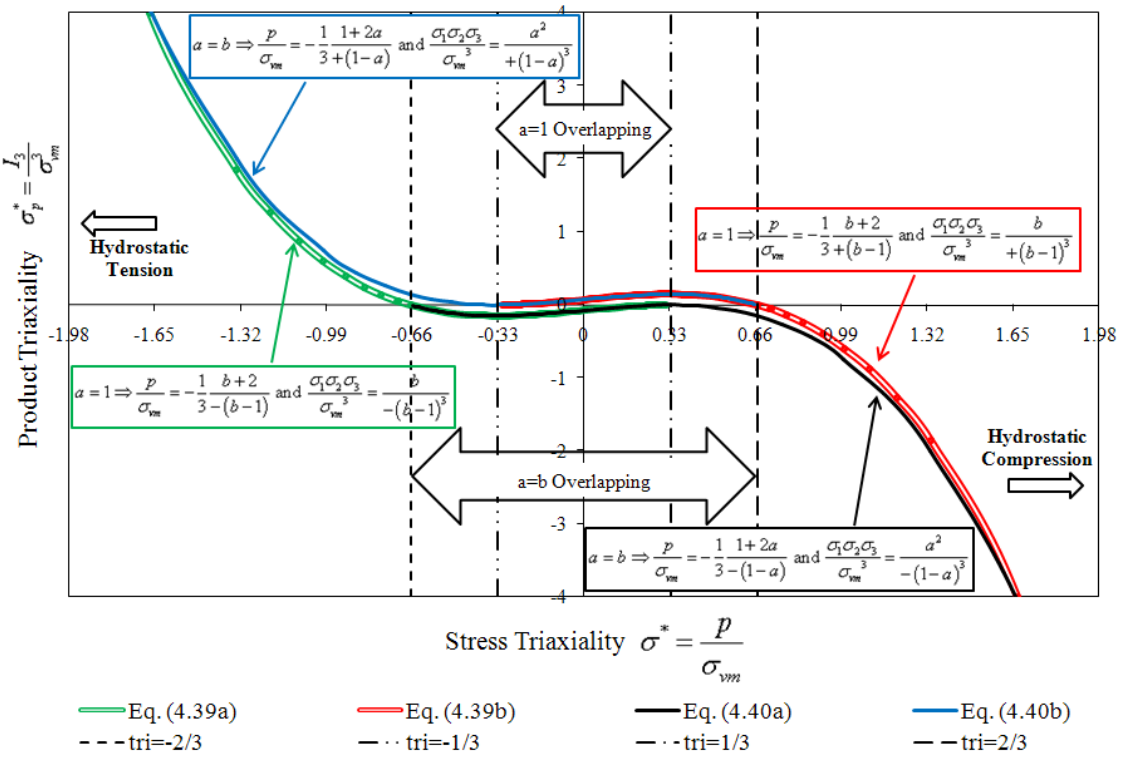

Figure 4-12: Stress-state envelope in the stress-triaxiality vs. product-triaxiality space.

Therefore, for any given stress-triaxiality, the largest magnitude of product-triaxiality occurs when two of the three principle stresses are equal. Depending on the sign, a state of hydrostatic compression or tension is found at the extremums. It should be noted that any state-of-stress must be within the bounds of the meridians defined by Equations (4.39) and (4.40), where the solution envelope extends until infinity as:

$$a, b = 1 \Rightarrow \frac{p}{\sigma_{vm}} \to \pm\infty \tag{4.41}$$

Failure locus or the meridians described by Equations (4.39) and (4.40) can also be related to the third deviatoric stress invariant by utilizing the relations in Equation (4.42). Therefore, it is possible to interchangeably use Lode-angle-parameter with product-triaxiality when illustrating the plane of stress-space as a projection of the three-dimensional failure surface.

$$\begin{aligned}
&I_3 = \sigma_1\sigma_2\sigma_3 \\
&J_3 = \mathrm{s}_1\mathrm{s}_2\mathrm{s}_3 = (\sigma_1 + p)(\sigma_2 + p)(\sigma_3 + p) \\
&\cos(3\vartheta) = \frac{27}{2}\frac{J_3}{\sigma_{vm}^3} \\
&\Rightarrow J_3 = \frac{2}{27}I_1^3 + \frac{1}{3}I_1I_2 + I_3 = I_3 + p^3 - \frac{p\sigma_{vm}^2}{3} \\
&\Rightarrow \frac{27}{2}\frac{J_3}{\sigma_{vm}^3} = \frac{27}{2}\left(\frac{I_3}{\sigma_{vm}^3} + \frac{p^3}{\sigma_{vm}^3} - \frac{p}{3\sigma_{vm}}\right) \\
&\Rightarrow -1 \le \theta_L = \frac{27}{2}\frac{J_3}{\sigma_{vm}^3} = \frac{27}{2}\left(\sigma_p^* + \sigma^{*3} - \frac{\sigma^*}{3}\right) \le +1
\end{aligned} \tag{4.42}$$

Figure 4-13(a) illustrates how the three-dimensional failure surface is projected on to the plane of stress-space with three distinct test points representing the uni-axial tension, shear and uni-axial compression, where Lode-angle-parameter is used by incorporating the third deviatoric stress invariant. Projected failure surface is shown in Figure 4-13(b), while the hatched stress-space represents the states-of-stress that an elementary particle can possibly experience. Using Lode-angle-parameter or the third deviatoric stress invariant on the projected failure locus provides a well-defined boundary on the invariant space; however, the conceivable limits towards the negative stress-triaxiality values are questionable and do not offer any practical bounds.

(a)

(b)

(c)

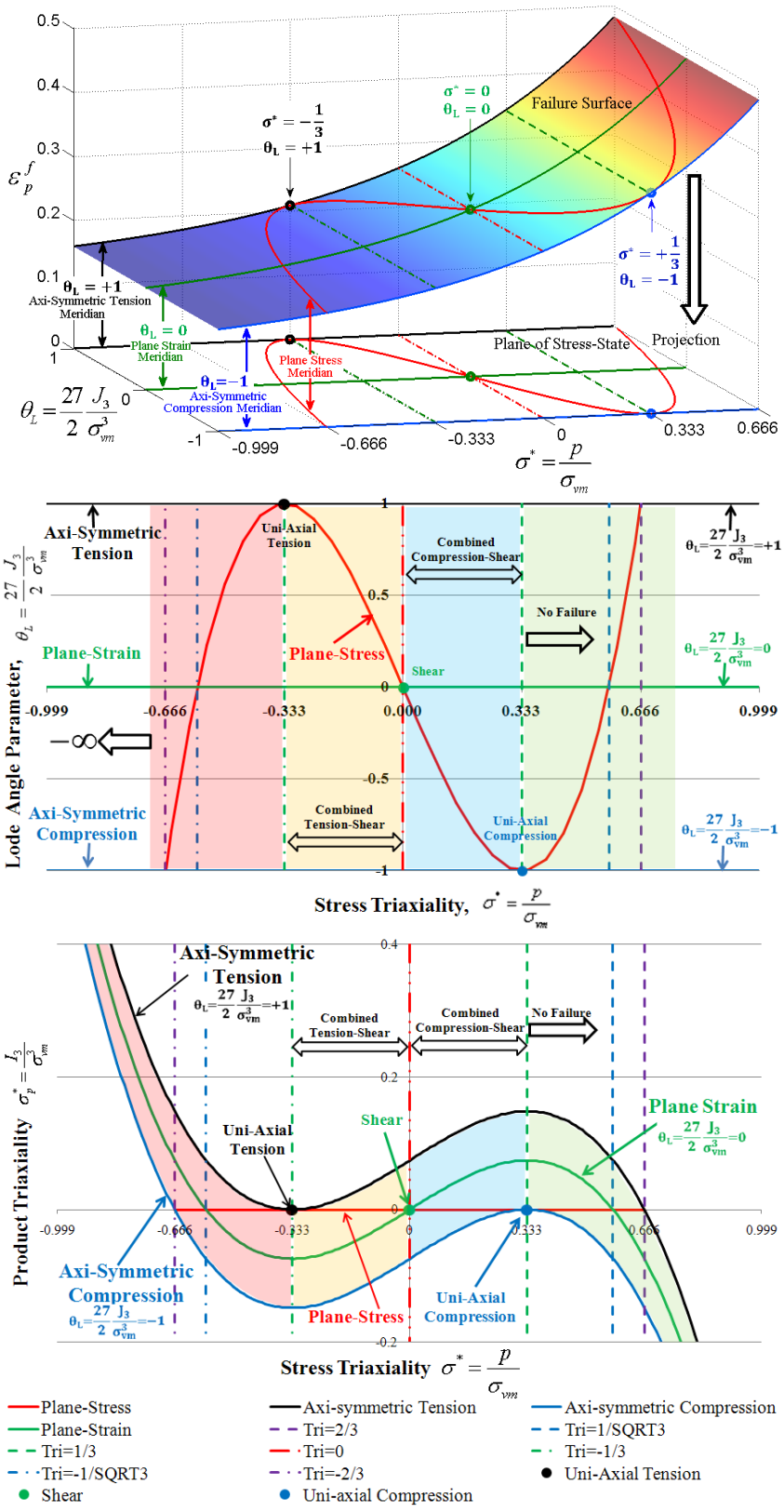

Figure 4-13: Representation of a three dimensional failure surface; (a) J-C relation, (b) projection on to the plane of stress-state defined by stress-triaxiality vs. Lode-angle-parameter and (c) projection on to the plane of stress-state defined by stress-triaxiality vs. product-triaxiality.

Since the stress invariants can interchangeably be used according to Equation (4.42), the same plane of stress-space can be illustrated with product-triaxiality by incorporating the third stress invariant in Figure 4-13(c). In this figure, the hatched areas also signify all states-of-stress that can be observed by an element. Having defined the Lode-angle-parameter as a primary boundary on the invariant space, incorporating the product-triaxiality provides a reasonable boundary on the space of interest. Especially towards the negative stress-triaxiality region, it is clearly seen that the region of interest can be limited since the corridor defined between the stress meridians tapers due to Equations (4.39) and (4.40).

Figure 4-13 also depicts how three distinct state-of-stress points on the failure surface can be illustrated on the projected planes of stress-states. Uni-axial tension, shear and uni-axial compression points on the failure surface are portrayed in Figures 4-13(b) and 4-13(c). Any point can similarly be positioned on both planes. However, due to the convenience in finding required test points for the material characterization phase in Chapter 5, the latter plane of stress-state is used more often. In the next sections, significant points and the region of interest on the stress-space are determined to help choose the states-of-stress that will be used to construct the failure surface after characterization of the plastic strain at failure for each stress-state point.

4.3.1 **Identification of the stress-states**

As the methodology of illustrating multiple states-of-stress by using stress-triaxiality, Lode-angle-parameter and product-triaxiality is defined, where all stress invariants are utilized, an intelligently contrived test matrix is needed to construct and span the stress-space with the required corresponding triaxiality values. The following sections are utilized to help identify the stress-states of each specimen that is chosen to have a particular stress-state during the testing.

4.3.1.1 Uni-axial state

The general states-of-stress can be identified in more detail with the following derivations:

Since $\sigma_1 \geq \sigma_2 \geq \sigma_3$, when a state of uni-axial stress exists either σ_1 will be greater than zero or σ_3 will be less than zero, and σ_2 will be zero in either case. If $\sigma_1 > 0$, then $a = b = 0$, and $\frac{p}{\sigma_{vm}} = -\frac{1}{3}$. If $\sigma_3 < 0$, then $\frac{p}{\sigma_{vm}} = \frac{1}{3}$. In both cases the product-triaxiality parameter is zero, (i.e., $\frac{\sigma_1\sigma_2\sigma_3}{\sigma_{vm}^3} = 0$).

4.3.1.2 Plane-stress state-of-stress

A condition of plane-stress, where one of the principle stresses is zero, can be represented by the principle stress parameters a or b being set equal to zero. In this case $\sigma_1 \geq 0$ and Equation (4.35) can be rewritten as either:

$$\begin{bmatrix} \sigma_1 & 0 & 0 \\ 0 & a\sigma_1 & 0 \\ 0 & 0 & b\sigma_1 \end{bmatrix} = \begin{bmatrix} \sigma_1 & 0 & 0 \\ 0 & a\sigma_1 & 0 \\ 0 & 0 & 0 \end{bmatrix} \Rightarrow 1 \geq a \geq 0 \tag{4.43}$$

with the stress-triaxiality term becoming:

$$\frac{p}{\sigma_{vm}} = -\frac{1}{3}\frac{1+a}{\sqrt{1+a^2-a}} \tag{4.44}$$

or

$$\begin{bmatrix} \sigma_1 & 0 & 0 \\ 0 & a\sigma_1 & 0 \\ 0 & 0 & b\sigma_1 \end{bmatrix} = \begin{bmatrix} \sigma_1 & 0 & 0 \\ 0 & 0 & 0 \\ 0 & 0 & b\sigma_1 \end{bmatrix} \Rightarrow 0 \geq b \geq -\infty \tag{4.45}$$

with the stress-triaxiality term becoming:

$$\frac{p}{\sigma_{vm}} = -\frac{1}{3}\frac{1+b}{\sqrt{1+b^2-b}} \tag{4.46}$$

and in both cases the product-triaxiality parameter is zero, (i.e., $\frac{\sigma_1\sigma_2\sigma_3}{\sigma_{vm}^3} = 0$).

So, for biaxial states-of-stress, either $\sigma_1 = \sigma_2$, $a = 1$ with the result of $\frac{p}{\sigma_{vm}} = -\frac{2}{3}$, or $\sigma_2 = \sigma_3$ with the result of $\frac{p}{\sigma_{vm}} = \frac{2}{3}$.

Equation (4.47) represents this case in a more generic way as:

$$\sigma_1 \geq 0 \Rightarrow \begin{bmatrix} \sigma_1 & 0 & 0 \\ 0 & a\sigma_1 & 0 \\ 0 & 0 & b\sigma_1 \end{bmatrix} = \begin{cases} \begin{bmatrix} \sigma_1 & 0 & 0 \\ 0 & a\sigma_1 & 0 \\ 0 & 0 & 0 \end{bmatrix} \Rightarrow 1 \geq a \geq 0 \Rightarrow \begin{cases} \frac{p}{\sigma_{vm}} = -\frac{1}{3}\frac{1+a}{\sqrt{1+a^2-a}} \\ \frac{\sigma_1\sigma_2\sigma_3}{\sigma_{vm}^3} = 0 \end{cases} \\ \begin{bmatrix} \sigma_1 & 0 & 0 \\ 0 & 0 & 0 \\ 0 & 0 & b\sigma_1 \end{bmatrix} \Rightarrow 0 \geq b \geq -\infty \Rightarrow \begin{cases} \frac{p}{\sigma_{vm}} = -\frac{1}{3}\frac{1+b}{\sqrt{1+b^2-b}} \\ \frac{\sigma_1\sigma_2\sigma_3}{\sigma_{vm}^3} = 0 \end{cases} \\ \begin{bmatrix} 0 & 0 & 0 \\ 0 & \sigma_2 & 0 \\ 0 & 0 & \sigma_3 \end{bmatrix} \Rightarrow \begin{cases} \sigma_2 \leq 0 \\ \sigma_3 \leq 0 \end{cases} \end{cases} \quad (4.47)$$

Considering isochoric plastic strains:

$$\varepsilon_p \approx \frac{\sigma_1}{3}\begin{bmatrix} 2-a & 0 & 0 \\ 0 & 2a-1 & 0 \\ 0 & 0 & -a-1 \end{bmatrix} \Rightarrow \begin{cases} 1 \geq a \geq 0 \\ b = 0 \end{cases} \Rightarrow \frac{\varepsilon_{p,2}}{\varepsilon_{p,1}} = \frac{2a-1}{2-a} \quad (4.48)$$

Plane-stress states for the stress-triaxiality versus product-triaxiality space are illustrated in Figure 4-14 with more details. It is also shown how the axi-symmetric tension, axi-symmetric compression and plane-strain meridians span the stress-space defined by the envelope represented by the Lode-angle-parameter.

Therefore, it is suggested here that the boundaries of the failure locus can be defined interchangeably by incorporating all three definitions of triaxiality. By using stress-triaxiality ($\frac{p}{\sigma_{vm}}$) vs. Lode-angle-parameter ($-1 \leq \theta_L = \frac{27}{2}\frac{J_3}{\sigma_{vm}^3} \leq +1$) or stress-triaxiality vs. product-triaxiality ($\frac{I_3}{\sigma_{vm}^3}$), a failure surface can be constructed after characterization of plastic strains at failure for every point of interest. Lode-angle-parameter can be used to categorize the stress meridians and the product-triaxiality can be used to categorize the limits of the state-of-stress.

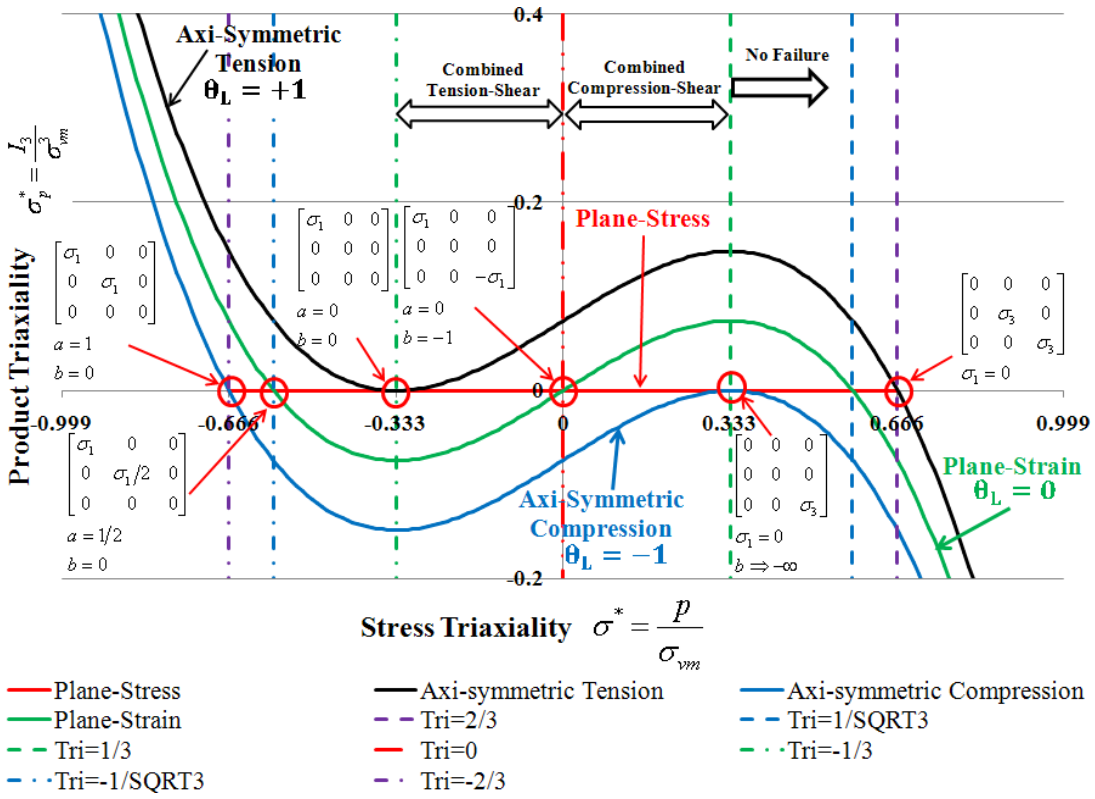

Figure 4-14: Plane-stress state conditions on the stress-space.

4.3.1.3 Axi-symmetric state-of-stress

A condition of axi-symmetric stress is observed when two principal stresses are equal. Axi-symmetric state-of-stress can exist in either tension or compression. The tension meridian is obtained when $a = b$ and compression is when $a = 1$.

Equation (4.49) represents this case in a more generic way as:

$$\begin{bmatrix} \sigma_1 & 0 & 0 \\ 0 & a\sigma_1 & 0 \\ 0 & 0 & a\sigma_1 \end{bmatrix} \Rightarrow \begin{cases} 1 \geq a \geq -\infty \\ b = a \end{cases} \Rightarrow \begin{cases} \dfrac{p}{\sigma_{vm}} = -\dfrac{1}{3}\dfrac{1+2a}{\sqrt{1+a^2-2a}} \\ \dfrac{\sigma_1\sigma_2\sigma_3}{\sigma_{vm}^3} = \dfrac{a^2}{(1+a^2-2a)^{3/2}} \end{cases}$$

$$\begin{bmatrix} \sigma_1 & 0 & 0 \\ 0 & \sigma_1 & 0 \\ 0 & 0 & b\sigma_1 \end{bmatrix} \Rightarrow \begin{cases} 1 \geq b \geq -\infty \\ a = 1 \end{cases} \Rightarrow \begin{cases} \dfrac{p}{\sigma_{vm}} = -\dfrac{1}{3}\dfrac{2+b}{\sqrt{1+b^2-2b}} \\ \dfrac{\sigma_1\sigma_2\sigma_3}{\sigma_{vm}^3} = \dfrac{b}{(1+b^2-2b)^{3/2}} \end{cases} \quad (4.49)$$

Considering isochoric plastic strains:

$$\varepsilon_p \approx \frac{\sigma_1}{3}\begin{bmatrix} 2-2a & 0 & 0 \\ 0 & a-1 & 0 \\ 0 & 0 & a-1 \end{bmatrix} \Rightarrow \begin{cases} 1 \geq a \geq -\infty \\ b = a \end{cases} \Rightarrow \frac{\varepsilon_{p,2}}{\varepsilon_{p,1}} = \frac{a-1}{2-2a} = -\frac{1}{2} \qquad (4.50)$$

Axi-symmetric stress-states for the stress-triaxiality vs. product-triaxiality space are illustrated in Figures 4-15 and 4-16 for both compression and tension meridians respectively.

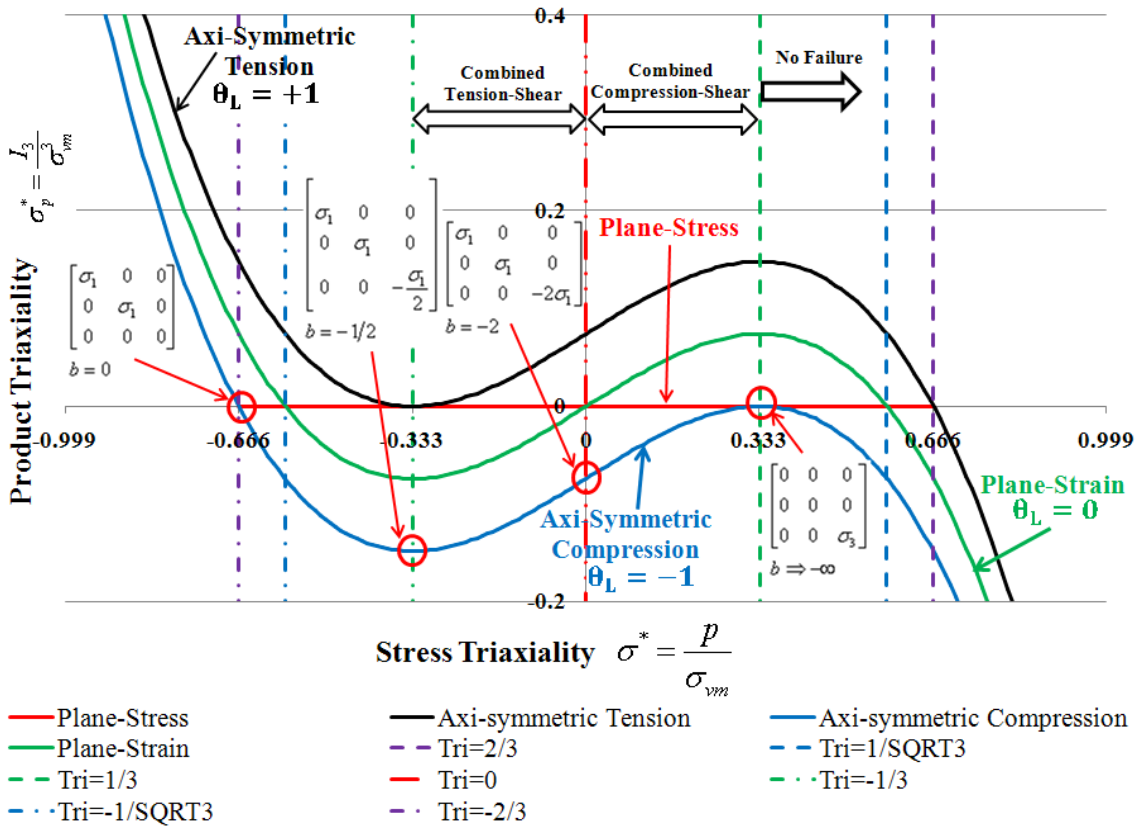

Figure 4-15: Axi-symmetric stress-state conditions on the compression meridian of the stress-space.

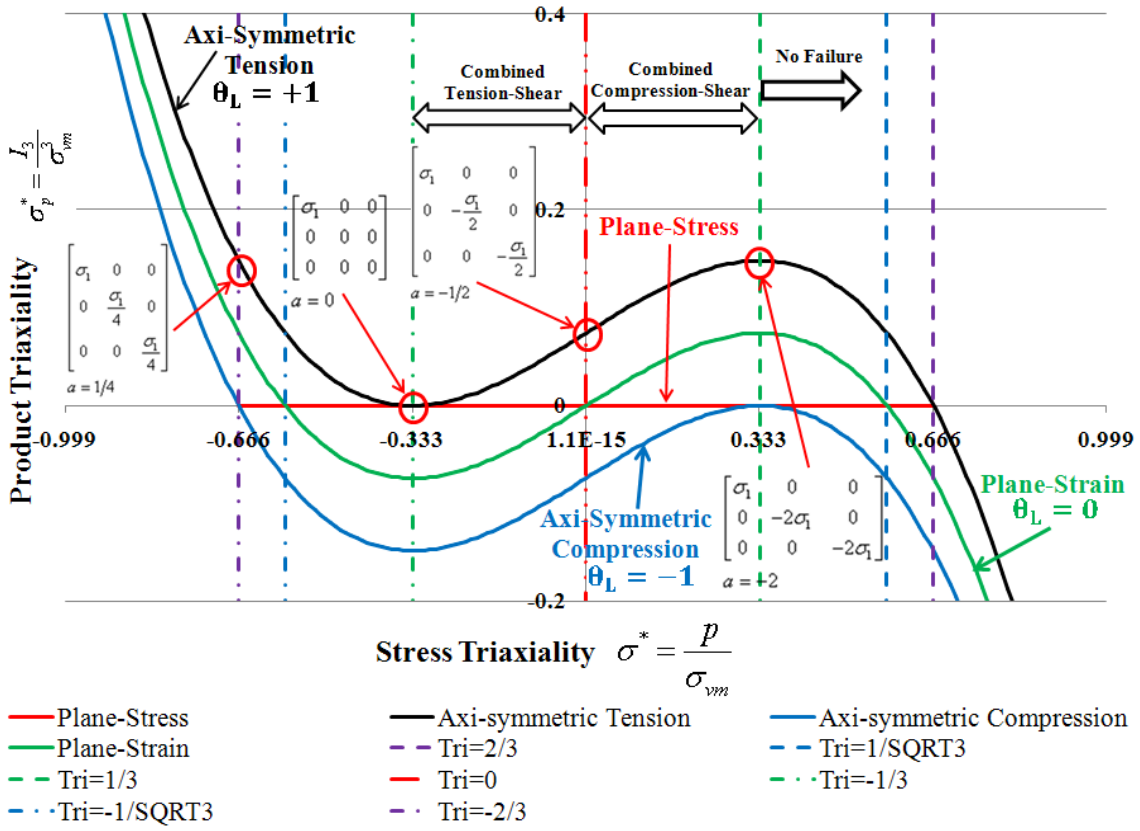

Figure 4-16: Axi-symmetric stress-state conditions on the tension meridian of the stress-space.

4.3.1.4 Plane-strain state-of-stress

A condition of Plane-strain stress observed where a principal deformation is zero. In terms of a and b, the principle stress parameters are:

$$\begin{bmatrix} \sigma_1 & 0 & 0 \\ 0 & a\sigma_1 & 0 \\ 0 & 0 & (2a-1)\sigma_1 \end{bmatrix} \Rightarrow \begin{cases} 1 \geq a \geq -\infty \\ b = 2a - 1 \leq a \end{cases} \Rightarrow \begin{cases} \dfrac{p}{\sigma_{vm}} = \pm\dfrac{1}{3}\dfrac{3a}{\sqrt{3+3a^2-6a}} \\ \dfrac{\sigma_1\sigma_2\sigma_3}{\sigma_{vm}^3} = \pm\dfrac{2a^2-a}{(3+3a^2-6a)^{3/2}} \end{cases} \tag{4.51}$$

Considering isochoric plastic strains:

$$\varepsilon_p \approx \mathbf{s} = \frac{\sigma_1}{3}\begin{bmatrix} 2-a-b & 0 & 0 \\ 0 & 0 & 0 \\ 0 & 0 & 2b-a-1 \end{bmatrix} \tag{4.52}$$

Plane-stress stress-states for the stress-triaxiality vs. product-triaxiality space are illustrated in Figure 4-17 for both compression and tension meridians respectively.

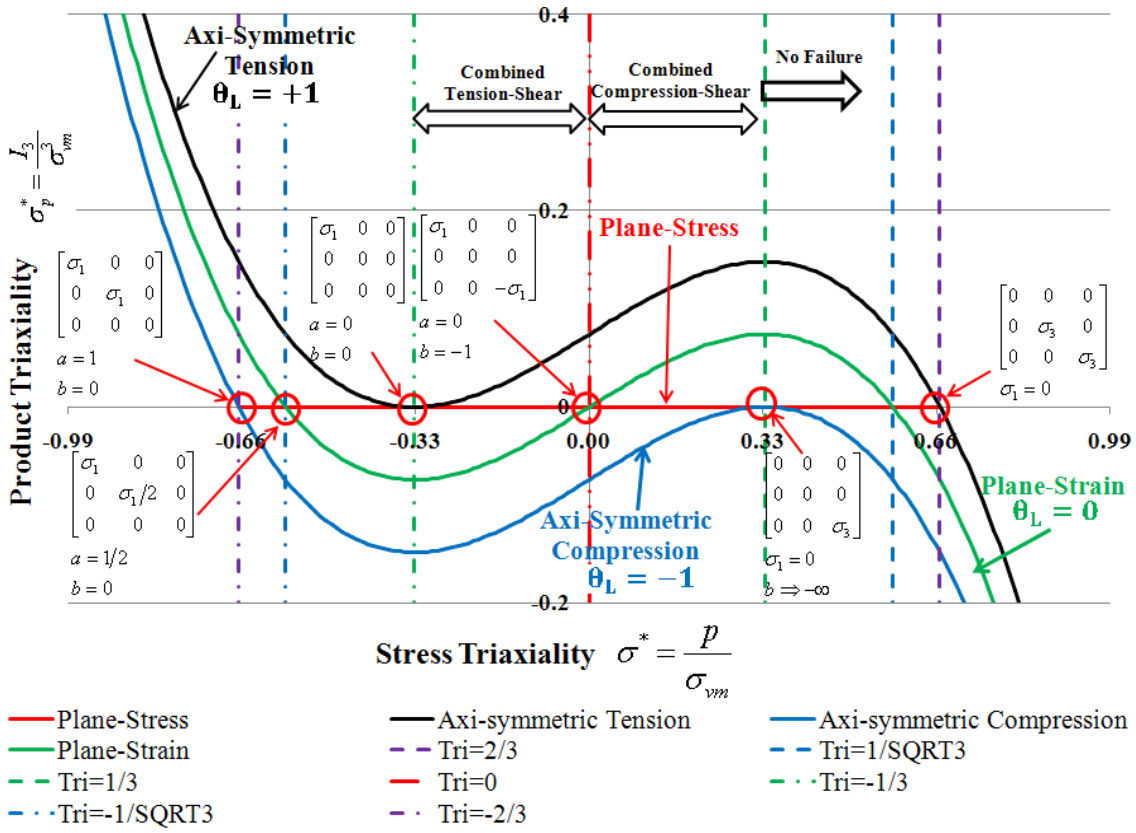

Figure 4-17: Plane-strain stress-state conditions on the plane-strain meridian of the stress-space.

4.3.2 **Notable points on the stress-state space**

The foregone calculations lead us to identify some of the most notable points that are summarized according to their stress-triaxiality, product-triaxiality and Lode-angle-parameter values as listed in Table 4-1 and illustrated in newly proposed stress-triaxiality versus product-triaxiality space in Figure 4-18. It is assumed that failure beyond a stress-triaxiality of $\sigma^* = +\frac{1}{3}$ is not possible; therefore, the test matrix and failure surface is defined up to the limiting stress-state of uni-axial compression.

Table 4-1: Notable points and their stress-state parameters.

States-of-stress	Stress-triaxiality σ^*	Product-triaxiality σ_p^*	Lode-angle-parameter θ_L	Illustration
Biaxial Tension	$-\frac{2}{3}$	0.0	-1.0	
Uni-axial Tension with Lateral Confinement (Plane-Strain Tension)	$-\frac{1}{\sqrt{3}}$	0.0	0.0	
Uni-axial Tension	$-\frac{1}{3}$	0.0	1.0	
Pure Shear	0.0	0.0	0.0	
Uni-axial Compression	$+\frac{1}{3}$	0.0	-1.0	

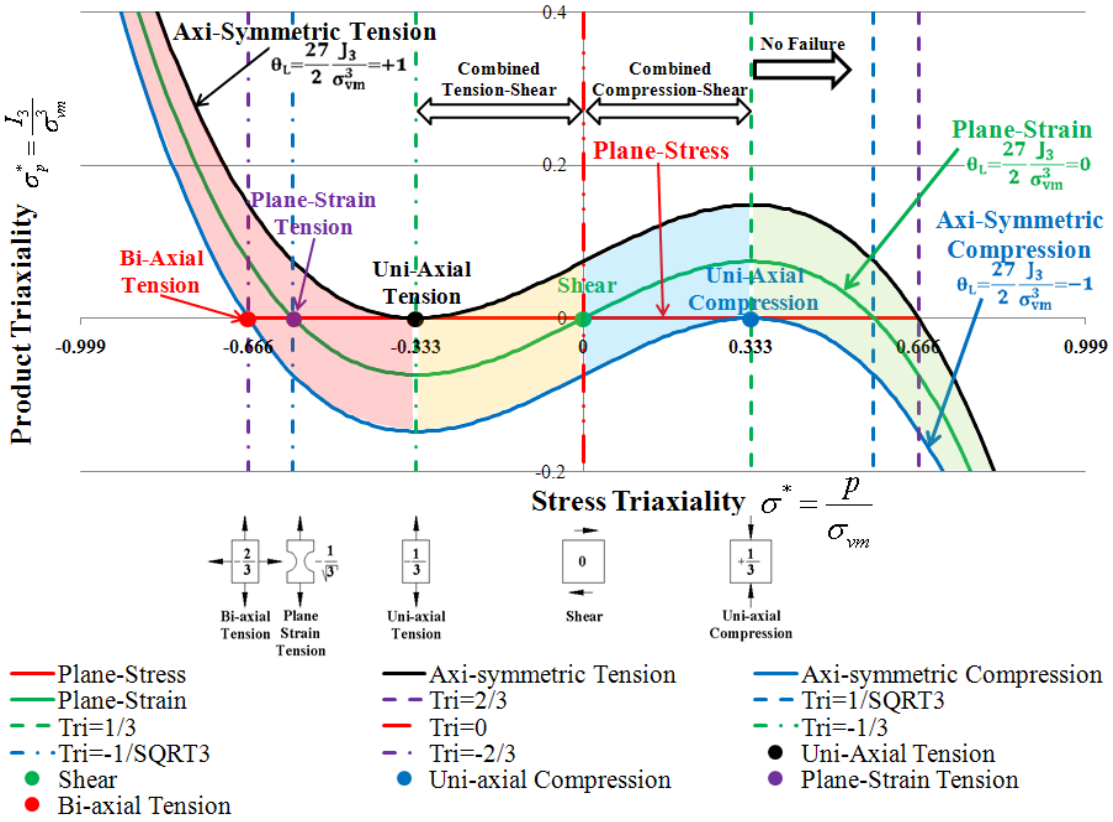

Figure 4-18: Notable points on stress-triaxiality versus product-triaxiality space.

Stress-triaxiality versus product-triaxiality space provides an objective tool to characterize the stress-state for any deformation pattern as illustrated in Figure 4-18 for five distinct states. Clearly, five stress-states are insufficient to construct a well-defined failure surface and more stress-state points are needed within the hatched area of the stress-state plane for a sufficient representation. These stress-state points have to be chosen with a reasonable resolution that a balance between the accuracy of the failure surface and the number of required stress-state points can be achieved since each stress-state point corresponds to a test and has to be characterized to find the plastic strain at failure. Therefore, there is a tradeoff between the cost of testing each chosen stress-state and the accuracy of the failure curve. Moreover, while choosing the states of interest, a methodology has to be developed to justify the region of curiosity and the capability of the chosen points for representing the entire failure surface independent of the local sensitivities. Consequently, in the following section, a methodology is suggested to help determine the region of interest on the stress-state plane for ductile materials under impact loading.

4.3.3 **Identification of the stress-states for structures under impact loading**

The results of the ballistic impact analyses that were reported in Section 3.2 are used to identify the stress-state history of the finite elements during the impact loading. It is found that the failure modes are changing from petalling to plugging as the thickness and the impact velocity changes, which suggests that the state-of-stress changes from tensile dominated necking to shear as illustrated in Figure 4-19.

To identify the possible modes of state-of-stress for individual finite elements, representative elements are selected within the impact region under the projectile. For thinner targets, due to petalling failure, more elements are selected in the vicinity of the petal formation. Figure 4-20 represents the set of elements selected per each thickness at the undeformed stage. Simulation results are selected from the higher end of the ballistic curve (i.e., higher velocities) considering that the dominant failure characteristics will be more pronounced. The triaxiality parameters (i.e., σ^*, σ_p^* and θ_L) are calculated at the peak values of the stresses for a number of finite elements, some of which failed and

some of which did not.

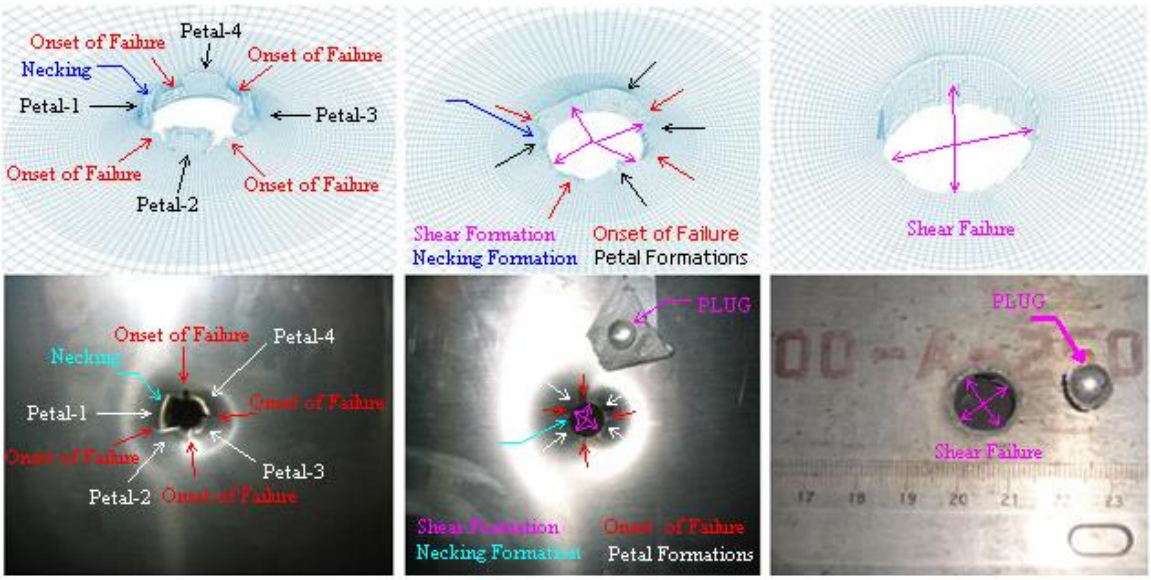

1.5875mm 3.75mm 6.35mm

Figure 4-19: Transition of the failure modes with target thickness under impact loading due to the state-of-stress.

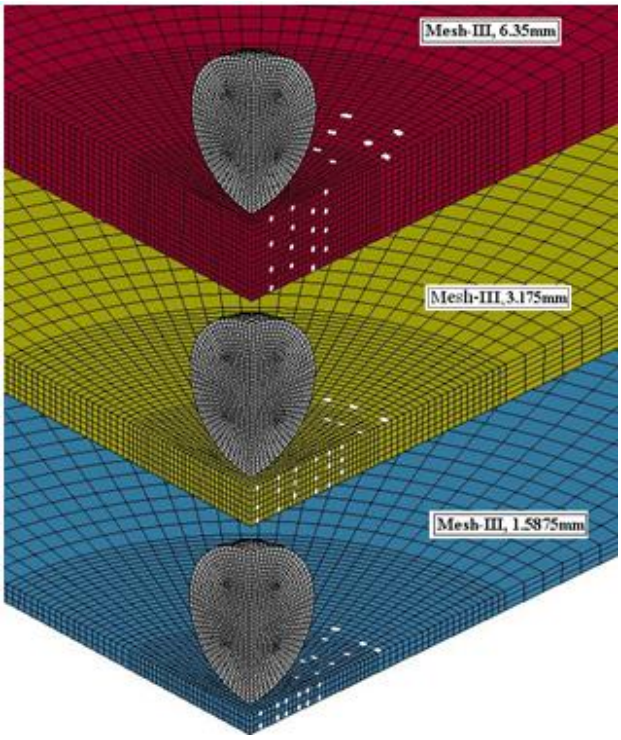

Figure 4-20: Selected elements for state-of-stress identification.

The triaxiality parameters vary considerably before the stresses reach levels near failure. Figure 4-21 summarizes and overlays the triaxiality parameters from the points collected for three different thicknesses on the stress-triaxiality versus product-triaxiality space. It should be noted that the selected elements are intended to be representative of the failure modes under impact regime only. It is also identified that the failing elements are accumulated around negative stress-triaxiality values, between axi-symmetric tension and axi-symmetric compression meridians. It is not a coincidence that for different thicknesses and impact speeds, for ductile materials under impact loading in general, stress-states that lead to failure are similar and populated within an envelope defined through negative values of the stress-triaxiality (i.e., $\sigma^* \leq -\frac{1}{3}$) versus product-triaxiality space. Therefore, an experimental program should be designed to cover this space (i.e., stress-space hatched in red) with a better resolution while constructing a failure surface for FE analysis. Clearly, fewer points are needed to represent the stress-states towards the positive values of the stress-triaxiality (i.e., $\sigma^* > -\frac{1}{3}$), where these regions are designated as combined tension-shear and combined compression-shear respectively (i.e., stress-spaces hatched in yellow and blue). No failure is assumed beyond a stress-triaxiality value of $\sigma^* = +\frac{1}{3}$, where it is also depicted in Figure 4-21 that several finite elements from the impact region are experiencing similar states-of-stress but do not fail. Therefore, the last stress-state point is chosen to be the uni-axial compression while constructing a failure surface and the region beyond that stress-triaxiality value (i.e., $\sigma^* > +\frac{1}{3}$), no test point is chosen as the stress-state approaches hydrostatic compression (i.e., stress-space hatched in green).

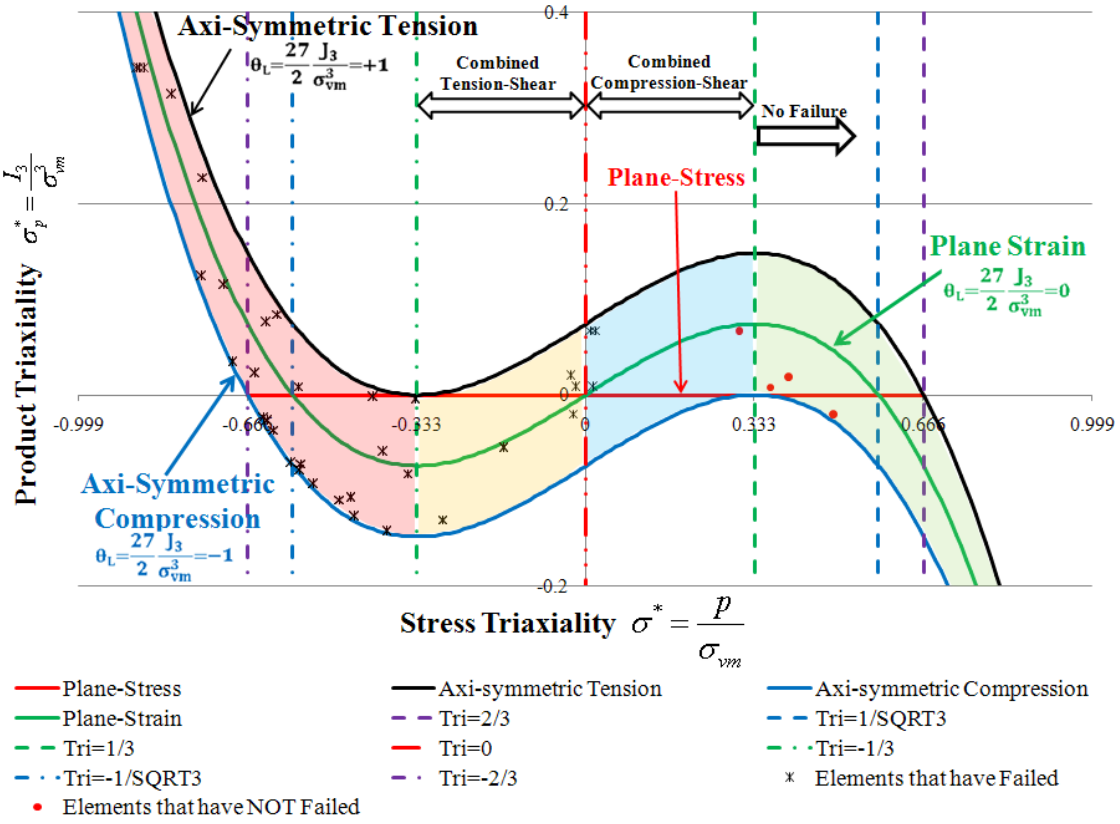

Figure 4-21: States-of-stress for the selected finite elements under the impact region as a function of stress-triaxiality and product-triaxiality.

4.4 Devising a testing program to characterize a generic failure locus

TRAUM utilizes an extended form of the accumulated failure algorithm, which is defined earlier by Equation (4.2) that depends upon multiple states-of-stress, strain rate, temperature and regularized with respect to the element size as formulized by Equation (4.53)

$$\varepsilon_p^f = f(\sigma^*, \theta_L)g(\dot{\varepsilon}_p)h(T)i(l_{cr})$$
$$D_{cr} = \int_0^{\varepsilon_p^f} \frac{d\varepsilon_p}{\varepsilon_p^f} \geq 1 \Rightarrow \text{failure} \tag{4.53}$$

where, $f(\sigma^*, \theta_L)$ represents a failure surface, which is constructed by characterized values of the effective plastic strains at failure for different states-of-stress at a nominal

strain rate and room temperature for a characteristic element size. The failure surface is then scaled by the factors defined by $g(\dot{\varepsilon}_p), h(T)$ and $i(l_{cr})$, which represent strain rate, temperature and regularization terms respectively.

Therefore, in the proceeding sections a methodology is introduced to help describe the stress-state dependent failure surface. A methodology is also described to form a failure locus by scaling the initially constructed stress-state dependent failure surface based on strain rate and temperature. Specimen design methodology and geometries for each selected stress-state is demonstrated. Targeted values of the stress-states, strain rates and temperatures for a fully defined failure locus are listed.

4.4.1 **Construction of a failure locus for multiple states-of-stress**

An intelligently contrived test matrix is developed by designing specific test specimens with different geometries that can be used to construct the whole failure locus for Al2024-T351 as a function of stress-triaxiality and Lode-angle-parameter defined by the factor in Equation (4.54).

$$f\left(\underbrace{\frac{p}{\sigma_{vm}}}_{\sigma^*}, \underbrace{\frac{27}{2}\frac{J_3}{\sigma_{vm}^3}}_{\theta_L}\right) \tag{4.54}$$

The boundaries of this failure locus are defined with a consideration on the stress-space defined by stress-triaxiality versus product-triaxiality (σ^* vs. σ_p^*). Different states-of-stress are attained by utilizing specimens that are representing axi-symmetric tension, plan-stress, plane-strain tension, shear, compression, combined tension-shear and bi-axial tension states. An inverse material characterization algorithm is then introduced to generate input data for the new material model (TRAUM). Consequently, the specimens with preliminary estimates of stress-triaxiality, Lode-angle-parameter, and product-triaxiality will be used to construct a failure surface. Parallel numerical simulations are used to verify the exact state-of-stress and the failure point, which are attained iteratively

until the desired values are achieved since the plastic deformation in the specimen causes changes in the predetermined stress-states.

Validated impact simulations reveal that the ductile materials undergoing impact loading fail under different states-of-stress as shown in Figure 4-21; however, the stress-states are populated around certain zones. Therefore, it is required to test materials under different stress-states and characterize the failure points to construct a failure locus having a bias on the zones of interest. It is usually a common practice to test axi-symmetric round specimens in tension to see the effects of confinement especially by using Bridgman's [162] [95] analysis of the stress-state at the necking localization of an axi-symmetric specimen. Characterizing and using effective plastic strain at failure as a function of state-of-stress is also widely practiced and described further by McClintock [115], Rice and Tracey [117] and Hancock and Mackenzie [119]. Many others including J-C [85], which is discussed in detail in Section 3.2, have utilized similar testing programs to characterize effective plastic strain at failure as a function of stress-triaxiality. J-C used an exponential curve fitting on the experimental data. Measuring the failure strain and the stress-state at the time of failure is not any easy task; therefore, parallel numerical simulations are typically used to inversely calculate the failure strains and stress-states. The common approach to characterize the failure point and corresponding stress-states is usually attained by trying to match the experimentally measured data, such as force vs. displacement curves. This is often described as a meticulous procedure since the behavior can be extremely nonlinear [1] [178] [180]. Besides, the stress-state is not the only variable that has an influence on the failure strain. There are other contributing factors to ductile failure such as; the strain rate effects, temperature etc., where in most cases the effects are coupled and can be difficult to identify [7] [8] [9] [10].

The variations in the state-of-stress and the range of the domain make it challenging to design an experimental program that can capture the whole failure locus. More recently, Bao [99], Bao and Wierzbicki [100], Barsoum and Faleskog [102], Xue [103], Bai [104], Bai and Wierzbicki [105] conducted test programs that have coupled numerical simulations and experiments with specimens having different geometries in order to cover a wide range of stress-states. Xue [103], Bai [104] have introduced failure

models with another stress-state indicator called the Lode-angle-parameter and their failure surfaces were illustrated in Figures 4-3 and 4-4, respectively. However, these failure surfaces fit different functions over the characterized test points for the values of equivalent plastic strain at failure representing different stress-states. Higher order surface fitting methodologies may put the overall accuracy at risk due to local sensitivities. Depending on the material of interest, changes in state-of-stress may cause considerable differences on the equivalent plastic strain at failure. Dramatic changes can be observed for Al2024-T351 when the stress-triaxiality changes in between $-\frac{1}{3} > \sigma^* > +\frac{1}{3}$ and Bao [99] suggested three distinct branches to represent the significant differences on the failure modes as illustrated in Figure 4-2. Consequently, while fitting a pre-determined higher order surface over the available stress-states, two critical details should be foresighted. First of all, the overall behavior of the failure surface should be kept stable and extreme oscillations due to the regions with local extremum should be prevented. Otherwise, higher order surface fitting can numerically lead to negative values of effective plastic strain at failure, which is unacceptable, when the failure surface needs to be extrapolated beyond the limits of the test matrix. Secondly, utilizing a pre-accepted function for the failure surface should not lead to even out the details for certain stress-states, where significant changes in the failure modes can be observed experimentally. Fitting a failure surface over a range of test points that are representing certain states-of-stress can be illustrated as in Figure 4-22(a) for a surface using J-C relation defined by Equation (3.4) and parameters given by Set-1 in Table 3-2.

The test points that are illustrated in Figure 4-22 signify different specimens used in this study, which will be discussed in more detail later in this Chapter and in Chapter 5. These test points are used to imply that the values of the effective plastic strain at failure for certain states-of-stress may not accurately be represented by a smooth surface fitting methodology (i.e., J-C). It can clearly be noticed that surface fitting to a number of test points flattens the sensitivity of the failure surface which leads to inaccurate representation. It should be noted that, Figure 4-22(b), which is a J-C representation, is not Lode-angle-parameter dependent. It is basically constructed by extending the failure curve that was found through curve fitting and only stress-triaxiality dependent (i.e.,

$\theta_L = \frac{27}{2}\frac{J_3}{\sigma_{vm}^3} = +1 = 0 = -1$). Figure 4-22(c) illustrates a projection of the J-C failure surface on to the plane of stress-states with a contour map and specifically selected states-of-stress points that a ruled failure surface can be constructed through a concept of 'bridging' with the suggested paths.

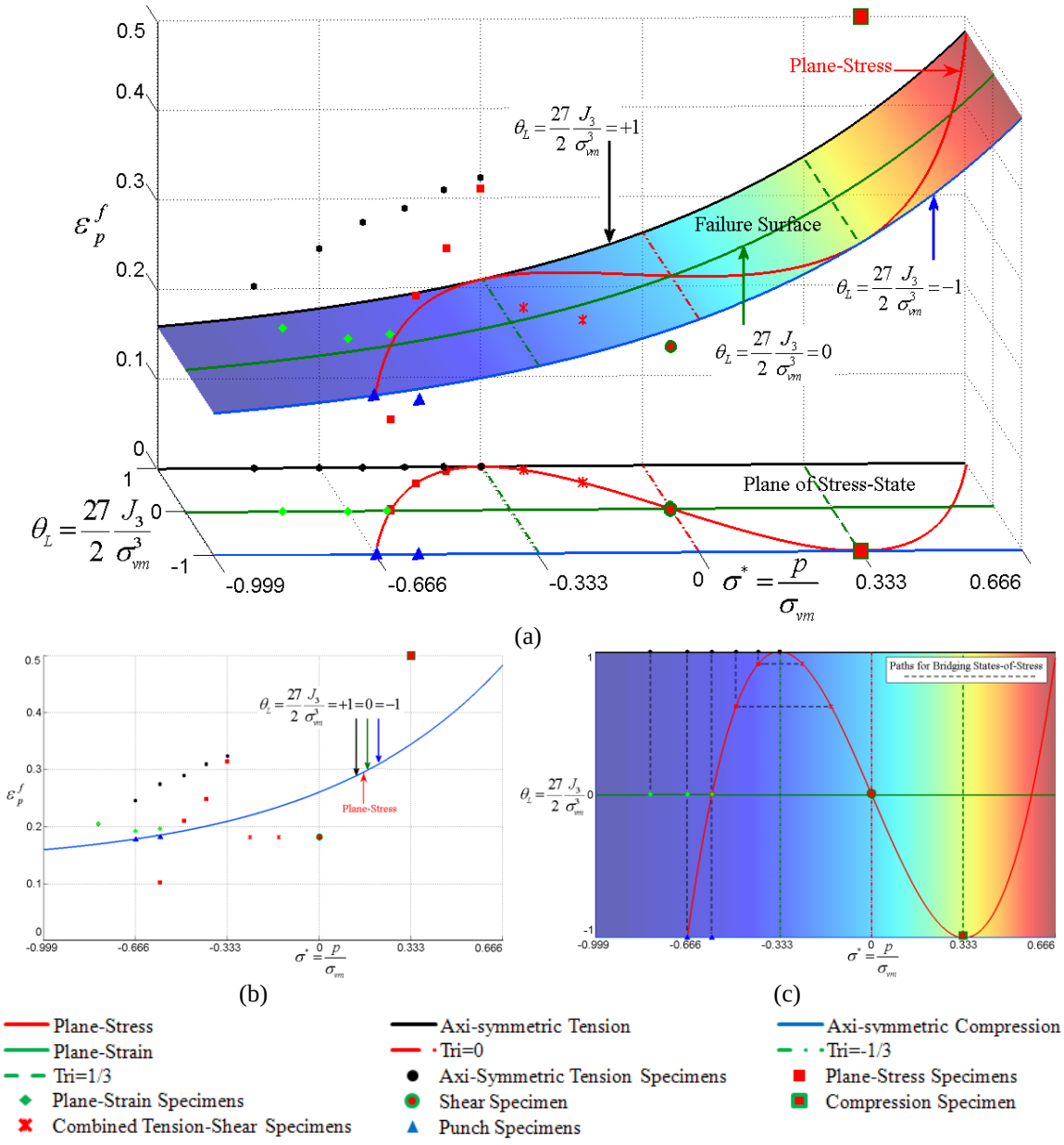

Figure 4-22: Representation of the J-C failure surface; (a) with test points suggested later in this Chapter, (b) projection on to the plane of stress-triaxiality vs. effective plastic strain at failure, showing no Lode-angle-parameter dependency and (c) projection on to the plane of stress-state defined by stress-triaxiality vs. Lode-angle-parameter showing the paths suggested for bridging the stress-states.

Similarly, the failure surface suggested by Bai [104] can be illustrated in Figure 4-23(a) with the same test points that are shown in Figure 4-22, which are representing certain stress-states that will be discussed further in the proceeding sections.

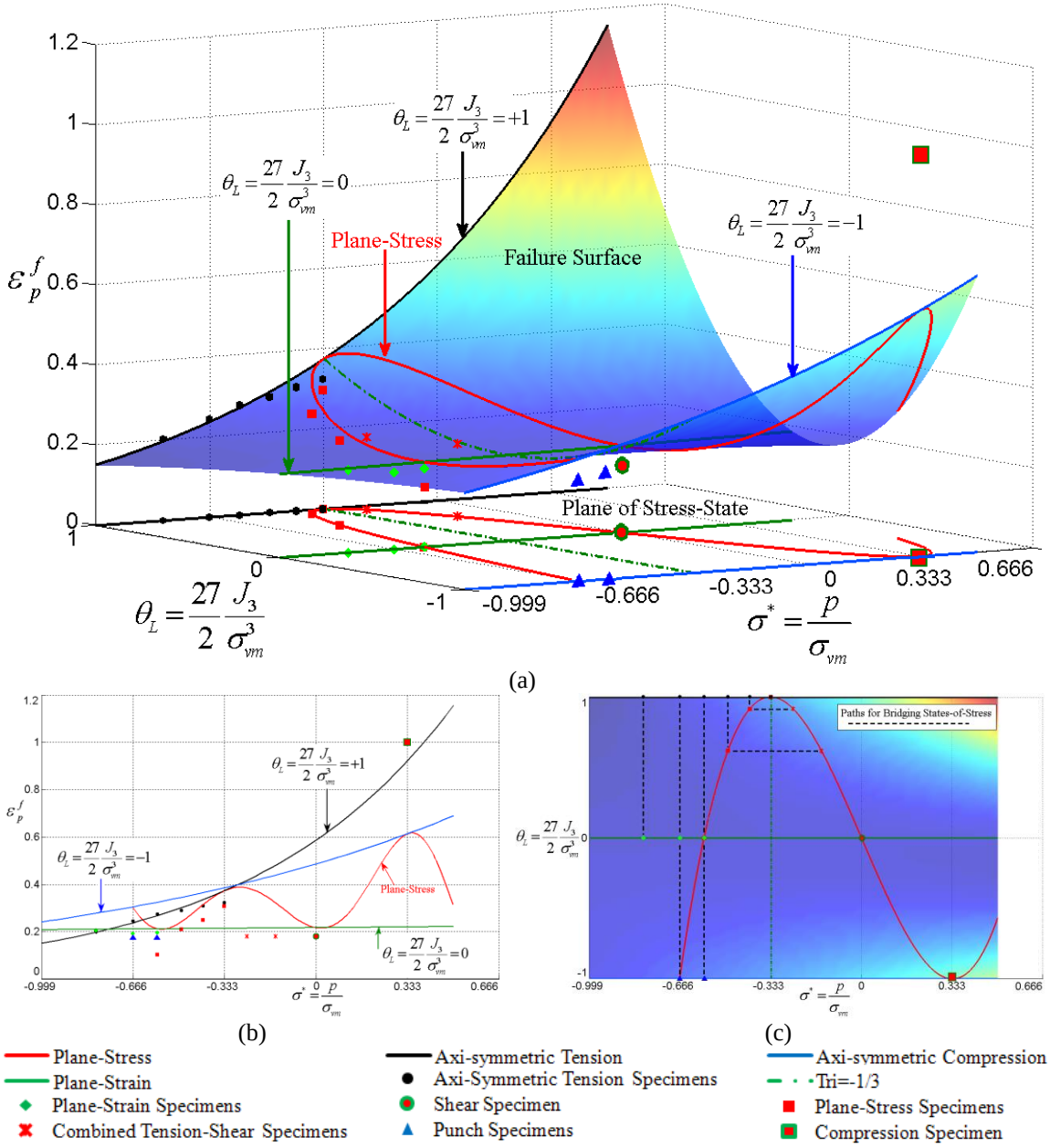

Figure 4-23: Representation of a Lode-angle-parameter dependent failure surface; (a) failure surface defined by surface fitting over the test points defined in [104], (b) projection on to the plane of stress-triaxiality vs. effective plastic strain at failure showing Lode-angle-parameter dependency with different stress meridians and (c) projection on to the plane of stress-state defined by stress-triaxiality vs. Lode-angle-parameter showing the paths suggested for bridging the stress-states.

It can clearly be observed that Lode-angle-parameter dependent failure surfaces have a better sensitivity in representing the failure response as functions of state-of-stress. Lode-angle-parameter dependency can be pronounced more by elaborating on the stress meridians as illustrated in Figure 4-23(b). However, Figure 4-23(b) also depicts that a surface fitting methodology, which is only concerned about minimizing the overall fitting error, may not necessarily captures the response of all stress-states and misses certain states-of-stress points or has to compromise even from matching a whole stress meridian. More importantly, every point on this space of stress-state corresponds to a test result, which is obtained through a rigorous characterization procedure and should not be compromised by a smoothing algorithm. Therefore, an alternative concept can be utilized to construct the failure surface with a bias on matching the invaluable testing points. Figure 4-23(c) illustrates the projection of the failure surface in Figure 4-23(a) on to the plane of stress-states with a contour map. Specific stress-state points are shown with the paths defined for 'bridging' concept.

The 'bridging' concept, which is outlined in Figure 4-24, starts by assuming a firm representation of certain states-of-stress values and the stress meridians that are considered for testing as briefly illustrated in Figures 4-22(c) and 4-23(c). These specific stress-states should be pronounced more while constructing the failure surface. The concept works by determining notable stress-states that have the same Lode-angle-parameters on the corresponding stress meridians with equidistant distribution of the stress-triaxiality values. Clearly, each stress meridian act as a natural boundary of the bridging.

During the identification of the testing points for bridging, overlapping stress-states can be found on the failure surface while determining the notable states-of stress for verification purposes, such as; a plane-stress case under uni-axial tension and an axi-symmetric case under uni-axial tension will lead to the same stress-state pair defined by: $(\sigma^*, \theta_L) = \left(-\frac{1}{3}, +1\right)$. Similarly, a plane-stress case under uni-axial tension with lateral confinement by the use of a notched geometry and a plane-strain case under uni-axial tension also share a common stress-state pair defined by: $(\sigma^*, \theta_L) = \left(-\frac{1}{\sqrt{3}}, 0\right)$. These

overlapping stress-states can be useful to verify whether similar stress-states lead to similar values of the effective plastic strain at failure even though they represent different types of specimens on different stress meridians.

Bridging can also be established between the same values of the Lode-angle-parameter with different values of the stress-triaxiality as illustrated in Figure 4-25 by combined tension-shear specimens. These two distinct specimens are identified to match the Lode-angle-parameters of the two plane-stress specimens with intermediate values of stress-triaxiality. Consequently, two unique cases are identified, where different states-of-stress are achieved by changing the type of loading on specimens rather than its geometry.

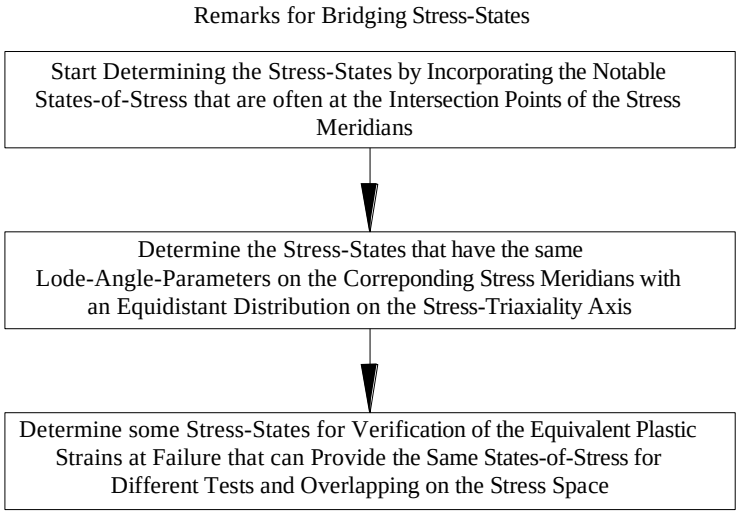

Figure 4-24: Outline of determining the stress-states while constructing the failure locus by bridging.

While designing the test matrix and the corresponding specimen geometries, the areas of interest for the projected states-of-stress are determined by the facilitation of Figure 4-25, where stress-states of the representative finite elements are illustrated for ductile materials under impact loading similar to the illustration in Figure 4-21 with the paths defined for bridging are overlaid.

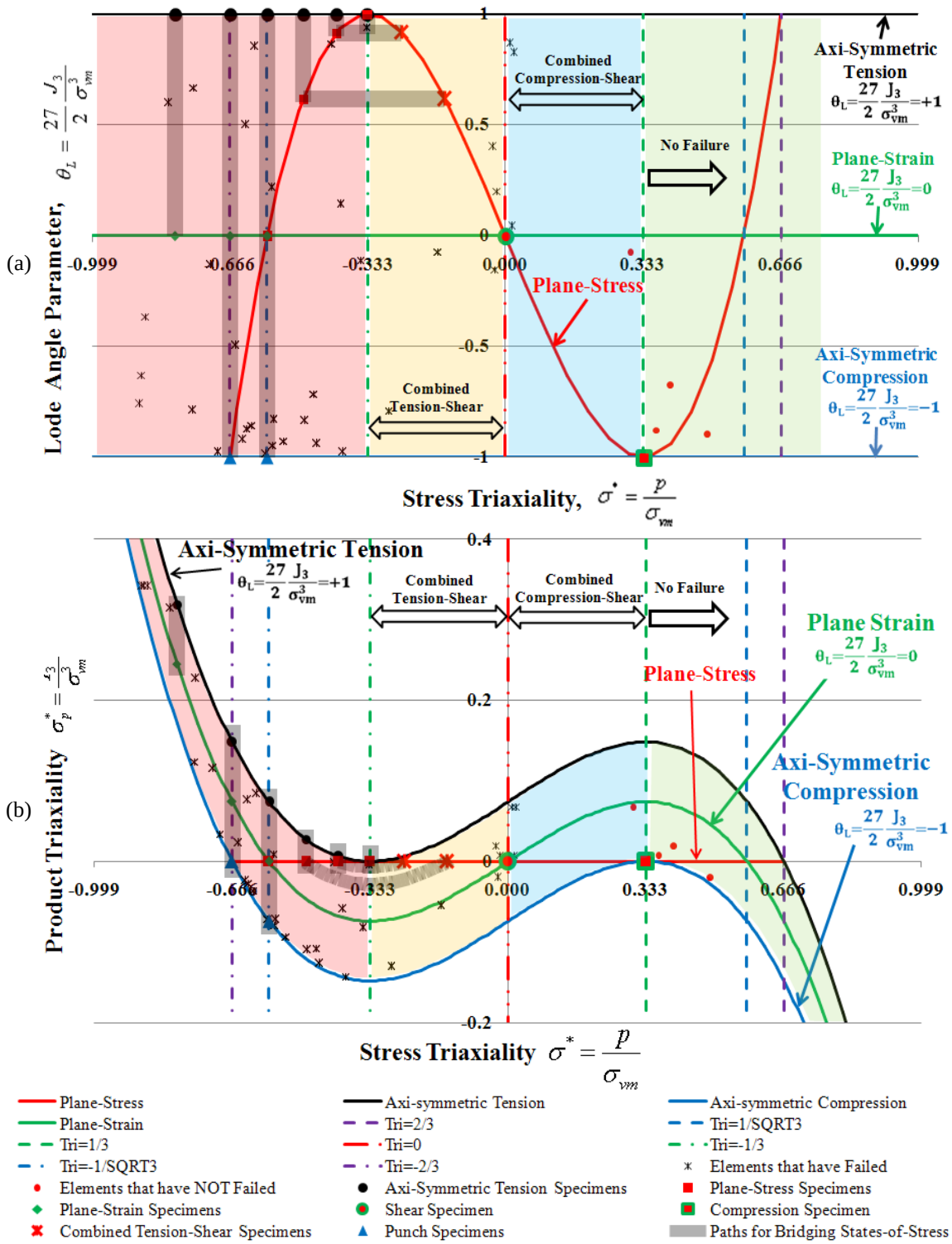

Figure 4-25: Identifying the bridging paths while constructing the failure locus through stress meridians and notable values of the stress-states considering the zone of interest suggested for ductile materials under impact loading; (a) representation of bridging on the plane of stress-state defined by stress-triaxiality vs. Lode-angle-parameter and (b) representation of bridging on the plane of stress-state defined by stress-triaxiality vs. product-triaxiality.

Figure 4-25(a) represents the paths for bridging on the plane of stress-state defined by stress-triaxiality vs. Lode-angle-parameter and Figure 4-25(b) on the plane of stress-state defined by stress-triaxiality vs. product-triaxiality. Both figures indicate that the region of interest, where the stress-states of the failing finite elements are populated and can be spanned by utilizing equivalent triaxiality parameters with equidistant distribution. Therefore, bridging provides a good way to interpolate between the Lode-angle-parameters for the selected stress-triaxiality values while only needing a small number of specimens.

Maximum stress-triaxiality value is identified when $\sigma^* = +\frac{1}{3}$, which correspond to the uni-axial compression state and no failure is assumed beyond that point as illustrated in Figure 4-25 and verified by the stress-state history of the finite elements that are under the region of impact. Although it is material and application dependent, for Al2024-T351, minimum stress-triaxiality value is identified when $\sigma^* = -0.8$, which is found by a judgment based on three different indications. The first indication is the population of the stress-triaxiality values of the finite elements that are under the impact region as illustrated in Figure 4-25. The second indication is a technological constraint on the shape of a potential specimen, where the most convenient test for this state is axi-symmetric tension. A very sharp notched geometry is necessary for an axi-symmetric specimen to provide the required confinement in order to reach that minimum value of stress-triaxiality. The last indication is found by utilizing the product-triaxiality parameter in the decision as discussed in Section 4.3, where it is stated that the solution envelope tapers towards the end of the stress meridians provided that the product-triaxiality is used to define the limits of the stress-triaxiality. Figure 4-25(b) illustrates this phenomenon, where the limits of the stress-triaxiality can clearly be captured within the limits of a reasonable solution. For even smaller stress-triaxiality values (i.e., $\sigma^* < -1.0$), spalling dominates failure due to the shock waves, rapid void growth and porosity [213], which is not within the scope of this dissertation.

Therefore, stress meridians (i.e., plane-stress, axi-symmetric tension, axi-symmetric compression and plane-strain) should be accepted as the boundaries or splines of a ruled failure surface as illustrated in Figure 4-26.

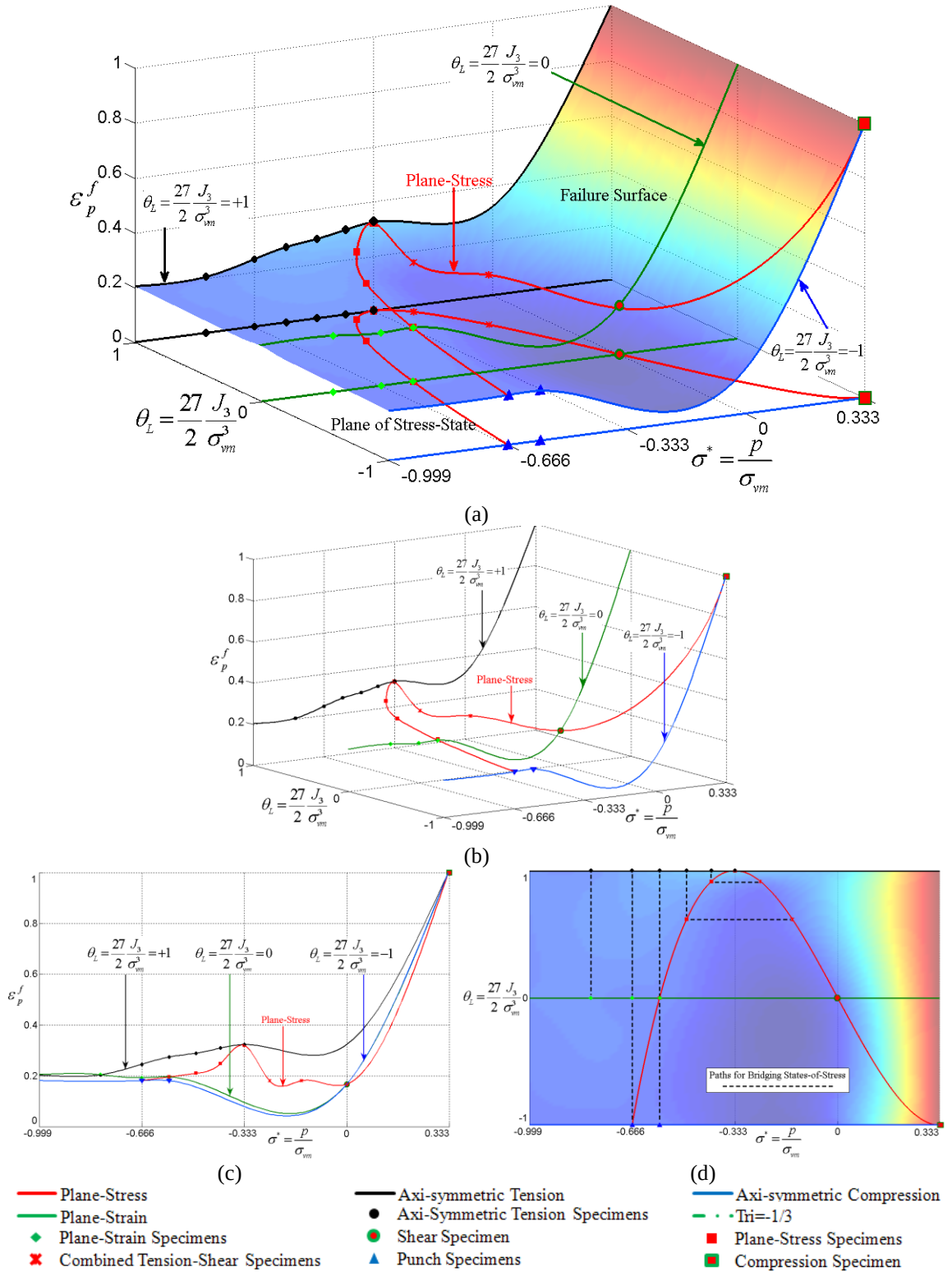

Figure 4-26: (a) Representation of a Lode-angle-parameter dependent ruled failure surface defined by stress meridians as splines swept from the test points defined later in this Chapter; (b) three-dimensional representation of the splines in stress space, (c) stress meridians projected on to the plane of stress-triaxiality vs. effective plastic strain at failure showing Lode-angle-parameter dependency and (d) representation of paths used for bridging stress-states.

The failure surface is then constructed by sweeping through these splines with the help of interconnecting stress-states suggested by bridging paths as shown in Figures 4-26(a) to 4-26(d). Three dimensional splines representing the stress meridians can individually be seen in Figure 4-26(b) with identified test points overlaid for each stress-state. Figure 4-26(c) illustrates how each spline of the stress meridian is obtained through the identified states-of-stress. It should be noted that the splines are forced to match each stress-state along the stress meridians so that the boundaries of the ruled surface can explicitly depend upon the test points.

It should also be noted that TRAUM explicitly depends upon characterized material data from test results; therefore, it can be foreseen that the accuracy of the model can easily be enhanced by increasing the number of the test points that span the failure locus. Tabulated structure of TRAUM can handle additional test points with flexibility and fidelity by redefining the failure surface with the additional value of effective plastic strain at failure for the corresponding stress-state.

Initially designed stress-state values for some of the points that are illustrated in Figure 4-25 may change during the plastic deformation especially after the instabilities like necking. Therefore, it should be noted that TRAUM can also handle changes in the initially assigned stress-state points by incorporating linear interpolation during the 'bridging' process.

4.4.2 **Construction of a failure locus for strain rate and temperature dependency**

Initial failure surface is constructed by utilizing values of effective plastic strain at failure that are characterized from different specimens, which represent different states-of-stress as discussed in Section 4.4.1. These specimens with different stress-states are tested at a nominal strain rate (i.e., $1.0s^{-1}$) and at room temperature (i.e., 294 K). In order to represent the strain rate and temperature dependency of the failure locus, scaling the initial failure surface is suggested as a convenient way with a multiplicative decomposition of the coupled terms [85]. Strain rate and temperature dependency of the initial failure surface is attained by two scaling factors that are used to offset the stress-state dependent failure surface as formulated in Equation (4.55).

$$\varepsilon_p^f = f(\sigma^*, \theta_L) g\left(\dot{\varepsilon}_p\right) h(T) i(l_{cr}) \tag{4.55}$$

where, $g\left(\dot{\varepsilon}_p\right)$ represents the strain rate dependent term and $h(T)$ represents the temperature dependent term that scales the failure strain. These scaling terms can comprise any number of test results that are performed at different strain rates and temperatures forming piecewise linear curves for scaling.

To identify the scaling curves, beginning with strain rate dependency, a stress-state is determined first from the initial failure surface. It is suggested to select a simple test for a convenient stress-state (i.e., specimen geometry and loading) since the same test will be performed at different strain rates and temperatures. In this study, plane-stress tension (i.e., $(\sigma^*, \theta_L) = \left(-\frac{1}{3}, +1\right)$) is identified as the baseline stress-state. To isolate the effects of strain rate dependency, all tests are performed at room temperature and no effects of adiabatic heating are assumed. Subsequently, the values of the effective plastic strain at failure can be identified for the selected strain rates. Each failure strain can then be normalized to the failure strain of the baseline in order to find a scaling factor for the corresponding strain rate. Finally, the scaling curve can be obtained by a collection of points representing the strain rates and the corresponding normalized failure strains as formulated in Equation (4.56).

$$\begin{aligned}
&\left(\sigma^*_{\text{baseline}},\ \theta_{L\,\text{baseline}},\ \ \dot{\varepsilon}_{p\,\text{baseline}},\ \ T_{\text{baseline}}\right) = \left(-\frac{1}{3}, +1, 1\text{s}^{-1}, 294\text{K}\right) \Rightarrow \varepsilon^f_{p\,\text{baseline}} \\
&\left(\sigma^*_{\text{baseline}},\ \theta_{L\,\text{baseline}},\ \ \dot{\varepsilon}_{p\,1},\ \ T_{\text{baseline}}\right) = \left(-\frac{1}{3}, +1, \dot{\varepsilon}_{p\,1}, 294\text{K}\right) \Rightarrow \varepsilon^f_{p\,1} \\
&\left(\sigma^*_{\text{baseline}},\ \theta_{L\,\text{baseline}},\ \ \dot{\varepsilon}_{p\,2},\ \ T_{\text{baseline}}\right) = \left(-\frac{1}{3}, +1, \dot{\varepsilon}_{p\,2}, 294\text{K}\right) \Rightarrow \varepsilon^f_{p\,2} \\
&\dot{\varepsilon}_{p\,\text{baseline}} < \dot{\varepsilon}_{p\,1} < \dot{\varepsilon}_{p\,2} \\
&\frac{\varepsilon^f_{p\,1}}{\varepsilon^f_{p\,\text{baseline}}} = g_1 \Rightarrow g\left(\dot{\varepsilon}_{p\,1}, g_1\right),\ \ \frac{\varepsilon^f_{p\,2}}{\varepsilon^f_{p\,\text{baseline}}} = g_2 \Rightarrow g\left(\dot{\varepsilon}_{p\,2}, g_2\right) \\
&\Rightarrow g\left(\dot{\varepsilon}_p\right) = \left\{g\left(\dot{\varepsilon}_{p\,\text{baseline}}, 1\right); g\left(\dot{\varepsilon}_{p\,1}, g_1\right); g\left(\dot{\varepsilon}_{p\,2}, g_2\right)\right\}
\end{aligned} \tag{4.56}$$

Strain rate depend failure locus can be illustrated as in Figure 4-27 emphasizing that the values of the effective plastic strains at failure are offset from the initial failure surface according to the scaling factors defined per each strain rate.

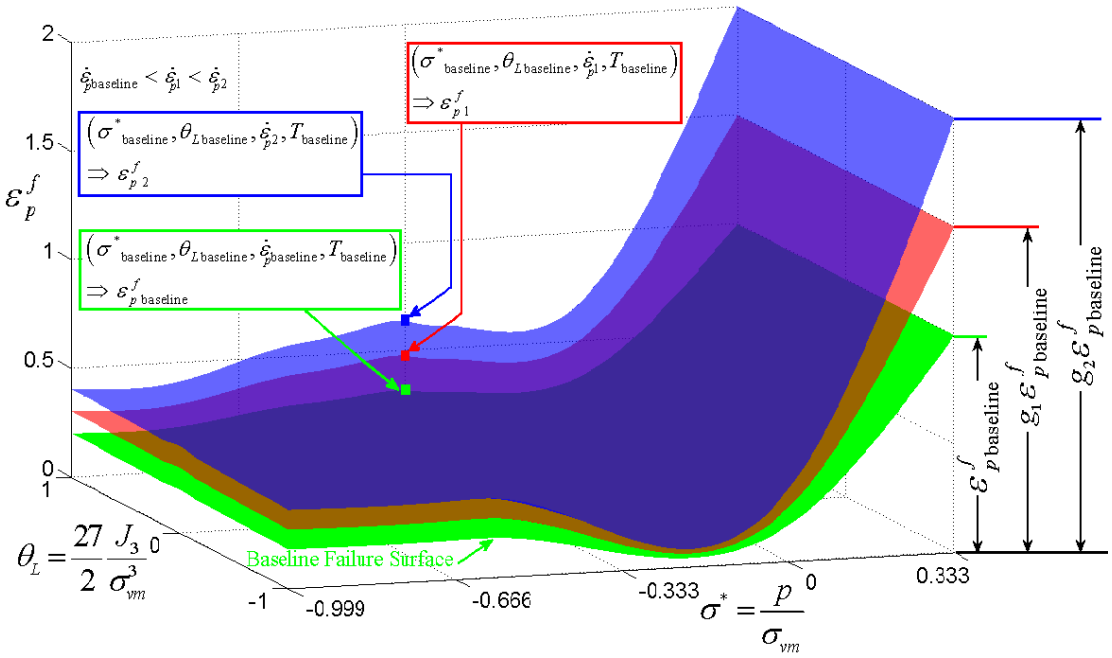

*Strain rate dependent scaling of the failure surface is exaggerated for demonstration purposes.

Figure 4-27: Strain rate dependent failure locus constructed by offsetting the initial failure surface.

It should be noted that the offset distances are exaggerated in Figure 4-27 for a better demonstration (i.e., $g_1\varepsilon^f_{p\,\text{baseline}} = 1.5$, $g_2\varepsilon^f_{p\,\text{baseline}} = 2$). Clearly, the amount of offset distances will be determined from characterization of the tests in Chapter 5 for the selected strain rates. It should also be noted that a logarithmic scale is utilized for defining the corresponding strain-rates assuming that there can be several orders of magnitude difference between the rates during the experimental program.

Figure 4-28 illustrates the baseline and the scaled stress-meridians according to the normalized scaling factors. The input format of the piecewise linear scaling term or curve $g(\dot{\varepsilon}_p)$ can also be seen in Figure 4-28. It should be noted that, for demonstration purposes, the effect of strain-rate on the effective plastic strain at failure is assume to be an increasing function. However, that may not necessarily be the case for the material of interest and increasing the strain-rate can lead to a steep drop in the effective plastic strain

at failure. Therefore, by utilizing strain rate and temperature dependent scaling curves, TRAUM can easily model the required response depending on the characterization of the failure strains at different strain-rates and temperatures.

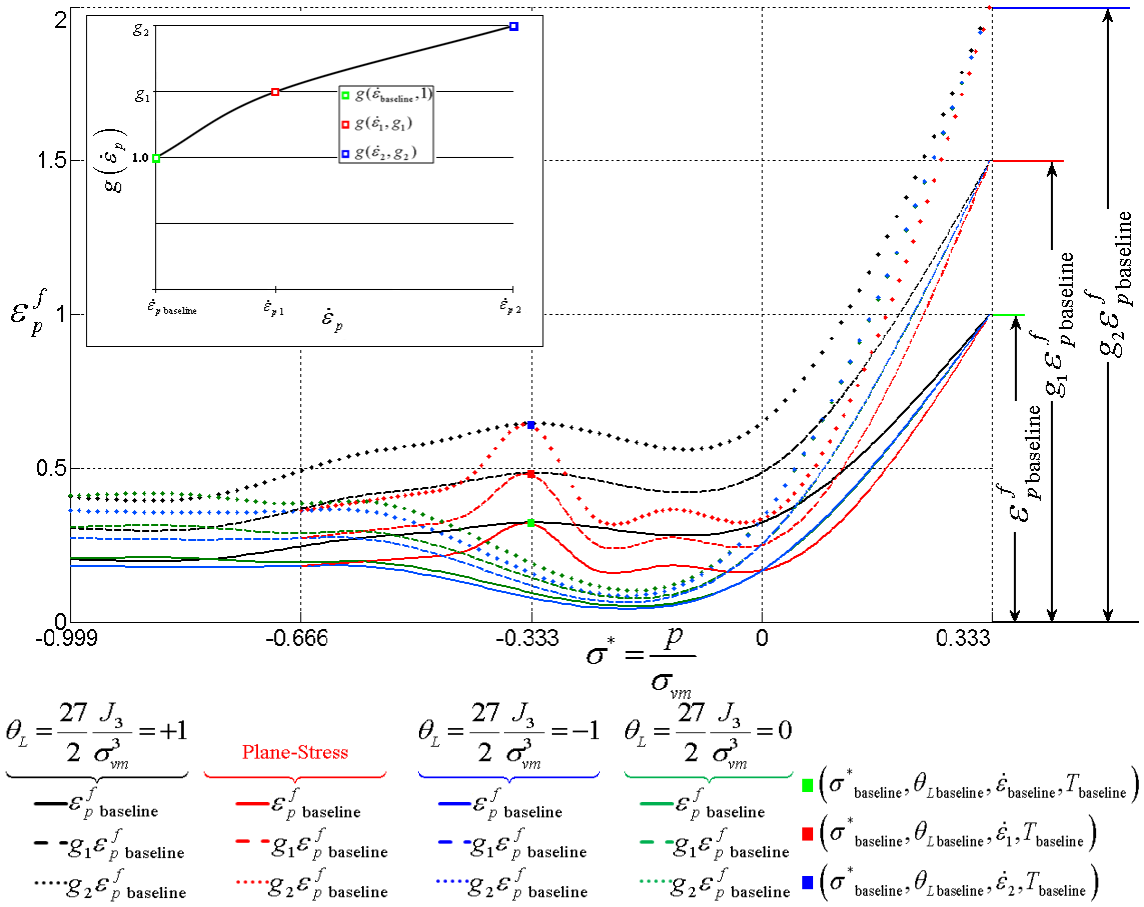

*Strain rate dependent scaling of the failure surface is exaggerated for demonstration purposes.

Figure 4-28: Strain rate dependent scaling factor (curve) and the scaled stress meridians of the failure surface.

Similarly, temperature dependency can also be represented as a piecewise linear scaling curve depending on the number of temperature dependent tests. Plane-stress tension (i.e., $(\sigma^*, \theta_L) = \left(-\frac{1}{3}, +1\right)$) is also considered as the baseline stress-state and to isolate the effects of temperature dependency, all tests are performed at the same strain rate (i.e., $1.0s^{-1}$). Subsequently, the values of the effective plastic strain at failure are identified for the selected temperatures. Each failure strain can then be normalized to the baseline to find a scaling factor corresponding to each temperature. Finally, the scaling

curve can be obtained by a collection of points representing the temperatures and the corresponding normalized failure strains as formulated in Equation (4.57).

$$
\begin{gathered}
\left(\sigma^*_{\text{baseline}},\ \theta_{L\,\text{baseline}},\ \dot{\varepsilon}_{p\,\text{baseline}},\ T_{\text{baseline}}\right) = \left(-\frac{1}{3}, +1{,}1\text{s}^{-1}, 294\text{K}\right) \Rightarrow \varepsilon^f_{p\,\text{baseline}} \\
\left(\sigma^*_{\text{baseline}},\ \theta_{L\,\text{baseline}},\ \dot{\varepsilon}_{p\,\text{baseline}},\ T_1\right) = \left(-\frac{1}{3}, +1{,}1\text{s}^{-1}, T_1\right) \Rightarrow \varepsilon^f_{p\,1} \\
\left(\sigma^*_{\text{baseline}},\ \theta_{L\,\text{baseline}},\ \dot{\varepsilon}_{p\,\text{baseline}},\ T_2\right) = \left(-\frac{1}{3}, +1{,}1\text{s}^{-1}, T_2\right) \Rightarrow \varepsilon^f_{p\,2} \\
T_{\text{baseline}} < T_1 < T_2 \\
\frac{\varepsilon^f_{p\,1}}{\varepsilon^f_{p\,\text{baseline}}} = h_1 \Rightarrow h(T_1, h_1),\quad \frac{\varepsilon^f_{p\,2}}{\varepsilon^f_{p\,\text{baseline}}} = h_2 \Rightarrow h(T_2, h_2) \\
\Rightarrow h(T) = \{h(T_{\text{baseline}}, 1); h(T_1, h_1); h(T_2, h_2)\}
\end{gathered}
\tag{4.57}
$$

Temperature depend failure locus can be illustrated as in Figure 4-29 emphasizing that the values of the effective plastic strains at failure are offset from the initial failure surface according to the scaling factors defined per each temperature.

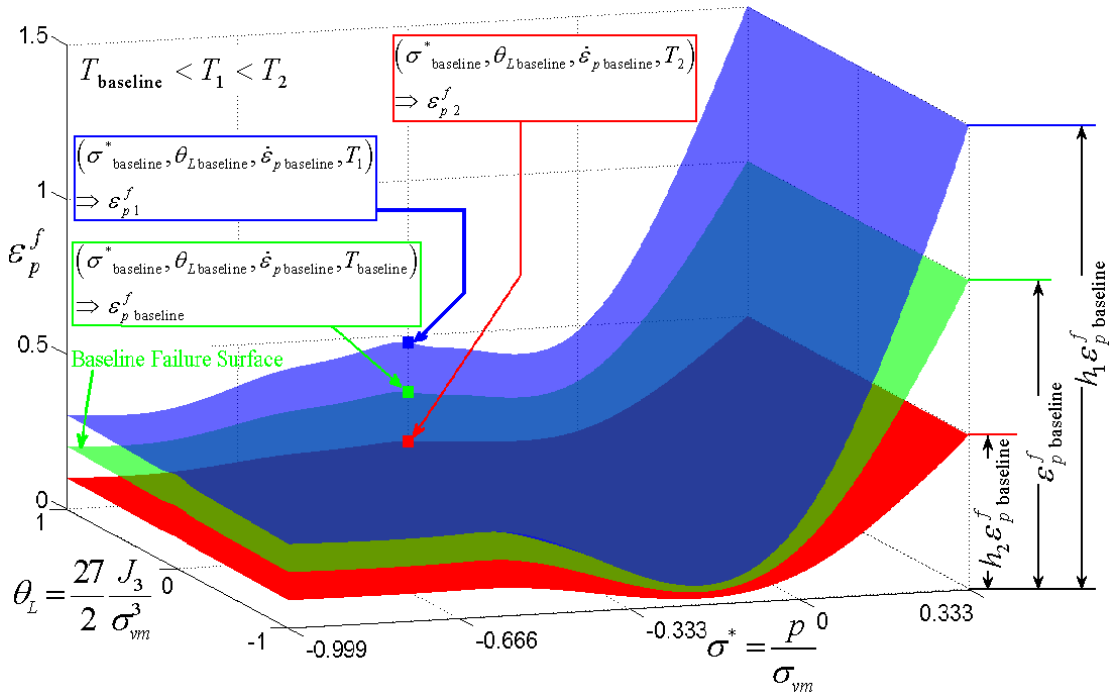

*Temperature dependent scaling of the failure surface is exaggerated for demonstration purposes.

Figure 4-29: Temperature dependent failure locus constructed by offsetting the initial failure surface.

It should be noted that the offset distances are exaggerated in Figure 4-29 for a better demonstration of the temperature dependency (i.e., $h_1\varepsilon_{p\,\text{baseline}}^{f} = 1.5$, $h_2\varepsilon_{p\,\text{baseline}}^{f} = 0.5$). Clearly, the amount of offset distances will be determined from characterization of the tests in Chapter 5 for the selected temperatures.

Figure 4-30 illustrates the baseline and the scaled stress-meridians according to the normalized scaling factors per each additional temperature. The input format of the piecewise linear scaling term or curve $h(T)$ can also be seen in Figure 4-30. A hypothetical case of increase in the failure strain due to a minor increase at the temperature is assumed first, where a drop in the failure strain is assumed for a much higher temperature. Clearly, failure is immediate at the melting temperature.

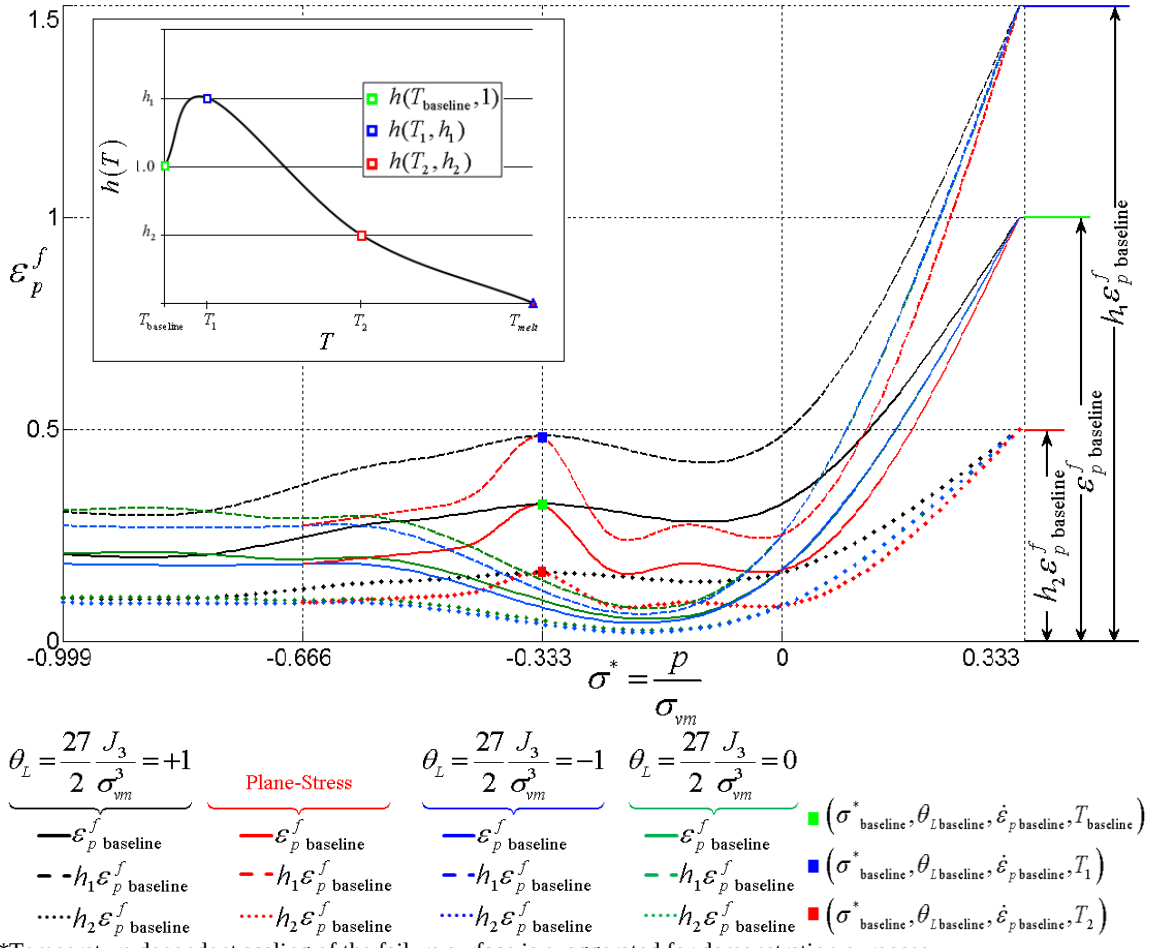

*Temperature dependent scaling of the failure surface is exaggerated for demonstration purposes.

Figure 4-30: Temperature dependent scaling factor (curve) and the scaled stress meridians of the failure surface.

4.4.3 **Key aspects of iterative specimen design algorithm for specific states-of-stress**

Design procedure of a specimen is critical in most cases since construction of the stress-state dependent failure locus, which is described in Section 4.4.1, relies profoundly on the attainment of the targeted states-of-stress. Specimen design procedure begins with a determination of the stress meridian, where the state-of-stress can be classified and associated with certain types of specimen geometries including the loading conditions as illustrated in Figure 4-25. Figure 4-31 also signifies the categorical representation of specific specimen geometries with the corresponding stress-states. Detailed design parameters for specimen geometries are obtained through an iterative algorithm, where targeted values of the state-of-stress are achieved by utilizing an inverse methodology that employs successive FE calculations.

The iterative procedure continues with an estimate on the desired state-of-stress that is initially determined by bridging concept from notable points on the plane of stress-state. An initial geometry is then designed for the targeted stress-state and a numerical model is developed for FE calculations. A semi-empirical estimation (i.e., Bridgman's analysis) is often used to find a reasonable initial design. However, during the deformation, stress-states do not stay constant and average values of the states-of-stress need to be calculated for the FE model. Consequently, initial geometry of the specimen is iteratively modified to achieve the targeted states-of-stress. Considering the types of specimen geometries that are selected for testing based on the stress meridians as illustrated in Figure 4-31, modifying the notch geometry is adopted as a convenient way of reaching the targeted state-of-stress values. Therefore, successive FE models are developed and simulated until the targeted stress-states are reached within a reasonable tolerance. In this study, the tolerance is selected as 5% difference between the targeted and calculated stress-states.

The same iterative procedure is followed for designing other specimens without a notched geometry, as well. For instance, Different punch geometries are designed for the punch tests that are illustrated in Figure 4-31(d); although, the same cylindrical specimen is used for testing. Details of the final specimen geometries are discussed in more detail in the proceeding sections.

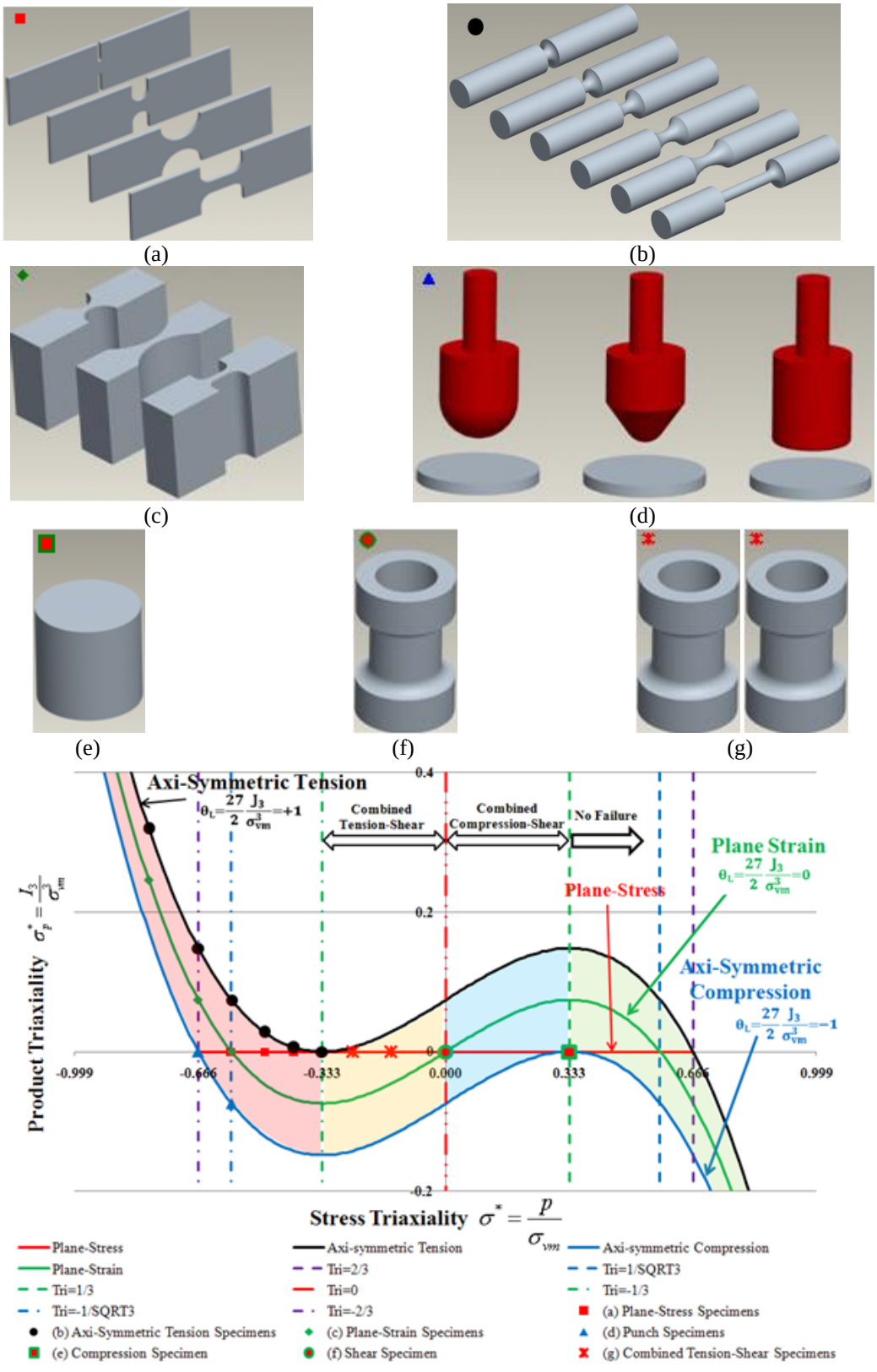

Figure 4-31: Specimen geometries and loading conditions categorically associated with certain stress meridians; (a) plane-stress, (b) axi-symmetric tension, (c) plane-strain, (d) punch, (e) compression, (f) shear (torsion) and (g) combined tension - shear (torsion) specimens.

A schematic flow diagram of the iterative specimen design algorithm can be illustrated as in Figure 4-32 and the corresponding steps are described in more for designing a notched axi-symmetric specimen under uni-axial tension detail as an example.

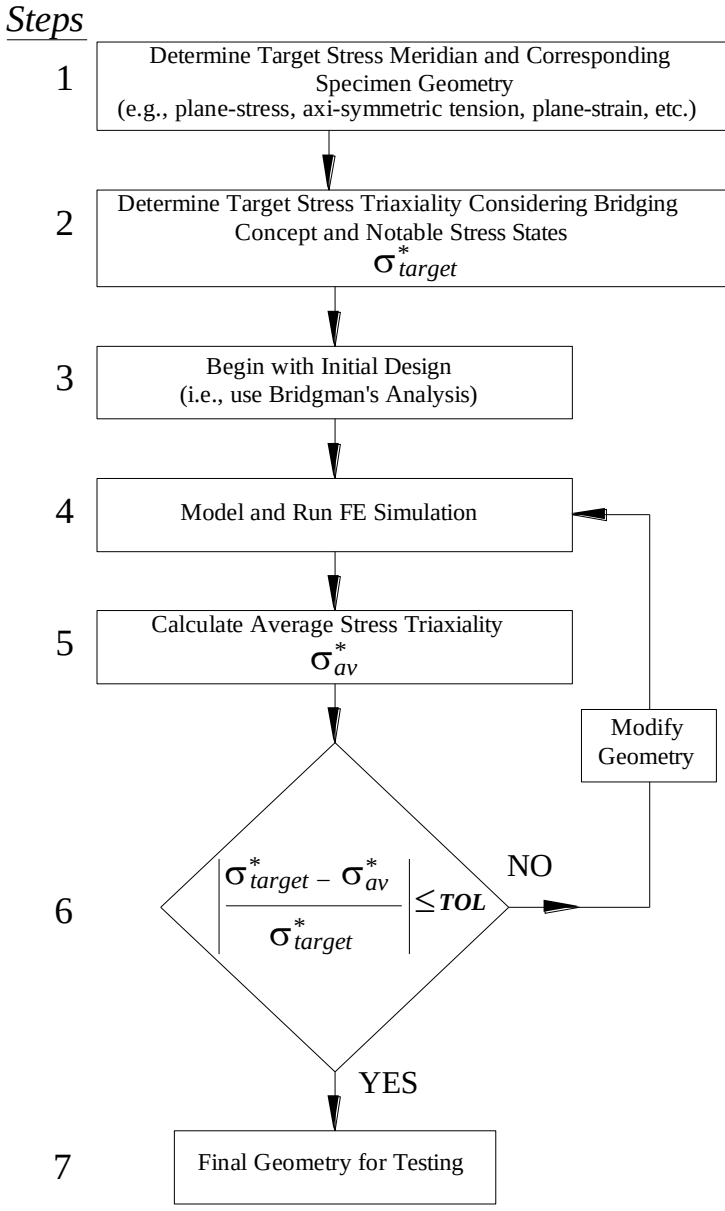

Figure 4-32: Flowchart for iterative specimen design procedure for desired states-of-stress.

Design procedure for a notched axi-symmetric tension specimen:

Step-1:

Iterative specimen design procedure begins by determining the targeted stress meridian and the corresponding specimen type. Figure 4-31 presents a template that can be used to justify the specimen shape associated with a specific state-of-stress. For an axi-symmetric stress-state in tension, axi-symmetric (i.e., round dogbone) geometry is suggested for the specimens as illustrated in Figure 4-31(b).

Step-2:

An axi-symmetric stress-state in tension leads to a Lode-angle-parameter of $\theta_L = +1$ and stress-triaxiality value needs to be determined to find a targeted state-of-stress for a reasonable testing point on the axi-symmetric tension meridian. While determining the targeted stress-triaxiality value, technological constraints such as the minimum notch radius, minimum and maximum specimen cross-section, the amount of applied force, strain rates and temperatures etc. should also be considered. As described in Section 4.3.3, a special attention is also required to select the targeted stress-state accordingly within an area of interest that is populated by the states-of-stress which are possessed by the finite elements failing under impact.

If every other variable is satisfied, selecting the stress-triaxiality from a list of notable stress-states is desirable. These notable points are often found at the overlapping (i.e., intersecting) points of the stress meridians as illustrated in Figure 4-18 before. However, limited number of notable stress-state points may not necessarily be enough to characterize the entire failure locus with good accuracy and additional points are needed for the intermediate values of the stress-triaxiality. In this case, for the notable stress-triaxiality values of $-\frac{1}{\sqrt{3}} \leq \sigma^* \leq -\frac{1}{3}$, two additional specimens are considered. These two specimens are chosen to be equidistant from the notable points along the axi-symmetric tension meridian considering the concepts described in Section 4.4.1 for bridging the stress-states between the stress meridians. Consequently, two targeted intermediate values of the stress-triaxiality are found as $\sigma^* \approx -0.41$ and $\sigma^* \approx -0.49$, respectively. For demonstration purposes of the iterative specimen design procedure, targeted stress-triaxiality value is selected as $\sigma^* \approx -0.49$. Therefore, it can be illustrated in Figure 4-33 that, the targeted stress-state will require an axi-symmetric tension

specimen and can provide a bridging with two other specimens that represent different states-of-stress. It is shown that the axi-symmetric specimen shares the same stress-triaxiality value (i.e., $\sigma^* \approx -0.49$) with a plane-stress specimen for bridging. Moreover, the plane-stress specimen shares a common Lode-angle-parameter (i.e., $\theta_L = +0.617$) with a combined tension-shear specimen for bridging, as well. Consequently, while targeting an axi-symmetric tension specimen with a stress-state defined by $(\sigma^*, \theta_L) = (-0.49, +1)$, two additional specimens from different stress meridians are also identified for testing by the use of bridging concept. These two additional specimens are illustrated in Figure 4-33 for a plane-stress and a combined tension-shear specimen with states-of-stress defined by $(\sigma^*, \theta_L) = (-0.49, +0.617)$ and $(\sigma^*, \theta_L) = (-0.147, +0.617)$, respectively. It should be noted that, for demonstration purposes, only a small portion of the stress meridian is plotted in Figure 4-33(b) while representing a Lode-angle-parameter of $\theta_L = +0.617$.

Step-3:

An initial design can be attained based on Bridgman's analysis [95] for axi-symmetric notched geometries in tension before necking as represented in Figure 4-34. According to Bridgman, stress-triaxiality is evaluated as:

$$\sigma^* = \frac{p}{\sigma_{vm}} = -\frac{1}{3} - \ln\left(\frac{a^2 + 2aR - 2r^2}{2aR}\right) \tag{4.58}$$

where, r is the radial coordinate at the minimum cross-section or at the gauge section, a is the radius of the gauge section and R is the radius of the notch. Based on this relation, stress-triaxiality leads to $\sigma^* = -\frac{1}{3}$ when $r = a$, while for $r = 0$ stress-triaxiality reduces to:

$$\sigma^* = -\frac{1}{3} - \ln\left(1 + \frac{a}{2R}\right) \tag{4.59}$$

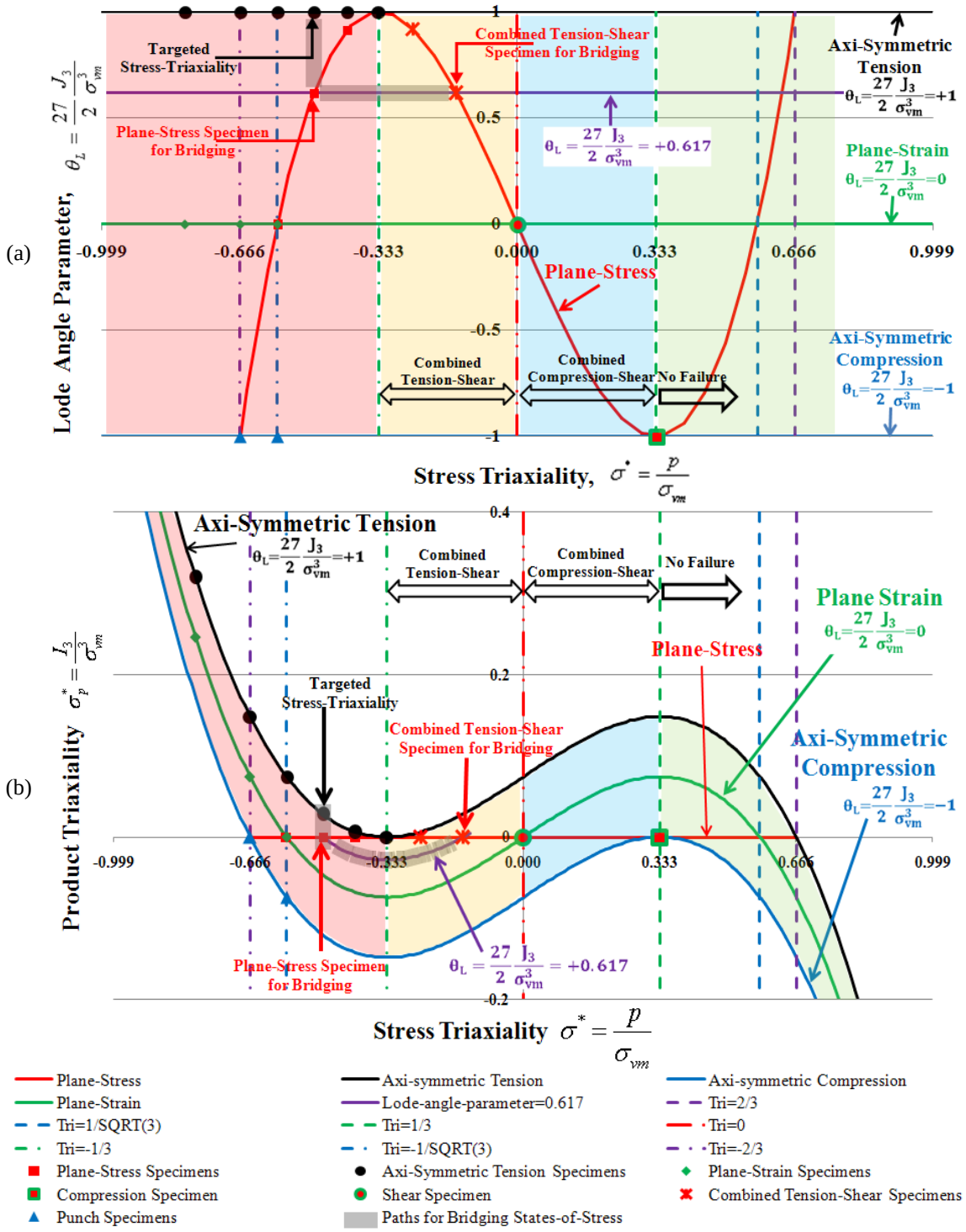

Figure 4-33: Determination of the targeted state-of-stress and the corresponding specimen geometry; (a) on the plane of stress-state defined by stress-triaxiality vs. Lode-angle-parameter, (b) on the plane of stress-state defined by stress-triaxiality vs. product-triaxiality.

Therefore, stress-triaxiality value of the initial design is calculated for a single finite element that is in the center of the specimen gauge region (i.e., $r = 0$) as illustrated in Figure 4-35. It should be noted that 1/8 of the model is hidden in this figure for illustration purposes.

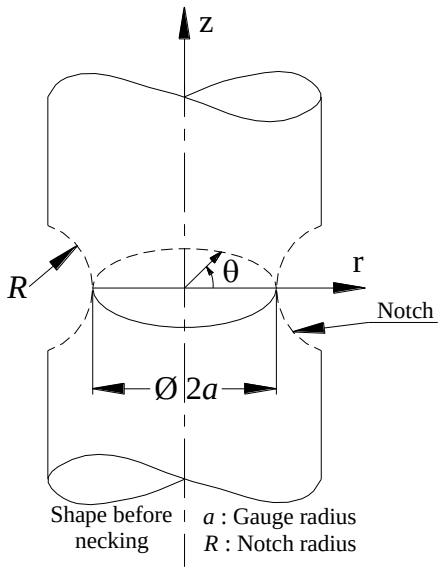

Figure 4-34: Axi-symmetric notched specimen geometry in tension for Bridgman's analysis.

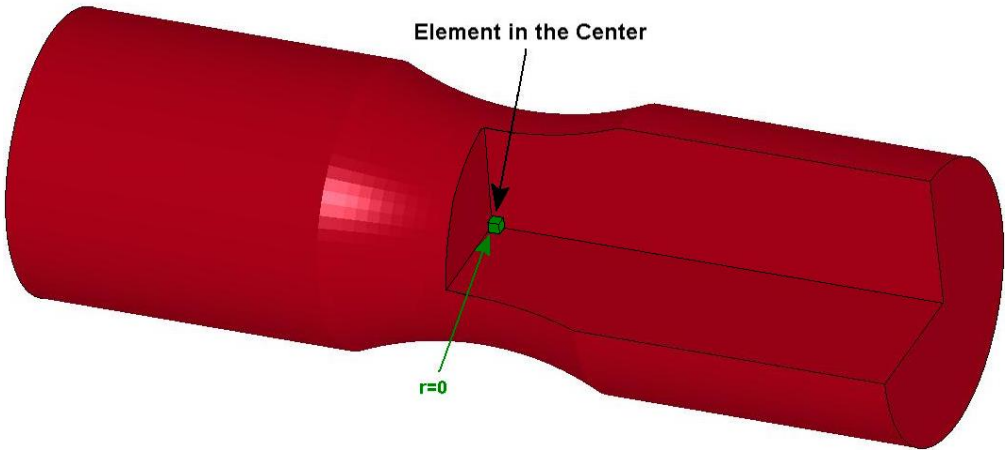

* 1/8 of the FE model is hidden for demonstration purposes.

Figure 4-35: Single finite element in the center of the specimen gauge region for stress-state calculations.

As the stress-meridian, corresponding specimen type and targeted stress triaxiality are determined, an initial gauge diameter can be determined based on the relation suggested by Equation (4.59). It should also be noted that the upper limits of the initial dimensions for the gauge section depend on at least two constraints. The first constraint is the dimensions of the source material, where the specimen is manufactured from. The second constraint is the capacity of the test apparatus, where the specimen is tested. The lower limit of the initial dimensions for the gauge section depends on the targeted strain rates that the specimen can be tested for. These constraints will be considered for the specimens that are designed for the testing program in the proceeding sections.

In order to demonstrate the iterative procedure, as an example, a gauge radius of $a = 5\ mm$ is accepted for the analysis to find an initial design and the notch radius R for the corresponding targeted stress-triaxiality value of $\sigma^*_{Target} = -0.49$ as illustrated in Figure 4-36.

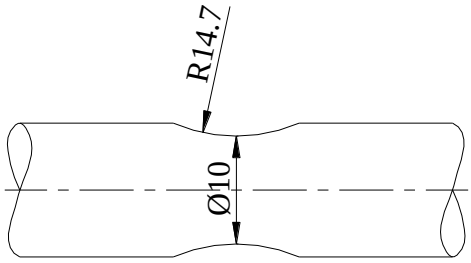

$$\sigma^* = \frac{p}{\sigma_{vm}} - \frac{1}{3} - \ln\left(1 + \frac{a}{2R}\right)$$
$$\sigma^*_{Target} = -0.49,\ \ a = 5\text{mm}$$
$$\Rightarrow R \approx 14.7\ \text{mm}$$

Figure 4-36: Bridgman's analysis utilized for the first iteration of an initial design procedure.

Step-4:

Three principle aspects related to non-linear FE analysis are reported to exhibit significant effects on the stress-state calculations. Therefore, while developing a FE model, the following points are addressed to help identify the sensitivities of the modeling methodology [1] [16]:

- Material properties
- Location of the calculation point within the gauge section
- Mesh size dependency

4.4.3.1 Dependency on the material properties

To address the effects of material properties on the stress-triaxiality calculation, a FE model is developed for the first iteration of the specimen design procedure and simulated using J-C as a stress-state sensitive material model utilizing the geometrical relations calculated in Figure 4-36. Bridgman's analysis suggests that stress-triaxiality is solely geometry dependent. However, it was mentioned that material properties also have significant effects on the stress-triaxiality [16]. Changes in the initial cross-section and notch geometry due to deformation, which is material dependent, lead to a change in the initially targeted stress-triaxiality. Therefore, to address the material property dependency of the stress-triaxiality, two material model parameters are employed from Table 4.2, which were also listed in Table 3.2 as Set-1 and Set-4 before.

Table 4-2: Set-1 and Set-4; J-C material model input data for the iterative specimen design procedure and successive FE simulations.

Material Characteristics			Sets	Strength Parameters				
Density [kg/m^3]	Poisson Ratio	Modulus of Elasticity [MPa]		Static Yield Limit [MPa]	Strain Hardening Modulus [MPa]	Strain Hardening Exponent	Strain Rate Coefficient	Thermal Softening Exponent
ρ	ν	E		A	B	n	C	m
2770	0.33	73084	Set-1	265	426	0.34	0.015	1.0
Reference Temp. [K]	Melting Temp. [K]	Specific Heat [J/kg-K]	Set-4	369	684	0.73	0.0083	1.7
				Failure Parameters				
				D_1	D_2	D_3	D_4	D_5
T_{room}	T_{melt}	C_p	Set-1	0.13	0.13	1.5	0.011	0.0
294	775	875	Set-4	0.31	0.045	1.7	0.005	0.0

The evolution of stress-triaxiality is calculated for the finite element in the center of the gauge section as illustrated in Figure 4-35. The results are compared for two sets of material properties in Figure 4-37, where it should be noted that each set comprises a different flow surface and a failure locus associated with the corresponding parameters as illustrated in Section 3 before. It can be observed that both the deformation characteristics and the failure point differ significantly according to the material properties, although the same material (i.e., Al2024-T351) is considered for the analysis. Therefore, it can be concluded that depending on the stock of material, ranges of strain rate and temperature

assumed during the characterization, and assessment of failure calculated values of the stress-states can vary significantly.

Considering that a new flow surface and a failure locus will be characterized in Chapter 5 from the test data specific to the material of interest and expecting that the initially targeted values of the stress-states will change, while designing an initial geometry for the specimens by utilizing existing material properties from literature, a reasonable tolerance is found to be desirable that can help approach to the targeted values of the stress-states during the iterations.

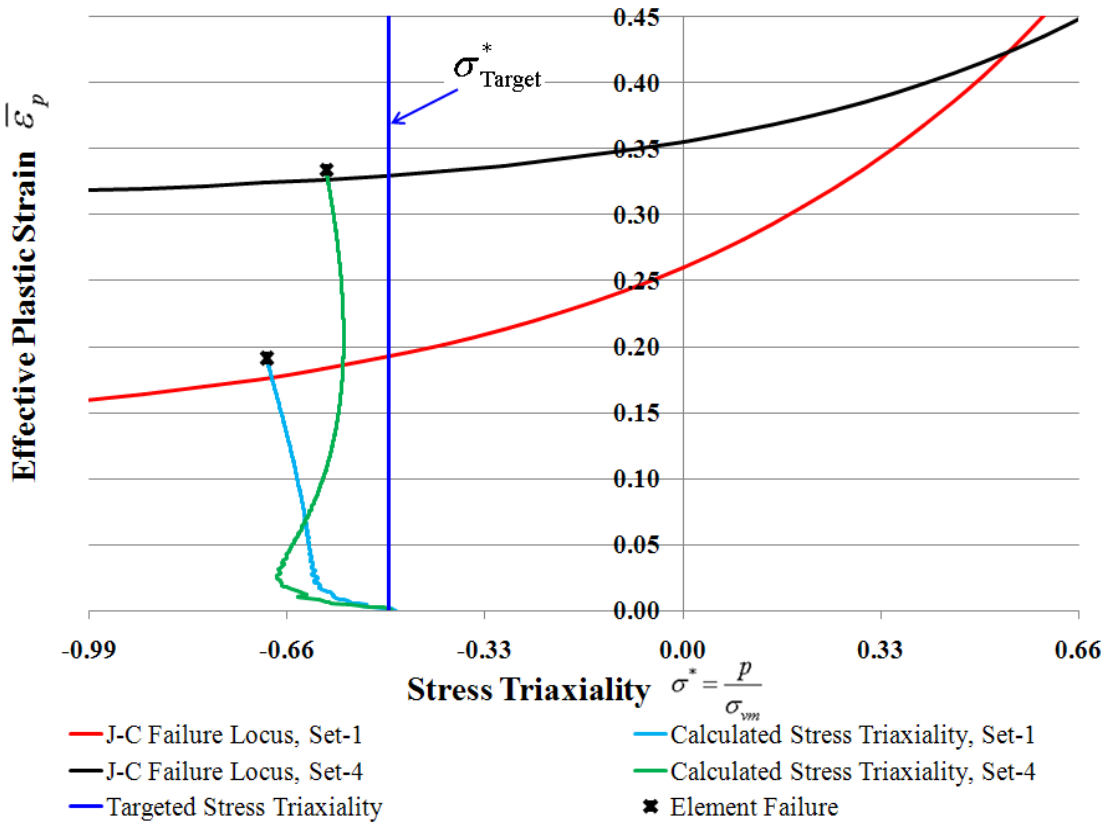

Figure 4-37: Dependency of the stress-triaxiality on the material properties.

4.4.3.2 Dependency on the location of the FE calculation

To address the effects of location dependency on the stress-triaxiality calculations within the gauge section, the FE model that is initially designed for the first iteration in Figure 4-36 is utilized for the analysis by using J-C and Set-4 material model parameters

from Table 4-2. As Equation (4.58) suggests, stress-triaxiality vary within the cross-section of the specimen. Therefore, a single finite element, which is at the center of the specimen gauge cross-section (i.e., $r = 0$), is often utilized for the calculations of the stress-states as illustrated by Figure 4.35 [1] [16]. This approach is also convenient as the Bridgeman's relation can be reduced to Equation (4.59) for the element in the center. Figure 4-38 illustrates two additional locations within the gauge section of the specimen, where the elements are selected for $r = \frac{a}{2}$ and $r = a$, respectively and the evolution of stress-triaxiality is compared to the targeted stress-triaxiality for the central element.

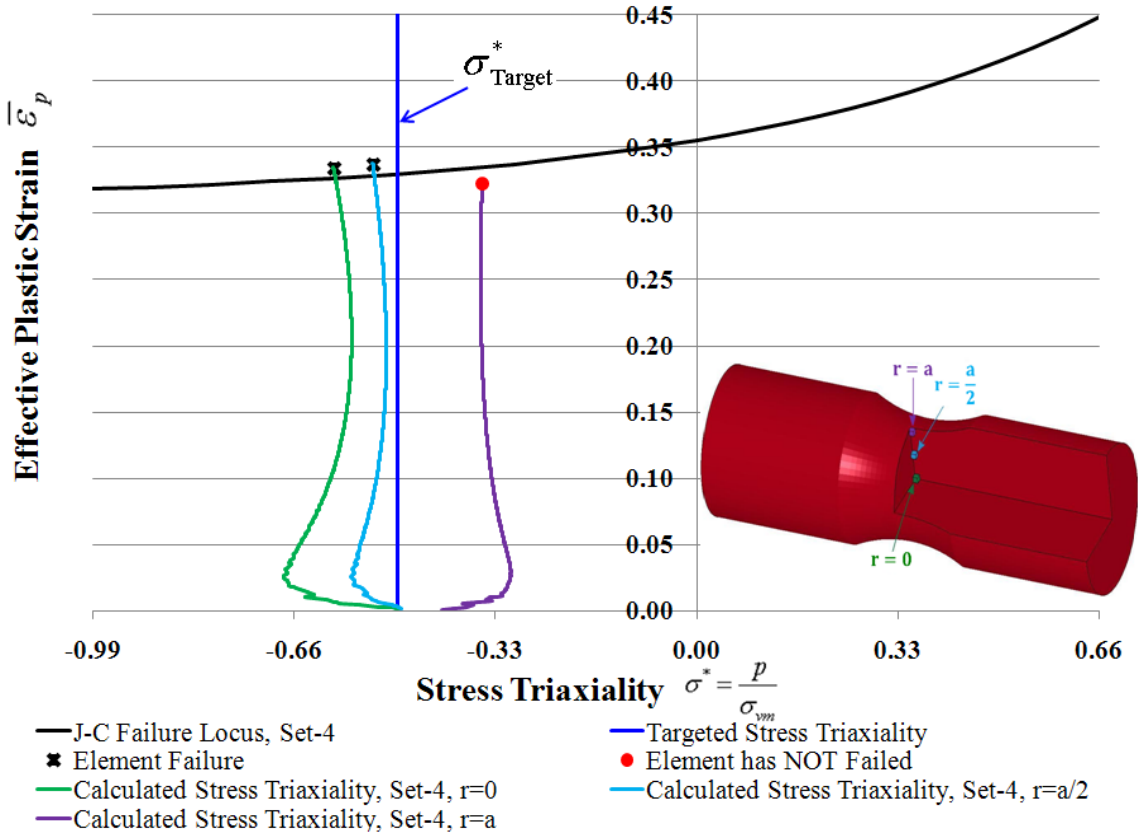

Figure 4-38: Dependency of the stress-triaxiality on the location of the calculation point within the gauge cross-section of the specimen.

During a ductile failure, the failure often initiates at the center of the specimen geometry and expected to form a 'cup-cone' failure mode as illustrated in Figure 2-2. Therefore, it is also beneficial to choose the stress-state calculation location at the central

element of the specimens for characterization of the effective plastic strains at failure. 'Cup-cone' formation is also achieved by the example that is illustrated to explain the iterative specimen design algorithm in Figure 4-38, where the finite elements at the locations $r = \frac{a}{2}$ and $r = 0$ are failing but the finite element at $r = a$ is not. As a result, unless otherwise mentioned, central elements are utilized for FE calculations and the characterization of the material parameters from this point forward.

4.4.3.3 Dependency on the mesh size and the significance of mesh regularization

Another important aspect of ductile deformation and failure is the mesh dependency. To address the effects of mesh size dependency on stress-triaxiality and failure strain calculation, five different FE models are developed by using different mesh sizes for the initial geometry that is shown in Figure 4-36. Figure 4-39 illustrates the FE models with the corresponding characteristic element lengths used to model the element in the center of the cross-section. It should be noted that the FE model is 3D axi-symmetric (i.e., round) specimen representing an axi-symmetric tension stress-state in tension.

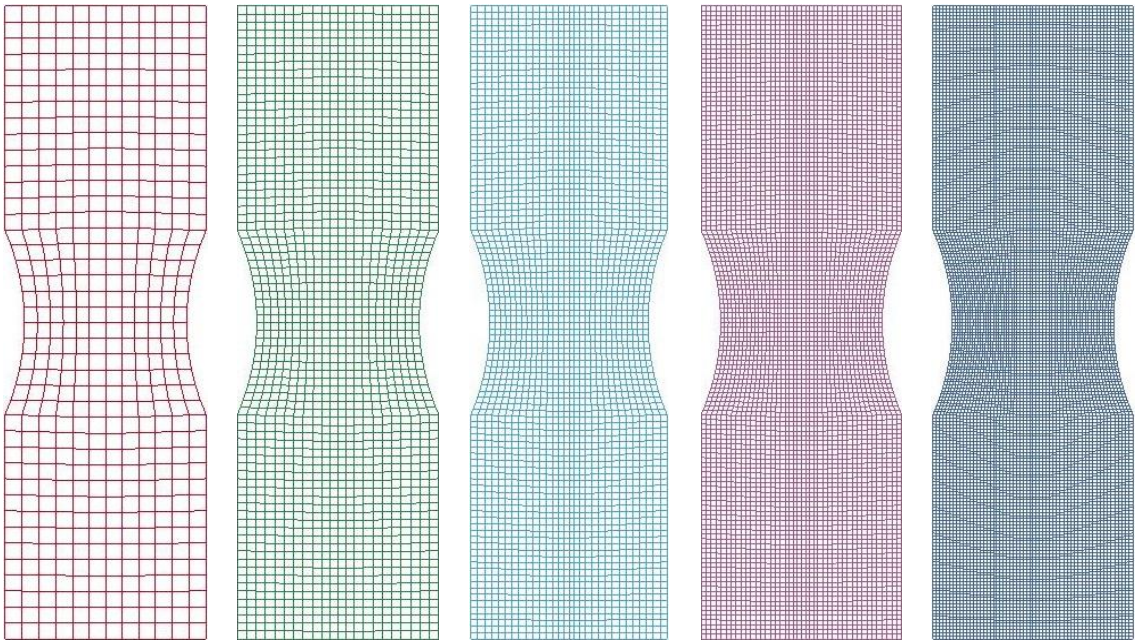

Figure 4-39: Cross-section of the FE model with different characteristic element lengths for the initial specimen geometry.

Evolution of the stress-triaxiality with respect to the effective plastic strain can be illustrated as in Figure 4-40 for five different characteristic element lengths. It should be noted that all models are simulated by utilizing J-C material model with Set-4 parameters from Table 4-2 and the calculations are plotted only for the element in the center of the specimen (i.e., $r = 0$) as illustrated in Figure 4-35. Element failure is attained when the accumulated effective plastic strain value exceeds the failure locus.

It can be concluded that calculated stress-triaxiality and the plastic strain values to failure are almost identical for different meshes as expected since J-C material model implies no mesh dependency. J-C model calculates the same plastic strain value for failure initiation independent of the mesh size.

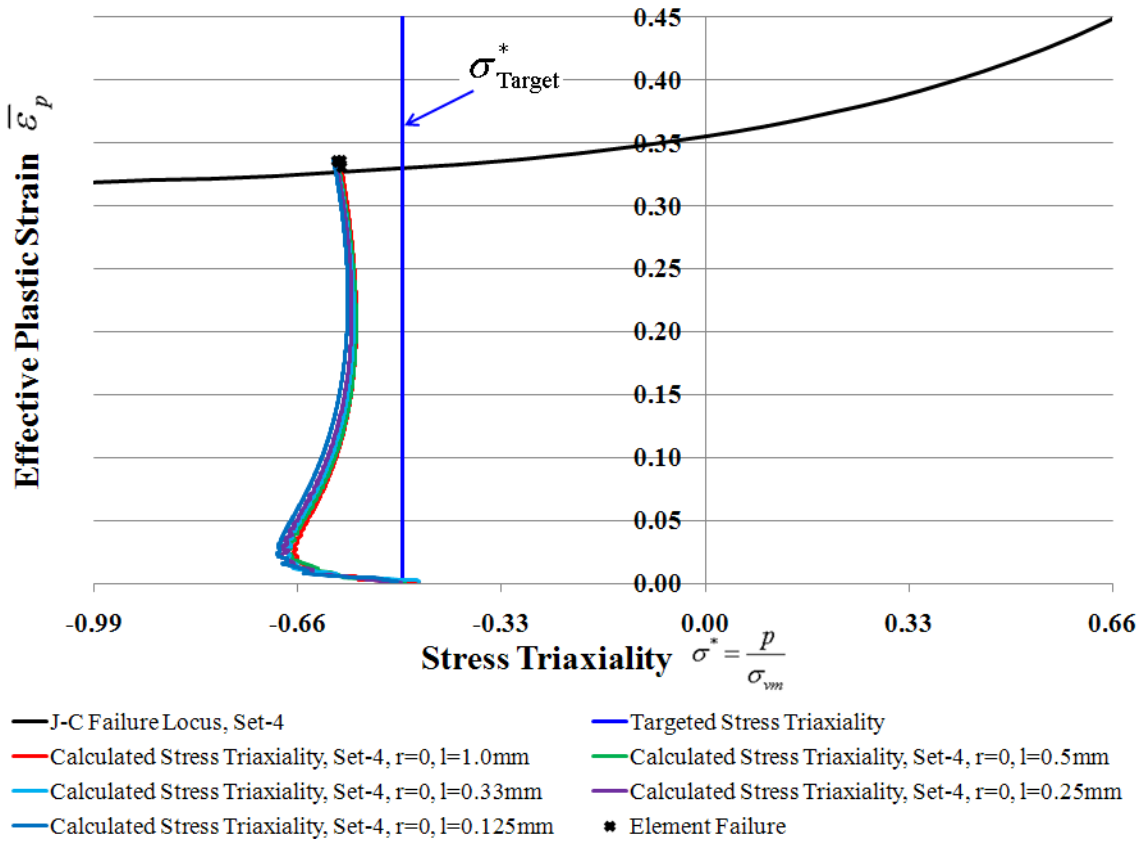

Figure 4-40: Evolution of stress-triaxiality with effective plastic strain when J-C material model is utilized for the simulations with different characteristic element lengths.

However, using a mesh independent value for plastic strain to failure during the simulations due to Equation (1.4) may have inconsistency on the overall displacement calculations since each element length leads to a different elongation corresponding to the same strain. Figure 4-41 represents the evolution of force and effective plastic strain with respect to the displacement comparing the results for different characteristic element lengths that are shown in Figure 4-39. It is illustrated that five different end displacements are calculated for the specimens with different element lengths, where only one of the models is shown to be matching the targeted displacement.

The evolution of force vs. displacement (or moment vs. rotation depending on the type of testing), which are directly obtained from test results, are often utilized to characterize the material properties from and to validate the accuracy of the FE simulations. Therefore, FE calculations with different mesh lengths are compared to each other in Figure 4-41 to show whether the response can be comparable to a test result for validation purposes.

It can be seen in Figure 4-41 that, by using a mesh independent failure strain calculation, all models with different characteristic element lengths fail almost at the same effective plastic strain value. The force responses are also found to be coherent since the geometry of the specimen, the constitutive relation used for each model, and the loading are all kept consistent.

Nevertheless, J-C failure model imposes that all elements should fail at the same strain due to Equation (1.4); the total elongations differ for each characteristic element length. Consequently, force vs. displacement measurements cannot be validated with a material model that has no mesh dependency on the calculation of plastic strain to failure. Moreover, effects of strain localization and thermal softening can also cause similar mesh dependency problems. Therefore, to solve pathological mesh problems, utilizing mesh regularization techniques are often suggested in conjunction with thermo/viscoplastic constitutive equations [194].

Stress-state, strain rate, temperature and mesh size dependency of the failure surface is attained by TRAUM with the scaling terms that are used to offset the stress-state dependent failure surface as formulated in Equation (4.60).

$$\varepsilon_p^f = f(\sigma^*, \theta_L) g(\dot{\varepsilon}_p) h(T) i(l_{cr}) \tag{4.60}$$

where, $g(\dot{\varepsilon}_p)$ represents the strain rate dependent term, $h(T)$ represents the temperature dependent term and $i(l_{cr})$ represents the regularization term that scales the effective plastic strain to failure depending on the characteristic element length. Regularization term is in the form of a piecewise linear curve that can comprise any number of different mesh sizes and corresponding scaling factors, which is similar to the strain rate and temperature dependent scaling terms that are illustrated in Figures 4-28 and 4-30.

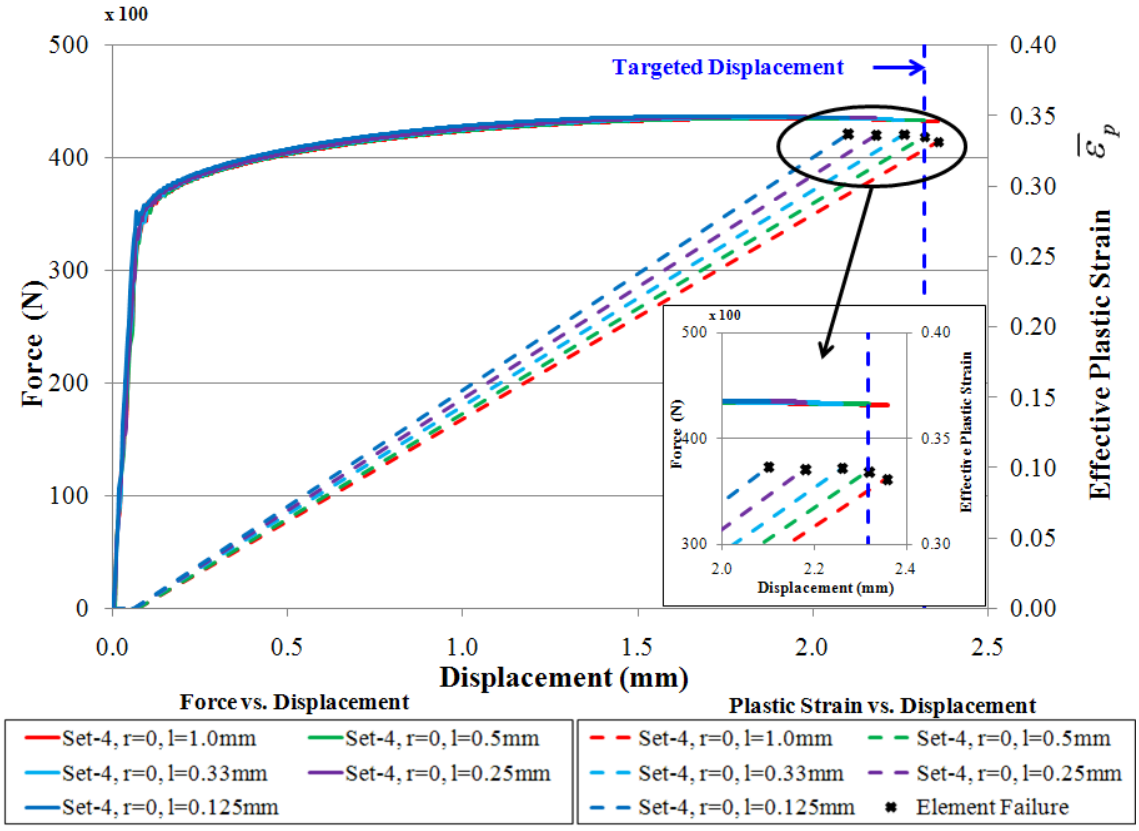

Figure 4-41: Effect of mesh size dependency on the prediction of end displacements.

Components of the regularization term can be found by simulating the initially designed specimen with different mesh lengths that are illustrated in Figure 4-39and finding the effective plastic strain to failure for each specimen targeting the displacement that is shown in Figure 4-41.

Since the targeted displacement is predicted with a characteristic element size of $l_{cr} = 0.5$ mm, it is assumed as a baseline for normalizing the other failure strains associated with the mesh lengths to find a scaling factor. The scaling curve can be obtained by a collection of points representing the characteristic element lengths and the corresponding normalized failure strains as formulated in Equation (4.57). It should be noted that the regularization term is obtain for a specific stress-state, strain rate and temperature that are accepted as a baseline.

$$
\begin{aligned}
&\left(\sigma^*_{\text{baseline}},\ \theta_{L\,\text{baseline}},\ \dot{\varepsilon}_{p\,\text{baseline}},\ T_{\text{baseline}},\ l_{\,\text{baseline}}\right) \Rightarrow \varepsilon^f_{p\,\text{baseline}} \\
&\left(\sigma^*_{\text{baseline}},\ \theta_{L\,\text{baseline}},\ \dot{\varepsilon}_{p\,\text{baseline}},\ T_{\text{baseline}},\ l_{\,1}\right) \Rightarrow \varepsilon^f_{p\,1} \\
&\left(\sigma^*_{\text{baseline}},\ \theta_{L\,\text{baseline}},\ \dot{\varepsilon}_{p\,\text{baseline}},\ T_{\text{baseline}},\ l_{\,2}\right) \Rightarrow \varepsilon^f_{p\,2} \\
&\left(\sigma^*_{\text{baseline}},\ \theta_{L\,\text{baseline}},\ \dot{\varepsilon}_{p\,\text{baseline}},\ T_{\text{baseline}},\ l_{\,3}\right) \Rightarrow \varepsilon^f_{p\,3} \\
&\left(\sigma^*_{\text{baseline}},\ \theta_{L\,\text{baseline}},\ \dot{\varepsilon}_{p\,\text{baseline}},\ T_{\text{baseline}},\ l_{\,4}\right) \Rightarrow \varepsilon^f_{p\,4} \\
&l_{\,1} > l_{\,\text{baseline}} > l_{\,2} > l_{\,3} > l_{\,4} \\
&\frac{\varepsilon^f_{p\,1}}{\varepsilon^f_{p\,\text{baseline}}} = i_1 \Rightarrow i(l_{\,1}, i_1),\ \ \frac{\varepsilon^f_{p\,2}}{\varepsilon^f_{p\,\text{baseline}}} = i_2 \Rightarrow i(l_{\,2}, i_2) \\
&\frac{\varepsilon^f_{p\,3}}{\varepsilon^f_{p\,\text{baseline}}} = i_3 \Rightarrow i(l_{\,3}, i_3),\ \ \frac{\varepsilon^f_{p\,4}}{\varepsilon^f_{p\,\text{baseline}}} = i_4 \Rightarrow i(l_{\,4}, i_4) \\
&\Rightarrow i(l_{cr}) = \{i(l_{\,1}, i_1); i(l_{\,\text{baseline}}, 1); i(l_{\,2}, i_2); i(l_{\,3}, i_3); i(l_{\,4}, i_4)\}
\end{aligned}
\tag{4.61}
$$

The results of the simulations that are before and after the regularization with different element lengths are summarized in Figure 4.42 comparing the end displacements and effective plastic strains to failure. It is shown that, different end displacements are obtained before the regularization when the same failure strain is utilized for different element lengths, where the biggest element size (i.e., $l_{cr} = 1$ mm) elongates more than the smallest element size (i.e., $l_{cr} = 0.125$ mm) before the failure. It is also shown that, by scaling the failure strains associated with the element lengths with the regularization term that is illustrated in Figure 4-42, end displacements are found to be approaching to the targeted value.

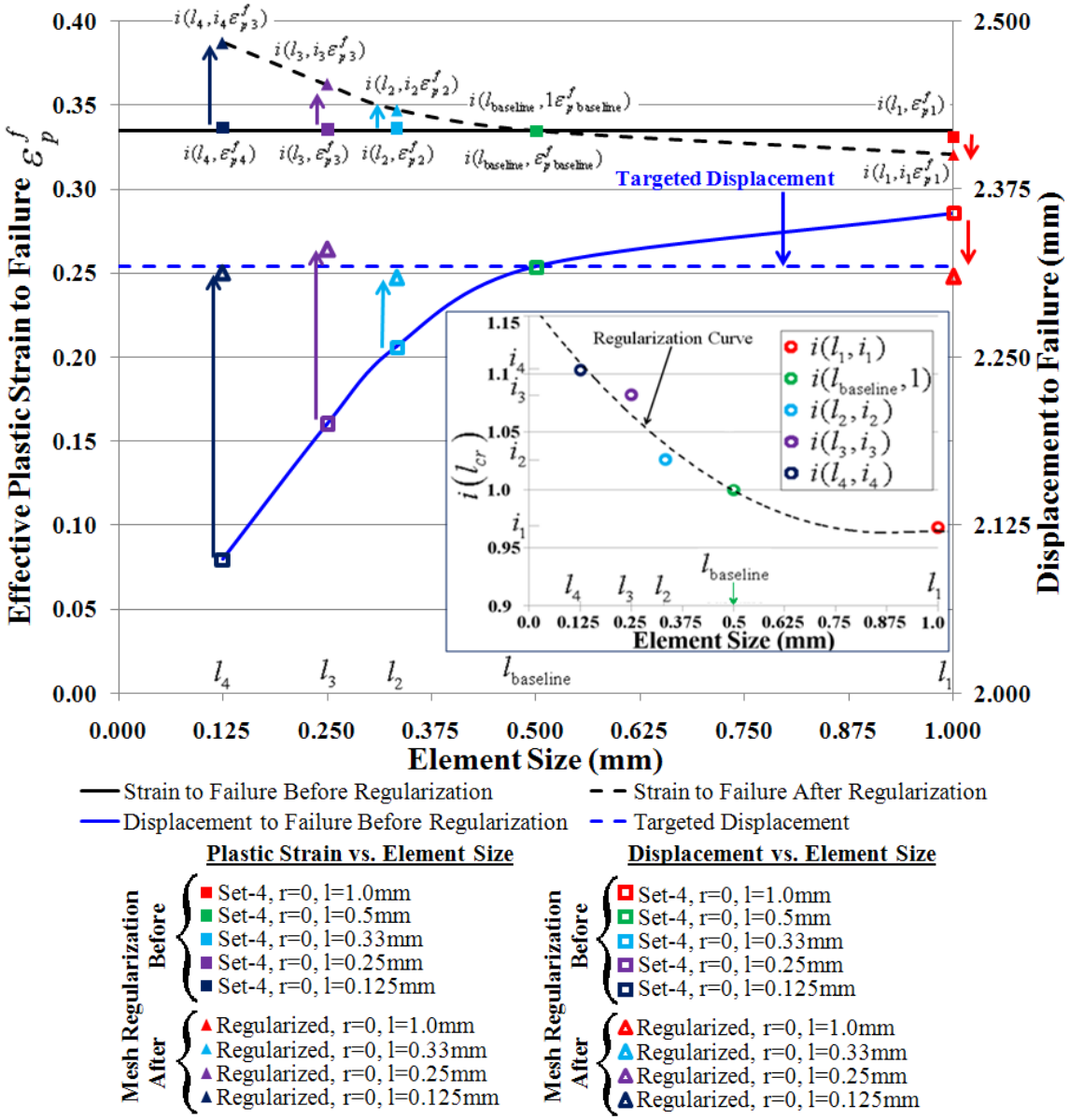

Figure 4-42: Effect of mesh size dependency on the prediction of end displacements.

The effects of mesh regularization can also be illustrated in Figure 4-43 for the force vs. displacement curves and the corresponding plastic strain accumulation. Compared to different end displacement predictions before the regularization in Figure 4-41, it can be observed that scaling the failure strains associated with element lengths have significant improvements.

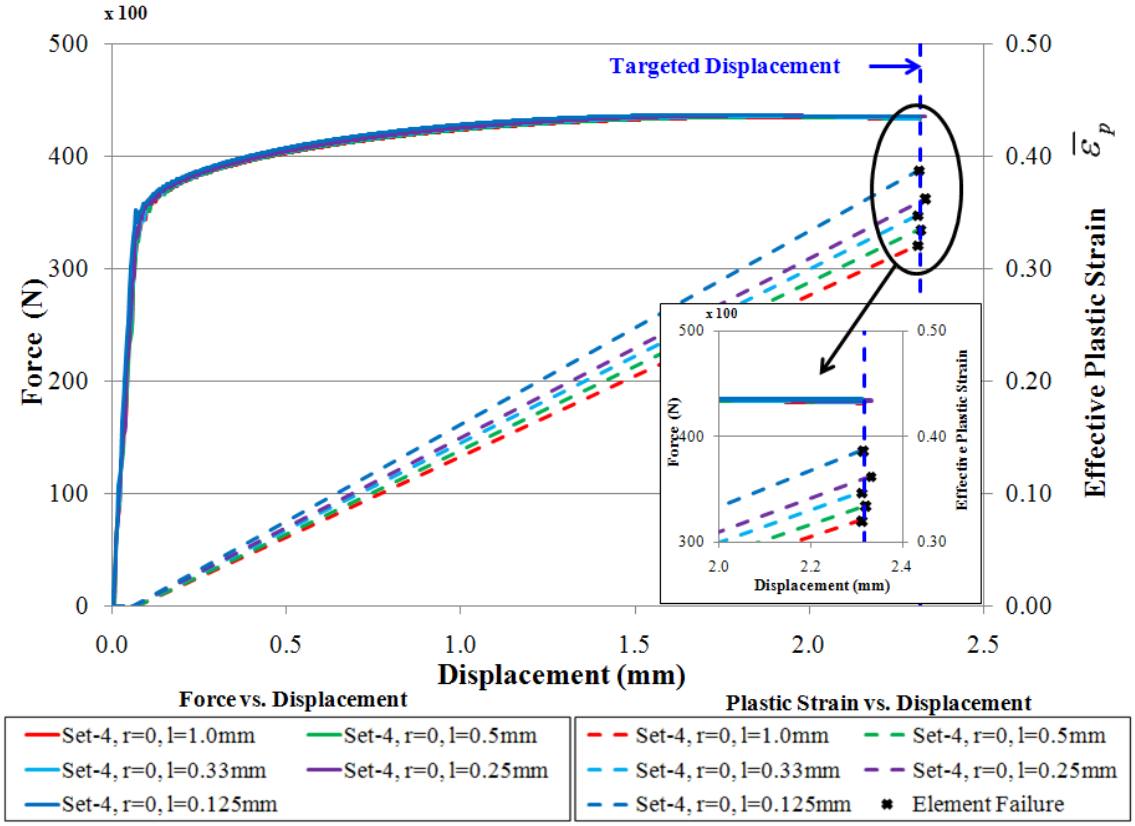

Figure 4-43: Effect of mesh regularization on the prediction of end displacements.

Three dimensional representation of the effects of regularization term on the failure surface that is described in Section 4.4.1 for multiple states-of-stress can be illustrated in Figure 4-44 emphasizing that the values of the effective plastic strains at failure are offset from the initial failure surface according to the scaling factors defined per each element length. It should be noted that the offset distances are exaggerated in Figure 4-44 (i.e., $i_1\varepsilon_{p\,\text{baseline}}^{f} = 0.5$, $i_2\varepsilon_{p\,\text{baseline}}^{f} = 1.5$) for a better demonstration of the mesh size dependency. Clearly, the amount of offset distances will be determined during the characterization for the baseline specimen in Chapter 5.

The effects of offsetting the stress meridians according to the regularization term that comprise normalized scaling factors per each additional element length can be illustrated in Figure 4-45. The input format of the piecewise linear scaling term or curve $i(l_{cr})$ can also be seen in Figure 4-45.

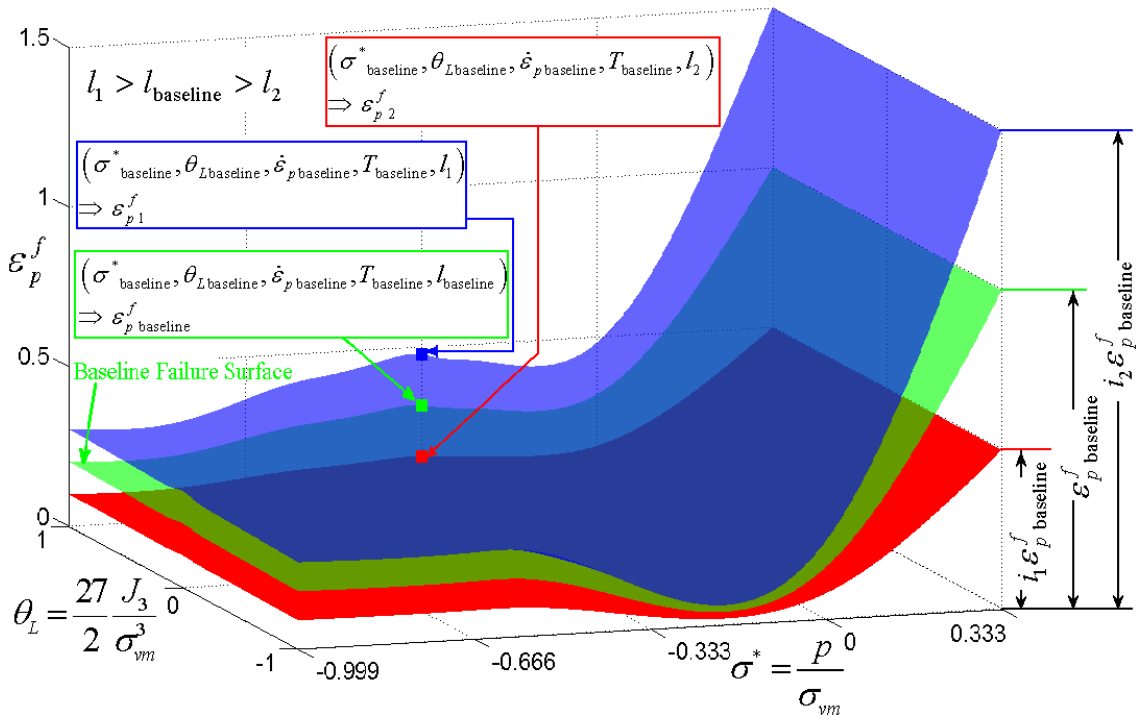

*Mesh size dependent scaling of the failure surface is exaggerated for demonstration purposes.

Figure 4-44: Mesh size dependent failure locus constructed by offsetting the initial failure surface.

Step-5:

Before starting the iterative FE simulations to find an initial specimen geometry that has a stress-triaxiality value within an acceptable tolerance to the targeted value, the material model parameters, location of the measurement and the element size has to be determined. It is shown in the previous steps that the state-of-stress depends on the material parameters, the location of the calculation point and the element size.

FE calculations for the stress-states depend on the flow surface and failure locus utilized in the material model. Figure 4-37 illustrates the comparison of stress-triaxiality calculations for two different sets of material model parameters (i.e., Set-1 and Set-4) when simulating the same initial specimen geometry with the same loading conditions. Set-4 is chosen for the successive FE calculations during the design iterations of the initial specimen geometries. Similarly, it is shown in Figure 4-38 that utilizing the element at the center of the specimen is a convenient way to calculate the evolution of the stress-state. Therefore, for the initial design procedure of the initial specimen geometries, unless otherwise stated, central element is used for the calculations. Figure 4-40 is used to

compare the stress-triaxiality histories for the finite elements with different sizes. It is shown in Figure 4-42 that elements with different characteristic lengths may lead to inaccurate calculation of the end displacements. Therefore, it is needed to decide on a mesh size before the successive FE calculations. An element length of $l_{cr} = 0.5$ mm is used for the example problem for demonstration in this section.

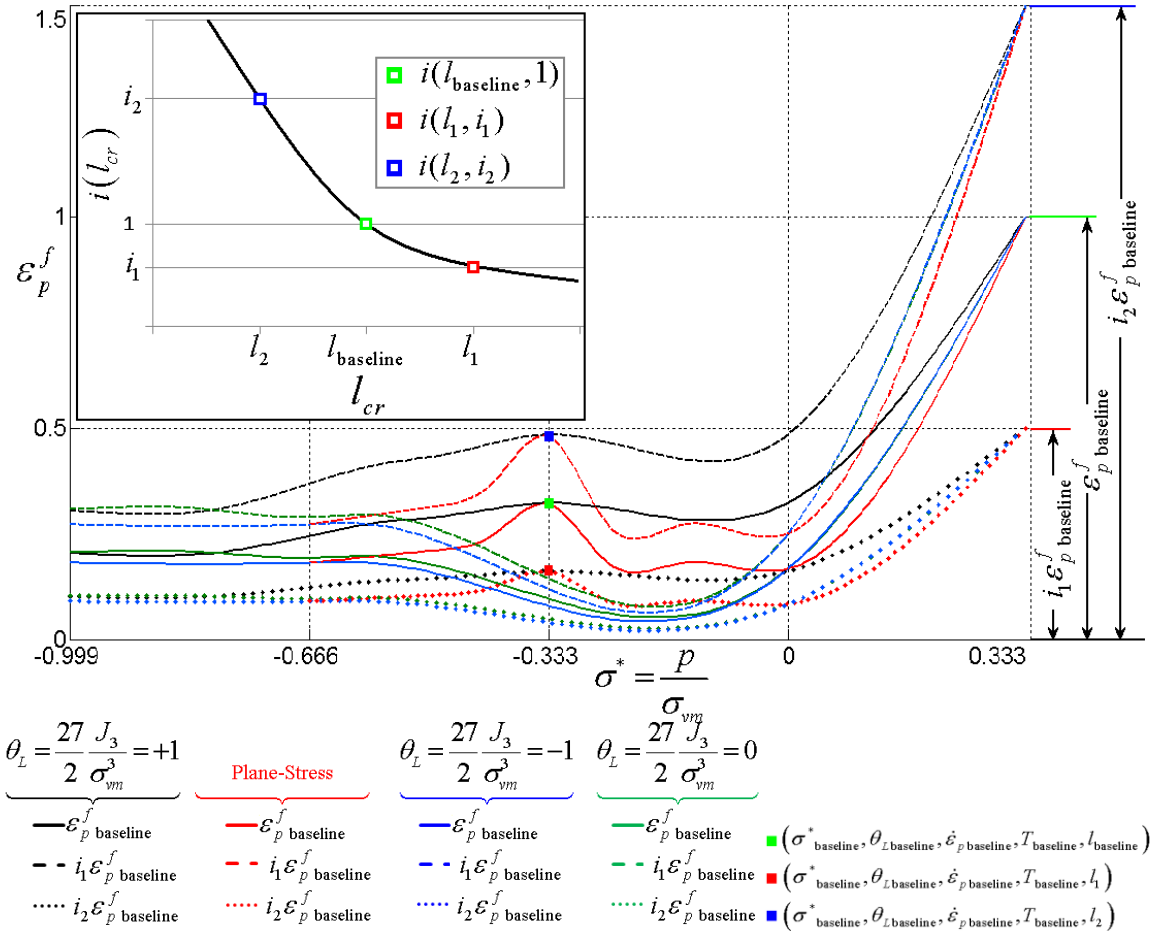

*Mesh size dependent scaling of the failure surface is exaggerated for demonstration purposes.

Figure 4-45: Mesh size dependent scaling factor (curve) and the scaled stress meridians of the failure surface.

It is reported that Bridgman's prediction for the un-deformed specimen geometry cannot be applied as plasticity takes over and necking dominates [1] [16]. States-of-stress, stress-triaxiality in particular, do not stay constant during the deformation and can exhibit major deviations from the initial state as illustrated in Figures 4-37, 4-38 and 4-40.

Therefore, an average value for the stress-state (i.e., stress-triaxiality) is often calculated through the effective plastic strain value as [100]:

$$\sigma_{av}^{*} = \left(\frac{p}{\sigma_{vm}}\right)_{av} = \frac{1}{\bar{\varepsilon}_p^f}\int_0^{\bar{\varepsilon}_p^f} \frac{p}{\sigma_{vm}}\, d\bar{\varepsilon}_p \tag{4.58}$$

Figure 4-46 illustrates the calculated stress-triaxiality for the first iteration with the averaged value compared to the initially targeted limit, which is found by Bridgman's analysis. It is found that the relative difference, which is described in Figure 4-32, between the calculated averaged and the targeted stress-triaxiality values are bigger than the tolerance. Therefore, successive FE calculations are necessary to find the initial design of the specimen for the targeted stress-triaxiality.

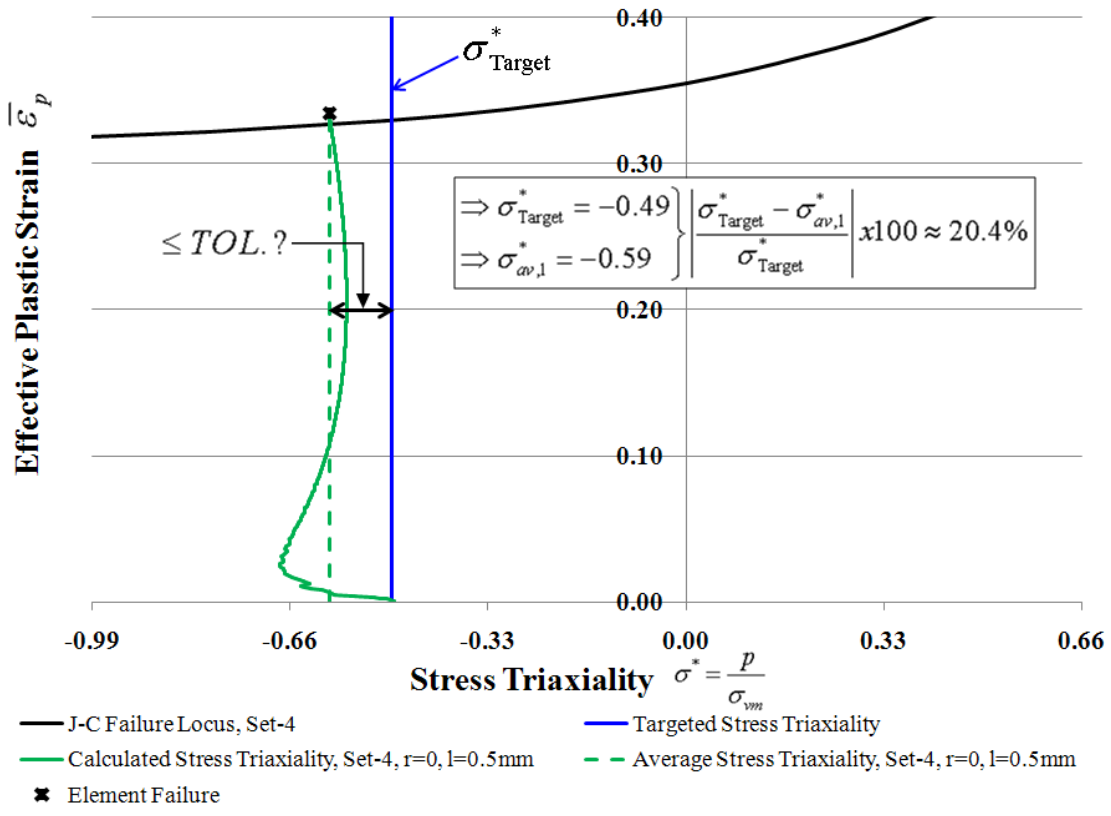

Figure 4-46: Averaged stress-triaxiality for the first iteration of the initial design.

Step-6:

The relative difference between the calculated and targeted values of the stress-triaxiality is found to be bigger than the tolerance. Consequently, the iterative procedure has to continue until a design can be attained that will approach to the targeted stress-triaxiality within the given tolerance. The number of required iterations can be reduced significantly by utilizing a modified Bridgman relation [106].

Considering that the calculated value of stress-triaxiality for the first iteration is significantly lower than the targeted value, a bigger notch radius ($R = 20$ mm) is randomly chosen for the second iteration keeping the cross-section identical with the first iteration (i.e., $a = 5\,mm$). Figure 4-46 illustrates the comparison of the averaged stress-triaxiality for the second iteration with the first iteration and the targeted value. It is also found for the second iteration that the relative difference is bigger than the tolerance.

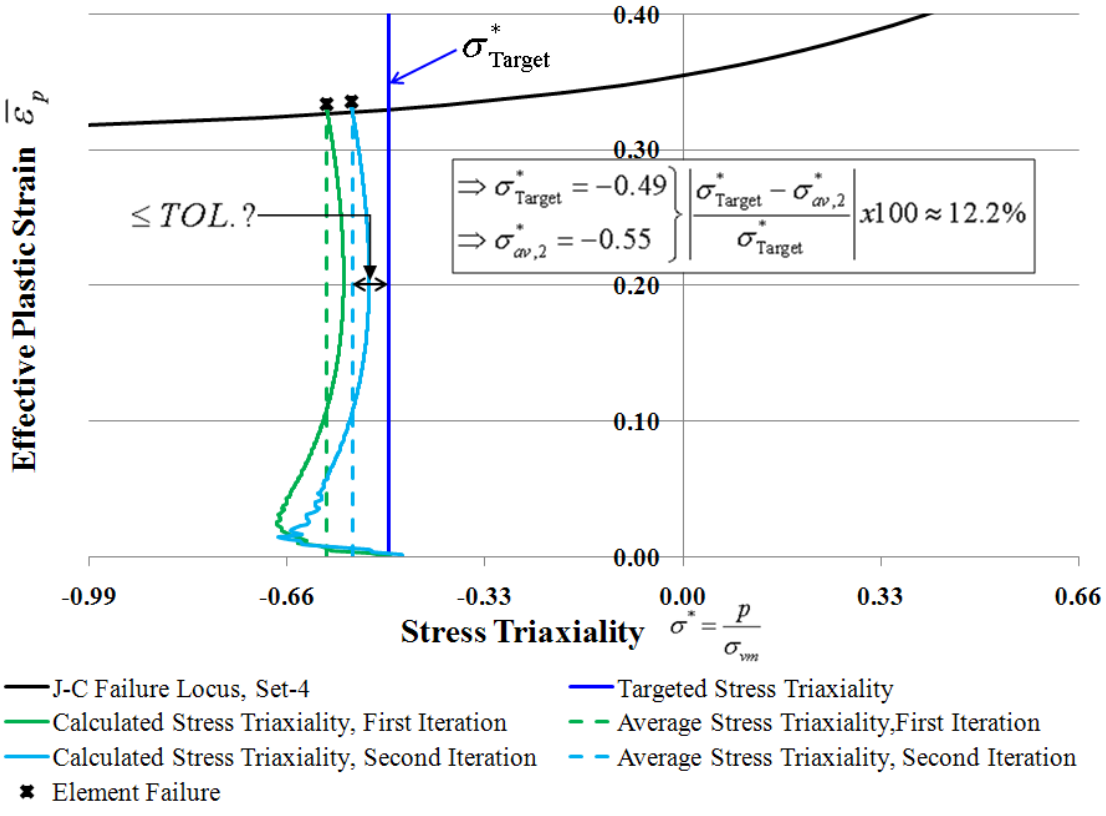

Figure 4-47: Averaged stress-triaxiality for the second iteration of the initial design.

Therefore, a third iteration is essential to find an initial geometry within the 5% difference of the targeted value of the stress-triaxiality. A modified Bridgman relation can be used to estimate the dimensions of the third specimen geometry as illustrated in Figure 4-48 keeping the minimum cross-section of the initial specimen identical with the previous iterations (i.e., $a = 5\,mm$). Different versions of the modified Bridgman relation can be found in the literature since stress-triaxiality depend on several independent factors including the geometry, material parameters, mesh size, etc. [106]. The new relation that is suggested in Figure 4-48 is found by curve fitting to the calculated average stress-triaxiality values of the first two iterations. While fitting a curve, Bridgman's analysis is considered as a baseline. Consequently, the notch radius for the third iteration can efficiently be found as $R = 26.4$ mm by the intersection point of the targeted value of the stress-triaxiality and the modified Bridgman relation.

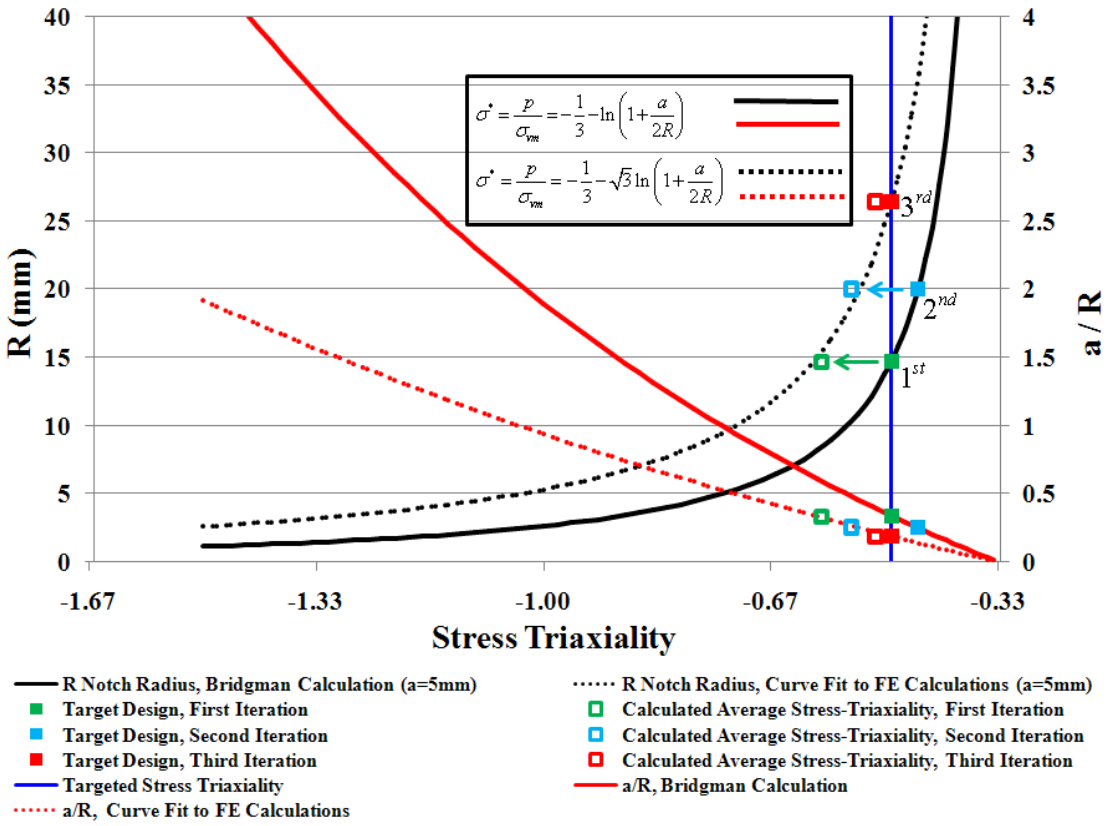

Figure 4-48: Modified Bridgman relation to find the initial specimen geometry for the targeted stress-triaxiality value.

Even though the calculated value for the third iteration also changes during the FE simulation, it is found that the third iteration satisfies the tolerance on the relative difference as illustrated in Figure 4-49. Therefore, it can be said that an initial design for targeted stress-triaxiality is found by only three successive iterations.

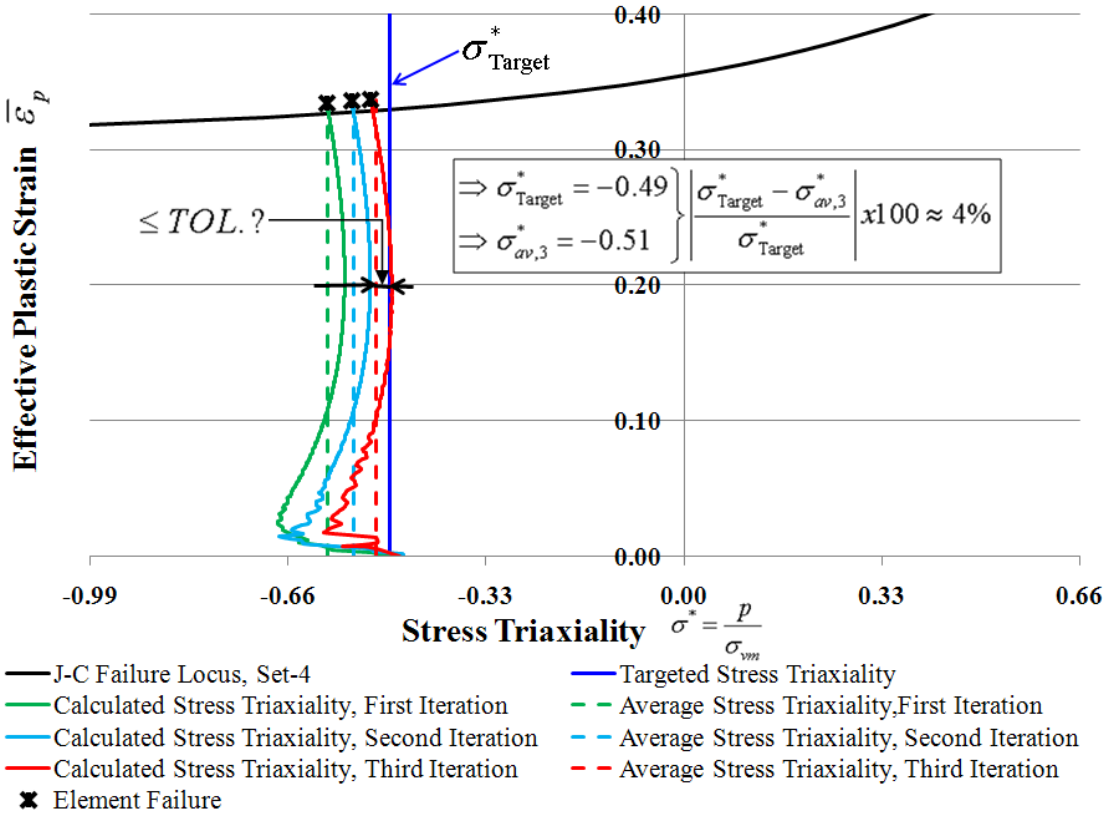

Figure 4-49: Averaged stress-triaxiality for the third iteration of the initial design.

Step-7:

The initial specimen dimensions are found as $a = 5\,mm$ and $R = 26.4$ mm for the example case targeting a stress-triaxiality value of $\sigma^*_{\text{Target}} = -0.49$. In the proceeding sections, similar methodology is attained to design specimens for specific states-of-stress. However, it should be noted that the targeted values of the stress-states that are predicted for the initial specimen geometries are subject to change. The decisive values will be calculated in Chapter 5 when the characterized flow surface and failure locus is utilized for the FE calculations of the specimens.

4.4.4 **Initial specimen geometries to characterize a failure locus depending on multiple states-of-stress**

Key steps of specimen design procedure are illustrated in Figure 4-32 and described in the previous section for axi-symmetric specimen geometry in tension for demonstration purposes. In this section, the same procedures are applied to find the initial specimen geometries, which are used to characterize a stress-state dependent failure locus for Al2024-T351. Specimen geometries are presented considering their geometries and loading conditions, which are categorically associated with specific states-of-stress and correspond to certain stress meridians as illustrated in Figure 4-31. It should be noted that in this section specimen geometries are iteratively found by utilizing Set-4 of the J-C material model and initially targeted values of the stress-states associated with the specimens can differ after the flow and failure loci are characterized and utilized during the FE calculations in Chapter 5.

4.4.4.1 Specimens for plane-stress tension

In order to achieve a plane-stress state in tension; thin, flat specimens are designed. It should be noted that the product-triaxiality values for thin, flat specimens should approach to zero since there is no third principle stress component for plane-stress state as:

$$\sigma_3 = 0 \Rightarrow \sigma_p^* = \frac{\sigma_1\sigma_2\sigma_3}{\sigma_{vm}^3} = \frac{I_3}{\sigma_{vm}^3} = 0 \tag{4.59}$$

Stress-triaxiality values for plane-stress state vary between $-\frac{1}{\sqrt{3}} \leq \sigma^* \leq \frac{1}{\sqrt{3}}$. Two specimens are designed to represent the plane-stress state considering the notable points at uni-axial stress-state in tension (i.e., $\sigma^* = -\frac{1}{3}$) and plane-strain state in tension (i.e., $\sigma^* = -\frac{1}{\sqrt{3}}$). As the value of the stress-triaxiality approaches $\sigma^* = -\frac{1}{\sqrt{3}}$, a form of confinement, which is often attained by appropriate notch geometry is applied to find the targeted stress-states. Therefore, the iterative scheme that is described in Figure 4-32 is

utilized to find feasible notch geometries by keeping the nominal cross-section of the specimen constant and modifying the notch radius. Two more equidistant points, which have stress-triaxiality values of $\sigma^* = -0.41$ and $\sigma^* = -0.49$, are selected to represent the plane-stress space with more resolution. Table 4-3 lists the values of the initially targeted stress-states associated with the corresponding plane-stress specimen geometries and FE models.

Table 4-3: Plane-stress specimens in tension associated with the targeted stress-states.

Specimen #	Specimen Geometry/FE Model	Initially Targeted Stress-State Values		
		σ^*	σ_p^*	θ_L
1	Specimen #1 Figure B-1	-0.333	0.0	1.0
2	Specimen #2 Figure B-2	-0.41	0.0	0.914
3	Specimen #3 Figure B-3	-0.49	0.0	0.616
4	Specimen #4 Figure B-4	-0.577	0.0	0.0

*Detailed geometries and corresponding FE models of the specimens are illustrated in Appendix-B

It is shown in Table 4-3 that a thin, flat specimen with a smooth gauge section (i.e., Specimen #1, Figure B-1) is designed to represent a stress-state of $\left(\sigma^*, \sigma_p^*, \theta_L\right) = \left(-\frac{1}{3}, 0, 1\right)$. This particular sample is assigned as the baseline for characterizing the strain rate dependent isothermal hardening curves, temperature dependent quasi-static hardening curves, and the scaling curves for offsetting the failure strain depending on the strain rate, temperature and critical element size.

Figure 4-50 illustrates the initially targeted stress-states for each specimen on the planes of stress-triaxiality vs. Lode angle parameter and stress-triaxiality vs. product-triaxiality, respectively.

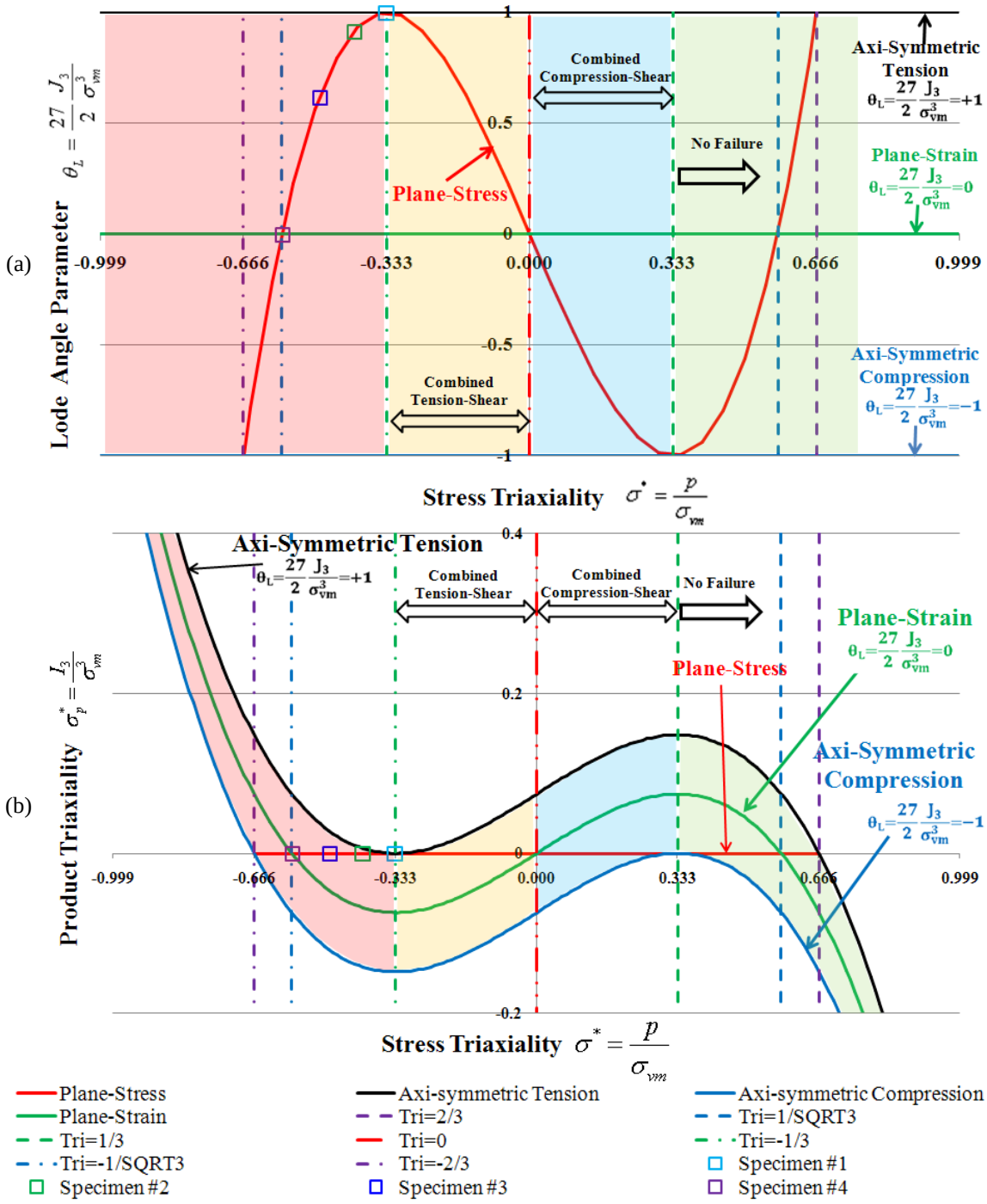

Figure 4-50: Determination of the targeted states-of-stress and the corresponding plane-stress specimen geometries on the planes defined by; (a) stress-triaxiality vs. Lode-angle-parameter and (b) stress-triaxiality vs. product-triaxiality.

After applying the specimen design procedures that are described in Section 4.4.3, targeted stress-states and calculated values are compared in Figure 4-51 for plane-stress

specimens, which are listed in Table 4-3. It should be noted that the states-of-stress are changing due to the deformation and as the effective plastic strain accumulates. Therefore, an average value is calculated by using the relation suggested by Equation (4.58) and compared with the targeted stress-states to verify the difference is within the tolerance given in Section 4.4.3.

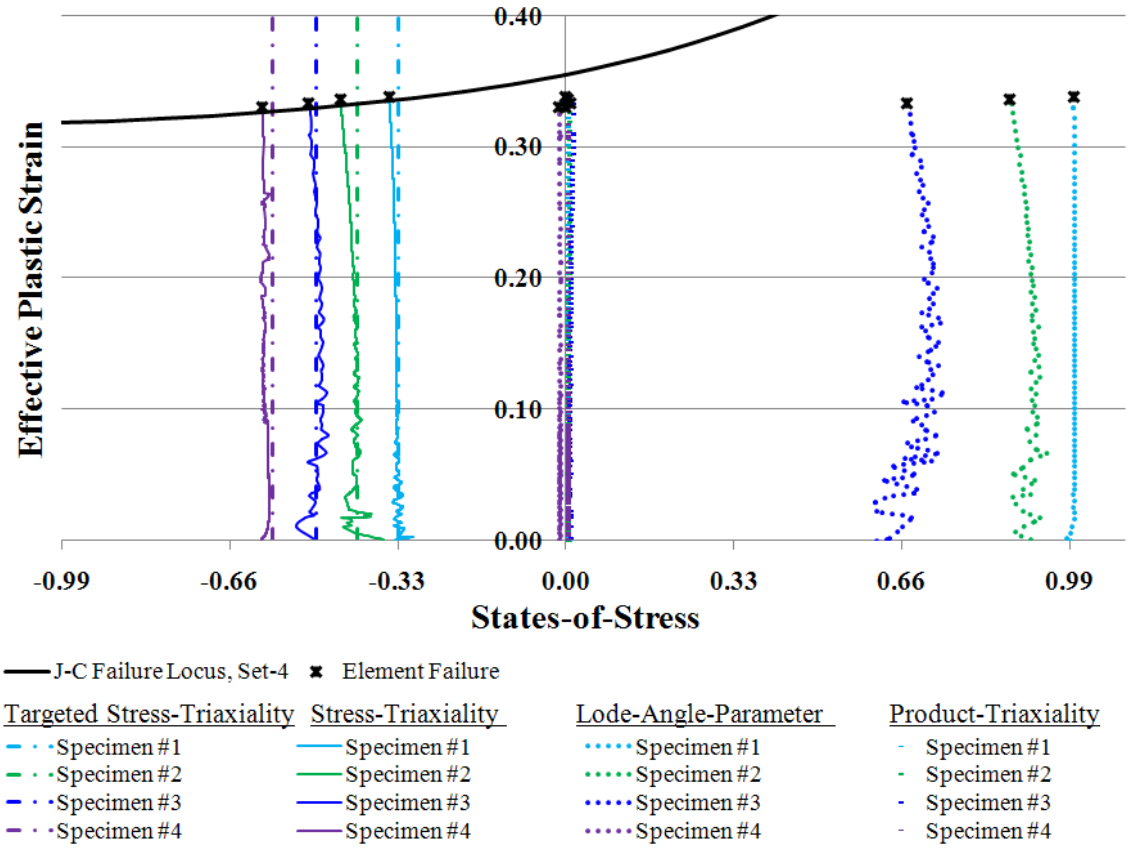

Figure 4-51: Comparison of the initially targeted and calculated states-of-stress for plane-stress specimens.

Set-4 of the J-C material model parameters are used for the FE calculations and the central elements in the gauge cross-section of the specimens are used for calculating the states-of-stress. It should be noted that the J-C failure locus is plotted to compare the failure initiation point on the plane defined by stress-triaxiality versus effective plastic strain and is not to illustrate a relation or dependency on the Lode-angle parameter and Product-triaxiality. It is shown that the calculated values of the stress-triaxiality for all

four specimen geometries are in good agreement with the initially targeted values. Product-triaxiality values are also shown to approach zero as required for a plane-stress state. Therefore, it can be concluded that the thickness of the specimens are selected thin enough to accomplish a plane-stress state in tension.

4.4.4.2 Specimens for axi-symmetric tension

Considering that the axi-symmetric extension meridian spans the stress-triaxiality space and reaches infinity at both ends depending on the stress ratios as shown in Figure 4-12, it is crucial to select the desired points such that the bridging can be accomplished across multiple states-of-stress while constructing the failure surface as illustrated by Figure 4-25. Figure 4-25 suggests potential regions of interest to help select specimen testing points such that the points already selected for the plane-stress state can be matched and the bridging between different states-of-stress accomplished. Therefore, the design sequence for axi-symmetric tension cases begins with a targeted stress-triaxiality value that has been found for a plane-stress case and then Bridgman's analysis can be utilized to find the initial notch diameter before necking since the minimum gauge diameter is a variable of choice. Consequently, the starting point for the initial design is the smooth axi-symmetric specimen, which has identical stress-states with the smooth plane-stress specimen as $\left(\sigma^*, \sigma_p^*, \theta_L\right) = \left(-\frac{1}{3}, 0, 1\right)$. The minimum stress-triaxiality value for specimens on the axi-symmetric extension meridian is attained by a confinement on the gauge section, which is iteratively found by using notch geometry through Bridgeman's relation. The sharpest notch radius is found for a stress-triaxiality value around $\sigma^* \approx -0.8$, where the failing finite elements are populated during a ballistic impact analysis as illustrated in Figure 4-21. One more stress-triaxiality target is selected to coincide with the biaxial stress-state in tension that has a stress-triaxiality of $\sigma^* = -\frac{2}{3}$, where the axi-symmetric compression meridian crosses the plane-stress. Therefore, for the six initially targeted states-of-stress values shown in Table 4-4, the iterative scheme described in Figure 4-32 is utilized to find feasible notch geometries while holding the specimen's nominal cross-section and iteratively modifying notch radius.

Table 4-4: Axi-symmetric specimens in tension associated with the targeted stress-states.

Specimen #	Specimen Geometry/FE Model	Initially Targeted Stress-State Values		
		σ^*	σ_p^*	θ_L
5	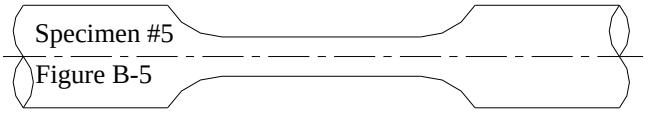 Specimen #5 Figure B-5	-0.333	0.0	1.0
6	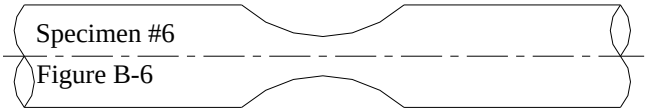 Specimen #6 Figure B-6	-0.41	0.006	1.0
7	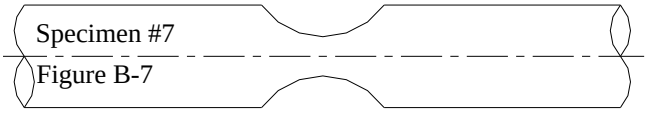 Specimen #7 Figure B-7	-0.49	0.028	1.0
8	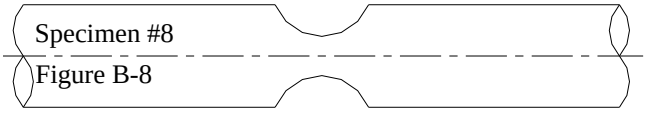 Specimen #8 Figure B-8	-0.577	0.074	1.0
9	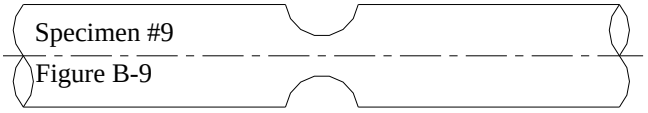 Specimen #9 Figure B-9	-0.666	0.148	1.0
10	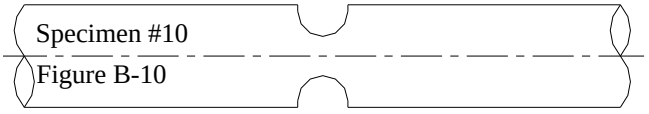 Specimen #10 Figure B-10	-0.8	0.319	1.0

*Detailed geometries and corresponding FE models of the specimens are illustrated in Appendix-B

Table 4-4 lists the values of the initially targeted stress-states associated with the corresponding axi-symmetric specimen geometries and FE models. It is shown that axi-symmetric specimen with a smooth gauge section (i.e., Specimen #5, Figure B-5) shares the same stress-states with the plane-stress specimen with a smooth gauge section (i.e., Specimen #1, Figure B-1). Therefore, as described in Figure 4-24, these particular overlapping stress-states are determined for verification purposes to test whether the failure initiates at the same effective plastic strain for the same states-of-stress independent of the specimen geometry or loading condition. Figure 4-52 illustrates the initially targeted stress-states for axi-symmetric specimens on the planes of stress-triaxiality vs. Lode angle parameter and stress-triaxiality vs. product-triaxiality.

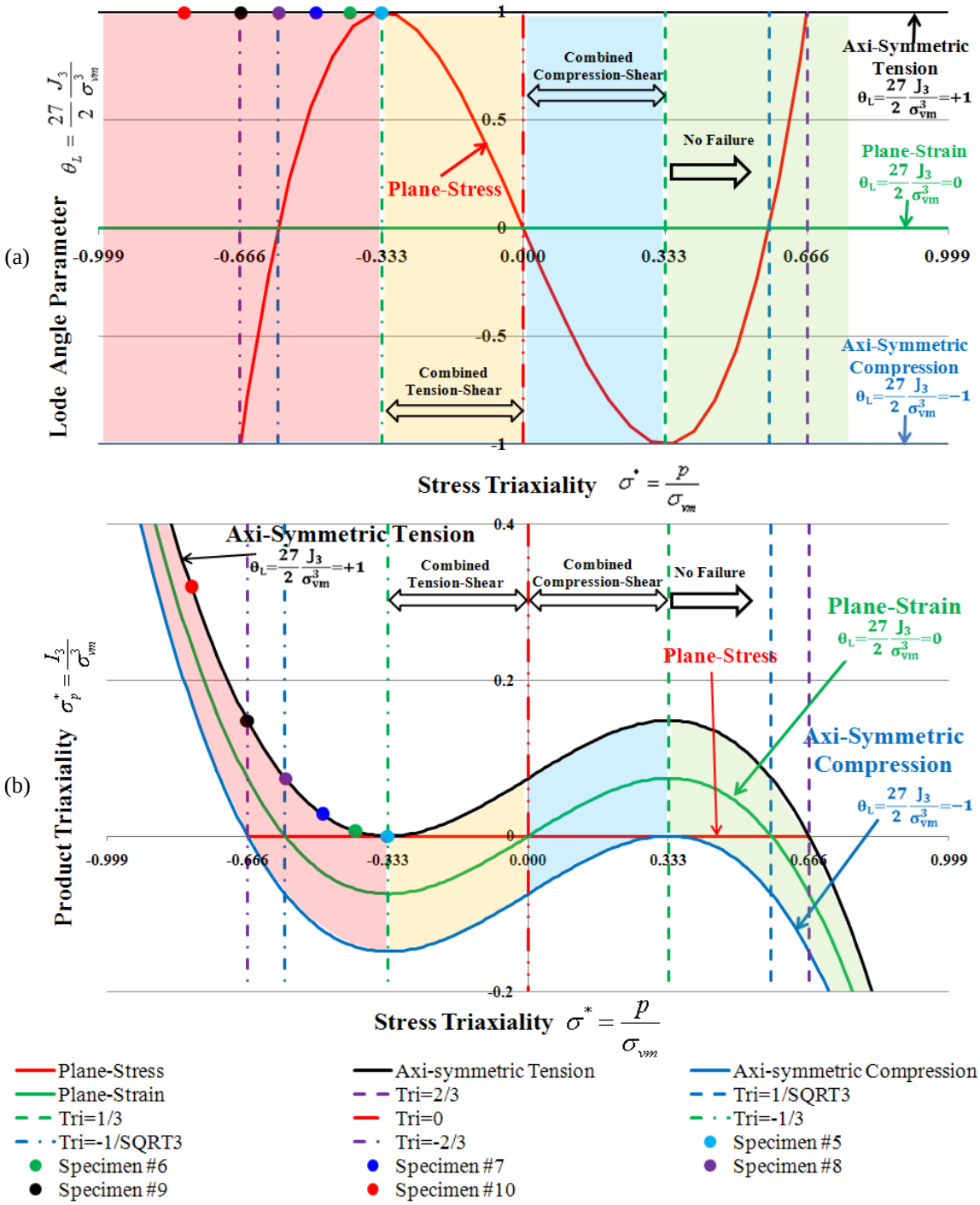

Figure 4-52: Determination of the targeted states-of-stress and the corresponding axi-symmetric specimen geometries on the plane defined by; (a) stress-triaxiality vs. Lode-angle-parameter and (b) stress-triaxiality vs. product-triaxiality.

It should be noted that the last three stress-states (i.e., Specimens #8, #9 and #10) are used for bridging the axi-symmetric tension meridian with the plane-strain state-of-stress.

Specimen design procedures that are described in Section 4.4.3 are used to find the initially targeted stress-states iteratively and calculated values are compared in Figure 4-53 for axi-symmetric specimens. Set-4 of the J-C material model parameters are used for the FE calculations and the central elements in the gauge cross-section of the specimens are used for calculating the states-of-stress. It is shown that the calculated averaged values of the stress-triaxiality for all six specimen geometries are in good agreement with the initially targeted values. J-C failure locus is plotted to illustrate the failure point as a function of stress-triaxiality and effective plastic strain. Lode-angle-parameter values are also shown that they are populated around unity as required for axi-symmetric stress-state in extension.

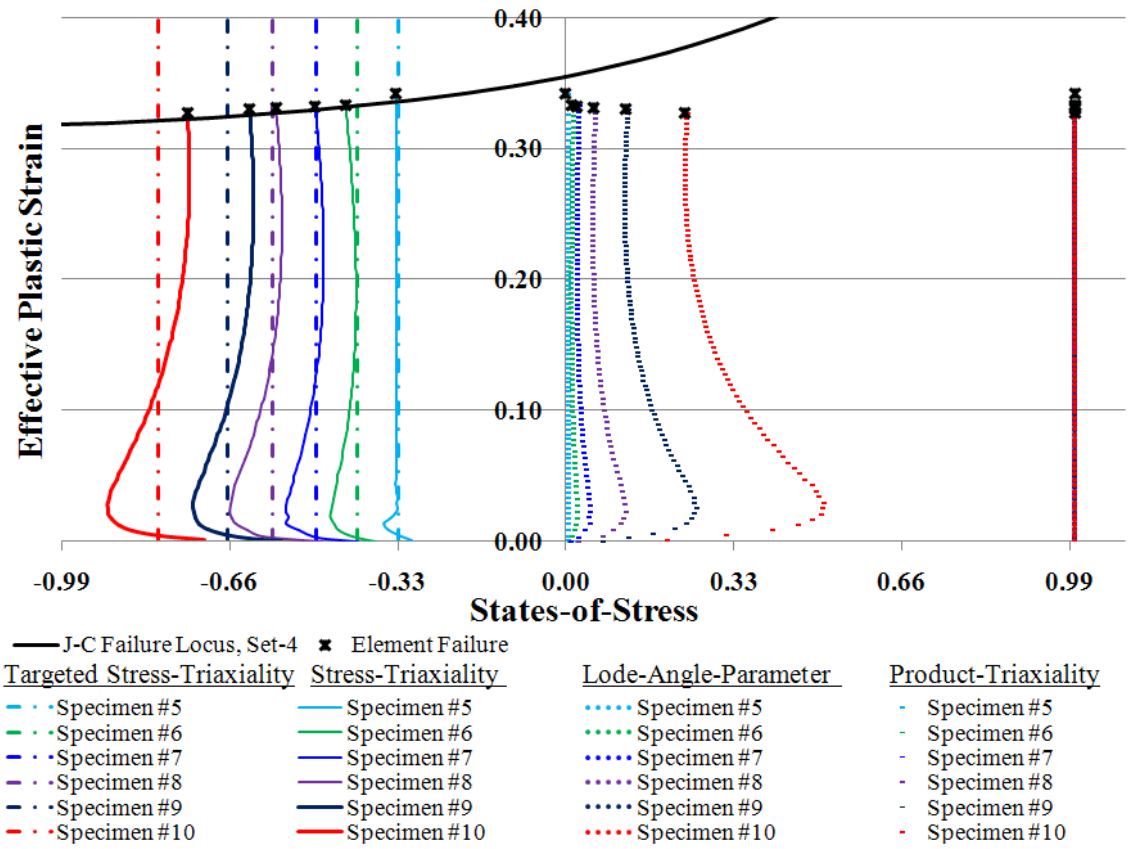

Figure 4-53: Comparison of the initially targeted and calculated states-of-stress for axi-symmetric specimens.

4.4.4.3 Specimens for plane-strain tension

Thick, grooved plates are designed in order to achieve stress-states on the plane-strain meridian. Three specimens are designed, beginning with a thick plate that has a smooth gauge section, considering the bridging across the plane-stress and axi-symmetric tension specimens. Therefore, stress-triaxiality for the first plane-strain specimen is determined as $\sigma^* = -\frac{1}{\sqrt{3}}$, where an overlapping stress-state is found at $\left(\sigma^*, \sigma_p^*, \theta_L\right) = \left(-\frac{1}{\sqrt{3}}, 0,0\right)$ that is also defined for Specimen #4. It should be noted that the Lode-angle-parameter values for thick, flat specimens should approach to zero since there is no third deviatoric stress component for plane-strain state as:

$$s_3 = 0 \Rightarrow \theta_L = \frac{27}{2}\frac{s_1 s_2 s_3}{\sigma_{vm}^3} = \frac{27}{2}\frac{J_3}{\sigma_{vm}^3} = 0 \tag{4.59}$$

A perfect plane-strain stress-state is achieved only if the thickness of the specimen is infinite, which will exceed the limits of the testing apparatus. Due to the technological constraints of the testing equipment, it is critical to determine necessary plate thickness of specimens such that the testing apparatus can accommodate the required forces, where the load cell that is used during the testing has a maximum capacity of ±20,000 lbf (~89 kN). Consequently, a reasonable plate thickness is iteratively found by using FE calculations, where the required load for testing and the stress-triaxiality predictions of the specimens with different thicknesses are examined. Stress-triaxiality calculations are attained by using a finite element in the center of the gauge section. The specimen that is designed to represent the plane-stress state (i.e., Specimen #1, Figure B-1) with a thickness of t=0.762mm is determined as a baseline for the iterations. Figure 4-54 represents an iterative analysis of the states-of-stress for the corresponding specimen thickness, where several FE models are developed to perceive the variation on the predicted stress-triaxiality. It is shown that a plane-strain state with stress-states $\left(\sigma^*, \sigma_p^*, \theta_L\right) = \left(-\frac{1}{\sqrt{3}}, 0,0\right)$ can be achieved by a specimen that is 64 times thicker than the baseline (i.e., 64t). Nevertheless, it is also shown that a specimen that is 32 times thicker

than the baseline (i.e., 32t) can also approach to the plane-strain state with a reasonable tolerance (i.e., 5%).

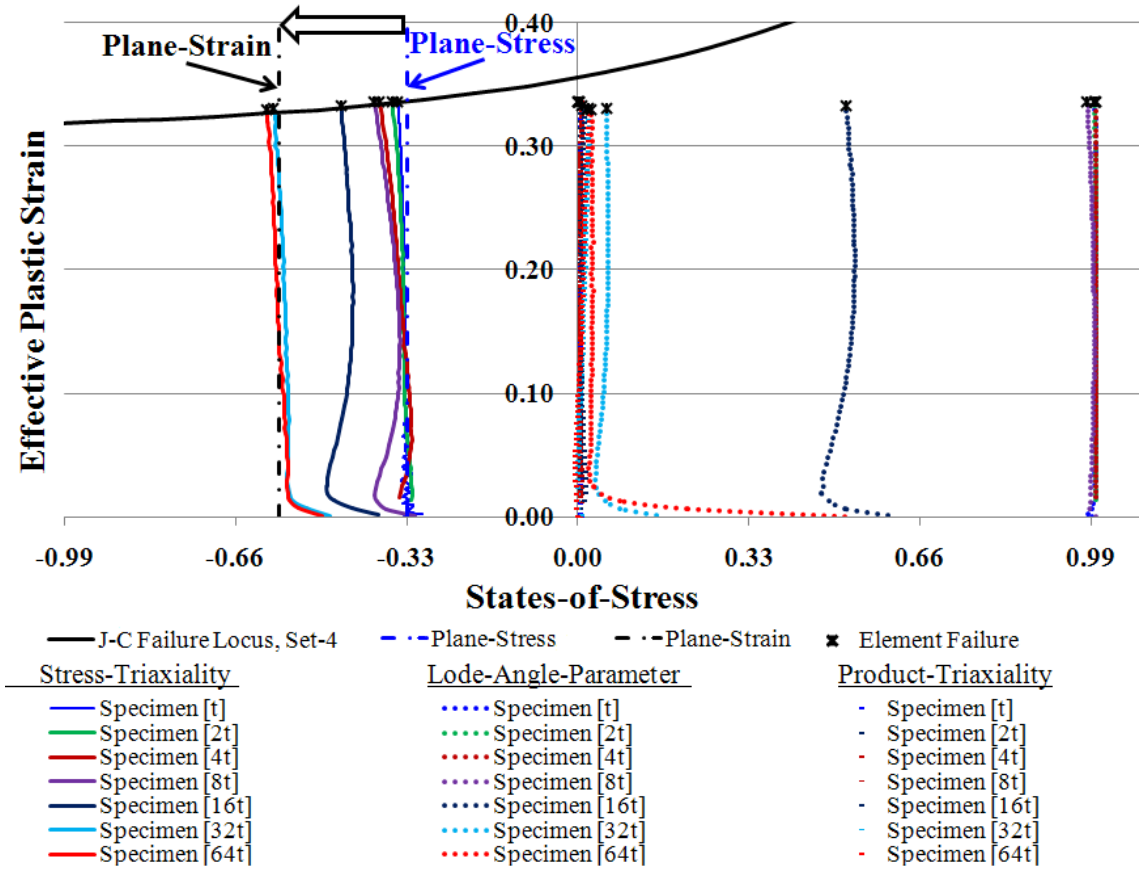

Figure 4-54: Determination of the best thickness for the plane-strain specimens considering the predictions on the states-of-stress.

Consequently, the force levels are compared in Figure 4-55 for a decisive selection of the specimen thickness based on the experimental limits. It can be observed from the figure that the thickest specimen (i.e., 64t) requires a load, which is dangerously close to the load carrying capacity of the test apparatus. On the other hand, 32t thick specimen requires only half of that capacity with a small compromise on the targeted stress-state. Therefore, it is concluded that a specimen that is approximately 32 times thicker than the plane-stress specimen can successfully capture plane-strain stress-states without challenging the limits of the test equipment.

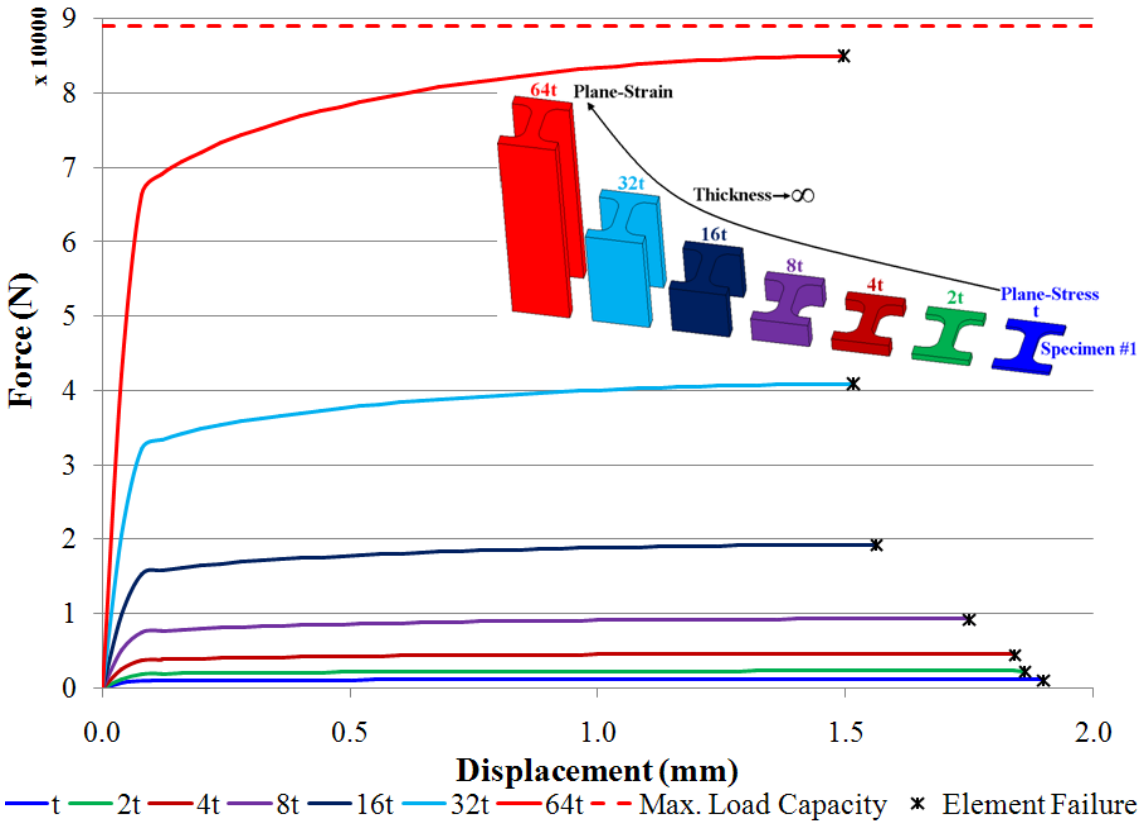

Figure 4-55: Determination of the best thickness for the plane-strain specimens considering the load carrying capacity of the test apparatus.

The second plane-strain specimen is designed to bridge points where the stress-triaxiality value is $\sigma^* = -\frac{2}{3}$ coinciding when the axi-symmetric compression meridian crosses the plane-stress meridian. This particular stress-triaxiality value is chosen to bridge with Specimen #9.

The third plane-strain specimen is designed to bridge points with Specimen #10, where the maximum value of stress-triaxiality is expected at $\sigma^* = -0.8$ considering Figure 4-21. These latter two plane-strain geometries are iteratively obtained by utilizing the procedures that are described in Section 4.4.3. Similar to the plane-stress and axi-symmetric specimens, a notch geometry is iteratively found while keeping the specimen's nominal cross-section constant.

Table 4-5 lists the values of the initially targeted stress-states associated with the corresponding plane-strain specimen geometries and FE models. Initially targeted stress-

states for plane-strain specimens on the planes of stress-triaxiality vs. Lode angle parameter and stress-triaxiality vs. product-triaxiality are illustrated in Figure 4-56.

Table 4-5: Plane-strain specimens in tension associated with the targeted stress-states.

Specimen #	Specimen Geometry/FE Model	Initially Targeted Stress-State Values		
		σ^*	σ_p^*	θ_L
11	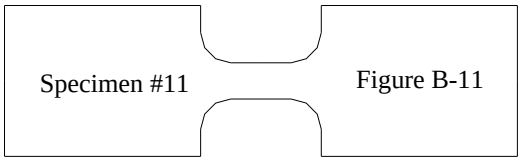	-0.577	0.0	0.0
12	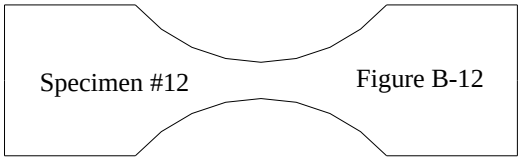	-0.666	0.074	0.0
13	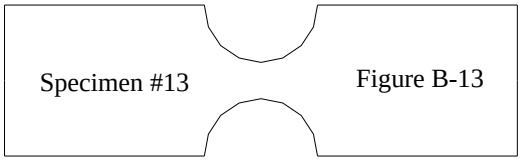	-0.8	0.245	0.0

*Detailed geometries and corresponding FE models of the specimens are illustrated in Appendix-B

Specimen design procedures that are described in Section 4.4.3 are used to find the initially targeted stress-states iteratively and calculated values are compared in Figure 4-57 for plane-strain specimens. Set-4 of the J-C material model parameters are used for the FE calculations and the central elements in the gauge cross-section of the specimens are used for calculating the states-of-stress. It is shown that the calculated averaged values of the stress-triaxiality for all three specimen geometries are in good agreement with the initially targeted values. J-C failure locus is plotted to illustrate the failure point as a function of stress-triaxiality and effective plastic strain. Lode-angle-parameter values are also shown that they are approaching to zero as the third deviatoric stress component diminishes for plane-strain state.

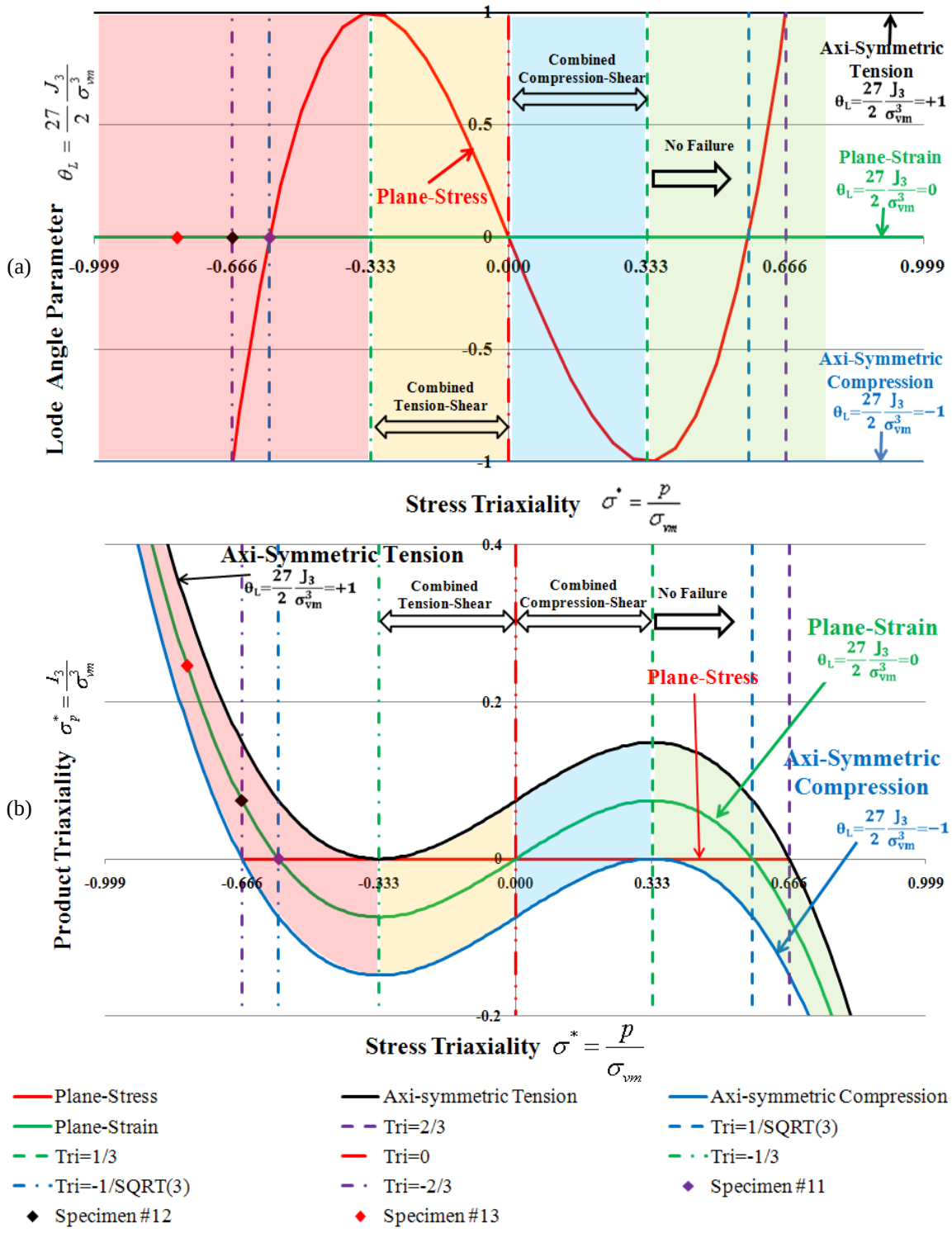

Figure 4-56: Determination of the targeted states-of-stress and the corresponding plane-strain specimen geometries on the plane defined by; (a) stress-triaxiality vs. Lode-angle-parameter and (b) stress-triaxiality vs. product-triaxiality.

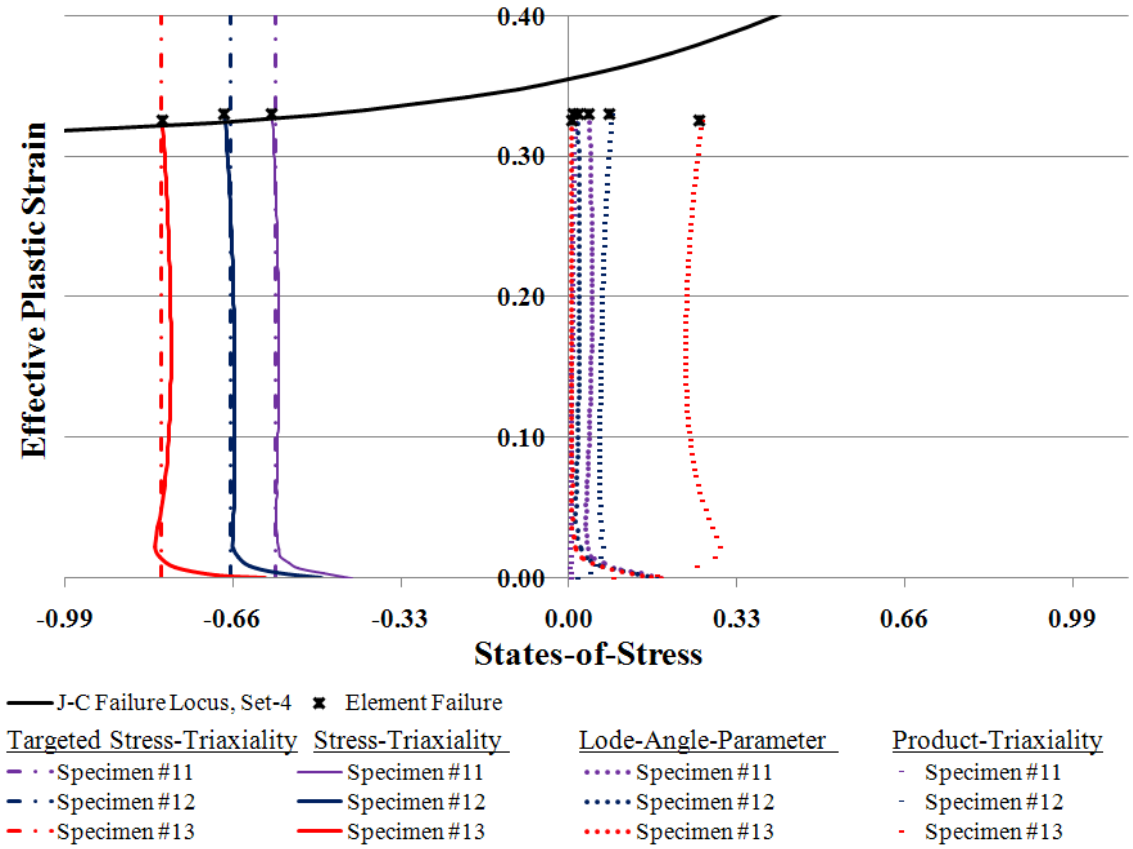

Figure 4-57: Comparison of the initially targeted and calculated states-of-stress for plane-strain specimens.

4.4.4.4 Specimens for uni-axial compression

In order to extend the coverage of the failure surface towards the positive values of the stress-triaxiality space, uni-axial compression specimens are used with cylindrical geometries. It is reported by Bridgman from a series of experiments [95] and more recently, with a parallel numerical and experimental study by Bao and Wierzbicki [106], that beyond a stress-triaxiality of $\sigma^* > +\frac{1}{3}$ no failure is expected for ductile materials. Therefore, the effective plastic strain required to achieve failure for the uni-axial compression is assumed 100% (i.e., $\bar{\varepsilon}_p^f = 1$). However, it should be noted that for the initial design stage of the specimens, failure is assumed based on the Set-4 of the J-C material model. States-of-stress are calculated for the central element in the gauge cross-section of the specimens. Simple cylindrical specimens with different diameter to height

ratios ($\frac{D}{H}$) are simulated first to check the effects of specimen geometry and friction coefficient on the state-of-stress for the central element in the middle of the specimen during a uni-axial compression test. Dimensions and the corresponding friction coefficients are listed in Table 4-6 for five different simulation models.

Figure 4-58 depicts the fact that for the central element stress-states are independent of the diameter to height ratio. It is also found that the effects of 'barrelling' due to surface friction during a uni-axial compression case have minor effects on the stress-state predictions. Considering that the upper and lower surfaces of the test apparatus were lubricated with molybdenum disulfide grease to minimize the effects of friction during the testing program [108], no friction is assumed for the initial design phase of the compression specimens. Therefore, a Specimen #14 is selected for the testing program with a diameter to height ratio of $\frac{D}{H} = 1$ (i.e., $\frac{D}{H} = \frac{3.048}{3.048}$) with no friction. Table 4-7 lists the values of the initially targeted stress-states associated with the corresponding compression specimen geometry and FE model.

Table 4-6: Model dimensions and friction coefficients for uni-axial compression simulations.

		Cylinder Height - *H* [mm]			
		3.048	3.81	5.08	6.35
Cylinder Diameter *D* [mm]	3.048	*D*/*H*=1, μ=0.0 *D*/*H*=1, μ=0.3 *D*/*H*=1, μ=0.5			
	5.08		*D*/*H*=1.33, μ=0.0	*D*/*H*=1, μ=0.0	*D*/*H*=0.8, μ=0.0

Table 4-7: Compression specimen with stress-state design parameters.

Specimen #	Specimen Geometry/FE Model	Initially Targeted Stress-State Values		
		σ^*	σ_p^*	θ_L
14	Specimen #14 Figure B-14	+0.333	0.0	-1.0

* Detailed geometry and corresponding FE model of the specimen is illustrated in Appendix-B

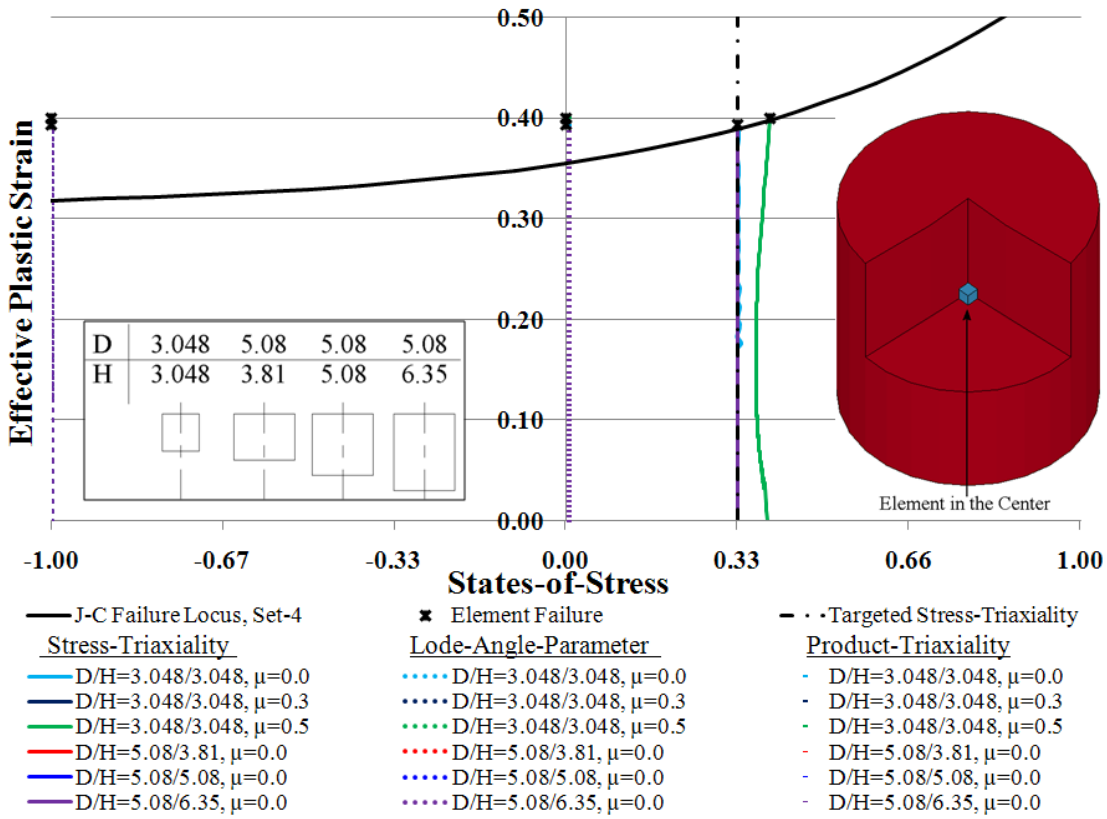

Figure 4-58: Effects of the diameter to height ratio and the coefficient of friction on the state-of-stress predictions.

It should be noted that the J-C failure locus is plotted to illustrate the failure point as a function of stress-triaxiality and effective plastic strain in Figure 4-58. During the testing program and characterization in the next Chapter, no failure is assumed for a uni-axial compression stress-state. Initially targeted stress-states for compression specimen on the planes of stress-triaxiality vs. Lode angle parameter and stress-triaxiality vs. product-triaxiality are illustrated in Figure 4-59.

4.4.4.5 Specimen for torsion / shear

Shear state is a notable stress-state, where all state-of-stress components yield to zero (i.e., $\sigma^*, \sigma_p^*, \theta_L = 0$). A spool shaped torsion test specimen with a thin wall, which is represented in Table 4-8, is designed for testing shear deformation and failure.

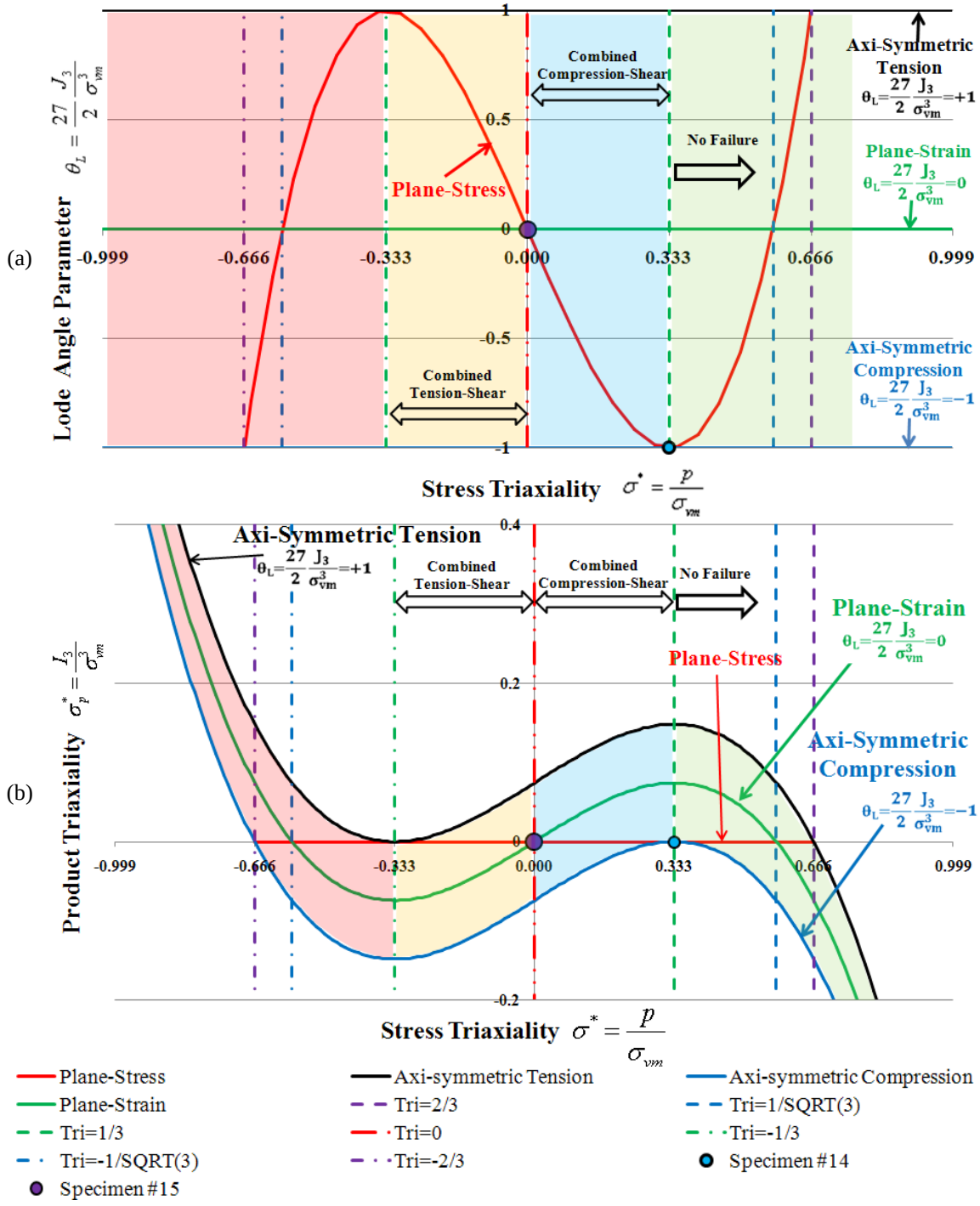

Figure 4-59: Determination of the targeted states-of-stress and the corresponding compression and torsion specimen geometries on the plane defined by; (a) stress-triaxiality vs. Lode-angle-parameter and (b) stress-triaxiality vs. product-triaxiality.

Table 4-8: Shear specimen with stress-state design parameters.

Specimen #	Specimen Geometry/FE Model	Initially Targeted Stress-State Values		
		σ^*	σ_p^*	θ_L
15	Specimen #15 Figure B-15	0.0	0.0	0.0

* Detailed geometry and corresponding FE model of the specimen is illustrated in Appendix-B

The wall thickness is iteratively found, where finding the optimum thickness requires a trade-off analysis between the limitations due to manufacturing constraints and the state-of-stress. A state of pure shear requires the wall thickness to be minimized, where technological constraints due to specimen production and instrumentation require a reasonable thickness. The location of the stress-state calculation along the thin walled gauge section also needs to be determined. Figure 4-60 illustrates the spool specimen geometry and three finite elements, where one on the outer surface (i.e., Element #1), one is on the inner surface (i.e., Element #3), and one is in the center (i.e., Element #2) of the section, are selected for stress-state calculations by utilizing Set-4 of the J-C material model parameters.

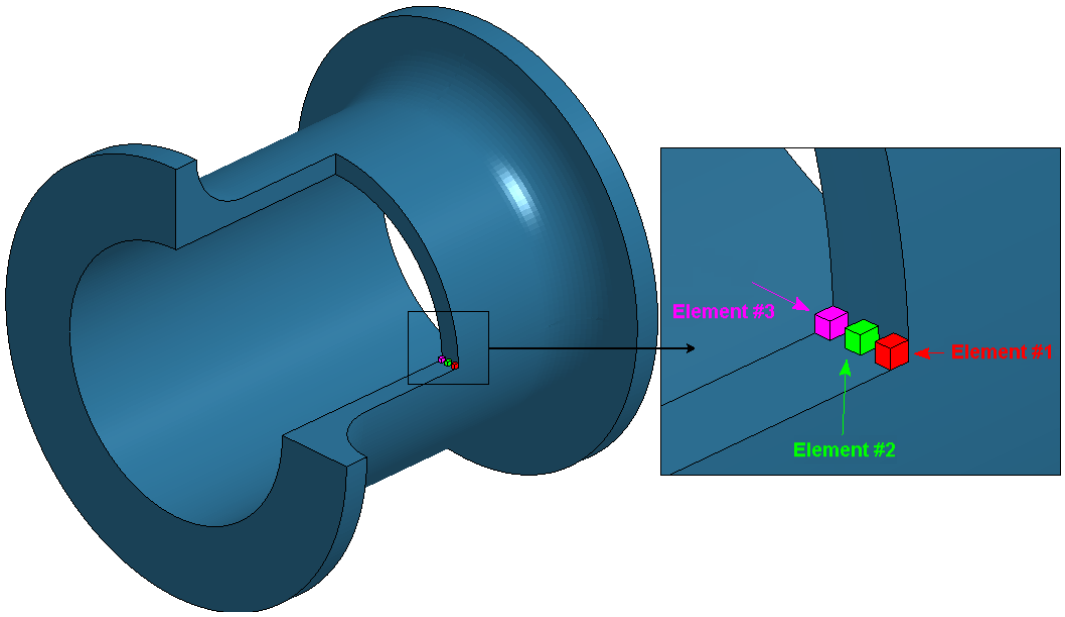

Figure 4-60: Alternative positions for calculating state-of-stress on shear specimen.

However, it is found that the failure often initiates at the end of the shoulder of the spool geometry under torsion and it is required to calculate the stress-states for the elements that are illustrated in Figure 4-61. The elements on the outer surface of the shear specimen are used to compare the stress-state predictions.

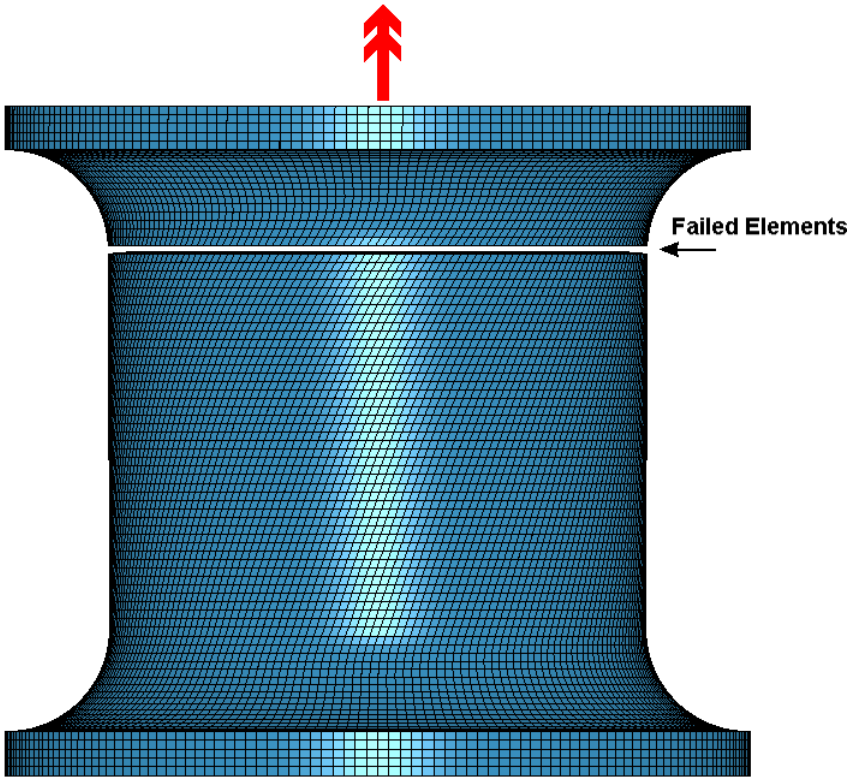

Figure 4-61: Position of the failure and the stress-state calculation for shear specimen.

It is shown in Figure 4-62 that the calculated values of the stress-triaxiality for all four positions on the specimen geometry are in good agreement with the initially targeted value for pure shear. J-C failure locus is plotted to illustrate the failure point as a function of stress-triaxiality and effective plastic strain. It should be noted that only the elements at the shoulder of the specimen fails due to torsion.

Figure 4-62 also illustrates that Lode-angle-parameter and product-triaxiality calculations for the elements inside the wall thickness and in the middle of the section (i.e., Element #2 and #3), are not ensuring the targeted stress-state for pure shear. Therefore, the elements on the outer surface of the spool geometry are selected for further

calculations of the states-of-stress. Initially targeted stress-states for shear specimen on the planes of stress-triaxiality vs. Lode angle parameter and stress-triaxiality vs. product-triaxiality are illustrated in Figure 4-59.

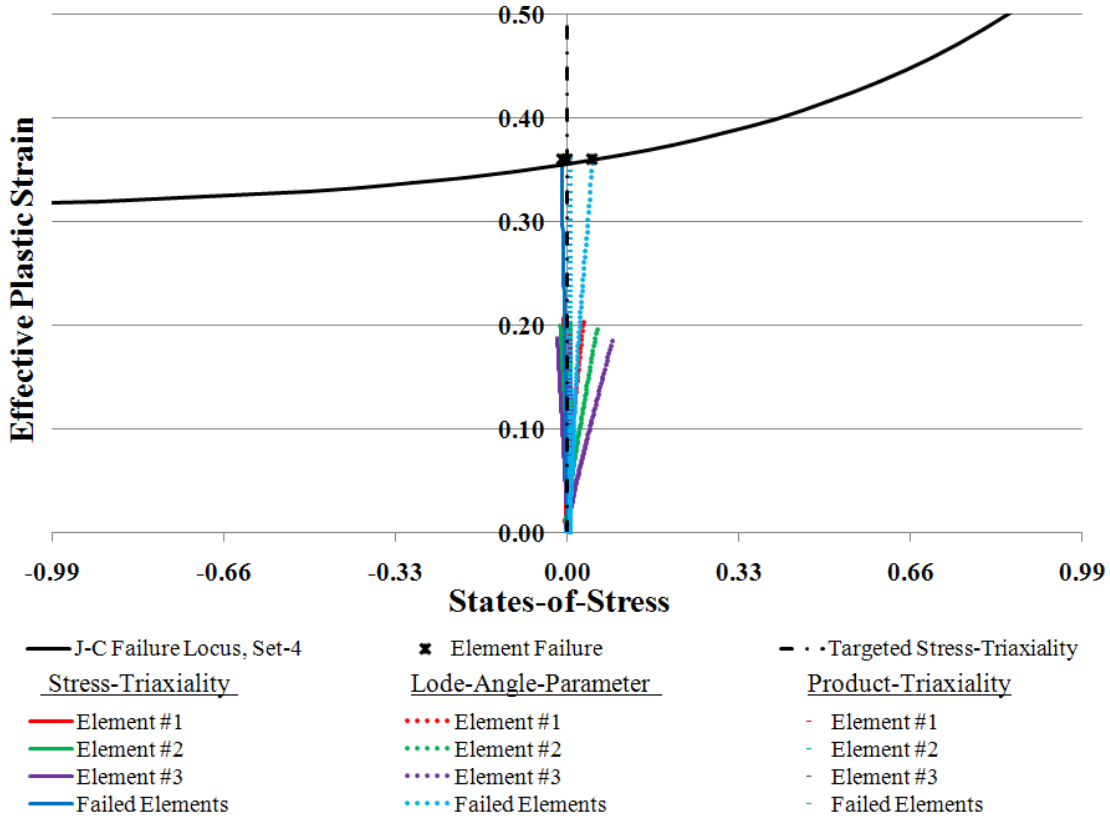

Figure 4-62: Comparison of the initially targeted and calculated states-of-stress for shear specimen.

4.4.4.6 Specimens for combined tension - shear

In the special case of combined tension-torsion, two specimens are designed with different stress-triaxiality values trying to match the Lode-angle-parameters of two of the intermediate plane-stress notched specimens. Stress-triaxiality values for these two notched plane-stress specimens are $\sigma^* = -0.41$ and $\sigma^* = -0.49$ namely for Specimen #2 and Specimen #3. Product-triaxiality values of these specimens are all zero on the σ^* vs. σ_p^* space. However, the failure characteristics are different and for characterization purposes on the σ^* vs. θ_L space, third deviatoric components are matched. Therefore, due to the bridging purposes that are illustrated by Figure 4-33, two combined tension-shear

specimens are needed. In that unique case Lode-angle-parameter is used for the bridging. Corresponding Lode-angle-parameters for Specimens #16 and #17 are calculated through the relation defined by Equation (4.60).

$$\left.\begin{matrix}\sigma_p^* = \frac{\mathrm{I}_3}{\sigma_{\mathrm{vm}}^3} = 0 \\ \sigma^* = \frac{p}{\sigma_{vm}} = \begin{cases}-0.41 \\ -0.49\end{cases}\end{matrix}\right\} \theta_L = \frac{27}{2}\frac{J_3}{\sigma_{\mathrm{vm}}^3} = \frac{27}{2}\left(\sigma_p^* + (\sigma^*)^3 - \frac{1}{3}\sigma^*\right) \Rightarrow \theta_L = \begin{cases}0.9145 \\ 0.6167\end{cases}$$

$$\text{Finding the roots for } -\frac{1}{3} \le \sigma^* \le 0 \qquad (4.60)$$

$$\frac{27}{2}\left((\sigma^*)^3 - \frac{1}{3}\sigma^*\right) = \theta_L = \begin{cases}0.9145 \\ 0.6167\end{cases} \Rightarrow \sigma^* = \begin{cases}-0.2505 \\ -0.1466\end{cases}$$

Figure 4-63 illustrates the bridging between the plane-stress specimens with intermediate stress-triaxiality and the combined tension - shear specimens on the planes of stress-triaxiality vs. Lode angle parameter and stress-triaxiality vs. product-triaxiality.

Similar studies of combined loading cases have been performed in the literature beginning with the pioneering work of Lode [109]. His research on tension and compression testing of tubes with internal pressure led to the proposed relations and engineering parameters those are still valid and very widely used today. Further details on this work can be found in Malvern [214].

In more recent studies, Barsoum and Faleskog [102] and Seidt [108] studied the failure characteristics of thin walled pipes while applying tension, compression and torsion at the same time. They have used ‘Lode parameter’ that is defined by Equation (4.61) for their characterization.

$$\mu = \frac{2\sigma_2 - \sigma_1 - \sigma_3}{\sigma_1 - \sigma_3} \qquad (4.61)$$

Utilization of different definitions by various authors for the ‘Lode’ parameter often causes confusion. In general, the differences among the different definitions for the Lode parameter can be illustrated using a structure under both normal force N and moment M, as illustrated in Figure 4-64.

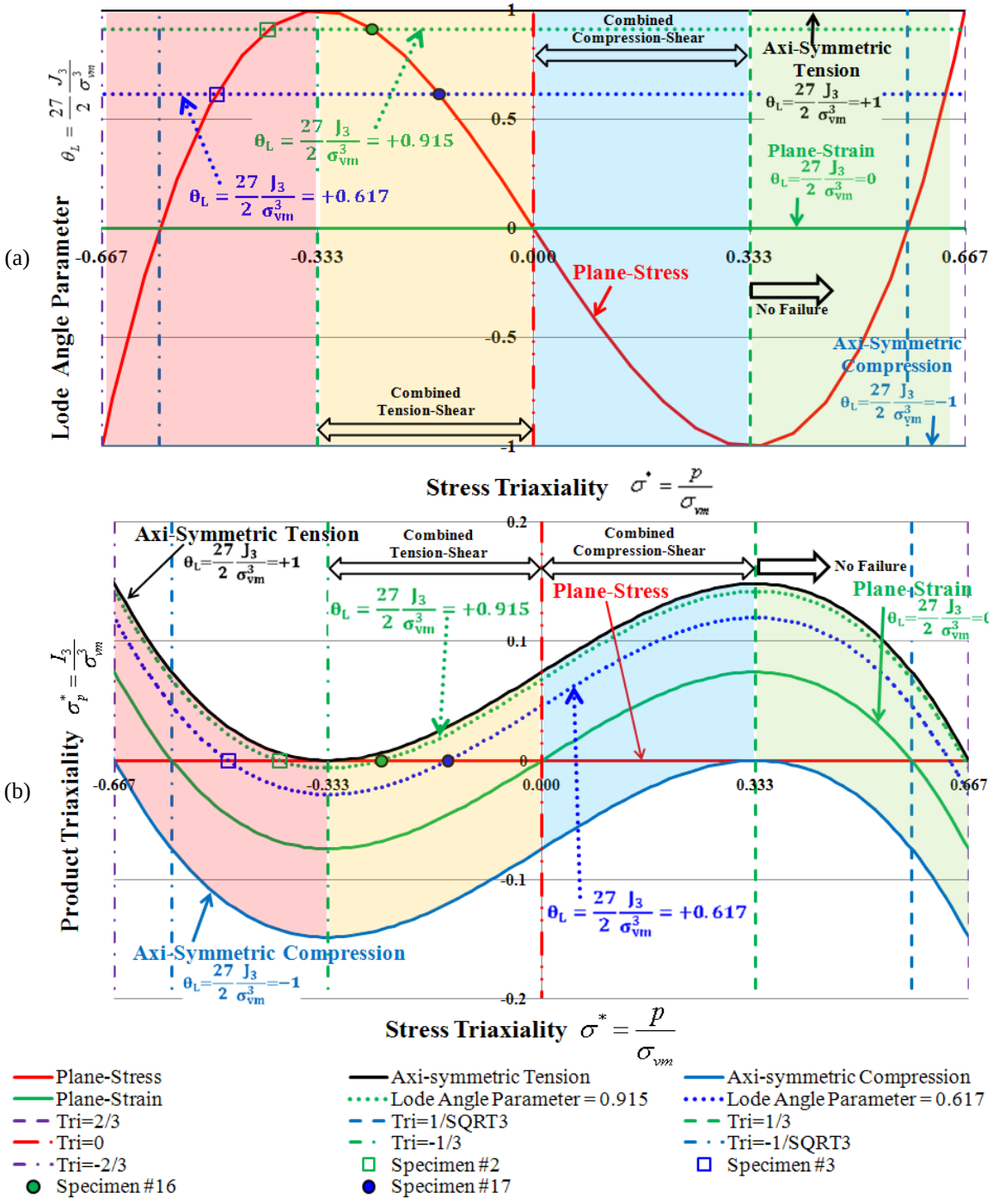

Figure 4-63: Determination of the targeted states-of-stress and the corresponding combined loading cases sharing the same Lode-angle-parameters with the plane-stress specimens on the plane defined by; (a) stress-triaxiality vs. Lode-angle-parameter and (b) stress-triaxiality vs. product-triaxiality.

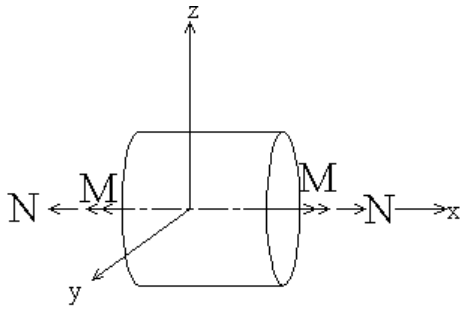

Figure 4-64: Combined loading under tension and torsion.

The stress-state under tension and shear can be written as:

$$\boldsymbol{\sigma} = \begin{bmatrix} \sigma_x & \tau_{xy} & 0 \\ \tau_{xy} & 0 & 0 \\ 0 & 0 & 0 \end{bmatrix} \tag{4.62}$$

The principle stresses can be written as:

$$\begin{aligned} \sigma_1 &= \frac{\sigma_x}{2} + \sqrt{\left(\frac{\sigma_x}{2}\right)^2 + \tau_{xy}^2} \\ \sigma_2 &= 0 \\ \sigma_3 &= \frac{\sigma_x}{2} - \sqrt{\left(\frac{\sigma_x}{2}\right)^2 + \tau_{xy}^2} \end{aligned} \tag{4.63}$$

The states-of-stress can then be compared by using this simple combined loading case as illustrated in Figure 4-65. It is shown that the stress-triaxiality changes in between $\pm\frac{1}{3}$ as the ratio of the tension and torsion varies. It is observed that the two different definitions of 'Lode' parameters are changing in between ± 1.

Loading ratios should be determined with care for combined states-of-stress. Therefore, it is critical to decide on the loading history and control of the experiment, where it is the loading condition that is modified to obtain different states-of-stress, not the geometry. Ratios between uni-axial stress and shear can be calculated as described by Equation (4.63) by combining the values in Equation (4.60) with the stress-state given in Equation (4.62).

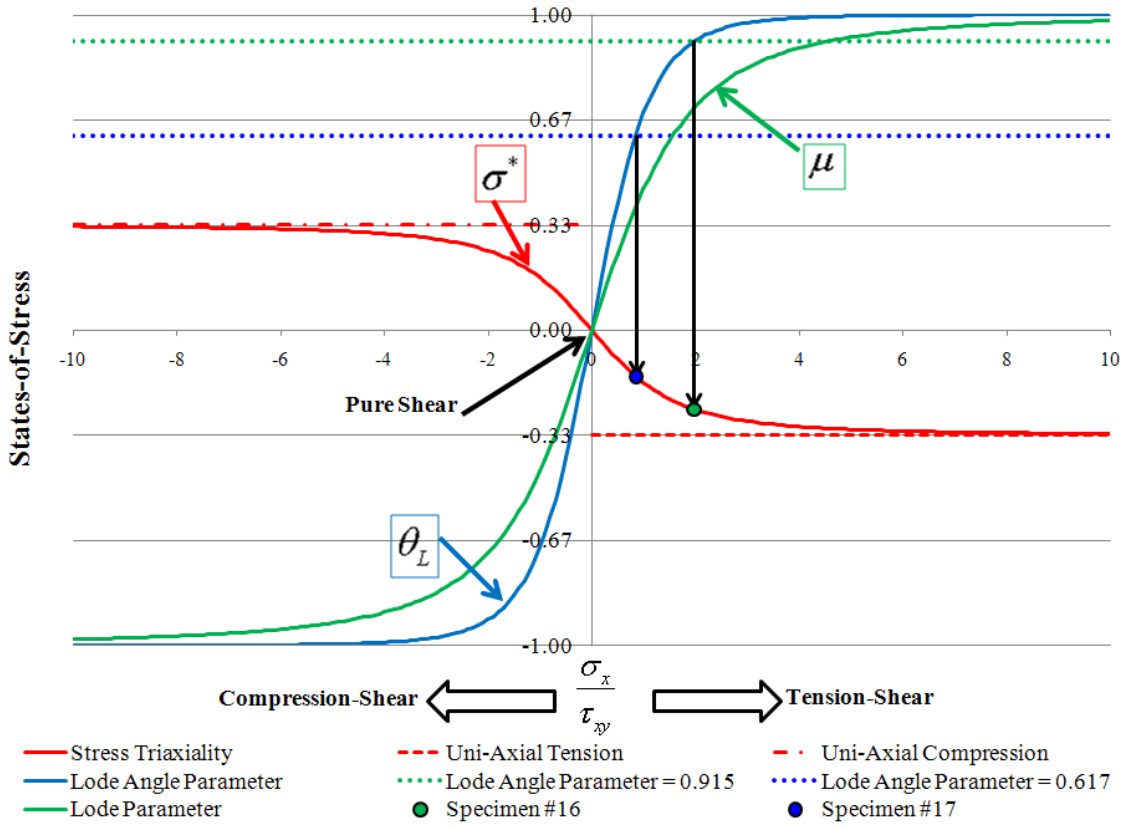

Figure 4-65: Comparison of the stress-states against proportion of combined loading.

$$\boldsymbol{\sigma} = \begin{bmatrix} \sigma_x & \tau_{xy} & 0 \\ \tau_{xy} & 0 & 0 \\ 0 & 0 & 0 \end{bmatrix}, p = -\frac{\sigma_x}{3} \Rightarrow \mathbf{s} = \begin{bmatrix} \frac{2}{3}\sigma_x & \tau_{xy} & 0 \\ \tau_{xy} & -\frac{1}{3}\sigma_x & 0 \\ 0 & 0 & -\frac{1}{3}\sigma_x \end{bmatrix}$$

$$\Rightarrow \sigma_{vm}^2 = \frac{3}{2}\left[\left(\frac{2}{3}\sigma_x\right)^2 + \left(-\frac{1}{3}\sigma_x\right)^2 + \left(-\frac{1}{3}\sigma_x\right)^2 + 2\tau_{xy}^2\right] \Rightarrow \sigma_{vm} = \sqrt{3\tau_{xy} + \sigma_x^2} \tag{4.64}$$

$$\Rightarrow \sigma^* = \frac{p}{\sigma_{vm}} = -\frac{\sigma_x}{3\sqrt{3\tau_{xy} + \sigma_x^2}} = \underbrace{\begin{cases} -0.2505 \\ -0.1466 \end{cases}}_{\text{From Equation (4.60)}} \Rightarrow \frac{\sigma_x}{\tau_{xy}} \approx \begin{cases} 1.973 \\ 0.848 \end{cases}$$

A more detailed discussion about the combined loading cases of tubes can be found at Seidt [108]. Table 4-9 present one specimen geometric design that is used for different combined loading conditions.

Table 4-9: Combined tension - shear specimen with corresponding loading ratios and stress-state design parameters.

Specimen #	Specimen Geometry/FE Model	Loading Ratios	Initially Targeted Stress-State Values		
			σ^*	σ_p^*	θ_L
16	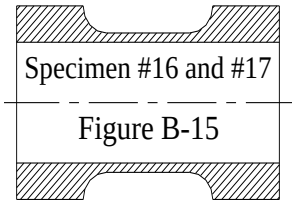 Specimen #16 and #17 Figure B-15	$\frac{\sigma_x}{\tau_{xy}} = 1.973$	-0.2505	0.0	0.915
17		$\frac{\sigma_x}{\tau_{xy}} = 0.848$	-0.1466	0.0	0.617

* Detailed geometry and corresponding FE model of the specimen is illustrated in Appendix-B

It is shown in Figure 4-66 that the calculated values of the stress-triaxiality for two different loading conditions are in good agreement with the initially targeted values for combined tension-shear specimen. J-C failure locus is plotted to illustrate the failure point as a function of stress-triaxiality and effective plastic strain. It should be noted that, due to the tension component, a necking region forms in the center of the spool geometry, where a finite element in the center of the specimen wall through the thickness is selected for stress-state calculations as illustrated in Figure 4-66.

4.4.4.7 Specimens for punch tests

Figure 4-21 suggests that there is a significant number of FEs failing around the equi-biaxial triaxiality region, where the points are approaching the axi-symmetric compression meridian. Therefore, utilizing a biaxial testing methodology is essential to cover the range of interest with accuracy. This region of interest is also a big concern for metal forming applications and different alternative testing methodologies are suggested such as; bulge testing, cruciform test and punch testing. Among these options, punch testing is found to be the most feasible due to the convenience in designing, building the set-up and producing the specimens. However, different alternative punch test methodologies exist depending on the shape of the punch and specimen or the strain path followed; such as Marciniak [172], Nakazima, Hasek and Keeler [215]. Nakazima and Hasek tests require variable specimen geometries, where in the Keeler test; the specimen geometry is kept the same while changing the geometry of the punch as illustrated in

Figure 4-67 [216]. A good review about the biaxial testing methodologies and metal forming applications can be found from Banadic, et al. [216].

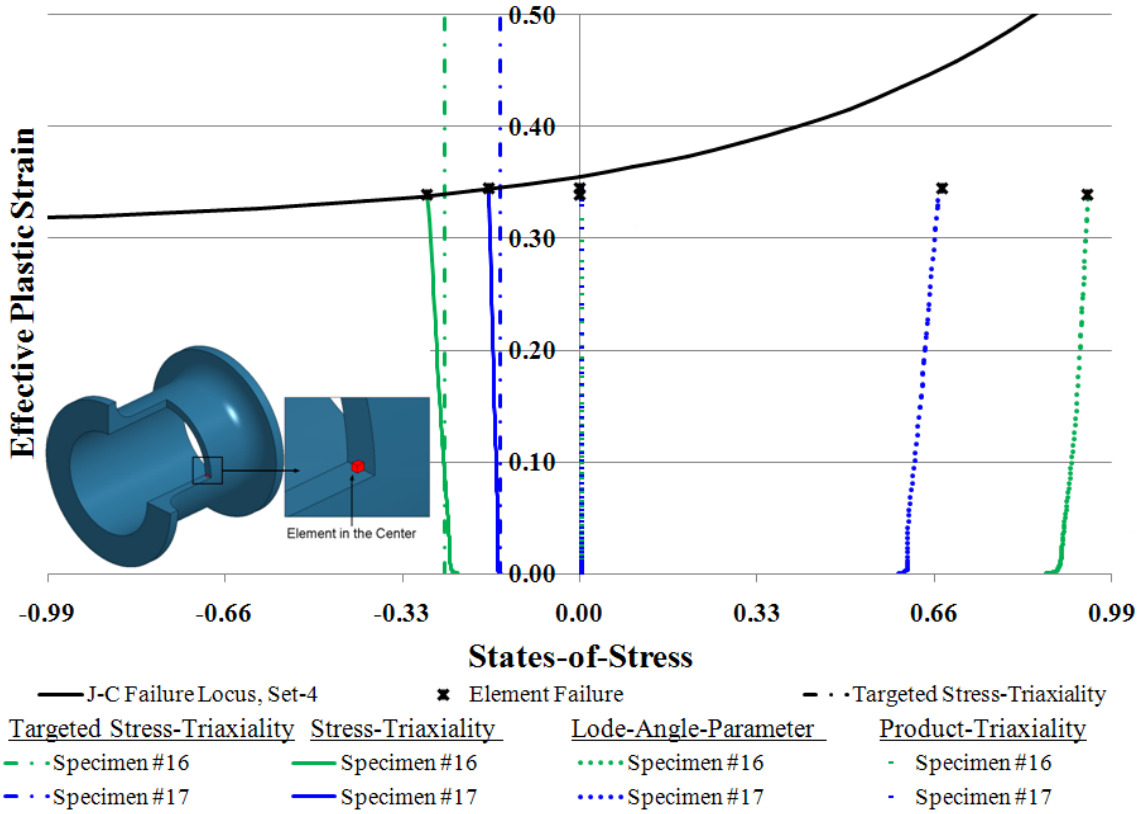

Figure 4-66: Comparison of the initially targeted and calculated states-of-stress for combined tension - shear specimens.

The states of interest for the punch test alternatives are illustrated as in Figure 4-68 on a Forming Limit Diagram (FLD), which is often used to predict formability and failure of sheet metals [216]. Depending on the area of interest, it can be justified that the Keeler tests are providing the most appropriate stress-states to the states observed during a ballistic impact since they cover a region between plane-stress and biaxial states. Lee, et al. has found that the stress-states during a punch test with hemispherical nose shape using a servo-hydraulic load frame provides near biaxial stress-states, where stress-triaxiality values were found to be in between $-0.62 \leq \sigma^* \leq -0.58$ depending on the coefficient of friction for a given punch radii [217]. Therefore, it can be said that, the

state-of-stress, deformation and failure behavior are similar for both ballistic impact simulations performed in Chapter 3 and punch tests.

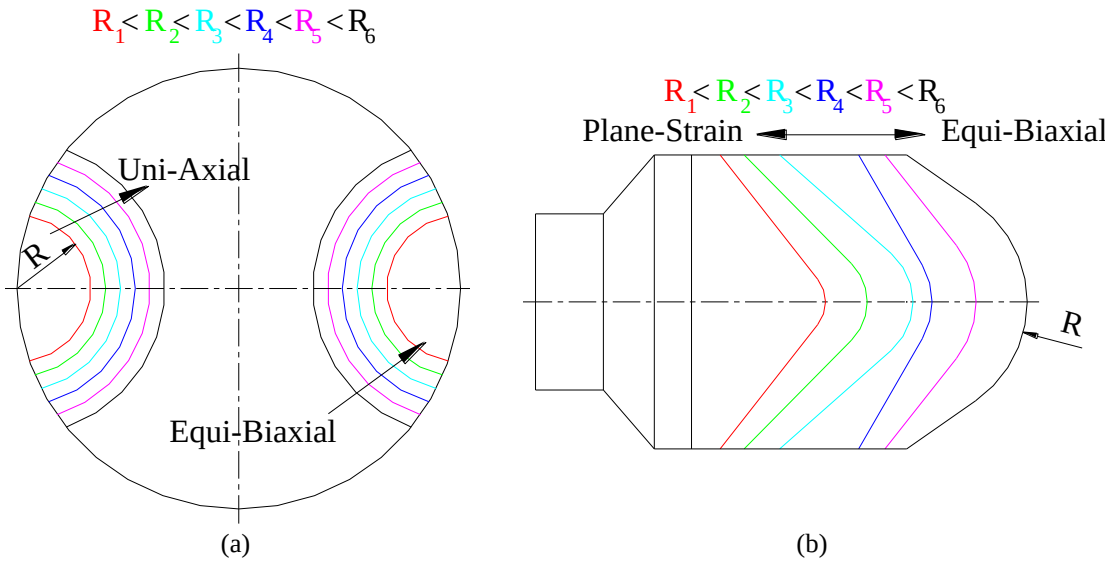

Figure 4-67: Punch test requirements for (a) Nakazima and Hasek test with different specimen geometries, (b) Keeler test with different punch radii, adapted after [216].

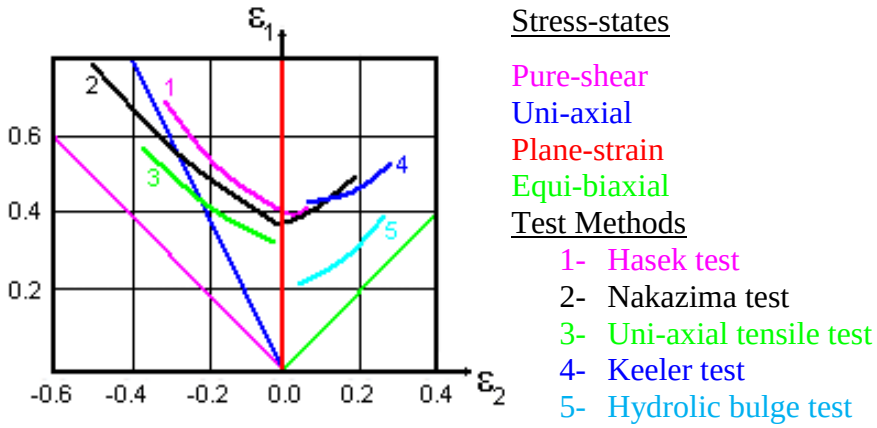

Figure 4-68: Characterization properties of different test methods and punch tests illustrated on a FLD, adapted after [216].

In addition to its convenience and accurate stress-state prediction capability, Keeler tests are also utilized for biaxial characterization because of their likelihood to provide insight into ballistic impact sensitivities such as nose shape effects. Borvik, et al. [14], experimentally observed the changes in the failure mode for Weldox460 E depending on

the nose shape geometry of the projectiles. Their results are illustrated in Figure 4-69 as shear, necking and petaling modes were reported for projectiles with different nose shapes.

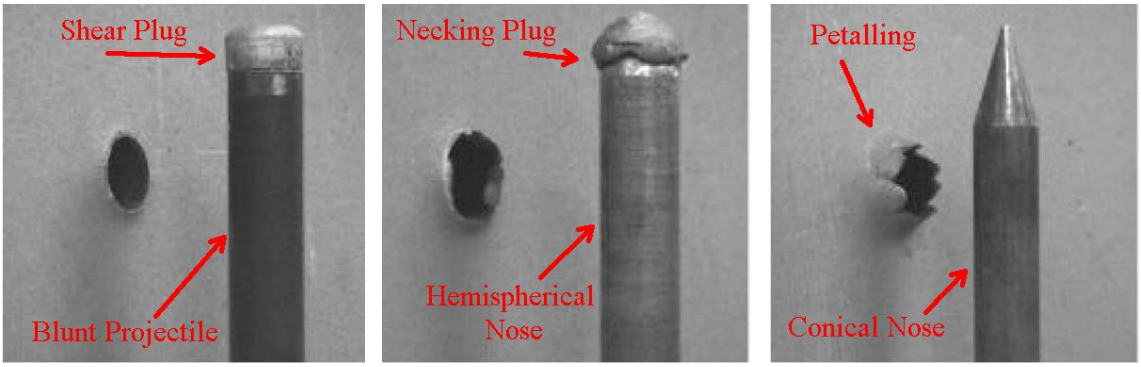

Figure 4-69: Effects of nose shape on the failure mode, adapted after [14].

Gupta, et al. [189] also experimentally investigated the role of nose shape on the impact performance evaluation of 1mm thick aluminum plates with hemispherical and blunt projectiles. Later on, they have extended their study by incorporating the effects of velocity and thickness [190]. Ben‐Dor, et al. provides the performance calculations for different nose shapes on different mediums [218]. Consequently, the effect of nose shape on the state-of-stress under the impact region and its contribution to the transition and change in the failure mode makes Keeler punch tests even more desirable.

Punch tests can also be used to predict adiabatic shear band formations and instabilities when adapted for dynamic characterization purposes and especially with a blunt nose shape. Roessig and Mason [219] have used a Split Hopkinson Bar (SHB) apparatus to test adiabatic shear localization of 1018 steel, 6061-T6 aluminum, and Ti-6Al-4V with a blunt punch. Rusinek, et al. [74] used a modified Hopkinson bar setup to study the effects of hemispherical projectile impact on mild steel and identified the change in the failure mode with the increase in impact speed. They have observed radial necking and petalling depending also on the lubrication used during the experiments as a contributing factor on the failure modes. Martinez, et al. [75] studied the AISI 304 steel under impact loading for perforation behavior assessment by a projectile with different nose shapes impacting at different speeds. Similarly, Seidt [108] implemented Keeler

punch geometries to a Split Hopkinson Pressure Bar (SHPB) apparatus and performed both low and high speed experiments on a more controlled environment, where force and displacement data was available to better understand the impact behavior through inverse FE simulations for characterization purposes [108]. Walters has used static and dynamic Hasek tests to characterize the Lode angle dependency on failure of Advanced High Strength Steels (AHSS) [220]. Dabboussi and Nemes [221] have performed quasi-static and dynamic SHPB shear punch experiments on 6061-T6, Ti-6Al-4V and austenitic, nitrogen-strengthened, stainless steel (Nitronic 33); characterized material properties through low speed tests for FE analysis and quantified the material ductility with high speed tests. Roessig and Mason [222] have continued their research with a numerical study on the shear instabilities during punch tests for three different materials. Li, et al. [223] also studied the shear dominant failure characteristics of Advanced High Strength Steels (AHSS) experimentally and numerically with square and circular punches for metal forming applications.

As a result, two punch tests with Keeler geometries are iteratively found, where a thin, cylindrical target (i.e., blank) is stamped by punches with two different nose shapes. As illustrated by Figures 4-67 and 4-68, a punch with a smaller nose radius leads to plane-strain state, where a bigger nose radius approaches to biaxial tension state.

Due to the considerations about bridging the notable stress-states, the first punch geometry that is represented in Figure 4-70(a) is designed to establish a link with Specimens # 4, #8 and #11 over the stress-triaxiality value of $\sigma^* = -\frac{1}{\sqrt{3}}$ respresenting a plane-strain stress-state, where a Lode-angle-parameter on the axi-symmetric compression meridian (i.e., $\theta_L = -1$) is aimed. The stress-state for this specimen is calculated from a finite element at the back side of the blank specimen as illustrated in Figure 4-70(b), where the failure initiates first. It should be noted that the failure initiation is observed for a ring of finite elements around the symmetry axis.

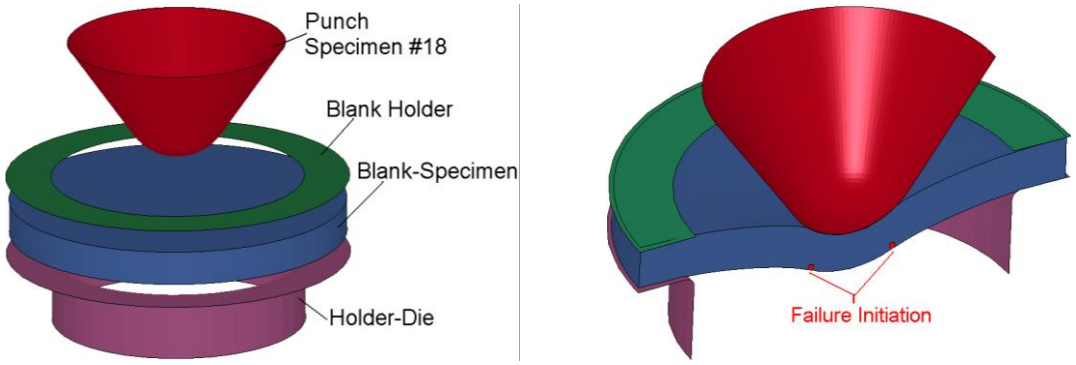

(a) (b)

Figure 4-70: (a) Test assembly for punch Specimen #18 and (b) location of the failure initiation point, where the state-of-stress is calculated for specimen design.

The second punch geometry that is represented in Figure 4-71(a) with a hemispherical nose shape is designed to establish a link with Specimens #9 and #12 over the stress-triaxiality value of $\sigma^* = -\frac{2}{3}$ respresenting a biaxial stress-state, where a Lode-angle-parameter on the axi-symmetric compression meridian (i.e., $\theta_L = -1$) is aimed. The stress-state for this specimen is also calculated from a finite element at the back side of the blank specimen as illustrated in Figure 4-71(b), where the failure initiates first. It should be noted that the failure initiation is observed for a ring of finite elements that are stretched around the symmetry axis.



(a) (b)

Figure 4-71: (a) Test assembly for punch Specimen #19 and (b) location of the failure initiation point, where the state-of-stress is calculated for specimen design.

The third punch geometry that is represented in Figure 4-72(a) has a blunt nose shape and designed to establish an overlapping stress-state with the pure shear (i.e., $\sigma^*, \sigma_p^*, \theta_L = 0$) specimen, which is described in Section 4.4.4.5 (i.e., Specimen #15). The failure initiates under the tip of the punch specimen as illustrated in Figure 4-72(b) and occur in the form of a shear band through the thickness. The details of the targeted stress-states and corresponding shapes of the punch test specimens are listed in Table 4-10.

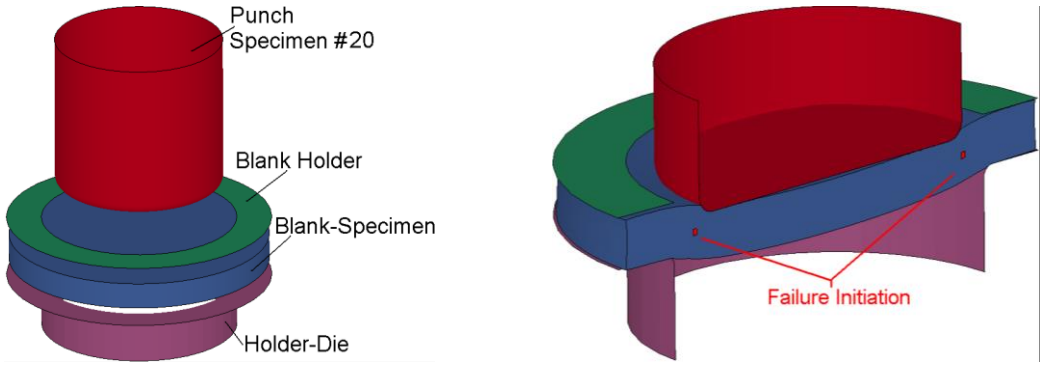

(a) (b)

Figure 4-72: (a) Test assembly for punch Specimen #20 and (b) location of the failure initiation point, where the state-of-stress is calculated for specimen design.

Table 4-10: Punch test specimens and test assembly with stress-state design parameters.

Specimen #	Specimen Geometry/FE Model	Initially Targeted Stress-State Values		
		σ^*	σ_p^*	θ_L
18	Specimen #18 Punch Figure B-16	-0.577	0.0741	-1.0
19	Specimen #19 Punch Figure B-17	-0.666	0.0	-1.0
20	Specimen #20 Punch Figure B-18	0.0	0.0	0.0

* Detailed geometry and corresponding FE model of the specimen is illustrated in Appendix-B

Figure 4-73 illustrates the calculated stress-states for the corresponding elements per each punch test specimen. It should be noted that Set-4 of the J-C material model parameters are utilized for the initial specimen calculations and J-C failure locus is plotted to illustrate the failure points as a function of stress-triaxiality and effective plastic strain. During the simulation of the punch test specimens, contact impact algorithms are defined between the punch, blank-holder, die and the blank-specimen in order to transfer the load from the punch to the specimen geometry, which introduces additional complexity on the evolution of the states-of-stress. However, it is shown that initially targeted stress-states are achieved with a good agreement for the selected elements at the failure zone. Initially targeted stress-states for punch test specimens on the planes of stress-triaxiality vs. Lode angle parameter and stress-triaxiality vs. product-triaxiality are illustrated in Figure 4-74.

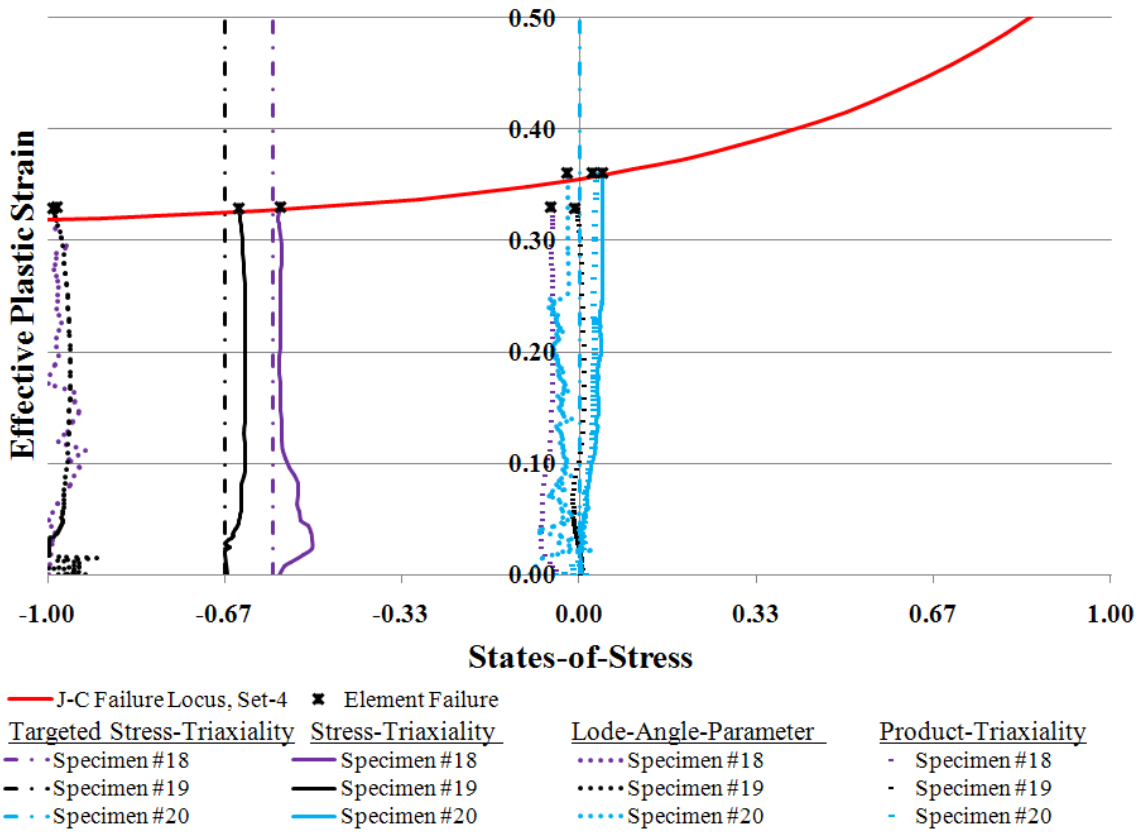

Figure 4-73: Comparison of the initially targeted and calculated states-of-stress for punch test specimens.

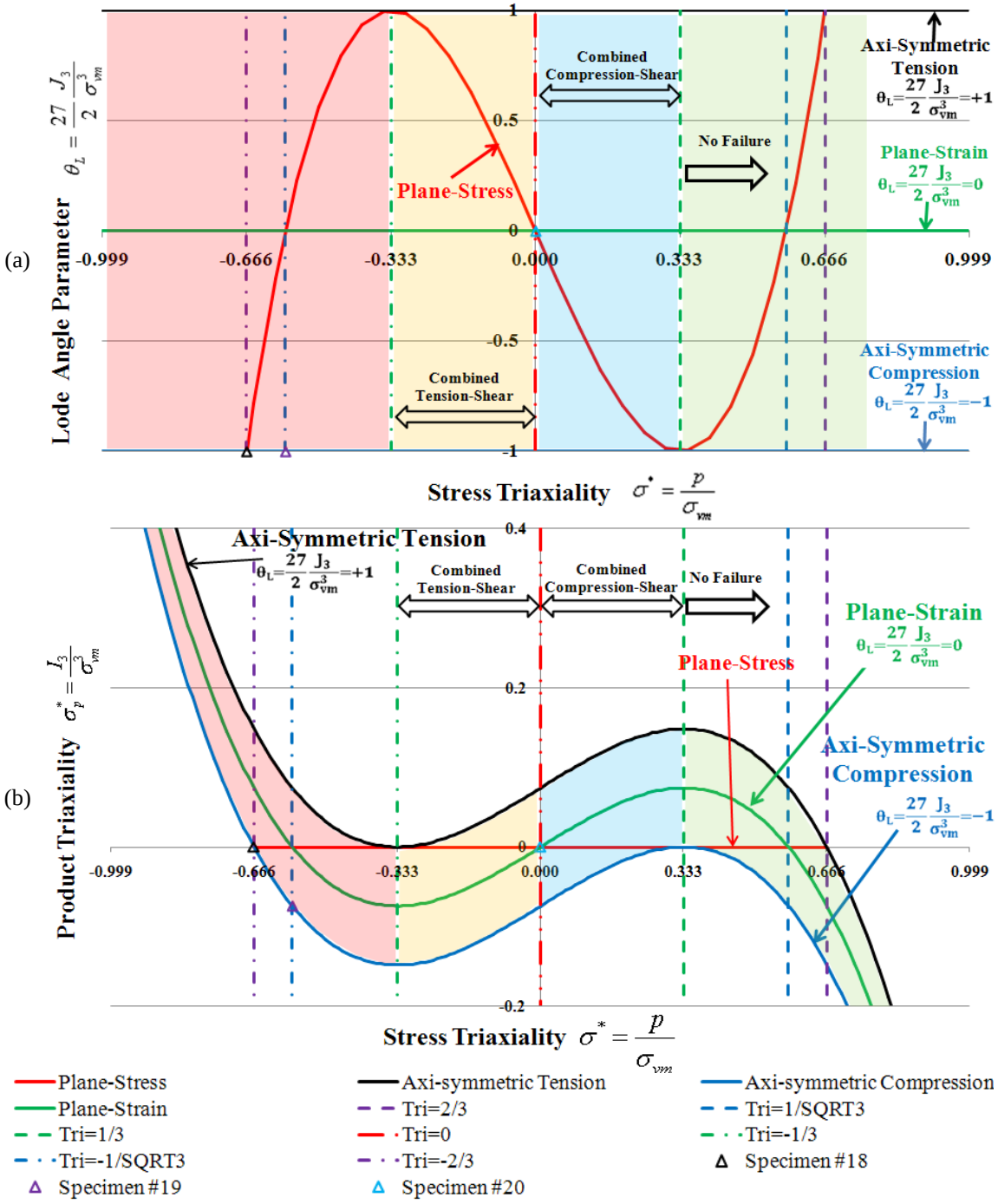

Figure 4-74: Determination of the targeted states-of-stress and the corresponding punch specimen geometries on the plane defined by; (a) stress-triaxiality vs. Lode-angle-parameter and (b) stress-triaxiality vs. product-triaxiality.

4.4.5 **Collection of specimens for the characterization of a failure locus depending on multiple states-of-stress**

To fill the failure locus illustrated by Figures 4-26 and 4-31 using the minimum number of test points, twenty specimens are designed with different shapes and loading conditions, which will lead to different states-of-stress. Table 4-11 summarizes all the design points with the corresponding stress-states. Technical drawings and FE models of the specimens are illustrated in Appendix-B and detailed information about the numerical models is provided in Chapter 5. Three points in this list coincide; they share the same stress-triaxiality and Lode-angle-parameter or product-triaxiality. The overlapping points will serve as a local verification to check whether the characterized failure strains are similar for different specimens that are sharing the same states-of-stress.

Initially targeted stress-states the specimens on the planes of stress-triaxiality vs. Lode angle parameter and stress-triaxiality vs. product-triaxiality are illustrated in Figure 4-75.

Table 4-11: Summary of specimens with initially targeted stress-state design parameters.

	θ_L				
σ^*	+1	+0.9145	+0.617	0.0	-1
+0.333					Specimen #14
0.0				Specimen #15 Specimen #20 Specimen #21	
-0.1466			Specimen #17		
-0.2505		Specimen #16			
-0.333	Specimen #1 Specimen #5				
-0.41	Specimen #6	Specimen #2			
-0.49	Specimen #7		Specimen #3		
-0.577	Specimen #8			Specimen #4 Specimen #11	Specimen #18
-0.666	Specimen #9			Specimen #12	Specimen #19
-0.8	Specimen #10			Specimen #13	

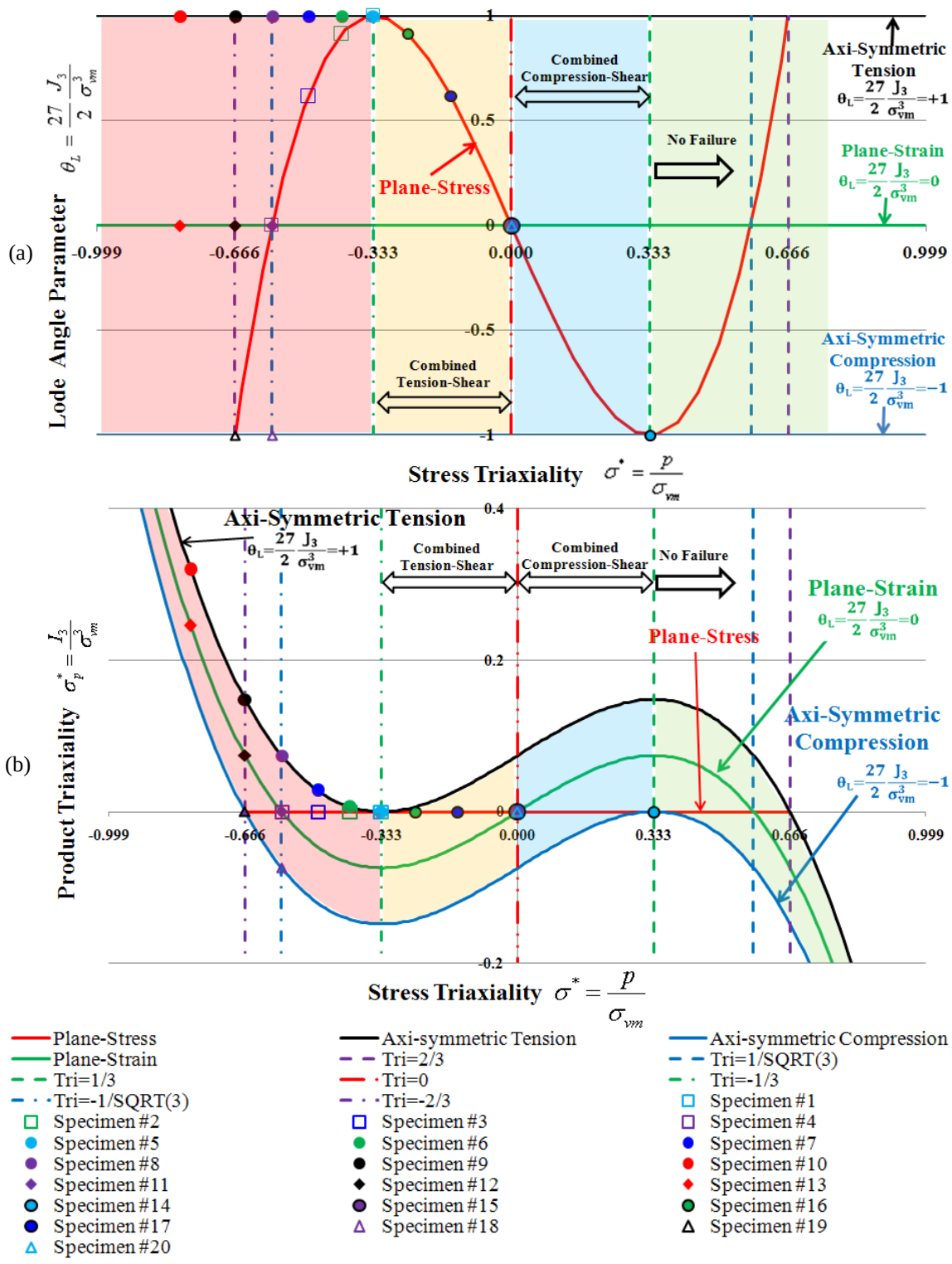

Figure 4-75: Overview of the test program and initially targeted states-of-stress for each specimen on the plane defined by; (a) stress-triaxiality vs. Lode-angle-parameter and (b) stress-triaxiality vs. product-triaxiality.

4.5 **Single element verification analysis for the new material model**

Single element FE models are used to test the stability, accuracy and robustness of TRAUM against J-C material model. Moreover, the tabulated input form of the new model for flow and failure surfaces is introduced. In the first part of this section, the new material model is reduced to behave similar to J-C material model having no dependency on the Lode-angle-parameter and no sensitivity on the element size to failure. The section proceeds with additional single element verification tests by incorporating stress-states that has Lode-angle-parameter and element size dependency showing that significant improvement can be achieved by using TRAUM.

4.5.1 **Single element analysis and verification of TRAUM with J-C material model for loading path dependency considering different values of stress-triaxiality**

4.5.1.1 Benchmark-problem definition

Fully integrated, hexahedral finite elements with equal lengths are used for the analysis at multiple values of the stress-triaxiality. Uni-axial tension cases are selected for the first benchmark as illustrated in Figure 4-76 with different boundary conditions. A displacement boundary condition, which provides a constant velocity as shown in Figure 4-77, is defined for the nodes on the top surface of the finite elements.

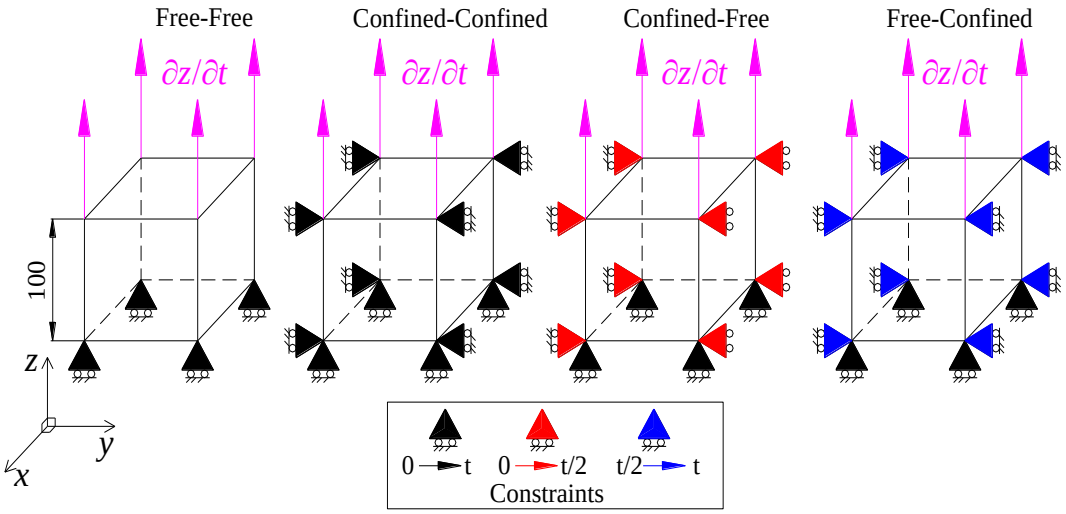

Figure 4-76: Single element models with the boundary conditions representing proportional and non-proportional loading conditions.

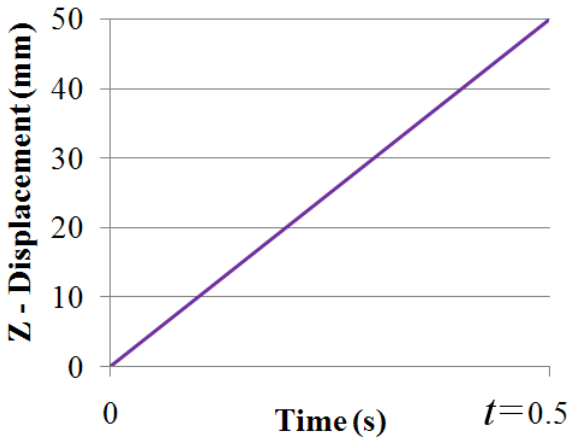

Figure 4-77: Applied displacement on the single finite element models.

According to the loading conditions, a free uni-axial tension (i.e., Free-Free) case represents a uni-axial state in tension, where there is no lateral confinement on the nodes. A confined uni-axial tension (i.e., Confined-Confined) case represents a plane-strain stress-state in tension, where the nodes of the element are constrained in the lateral direction and cannot move when pulled by enforcing a displacement field as illustrated in Figures 4-76 and 4-77. The loading and boundary conditions do not change for the first two elements during the entire simulation.

In order to test the path dependent failure accumulation, non-proportional loading conditions are utilized by introducing a jump condition for the subsequent cases (i.e., Confined-Free and Free-Confined), where the boundary conditions are switched in the middle of the simulation (i.e., t = t/2 or t = 0.25s). The first jump condition is attained by releasing the lateral constraints on the nodes of the element when t = t/2. The second jump condition is attained by constraining the nodes of the finite element laterally when t = t/2, which were free in the beginning of the simulation.

The evolution of the stress-states for each single element are listed in Table 4-12 and illustrated in Figure 4-78 on the planes of stress-triaxiality vs. Lode angle parameter and stress-triaxiality vs. product-triaxiality, respectively. In this figure, the effects of the jump conditions are also illustrated by corresponding arrows defining the path of the stress-states that are changing with the boundary conditions.

Table 4-12: Evolution of the corresponding states-of-stress for different loading conditions.

Loading Conditions	Evolution of the Stress-State Values					
	σ^*		σ_p^*		θ_L	
	$t=0\rightarrow\frac{t}{2}$	$t=\frac{t}{2}\rightarrow t$	$t=0\rightarrow\frac{t}{2}$	$t=\frac{t}{2}\rightarrow t$	$t=0\rightarrow\frac{t}{2}$	$t=\frac{t}{2}\rightarrow t$
Free-Free	-0.333	-0.333	0.0	0.0	+1.0	+1.0
Confined-Confined	-0.577	-0.577	0.0	0.0	0.0	0.0
Confined-Free	-0.577	-0.333	0.0	0.0	0.0	+1.0
Free-Confined	-0.333	-0.577	0.0	0.0	+1.0	0.0

Single element benchmark tests are performed by utilizing Set-4 of the J-C material model parameters that are listed in Table 4-13 [58]. The flow surface for J-C is defined by Equation (4.65) incorporating the coefficients from Table 4-13. The illustration of the flow surface for J-C is shown in Figures 3-6(b) and Figures 3-6(d) for strain-rate dependent hardening surface at room temperature (i.e., 294K) and temperature dependent softening surface at a nominal strain rate of $1.0s^{-1}$.

$$\sigma_y = \left(A + B\left(\varepsilon_p\right)^n\right)(1 + C\ln\dot{\varepsilon}^*)(1 - T^{*m}) \tag{4.65}$$

Table 4-13: J-C material model input data used for single element simulations [58].

Material Characteristics			Strength Parameters				
Density [kg/m^3]	Poisson Ratio	Modulus of Elasticity [MPa]	Static Yield Limit [MPa]	Strain Hardening Modulus [MPa]	Strain Hardening Exponent	Strain Rate Coefficient	Thermal Softening Exponent
ρ	ν	E	A	B	n	C	m
2770	0.33	73084	369	684	0.73	0.0083	1.7
Reference Temp. [K]	Melting Temp. [K]	Specific Heat [J/kg-K]	Failure Parameters				
T_{room}	T_{melt}	C_p	D_1	D_2	D_3	D_4	D_5
294	775	875	0.31	0.045	1.7	0.005	0.0

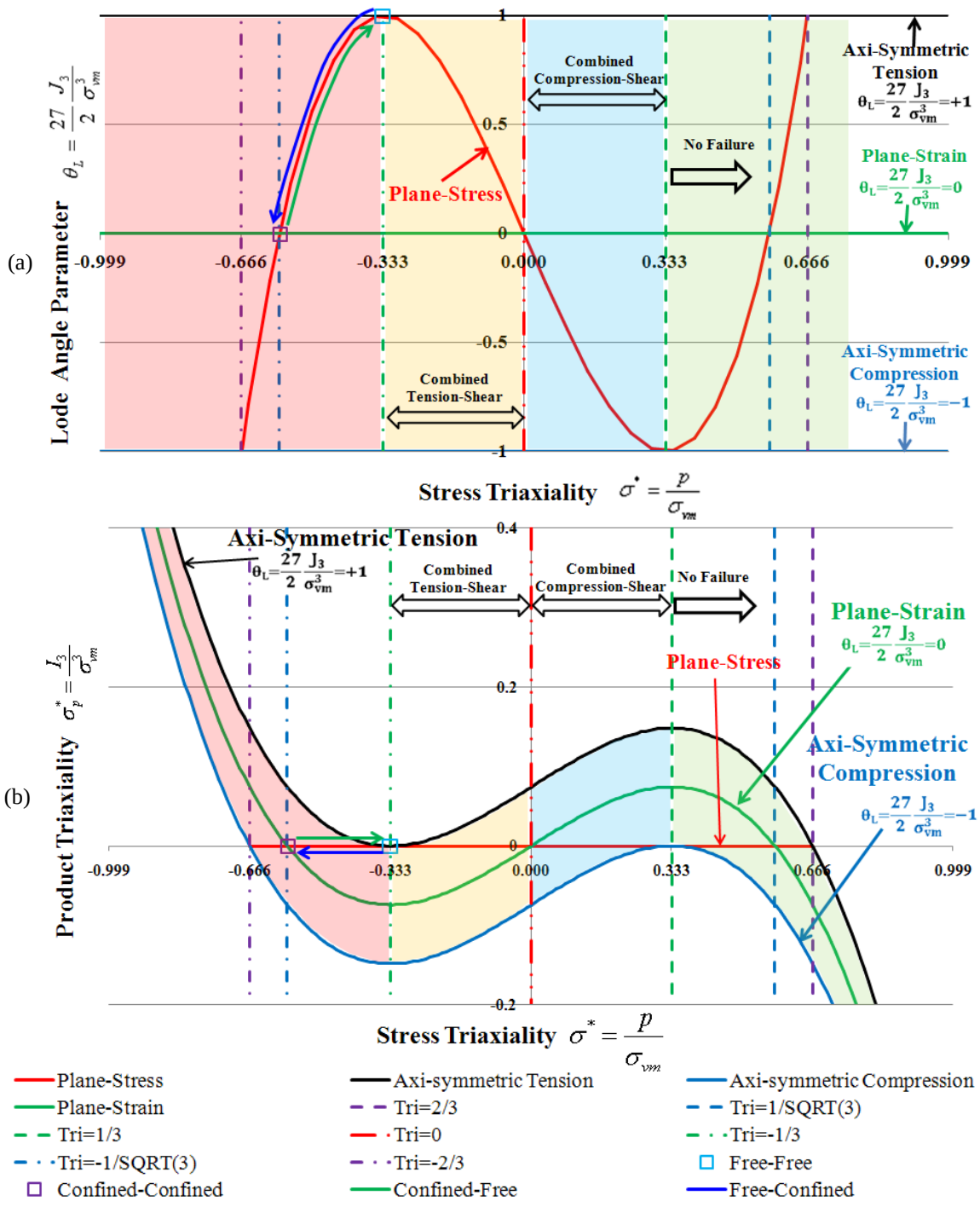

Figure 4-78: States-of-stress for each finite element on the plane defined by; (a) stress-triaxiality vs. Lode-angle-parameter and (b) stress-triaxiality vs. product-triaxiality.

TRAUM utilizes an explicitly defined tabulated form of the flow surface as an input by using a multiplicative decomposition that is formulated by Equation (4.66).

Isothermal hardening curves $k1(\varepsilon_p, \dot{\varepsilon}_p)$ at room temperature and temperature dependent quasi-static hardening curves $kt(\varepsilon_p, T)$ at a nominal strain-rate are calculated from Equations (4.67) and (4.68) by incorporating the J-C parameters that are listed in Table 4-13. Figure 4-79(a) illustrates the J-C flow surface with the rate dependent isothermal hardening curves that are calculated by using Equation (4.67) in order to generate the tabulated input data for TRAUM as shown in Figure 4-79(b).

$$\sigma_y = k1(\varepsilon_p, \dot{\varepsilon}_p) kt(\varepsilon_p, T) \tag{4.66}$$

$$\begin{aligned} T^* &= \frac{T - T_{room}}{T_{melt} - T_{room}} \\ T &= 274\text{K} = T_{room} \\ \Rightarrow k1(\varepsilon_p, \dot{\varepsilon}_p) &= \left(A + B(\varepsilon_p)^n\right)(1 + C\ln\dot{\varepsilon}^*) \end{aligned} \tag{4.67}$$

$$\begin{aligned} \dot{\varepsilon}^* &= \frac{\dot{\varepsilon_p}}{\dot{\varepsilon}_0} \\ \dot{\varepsilon}_p &= 1.0\text{s}^{-1} \Rightarrow \dot{\varepsilon}^* = 1 \\ \Rightarrow\ kt(\varepsilon_p, T) &= \left(A + B(\varepsilon_p)^n\right)(1 - T^{*m}) \end{aligned} \tag{4.68}$$

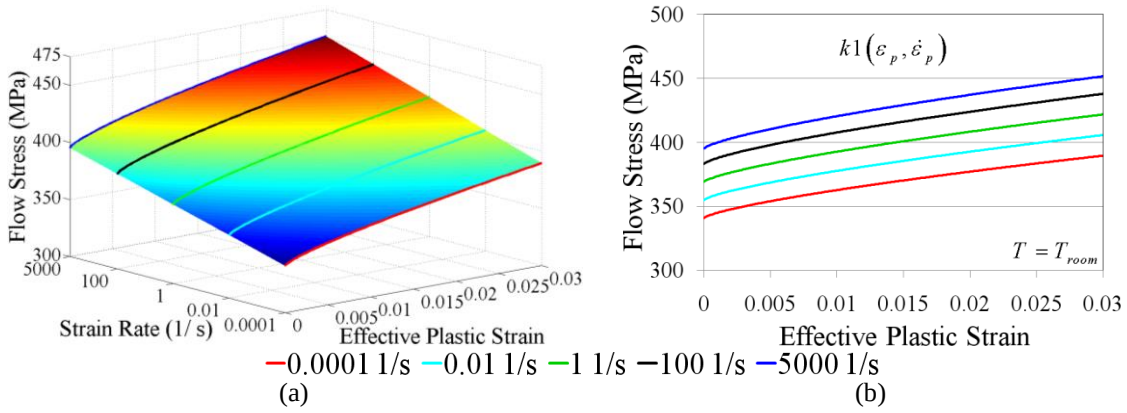

Figure 4-79: Stain-rate dependent flow surface at room temperature representing; (a) Set-4 of the J-C material model parameters and (b) tabulated format of the J-C flow surface for TRAUM.

Similarly, Figure 4-80(a) illustrates the J-C flow surface with the temperature dependent quasi-static hardening curves that are calculated by using Equation (4.68) in order to generate the tabulated input data for TRAUM as shown in Figure 4-80(b).

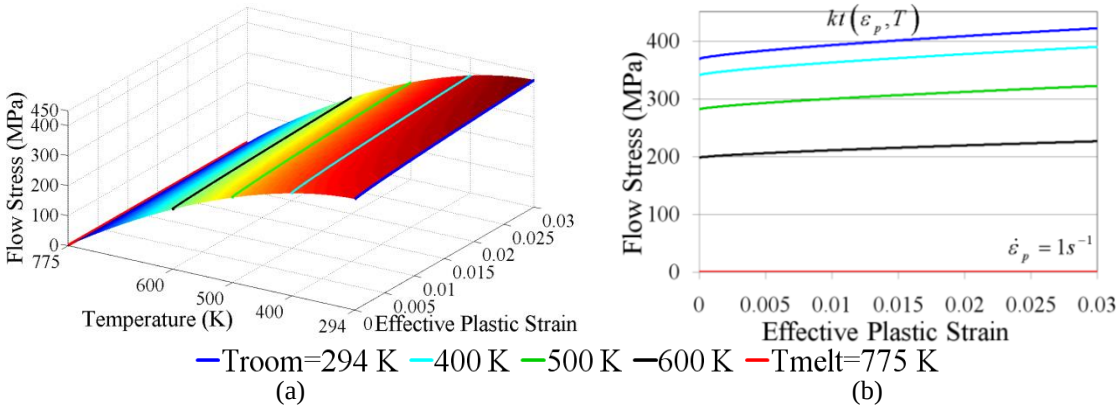

Figure 4-80: Temperature dependent flow surface at a nominal strain rate of 1.0s^{-1} representing; (a) Set-4 of the J-C material model parameters and (b) tabulated format of the J-C flow surface for TRAUM.

It should be noted that while representing the J-C flow surface in a tabulated format, only a small number of hardening curves are calculated for illustration purposes and additional input curves may be required based on the characteristics of the flow surface. Clearly, the number of hardening curves can be determined based on the availability of the strain-rate and temperature dependent experimental data during the characterization phase of a material.

The failure locus for J-C is defined by Equation (4.69) by incorporating the coefficients from Table 4-13. The illustration of the strain rate and temperature dependent failure loci for J-C is shown in Figures 3-10 and 3-11.

$$\varepsilon_p^f = [D_1 + D_2 \exp(D_3 \sigma^*)][1 + D_4 \ln \dot{\varepsilon}^*][1 + D_5 T^*] \tag{4.69}$$

TRAUM utilizes an explicitly defined tabulated form of the failure surface as an input by using a formulation as a function of state-of-stress $f(\sigma^*, \theta_L)$, strain rate $g(\dot{\varepsilon}_p)$, temperature $h(T)$ and regularized element length $i(l_{cr})$ that is defined by Equation (4.70).

$$\varepsilon_p^f = f(\sigma^*, \theta_L) g(\dot{\varepsilon}_p) h(T) i(l_{cr}) \tag{4.70}$$

Since J-C does not take the Lode-angle-parameter or the product-triaxiality into account, TRAUM tabulated failure surface format can be reduced by only calculating the stress-triaxiality dependent failure locus using Equation (4.71) for a nominal strain-rate at room temperature as illustrated in Figure 4-81(a). It should be noted that the equivalent plastic strain at failure is described by a tabulated nature as a function of stress-triaxiality and Lode-angle-parameter to construct the failure surface for TRAUM as illustrated in Figure 4-81(b). Therefore, the same failure locus can be used for all values of the Lode-angle-parameter. Similar to the representation of the flow surface, only a small number of curves are used for illustration purposes when the failure surface for TRAUM is constructed. Clearly, the number and complexity of the tabulated failure loci can be determined depending on the experimental program.

$$\begin{aligned} &\dot{\varepsilon}_p = 1.0\text{s}^{-1}, T = T_{room},\ \theta_L = \text{constant} \\ &f(\sigma^*, \theta_L) = [D_1 + D_2 \exp(D_3 \sigma^*)] \end{aligned} \tag{4.71}$$

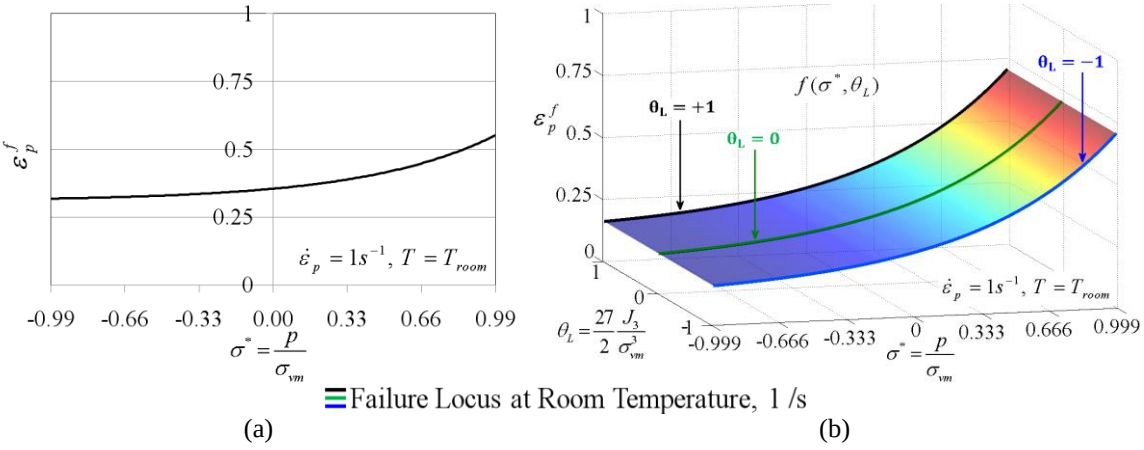

Figure 4-81: Failure surface at room temperature and a nominal strain rate of 1.0s^{-1} representing; (a) tabulated format of the J-C failure locus for TRAUM and (b) TRAUM's three dimensional representation for Set-4 of the J-C material model parameters.

The failure locus is scaled by utilizing strain-rate and temperature dependent factors (i.e., curves) that are generated for a baseline at a nominal strain rate of $1.0s^{-1}$ and room temperature as previously illustrated by Figures 3-10 and 3-11 for J-C and 4-28 and 4-30 for TRAUM. Scaling curves can be calculated by using Equation (4.72) with the corresponding parameters from Table 4-13. Figure 4-82(a) illustrates the strain-rate dependent scaling curve and assumes a positive effect on the failure strain with the increasing strain-rates. Figure 4-82(b) illustrates the temperature dependent scaling curve, which has no effect on the failure strain as $D_5 = 0$ for J-C Set-4 [58].

$$g(\dot{\varepsilon}_p) = [1 + D_4 \ln\dot{\varepsilon}^*]$$
$$h(T) = [1 + D_5 T^*] \tag{4.72}$$

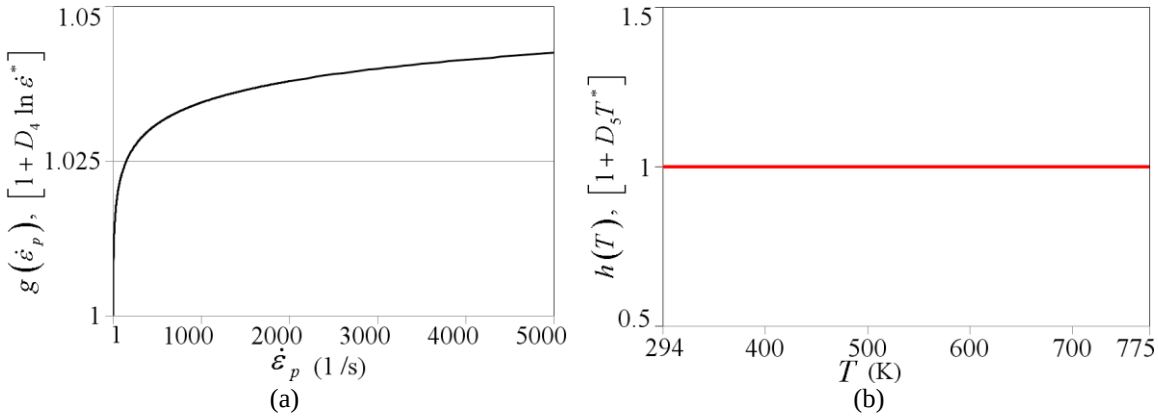

Figure 4-82: Scaling factors for TRAUM offsetting the failure locus with; (a) strain-rate dependent scaling curve normalized for a nominal-strain rate of $1.0s^{-1}$ (b) temperature dependent scaling curve normalized for room temperature.

TRAUM utilizes a mesh regularization factor to scale the failure locus based on the targeted displacements for finite elements with different edge lengths as described in Section 4.4.3.3 and illustrated by Figure 4-45. However, J-C model does not consider the effects of mesh size on failure. Therefore, a scaling factor of unity is utilized for the regularization term $i(l_{cr})$ in the TRAUM failure surface definition as illustrated in Figure 4-83.

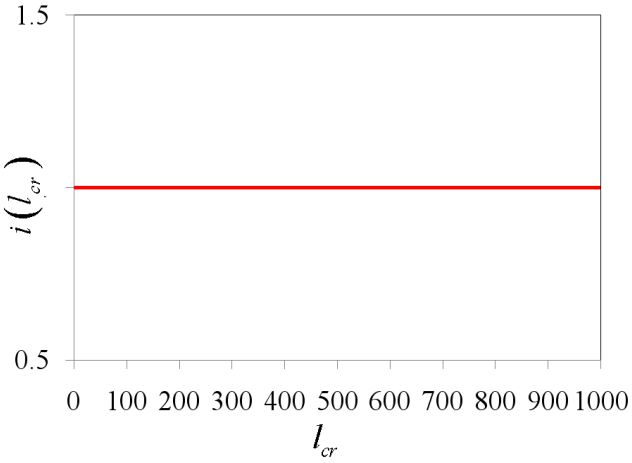

Figure 4-83: Scaling factor for TRAUM offsetting the failure locus with element size dependent scaling curve.

4.5.1.2 Benchmark-problem results

Single element benchmark models are simulated with the single finite elements and boundary conditions described in Figure 4-76 and with the loading condition in Figure 4-77. TRAUM input data is generated by reducing some of the features to represent the Set-4 of the J-C material model parameters. J-C and TRAUM responses are compared to show that the reduced TRAUM features are fully capable of finding identical results.

The amount of displacements are calculated and compared in Figure 4-84 with the corresponding TRAUM input data. It is found that the J-C and TRAUM displacements and failure predictions for the finite elements are identical for all boundary conditions. Based on the characteristics of the failure locus that is illustrated in Figure 4-81(a), it is shown that the plane-strain stress-state, which is represented with 'Confined-Confined' boundary conditions fails first and the uni-axial stress state that is represented with 'Free-Free' boundary conditions fails the last. That can be explained by the fact that the required effective plastic strain to failure monotonically increases towards the positive values of the stress-triaxiality, where a bigger failure strain is required at the uni-axial stress-state for the finite element to fail compared to a plane-strain stress-state.

It is also shown that two elements with non-proportional boundary conditions fail in between the proportional cases, where the element that starts with a plane-strain stress-state (i.e., 'Confined-Free' boundary condition) fails before the element that starts with a

uni-axial stress-state (i.e., 'Free-Confined' boundary condition). Figure 4-84 illustrates the displacement path after the jump condition, where the corresponding nodes of the element are either confined or released as shown in Figure 4-76.

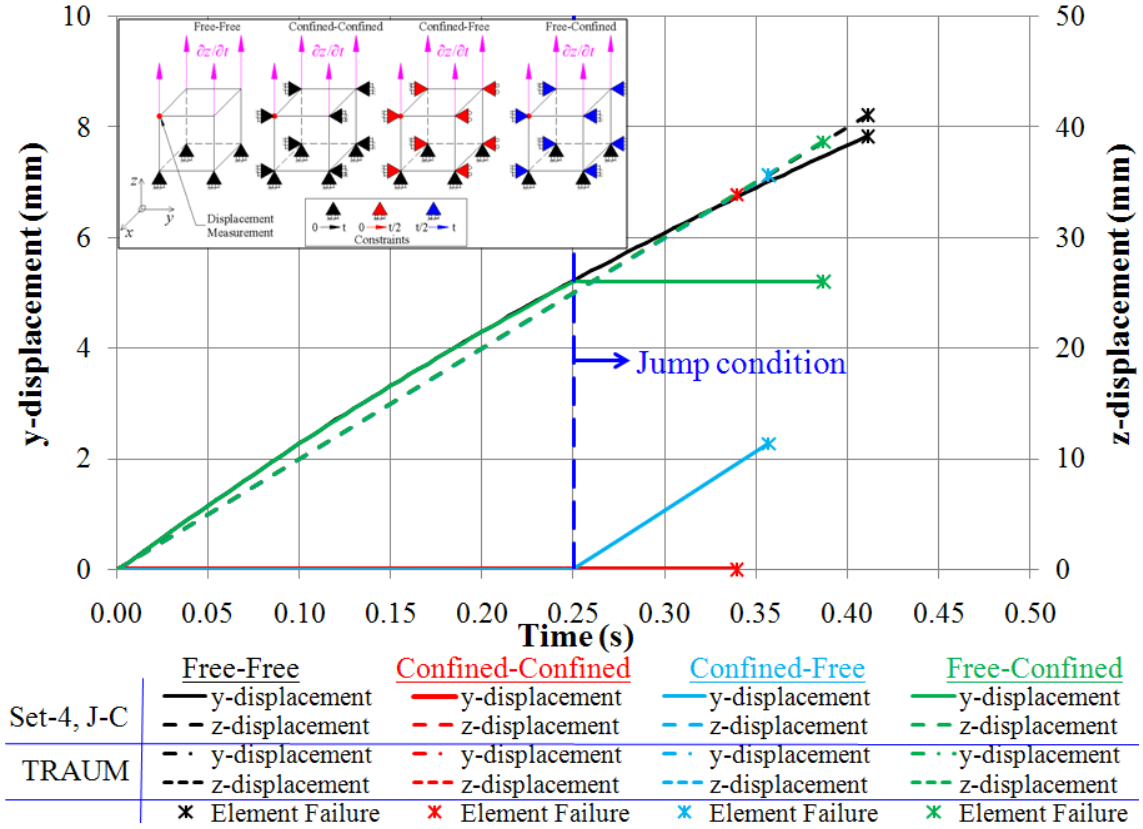

Figure 4-84: Comparison of the displacements for different boundary conditions on single elements.

The verification of load path dependence is shown with the evolution of the effective plastic strain at failure as a function of stress-triaxiality in Figure 4-85 with the jump conditions, where it should be noted that identical results are obtained for J-C and TRAUM. The results verify that the targeted stress-states which are illustrated in Figure 4-78 for single elements are achieved including the cases with the jump condition. It should also be noted that the jump conditions are defined at the same time for each non-proportional loading cases. However, it is shown that the plastic strain evolves more rapidly for plane-strain stress-state that accumulates a higher plastic strain compared to a uni-axial stress-state.

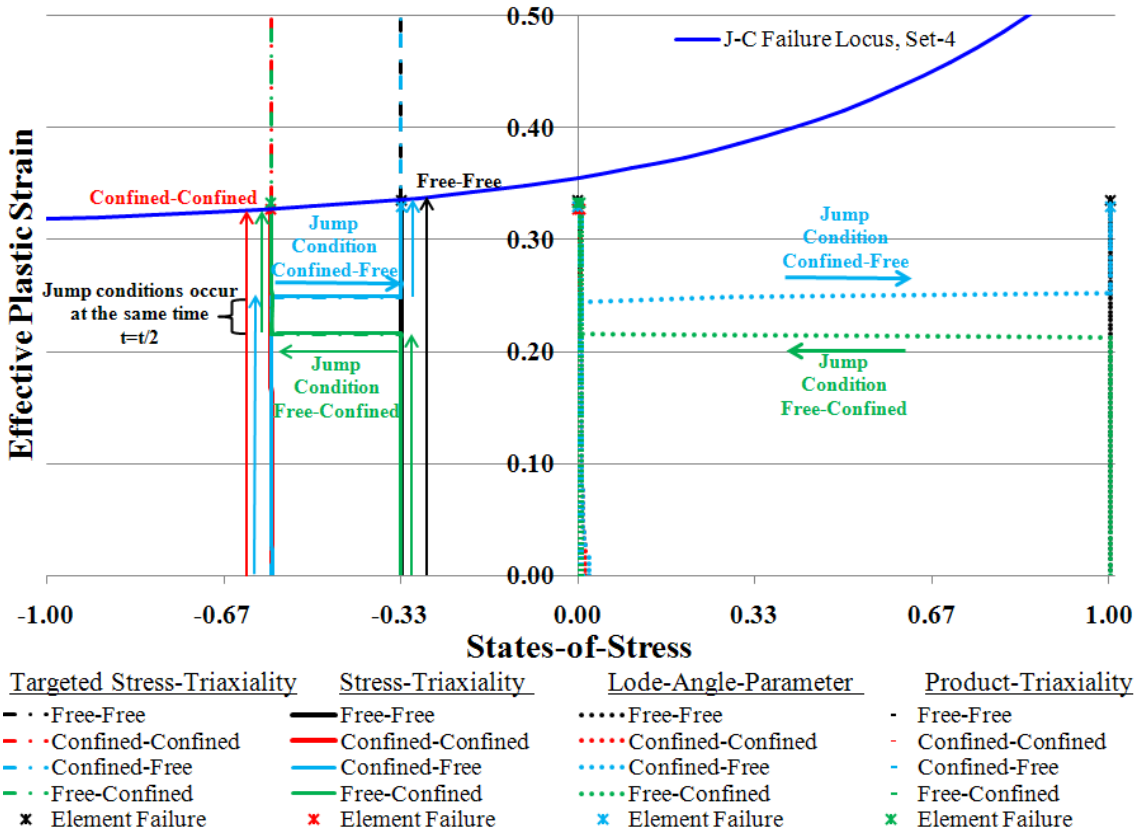

Figure 4-85: Evolution of the effective plastic strain to failure paths as a function of stress-triaxiality for proportional and non-proportional loading indicating identical J-C and TRAUM results.

Effective stress and effective plastic strain histories of the elements with different boundary conditions are compared in Figure 4-86 to identify the path dependency of the response. Continuous lines represent the effective stress versus displacement and the dotted lines represent the effective plastic strain versus displacement for different boundary conditions. The effects of the jump condition can clearly be seen as the response of the finite elements change when the boundary conditions are switched (i.e., t = t/2). Two non-proportional cases fail at different failure strains due to differences in the loading history and path dependency of the failure accumulation. The elements with plan-strain stress-state in the beginning reach higher stresses and accumulate plastic strain more rapidly compared to the elements with uni-axial stress-state.

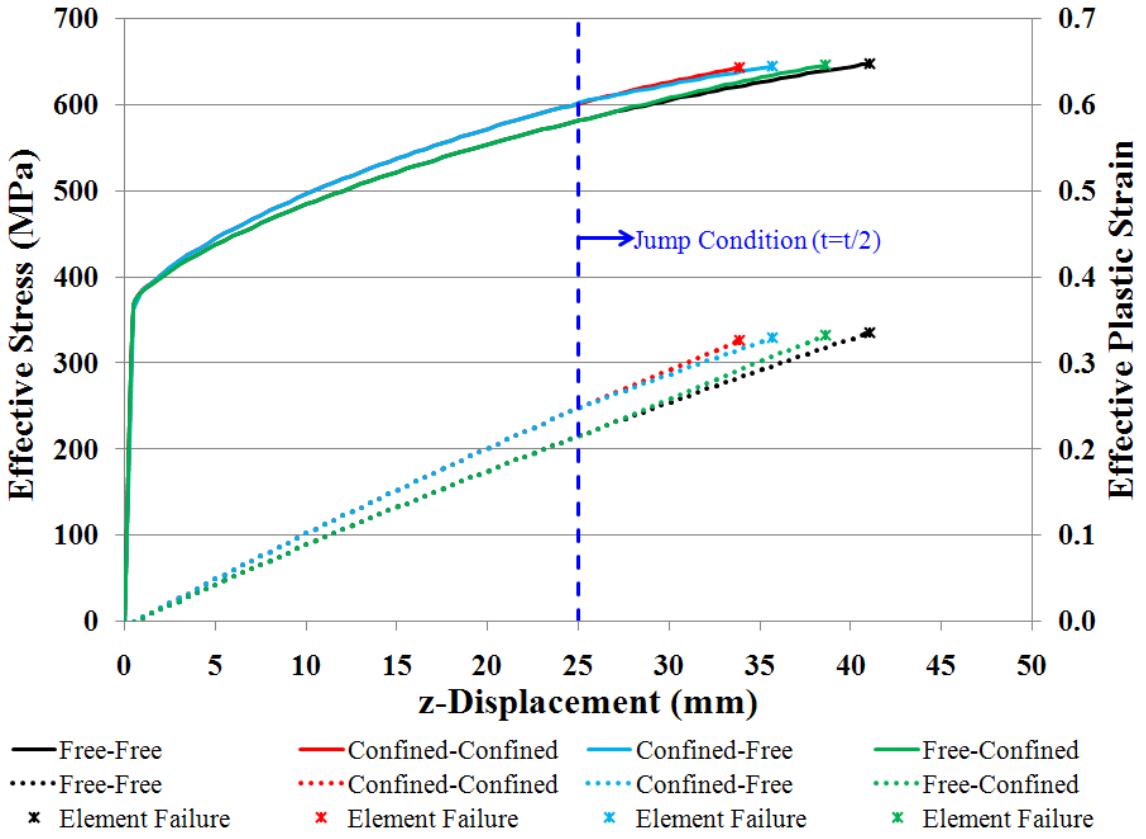

Figure 4-86: Comparison of effective stress and effective plastic strain response for different boundary conditions.

Identical results are obtained for the stress-strain response for J-C and TRAUM as illustrated In Figure 4-87. Therefore, it is concluded that TRAUM can accurately predict failure accumulation depending on the path dependent loading history. It should be noted that TRAUM utilizes a tabulated input for the flow and failure surfaces, which are defined by several number of piecewise linear curves as illustrated in Figures 4-79 and 4-80. The number of curves is often determined by the available experimental data and it is expected that more accuracy can be achieved if more curves are used to define the surfaces.

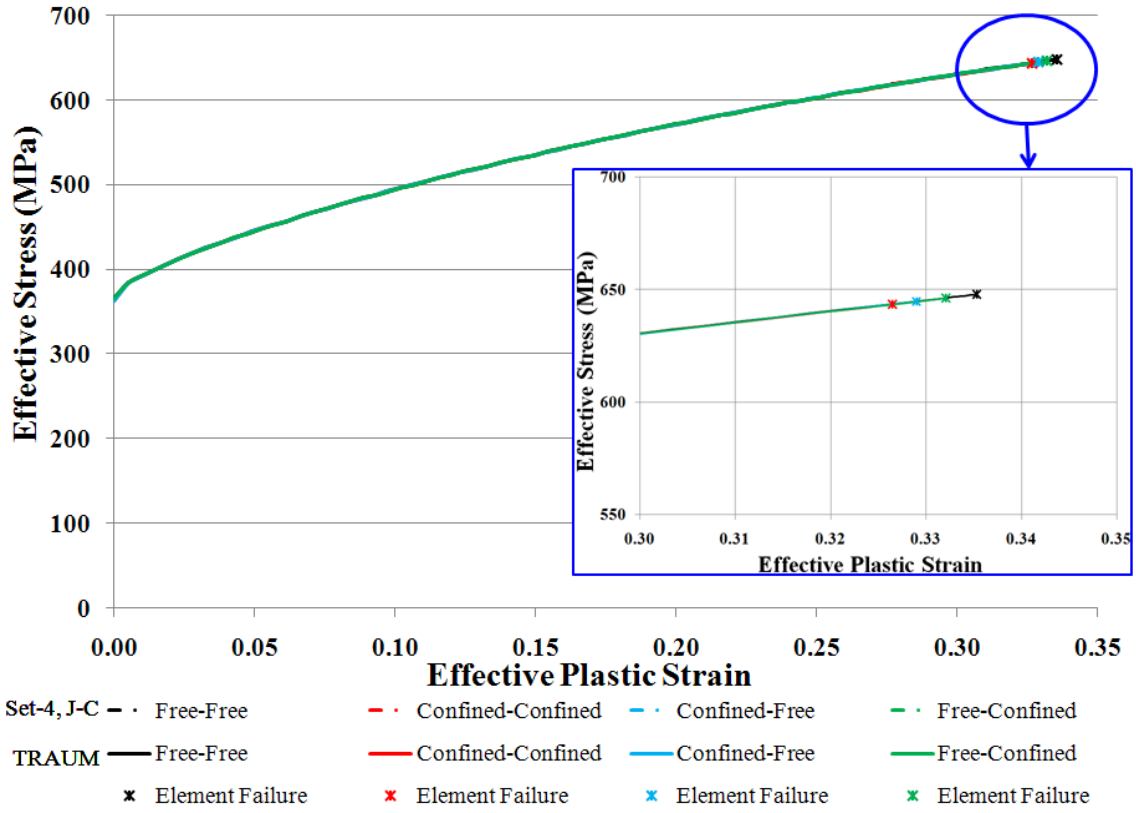

Figure 4-87: Comparison of the stress-strain response for J-C and TRAUM with different boundary conditions.

4.5.2 **Single element analysis and verification of TRAUM with J-C material model for mesh size dependency on the prediction of failure**

4.5.2.1 Benchmark-problem definition

In order to show the uni-directional effects of regularization, fully integrated, hexahedral finite elements with different lengths are used for the analysis as illustrated in Figure 4-88. Initially, the effect of element size on the failure prediction is demonstrated by illustrating the results from a mesh size dependent material model, where J-C is employed for the analysis. During an experiment, force versus displacement response of a material is often the property that is directly measurable. Therefore, independent of the mesh size, it is required to achieve the same amount of overall displacement before failure when simulating the material. It is shown with this problem that by using TRAUM, single finite elements can reach to the same elongation before failure.

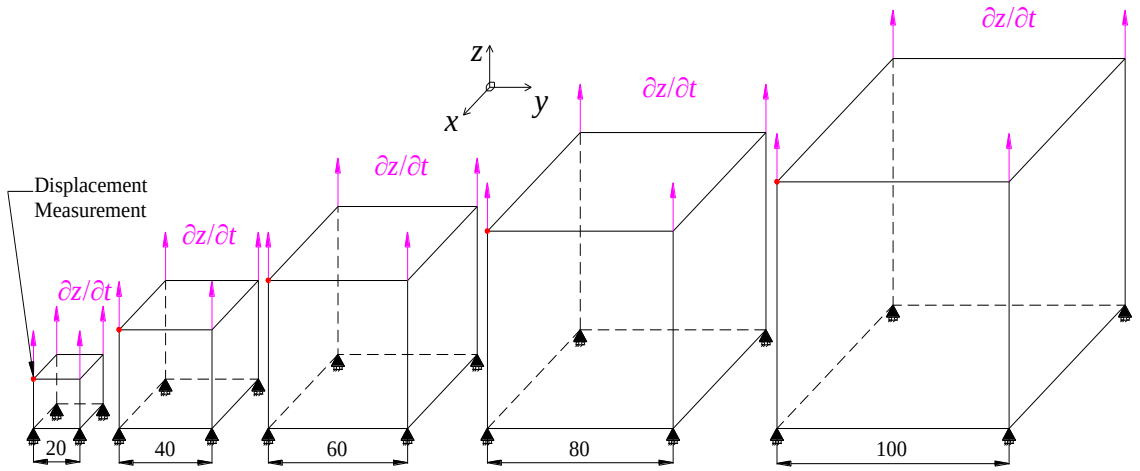

Figure 4-88: Single element models for regularization.

A uni-axial stress-state is chosen for the analysis that gives a stress-state of $\left(\sigma^*, \sigma_p^*, \theta_L\right) = \left(-\frac{1}{3}, 0, -1\right)$. The same displacement boundary condition, which provides a constant velocity as shown in Figure 4-77, is applied for the nodes on the top surface of the finite elements. Other nodes are constrained during the analysis.

4.5.2.2 Benchmark-problem results

The accumulation of the effective plastic strain is illustrated in Figure 4-89 with respect to the overall displacement of the free nodes. It is shown that the failure strain is the same for all element lengths and therefore the failure initiates at different values of the total displacement when J-C material model is used. Consequently, it is often a common practice to generate different material model parameter sets for different mesh lengths. However, considering geometrical non-linearity and complex mesh patterns, it is not trivial to predict the required range of mesh size and corresponding material model data. Moreover, considering todays' large finite element models, associating the material input data that is prepared for specific element lengths with the corresponding mesh is not any easy task. Therefore, TRAUM suggests a scaling factor for the characterized values of the failure locus considering a critical element size to solve the mesh size dependency.

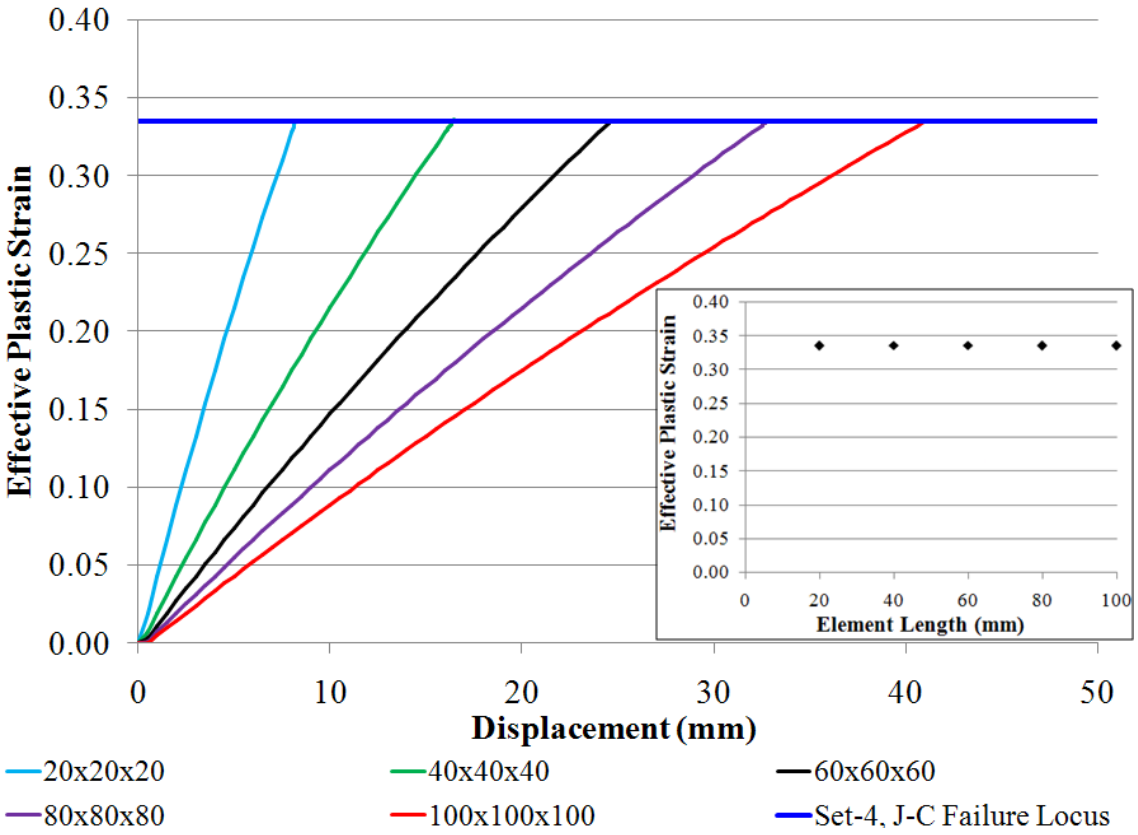

Figure 4-89: Evolution of the effective plastic strains to failure with different element lengths for J-C.

In order to benchmark the results with J-C, the same tabulated inputs are utilized for TRAUM, which are illustrated by Figures 4-79 - 4-82 to construct the flow and the failure surfaces. However, to activate the mesh regularization scheme that is described in Section 4.4.3.3, a mesh size dependent scaling curve for the effective plastic strain at failure needs to be generated replacing the input curve that is illustrated in Figure 4-83. TRAUM utilizes a scaling term $i(l_{cr})$ for the characterized values of the effective plastic strains at failure with respect to the element lengths that are considered for the simulation as illustrated in Figure 4-90. It should be noted that an element length of 20 mm is selected as a baseline for the analysis. It is shown that the implementation of the regularization term scales the values of the effective plastic strain at failure or offsets the failure locus depending on the element size. Therefore, each element reaches to the exact total displacement before failure initiates. Consequently, experimental results can be achieved with different element length once a regularization term is characterized.

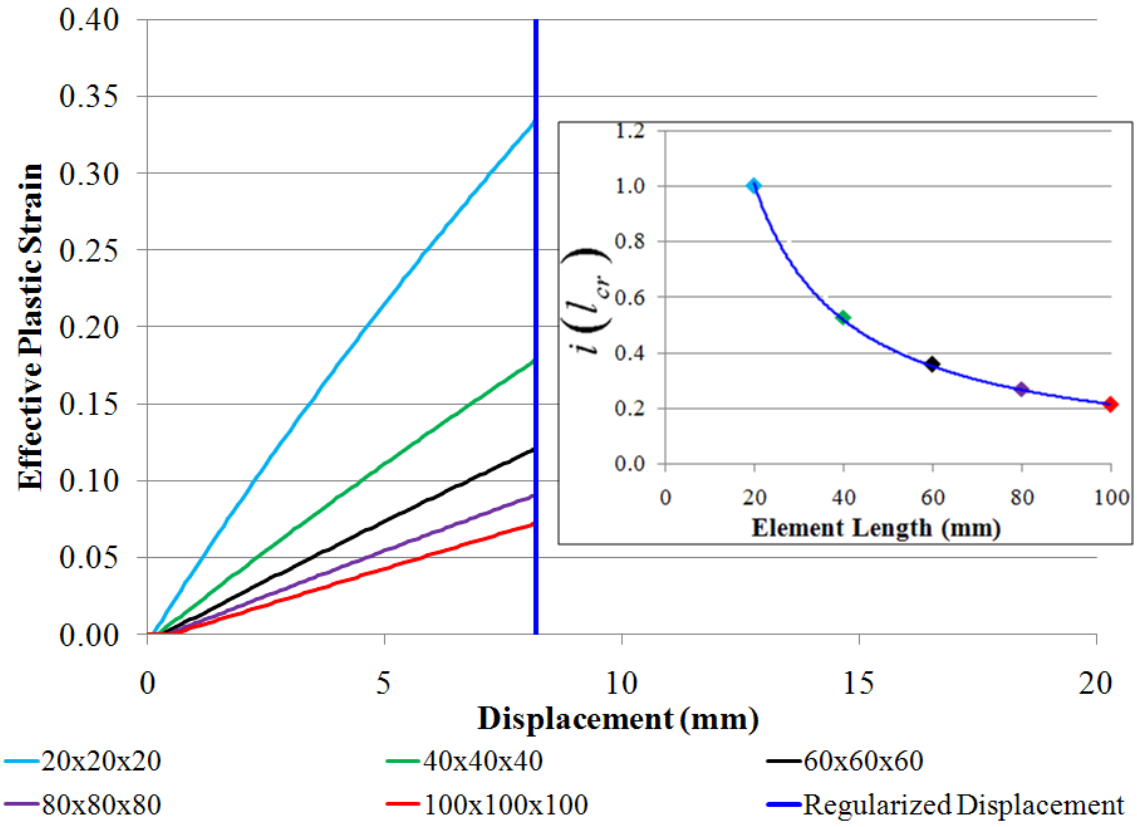

Figure 4-90: Evolution of the effective plastic strain to failure with different element lengths for TRAUM.

4.5.3 **Single element analysis and verification of TRAUM with J-C material model for a non-monotonic representation of the failure locus**

4.5.3.1 Benchmark-problem definition

Figure 1-4 illustrates the differences between three different J-C failure loci and the experimentally driven failure locus suggested by Boa [99] based on the stress-triaxiality. It is shown that a single monotonic function (i.e., J-C failure criteria) may not necessarily be able to capture the whole failure behavior of a ductile material considering different states-of-stress. Therefore, TRAUM is utilized in this benchmark problem to show that any failure locus can be employed as a failure rule if the material can be tested and characterized for failure strains as a function of stress-triaxiality and Lode-angle-parameter.

Fully integrated, hexahedral finite elements with equal lengths are used for the analysis with different boundary and loading conditions representing notable values of stress-triaxiality. Figure 4-91 illustrates the notable stress-states with the corresponding boundary conditions for each element. A displacement boundary condition, which provides a constant velocity as shown in Figure 4-77, is defined for different directions and nodes as illustrated in Figure 4-91.

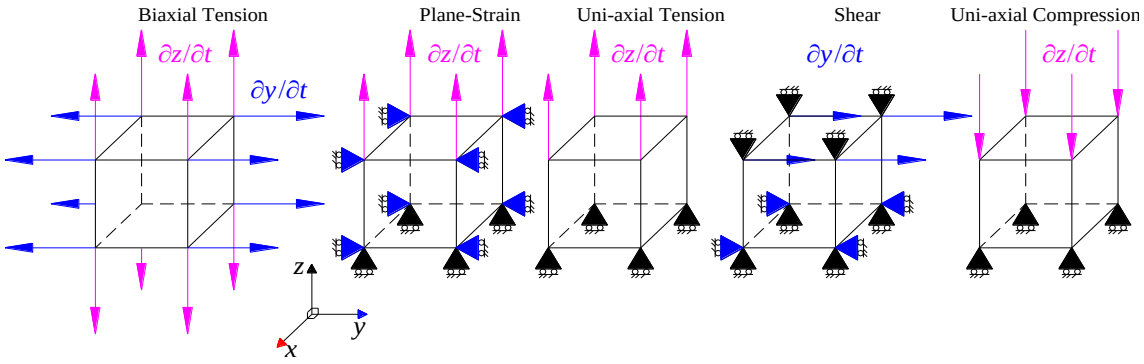

Figure 4-91: Single element models representing notable stress-triaxialities.

The corresponding stress-states for each single element are illustrated in Figure 4-92 on the planes of stress-triaxiality vs. Lode angle parameter and stress-triaxiality vs. product-triaxiality, respectively. It can clearly be seen that the stress-space with this five single elements are simulated for the entire plane-stress meridian. It should also be noted that several different Lode-angle-parameters are achieved by this benchmark problem, which is desirable test a failure locus for diverse values of the stress-states.

In order to compare the failure prediction with J-C, the same tabulated inputs are utilized for TRAUM, which are illustrated by Figures 4-79 and 4-80 to construct the flow surface. However, the failure surface is constructed by the failure locus suggested by Bao [99] replacing the J-C failure locus that is shown in Figure 4-81. Figure 4-93 depicts Bao's failure locus in a tabulated format that is utilized by TRAUM. It should be noted that, Bao's failure locus does not have Lode-angle-parameter dependency; therefore, a constant behavior is assumed for the failure surface along the axis representing the Lode-angle-parameter.

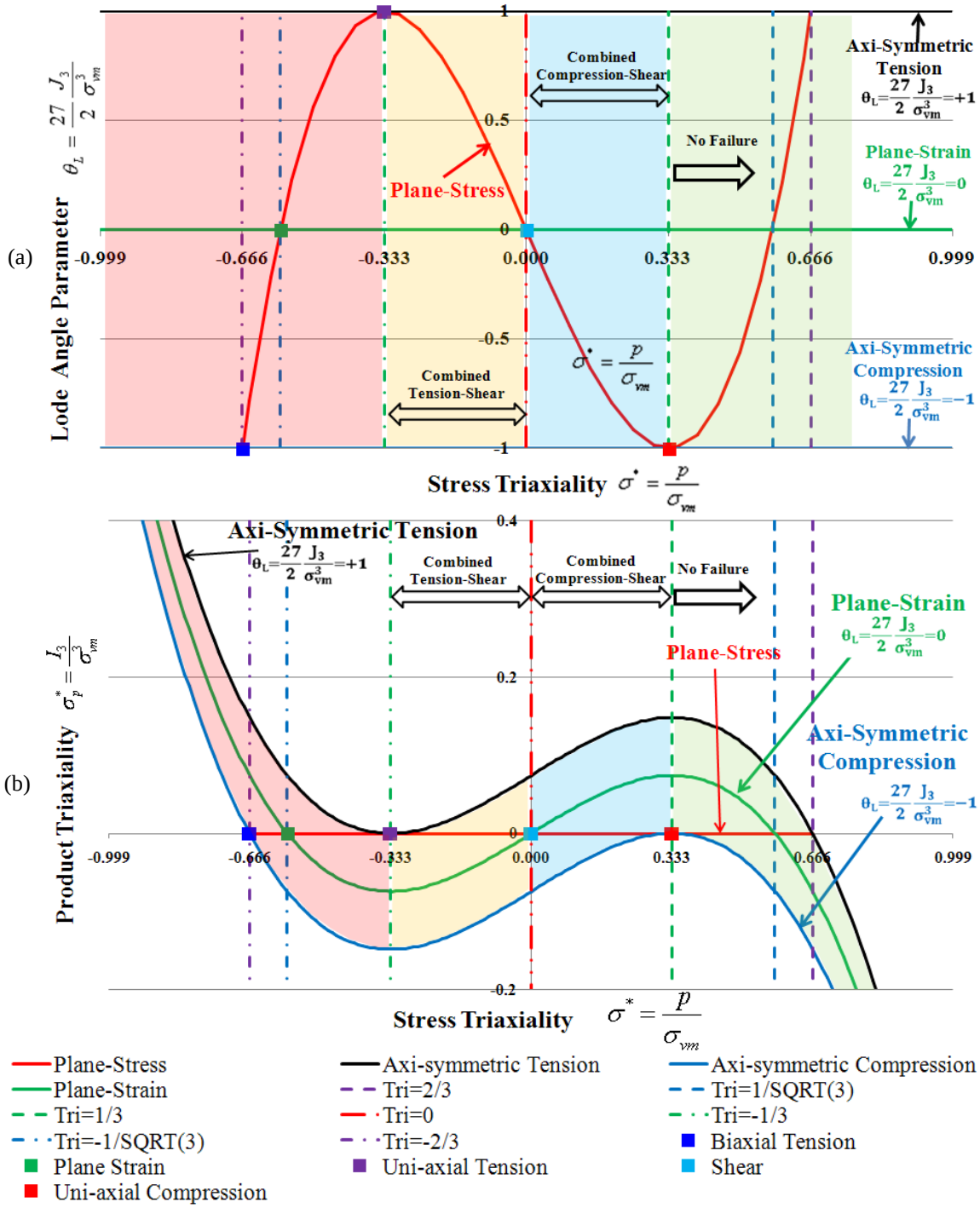

Figure 4-92: States-of-stress for each finite element on the plane defined by; (a) stress-triaxiality vs. Lode-angle-parameter and (b) stress-triaxiality vs. product-triaxiality.

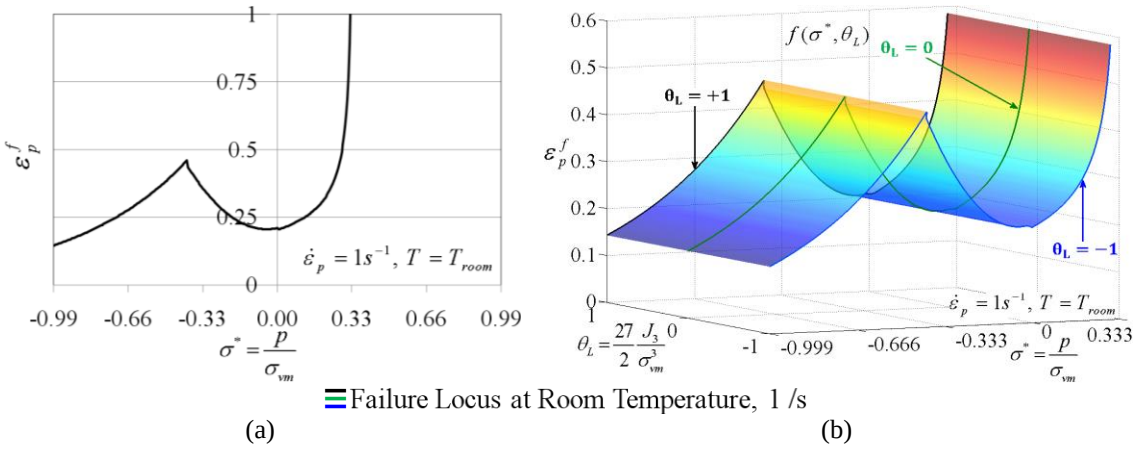

(a) (b)

Figure 4-93: Failure surface at room temperature and a nominal strain rate of 1.0s^{-1} representing; (a) tabulated format of the Bao's failure locus for TRAUM and (b) Bao failure locus in three dimensional representation with constant Lode-angle-parameter dependency.

4.5.3.2 Benchmark-problem results

Failure predictions for monotonic and non-monotonic failure loci are compared in Figure 4-94, where the failure points for J-C Set-4 and Bao failure locus are marked for the corresponding states-of-stress. It is known that J-C parameters are often calibrated to fit a monotonically increasing function as a failure locus while ignoring some of the points that may jeopardize the smoothness [85] [101]. It is shown in this benchmark problem that only the uni-axial tension and plane-strain stress-states are able to predict failure within reasonable closeness. It should also be noted that using a monotonic failure locus may not necessarily be always conservative while predicting failure. It is shown that J-C failure locus under-predicts the failure for the intermediate stress-triaxialities between the uni-axial tension and plane-strain states. Moreover, according to Bao's failure locus, failure is not assumed for stress-triaxialities that are above $\sigma^* > +\frac{1}{3}$ or uni-axial compression stress-state [99] [106]. In that case, using J-C initiates premature failure of the elements under compression, which may have dramatic effects on the failure prediction of ductile materials. On the other hand, Bao's failure locus is essentially described by a combination of three curves, which are also defined by curve fitting for three distinct branches of the failure space as a function of stress-triaxiality [99]. Therefore, the methodology for constructing the failure locus cannot be generalized and

applied to every material of interest, which may have different failure characteristics and consequently different shapes for the failure locus. A need for a generic representation of a failure locus provides TRAUM to present the opportunity to tabulate any failure characteristics based on the experimental data as it is demonstrated in Figures 4-93 and 4-94 for Bao's failure locus.

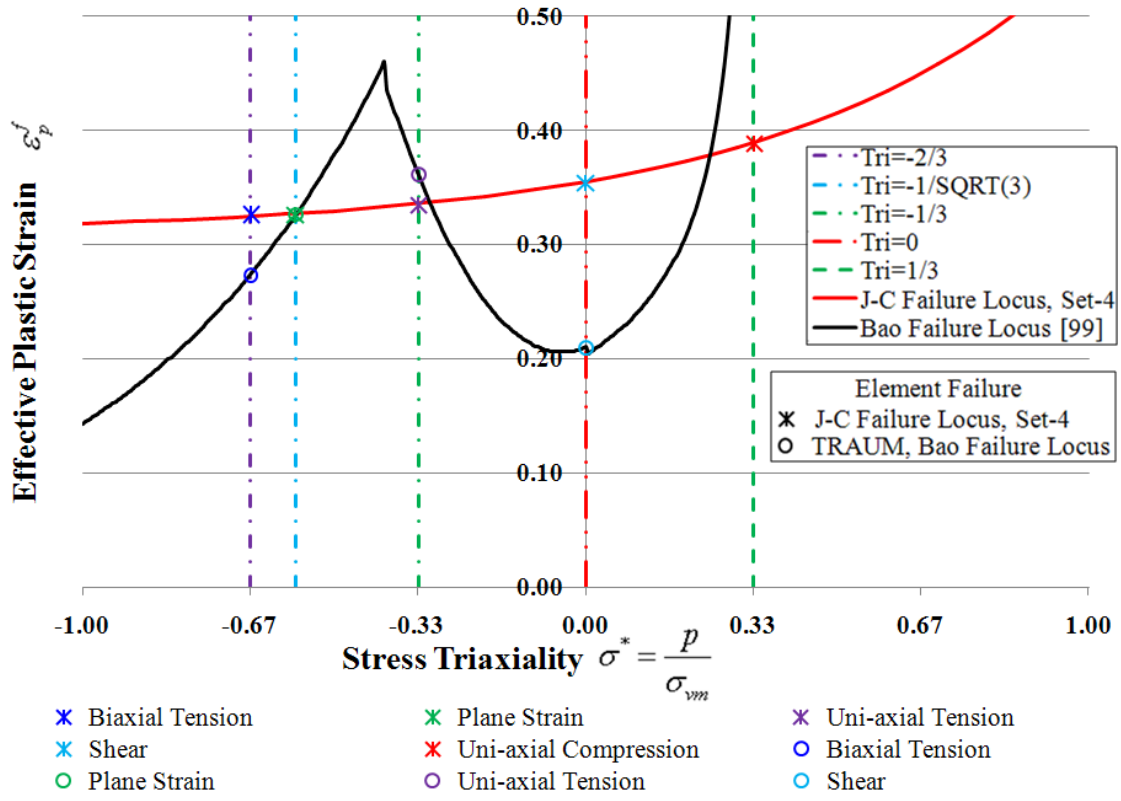

Figure 4-94: Comparison of the failure predictions for different states-of-stress when a non-monotonic failure locus is utilized by TRAUM.

4.5.4 **Single element analysis and verification of TRAUM for a Lode-angle-dependent failure surface**

4.5.4.1 Benchmark-problem definition

It should be noted that a reduced tabulated input format is used for the single element benchmark analysis for the previous cases above, where a constant Lode-angle-parameter is considered over the entire stress-space as illustrated in Figures 4-81(b) and 4-93(b).

However, Barsoum and Faleskog [102] and Xue [103] showed that failure profoundly depends on the third deviatoric stress invariant, where Xue represented the described failure surface for Bao's experimental results as illustrated in Figures 1-5 and 4-3 [103]. Therefore, in this benchmark problem, it is required to generate a unique failure locus for each Lode-angle-parameter as a function of stress-triaxiality. In order to test the Lode-angle-parameter dependency on failure prediction, Bao's and Xue's failure surfaces are compared, where both are simulated with TRAUM.

Three fully integrated, hexahedral finite elements with equal lengths are used for the analysis with different loading conditions representing notable values of Lode-angle-parameter, where all have the same stress-triaxiality. Figure 4-95 illustrates the notable stress-states with the corresponding loading conditions for each element. Each finite element is loaded with a different pressure field. Only two surfaces (i.e., upper and lower surfaces) of the finite element that is representing the axi-symmetric boundary conditions are loaded with a pressure field as illustrated in Figure 4-95. All six surfaces of the other elements are loaded by different pressure fields with different ratios.

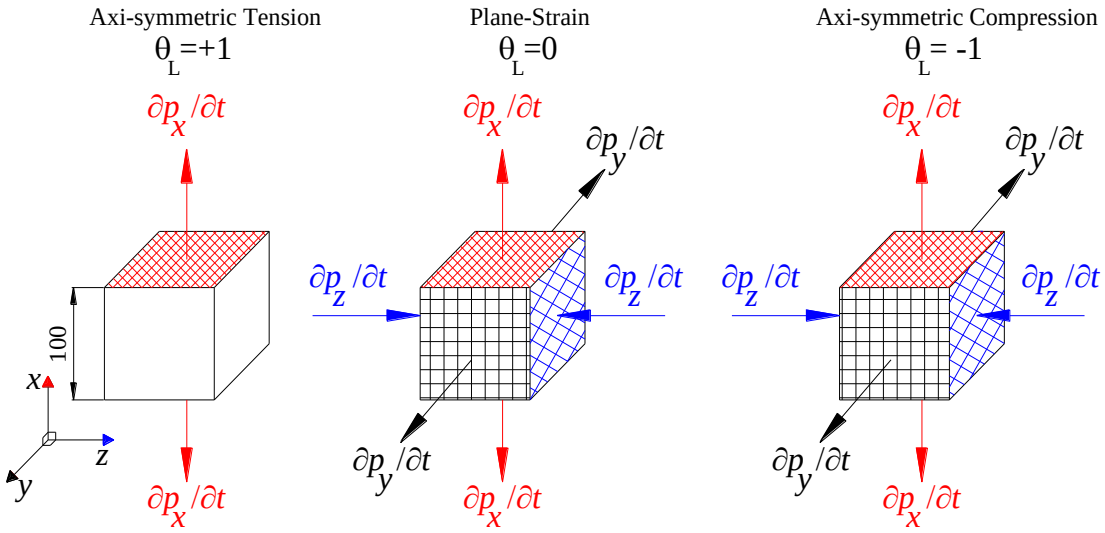

Figure 4-95: Single element models representing notable Lode-angle-parameters.

Recalling Section 4.3.1, the stress-states are identified by incorporating the principle stresses as defined by the relations in Equation (4.73). However, simply applying a street field with the required ratios to find the desired states-of-stress would not be an objective

comparison considering that different amounts of effective stress can clearly lead to different deformation and failure accumulation. Therefore, the loading conditions that are defined for the axi-symmetric tension case is selected as a baseline and all other loading conditions are normalized according to the effective stress to have an objective comparison. It should be noted that targeted stress-states can be achieved by keeping certain ratios of the principle stresses according to the methodology defined in Section 4.3.1.

$$\begin{aligned}
&\text{Axi-symmetric Tension}\ \left\{\sigma_1\begin{bmatrix}1&0&0\\0&0&0\\0&0&0\end{bmatrix}\right. \Rightarrow \quad \sigma^* = -\frac{1}{3}, \theta_L = +1, \sigma_p^* = 0,\ \sigma_{vm} = \sigma_1(\text{baseline}),\ \text{Objective Ratio} = \frac{\sigma_{vm,\ \text{baseline}}}{\sigma_{vm}} = \frac{\sigma_1}{\sigma_1} = 1\\
&\text{Plane Strain}\ \left\{\sigma_1\begin{bmatrix}1&0&0\\0&-\frac{1}{2}+\sqrt{\frac{3}{4}}&0\\0&0&-2+\sqrt{3}\end{bmatrix}\right. \Rightarrow \quad \sigma^* = -\frac{1}{3}, \theta_L = 0, \sigma_p^* = -0.074,\ \sigma_{vm} \approx 1.098\sigma_1,\ \text{Objective Ratio} = \frac{\sigma_{vm,\ \text{baseline}}}{\sigma_{vm}} = \frac{\sigma_1}{1.098\sigma_1} \approx 0.911\\
&\text{Axi-symmetric Compression}\ \left\{\sigma_1\begin{bmatrix}1&0&0\\0&1&0\\0&0&-\frac{1}{2}\end{bmatrix}\right. \Rightarrow \quad \sigma^* = -\frac{1}{3}, \theta_L = -1, \sigma_p^* = -0.148,\ \sigma_{vm} \approx 1.5\sigma_1,\ \text{Objective Ratio} = \frac{\sigma_{vm,\ \text{baseline}}}{\sigma_{vm}} = \frac{\sigma_1}{1.5\sigma_1} \approx 0.666
\end{aligned} \tag{4.73}$$

The new values of the principle stresses and the corresponding states-of-stress are defined by Equation (4.74) after normalizing the values for the same amount of effective stress. Figure 4-96 depicts the single element models with the corresponding loading conditions, where it should be noted that the loads are applied to the entire surface within the described directions. Figure 4-97 illustrates the pressure boundary condition that is applied to the surfaces of the finite elements with the scaling factors described by Equation (4.74).

The corresponding stress-states for each single element are illustrated in Figure 4-98 on the planes of stress-triaxiality vs. Lode angle parameter and stress-triaxiality vs. product-triaxiality, respectively.

$$\text{Axi-symmetric Tension} \left\{\sigma_1 \begin{bmatrix} 1 & 0 & 0 \\ 0 & 0 & 0 \\ 0 & 0 & 0 \end{bmatrix} \Rightarrow \sigma^* = -\frac{1}{3}, \theta_L = +1, \sigma_p^* = 0 \quad \sigma_{vm} = \sigma_1 \right.$$

$$\text{Plane Strain} \left\{\sigma_1 \begin{bmatrix} 0.911 & 0 & 0 \\ 0 & 0.333 & 0 \\ 0 & 0 & -0.244 \end{bmatrix} \Rightarrow \sigma^* = -\frac{1}{3}, \theta_L = 0, \sigma_p^* = -0.074 \quad \sigma_{vm} = \sigma_1 \right. \tag{4.74}$$

$$\text{Axi-symmetric Compression} \left\{\sigma_1 \begin{bmatrix} 0.666 & 0 & 0 \\ 0 & 0.666 & 0 \\ 0 & 0 & -0.333 \end{bmatrix} \Rightarrow \sigma^* = -\frac{1}{3}, \theta_L = -1, \sigma_p^* = -0.148 \quad \sigma_{vm} = \sigma_1 \right.$$

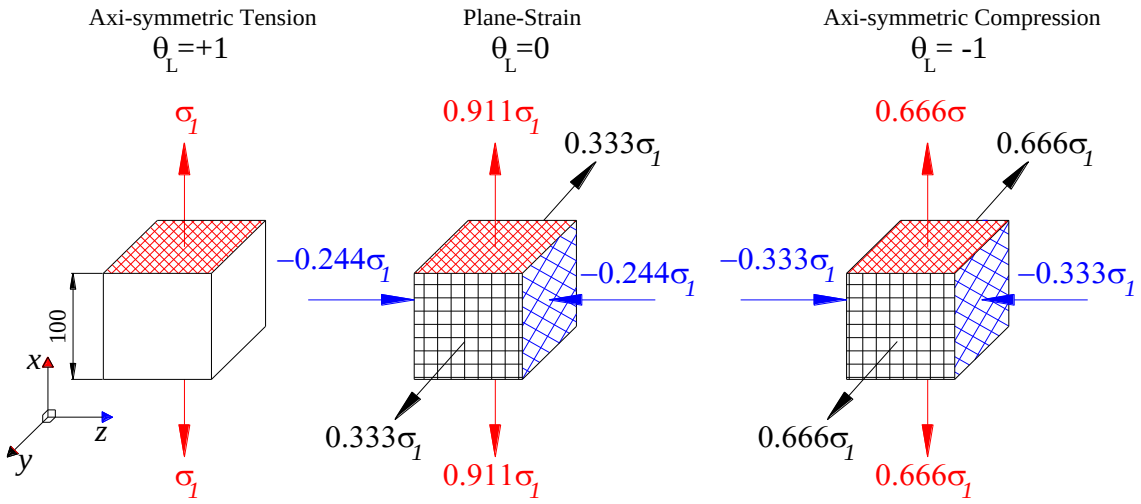

Figure 4-96: Single element models representing notable Lode-angle-parameters.

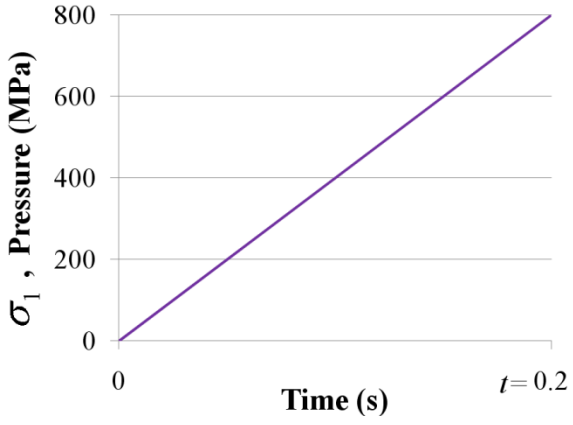

Figure 4-97: Applied pressure on the single finite element models without the scaling factors.

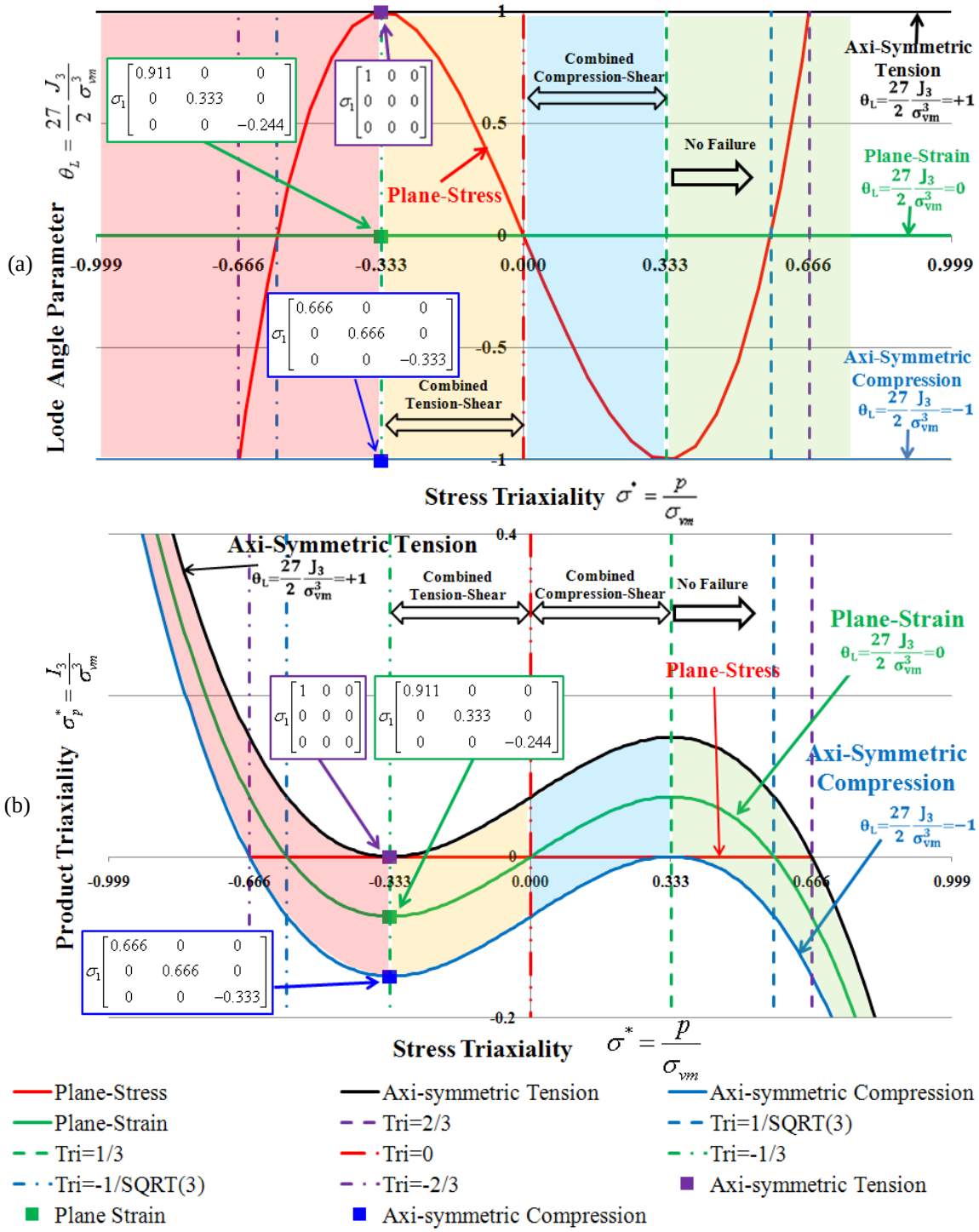

Figure 4-98: States-of-stress for each finite element on the plane defined by; (a) stress-triaxiality vs. Lode-angle-parameter and (b) stress-triaxiality vs. product-triaxiality.

It is shown in Figure 4-98 that three finite elements share the same value for the stress-triaxiality and have different Lode-angle-parameters due to the differences in the loading conditions. Therefore, it is expected that these elements have different effective strains to failure. However, this can only be achieved by incorporating a Lode-angle-parameter dependency on the description of the failure surface. Figure 4-99 illustrates Xue's failure surface in a tabulated format that is utilized by TRAUM. It should be noted that, Xue's failure surface has a symmetric surface fitting accepting plane-strain meridian as a symmetry axis [103]. Consequently, it is expected to have the same failure strains for axi-symmetric tension (i.e., $\theta_L = +1$) and axi-symmetric compression (i.e., $\theta_L = -1$). The scaling factors that are utilized by TRAUM are considered according to Figures 4-82 and 4-83 since the strain-rate, temperature and element lengths are kept the same for the benchmark problem.

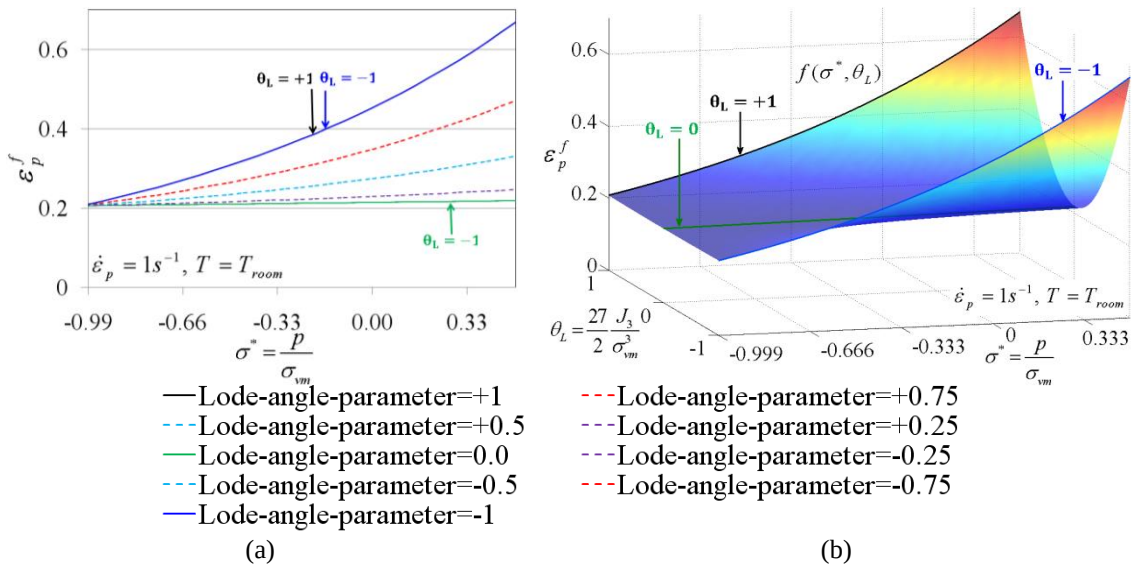

Figure 4-99: Failure surface at room temperature and a nominal strain rate of 1 s^{-1} representing (a) tabulated format of the Xue's failure surface for TRAUM and (b) Xue's failure surface.

The flow surface, which is represented by Figures 4-79 and 4-80, is used as a tabulated input for the simulations. It should be noted that both Bao [99] and Xue [103] have characterized and used a flow surface that has no temperature or strain-rate dependency. Therefore, Set-4 of the J-C material model is considered for the analysis.

4.5.4.2 Benchmark-problem results

Failure predictions for a Lode-angle-parameter dependent failure surface are compared in Figure 4-100, where the failure points for Bao's and Xue's failure surface are marked for the corresponding states-of-stress. It should be noted that all three stress-states share the same stress-triaxiality, where Lode-angle-parameters are changing with the loading ratios following axi-symmetric tension, plane strain and axi-symmetric compression meridians, respectively. TRAUM tabulated input for Bao's failure surface predicts identical results for all three cases. It is shown that, when Xue's failure surface is utilized by TRAUM for a plane strain loading condition, failure is predicted to occur earlier than the axi-symmetric cases, which would not be possible otherwise if a Lode-angle-parameter dependent failure surface was not utilized.

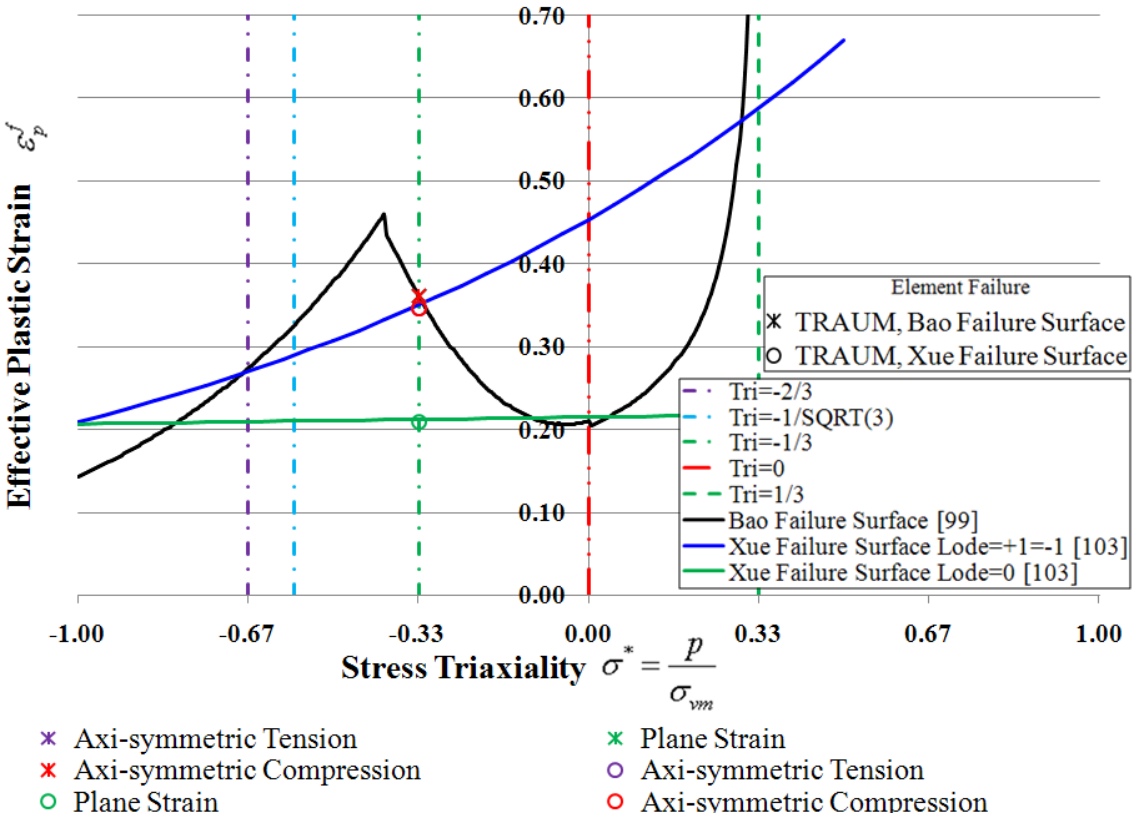

Figure 4-100: Comparison of the failure predictions for different states-of-stress when a Lode-angle-dependent failure surface is utilized by TRAUM.

It should be noted that with the help of additional experimental data, Xue's failure surface is further modified to reflect differences between the axi-symmetric tension and compression meridians breaking the symmetric surface fitting assumption [104]. Therefore, there is a need to explicitly describe a failure surface depending on the states-of-stress, strain-rate and temperature, which is also mesh size independent like TRAUM. Considering all benchmark and verification problems, it can be concluded that TRAUM can successfully predict the failure behavior of ductile materials.

4.6 **Summary**

In this Chapter, a thermo-elastic/viscoplastic material model with regularized, stress-state dependent failure algorithm is developed. The procedures and techniques used during the implementation of the material model into a non-linear explicit dynamics FE code are presented. Given the name 'TRAUM', the new material model is capable of predicting ductile deformation and failure of materials under impact loading.

Along with the methodology, derivations about the constitutive relation and regularized accumulated failure algorithm are presented with their corresponding numerical implementation schemes. A generic failure locus for ductile materials based on multiple states-of-stress is developed. This locus represents the stress-states as a function of stress-triaxiality and product-triaxiality, which is directly related to the Lode-angle-parameter and third invariant of the stress tensor.

Based on the numerical simulation results and observed differences in the failure modes depending on the target thickness, speed of the projectile, nose shape and orientation, it is found that one of the most dominant factors on the transition of the failure mode is the state-of-stress. The stress-states that are dominant on structures under impact loading are found and overlaid on the product-triaxiality versus stress-triaxiality space. The population of the failure points on the stress-state diagram indicates that most of the failures occur within the envelope defined between the negative part of the stress-triaxiality, which corresponds to axi-symmetric tension, plane strain tension and axi-symmetric compression meridians.

Therefore, an experimental program is devised to cover the range of interest on the stress-state diagram. The experimental program suggests testing specimens with different

geometries or loading conditions to achieve the variances in the state-of-stress. An iterative specimen design algorithm is also introduced and used while designing the specimens aiming a bridging can be achieved through the average targeted stress-states while constructing the failure locus. Shapes of the designed specimens can be found in Appendix–B with their corresponding FE models. Figures 4-75 summarized the targeted stress-states for the specimens on the stress-spaces defined by stress-triaxiality vs. Lode angle parameter and stress-triaxiality vs. product-triaxiality.

Finally, the stability, accuracy and robustness of TRAUM benchmarked against J-C, Bao and Xue's failure surface definitions by utilizing single element simulations. It is shown that the new material model can successfully predict proportional and non-proportional loading conditions where strain rate and temperature dependent test cases are verified accurately. Mesh regularization, failure under different states-of-stress and Lode-angle-dependent failure prediction is also benchmarked for the new material model. TRAUM input definitions are described for tabulated representation of flow and failure surfaces.

The TRAUM material model is fully developed and implemented. Special specimens are designed for an experimental program to characterize the material data required for TRAUM input. The results of the experimental program and material characterization are demonstrated in the following Chapter.

CHAPTER 5 - **Experimental program**

5.1 **Introduction**

It is shown in the previous Chapters that during the ballistic impact simulations, failure predominantly occurs for certain values of the state-of-stress. This region can be defined by an envelope, which can be described between the meridians of certain stress-states. It is also shown that one of the widely used material models may not be accurate enough for predicting failure when the failure characteristics do not exhibit a monotonic trend or depend on an extra stress invariant. The significance of the mesh dependency on failure prediction is also pronounced.

As a result, a thermo-elastic/viscoplastic material model with regularized failure, TRAUM, is introduced with a stress-state dependent failure locus. This failure locus is defined through stress-triaxiality and Lode-angle-parameter, which incorporates all three stress invariants. The failure locus is also regularized and then scaled based on the mesh size. Specifically designed specimens are used to construct this failure locus based on the targeted values of the stress-states, where a failure surface is formed from the characterized values of the effective plastic strains at failure for every specimen specific to certain states-of-stress.

In this Chapter, details about the testing procedures are explained and a more detailed description of the characterization methodology is attained. Temperature and strain-rate dependent flow and failure surfaces for Al2024-T351 are obtained and input data for TRAUM is generated.

Material testing was performed within the framework of uncontained aircraft engine failure joint research program and the experimental results were provided by Seidt [108], where a more detailed analysis of the experimental program can be found.

5.2 **Material of interest**

Al2024 aluminum alloy, which is also known as UNS A92024 or ISO AlCu4Mg1 [224], is selected as the material of interest for impact performance evaluation. Al2024 is a heat-treatable Al-Cu-Mg alloy, which is available in a wide variety of product forms and tempers. Due to its good strength to weight ratio, good machining and fatique

characteristics, it is widely used in aerospace applications especially for wing and fuselage structures [225]; therefore, is a good candidate for investigating dynamic deformation and failure behavior. Its common usage also attracts significant academic attention [99] [103], which makes Al2024 an ideal candidate for comparing new findings against the results in literature.

The alloying variances of Aluminum can be illustrated in Figure 5-1 for principle elements. The main alloying component for 2024 is copper, where other elements exist in the composition as secondary phase particles or inclusions. The Al2024-T351 material that is used to generate the specimens and tested in this research was acquired from Kaiser Aluminum and conformed to the specifications defined in Table 5-1.

Table 5-1: Material specifications for Al2024-T351.

Specification	Form	Gauge [mm]	Width [mm]	Length [mm]
AMS 4037	Bare sheet and plate	12.7 (1/2″)	1231.9 (48.5″)	3670.3 (144.5″)
AMS-QQ-A-250/4	Bare sheet and plate			

The chemical composition of the material is listed in Table 5-2. Srivatsan, et al. discussed the role of secondary particles on the impact performance of Al2024-T351 while investigating notch sensitivity [226]. They found that AlCuMn dispersoid particles in the composition have a significant effect on the failure. Bao stated that AICuFeMn particles were around 10 μm in size and played the most significant role on failure, where the initial void nucleation was observed around these cracking particles [99]. Bao also reports other secondary particles like AICuMg, AIMgSi, AIZnMg, AIZnMgCu, which were measured around 2 μm in size [99]. An in depth investigation about the phase diagrams of Al2024 with Mg-Cu-Si-Fe, dispersoid formations based on the solidification characteristics and microstructure can be found from Ives, et al. [227].

Table 5-2: The chemical composition of aluminum alloy Al2024-T351.

Alloy	Chemistry [weight %]										
Al2024-T351	Si	Fe	Cu	Mn	Mg	Cr	Zn	Ti	V	Zr	Other
	0.08	0.22	4.47	0.59	1.37	0.01	0.18	0.02	0.01	0.01	0.04

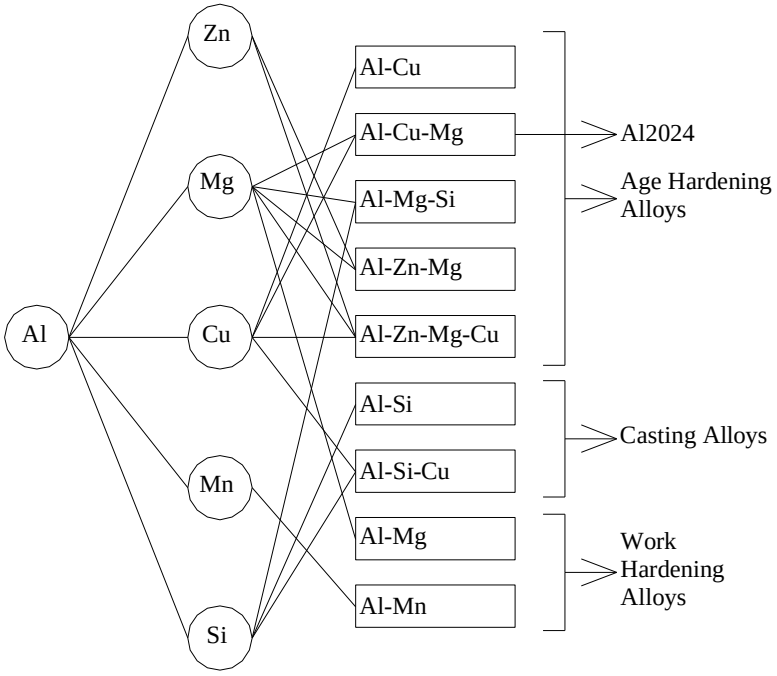

	Wrought Alloys								Cast Alloys	
Series	1XXX	2XXX	3XXX	4XXX	5XXX	6XXX	7XXX	8XXX	2XX.X	3XX.X
Composition	Al	Al-Cu	Al-Mn	Al-Si	Al-Mg	Al-Mg-Si	Al-Zn-Mg	Al-Li	Al-Cu-Ag	Al-Si-Mg

Figure 5-1: Principle Aluminum alloys and Al2024, adapted after [228].

The mechanical properties of the alloy vary significantly with temper treatment, where T3 type tempers are notable for their high toughness. They are solution heat treated at 495°C, cold worked, and naturally aged to a substantially stable condition [228]. The T3 temper form is used for materials up to 6.35 mm (1/4″) thick, and the T351 temper form is used for thicker plates [225]. During the T351 temper treatment, the metal is stress relieved by stretching a controlled amount, which is around 1.5-3%, and naturally aged. No further straightening is applied after stretching [229] [230].

Specimens that are designed in Chapter 4 were manufactured from 12.7mm plates. The specimens were aligned with the rolling direction to minimize transverse and anisotropic effects since the material model is developed assuming isotropic plasticity. All specimens were manufactured from the same lot of material to ensure material property consistency. Figure 5-2 illustrates the alignment of the specimens on an orthogonal material axis adjusted to the rolling direction.

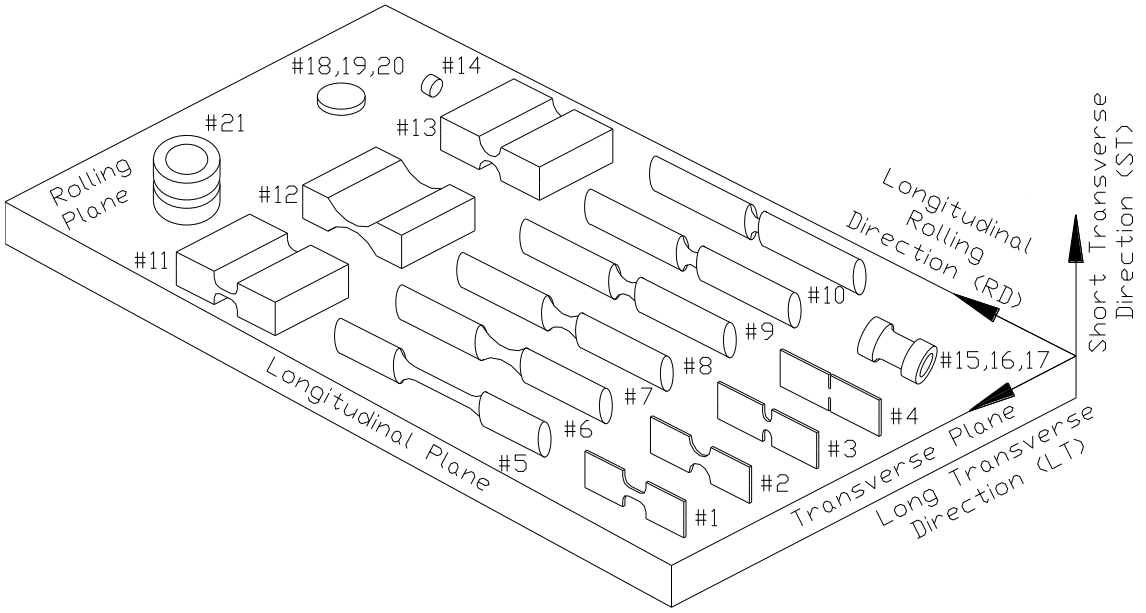

Figure 5-2: Orthogonal directions of the rolled plate and specimen orientations.

5.3 **Methodology**

In this Chapter, dynamic deformation and failure behavior of Al2024-T351 Aluminum alloy is characterized and required input data for TRAUM is attained.

Lee [231] states that 'poorly understood and presented calibration procedures' are one of the biggest challenges in the application of a failure criteria considering that several numbers of parameters, which are strongly coupled, are needed to represent physics based material models or significant amounts of material tests and complex numerical simulations are required to calibrate phenomenological material models. Challenges in characterization do not only exist on 'the lack of the technology and tools necessary for performing high speed deformation and temperature measurements with requisite accuracy' [6] but also comprise the lack of adequate computational mechanics tools that are required to 'simulate the processes in practically reasonable computational times and high accuracy' [6]. Therefore, a well-established experimental-numerical framework was required and evolved significantly especially during the last decade to overcome these challenges, which has stimulated several research studies about modeling dynamic ductile deformation and failure behavior of materials [6] [99] [103] [231]. In this Chapter, a similar synchronized experimental-computational characterization framework is adopted,

where full field analyses of deformation and failure and directly measured forces are compared with concurrent finite element simulations to attain the required input for TRAUM.

The steps of the characterization methodology can be illustrated as in Figure 5-3. The first step is to obtain a quasi-static hardening curve at room temperature. The hardening curve is the foundation for characterization of the failure strains at room temperature and quasi-static loading conditions. However, characterizing a hardening curve can be very challenging considering the instabilities that occur during plastic deformation of a material. Due to friction at both ends of a compression specimen, 'barrelling' may lead to non-uniform flow and deformation and therefore is not desirable. Tension tests exhibit instability when the specimen necks during plastic deformation. This instability is most commonly known as necking instability, where the deformation loses its homogeneous distribution (i.e., elastic Poisson deformation) and localizes. In this section, the hardening curve is characterized by correlating with the test data (i.e., force vs. displacement) using an iterative-inverse methodology that is straight forward and requires minimum number of FE simulations. A plane-stress specimen, which is illustrated in Figure B-1 (i.e., Specimen #1) with a smooth gauge section, is utilized for the characterization of the true stress - true strain curve. Digital Image Correlation (DIC) was used for most cases, unless otherwise stated to obtain specimen displacements and strains. This method is desirable because it provides better understanding of the full strain-displacement field and avoids errors or discrepancies that may arise due to tooling or instrumentation [108]. A brief overview of DIC is given in the next section.

High strain-rate and temperature dependent hardening curves are characterized similarly in the subsequent step to generate the tabulated flow surface for TRAUM.

Beginning with the third step, failure locus is characterized for the material of interest. However, during the characterization of the failure strains for different states-of-stress, it must be recognized that the results will be mesh size dependent unless a mesh regularization scheme is implemented. Therefore, before characterizing the failure strains at different stress-states, a regularization curve is determined as described in Section 4.4.3.3 by utilizing different FE models for the plane-stress smooth specimen (i.e., Specimen #1).

The next step is the characterization of effective plastic strains at failure (i.e., failure strains) for every specimen designed in Chapter 4 based on the corresponding stress-states. Bao [99] suggests a 'trial-and-error' technique to characterize specimens after necking instability by using an iterative inverse calculation of displacement field using FE models to calculate the best response. Lee [231] suggests an alternative 'quick calibration method' for calibration of the failure strains within 10% error, which is promising. However, both methods are mesh dependent and assume that the failure loci is constructed by a surface fitting methodology based on a parabolic function, which is generated by minimizing the average error for the failure strains that are characterized for different specimens and stress-states [104]. Having the advantage that TRAUM integrated a mesh regularization scheme for the failure prediction by utilizing a scaling curve, during characterization of the failure loci, Bao's 'trial-and-error' methodology is adopted considering that every stress-state can lead to a unique failure strain and needs to be treated individually. Tabulated nature of TRAUM provides the advantage of constructing any continuous surface structure over the characterized strains.

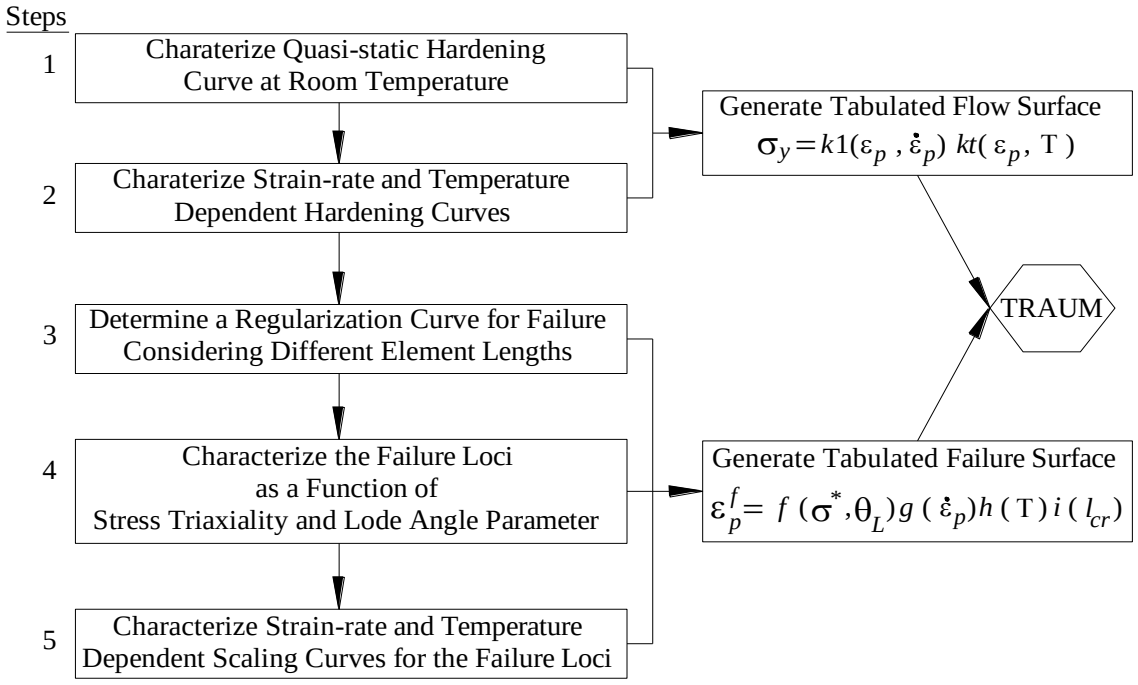

Figure 5-3: Steps for material characterization.

The last step is to characterize the strain-rate and temperature dependent scaling curves for the failure loci that will provide the full failure description by scaling the failure strains depending on the strain-rate and temperature.

As a result, a tabulated failure locus is constructed for TRAUM as a function of stress-triaxiality, Lode-angle-parameter and scaling terms for strain-rate, temperature and mesh size.

5.4 **Digital Image Correlation (DIC)**

One of the most important stages of experimental solid mechanics is to quantify or characterize the material properties with regard to a constitutive law after a measurement stage [232]. The full-field analysis of displacements from mechanical tests is a key component to bridge the gap between experiments and simulations by utilizing different optical technologies for measurements. The DIC method is widely used for full-field deformation measurements due to its advantages of simple equipment, high precision and non-contact measurement [233] [234] [235] [236] [237] [238] [239] [240] [241] [242]. Moreover, with the implementation of three dimensional capabilities with binocular stereovision techniques, DIC applications are desirable for deformations that have out-of-plane components [243] [244].

Several different digital optical methods, each coupled with its own computational scheme to process the digital images are currently available to characterize different specimen shapes under different loading conditions. Avril, et al. presents a review of four kinematic automated methods that were used to characterize material model parameters using full-field measurements for four different types of specimens [245]. DIC was utilized for biaxial tensile test on a perforated cruciform specimen by Cooreman [246]. Kajberg and Wikman [247] used DIC for high-strain rate measurements on a SHPB apparatus to inversely calculate viscoplastic material model parameters for J-C. More recently Seidt [108] used three-dimensional DIC to measure full field behavior of Al2024-T351 under quasi-static through high-strain rate conditions. Orteu provides an extensive review on three dimensional applications in experimental mechanics [248]. A binocular stereovision technique was used during the measurement of the displacement fields through the course of this study using the experimental finding by Seidt [108].

Binocular stereovision technique can be explained by using Figure 5-4. According to Orteu, from a pair of images, it is possible to compute the 3D coordinates of a physical 3-D point by triangulation assuming that:

1- The geometry of the relative position and orientation of the two cameras is known, which is satisfied by an off-line camera calibration procedure;

2- The two image points in Figure 5-4(a); p_1 and p_2, are matched to the same corresponding physical point P, which is satisfied by stereo-matching calculations.

where, $P(X,Y,Z)$ is the 3D point to be measured, $p_1(u_1, v_1)$ and $p_2(u_2, v_2)$ are its stereo projections in the images, C_1 and C_2 are the optical centers of the two cameras.

From the pair of stereo images taken at time t_0 and t_1, the 3D shapes of the object can be computed. By matching the two with temporal matching or tracking and correlation-based stereo-matching, the 3D displacement vector corresponding to each image point can be computed as shown in Figure 5-4(b) [248].

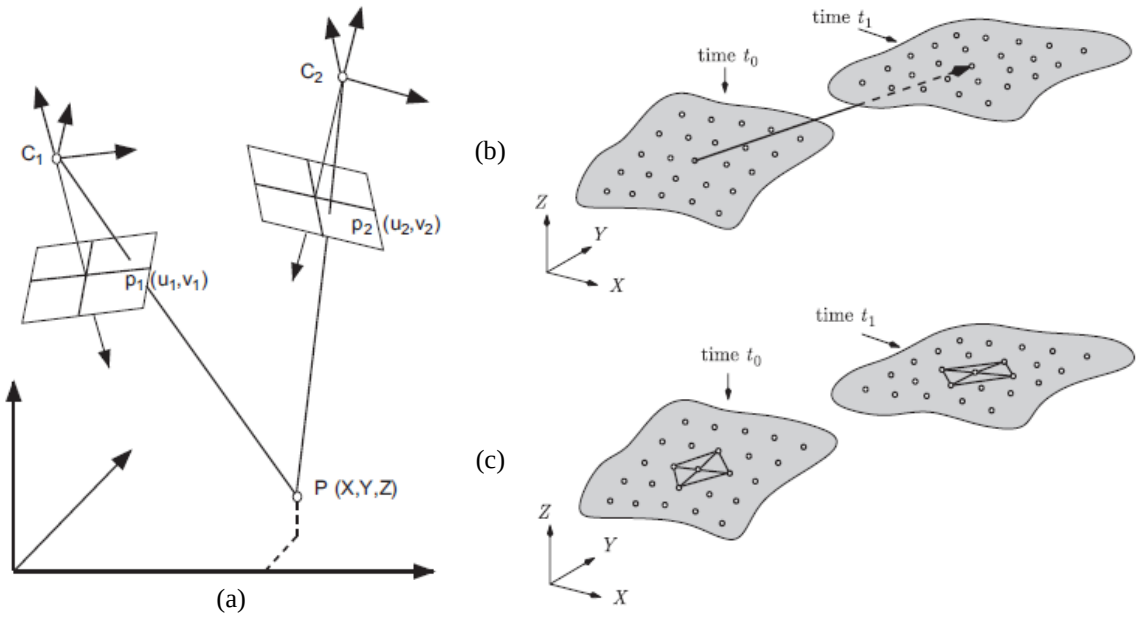

Figure 5-4: Binocular stereovision technique; (a) calculation of image point by triangulation, (b) temporal calculation of 3D displacement field and (c) temporal calculation of 3-D strain field, after [248].

The strain field can be computed by analyzing the initial and final configuration of an array of points marked on the surface. Each square element of the grid pattern is divided

into triangular sub-elements. The principal strains in each element are determined by comparing the undeformed and deformed triangles. With 3D DIC, no regular grid is marked on the surface of the object but the 3D mesh resulting from the 3D reconstruction of a Delaunay triangular mesh defined in an image can be computed as shown in Figure 5-4(c) [248].

Figure 5-5 illustrates two different binocular systems that were used by Seidt [108] for the measurement of the specimens that are utilized in this Chapter for characterization and in Chapter 6 for validation purposes. The first system in Figure 5-5(a) consists of two Point Gray Research GRAS-20S4M-C cameras with 1624 pixel by 1224 pixel resolution for quasi-static testing. The second system in Figure 5-5(b) consists of two Photron SA1.1 cameras with 1024 pixel by 1024 pixel resolution for high strain-rate testing [108].

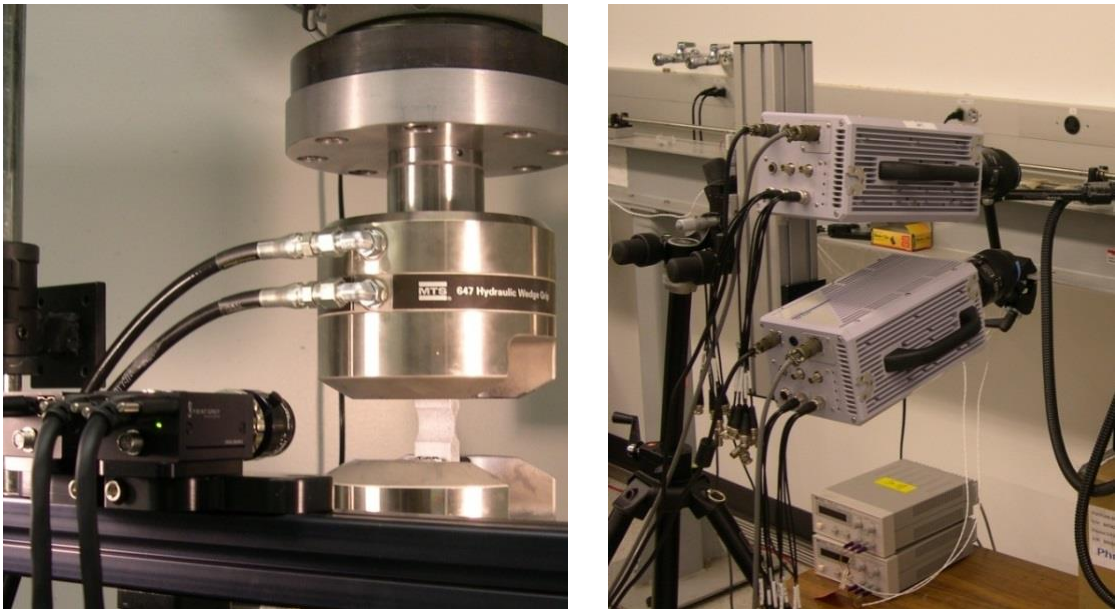

(a) (b)

Figure 5-5: Binocular stereovision camera systems for; (a) quasi-static testing and (b) dynamic testing, after [108].

5.5 **Characterization of the quasi-static hardening curve at room temperature**

Characterization of the quasi-static hardening curve at room temperature is the first step that is defined by Figure 5-3. Quasi-static tension tests on smooth plane-stress

specimens (Specimen #1) were performed at room temperature [108]. These specimens were fabricated in the rolled direction of the aluminum plate. Tests were carried out at three different speeds to achieve nominal strain-rates of 1.0×10^{-4} s^{-1}, 1.0×10^{-2} s^{-1} and 1.0 s^{-1} by using a Servo-Hydraulic Loading Frame (SHLF) apparatus that is shown in Figure 5-6 [108].

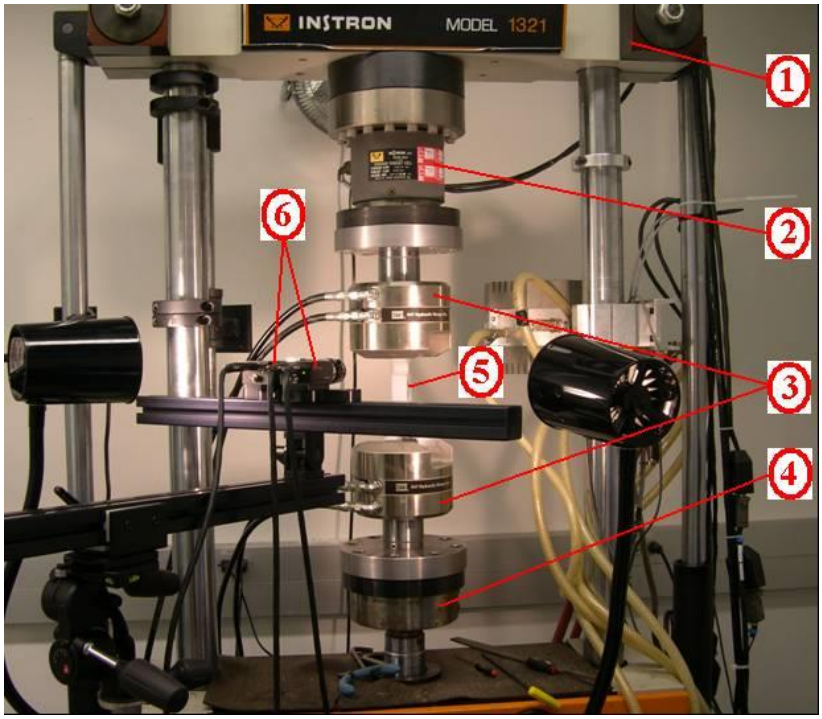

1: Servo-Hydraulic Loading Frame (SHLF)
2: Load Cell
3: Hydraulic Grips
4: Actuator
5: Specimen
6: DIC-Binocular Cameras

Figure 5-6: Servo-hydraulic Load Frame, after [108].

The test conditions, which are used to characterize the initial quasi-static hardening curve, are summarized in Table 5-3 for three different testing speeds. Each test was performed at least three times for consistency unless otherwise stated. In order to identify the test cases that are used during the characterization and validation procedure, a unique numbering scheme is followed that is defined by two successive numbers, where the first number is specifically designated to identify the major testing parameters (i.e., specimen, apparatus, loading condition, targeted strain-rate and temperature). The successive number identifies the repeated test case with an expression to represent whether the measurement for the displacement field was obtained from an extensometer or Digital Image Correlation (DIC). A suffix 'e' is added if the measurement is from an

extensometer. Figure 5-7 defines the numbering scheme for a unique test that is performed by using the parameters that are summarized in Table 5-3. Complete list of test results and corresponding true stress versus true strain data can be found in Appendix–C for reference. Complete list of tests are also listed in Appendix–D.

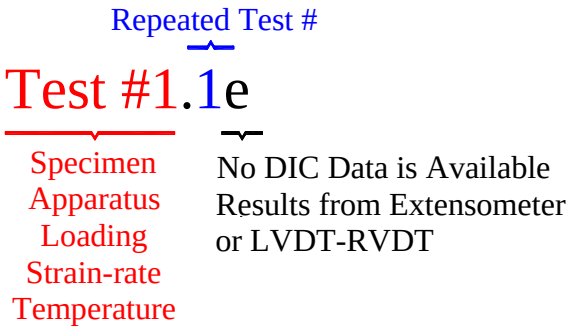

Figure 5-7: Numbering scheme for test results.

Table 5-3: Test cases that are used to characterize quasi-static hardening curve at room temperature.

Test #	Specimen #	Test Apparatus	Loading	Actuator Velocity [mm/s]	Targeted Equivalent Strain Rate [s^{-1}]	Temperature [K]	Extensometer Gage Length L_0 [mm]
1 [Figure C-1]† [Table C-1] ‡	1 [Figure B-1]§	SHLF*	Uni-axial Tension	5.08×10^{-4}	1.0×10^{-4}	Room Temperature	4.0
2 [Figure C-2]† [Table C-2] ‡				5.08×10^{-2}	1.0×10^{-2}		
3 [Figure C-3]† [Table C-3] ‡				5.08	1.0		

* Servo-Hydraulic Loading Frame (SHLF).
† Test results for the corresponding specimen, strain-rate and temperature illustrated in Appendix–C.
‡ Test results for the corresponding specimen, strain-rate and temperature listed in Appendix–C.
§ Detailed geometries and corresponding FE models of the specimens are illustrated in Appendix–B.

Overall behavior of the force vs. displacement and true stress vs. true strain curves from the test results that are listed in Table 5-3 are plotted at different strain-rates in Figures C-1, C-2 and C-3 for the test parameters, which are specified in Tables C-1, C-2 and C-3, respectively. It should be noted that the true stress vs. true strain curves are generated for the 'nominal' values and the effects of instabilities (i.e., necking) are not reflected on the behavior.

A good repeatability was obtained for the flow behavior within the test results considering small differences in the specimen geometries and measured strain-rates [108]. It is shown with Figures C-1, C-2 and C-3 that the behavior of the flow stress for three different strain-rates, which are two orders of magnitude apart, is very close and stays within maximum 3% difference. It is also pronounced that the especially tensile and compressive flow stresses below $1.0x10^{3}s^{-1}$ are relatively strain-rate independent and even a strain-rate softening behavior is common for aluminum alloys at these quasi-static strain rates [249] [250]. Even though, failure strains differ significantly as illustrated in Figure 5-8, flow characteristics are very close to each other and can even be represented by a single curve that can just be scaled to represent a strain-rate hardening behavior in order to avoid any numerical instability. Therefore, in the proceeding section, a baseline hardening curve is characterized for scaling purposes. It should be noted in Figure 5-8 that the strain rates represent the targeted equivalent rates.

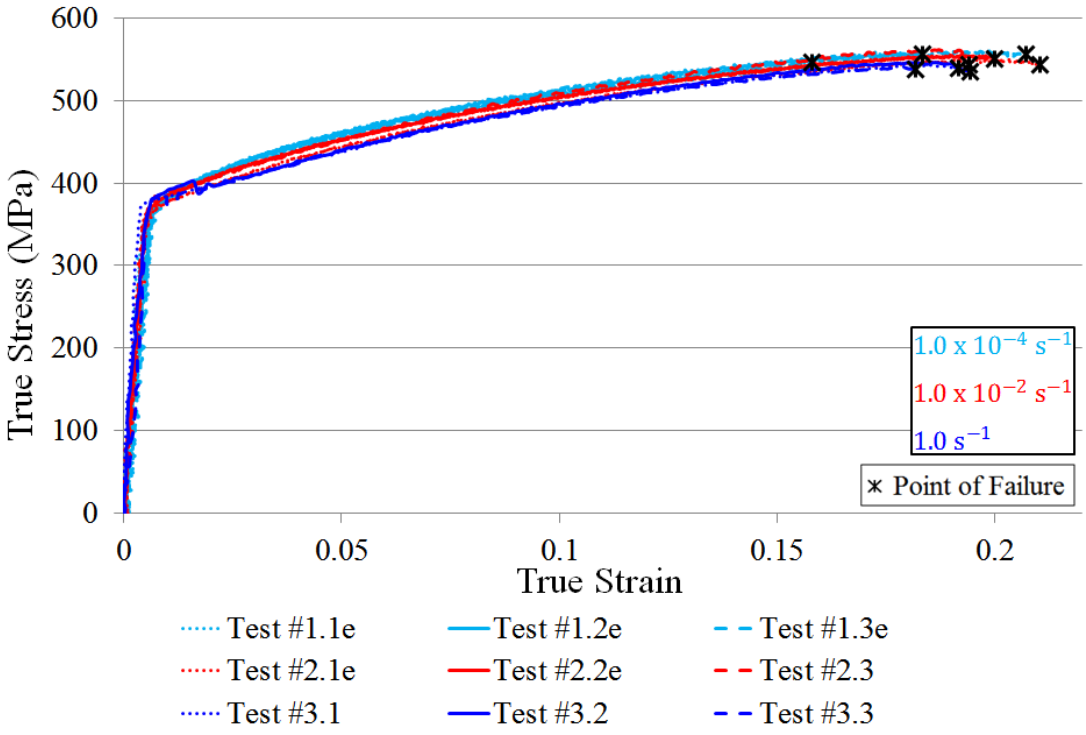

Figure 5-8: Flow and failure behavior of Al2024-T351 for quasi-static uni-axial tension at room temperature.

However, when the quasi-static test results are overlayed in Figure 5-8 a flow softening behavior is exhibited for Al2024-T351 with increasing strain-rates, which is not within the scope of this dissertation. Therefore, to satisfy numerical stability and considering that the quasi-static testing conditions still provide a state of isothermal testing, a common hardening curve is generated for the lowest strain-rate and scaled an amount of 3% to represent a positive strain-rate dependency, which will also prevent a risk of cross over among the hardening curves [251]. A common hardening curve is characterized in the proceeding sections for all three strain-rates once a stable base for the quasi-static flow behavior is identified. Clearly, failure strains, which differ significantly as illustrated in Figure 5-8, are also characterized during the development of the failure surface.

Phenomenologically, oscillatory deformation characteristics and the anomaly in the flow behavior due to temperature and strain-rate dependency, which is often recognized by strain-rate softening as illustrated in Figure 5-8, are explained by Dynamic Strain Aging (DSA). The instabilities (i.e., irregular oscillatory deformation modes) associated with DSA are commonly referred as the Portevin-Le Châtelier (PLC) effect [252] [253].

5.5.1 **Dynamic strain aging and Portevin–Le Châtelier effect**

Three hardening curves from three different strain-rates are depicted in Figure 5-9 and it is shown that Al2024-T351 has Dynamic Strain Aging (DSA) due to the effects of point defects, dispersoids and secondary pahese particles that are discussed in Section 5.2 [99] [226]. Given enough time, Cu, Mg and Fe based particles diffuse towards mobile dislocations and temporarily arrest them [254]. It is a common phenomenon for several different Aluminum alloys that is observed only at certain strain-rates and temperatures and often referred as the Portevin–Le Châtelier (PLC) effect [252] [253] [254] [255] [256] [257] [258] [259]. The characteristics of DSA are higher flow stresses and greater strain hardening at lower strain-rates than for higher ones. Two of the most significant characteristics of PLC are the serrated stress–strain curves as shown in Figure 5-9, discontinuous plastic flow that is often called as ‘jerky-flow’ and propagating deformation bands during plastic straining. Different types of serrated flows are described by Brindley and Worthington [260] for single and polycrystalline materials based on the

activation energies for the onset of serrated yielding. It is shown in Figure 5-9 that, as an Al-Cu-Mg alloy, Al2024 emerges a 'Type-B' serrated yielding until a strain-rate of $1.0x10^{-2}s^{-1}$, where onset of serrated yielding varies with the strain-rate that determines the activation energy.

Material returns to its stable behavior when certain strain-rate and temperature regime characteristics are outside the critical area. Therefore, it is important to identify the most appropriate strain-rate to begin characterization for the flow and failure surfaces. Due to the fact that this dissertation targets strain-rates significantly higher than the outlined regime for DSA, these effects are only discussed for completeness in the characterization methodology.

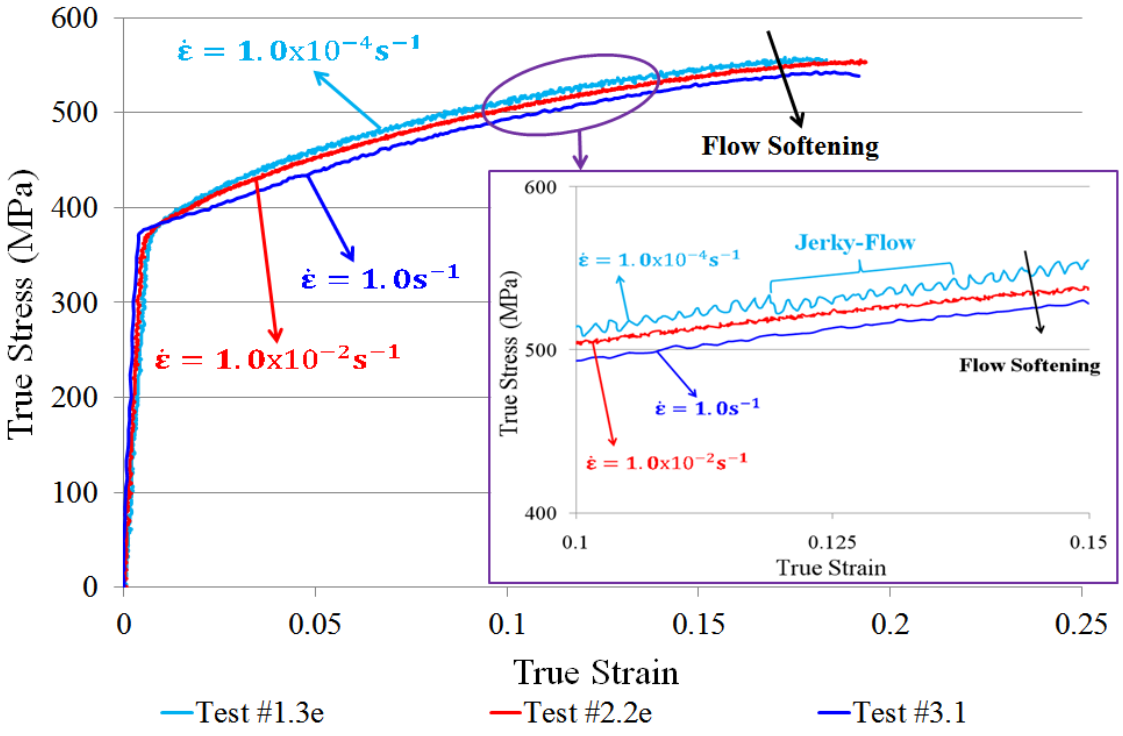

Figure 5-9: DSA and PLC effect for Al2024-T351.

Zaiser and Hahner [253] suggested using an N-shaped curve for stainless steel as a function of effective stress and characteristic strain-rate as illustrated in Figure 5-10(a), where three zones are defined to identify the stability of the regions. The first Zone is defined as the 'slow regime', where the strain-rates are lower than the critical DSA strain-

rates for stability. Dislocations have enough time and are efficiently aged providing positive strain-rate sensitivity. The second Zone is defined as the 'intermediate regime', where the strain-rates are within the unstable region. Negative strain-rate sensitivities are observed, where an increase in the strain-rate does not give a rise to the effective pinning strength and reduces the contribution of the thermal flow stress. The third Zone is defined as the 'fast regime' where sensitivity of the strain-rates becomes positive again. In this Zone, dislocations occur at high rates that can overcome the 'solute kinetics.' Consequently, dislocations can occur through an 'array of solute atoms' [253].

PLC effect for Al2024 alloy is reported by Bohlke, et al. [254], Bondar, et al. [261] and Liang, et al. [262]. Bohlke, et al. reported experimental results that can be evaluated in a similar fashion by utilizing a N-shaped stability map that is constructed as a function of critical stress and strain-rate for Al2024 as illustrated in Figure 5-10(b) [254]. They have used the cross-head readings for the calculation of the 'critical' stress and strain considering that the regular extensometers can only measure the local strain field and are not capable of representing the deformation field outside the span of the extensometer. Bohlke, et al. have also provided a critical strain based stability map for Al2024, where a similar behavior can be observed as illustrated in Figure 5-10(c) [254]. They have reported that for the strain-rates around $1.0x10^{-2}s^{-1}$, saw-tooth profile for the stress vs. strain graph smoothes and the 'unstable behavior disappears altogether' providing a plateau for the critical strains, where they have observed no strain-rate dependency on the critical strain.

In a different study, Bondar, et al. found similar experimental results for Al2024 that an N-shaped diagram can be constructed to provide insight about the stability regime based on the strain-rates as illustrated in Figure 5-10(d) [261].

Clearly, PLC effect is sensitive to some other properties such as the type of grain size, texture, heat treatment and state-of-stress [259] [262]. However, based on the stability maps for Al2024 that are shown in Figure 5-10, a characterization can be justified beginning with a strain-rate of $1.0x10^{-2}s^{-1}$, which is Test #2 defined in Table 5-3 and illustrated in Figure C-2. Results from the lower strain-rates are not desirable for characterization of the flow behavior. Figure 5-8 suggests that the difference between the flow stresses is only around three percent for quasi-static test cases. Therefore, the first

stable test result (i.e., Test #2) is used to characterize the quasi-static hardening curve at room temperature.

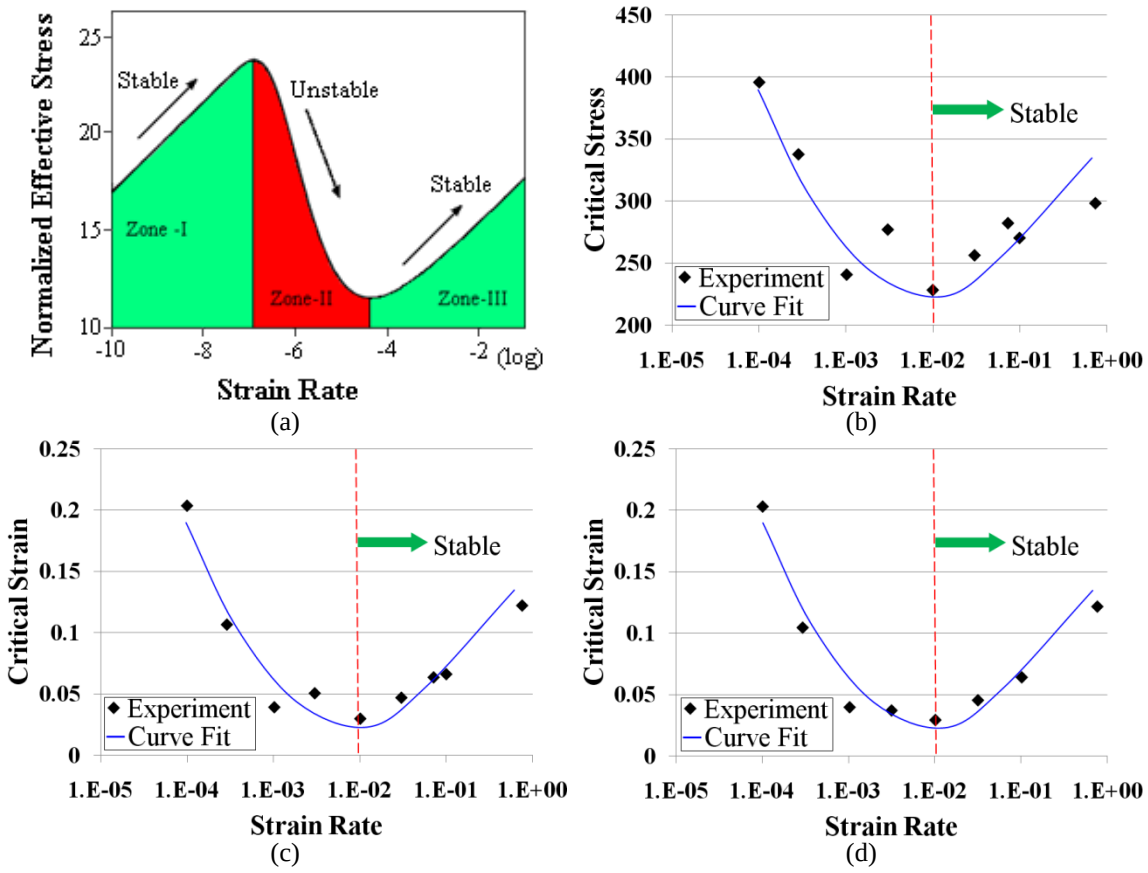

Figure 5-10: Stability maps for PLC effect; (a) Generic N-shaped stability map, adapted after [253], (b) stability map for Al2024 based on critical stress, digitized and adapted after [254], (c) stability map for Al2024 based on critical strain, digitized and adapted after [254] and (d) stability map for Al2024 based on critical strain, digitized and adapted after [261].

5.5.2 **Iterative methodology for the characterization of the hardening curve**

It is found that Al2024-T351 has flow softening. A maximum amount of three percent difference is observed between the flow stresses of the quasi-static uni-axial tension tests. It is also found that characterization of a stable hardening curve can start from a strain-rate of $1.0x10^{-2}s^{-1}$ considering the PLC effect. Moreover, considering that the impact performance evaluation of ductile materials will require strain-rates significantly higher and to keep numerical stability by assuming only strain-rate hardening a base hardening curve is characterized for a rate of $1.0x10^{-2}s^{-1}$. The base hardening curve is then scaled to

match other quasi-static test results while avoiding any cross overs among the hardening curves.

During the characterization, direct measurements from the load cell and DIC measurements are used to match the force vs. displacement field with the calculated finite element results. In order to eliminate any potential compliance in the testing apparatus (e.g., SHLF, grips), DIC measurements are desirable when possible. Therefore, Test #2.3 is chosen to represent the hardening behavior. A sample of the DIC strain field can be seen in Figure 5-11 for the plane-stress smooth specimen.

The gauge length of the specimen can be effectively chosen between any two points within the full field and be compared with the simulation results. Extension of the gauge length can be observed in Figure 5-11, which was initially selected as 4 mm.

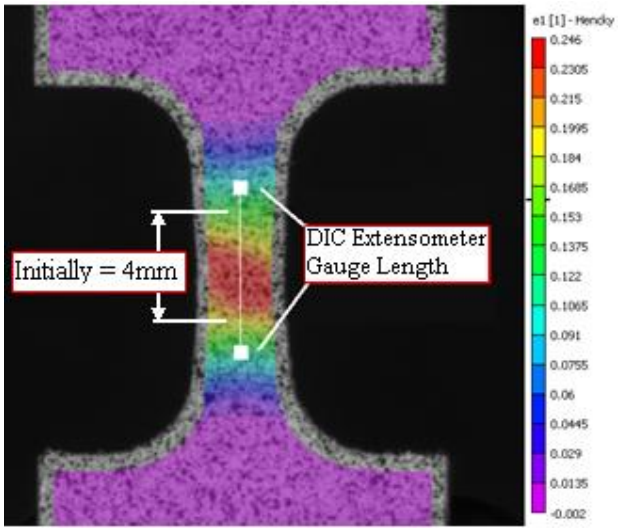

Figure 5-11: Illustration of the strain field with a given DIC extensometer.

Figure 5-12(a) illustrates the force vs. displacement data in raw (i.e., as-measured) format without any smoothing or curve fitting for Test #2.3 until the failure point. Engineering stress vs. engineering strain curve is obtained by using the DIC gauge length and the gauge width defined in Table C-2 as:

$$\sigma^0 = \frac{P}{A} = \frac{P}{wt}, \varepsilon^0 = \frac{L - L_0}{L_0} \tag{5.1}$$

where, σ^0 represents the engineering stress and ε^0 is the engineering strain. P is the load and A represents the initial area. w, t, L_0 and L represent the initial gauge width, thickness, length and final gauge length, respectively.

Figure 5-12(b) illustrates the engineering stress vs. engineering strain curve with the elastic modulus and yield point. Young's Modulus is found from the slope of the linear part of the $\sigma^0 - \varepsilon^0$ curve. Yield point is determined by using the traditional 0.2 percent strain-offset or proof-stress approach due to Hooke's law. The corresponding Young's Modulus and yield point is identified as:

$$\begin{aligned} E &\approx 73000\text{MPa} \\ \sigma_y &\approx 364\text{MPa} \\ \varepsilon_y &\approx 0.0052 \end{aligned} \tag{5.2}$$

where, E is the Young's Modulus, σ_y is the yield stress and ε_y is strain at yield point.

Assuming that the deformation within the gauge section will remain homogeneous until necking and volume is constant, true stress vs. true strain curve can be calculated according to the relation in Equation (5.3) and illustrated in Figure 5-12(c).

$$\begin{aligned} \varepsilon &= \ln(1 + \varepsilon^0) \\ \sigma &= \sigma^0(1 + \varepsilon^0) \end{aligned} \tag{5.3}$$

where, σ represents the true stress and ε is the true strain.

Figure 5-12(d) illustrates true stress vs. true plastic strain curve that is obtained by subtracting the elastic part from the true strain as:

$$\varepsilon^p = \varepsilon - \frac{\sigma_y}{E} \tag{5.4}$$

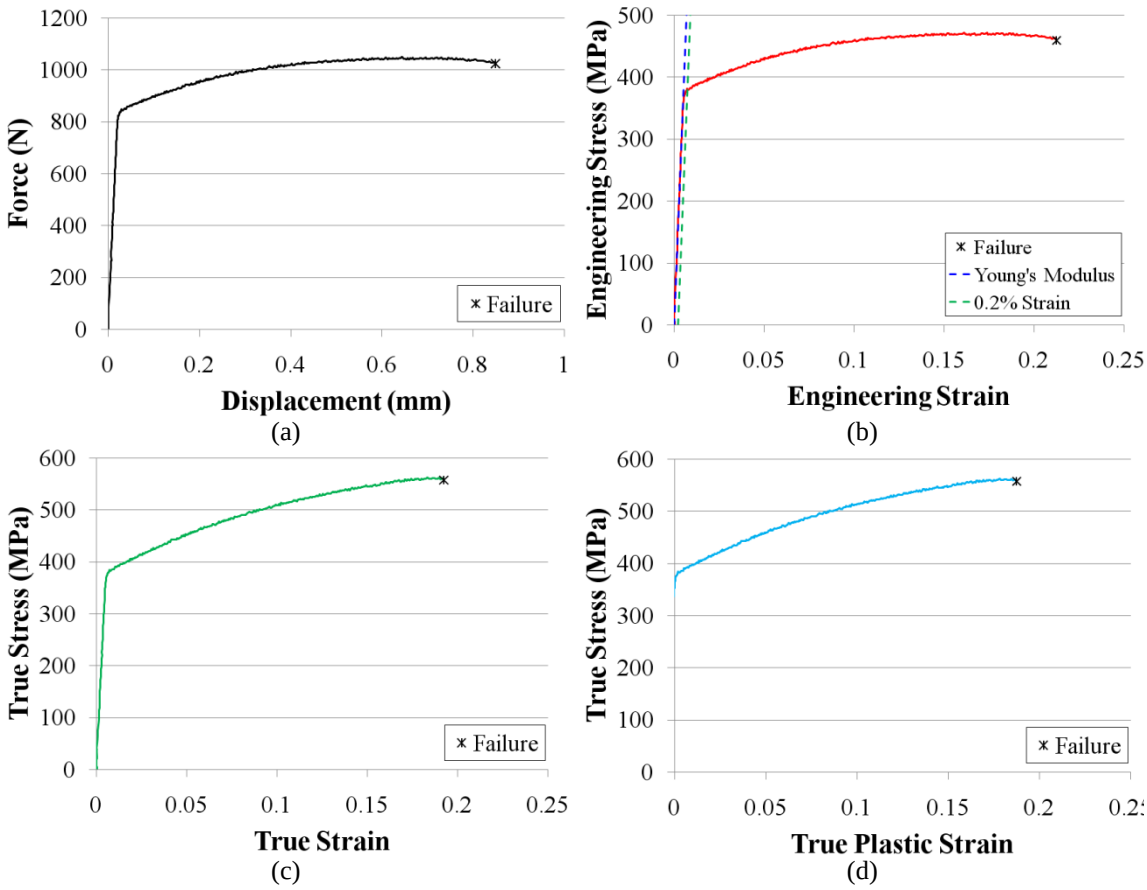

Figure 5-12: Methodology to obtain true plastic strain vs. stress raw data; (a) Force vs. displacement curve, (b) engineering stress vs. strain curve, (c) true stress vs. strain curve and (d) true plastic strain vs. stress curve.

Figure 5-11(d) shows the true stress vs. true plastic strain curve that is calculated from the raw (i.e., as-measured) force vs. displacement curve by applying the relations in Equations (5.1) - (5.4). It should be noted that the hardening curve, which is characterized from a uni-axial tensile test, is applicable only until the necking point due to tensile instability as the Equations (5.1) - (5.4) assume that the deformation and stress-state will remain homogeneous and that the state-of-stress will remain constant. Beyond the necking point, state-of-stress is not uni-axial tension anymore and the state-of-strain is no longer homogeneous. Therefore, the hardening curve cannot be used for FE simulations without correction [94] [251] [263] [264]. Flow behavior also becomes mesh dependent after the necking point, which can increase the number of FE simulations dramatically based on the mesh size. Therefore, a semi-empirical technique is introduced in this

section for the iterative methodology, where the number of FE simulations can be reduced considering the mesh sensitivity.

The methodology starts by identifying the necking point. A quadratic nine point-average Savitzky and Golay smoothing algorithm [265] is utilized first to filter the true stress vs. true plastic strain raw (i.e., as-measured) data as illustrated in Figure 5-12. The smoothing procedure can be customized depending on how noisy the test data is. The key is to smooth the curve without losing any significant details.

Considère's criterion for diffuse necking, which identifies the plastic instability when the increase in stress due to decrease in the cross-sectional area is greater than the increase in load bearing capacity of the specimen due to work hardening, is then applied to find the necking point [95] [266] [267] [268]. Diffuse necking begins at a point, where the rate of strain hardening is equal to the true stress as shown in Figure 5-13 by utilizing the smoothed true stress vs. true strain curve as [94]:

$$\frac{d\sigma}{d\varepsilon} = \sigma \tag{5.5}$$

Necking point is determined as:

$$\begin{aligned} \sigma_n &\approx 544\text{MPa} \\ \varepsilon_n &\approx 0.148 \end{aligned} \tag{5.6}$$

Figure 5-14 illustrates and Table 5-4 summarizes notable points on three hardening curves respectively based on the relations described in Equations (5.1) – (5.5). These points are used later in this section to describe the iterative methodology for the characterization of the hardening curve after necking.

It should be noted that while Considère's criterion is derived from a power law representing the stress-strain behavior (i.e., Hollomon's equation [269]); it also works for stress-strain behaviors which do not obey a power law but still exhibit a smooth hardening characteristics. Therefore, Considère's criterion should be applied to the materials with PLC effect under the condition that the results are measured inside one of the safe zones as described by Figure 5-10(a). Outside the safe zone, strain hardening

rates exhibit a highly oscillatory behavior due to the PLC effect that can cross over with the hardening curve at multiple locations, where the Considère's criterion is not met and can lead to an erroneous identification of the necking point [270] [271] [272].

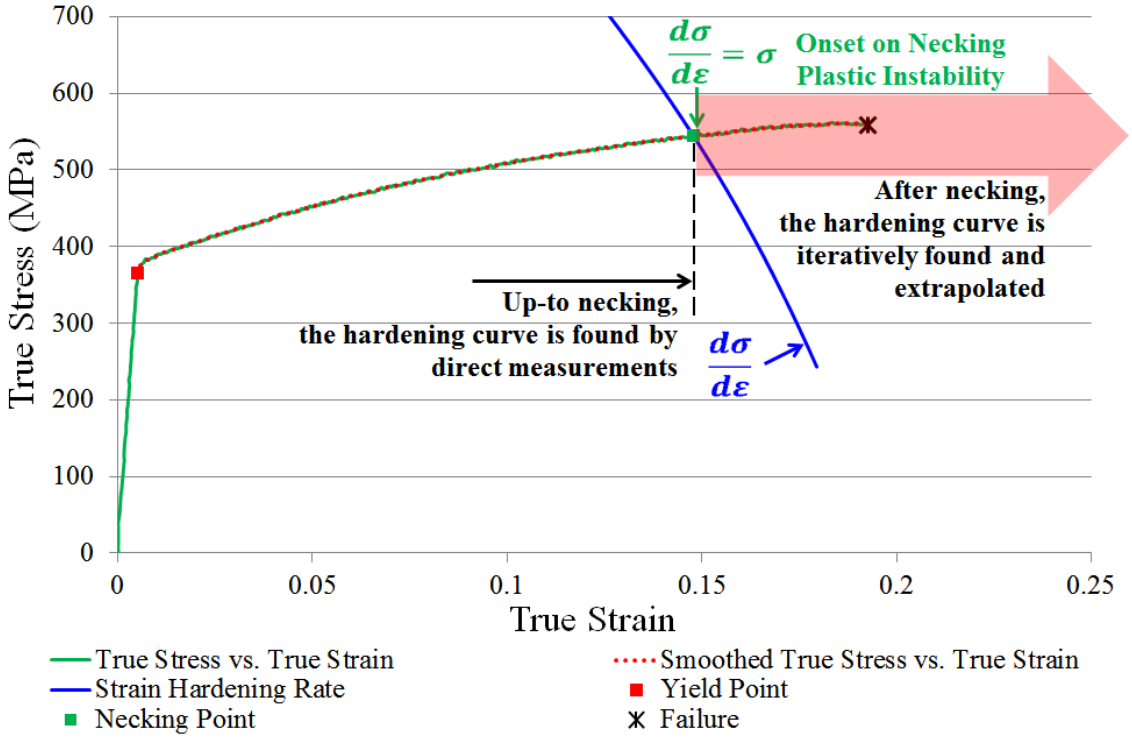

Figure 5-13: Smoothed true stress vs. true strain curve and the onset on necking.

Table 5-4: Notable points on hardening curves.

Notable Points	Engineering Stress vs. Strain	True Stress vs. Strain	True Stress vs. Plastic Strain
■ Yield Point	$\sigma_y \approx 364\text{MPa}$ $\varepsilon_y \approx 0.0052$		
■ Necking Point	$\sigma_n^0 \approx 469\text{MPa}$ $\varepsilon_n^0 \approx 0.159$	$\sigma_n \approx 544\text{MPa}$ $\varepsilon_n \approx 0.148$	$\sigma_n \approx 544\text{MPa}$ $\varepsilon_n^p \approx 0.143$
✱ Failure Point	$\sigma_f^0 \approx 461\text{MPa}$ $\varepsilon_f^0 \approx 0.212$	$\sigma_f \approx 559\text{MPa}$ $\varepsilon_f \approx 0.192$	$\sigma_f \approx 559\text{MPa}$ $\varepsilon_f^p \approx 0.1875$

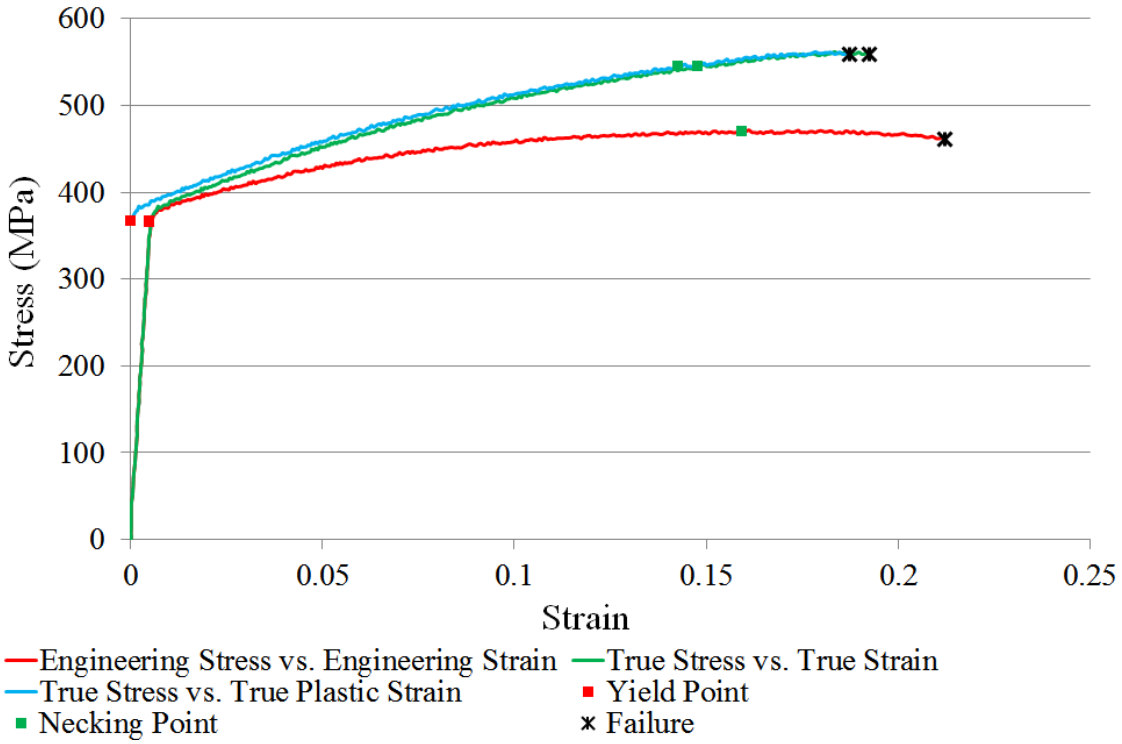

Figure 5-14: Yield, necking and failure points on the hardening curves.

Considering the applications where post necking behavior is expected and the total strain value will exceed the onset on necking, a methodology has to be developed to obtain the true stress vs. true strain relation after necking as the relation given by Equation (5.3) is not valid anymore beyond necking [94] [251] [263] [264]. It should also be noted that the true stress vs. true strain relation that is characterized from a uni-axial tensile test until the failure point can only cover up to twenty percent strain (i.e., for Al2024-T351) because the effects of strain localization do not permit further deformations. Therefore, true stress vs. true strain relation should be extrapolated for applications that will require larger deformations before failure [251].

There are two common approaches that can be followed to approximate the true stress vs. true strain relation after necking [99] [104]. The first approach is using a scaling technique, where true stress is estimated by applying a correction or weighting factor on the equivalent stress based on the continuous measurements of the neck geometry evolution. Bridgeman [95], Le Roy [120] and Alves and Jones [16] have used correction techniques based on the Bridgeman relation. For axi-symmetric cylindrical specimens in

uni-axial tension, Bridgeman's correction for diffuse necking scales the equivalent stress with a semi-empirical relation depending on the altering neck geometry as illustrated in Figure 5-15 [95]. However, Bridgeman's correction necessitates three conditions that must be satisfied:

1- A uniform distribution of the strain within the gauge cross-section;

2- An accurate measurement of the evolution of the neck geometry that has an idealized pre-determined shape;

3- A constant ratio between the principle stresses during the loading, where the total strains can easily be related to stresses empirically [263].

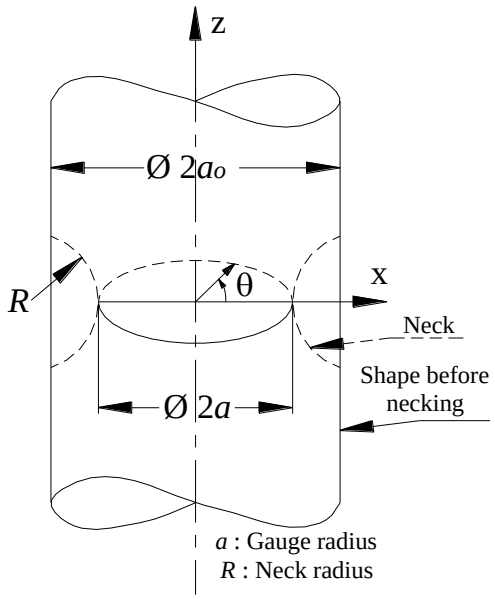

$$\bar{\varepsilon} = 2\ln\left(\frac{a_0}{a}\right)$$

$$\sigma_{xx} = \sigma_{yy} = \bar{\sigma}\ln\left(\frac{a^2 + 2aR - x^2}{2aR}\right)$$

$$\sigma_{zz} = \bar{\sigma}\left[1 + \ln\left(\frac{a^2 + 2aR - x^2}{2aR}\right)\right]$$

Figure 5-15: Bridgman's correction for diffuse necking on axi-symmetric cylindrical specimen geometry in tension.

Nevertheless, Alves and Jones reported large differences between the FE simulations and Bridgeman's correction for predicting equivalent strain and stress-triaxiality [16]. Bao also found significant differences between the FE simulations and Bridgeman's correction during the evolution of equivalent stress and equivalent strain predictions, which were calculated for the minimum cross-section of the gauge section of an axi-symmetric cylindrical specimen [99] [273].

Unlike axi-symmetric cylindrical specimens in tension, specimens with a rectangular cross-section exhibit an additional necking instability, which is called localized necking. Both necking mechanisms are schematically illustrated in Figure 5-16 for a rectangular bar under uni-axial tension. Due to non-homogeneous progress of the deformation within the necking zone and localized necking, three conditions that are required for correction methodologies (i.e., Bridgman's correction) are no longer fulfilled given:

1- A non-uniform distribution of the strain within the gauge cross-section;

2- A complex necking geometry with un-symmetrical and non-uniform evolution;

3- A variable ratio between the principle stresses during the loading, where the stress distribution at the gauge region can be calculated by using the incremental theory of plasticity [263].

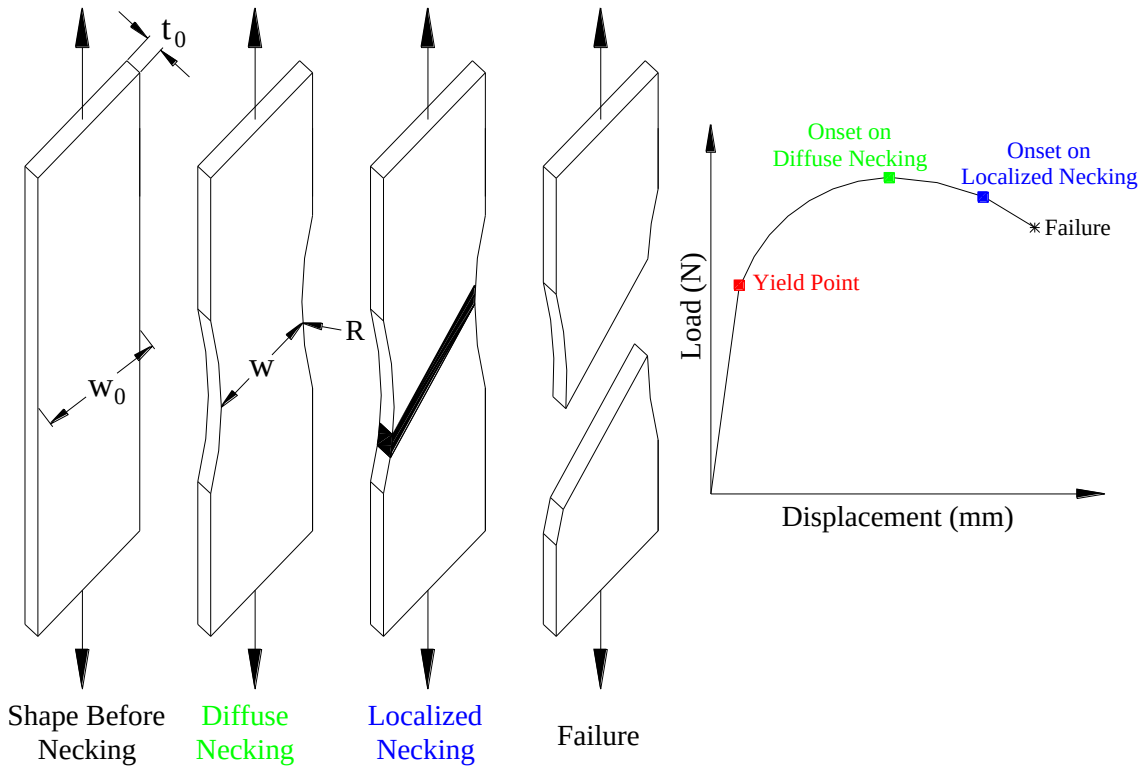

Figure 5-16: Schematic illustration of the necking mechanisms developing during the progressive deformation of a rectangular bar under uni-axial tension up to failure.

Although there has been major improvements to Bridgeman's correction such as the 'MLR model' that has been suggested by La Rosa, et al. [274] and Mirone [275] [276]

[277] recently in a series of investigations with several different materials and notch geometries, for specimens with a rectangular cross-section (i.e., strips, sheet metals) there is no standardized method that can be applied [263] [264] [278] [279] [280].

The second approach to approximate the true stress vs. true strain relation after necking is a trial-and-error method, where the true stress vs. strain relation after necking is adjusted inversely with successive FE simulations by using a weighting or penalty factor that is applied on the initial true stress vs. true strain input based on the comparison between the measured and calculated force vs. displacement (i.e., load vs. elongation or area reduction) responses [99] [263] [281]. Single or multiple objective functions can be assumed to modify the initial true stress vs. true strain relation while trying to minimize the differences between the FE simulation and the test results. One of the most common approaches is to use a penalty factor on the initial true stress vs. true strain relation based on a relative error, which is calculated from the overall difference between the load vs. elongation response or the difference between the targeted load at a particular elongation [282] [268]. Optimization techniques are often utilized to reduce the number of required FE simulations during the inverse determination of the material parameters or in that case the shape of the true stress vs. true strain curve by approximating the material response with special functions [251] [283] [284] [285] [286] [287]. Koc and Stok [288] compared the predictive performance of some of the most commonly used functions that are utilized to describe the flow behavior of a austenitic stainless steel and a low alloy steel, where it was suggested that the 'fitting accuracy is the most important factor' because there is no significant difference among Hollomon's, Swift's and Ludwig's law in describing the flow curves of materials beyond necking. However, it should be noted that these functions should be used with care especially during the calculations for very high strains if they are based on an extrapolation of the stress vs. strain curve depending on the data before necking as formulated by Ling [263] for a power law. It should also be noted that computationally costly non-linear FE simulations, which are repeated with several different variables to minimize the difference between the experimentally measured data and the simulated response, are required to identify the material model parameters when non-linear optimization techniques are utilized. Therefore, Stander, et al. [287] used a successive response surface methodology to reduce the cost of the overall optimization

process by incorporating an approximation function over the responses and by utilizing a *D*-optimality criterion for the sampling, where convergence was achieved within only ten successive iterations.

Physics based constitutive models, such as the Gurson-Tvergaard-Needleman (GTN) model, are often used to describe the flow and yield surface [123] [124] [129] [289]. Duan, et al. [272] discussed the characterization details of the GTN model and acknowledged some weaknesses such as having too many parameters, parameters without physical meaning and difficulties in determining some of the parameters experimentally. They also mentioned that GTN model calibration for some ductile materials, such as AA5754, AA6111, DQAK, and DP600, is not appropriate considering that the void nucleation is not observed until the 'intense-shear band formation', which occurs very close to the fracture surface, and suggested using Hollomon's [269] and Voce's [290] law instead.

Remarkable improvements are achieved during the last decade for measuring the evolution of the deformed specimen geometry by using DIC or Digital Speckle Photography (DSP), where the local strains are also taken into account during the calculation of the true stress vs. strain relation [247]. Scheider, et al. [291] used a second order polynomial to represent the correction function for different materials based on the DIC measurements and inverse calculations.

An iterative method is often preferred to predict the part of the hardening curve beyond the necking point by using FE models with different mesh sizes and changing the curve by a power or Swift's law [292] sequentially until finding the best results. Automated algorithms can also be utilized to solve this exhaustive procedure. However, neither method really gets around the need for a trial and error approach to solve the problem. A new approach here is suggested depending on the number of elements that might contribute to the necking.

Consider Figure 5-17; beyond the necking point all plastic strains will localize in a very small area which will be within the neck. As we know the necking and failure points from Table 5-4, we can compute the additional elongation of the specimen after necking as:

$$\Longrightarrow L_0 = nl_0$$

$$\left.\begin{array}{l}\text{Engineering Strain at Necking} \\ \varepsilon_n^0 = \dfrac{L_n - L_0}{L_0} \Longrightarrow \varepsilon_n^0 L_0 = L_n - L_0 \\ \text{Engineering Strain at Failure} \\ \varepsilon_f^0 = \dfrac{L_f - L_0}{L_0} \Longrightarrow \varepsilon_f^0 L_0 = L_f - L_0\end{array}\right\} \Delta L = L_f - L_n = L_0\left(\varepsilon_f^0 - \varepsilon_n^0\right) \tag{5.7}$$

where, L_0 is the initial gauge length, n is the number of elements, l_0 is the initial length of the single element. L_n and L_f are the gauge lengths, where ε_n^0 and ε_f^0 are the engineering strains at the necking and failure points, respectively. Given the values in Table 5-4 and a gauge length of $L_0 = 4\text{mm}$, additional elongation to failure after necking can be calculated as:

$$\Delta L = L_f - L_n = L_0\left(\varepsilon_f^0 - \varepsilon_n^0\right) = 4(0.212 - 0.159) = 0.211\text{mm} \tag{5.8}$$

The local strain can be estimated by relating this elongation to the mesh length since all deformation will localize in a single row of elements. Consider that the specimen is meshed with 4, 8 and 12 elements over the width, where the width of the sample is given as $w = 2.9972\text{mm}$. True failure strain for each element characteristic length can be obtained.

$$\begin{aligned} l_0 &= \frac{w}{n} = \frac{2.9972}{4 \vee 8 \vee 12} \\ \varepsilon_f &= \ln\frac{l}{l_0} = \ln\left(\frac{\Delta l}{l_0} + 1\right) = \ln\left(\frac{\Delta l_n + \Delta l_f}{l_0} + 1\right) = \ln\left(\varepsilon_n^0 + \frac{\Delta L}{l_0} + 1\right) \\ &= \ln\left(0.159 + \frac{0.211}{l_0} + 1\right) \end{aligned} \tag{5.9}$$

where, $\frac{l}{l_0}$ is the stretch ratio of a single element, $\Delta l_f = \Delta L$ is the additional elongation of a single element after necking assuming all elongation due to necking occurs in a single element and $\frac{\Delta l_n}{l_0} = \varepsilon_n^0$ is the engineering strain of every element at necking.

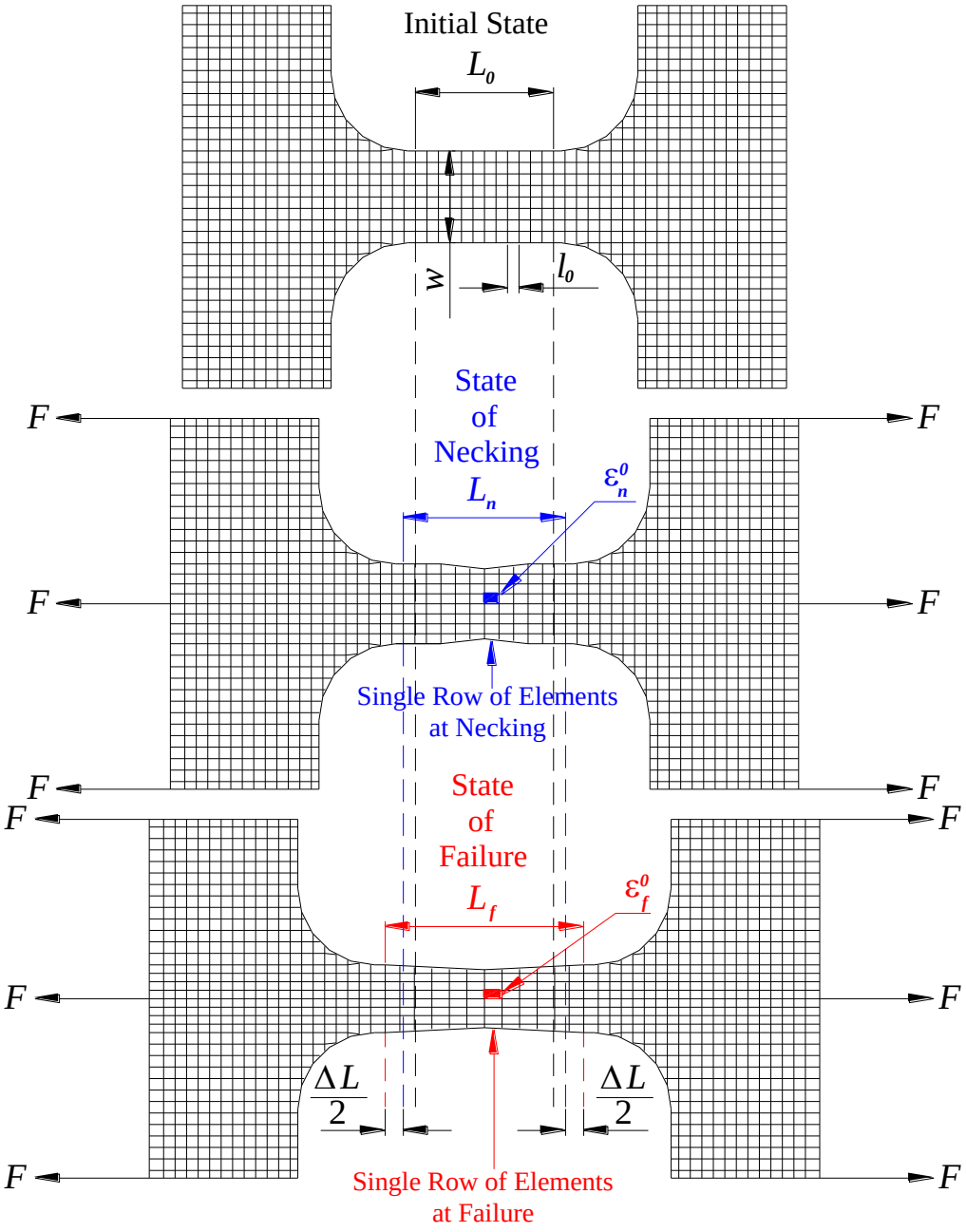

Figure 5-17: Determination of the hardening curve beyond the necking point.

The failure stress in a single element can be found similarly:

$$\sigma_f = \sigma_f^0 = 461\text{MPa}\,\frac{l}{l_0} \tag{5.10}$$

Therefore, plastic strain at failure of a single element is:

$$\varepsilon_f^p = \varepsilon_f - \frac{\sigma_f}{E} \tag{5.11}$$

Table 5-5 lists the failure strain and stress prediction depending on the number of elements used in the neck area. However, physically, localization is gradual rather than immediate and the procedure should be repeated assuming that localization takes place in n^*= 2 and 3 element rows rather than only 1. In reality, a transition takes place with the deformation localizing gradually from the entire gage length to a single element row. Therefore, inspecting the different number of element rows at the neck region, failure strain and stress prediction depend on the number of elements as shown in Table 5-6.

Table 5-5: Predicted failure parameters for number of elements in the neck area.

Number of Elements n	Stretch Ratio $\frac{l}{l_0}$	Failure Strain ε_f	Failure Stress (MPa) σ_f	Plastic Failure Strain ε_f^p
4	1.441199	0.365476	664.3929	0.356374
8	1.722872	0.543992	794.2438	0.533112
12	2.004544	0.695417	924.0947	0.682758

Table 5-6: Predicted failure parameters for different row of elements in the neck area.

Number of Elements / Number of Rows at Neck n/n^*	Stretch Ratio $\frac{l}{l_0}$	Failure Strain ε_f	Failure Stress (MPa) σ_f	Plastic Failure Strain ε_f^p
4 / 1	1.441199	0.365476	664.3929	0.356374
4 / 2	1.300363	0.262644	599.4674	0.254432
4 / 3	1.253418	0.225874	577.8256	0.217959

A power law can then be used to represent the hardening curve after necking by using the following systems of equations:

$$\sigma_y = k\left(\varepsilon_e + \varepsilon_p\right)^m \Longrightarrow \begin{cases} \sigma_n = k\left(\varepsilon_e + \varepsilon_n^p\right)^m \\ \sigma_f = k\left(\varepsilon_e + \varepsilon_f^p\right)^m \end{cases} \tag{5.12}$$

$$\frac{\partial \sigma_y}{\partial \varepsilon_p} = kn\left(\varepsilon_e + \varepsilon_p\right)^{m-1} \Longrightarrow \sigma_n = k\left(\varepsilon_e + \varepsilon_n^p\right)^m \approx kn\left(\varepsilon_e + \varepsilon_n^p\right)^{m-1}$$
$$\Longrightarrow \varepsilon_e = m - \varepsilon_n^p$$
$$\Longrightarrow \sigma_f = \frac{\sigma_n}{m^m}\left(m + \varepsilon_f^p - \varepsilon_n^p\right)$$

Three non-linear equations are derived and solved by using the values for stress and plastic strain at necking and failure for four elements over the width as:

$$\sigma_y = k\left(\varepsilon_e + \varepsilon_p\right)^m \Longrightarrow \begin{cases} \sigma_n = km\left(\varepsilon_e + \varepsilon_n^p\right)^{m-1} \\ \sigma_n = k\left(\varepsilon_e + \varepsilon_n^p\right)^m \\ \sigma_f = k\left(\varepsilon_e + \varepsilon_f^p\right)^m \end{cases} \tag{5.13}$$

The coefficients of the solution are listed in Table 5-7 and the corresponding curves are plotted in Figure 5-16.

Table 5-7: Predicted coefficients for the power law plasticity for different row of elements at the necking area.

Number of Elements / Number of Rows at Neck	Stretch Ratio	Failure Strain	Failure Stress (MPa)	Plastic Failure Strain	Power Law Coefficients		
n/n^*	$\frac{l}{l_0}$	ε_f	σ_f	ε_f^p	k	ε_e	m
4 / 1	1.441199	0.365476	664.3929	0.356374	457.664	1.0198	1.1626
4 / 2	1.300363	0.262644	599.4674	0.254432	785.228	0.1847	0.328
4 / 3	1.253418	0.225874	577.8256	0.217959	709.737	-0.014	0.1294

Figure 5-18 illustrates the comparison of the hardening curves that are extrapolated by using the coefficients of the power law plasticity beyond the necking point. Extrapolation is performed until a plastic strain of 100% is reached considering that the material should fail before. It should be noted that the number of elements that are contributing to necking have a significant effect on the prediction of the hardening characteristics. It should also be noted that $m > 1$ is not a realistic value for metals. Therefore, an inverse methodology should be followed while estimating the characteristics of the true stress vs. true plastic strain curves as an input for the material model. The predictive performance of a hardening curve can be evaluated by using a

direct comparison of the force vs. displacement curves as illustrated in Figure 5-19 by utilizing the smooth plane-stress specimen in Figure B-1. Fully integrated, eight-noded 3D solid elements are used for the model. Figure 5-19 illustrates the comparison between the FE prediction and the force versus displacement of Test #2.3. The FE calculation and comparison for the hardening curve in Figure 5-19 does not include the failure algorithm yet. The failure strains for the specimens are characterized in the proceeding sections.

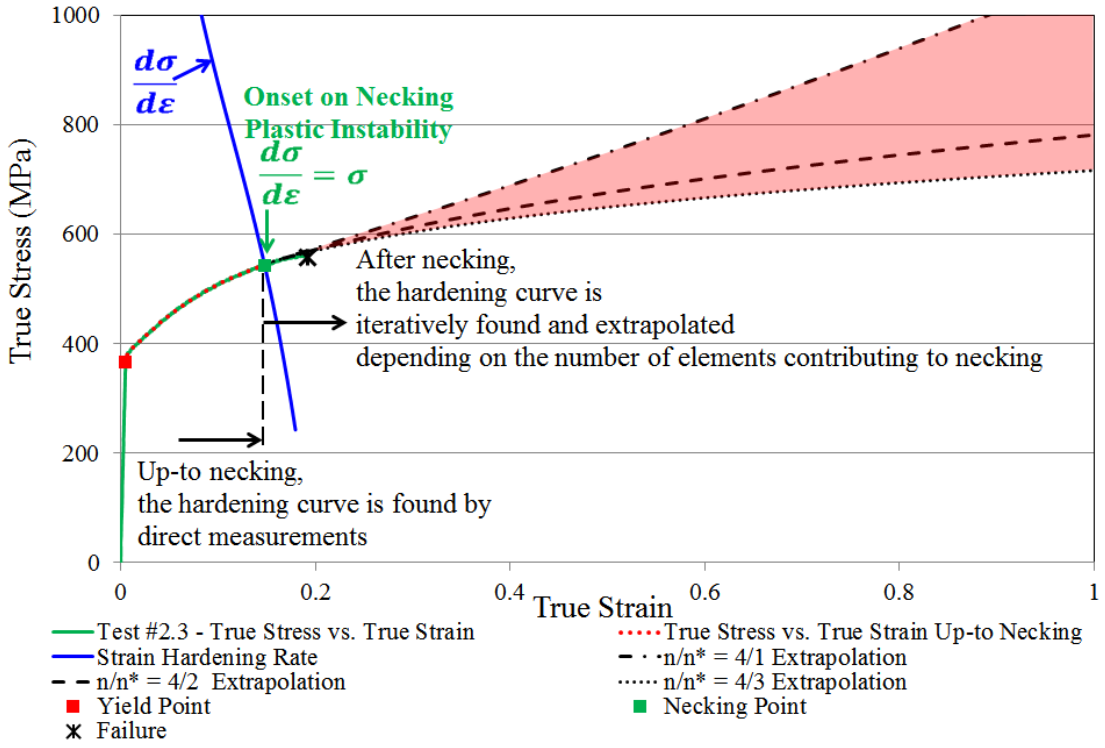

Figure 5-18: Hardening curves for different number of rows in the neck area beyond necking point.

Table 5-8 lists the amount of error between the force vs. displacement curve of the Test #3.2 and the simulation results when the power law plasticity is utilized as an input curve with the given coefficients in Table 5-7. The error is the normalized difference between the areas under the force vs. displacement curves.

It is concluded that the best curve approximation to the experimental results is reached by the $n/n^* = 4/3$ extrapolation. Therefore, it is chosen to represent the baseline for quasi-static hardening characteristics for Al2024-T351. It should be noted that the first part of the hardening curve up-to necking is explicitly used in this analysis.

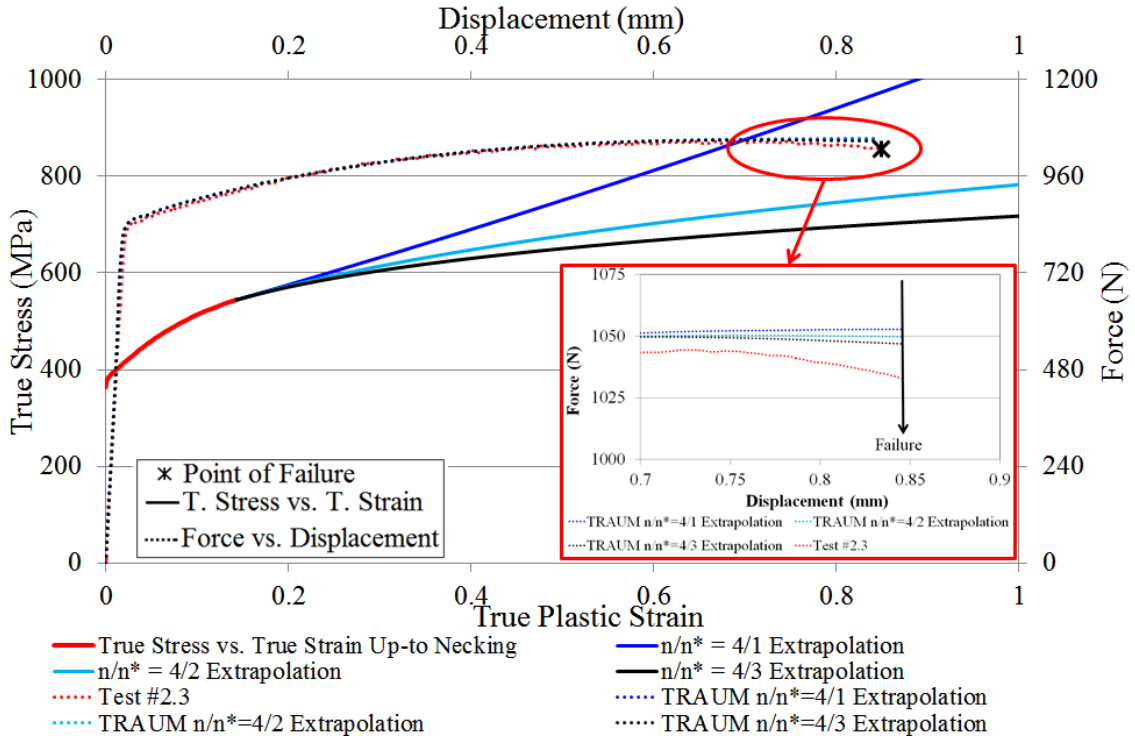

Figure 5-19: Comparison of the prediction performance of the extrapolated hardening curves.

Table 5-8: Amount of error between the test and the simulation results for different hardening characteristics.

Number of Elements / Number of Rows at Neck n/n^*	Error %
4 / 1	1.1047
4 / 2	0.5343
4 / 3	0.3847

Deformation and failure behavior of Al2024-T351 has been investigated by many other researchers. Figure 5-20 represents a comparison between the quasi-static hardening curves in the literature and the newly characterized curve. The curves are suggested by Lesuer [41], Johnson and Cook [84], Bai and Wierzbicki [105], Seidt [108], MIL-HDBK-5H [225], Teng and Wierzbicki [293] and Bai, et al. [294]. The effects of using different

flow behavior is also studied by Mahmoud and Lease for Crack-Tip-Opening-Angle (CTOA) predictions, where the influence of the hardening behavior was discussed [295].

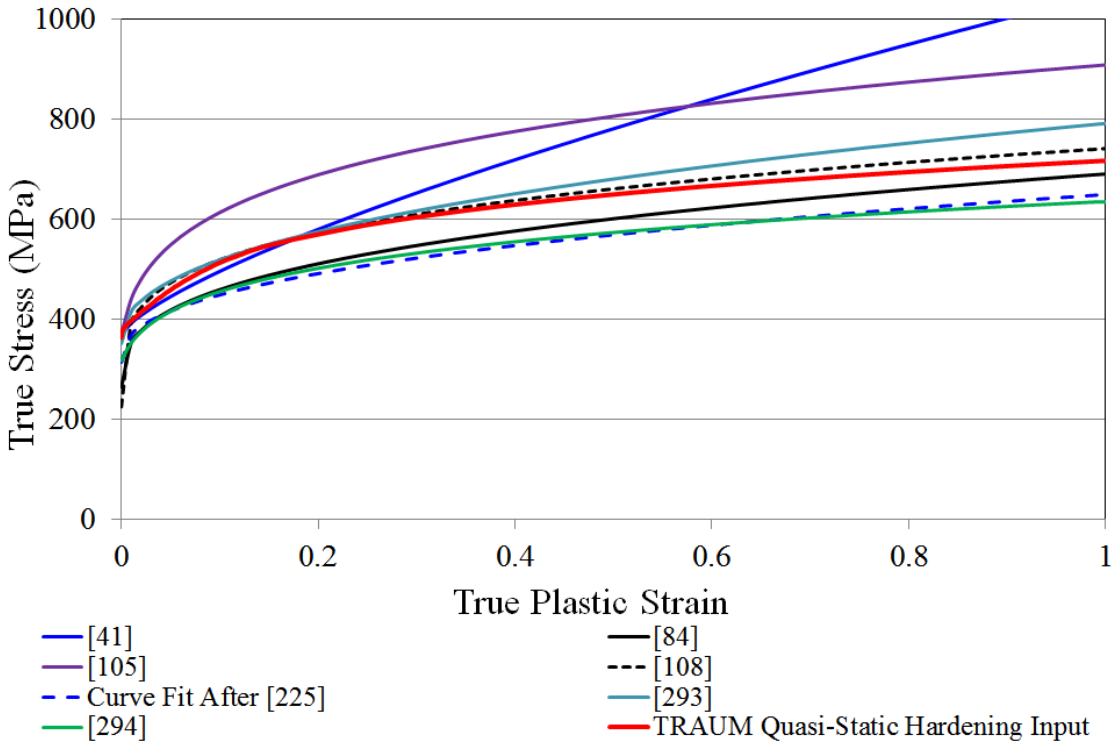

Figure 5-20: Comparison of the quasi-static hardening curves for Al2024-T351 by other researchers.

The distribution and differences in the hardening characteristics are noticeable for some of the cases, where the main difference is due to the utilization of compression or torsion tests for the characterization process. Nevertheless, it is a common practice to carry material model parameters assuming that the mechanical and characteristic properties of each material will be equivalent independent of the supplier, specific lot and the differences during the manufacturing stage, which can affect the characteristics significantly. Therefore, it is advisable to characterize each material rather than just plugging in the coefficients or parameters that can be obtained from the literature. TRAUM encourages and promotes tabulated inputs of the flow and failure surfaces rather than carrying parameters that can only partially capture the behavior.

The mesh sensitivity of the flow behavior is investigated by using seven different characteristic element sizes for the quasi-static uni-axial test at room temperature (i.e.,

Test #2.3). The element dimensions are listed in Table 5-9 and the corresponding figures for the mesh patterns are illustrated in Appendix–E. It is shown in Figure 5-21 that the flow behavior is consistent even though very diverse characteristic element lengths are used with the same input for the hardening curve. It can be seen that with the increasing mesh density, the flow behavior can be predicted more accurately.

Table 5-9: Mesh patterns that are used to test the mesh dependency of the flow behavior for the characterized quasi-static hardening curve.

Mesh Pattern #	Specimen #	Element Dimensions [mm]			Corresponding Notation for the Mesh Pattern	Characteristic Element Length [mm]
		l_x	l_y	l_z	Thickness*/Number of Elements	
1 [Figure E-1]†	1 [Figure B-1]§	0.8000	0.7493	0.7417	[t/1]	0.7417
2 [Figure E-2]†		0.3636	0.3747	0.3708	[t/2]	0.3636
3 [Figure E-3]†		0.2500	0.2498	0.2472	[t/3]	0.2472
4 [Figure E-4]†		0.1905	0.1873	0.1854	[t/4]	0.1854
5 [Figure E-5]†		0.1538	0.1499	0.1483	[t/5]	0.1483
6 [Figure E-6]†		0.0769	0.0749	0.0742	[t/10]	0.0742
7 [Figure E-7]†		0.0385	0.0375	0.0371	[t/20]	0.0371

§ Detailed geometry of the specimen is illustrated in Appendix–B.
† Corresponding FE models are illustrated in Appendix–E.
* Thickness for Test #3.2 : [t = 0.74168 mm]

However, the repeatability of the predicted flow behavior suggests that a fixed mesh size can be utilized for simulating the flow behavior since the maximum difference does not exceed 1%. Therefore, to generate the strain-rate and temperature dependent flow surface of Al2024-T351, an element length of 0.15mm is chosen for convenience considering the computational costs and accuracy. It should also be noted that the comparison in Figure 5-21 does not include the effects of regularized failure yet and the simulations were interrupted manually when the displacement at failure is reached.

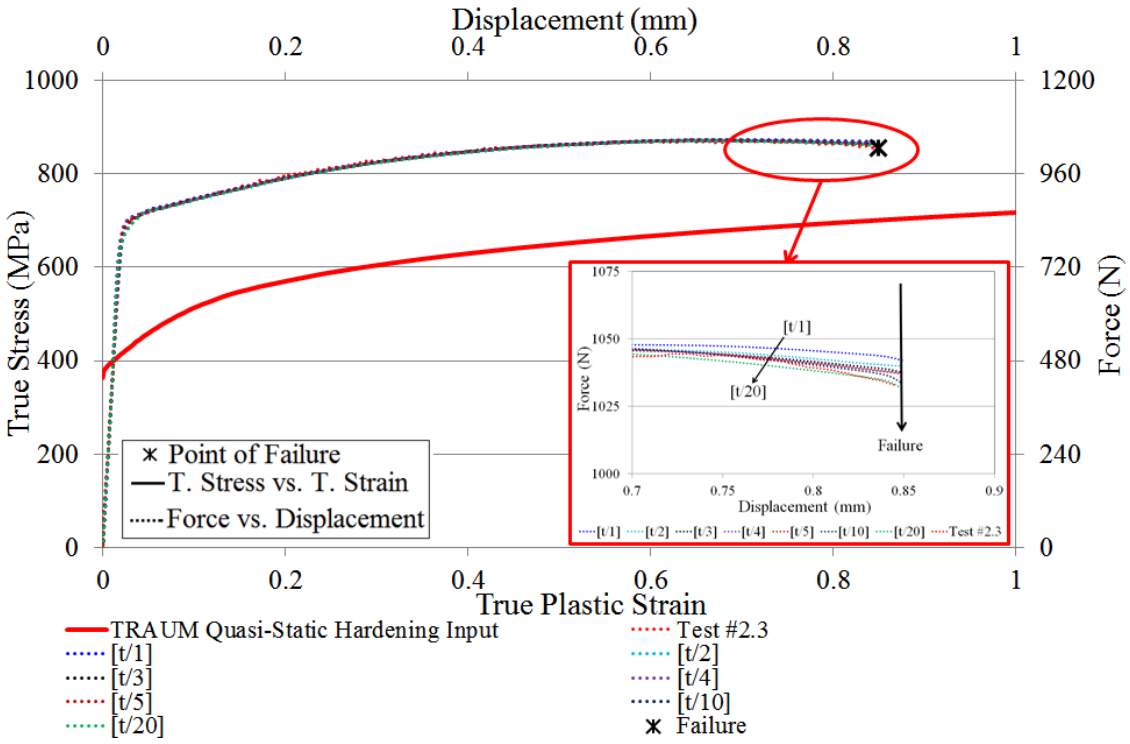

Figure 5-21: Characterized quasi-static hardening curve at room temperature for Al2024-T351 and predicted force vs. displacement curves with different characteristic element lengths.

5.5.3 **Verification of the quasi-static hardening curves for axi-symmetric tension at room temperature**

It is shown in Figure 5-8 that the flow characteristics of the quasi-static uni-axial tests at room temperature are close to each other and can be represented by scaling a baseline according to the strain-rate dependency, where a strain-rate hardening is desirable to assure numerical stability. By using an iterative methodology, the baseline for the hardening behavior is characterized and illustrated in Figure 5-21. The baseline is scaled 1% and positive strain-rate hardening characteristics are imposed on the behavior for the quasi-static regime at room temperature as illustrated in Figure 5-22.

Characterized input curves are verified by comparing with the force vs. displacement curves for different strain-rates. The verification results are illustrated in Appendix–F. Figure F-1 shows the comparison of the TRAUM simulations with the corresponding test results by using the input curves that are given in Figure 5-22 at a targeted strain rate of $1.0x10^{-4}s^{-1}$. Similarly, Figures F-2 and F-3 illustrate the comparisons for targeted strain-

rates $1.0x10^{-2}s^{-1}$ and $1.0s^{-1}$, respectively. Given the repeatability of the test results, it is verified that the characterized hardening curves can accurately capture the flow behavior and can be used for validation purposes.

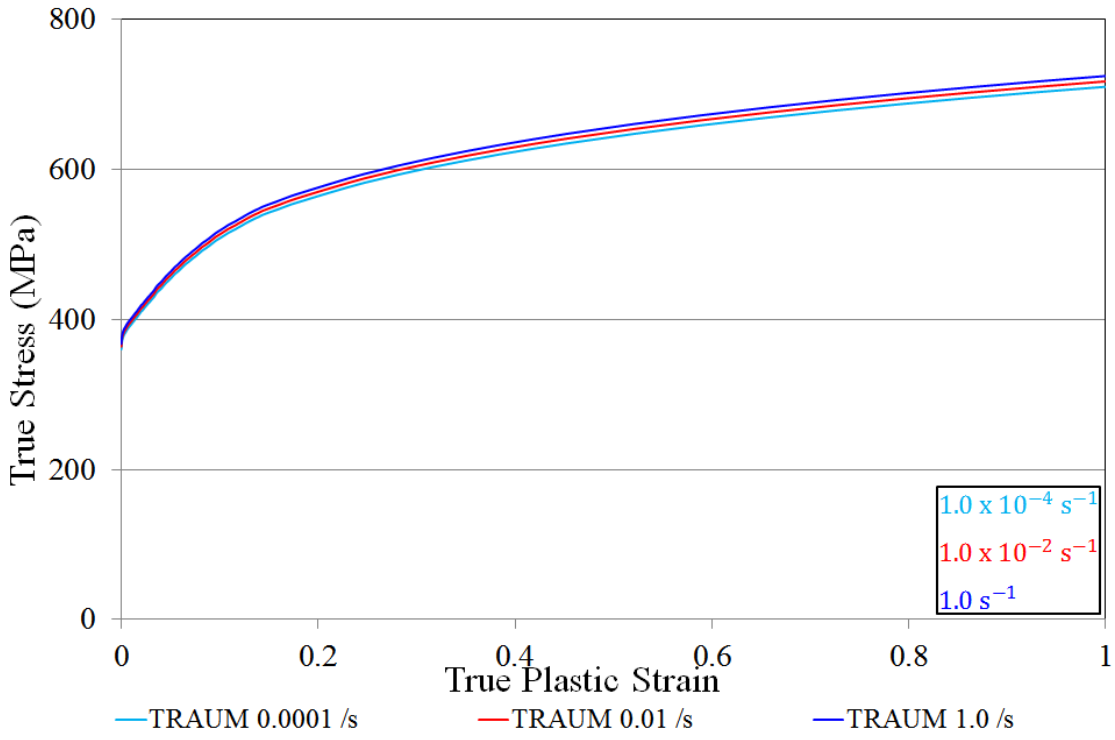

Figure 5-22: Strain-rate dependent quasi-static hardening curves at room temperature.

Quasi-static hardening curves are also verified by using a smooth axi-symmetric specimen test under uni-axial tension at room temperature. Considering that the smooth plane-stress and the smooth axi-symmetric specimens share the same stress-triaxiality and Lode-angle-parameters, the accuracy of the characterized hardening curves can be verified by comparing the flow behavior of two different test cases with the same state-of-stress. Table 5-10 lists the details about the test cases for the axi-symmetric specimens in uni-axial tension. More information can be found in Appendix–C for the test cases, where Table C-4 lists the parameters of the tests and Figure C-4 illustrates the force vs. displacement and true stress vs. true strain curves for 'nominal' values. Accuracy of the hardening curves are verified in Figure F-4 with TRAUM by comparing force vs.

displacement curves for two different gauge lengths, where global and local effects during the flow and failure are shown.

Table 5-10: Test cases that are used to verify quasi-static hardening curve at room temperature.

Test #	Specimen #	Test Apparatus	Loading	Actuator Velocity [mm/s]	Targeted Equivalent Strain Rate [s^{-1}]	Temperature [K]	Extensometer Gage Length L_0 [mm]
4 [Figure C-4]† [Table C-4]‡	5 [Figure B-5]§	SHLF*	Uni-axial Tension	2.413×10^{-1}	1.0×10^{-2}	Room Temperature	22.3
				2.413×10^{-1}			
				2.413×10^{-1}			4.0

* Servo-Hydraulic Loading Frame (SHLF).
† Test results for the corresponding specimen, strain-rate and temperature illustrated in Appendix–C.
‡ Test results for the corresponding specimen, strain-rate and temperature listed in Appendix–C.
§ Detailed geometries and corresponding FE models of the specimens are illustrated in Appendix–B.

It is shown in Figure 5-23 that the flow characteristics of two different test specimens, which are sharing the same stress-triaxiality and Lode-angle-parameter, are identical and can be predicted accurately by TRAUM.

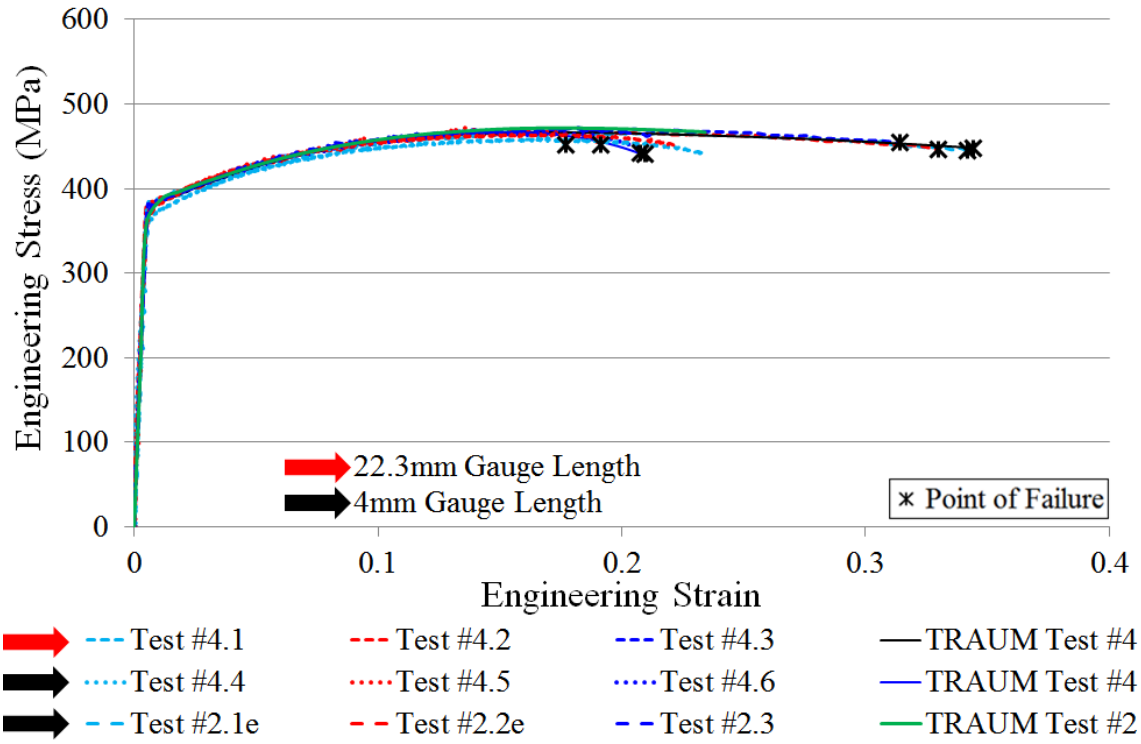

Figure 5-23: Verification of the hardening curves for plane-stress and axi-symmetric specimens sharing the same stress-triaxiality.

Engineering stress vs. engineering strain behavior describes the flow behavior is following the same path until the localization of failure, which will be characterized and regularized later in this chapter. It is verified that by using the same hardening curves as input, calculated stress vs. strain response is found identical and it can be concluded that the flow behavior of the material can accurately be represented by the hardening curves that are illustrated in Figure 5-22 for quasi-static regime at room temperature.

Further comparisons are assessed in the proceeding sections during the characterization of the failure strains for specimens with different states-of-stress.

5.5.4 **Verification of the quasi-static hardening curves for uni-axial compression at room temperature**

The hardening curves that are characterized by using tension tests and illustrated in Figure 5-22 are verified by using quasi-static uni-axial compression tests at room temperature. Beyond the necking point, tension tests do not provide a uni-axial state-of-stress and should be corrected as discussed in Section 5.5.2. Therefore, it is common to extrapolate the stress vs. strain relation by using compression tests that can provide more information after necking. However, compression tests also present risks on non-homogeneous stress distribution due to the friction between the specimen and the platens of the SHLF, which will cause 'barrelling' effect. In principle, if the diameter to height ratio $\left(\frac{D}{H}\right)$ of the specimens approaches to zero, which means testing an infinitely long cylinder, the effects of friction can be avoided. However, long cylinders will experience buckling even before reaching to a point of yield and cannot be used to represent a homogeneous state of uni-axial flow for compression. Johnson and Mellor [296], Cook and Larke [297], Schey, et al. [298] and Bao [99] used cylinders with different aspect ratios to develop hardening curves from uni-axial compression tests, where the curves are extrapolated depending on the amount of 'barrelling' per each ratio $\left(\frac{D}{H}\right)$. However, in this section only a verification of the von Mises plasticity will be performed by utilizing the curves that are illustrated in Figure 5-22 without a need to further testing additional cylinders with different ratios. This verification will allow justifying the assumption of

using von Mises (J_2) plasticity for TRAUM as illustrated in Figure 1-8. Moreover, Li, et al. suggested using a compression specimen which has an aspect ratio of $\frac{D}{H} = 1$ for uni-axial quasi-static compression experiments while testing Al2024 with different aspect ratios, lubrication conditions and strain rates [299]. They have concluded that the best specimen geometry to characterize flow and failure behavior of the material independent of the lubrication conditions for compression minimizing the effects of 'barrelling' would have an aspect ratio of $\frac{D}{H} = 1$.

Seidt performed quasi-static compression tests for Al2024-T351 on a SHLF that is illustrated in Figure 5-6 with a secondary Linear Variable Differential Transformer (LVDT) fixture that is shown in Figure 5-24 [108].

The details of the three test cases that are used to verify quasi-static hardening curves for uni-axial compression at room temperature are listed in Table 5-11. More information can be found in Appendix–C for the test cases, where true stress vs. true strain curves are generated from the force vs. displacement curves by using the following relations assuming that the volume is conserved as:

$$D^2 H = D_0^2 H_0 \tag{5.14}$$

where, D and D_0 are the current and initial diameters and H and H_0 are the current and initial specimen heights, respectively.

True stress vs. true strain curves are then generated according to:

$$\begin{aligned} \sigma &= \frac{P}{A} = \frac{P}{\frac{\pi D^2}{4}} = \frac{4PH}{\pi D_0^2 H_0} \\ \varepsilon &= \ln\left(\frac{A}{A_0}\right) = \ln\left(\frac{H_0}{H}\right) \end{aligned} \tag{5.15}$$

where, P is the load, A and A_0 are the current and initial areas, respectively.

It is shown with Figures C-5, C-6 and C-7 that the quasi-static hardening characteristics of Al2024-T351 exhibit similar strain rate sensitivity under uni-axial compression. The yield point, Young's Modulus and hardening characteristics are also

similar, which can be represented by the same flow curves that are shown in Figure 5-22. It is also shown that DSA and PLC effects are not necessarily become specific to stress-states under tension and can be effective also for compression.

Figure 5-25 illustrates the flow softening behavior of the material at quasi-static compression regime. Test #5.1e is found to be an outlier and excluded from further analysis. It should be noted in Figure 5-25 that the strain rates represent the targeted equivalent rates.

Input curves, which are characterized in Figure 5-22, are verified by comparing with the force vs. displacement curves at different strain-rates for uni-axial compression and illustrated in Appendix–F. Figure F-5 shows the comparison of the TRAUM simulations with the corresponding test results by using the input curves that are given in Figure 5-22 at a targeted strain rate of $1.0\text{x}10^{-4}\text{s}^{-1}$. Similarly, Figures F-6 and F-7 illustrate the comparisons for targeted strain-rates $1.0\text{x}10^{-2}\text{s}^{-1}$ and $1.0\ \text{s}^{-1}$, respectively. Given the repeatability of the test results, it is verified that the characterized hardening curves can accurately capture the flow behavior and can be used for validation purposes even for stress-states beyond tension. The results support the assumption that flow at compression can still be predicted accurately by using hardening curves that are characterized from uni-axial tension when J_2 flow rule is utilized.

Table 5-11: Test cases that are used to verify quasi-static hardening curves for uni-axial compression at room temperature.

Test #	Specimen #	Test Apparatus	Loading	Actuator Velocity [mm/s]	Targeted Equivalent Strain Rate [s^{-1}]	Temperature [K]	Gage Length H [mm]
5 [Figure C-5]† [Table C-5] ‡	14 [Figure B-14]§	SHLF*	Uni-axial Compression	3.048×10^{-4}	1.0×10^{-4}	Room Temperature	3.048
6 [Figure C-6]† [Table C-6] ‡				3.048×10^{-2}	1.0×10^{-2}		
7 [Figure C-7]† [Table C-7] ‡				3.048	1.0		

* Servo-Hydraulic Loading Frame (SHLF).
† Test results for the corresponding specimen, strain-rate and temperature illustrated in Appendix–C.
‡ Test results for the corresponding specimen, strain-rate and temperature listed in Appendix–C.
§ Detailed geometries and corresponding FE models of the specimens are illustrated in Appendix–B.

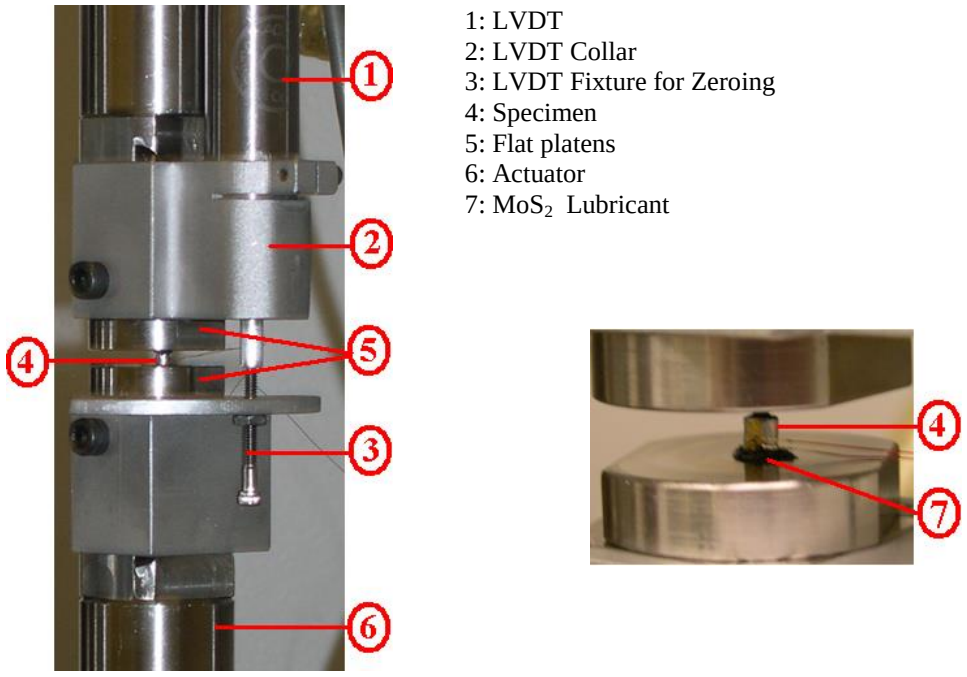

Figure 5-24: Quasi-static compression test setup with LVDT fixture, after [108].

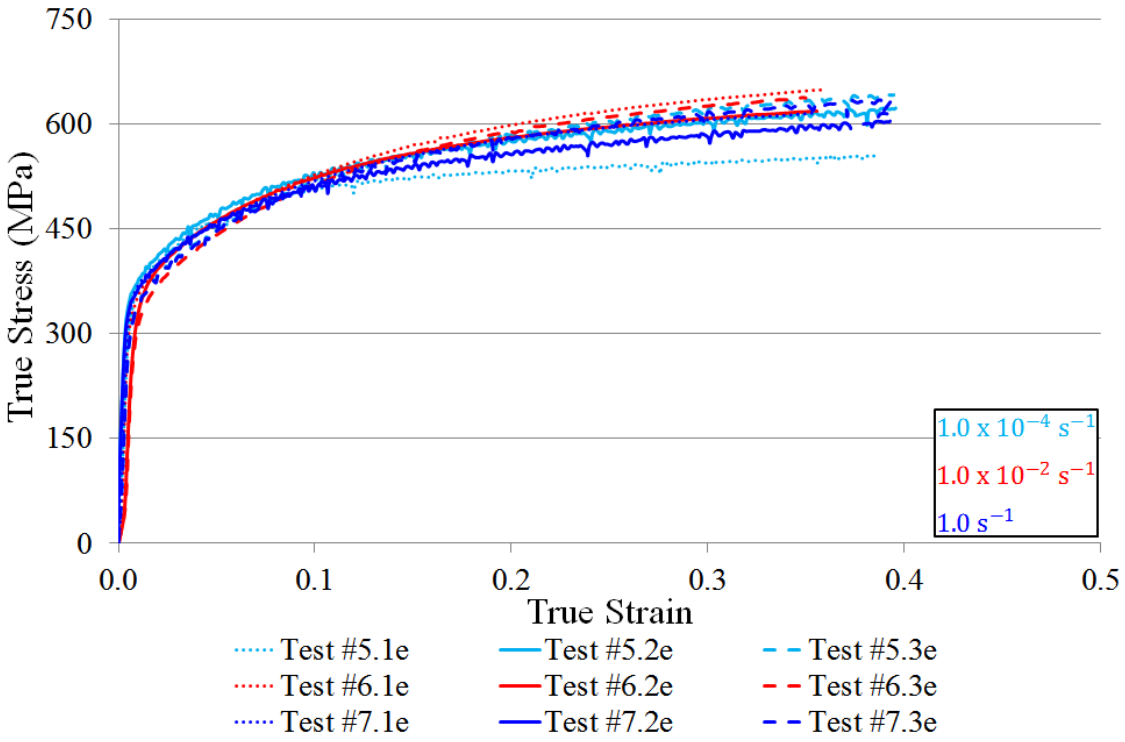

Figure 5-25: Flow and failure behavior of Al2024-T351 for quasi-static uni-axial compression at room temperature.

5.5.5 **Verification of the quasi-static hardening curves for torsion at room temperature**

A spool shaped torsion test specimen with a thin wall that is illustrated in Figure B-15 was utilized for quasi-static torsion tests by using the SHLF which is illustrated in Figure 5-6 [108]. DIC was used to track the rotational displacements and strain field for the torsion cases, where it was discussed that more accurate measurements were achieved compared to a Rotary Variable Differential Transformer (RVDT).

Table 5-12 lists the details of the torsion tests and more information can be found in Appendix–C, where Table C-8 lists the details about the test parameters. Figure C-8 illustrates moment vs. rotation curves and corresponding shear stress vs. shear strain curves, which are calculated according to:

$$\tau = \frac{T r_m}{J}$$
$$\gamma = \frac{\phi r_o}{L_0} \tag{5.16}$$

where, T is the torque, r_m is the mean gage radius, J is the polar moment of inertia, ϕ is the twist angle, r_o is the outer radius of the gauge and L_0 is the gage length.

Table 5-12: Test cases that are used to verify quasi-static hardening curves for torsion at room temperature.

Test #	Specimen #	Test Apparatus	Loading	Actuator Velocity [^{o}/s]	Targeted Shear Strain Rate [s^{-1}]	Temperature [K]	Gage Length L_0 [mm]
8 [Figure C-8]† [Table C-8] ‡	15 [Figure B-15]§	SHLF*	Torsion	1.48	1.0	Room Temperature	6.35

* Servo-Hydraulic Loading Frame (SHLF).
† Test results for the corresponding specimen, strain-rate and temperature illustrated in Appendix–C.
‡ Test results for the corresponding specimen, strain-rate and temperature listed in Appendix–C.
§ Detailed geometries and corresponding FE models of the specimens are illustrated in Appendix–B.

The dimensions are illustrated by Figure 5-26 for convenience. It should be noted that DIC strains are measured from the outer surface of the specimens. Considering the relative movement of two gauge points, the overall angular displacement can be found as:

$$\left.\begin{aligned}\phi_1 &= arctan\left(\frac{\Delta x_1}{\Delta y_1}\right)\\ \phi_2 &= arctan\left(\frac{\Delta x_2}{\Delta y_2}\right)\end{aligned}\right\} \phi = \phi_1 - \phi_2 \tag{5.17}$$

Effective stress vs. effective strain behavior is also illustrated in Figure C-8 by using the following relation for stress considering the stress-state during torsion as:

$$\begin{bmatrix} 0 & \tau_{xy} & 0 \\ \tau_{yx} & 0 & 0 \\ 0 & 0 & 0 \end{bmatrix} \Longrightarrow \bar{\sigma} = \left(\frac{3}{2} S_{ij} S_{ij}\right)^{\frac{1}{2}} = \sqrt{3}\tau_{xy} \tag{5.18}$$

where, $S_{ij} = \sigma_{ij} - \sigma_m \delta_{ij}$ is the deviatoric stress tensor. It is shown in Figure 4-62 that all other components of stress tensor are zero giving a pure shear state during the torsion.

Similarly, effective shear strains can be calculated according to:

$$\begin{bmatrix} 0 & \gamma_{xy} & 0 \\ \gamma_{yx} & 0 & 0 \\ 0 & 0 & 0 \end{bmatrix} \Longrightarrow \bar{\varepsilon} = \left(\frac{2}{3} d\varepsilon'_{ij} d\varepsilon'_{ij}\right)^{\frac{1}{2}} = \frac{1}{\sqrt{3}} \gamma_{xy} \tag{5.19}$$

where, $d\varepsilon'_{ij} = d\varepsilon_{ij} - \frac{1}{3} d\varepsilon_{kk} \delta_{ij}$ is the deviatoric strain tensor increment.

Hardening curves that are illustrated in Figure 5-22 are also verified for torsion tests and the results are shown in Appendix-F by Figure F-8. It is shown that the yield point and the hardening behavior are slightly over predicted when the hardening curves that are characterized from uni-axial tension tests are used. However, it is seen that the differences are not as significant compared to the repeatability of the failure strains in Figure C-8, where almost 100% difference is observed and identified as the major source of interest. Figure 5-27 illustrates the differences between the hardening behavior of the material under uni-axial tension, axi-symmetric tension, uni-axial compression and torsion for a nominal strain-rate of $1.0\times10^{-2}s^{-1}$ at room temperature. It is shown that both tension responses are found as identical, which is also depicted by Figure 5-23. The quasi-static hardening curve for TRAUM is characterized from the tension tests and extrapolated according to the procedures described in Section 5.5.2 considering the

findings that are illustrated in Figure 4-21, which is suggesting that under impact loading majority of the failure occurs under the state-of-tension. It should also be noted that no failure is assumed beyond a stress-triaxiality of $\sigma^* = +\frac{1}{3}$, which corresponds to a stress-state in uni-axial compression.

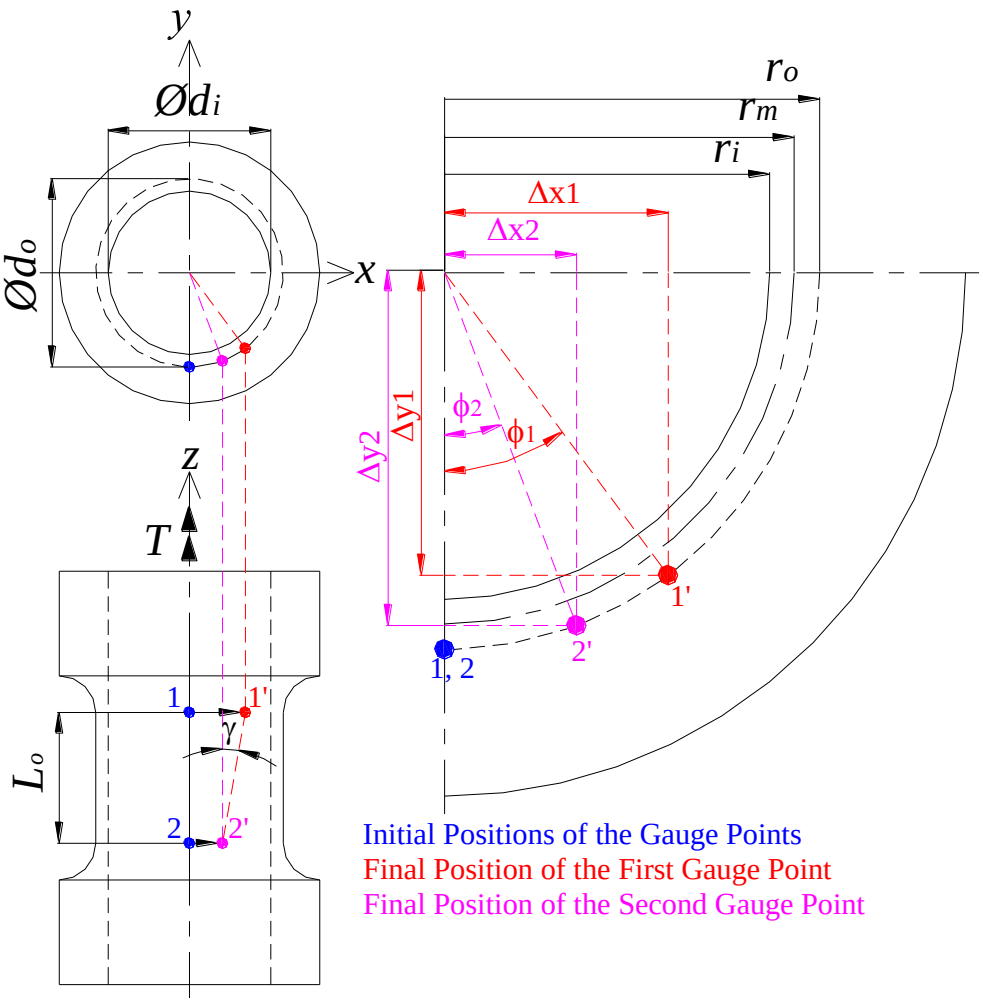

Figure 5-26: Calculation of the shear strains with respect to DIC measurements.

Differences between the flow characteristics of Al2024-T3/T351 that are illustrated in Figure 5-20 primarily depend on the choice of the stress-state for characterization purposes, which is often compression since it provides more information on the flow covering a larger portion on the plastic strain axis. Shear tests are also preferred to avoid any potential risks of instability due to necking or 'barrelling', which are common in

tension and compression. However, it is shown that stress-states towards the tension regime are more significant during the deformation and failure under impact loading of structures. Therefore, the 95% confidence interval of the hardening behavior is shown in Figure 5-27 by comparing the true stress vs. true strain curves that are generated from engineering stress vs. engineering strain curves for tension and compression and the effective stress vs. effective strain curve that is generated from shear stress vs. shear strain curve for shear. It can be seen that all flow behavior can be captured within the confidence interval provided that the characterized hardening behavior that is illustrated in Figure 5-22 is utilized as an input for the simulations.

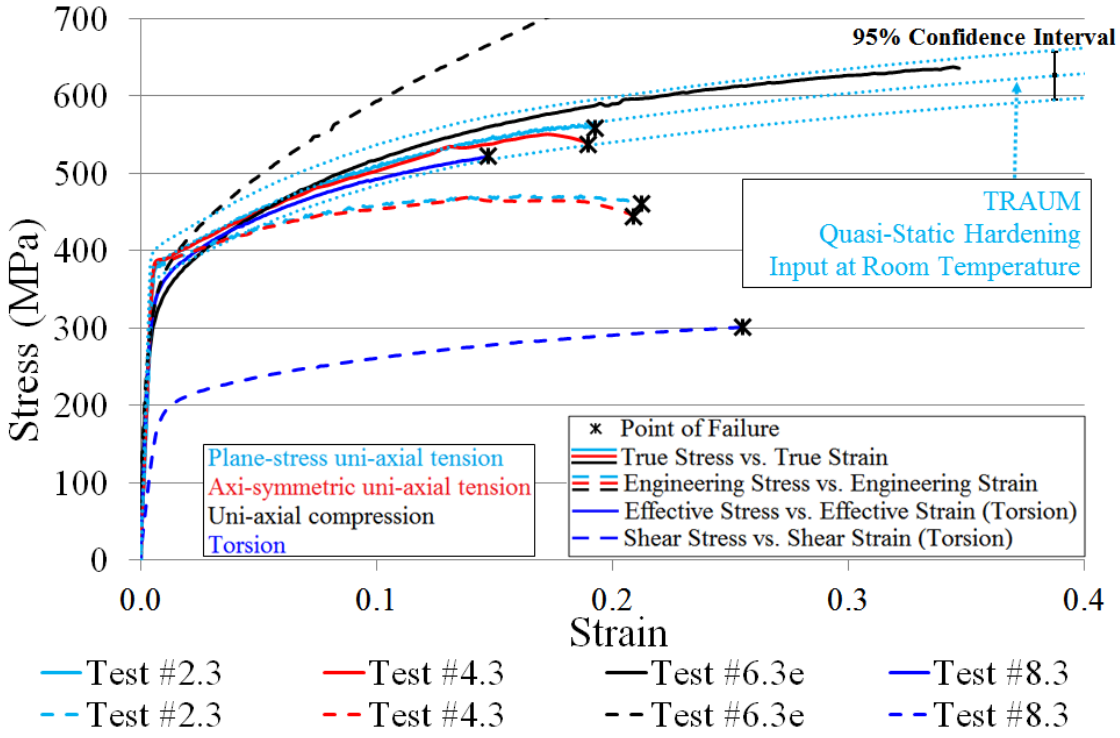

Figure 5-27: Comparison of the flow behavior for specimens with different states-of-stress.

5.6 Characterization of the temperature dependent quasi static hardening curves

As described in Section 5.3 and illustrated by Figure 5-3, temperature dependent hardening curves are required to build the flow surface of the material, where true stress vs. true plastic strain curves are characterized individually for each temperature according to the tabulated input approach with TRAUM.

5.6.1 **Determination of the testing range for temperature dependent behavior**

Temperature dependency of the flow behavior for structures under impact loading is critical, where both the changes in the ambient and the body itself due to the plastic work or deformation heating can affect the strength significantly. Sub-zero operating temperatures are often responsible from an increase in the strength but a decrease in the ductility, where softening and an increase in the ductility are often seen with the elevated temperatures [184]. Considering the ballistic impact simulations that are shown in Chapter 3 for three different target thicknesses of Al2024-T3/T351, estimated temperature changes due to the plastic work within the impact zone are illustrated by Figures 5-28, 5-29 and 5-30 for targets at 1.5875, 3.75 and 6.35mm thicknesses, respectively. It should be noted that only a quarter of the full finite element model is shown for better illustration purposes with Mesh-III topology that is described in Chapter 3. The failure modes are found as necking and petalling for 1.5875mm targets, a hybrid petalling and plugging for 3.75 mm targets and plugging for 6.35mm thick targets, correspondingly. It can clearly be seen that the temperature distribution localizes and the temperature rises with the increasing target thickness as the maximum temperatures are calculated as 360, 560 and 800K, respectively for each thickness above the ballistic limit. This behavior can also be used to explain the fact that the change in the failure mechanisms are affected by the temperature distribution, where it is common to observe shear band formations due to adiabatic heating for thicker targets and higher impact velocities [300] [301] [302]. Figures 5-28 - 5-30 can also be used to justify the range for testing different temperatures to characterize the flow and failure properties. Considering the Background and Motivation of this dissertation that is described in Section 1.2 and the material of interest that is defined in Section 5.2 as Al2024-T351, it is required to test both sub-zero and elevated temperatures to cover the operational conditions of the aerospace structures under impact loading.

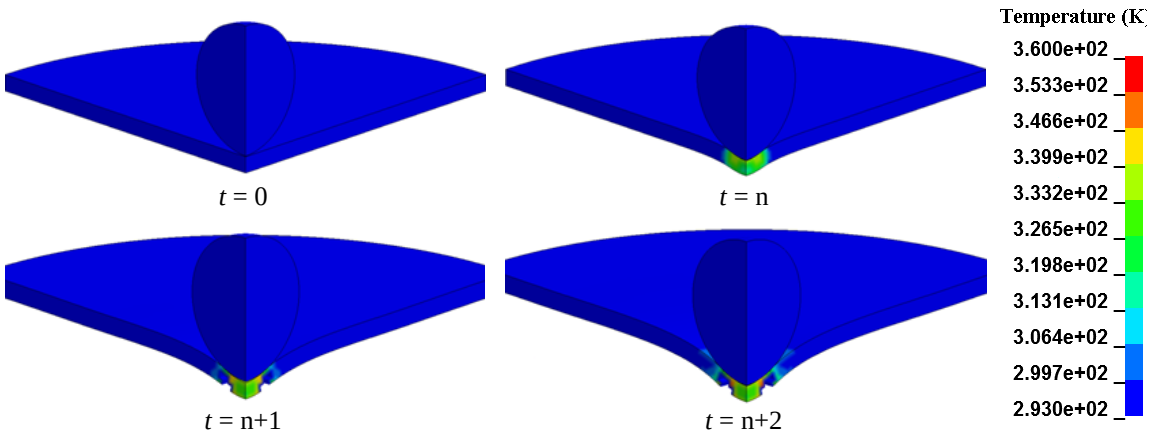

Figure 5-28: Temperature increase due to the plastic work for 1.5875mm thick targets under impact.

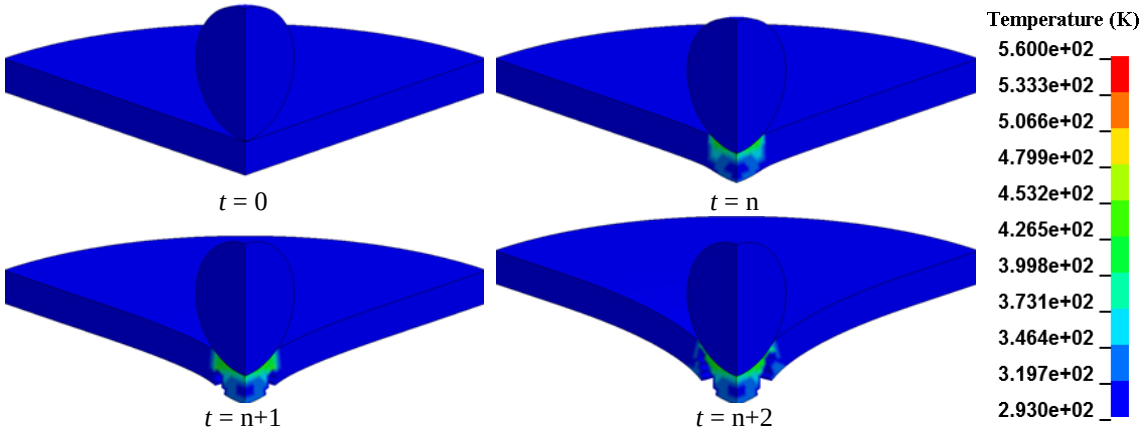

Figure 5-29: Temperature increase due to the plastic work for 3.75mm thick targets under impact.

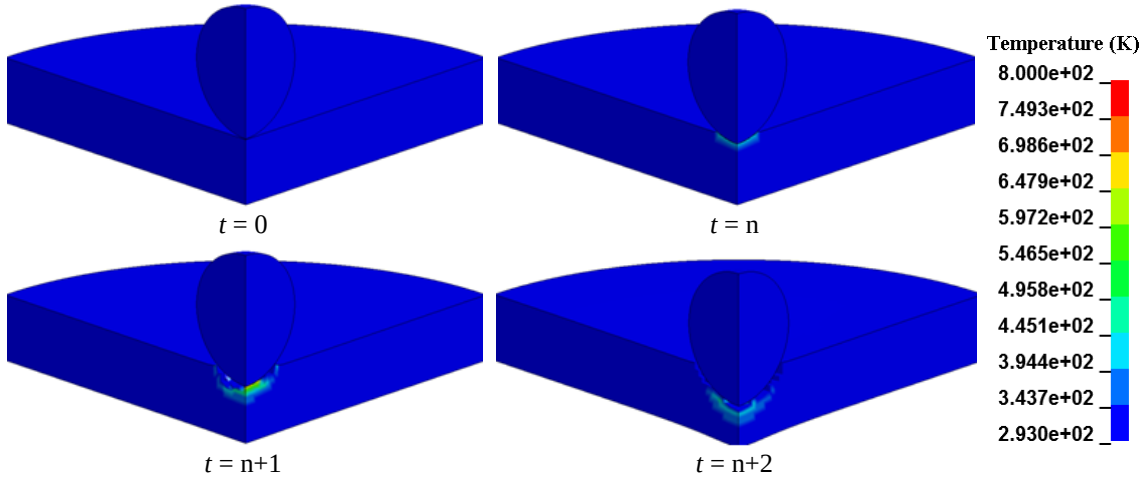

Figure 5-30: Temperature increase due to the plastic work for 6.35mm thick targets under impact.

A ‘remarkable characteristic’ of Al2024-T3/T351 was mentioned by Martinez as the ‘strong’ increase of the strain hardening behavior and the corresponding improvement in ductility with the decrease in temperature, where the ‘service temperature’ of Al2024-T3 was suggested between 213K and 293K for aeronautical applications [303]. Lispski and Mrozinski have also suggested a corridor of operating temperatures for Al2024-T3 up to 393K, which was recommended by the supplier as the maximum operating temperature [304]. In this dissertation, the range of testing is chosen between 223K and 723K considering the operational conditions and the temperature rise due to adiabatic heating [108]. Further testing was not required considering that the localized shear band formations were reported even without a phase change was observed [302]. Therefore, it was concluded that the predicted temperature rises that are illustrated by Figures 5-28 - 5-30 would be sufficient to cover the range of interest for Al2024-T351 to simulate impact problems accurately.

5.6.2 **Temperature dependent Young’s modulus, Poisson’s ratio and specific heat**

Lispski and Mrozinski reported that up to 10% decrease in the strength properties of Al2024-T3 was observed at a temperature of 393K and measured that this drop reaches 70 to 85 percent at a temperature of 473K. However, the effects of testing apparatus and compliance were not discussed in their measurements, where the elastic modulus was determined from uni-axial tensile tests as the ‘static’ method of finding Young’s modulus [304]. Investigating the behavior of several metals at elevated temperatures, Gordon, et al. reported differences between the ‘static’ and ‘dynamic’ elastic moduli, which were derived from conventional stress vs. strain curves and by determining the velocity of propagating elastic waves, respectively [305]. They have found that both methods agree well in the low stress levels, where the rate effects were not significant. However, at higher stress levels, where the stress vs. strain relation was not linear anymore, and the rate effects should be considered, ‘dynamic’ method was found to provide higher modulus and should be preferred since the measurements were prone to accumulate less errors due to compliance [305]. Elastic moduli for tension and compression were also reported to be identical at cryogenic and elevated temperatures, which are consistent with

the findings in Section 5.5 for the ‘static’ determination of the mechanical properties [225]. Evolution of the elastic moduli with respect to temperature from several different sources are compared in Figure 5-31 for Al2024, which also illustrates the deviation between ‘static’ and ‘dynamic’ methods. It is shown that both methods provide identical behavior up to 422K and ‘static’ modulus rapidly drops with increasing temperature.

Gordon, et al. measured the change in Young’s Modulus with respect to temperature for Al2024-T4. It should be noted that all Al2024 series aluminum alloys have the same elastic modulus independent of the initial temper characteristics [306]. Vosteen has also verified these results by utilizing flexural beam vibration tests for Al2024-T3 with ‘dynamic’ determination of the elastic modulus [307]. Similarly, Hill and Shimmin tested Al2024-T4 and several other metal alloys at elevated temperatures to determine the ‘dynamic’ elastic modulus and reported a rapid decrease in modulus as a result of the solution of $Cu_2Mg_2Al_5$ precipitates at around 533K [308]. Brammer and Percival measured elastic waves in slender rods by the deposition of laser energy pulses at temperatures between 295 and 811K and determined that Young’s modulus decreases 40% and Poisson’s ratio increases 7% in specimens that were made of Al2024-T6 and cut parallel to the rolling direction [309]. Specific heat for aluminum alloys is also known to be temperature dependent [310]. Figure 5-31 illustrates the temperature dependent characteristics of the Young’s modulus, Poisson’s ratio and the specific heat for Al2024.

In this dissertation, Poisson’s ratio and specific heat are assumed to stay constant and the values are chosen at room temperature. Figure 5-31 illustrates that for the chosen range of testing, the evolution of Young’s modulus with respect to temperature cannot be represented ‘satisfactorily’ by a linear function [309]. Therefore, tabulated form of a second order polynomial is used to represent the test data that is shown in Figure 5-32 for TRAUM input, which is forced to intercept the Young’s modulus exactly at room temperature. This polynomial is programmed to use a curvature similar to the other published data for temperature dependent modulus of Al2024 that are illustrated in Figure 5-31. The same curvature is extended to find the Young’s modulus at cryogenic temperatures assuming that the trend will not change due to the effects like ductile-to-brittle transition considering that the material of interest has fcc crystal structure. Figures 5-31 and 5-32 show that the testing range for the material is cut before the solidus

boundary is reached and no phase change is considered. However, dynamic recovery and recrystallization can still be expected within the given range [108].

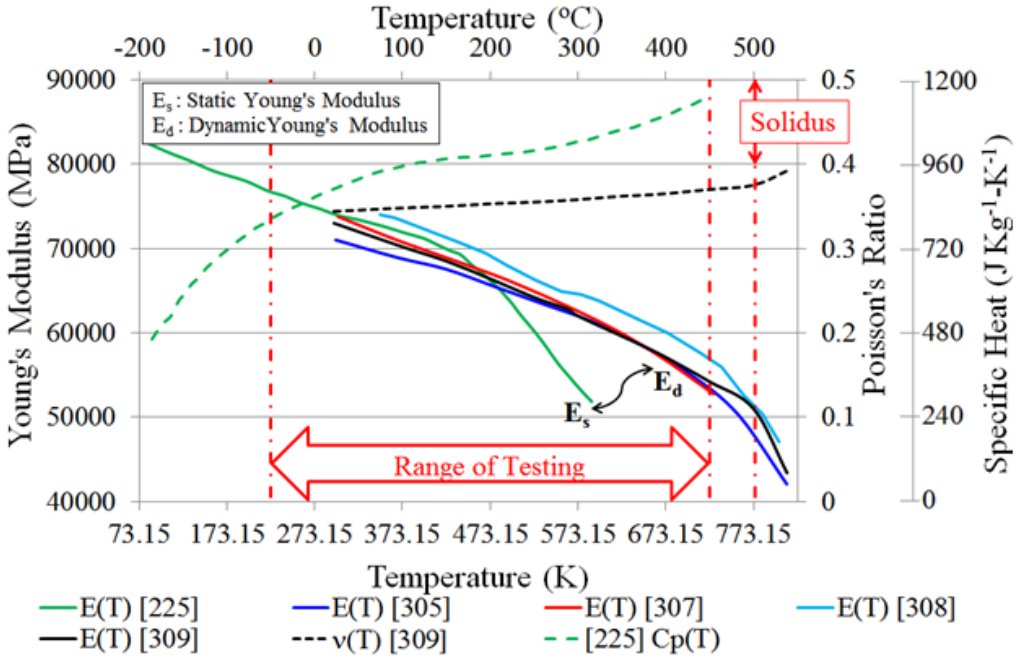

Figure 5-31: Temperature dependent Young's modulus and Poisson's ratio for Al2024.

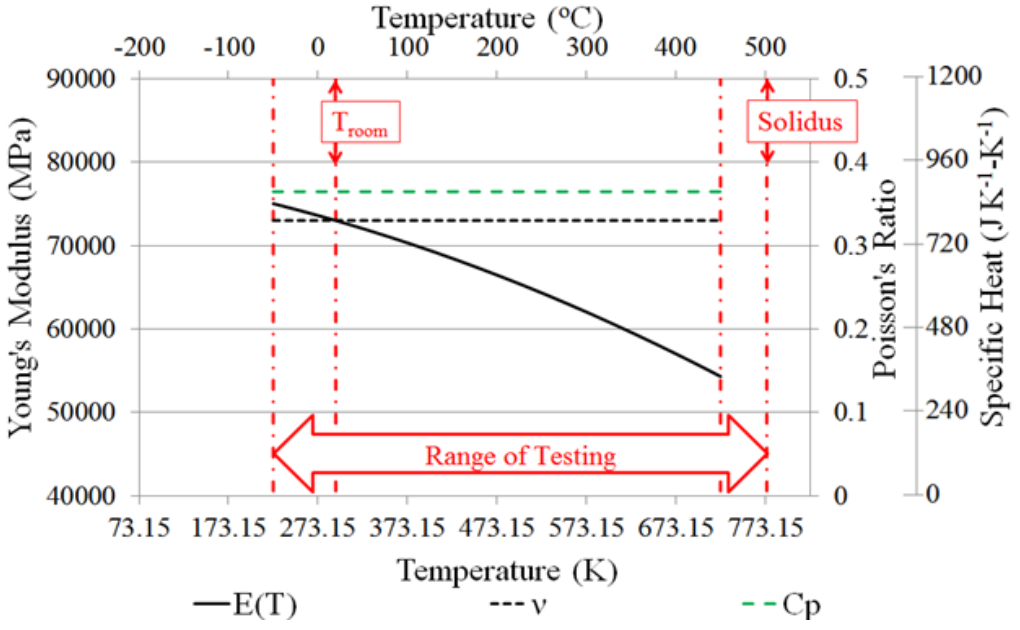

Figure 5-32: Evolution of tabulated Young's modulus and constant Poisson's ratio for Al2024-T351.

5.6.3 **Apparatus for temperature dependent testing**

Five different temperatures including room temperature were chosen for testing the temperature dependent behavior of Al2024-T351. Two different furnaces were used for elevated temperature testing at around 423, 573 and 723K and a cryogenic chamber was used to test the material at around 223K [108]. It should be noted that all temperature dependent tests were carried out at quasi-static testing conditions (i.e., $1s^{-1}$) by utilizing the SHLF that is shown in Figure 5-33 as the main apparatus. All temperature dependent tests were repeated for tension, compression and torsion specimens at quasi-static conditions. DIC measurements were not possible for high and low temperature testing due to the fact that the instrumentation of the furnaces and cryogenic chamber did not allow direct visual contact with the specimens. The limits of the high temperature testing were also exceeded for the extensometers, strain gauges and other LVDT equipment. The limited space inside the high temperature testing furnace was also an additional restriction for the measurement equipment [108]. Therefore, LVDT and RVDT measurements from the Instron SHLF were used to keep the consistency between the temperature dependent tests. These measurements were also verified with strain gauge measurements until certain temperatures and strains to test machine and adapter compliance and satisfactory correlation was achieved provided that a modulus correction for the temperature dependent Young's modulus was applied.

Figure 5-33 illustrates the test apparatus equipped with an ATS 3620 convection furnace, an interface cell and Inconel 718 push/pull rods. ATS 3620 convection furnace was utilized for testing temperatures at around 423K. A Research, Inc., E4-2 IR furnace was used to achieve higher temperatures for testing at 573 and 723K by using the same SHLF as illustrated in Figure 5-34. Low temperature testing was achieved by using a cryogenic chamber that is illustrated in Figure 5-35 at around 223K by letting liquid nitrogen through copper tubing into the chamber with no direct contact with the specimens [108]. Temperature distribution is monitored and regulated during the temperature dependent testing of the specimens by using multiple thermocouples that were attached to several different locations on the specimens and the testing apparatus.

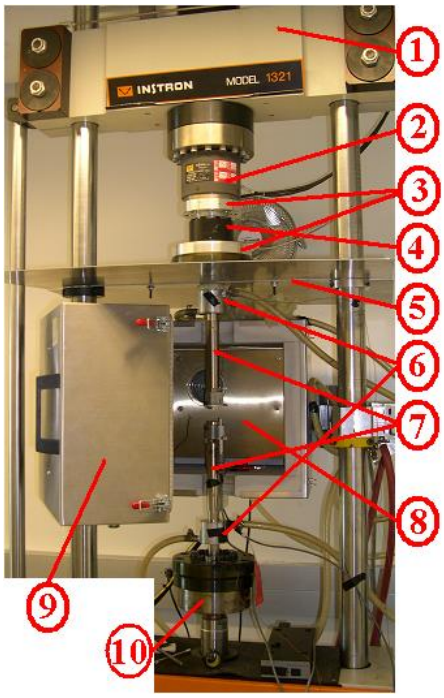

1: Servo-Hydraulic Loading Frame (SHLF)
2: Load Cell
3: Mounting plates
4: Interface cell
5: Heat barrier
6: Upper and lower cooling sleeves
7: Upper and lower push/pull rods
8: Back door of ATS 3620 furnace
9: Front door of ATS 3620 furnace
10: Actuator

Figure 5-33: Servo-hydraulic Load Frame with ATS 3620 furnace, after [108].

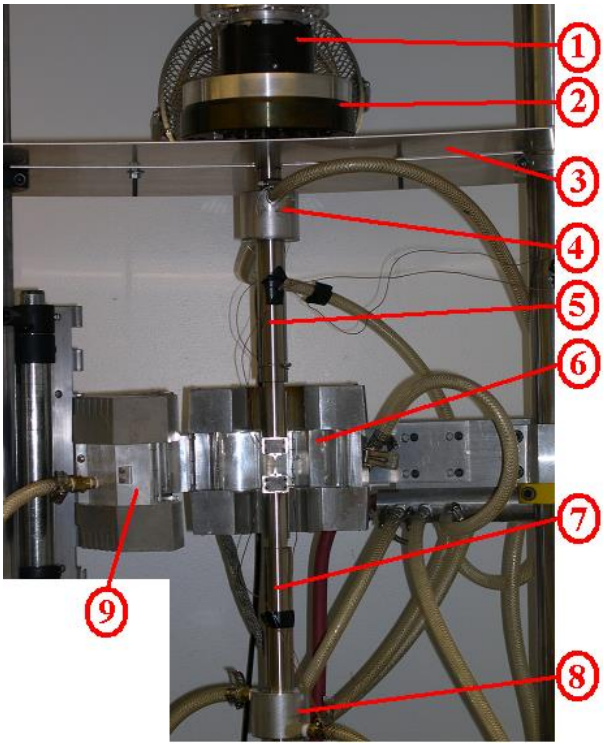

1: Interface cell
2: Mounting plates
3: Heat barrier
4: Upper cooling sleeve
5: Upper push/pull rod
6: Back door of E4-2 IR furnace
7: Lower push/pull rod
8: Lower cooling sleeve
9: Front door of E4-2 IR furnace

Figure 5-34: Servo-hydraulic Load Frame with Research, Inc., E4-2 IR furnace, after [108].

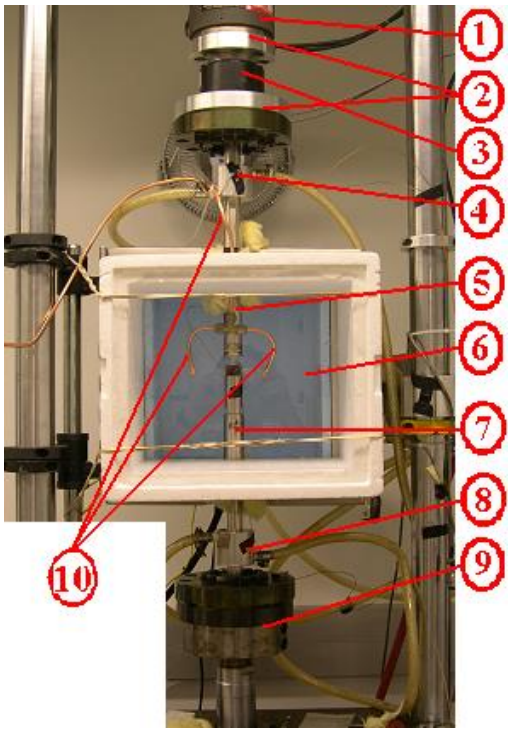

1: Load Cell
2: Mounting plates
3: Interface cell
4: Upper heating sleeve
5: Upper push/pull rod
6: Cryogenic chamber
7: Lower push/pull rod
8: Lower heating sleeve
9: Actuator
10: Copper tubing for liquid nitrogen

Figure 5-35: Servo-hydraulic Load Frame with cryogenic chamber, after [108].

Figure 5-36(a) illustrates four thermocouples within the furnaces, where two of them were attached to a plane stress uni-axial tension specimen. Two thermocouples were attached to the clamps, where the upper thermocouple was used by the controller. Figure 5-36(b) illustrates three thermocouples within the cryogenic chamber, where two of them were attached to the tension specimen and one of them was attached to the lower clamp that was used by the controller [108]. Figure 5-37 illustrates the evolution of the temperatures that were measured from the thermocouples and the points of testing for the corresponding tests ranging from 223K to 723K. It is shown with Figure 5-37 that the targeted test temperatures were reached without sudden heating or cooling, keeping the temperature gradients minimal.

The details of the temperature dependent quasi-static tests are listed in Table 5-13 for uni-axial tension by using a plane-stress specimen. More information about the repeatability of the temperature dependent tests can be found in Appendix-C. It should be noted that the true stress vs. true strain values in Appendix-C are calculated for nominal values and the flow curves are characterized in the proceeding sections.

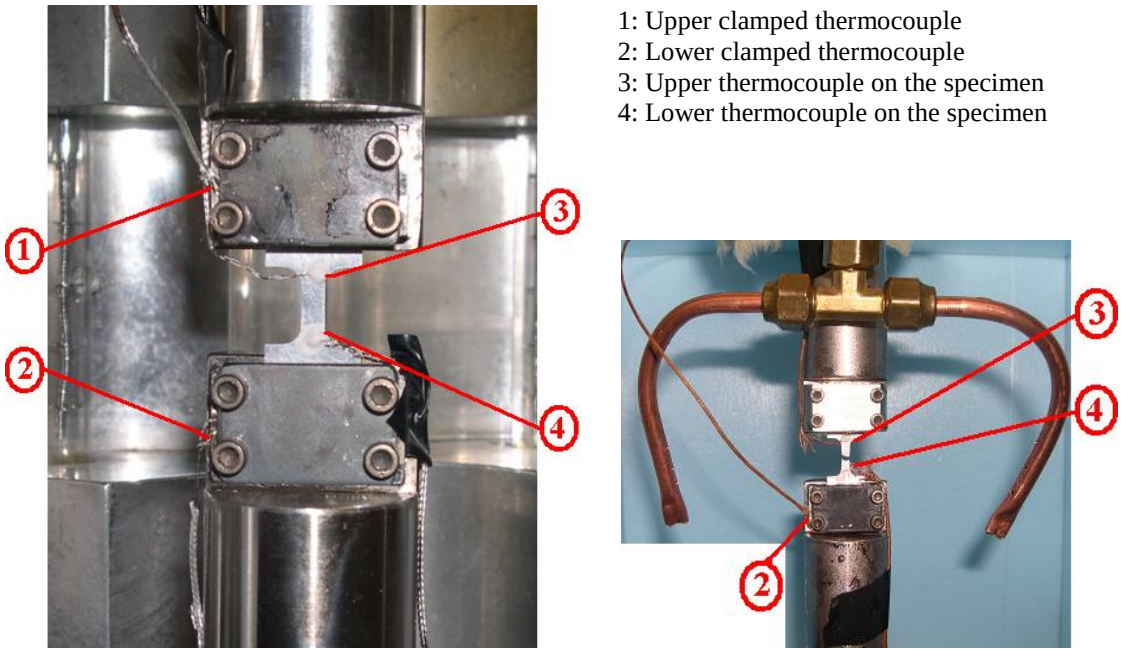

(a) (b)

Figure 5-36: Instrumentation of the tension specimens with thermocouples for (a) high temperature and (b) low temperature testing, after [108].

Table 5-13: Test cases that are used to characterize temperature dependent quasi-static hardening curves for uni-axial tension.

Test #	Specimen #	Test Apparatus	Loading	Actuator Velocity [mm/s]	Targeted Equivalent Strain Rate [s^{-1}]	Targeted Temperature [K]	Extensometer Gage Length L_0 [mm]
9 [Figure C-9]† [Table C-9]‡	1 [Figure B-1]§	SHLF*	Uni-axial Tension	5.08	1.0	423	5.08
10 [Figure C-10]† [Table C-10]‡						573	
11 [Figure C-11]† [Table C-11]‡						723	
12 [Figure C-12]† [Table C-12]‡						223	

* Servo-Hydraulic Loading Frame (SHLF).
† Test results for the corresponding specimen, strain-rate and temperature illustrated in Appendix–C.
‡ Test results for the corresponding specimen, strain-rate and temperature listed in Appendix–C.
§ Detailed geometries and corresponding FE models of the specimens are illustrated in Appendix–B.

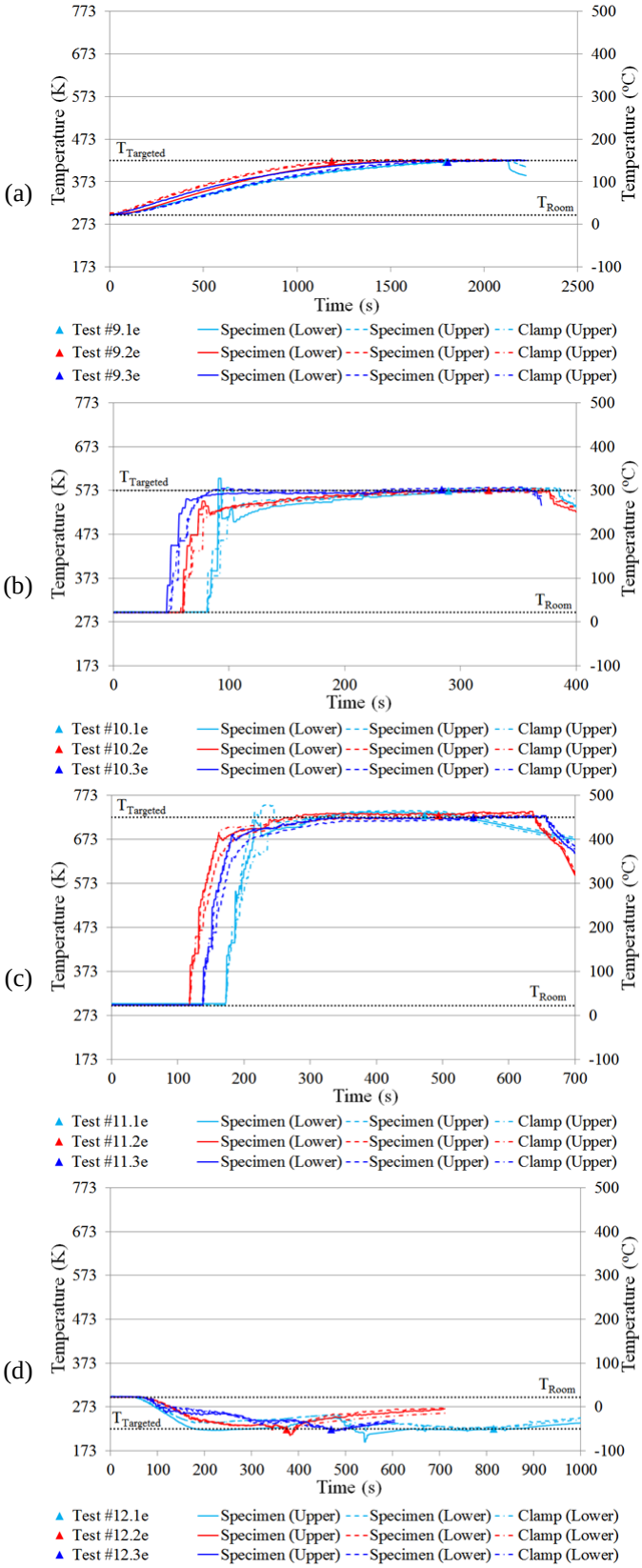

Figure 5-37: Evolution of temperatures within the testing apparatus for quasi-static uni-axial tension at targeted values of; (a) 423K, (b) 573K, (c) 723K and (d) 223K.

It is shown in Figure 5-37 that the tests were performed as soon as the targeted temperatures were achieved. Average specimen temperatures, which were measured directly from the thermocouples that were attached to the specimens (i.e., average of the upper and lower thermocouples), are illustrated in Figure 5-38. It is shown that at the time of testing, averaged specimen temperatures are within ±5K of the targeted test temperatures. Therefore, it is concluded that the targeted values of the temperature dependent flow curves can directly be used for characterization. Averaged values of the measured temperatures are also listed in Appendix-C by Tables C-9 – C-12 for each test.

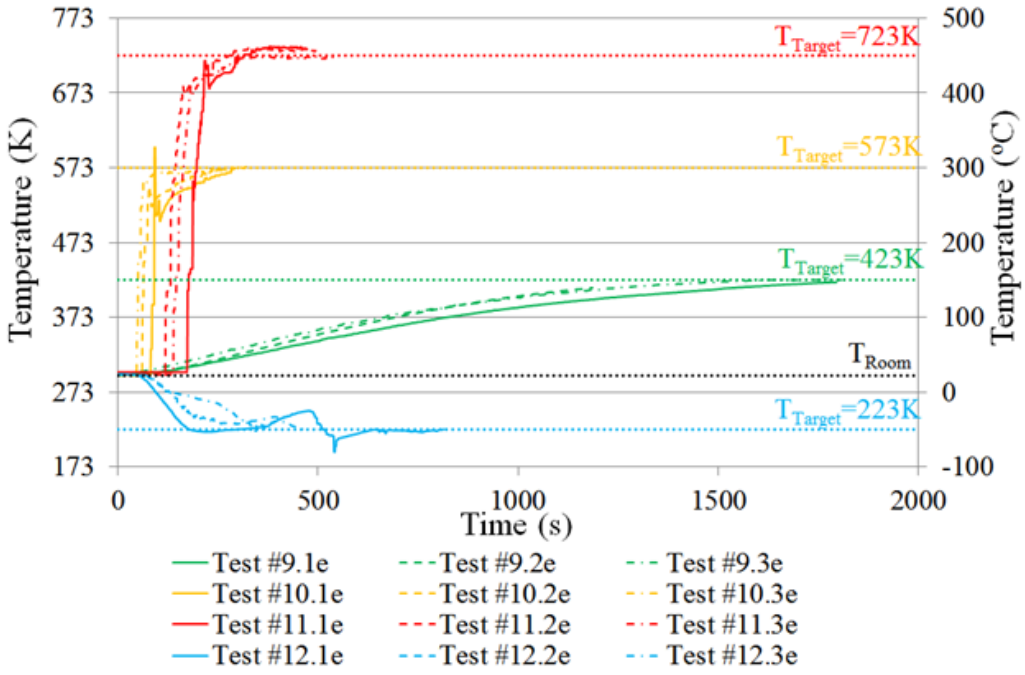

Figure 5-38: Temperature profiles of the tension specimens until the targeted testing temperatures.

Similarly uni-axial compression specimen temperatures were monitored during the quasi-static testing by using thermocouples attached to the clamps and the specimen. Figure 5-39(a) illustrates thermocouples within the furnaces and Figure 5-39(b) illustrates thermocouples within the cryogenic chamber [108]. Figure 5-40 illustrates the evolution of the temperatures that were measured from the thermocouples and the points of testing for the corresponding tests ranging from 223K to 723K. The details of the temperature

dependent quasi-static tests are listed in Table 5-14 for uni-axial compression. More information about the repeatability of the temperature dependent tests can be found in Appendix-C.

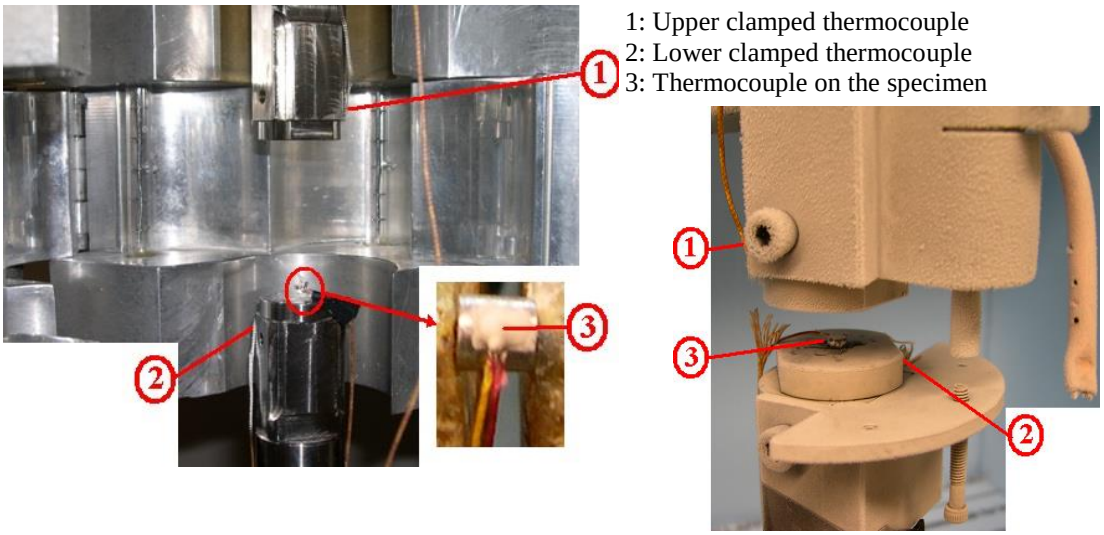

Figure 5-39: Instrumentation of the compression specimens with thermocouples for (a) high temperature and (b) low temperature testing, after [108].

Table 5-14: Test cases that are used to characterize temperature dependent quasi-static hardening curves for uni-axial compression.

Test #	Specimen #	Test Apparatus	Loading	Actuator Velocity [mm/s]	Targeted Equivalent Strain Rate [s^{-1}]	Targeted Temperature [K]	Gage Length H [mm]
13 [Figure C-13]† [Table C-13]‡	14 [Figure B-14]§	SHLF*	Uni-axial Compression	3.048	1.0	423	3.048
14 [Figure C-14]† [Table C-14]‡						573	
15 [Figure C-15]† [Table C-15]‡						723	
16 [Figure C-16]† [Table C-16]‡						223	

* Servo-Hydraulic Loading Frame (SHLF).
† Test results for the corresponding specimen, strain-rate and temperature illustrated in Appendix–C.
‡ Test results for the corresponding specimen, strain-rate and temperature listed in Appendix–C.
§ Detailed geometries and corresponding FE models of the specimens are illustrated in Appendix–B.

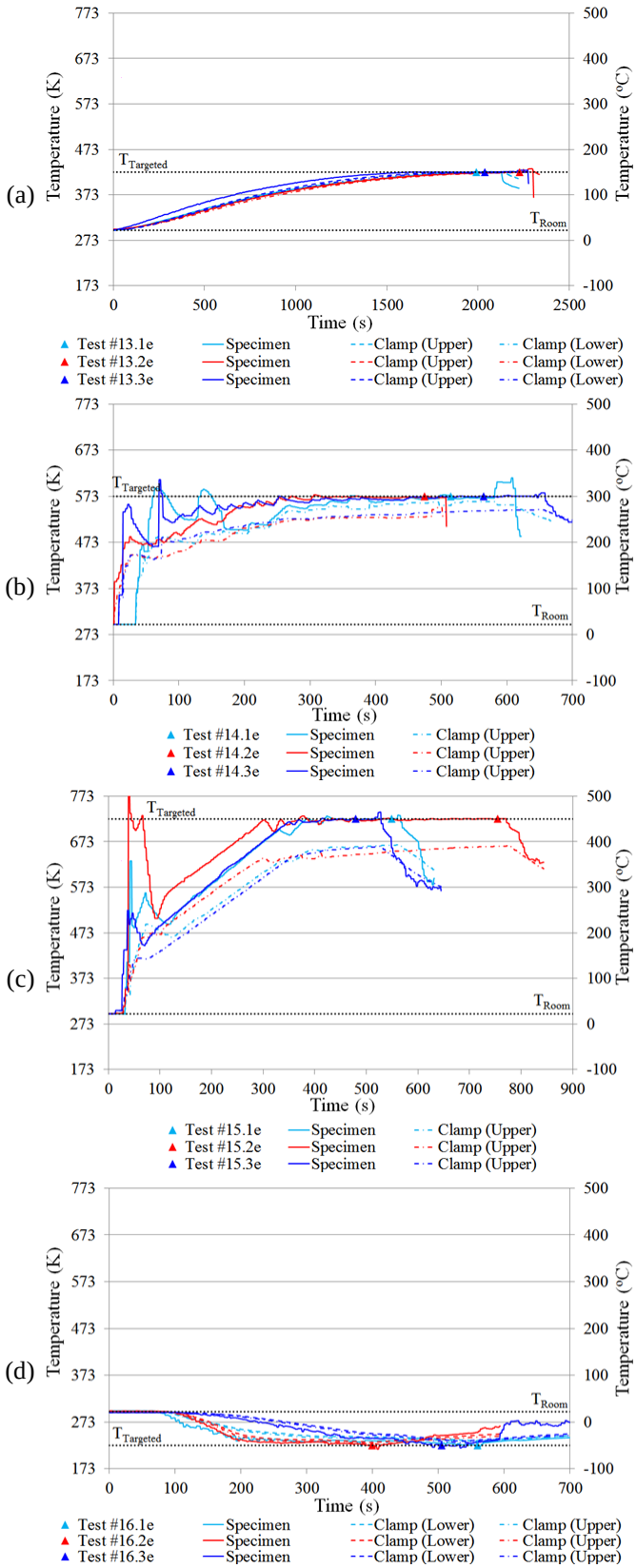

Figure 5-40: Evolution of temperatures within the testing apparatus for quasi-static uni-axial compression at targeted values of; (a) 423K, (b) 573K, (c) 723K and (d) 223K.

Figure 5-40 shows that the targeted test temperatures were reached without sudden heating or cooling, keeping the temperature gradients minimal. Considering that the compression specimens are relatively smaller and the temperature distribution within the specimen will be minimal, a comparison of the temperature profiles measured for each test is illustrated in Figure 5-41. Specimen temperatures are directly used in this case as the average temperatures which are listed in Appendix-C by Tables C-13 – C-16.

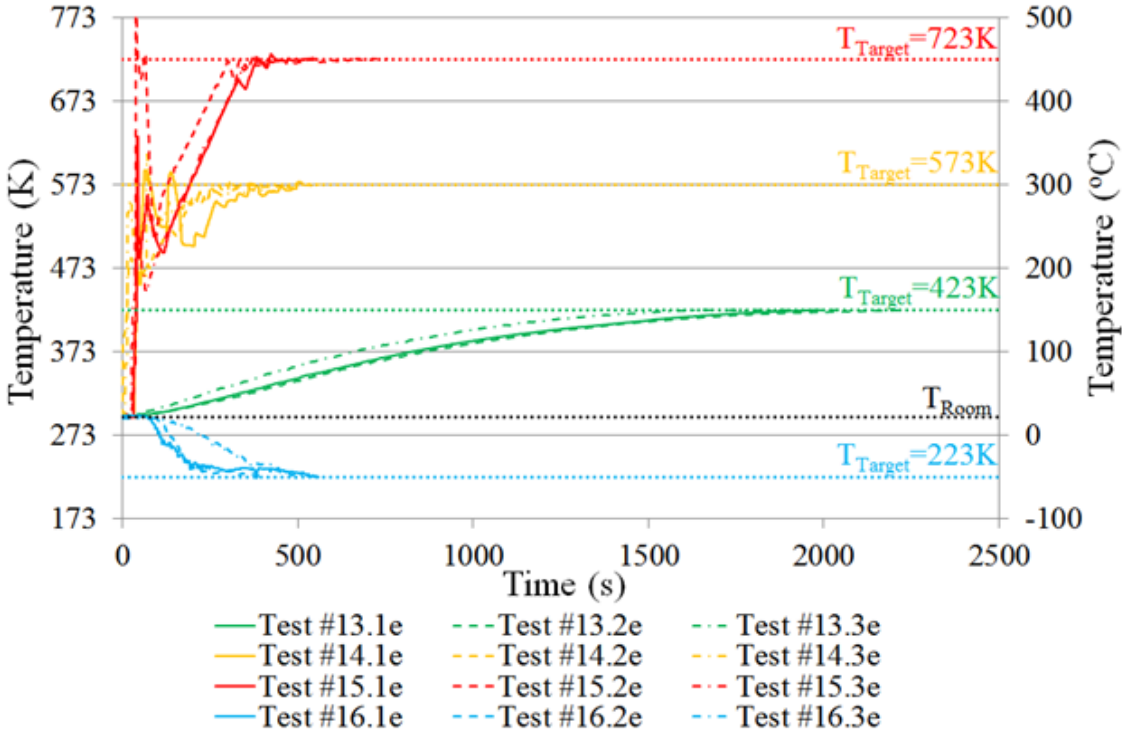

Figure 5-41: Temperature profiles of the compression specimens until the targeted testing temperatures.

A spool shaped specimen is used for the quasi-static testing of the flow behavior under torsion. The specimens were tested by using the SHLF that was illustrated in Figure 5-6 with torsion grips and holding adaptors to attach the specimens as illustrated in Figure 5-42 [108]. Spool shaped specimens were connected by using epoxy and also were pinned to both adaptors, (i.e., upper and lower), which had hexagonal shaped end geometries that were used to be inserted into the torsion grips. A set of screws were then

used to fix the adaptors to the grips. A LVDT-based torsional extensometer was used to measure the arc length of the apparatus beside the integrated RVDT of the Instron SHLF. The accuracy of this system was discussed by Seidt [108]. It should be noted that no DIC measurements were available when this apparatus was utilized.

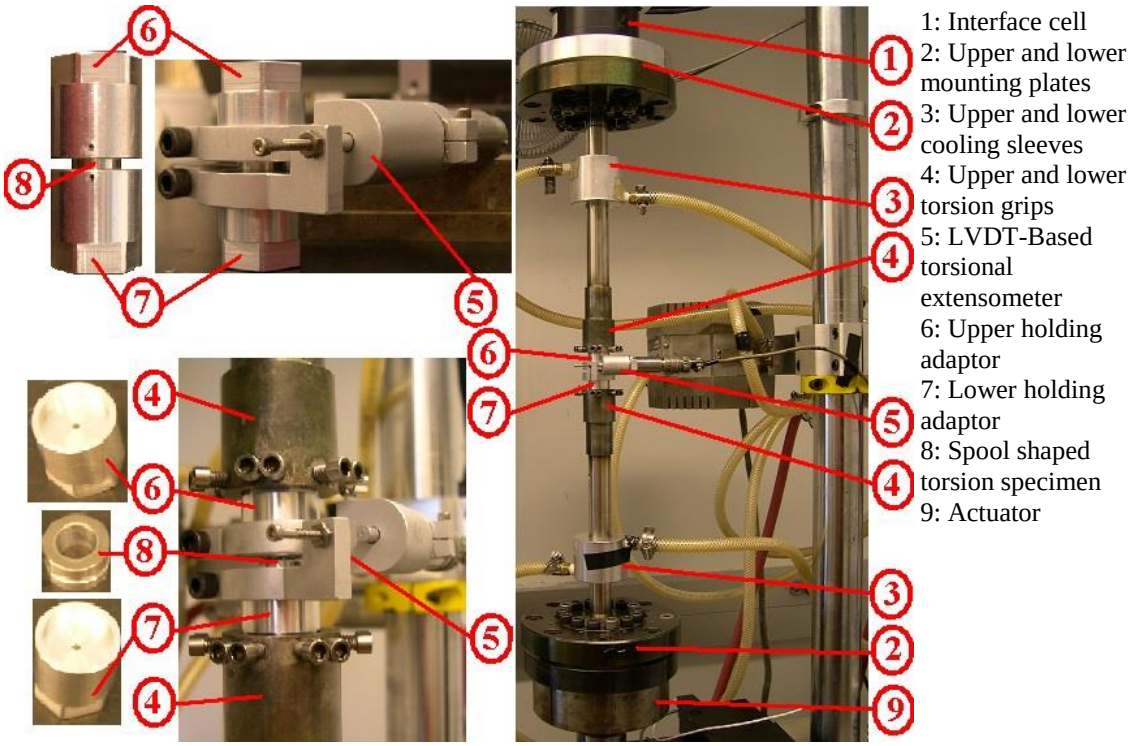

Figure 5-42: Servo-hydraulic Load Frame with torsion grips, after [108].

Figure 5-43(a) illustrates four thermocouples within the furnaces, where two of them were attached to the grips, one of them was attached to the specimen and the last one was attached to the LVDT. Figure 5-43(b) illustrates four thermocouples within the cryogenic chamber with a similar sequence. The details of the temperature dependent quasi-static tests are listed in Table 5-15 for torsion by using a spool shaped specimen. More information about the repeatability of the temperature dependent tests can be found in Appendix-C. It should be noted that the effective stress vs. effective strain values in Appendix-C are calculated for nominal values and the flow curves are characterized in the proceeding sections.

Table 5-15: Test cases that are used to characterize quasi-static hardening curves for torsion.

Test #	Specimen #	Test Apparatus	Loading	Actuator Velocity [^{o}/s]	Targeted Shear Strain Rate [s^{-1}]	Targeted Temperature [K]	Gage Length L_0 [mm]
17 [Figure C-17]† [Table C-17]‡	21 [Figure B-19]§	SHLF*	Torsion	3.781×10^{-3}	1.0×10^{-4}	Room Temperature	2.54
18 [Figure C-18]† [Table C-18]‡				3.781×10^{-1}	1.0×10^{-2}		
19 [Figure C-19]† [Table C-19]‡				37.81	1.0		
20 [Figure C-20]† [Table C-20]‡						423	
21 [Figure C-21]† [Table C-21]‡						573	
22 [Figure C-22]† [Table C-22‡						723	
23 [Figure C-23]† [Table C-23]‡						223	

* Servo-Hydraulic Loading Frame (SHLF).
† Test results for the corresponding specimen, strain-rate and temperature illustrated in Appendix–C.
‡ Test results for the corresponding specimen, strain-rate and temperature listed in Appendix–C.
§ Detailed geometries and corresponding FE models of the specimens are illustrated in Appendix–B.

Figure 5-44 illustrates the evolution of the temperatures that were measured from the thermocouples and the points of testing for the corresponding tests ranging from 223K to 723K. It is shown with Figure 5-44 that the targeted test temperatures were consistently reached without sudden heating or cooling, keeping the temperature gradients minimal. Only the comparison between the temperatures that were measured from the specimen and the lower grip were compared for better illustration purposes considering that the measured temperatures were close to each other. Figures 5-44

Temperature profiles of the torsion specimens are given in Figure 5-45. It is shown that all tests were in agreement with the targeted temperatures. Therefore, targeted values for the temperature dependent testing are directly used during the characterization of the flow curves, which are listed in Appendix-C by Tables C-20 – C-23.

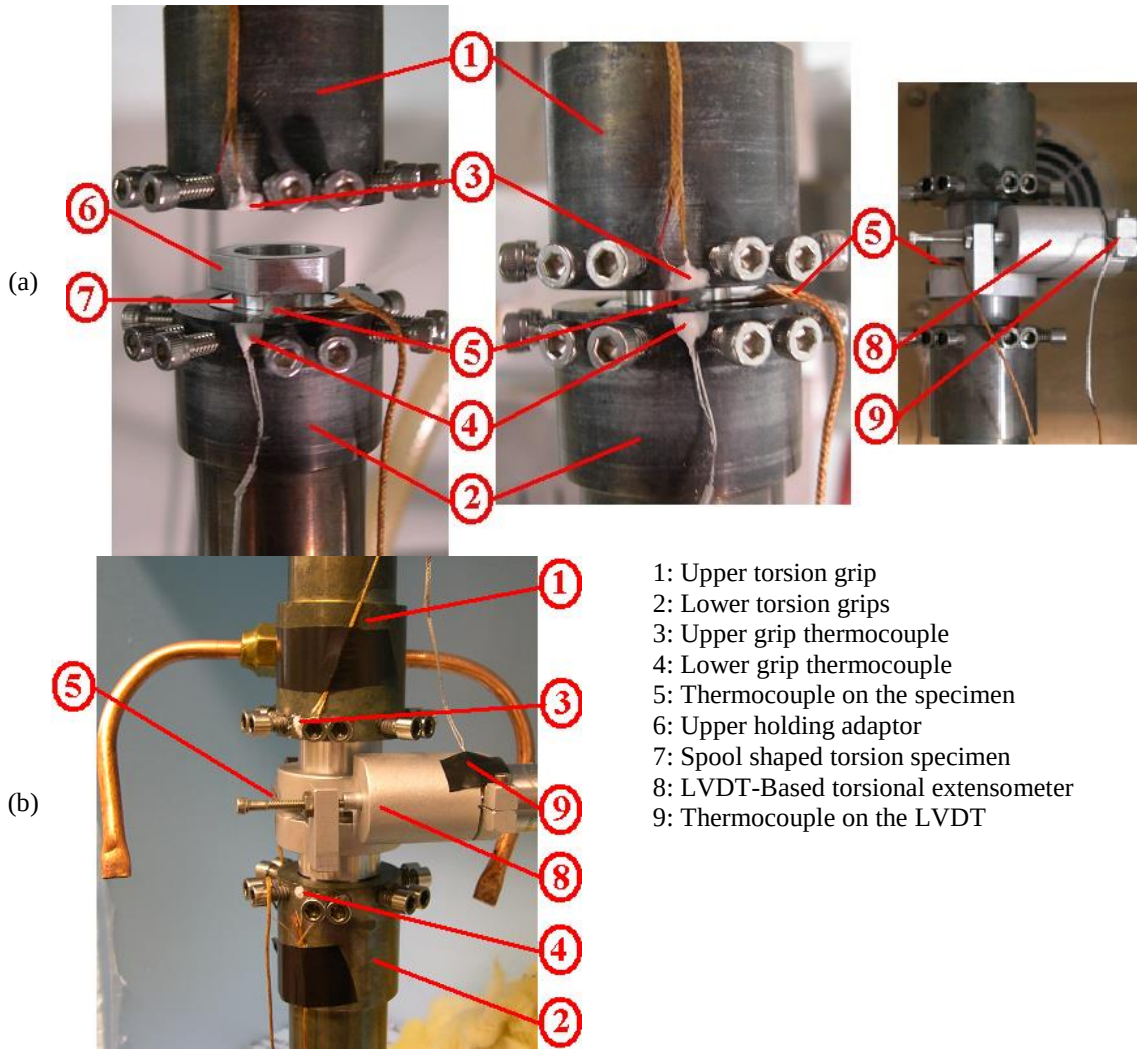

Figure 5-43: Instrumentation of the torsion specimens with thermocouples for (a) high temperature and (b) low temperature testing, after [108].

5.6.4 **Assessment of the quasi-static testing conditions considering the deformation heating and the isothermal assumption**

It is often assumed that at quasi-static testing conditions the deformation heating will not be significant and the specimen will have enough time to dissipate the generated heat to the surrounding usually by conduction through the testing apparatus and grips. When the high thermal conductivity and 'strain-rate insensitive' nature of Al2024 are considered, this assumption can mistakenly be justified. However, Charpentier, et al. showed that due to the deformation heating, flow curves for $\dot{\varepsilon} > 1.0\text{x}10^{-2}\text{s}^{-1}$ do not

correspond to isothermal conditions and a correction is needed for Al2024 [311]. Martínez used an infrared camera to record the temperature profile during a quasi-static uni-axial tensile test for Al2024-T3 at $10^{-3}s^{-1}$ and showed that the temperature rise should be considered especially when a tensile instability (i.e., necking) takes place. Using a high-speed HgCdTe photoconductive detector, Hodowany, et al. measured a temperature rise of nearly 15K within an engineering plastic strain of 20% between $1.0s^{-1}$ and $3000s^{-1}$ for Al2024-T3 [312]. Consequently, a correction on the flow stress should be applied even at quasi-static testing conditions, where isothermal hardening curves should be generated from the adiabatic flow curves. For a coupled thermo-mechanical problem the heat conduction problem suggests a relation for strain and temperature. For a material in uni-axial tension, the temperature balance can be expressed according to:

$$\lambda\nabla^2 T - \dot{T} = -\frac{\dot{\beta}\sigma_{ij}\dot{\varepsilon}_{ij}^{p}}{\rho C_p} + \frac{\alpha}{\rho C_p}\frac{E}{1-2\nu}T_0\dot{\varepsilon}_{kk}^{e} \tag{5.20}$$

where, T is the temperature, $T_0$is the initial or reference temperature, β is the Taylor–Quinney coefficient that represents the proportion of plastic work converted into heat, ρ is the density, σ_{ij} are the stress components, $\dot{\varepsilon}_{kk}^{e}$ and $\dot{\varepsilon}_{ij}^{p}$ are the elastic and the plastic strain components, respectively. The specific heat at constant pressure is represented by C_p, where λ is the thermal diffusivity and α is the thermal expansion coefficient.

For a dynamic equilibrium, thermo-elastic effects are assumed to have negligible contribution and even a negative effect on the temperature, where Lee and Shaue have reported nearly 0.8K decrease in temperature up to the yield point for Al2024-T3 under uni-axial tension at $2.0\text{x}10^{-2}s^{-1}$ [313]. Martinez has also reported a temperature decrease due to thermo-elasticity for Al2024-T3 [303]. Therefore, the thermo-elastic component of the equilibrium can be ignored as:

$$\frac{\alpha}{\rho C_p}\frac{E}{1-2\nu}T_0\dot{\varepsilon}_{kk}^{e} = 0 \tag{5.21}$$

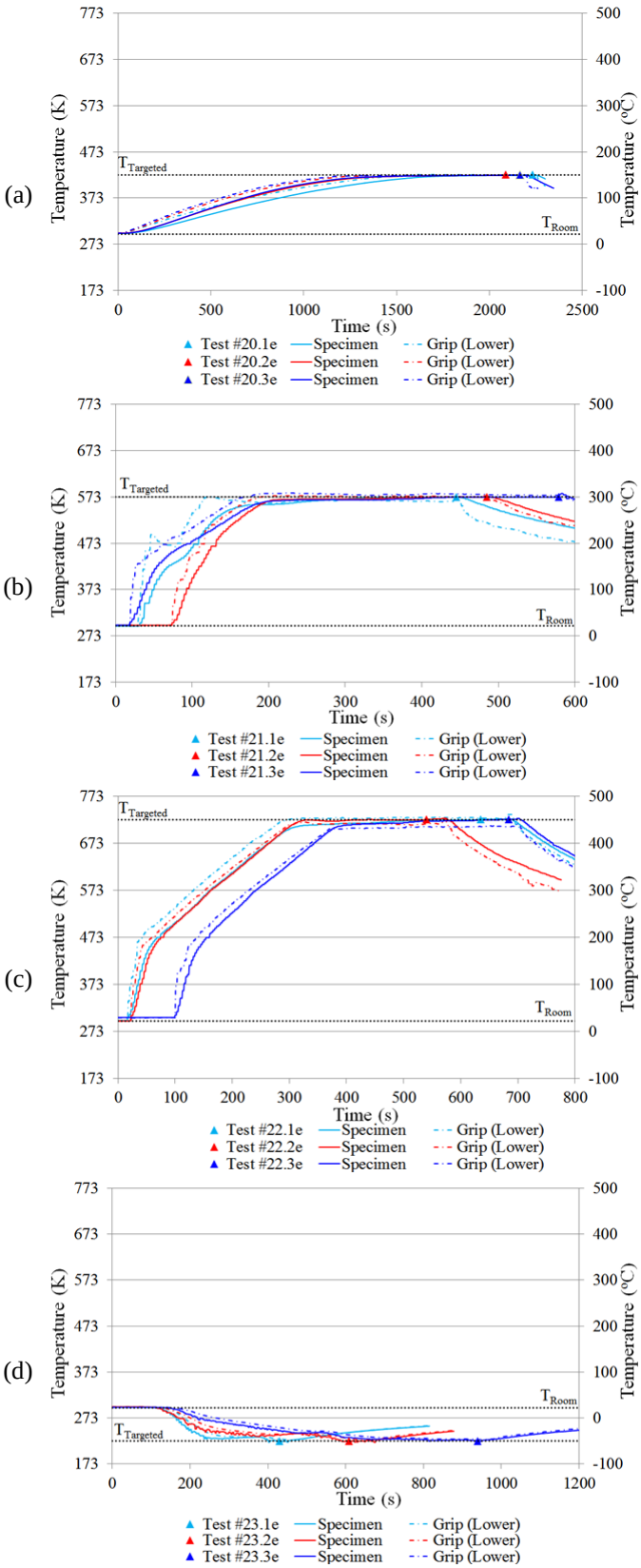

Figure 5-44: Evolution of temperatures within the testing apparatus for quasi-static torsion at targeted values of; (a) 423K, (b) 573K, (c) 723K and (d) 223K.

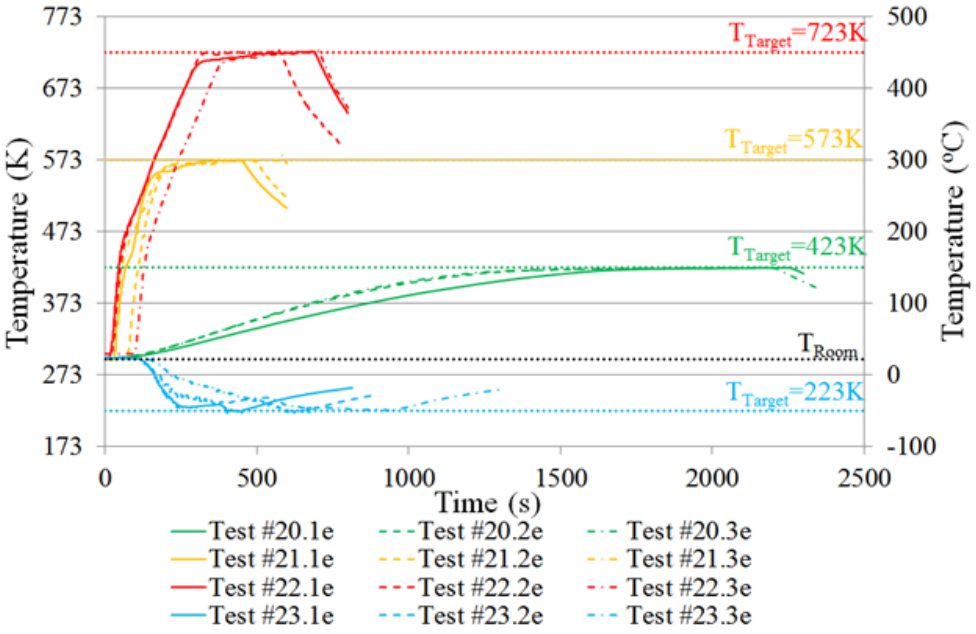

Figure 5-45: Temperature profiles of the torsion specimens until the targeted testing temperatures.

For an adiabatic process, where the deformation rate is high enough and no heat transfer between the specimen and the surrounding or within the specimen itself is expected, the heat conduction term can also be ignored as:

$$\lambda \nabla^2 T \dot{=} 0 \tag{5.22}$$

Consequently, assuming that the heat capacity C_p, Taylor–Quinney coefficient that represents the proportion of plastic work converted into heat β and the density ρ are constants, after integrating, the temperature increment becomes:

$$\Longrightarrow \dot{T} = \frac{\beta \sigma_{ij} \dot{\varepsilon}_{ij}^{p}}{\rho C_p} \Longrightarrow \Delta T(\varepsilon_p) = \frac{\beta}{C_p \rho} \int_0^{\varepsilon_p} \sigma d\varepsilon_p = T - T_{room} \tag{5.23}$$

where, T_{room} is the room/current temperature, σ is the flow stress and ε_p is the plastic strain, respectively.

The integral part of the equation corresponds to the irreversible energy stored in the body due to the plastic work. C_p is the specific heat at constant pressure and assumed constant as illustrated in Figure 5-32 for room temperature.

The amount of plastic work converted into heat is discussed extensively by Bever, et al. [314] and Rosakis et al. [315] within a thermodynamic framework. Hodowany, et al. [312] found that the amount of work changes between 60% to %100 depending on the amount of strain and strain rate for metals, where they have found no rate dependency for Al2024-T3. Mason et al. [316] found that, for strain-rate independent solids, the Zehnder's Model [317] provides an 'acceptable' prediction on the amount of work converted into heat, where they have measured rates between $10^{-3}s^{-1}$ to $10^{3}s^{-1}$. Zehnder assumed that the dislocation density increases with strain at a rate that is proportional to the work hardening exponent and formulated β as a function of the strain [317].

If n is the strain-hardening exponent of a power law hardening material as:

$$\sigma = \sigma_0 \left(\frac{\varepsilon}{\varepsilon_0}\right)^n \tag{5.24}$$

where, σ_0 and ε_0 are the yield stress and strain, respectively. The amount of plastic work converted into heat is found as:

$$\beta = \frac{\left(\frac{\varepsilon}{\varepsilon_0}\right)^{1-n} - 2nC_1}{\left(\frac{\varepsilon}{\varepsilon_0}\right)^{1-n} - n} \tag{5.25}$$

where, C_1 is a tuning parameter depending on the material. Zehnder model starts with a low value of β and increases with the accumulated plastic strain. The model can incorporate strain-rate sensitivity through hardening exponent if rate dependency present. Some fcc metals and especially aluminum alloys with low strain hardening behavior are found to behave according to Zehnder's Model [318].

There are also other models for β, which are considering strain-rate, temperature and stored energy of cold work [315] or using an extra coefficient for tuning the fraction of

heat retained in the body [319]. However, considering the strain-rate 'insensitive' properties of AL2024-T351 and since it is conservative to incorporate a relatively higher dependency of β, it is assumed to be a constant at 0.9, which is suggested as a proper value for metals under impact loading [204] [318]. Figure 5-46 illustrates the simulation results for Test #3.3 at $1.0s^{-1}$ under uni-axial tension and the calculated temperature increase with respect to the plastic strain for a finite element which is in the center of the neck region. It should be noted that the adiabatic stress vs. strain curve is utilized for the analysis, which is characterized in Section 5.5.2 but no correction for deformation heating or temperature softening is assumed. Both strain dependent behavior of the Zehnder's Model and constant assumption for β are also illustrated on the same strain space. With the increasing strain, both assumptions converge. However, it is a conservative assumption to use a higher value for β at the beginning of the strain accumulation that is converted into heat. It is shown that the temperature increase for a true strain of nearly 20% reaches 38K and the quasi-static test cannot be considered as isothermal, where an adiabatic to isothermal conversion procedure is required to characterize the input data for the constitutive model when thermal softening is activated.

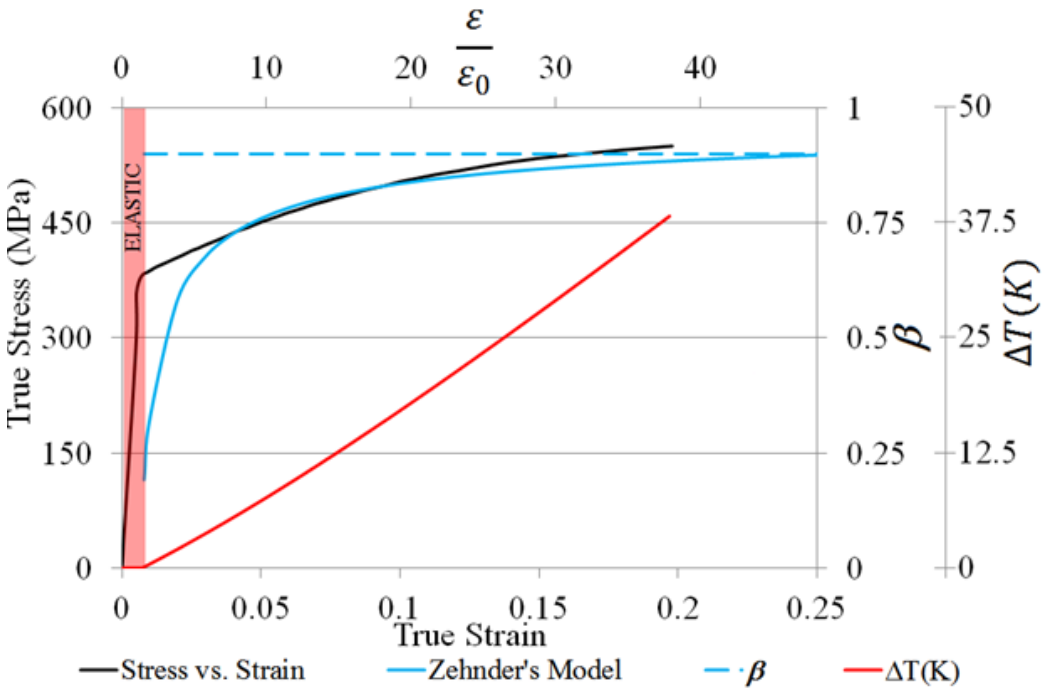

Figure 5-46: Evolution of temperature with respect to strain at quasi-static testing and the amount of plastic work converted into heat.

For the initial conditions, which are demonstrated in Figure 54-7(a) at time t_0, the specimen is assumed at room temperature. Several points are selected along the symmetry axis of the specimen for quantitative assessment of the evolution of the temperature profile. Temperature distribution on the specimen can be illustrated in Figure 5-47(b) at time t_n; just before failure occurs. Localization of the temperature profile can be noticed especially at the necked section of the specimen.

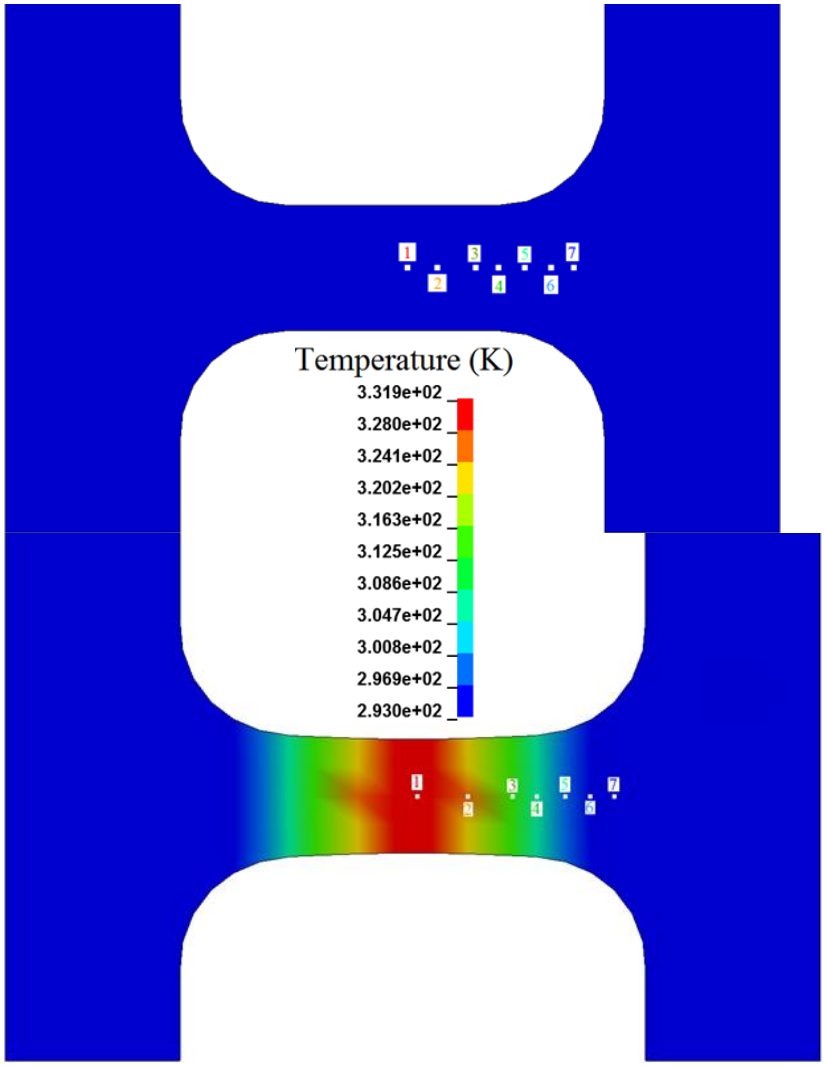

Figure 5-47: Evolution of temperature at quasi-static testing due to the plastic work; (a) initial conditions and (b) before failure.

The temperature profile within the specimen with respect to deformation can also be illustrated by Figure 5-48, where temperature values of the selected points along the symmetry axis are depicted beginning with the point that is at the center of the gauge length and eventually necking. The temperature history of the points are described with respect to the incremental solution steps of the finite element calculations, where t_i represents the initial time (i.e., $t_i \ ; i = 0, \dots, n$) and t_n represents the last time step before failure occurs. The results that are from the half of the specimen are illustrated for simplicity and it is assumed that the first point is always on the vertical symmetry axis. The initial gauge length of the specimen is shown with respect to the positions of the selected points. Solid black lines for each selected point represent the deformation paths and the corresponding readings for temperature as the specimen deforms. It can be seen that, due to plastic work, the initial temperature increases at around 38K at the center of the specimen, where tensile instability is observed.

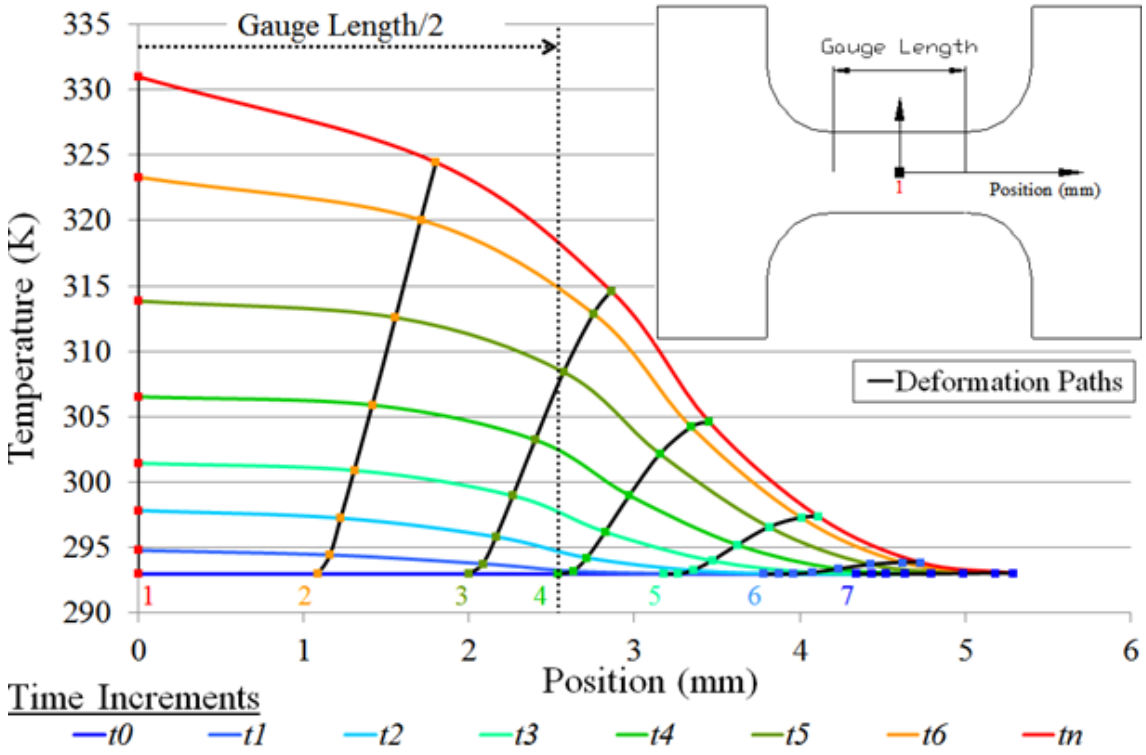

Figure 5-48: Evolution of temperatures at the selected points along the specimen with respect to deformation.

It should be noted that, both Figures 5-47 and 5-48 demonstrate results of the thermo-mechanical problem with adiabatic assumption according to Equation (5.23), where no heat transfer from the specimen is allowed but temperature softening is not activated by only using one hardening curve for each temperature and strain-rate. Therefore, a coupled heat conduction component should be incorporated into the balance equation and verify whether a full adiabatic assumption can be applied for quasi-static conditions by solving a coupled thermo-mechanical problem. If Equation (5.20) is rearranged as:

$$\rho C_p \Delta T = \beta \int_0^{\varepsilon_p} \sigma d\varepsilon_p - \kappa \nabla^2 T \tag{5.26}$$

where, κ is the thermal conductivity coefficient. Note that in Cartesian coordinates:

$$\nabla^2 T = \Delta T = \frac{\partial^2 T}{\partial x^2} + \frac{\partial^2 T}{\partial y^2} + \frac{\partial^2 T}{\partial z^2} \tag{5.27}$$

The coupled thermo-mechanical problem is illustrated in Figure 5-49 by the corresponding boundaries and initial conditions. One side of the specimen is pulled in the positive x-axis, where the other side is constrained. The specimen has a boundary with an initial temperature at both ends and assumed to have perfect contact with the grips or the testing apparatus, where this particular region constitutes a large heat sink with constant temperature. The heat that is generated due to the plastic work will be diffused by the flux $\vec{q}$ towards the ends of the specimen with lower temperature differentials. The problem is discretized and solved as a coupled thermo-mechanical field by using a fully implicit time integration scheme, which is unconditionally stable and can even accommodate long duration unsteady-state heat transfer problems by utilizing LS-DYNA as the non-linear FE solver. The material constants that are used to describe the thermal material properties are listed in Table 5-16.

The results are illustrated in Figure 5-50 for the coupled thermo-mechanical problem, where a comparison is demonstrated with the sole mechanical case and the case with heat conduction. The dashed lines in Figure 5-50 depict the temperature evolution and the

deformation history of the selected points along the symmetry axis of the specimen. It is clearly seen that the final temperature of the central point in the middle of the neck region is lower than the case when no heat conduction is considered. It is also shown that the temperatures of the end points rise due to the heat flow, which is not the case if heat conduction is not allowed. It should be noted that the results of the transient heat transfer problem are illustrated only for representative time increments, which corresponds to specifically selected intervals in time until the point of failure is reached at t_n during the uni-axial tensile test at the specified strain-rate.

Table 5-16: Test cases that are used to characterize quasi-static hardening curves for torsion.

Density ρ [kg/m^3]	Specific Heat Capacity C_p [J/Kg-K]	Thermal Conductivity Coefficient κ [W/m-K]
2780	875	121

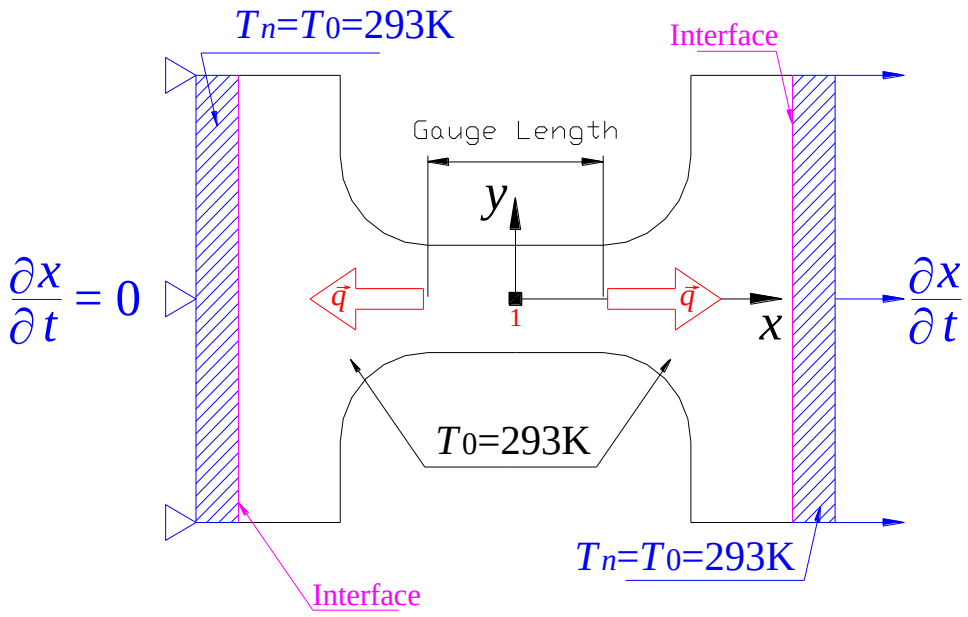

Figure 5-49: Thermo-mechanical problem for uni-axial tension.

Figure 5-50 also verifies that the temperature balance is in the path of convergence according to Equation (5.26), where the generated heat is transferred within the body towards the regions with lower temperatures trying to approach to equilibrium for the

diffusion problem within the given timeframe for quasi-static testing. Clearly, it is expected that if enough time is given, the whole specimen will reach to a constant temperature distribution. However, it should be noted that a failure state is also reached and limits the time dependent diffusion. Therefore, the evolution of temperature profiles and energies are illustrated as a function of position or strain (i.e., deformation).

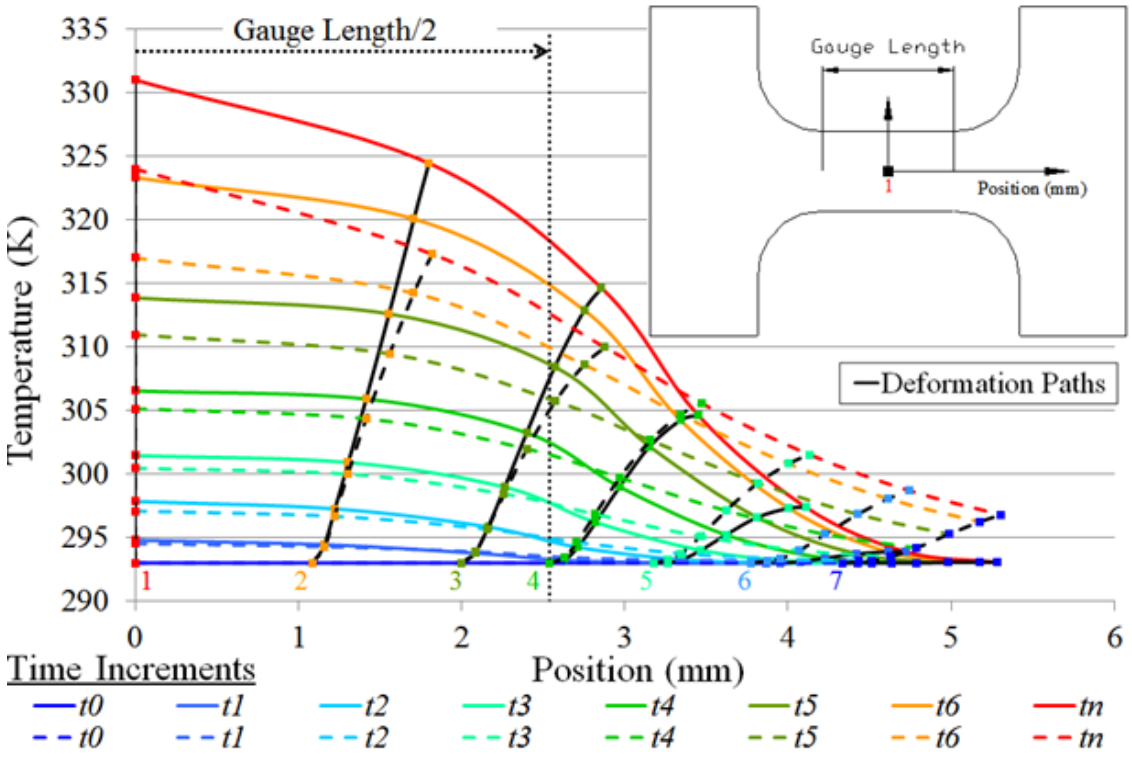

Figure 5-50: Evolution of temperatures with respect to deformation for coupled thermo-mechanical problem.

Figure 5-51 illustrates the temperature distribution and evolution of the temperatures within the specimen under quasi-static, uni-axial tensile loading, where two cases are compared to show the significance of incorporating heat conduction in the solution. First three increments of the solution are not illustrated for brevity. It is noticeable to observe the diffusion towards the ends of the specimen, where a constant temperature heat sink is assumed. It is also remarkable to see that the temperatures of the necked region become more homogeneous if heat conduction is permitted.

Time	Without Heat Conduction	Coupled Thermo-mechanical Solution with Heat Conduction

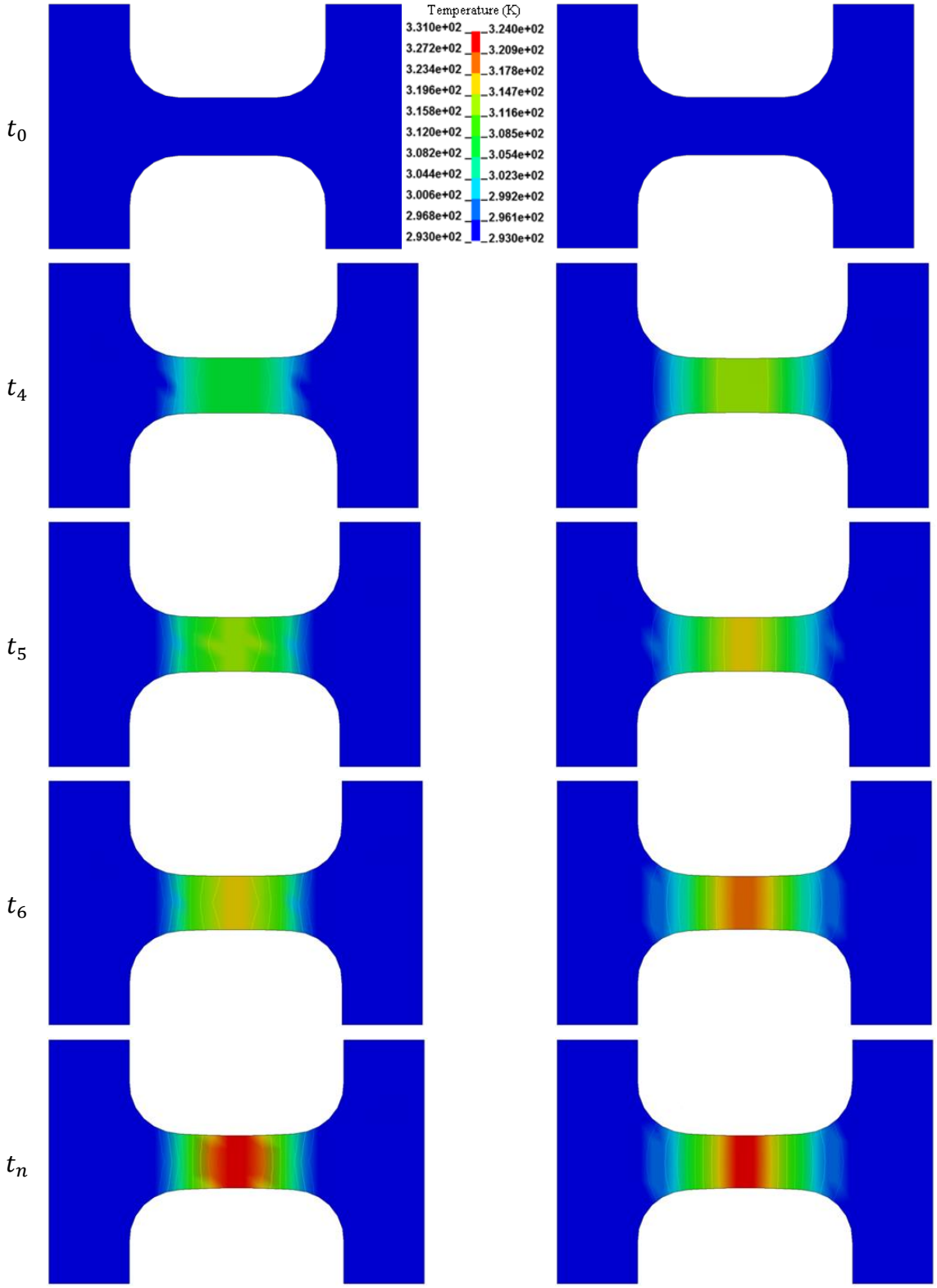

Figure 5-51: Temperature distribution within the specimen based on the formulation of the thermo-mechanical problem.

Heat transfer occurs due to the temperature gradient within the specimen, which generates a heat flux towards the regions with lower temperatures as illustrated in Figure 5-52 for the selected time increments. The flux vectors signify the direction and magnitude of the heat flow.

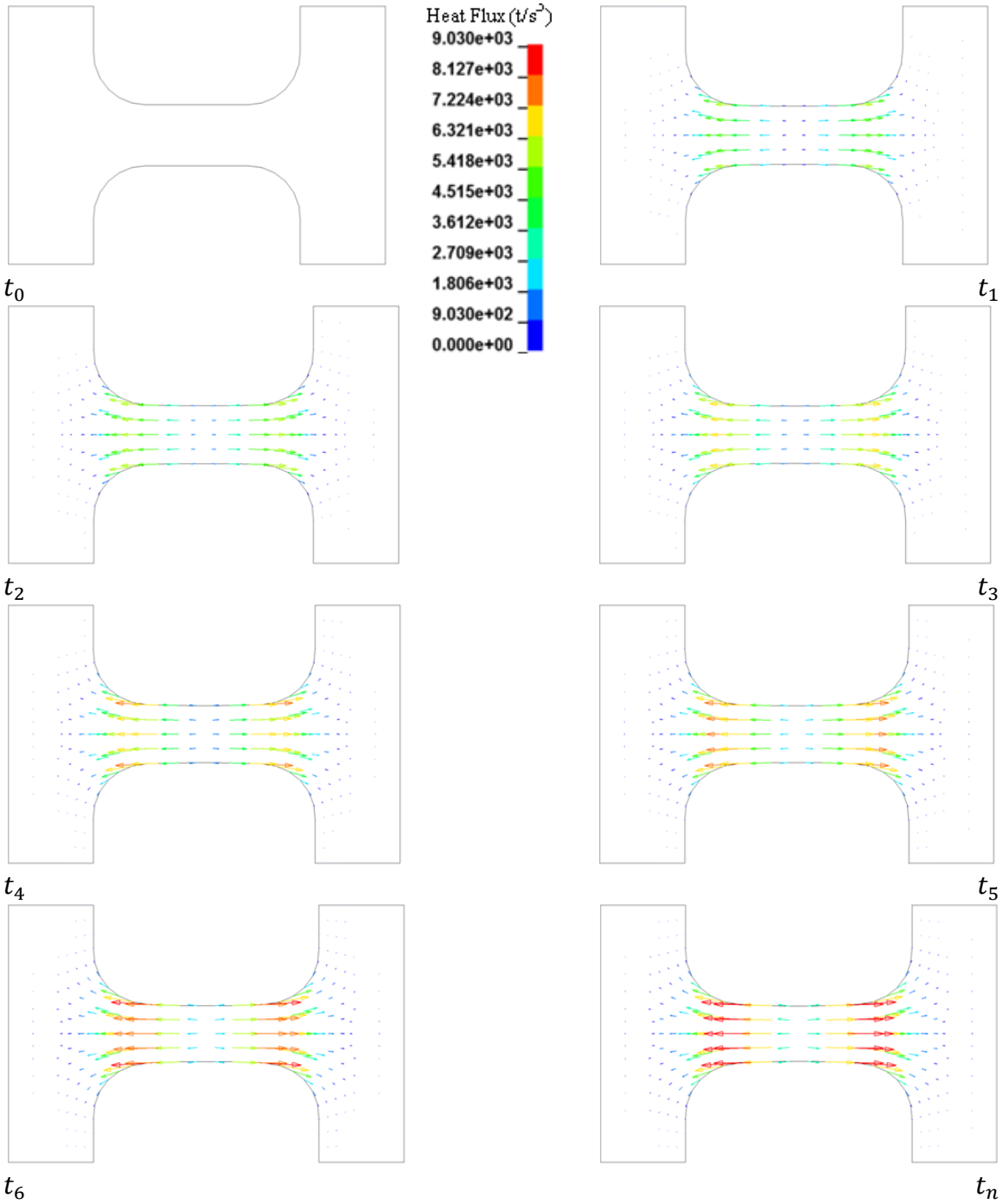

Figure 5-52: Heat flux within the specimen due to the thermo-mechanical problem.

It is shown that a significant amount of heat is transferred through the shoulder geometry of the specimen and it can be concluded that the specimen geometry and the type of gripping can play an important role in achieving isothermal conditions especially while testing at high rates of deformation and temperature dependent testing [320].

As a result of the plastic work that is converted into heat and conducted through the specimen, Figure 5-53 illustrates the calculated total proportion of the energy for the whole specimen overlaid with the total temperature increase. It should be noted that the maximum temperature increase is observed at the center of the neck formation and conducted across the shoulder of the specimen. Figure 5-53 exhibits the total change in the temperature during the quasi-static testing at a strain-rate of $1.0s^{-1}$. It is remarkable to observe that the calculated profile of β is in good agreement with both Zehnder's dislocation based model and Macdougall's experimental observations for an Aluminum alloy, where he has used infrared radiometry and thermocouples to verify the proportion of plastic work converted into heat [318].

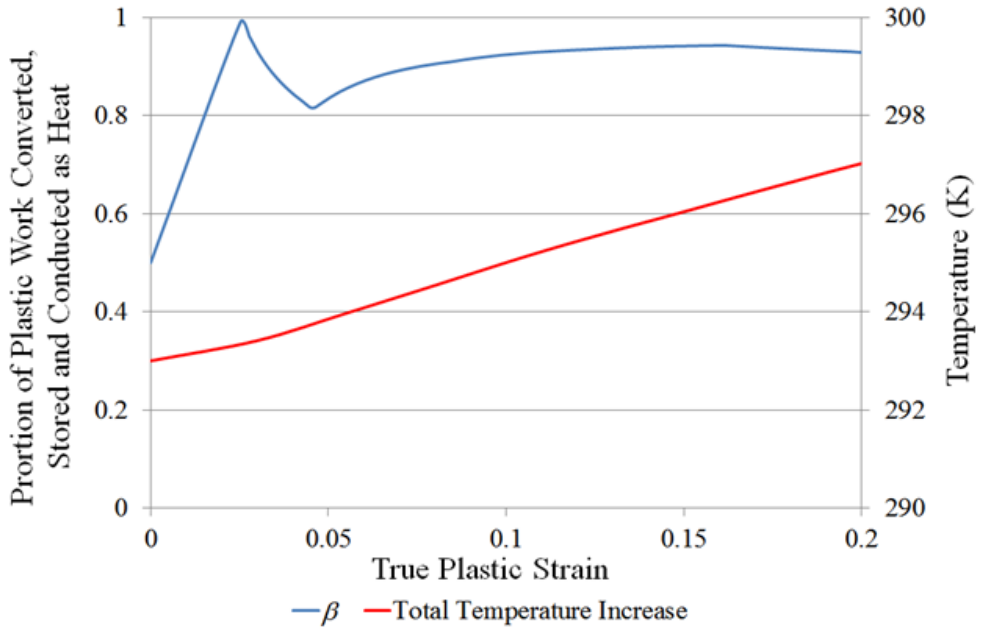

Figure 5-53: The amount of plastic work converted into heat and the corresponding total temperature increase.

The results suggest that β increases with the increasing plastic strain and even exceeds 90% (i.e., 0.9) until around 5% strain. As the dynamic equilibrium is reached, β attains a monotonic, steady-state regime around 0.9 until the failure. The rather monotonic increase in the total temperature indicates the existence of localized temperature increases. Consequently, a constant value for the proportion of plastic work into heat is utilized (i.e., $\beta = 0.5$) for the simulations during the course of this dissertation.

It is shown that quasi-static tests are not ideally isothermal but quasi-adiabatic and temperature softening also needs to be considered during the characterization of the isothermal hardening curves for TRAUM. To characterize the isothermal hardening curves, quasi-adiabatic behavior is used as the baseline. A one step inverse calculation is performed to elevate the strength of the material for the corresponding true plastic strain proportional to the amount of heat generated within the body or the plastic work. Clearly, the effects of heat conduction are also required to be considered during the calculation as described by Equation (5.26). Therefore, to characterize isothermal hardening curve for a corresponding temperature and strain-rate, a coupled thermo-mechanical simulation is also needed. Figure 5-54 illustrates the comparison of the test results when the characterized quasi-adiabatic hardening curves are used with and without the temperature softening behavior of TRAUM, which is activated by incorporating tabulated temperature dependent hardening curves $kt(\varepsilon_p, T)$ from Equation (4.6). In this figure, it should be first noticed that the test results (i.e., Test #2.3 with force vs. displacement curve that is dotted and in red color) are validated (i.e., force vs. displacement curve that is dashed and in green color) by utilizing an adiabatic hardening curve (i.e., true stress vs. true strain curve in green color) without considering the effects of temperature softening. However, when the temperature softening effects are activated with the corresponding temperature dependent flow surface kt, the calculated response softens (i.e., force vs. displacement curve that is dotted and in green color) and the correlation is lost, as expected. Therefore, an adiabatic to isothermal inverse conversion of the strength is required to account for the amount of temperature softening with respect to the plastic work by considering the amount of plastic work converted into heat and the conduction of the generated heat within the specimen. Consequently, an isothermal hardening curve (i.e., true stress vs.

true strain curve in blue color) is calculated by considering the retained energy due to the plastic work and the correlation with the test result can be achieved again (i.e., force vs. displacement curve that is dotted and in blue color) when the temperature softening effects are active. Using adiabatic hardening curves to describe the flow surface artificially softens the material if adiabatic heating feature of TRAUM is active according to Equation (4.7). Thus, isothermal hardening curves are characterized in the next sections by using an automated methodology that will identify the baseline adiabatic hardening curve according to the mesh sensitivities and variations of the test results and then obtain the isothermal hardening curves at the final stage by an inverse thermo-mechanical calculation of the retained energies.

However, it should be noted that quasi-static temperature changes within the specimen or transient temperature differential effects were not measured during the temperature or strain-rate dependent testing of Al2024-T351. Figures 37, 38, 40, 41, 44 and 45 are illustrating the temperature profiles of the testing chamber and the specimen to verify the ambient temperature stability only during the testing.

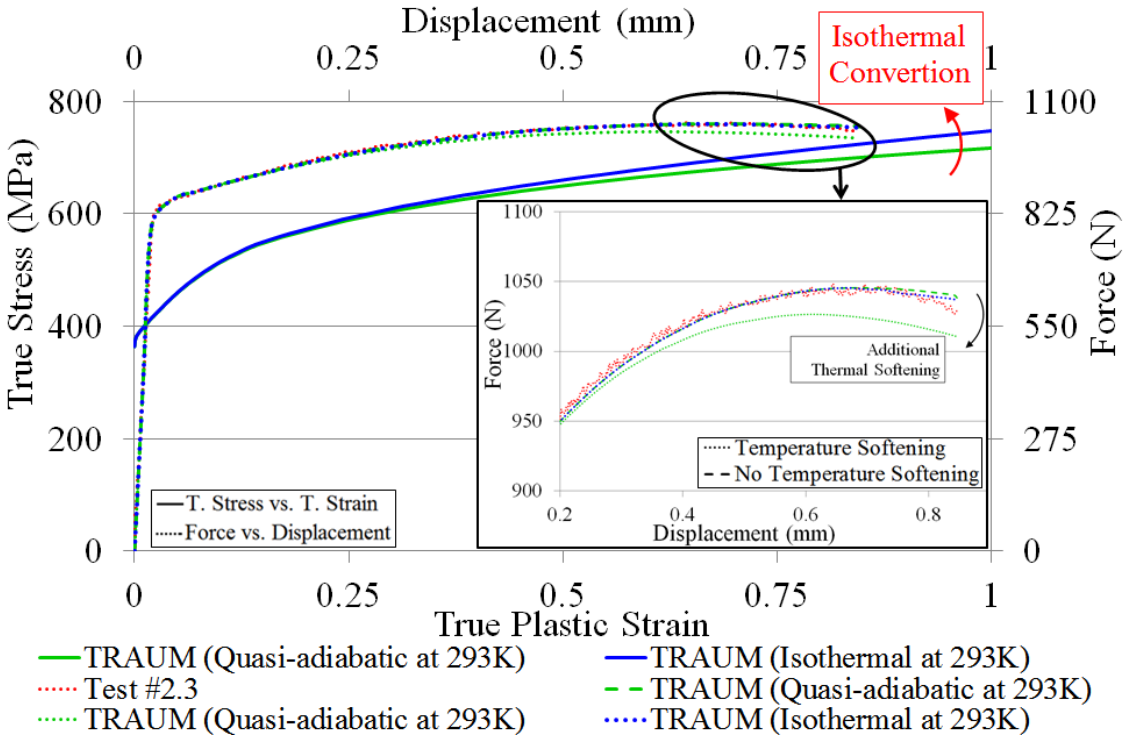

Figure 5-54: Calculating isothermal hardening curves from adiabatic hardening curves.

5.6.5 **A multi-case automated material characterization methodology by using AO algorithm based on SRSM**

An iterative characterization methodology is described in Section 5.5.2 to obtain quasi-static, quasi-adiabatic hardening curves at room temperature by incorporating a power law plasticity assumption on the extrapolated part after necking. It is shown in Sections 5.5.3 – 5.5.5 that the described method can successfully be used to generate accurate hardening curves.

Therefore, a similar method can be used to automatically characterize the flow surface of a material by generating temperature dependent flow curves for a more generic usage by utilizing an inverse parameter identification algorithm that is schematically illustrated in Figure 5-55 as an error minimization criterion [283]. The algorithm is divided in four major tasks, which are pre-processing (in red color), optimization (in black color), numerical solver (in blue color) and thermo-mechanical compensation cycle for adiabatic heating (in green color).

The pre-processor is a user defined routine that is responsible from generating the input curves, which will be used by the FE models and the reference curves that will be used to evaluate the objective functions. LS-OPT is used as the optimizer, where a Successive Response Surface Methodology (SRSM) will be utilized for optimization [321]. Non-linear simulations will be performed by using LS-DYNA as the solver [96]. The compensation of the adiabatic heating is calculated for a single cycle that requires a coupled non-linear thermo-mechanical simulation. The retained energy within the specimen due to the adiabatic effects are calculated based on the methodology that is described in the previous section and then is used to generate the isothermal hardening curves for the specific strain-rate and temperature. The automation of the tasks is maintained by a framework, which is developed within MATLAB [322].

It should be noted that the automated material characterization methodology is described in the successive sections only for a demonstration case for brevity and is then used to characterize the isothermal flow surface by considering the corresponding strain-rate and temperature dependent test results, which are detailed in Appendix-C.

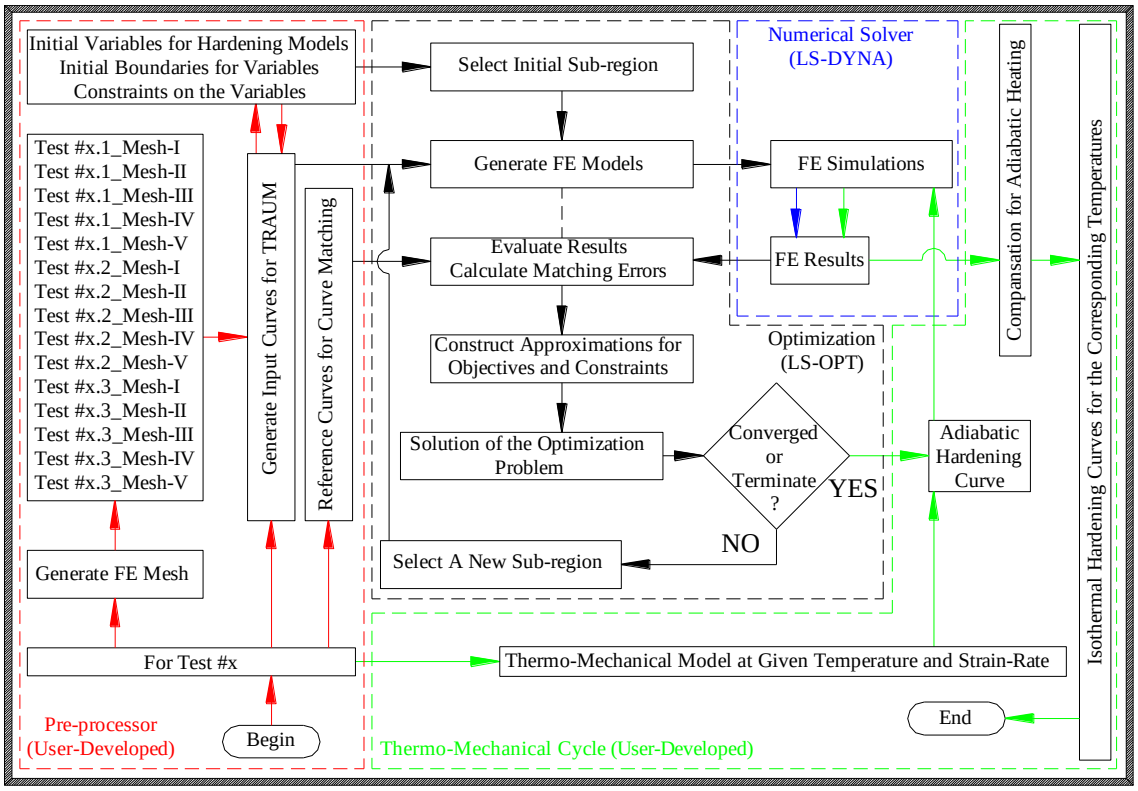

Figure 5-55: Flow diagram of the automated parameter identification process for material characterization by using SRSM for temperature dependent tests.

Several different factors are addressed while developing an automated scheme by coupling an Approximate Optimization (AO) algorithm with FE simulations to construct SRS for the prediction of the flow curves by parameter identification. Figure 5-56 illustrates the flow chart of the first task, where the initial input and the reference curves are generated. The methodology begins with a smoothing stage, where the targeted reference response curves are generated within the framework of automated material characterization process by utilizing MATLAB as the main user interface [322]. Especially with the temperature dependent flow, it is not uncommon to find PLC effects becoming more dominant and the serrated flow behavior can oblige automated characterization to become more complex in nature. A nine point average quadratic smoothing is applied to generate stress vs. strain curves. It is also necessary to apply a modulus correction on the engineering stress vs. engineering strain curves, which are generated according to Equation (5.1) for each test case, based on the temperature

dependent Young's modulus that is shown in Figure 5-32. The experimental curves can then be used as the targeted reference curves while minimizing the residuals from the simulated response, which is often referred as the 'distance function' of the objectives [287].

The objective function can be represented as a composite form or a combination of several different objective functions primarily based on the minimization of the 'distance functions' or error with respect to the experimentally measured curve depending on minimizing the Mean Squared Error (MSE) concept [287].

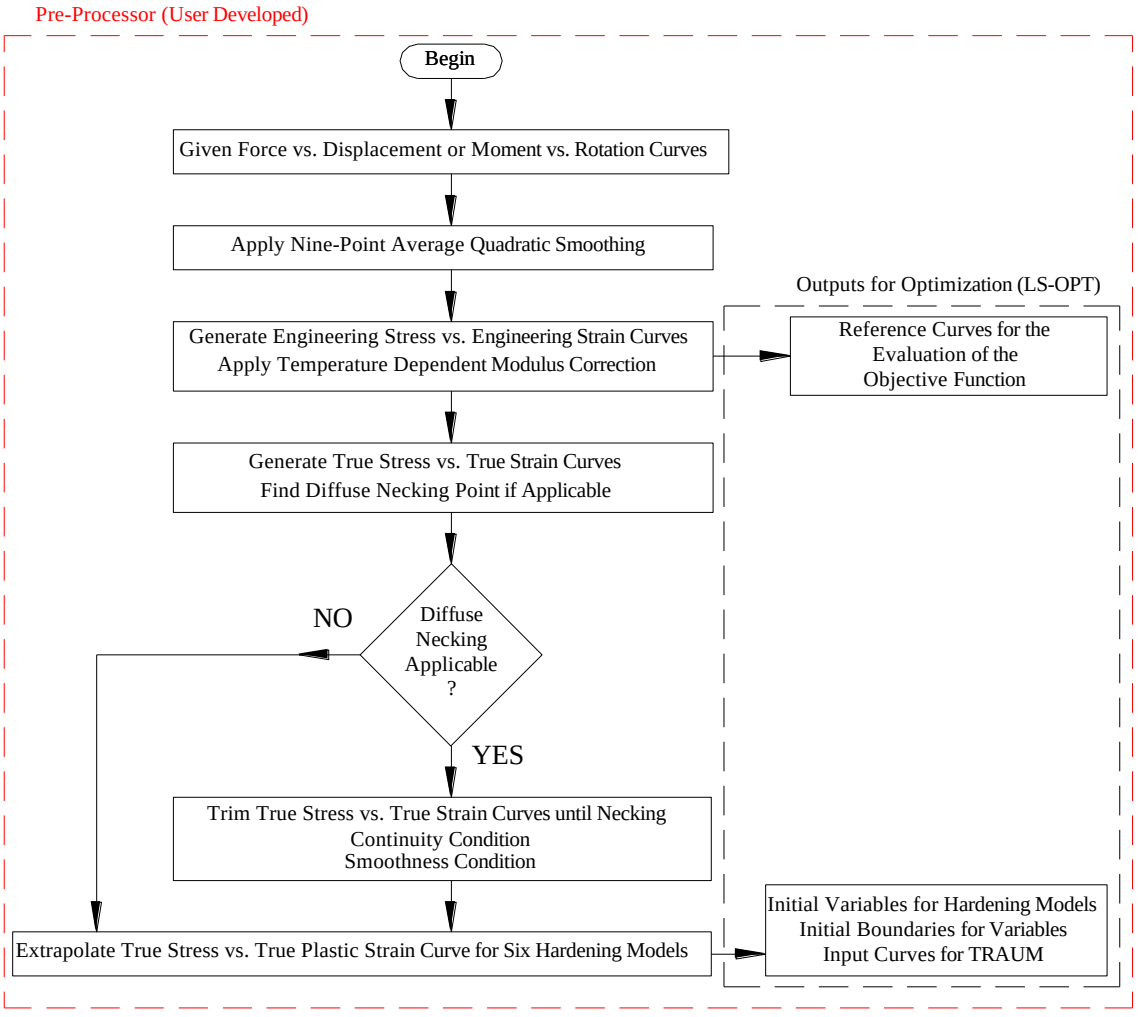

Figure 5-56: First stage of the automated parameter identification process for material characterization by using SRSM for temperature dependent tests.

The true stress vs. true strain curves can directly be generated according to Equation (5.3) and the diffuse necking points can be found according to Equation (5.28) by using Considère's criterion that is also defined by Equation (5.5). The true stress vs. true plastic strain curves until the necking point can be generated according to Equation (5.4) or a curve fitting can be used to find an equivalent analytical representation by estimating the initial parameters of a hardening model.

$$d \ln \sigma = d\varepsilon \tag{5.28}$$

However, with the increasing oscillations due to PLC effect, using Considère's criterion may not be sufficient to identify the onset of diffuse necking. Moreover, during the elevated temperature testing, necking may occur very rapidly and the material can almost demonstrate an elastic-perfectly-plastic behavior, where it is not often possible to identify necking. Therefore, the whole true stress vs. true plastic strain curve that was generated in the previous step or an equivalent analytical model is directly used as the flow curve. However, an automated characterization algorithm is needed to test several different hardening models for the best correlation of the flow up to uniform elongation and should accurately predict large strain behavior after extrapolation. Effects of temperature softening, dynamic recovery and recrystallization may also require the algorithm to predict a non-monotonic hardening curve for the representation of the flow. Therefore, several different analytical hardening representations are considered at the same time by incorporating six different models and comparing each for the most accurate prediction [251]. It should be noted that the hardening models will be treated as a discrete variable and the model which provides the minimum LSE will be determined automatically by the optimization algorithm as the most successful flow model. Table 5-16 lists six different hardening models that are used to predict the flow behavior with different number of variables, which will be found as a result of the non-linear optimization. The initial values of these variables are estimated by using the curve fitting feature of MATLAB [322]. Upper and lower boundaries of the initial estimations are also found within 95% confidence interval that will determine the initial boundaries of the independent variables during the optimization stage. It should be noted that TRAUM can

accept tabulated input curves to generate the flow and failure surfaces. On the other hand, it would be computationally costly to predict a tabulated curve by using an inverse method since the whole hardening curve should be represented with numerous number of independent variables as a function of true plastic strain [323]. Clearly, the cost of the non-linear optimization is reduced significantly if the number of independent variables is reduced, which is directly effecting the number of required non-linear FE simulations. Therefore, the analytical hardening models that are listed in Table 5-17 to characterize the flow have a maximum of four independent variables due to a concern of cost reduction during the optimization procedure.

Table 5-17: List of hardening models.

Hardening Models	Discription	Variables	
Hollomon [269]	$\sigma(\varepsilon^p) = C_1 \varepsilon^{p\,C_2}$	$\{C_1,\ C_2\}$	(5.29)
Ludwik [324]	$\sigma(\varepsilon^p) = C_1 + C_2 \varepsilon^{p\,C_3}$	$\{C_1,\ C_2,\ C_3\}$	(5.30)
Swift [292]	$\sigma(\varepsilon^p) = C_1 (C_2 + \varepsilon^p)^{C_3}$	$\{C_1,\ C_2,\ C_3\}$	(5.31)
Voce [290]	$\sigma(\varepsilon^p) = C_1 + (C_2 - C_1)\, e^{-C_3 \varepsilon^p}$	$\{C_1,\ C_2,\ C_3\}$	(5.32)
Hockett/Sherby [325]	$\sigma(\varepsilon^p) = C_2 - (C_2 - C_1)\, e^{-C_3 \varepsilon^{p\,C_4}}$	$\{C_1,\ C_2,\ C_3,\ C_4\}$	(5.33)
Ghosh [326]	$\sigma(\varepsilon^p) = C_1 + C_2 (C_3 + \varepsilon^p)^{C_4}$	$\{C_1,\ C_2,\ C_3,\ C_4\}$	(5.34)

Initials of the models are used for comparison as:
H : **H**ollomon, **L**udwik : **L**, **S**wift :**S**, **V**oce : **V**, **H**ockett/**S**herby :**H/S**, **G**hosh :**G**

According to Figure 5-56, if a diffuse necking point can be identified; the curve fitting algorithm will trim the flow curve at onset of necking ε_n as illustrated by Figure 5-18 and the rest of the curve is found by the optimization algorithm by using the analytical hardening models in Table 5-17. However, two constraints are applied in this case to impose continuity and smoothness of the hardening curve based on Equations (5.35) and (5.36).

$$\varepsilon_n \equiv \varepsilon_n|_{\varepsilon=\varepsilon_n},\ \sigma_n \equiv \sigma_n|_{\varepsilon=\varepsilon_n} \tag{5.35}$$

$$\varepsilon_n \equiv \varepsilon_n|_{\varepsilon=\varepsilon_n},\ E_t \equiv E_t|_{\varepsilon=\varepsilon_n} \tag{5.36}$$

where, ε_n is the strain at necking, σ_n is the stress at necking and $E_t = \frac{d\sigma}{d\varepsilon}$ is the tangent or hardening modulus.

Repeatability of the tests is also considered during the parameter identification, where each test was repeated at least three times unless otherwise stated. Differences in strain-rates, temperatures and specimen geometries are considered during the prediction of the corresponding flow curves, which suggests a multi-case (i.e., multi-objective) implementation of the objective function during optimization. Consequently, each repeated test case is treated as independent and the comparison between the experimentally measured engineering stress vs. engineering strain curve and the numerically calculated response is evaluated separately to find the objective function. Each objective is then combined to form a multi-case objective and the best solution for all is found as the minimum of the multi-objective functions. Although this method is more costly, it is recommended since the sensitivities of the contributing factors on the response and the uncertainty of the test results are not identified.

Flow behavior is also mesh dependent as illustrated in Figure 5-21. Therefore, mesh size should be considered during the characterization of the hardening behavior, where five different mesh lengths, which are referred as Mesh Patterns #3 - #7 in Table 5 (i.e., as illustrated in Appendix-E) are utilized for each test case. Therefore, each individual test is modeled by fifteen different FE models and the optimum is found for all fifteen models, where the models with a characteristic element length of 0.1483mm and referred as [t/5] in Table 5-9 are assumed to have 200% more significance by assigning a weight factor considering that the same mesh size will also be utilized during the characterization of the failure strains in the proceeding sections.

Deciding on the curve matching methodology is also a concern during the comparison of an experimental curve and a calculated response. A combination of two different approaches is used for the parameter identification algorithm. The first approach is a more common Ordinate-based Curve-Matching (OCM) methodology, where error is quantified by the sum of the squares of the distances in the values between the targeted experimental points and the interpolated points on the computed curve [321]. This method works efficiently when both curves are monotonic, have similar lengths and no oscillations are expected, where control points do not explicitly depend on the abscissa.

Figure 5-57 illustrates the features of an OCM between stress-strain curves, where $g(\varepsilon)$ represents the experimental curve that is defined by experimental points $g_n(\varepsilon)$ and $f(z,\varepsilon_n)$ is the computed response curve that is represented by a response surface. A typical curve $f(z,\varepsilon)$is then represented by N number of response surfaces. The error is defined by e_n and the combined MSE of the whole domain can be calculated as:

$$E_1 = \frac{1}{N}\sum_{n=1}^{N} W_n \left(\frac{f(z,\varepsilon_n) - g(\varepsilon_n)}{s_n}\right)^2 = \frac{1}{N}\sum_{n=1}^{N} W_n \left(\frac{e_n}{s_n}\right)^2 \tag{5.37}$$

where, W_n are the weighting factors and s_n are the scale factors, which are taken as unity since all points are assumed to have equal importance and contribution except Mesh Patterns #5 as mentioned for the mesh sensitivity.

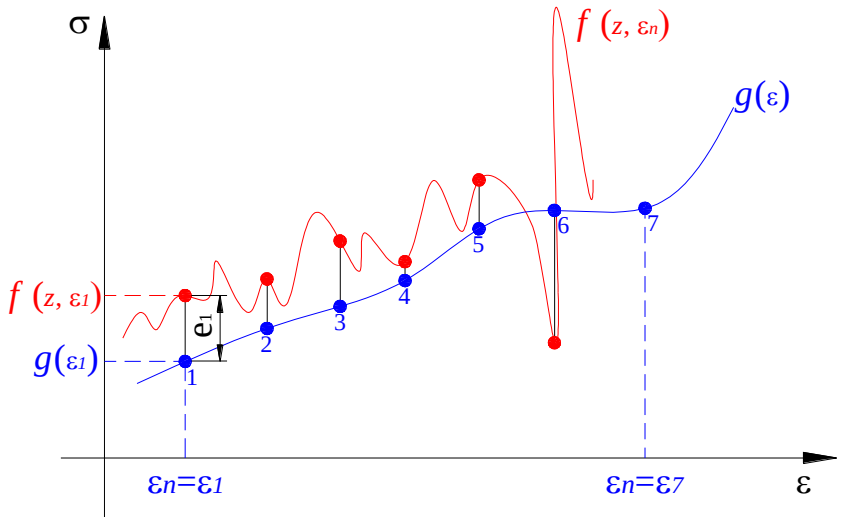

Figure 5-57: Features of OCM methodology.

Although OCM methodology is fast and effective, it has some limitations in matching curves with steep deviations as illustrated around Point#6 in Figure 5-57. Therefore, the method is supported with a secondary algorithm to characterize failure strains when the stress vs. strain curve rapidly drops. Another limitation of the OCM is a strict dependency of the range of two curves. As illustrated around Point#7 in Figure 5-57, if computed and targeted curves do not coincide at any location of the domain, the algorithm can become

instable as the error of that point will not be possible to quantify. Oscillations on the matching curves are also not desirable when the OCM is utilized as illustrated around Point#6 in Figure 5-57, which may find a non-unique solution and become unstable. Considering PLC effects at elevated temperature testing, this limitation also justifies that a secondary curve matching algorithm should be utilized in addition to OCM.

Partial Curve Mapping (PCM) methodology [327] [328] is the secondary algorithm that is utilized to find the error between the experimentally obtained engineering stress vs. engineering strain curves and the calculated responses. The method depends on a strategy which is using a matching metric that is computed by using the volume between the experimental the computed curve section. PCM technique is advisable for material models that utilize tabulated or piecewise-linear inputs (i.e., TRAUM) considering that the method assumes both experimental and computed curves to be polygonal and takes the continuity of the curves into account [327]. It is also reported that the method provides good matching accuracy with hysteretic curves since both curves are normalized and becomes independent of the actual curve length [329]. Therefore, PCM is preferred for characterizing hardening curves especially when the PLC effects are significant. The method aims to find the best match between the curves a and a'' as illustrated in Figure 5-58 by finding the minimum sum of volumes as formulated in Equation (5.30) [327].

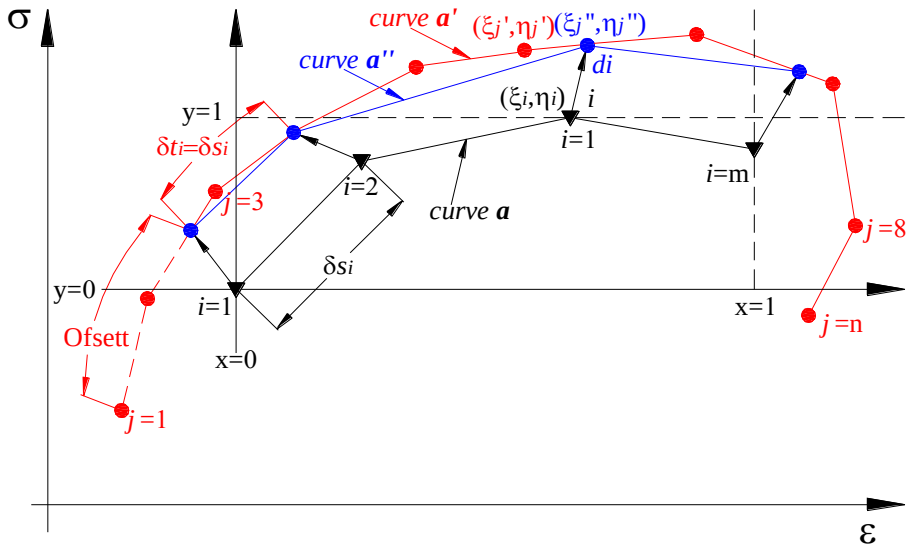

Figure 5-58: Features of PCM methodology, adapted from [327].

$$E_2 = \min_{p} \sum_{i=1}^{m} \frac{d_i - d_{i-1}}{2} \times \frac{\sqrt{(\xi_i - \xi_{i-1})^2 + (\eta_i - \eta_{i-1})^2}}{s} \qquad ; (i = 2,3, \dots, m) \quad (5.38)$$

where, d_i are the distances between the point pairs and s is the total polygon length for curve a. The total length of the curve a' is represented by t in Figure 5-58 and an offset increment can be accommodated by a 'slide' control within the increments [327].

Segment lengths of each polygon can be calculated for curve a as:

$$\delta s = \sqrt{(\xi_i - \xi_{i-1})^2 + (\eta_i - \eta_{i-1})^2} \qquad ; (i = 2,3, \dots, m) \quad (5.39)$$

It should be noted that the vertices of the original curve a is used as a boundary with a range of $[(0,0); (1,1)]$. Coordinates are normalized as:

$$\xi_i = \frac{x_i - x_{min}}{x_{max} - x_{min}} , \qquad \eta_i = \frac{y_i - y_{min}}{y_{max} - y_{min}} \qquad ; (i = 1,2, \dots, m) \quad (5.40)$$

The vertices of the mapped curve a' and the final mapped curve a'' are also normalized to the boundaries of the original curve a as:

$$\xi'_j = \frac{x_j - x_{min}}{x_{max} - x_{min}} , \qquad \eta'_j = \frac{y_j - y_{min}}{y_{max} - y_{min}} \qquad ; (j = 1,2, \dots, n) \quad (5.41)$$

Therefore, the combined objective function of the parameter identification problem can be expressed by uniting the minimum of sum of the errors of OCM and PCM techniques and reducing the problem into a single objective function as:

$$\min E = \min(E_1 + E_2) \quad (5.42)$$

Parameter identification algorithms are often formulated as unconstrained optimization problems if additional constraints are not prescribed, where appropriate rules that are related to the continuity, monotonicity or smoothness of the design space can be imposed on the selection of the parameters [287]. Therefore, a constrained SRSM

is utilized for the optimization problem considering the constraints that are defined by Equations (5.35) and (5.36).

The optimization problem can be formulated by considering the vector of stress response values during a tensile test as:

$$\boldsymbol{\sigma} = \boldsymbol{\sigma}(\mathbf{C}, \boldsymbol{\varepsilon}) \tag{5.43}$$

where, $\mathbf{C}$ is the vector of material parameters, which is also referred as the vector of design variables. An operational vector is defined by $\boldsymbol{\varepsilon}$ to turn objectives into physically known variables. Clearly, stress and strain variables that are used during the optimization are engineering values and are found by using Equation (5.1). If the material parameters $\left(\mathbf{C}^{\text{real}}\right)$ were known, the system could have written as:

$$\boldsymbol{\sigma}^{\text{real}} = \boldsymbol{\sigma}\left(\mathbf{C}^{\text{real}}, \boldsymbol{\varepsilon}\right) \tag{5.44}$$

However, material parameters are usually unknown and only engineering stresses can be obtained from Equation (5.1) by experimentally measured force responses. The parameter identification problem is then formulated to obtain the approximation such that the approximated stresses approach to the real stresses as:

find:	$\mathbf{C}^{\text{approximate}}$		(5.45)
given:	$\boldsymbol{\varepsilon}$		(5.46)
minimize:	$\mathbf{E} = \left(\mathbf{E}_1\left(\mathbf{C}^{\text{approximate}}\right) + \mathbf{E}_2\left(\mathbf{C}^{\text{approximate}}\right)\right)$		(5.47)
subjected to:	$\mathbf{B}_i\left(\mathbf{C}^{\text{approximate}}\right) = 0$	$;(i = 1,2)$	(5.48)
such that:	$\boldsymbol{\sigma}\left(\mathbf{C}^{\text{approximate}}, \boldsymbol{\varepsilon}\right) \Longrightarrow \boldsymbol{\sigma}^{\text{real}}$		(5.49)
within the design space:	$C_j^{Lower} \leq C_j \leq C_j^{Upper}$	$;(j = 1,2,3,4)$	(5.50)
within the discrete design space:	$C_p = \{\mathrm{H}, \mathrm{L}, \mathrm{S}, \mathrm{V}, \mathrm{H/S}, \mathrm{G}\}$	$;(p = 1,2,\ldots,6)$	(5.51)

where, $\mathbf{C}^{\text{approximate}}$ are the approximated design variables or the material parameters to be found, $\mathbf{E}$ is the combined objective function based on the minimization of the difference between the targeted and approximated values by using Equation (5.42) and $\mathbf{B}_i$ are the constraint functions based on Equations (5.35) and (5.36). The parameters that are

used to define the number of constraint functions, continuous and discrete design variables are respectively given by i, j and k. C_j^{Lower} and C_j^{Upper} are the lower and upper bounds of the continuous design variables, where C_p represents the set of discrete design variables and the set comprises the six hardening models that are defined in Table 5-17.

It should be noted that the optimization problem comprises both continuous and discrete variables, where material hardening models are discrete and their corresponding parameters are continuous variables. This technique is referred as the mixed-variable optimization [284]. A more effective strategy is to replace the optimization problem in Equations (5.45) – (5.51) with a series of simpler approximate sub-problems [330] [285] [321]. In this approach, solutions of the sub-problems are expected to yield the optimum of the original optimization problem. The *k*-th sub-problem in this approach is defined as:

find:	$\mathbf{C}^{\text{approximate}}$		(5.52)
given:	$\boldsymbol{\varepsilon}$		(5.53)
minimize:	$\tilde{\mathbf{E}}^{(k)} = \left(\mathbf{C}^{\text{approximate}}\right)$		(5.54)
subjected to:	$\tilde{\mathbf{B}}_i^{(k)}\left(\mathbf{C}^{\text{approximate}}\right) = 0$	$; (i = 1,2)$	(5.55)
such that:	$\tilde{\boldsymbol{\sigma}}^{(\mathbf{k})}\left(\mathbf{C}^{\text{approximate}}, \boldsymbol{\varepsilon}\right) \Longrightarrow \boldsymbol{\sigma}^{\text{real}}$		(5.56)
within the part of the design space (i.e., sub-region):	$C_j^{Lower(k)} \leq C_j \leq C_j^{Upper(k)}$	$; (j = 1,2,3,4)$	(5.57)
within the part of the discrete design space (i.e., sub-region):	$C_p^{(k)} = \{\mathrm{H}, \mathrm{L}, \mathrm{S}, \mathrm{V}, \mathrm{H/S}, \mathrm{G}\}$	$; (p = 1,2, \ldots, 6)$	(5.58)

where, $C_j^{Lower(k)}$ and $C_j^{Upper(k)}$ define the bounds of the *k*-th sub-region and $C_j^{Lower(k)} \geq C_j^{Lower}$, and $C_j^{Upper(k)} \leq C_j^{Upper}$.

Equations (5.52) – (5.58) are solved by replacing the objective and constraint functions with successive response surface approximations in the *k*-th sub-region by using least square error curve fitting, where they are utilized as simplified mathematical representations of the computationally costly FE simulations. Therefore, the method is often referred as SRSM [321] [198]. The sub-problem in Equations (5.52) – (5.58) is solved by using LS-OPT, which implements AO based on SRSM [321].

During the successive AO approach, the optimal point of the *k*-th sub-problem becomes a starting point for the next (i.e., *k*+1-th) sub-problem. The process of creating new sub-problems with new approximations and solving for optimums is repeated until

the convergence criterion is reached. Convergence criterion that is used in this study is the relative change in the approximate objective values in the last two iterations and its value is considered as 1%.

Construction of approximations by RSM and the adjustment of size of successive sub-regions are the two important features of the successive AO. While constructing the approximations by RSM, the type of an approximation function is determined first. This information is needed to select only sufficient number of design points to create the approximation efficiently. A function $\tilde{\boldsymbol{\sigma}}^{(\mathbf{k})}(\mathbf{C})$ that approximates $\boldsymbol{\sigma}\left(\mathbf{C}^{\text{real}}\right)$ (if k are dropped for brevity) can be defined in terms of basis functions φ_l, which are functions of design variables and some calibration parameters a_l in the form of:

$$\tilde{\boldsymbol{\sigma}}(\mathbf{C}) = \sum_{l=1}^{L} a_l \, \varphi_l \, (\mathbf{C}) \tag{5.59}$$

LS-OPT offers two types of basis functions [321]. An approximation that is corresponding to a linear model is defined as:

$$\varphi = [1, x_1, x_2, \dots, x_n]^T \tag{5.60}$$

An approximation that is corresponding to a quadratic model is defined as:

$$\varphi = [1, x_1, x_2, \dots, x_n, x_1^2, x_1 x_2, \dots, x_1 x_n, \dots, x_n^2]^T \tag{5.61}$$

Basis functions should be selected to yield an approximate function, which is accurate enough to achieve fast convergence and simple enough to be used in numerous repeating FE simulations. Therefore, both linear and quadratic models can be compared for the best accuracy and efficiency. Linear models often require fewer number of design points but may need more number of iterations to converge, where quadratic model requires more design points but less number of iterations.

The next step in constructing the approximations by RSM is to select adequate number of design points to create the approximation in the sub-region using statistical experimental design techniques (i.e., *D*-optimality). In the final stage, the approximation

model is fitted to the simulation results at the selected design points using the least-squares method. The results $\boldsymbol{\sigma} = \left[\sigma^{(1)}, \sigma^{(2)}, \dots, \sigma^{(P)}\right]^T$ of the simulations at carefully selected P number of design points are obtained under the condition that $P \geq L$. The unknown calibration parameters $\mathbf{a} = \left[a^{(1)}, a^{(2)}, \dots, a^{(L)}\right]^T$ can be easily determined by using least-squares method, which will be based on the errors between the simulations and the approximations. The error between the simulations and approximation for the *i*-th design point $\mathbf{C}_i$ can be written as:

$$\varepsilon_i = \sigma^{(i)} - \tilde{\sigma}^{(i)} = \sigma^{(i)} - \sum_{l=1}^{L} a_l \, \varphi_l(\mathbf{C}_i) \tag{5.62}$$

Consequently, the sum of the square of the errors at P number of design points can be written as:

$$E(\mathbf{a}) = \sum_{i=1}^{P} \varepsilon_i^2 = \sum_{i=1}^{P} \left[\sigma^{(i)} - \sum_{l=1}^{L} a_l \, \varphi_l(\mathbf{C}_i)\right]^2 \tag{5.63}$$

Least square error method requires the determination of the unknown parameters $\mathbf{a}$ to minimize $E(\mathbf{a})$, where the solution vector to the unknown coefficients can be written as:

$$\mathbf{a} = [\mathbf{X}^T\mathbf{X}]^{-1}\mathbf{X}^T\boldsymbol{\sigma} \tag{5.64}$$

where, $\mathbf{X} = \varphi_l(\mathbf{C}_i)$ is the matrix of basis functions evaluated at the design points.

LS-OPT selects P number of design points in the current sub-region by using a Genetic Algorithm (GA), which applies *D*-optimal criterion on the statistical factorial experimental design [321]. During the selection procedure, factorial experimental design is created first by a $\boldsymbol{n}$ dimensional hypercube with $r^{\boldsymbol{n}}$ number of design points consisting of r number of points spaced at regular intervals in each variable direction. To create an approximation in the order of r, at least $(r+1)^{\boldsymbol{n}}$ factorial designs must be used, where P number of design points are selected out of $(r+1)^{\boldsymbol{n}}$ candidate points. *D*-optimal design criterion selects the best set of design points from a basis design by maximizing the

determinant of $[\mathbf{X}^T\mathbf{X}]$ matrix as a measure for the accuracy of the approximation [321]. The default *D*-optimal point selection algorithm of LS-OPT selects $\text{int}\big(1.5(\boldsymbol{n}+1)\big)+1$ number of points for a linear approximation if $\boldsymbol{n}$ is the number of independent variables and a quadratic approximation selects $\text{int}\big(0.75(\boldsymbol{n}+1)(\boldsymbol{n}+2)\big)+1$ number of points, which leads to 50% more points than the minimum required as a safety metric. Table 5-18 lists the number of required design points for each hardening model with respect to the number of independent variables considering the order of the approximation function.

Table 5-18: List of hardening models.

Hardening Models	Number of Continuous Variables ($\boldsymbol{n}$)	*D*-optimal Approximations	
		Linear	Quadratic
Hollomon	2	5	10
Ludwik	3	7	16
Swift	3	7	16
Voce	3	7	16
Hockett/Sherby	4	8	23
Ghosh	4	8	23

The size and the position of successive sub-regions are highly influential on the accuracy of the approximations to be constructed. Generally the smaller the size of the sub-region is, the greater the accuracy of the approximation. The SRSM builds a new response surface approximation from the design points that are selected in each iteration for a region of interest, where the size and the location of the sub-region is adjusted for the next successive iteration depending on the oscillation and the accuracy of the predicted optimum of the current iteration to the initial (i.e., previous) design. A combination of panning and zooming parameters are calculated based on the distance between the optimum and the initial design in the sub-region. For a two dimensional illustration of a design space, Figure 5-59(a) shows a pure panning for the second sub-region, where a different optimum is found for each iteration. Figure 5-59(b) illustrates a pure zooming for the next sub-region, where an equivalent optimum is found. Figure 5-59(c) illustrates a combination of panning and zooming for the successive sub-regions [321] [331]. It should be noted that the bounds and range of the sub-regions may vary over the iterations depending on the adjustment parameters, which are also depending on the order of the approximation function. The default options of LS-OPT for the sub-

region determination are used during the parameter identification process and the changes within the design space are illustrated in the proceeding sections.

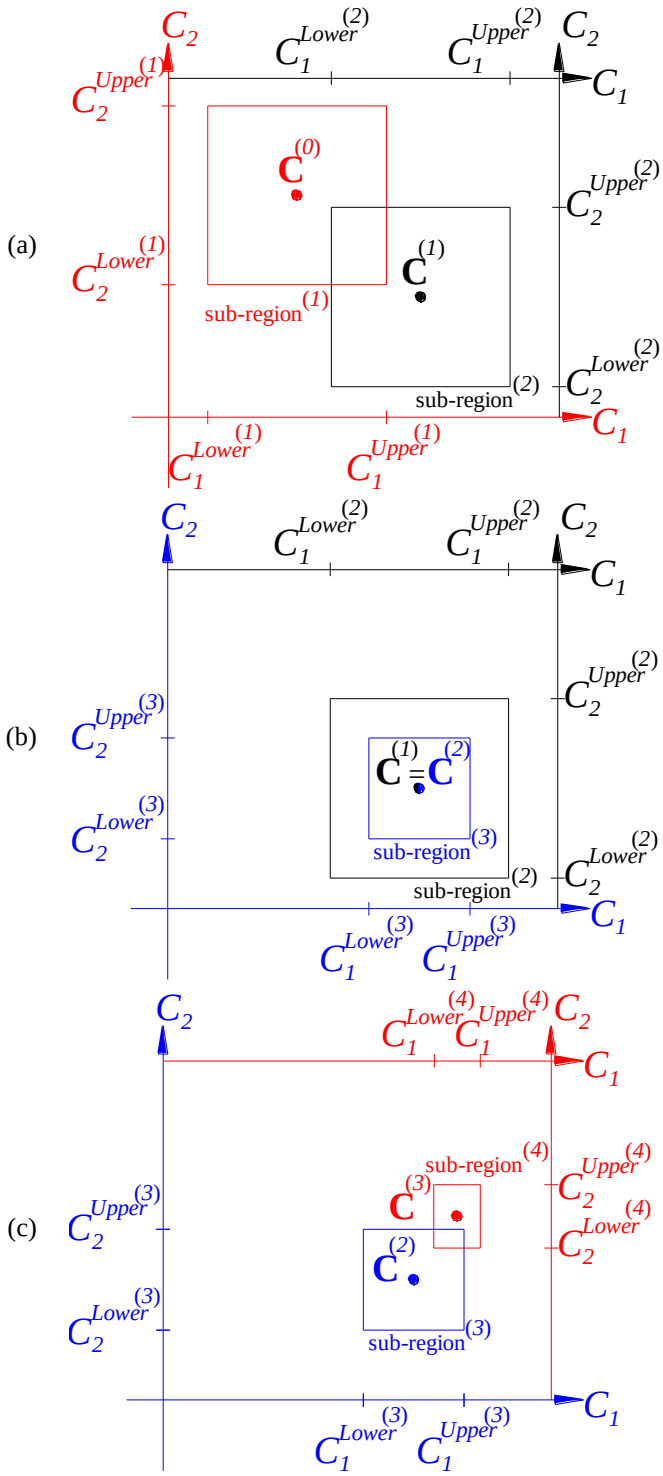

Figure 5-59: Adjustment of the successive sub-regions in SRSM by using; (a) pure panning, (b) pure zooming and (c) a combination of panning and zooming, adapted from [321].

A verification of the automated characterization methodology that is described in Figure 5-55 is demonstrated and verified for Test #2 by comparing the results with the characterized hardening curve in Section 5.5.2. The optimization problem can be written for Test #2 as formulated by Equations (5.45) – (5.51), where the initial design space for the variables and the boundaries of these variables are listed in Table 5-19. It should be noted that the initial design space **C**, targeted curves $\boldsymbol{\sigma}^{\text{real}}$ and the constraints **B** are generated according to the procedures that are described by Figure 5-55.

Initial design space for each hardening model is illustrated in Figure 5-60 by using the parameters that are found for the experimental hardening curve until necking and listed in Table 5-19. Clearly, the hardening models correlate well until the onset of diffuse necking and exhibit a large divergence at larger strains based on the characteristics of the hardening models. Therefore, extrapolation of the models for large strains is determined by using AO method. The method is based on minimizing the error between the experimental engineering stress vs. engineering strain curve and the corresponding results from the simulations. The differences between the experiment and the simulations are illustrated in Figure 5-60(b) for the initial design space.

According to the multi-case approach, three repeated tests are used with five different mesh sizes as described by Figure 5-55. However, the proceeding results are presented only for Test #2.3 and the models with a characteristic element length of 0.1483mm, which is referred as [t/5] in Table 5-9 and illustrated in Figure E-5.

Stander, et al. have shown that a similar algorithm has converged with only ten iterations by using a linear approximation of the response functions for a ‘power-law’ material model, which has only two independent variables [287]. Therefore, fifteen iterations are used as a termination criterion for the parameter identification algorithm with linear approximations that is described in Figure 5-55 considering that additional complexities are added to the problem, which are the contributions of multi-case problem, discrete variables, hardening models with more independent variables, constraints on the parameters and a combined objective function.

Table 5-19: List of the values for the initial design variables and the bounds for the corresponding hardening models.

Design Space						Objective Function (Combined Error) $E = (E_1 + E_2)$
Discrete Variables	Continuous Variables	Initial Design Space			Optimum*	
		Lower	Initial	Upper		{Initial} | (Optimum)* [% Improvement]
C_p	C_j	$C_j^{Lower^0}$	$C_j^{\ 0}$	$C_j^{Upper^0}$	$C_j^{\text{approximate}}$	
Hollomon	C_1	700	737.7	800	712.35925	{4.22×10^{-3}} (2.94×10^{-3})
	C_2	0.14	0.1574	0.17	0.140101	[30.33]
Ludwik	C_1	350	364.6	400	366.23363	{$2.66\text{E}\times10^{-4}$} ($1.67\times10^{-4}$)
	C_2	600	639.3	700	601.36541	
	C_3	0.5	0.6388	0.8	0.6253235	[37.22]
Swift	C_1	600	823.4	900	728.68205	(1.40×10^{-4}} (8.66×10^{-5})
	C_2	0.01	0.03658	0.05	0.0137006	
	C_3	0.1	0.2384	0.3	0.1627388	[38.14]
Voce	C_1	500	618.7	650	595.54815	{1.67×10^{-4}} (7.29×10^{-5})
	C_2	300	377.8	400	374.67036	
	C_3	8.0	8.251	10.0	9.9587743	[56.35]
Hockett/ Sherby‡	C_1	330	379.3	400	376.01307	{1.24×10^{-4}} (3.98×10^{-5})†
	C_2	1200	1973	2300	1245.4859	
	C_3	0.7	1.343	1.9	0.9000002	
	C_4	-0.32	-0.2668	-0.1	-0.314804	[67.9]
Ghosh	C_1	-1500	-1195	-1000	-1379.627	{1.13×10^{-4}} (7.05×10^{-5})
	C_2	1850	1980	2100	2100	
	C_3	0.03	0.05187	0.06	0.0303069	
	C_4	0.04	0.0787	0.1	0.0517836	[37.61]

*Optimum values are found after 15 iterations by using AO with SRSM and linear approximations.
†Minimum of all combined objective functions, optimum point.
‡Discrete variable with the minimum combined error, best hardening model.

Results of the automated AO algorithm are listed in Table 5-19 for continuous and discrete variables. The minimum combined error function is found after fifteen successive iterations for each discrete variable and mesh size. Hockett/Sherby hardening model provided the best correlation with the test results based on the curve matching. It should be noted that the AO method is sensitive to the initial design point and the amount of improvement often depends on the starting design, shape and size of the design space and the distance of the optimum solution to the starting point. Therefore, it is often a common practice to begin with a different initial design point to check whether a global optimum is found [285]. However, considering that *D*-optimality criterion is used for point selection and a considerable amount of successive iterations are utilized, it is concluded that the global optimum is achieved.

(a)

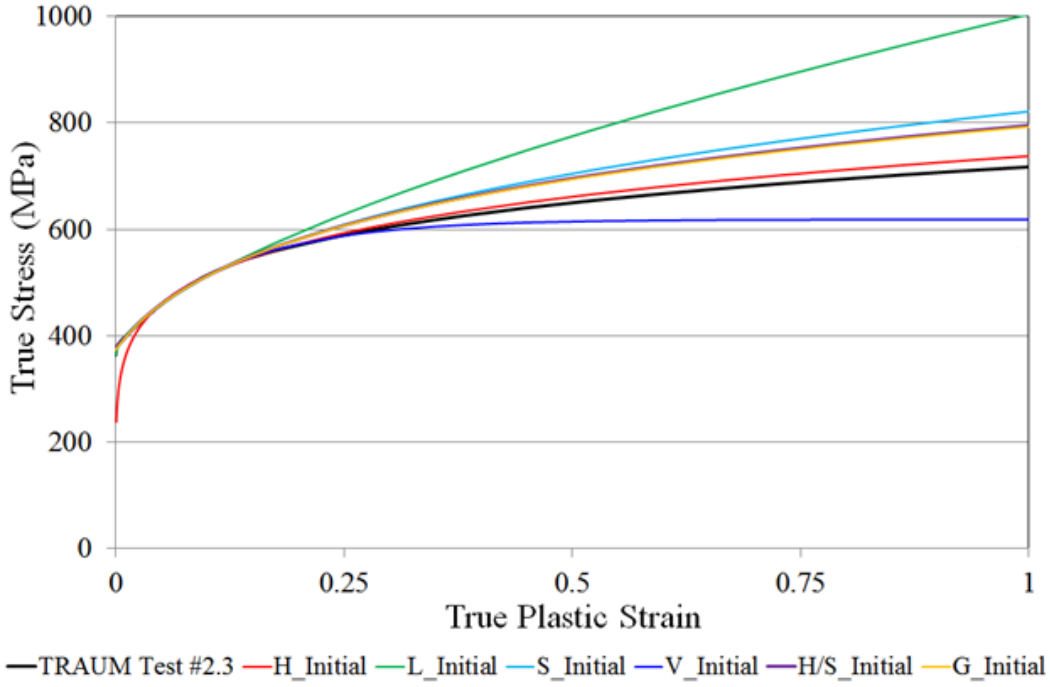

(b)

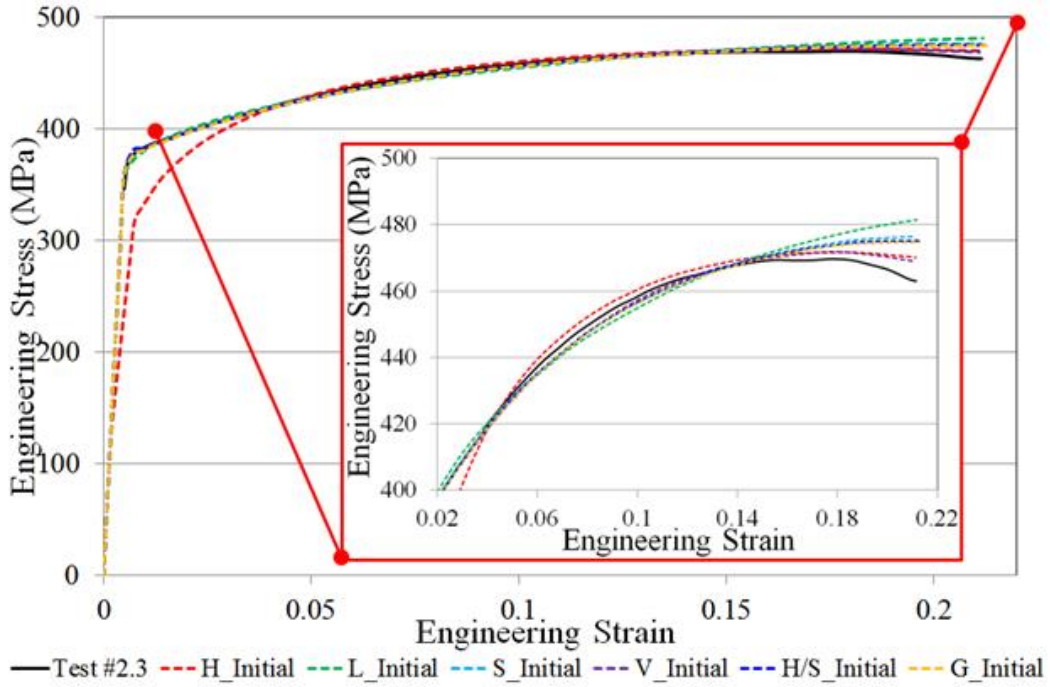

Figure 5-60: Initial conditions: (a) initial design space and inputs for TRAUM and (b) initial response functions compared with the targeted response.

The convergence behavior of the objective functions for each discrete variable is illustrated in Figure 5-61, where it is shown that the combined errors from the curve

matching are rapidly minimized. It should be noted that both *y*-axes in Figure 5-61 represent the same error function with different scales for better illustration. The legends on both sides show the discrete variables that are using the corresponding scales depending on the side that they are assigned. It is found that the algorithm can successfully converge just after five iterations. The convergence takes longer for models with a larger initial design space and boundaries (i.e., Swift Model). It is also clear that the farther the initial design point from the optimum is, the longer it takes to converge. Although it is expected that the models with more independent variables will converge slower, no dramatic changes are observed. The evolution of the design variables for the optimum solutions per each iteration are illustrated by using the successive Figures 5-62 - 5-67 for the corresponding hardening models, where the boundaries of the design space are also represented to show the dynamic attribute of the optimization scheme that is updating the region of interest in every iteration.

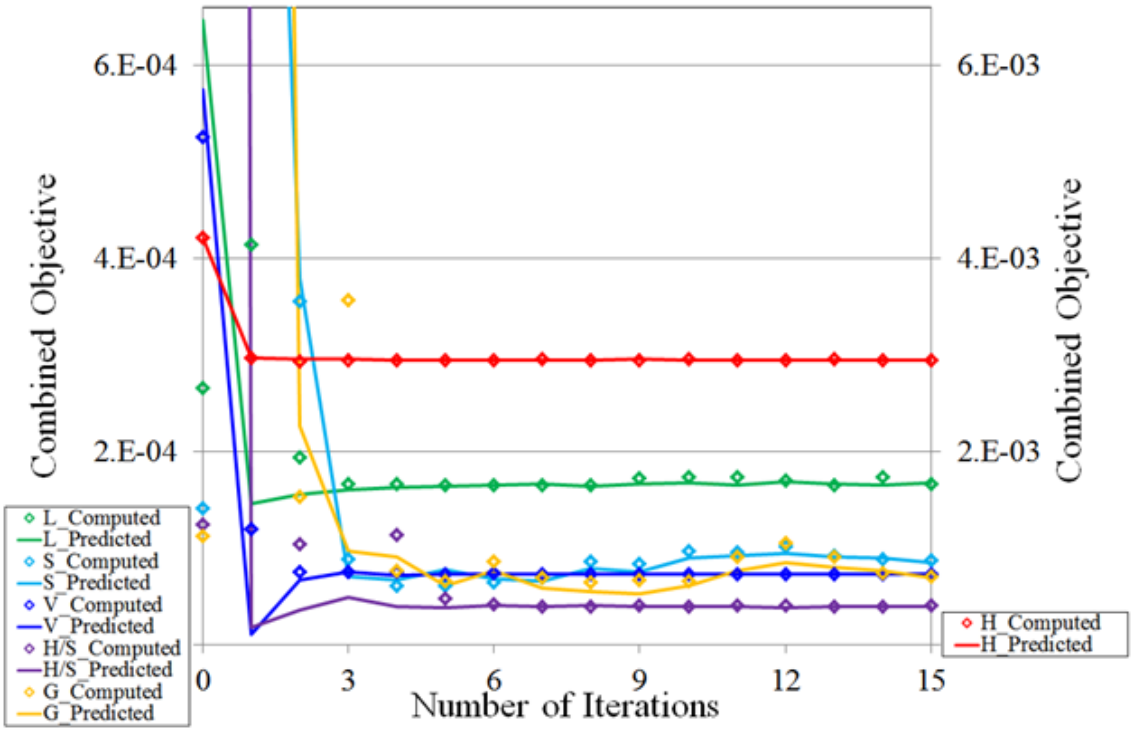

Figure 5-61: History of optimization: evolution of combined objective functions for each discrete variable.

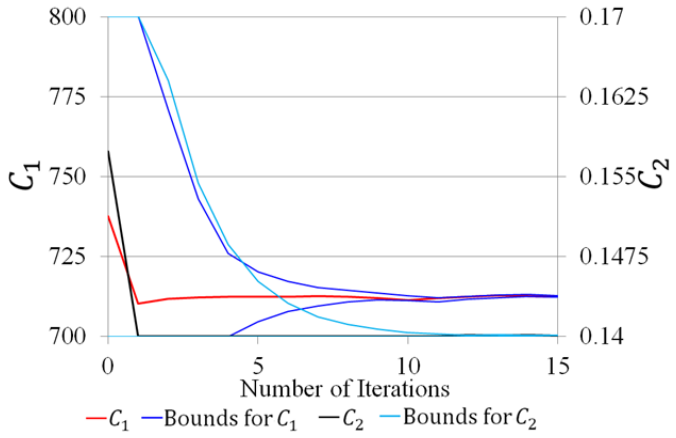

Figure 5-62: History of optimization: evolution of design variables for Hollomon Model.

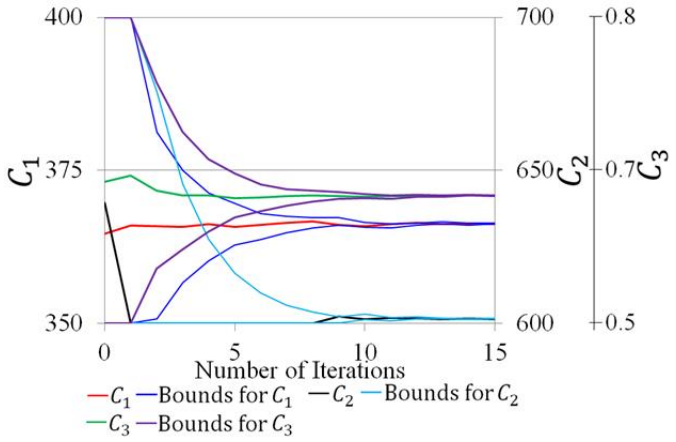

Figure 5-63: History of optimization: evolution of design variables for Ludwik Model.

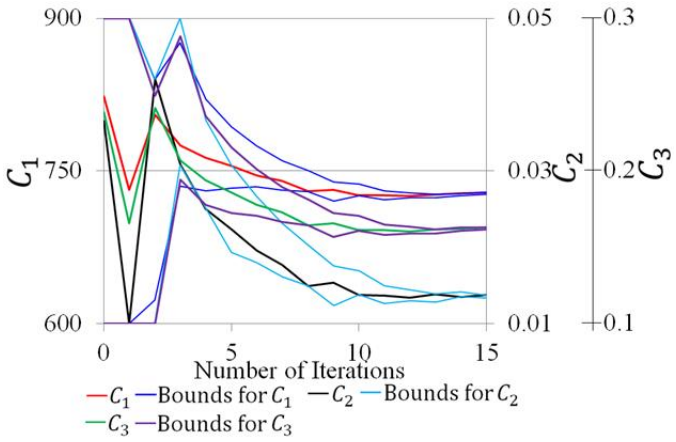

Figure 5-64: History of optimization: evolution of design variables for Swift Model.

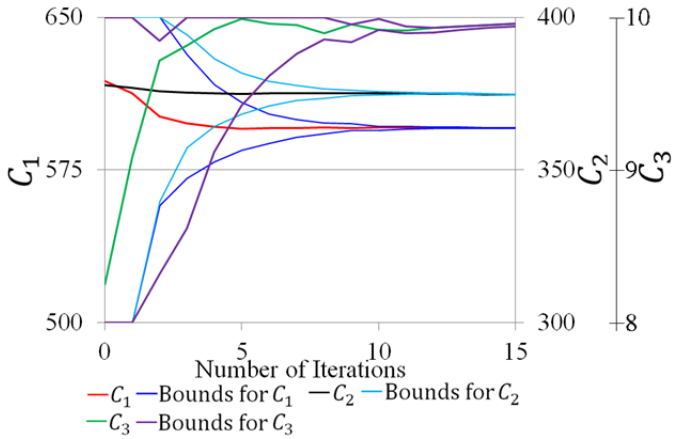

Figure 5-65: History of optimization: evolution of design variables for Voce Model.

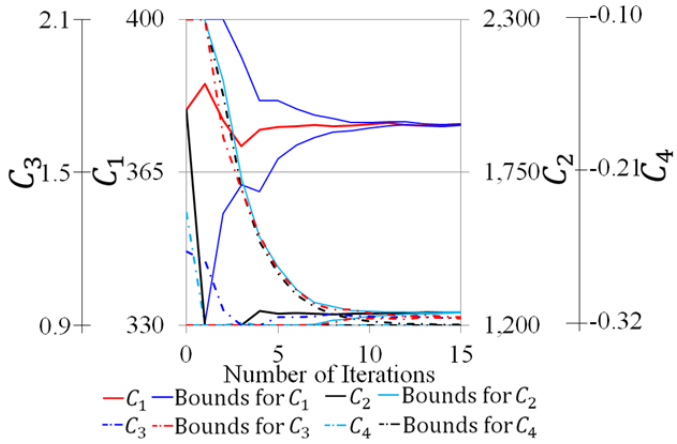

Figure 5-66: History of optimization: evolution of design variables for Hockett/Sherby Model.

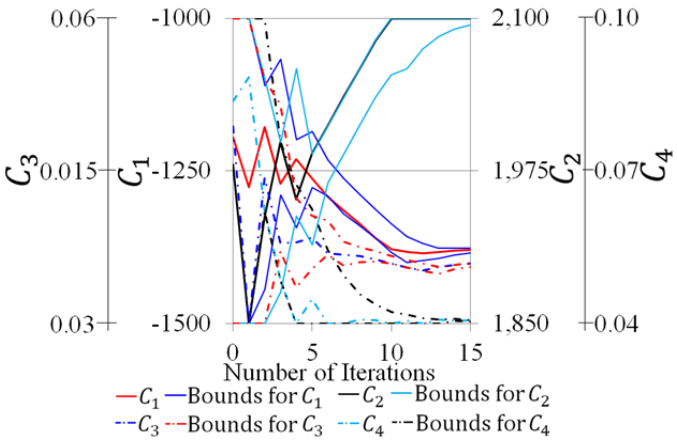

Figure 5-67: History of optimization: evolution of design variables for Ghosh Model.

Figures 5-62 - 5-67 emphasize that, depending on the range of the initial design space and the location of the optimum with respect to the initial design point, at least fifteen iterations are required for the best overall convergence of the design variables when linear approximations are utilized to construct the response surface for the AO algorithm. It can clearly be seen that the algorithm applies a penalty for the approximated solution to force for a convergence by using the boundaries as a contracting corridor to the optimum design point. This path of solutions are adapted by modifying the sampling (i.e., point selection) region by utilizing the 'panning' and 'zooming' features that are illustrated in Figure 5-59 while approaching to the optimum. Figure 5-68 illustrates the adapted sub-regions for Hollomon Model, where the design space of the two independent variables are modified in every iteration by a combined 'panning' and 'zooming' approach. The evolution of the subsequent sub-regions can be explained better when Figures 5-62 and 5-68 are evaluated together, where it is shown that the variable C_2 converges to the lower boundary of the design space and the range of the sub-regions contract from that point forward.

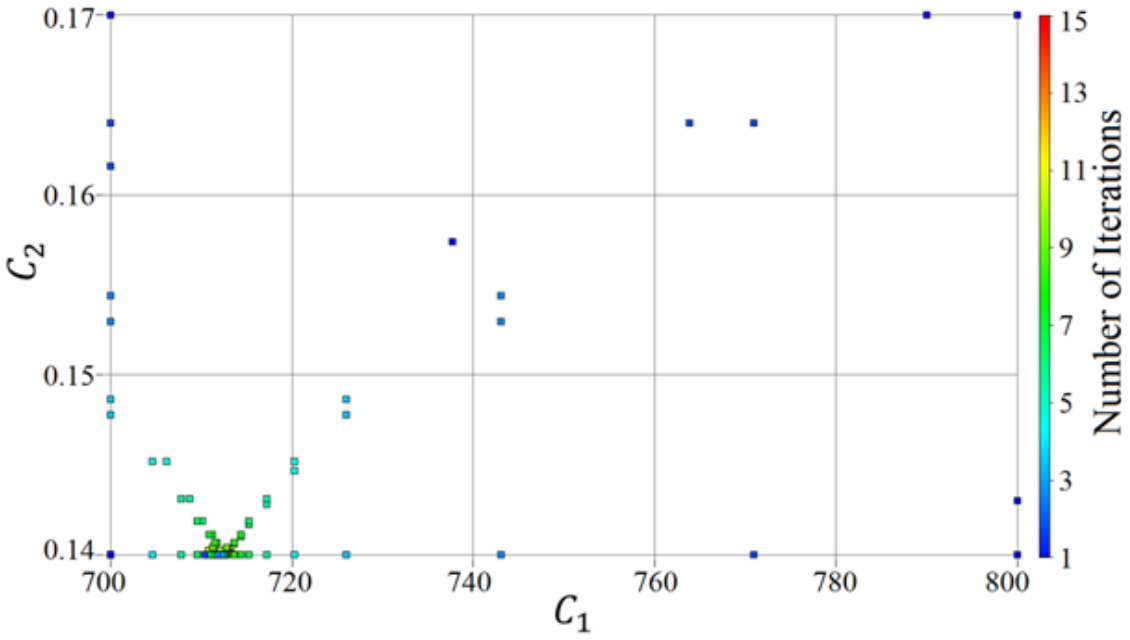

Figure 5-68: History of optimization: evolution of design space and sub-regions for H Model.

It should be noted that Hollomon hardening model has only two variables and the design space can be constructed and illustrated on a plane. However, hyper-surfaces need to be constructed for the models with more variables. Since Hockett/Sherby hardening model has provided the best correlation with the test results and it has four variables, the design space and the evolution of the sub-regions are illustrated in Figures 5-69(a) and 5-69(b) for H/S model with different combinations of three variables for better visualization of the design space, which is in higher dimensions.

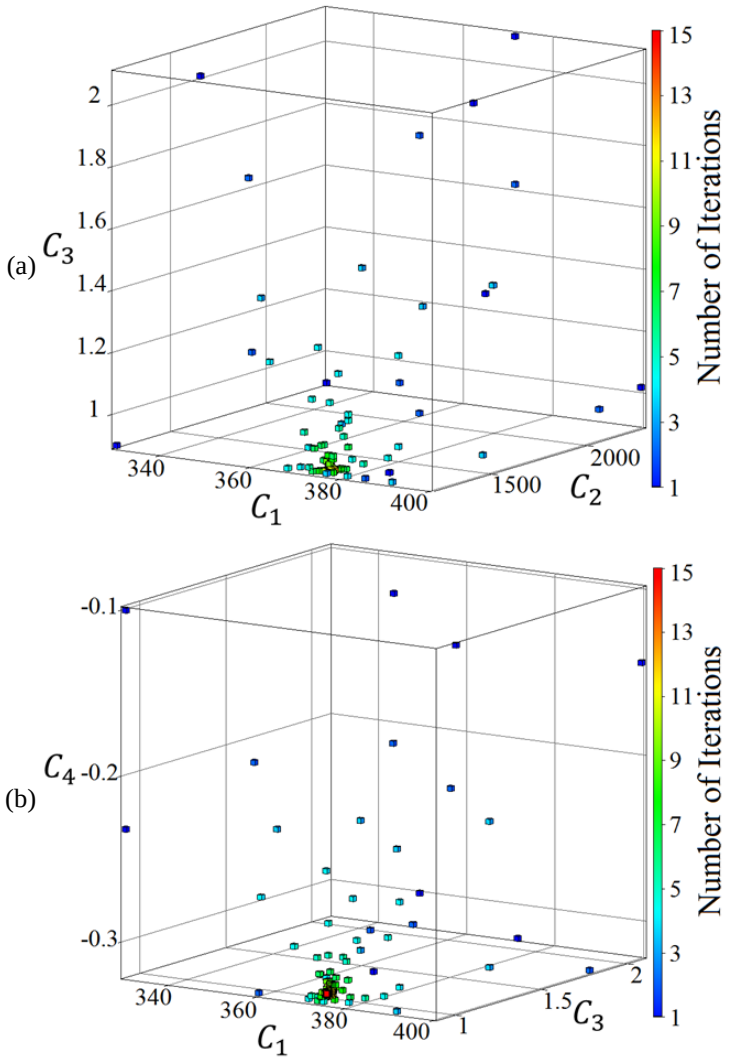

Figure 5-69: History of optimization: evolution of design space and sub-regions for H/S Model with different combinations of variables showing; (a) C_1, C_2, C_3 **and (b)** C_1, C_3, C_4**.**

The design space can also be projected on a plane and illustrated in a similar fashion as visualized in Figures 5-70(a), 5-70(b) and 5-70(c) keeping one of the variables as a baseline, where the evolution of the other variables are investigated with respect to C_1.

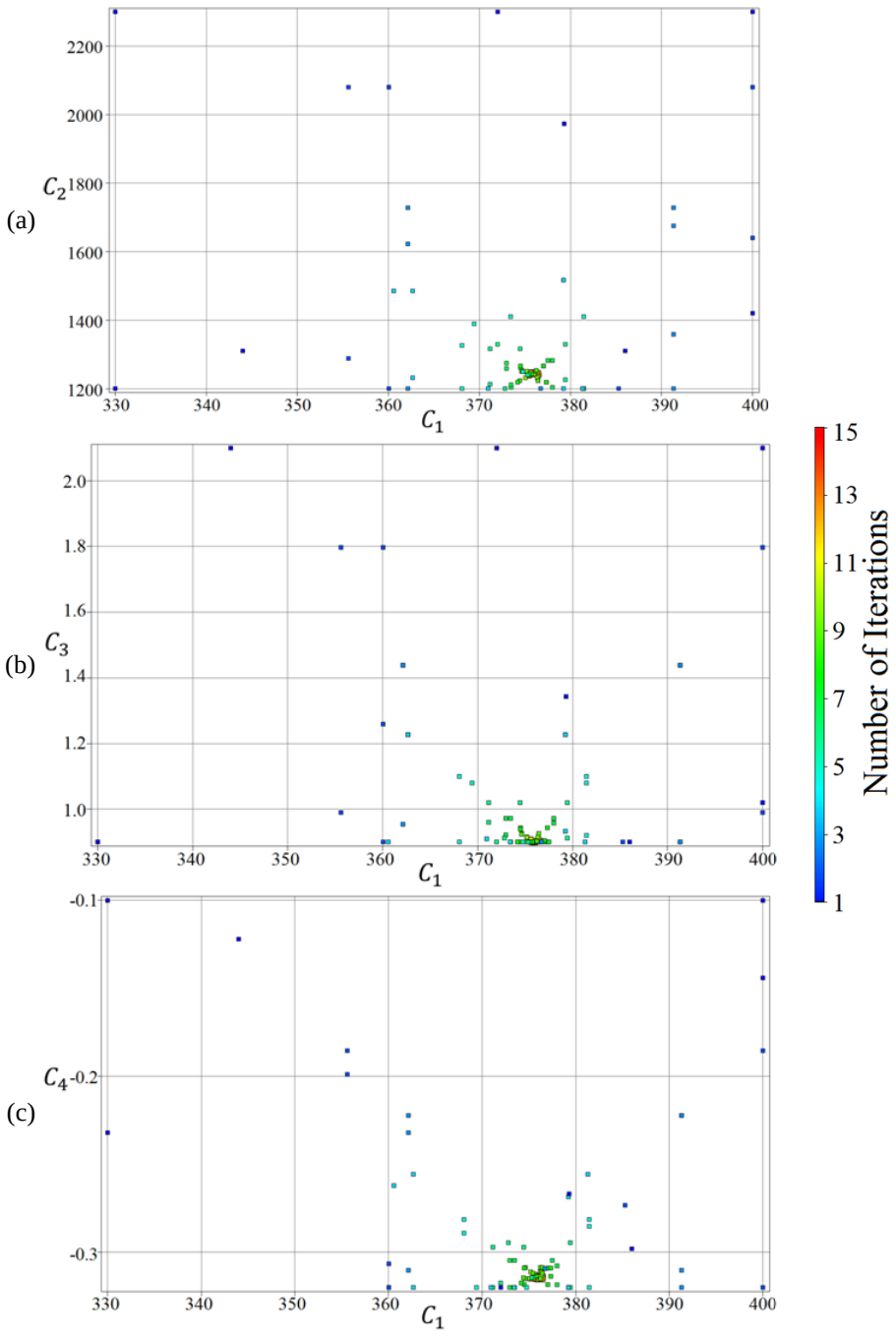

Figure 5-70: History of optimization: evolution of design space and sub-regions for H/S Model on a plane with different combinations of variables showing; (a) C_1, C_2 , (b) C_1, C_3 and (c) C_1, C_4.

Figures 5-71(a), 5-71(b) and 5-71(c) describe the relations between the other variables of the H/S model, where the evolution of the sub-regions are projected on a planar design space.

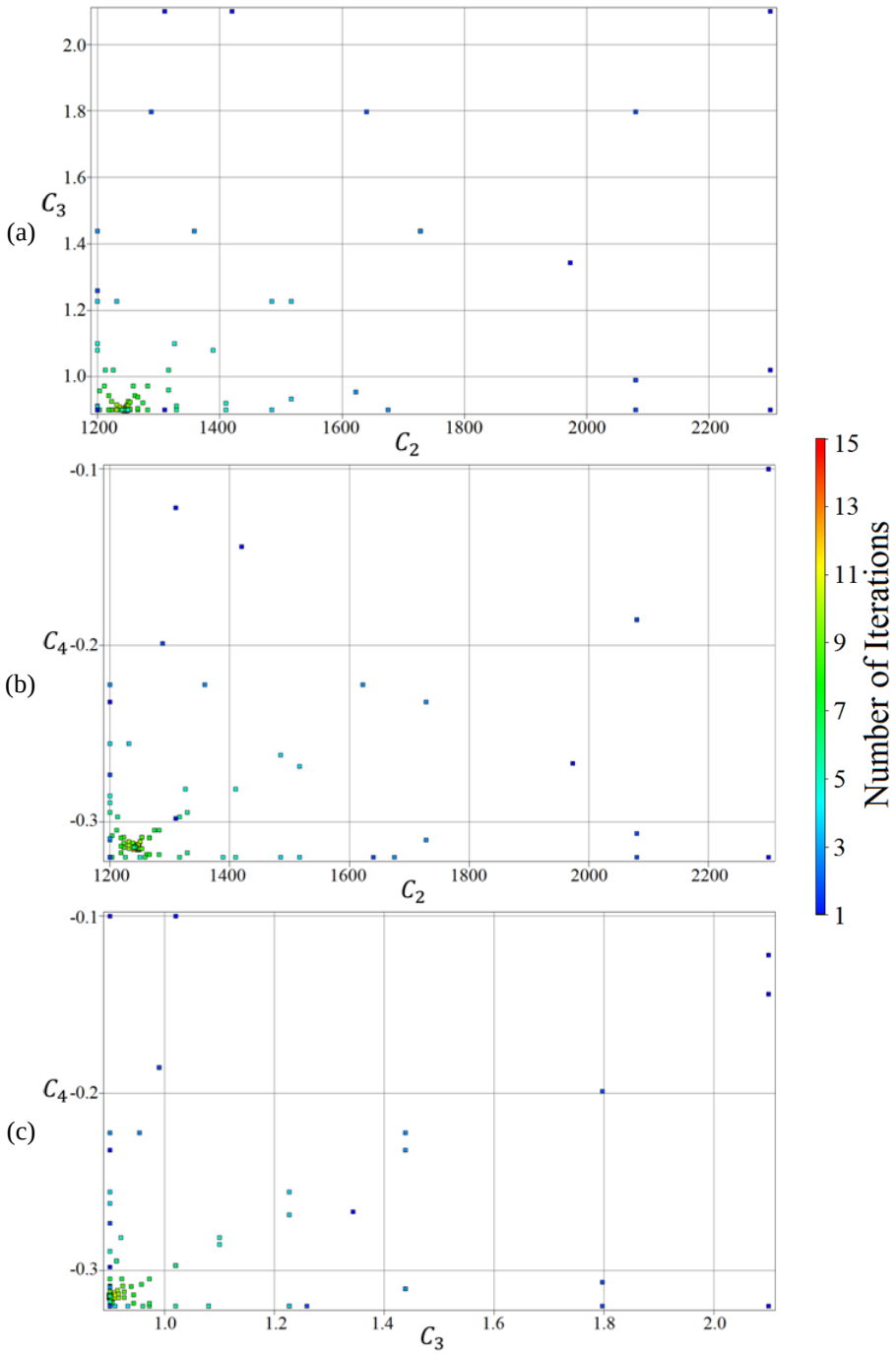

Figure 5-71: History of optimization: evolution of design space and sub-regions for H/S Model on a plane with different combinations of variables showing; (a) C_2, C_3 **, (b)** C_2, C_4 **and (c)** C_3, C_4**.**

These results are consistent with the results that are presented in Figure 5-66, which verify that all other variables converge towards the lower boundaries of the design space. Only C_1 converges to an optimum closer to the initial design point. This is one of the justifications for utilization of AO method for parameter identification and characterization because the curve matching metrics can dramatically be improved with optimization compared to the initial parameter identification, which is often performed by using ordinary curve fitting.

The point selection strategy of the optimization algorithm can also be illustrated by Figures 5-72 – 5-74 using a normalized network of design points, where it is shown that all variables are in fact normalized to keep the algorithm stable independent of the gradients within the variables. Variables which are several orders of magnitude apart can also cause artificial weighting and can favor the variable with a larger figure. The combination of the design variables and the network of all other attempted design points can clearly be seen for successive iterations, where the algorithm rapidly starts to converge towards the optimum combination of points especially after the 5th iteration. Eight simulations (i.e., design points) were required during the each iteration since H/S hardening model has four independent continuous variables and a linear approximation function is used for the predictions. It should be noted that optimization history for multi-case mesh dependent network are not shown for brevity reasons.

Values for the combined error functions are also illustrated by Figures 5-72 – 5-74 for each design point, where it is clearly seen that the objective functions are minimized successively towards the optimal solution. It should be noted that the range of the error function in the first iteration is ten times more in Figure 5-72(a) due to the large matching errors that are found for the design points during the initial iteration.

Figures 5-72 – 5-74 also demonstrate the engineering stress vs. engineering strain responses that are calculated by successive iterations for each design point. The wellness of the curve matching with respect to the test result can be quantified easily with successive iterations. It should be noted that the optimization history for Test # 2.1e and Test #2.2e are not shown for brevity reasons.

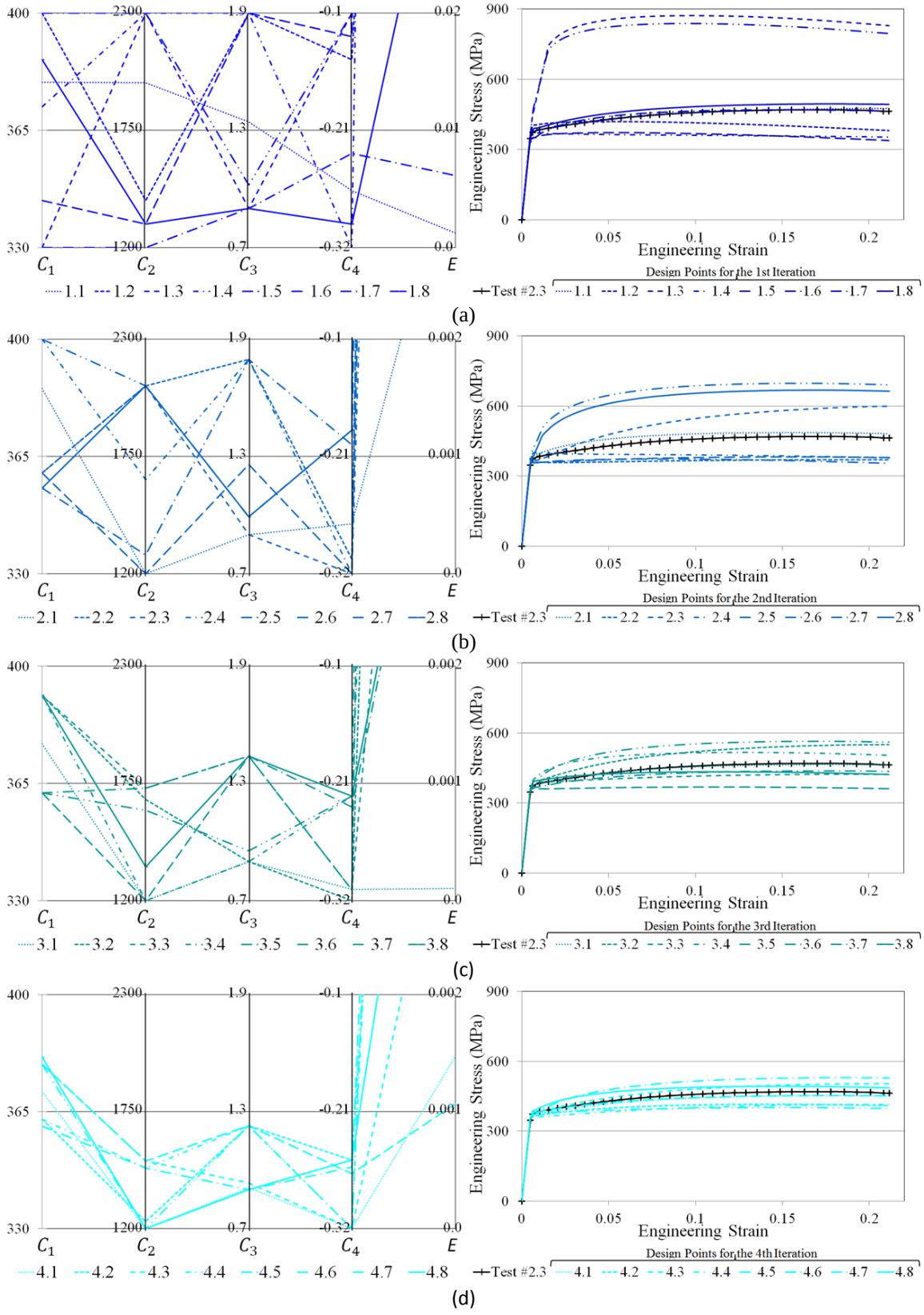

Figure 5-72: History of optimization: selection of design points and the corresponding responses for the iterations; (a) 1st, (b) 2nd, (c) 3rd and (d) 4th.

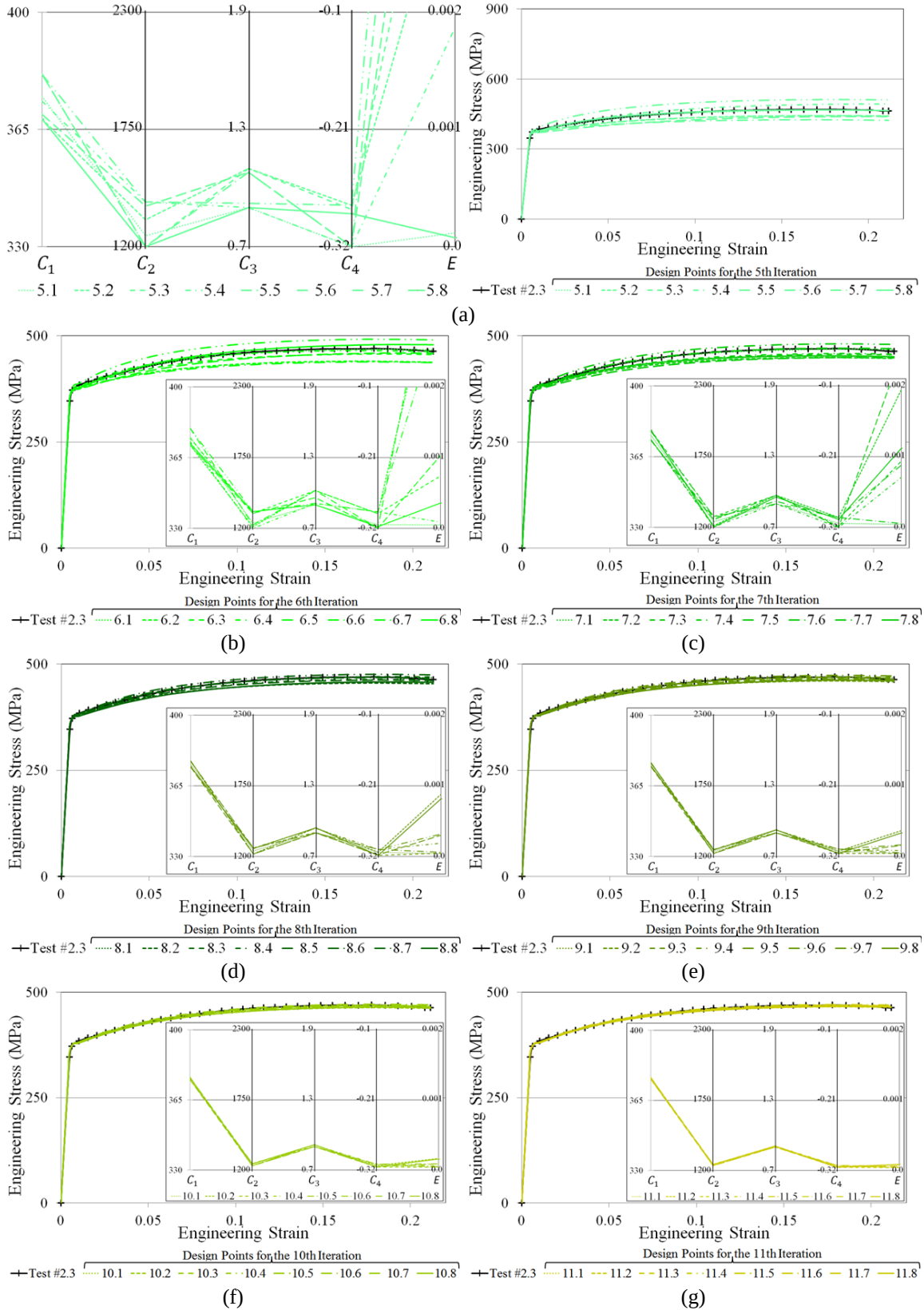

Figure 5-73: History of optimization: selection of design points and the corresponding responses for the iterations; (a) 5th, (b) 6th, (c) 7th, (d) 8th, (e) 9th, (f) 10th and (g) 11th.

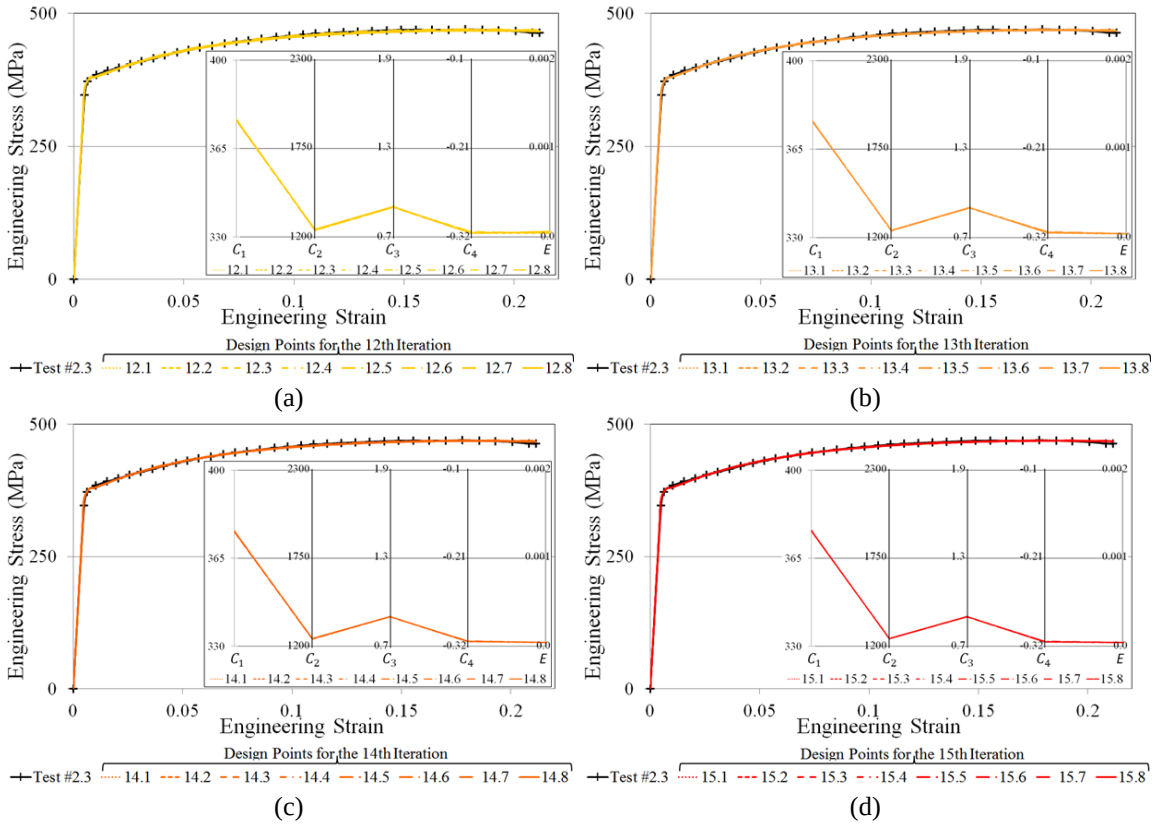

Figure 5-74: History of optimization: selection of design points and the corresponding responses for the iterations; (a) 12th, (b) 13th, (c) 14th and (d) 15th.

Comparison of the response curves depict that the error functions are efficiently minimized by the successive iterations. The scale of the engineering stress response is modified after the 6th iteration that is shown by Figure 5-73(b), where the differences between the test and the simulation results disappear significantly. It should be noted that these optimization histories are only shown for the best solution option, which is provided by the H/S hardening model.

A summary of the optimum solutions can be illustrated as in Figure 5-75 for each hardening model (i.e., discrete variable) by using the parameters that are listed in Table 5-19. The optimum solutions depict that within the range of testing, which is determined by the failure strain, all models match with the experiment within a certain degree of success that are also quantified in Table 5-19 by comparing the values of the combined error functions and the amount of improvement with respect to the initial design point. Therefore, the best matching combination can be determined objectively.

It is found that Hollomon hardening model can be relatively efficient in representing the flow behavior with only two variables to identify, where fewer amounts of design points are required during the iterations. However, the initial hardening region is found to be less successful compared to the other models, where majority of the error accumulates just after the plastic flow begins. Consequently, Hollomon model can be a good alternative and baseline for any material characterization problem, where computational costs are significant.

Ludwik hardening model is found to provide a better approximation in the beginning of the plastic flow and can provide a good estimate up to the necking point. However, it demonstrates a strong hardening behavior and the form of the model do not allow a monotonically decreasing tangent modulus. It should be noted that the parameters for the model are determined with two constraint conditions to satisfy continuity and smoothness. Therefore, some power laws can be divergent at the large strain region when extrapolated without sufficient test results.

Voce hardening model is found as one of the most successful models with three variables. However, contrary to Ludwik hardening model, Voce exhibits a dramatic softening after necking and can be preferred during the characterization of the temperature dependent hardening curves.

Swift, Hockett/Sherby and Ghosh hardening models have exhibited major improvements compared to their initial design points. It is noticeable that these models have converged to similar characteristics beyond the necking point when the flow curves are extrapolated as illustrated in Figure 5-75(a), where all models are also compared with the iteratively characterized hardening curve in Section 5.5.2 that was also using a Swift law for extrapolation.

The automated parameter identification scheme that is described in this section is utilized to characterize the temperature and strain-rate dependent flow behavior in the proceeding sections. The flow surface for TRAUM is generated by using tabulated inputs comprised of hardening curves, which are characterized by using different hardening models. Therefore, TRAUM demonstrates an advantage of using multiple hardening behaviors when necessary to construct the flow surface of a material. The fourth step during the characterization procedure is to obtain the isothermal hardening curves by

using thermo-mechanical simulation results as described in Section 5.6.4. The next section describes the characterization of temperature dependent flow surface by using AOM.

(a)

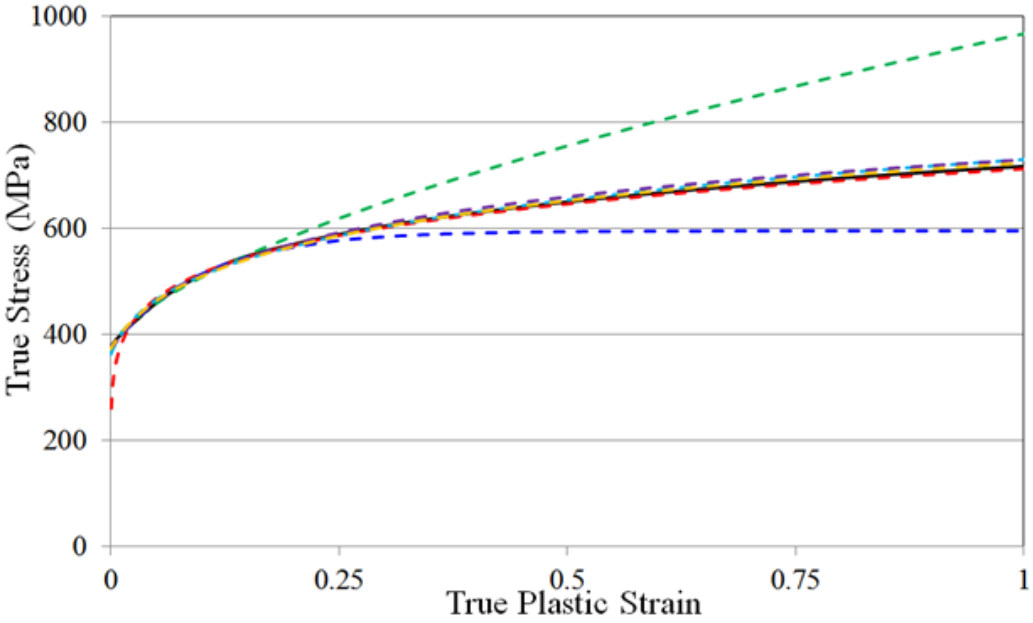

(b)

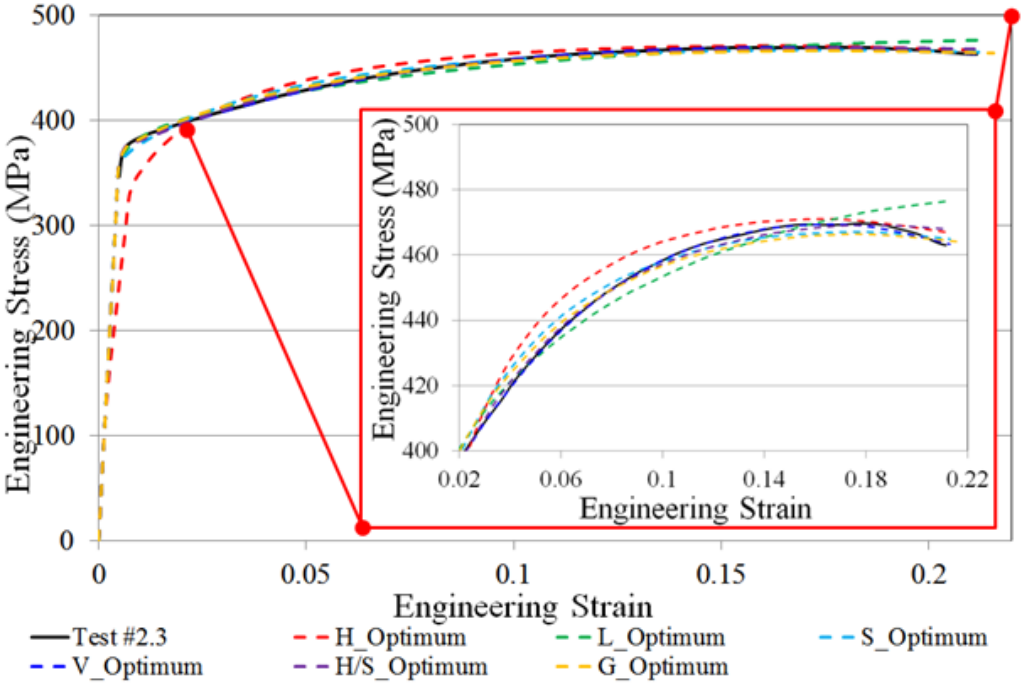

Figure 5-75: Optimum conditions; (a) optimum design space and inputs for TRAUM and (b) optimum response functions compared with the targeted response.

5.6.6 **Characterization of the temperature dependent hardening curves at quasi-static conditions by using automated AO with SRSM**

Temperature dependent flow surface of Al2024-T351 is characterized around a nominal strain rate of $1.0s^{-1}$ for tension, compression and torsion tests by utilizing the AOM that has been described in Section 5.6.5. Adiabatic (i.e., quasi-adiabatic) hardening curves are determined for each temperature by using the automated optimization algorithm with SRSM as illustrated in Figure 5-55. TRAUM constructs the flow surface by using linear interpolations between the tabulated hardening curves, which may have different characteristics. Therefore, different hardening behavior can easily be implemented.

Temperature dependent hardening behavior for uni-axial tension is characterized by using Tests #2, #9, #10, #11 and #12, which are listed by Tables 5-2 and 5-13. Further details and repeatability of the tests are given in Appendix-C. It can clearly be seen from Figures C-9, C-10 and C-11 that elevated temperature testing also causes severe PLC effects, which have to be considered during the characterization. All three major types of flow behavior specific to the PLC effect can also be identified after Lüders band formations for high temperature tests. Lipski and Mrozinski tested the temperature dependent behavior of Al2024–T3 between 273K and 473K and found intense PLC effects between 323K and 348K [304]. They have observed that the PLC effects were 'virtually unnoticeable' at the temperature of 473K. However, it should be noted that they have tested the material at a nominal strain rate of $8.77x10^{-4}s^{-1}$, which is at least three orders of magnitude slower than the testing speed that is used for Tests #9 - #11. Moreover, Chatterjee, et al. have reported that the dynamics of PLC effect on aluminum alloys can be chaotic and mentioned about the need to investigate the temperature and strain-rate dependent properties of materials considering the complex nature of the PLC effect [332]. It should be noticed that the effects of PLC disappear at a temperature of 223K as illustrated in Figure C-12.

During the elevated temperature testing, dynamic recovery and recrystallization are also responsible from the rise of the oscillation frequency and the amplitude of flow. Severe oscillations are noticeable at 573K and 723K, where the flow is distracted by

newly forming grains and boundaries as the deformation evolves. Both flow curves exhibit dynamic equilibrium between the work hardening due to dislocation accumulation and the softening due to dynamic recrystallization. It is seen from the Figures C-10 and C-11 that the flow reaches to a plateau with the recovery until the activation energy for the recrystallization is attained, where the microstructure reforms consisting of a dynamic mixture of grains with various dislocation densities that are often strain-free. Therefore, strain-softening of a polycrystalline is typical at quasi-static and elevated temperatures testing [333]. However, simulating dynamic strain-softening by using finite elements require regularization since the uniqueness of the problem is compromised and the partial differential equations of motion or equilibrium change the type from hyperbolic to elliptic form and become ill-posed at the onset of softening, where a negative tangent modulus is found at the hardening curve [334]. Consequently, the solution is mesh dependent and due to the instabilities like localization, the deformation localizes in one single element (i.e., or a single row of elements) and the load bearing capacity reduces significantly. Therefore, to achieve the large displacements that were measured for high temperature testing and still be able to predict the loading accurately, regularization feature of TRAUM is activated for Mesh Pattern #5 and the failure strain of the elements are characterized. The regularization procedures for strain-rate, temperature and characteristic element size are described in the proceeding sections.

Figure 5-76 illustrates the temperature dependent quasi-adiabatic and isothermal hardening curves that are characterized for uni-axial tension tests. Each hardening curve is designated by the corresponding temperature. These hardening curves are the optimum solutions of the characterization that is described in Section 5.6.5, which have provided the best correlation with the test results for five different mesh sizes. Moreover, three repetitive tests are also considered during the curve matching. One of the three tests for each temperature is illustrated in Figure 5-76 with the corresponding hardening curves. While simulating the strain softening behavior, localization of the finite elements is noticeable and may risk the stability of the solution if regularization of the mesh size is not used. At higher temperatures, saturation is achieved very early, where even an onset of localized necking cannot be described that is followed by an almost perfectly plastic behavior. Figures F-9 - F-12 illustrate the verification of the simulation results when the

hardening curves that are shown in Figure 5-76 are utilized to calculate the corresponding force vs. displacement responses for each temperature.

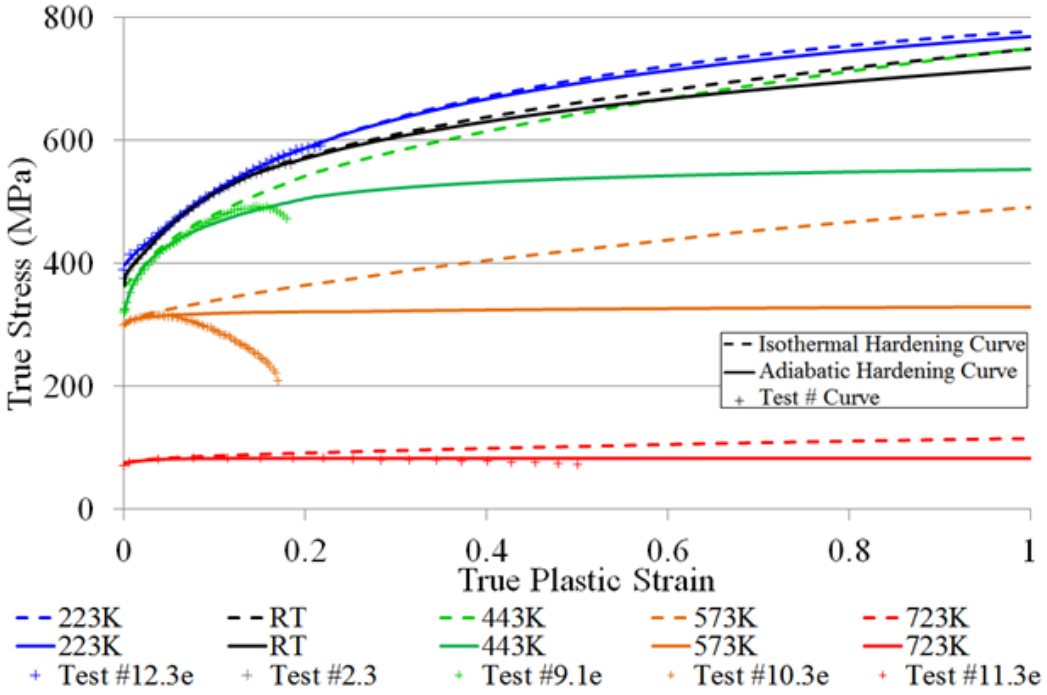

Figure 5-76: Temperature dependent, quasi-static flow surface that is characterized from uni-axial tension tests.

Isothermal hardening curves are calculated by an additional coupled thermo-mechanical simulation of the specimen at the given temperature and strain-rate, where temperature softening and heat conduction is permitted. The retained energy within the body is then inversely added to the strength of the material as illustrated in Figure 5-76 for the corresponding temperatures. It should be noted that with the isothermal hardening curves, TRAUM can incorporate adiabatic heating and temperature softening according to Equation (4.7). On the other hand, it is clear that artificial heating occurs if both adiabatic hardening curves and temperature dependency due to the plastic work are considered at the same time. Figure 5-76 exhibit that the specimen at 443K and 573K can retain more energy than any other state. Therefore, a dramatic increase of the hardening behavior is calculated as the material ductility increases with the increasing temperature and the hardening curve should accommodate the large elongation without numerical instability and localization. It is also shown that the tabulated form of defining the flow

surface is a desirable tool for materials that can exhibit different hardening characteristics with respect to temperature or strain-rate dependency as shown in Figure 5-76 for a transition from a power law hardening to almost perfectly plastic behavior.

Similarly, temperature dependent hardening adiabatic and isothermal curves are characterized for uni-axial compression by using Tests #7, #13, #14, #15 and #16, which are listed by Tables 5-11 and 5-14. More information about these tests that are used to characterize the temperature dependent flow surface can be found in Appendix-C. It is noticeable to see that the PLC effects are not observed for compression. Characterized hardening curves are illustrated in Figure 5-77 for compression and verifications of the temperature dependent hardening curves are presented in Appendix-F. Figures F-13 – F-16 represent the correlation between the uni-axial compression tests and the corresponding simulations with TRAUM when the flow surface that is illustrated in Figure 5-77 is utilized.

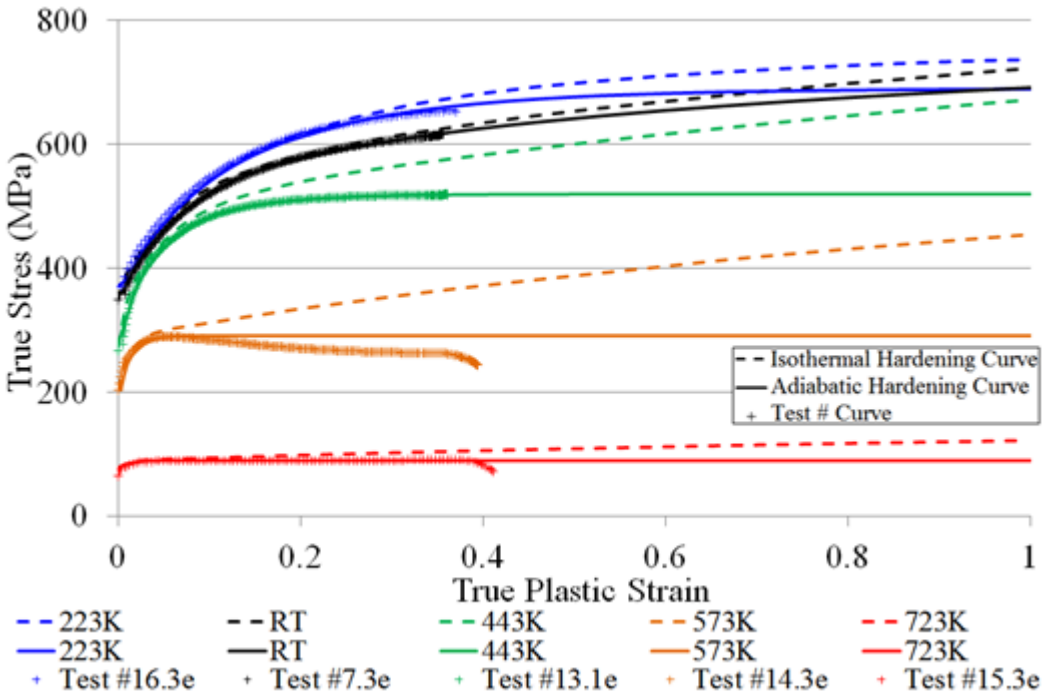

Figure 5-77: Temperature dependent, quasi-static flow surface that is characterized from uni-axial compression tests.

Isothermal hardening curves that are calculated for compression after a single inverse coupled thermo-mechanical iteration as described for uni-axial tension in Section 5.6.5.

Figure 5-55 illustrates the flow of the fourth cycle when a heat transfer problem is solved along with the plasticity and the heat generated due to the plastic work is conducted through the testing apparatus or grips (i.e., platens during the uni-axial compression). The boundary and initial conditions are illustrated in Figure 5-78 for the uni-axial compression problem describing the upper and lower platens as infinitely large heat sinks at constant temperature and a thermal contact-impact algorithm is defined between the upper and lower surfaces of the compression specimen to transfer the heat generated within the specimen during the plastic deformation. Friction is also defined between the platens and the specimen.

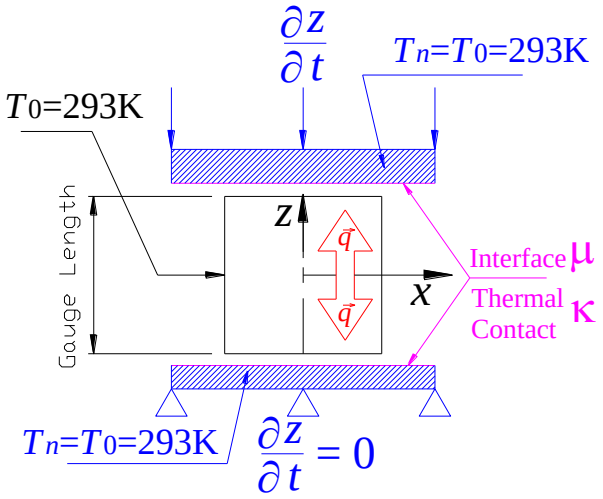

Figure 5-78: Thermo-mechanical problem for uni-axial compression.

Figure 5-79 illustrates the comparison of the evolution of temperature profile within the compression specimen with respect to the consideration of adiabatic conditions and heat transfer through the platens in contact with the upper and lower surface of the specimen. It can be seen that the specimen experiences a homogeneous temperature profile when no effects of heat transfer is assumed and a significant amount of plastic work is converted and equally distributed for each finite element within the body. However, when heat conduction is coupled, the heat flux due to the temperature difference within the body creates a heat differential and a significant portion of the heat generated can be dissipated through the test apparatus.

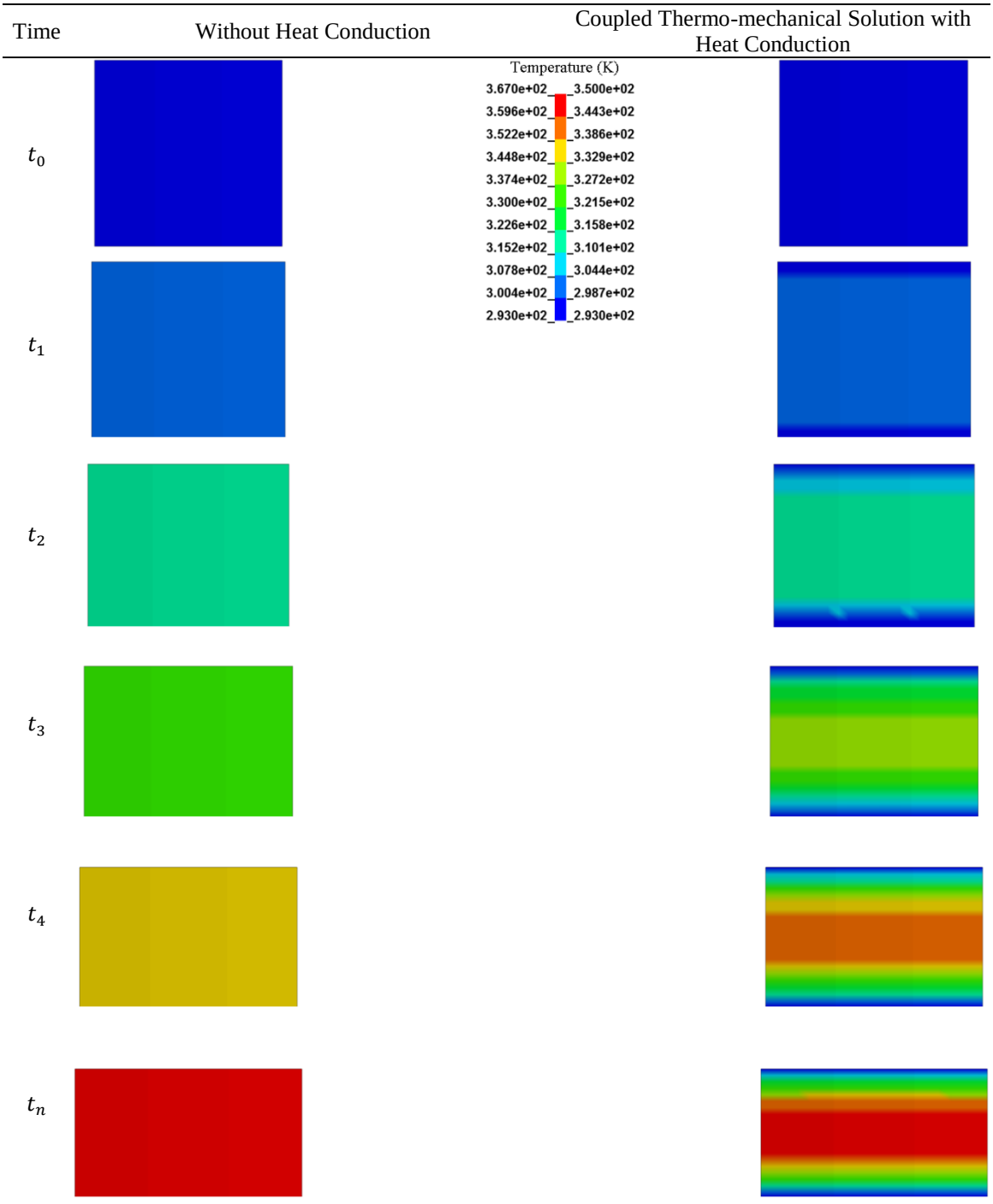

Figure 5-79: Temperature distribution within the specimen for the thermo-mechanical problem with uni-axial compression.

The heat flux within the body is illustrated for the time increments in Figure 5-80, where it can be observed that most of the heat is transferred at the contact interface

reducing the temperatures of the boundaries and causing a localized distribution of heat at the center of the specimen, which then can be responsible from adiabatic shear bands.

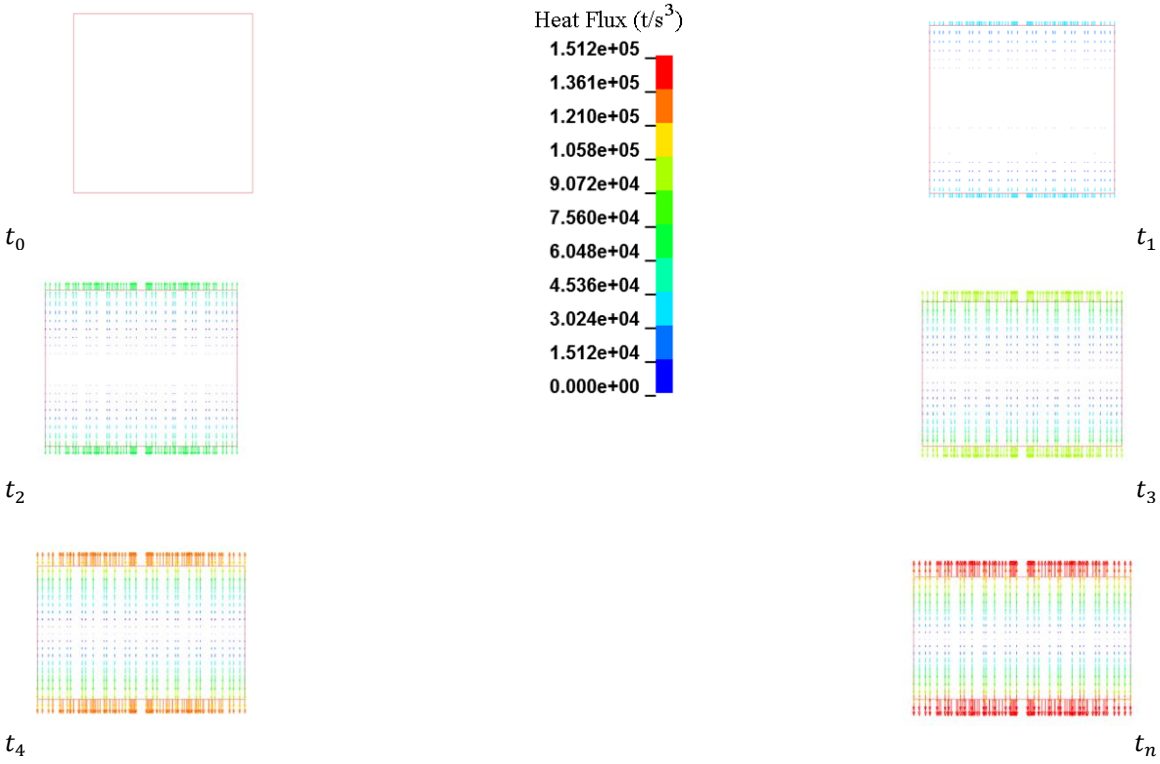

Figure 5-80: Heat flux within the specimen due to the thermo-mechanical problem with uni-axial compression.

Adiabatic and isothermal hardening curves for torsion are also found by AOM that is described by Figure 5-55. Tests #17 - #23 are used, which are listed by Table 5-15. More information about these tests that are used to characterize the temperature dependent flow surface can be found in Appendix-C. It is noticeable to see that the PLC effects also disappear for torsion. Characterized hardening curves are illustrated in Figure 5-81 for torsion and verifications are presented in Appendix-F. Figures F-17 – F-23 illustrates the verification of the hardening curves for quasi-static torsion specimen that is illustrated by Figure B-19, where a different torsion specimen with a different material orientation is utilized to characterize the flow behavior.

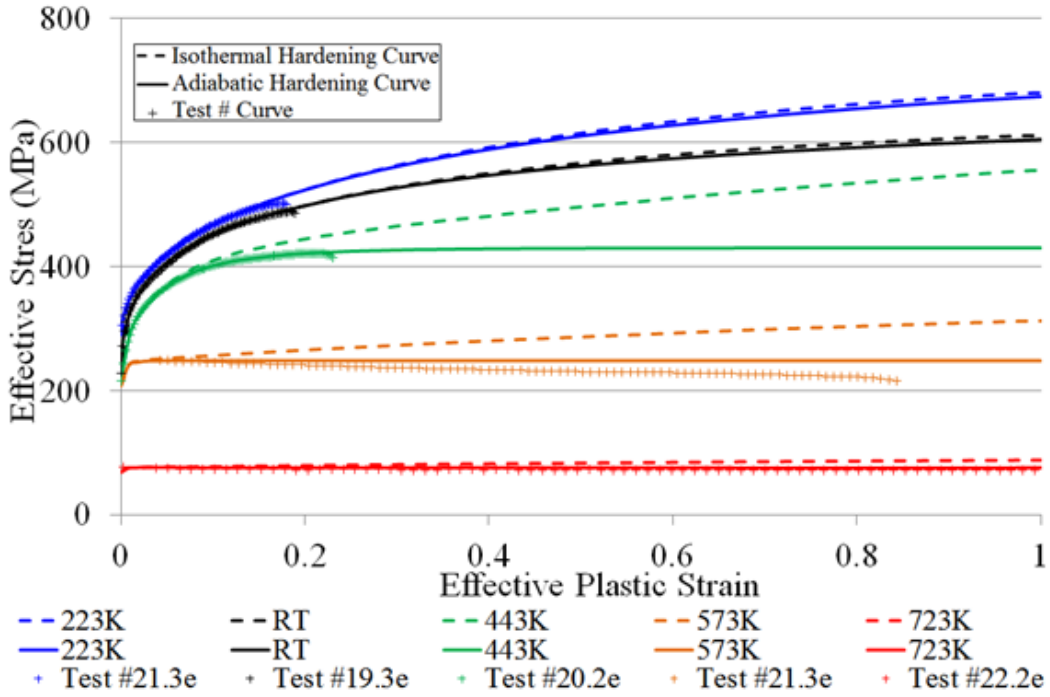

Figure 5-81: Temperature dependent, quasi-static flow surface that is characterized from torsion tests.

Isothermal hardening curves for torsion are also calculated in accordance with the methods that are described in Section 5.6.5. However, due to the special testing apparatus that is illustrated by Figures 5-42 and 5-43 for torsion, the boundary and initial conditions for the coupled thermo-mechanical problem is formulated as shown in Figure 5-82 for the cross-section of the specimen with spool shaped geometry. The upper and lower boundaries of the specimen are assumed at constant temperature (i.e., room temperature) by defining an infinitely large heat sink and the initial temperatures of the whole apparatus and specimen are also defined correspondingly. The heat conduction is assumed to occur through the interfaces, which are considered to conduct heat according to the thermal properties that are listed by Table 5-16.

The differences during the evolution of temperature profiles with two cases are illustrated in Figure 5-83 for specific time increments, where the temperature localization at the gauge section is shown depending on whether the heat conduction is considered. It should be noted that half of the specimen geometry is masked for illustrating the details of the gauge section better.

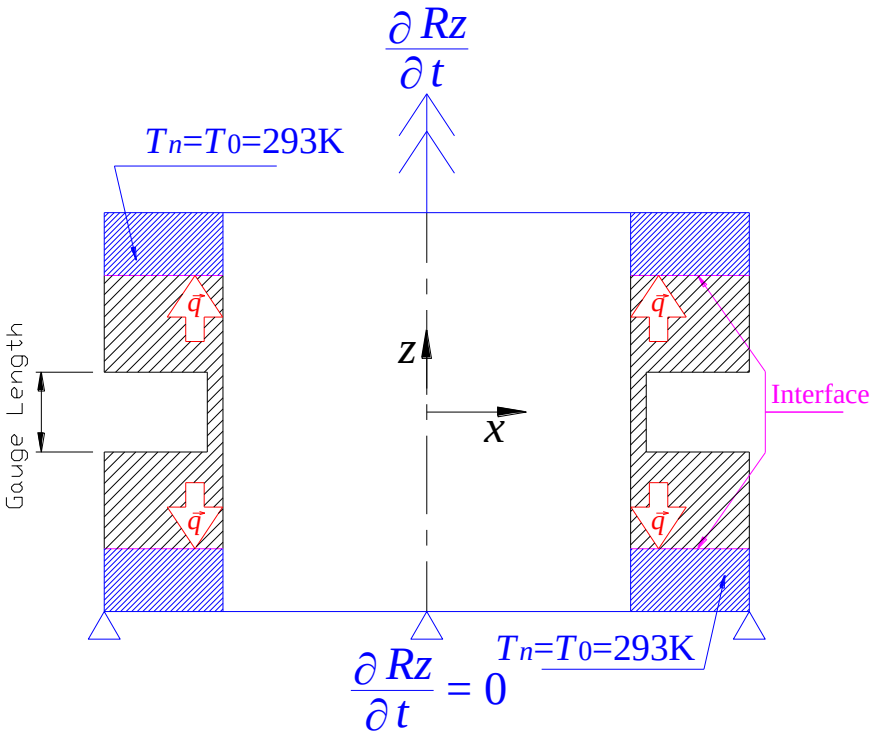

Figure 5-82: Thermo-mechanical problem for torsion.

It is shown that torsion specimens generate a significant amount of heat due to the large plastic deformation and the temperature increases within the gauge section, which primarily affects the flow behavior of the material. Considering Al2024-T351 is found to be rather 'strain-rate independent' at quasi-static conditions, thermally activated deformation should be noted as the main reason for the dislocations that has substantial contribution on temperature dependent flow, heat generation and transfer. Therefore, temperature gradient and retained energies are critical and should be calculated during the simulations for predicting the activation energies accurately.

The vectors of heat flux for the torsion specimen are illustrated in Figure 5-84 for the corresponding time increments, where the influence of the shoulder geometry on heat transfer is corroborated again by elaborating the amount of flux generated towards the interfaces of the specimen with the torque apparatus. It is therefore, the temperature distribution within the cross-section of the specimen with heat conduction is more homogenous than the localized behavior seen if the conduction is not permitted.

Time	Without Heat Conduction	Coupled Thermo-mechanical Solution with Heat Conduction

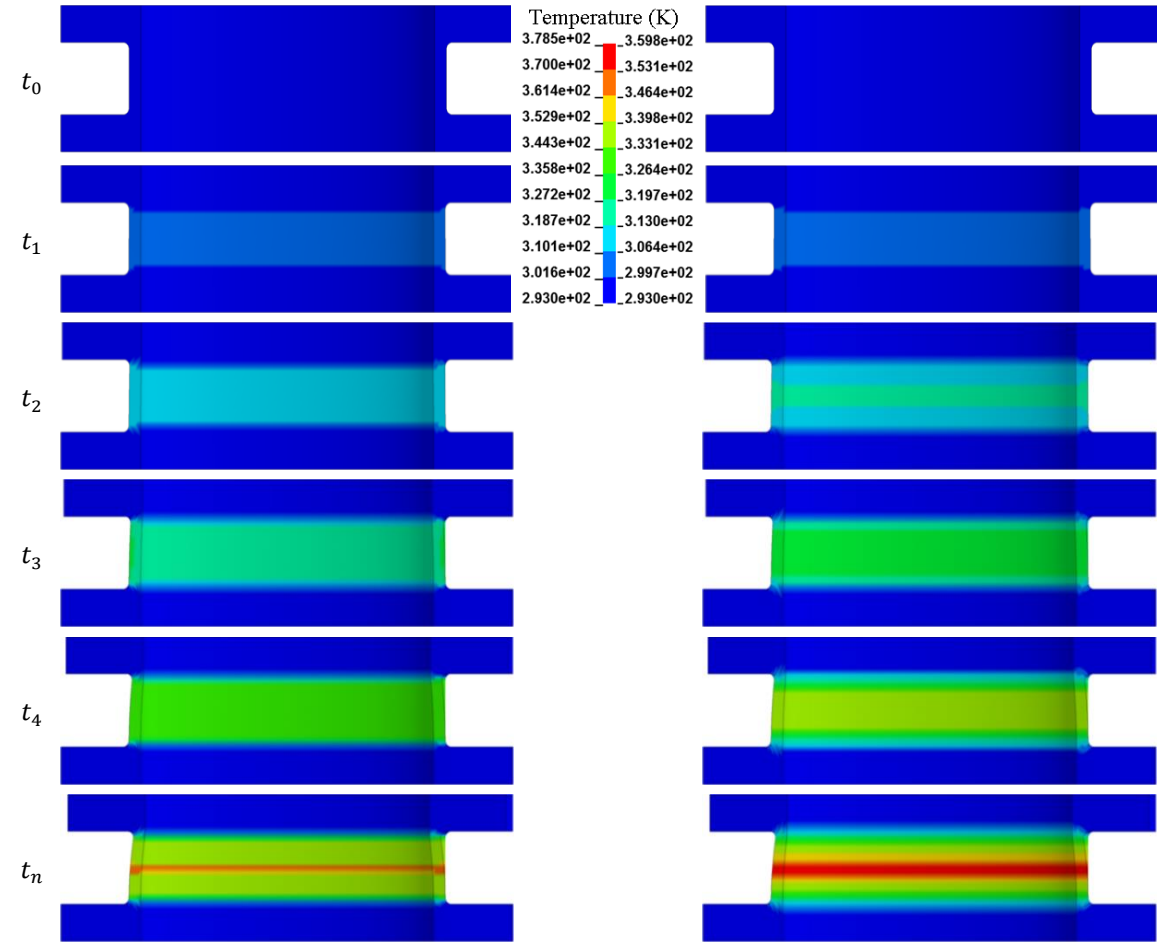

Figure 5-83: Temperature distribution for the thermo-mechanical problem with torsion.

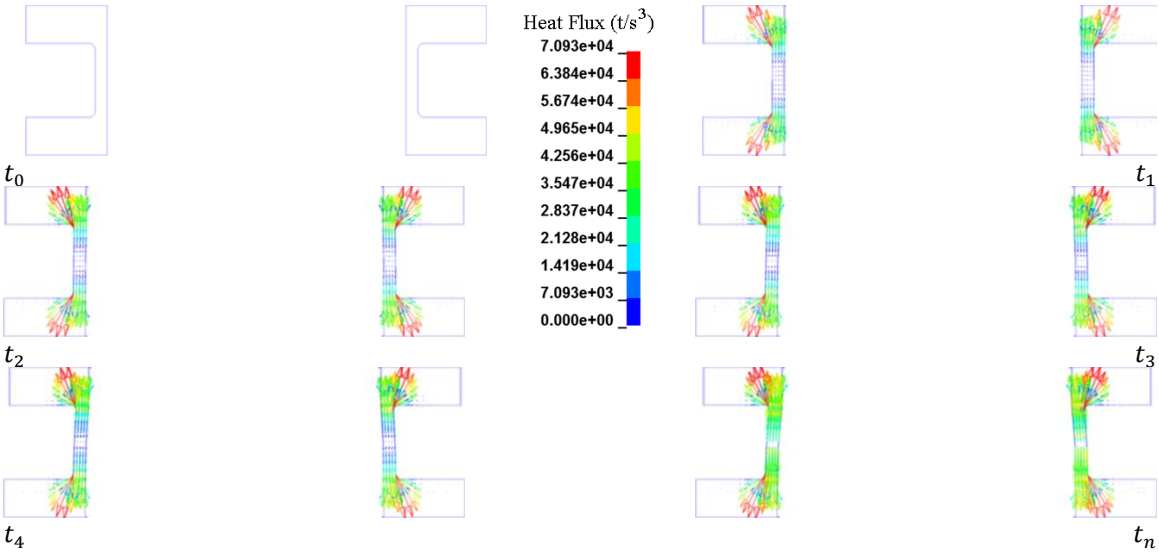

Figure 5-84: Heat flux within the specimen due to the thermo-mechanical problem with torsion.

It should be noted that, as illustrated in Figure 5-2, Specimen #21 has a different orientation of deformation plane. Therefore, the flow curves that are characterized for Specimen #21 are used only for comparison purposes of the flow behavior. Characterization of the failure strains for the proceeding sections will be performed only for the specimens that have the same orientation and do not exhibit a strong stress differential effect as illustrated in Figure 5-85. It is shown that the effective stress vs. effective strain behavior, which is found by using the quasi-static torsion tests with Specimen #21, is outside the confidence interval of the hardening behavior that is characterized for uni-axial tension and compression specimens with the same orientation. Therefore, different plasticity models can be recommended to include stress differential effects and anisotropy within the material especially considering that the hardening curves are often extrapolated to cover large strains for input data of the material model.

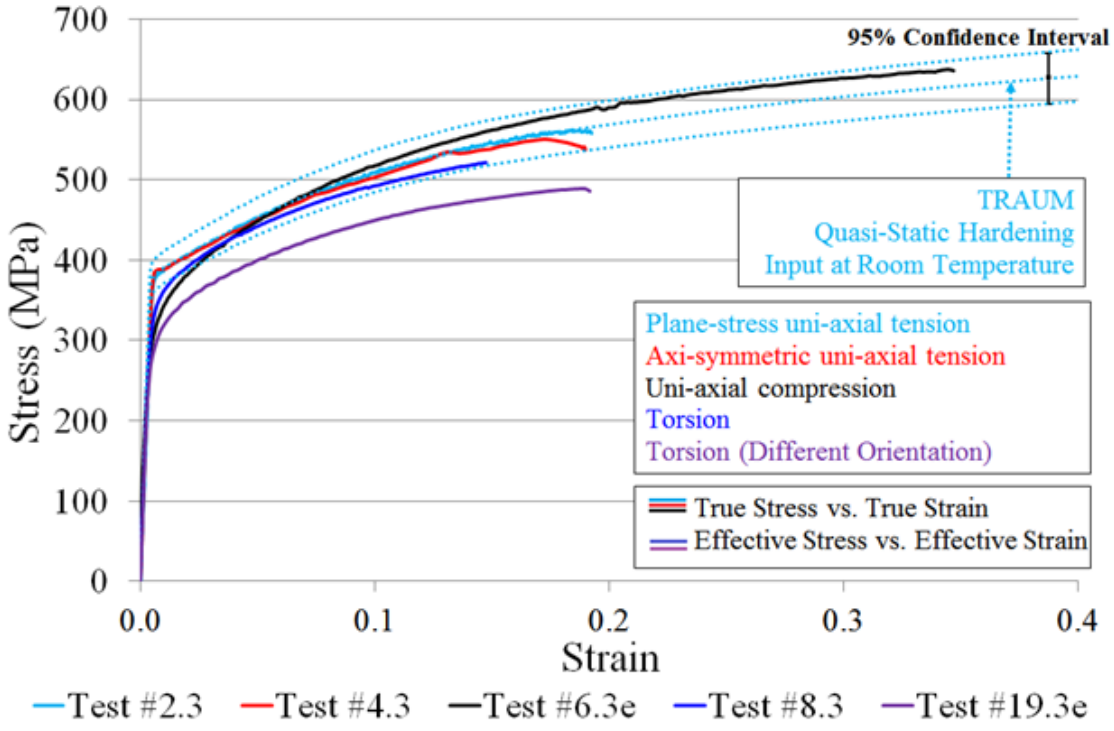

Figure 5-85: Comparison of the flow behavior for specimens with different orientation and states-of-stress.

5.7 **Characterization of the strain-rate dependent hardening curves at room temperature**

As described in Section 5.3 and illustrated by Figure 5-3, strain-rate dependent isothermal hardening curves are required to build the flow surface of the material, where true stress vs. true plastic strain curves are characterized for each strain-rate according to the tabulated input approach with TRAUM.

5.7.1 **Determination of the testing range for strain-rate dependent behavior**

Strain-rate dependency of the flow behavior for structures under impact loading is significantly important, where the strength and ductility of the material can dramatically be affected due to strain-rate hardening and thermal softening. High rate deformation process becomes adiabatic, where the heat generated due to the plastic work is arrested within the body and cannot find enough time to propagate or be conducted [204] [9] [184]. Therefore, body temperature of a rapidly deforming material can increase significantly as illustrated by Figures 5-28 - 5-30. Considering the ballistic impact simulations that are shown in Chapter 3 for three different target thicknesses of Al2024-T3/T351, estimated effective strain-rates within the impact zone are illustrated by Figures 5-86, 5-87 and 5-88 for targets at 1.5875, 3.75 and 6.35mm thicknesses, respectively. The Mesh-III pattern, which is used for ballistic impact analysis in Chapter 3, is utilized for the prediction of the targeted ranges of strain-rates. It should be noted that only one quarter of the finite element model is shown for illustration purposes. It is concluded in Chapter 3 that the deformation and failure modes of the material changes as the thickness changes, where it is found that the failure modes are directly affected by the state-of-stress. On the other hand, temperature and strain-rate history around the impact zone are the influential factors which are also determining the failure modes. It is clearly seen that the range of the maximum strain-rates increase as the thickness of the target material increases, where the failure modes change from petalling to shearing. A significantly high deformation speed is required to accumulate and localize enough heat that is necessary to initiate an adiabatic shear band [77].

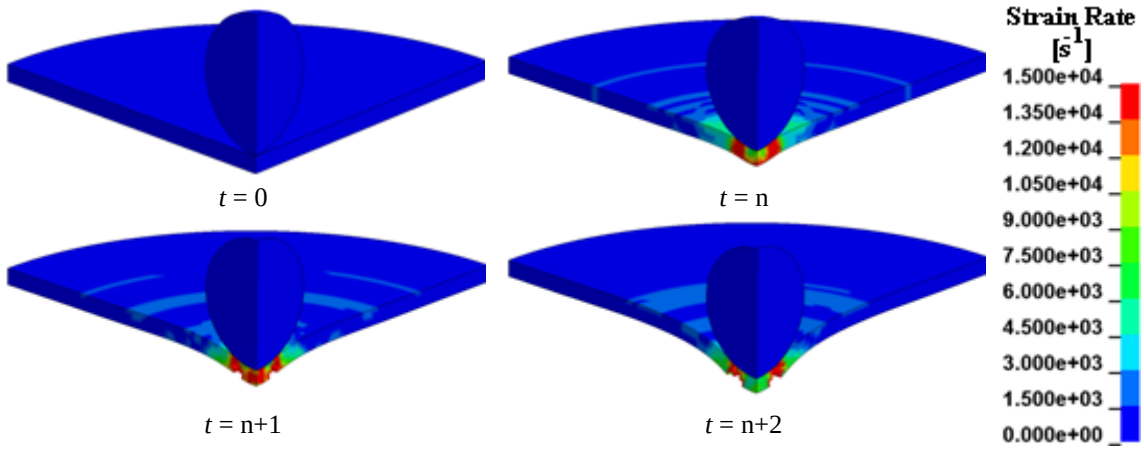

Figure 5-86: Strain-rates achieved for 1.5875mm thick targets under impact.

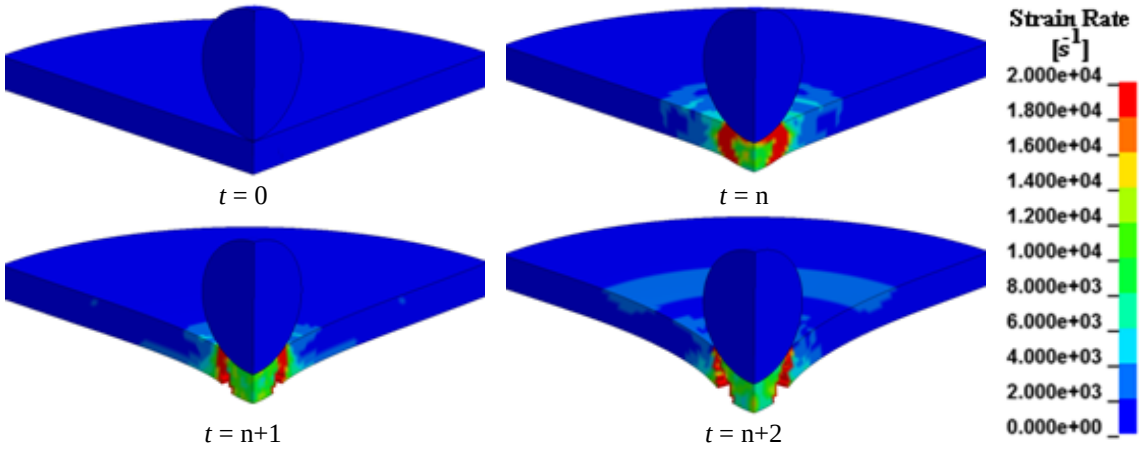

Figure 5-87: Strain-rates achieved for 3.75mm thick targets under impact.

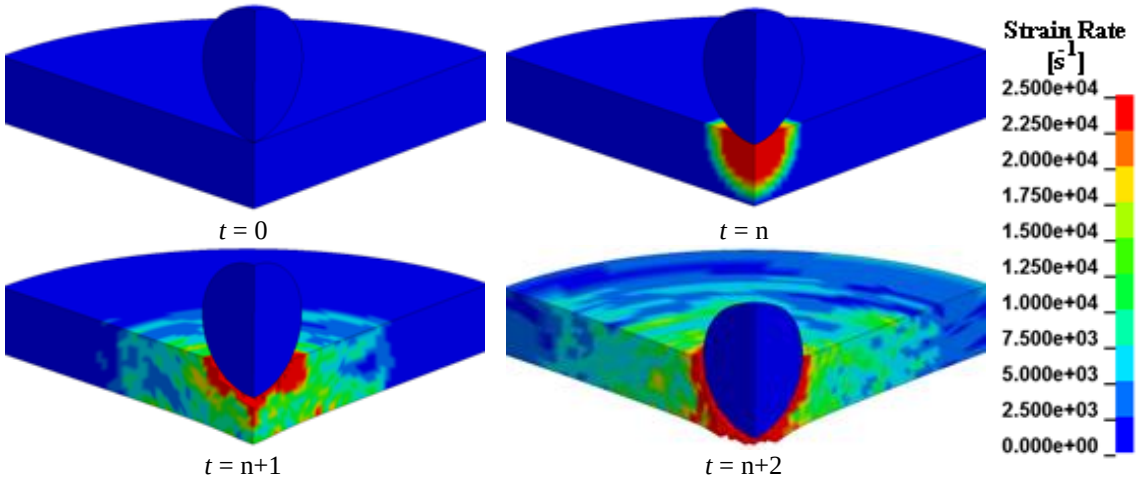

Figure 5-88: Strain-rates achieved for 6.35mm thick targets under impact.

Borvik, et al. predicted a maximum strain-rate of $6x10^{5}s^{-1}$ for 8mm thick Weldox 460 E steel plates impacted by blunt cylindrical projectiles with speeds as high as 298 ms^{-1}, where shear band and plugging formations were observed [335]. Considering that Al2024-T351 has a much lower strength, the given problem has a lower target thickness and the projectile has a spherical nose shape, it would be justifiable to expect lower strain-rates for the range of the problem that is described in Chapter 3. Anticipated results are depicted by Figures 5-86 - 5-88, where the thickest target material is experiencing a maximum strain-rate in the range of $2.5x10^{4}s^{-1}$. Consequently, it is desirable to cover or approach to these strain-rates during the testing program in order to have a better representation of the material behavior under impact loading.

Dynamic behavior of Al2024 has been investigated by several other sources before. Johnson, et al. have tested the high strain-rate and failure properties of Al2024-T351 up to $123s^{-1}$ by using a torsion Hopkinson bar apparatus and have characterized both adiabatic and isothermal behavior, where a shear strain-rate up to $1.0x10^{1}s^{-1}$ and below is assumed isothermal [336].They also have discovered that Al2024-T351 may fail before an instability forms. Set-1 of the material model parameters for J-C model in Chapter 3 is taken from this source. Mason et al. have investigated the adiabatic heating characteristics of Al2024 and the role of the Taylor-Quinney coefficient with respect to the strain-rate and the amount of deformation [316]. They have found that the amount of plastic work that is converted into heat changes dramatically with the amount of plastic work. Li, et al. have also tested Al2024 with three different strain rates under uni-axial compression for lubricated and un-lubricated conditions with various aspect ratios [299]. They have found 9.35% increase of the flow stress for un-lubricated conditions and 6.72% increase of the flow stress for lubricated conditions as the strain-rates are increased from approximately $10^{-3}s^{-1}$ to $3.5\times10^{3}s^{-1}$ for a specimen aspect ratio of one, which is the suggested height to diameter ratio for compression specimens. Hodowany, et al. have used a Kolsky bar apparatus to test Al2024-T3 for large strains from $1.0x10^{-3}s^{-1}$ to $3000s^{-1}$ and found that the stress vs. strain response of the isothermal and adiabatic flow curves was ‘nearly the same’ over the 30% strain range [312]. Lesuer tested Al2024-T3 in compression at a nominal strain rate of $4000s^{-1}$and in tension at a nominal strain

rate of 8000s^{-1} considering different material orientations and found that the stock is isotropic [41]. High-strain rate testing also revealed that the beyond 4000s^{-1} Al2024-T3 is slightly strain rate dependent. A temperature rise of 70°C for tension and 90°C increase in compression was predicted with the characterized material properties. Set-2, Set-3 and Set-3 of the material model parameters, which are used in Chapter 3, are used from this source. Bao has tested stress-state dependent failure characteristics of Al2024-T351 at quasi-static conditions, where he has performed tension and compression tests on the material and discovered signs of anisotropy [99]. Seidt has performed extensive testing with different strain-rates, temperatures and specimens with different geometries to cover the dynamic ductile deformation and failure behavior of Al2024-T351 [108]. He has tested the material at quasi-static conditions with strain-rates from $1.0x10^{-4}s^{-1}$ to 1.0 s^{-1}. At high-strain rate conditions, he has tested Al2024-T351 up to $1.8x10^{3}$ for tension, $1.1x10^{4}$ for compression and $2.8x10^{3}$ for torsion at room temperature. Seidt also investigated the temperature dependent behavior of Al2024-T351 and performed quasi-static tests from 223K up to 723K. His test program also characterized a failure space with respect to the state-of-stress that each specimen was specifically designed for. Seidt pronounced strong anisotropic and stress differential effects for Al2024-T351. Panov also found anisotropic behavior during the testing of Al2024 for quasi-static conditions at various temperatures from 223K up to 473K. He also reported that the material is not strain-rate dependent between $6.4x10^{-4}s^{-1}$ and $6.4s^{-1}$ [337].

5.7.2 **Apparatus for strain-rate dependent testing**

Adapted versions of split Hopkinson (Kolsky) bar (SHB) apparatuses are used to determine the dynamic properties of Al2024-T351 at high strain-rates for compression, tension, and torsion. Split Hopkinson Bar (SHB) technique has become a standard for testing and characterization of the high strain-rate properties especially after 1970s [338]. The method is very well known for years and well documented in the literature [339] [340] [341] [342] [343] [344] [345] [346], where more information can be found by Bell [347], Meyers [184], Gray [348], Johnson [349], Zukas [9], Field, et al. [338], Chen and Song [350]. SHB apparatus is preferred for testing between the rates of $10^{2}s^{-1}$ – $10^{4}s^{-1}$ often depending on the impedance of the material. The adaptations of the apparatus are

described by Gray [348] for compression, by Staab and Gilat [351] for tension and by Gilat [352] for torsion. It should be noted that, the material data, which is characterized in this Chapter, is provided within the joint material research program and more information about testing, specimen attachments, instrumentation, data acquisition and filtering can be found from Seidt [108]. Therefore, the testing apparatuses, which are used by Seidt, are briefly described in the proceeding sections in order to explain the procedures that are used to characterize the material behavior for TRAUM.

5.7.2.1 Compression Split Hopkinson Bar (CSHB) apparatus

During the CSHB testing, a striker bar is fired by a gas gun such that it impacts the end of the incident bar. As a result of the impact, an elastic compression wave is generated and propagated along the incident bar until the interface is reached with the specimen (i.e., Specimen #14). The three bar Kolsky apparatus that is used by Seidt for testing high strain-rate behavior of Al2024-T351 is shown in Figure 5-89 [108].

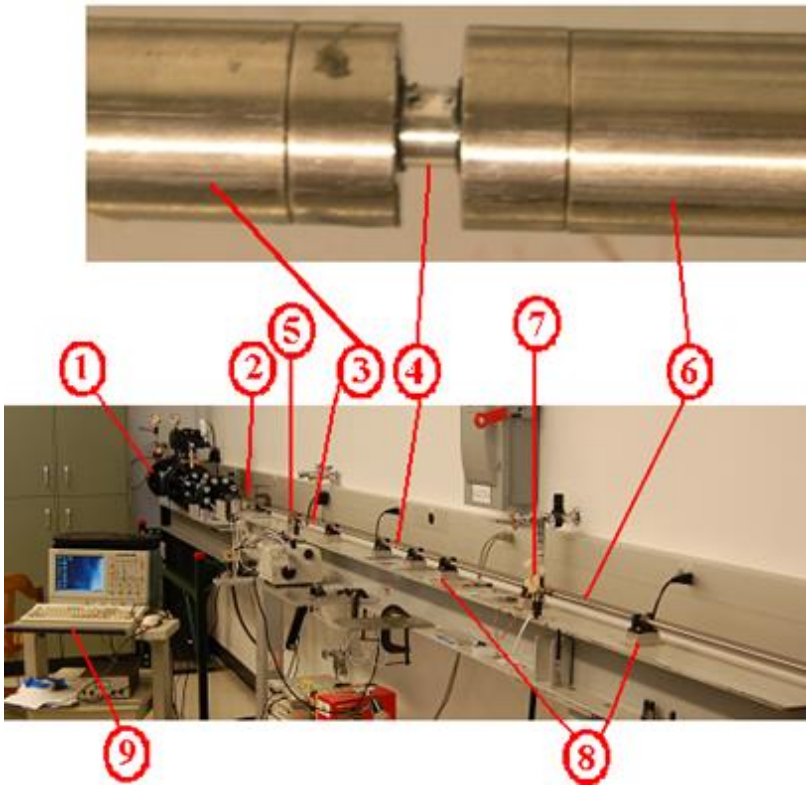

1: Gus gun
2: Striker bar
3: Incident bar
4: Specimen
5: Gauge A
6: Transmitter bar
7: Gauge B
8: Support bearings
9:Oscilloscope and data acquisition

Figure 5-89: CSHB apparatus, after [108].

A schematic illustration of the CSHB apparatus can be seen in Figure 5-90, where Lagrangian *x-t* (i.e., time-distance) diagram is used to show the time coincident propagation of the waves along the apparatus as a result of the initial impact.

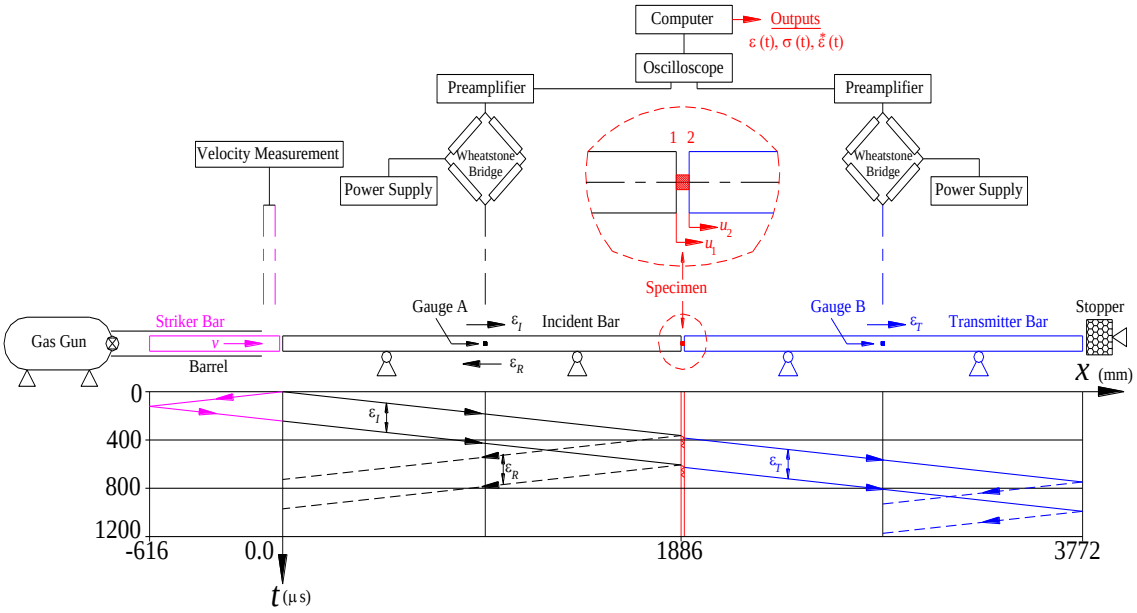

Figure 5-90: Schematic CSHB apparatus and the Lagrangian diagram for wave propagation, modified after [108].

The speed of the elastic wave propagation for the bars, which have identical cross-sectional properties and made from the same material, can be found as:

$$c_{bar} = \sqrt{\frac{E_{bar}}{\rho_{bar}}} \tag{5.65}$$

where, E_{bar} and ρ_{bar} are the Young's modulus and the density of the bar material, respectively. Knowing the initial impact velocity v of the striker bar, the amplitude of the incident wave $\varepsilon_I(t)$ that will be measured by the strain gauge on the incident bar (i.e., Gauge A) can be calculated as:

$$\varepsilon_I = \frac{v}{2c_{bar}}; \quad t_{pulse} = \frac{2L_{striker}}{c_{bar}} \tag{5.66}$$

Where, $L_{striker}$ is the length of the striker and t_{pulse} is the time needed by the pulse to return to the contact interface assuming that the striker and the input bar remain in contact until the pulse that is generated in the striker reflects from its back end as a tensile pulse. Figure 5-91 illustrates typical wave forms for incident and transmitted waves that were measured during Test #26.1e from Gauge A and Gauge B, respectively. The amplitude ε_I and length t_{pulse} of the pulse are shown to be very close to the calculated values. The length of the compression pulse is proportional to twice the length of the striker length, where a 616mm long striker bar was used by Seidt that was made from Ti-6Al-4V with a diameter of 12.7mm; the lengths of the incident and transmitter bars were 1886mm, respectively [108]. It is also noticeable that the Pochhammer-Chree oscillations appear due to the lower velocity of the short wavelength components, which causes dispersion and rides on the waves propagating along the bar [353].

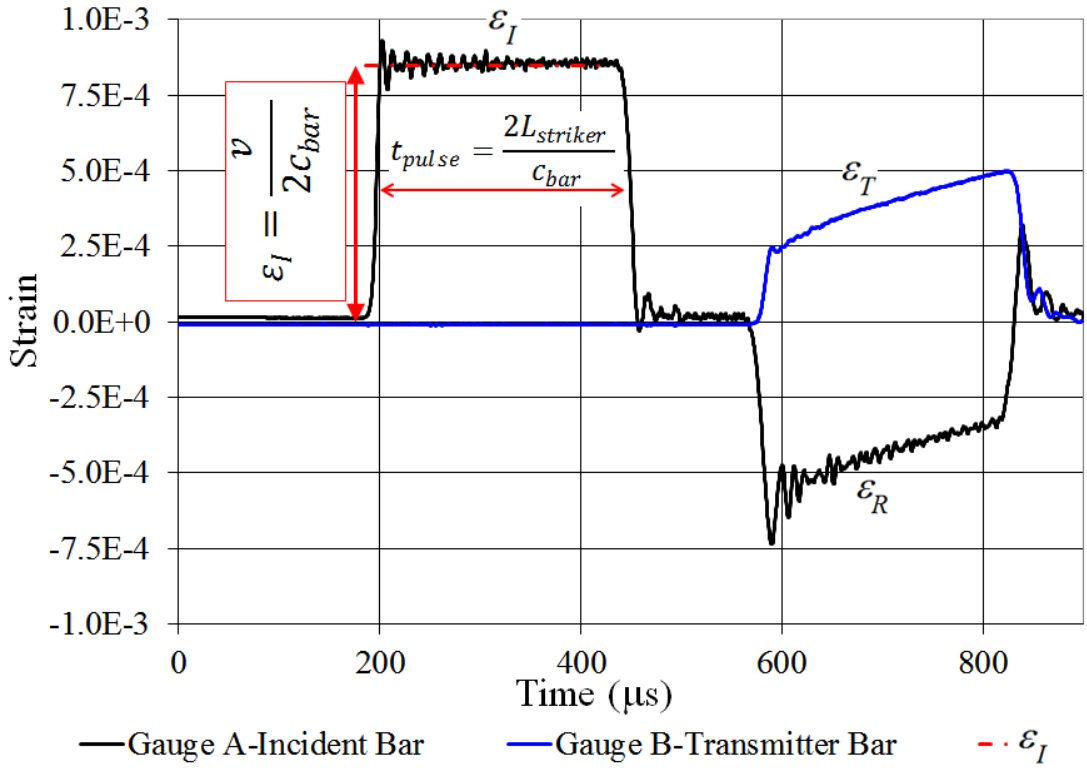

Figure 5-91: Evolution of the wave forms on incident and transmitter bars for Test #26.1e on CSHB apparatus.

When the compression wave or the incident wave propagates along the incident bar and reaches to the specimen, part of the wave is transmitted to the transmitter bar through the specimen and continues to be in compressive form as the transmitted wave; remaining part of the wave reflects at the boundary back to the incident bar in a tensile form and referred as the reflected wave. All bars assumed to stay elastic during the procedure. The specimen deforms plastically provided that the amplitude of the incident wave overcomes the yield strength of the specimen material. The amplitudes of the incident, transmitted and reflected waves are measured by strain gauges mounted on the incident and transmitted bars as ε_I, ε_T and ε_R, respectively. The amplitude of the transmitted wave is measured by Gauge B and the reflected wave is measured by Gauge A, correspondingly.

It should be noted that all three bars are assumed perfectly axi-symmetric with proper diameter to length aspect ratios and one-dimensional elastic wave propagation theory can be applied to solve the equations of motion and energy, where velocity, displacement and pressure fields at both faces of the specimen can be obtained as a function of time from three strain-time histories of $\varepsilon_I(t)$, $\varepsilon_T(t)$ and $\varepsilon_R(t)$ as:

Velocities: $$v_1(t) = c_{bar}\big(\varepsilon_I(t) - \varepsilon_R(t)\big) \quad ; \quad v_2(t) = c_{bar}\varepsilon_T(t) \tag{5.67}$$

Displacements: $$u_1(t) = \int_0^t v_I(t)dt \quad ; \quad u_2(t) = \int_0^t v_2(t)dt \tag{5.68}$$

Forces: $$F_1(t) = E_{bar}A_{bar}\big(\varepsilon_I(t) + \varepsilon_R(t)\big) \quad ; \quad F_2(t) = E_{bar}A_{bar}\varepsilon_T(t) \tag{5.69}$$

where, 1 and 2 denote the incident and transmitted sides of the specimen as illustrated in Figure 5-90. Time interval 't' is the time when the wave arrives at the end of the specimen. E_{bar} and A_{bar} are the Young's modulus and cross-sectional areas of the pressure bars.

Assuming that the system is in dynamic force equilibrium as:

$$F_1(t) \cong F_2(t);\ \big(\varepsilon_I(t) + \varepsilon_R(t)\big) \cong \varepsilon_T(t) \tag{5.70}$$

With this approximation, the strain-rate $\dot{\varepsilon}(t)$ and the stress $\sigma(t)$ in the specimen are proportional to the reflected $\varepsilon_R(t)$ pulse and the transmitted pulse $\varepsilon_T(t)$, respectively. Nominal strain rate, strain and stress within the specimen can be found as:

$$\dot{\varepsilon}(t) = \frac{v_1(t) - v_2(t)}{h_0} = \frac{c_{bar}}{h_0}\left(\varepsilon_I(t) - \varepsilon_R(t) - \varepsilon_T(t)\right) \cong -\frac{2c_{bar}}{h_0}\varepsilon_R(t) \tag{5.71}$$

$$\varepsilon(t) = \int_0^t \dot{\varepsilon}(t)\,dt \cong -\frac{2c_{bar}}{h_0}\int_0^t \varepsilon_R(t)dt \tag{5.72}$$

$$\sigma(t) = \frac{F_1(t) + F_2(t)}{2A_0} = \frac{1}{2}E_{bar}\left(\frac{A_{bar}}{A_0}\right)\left(\varepsilon_I(t) + \varepsilon_R(t) + \varepsilon_T(t)\right) \cong E_{bar}\left(\frac{A_{bar}}{A_0}\right)\varepsilon_T(t) \tag{5.73}$$

where, h_0 and A_0 are the initial length and cross-sectional area of the specimen, respectively.

Figure 5-92 illustrates the history of nominal values of strain, stress and strain rate after a data reduction by assuming that time starts when the first wave front reaches the specimen. It is shown that the calculated strain-rate is not constant and noticeable amount of oscillations are recorded especially within the 'rise-time' during the elastic loading. Therefore, the initial part of the stress vs. strain relation is not used during the characterization procedure, where the dynamic equilibrium is compromised. To determine the nominal strain-rate, averaged strain-rate is calculated for the range beyond the 'rise-time'.

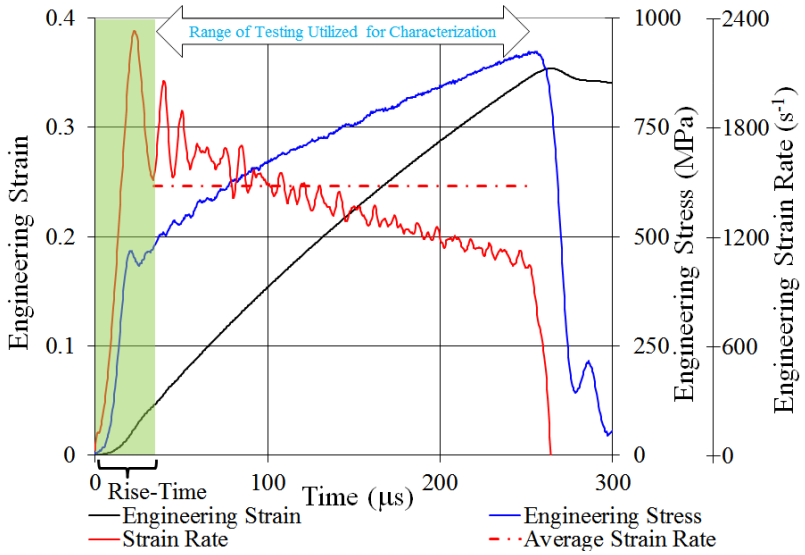

Figure 5-92: History of the specimen for Test #26.1e on CSHB apparatus.

The ‘single-wave’ analysis, which is defined by Equations (5.71) - (5.73), utilizes only the reflected wave when calculating the strain and uses only the transmitted wave to find the nominal stress [348]. If the dynamic equilibrium assumption is in question, ‘two-wave’ or ‘three-wave’ analyses can be used to determine the stress-time history, where incident and reflected waves are also taken into account during the verification of dynamic equilibrium [348] [344] [354] [353]. Equations (5.74) and (5.75) represent the nominal stress within the specimen when ‘two-wave’ and ‘three-wave’ analyses are applied, respectively [348].

$$\sigma(t) \cong E_{bar}\left(\frac{A_{bar}}{A_0}\right)\left(\varepsilon_I(t) + \varepsilon_R(t)\right) \tag{5.74}$$

$$\sigma(t) = \frac{1}{2}E_{bar}\left(\frac{A_{bar}}{A_0}\right)\left(\varepsilon_I(t) + \varepsilon_R(t) + \varepsilon_T(t)\right) \tag{5.75}$$

For an ‘acoustically hard material’ with a smaller diameter than the pressure bars, the axial stress distribution of the specimen is found to be non-uniform in the linear elastic phase of deformation. Stress equilibrium is not reached during the linear elastic range, where it is minimal but not still completely achieved during the plastic deformation [355]. Especially during the initial ‘rise-time’ or ‘ring up-time’, the interactions of the waves and reverberation within the specimen causes compromise in the assumption of dynamic force equilibrium and severe oscillations can be observed when the flow behavior is characterized [184] [356]. Due to these effects, it is also not completely possible to achieve a constant strain-rate. Several methods are suggested to help lessening these effects such as pulse shaping, striker nose shape design, specimen chamfering and interface geometry design [348] [357]. Inertial and friction effects are also effective on the interface between the bars and the specimen, which are responsible from a fraction of the wave dispersion. However, it is not completely possible to solve the problem since it is a tradeoff between using a thinner specimen with a smaller $\frac{h_0}{A_0}$ ratio and lower the amount of inertial effects but increase the friction or using a thicker specimen with a bigger $\frac{h_0}{A_0}$ ratio and lower the amount of friction but increase the inertial effects.

According to Gray [348], radial and longitudinal inertial and friction effects can be reduced by minimizing the areal-mismatch between the bar and specimen by a ratio of $\frac{A_{bar}}{A_0} \approx 1.5625$ and by using a specimen with a ratio of $0.64 \leq \frac{h_0}{A_0} \leq 1.27$ when a material with a Poisson's ratio of $\nu = 0.333$ is considered. On the other hand, Follansbee suggests a ratio of $1.9 \leq \frac{h_0}{A_0} \leq 2.55$ to minimize the friction effects [357]. Therefore, a calculated compromise is necessary, where a unified approach to inertia and friction can be used through the consideration of energy balance as suggested by Malinowski and Klepaczko considering a 'three-wave' analysis concluding that a ratio of $0.64 \leq \frac{h_0}{A_0} \leq 1.27$ would be appropriate for aluminum [358] [355]. It should be noted that for a plastically deforming solid that obeys the Taylor-von Karman Theory to achieve a uni-axial stress state in the specimen, the optimum thickness of the specimen depends on the 'rise-time t', which is estimated as the time required for π reverberations in the specimen given by [359] [355]:

$$t^2 \geq \frac{\pi^2 \rho_0 h_0}{\frac{\partial \sigma}{\partial \varepsilon}} \tag{5.76}$$

where, ρ_0 is the density of the specimen and $\frac{\partial \sigma}{\partial \varepsilon}$ is the Stage-II (i.e., athermal) work-hardening rate of the true stress-strain diagram of the specimen.

Figure 5-93(a) illustrates the comparison between the nominal stress calculations with respect to the consideration on dynamic equilibrium by incorporating different waves in the calculation. Equations (5.73) – (5.75) are compared to verify whether the equilibrium is achieved.

Figure 5-93(b) is used to show that according to Equation (5.76), minimum $37.14\mu s$ is necessary to have π number of reverberations within the specimen and achieve dynamic equilibrium with the plastic state. Equation (5.76) implicitly corresponds to a strain of $\varepsilon = 0.052$ and the borderline for equilibrium is illustrated by Figure 5-93(b). It should be noted that the borderline is calculated for each high strain-rate test and the

characterization of the hardening curves are performed beyond the boundary of dynamic equilibrium.

(a)

(b)

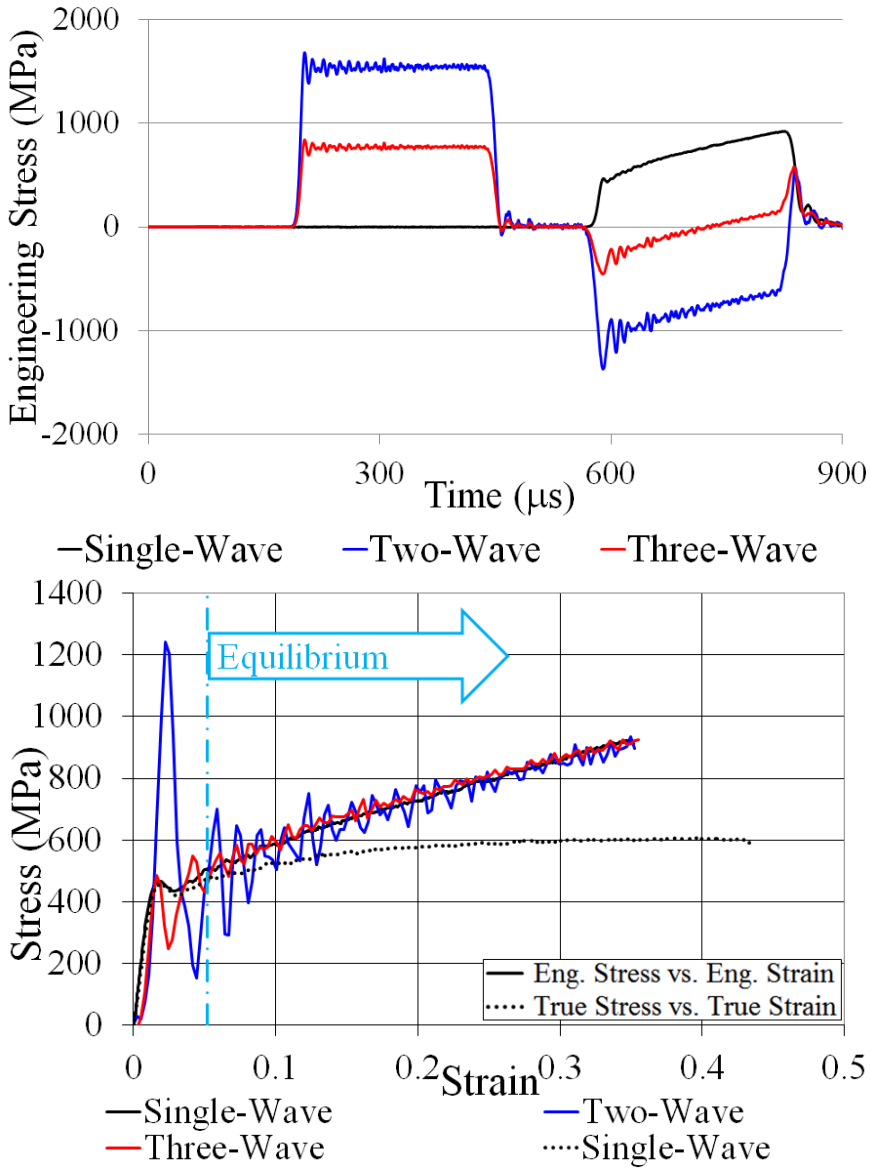

Figure 5-93: Boundary of dynamic equilibrium for Test #26.1e on CSHB apparatus; (a) wave analyses for nominal stress measurements and (b) determination of the boundary for equilibrium based on the wave analyses.

It should be noted that the specimen design and the lot of the specimen material for high strain-rate testing were kept the same with the quasi-static cases in order not to avoid any size effects or material mismatch.

5.7.2.2 Tension Split Hopkinson Bar (TSHB) apparatus

Hopkinson bar apparatuses can also be used for testing high strain-rate properties in tension with similar concepts that are described for compression. Clearly, the traditional Kolsky apparatus needs additional features to incorporate methods of generating a tensile pulse in loading, and appropriate geometries for the specimen and gripping. Three general types of TSHB apparatuses are reported, where the first type is conducted in the same manner as CSHB with only a 'top-hat' shaped specimen geometry and a tubular transmitter bar [348] [344]. However, complex specimen geometry and complications in measuring the gauge section, which will be inside the tubular transmitter bar, are some of the disadvantages during the high strain-rate testing. The second type is a direct loading apparatus, where the pulse can be generated with several different methods including directly impacting an anvil attached to the bar, explosive detonation or applying a pulse through a loading tube as described by Harding [360] and Albertini and Montagnani [361]. The third type uses a collar geometry that fits around the specimen and transfers the compression wave to the transmitter bar, where the specimen is threaded firmly between the both incident and the transmitter bar and forced in tension as the transmitter bar is loaded by the collar [362]. However, the interaction of the collar with the specimen and the bars bring additional problems of uncertainty and equilibrium particularly with a difficulty in estimating the preloading on the specimen and the collar.

Staab and Gilat [351] and Seidt [108] used a direct loading method with a preloaded clamped incident bar, where the loading is released by fracturing a pin and the attached specimen is directly subjected to a tensile pulse proportional to half of the amount of preloading on the incident bar before the pin was released. Figure 5-94 illustrates the TSHB apparatus that was used by Seidt, which utilizes direct loading method [108]. The time coincident Lagrangian wave propagation diagram and the instrumentation of the TSHB apparatus are also shown schematically by Figure 5-95.

The load P is applied by pulling a portion of the incident bar up to the clamped location with a pulley-rope system supported by a hydraulic cylinder. When the clamp is released by breaking a pin, the preloaded incident bar generates a tensile wave with amplitude of ε_I, which travels along the incident bar towards the strain gauges and the

specimen (i.e., Specimen #1). The amplitude of the pulse is proportional to the half of the applied load and the duration of the pulse can be found as [351]:

$$\varepsilon_I = \frac{P}{2E_{bar}A_{bar}}; \quad t_{pulse} = \frac{2L_{constrained}}{c_{bar}} \tag{5.77}$$

where, E_{bar} is the Young's modulus, A_{bar} is the cross-sectional area of the incident bar and $L_{constrained}$ is the constrained part of the incident bar behind the clamp and preloaded in tension with a rope-pulley system.

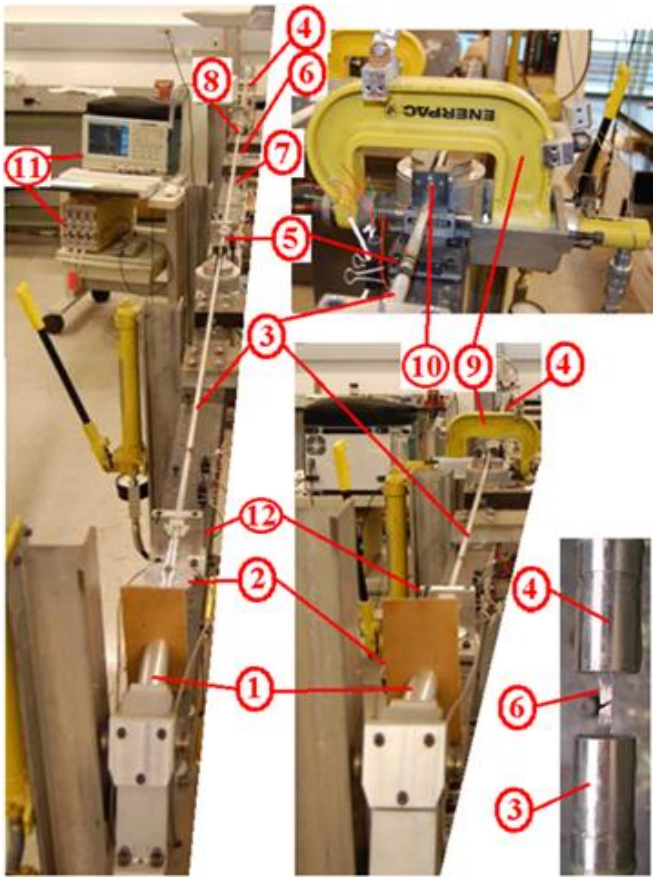

1: Hydraulic cylinder
2: Rope-pulley system
3: Incident bar
4: Transmitter bar
5: Gauge A
6: Specimen
7: Gauge B
8: Gauge C
9: Clamp
10: Pin
11: Oscilloscope and data acquisition
12: Support bearings

Figure 5-94: TSHB apparatus, after [108].

Seidt used 7075-T6 aluminum rods with a diameter of 12.7mm during his tests by TSHB [108]. The length of the clamped part of the incident bar was 1562mm, which has provided a 616.9μs long initial tensile pulse. Figure 5-96 illustrates typical wave forms

for incident and transmitted waves that were measured during Test #24.1e from Gauge A, Gauge B and Gauge C, respectively. The amplitude ε_I and the duration t_{pulse} of the pulse are shown to be very close to the calculated values.

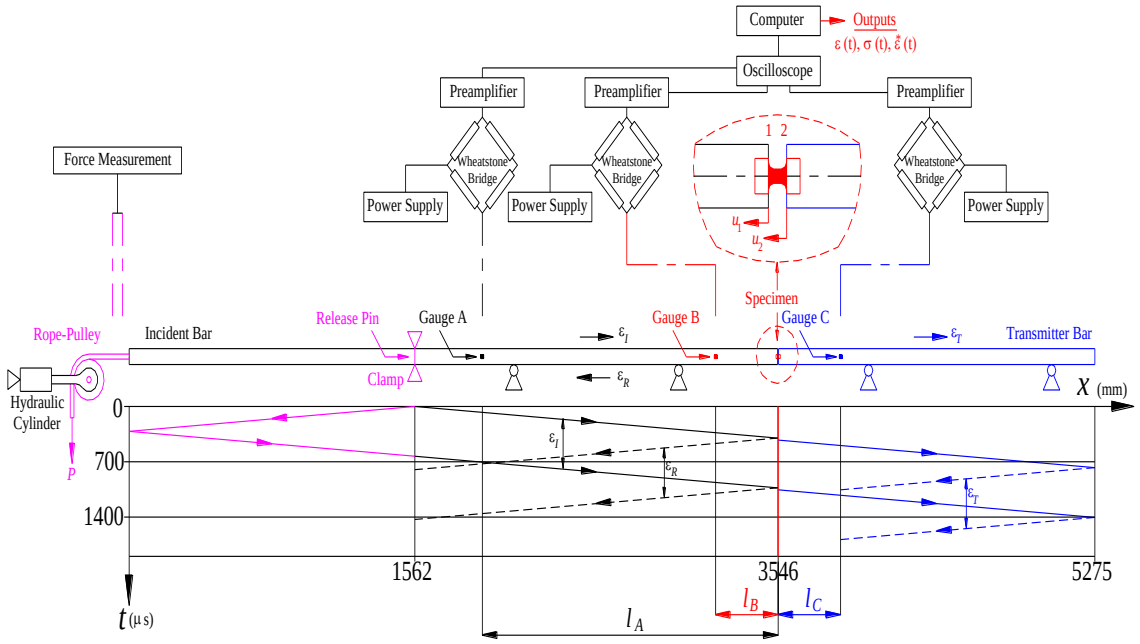

Figure 5-95: Schematic TSHB apparatus and the Lagrangian diagram for wave propagation, modified after [108].

When the propagating wave $\varepsilon_I(t)$ reaches to the interface between the specimen and the incident bar, part of the wave transmits to the transmitter bar and continues in the form of tension wave $\varepsilon_T(t)$; the remaining part of the wave reflects back to the incident bar and propagates as a compression wave $\varepsilon_R(t)$. If the magnitude of the pulse is enough, the specimen deforms plastically. The velocities at the interfaces can be calculated by Equations (5.78) and (5.79) using the force histories of the strain gauges at the designated points as illustrated in Figure 5-95 if $F_A(t)$, $F_B(t)$ and $F_C(t)$ are the forces that are measured from strain gauge locations at A, B and C, respectively [351]. It should be noted that l_A, l_B and l_C are the distances from the interface to the designated points of the strain gauges. It is seen that only a small amount of 'rise-time' is found at the beginning of the pin release time and both amplitude and duration of the pulse are in accordance with the calculations, where the inertial effects of rope-pulley system with the incident

bar did not have a significant alteration or compliance. Seidt mentioned that such effects were avoided by the choice of the strain gauge locations, where it should be noted that the free length of the incident bar was 1984mm and the transmitter bar was 1729mm long [108].

$$v_1(t) = \frac{1}{\rho_{bar} c_{bar} A_{bar}} \left[F_A\left(t - \frac{l_A}{c_{bar}}\right) + F_A\left(t - \frac{l_A}{c_{bar}} + 2\frac{l_B}{c_{bar}}\right) - F_B\left(t + \frac{l_B}{c_{bar}}\right) \right] \quad (5.78)$$

$$v_2(t) = \frac{1}{\rho_{bar} c_{bar} A_{bar}} \left[F_C\left(t + \frac{l_C}{c_{bar}}\right) \right] \quad (5.79)$$

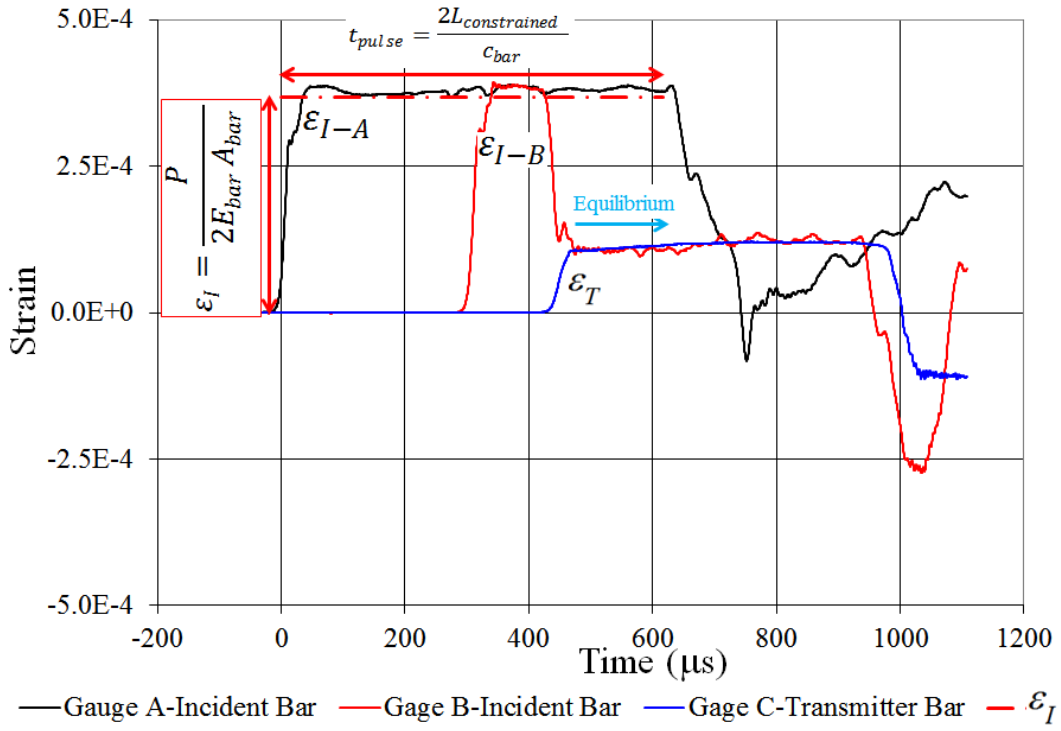

Figure 5-96: Evolution of the wave forms on incident and transmitter bars for Test #XX on TSHB apparatus.

Figure 5-96 also illustrates that a state of dynamic force equilibrium is achieved by comparing the strain readings from the Strain Gauges B and C, which are mounted on the incident and the transmitter bars, respectively. Considering that the Strain Gauges B and C are located equidistant to the specimen and the interface (i.e., $l_B = l_C$), as the specimen deforms plastically, both signals converge to force equilibrium. Consequently, the

problem is then treated similar to the CSHB and the transmitted pulse is assumed proportional to the engineering stress in the specimen and the reflected pulse is proportional to the strain-rate, which can be calculated as:

$$\dot{\varepsilon}(t) = \frac{v_1(t) - v_2(t)}{L_0} \tag{5.80}$$

$$\varepsilon(t) = \int_0^t \dot{\varepsilon}(t)\, dt \tag{5.81}$$

$$\sigma(t) = E_{bar}\left(\frac{A_{bar}}{A_0}\right)\varepsilon_T(t) = \frac{F_C}{A_0}\left(t + \frac{l_C}{c_{bar}}\right) \tag{5.82}$$

where, L_0 is the gauge length and A_0 is the initial cross-section of the tension specimen.

Figure 5-97 illustrates the history of nominal values of strain, stress and strain rate after a data reduction by assuming that time starts when the first wave front reaches the specimen. It is shown that the calculated average strain-rate is almost constant at around 505s^{-1} considering the high dynamic loading conditions.

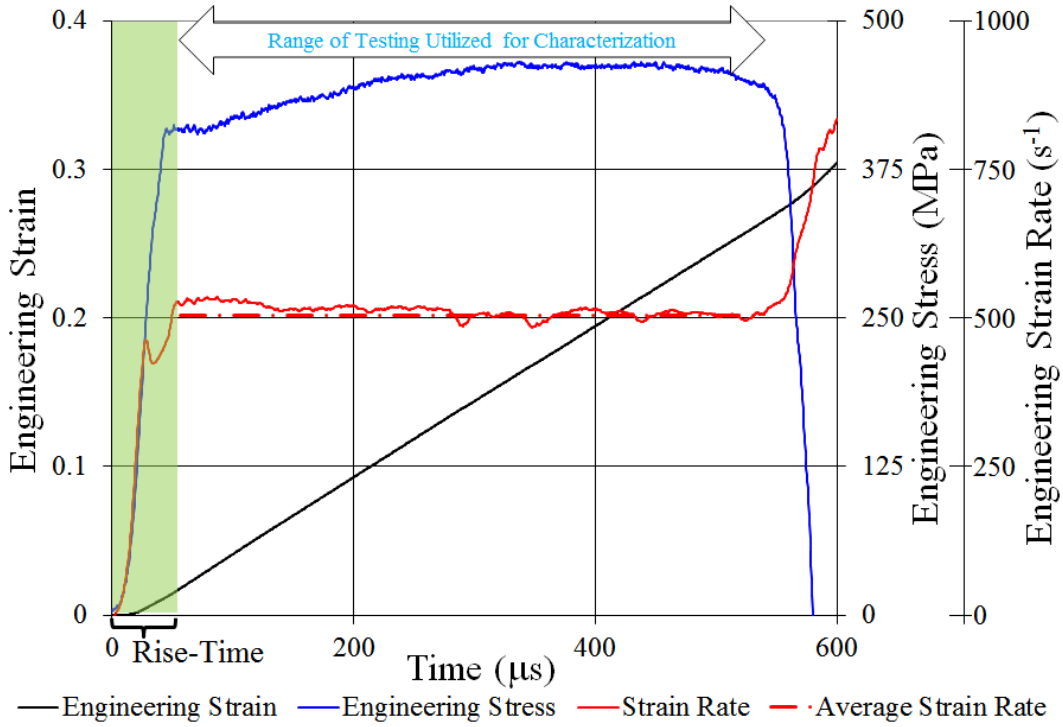

Figure 5-97: History of the specimen for Test #24.1e on TSHB apparatus.

Assuming volume constancy and homogeneous deformation without tensile instability, true stress vs. true strain relation is found and illustrated in Figure 5-98 for the nominal stress-strain values that are found by utilizing Equations (5.81), (5.82) and (5.3). Tensile instability is already considered during the characterization of the flow surface as described in Section 5.6.5 and similar methodology is followed for the characterization of the high strain-rate behavior.

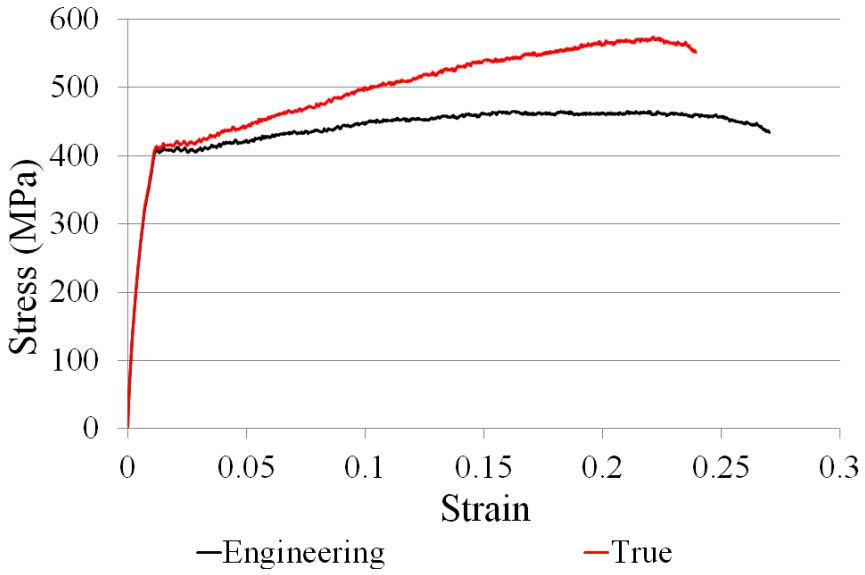

Figure 5-98: Flow behavior for Test #24.1e on TSHB apparatus.

5.7.2.3 Shear Split Hopkinson Bar (SSHB) apparatus

High strain-rate properties of materials can be tested under shear loading [363] with greater accuracy [364] by using adapted versions of Kolsky bar apparatus, which are modified to apply torque on the specimen instead of compression or tension often by using specimens with tubular or spool geometry [365] [366]. The torque can be applied by two means, where using explosives or direct loading with a stored torque device similar to that of the tension apparatus are recognized as the most common [367]. Several advantages of using a SSHB over the uni-axial options, which are described in the previous sections, are pronounced including the benefits of avoiding dispersive

characteristics with the primary mode of torsional waves in the bar. Therefore, dispersion corrections are not necessary anymore if special care is attained in order not to cause any bending waves during the test. This advantage provides the opportunity to place the strain gauges closer to the specimen by design since the three-dimensional end effects are also avoided [367]. A second advantage is recognized as the capability of sustaining large shear strains so that the material can be tested over large strain regimes without the limitations of compression (i.e., friction, Poisson's ratio effect-radial component of deformation, inertial effects, multi-axial state-of-stress) and tension (i.e., tensile instability-necking, inertial effects, multi-axial state-of-stress) [368]. However, shear bands are reported to be one of the most significant limitations during a torsional loading, where uniform strain distribution is compromised [369].

Seidt used a direct loading SSHB apparatus during his tests as illustrated in Figure 5-99, where the torque T was applied by using a wheel that was attached to the incident bar and was initially loaded by a rope-pulley system [108] [352] [370]. Part of the incident bar was initially constrained with a clamp mechanism, which was released when a pin was broken. Consequently, the incident bar was loaded with an elastic shear pulse $\gamma_I(t)$ that was proportional to the half of the stored torque and propagated along the bar with a surface amplitude and duration of:

$$\gamma_I = \frac{T r_{bar}}{2 G_{bar} J_{bar}}; \quad t_{pulse} = \frac{2 L_{constrained}}{c_{bar}^T} \tag{5.83}$$

where, r_{bar} is the radius, G_{bar} is the shear modulus and J_{bar} is the polar moment of inertia of the incident bar. $L_{constrained}$ is the constrained part of the incident bar behind the clamp. The speed of the transverse elastic wave propagation for the bars can be found as:

$$c_{bar}^T = \sqrt{\frac{G_{bar}}{\rho_{bar}}} \tag{5.84}$$

The time coincident Lagrangian wave propagation diagram and the instrumentation of the SSHB apparatus are also shown schematically by Figure 5-100. The diameter of the

bars that were used during the testing was made of 7075-T6 aluminum with a diameter of 22.225mm. The length of the constrained part of the incident bar was 1227mm, which has provided a 792μs long initial tensile pulse. The free part of the incident bar was 2283mm long and the length of the transmitter bar was 2026mm [108]. Figure 5-101 illustrates typical wave forms for incident and transmitted waves that were measured during Test #31.1e from Gauge A, Gauge B and Gauge C, respectively. The amplitude γ_I and the duration t_{pulse} of the pulse are shown to be very close to the calculated values after a moderate 'rise-time'. As the shear wave $\gamma_I(t)$ reaches to the interface between the specimen (i.e., Specimen #21) and the incident bar, part of the wave transmits to the transmitter bar and continues in the same form of shear wave $\gamma_T(t)$; the remaining part of the wave reflects back to the incident bar and propagates in the opposite sign $\gamma_R(t)$. If the magnitude of the pulse is enough, the specimen deforms plastically.

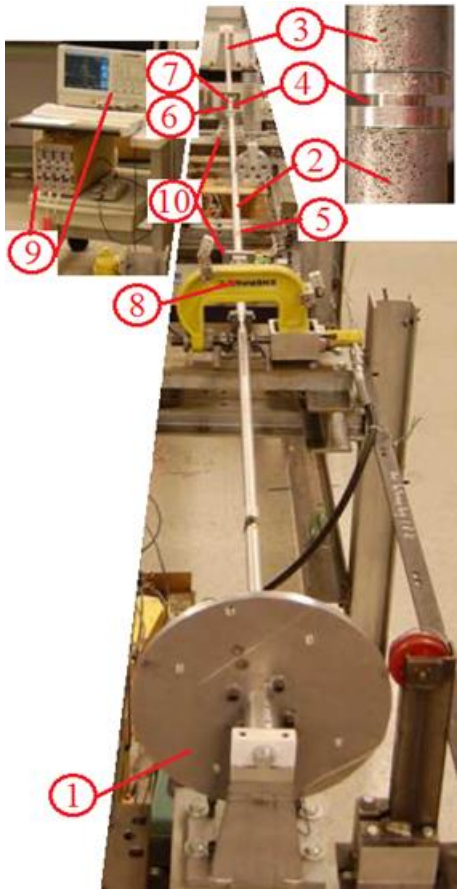

1: Torque wheel
2: Incident bar
3: Transmitter bar
4: Specimen
5: Gauge A
6: Gauge B
7: Gauge C
8: Clamp
9: Oscilloscope and data acquisition
10: Support bearings

Figure 5-99: SSHB apparatus, after [108].

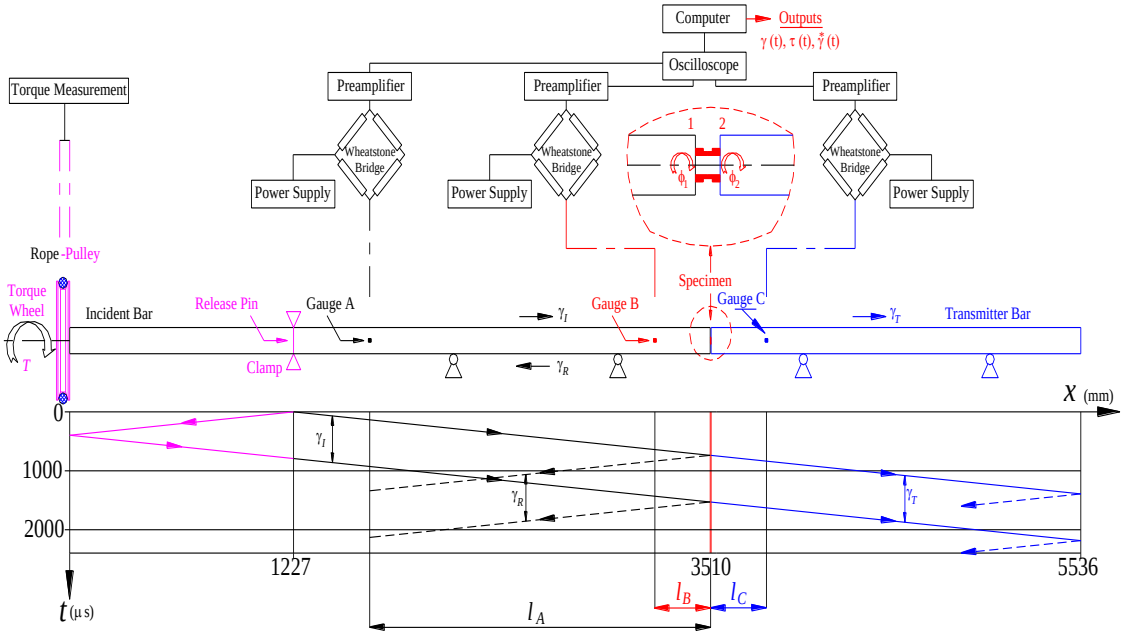

Figure 5-100: Schematic SSHB apparatus and the Lagrangian diagram for wave propagation, modified after [108].

The angular velocities at the interfaces can be calculated by Equations (5.85) and (5.86) using the torque histories of the strain gauges at the designated points as illustrated in Figure 5-100 if $T_A(t)$, $T_B(t)$ and $T_C(t)$ are the torque histories that are measured from strain gauge locations at A, B and C, respectively [351]. It should be noted that l_A, l_B and l_C are the distances from the interface to the designated points of the strain gauges.

$$\omega_1(t) = \frac{1}{\rho_{bar} c_{bar}^T J_{bar}} \left[T_A\left(t - \frac{l_A}{c_{bar}^T}\right) + T_A\left(t - \frac{l_A}{c_{bar}^T} + 2\frac{l_B}{c_{bar}^T}\right) - T_B\left(t + \frac{l_B}{c_{bar}^T}\right) \right] \tag{5.85}$$

$$\omega_2(t) = \frac{1}{\rho_{bar} c_{bar}^T J_{bar}} \left[T_C\left(t + \frac{l_C}{c_{bar}^T}\right) \right] \tag{5.86}$$

Figure 5-101 illustrates that a state of dynamic force equilibrium is achieved by comparing the strain readings from the Strain Gauges B and C, which are mounted on the incident and the transmitter bars, respectively. These strain gauges are located equidistant to the specimen and the interface (i.e., $l_B = l_C$), where both signals converge to torque equilibrium as the specimen deforms plastically.

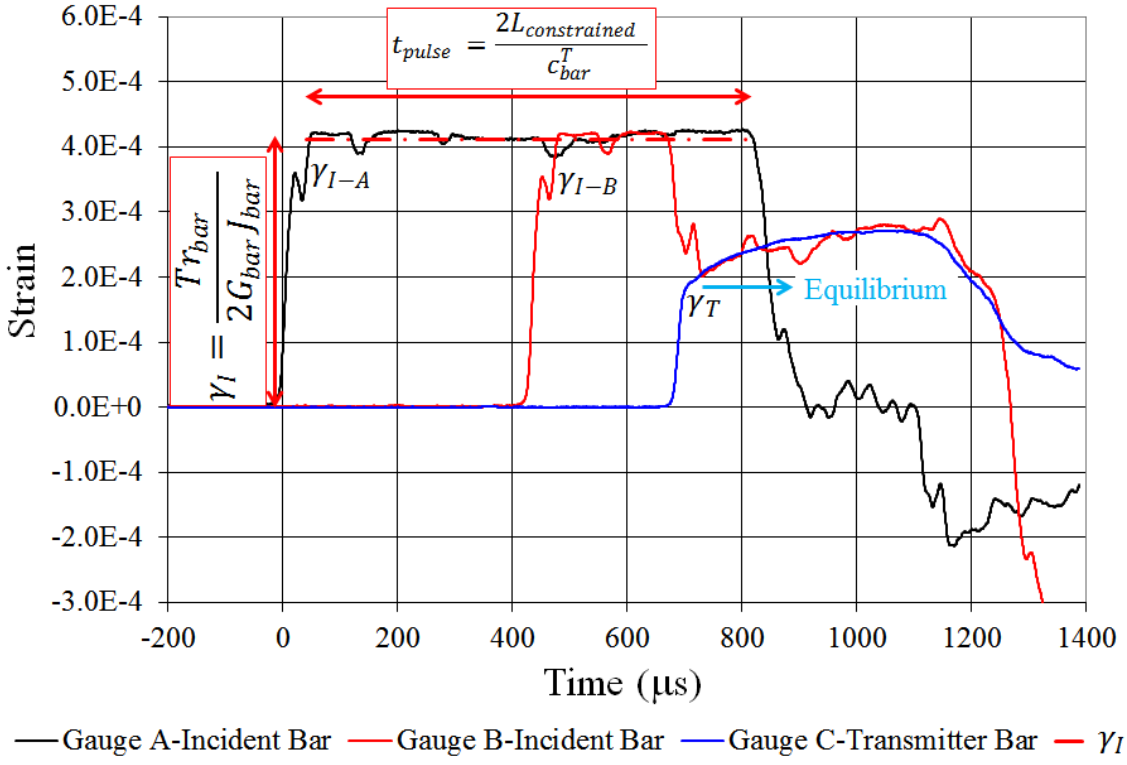

Figure 5-101: Evolution of the wave forms on incident and transmitter bars for Test #31.1e on SSHB apparatus.

Consequently, the problem is then treated similar to the TSHB and the transmitted pulse is assumed proportional to the shear stress in the specimen and the reflected pulse is proportional to the strain-rate, which can be calculated as:

$$\dot{\gamma}(t) = \frac{r_m\left(\omega_1(t) - \omega_2(t)\right)}{L_0} \tag{5.87}$$

$$\gamma(t) = \int_0^t \dot{\gamma}(t)\, dt \tag{5.88}$$

$$\tau(t) = G_{bar}\left(\frac{J_{bar}}{J_0}\right)\left(\frac{r_m}{r_{bar}}\right)\gamma_T(t) = \frac{T_C}{J_0} r_m \left(t + \frac{l_C}{c_{bar}^{T}}\right) \tag{5.89}$$

where, r_m is the mean gauge radius, L_0 is the gauge length and J_0 is the polar moment of inertia of the spool shaped specimen.

Figure 5-102 illustrates the history of nominal values of strain, stress and strain-rate after a data reduction by assuming that time starts when the first wave front reaches the specimen. It is shown that after a moderate 'rise-time', averaged strain-rate is found around $901s^{-1}$.

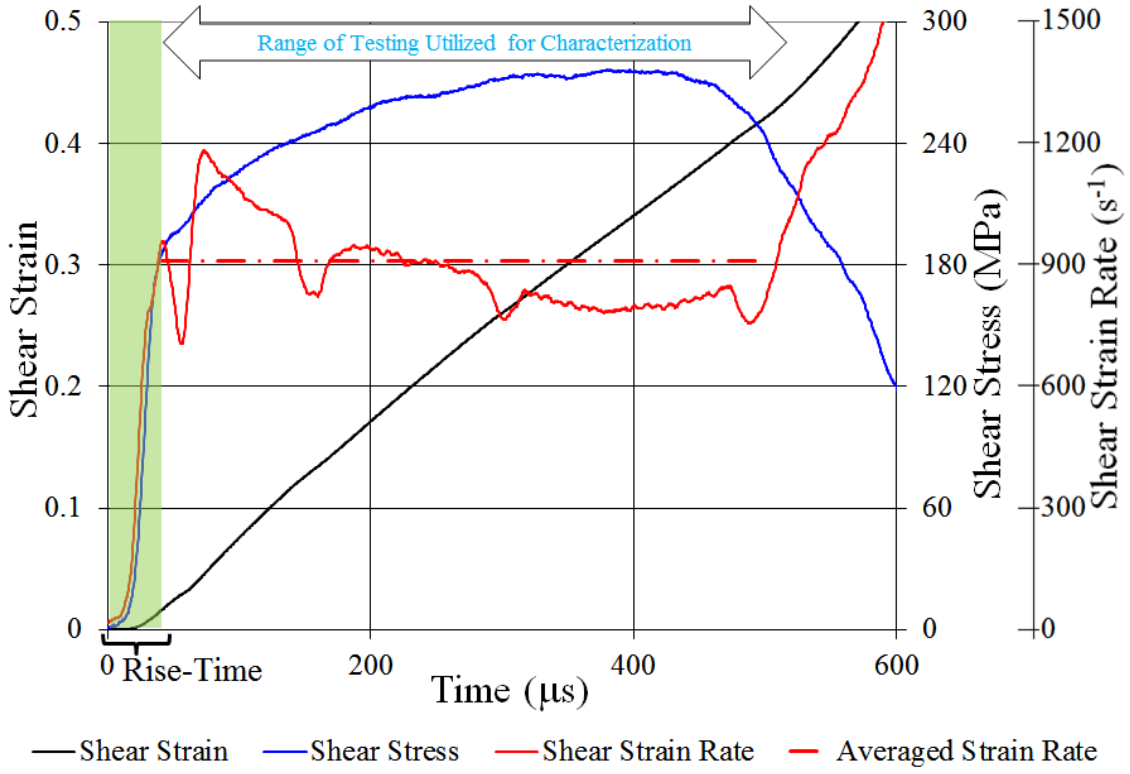

Figure 5-102: History of the specimen for Test #31.1e on SSHB apparatus.

Assuming volume constancy and homogeneous deformation without shear bands or instability, effective stress vs. effective strain relation is found and illustrated in Figure 5-103 for the nominal stress-strain values that are found by utilizing Equations (5.88), (5.89) and (5.18), (5.19).

In the proceeding sections, high strain-rate material properties are characterized at room temperature for different states-of-stress by using the methodologies and relations that are described for each SHB apparatuses.

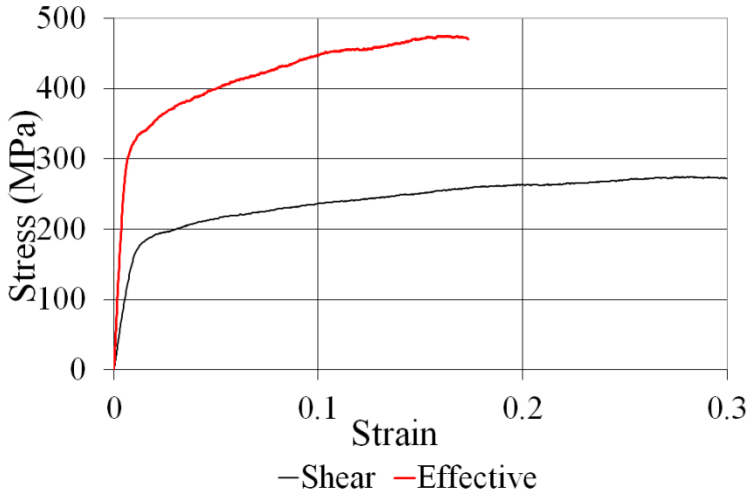

Figure 5-103: Flow behavior for Test #31.1e on SSHB apparatus.

5.7.3 **Modifications on the automated material characterization methodology considering high strain-rate testing, adiabatic heating and dynamic force equilibrium**

A detailed description of the effects of adiabatic heating is depicted in Section 5.6.4 for quasi-static testing conditions. For high strain-rate deformation, the adiabatic conditions are more evident, where there is just not enough time for heat transfer that can occur between the specimen and the surrounding or within the specimen. Consequently, the heat conduction terms of the balance equation is ignored as shown in Equation (5.22). As a result, Equation (5.23) applies to high strain-rate deformation and it is shown that it is permissible to assume 90% of the plastic work is converted into heat for Al2024-T351. As the deformation rates are more rapid than the quasi-static testing, and the amount of heat generated within the specimen cannot escape and is stored, a correction is necessary to obtain the iso-thermal hardening curves since TRAUM already have an incorporated adiabatic heating treatment, which is applied by Equation (4.7). Therefore, in this section automated material characterization procedure that is illustrated by Figure 5-55 is adapted for high strain-rate cases, where the additional iteration for solving a thermo-mechanical problem is not required and the correction from the adiabatic to isothermal conditions can directly be applied after the adiabatic curves are characterized. The new algorithmic flow of the characterization process can be illustrated in Figure 5-104.

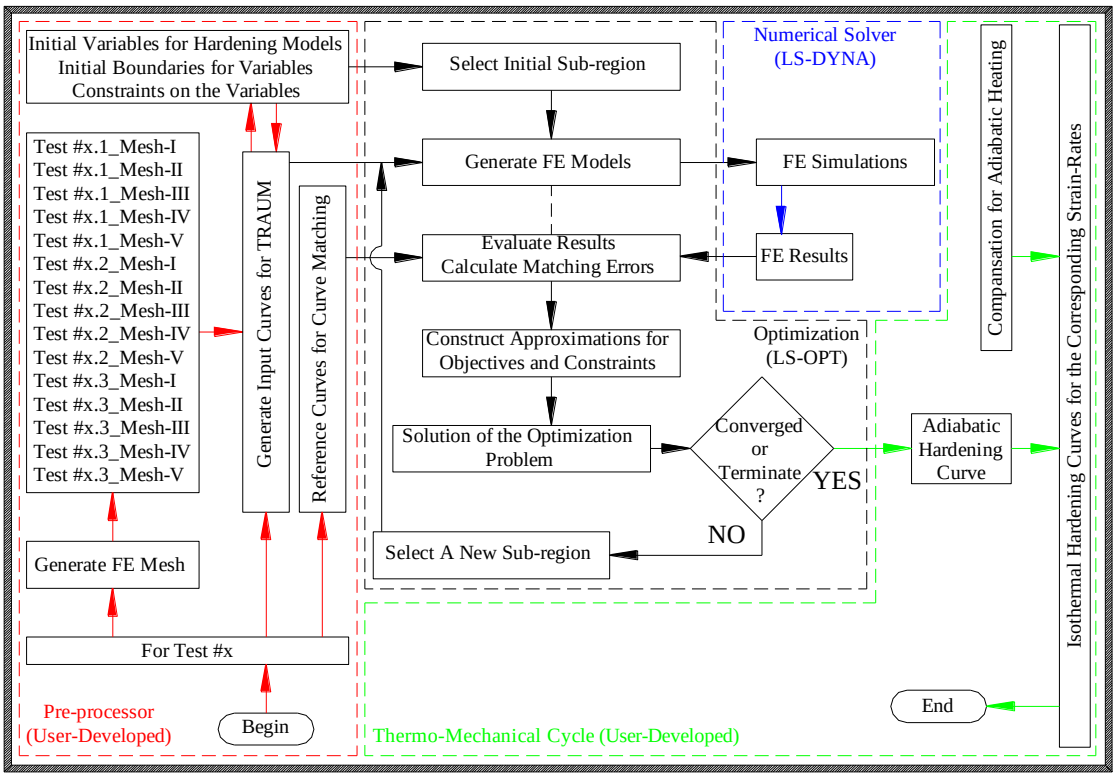

Figure 5-104: Flow diagram of the automated parameter identification process for material characterization by using SRSM for rate dependent tests.

The first step of the automated process is also slightly modified as shown in Figure 5-105. It should be noted that due to the highly dynamic nature of the testing, it is required to determine an averaged strain-rate for each test during the characterization based on the described relations in Section 5.7.2. Consequently, it is also required to determine the boundaries of the characterization, where an averaged strain-rate can be determined. As illustrated in Figure 5-105, the algorithm is also modified to consider the part of the hardening curve that is within the boundaries of dynamic force equilibrium. Therefore, particularly the initial parts of the hardening curves are not used during the characterization, which are representing the 'rise-time' of the behavior. Therefore, the averaged strain-rates are also calculated between the boundaries that are manifested by the dynamic force equilibrium and the failure point of the specimen based on the plastic strain at failure.

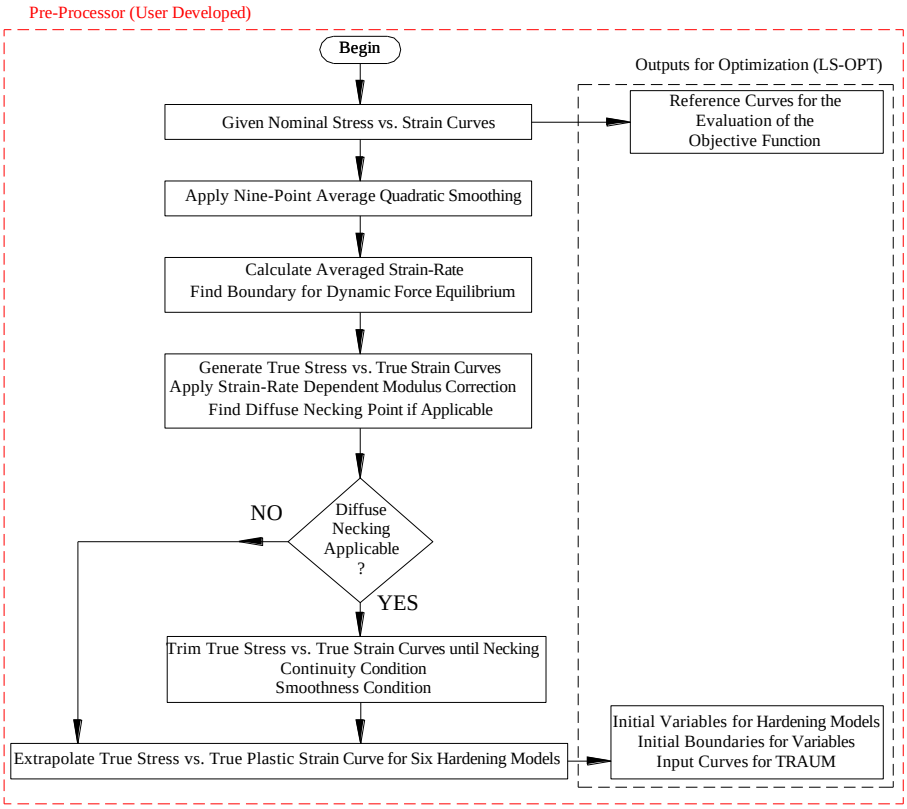

Figure 5-105: First stage of the automated parameter identification process for material characterization by using SRSM for rate dependent tests.

5.7.4 **Characterization of the strain-rate dependent hardening curves at room temperature by using automated AO with SRSM**

Strain-rate behavior of Al2024-T351 is characterized based on the test results that are provided by Seidt, where he used SHB apparatuses for testing the material in tension, compression and shear [108]. In this section, the AO methodology, which is illustrated by Figure 5-104, is applied to characterize the strain-rate dependent flow surface.

5.7.4.1 Characterization of the high strain-rate rate dependent flow in tension

Strain-rate dependent hardening curves are characterized based on the methodology that is described in Sections 7.7.2.2 and 5.7.2.2 by using the AOM that is illustrated in Figure 5-104.

Table 5-20 lists the TSHB tests that are targeting two strain-rates by using the plane-stress specimen with smooth gauge section (i.e., Specimen #1), which is also used during the characterization of the quasi-static hardening and temperature dependent hardening behavior, in order to avoid any size effects or specimen related uncertainties. More information about the specimen dimensions, repeatability of the test results and calculated averaged strain-rates can be found in Appendix-C.

Table 5-20: Test cases that are used to characterize dynamic hardening curves with TSHB at room temperature.

Test #	Specimen #	Test Apparatus	Loading	Targeted Equivalent Strain Rate [s^{-1}]	Temperature [K]	Extensometer Gage Length L_0 [mm]
24 [Figure C-24]† [Table C-24]‡	1 [Figure B-1]§	TSHB*	Uni-axial Tension	500	Room Temperature	5.08
25 [Figure C-25]† [Table C-25]‡				1500		

* Tension Split Hopkinson Bar (TSHB).
† Test results for the corresponding specimen, strain-rate and temperature illustrated in Appendix–C.
‡ Test results for the corresponding specimen, strain-rate and temperature listed in Appendix–C.
§ Detailed geometries and corresponding FE models of the specimens are illustrated in Appendix–B.

It should be noted that due to the equilibrium considerations the averaged strain rates can differ significantly from the targeted strain-rates as the range of the stable and uniform deformation is chosen by the characterization algorithm. Summary of the flow behavior of Al2024-T351 under uni-axial tension is illustrated in Figure 5-106, where all three repeated tests per each strain-rate are shown for comparison. Strain-rate independent (i.e., strain-rate softening) characteristics at the low rate regime and minor strain-rate hardening behavior after $500s^{-1}$ are noticeable. Oscillatory characteristics are observable for the high-rate testing by TSHB, which required a consideration on determining an averaged strain-rate and a boundary for characterizing the flow behavior by ignoring the initial part of the hardening curve especially during the 'rise-time'.

Isothermal hardening curves are calculated based on the amount of plastic work that is converted into heat during the high strain-rate deformation. Figure 5-107 illustrates the isothermal and the adiabatic hardening curves for the corresponding strain-rates. It is noticeable that as the strain-rate increases, the amount of heat generated and retained in

the body also increases, which causes the isothermal curve to compensate for more energy. Verifications of the hardening curves with TRAUM are illustrated by Figures F-24 and F-25 in Appendix-F for the corresponding high-rate tensile tests. These comparisons also signify that a modulus correction was necessary to achieve the correct Young's modulus during the characterization of the rate-dependent flow as illustrated in Figure 5-105.

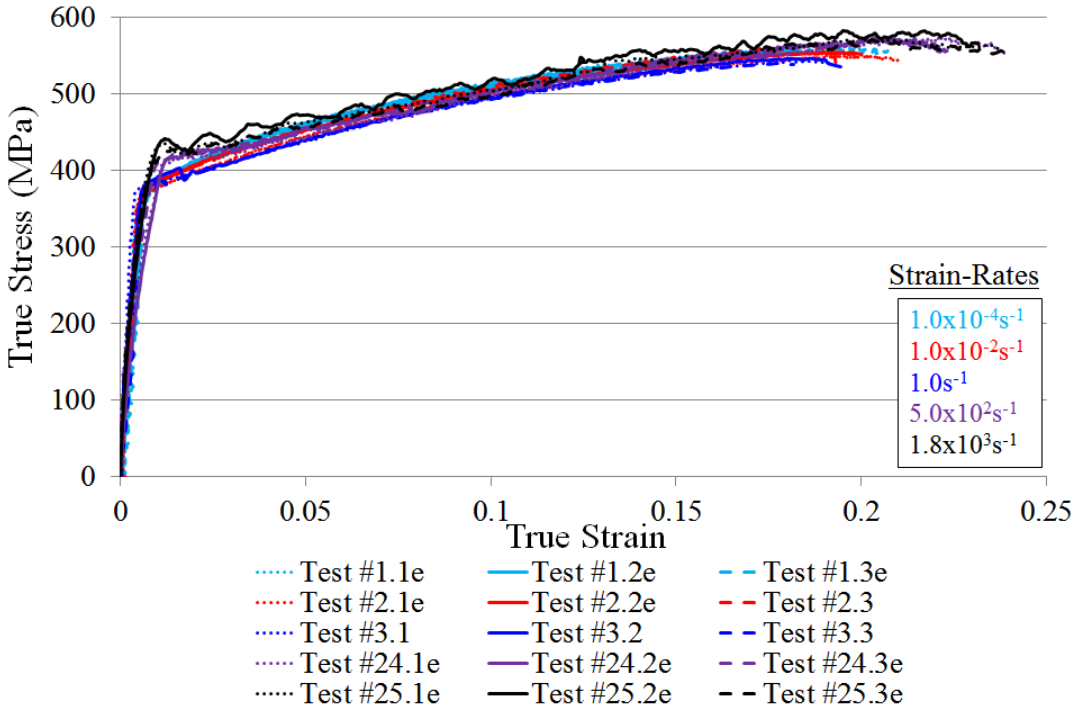

Figure 5-106: Flow behavior of Al2024-T351 for uni-axial tension at room temperature.

5.7.4.2 Characterization of the high strain-rate dependent flow in compression

By using the AOM that is described in Section 7.7.2.2 strain-rate dependent flow behavior of Al2024-T351 is characterized by using the CSHB and the procedures that are defined in Section 5.7.2.1.

Table 5-21 lists the CSHB tests that are primarily targeting two strain-rates by using the axi-symmetric compression specimen (i.e., Specimen #14). More information about the specimen dimensions, repeatability of the test results and calculated averaged strain-rates can be found in Appendix-C.

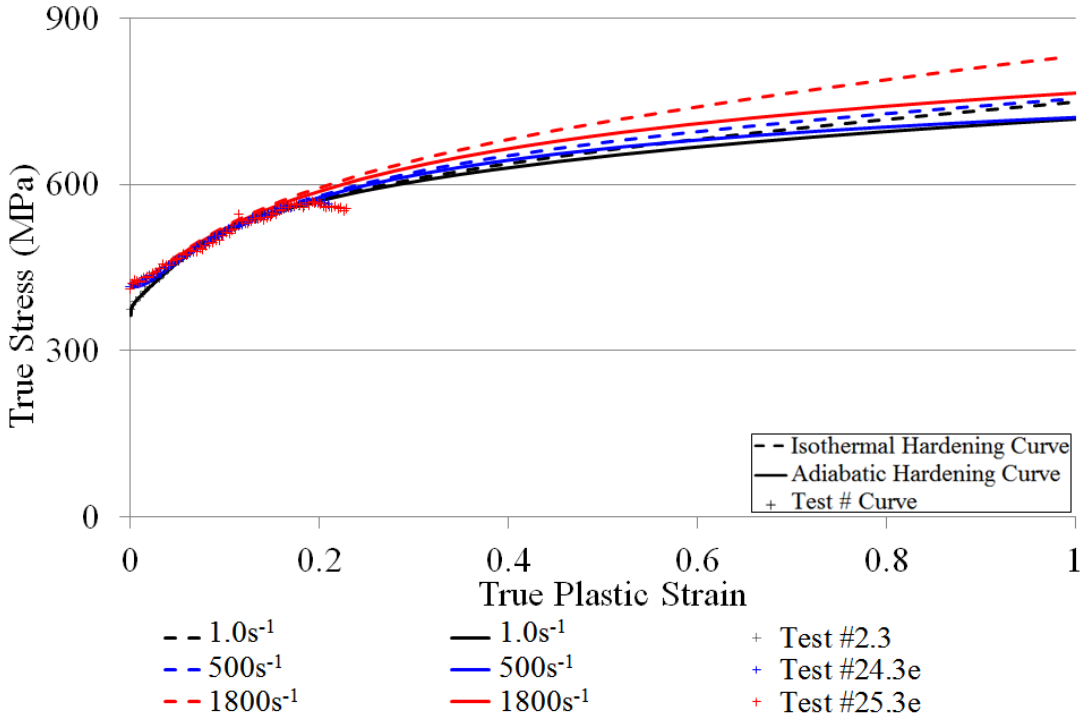

Figure 5-107: Strain-rate dependent flow surface that is characterized from TSHB tests at room temperature.

Table 5-21: Test cases that are used to characterize dynamic hardening curves with CSHB at room temperature.

Test #	Specimen #	Test Apparatus	Loading	Targeted Equivalent Strain Rate [s^{-1}]	Temperature [K]	Extensometer Gage Length L_0 [mm]
26 [Figure C-26]† [Table C-26]‡	14 [Figure B-1]§	CSHB*	Uni-axial Compression	2000	Room Temperature	5.08
27 [Figure C-27]† [Table C-27]‡				5500		
28†† [Figure C-28]† [Table C-28]‡				9000		2.54
29†† [Figure C-28]† [Table C-28]‡				10000		
30†† [Figure C-28]† [Table C-28]‡				11000		

* Compression Split Hopkinson Bar (CSHB).
† Test results for the corresponding specimen, strain-rate and temperature illustrated in Appendix–C.
‡ Test results for the corresponding specimen, strain-rate and temperature listed in Appendix–C.
§ Detailed geometries and corresponding FE models of the specimens are illustrated in Appendix–B.
†† These tests were performed for only one case and were not repeated.

On the other hand, due to the limitations in SHB testing and specimen design considering a stable and uniform flow, the maximum achievable strain-rates were around $5000s^{-1}$ [108]. However, the range of strain-rates are much higher that are required for successfully simulating a ballistic impact as illustrated in Figures 5-86 – 5-88. Therefore, CSHB apparatus and the specimen dimensions are modified to increase the strain-rates up to $1.1x10^{4}s^{-1}$ [371]. In order to avoid complications due to increasing inertia and being able to achieve higher strain-rates by using the same three bar Kolsky apparatus, a smaller gauge length was used for the axi-symmetric compression specimen. However, these tests were performed for only once and were not repeated. Details of these higher rate tests are also listed in Table 5-21and more information can be found in Appendix-C. A summary of the flow behavior of Al2024-T351 under uni-axial compression is illustrated in Figure 5-108 for several different averaged strain-rates. It is seen that the hardening characteristics differ significantly beginning with a strain-rate of $5.0x10^{3}s^{-1}$ due to the change in the dislocation mechanism, where thermally activated dislocations are replaced by viscous-drag/inertia activated dislocations [372] [373].

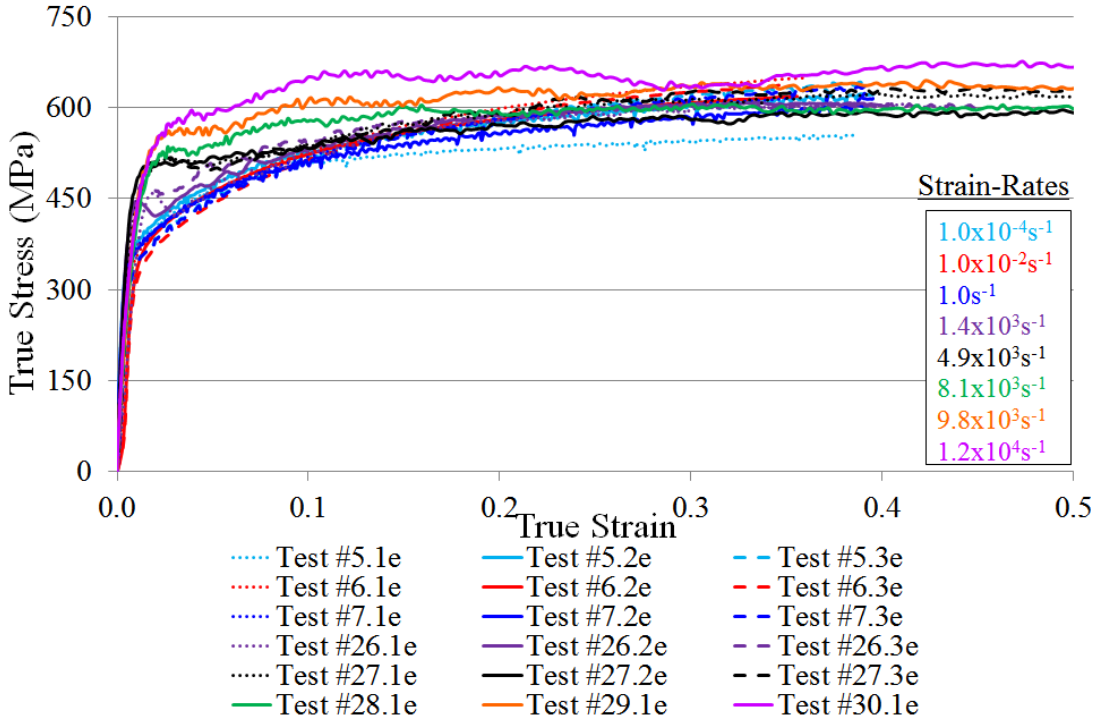

Figure 5-108: Flow behavior of Al2024-T351 for uni-axial compression at room temperature.

It is also seen by the adiabatic test curves in Figure 5-108 that the thermal softening of the material, especially after 25% strain, alters the hardening mechanism and the material softens significantly even at higher strain-rates, where drag activated dislocations are dominant.

Isothermal hardening curves are calculated based on the amount of plastic work that is converted into heat during the high strain-rate deformation. Figure 5-109 illustrates the isothermal and the adiabatic hardening curves for the corresponding strain-rates. Verifications of the hardening curves with TRAUM are illustrated by Figures F-26 - F-28 in Appendix-F for the corresponding high-rate compression tests.

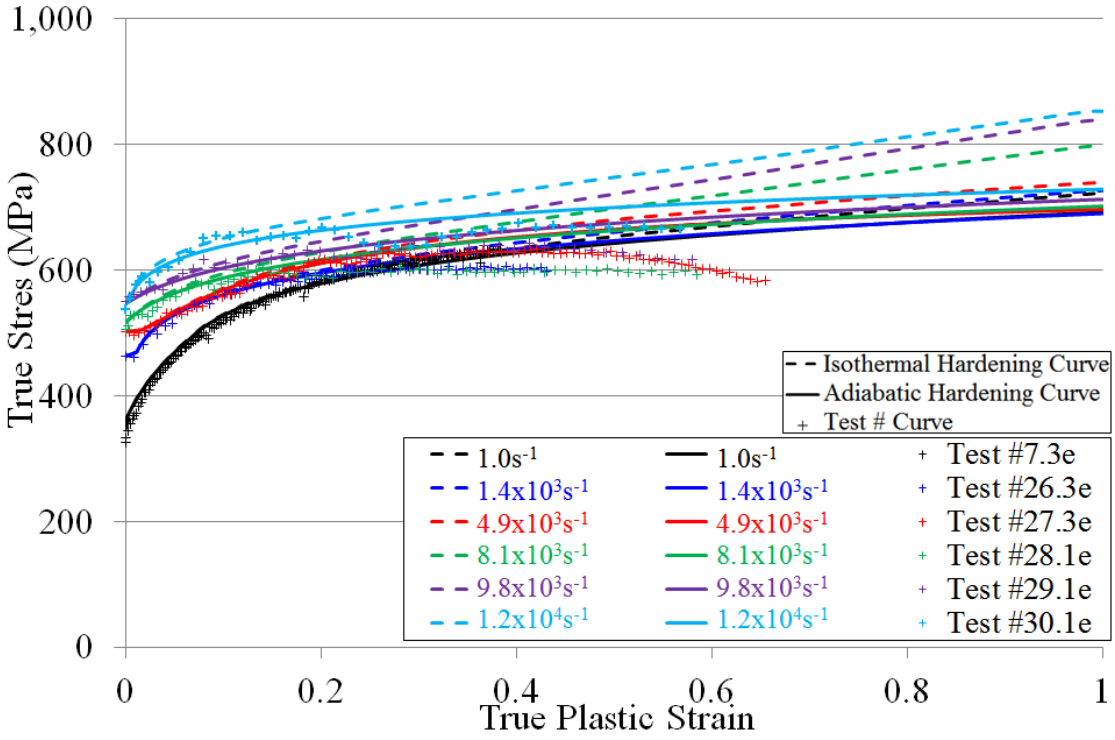

Figure 5-109: Strain-rate dependent flow surface that is characterized from CSHB tests at room temperature.

5.7.4.3 Characterization of the high strain-rate dependent flow in shear

Similar methodology is applied for characterizing the dynamic flow properties of Al2024-T351 under shear that were measured by using a SSHB apparatus.

Table 5-22 lists the CSHB tests that are primarily targeting two strain-rates by using the spool shaped torsion specimen (i.e., Specimen #21). More information about the specimen dimensions, repeatability of the test results and calculated averaged strain-rates can be found in Appendix-C.

Table 5-22: Test cases that are used to characterize dynamic hardening curves with SSHB at room temperature.

Test #	Specimen #	Test Apparatus	Loading	Targeted Shear Strain Rate [s^{-1}]	Temperature [K]	Gage Length L_0 [mm]
31 [Figure C-29]† [Table C-29] ‡	21 [Figure B-19]§	SSHB *	Torsion	866	Room Temperature	1.3462
32 [Figure C-30]† [Table C-30] ‡				5000		

* Shear Split Hopkinson Bar (SSHB).
† Test results for the corresponding specimen, strain-rate and temperature illustrated in Appendix–C.
‡ Test results for the corresponding specimen, strain-rate and temperature listed in Appendix–C.
§ Detailed geometries and corresponding FE models of the specimens are illustrated in Appendix–B.

Summary of the flow behavior of Al2024-T351 under shear loading is illustrated in Figure 5-110, where all three repeated tests per each strain-rate are shown for comparison. Strain-rate independent (i.e., strain-rate softening) characteristics at the low rate regime and minor strain-rate hardening behavior after $500s^{-1}$ are noticeable for the torsion tests similar to the results that are found in uni-axial tension. However, torsion tests exhibit a smooth flow behavior, which is a sign that the flow is not affected from instabilities. Isothermal hardening curves are calculated based on the amount of plastic work that is converted into heat during the high strain-rate deformation. Figure 5-111 illustrates the isothermal and the adiabatic hardening curves for the corresponding strain-rates. A comparison is presented with the quasi-static test results to show the insignificant rate dependency of the material up to $5000s^{-1}$.

Verifications of the hardening curves with TRAUM are illustrated by Figures F-29 and F-30 in Appendix-F for the corresponding high-rate torsion tests.

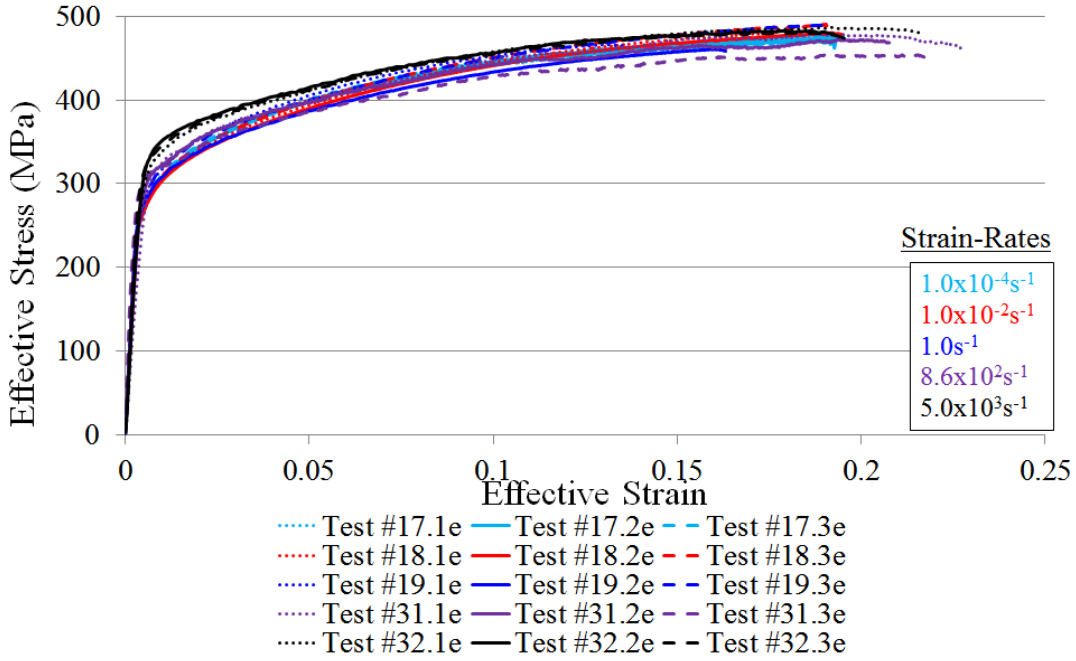

Figure 5-110: Flow behavior of Al2024-T351 for torsion at room temperature.

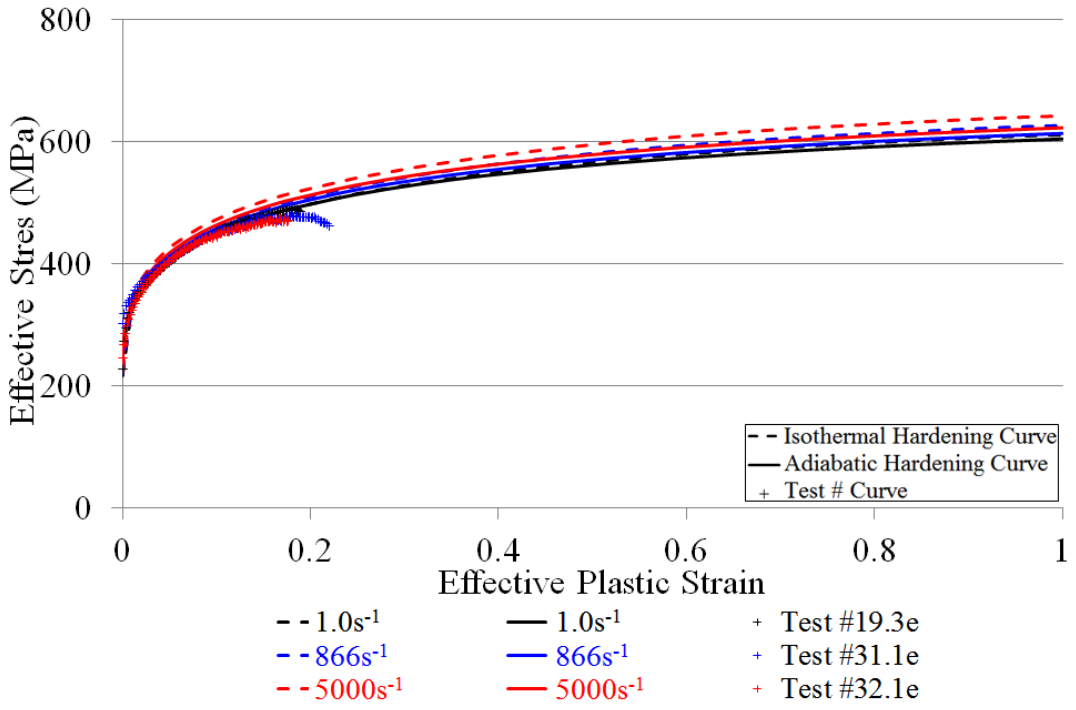

Figure 5-111: Strain-rate dependent flow surface that is characterized from SSHB tests at room temperature.

5.8 **Adiabatic and isothermal flow surface for Al2024-T351**

Based on the methodology that is described in section 5.3 and illustrated by Figure 5-3, tabulated flow surface of Al2024-T351 s characterized and represented by a set of hardening curves that are used to construct the flow surface. Hardening characteristics first characterized for the adiabatic conditions and test results. An additional step is performed to find the isothermal flow behavior considering the heat generation within the body due to the plastic work. TRAUM utilizes the strain-rate dependent hardening curves at room temperature and temperature dependent hardening curves at a nominal strain-rate d $1.0s^{-1}$ as described by Equation (4.6). Consequently, verified hardening characteristics and the flow surfaces of Al2024-T351 are illustrated by Figures 5-112 – 5-114.

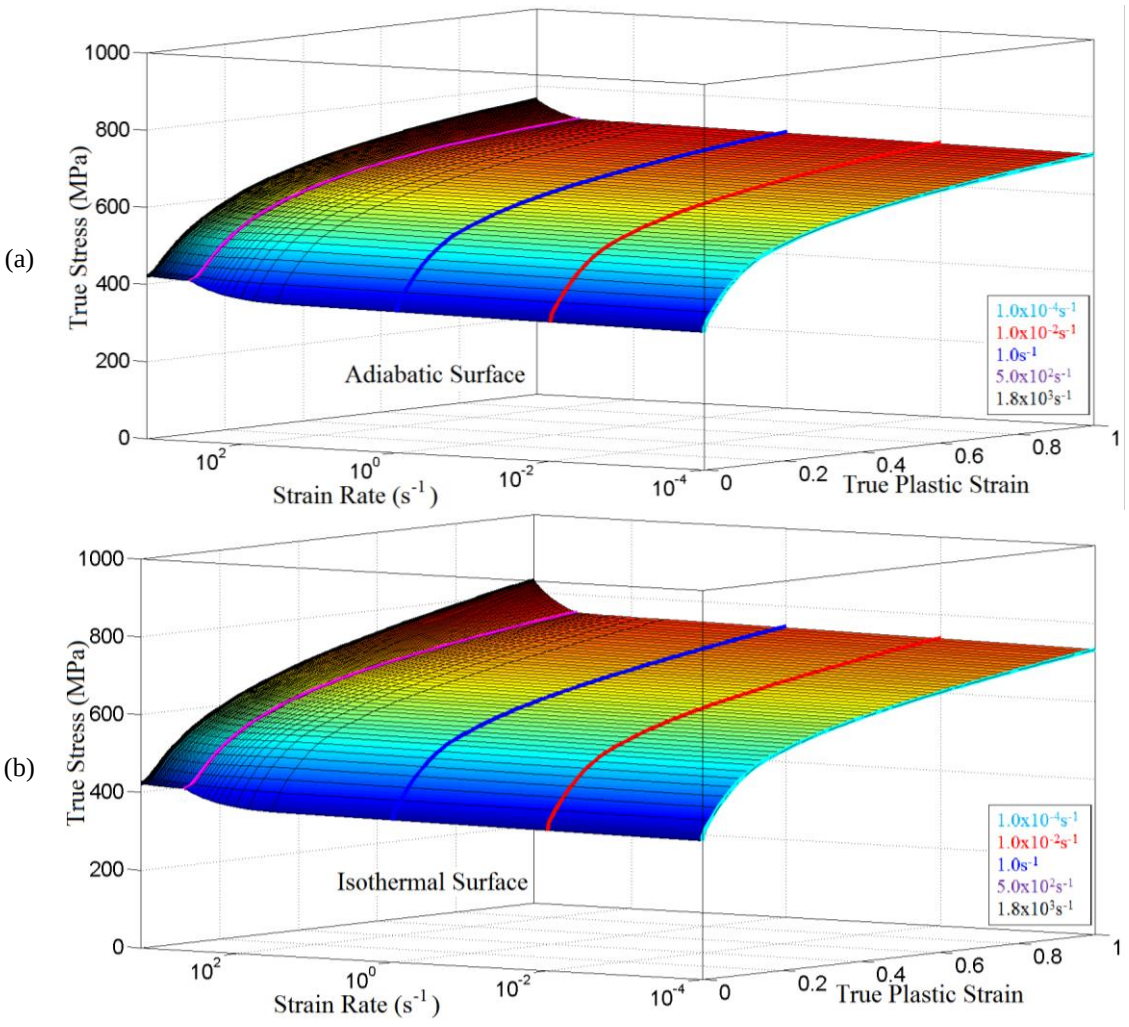

Figure 5-112: Strain-rate dependent flow surfaces that are characterized from uni-axial tension tests; (a) adiabatic and (b) isothermal.

Figures 5-112 – 5-114 exhibits the strain-rate dependent flow surface for both adiabatic and isothermal conditions. The figures summarize the required inputs for TRAUM for different test conditions including uni-axial tension, compression and shear. It should be noted that since tabulated inputs are used to construct the flow surface during the simulations, linear interpolations between the input curves are used to find the required state variables for the solution of the plasticity problem. Rate dependent flow surfaces clearly show that the Al2024-T351 has insignificant rate-dependency up to $5000s^{-1}$, where thermally activated dislocations are dominant as a typical fcc material.

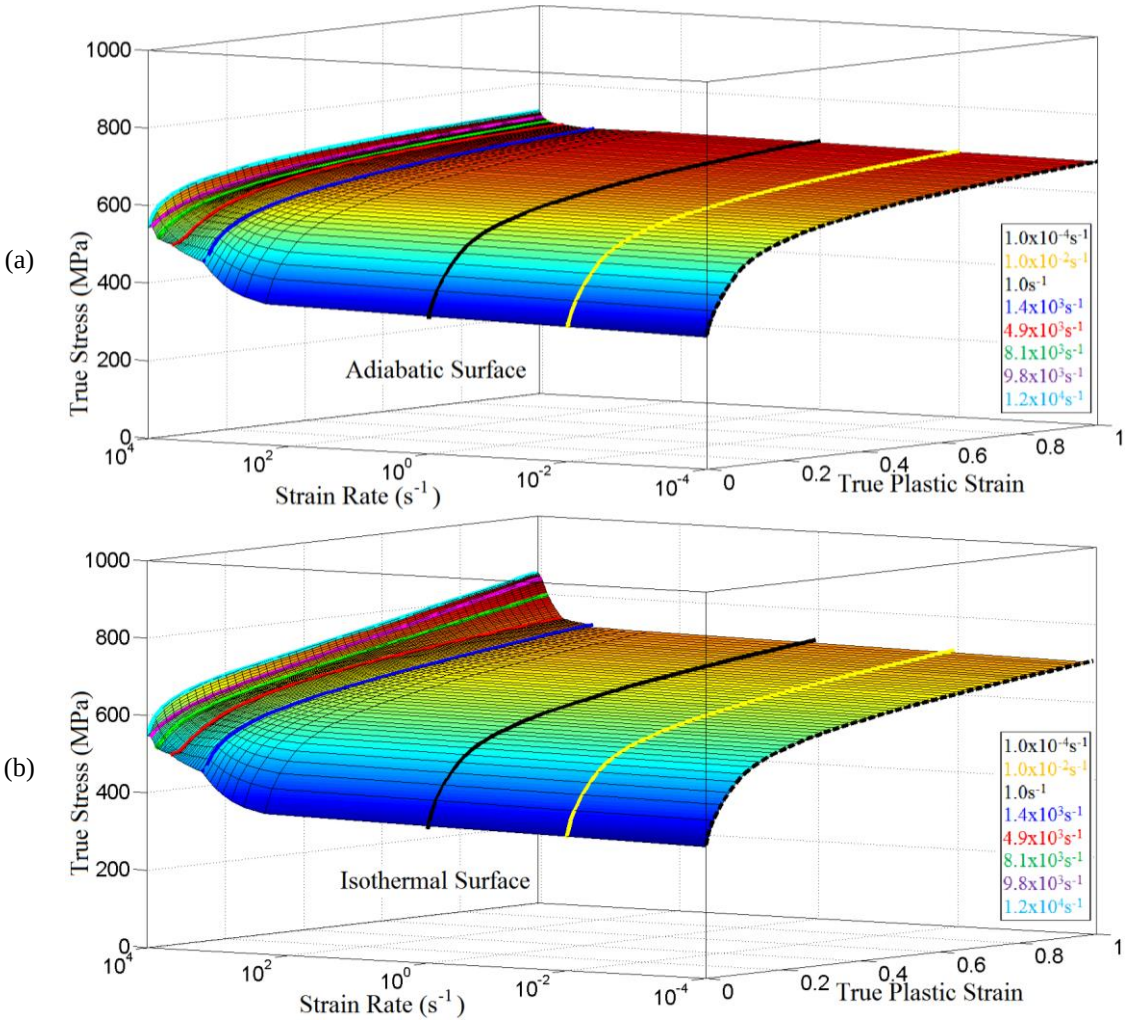

Figure 5-113: Strain-rate dependent flow surfaces that are characterized from uni-axial compression tests; (a) adiabatic and (b) isothermal.

It is clearly seen that after $5000s^{-1}$, the material exhibits an increasing rate-dependency as the viscous drag becomes more dominant. However, it was not possible to test the material for even higher strain-rates due to the limitations of the Hopkinson bar apparatuses. It is advisable to consider testing the material by utilizing other equipment for much higher strain-rates considering that the expected strain-rates for a ballistic impact can reach to levels that are another order of magnitude higher than the currently investigated [12] [9] [13].

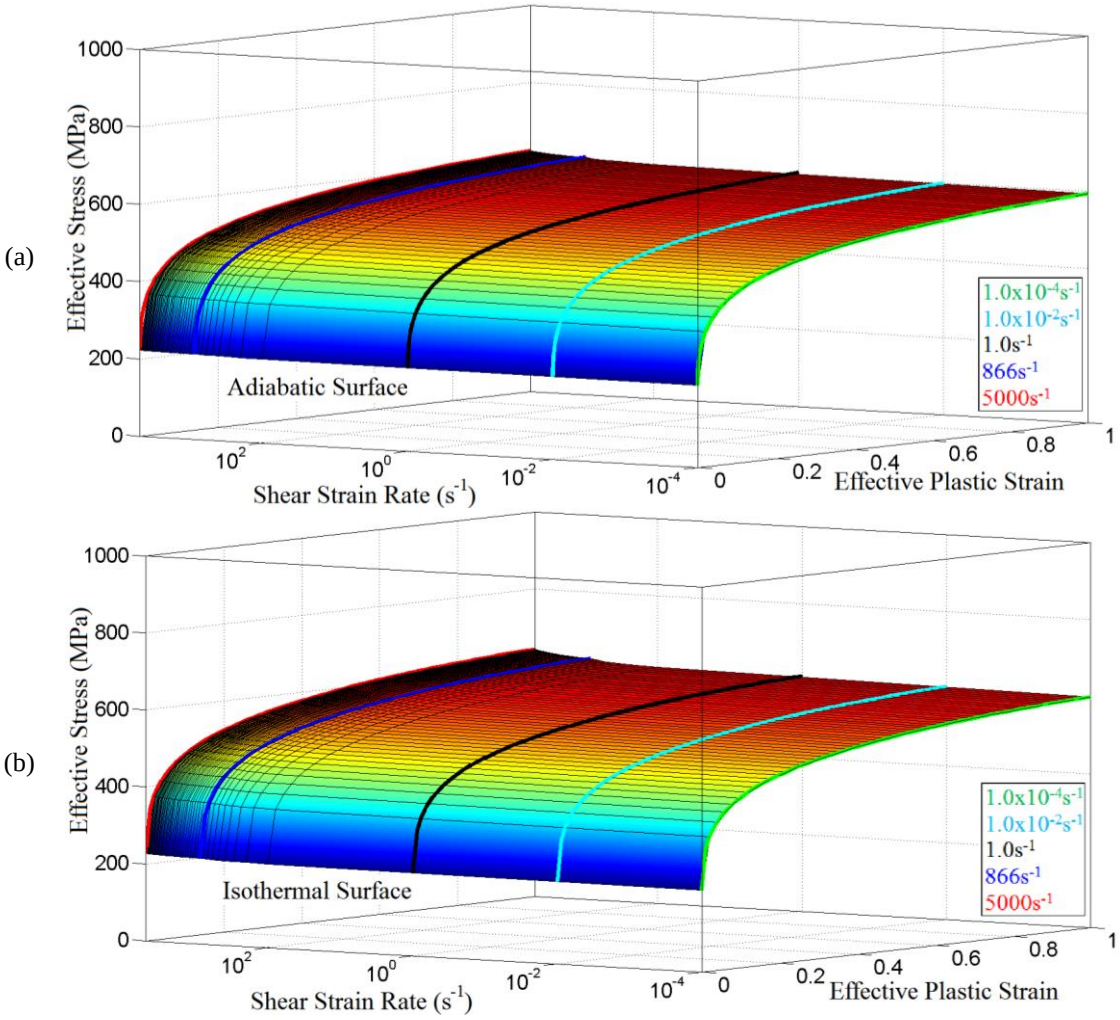

Figure 5-114: Strain-rate dependent flow surfaces that are characterized from torsion tests; (a) adiabatic and (b) isothermal.

Similarly, temperature dependent flow behavior is characterized by constructing both adiabatic and isothermal hardening curves. Figures 5-115 – 5-117 illustrate the temperature dependent flow surfaces for both adiabatic and isothermal conditions under uni-axial tension, compression and torsion, respectively. These flow surfaces are representing the tabulated input format of TRAUM and it should be noted that during the finite element simulations the state variables are found by linear interpolations. Temperature dependent behavior is only characterized by using the quasi-static test results. However, it is shown that even at low speed testing, the amount of heat generated and retained in the body due to the plastic work should be considered, especially within the vicinity of necking.

(a)

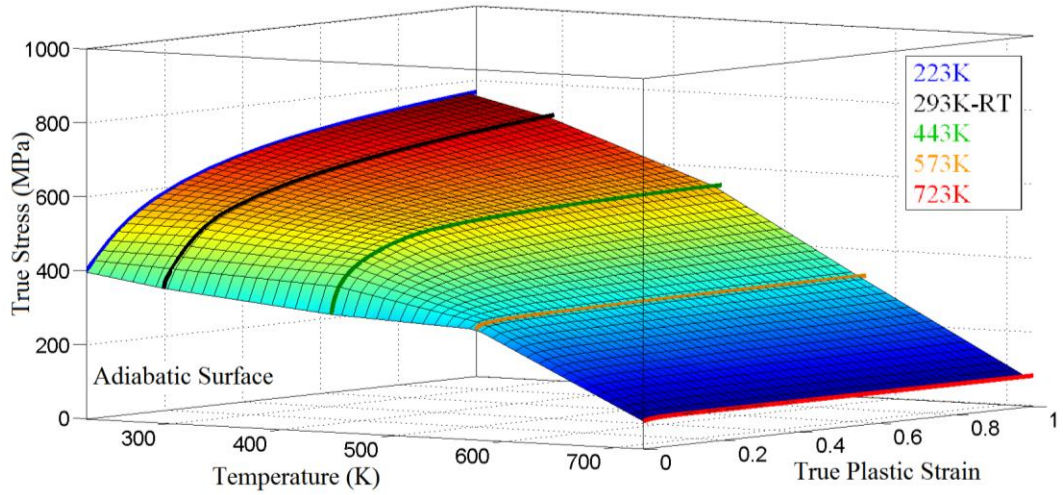

(b)

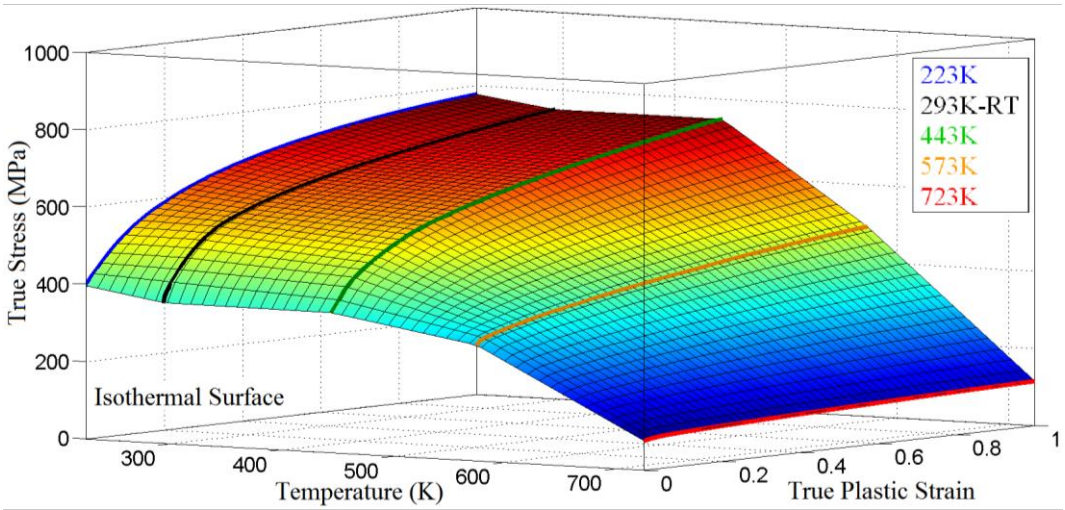

Figure 5-115: Temperature dependent flow surfaces that are characterized from uni-axial tension tests; (a) adiabatic and (b) isothermal.

During the high temperature testing, it is shown that a significant amount of increase in the failure strains or elongation is observable especially beyond that the recrystallization and dynamic recovery temperature. Consequently, the finite element model should be able to handle increasing failure strains. The required treatment is discussed in more detail in the proceeding sections when the temperature dependent failure strain scaling is implemented.

(a)

(b)

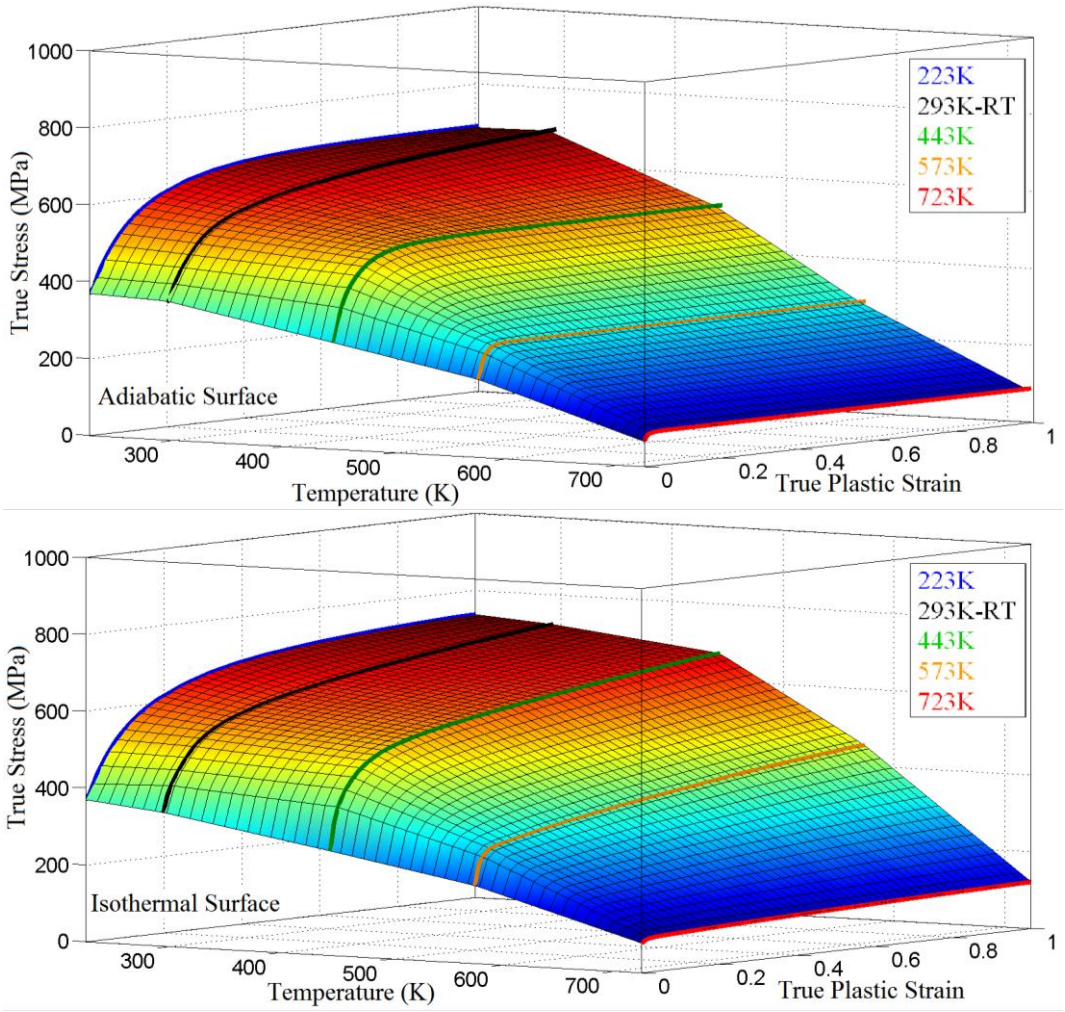

Figure 5-116: Temperature dependent flow surfaces that are characterized from uni-axial compression tests; (a) adiabatic and (b) isothermal.

(a)

(b)

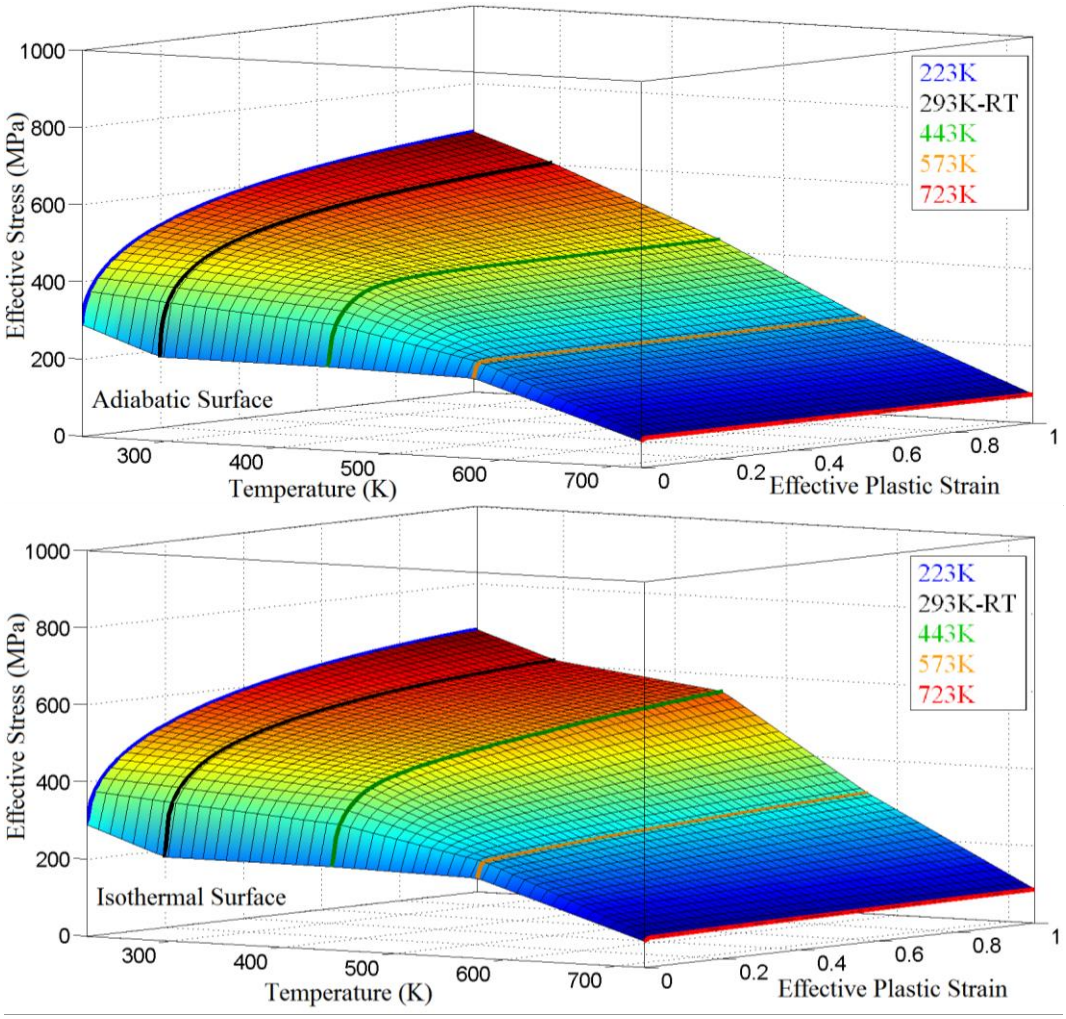

Figure 5-117: Temperature dependent flow surfaces that are characterized from torsion tests; (a) adiabatic and (b) isothermal.

5.9 **Determination of the regularization curve**

Flow surface of Al2024-T351 is characterized considering the temperature and strain-rate dependency in the previous sections. Based on the methodology that is described in Section 5.3 and illustrated by Figure5-3, a mesh regularization step is necessary before characterizing the ductile failure properties of the material. It was reported that, finite element simulations are sensitive to mesh size or the level of the discretization especially when failure and thermal softening is considered [195] [99] [180] [231] [374]. Mesh dependent nature of the numerical methods in predicting failure and softening

substantiates a regularization algorithm to be implemented for a stable and unique solution.

By using a similar 'trial-and-error' technique that is defined by Bao [99], a plastic strain value at failure is identified for each specimen. This methodology is a line search algorithm that finds the best corresponding effective plastic strain at failure by comparing the force vs. displacement curves with the test results. Figure 5-118 illustrates the results of the FE calculation with different values of the plastic strain trying to find the best value, which can predict the elongation at failure. The best value of the failure strain is selected for this particular state-of-stress as the 'failure point'. In this case, The 'failure point' is found for a plastic strain of $\varepsilon_p^f = 0.24$, where a comparison is made with Test #2.3 and the best correlation for the required amount of displacement is found.

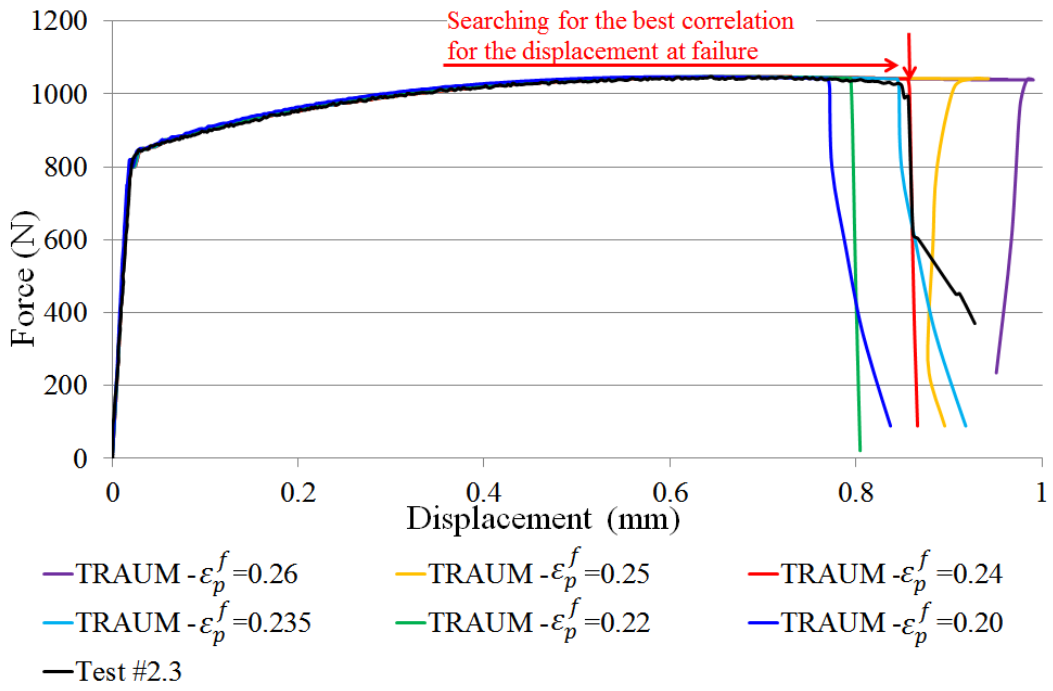

Figure 5-118: Iterative, 'trial and error' failure strain characterization.

The rest of the specimens, which are designed in Chapter 4, are characterized similarly and their corresponding 'failure points' are found to construct a failure locus based on their states-of-stress values that the specimens were loaded. However, the

failure strains are mesh dependent and there needs to be a regularization scheme implemented to adjust the characterized strains for different mesh sizes [375]. When the same failure strain is used with different mesh lengths, the amount of displacement to failure differs significantly as illustrated in Figure 5-119 for seven different characteristic element lengths, which are listed by Table 5-23 for their corresponding element dimensions. Therefore, regularization on the failure strains is necessary as a function of the characteristic element length.

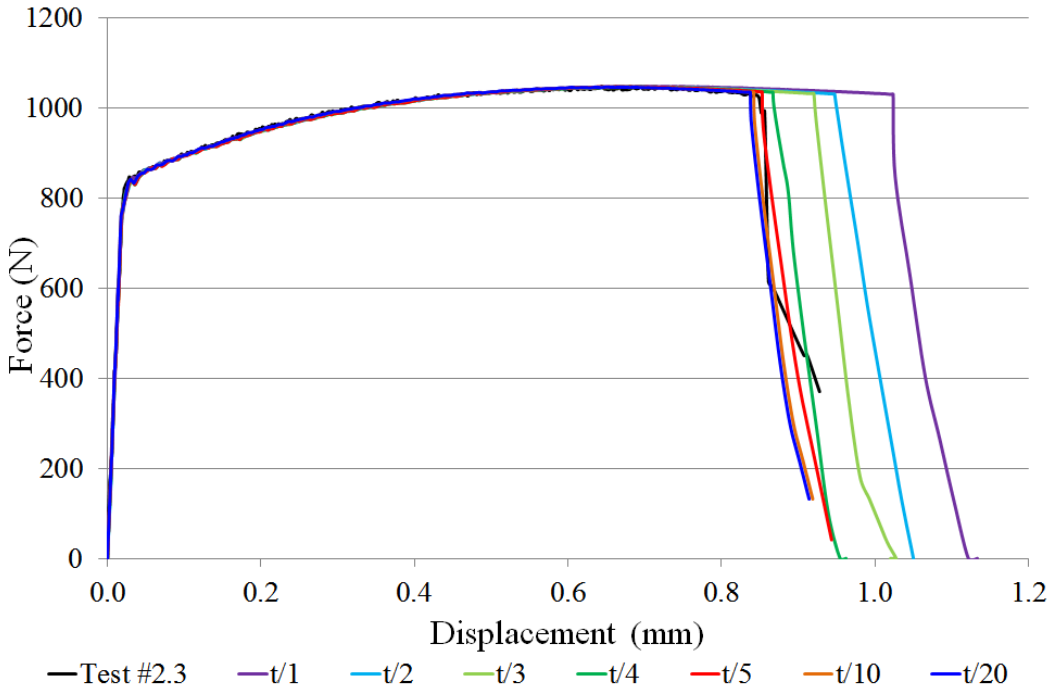

Figure 5-119: Force vs. displacement predictions for different characteristic element lengths before regularization for the same failure strain.

The specimen that was employed for the characterization of the regularization curve as described in Section 4.4.3.3 is illustrated in Figure B-1, which is the plane-stress specimen with a smooth gauge region (i.e., Specimen #1). It is also depicted in Section 4.4.3.3 is that the regularization methodology requires a baseline for the reference mesh size and scales the failure strains based on the initially selected critical element length. Considering the overall dimensions of the specimens in this research, a characteristic length of around 0.14mm - 0.15mm is chosen, which can be used to model the specimens

with reasonable accuracy and computational cost. Table 5-23 lists the alternative element lengths that are used to model the same specimen, where the baseline is chosen for [t/5] that can accommodate five elements through the thickness of the plane-stress specimen. Six other FE models are developed with different mesh sizes to characterize the failure strains. Figures E-1 – E-7 illustrates the corresponding FE models of Specimen #1 that are used to generate the regularization curve.

Table 5-23: Characteristic element lengths used for the regularization models.

	FE Models with Different Characteristic Element Lengths						
	[t/1] *	[t/2] *	[t/3] *	[t/4] *	[t/5] *	[t/10] *	[t/20] *
Length [mm]	0.762	0.381	0.254	0.1905	0.1504	0.0762	0.031
Model	Figure E-1	Figure E-2	Figure E-3	Figure E-4	Figure E-5	Figure E-6	Figure E-7

*t=0.762mm

The iterative method is used to analyze each case and the best failure strains are found at the end of the line search as illustrated in Figure 5-120.

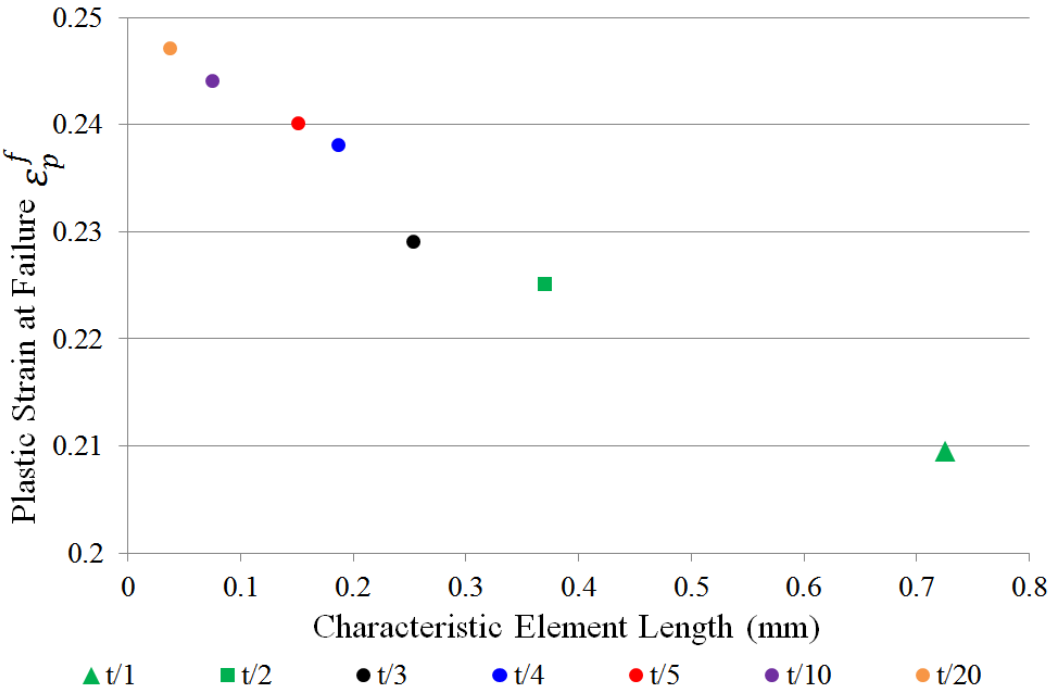

Figure 5-120: Plastic strains at failure for the corresponding characteristic element lengths.

However there is a need to outline the boundaries of the regularization since the numerical discretization can only present an accurate solution within the boundaries of numerical sensitivities. It should be noted that mesh should be fine enough to be able to capture the physical deformation during a localized necking, where it is accepted that the specimen often experiences a diffuse necking stage prior to the localization starts and no homogeneous deformation is expected. Consequently, an empirical approach to the determination of the regularization curve can be made considering Figure 5-121 as the simplified illustration of the specimen geometry and relations during a localized necking [376]. This analytical approach assumes that all displacements within the gauge section concentrate within the localized area after the numerical prediction of the localization as:

$$l^f_{physical} - l^n_{physical} = L^f - L^n \tag{5.90}$$

Initial State

L^0 : Undeformed gauge length

$l^0_{critical}$: Undeformed element characteristic length

$l^0_{physical}$: Undeformed physical size of the neck

State-of-Localization

L^n : Gauge length at localization

$l^n_{critical}$: Element characteristic length at localization

$l^n_{physical}$: Physical size of the neck at localization

ε^n_0 : Engineering strain at localization

State-of-Failure

L^f : Gauge length at failure

$l^f_{critical}$: Element characteristic length at failure

$l^f_{physical}$: Physical size of the neck at failure

ε^f_0 : Engineering strain at failure

ε^f : True strain at failure

ε^f_p : Predicted failure strain

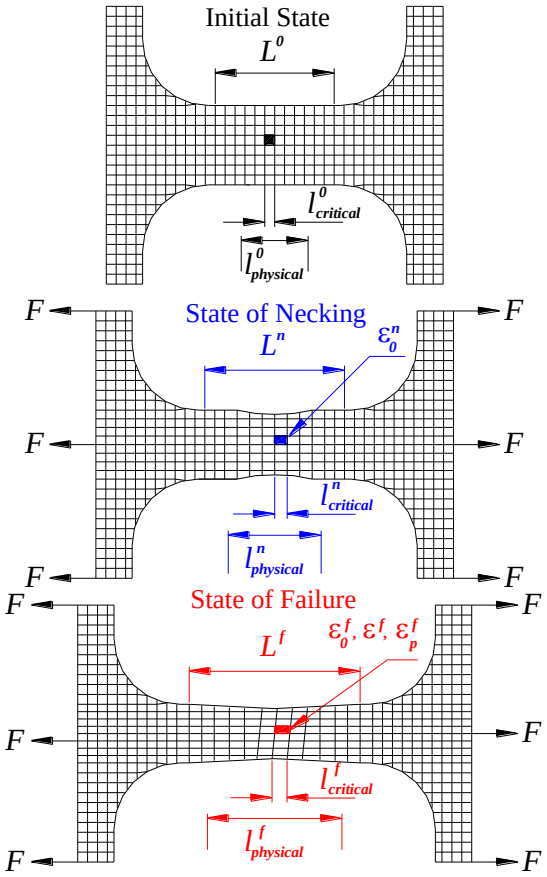

Figure 5-121: Geometrical representation of a neck and material properties for the empirical determination of the regularization boundaries.

It is also assumed and illustrated in Figure 5-121 that after necking, all additional displacement concentrates in the localized element row as:

$$l^f_{critical} - l^n_{critical} = L^f - L^n \tag{5.91}$$

Therefore, the true strain at failure can be found as:

$$\begin{aligned} \varepsilon^f &= \ln\left(\frac{l^f_{physical}}{l^0_{physical}}\right) = \ln\left(\frac{l^n_{physical}}{l^0_{physical}} + \frac{l^f_{physical} - l^n_{physical}}{l^0_{physical}}\right) \\ &= \ln\left(\varepsilon^n_0 + 1 + \frac{L^f - L^n}{L^0}\frac{L^0}{l^0_{physical}}\right) = \ln\left(\varepsilon^n_0 + 1 + \left(\varepsilon^f_0 - \varepsilon^n_0\right)\frac{L^0}{l^0_{physical}}\right) \end{aligned} \tag{5.92}$$

Solving the equation for the engineering strain at failure as:

$$\varepsilon^f_0 = \frac{l^0_{physical}}{L^0}\left(e^{\varepsilon^f} - \varepsilon^n_0 - 1 + \varepsilon^n_0\frac{L^0}{l^0_{physical}}\right) \tag{5.93}$$

Engineering strain at failure depends upon the gauge length, which will converge to the engineering strain at necking if the initial length is infinitely long as:

$$\text{if } L^0 \to \infty \Rightarrow \varepsilon^f_0 = \varepsilon^n_0 \tag{5.94}$$

Consequently, the predicted failure strain in the numerical model can be calculated as:

$$\begin{aligned} \varepsilon^f_p &= ln\left(\frac{l^f_{critical}}{l^0_{critical}}\right) = \ln\left(\frac{l^n_{critical}}{l^0_{critical}} + \frac{l^f_{critical} - l^n_{critical}}{l^0_{critical}}\right) \\ &= \ln\left(\varepsilon^n_0 + 1 + \frac{L^f - L^n}{L^0}\frac{L^0}{l^0_{critical}}\right) = \ln\left(\varepsilon^n_0 + 1 + \left(\varepsilon^f_0 - \varepsilon^n_0\right)\frac{L^0}{l^0_{critical}}\right) \\ &= \ln\left(\varepsilon^n_0 + 1 + \left(\frac{l^0_{physical}}{L^0}\left(e^{\varepsilon^f} - \varepsilon^n_0 - 1 + \varepsilon^n_0\frac{L^0}{l^0_{physical}}\right) - \varepsilon^n_0\right)\frac{L^0}{l^0_{critical}}\right) \end{aligned} \tag{5.95}$$

A field of bifurcation can then be written for the regularization curve describing a set of possible solutions for the strains at failure as a function of the characteristic length as:

$$\varepsilon_p^f = \ln\left(\varepsilon_0^n + 1 + \frac{l^0_{physical}}{l^0_{critical}}\left(e^{\varepsilon^f} - \varepsilon_0^n - 1\right)\right) \tag{5.96}$$

In that case, the strain at failure can be written independent of the gauge length, which can be verified for the critical and physical element lengths that will become material properties as:

$$\text{if } l^0_{critical} \to l^0_{physical} \Rightarrow \varepsilon_p^f = ln\left(e^{\varepsilon^f}\right) = \varepsilon^f \tag{5.97}$$

The boundaries of the solution are determined by the bifurcation and the limit solution, where the maximum element size and the corresponding failure strain can be found for the coarse meshes as:

$$\text{if } l^0_{critical} \gg l^0_{physical} \Rightarrow \varepsilon_p^f = ln(\varepsilon_0^n - 1) \tag{5.98}$$

Therefore, the maximum element size should be kept within the verified limits of the regularization study and should not be extrapolated for bigger elements as the material characteristic length becomes the necking strain. The same applies to the smaller element lengths as the regularization curve scales the failure strain asymptotically, the element size should not be extrapolated beyond the verified limits. Figure 5-122 illustrates the bifurcation region that is generated over the set of points, which are characterized for seven different characteristic element lengths and illustrated in Figure 5-120. It is shown that by considering all element lengths (i.e., all regularization points from Figure 5-120), the limits of the solution (i.e., in blue color) that is suggested by Equation (5.96) indicate significant differences for the prediction of the failure strain for smaller element lengths, where localized necking is expected to be predicted. On the other hand, by ignoring the points, which are prospected to miss the prediction of localized necking, the solution of

Equation (5.96) outlines the feasible limits of the regularization region.

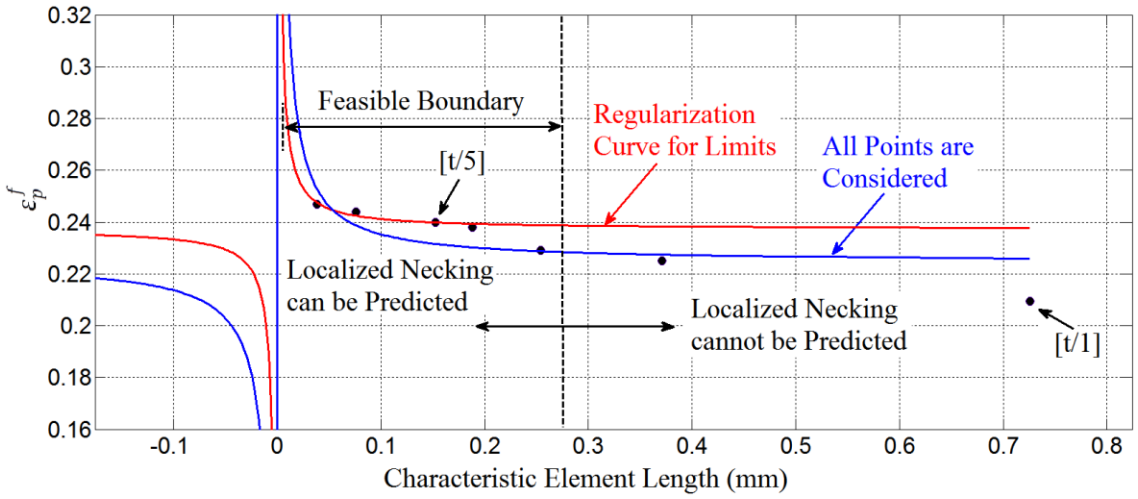

Figure 5-122: Regularization curve for six different characteristic element lengths.

Consequently, the red line that is illustrated in Figure 5-122 is accepted as the basis of the regularization curve, where a normalization procedure is performed according to the methodology that is described in Section 4.4.3.3. TRAUM utilizes the regularization curve as a scaling curve as a function of the characteristic element lengths, where the baseline is chosen as the mesh size that is used for the characterization of the failure strains. Therefore, the regularization curve $i(l_{cr})$ for TRAUM can be generated by assuming the failure strain for [t/5] model as the baseline and normalizing the rest of the failure strains as illustrated in Figure 5-123. As a result, the same amount of displacement can be achieved with different element sizes if the regularization curve that is illustrated in Figure 5-123 is utilized for failure prediction of Test #2.3 conditions.

The force vs. displacement responses of different models are illustrated in Figure 5-124 after the regularization is activated. It is clear that the algorithm scales the failure strain for each element according to the regularization curve that is shown in Figure 5-123. The differences in the displacement predictions for the models with bigger elements are expected since they are beyond the limits of the localized neck region and cannot handle such localizations successfully. Considering that the failure is gradual and with the instability that needs to be predicted and solved, it is still noticeable to achieve a

regularized displacement at this level. With the regularized failure, TRAUM is able to predict localized necking and the force vs. displacement field at the same time for smaller element sizes that are within the boundary of the feasible solution that is described and illustrated in Figure 5-122. It can be seen from Figure 5-129 and Figures G-1 - G-3 that at least three elements through the thickness are needed to predict localized necking.

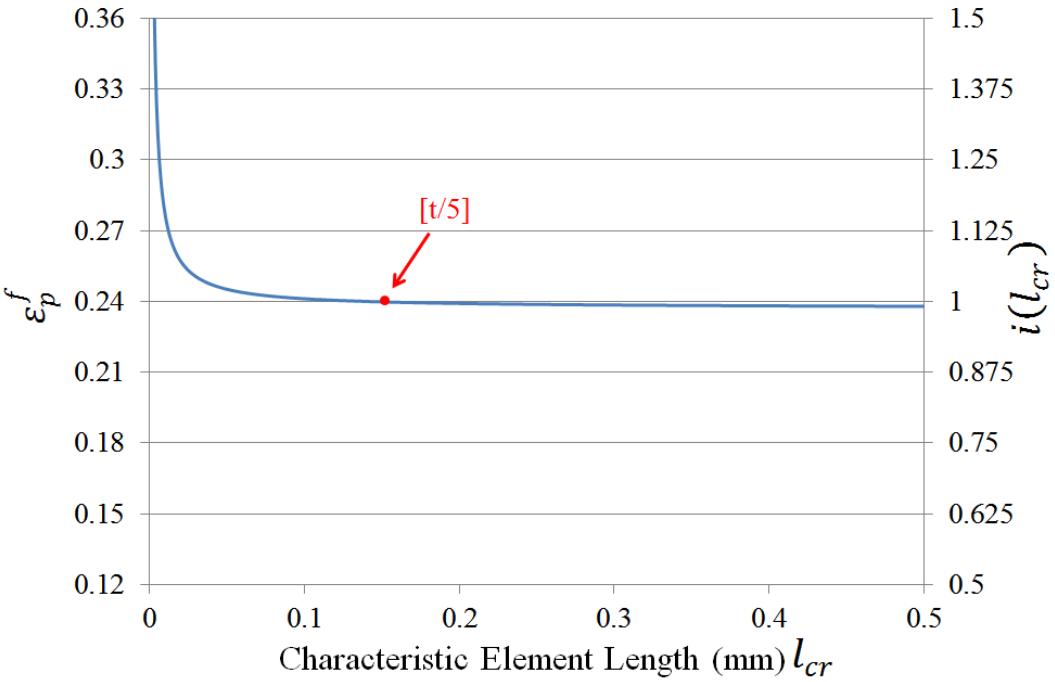

Figure 5-123: Regularization curve for TRAUM.

5.9.1 **Localized tensile instability**

Localized tensile necking instability has received a good deal of attention because the characteristic behavior of diffuse and localized necking have significant effects on local deformation and failure. Hill [94] formulated localized necking as a special case in thin anisotropic strips in tension, as shown in Figure 5-125, by stress characteristics depending on zero extension in the necking zone. Therefore, the slopes for $\frac{dy}{dx}$ of the characteristics should satisfy the known anisotropic relations as:

$$d\varepsilon_s = d\varepsilon_x dx^2 + 2d\gamma_{xy} dxdy + d\varepsilon_y dy^2$$

or

$$\left[(G+H)\sigma_x - H\sigma_y\right]dx^2 + 2N\tau_{xy}dxdy + \left[(F+H)\sigma_y - H\sigma_x\right]dy^2 = 0 \tag{5.99}$$

$$\text{Let } \frac{dy}{dx} = \tan(\theta+\alpha)$$

$$\Rightarrow a\tan^2\theta + 2b\tan\theta - c = 0$$

where,

$$\sigma = \frac{1}{\sqrt{F\sin^2\alpha + G\cos^2\alpha + H + (2N - F - G - 4H)\sin^2\alpha\cos^2\alpha}}$$

$$\Rightarrow \mathrm{a} = \mathrm{H} + (2N - F - G - 4H)\sin^2\alpha\cos^2\alpha$$

$$\Rightarrow \mathrm{b} = [(N - F - 2H)\sin^2\alpha - (N - G - 2H)\cos^2\alpha]\sin\alpha\cos\alpha \tag{5.100}$$

$$\Rightarrow \mathrm{c} = \mathrm{a} + F\sin^2\alpha + G\cos^2\alpha = 1/\sigma^2$$

Considering an isotropic material, Hill's analyses reduce as:

$$F = G = H = \frac{N}{3}$$

$$b = 0$$

$$c = 2a \tag{5.101}$$

$$\Rightarrow \tan\theta = \sqrt{2} \Rightarrow \theta = \pm 54.7^{\circ}$$

where, two equally possible necking directions are identified with a distinct angle of crack formation [94].

From the discontinuities of relative velocity **v**, Hill also considered a necking that makes an angle ψ with the velocity vector that has a magnitude v as illustrated in Figure 5-126 [377]. Treating the strain-rate in the neck as if it were uniform and based on the assumption of the general plane-stress theory, it is accepted that the velocity vector is perpendicular to the direction of the extension along the neck.

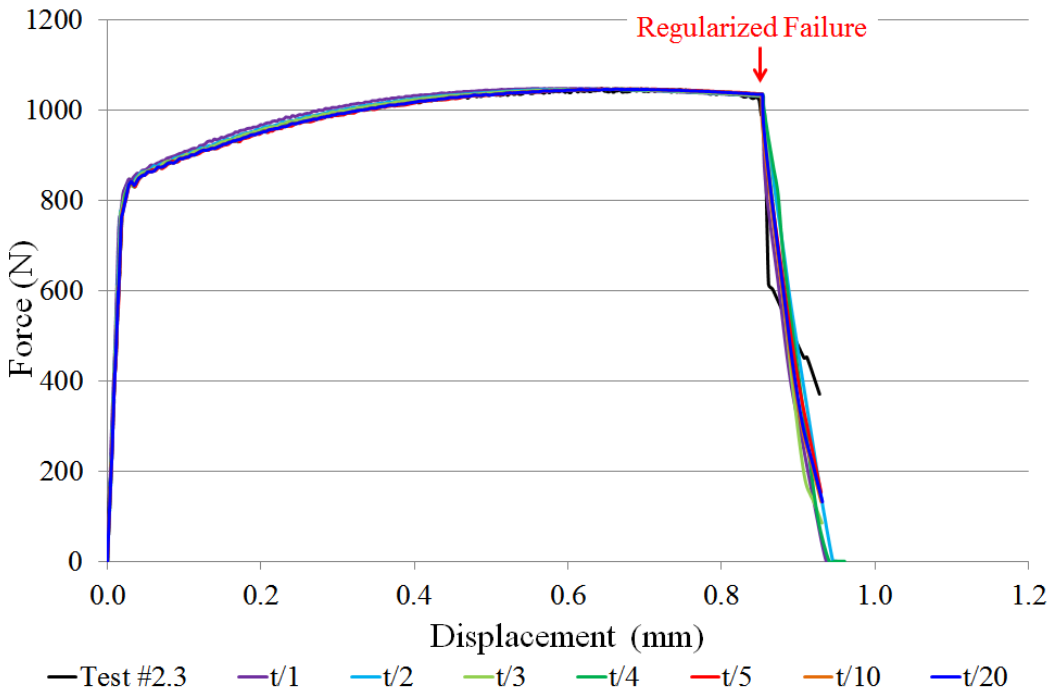

Figure 5-124: Force vs. displacement predictions for different mesh sizes after regularization.

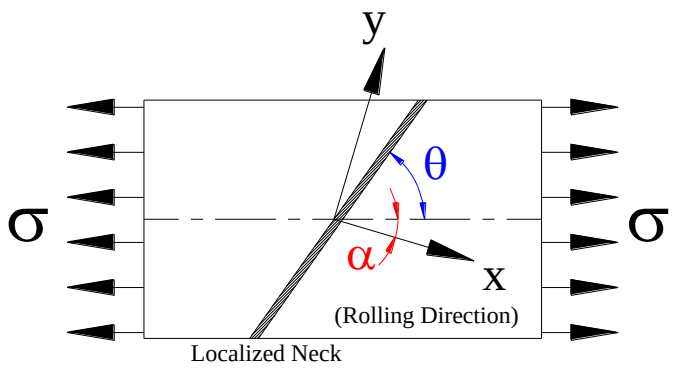

Figure 5-125: Analysis of an oblique necking of an anisotropic strip in tension, adapted after [94].

When $\psi = 0$, there is no necking but only a relative sliding [377]. The strain-rate tensor in the neck has principal components in the form of:

$$\dot{\boldsymbol{\varepsilon}} = \frac{v}{2b}\begin{bmatrix} 1+sin\psi & & \\ & -1+sin\psi & \\ & & -2sin\psi \end{bmatrix} \tag{5.102}$$

The plastic work rate for unit length of the neck is written as:

$$bh\dot{W} = bh(\sigma_1\dot{\varepsilon}_1 + \sigma_2\dot{\varepsilon}_2) = \frac{1}{2}hv\big((\sigma_1 - \sigma_2) + (\sigma_1 + \sigma_2)sin\psi\big) \tag{5.103}$$

If f denotes the yield function, the plastic potential can be written as:

$$\frac{\partial f}{\partial \sigma_1}\Big/\frac{\partial f}{\partial \sigma_2} = \dot{\varepsilon}_1/\dot{\varepsilon}_2 \tag{5.104}$$

where, $f(\sigma_1, \sigma_2)$ is constant and depends upon the degree of hardening.

Hence, the angle of the velocity vector with respect to the neck orientation can be found from:

$$sin\psi = \frac{\dot{\varepsilon}_1 + \dot{\varepsilon}_2}{\dot{\varepsilon}_1 - \dot{\varepsilon}_2} = \left(\frac{\partial f}{\partial \sigma_1} + \frac{\partial f}{\partial \sigma_2}\right)\Big/\left(\frac{\partial f}{\partial \sigma_1} - \frac{\partial f}{\partial \sigma_2}\right) \tag{5.104}$$

where, for real ψ, $-\frac{\partial f}{\partial \sigma_1} \leq \frac{\partial f}{\partial \sigma_2} \leq 0$. For the particular case of uni-axial tension of the plane-stress specimens $\dot{\varepsilon}_1/\dot{\varepsilon}_2 = -2$; the corresponding angle is $\psi = sin^{-1}\frac{1}{3} = 19^o28'$; the neck orientation to the direction of traction is $\frac{1}{4}\pi + \frac{1}{2}\psi = 54^o44'$and the orientation of the velocity vector is $\frac{1}{4}\pi - \frac{1}{2}\psi = 35^o16'$ [377].

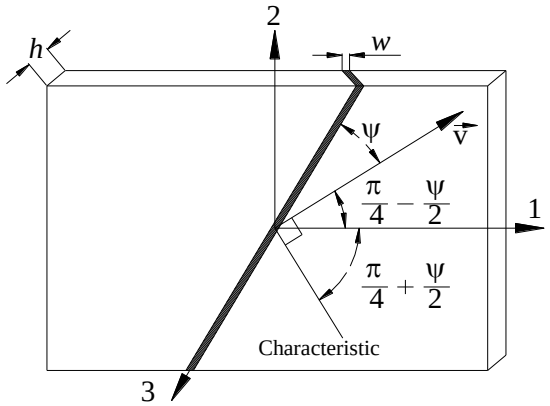

Figure 5-126: Discontinuities of relative velocity, adapted after [377].

Lemaitre [145] used Maxwell's compatibility equation to solve the uni-axial tension case illustrated in Figure 5-127 considering the discontinuities of the strain-rates in the necking area with the field given by:

$$[\sigma] = \begin{bmatrix} \sigma & 0 & 0 \\ 0 & 0 & 0 \\ 0 & 0 & 0 \end{bmatrix}, [\varepsilon] = \begin{bmatrix} \varepsilon & 0 & 0 \\ 0 & -\nu^* \varepsilon & 0 \\ 0 & 0 & -\nu^* \varepsilon \end{bmatrix} \tag{5.105}$$

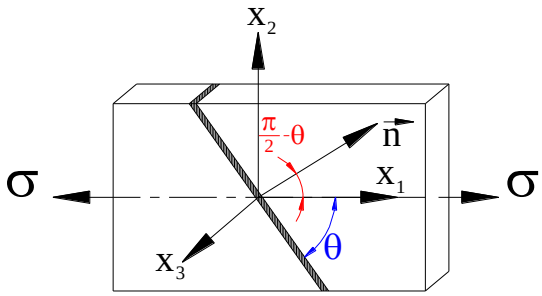

Figure 5-127: Crack initiation in tension, after [145].

Assuming that the shear strain is ε_{12} and discontinuity of its rate form diminishes, from the compatibility equation:

$$[\dot{\varepsilon_{12}}] = \frac{1}{2}(g_1 n_2 + g_1 n_2) = 0 \tag{5.106}$$

where, the components of the unit vectors are defined on plane x_1, x_2 with respect to x_1 axis as:

$$\vec{n}: \begin{bmatrix} sin\theta \\ cos\theta \\ 0 \end{bmatrix}, \vec{g}: \begin{bmatrix} \gamma sin\chi \\ \gamma cos\chi \\ 0 \end{bmatrix}, sin(\chi + \theta) = 0 \Rightarrow \chi + \theta = k\pi, k = 0, \pm 1, \pm 2, \ldots,$$
$$\Rightarrow \vec{g}: \begin{bmatrix} -\gamma sin\theta \\ +\gamma cos\theta \\ 0 \end{bmatrix}. (-1)^k \tag{5.107}$$

Writing the discontinuities of the normal strain rates:

$$\begin{aligned}[\![\dot{\varepsilon_{11}}]\!] &= g_1 n_1 = -\gamma \sin^2\theta . (-1)^k \\ [\![\dot{\varepsilon_{22}}]\!] &= g_2 n_2 = +\gamma \sin^2\theta . (-1)^k \end{aligned} \tag{5.108}$$

From the strain field showing that failure orientation will not depend on the constitutive equation but only on Poisson's ratio [145]:

$$\begin{aligned} &\varepsilon_{22} = -\nu^* \varepsilon_{11} \Rightarrow [\![\dot{\varepsilon_{22}}]\!] = -\nu^* [\![\dot{\varepsilon_{11}}]\!] \\ &\Rightarrow \cos^2\theta = \nu^* \sin^2\theta [\![\dot{\varepsilon_{22}}]\!] \Rightarrow \tan\theta = \pm\sqrt{\frac{1}{\nu^*}} \end{aligned} \tag{5.109}$$

Consequently, a similar result can be obtained through a different approach for tensile instability assuming the rest of the specimen outside the necking region can be assumed to behave rigidly:

$$\begin{aligned} \theta &= \tan^{-1}\sqrt{\frac{1}{\nu^*}} \\ \nu^* = 0.5 &\Longrightarrow \theta = \pm 54.7^{\mathrm{o}} \end{aligned} \tag{5.110}$$

where, θ is the classical angle of the Lüders bands, which may be observed from the experiments easily [145]. However, PLC effect and Lüders bands that are forming as the necking instability takes place after yield should not be confused. Although they co-exist and may cause the same form of strain localization, they have phenomenological differences. Rizzia and Hahner [257] discuss their distinct features. The PLC effect is more pronounced in axi-symmetric specimen characterization in the proceeding sections.

More discussion about the tensile instabilities and bifurcation can be found by Marciniak [378] and more recently by Bao [99], Lee [231] and Li [379].

Localized necking is clearly observed during the testing of smooth flat specimens. Figure 5-128(a) shows the specimen on the testing apparatus and 5-128(b) shows the

pristine and deformed specimens with the necking profile and failure surface, which is a specific angle, calculated and shown to be characteristic for this state.

When localization occurs, the structure loses stability and a localized neck forms at high speed. The band formations and the profile of the cross-section in the gauge area can be seen in Figures 5-129 - 5-131. These figures illustrate the evolution of deformation in the necking area during simulations by using TRAUM with the characterized flow surface and the failure strain.

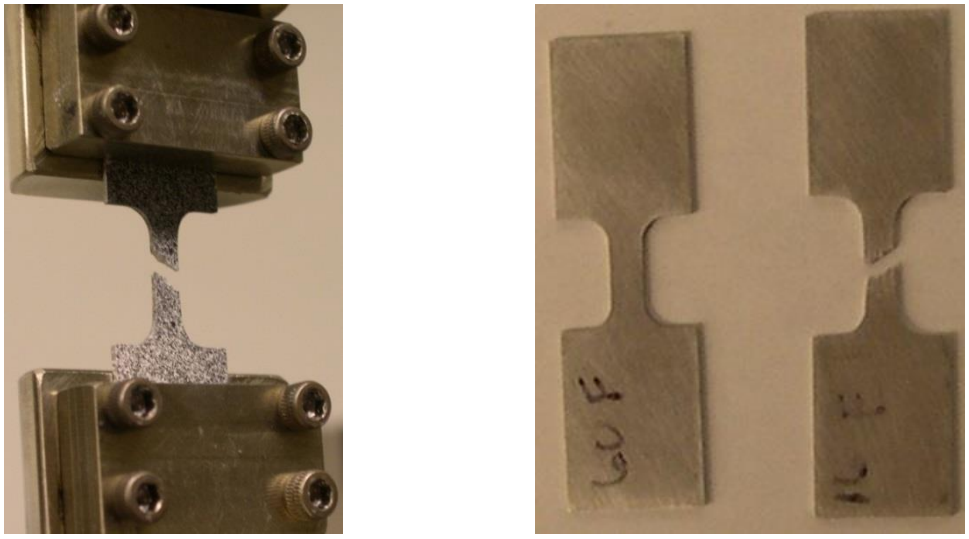

(a) (b)

Figure 5-128: Uni-axial tension experiment on SHLF apparatus with Specimen #1; (a) pristine specimen and (b) post-test specimen with localized necking, after [108].

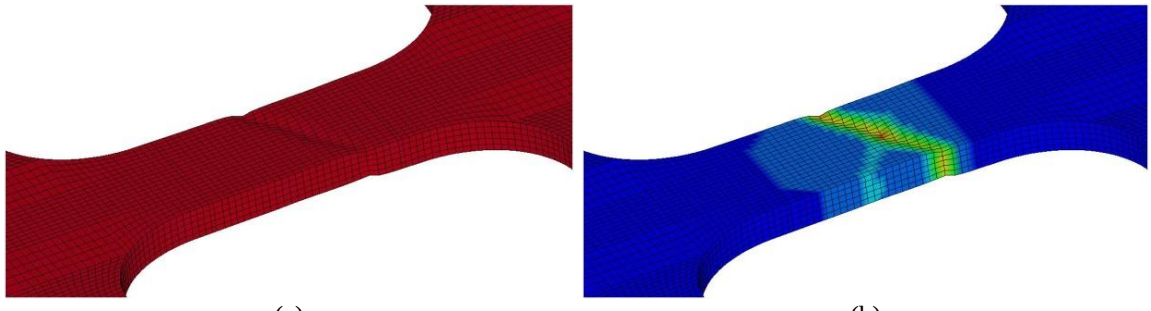

(a) (b)

Figure 5-129: Formation of the localized necking instability; (a) FE deformation and (b) localization of the effective plastic strain at necking.

Figure 5-130 illustrates the plastic strain localization at the neck region by the distinctive crack orientation that is analytically predicted. Figure 5-131 elaborates the fact that the orientation of the crack angle is random. However, the formation of a localized neck is strictly mesh dependent and Figure 5-131 illustrates the localized neck formation by utilizing [t/5] and [t/10] models for the plane-stress specimen, where five and ten elements through the thickness of the specimen gauge region is used, respectively.

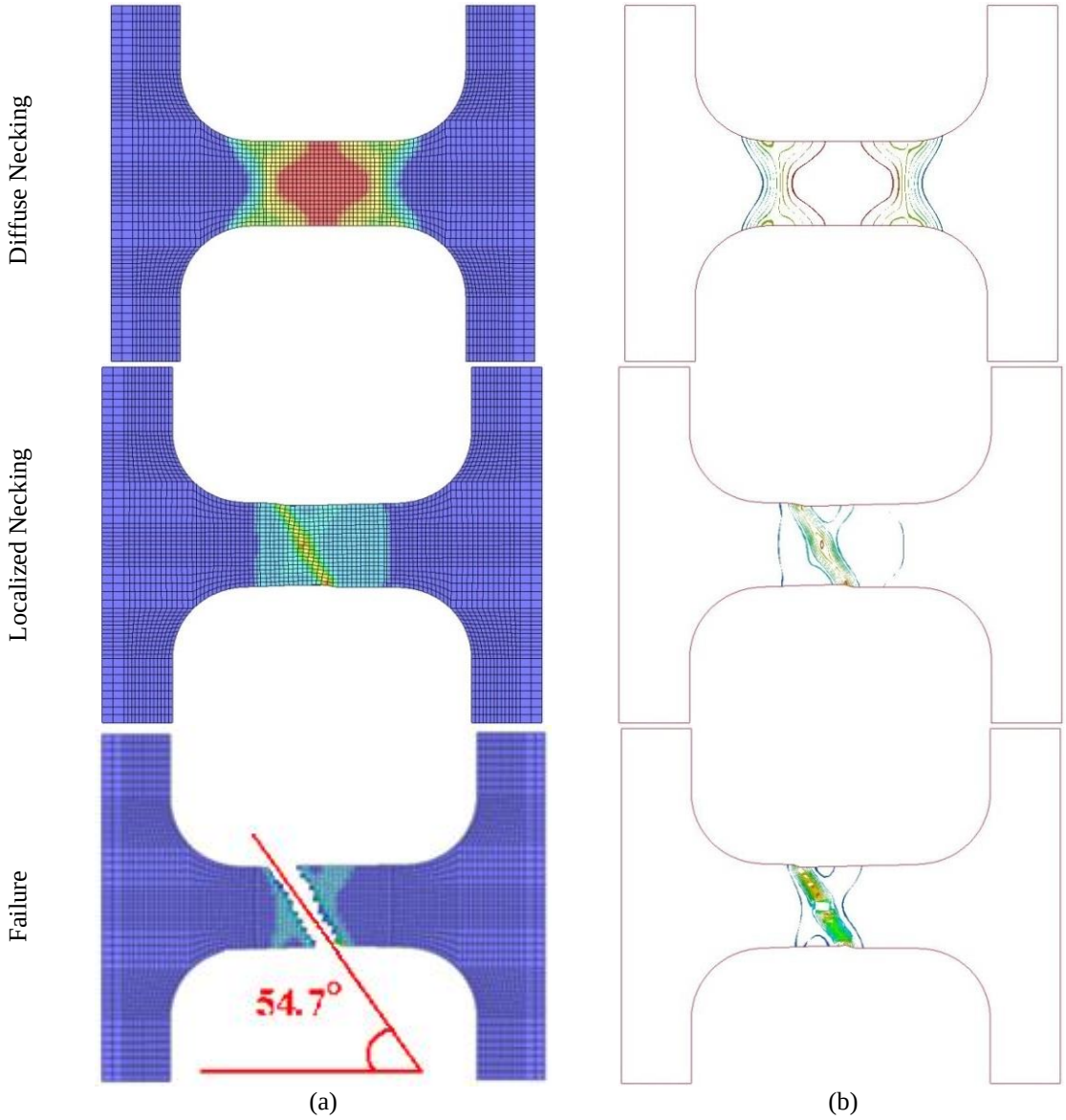

Figure 5-130: Evolution of deformation and failure; (a) fringe plot of plastic strains and (b) iso-surface plot of plastic strains.

Predictions with other mesh patterns can be found in Appendix-G, from Figures G-1 – G-3, where the figures also reflect the plastic strain fields. Figure G-2 infers that localization within the neck cannot be predicted with elements above a certain size. The regularization algorithm can still satisfy the total elongation at failure, as shown in Figure 5-121. However, the failure mode cannot be found accurately if localized necks are of interest.

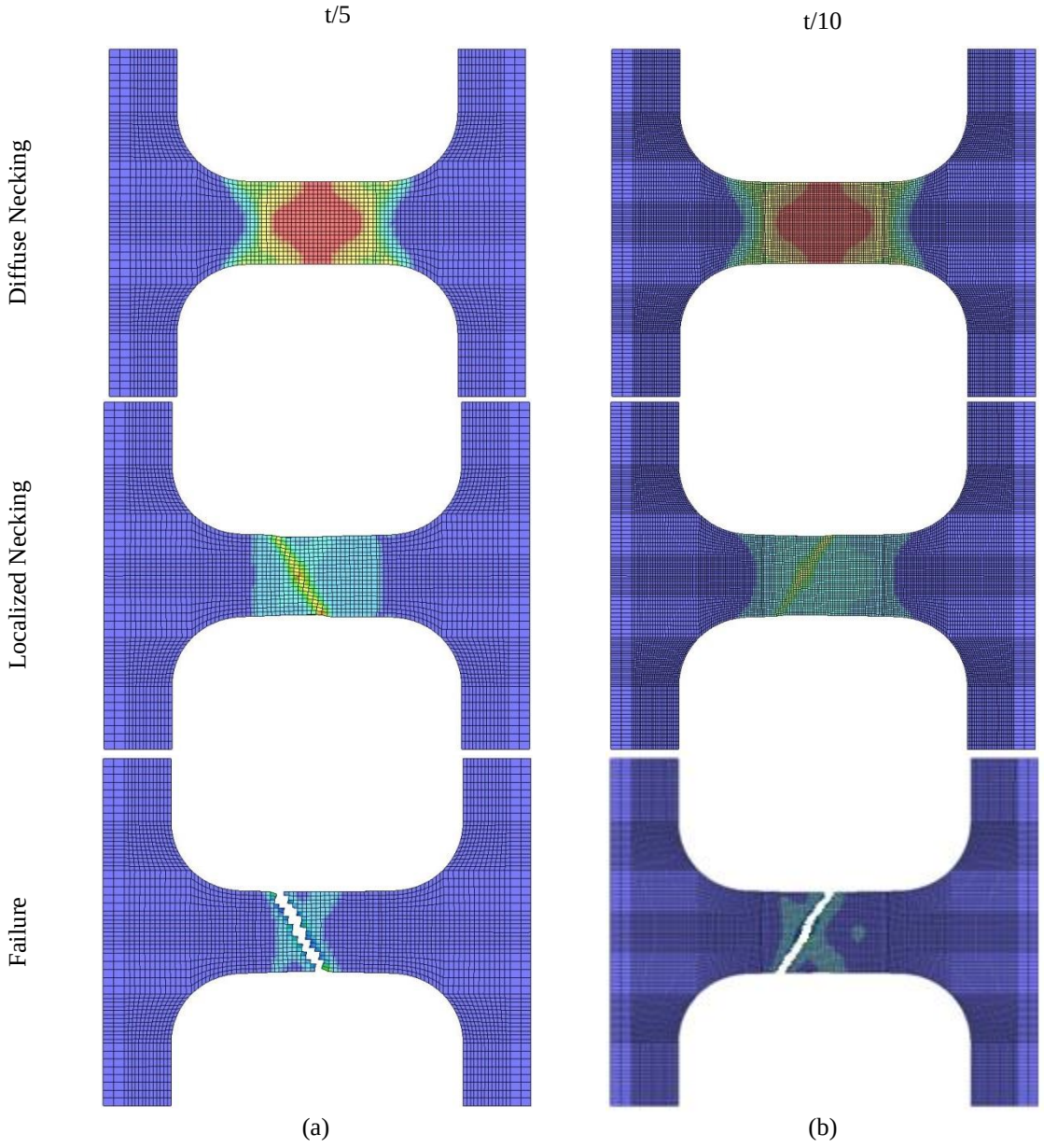

Figure 5-131: Randomness of the localized neck depending on the characteristic element length; (a) for [t/5] model and (b) for [t/10] model.

It should also be noted that the last two FE models in the regularization set (i.e., [t/1] and [t/2]), where the localized necking could not be predicted accurately, also imply that minimum three elements through the thickness are needed to predict localized necking for the plane-stress specimen.

5.10 **Characterization of the failure locus**

Having a flow surface characterized and regularized in the previous sections, characterization of the failure locus is attained through the set of specimens designed with different geometries that have different stress-states during the failure initiation and accumulation. These specimens are categorized according to their targeted stress-states as described in detail in Chapter 4. However, it should be noted that the initially utilized flow behavior is different than the newly characterized flow surfaces. Consequently, initially targeted stress-states should be reassessed by using the new flow surfaces and the corresponding states-of-stress for each specimen design should be confirmed. Determination of the failure strains is achieved in a similar fashion to the methodology that is described in the previous section for the smooth plane-stress specimen. Displacements at failure are iteratively matched by changing the effective plastic strains at failure until a good agreement is found. The stress-states in terms of stress-triaxiality, Lode-angle-parameter and product-triaxiality for each specimen are calculated by averaging over the failure strain as [99]:

$$\frac{1}{\varepsilon_p^f}\int_0^{\varepsilon_p^f}(\text{state}-\text{of}-\text{stress})d\varepsilon_p \tag{5.111}$$

The key point is that the experimental study has to be repeated at least three times per loading condition for each specimen geometry to ensure experimental repeatability [108]. Therefore, unless otherwise stated, all specimens are characterized to all three repeated test results. The arithmetic mean of the calculated stress-states is then used to construct the failure locus. While characterizing the failure strains, FE models that are illustrated in Appendix–B are utilized with a characteristic length of around 0.1524mm (i.e., [t/5]).

Since it has already been shown that failure strains are mesh dependent, the characterization and validation for all failure strains are regularized using the regularization curve that is shown in Figure 5-120. To construct the failure surface that is used as a baseline for scaling, failure strains are characterized as a function of state-of-stress for quasi-static conditions at strain-rates of $1.0s^{-1}$ and $1.0x10^{-2}s^{-1}$. The Servo Hydraulic Load Frame (SHLF) that is shown in Figure 5-6 was utilized for the experiments [108]. Subsequently, strain-rate and temperature dependent scaling curves are characterized to scale the failure surface that is constructed as the baseline.

5.10.1 **Plane-stress tension specimens**

Four different plane-stress specimen geometries were developed to characterize the failure strains for the corresponding stress-states. These specimens are shown in Figure 5-132 and the design details are provided in Chapter 4. All specimens were tested in quasi-static conditions at room temperature. DIC was utilized to measure the displacement field and SHLF was used for testing [108]. Details of the testing are listed in Table 5-24.

DIC technique provides the opportunity to determine the gauge length for each specimen virtually with the added convenience of being able to select any two points on the specimen that can correspond to the FE model mesh. The gauge points for the corresponding specimens are illustrated in Figure 5-133. The gauge length for Specimen #1 is selected within the smooth section of the specimen to provide information for the homogeneous deformation and flow. The rest of the gauge lengths are selected outside the notch geometries due to the fact that the localization occurs immediately within the notch. It should be noted that all plane-stress specimen tests are performed at a strain-rate of $1.0s^{-1}$ and the only exception is the Test #2.3, which is primarily used as the baseline for the characterization of the flow surface. Therefore, the plastic strain at failure is first verified for the reference test at $1.0x10^{-2}s^{-1}$ and the rest of the failure strains are consistently characterized for the targeted strain-rates as listed by Table 5-24.

The test conditions that are described by Table 5-24 are simulated by using the FE models that are illustrated in Appendix–B with Figures B-1 - B-4. Each model is developed by using five elements through the thickness to keep the characteristic element size similar to the [t/5] model.

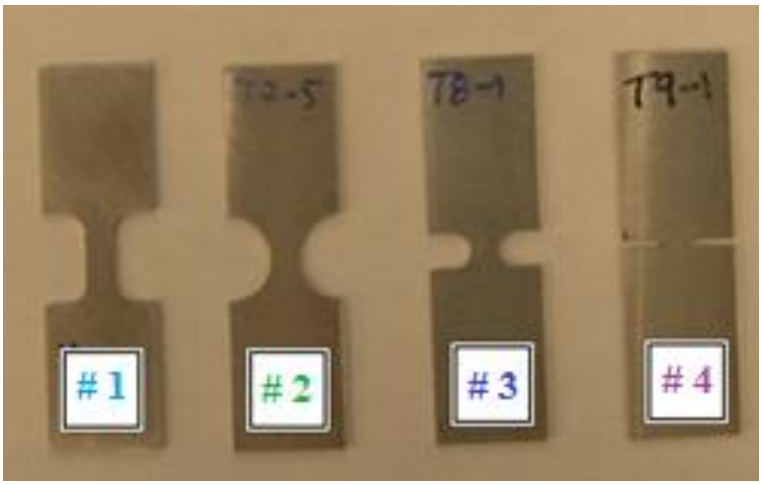

Figure 5-132: Plane-stress tension specimens, after [108].

Table 5-24: Test cases for characterization of the quasi-static failure strains at room temperature for plane-stress tension specimens.

Test #	Specimen #	DIC Gauge Length [mm]	Test Apparatus	State-of-Stress and Loading	Initially Targeted				
					Stress-State Values			Strain Rate	Temp.
					σ^*	σ_p^*	θ_L	[s^{-1}]	[K]
2.3 [Figure C-2]† [Table C-31]‡	1 [Figure B-1]§	4.0	SHLF*	Plane-Stress in Tension	$-\frac{1}{3}$	0.0	1.0	1.0×10^{-2}	RT††
3.1 [Figure C-3]† [Table C-31]‡								1.0	
3.2 [Figure C-3]† [Table C-31]‡									
33 [Figure C-31]† [Table C-32]‡	2 [Figure B-2]§	11.3			-0.41	0.0	0.9145		
34 [Figure C-32]† [Table C-33]‡	3 [Figure B-3]§	6.6			-0.49	0.0	0.617		
35 [Figure C-33]† [Table C-34]‡	4 [Figure B-4]§	3.8			$-\frac{1}{\sqrt{3}}$	0.0	0.0		

* Servo-Hydraulic Loading Frame (SHLF).
† Test results for the corresponding specimen, strain-rate and temperature illustrated in Appendix–C.
†† Room temperature.
‡ Test results for the corresponding specimen, strain-rate and temperature listed in Appendix–C.
§ Detailed geometries and corresponding FE models of the specimens are illustrated in Appendix–B.

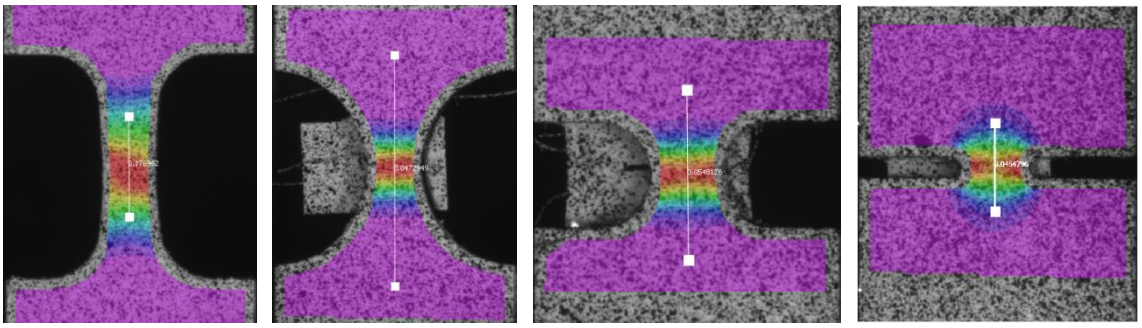

Specimen #1 Specimen #2 Specimen #3 Specimen #4

Figure 5-133: Positions of the DIC gauge lengths for plane-stress tension specimens.

It should be noted that, even though the failure strains are regularized, the methodology that is described in Section 4.4.3.3 suggests constructing a failure surface for a baseline characteristic element size and then scaling it according to the regularization curve that is illustrated by Figure 5-123.

Plastic strain at failure is iteratively found by comparing force vs. displacement curves. Figure 5-134 summarizes the evolution of the state variables (i.e., ε_p^f, σ^*, σ_p^* and θ_L) for the displacement field that is measured for Specimen #1. The figure illustrates only one set of characterized stress-states for brevity. Repetitive analyses are performed for the conditions that are listed in Table 5-24. The same characterization procedure is applied for all three tests that are also illustrated in Figure 5-134 to find the limits and an averaged value for the state variables. Similar procedures are applied to other plane-stress specimens and the results are illustrated in Appendix-H by Figures H-1 - H-3, respectively.

It is found that for the smooth gauge section, the state-of-stress remains homogeneous until necking. Figure 5-135 depicts the force vs. displacement results for each specimen. It is observed that for the same initial cross-section, just because of the differences in the state-of-stress; as the notch geometry sharpens the required force increases while the displacement to failure drops significantly. The differences in the elastic parts of the responses are due to the choice of different DIC gauge lengths for the specimens. Therefore, initial slope of the curves lead to differences in elongation for the same amount of traction.

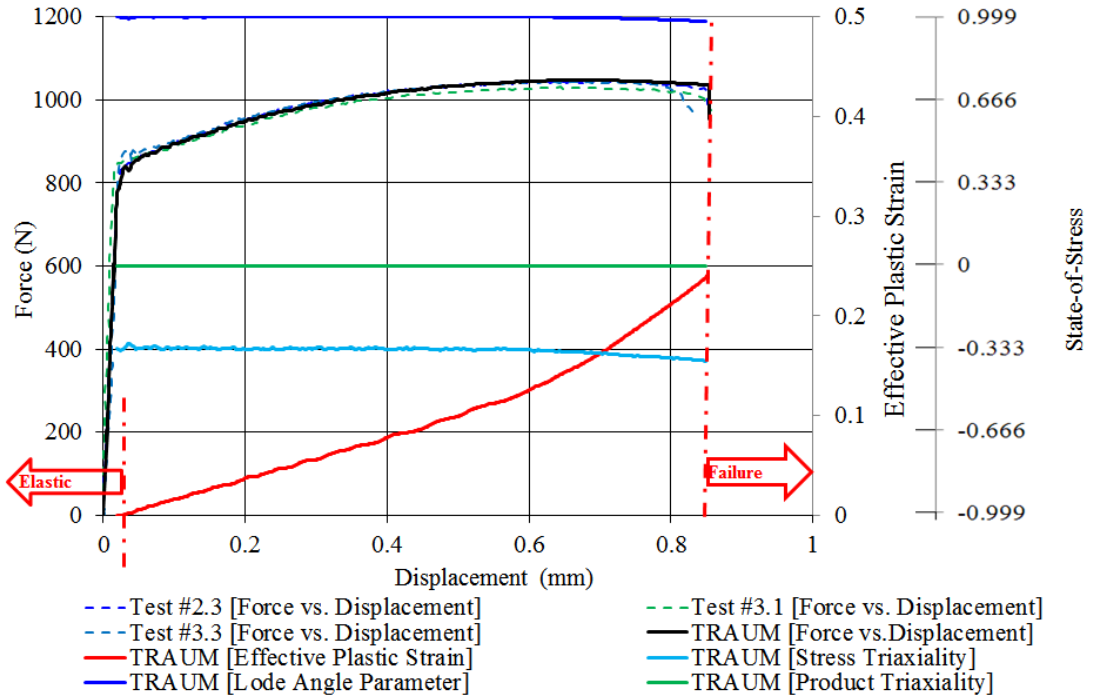

Figure 5-134: Characterization of the stress-states and failure strain for Specimen #1.

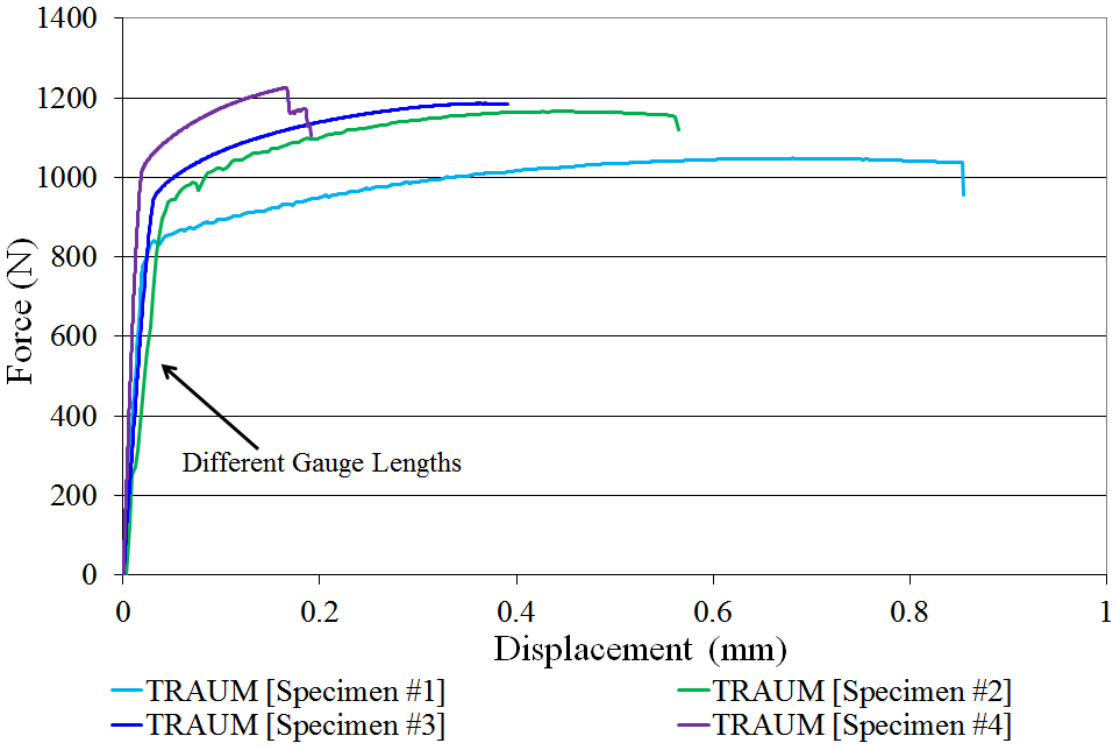

Figure 5-135: Force vs. displacement results for plane-stress specimens.

According to the results that are characterized by Figure 5-134 and Figures H-1 - H-3, plastic strains at failure and the corresponding states-of-stress are summarized by Table 5-25, where for all three repetitive test conditions an arithmetic mean is calculated for constructing the failure locus according to Equation (5.111). Arithmetic mean of the failure strains are used for the representative failure strain for each stress-state.

Table 5-25: Characterized plastic strains at failure and corresponding stress-states for plane-stress specimens in tension.

Test ‡ #	Specimen Geometry/FE Model*		Plastic Strain at Failure	Calculated Stress-State Values†		
			ε_p^f	σ_{av}^*	$\sigma_{p,av}^*$	$\theta_{L,av}$
2, 3	1 Figure B-1	Min.	0.24	-0.337	0.0	0.999
		Max.	0.255	-0.335	0.0	0.999
		Av.**	0.249	-0.336	0.0	0.999
33	2 Figure B-2	Min.	0.238	-0.434	0.002	0.885
		Max.	0.259	-0.432	0.003	0.888
		Av.**	0.248	-0.433	0.002	0.888
34	3 Figure B-3	Min.	0.190	-0.50	0.004	0.642
		Max.	0.229	-0.493	0.006	0.657
		Av.**	0.21	-0.497	0.006	0.649
35	4 Figure B-4	Min.	0.095	-0.580	-0.02	-0.03
		Max.	0.114	-0.578	0.0	0.0
		Av.**	0.102	-0.579	-0.001	-0.02

*Geometries and corresponding FE models of the specimens can be found in Appendix–B.
**Each test is repeated three times and the average represents the arithmetic mean.
‡ Test results can be found in Appendix–C.
† Stress-state values are averaged according to Equation (5.111)

Three dimensional representation of the failure space for plane-stress specimens is illustrated in Figure 5-136 by using the stress-triaxiality, Lode-angle-parameter and product-triaxiality with respect to the plastic strain at failure. The evolution of the stress-states and the plastic strains are illustrated with continues lines for only one test condition and representing each specimen with different colors, where the dashed lines are representing the averaged stress-states and the arithmetic mean of the three repetitive cases for each specimen correspondingly. During the construction of the failure surface the averaged values of the stress-states and the arithmetic mean of the failure strains are

used, which are listed in Table 5-25. For a better assessment of the evolution of the stress-states, the histories can be projected on to the planes defined by Lode-angle-parameter vs. stress-triaxiality as in Figure 5-137(a) and product-triaxiality vs. stress-triaxiality as in Figure 5-137(b), respectively.

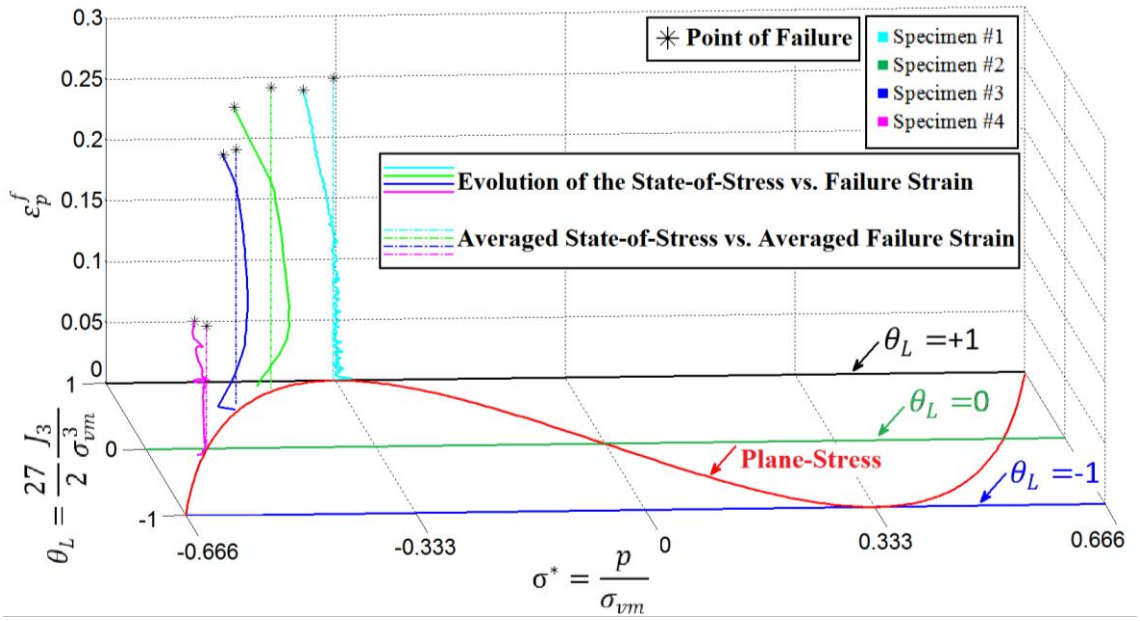

(a)

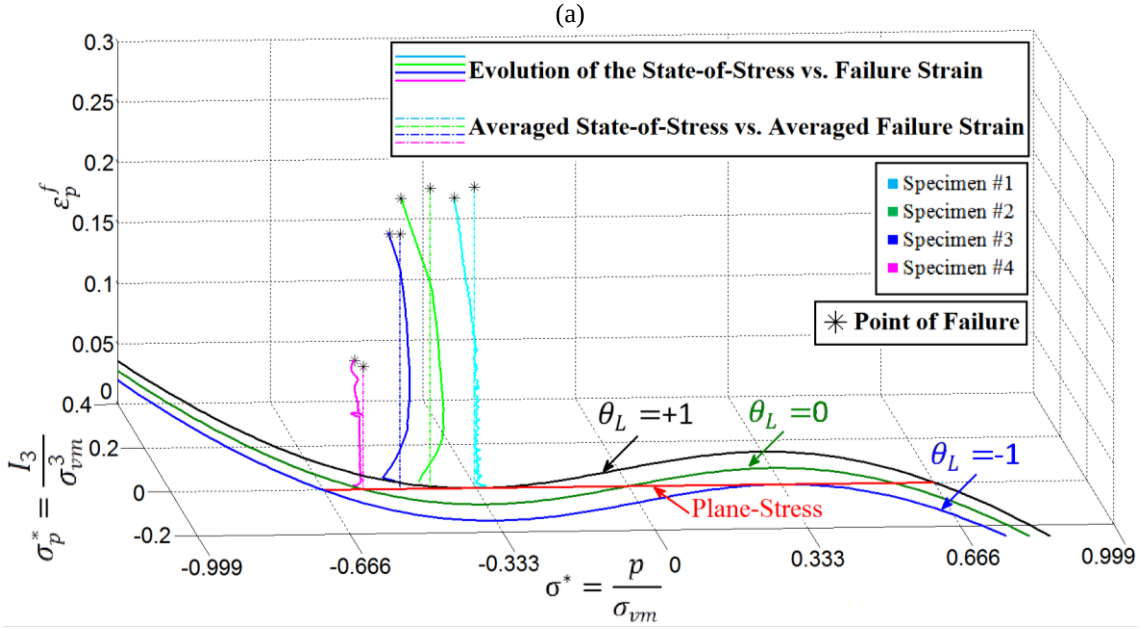

(b)

Figure 5-136: Evolution of the stress-state dependent failure in three dimensional failure space for plane-stress specimens represented by; (a) the space defined by stress-triaxiality vs. Lode-angle-parameter and (b) the space defined by stress-triaxiality vs. product-triaxiality.

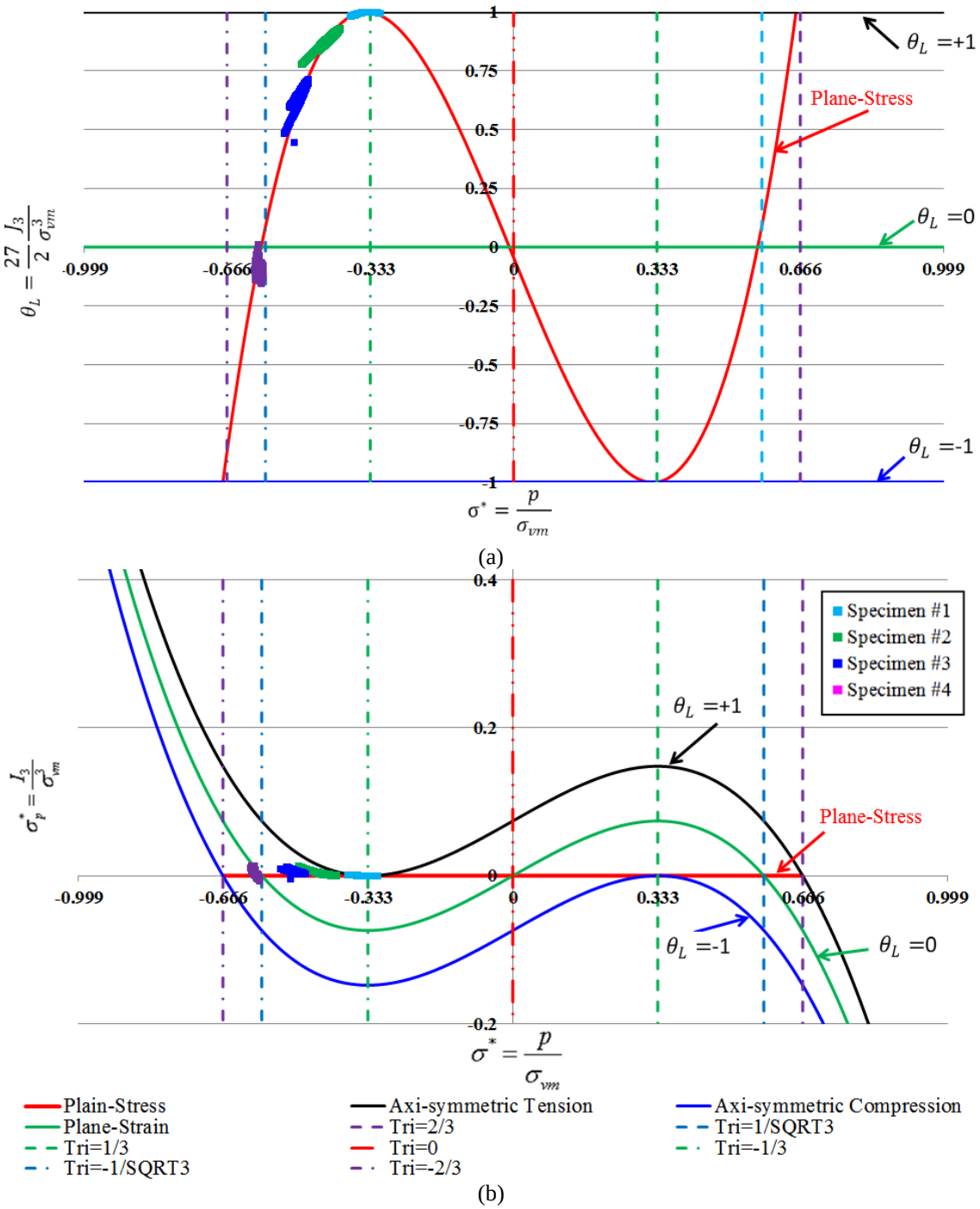

Figure 5-137: Evolution of the stress-state dependent failure for plane-stress specimens projected on; (a) the plane defined by stress-triaxiality vs. Lode-angle-parameter and (b) the plane defined by stress-triaxiality vs. product-triaxiality.

The history of the states-of-stress that are represented by the node clouds in Figure 5-137 suggests that the plane-stress conditions are successfully satisfied during the experiments and the distribution is reasonable. The stress-state points accumulate around the designated positions within the plane-stress line. Therefore, initially targeted stress-states, which are described by Figures 4-31 and 4-75, are achieved for 'bridging' the states-of-stress over the failure surface.

Figure 5-136 can also be projected on a plane that is defined by the plastic strain and the corresponding state-of-stress as illustrated in Figure 5-138. It can be observed from Figure 5-138 that although the stress-states are evolving as the plasticity takes place; they remain stable during the deformation for the central element that is in the middle of the specimen gauge region. Due to the confining effects of the notch geometry, stress-triaxialities are decreasing as the gauge length and radius decrease. Lode-angle-parameters are also variable. However, product-triaxiality values show that the central elements are remaining in an almost perfectly plane-stress state-of-stress.

All stress-state parameters are calculated from the central element in the middle of the cross-section as described in Section 4.4.3 and illustrated by Figure 4-35. It is observed for all cases that as soon as the failure occurs, the specimen separates in two parts. Therefore, the force vs. displacement curve often coincides or exceeds the plastic strain curve in the maximum time or displacement field as represented by Figure 5-134, and Figures H-1 - H-3. That is purely because the failure first initiates in the central element and propagates towards the edges or to the root of the notch geometry. However, for Specimen #4 with the sharpest notch, failure first initiates at the notch root of the specimen geometry rather than in the middle. Therefore, the force reading from the force vs. displacement curve starts to drop before the failure occurs in the central element. Figure 5-139 shows the evolution of the stress-states for the corresponding elements in the form of a node cloud. The central element stays on the plane-stress meridian as planned and have a stress-triaxiality approaching to the plane-strain meridian that will provide a point of 'bridging' across the stress-states with other specimens. However, the element at the root of the notch is experiencing an almost axi-symmetric tension state-of-stress. Clearly, two elements in a very simple specimen under quasi-static loading conditions and room temperature can experience two different states-of-stress

simultaneously even within a very small region. Therefore, two elements should have different plastic failure strains for failure and ultimately fail at different times. This small case is also another justification for developing a stress-state dependent failure law.

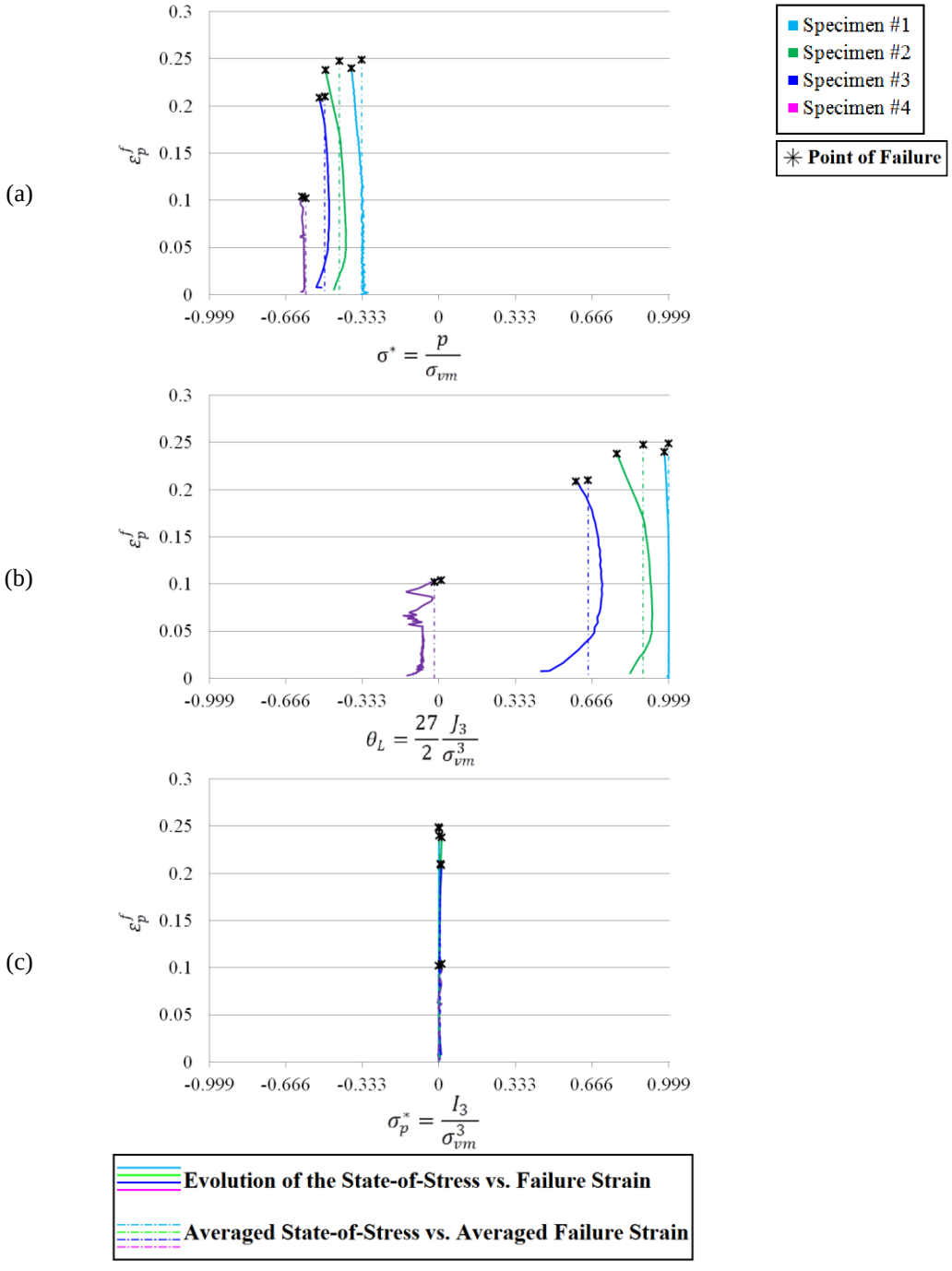

Figure 5-138: Evolution of plastic strain and states-of-stress for plane-stress specimens with averaged values as a function of; (a) stress-triaxiality, (b) Lode-angle-parameter and (c) product-triaxiality.

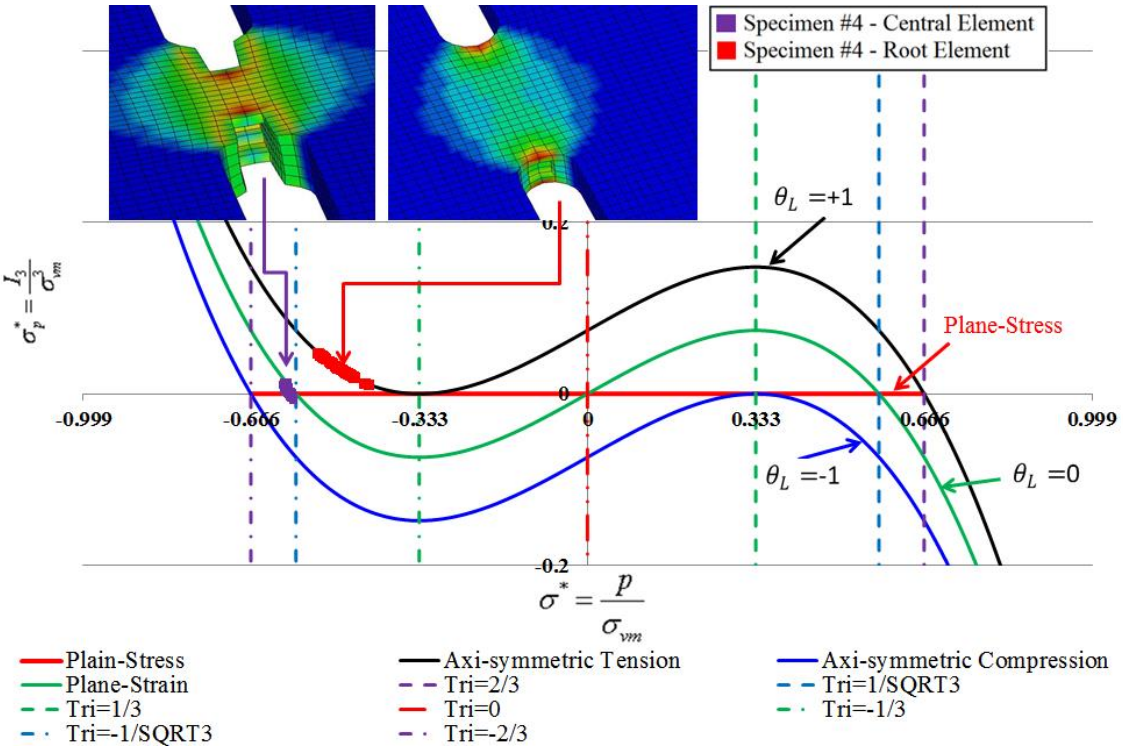

Figure 5-139: Evolution of the state-of-stress for the central and root elements in the notch geometry.

5.10.2 **Axi-symmetric tension specimens**

Six different specimen geometries are developed to characterize the plastic strain at failure for different stress-states of axi-symmetric tension. These specimens are illustrated in Figure 5-140 and the design details are provided in Chapter 4. All specimens were tested at quasi-static conditions and at room temperature. Details of the testing are listed in Table 5-26.

DIC was utilized to measure the displacement fields and SHLF was used for testing [108]. DIC gauge lengths are illustrated in Figure 5-141. The gauge length for Specimen #5 is selected within the smooth section of the specimen to provide information for the necking. The rest of the gauge lengths are selected on the shoulders of the notch geometries within a distance from a possible localization. Details of the axi-symmetric testing and specimen dimensions can be found in Appendix-C.

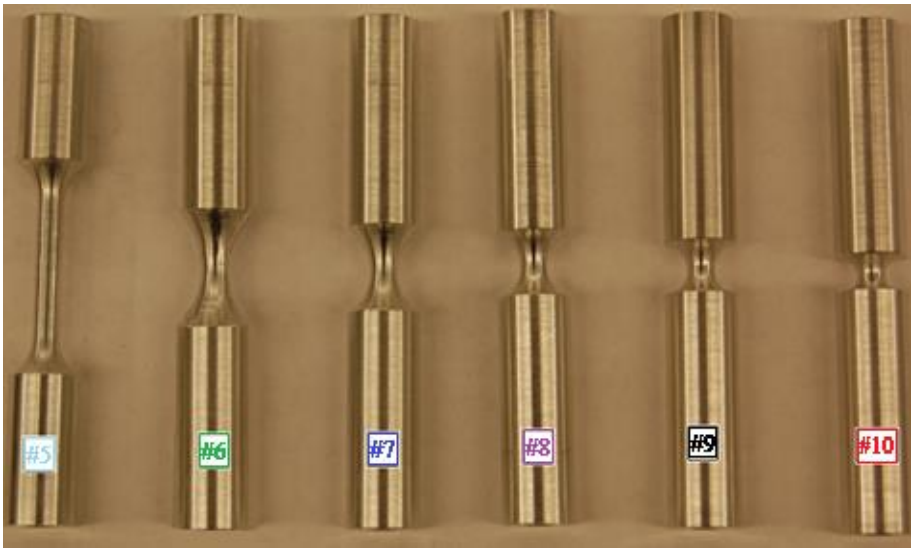

Figure 5-140: Axi-symmetric tension specimens, after [108].

The test conditions that are described by Table 5-26 are simulated by using the FE models which are illustrated in Appendix–B by Figures B-5 - B-10. The characteristic element lengths are chosen as 0.15mm in the middle of each specimen, which is consistent with the element length of the [t/5] model. This consistent characteristic element length is preferred since it can capture any localized instabilities but also can present computationally efficient solution times. Plastic strains at failure are characterized by comparing displacements at failure by using a similar approach that is described for the plane-stress specimens. Figure 5-142 depicts the force vs. displacement results for each specimen that is calculated for a specific test for a characterized value of the plastic strain at failure. It is observed that specimens with notch geometries follow the same characteristics as the plane-stress specimens, where the required forces increase with a significant reduction in the displacements to failure as the radii decrease. The differences in the elastic parts of the responses are also a result of using different DIC gauge lengths due to the notch geometry.

Figure 5-143 illustrates the characterization of the failure strain with respect to the evolution of the states-of-stress over the displacement field for Specimen #5. The failure strain is found for the corresponding plastic strain that matches the force vs. displacement curve of the specific test result. Three repetitive tests are shown in Figure 5-143, where

only one set of characterization data is illustrated for brevity. It is clearly seen that the stress-state remains stable during the test until the localization. Consequently, the states-of-stress are found to be very close to the ideal axi-symmetric tension state for Specimen #5 for the given conditions.

Table 5-26: Test cases for characterization of the quasi-static failure strains at room temperature for axi-symmetric tension specimens.

Test #	Specimen #	DIC Gauge Length [mm]	Test Apparatus	State-of-Stress and Loading	Initially Targeted			
					Stress-State Values			Strain Rate [s^{-1}]
					σ^*	σ_p^*	θ_L	
4.4 [Figure C-4]† [Table C-35] ‡	5 [Figure B-5]§	4.0	SHLF*	Axi-Symmetric in Tension	$-\frac{1}{3}$	0.0	1.0	1.0×10^{-2}
4.5 [Figure C-4]† [Table C-35] ‡								
4.6 [Figure C-4]† [Table C-35] ‡								
36 [Figure C-34]† [Table C-36] ‡	6 [Figure B-6]§	17.9			-0.41	0.006	1.0	
37 [Figure C-35]† [Table C-37] ‡	7 [Figure B-7]§	13.5			-0.49	0.028	1.0	
38 [Figure C-36]† [Table C-38] ‡	8 [Figure B-8]§	10.2			$-\frac{1}{\sqrt{3}}$	0.074	1.0	
39 [Figure C-37]† [Table C-39] ‡	9 [Figure B-9]§	7.7			$-\frac{2}{3}$	0.148	1.0	
40 [Figure C-38]† [Table C-40] ‡	10 [Figure B-10]§	5.0			-0.8	0.319	1.0	

* Servo-Hydraulic Loading Frame (SHLF).
† Test results for the corresponding specimen, strain-rate and temperature illustrated in Appendix–C.
‡ Test results for the corresponding specimen, strain-rate and temperature listed in Appendix–C.
§ Detailed geometries and corresponding FE models of the specimens are illustrated in Appendix–B.

The same characterization procedures are applied to the rest of the axi-symmetric specimens in tension and the results are illustrated in Appendix-H by Figures H-4 to H-8, respectively. According to the results that are characterized by Figure 5-143 and Figures H-4 - H-8, plastic strains at failure and the corresponding states-of-stress are summarized by Table 5-27, where for all three repetitive test conditions the stress-states are averaged according to Equation (5.111). Arithmetic mean of the failure strains are used as the representative failure strain for the failure locus.

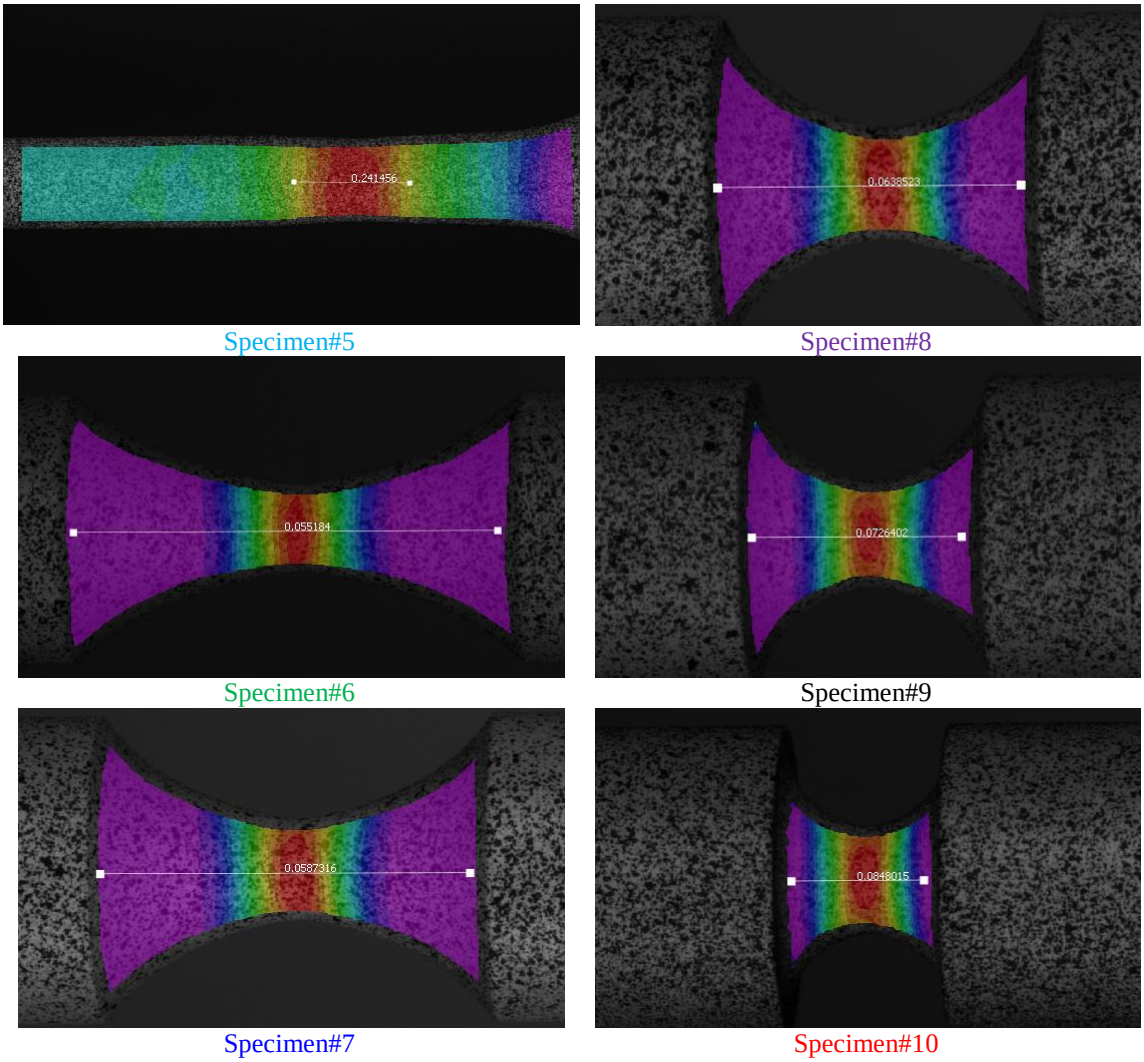

Figure 5-141: Positions of the DIC gauge lengths for axi-symmetric tension specimens.

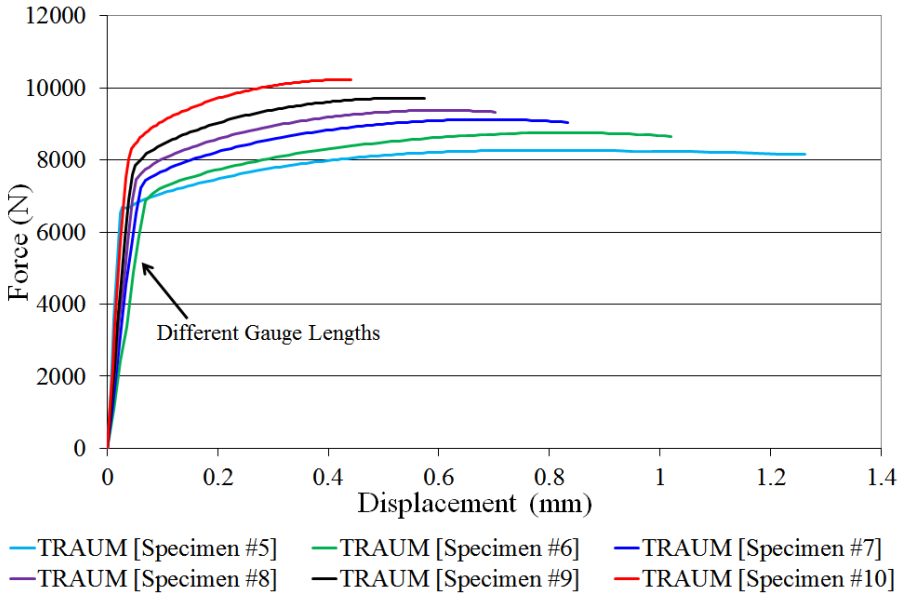

Figure 5-142: Force vs. displacement results for axi-symmetric specimens.

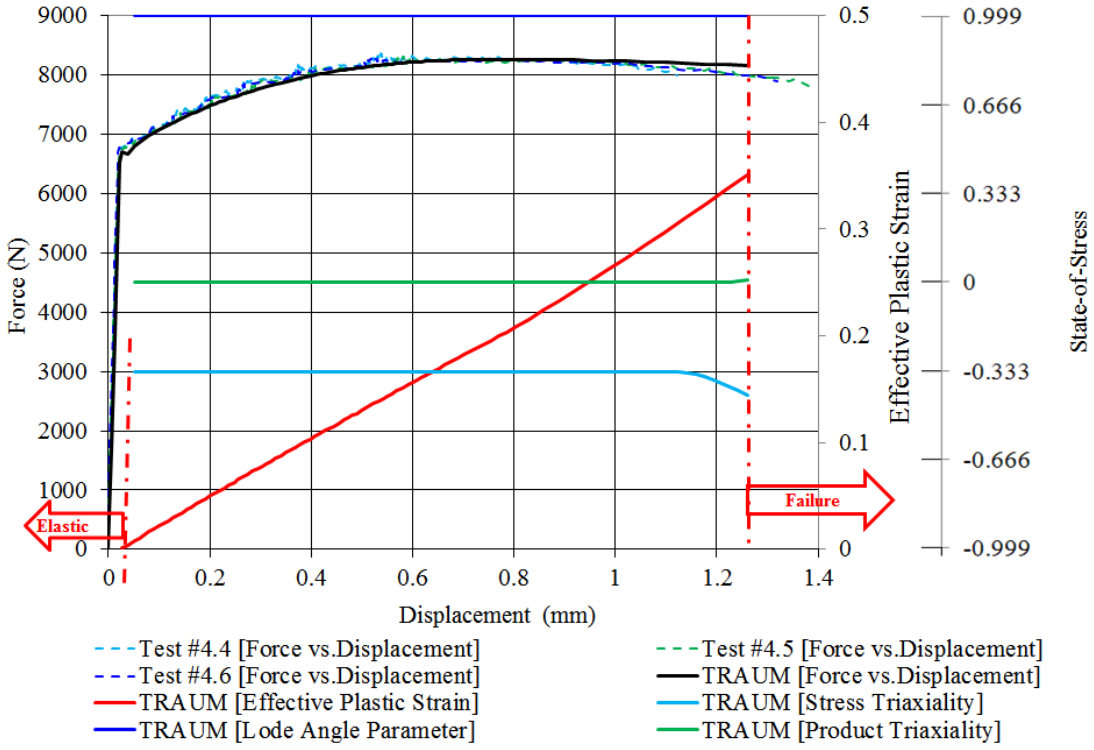

Figure 5-143: Characterization of the stress-states and failure strain for Specimen #5.

Table 5-27: Characterized plastic strains at failure and corresponding stress-states for axi-symmetric specimens in tension.

Test ‡ #	Specimen Geometry/FE Model*		Plastic Strain at Failure	Calculated Stress-State Values†		
			ε_p^f	σ_{av}^*	$\sigma_{p,av}^*$	$\theta_{L,av}$
4	5 Figure B-5	Min.	0.28	-0.355	0.001	0.999
		Max.	0.37	-0.343	0.003	0.999
		Av.**	0.323	-0.348	0.002	0.999
36	6 Figure B-6	Min.	0.3	-0.526	0.048	0.999
		Max.	0.317	-0.523	0.05	0.999
		Av.**	0.309	-0.525	0.049	0.999
37	7 Figure B-7	Min.	0.286	-0.608	0.096	0.999
		Max.	0.291	-0.607	0.097	0.999
		Av.**	0.289	-0.607	0.096	0.999
38	8 Figure B-8	Min.	0.273	-0.675	0.164	0.999
		Max.	0.275	-0.677	0.167	0.999
		Av.**	0.274	-0.675	0.164	0.999
39	9 Figure B-9	Min.	0.24	-0.763	0.265	0.999
		Max.	0.249	-0.76	0.266	0.999
		Av.**	0.245	-0.763	0.265	0.999
40	10 Figure B-10	Min.	0.2	-0.857	0.435	0.999
		Max.	0.21	-0.853	0.44	0.999
		Av.**	0.204	-0.856	0.44	0.999

*Geometries and corresponding FE models of the specimens can be found in Appendix–B.
**Each test is repeated three times and the average represents the arithmetic mean.
‡ Test results can be found in Appendix–C.
† Stress-state values are averaged according to Equation (5.111)

Three dimensional representation of the failure space for axi-symmetric specimens is illustrated in Figure 5-144 by using the stress-triaxiality, Lode-angle-parameter and product-triaxiality with respect to the plastic strain at failure. Averaged values of the stress-states and the arithmetic mean of the failure strains are also illustrated for three repeated cases of each specimen. During the construction of the failure surface the averaged values of the stress-states and the arithmetic mean of the failure strains are used, which are listed in Table 5-27. It should be noted that the case illustrated for Specimen #5 in Figure 5-144 has a significantly different failure strain compared to the mean failure strain that is found by the arithmetic mean, which is due to the PLC effect during the flow. Consequently, the axi-symmetric specimen with a smooth gauge length at a strain

rate of $1.0x10^{-2}s^{-1}$ has experienced the complications of 'serrated flow' and the plastic strain at failure could only be justified through the general trend that is found from the projections of the failure strain and the stress-states.

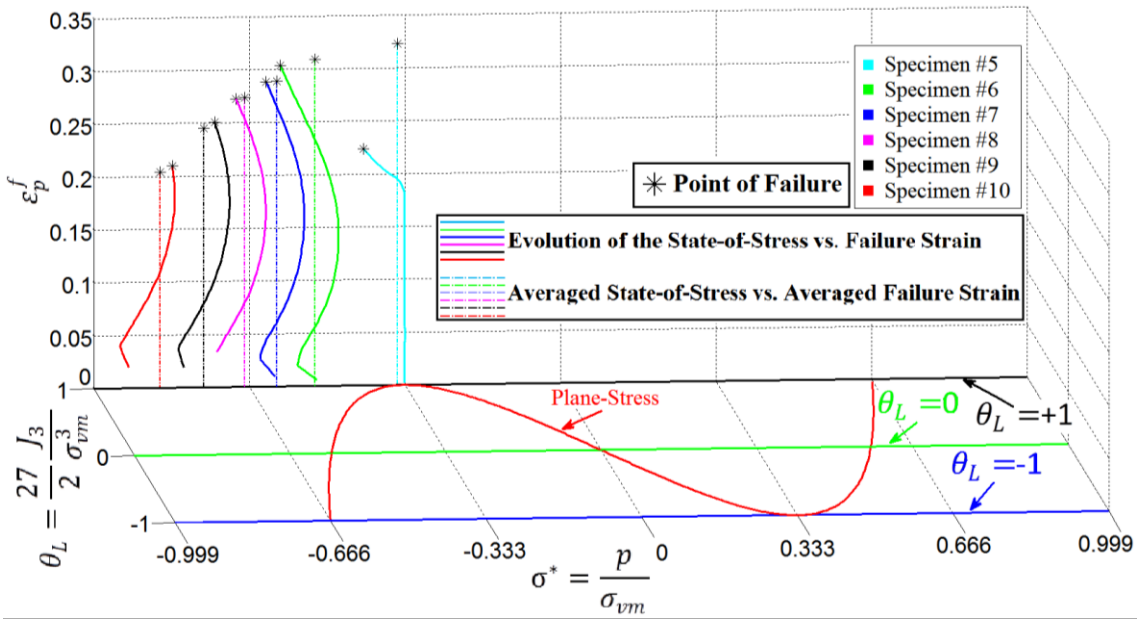

(a)

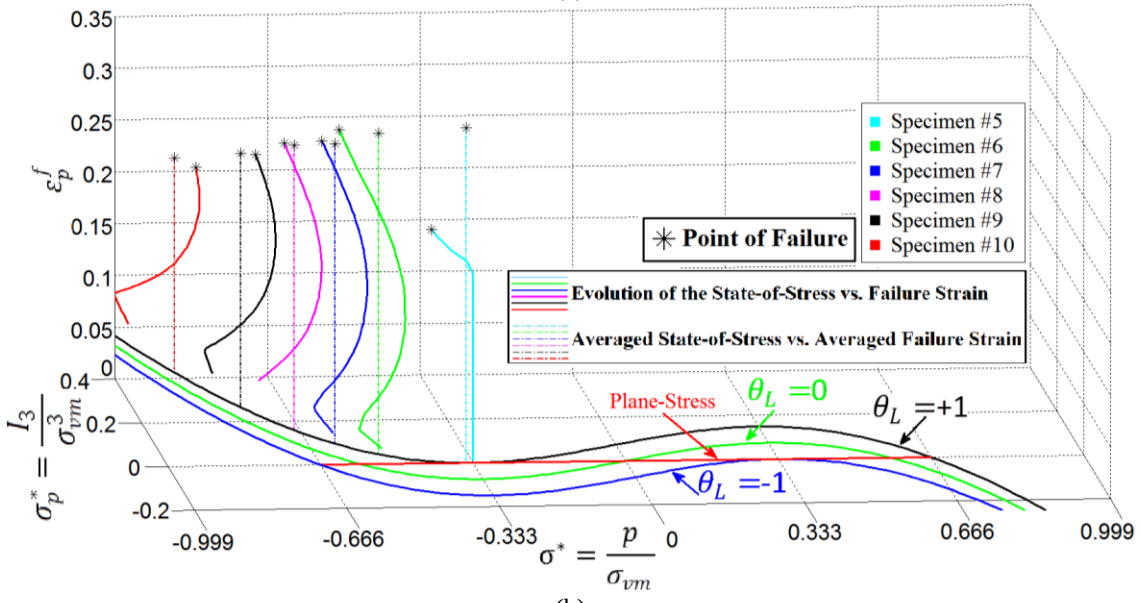

(b)

Figure 5-144: Evolution of the stress-state dependent failure in three dimensional failure space for axi-symmetric specimens represented by; (a) the space defined by stress-triaxiality vs. Lode-angle-parameter and (b) the space defined by stress-triaxiality vs. product-triaxiality.

For a better assessment of the evolution of the stress-states, the histories of the stress-states can be projected on the planes defined by Lode-angle-parameter vs. stress-triaxiality as in Figure 5-145(a) and product-triaxiality vs. stress-triaxiality as in Figure 5-145(b), respectively.

The histories of the states-of-stress that are represented by the node clouds in Figure 5-145 suggests that the axi-symmetric conditions are successfully achieved during the experiments and a good distribution of the stress-states are obtained that are essential for 'bridging' the corresponding specimens as described by Figures 4-31 and 4-75. The stress-state points accumulate around the designated axi-symmetric meridian for the central elements of the specimens in the middle of the gauge section.

Figure 5-144 can also be projected on a plane that is defined by the plastic strain and the corresponding state-of-stress as illustrated in Figure 5-146. It is shown that the axi-symmetric tension meridian is followed by the central element of the specimens during the entire evolution of the stress-states, where the stress-triaxiality and product-triaxiality values reduce as a result of the confined deformation that is effected by the notch geometry in the gauge section. All stress-state parameters are averaged according to Equation (5.111) and the failure strains are characterized as the mean of the three successive tests for each stress-state condition.

The effects of 'serrated flow' and the morphology of the PLC bands propagating over the axi-symmetric specimen with a smooth gauge section were measured by using DIC and illustrated in Figure 5-147 for specific time increments up to failure at time t_n [380]. The distribution of the true strains are shown for the gauge section, where it is seen that beginning with the initial time t_0, the localization of the strain field moves back and forth along the gauge section until localized necking forms at time t_{12}. The shape of the PLC bands is related to the material properties, the geometry of the specimen, and the type and rate of the loading. The band formation also influences the shape of the localized necking and eventually the shape of the failure surface, where in the case of an axi-symmetric round specimen in tension a conical shape is observed that was also reported by Zhang, et al. [381]. The effects of Al and Al-Cu alloys were investigated before both experimentally and numerically by the help of image correlation and similar result have been pronounced for axi-symmetric specimens [254] [259] [382] [383].

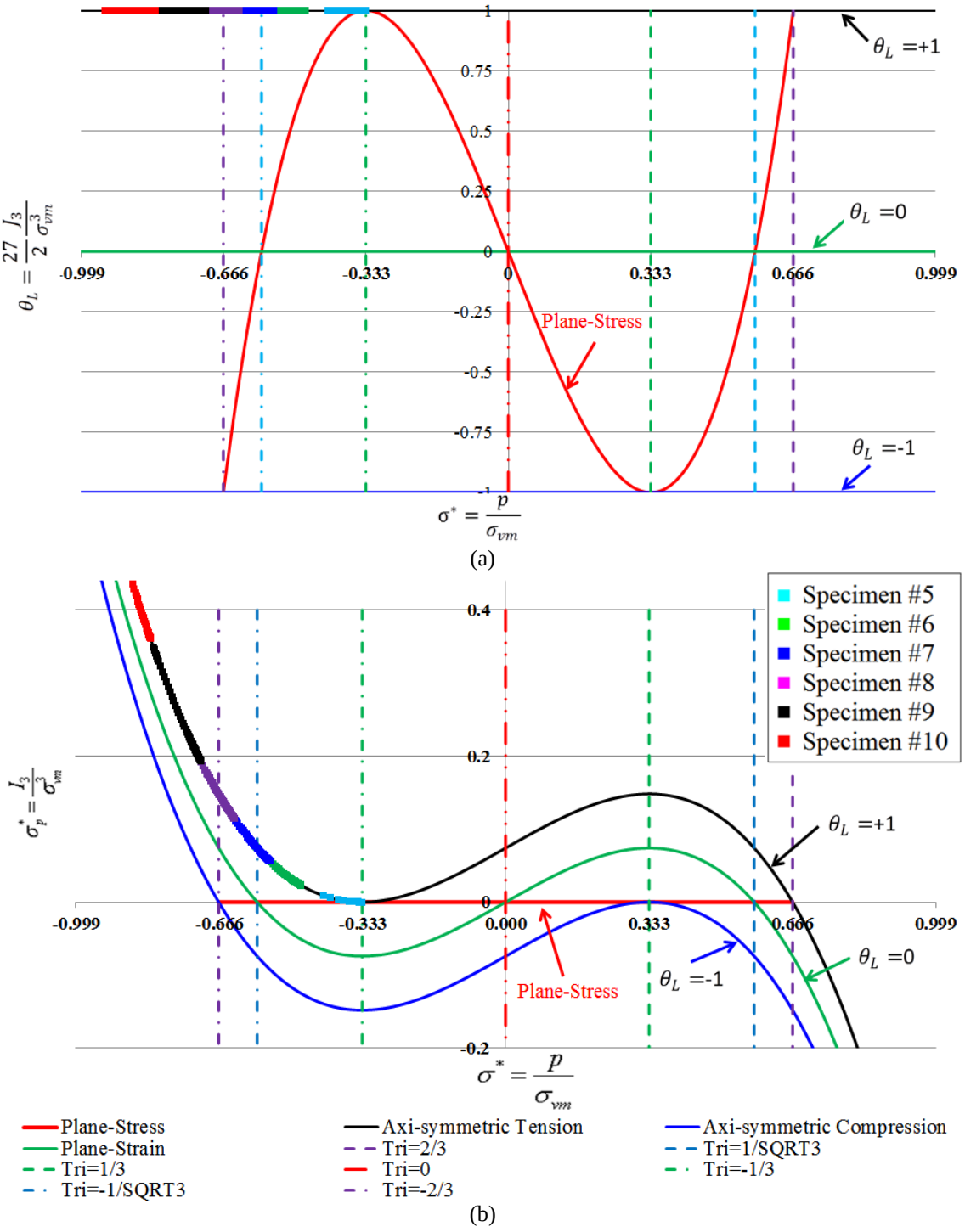

Figure 5-145: Evolution of the stress-state dependent failure for axi-symmetric specimens projected on; (a) the plane defined by stress-triaxiality vs. Lode-angle-parameter and (b) the plane defined by stress-triaxiality vs. product-triaxiality.

(a)

(b)

(c)

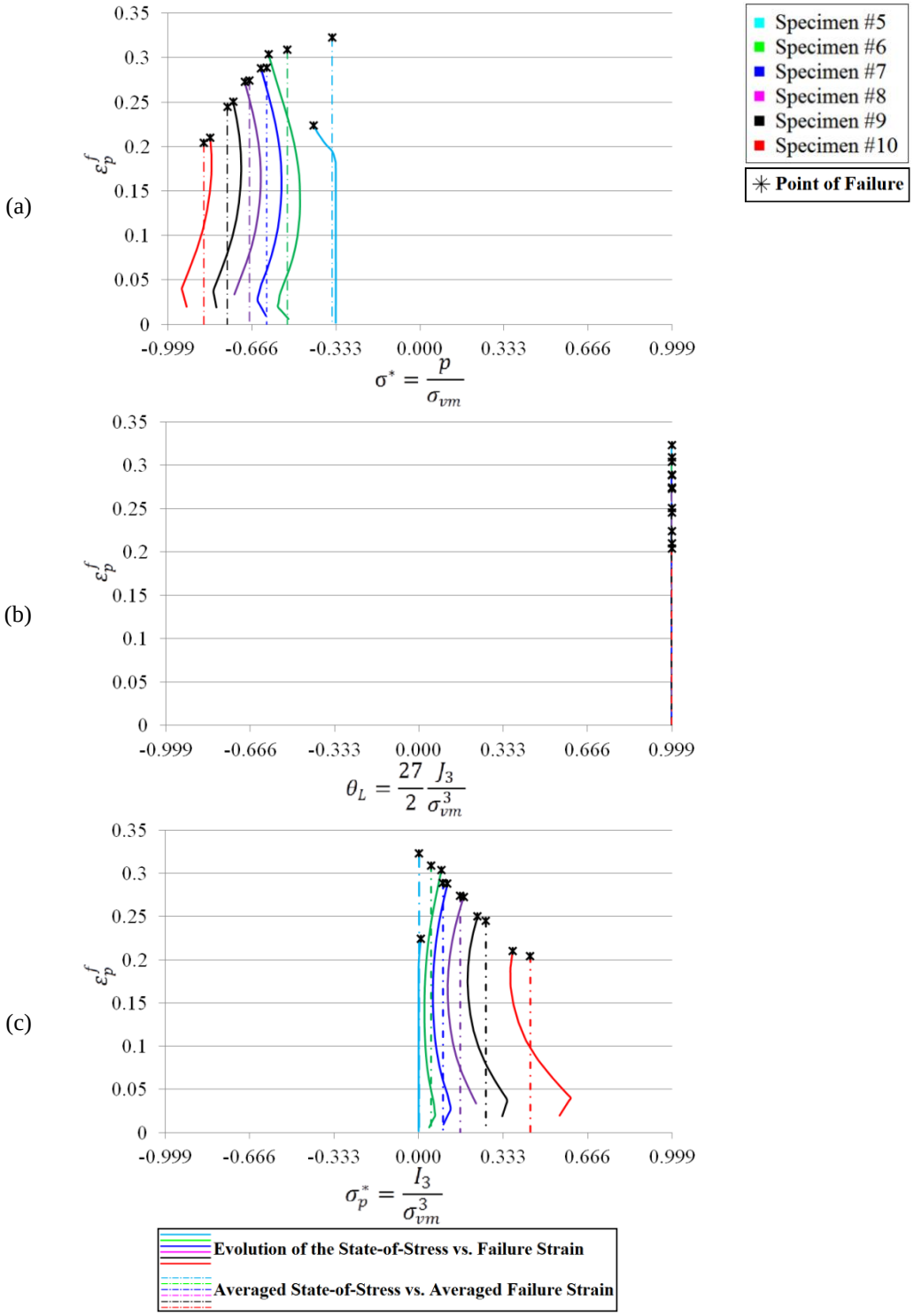

Figure 5-146: Evolution of plastic strain and states-of-stress for axi-symmetric specimens with averaged values as a function of; (a) stress-triaxiality, (b) Lode-angle-parameter and (c) product-triaxiality.

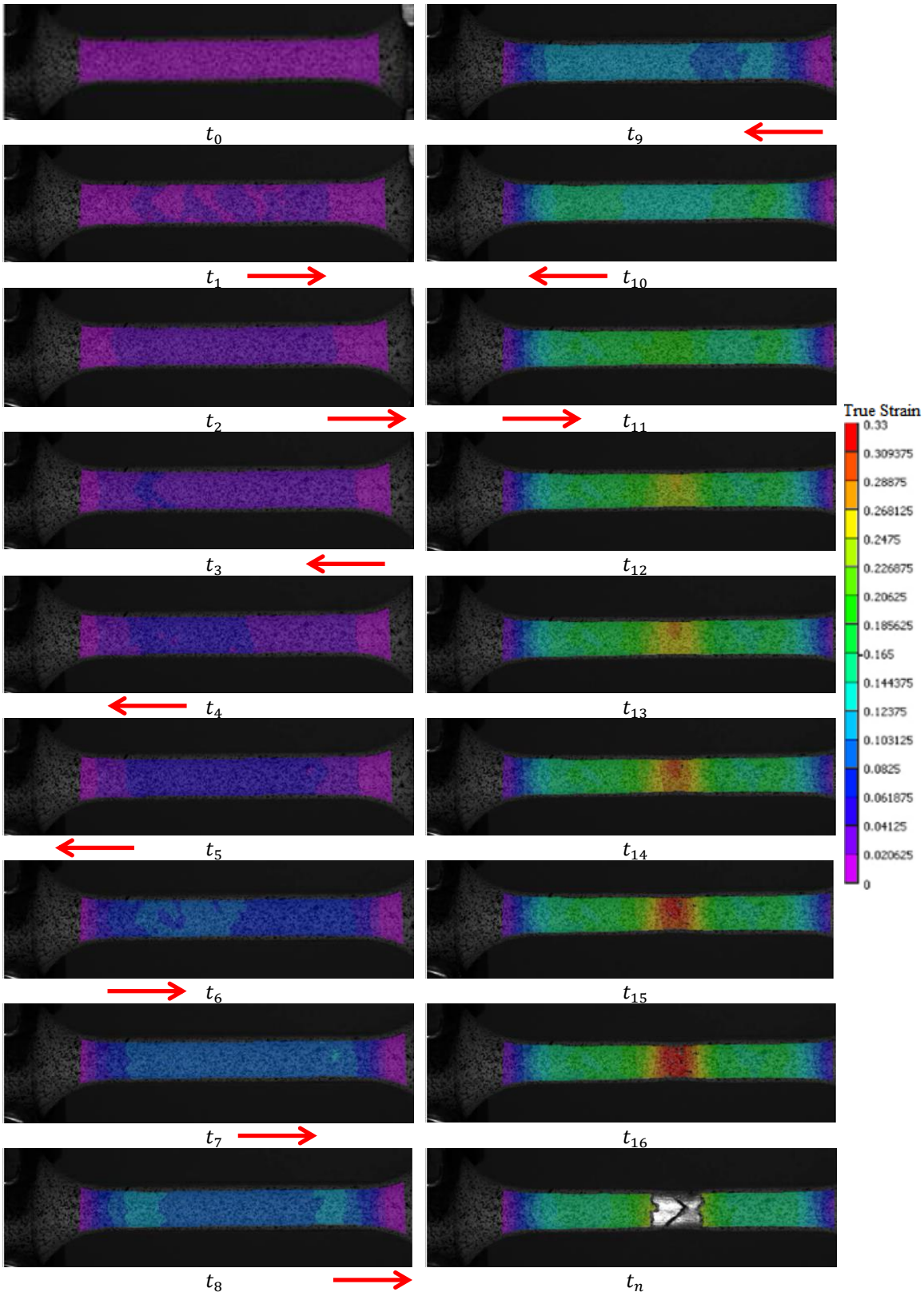

Figure 5-147: Morphology of the PLC bands propagating along the smooth gauge section of the axi-symmetric specimen in tension, after [380].

Specimens with the notch geometry were also reported to be prone to the effects of PLC bands. However, it was shown that the bands have escaped from the notched zone and arrested outside the localization due to the confinement within the gauge section [382]. Therefore, for the axi-symmetric specimens with notch geometries, consistent failure behavior is observed with the change in the states-of-stress as the localized necking within the gauge section evolves more rapidly.

5.10.3 **Plane-strain tension specimens**

Three different specimen geometries are characterized to find the plastic strain at failure for plane-strain stress-state in tension. These specimens are illustrated in Figure 5-148 and the design information is provided in Chapter 4. All specimens are tested at quasi-static conditions and room temperature. DIC was utilized to measure the displacement field and SHLF was used for testing [108]. DIC gauge lengths, which are virtually determined, are illustrated in Figure 5-149. The gauge length for Specimen #11 is selected within the smooth section of the specimen to provide information for the necking. The rest of the gauge lengths are selected on the shoulders of the notch geometries within a distance from a possible localization. Details of the plane-strain testing are listed in Table 5-28 and test conditions of the testing and specimen dimensions can be found in Appendix-C.

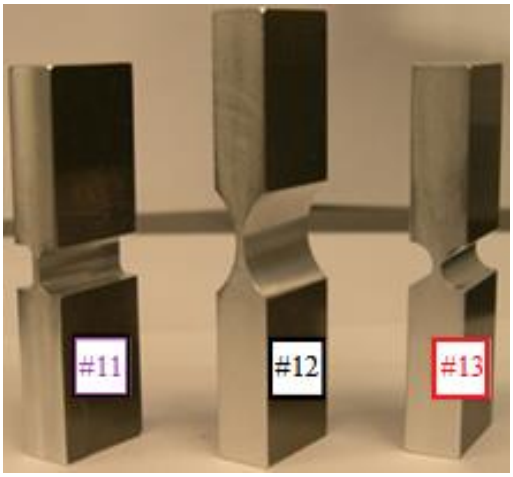

Figure 5-148: Plane-strain tension specimens, after [108].

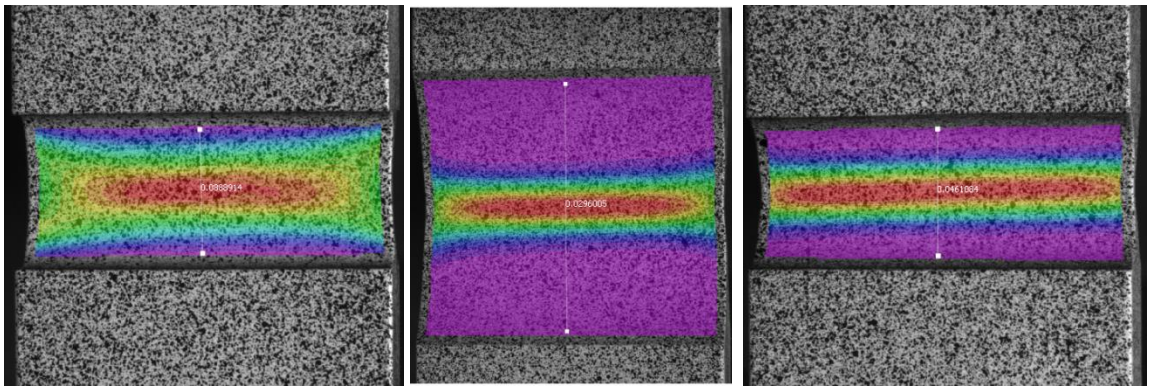

Specimen#11 Specimen#12 Specimen#13

Figure 5-149: Positions of the DIC gauge lengths for plane-strain tension specimens.

Table 5-28: Test cases for characterization of the quasi-static failure strains at room temperature for plane-strain tension specimens.

Test #	Specimen #	DIC Gauge Length [mm]	Test Apparatus	State-of-Stress and Loading	Initially Targeted			
					Stress-State Values			Strain Rate [s^{-1}]
					σ^*	σ_p^*	θ_L	
41 [Figure C-39]† [Table C-41] ‡	11 [Figure B-11]§ 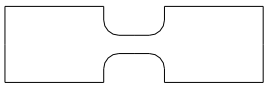	5.08	SHLF*	Plane-Strain in Tension	$-\frac{1}{\sqrt{3}}$	0.0	0.0	1.0×10^{-2}
42 [Figure C-40]† [Table C-42] ‡	12 [Figure B-12]§ 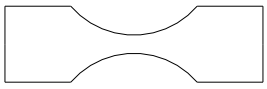	19.5			$-\frac{2}{3}$	0.074	0.0	
43 [Figure C-41]† [Table C-43] ‡	13 [Figure B-13]§ 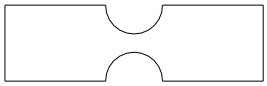	8.0			-0.8	0.245	0.0	

* Servo-Hydraulic Loading Frame (SHLF).
† Test results for the corresponding specimen, strain-rate and temperature illustrated in Appendix–C.
‡ Test results for the corresponding specimen, strain-rate and temperature listed in Appendix–C.
§ Detailed geometries and corresponding FE models of the specimens are illustrated in Appendix–B.

The test conditions that are described by Table 5-28 are simulated by using the FE models which are illustrated in Appendix–B by Figures B-11 - B-13. The characteristic element lengths are chosen as 0.15mm in the middle of each specimen, which is consistent with the element length of the [t/5] model. Plastic strains at failure are

characterized by comparing displacements at failure by using a similar approach that is described for the plane-stress and axi-symmetric specimens. Figure 5-150 shows the force vs. displacement results for each specimen that is calculated for a specific test for a characterized value of the plastic strain at failure. It is observed that specimens with notch geometries follow the same characteristics as the plane-stress and axi-symmetric specimens, where the required forces increase with a significant reduction in the displacements to failure as the radii decrease. The differences in the elastic parts of the responses are also a result of using different DIC gauge lengths due to the notch geometry.

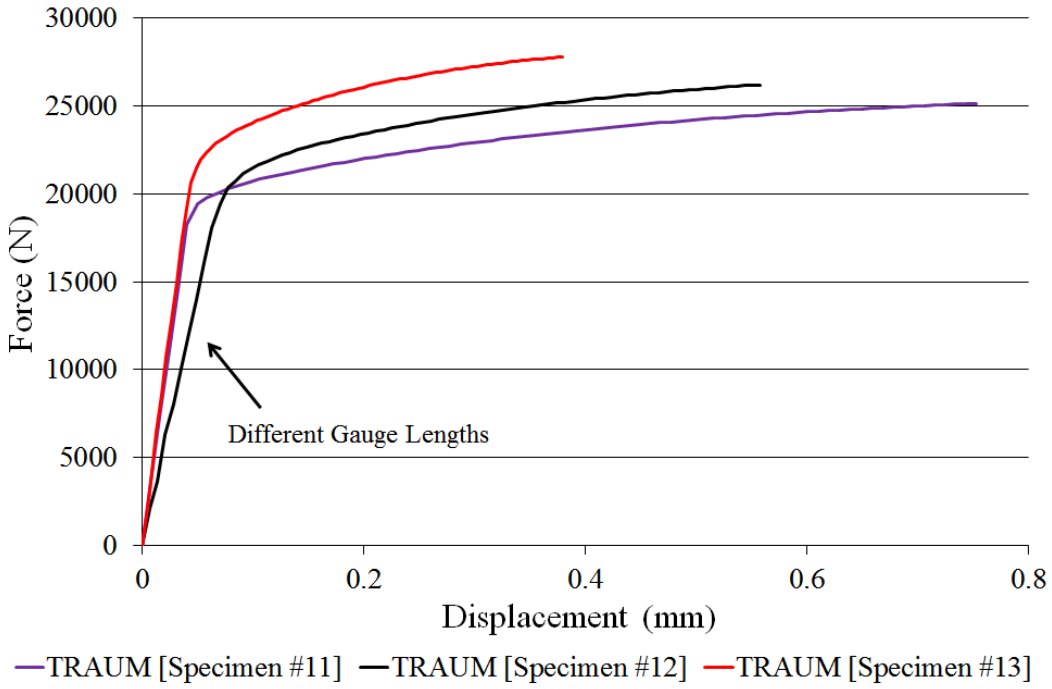

Figure 5-150: Force vs. displacement results for plane-strain specimens.

Figure 5-151 illustrates the characterization of the failure strain with respect to the evolution of the states-of-stress over the displacement field for Specimen #11. The failure strain is found for the corresponding plastic strain that matches the force vs. displacement curve of the specific test result. Three repetitive tests are shown in Figure 5-151, where only one set of characterization data is illustrated for brevity.

The same characterization procedures are applied to the rest of the plane-strain specimens in tension and the results are illustrated in Appendix-H by Figures H-9 and H-10, respectively. According to the results that are characterized by Figure 5-151 and Figures H-9 and H-10, plastic strains at failure and the corresponding states-of-stress are summarized by Table 5-29, where for all three repetitive test conditions the stress-states are averaged according to Equation (5.111). Arithmetic mean of the failure strains are used as the representative failure strain for the failure locus.

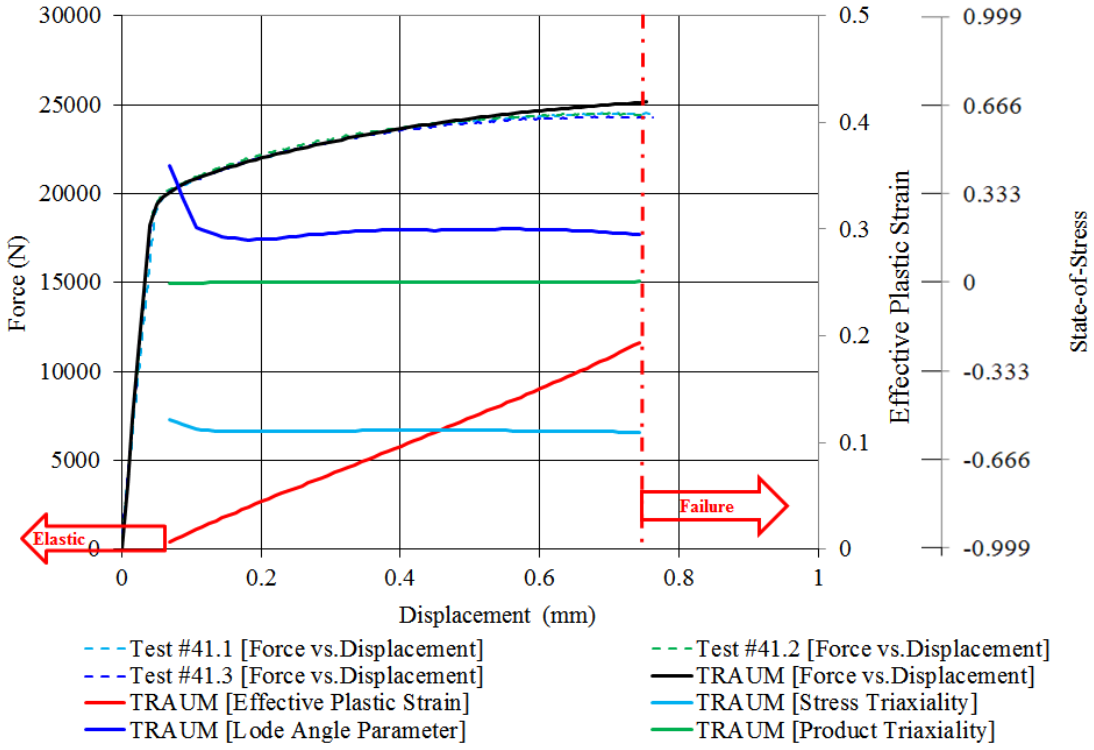

Figure 5-151: Characterization of the stress-states and failure strain for Specimen #11.

Three dimensional representation of the failure space for plane-strain specimens is illustrated in Figure 5-152 by using the stress-triaxiality, Lode-angle-parameter and product-triaxiality with respect to the plastic strain at failure. Averaged values of the stress-states and the arithmetic mean of the failure strains are also illustrated for three repeated cases of each specimen. During the construction of the failure surface the averaged values of the stress-states and the arithmetic mean of the failure strains are used, which are listed in Table 5-29.

Table 5-29: Characterized plastic strains at failure and corresponding stress-states for plane-strain specimens in tension.

Test ‡ #	Specimen Geometry/FE Model*		Plastic Strain at Failure	Calculated Stress-State Values†		
			ε_p^f	σ_{av}^*	$\sigma_{p,av}^*$	$\theta_{L,av}$
41	11 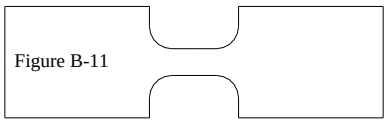 Figure B-11	Min.	0.19	-0.566	0.002	0.146
		Max.	0.21	-0.563	0.003	0.148
		Av. **	0.196	-0.564	0.002	0.147
42	12 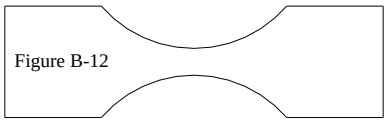 Figure B-12	Min.	0.188	-0.609	0.037	0.2
		Max.	0.21	-0.604	0.04	0.21
		Av. **	0.192	-0.606	0.038	0.208
43	13 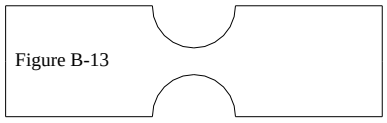 Figure B-13	Min.	0.195	-0.733	0.155	0.1
		Max.	0.21	-0.73	0.157	0.11
		Av. **	0.205	-0.732	0.156	0.103

*Geometries and corresponding FE models of the specimens can be found in Appendix–B.
**Each test is repeated three times and the average represents the arithmetic mean.
‡ Test results can be found in Appendix–C.
† Stress-state values are averaged according to Equation (5.111)

The histories of the stress-states can be projected on the planes defined by Lode-angle-parameter vs. stress-triaxiality as in Figure 5-153(a) and product-triaxiality vs. stress-triaxiality as in Figure 5-153(b), respectively. The evolution of the states-of-stress that are represented by the node clouds in Figure 5-153 suggests that close results to the plane-strain conditions are achieved during the experiments. However, due to the finite thickness of the specimens, the Lode-angle-parameter varies and is not exactly on the targeted plane-strain meridian. Clearly, an ideal plane-strain case should have an infinite thickness, where the third deviatoric stress invariant and consequently the Lode-angle-parameter disappear. Since it is impossible to test an infinitely thick specimen, specimens with finite thicknesses are designed in Chapter 4 by calculating the corresponding stress-states that are desired for 'bridging'. As a result, it is shown that especially the plane-strain specimen with a smooth gauge section (i.e., Specimen #11) provides stress-states that are in between plane-stress and plane-strain conditions when the history of the specimen is averaged. On the other hand, the failure points for the plane-strain specimens are found to be on the corresponding meridian. Therefore, it can be justified that the

characterized values of the failure strains can be used for the states-of-stress that are listed by Table 5-29 after averaging.

It is also observed from Figure 5-154 that the plastic strains at failure are not as sensitive to the state-of-stress compared to the other states tested before.

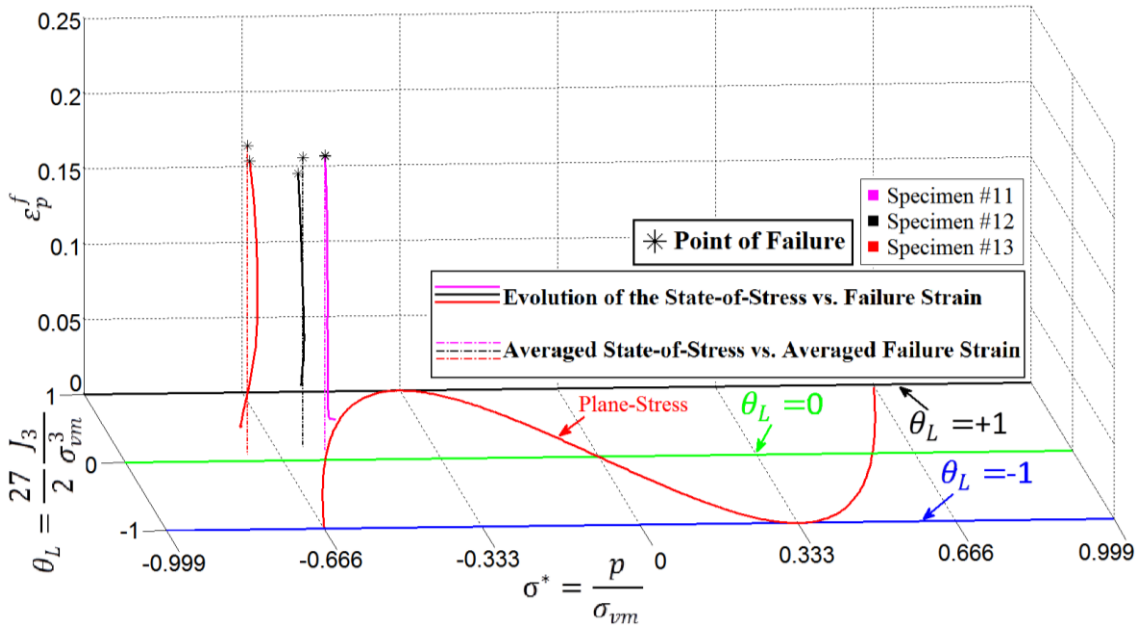

(a)

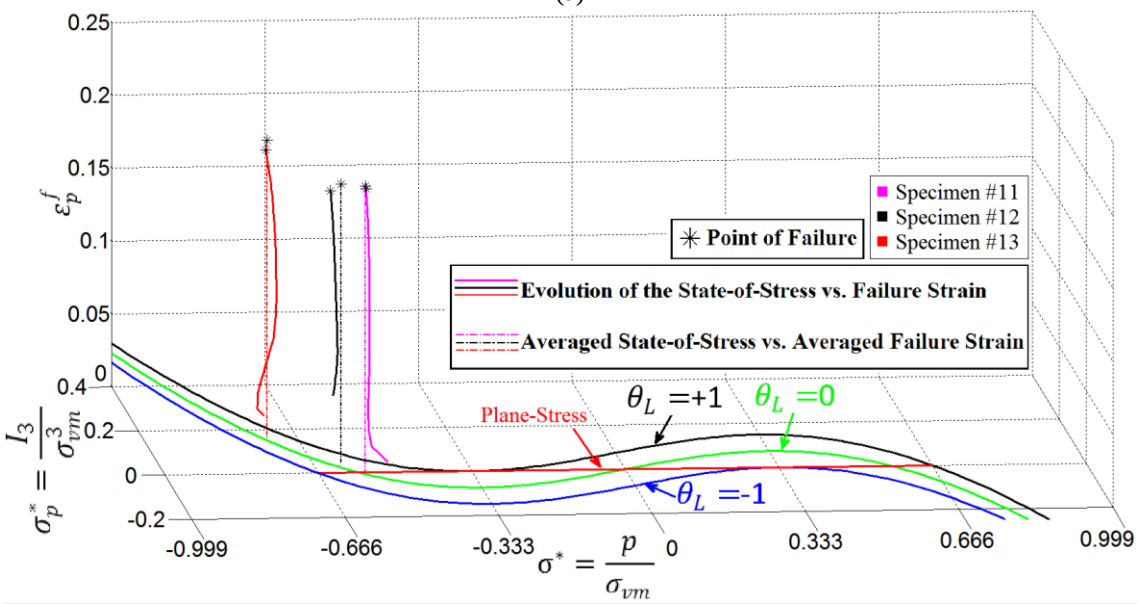

(b)

Figure 5-152: Evolution of the stress-state dependent failure in three dimensional failure space for plane-strain specimens represented by; (a) the space defined by stress-triaxiality vs. Lode-angle-parameter and (b) the space defined by stress-triaxiality vs. product-triaxiality.

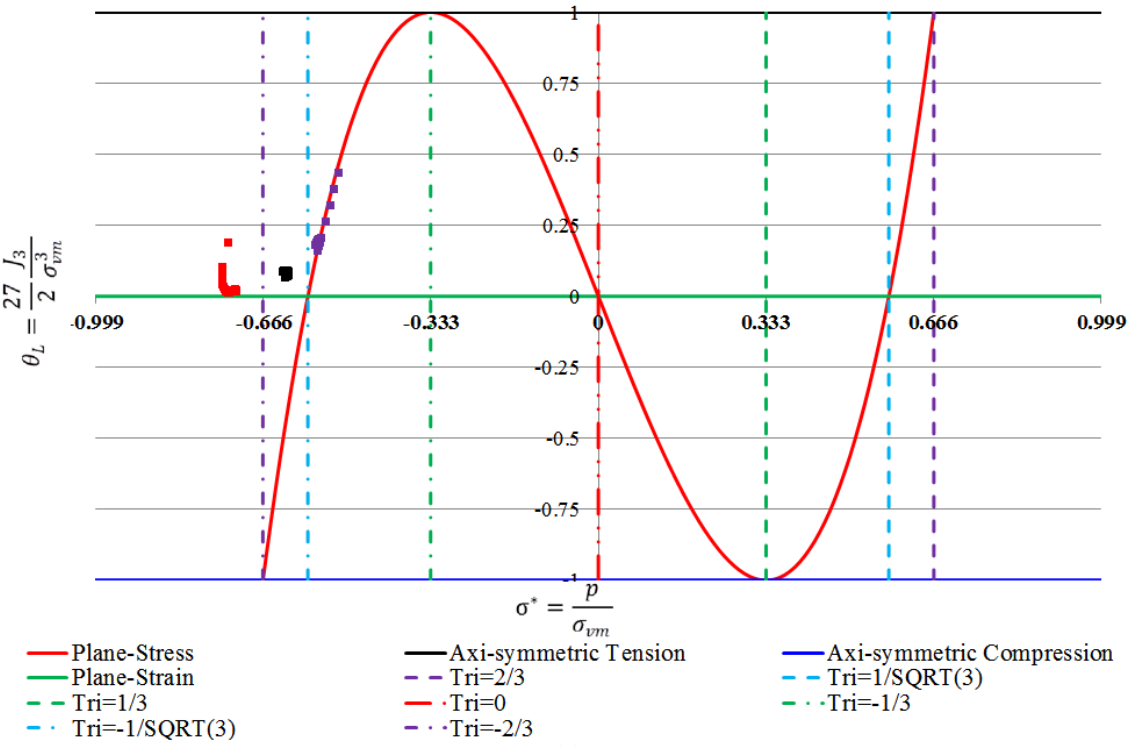

(a)

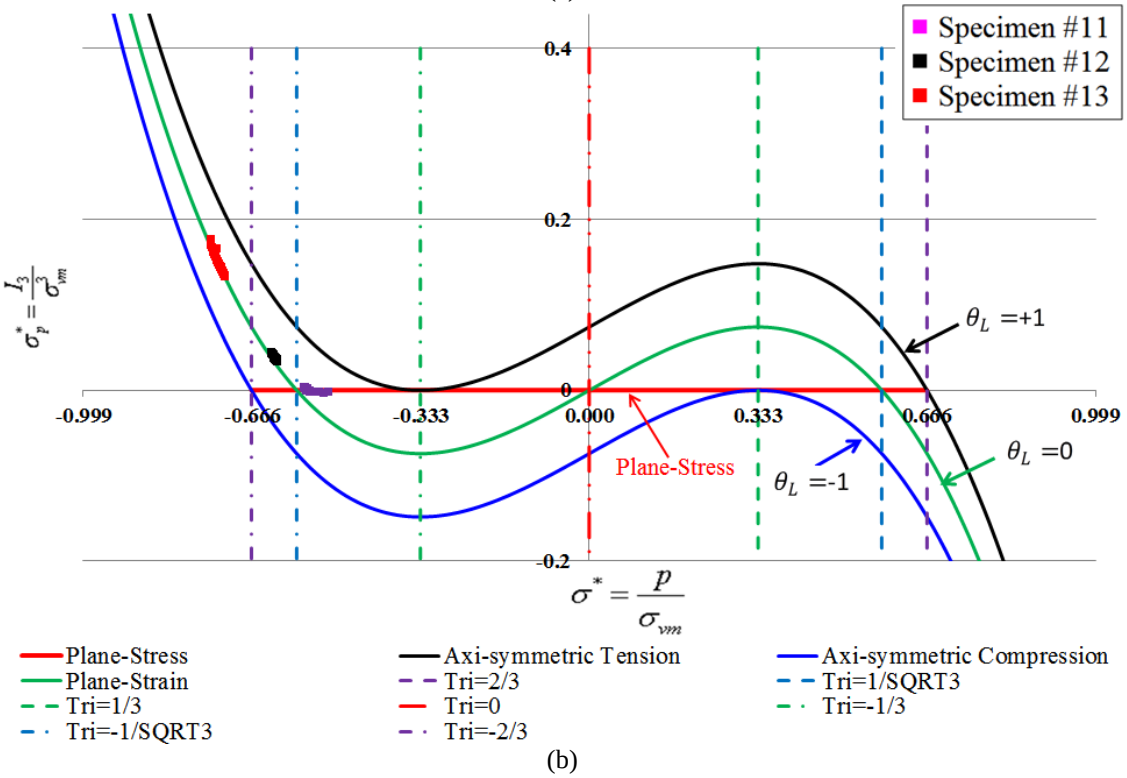

(b)

Figure 5-153: Evolution of the stress-state dependent failure for plane-strain specimens projected on; (a) the plane defined by stress-triaxiality vs. Lode-angle-parameter and (b) the plane defined by stress-triaxiality vs. product-triaxiality.

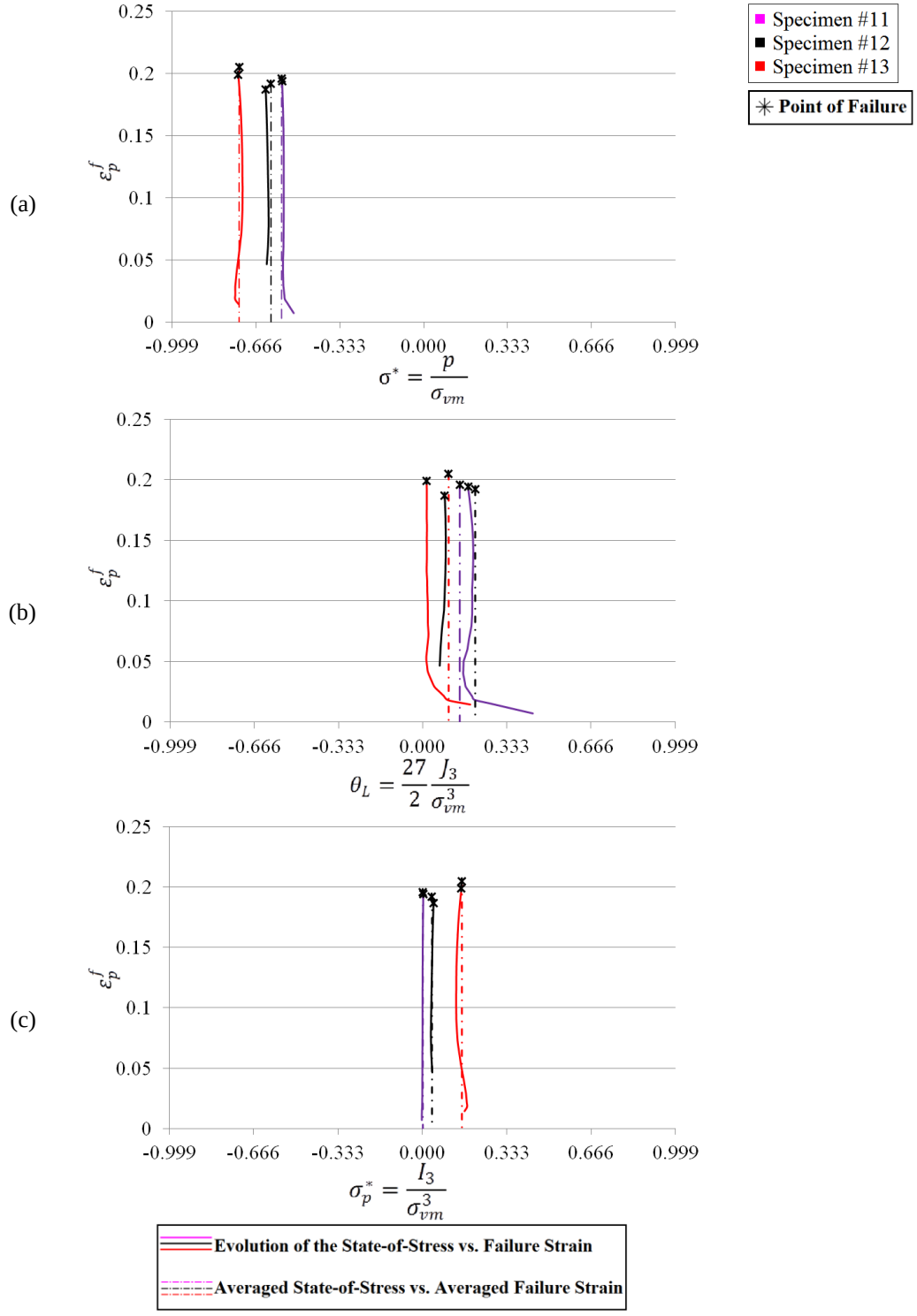

Figure 5-154: Evolution of plastic strain and states-of-stress for plane-strain specimens with averaged values as a function of; (a) stress-triaxiality, (b) Lode-angle-parameter and (c) product-triaxiality.

5.10.4 **Uni-axial compression specimen**

An axi-symmetric uni-axial compression specimen with equal length to diameter ratio is designed in Chapter 4 and illustrated by Figure 5-155. The specimen was tested with the SHLF as shown in Figure 5-24. To minimize the effects of friction and consequently 'barrelling' of the specimen, grease was applied to both loading surfaces [108]. DIC data was not available for this case. Therefore, the total height of the specimen is used as the gauge length. All specimens were tested at quasi-static conditions and at room temperature. Details of the testing are listed in Table 5-30.



Figure 5-155: Uni-axial compression specimen, after [108].

Table 5-30: Test cases for characterization of the quasi-static failure strains at room temperature for uni-axial compression specimens.

Test #	Specimen #	Gauge Length [mm]	Test Apparatus	State-of-Stress and Loading	Initially Targeted			
					Stress-State Values			Strain Rate [s^{-1}]
					σ^*	σ_p^*	θ_L	
6 [Figure C-6]† [Table C-44]‡	14 [Figure B-14]§ 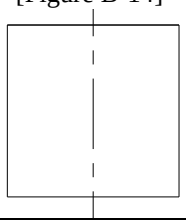	3.048	SHLF*	Uni-axial Compression	$+\frac{1}{3}$	0.0	-1.0	1.0×10^{-2}

* Servo-Hydraulic Loading Frame (SHLF).
† Test results for the corresponding specimen, strain-rate and temperature illustrated in Appendix–C.
‡ Test results for the corresponding specimen, strain-rate and temperature listed in Appendix–C.
§ Detailed geometries and corresponding FE models of the specimens are illustrated in Appendix–B.

The cut-off value for the stress-triaxiality for ductile materials were experimentally found as $\sigma^* = +\frac{1}{3}$ by Bridgman [95] and recently both experimentally and numerically

verified by Bao [99], and Bao and Wierzbicki [100]. Therefore, failure is not assumed for uni-axial compression case. However, in order to verify the stress-states, the force vs. displacement curves are compared for quasi-static uni-axial compression tests at room temperature and the results are illustrated by Figure F-6 in Appendix-F for verification.

The test conditions that are described by Table 5-30 are simulated by using the FE model that is illustrated in Appendix–B with Figure B-14 by using an element characteristic length of 0.15mm at the center of the specimen. In this case no failure is attained. The force vs. displacement curves and the corresponding stress-states are calculated by averaging the states-of-stress until the maximum plastic strain that the simulations are interrupted since no failure is assumed. Figure 5-156 summarizes all state variables on the displacement field for Specimen #14.

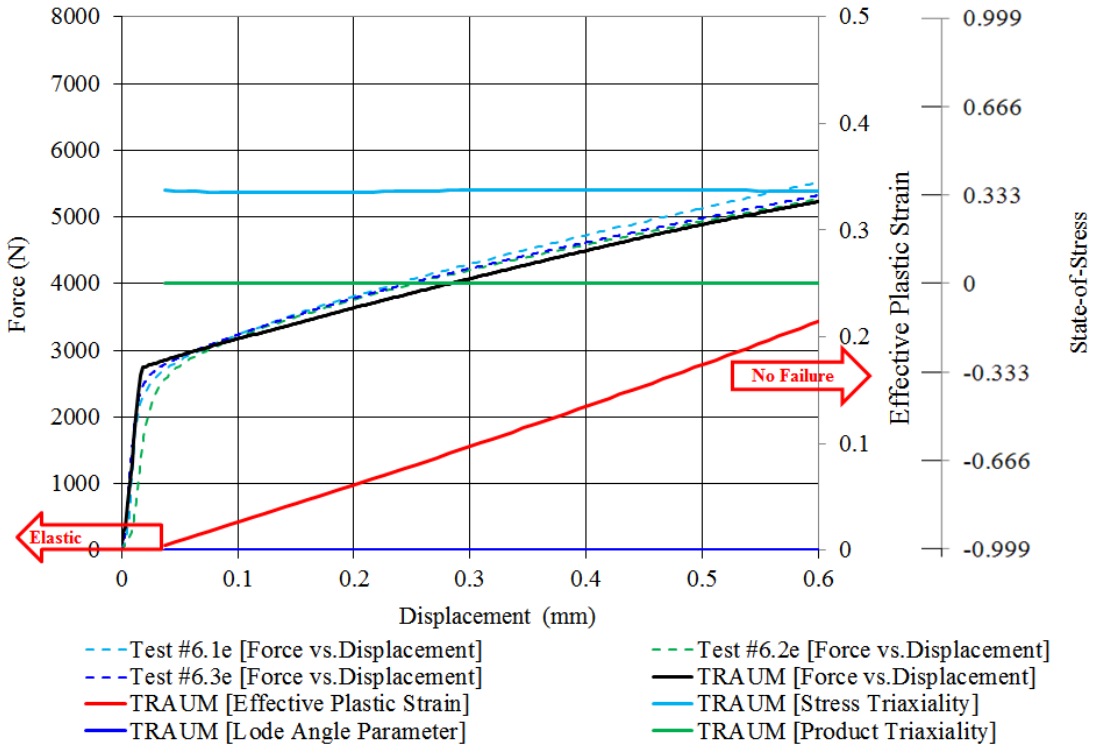

Figure 5-156: Characterization of the stress-states and failure strain for Specimen#14.

The results for the uni-axial compression specimen are summarized in Table 5-31 and since no failure is assumed for this state-of-stress, the plastic strain values at failure are fixed at 100% plastic strain.

Table 5-31: Characterized plastic strains at failure and corresponding stress-states for plane-strain specimens in tension.

Test ‡ #	Specimen Geometry/FE Model*		Plastic Strain at Failure	Calculated Stress-State Values†		
			ε_p^f	σ_{av}^*	$\sigma_{p,av}^*$	$\theta_{L,av}$
6	14 Figure B-14	Min.	1.0	+0.333	0.0	-1.0
		Max.	1.0	+0.333	0.0	-1.0
		Av. **	1.0	+0.333	0.0	-1.0

*Geometries and corresponding FE models of the specimens can be found in Appendix–B.
**Each test is repeated three times and the average represents the arithmetic mean.
‡ Test results can be found in Appendix–C.
† Stress-state values are averaged according to Equation (5.111)

Three dimensional representation of the failure space for compression specimens is illustrated in Figure 5-162 by using the stress-triaxiality, Lode-angle-parameter and product-triaxiality with respect to the plastic strain at failure. The projections of the stress-states are also illustrated in Figures 5-163 and 5-164, where it is shown that the specimens stays within the axi-symmetric compression meridian and the failure strain is so high compared to the other stress-states that it cannot be seen in the same scale plot.

5.10.5 **Shear/torsion specimen**

Using the torque capability of the SHLF, the spool geometry that is shown in Figure 5-157(a) and illustrated in Figure B-15 was tested to obtain a pure shear stress-state [108]. DIC was used to measure the rotational displacements during the experiment, where the location of the DIC gauge length is illustrated in Figure 5-157(b) [108]. The FE model of this specimen is simulated by holding one side of the spool geometry and applying a rotational velocity to the other side while leaving the nodes free to move on the axial direction. For this specimen, moment vs. rotation behavior is used to find the applicable failure strain. The moment is calculated through the critical cross-section of the specimen, which is assumed to be in the middle of the spool gauge length. The test conditions are listed in Table 5-32.

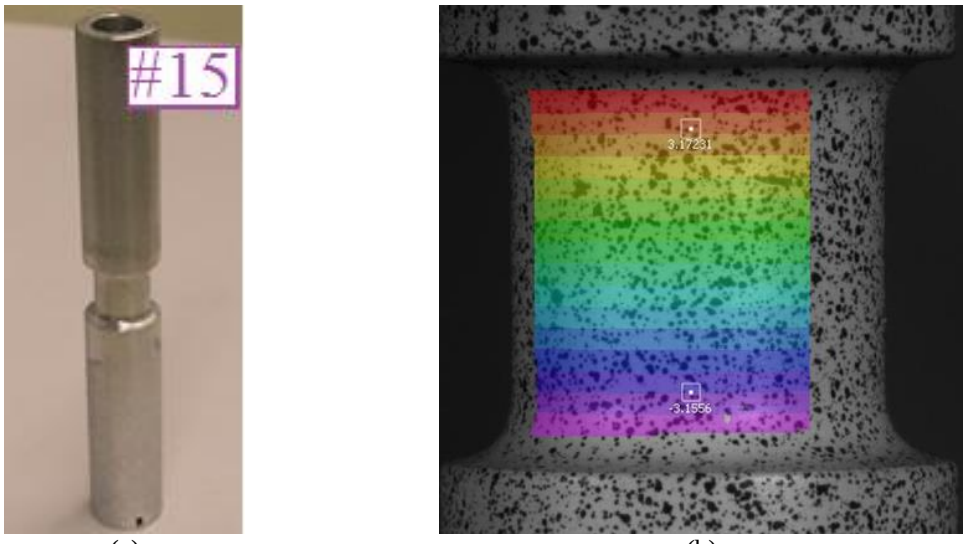

(a) (b)

Figure 5-157: Torsion specimen; (a) spools shaped specimen geometry for torsion and (b) position of the DIC gauge length for torsion specimen, after [108].

Table 5-32: Test cases for characterization of the quasi-static failure strains at room temperature for torsion specimens.

Test #	Specimen #	DIC Gauge Length [mm]	Test Apparatus	State-of-Stress and Loading	Initially Targeted			
					Stress-State Values			Strain Rate [s^{-1}]
					σ^*	σ_p^*	θ_L	
8 [Figure C-8]† [Table C-45] ‡	15 [Figure B-15]§ 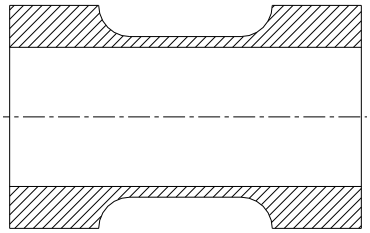	6.35	SHLF*	Torsion	0.0	0.0	0.0	1.0

* Servo-Hydraulic Loading Frame (SHLF).
† Test results for the corresponding specimen, strain-rate and temperature illustrated in Appendix–C.
‡ Test results for the corresponding specimen, strain-rate and temperature listed in Appendix–C.
§ Detailed geometries and corresponding FE models of the specimens are illustrated in Appendix–B.

Moment vs. rotation curve and the corresponding stress-states are calculated by using the FE that is shown in Figure B-15. Figure 5-158 summarizes all state variables as a function of rotation for Specimen #15. Although maximum rotation at failure is predicted exactly and the plastic strain at failure is characterized, it is observed from Figure 5-158 that the moment level prediction is slightly higher. Considering that most ductile metals

assumed to behave according to von Mises plasticity, TRAUM is formulated by implementing the J_2 flow rule. Therefore, the plasticity algorithm assumes a perfect ellipse on the invariant space. However, some materials, especially cold rolled materials may not necessarily behave according to J_2 flow theory. Therefore, a higher order yield criteria may be required. It is also reported by Seidt that Al2024-T351 has anisotropic behavior [108]. Since the manufactured surfaces of the spool geometry lies within the two orthogonal axes of the plate as illustrated in Figure 5-2, different behavior can be explained by presence of anisotropy. On the other hand, the predictive capability of this particular test is within the repeatability of the test results as illustrated by Figures 5-158 and C-8, where almost 80-85% difference in the plastic strain at failure was observed between the test results. Moreover, repeatability of the moment levels during the test results show that the numerical predictions still present adequate results for the shear dominant deformation even by using von Mises plasticity as the yield criterion.

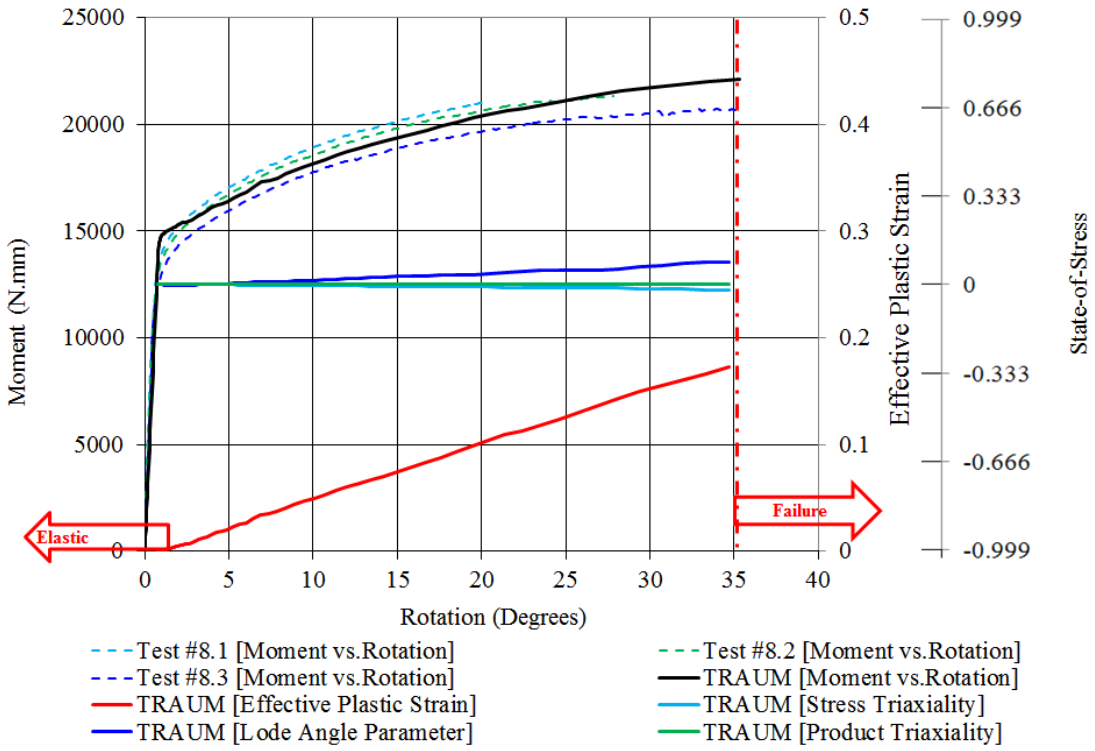

Figure 5-158: Characterization of the stress-states and failure strain for Specimen #15.

The overall results for pure-shear specimens are summarized in Table 5-33, where the averaged stress-states and the mean for the failure strain can be found for the corresponding states-of-stress.

Table 5-33: Characterized plastic strains at failure and corresponding stress-states for torsion specimens.

Test ‡ #	Specimen Geometry/FE Model*		Plastic Strain at Failure	Calculated Stress-State Values†		
			ε_p^f	σ_{av}^*	$\sigma_{p,av}^*$	$\theta_{L,av}$
8	15 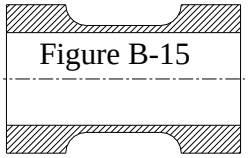	Min.	0.179	0.0	0.0	0.0
		Max.	0.184	0.0	0.01	0.05
		Av. **	0.181	0.0	0.01	0.04

*Geometries and corresponding FE models of the specimens can be found in Appendix–B.
**Each test is repeated three times and the average represents the arithmetic mean.
‡ Test results can be found in Appendix–C.
† Stress-state values are averaged according to Equation (5.111)

Three dimensional representation of the failure space for torsion specimens is illustrated in Figure 5-162 by using the stress-triaxiality, Lode-angle-parameter and product-triaxiality with respect to the plastic strain at failure. The projections of the stress-states are also illustrated in Figures 5-163 and 5-164, where pure shear behavior is accurately obtained for the central element that is in the middle of the gauge section of the spool geometry.

5.10.6 **Combined tension/torsion specimens**

Two combined tension/torsion specimens are designed to match the Lode-angle-parameters of the two intermediate notched plane-stress specimens that are designed in Chapter 4. These specimens share the same geometry as illustrated in Figure 5-159(a) and the required stress-state is achieved by controlling tension/torsion proportions of the loading. All specimens were tested at quasi-static conditions and at room temperature. Details of the testing are listed in Table 5-34. DIC was utilized to measure the displacement fields and SHLF was used for testing [108]. DIC gauge length is illustrated on the spool geometry in Figure 5-159(b), where both vertical and rotational displacements were tracked for the corresponding points that are defining the virtual

extensometer on the specimen. Details of the combined tension/torsion testing and specimen dimensions can be found in Appendix-C.

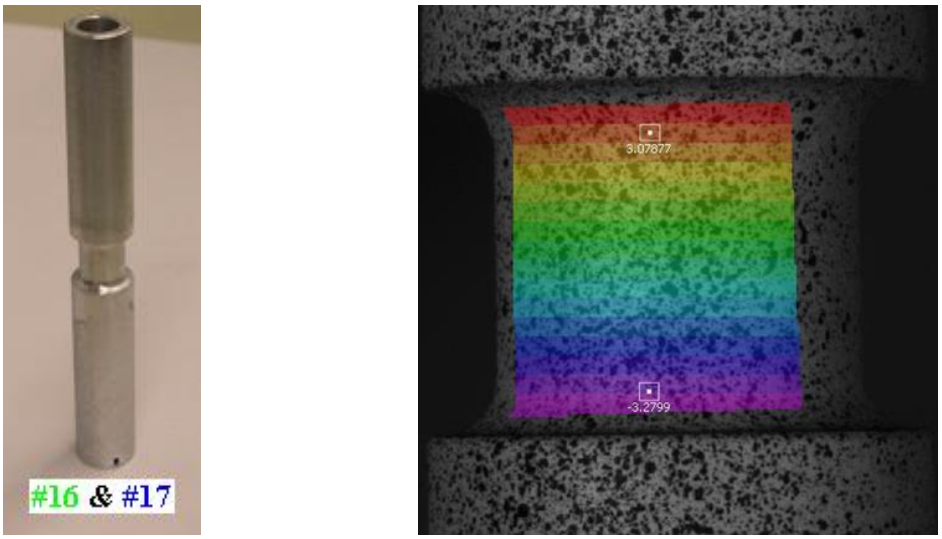

(a) (b)

Figure 5-159: Combined tension/torsion specimen; (a) spools shaped specimen geometry and (b) position of the initial DIC gauge length for combined tension/torsion specimen, after [108].

Table 5-34: Test cases for characterization of the quasi-static failure strains at room temperature for combined tension/torsion specimens.

Test #	Specimen #	DIC Gauge Length [mm]	Test Apparatus	State-of-Stress and Loading	Initially Targeted				
					Stress-State Values				Strain Rate
					$\frac{\sigma_x}{\tau_{xy}}$	σ^*	σ_p^*	θ_L	[s^{-1}]
44 [Figure C-42]† [Table C-46]‡	16 [Figure B-15]§ 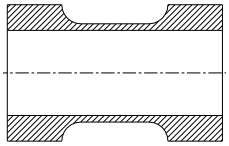	6.35	SHLF*	Combined Tension/ Torsion	1.973	-0.2505	0.0	0.915	1.0
45 [Figure C-43]† [Table C-47]‡	17 [Figure B-15]§ 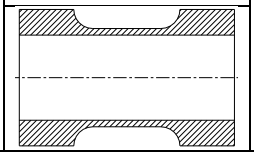				0.848	-0.1466	0.0	0.617	

* Servo-Hydraulic Loading Frame (SHLF).
† Test results for the corresponding specimen, strain-rate and temperature illustrated in Appendix–C.
‡ Test results for the corresponding specimen, strain-rate and temperature listed in Appendix–C.
§ Detailed geometries and corresponding FE models of the specimens are illustrated in Appendix–B.

Figure 5-160 and 5-161 summarizes the evolution of the state variables (i.e., ε_p^f, σ^*, σ_p^* and θ_L) for the displacement and rotation field that are measured for Specimen #16 and Specimen #17. The figures illustrate only one set of characterized stress-states for brevity. Repetitive analyses are performed for the conditions that are listed in Table 5-34. The same characterization procedure is applied for all three tests that are also illustrated in Figures 5-160 and 5-161 to find the limits and an averaged value for the state variables. Averaged stress-states and the mean of the failure strains are summarized by Table 5-35.

Table 5-35: Characterized plastic strains at failure and corresponding stress-states for torsion specimens.

Test ‡ #	Specimen Geometry/FE Model*		Plastic Strain at Failure	Calculated Stress-State Values†			
			ε_p^f	$\frac{\sigma_x}{\tau_{xy}}$	σ_{av}^*	$\sigma_{p,av}^*$	$\theta_{L,av}$
44	16 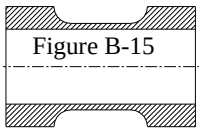	Min.	0.179	2.5	-0.2761	0.0	0.9418
		Max.	0.197	2.7	-0.2842	0.0	0.9583
		Av. **	0.182	2.5867	-0.28398	0.0	0.949661
45	17 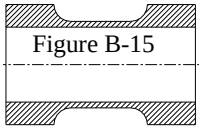	Min.	0.1931	1.14	-0.1732	0.0	0.7247
		Max.	0.212	1.17	-0.1833	0.0	0.7416
		Av. **	0.19879	1.1567	-0.175451	0.0	0.72515

*Geometries and corresponding FE models of the specimens can be found in Appendix–B.
**Each test is repeated three times and the average represents the arithmetic mean.
‡ Test results can be found in Appendix–C.
† Stress-state values are averaged according to Equation (5.111)

Three dimensional representation of the failure space for combined loading specimens is illustrated in Figure 5-162 by using the stress-triaxiality, Lode-angle-parameter and product-triaxiality with respect to the plastic strain at failure. It can be seen that these specimens follow the plane-stress meridian as initially targeted for 'bridging' with the two intermediate notched plane-stress specimens sharing the same Lode-angle-parameter or meridian.

The projections of the stress-states are also illustrated in Figures 5-163 and 5-164, where the transition of the state-of-stress can clearly be observed from uni-axial tension towards pure shear.

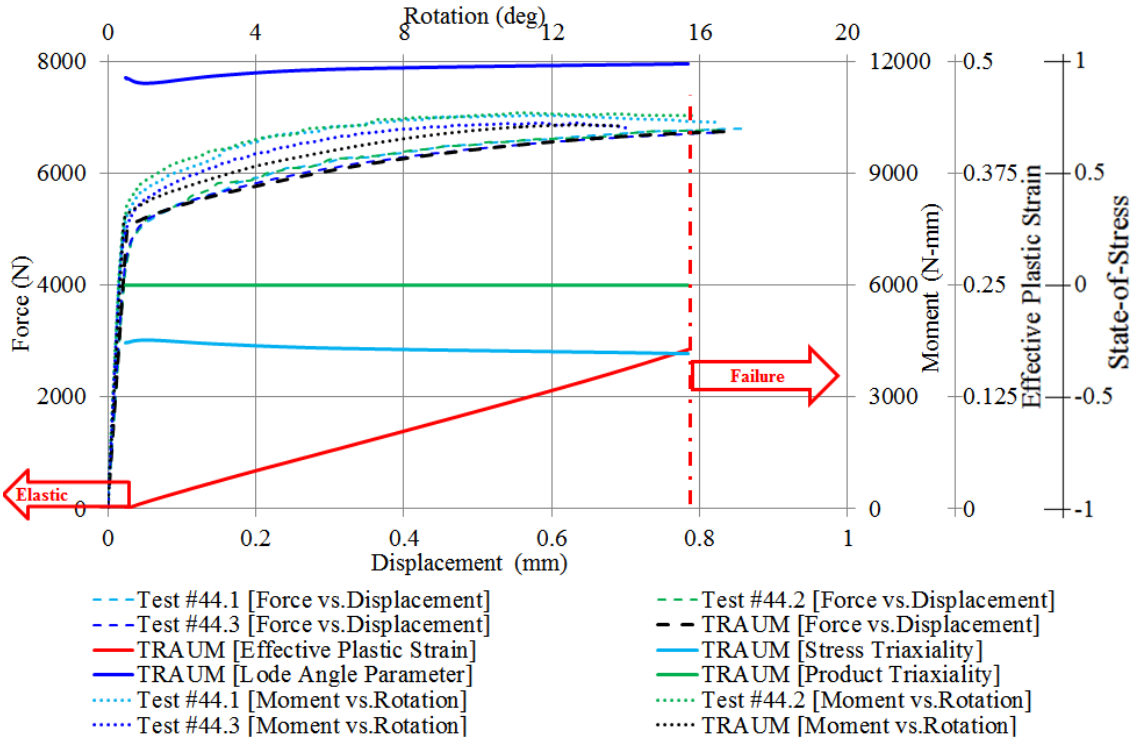

Figure 5-160: Characterization of the stress-states and failure strain for Specimen #16.

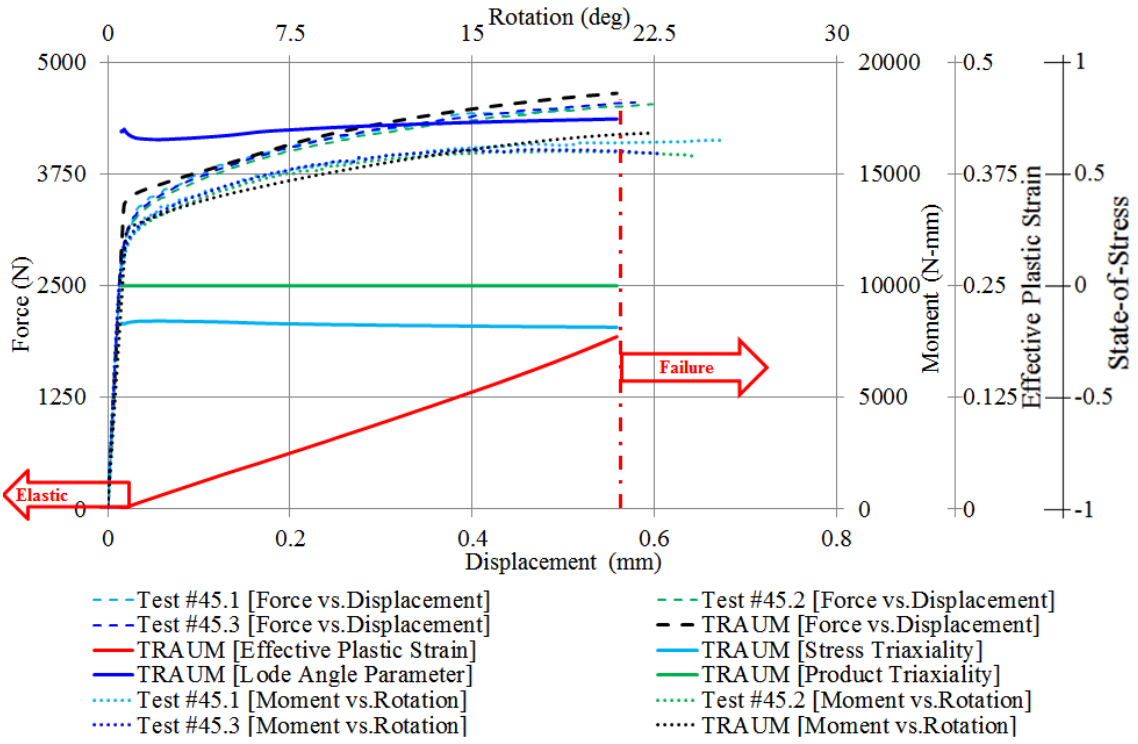

Figure 5-161: Characterization of the stress-states and failure strain for Specimen #17.

It should be noted that different stress-states for the combined loading specimens are achieved by using different proportions of loading as described in Section 4.4.4.6 by Figure 4-65. Therefore, small changes during the loading (i.e., profile of loading) can slightly change the targeted stress-states.

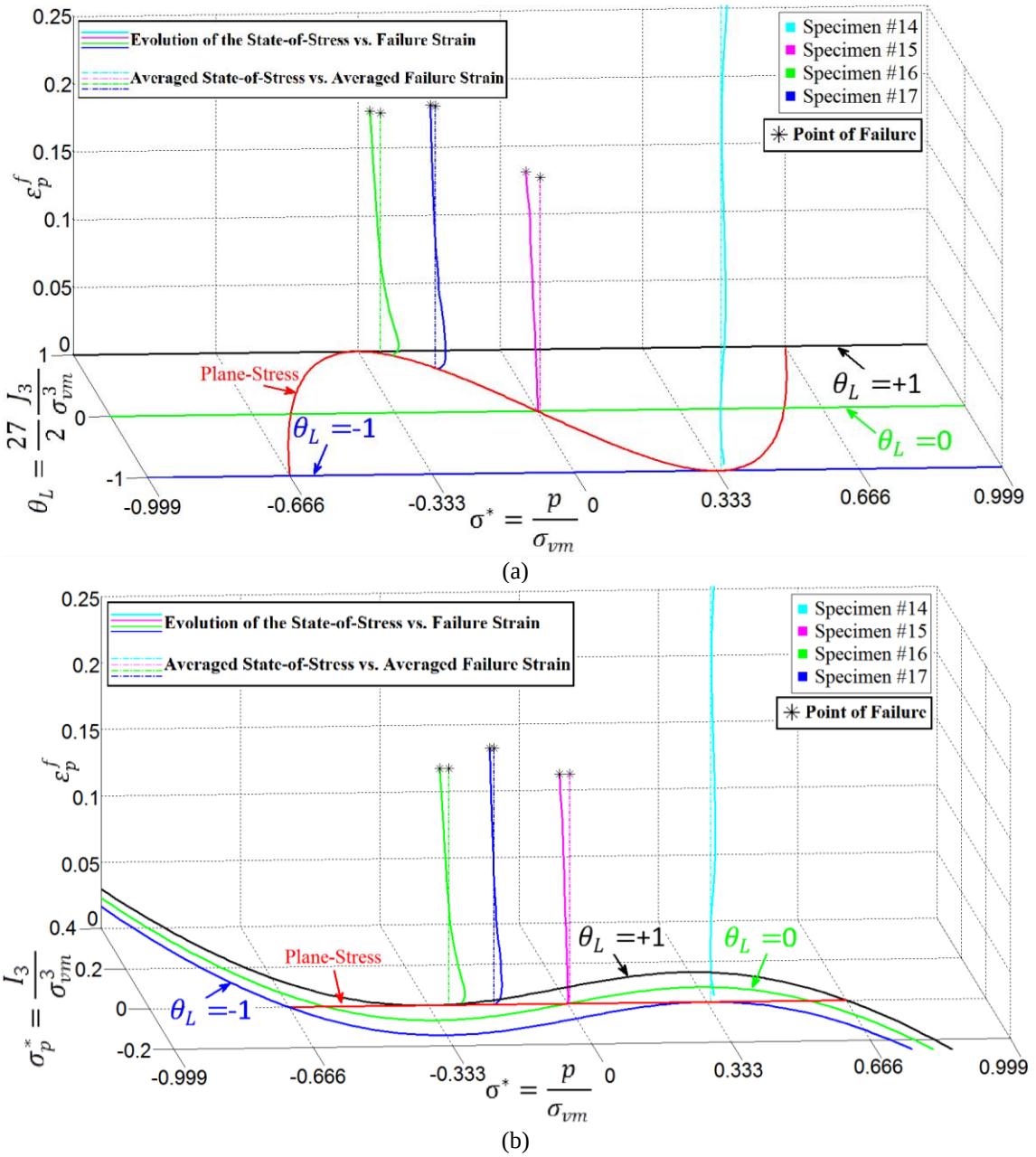

Figure 5-162: Evolution of the stress-state dependent failure in three dimensional failure space for uni-axial compression, torsion and combined tension/torsion specimens represented by; (a) the space defined by stress-triaxiality vs. Lode-angle-parameter and (b) the space defined by stress-triaxiality vs. product-triaxiality.

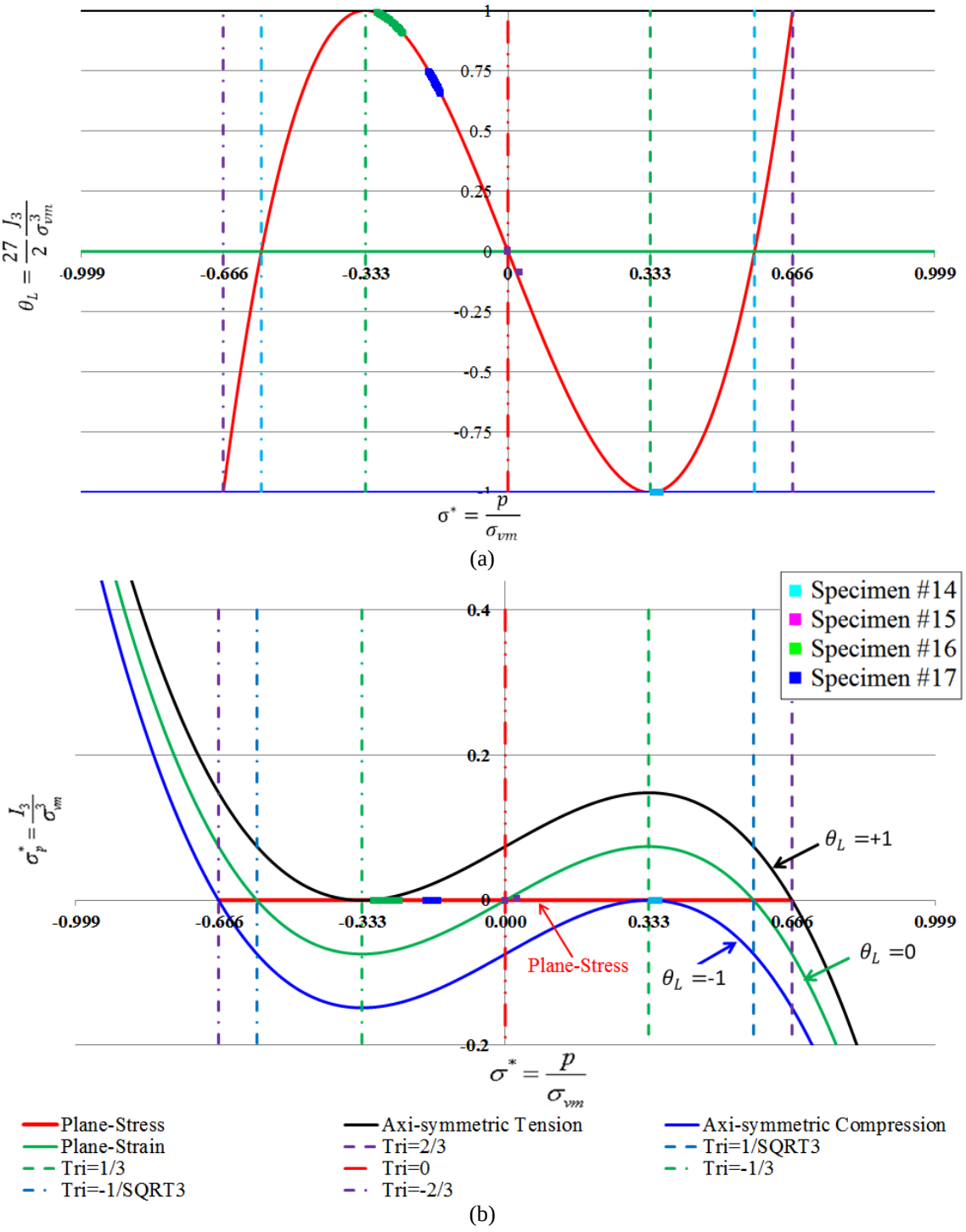

Figure 5-163: Evolution of the stress-state dependent failure for uni-axial compression, torsion and combined tension/torsion specimens projected on; (a) the plane defined by stress-triaxiality vs. Lode-angle-parameter and (b) the plane defined by stress-triaxiality vs. product-triaxiality.

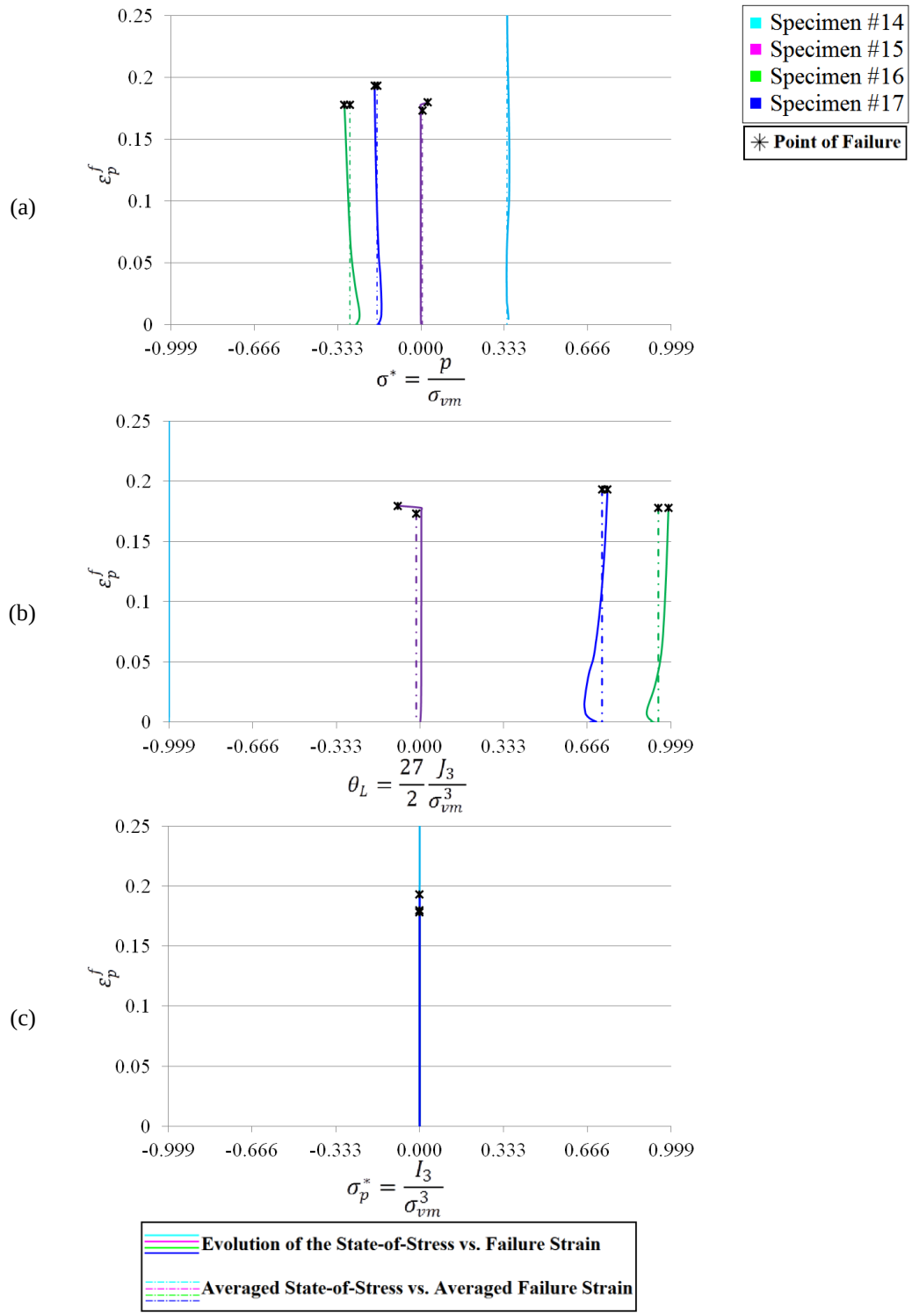

Figure 5-164: Evolution of plastic strain and states-of-stress for uni-axial compression, torsion and combined tension/torsion specimens with averaged values as a function of; (a) stress-triaxiality, (b) Lode-angle-parameter and (c) product-triaxiality.

5.10.7 **Punch test specimens**

Three punch shapes are designed in Section 4.4.4.7 to obtain states-of-stress that are similar to and often expected to occur during a ballistic impacts as illustrated by Figure 4-21 [107]. These punch geometries are designed with different nose shapes that can initiate different failure modes on a disk like 1.473mm thick specimen as the interaction between the two evolves from plane-strain to equi-biaxial and in the case of the blunt nose, pure shear. It should be noted that during the punch tests the 'specimen' indicates the shape of the punch but not the disk, which is primarily a disk as illustrated in Figures B16- B-18. SHLF and the load cell was used for testing the material at low rates, where DIC was utilized to measure the displacement off the punch as it is moving inside the specimen assembly as illustrated in Figure 5-165 [108] [384]. Details of the testing are listed by Table 5-26 for quasi-static conditions and room temperature.

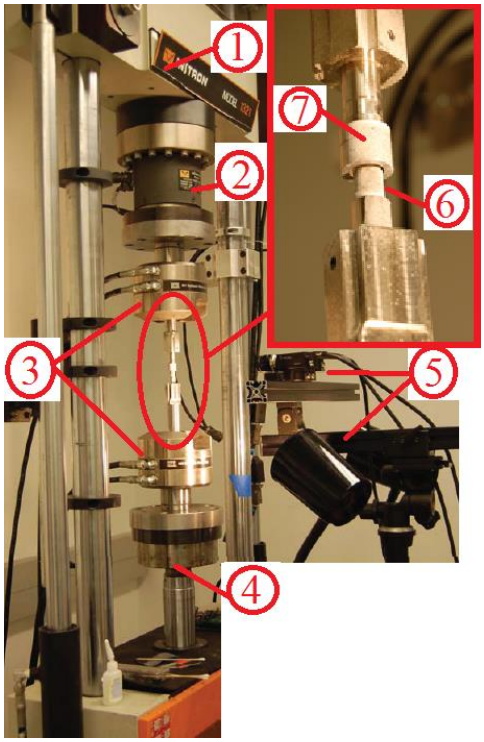

1: Servo-Hydraulic Loading Frame (SHLF)
2: Load Cell
3: Hydraulic Grips
4: Actuator
5: DIC-Binocular Cameras and Lighting
6: Punch
7: Specimen Assembly

Figure 5-165: Quasi-static punch testing apparatus by SHLF and DIC set-up, modified after [384].

Table 5-36: Test cases for characterization of the quasi-static failure strains at room temperature for punch test specimens.

Test #	Specimen #	Test Apparatus	State-of-Stress and Loading	Initially Targeted			
				Stress-State Values			Actuator Velocity [mms^{-1}]
				σ^*	σ_p^*	θ_L	
46 [Figure C-44]† [Table C-48]‡	18 [Figure B-16]§ 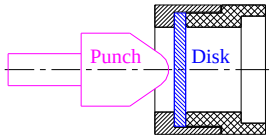	SHLF*	Plane-Strain	$-\frac{1}{\sqrt{3}}$	0.0741	-1.0	0.233
47 [Figure C-44]† [Table C-48]‡	19 [Figure B-17]§ 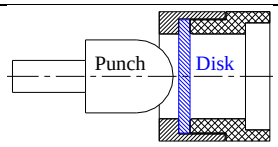		Equi-Biaxial	$-\frac{2}{3}$	0.0	-1.0	
48 [Figure C-44]† [Table C-48]‡	20 [Figure B-18]§ 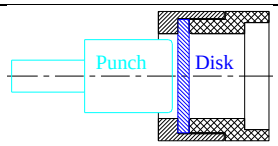		Shear	0.0	0.0	0.0	

* Servo-Hydraulic Loading Frame (SHLF).
† Test results for the corresponding specimen, strain-rate and temperature illustrated in Appendix–C.
‡ Test results for the corresponding specimen, strain-rate and temperature listed in Appendix–C.
§ Detailed geometries and corresponding FE models of the specimens are illustrated in Appendix–B.

Figure 5-166 illustrates the characterization of the failure strain with respect to the evolution of the states-of-stress over the displacement field for Specimen #18. The failure strain is found for the corresponding plastic strain that matches the force vs. displacement curve of the specific test result. It is clearly seen that the stress-states remain stable during the test until the failure even though the force response of the FE model globally exhibits oscillations due to the contact that is defined between the disk and the punch. It should be noted that the punch and the rest of the specimen assembly fixture are assumed to be rigid during the simulations. The disk material is assumed to be free inside the assembly. However, during the test the small disk was epoxied to the internal boundaries of the fixture. Figure 5-167 illustrates the states-of-stress at the time of failure and after the failure occurred with the characterization of the failure strain at the same time. It should be noted that the rest of the specimen assembly is hidden and only half of the punch

geometry is shown in transparent for better illustration. The specimen is also not shown in complete size to limit the area of interest within the vicinity of initial failure and characterization. The results clearly show that the material is experiencing the stress-states that are very close to the targeted values, which are given in Table 5-36. The results are also quantitatively supported by Figure 5-166, where the effective plastic strain at failure can clearly be identified with the corresponding states-of-stress while the rest of the model is also verified that the force vs. displacement behaviors are coincident.

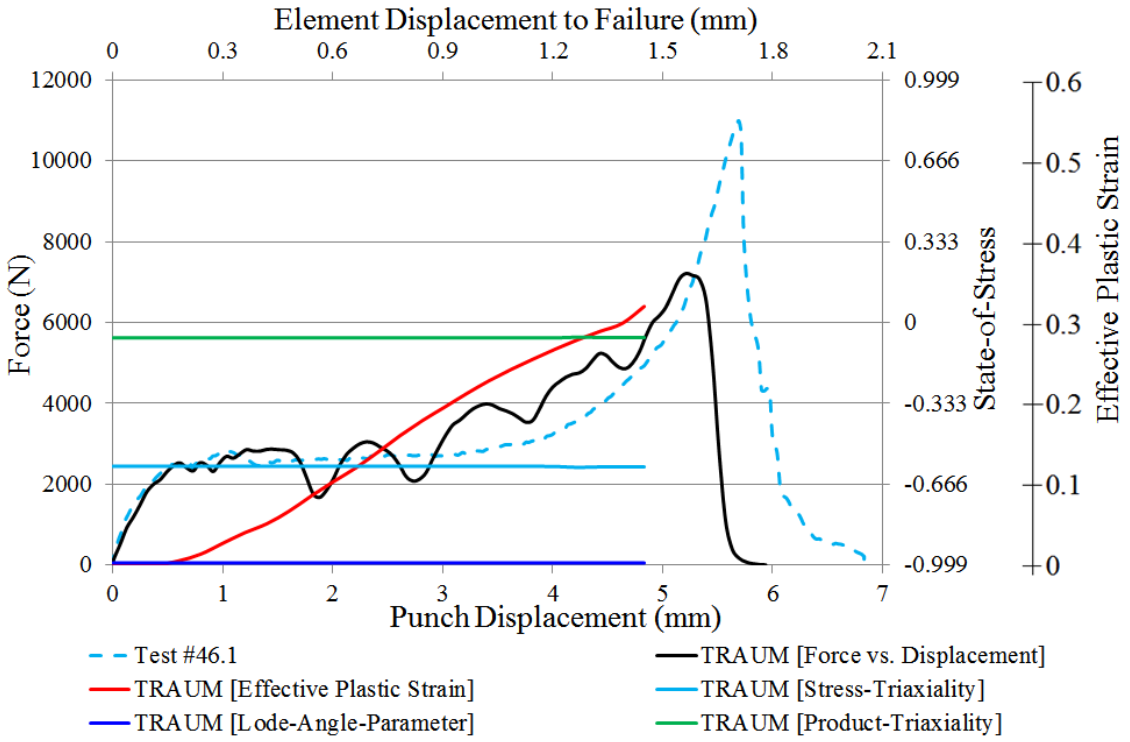

Figure 5-166: Characterization of the stress-states and failure strain for Specimen #18.

Similar methodology is applied for Tests #47.1 and #48.1 correspondingly to identify the failure strain at the representative elements on the specimen. The results of the characterization of the failure strains are illustrated in Figures H-11 and H-12 for Tests #47.1 and #48.1, respectively. It is shown that quasi-static deformation process of the punch test successfully exhibit the stress-states that are required to build the 'bridging' between the corresponding plane-stress, plane-strain and axi-symmetric states. The results of the states-of-stress and the failure strains are summarized in Table 5-37.

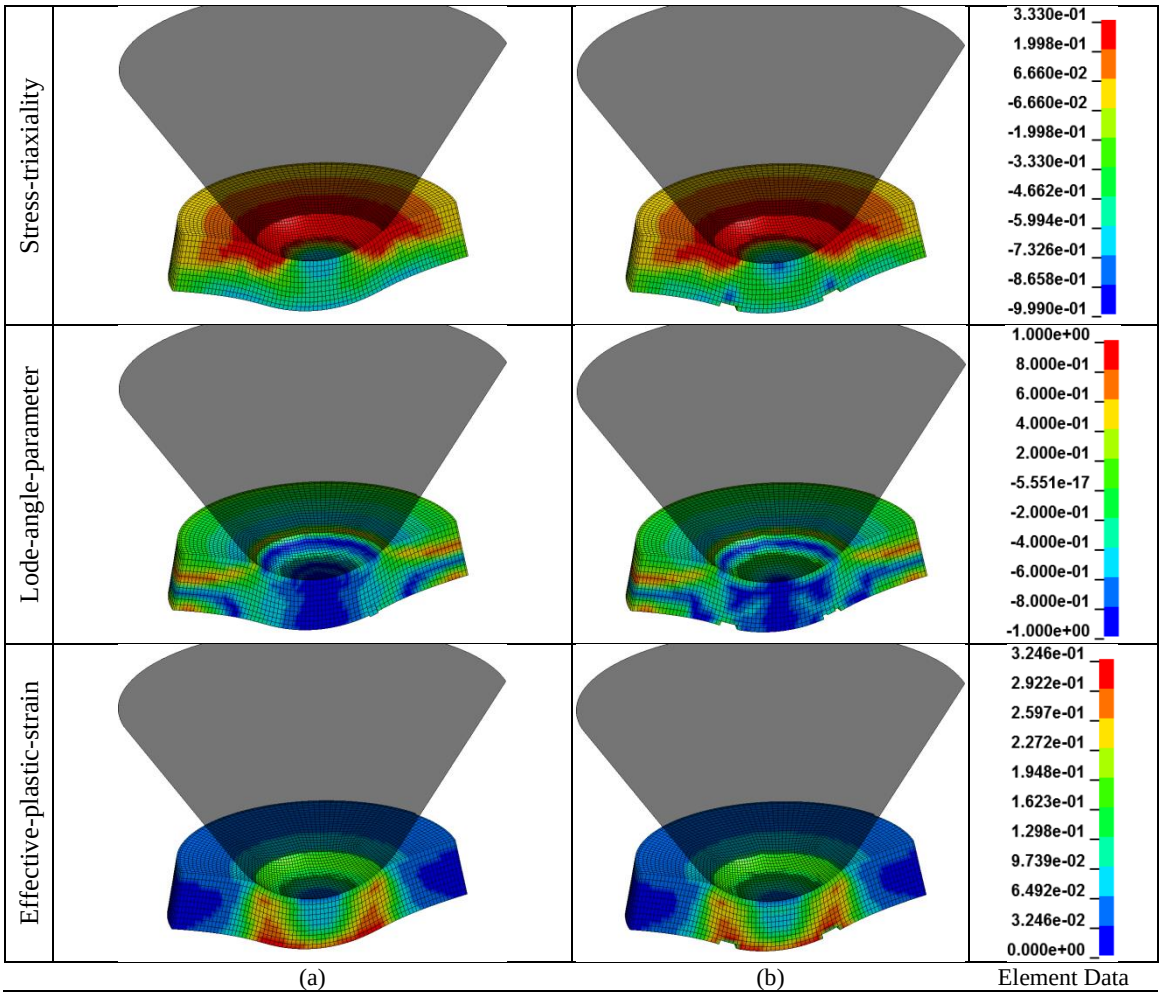

Figure 5-167: Characterization of the stress-states and failure strain for Specimen #18; (a) just before failure and (b) after the initial failure.

Since each quasi-static punch test was performed only once, the failure strains that are found by the characterization are directly used for the corresponding states-of-stress. Although, punch tests are considered relatively more complicated tests, where there are risks of compliance with the testing apparatus and fixture, the results suggest otherwise as the evolution of the flow and failure are observed to be rather stable and consistent. Due to the dynamics of the testing, better correlations can be achieved on the force vs. deflection characteristics if the uncertainties were known in more detail such as the specimen-adhesive-fixture interaction, friction and misalignment.

Table 5-37: Characterized plastic strains at failure and corresponding stress-states for punch test specimens.

Test ‡ #	Specimen Geometry/FE Model*	Plastic Strain at Failure	Calculated Stress-State Values		
		ε_p^f	σ_{av}^*	$\sigma_{p,av}^*$	$\theta_{L,av}$
38	18 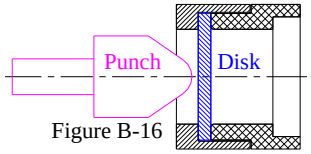 Figure B-16	0.32	-0.5919	-0.0632	-0.9903
39	19 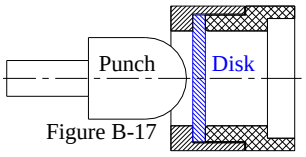 Figure B-17	0.3312	-0.6669	0.0008	-0.9940
40	20 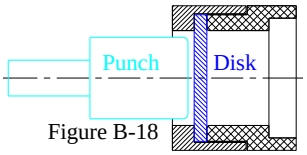 Figure B-18	0.2003	0.0133	0.0038	-0.0090

*Geometries and corresponding FE models of the specimens can be found in Appendix–B.
‡ Test results can be found in Appendix–C.

When the histories of the stress-states are projected on the planes defined by Lode-angle-parameter vs. stress-triaxiality as in Figure 5-168(a) and product-triaxiality vs. stress-triaxiality as in Figure 5-168(b), it is seen that the targeted stress-states are successfully achieved. The evolution of the states-of-stress that is represented by the node clouds in Figure 5-168 suggests that punch tests can be utilized for testing biaxial and compression meridians with a convenient testing apparatus, where the ballistic impact related stress-states can be obtained in a controlled manner when restricted options are also applied [108]. However, it should be noted that different elements that are selected through the thickness of the disk specimen for the punch tests can carry different histories, which are not as consistent as the central elements that are used during the characterization of the uni-axial tests.

As the quasi-static characterization of the failure strains for the specimens that are designed in Chapter 4 for 'bridging' is complete, the failure surface can be constructed over the space defined by the states-of-stress and plastic strain at failure according to Figure 5-3.

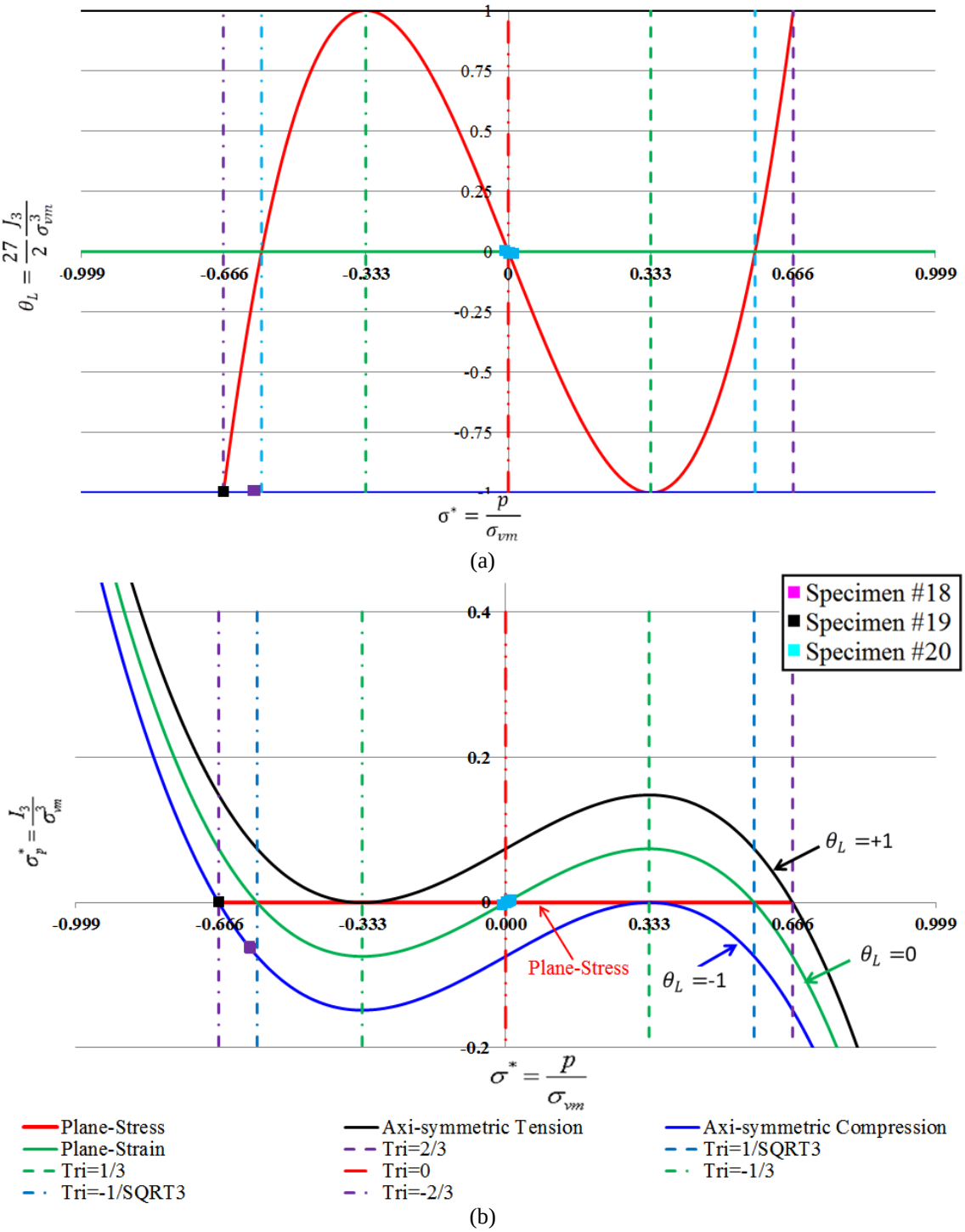

Figure 5-168: Evolution of the stress-state dependent failure for punch test specimens projected on; (a) the plane defined by stress-triaxiality vs. Lode-angle-parameter and (b) the plane defined by stress-triaxiality vs. product-triaxiality.

5.11 **Construction of the failure surface for quasi-static conditions and room temperature**

It should be noted that initially targeted states-of-stress for the specimens that are designed in Chapter 4 are no longer accountable, and before constructing a failure surface corresponding modifications on each 'bridging' point is desirable. A reassessment of the stress-states for each specimen can be performed by using the averaged values of the states-of-stress that are calculated in Section 5.10. Figure 5-169 illustrates the stress-states of the specimens after incorporating the newly characterized flow surface for Al2024-T351 simulations with TRAUM. The stress-states are in good agreement with the initially designed stress-space that is illustrated by Figure 4-75 after newly characterized flow surface is utilized. It is also shown that the stress-states span the entire space with a good resolution and cover the representative states-of-stress that this dissertation is focused on as illustrated by Figure 4-25. Therefore it can be concluded that the calculated stress-states in Section 5.10 can be used for 'bridging' and constructing the failure surface.

The distribution of the averaged values and the limits states-of-stress with the characterized mean values and limits of the failure strains can be illustrated on the plane defined by plastic strain at failure vs. stress-triaxiality as in Figure 5-170. It should be noted that since a failure strain of 100% is assumed for compression specimen (i.e., Specimen # 14), it is not shown on the scale that is used with this figure. Figure 5-170 also suggests that stress-triaxiality is the most significant way of representing states-of-stress since all stress-states can be represented on this scale without any bias on any specific state. Figure 5-171 illustrates the same distribution on a plane defined by plastic strain at failure vs. Lode-angle parameter. The figure clearly suggests that the axi-symmetric meridians cannot be represented with an equally sensitive fashion but a linear function if the Lode-angle-parameter was the only state variable considered to represent the space of stress-state. On the other hand, Lode-angle-parameter presents an opportunity to represent plane-stress meridian with higher accuracy and can be preferred for simulating sheet metal applications of ductile failure. Figure 5-172 illustrates the distribution of stress-space and failure strain on a plane defined by plastic strain at failure vs. product-triaxiality.

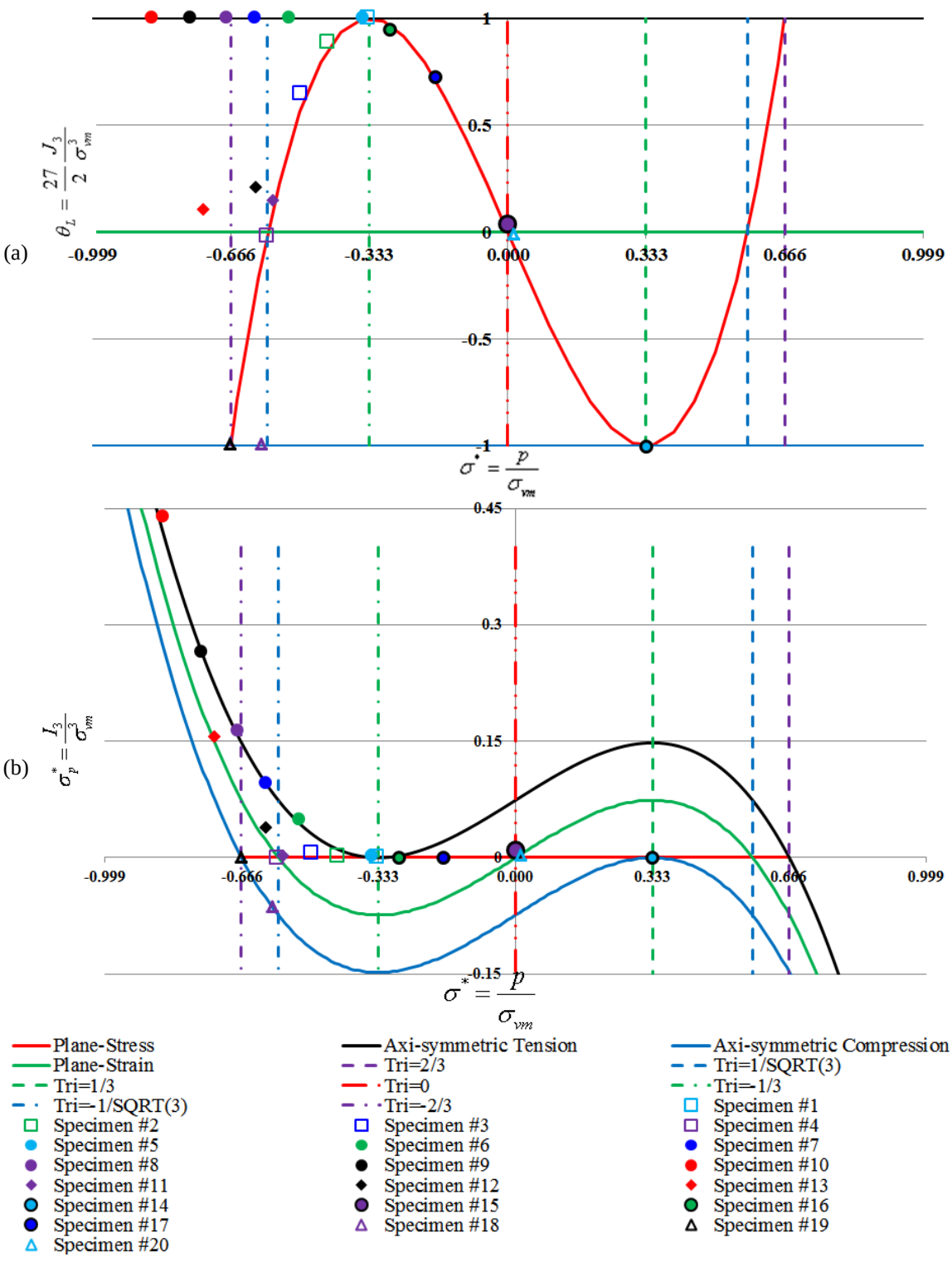

Figure 5-169: Overview of the test program after characterized flow surface is attained for the calculation of the targeted states-of-stress for each specimen on the plane defined by; (a) stress-triaxiality vs. Lode-angle-parameter and (b) stress-triaxiality vs. product-triaxiality.

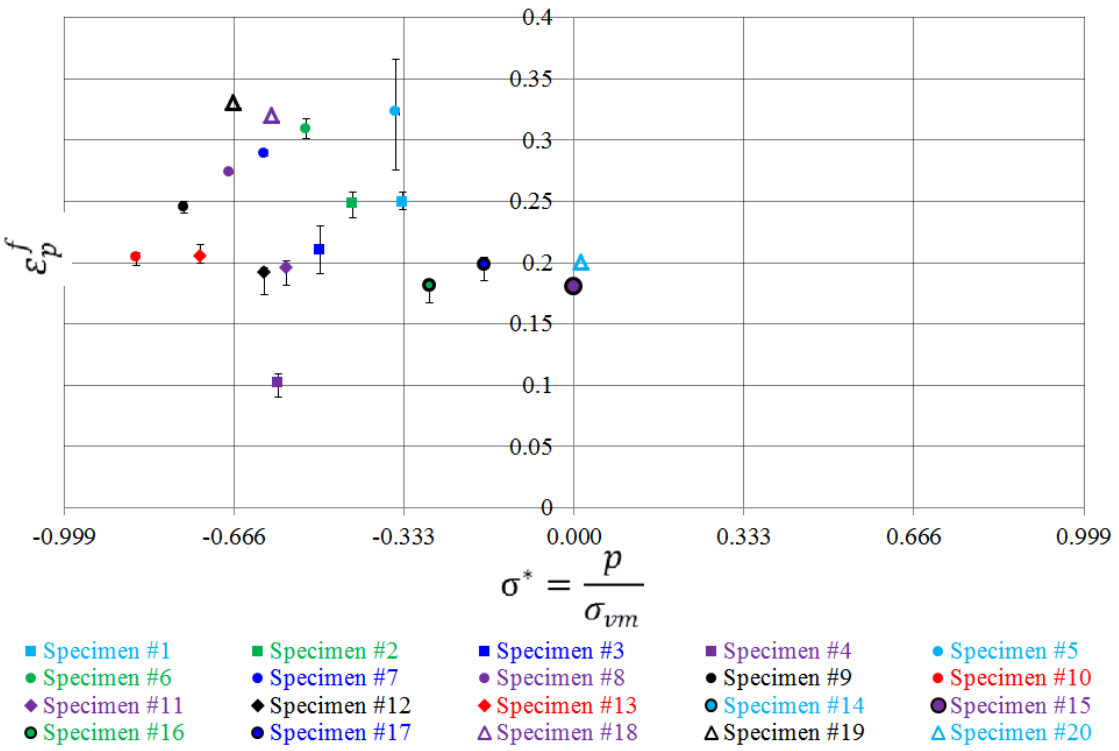

Figure 5-170: Stress-state dependent failure strains and their limits on the plane defined by stress-triaxiality vs. plastic strain at failure.

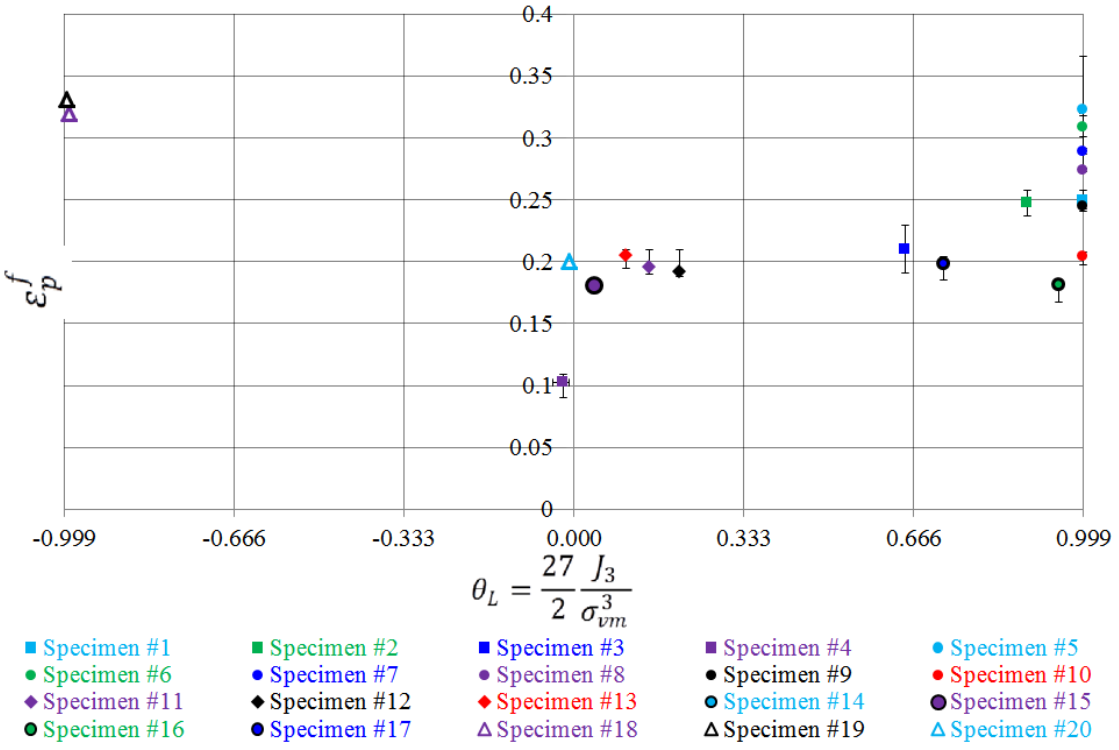

Figure 5-171: Stress-state dependent failure strains and their limits on the plane defined by Lode-angle-parameter vs. plastic strain at failure.

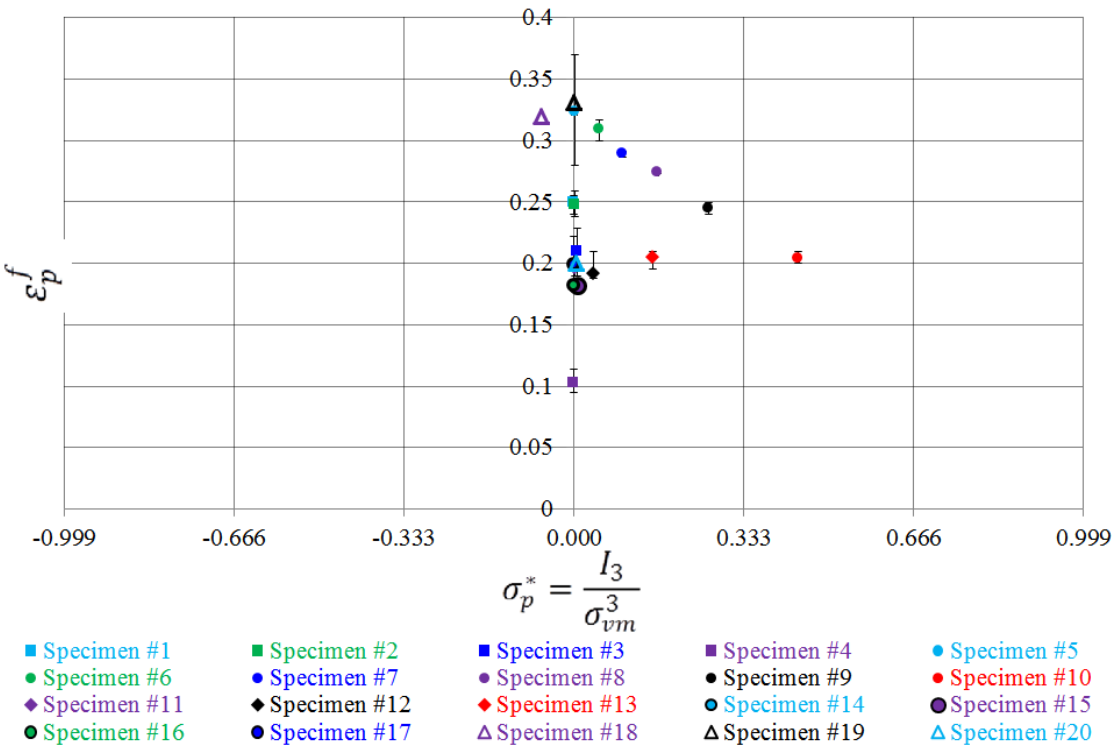

Figure 5-172: stress-state dependent failure strains and their limits on the plane defined by product-triaxiality vs. plastic strain at failure.

The figure suggests that the axi-symmetric meridians are represented with higher accuracy compared to the plane-stress meridian. Especially for the case of axi-symmetric tension, where there are more specimens to define the meridian with, a high order representation of the relation can be possible. Therefore, it is advisable to utilize product-triaxiality for the applications; where multi-axial state-of-stress is considered during the evolution of the plastic strains with axi-symmetric meridians are actively contributing.

The failure space can then be illustrated in three-dimensional form with the characterized points for each state-of-stress as illustrated in Figure 5-173, where a failure surface will be constructed over the entire domain bounded by the stress meridians. The surface is built as a ruled facet and is compelled to follow the stress meridians that are also constructed by using three dimensional splines. The failure surface is constructed by using bivariate tensor product splines, which are utilized considering their capability in predicting highly non-linear surfaces independent of the directionality of the data that also harmonizes with the ‘bridging’ methodology.

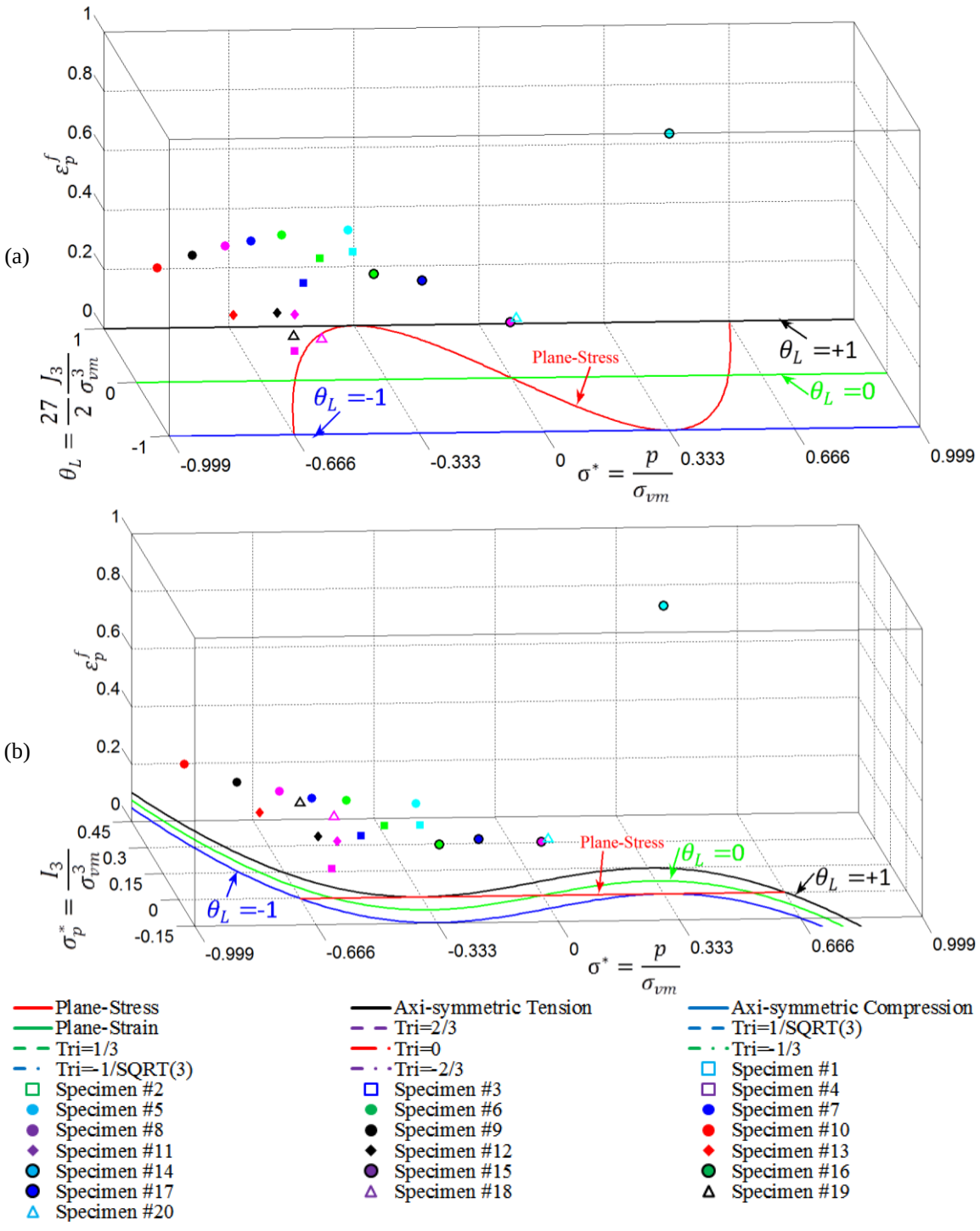

Figure 5-173: Three dimensional representation of the characterized failure points for each state-of-stress based on the averaged values and mean failure strain on the plane defined by; (a) stress-triaxiality vs. Lode-angle-parameter and (b) stress-triaxiality vs. product-triaxiality.

It should be noted that in Chapter 4 'bridging' the states-of-stress is suggested as a guideline to construct a failure surface with minimum number of test results without a compromise in the accuracy of the response. Having technological limitations and considering the cost of testing, it is often not possible to obtain enough number of test points to define the failure surface as a function of state-of-stress for the entire range of interest. On the other hand, pre-determined monotonic surface shapes are often utilized with an error minimization algorithm over-fitting the data. Therefore, TRAUM is supported by a user-defined surface characterization methodology that avoids over-fitting the available data but is independent of the direction of the state-of-stress and is sensitive to the selected representative states that are chosen for the specimens by implicitly incorporating the required state intervals. Figure 5-174 illustrates the stress-meridians that are used for the ruled surface boundaries. It should be noted that these meridians are obtained by a three dimensional smoothing spline functions and therefore represent approximation of the test data. Consequently, it can be said that the methodology is not an interpolant but a ridge estimator, where the bias is towards the accuracy of the prediction by controlling the smoothness of the spline functions.

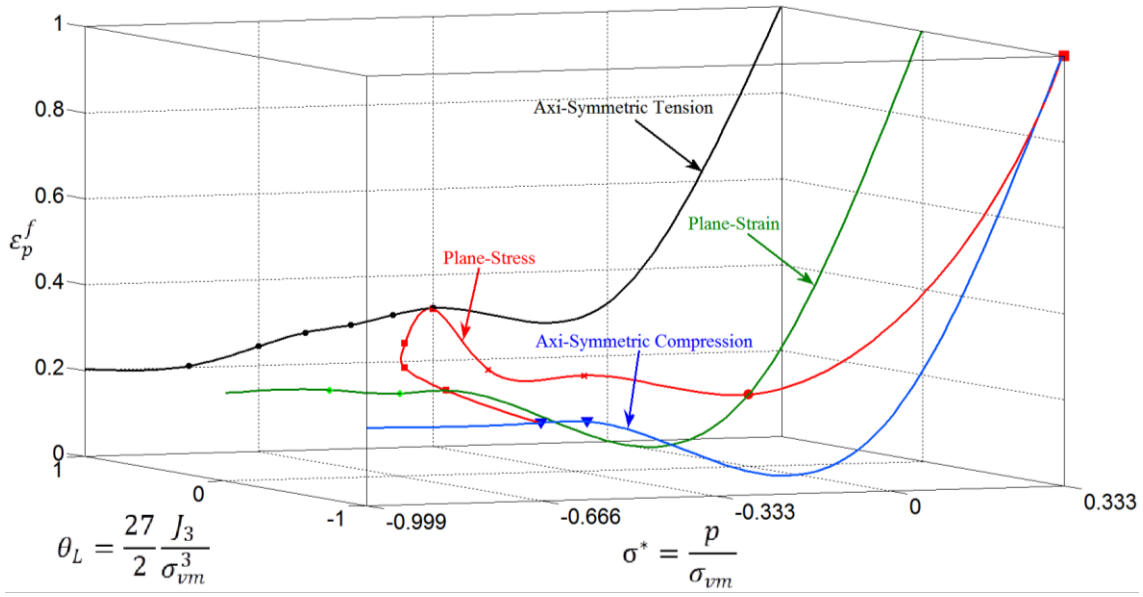

Figure 5-174: Three dimensional B-splines that are used to construct the boundaries of the ruled failure surface from the corresponding stress meridians.

Each pre-determined states-of-stress during the 'bridging' for the specimen design also serve as the 'internal knots' of the three dimensional B-splines, which will be constructed over the failure space independent of the directions of the state-of-stress. The directions are chosen to be the stress-triaxiality vs. Lode-angle-parameter to represent the stress space. Using bivariate approach provides the opportunity to choose the desired stress-states for testing as initially planned in Chapter 4 with almost equally spaced intervals on both stress-triaxiality and Lode-angle-parameter axes, which is a desired feature for spline functions when the 'internal knots' are defined. The methodology is programmed to search for the best failure strains by minimizing the error between the test results and the failure surface that is constructed by using the bivariate B-splines. Therefore, it can be said that the methodology will simultaneously be finding the discrete least-square approximation to the smoothening spline approximations. More details about the methodology and recent applications can be found from de Boor [385] [386].

Considering a least-squares approximation to the test data defined as a function of states-of-stress over the range covered by the testing program as:

$$\varepsilon_p^f(i,j) = f\left(\sigma^*(i), \theta_L(j)\right) \quad , \; i = 1, \dots, I; \; j = 1, \dots, J \tag{5.112}$$

where, $\varepsilon_p^f(i,j)$ represents the failure strains that are characterized from the corresponding specimens and illustrated in Figure 5-173(a) as a function of the stress-triaxiality $\sigma^*(i)$ and the Lode-angle-parameter $\theta_L(j)$. The indices represent the number of available test points. The set of splines in the direction of the Lode-angle-parameter can then be found by also applying the least squares as:

$$\sum_{j=1}^{J} \left| \varepsilon_p^f(i,j) - SP_{Lode}\left(n_{Lode}, knot_{Lode}, \theta_L(j), \varepsilon_p^f(i,j)\right) \right| \quad , i = 1, \dots, I \tag{5.113}$$

where, n_{Lode} is the order of the spline function that is chosen to represent the behavior of the set of splines in the direction of the Lode-angle-parameter and is taken to be as a

cubic function. $knot_{Lode}$ is the knot sequence for the Lode-angle-parameter, where equally spaced values of the states-of-stress that are used for 'bridging' purposes are used to implicitly define the sensitivity of the approximation based on the testing. Consequently, the knot sequence in the direction of Lode-angle-parameter can be defined as:

$$knot_{Lode} = [-1.0, 0.0, 0.617, 0.9145, 1.0] \tag{5.114}$$

The results of the discrete least-squares approximations with B-splines in the direction of the Lode-angle-parameter are illustrated in Figure 5-175. It should be noted that these results do not form a surface yet and are used to obtain a matrix of coefficients representing the least squares and spline approximation of the domain. Therefore, the set of splines that are calculated in Equation (5.113) can alternatively be represented in the form of a function of coefficients as:

$$SP_{Lode}\left(n_{Lode}, knot_{Lode}, \theta_L(j), \varepsilon_p^f(i,j)\right) \mapsto \sum_r \theta_L^{coeff}(j,r)\, B_{r,n_{Lode}}(\theta_L) \qquad , j = 1, \dots, J \tag{5.115}$$

where, $\theta_L^{coeff}(j,r) \rightarrow \theta_L^{coeff}(J,r)$ suggests that each coefficient vector is represented by a spline of the same order and with an appropriate knot sequence $knot_{stress-triaxiality}$.

Similarly, by choosing an appropriate order $n_{stress-triaxiality}$ (i.e., cubic order) and assigning the stress-states that are used for 'bridging' the specimens that designed in Chapter 4, the set of splines in the direction of the stress-triaxiality can be written as:

$$SP_{stress-triaxiality}\left(n_{stress-triaxiality}, knot_{stress-triaxiality}, \sigma^*(i), \theta_L^{coeff}(r,j)\right) \quad \begin{matrix} , i = 1, \dots, I \\ , j = 1, \dots, J \end{matrix} \tag{5.116}$$

where, $knot_{Stress-triaxiality}$ is the knot sequence for the stress-triaxiality, where equally spaced values of the states-of-stress that are used for 'bridging' purposes are used to implicitly define the sensitivity of the approximation based on the testing. Consequently, the knot sequence in the direction of stress-triaxiality can be defined as:

$$knot_{stress-triaxiality} = [-0.999, -0.8, -0.666, -0.577, -0.49, -0.41, -0.333, -0.2505, -0.1466, 0.0, 0.333] \quad (5.117)$$

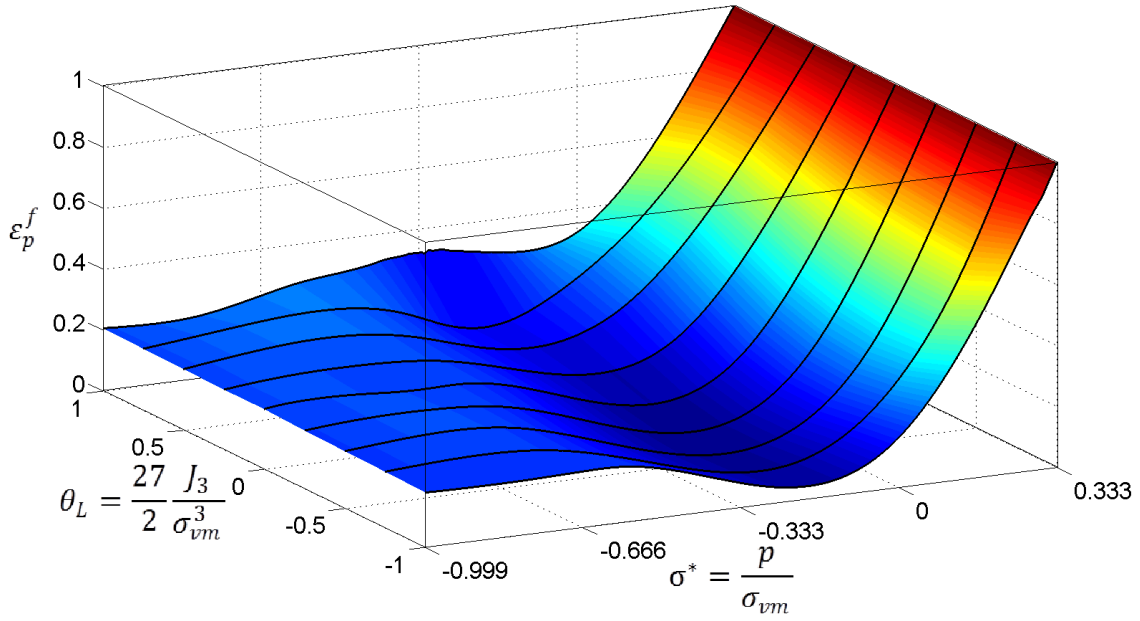

Figure 5-175: B-spline approximations in the direction of Lode-angle-parameter that are used to construct the three dimensional failure surface with bivariate splines.

Consequently, the coefficients of the resulting set of splines that are found from the approximations in Equation (5.116) provide the bivariate spline approximation to the original test data as:

$$\varepsilon_p^f\left(\sigma^*(i), \theta_L(j)\right) \mapsto \sum_q \sum_r \sigma^{*coeff}(q,i)\theta_L^{coeff}(j,r)\, B_{q,n_{stress-triaxiality}}(\sigma^*) B_{r,n_{Lode}}(\theta_L) \quad \begin{matrix} , i = 1, \dots, I \\ , j = 1, \dots, J \end{matrix} \quad (5.118)$$

Figure 5-176 illustrates the resultant failure surface, which is a ruled facet defined by the boundaries that are in fact the stress-meridians and the corresponding stress-states that are designed for testing specific specimen geometries. The surface is constructed by using B-splines of the cubic order by assigning the stress-states that are chosen during the 'bridging' as the internal control knots.

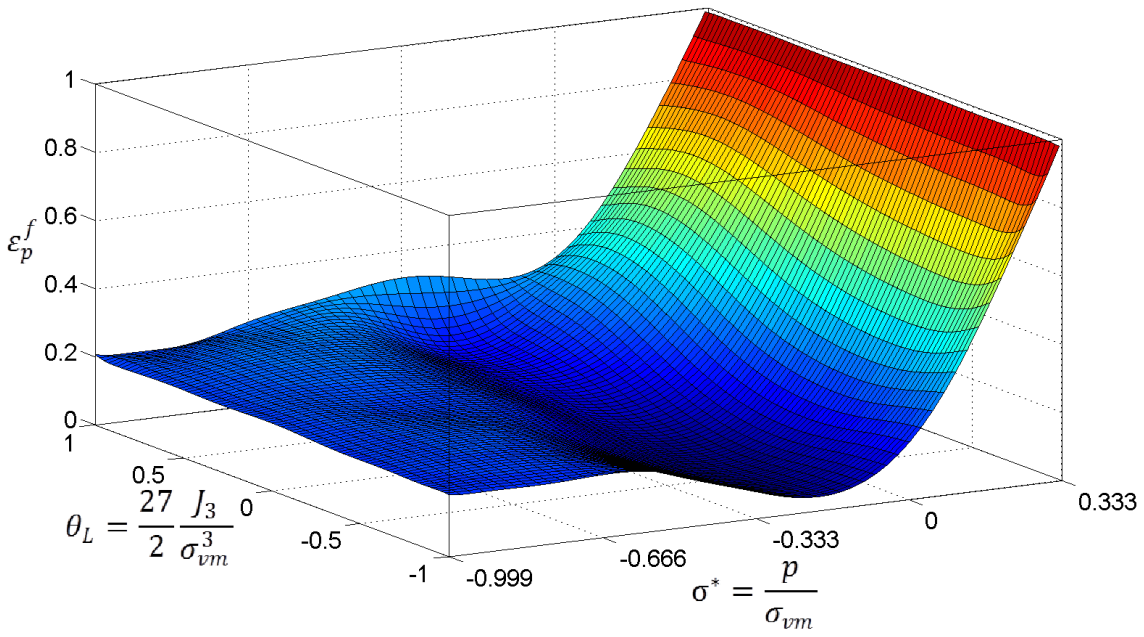

Figure 5-176: Bivariate spline approximation to the original test data or the failure strain for quasi-static conditions and room temperature for TRAUM.

It should be noted that the sequence of constructing the surface does not matter when the multivariate approximation process with spline smoothing or interpolation are used to identify the coefficient matrix since the resulting approximation has coefficients that depend linearly on the given data and not biased. Therefore, it is clear that if stress-triaxiality axis was chosen to characterize the coefficient matrix first, the difference for the resultant surface would be due to the round-off error only [385] [387]. The total amount of relative error for the approximation can be calculated as:

$$\begin{matrix} \varepsilon_p^f(\sigma^*(i), \theta_L(j)) \\ - SP_{stress-triaxiality}\left(n_{stress-triaxiality}, knot_{stress-triaxiality}, \sigma^*(i), \theta_L^{coeff}(r,j)\right) \end{matrix} \begin{matrix} , i = 1, \dots, I \\ , j = 1, \dots, J \end{matrix} \quad (5.119)$$

The error field can be illustrated as in Figure 5-177 for the entire range of stress-space. It is shown that by only utilizing cubic splines for a small number of available test data that are defined with the 'bridging' methodology, it is still possible to achieve a good estimate of the failure locus. It is shown that the maximum error over the entire stress

space is less than four orders of magnitude. Therefore, it is concluded that the failure surface can accurately be modeled by using B-splines.

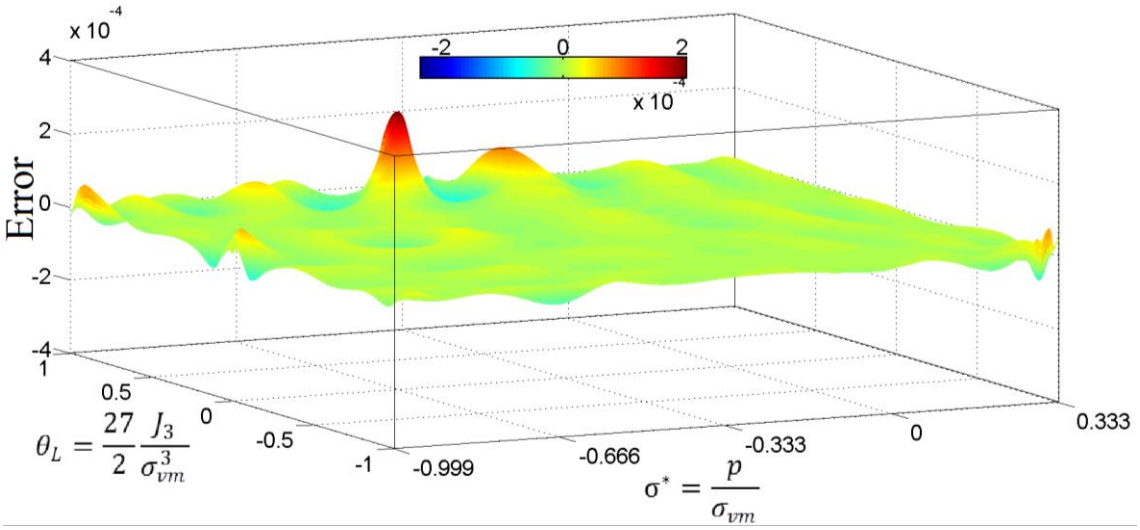

Figure 5-177: Relative error for the B-spline approximation of the failure space.

Failure surface and the stress meridians, which are approximated by the spline functions, are overlaid in Figure 5-178(a) to illustrate the formation of the surface boundaries. Figure 5-178 is characterized for Al2024-T351 for the quasi-static conditions at room temperature as a function of stress-triaxiality, Lode-angle-parameter and the failure strains. Tabulated form of the failure surface is utilized by TRAUM for the finite element simulations in the proceeding chapters for validation studies. The accuracy and quality of the failure surface with the experimental data is illustrated in Figure 5-178(b), where it is shown that no over-fitting or noise due to the higher order curve fitting are observed. It should be noted that TRAUM utilizes a tabulated form of the failure surface. Therefore, it is advisable to consider using as many curves as possible to define the entire range of the failure space since the failure algorithm will use only linear interpolations between two stress-states unless a higher resolution output is provided. It is clear that the accuracy of the failure predictions can directly be related to the resolution of the input data.

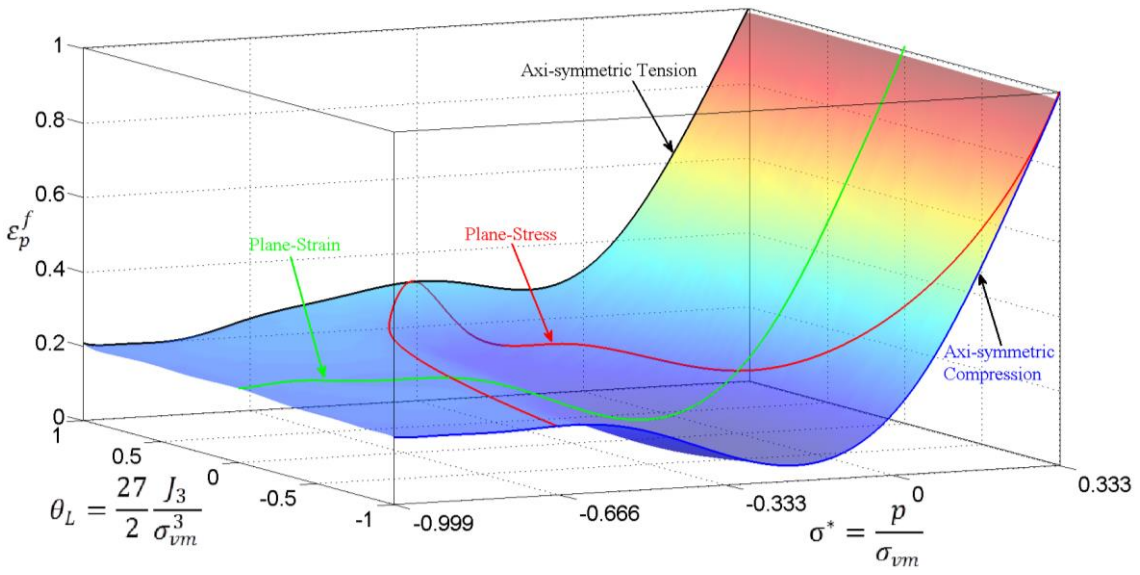

(a)

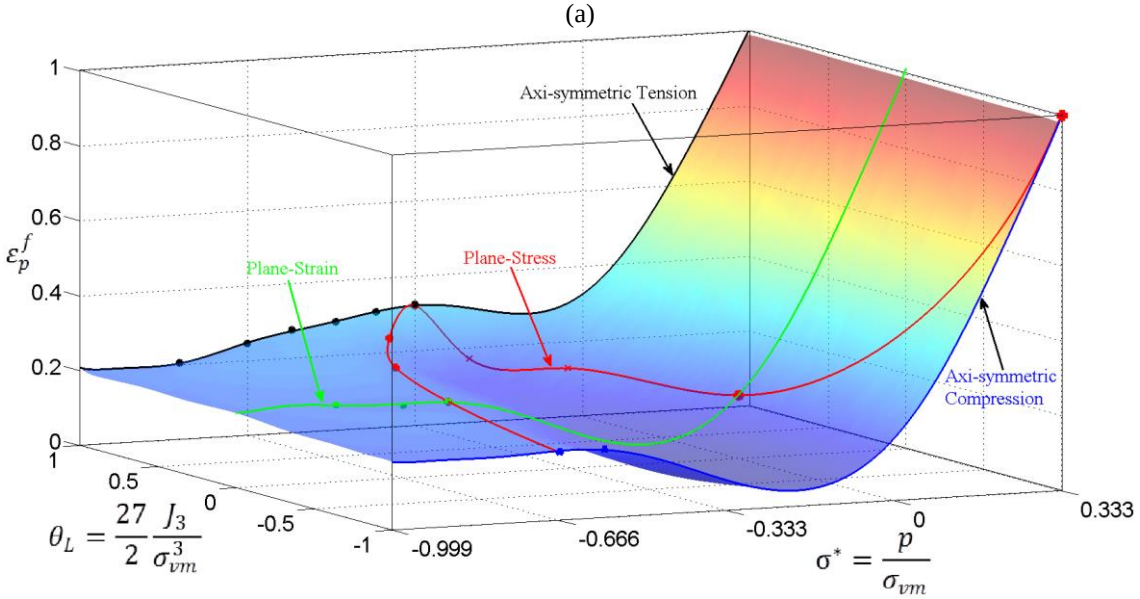

(b)

Figure 5-178: Failure surface for quasi-static conditions and room temperature with; (a) the bounding stress-meridians and (b) with the corresponding specimens representing the failure characteristics.

The matrix of coefficients of the bivariate tensor product splines are given in Table 5-38. The failure surface that is illustrated in Figure 5-176 and 5-178 can be obtained by using cubic spline functions, where the coefficients from Table 5-38 are used with the sequence of knots that are defined by Equations (5.114) and (5.117) for the given directions, respectively.

Table 5-38: Matrix of coefficients for the bivariate spline approximations of the failure surface.

Stress-triaxiality Direction	Lode-angle-parameter Direction						
	0.18265706	0.180722626	0.1974418818	0.196306654	0.205348781	0.201961635	0.203089647
	0.181032609	0.191681800	0.2099066962	0.210177937	0.208126860	0.199997205	0.202758396
	0.173904423	0.234911590	0.1800445948	0.248578299	0.237540132	0.186508293	0.183767542
	0.165770283	0.243136402	0.1479014422	0.258919159	0.243530627	0.246163831	0.245468272
	0.193271126	0.093970635	0.2382964411	0.199214185	0.298203036	0.26822448	0.286848736
	0.108245050	0.020107982	0.1337607453	0.137335649	0.146571604	0.319868489	0.315860365
	0.045576764	0.010992641	0.0027318219	0.153835620	0.089918292	0.208223276	0.327902561
	0.031663882	0.043540571	-0.035688561	0.167582959	0.219363361	0.289201300	0.266731299
	0.198997061	0.134966310	0.0301375074	0.415554552	0.400592855	0.285091656	0.295897275
	0.634722892	0.508244207	0.6695618059	0.754049180	0.736247671	0.721057295	0.716323757
	0.994459899	1.038933808	0.9990188243	1.008870554	1.009115837	1.00585365	1.007920084

5.12 **Characterization of the strain-rate dependent scaling curve for the failure surface**

According to Figure 5-3, a scaling curve for the failure surface is required to offset the failure strains that are characterized for the quasi-static conditions and represented in the form of a surface as a function of states-of-stress in the previous section. The methodology for the characterization of the scaling curve is described in Section 4.4.2.

The baseline for the normalization of the failure strain over the strain-rates is chosen as $1.0s^{-1}$ and the plane-stress specimen with a smooth gauge section is chosen for the characterization of the strain-rate dependency on failure at room temperature. It is shown in Figures 5-179(a) – 5-179(e) that the strain at failure changes drastically with the strain-rate. Details of the rate-dependent tests can be found in Appendix-C.

Although Al2024-T351 is found to have relatively strain-rate insensitive flow behavior up to the viscous-drag activated dislocation boundary, it is clearly seen that the failure behavior is affected with the strain-rate. Consequently, the failure strains that are characterized for the quasi-static conditions should be scaled according to the amount of strain-rate that each finite element will experience during the simulations. The line search methodology is applied while characterizing the plastic strains at failure for the plane-stress specimen for the corresponding tests while engineering stress vs. engineering strain curves are matched for the comparison as illustrated in Figure 5-179. The best matching

values of the plastic strains are assumed as the failure strains and for three repeated test results arithmetic mean of the failure strains are calculated for the corresponding strain-rate as shown in Figure 5-179(f) for the resultant engineering strain that are found by the simulations.

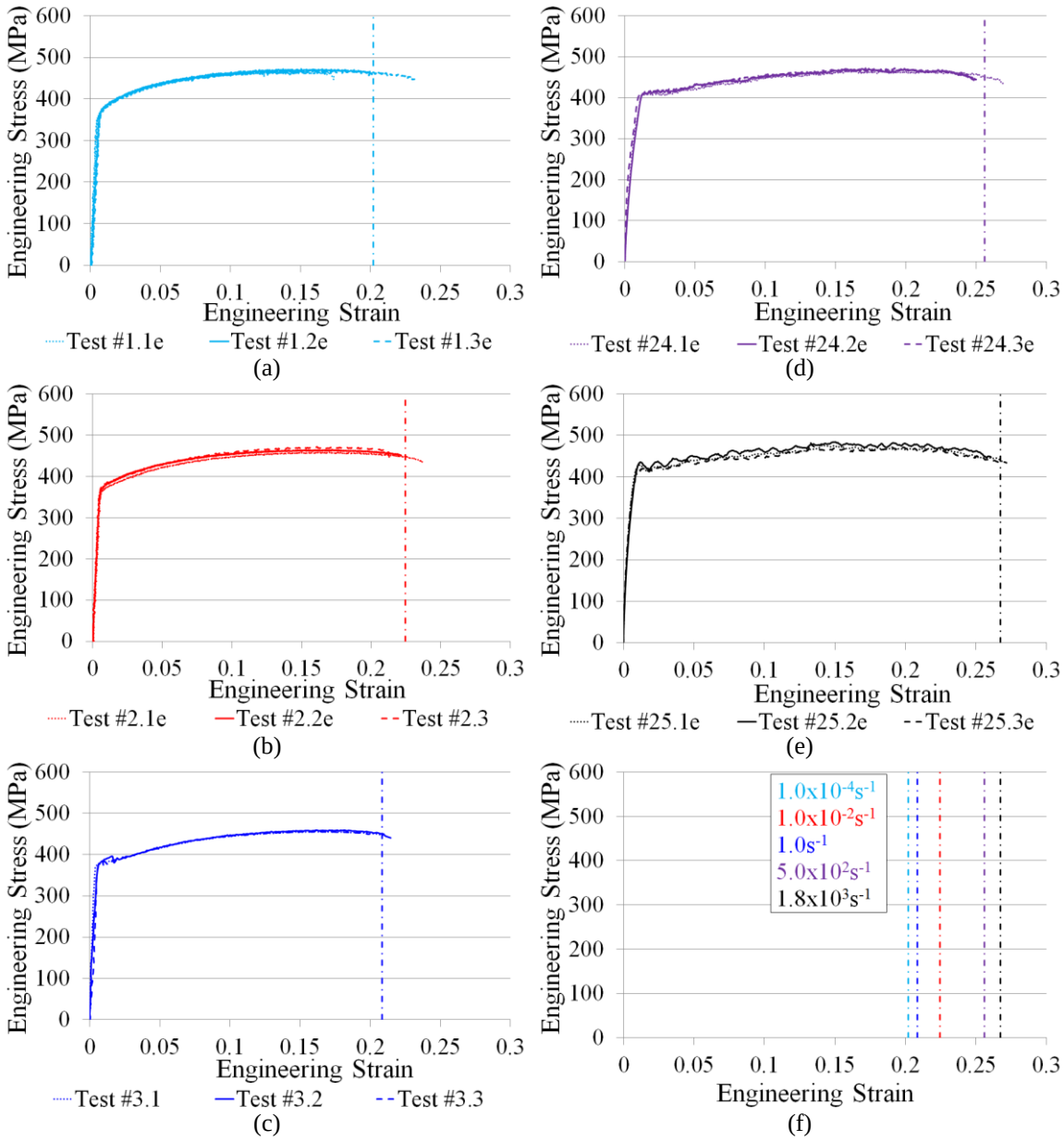

Figure 5-179: Comparison of the test results with the predicted failure that is found by TRAUM simulations by using the characterized values of the failure strains for the corresponding strain-rates showing; (a)-(e) the comparison of the failure point for each strain-rate and the mean of the TRAUM simulations and (f) the comparison of the mean values of the plastic strain at failure for TRAUM simulations at each strain-rate.

The scaling curve $g(\dot{\varepsilon}_p)$ is illustrated in Figure 5-180 as a function of logarithmic strain–rate vs. failure strain and logarithmic strain-rate vs. normalized scaling factor corresponding to the strain-rate, where the baseline is assumed to be $1.0s^{-1}$. It should be noted that the failure strain reduces slightly in between $1.0x10^{-2}s^{-1}$ and $1.0s^{-1}$ and the monotonically increases for the higher strain-rates.

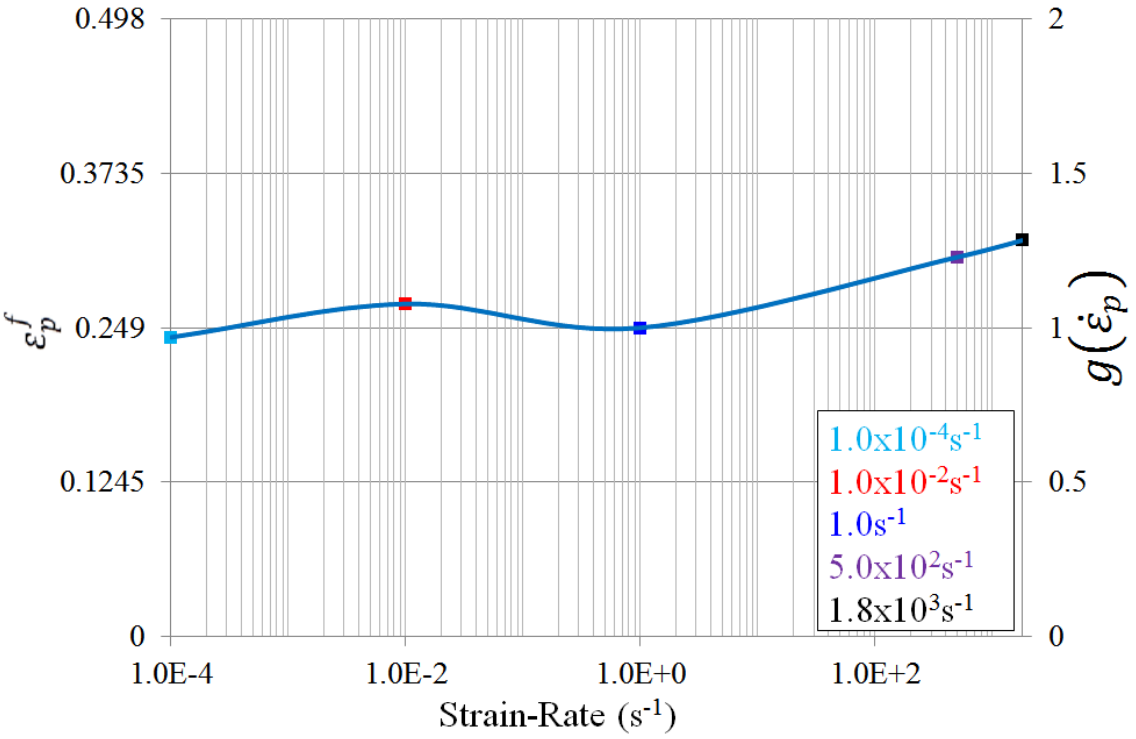

Figure 5-180: Strain-rate dependent scaling curve for the failure surface for TRAUM.

The scaling curve is used to modify the characterized values of the failure surface according to Equation (4.55) as illustrated in Figure 5-181, where the failure surface is scaled based on the normalized factors and the corresponding value of the strain-rate. It should be noted that the intermediate values of the rate dependent failure strains are found from linear interpolations.

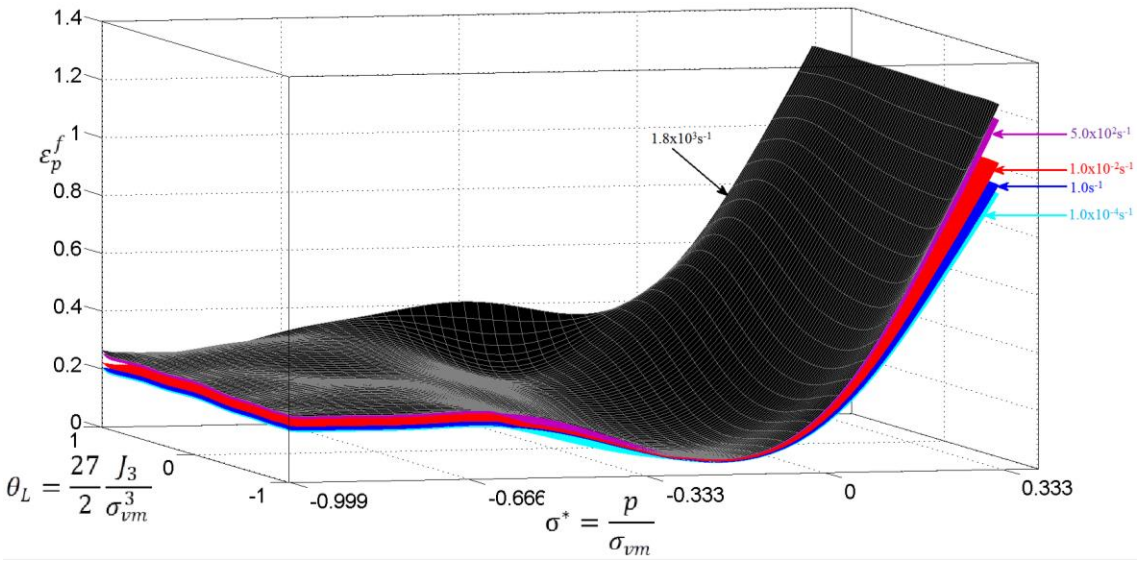

Figure 5-181: Strain-rate dependent failure surfaces for TRAUM.

5.13 **Characterization of the temperature dependent scaling curve for the failure surface**

Based on the methodology that is illustrated by Figure 5-3, a scaling curve for the failure surface is required to offset the failure strains based on the temperature. The failure surface that is constructed in Section 5.11 is characterized for the room temperature and represented in the form of a surface as a function of states-of-stress. Consequently, the failure strains are required to be scaled based on the methodology that is described in Section 4.4.2. The baseline for the normalization of the failure strain over the different temperatures is chosen as Room Temperature (RT) and the plane-stress specimen with a smooth gauge section is chosen for the characterization of the temperature dependency on failure at a nominal strain-rate of $1.0s^{-1}$. It is shown in Figures 5-182(a) – 5-182(e) that the strain at failure changes drastically with the temperature. Details of the temperature tests can be found in Appendix-C.

Engineering stress vs. engineering strain curves are matched for the comparison as illustrated in Figure 5-182 to find the best plastic strain at failure for each specific temperature and test. The best matching values of the plastic strains are assumed as the failure strains and for three repeated test results arithmetic mean of the failure strains are calculated for the corresponding strain-rate as shown in Figure 5-182(f) for the resultant engineering strain that are found by the simulations. However, for 723K the plastic strain

at failure is found unrealistically high and assumed to be beyond the stability limits of the simulation. The excessive amount of localization is not desirable, which ultimately localizes to a single row of elements and lose the ellipticity of the problem. Therefore, the maximum extend of the plastic strain value is characterized to an upper limit of 50% for this temperature as illustrated in 5-182(e).

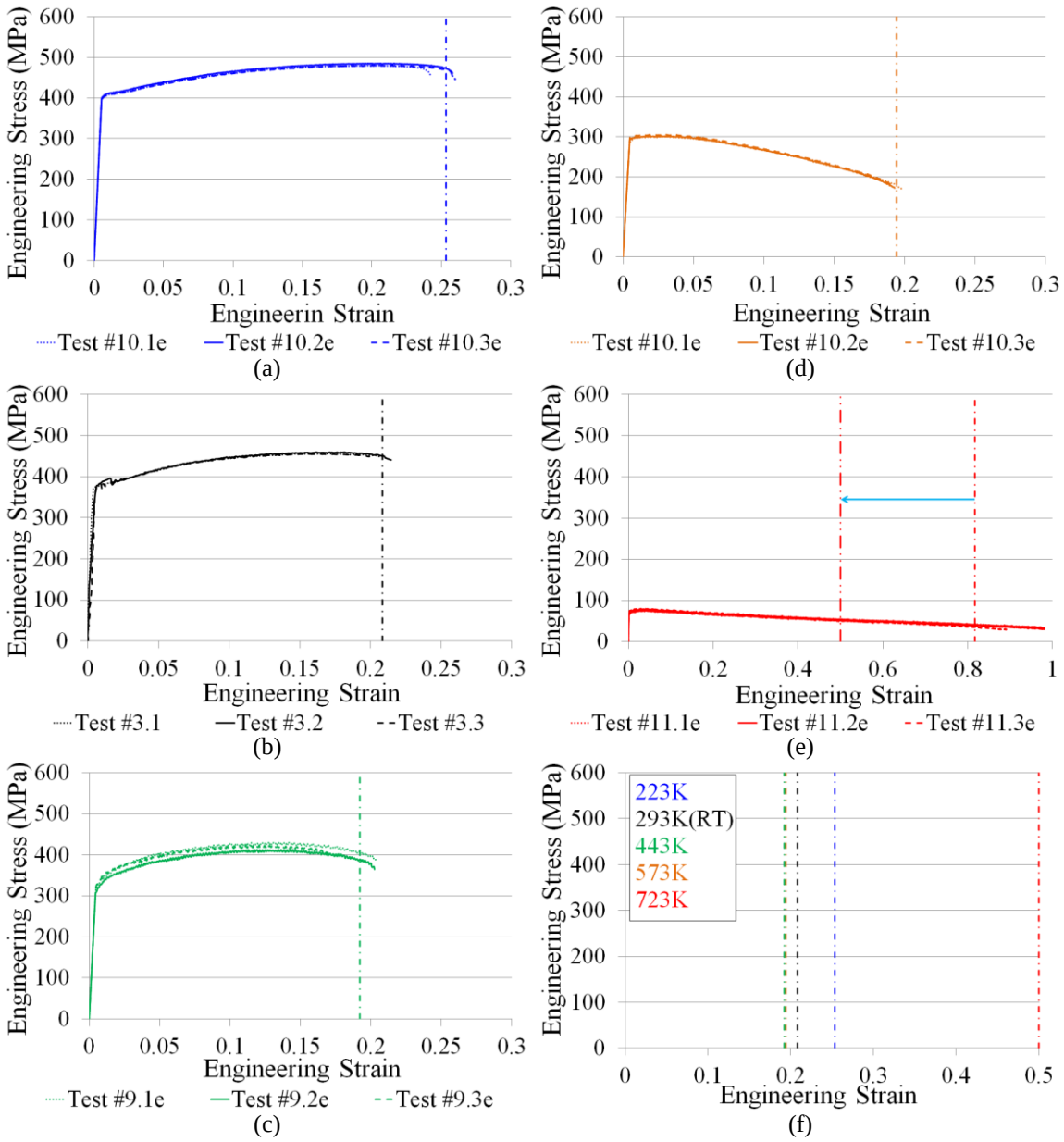

Figure 5-182: Comparison of the test results with the predicted failure that is found by TRAUM simulations by using the characterized values of the failure strains for the corresponding temperatures showing; (a)-(e) the comparison of the failure point for each temperature and the mean of the TRAUM simulations and (f) the comparison of the mean values of the plastic strain at failure for TRAUM simulations at each temperature.

The scaling curve $h(T)$ is illustrated in Figure 5-183 as a function of temperature vs. failure strain and temperature vs. normalized scaling factor corresponding to the current temperature, where the baseline is assumed to be at 293K. It is noticeable that the failure strain rises with the decreasing temperature and stays on a plateau during the dynamic recovery and recrystallization phase.

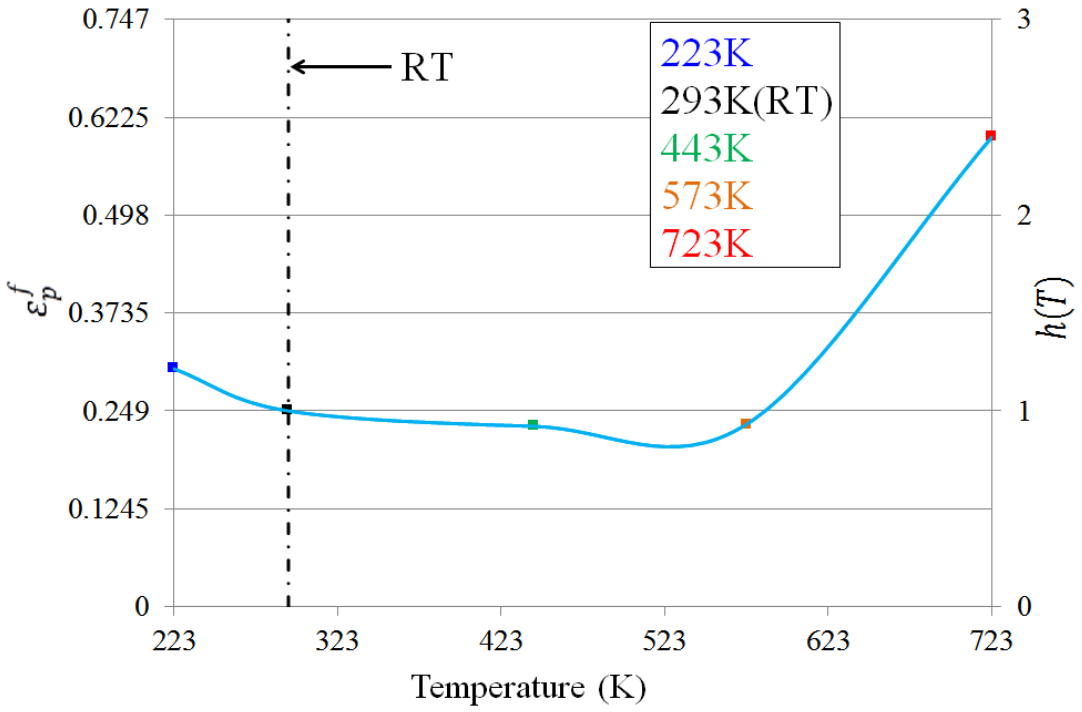

Figure 5-183: Temperature dependent scaling curve for the failure surface for TRAUM.

The scaling curve is used to modify the characterized values of the failure surface according to Equation (4.55) as illustrated in Figure 5-184, where the failure surface is scaled based on the normalized factors and the corresponding value of the temperature. It should be noted that the intermediate values of the temperature dependent failure strains are found from linear interpolations.

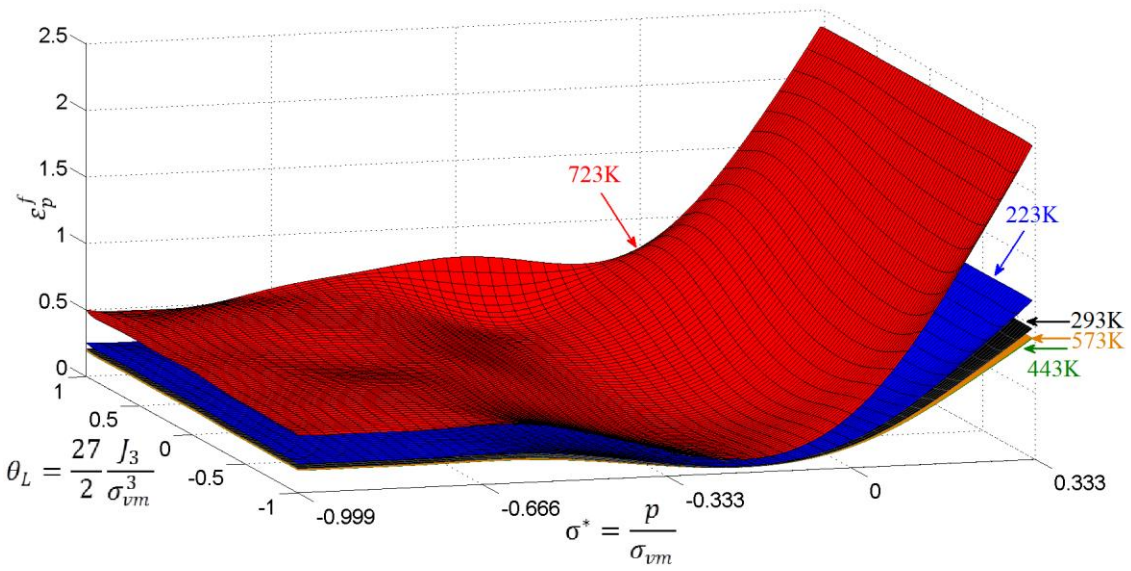

Figure 5-184: Temperature dependent failure surfaces for TRAUM.

5.14 **Summary and conclusions**

Material instabilities and the constraints of testing technology require implementation of alternative methods for characterization of material behavior. In this Chapter, Al2024-T351 aluminum alloy is first characterized by using a coupled semi-empirical and iterative, 'trial-and-error' methodology [99]. The methodology explicitly depends on a Swift law representation of the hardening curve after the necking point by assuming the number of elements contributing to the necking.

It is found that the Al2024-T351 has negative strain-rate sensitivity, DSA and PLC effect during the quasi-static loading conditions. Consequently, a more sophisticated characterization methodology is developed by using AOM and utilizing SRSM. During the characterization, verification of the data is attained rigorously and the results are presented throughout the chapter or in the appendixes. Temperature and strain-rate dependent flow surfaces are characterized for both adiabatic and isothermal conditions. It is shown that the deformation heating should be considered even during the quasi-static testing. Coupled thermo-mechanical simulations are performed to calculate the effects of adiabatic heating and heat transfer from the specimen during the testing.

A mesh regularization curve is characterized based on a bifurcation assumption depending on the mesh size. It is shown that even though the elongation at failure can be

achieved by modifying the plastic strain at failure, it is not possible for coarse meshes to predict localized necking. Therefore, the regularization scheme should only be considered for the range that is verified. With the regularization algorithm activated the characterization of the failure strains are attained.

The failure surface is characterized from the specifically designed specimens in Chapter 4 for representing different states-of-stress. The failure strains are found by a line search approach for the best plastic strain at failure while correlating with the test results. The results of the failure strain characterization are also illustrated in the failure space defined by using different states-of-stress.

The stress-states of the specimens are calculated by simple averaging of the invariants over in the failure strain and used to construct the failure locus. 3D-spline functions are utilized to define the stress-meridians, which are used as the boundaries of the failure surface. Bivariate tensor product splines are used to approximate the failure surface from the characterized failure strains of each specimen. This methodology is found to present the advantages of being direction independent and being able to represent highly non-linear surfaces with minimum number of required test points without a compromise in accuracy. It is also found in harmony with the 'bridging' methodology that is described in Chapter 4 as a methodology to link the stress-states of particular specimens for better representation of the failure space with almost equally partitioned intervals.

Temperature and strain-rate dependent scaling curves are characterized for scaling the failure surface accordingly. The scaling curves are characterized based on the methodology that is described in Chapter 4 by assuming a condition for baseline, which is the testing conditions that are used during the characterization of the stress-state dependent failure surface (i.e., at RT and $1.0s^{-1}$). The rest of the testing conditions are then normalized to the value at the baseline and scaled accordingly.

The methodology described above may sound exhaustive and time consuming. However, the method provides and/or compels the input data for a material to be very precise. The success of a material model like TRAUM, which utilizes fully tabulated test results as an input and fully depends on the refinement of the experimental characterization, it can be concluded that the model will be only as good as the test data.

CHAPTER 6 - **Validation of the material test results**

6.1 **Introduction**

Development of a new material model is justified and the procedures for the implementations are described in the previous chapters. It is shown that ductile failure of materials can be predicted more accurately by a failure algorithm depending on the state-of-stress, where all three stress invariants are considered. It is also shown in the previous chapters that a mesh regularization algorithm is necessary and should be utilized to predict failure more accurately. Therefore, a new thermo-viscoplastic material model with regularized stress-state dependent failure algorithm, TRAUM, is developed and implemented.

Moreover, a material testing program is designed and results are characterized for the new material model in Chapter 5. Flow and a failure surfaces for Al2024-T351 are generated based on tabulated input curves. In this Chapter, the characterized material properties are used to validate the model based on the cases in the material testing program. The material input data can be summarized based on the characterization methodology that is followed in chapter 5 as illustrated in Figure 6-1.

DIC is used to compare the full field strain predictions. It should be noted that the FE calculations are compared with both quantitatively and qualitatively by utilizing DIC and force vs. displacement behavior. Therefore, simulation results are expected to predict both the initiation of failure and also capture the evolution of the deformation towards failure. All fringe plots (i.e., contour plots for strain) in this Chapter represent the true plastic strain in the principle direction of force. DIC is used to measure the displacement field on the surface of the specimens. Therefore, the failure strains at the time of failure is expected to be different than the central element of the specimens, where most often ductile failure initiates and the failure characterization is performed for. Consequently, it is an objective assessment to test whether the failure surface, which is characterized from the central elements of the specimens, is able to predict failure for extends of the failure space that is defined by the states-of-stress. It should be noted that the cross-section of the specimens experience different stress-states during the evolution of the deformation.

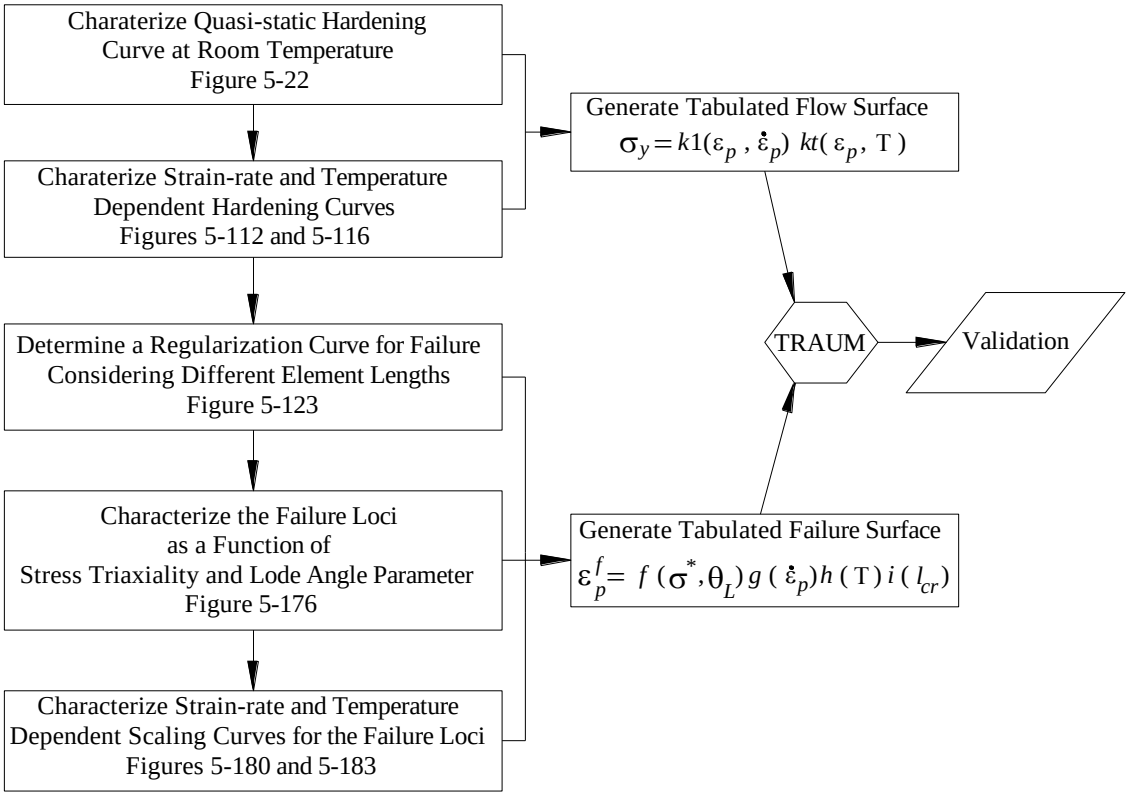

Figure 6-1: Characterized material input data for TRAUM and the path towards validation.

6.2 **Plane-stress tension specimens**

Plane-stress specimens are simulated by using the flow and failure surfaces that are characterized in Chapter 5. Figure 6-2(a) illustrates the strain field measurement of Specimen #1, where Figure 6-2(b) shows the simulation results when TRAUM is utilized with the characterized material data. Figure 6-2(c) represents the comparison of the force vs. displacement response between the test and FE simulation results. It is clearly seen that the model is in excellent agreement with the test results. However, since DIC sampling rate was not high enough, rapidly occurring localized necking instability was not captured. Therefore, comparison for the DIC and FE simulation illustrates the measurement at the initiation of diffuse necking.

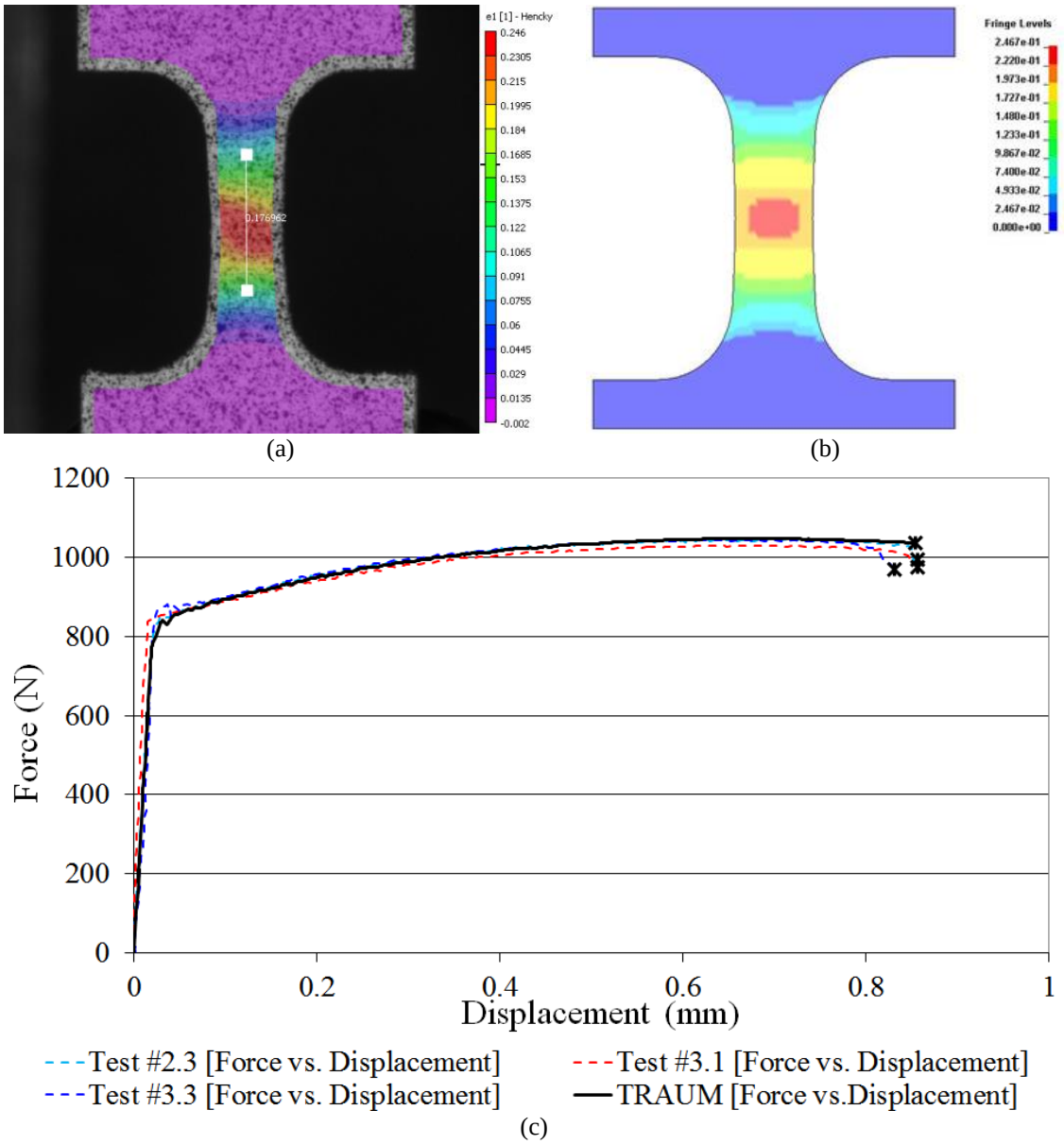

Figure 6-2: Quasi-static test results for Specimen #1; (a) DIC strain field measurement, (b) Test #2 surface strain prediction with TRAUM and (c) force vs. displacement comparison between Test #2 and Test #3 results and TRAUM predictions.

Similarly, Figure 6-3(a), Figure 6-4(a) and Figure 6-5(a) illustrate the strain field measurements of Specimen #2, Specimen #3 and Specimen #4, successively. Figure 6-3(b), Figure 6-4(b) and Figure 6-5(b) represent simulation results when the new material model is utilized with the characterized data set. Comparison of the force vs. displacement responses between the test results and FE simulations are represented by Figure 6-3(c), Figure 6-4(c) and Figure 6-5(c). It should be noted that the initial slope of force vs. displacement curves for the notched specimens differ due to the differences in

the initial gauge lengths. It should be emphasized that the flow behavior of the plane-stress specimens correlate well with the test results as illustrated through the force vs. displacement curves as an indication of the success of the characterized hardening curves. The failure point for the plane-stress notched specimens is found to occur within the repeatability of the test results and this is clearly showing that the failure to displacement is predicted accurately for variable states-of-stress.

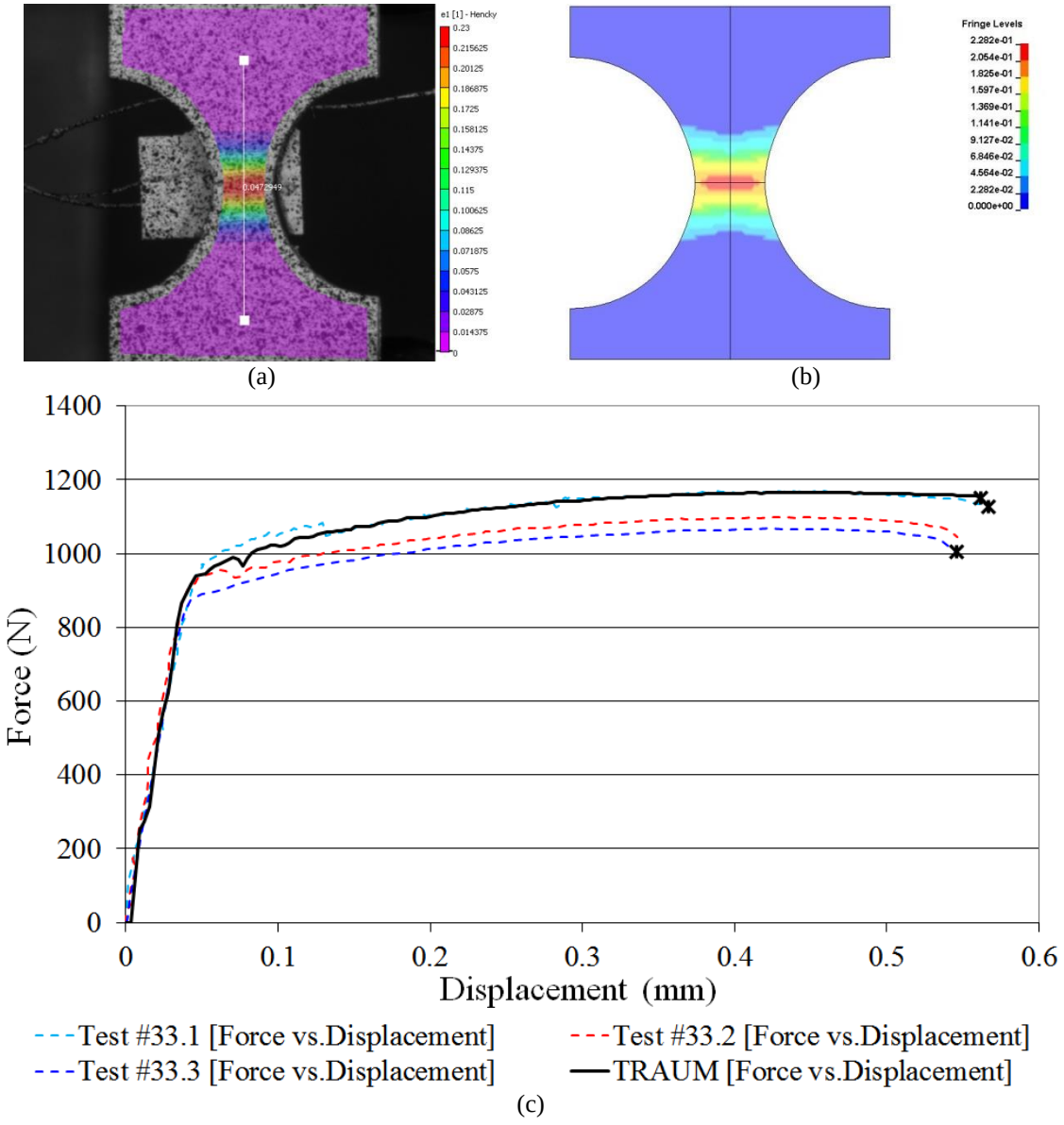

Figure 6-3: Quasi-static test results for Specimen #2; (a) DIC strain field measurement, (b) Test #33 surface strain prediction with TRAUM and (c) force vs. displacement comparison between Test #33 results and TRAUM predictions.

As a general rule, it is also observed that the amount of load increases as the notch radius gets smaller and the displacement to failure also reduces. Therefore, it can be concluded that a decreasing stress-triaxiality requires higher loads with less displacement to failure [273]. Upper and lower limits of the displacement to failure for the plane-stress specimens are also a good justification of using a tabulated material model, where the repeatability of the test results significantly influences the achievable accuracy.

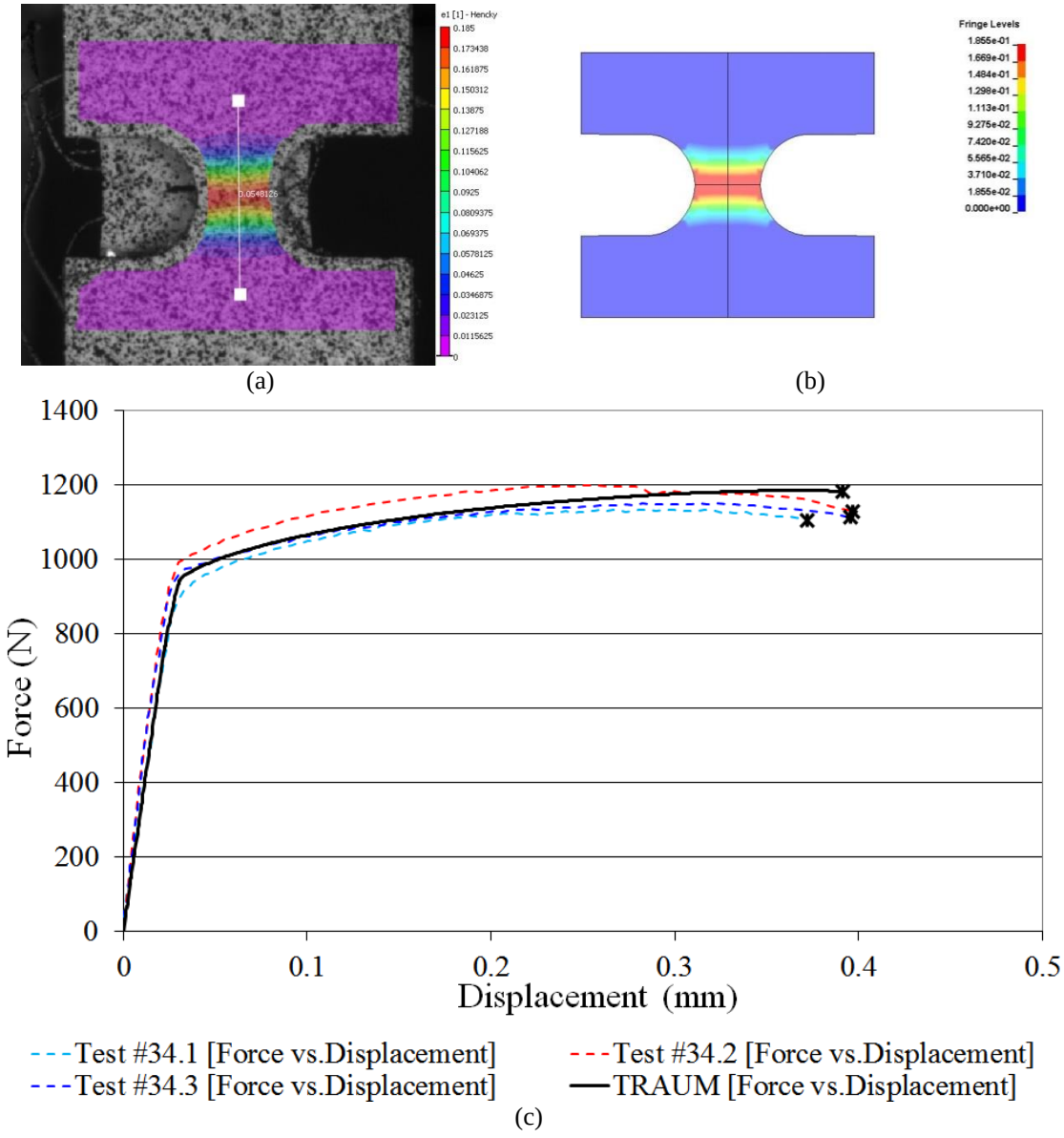

Figure 6-4: Quasi-static test results for Specimen #3; (a) DIC strain field measurement, (b) Test #34 surface strain prediction with TRAUM and (c) force vs. displacement comparison between Test #34 results and TRAUM predictions.

Figure 6-5 illustrates the results for Specimen #4 which differs from the other plane-stress specimens as the failure starts at the shoulder of the notch geometry rather than the center of the specimen. This is due to the confined boundary conditions at the shoulder of the specimen because of the notch geometry as the stress-state changes dramatically and no longer at plane-stress state. Therefore, predicting the failure of sharp notched specimen illustrates the limits of the new material model since the failure occurs in a region with a very high gradient of the state-of-stress.

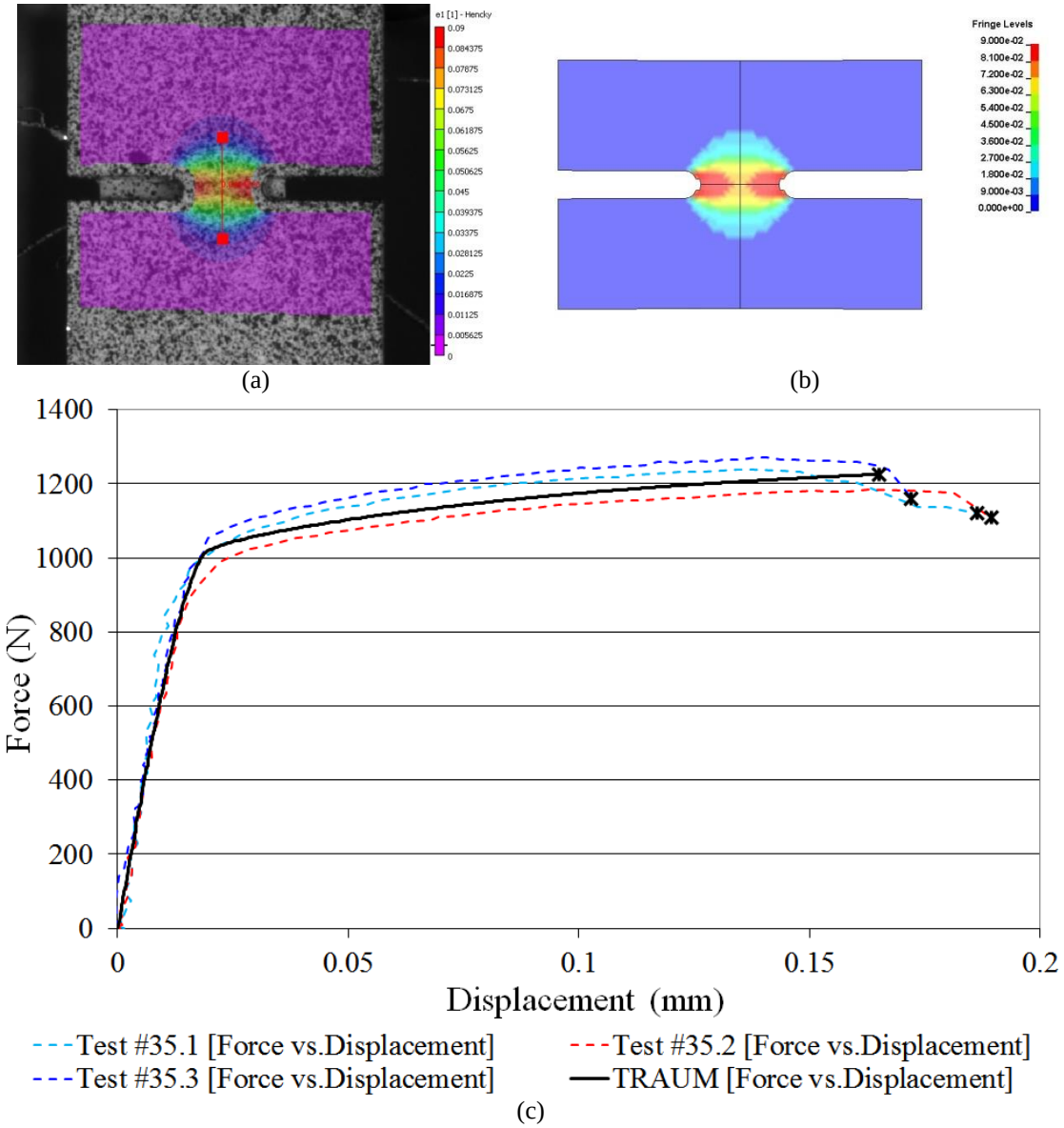

Figure 6-5: Quasi-static test results for Specimen #4; (a) DIC strain field measurement, (b) Test #35 surface strain prediction with TRAUM and (c) force vs. displacement comparison between Test #35 results and TRAUM predictions.

6.3 **Axi-symmetric tension specimens**

Axi-symmetric specimens are simulated by using the flow and failure curves that are characterized in Chapter 5. Figure 6-6(a) illustrates the strain field measurement of the Specimen #5, where Figure 6-6(b) is the simulation results when TRAUM is utilized with the characterized values of the material data. Figure 6-6(c) represents the force vs. displacement comparison of the FE simulation results, respectively.

It is shown that the model is in good agreement with the test results. However, even the repeatability of the test results for this case is affected by the influence of PLC effect. Therefore, it is acceptable to find that the predicted failure point is within the corridor of the successive test results. DIC measurement in Figure 6-6(a) shows the influence of the PLC effect, where the strain localization has moved due to the serrated flow behavior in the material. Therefore, the FE predictions of failure should be judged according to the fact that failure could have happened anywhere within the smooth gauge region for Specimen #5. Similarly, the high variations of the displacement to failure can be explained by the uncertainty brought due to the PLC effect, where the evolution of the failure depends upon to the microstructure.

Figure 6-7(a), Figure 6-8(a), Figure 6-9(a), Figure 6-10(a) and Figure 6-11(a) illustrate the strain field measurements of Specimen #6, Specimen #7, Specimen #8, Specimen #9 and Specimen #10, successively. Figure 6-7(b), Figure 6-8(b), Figure 6-9(b), Figure 6-10(b) and Figure 6-11(b) represent simulation results when TRAUM is utilized with the characterized data set. Figure 6-7(c), Figure 6-8(c), Figure 6-9(c), Figure 6-10(c) and Figure 6-11(c) represent the force vs. displacement comparison of the FE simulation results.

It should be noted that, with the decreasing stress-triaxiality the required force to failure also increases for axi-symmetric specimens, where the displacement to failure decreases.

(a)

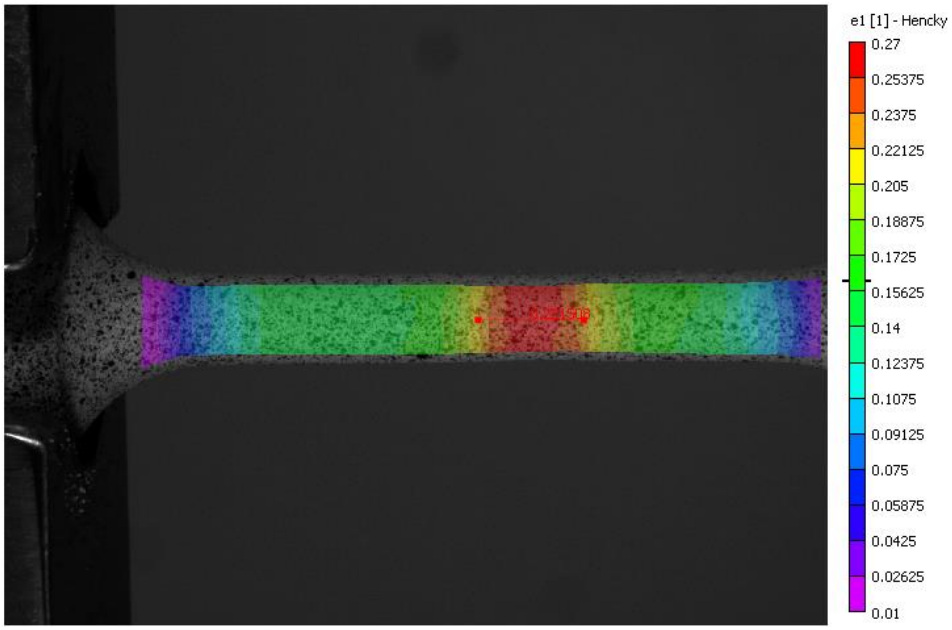

(b)

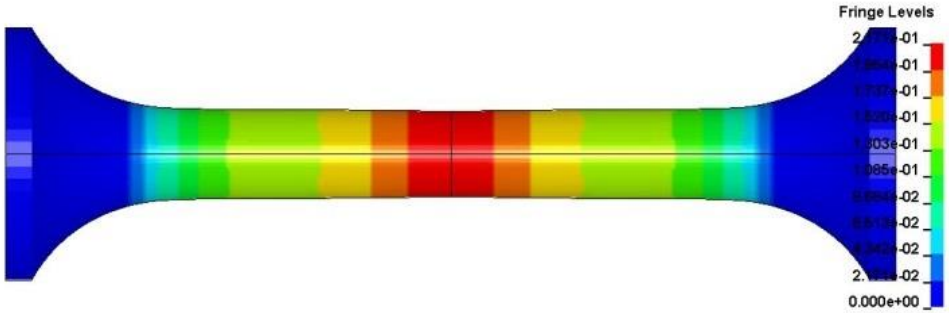

(c)

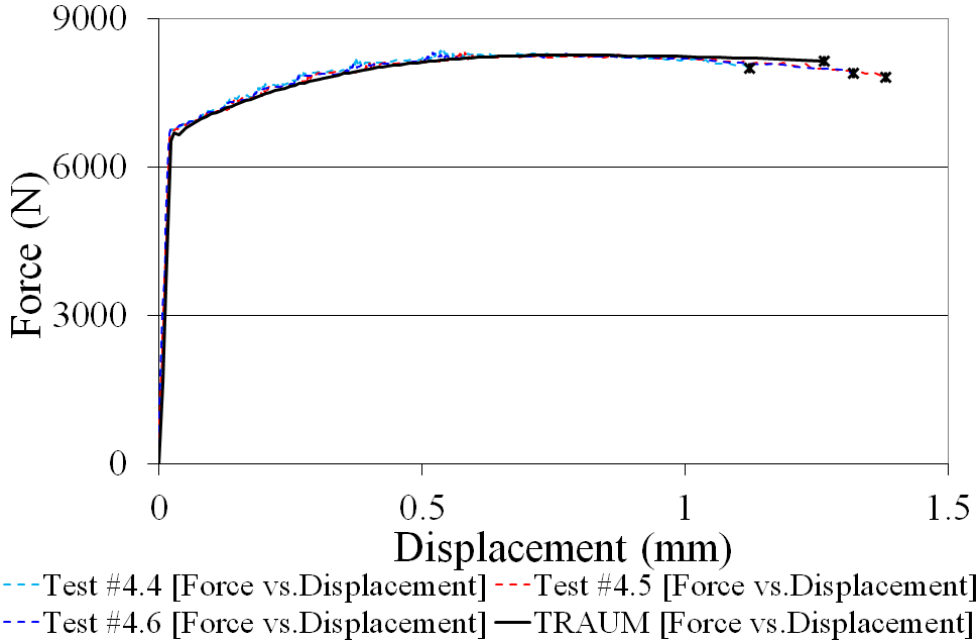

Figure 6-6: Quasi-static test results for Specimen #5; (a) DIC strain field measurement, (b) Test #4 surface strain prediction with TRAUM and (c) force vs. displacement comparison between Test #4 results and TRAUM predictions.

(a)

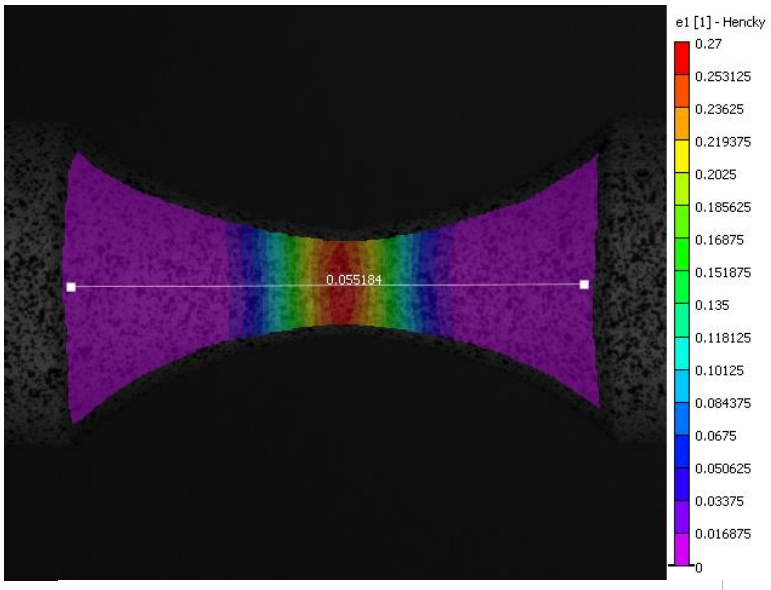

(b)

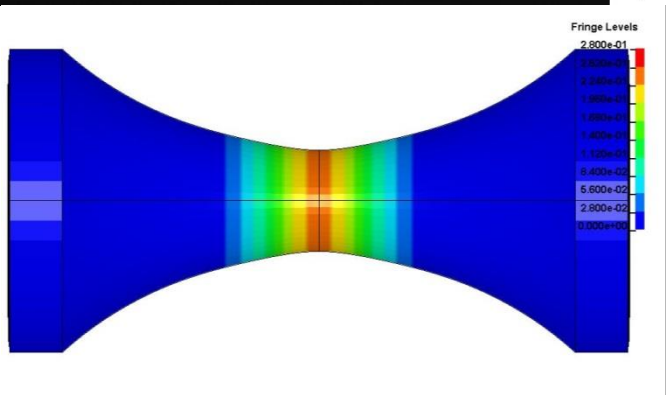

(c)

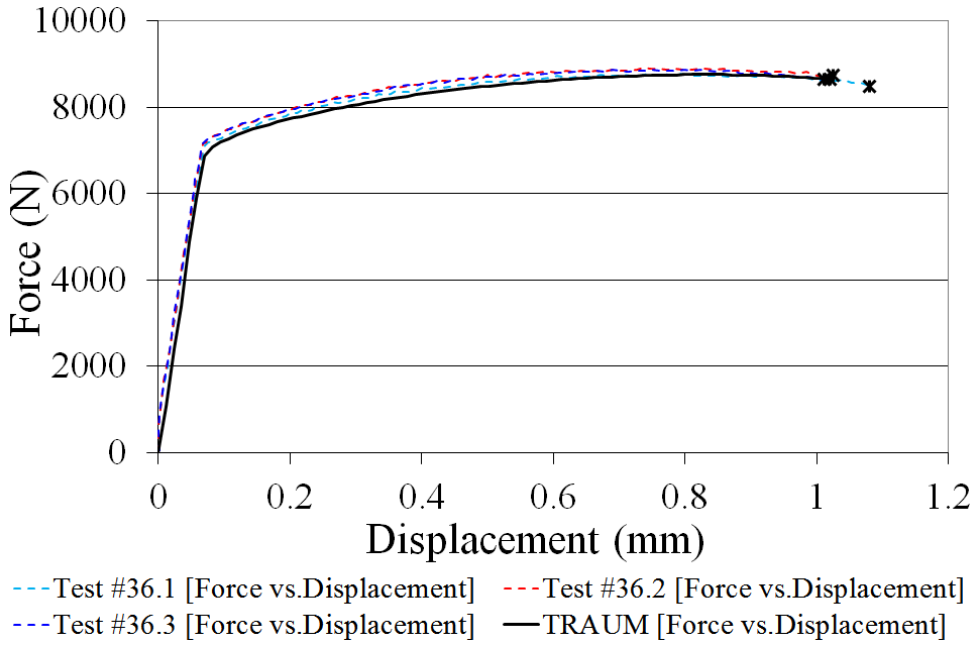

Figure 6-7: Quasi-static test results for Specimen #6; (a) DIC strain field measurement, (b) Test #36 surface strain prediction with TRAUM and (c) force vs. displacement comparison between Test #36 results and TRAUM predictions.

(a)

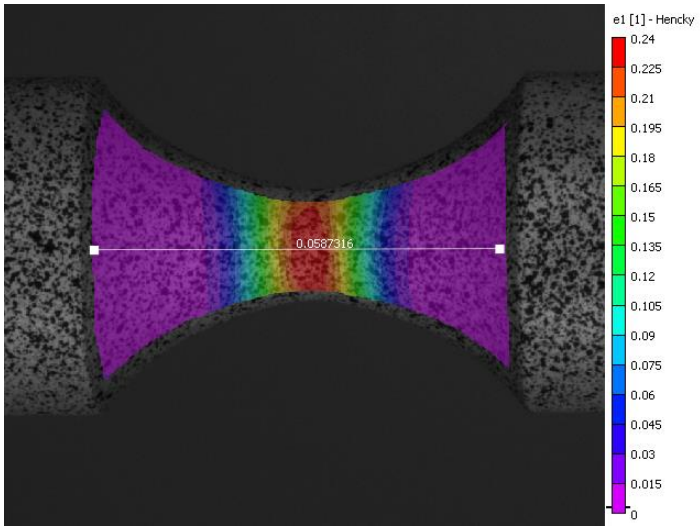

(b)

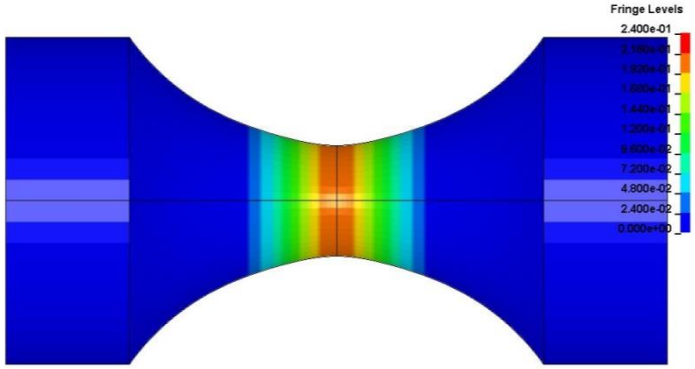

(c)

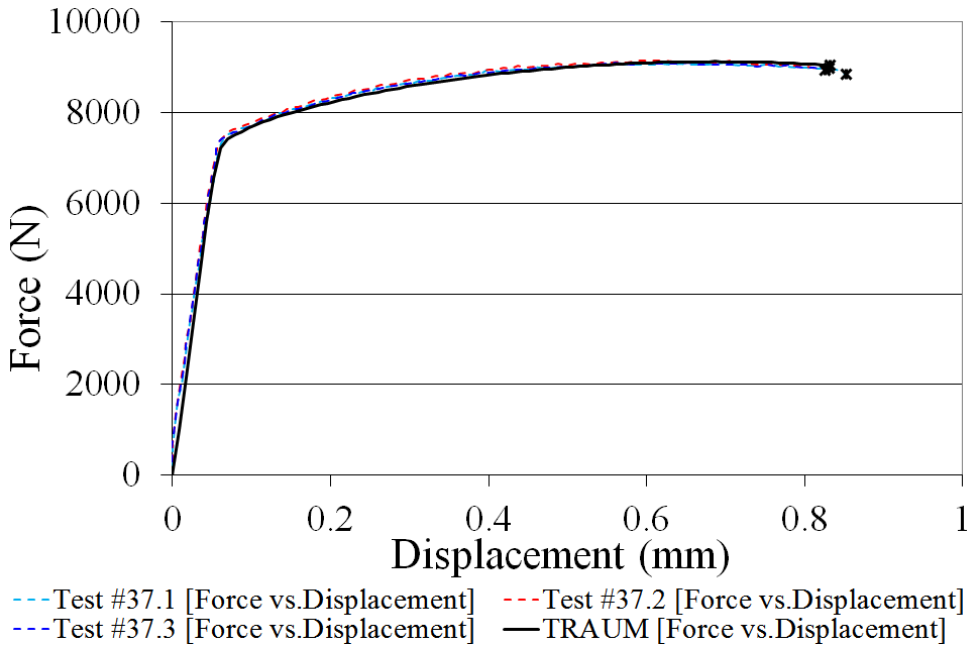

Figure 6-8: Quasi-static test results for Specimen #7; (a) DIC strain field measurement, (b) Test #37 surface strain prediction with TRAUM and (c) force vs. displacement comparison between Test #37 results and TRAUM predictions.

(a)

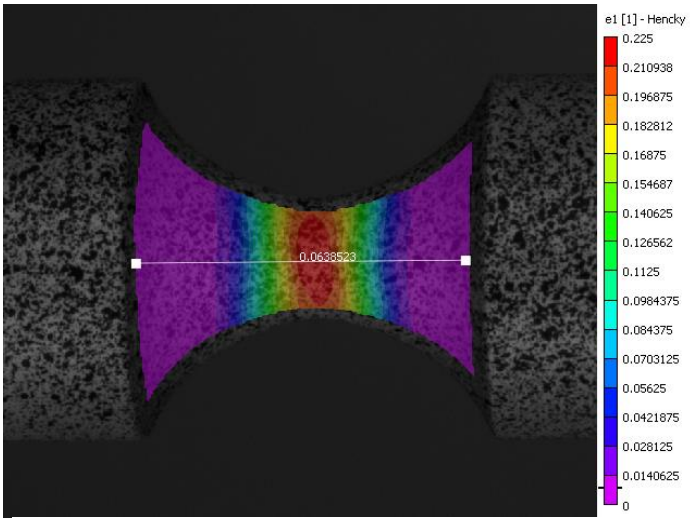

(b)

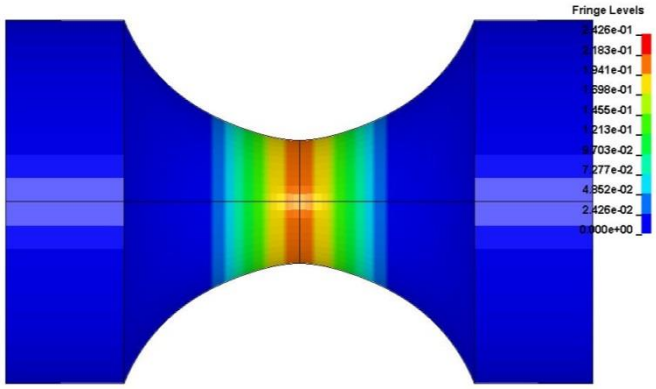

(c)

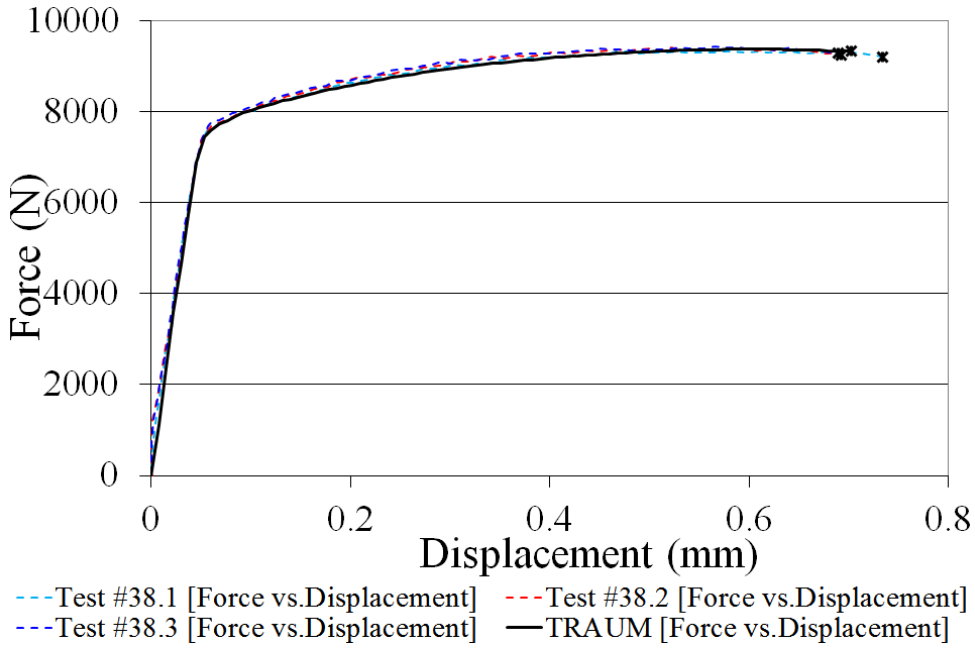

Figure 6-9: Quasi-static test results for Specimen #8; (a) DIC strain field measurement, (b) Test #38 surface strain prediction with TRAUM and (c) force vs. displacement comparison between Test #38 results and TRAUM predictions.

(a)

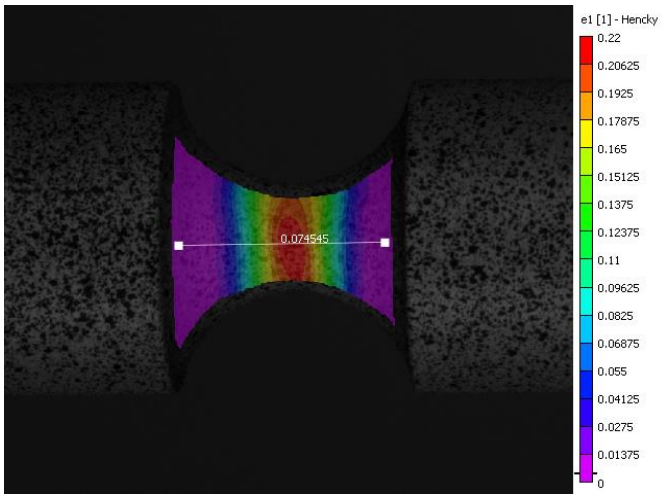

(b)

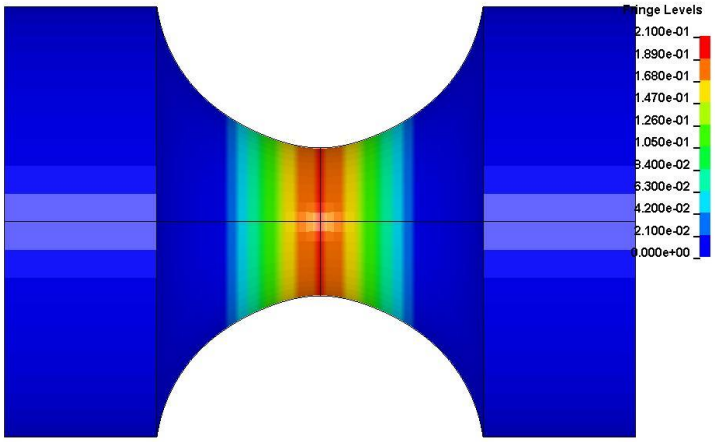

(c)

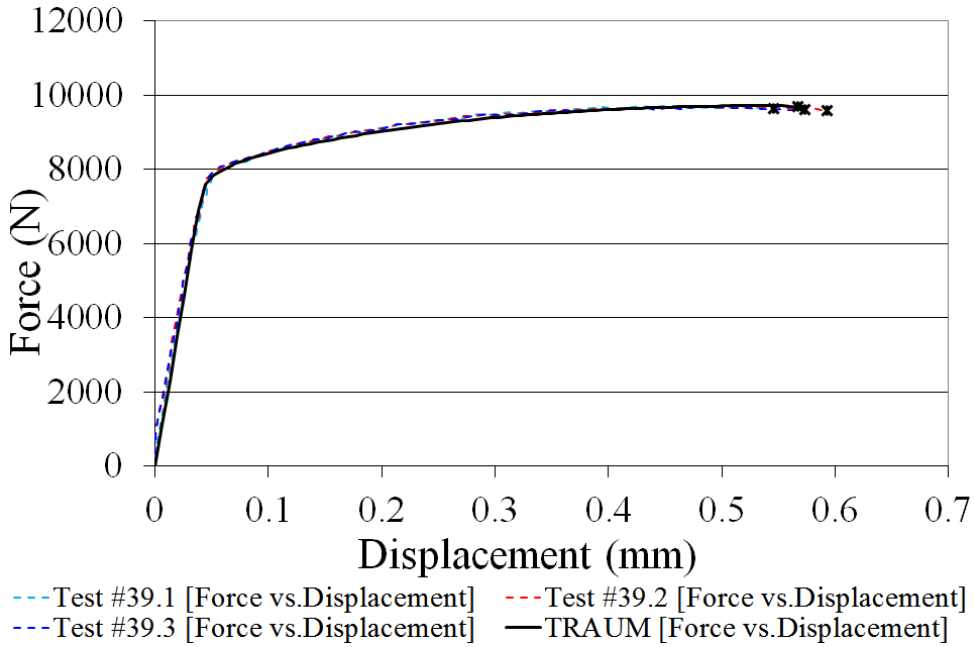

Figure 6-10: Quasi-static test results for Specimen #9; (a) DIC strain field measurement, (b) Test #39 surface strain prediction with TRAUM and (c) force vs. displacement comparison between Test #39 results and TRAUM predictions.

(a)

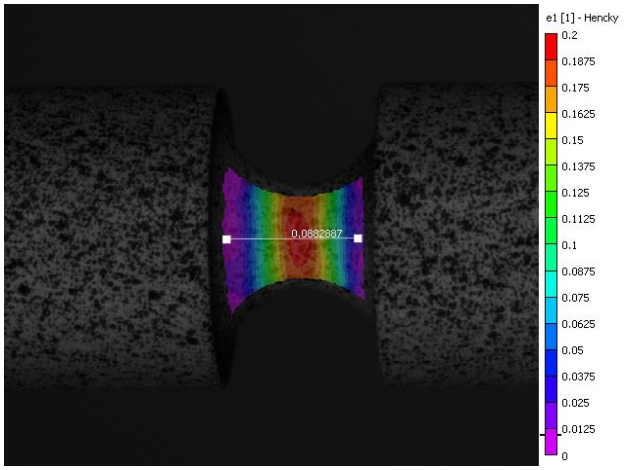

(b)

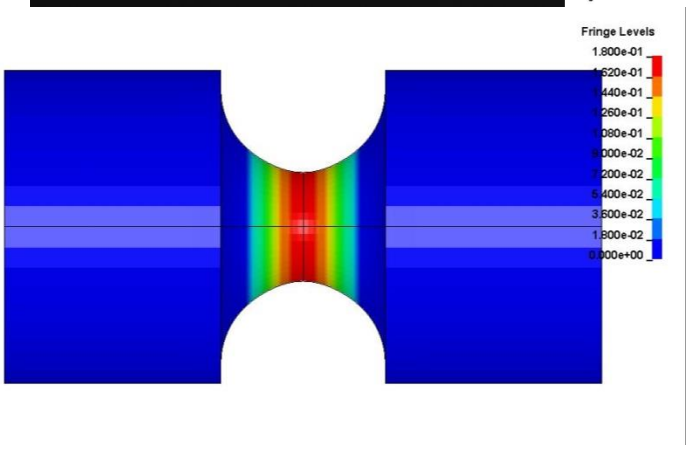

(c)

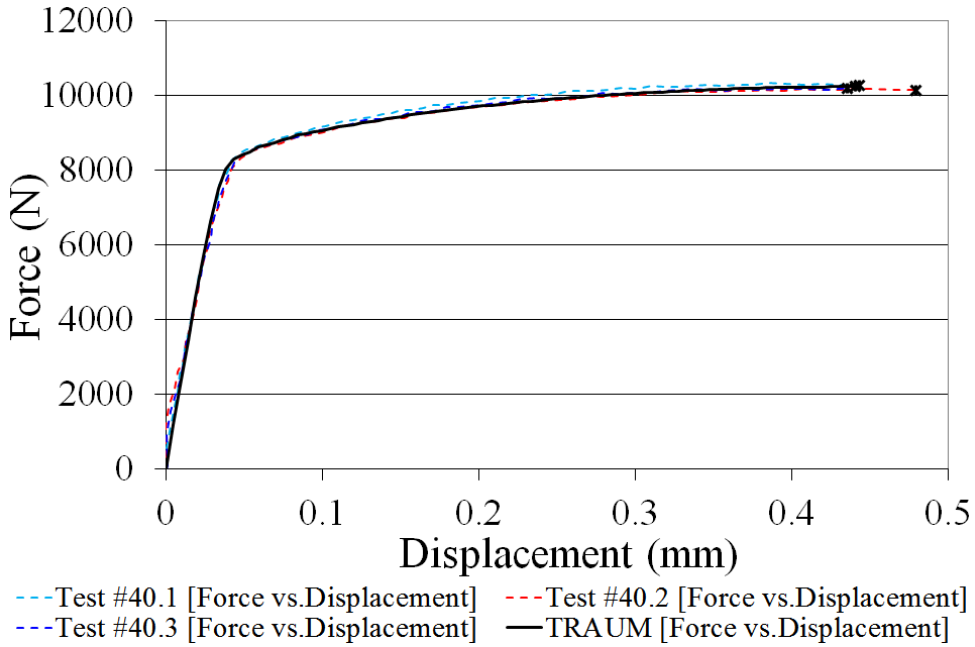

Figure 6-11: Quasi-static test results for Specimen #10; (a) DIC strain field measurement, (b) Test #40 surface strain prediction with TRAUM and (c) force vs. displacement comparison between Test #40 results and TRAUM predictions.

6.4 **Plane-strain tension specimens**

Plane-strain specimens are simulated by using the flow and failure curves that are characterized in Chapter 5. Figure 6-12(a) illustrates the strain field measurement of the Specimen #11, where Figure 6-12(b) represents the simulation results when TRAUM is utilized with the characterized values of the material data. Figure 6-12(c) represents the force vs. displacement comparison of the FE simulation results.

Similarly, Figure 6-13(a) and Figure 6-14(a) illustrate the strain field measurement of the Specimen #12 and Specimen #13, successively. Figure 6-13(b) and Figure 6-14(b) represent simulation results when TRAUM is utilized with the characterized data set. Figure 6-13(c) and Figure 6-14(c) represent the force vs. displacement comparison of the FE simulation results.

It is also found with plan-strain specimens that the ductility decreases with the decreasing stress-triaxiality as the failure strains reduces significantly and brittle failure patterns appear. It should also be noted that the new material model utilizes a von Mises plasticity algorithm and the flow stresses for a plane-strain condition is over predicted as illustrated in Figure 6-12(c), Figure 6-13(c) and Figure 6-14(c). However, the displacements at failure are accurately predicted based on the characterized values of the plastic strains at failure that are found in Chapter 5.

(a)

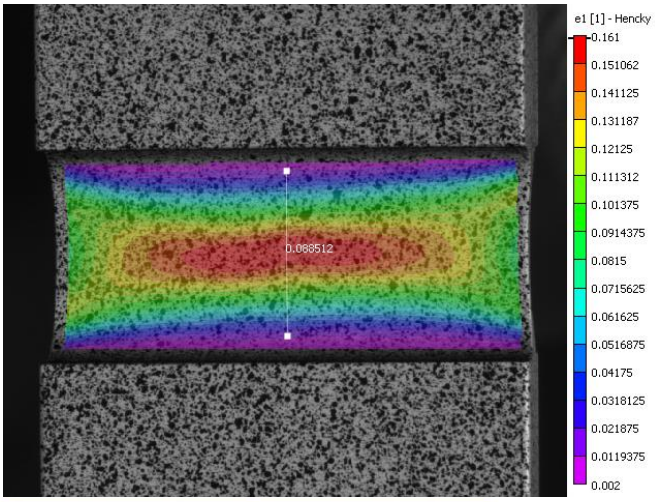

(b)

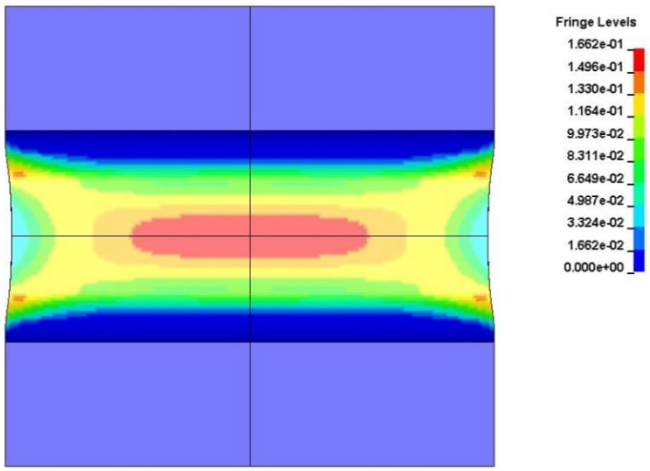

(c)

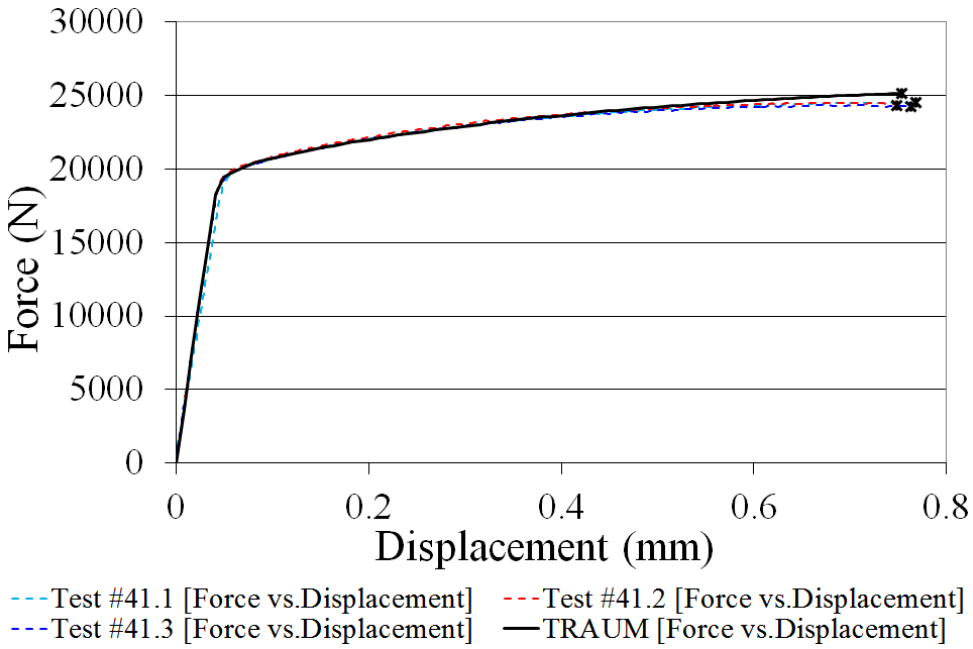

Figure 6-12: Quasi-static test results for Specimen #11; (a) DIC strain field measurement, (b) Test #41 surface strain prediction with TRAUM and (c) force vs. displacement comparison between Test #41 results and TRAUM predictions.

(a)

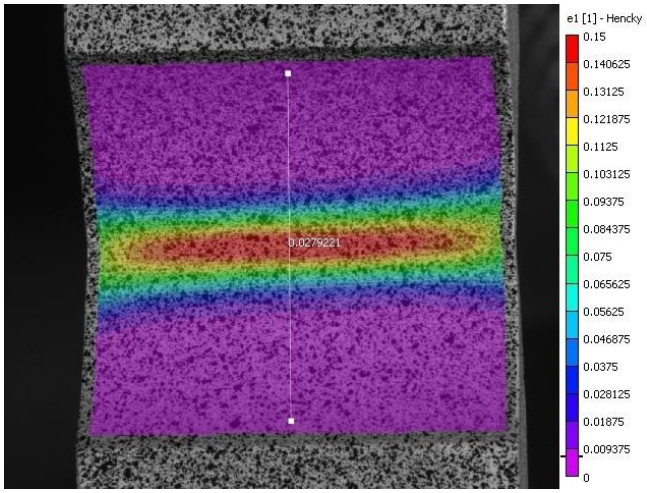

(b)

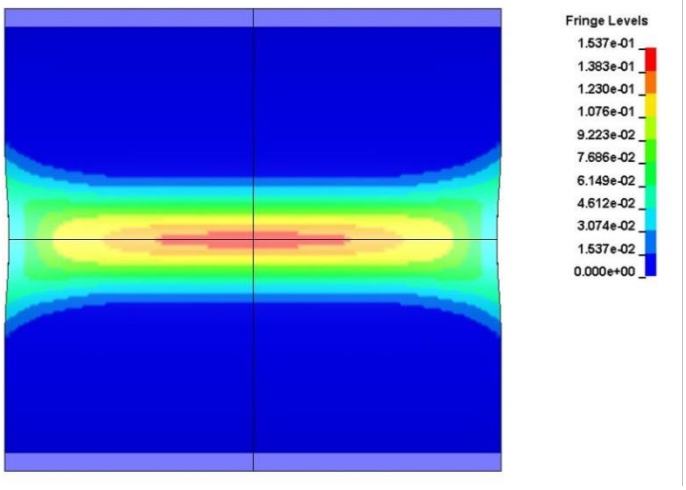

(c)

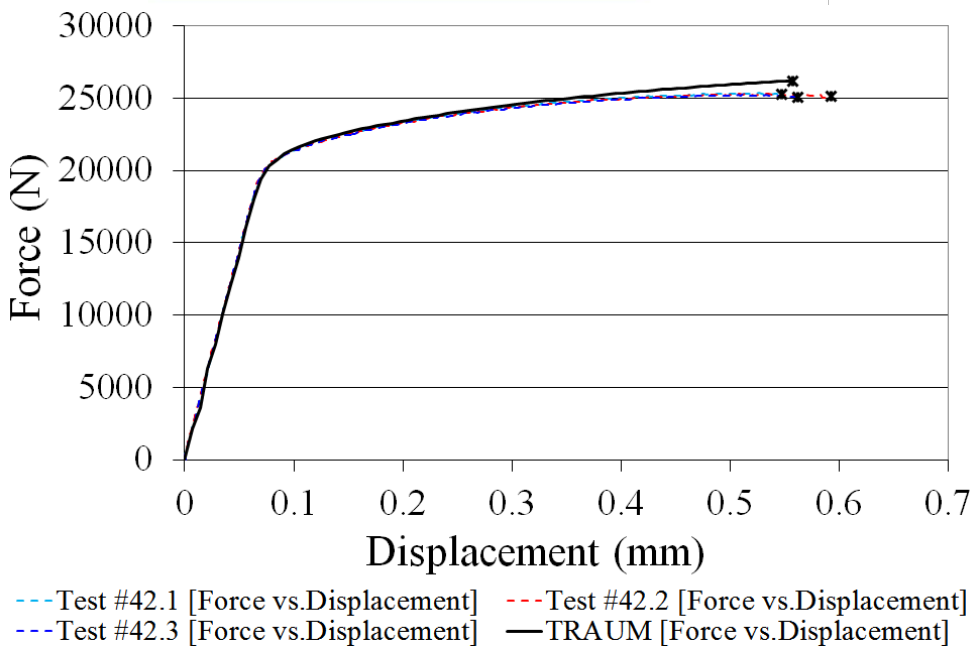

Figure 6-13: Quasi-static test results for Specimen #12; (a) DIC strain field measurement, (b) Test #42 surface strain prediction with TRAUM and (c) force vs. displacement comparison between Test #42 results and TRAUM predictions.

(a)

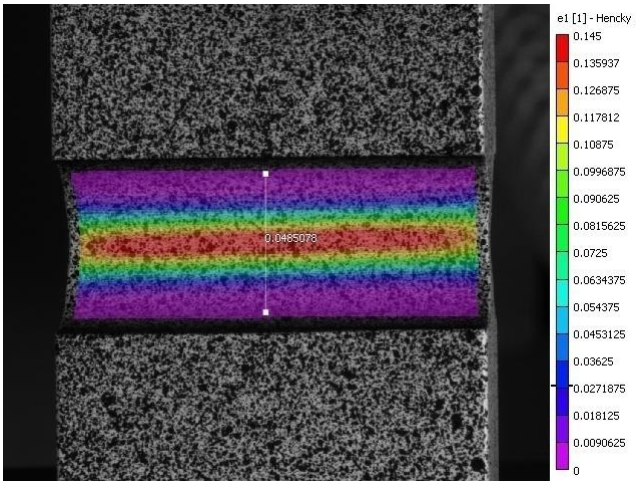

(b)

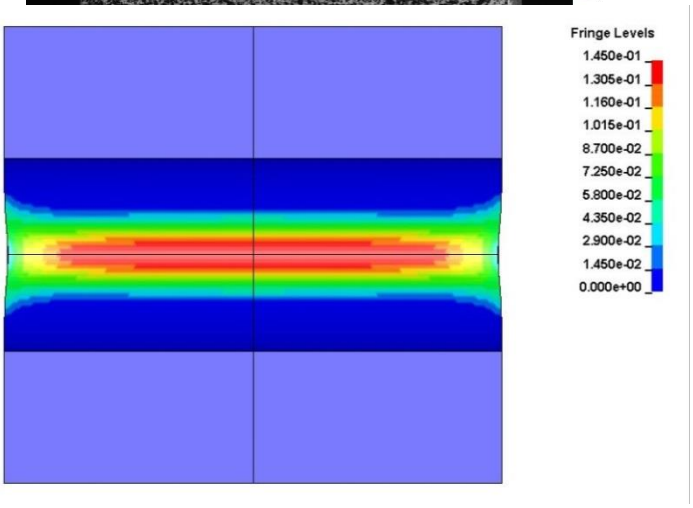

(c)

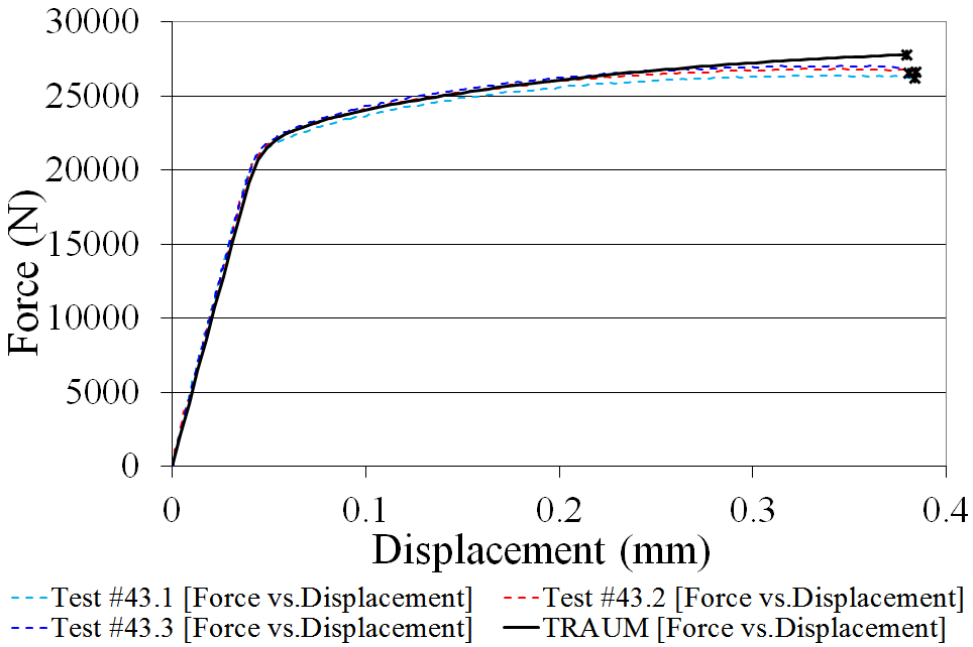

Figure 6-14: Quasi-static test results for Specimen #13; (a) DIC strain field measurement, (b) Test #43 surface strain prediction with TRAUM and (c) force vs. displacement comparison between Test #43 results and TRAUM predictions.

6.5 **Uni-axial compression specimen**

Uni-axial compression specimen is simulated by using the flow and failure curves that are characterized in Chapter 5. Figure 6-15(a) illustrates the simulation results when TRAUM is utilized with the characterized values of the material data. Figure 6-15(b) represents the comparison of the force vs. displacement response between the test and FE simulation results. DIC measurements were not used for the compression specimens [108]. Failure is not assumed during the ductile deformation of the uni-axial compression specimen. Therefore, a homogeneous distribution of the plastic strain is predicted for the simulation until forty percent strain as illustrated in Figure 15(a).

(a)

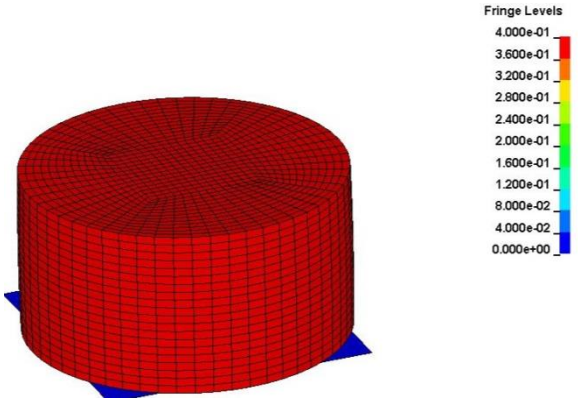

(b)

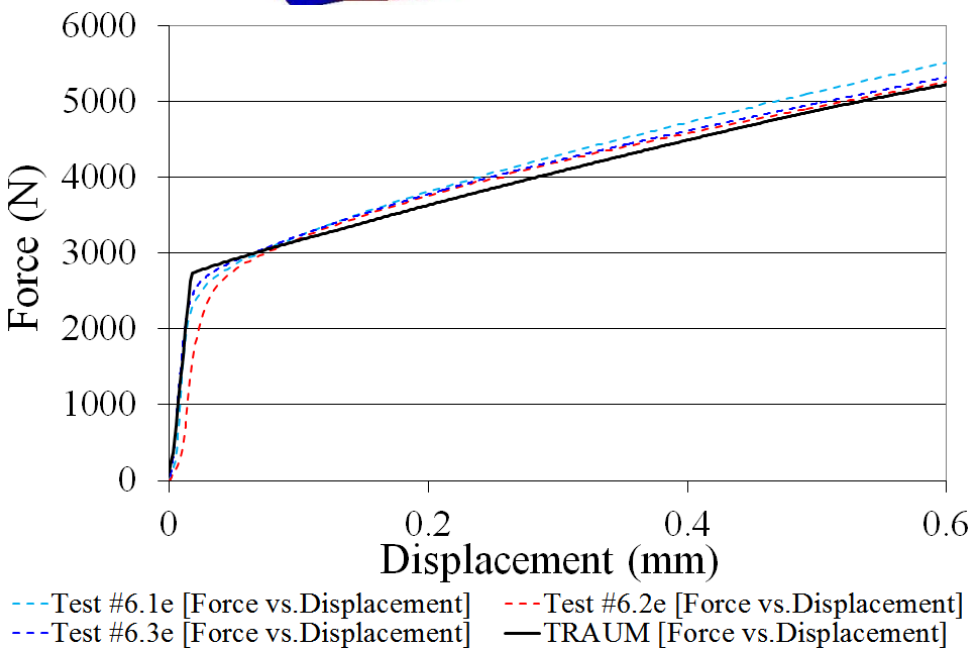

Figure 6-15: Quasi-static test results for Specimen #14; (a) Test #6 surface strain prediction with TRAUM and (b) force vs. displacement comparison between Test #6 results and TRAUM predictions.

6.6 **Shear/torsion specimen**

Shear specimen is simulated by using the flow and failure curves that are characterized in Chapter 5. Figure 6-16(a) illustrates the strain field measurement of the Specimen #15, where Figure 6-16(b) represents the simulation results when TRAUM is utilized with the characterized values of the material data. Figure 6-16(c) represents the comparison of the moment vs. rotation response between the test and FE simulation results.

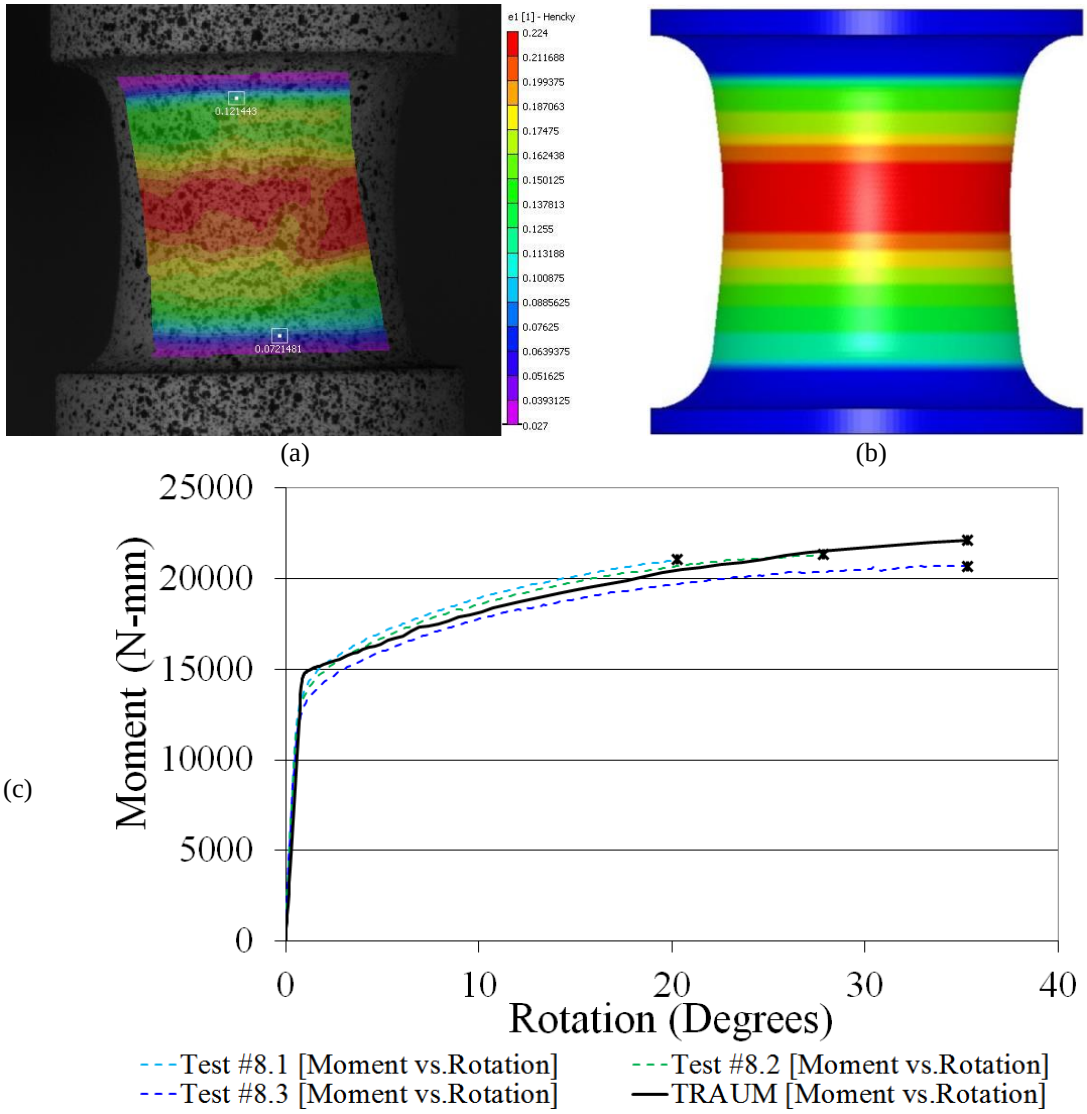

Figure 6-16: Quasi-static test results for Specimen #15; (a) DIC strain field measurement, (b) Test #8 surface strain prediction with TRAUM and (c) force vs. displacement comparison between Test #8 results and TRAUM predictions.

6.7 **Combined tension/torsion specimens**

Combined tension/torsion specimens are simulated by using the flow and failure curves that are characterized in Chapter 5. Figure 6-17(a) and Figure 6-18(a) illustrate the strain field measurements of the Specimen #16 and Specimen #17, where Figure 6-17(b) and Figure 6-18(b) represent the simulation results when TRAUM is utilized with the characterized values of the material data, respectively. Figure 6-17(c) and Figure 6-18(c) represent the comparison of the moment vs. rotation and force vs. displacement responses between the test and FE simulation results.

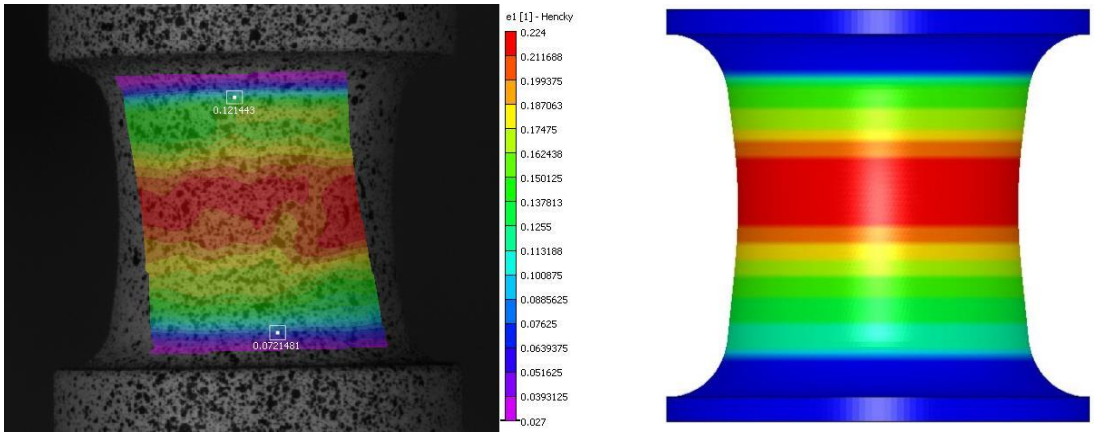

(a) (b)

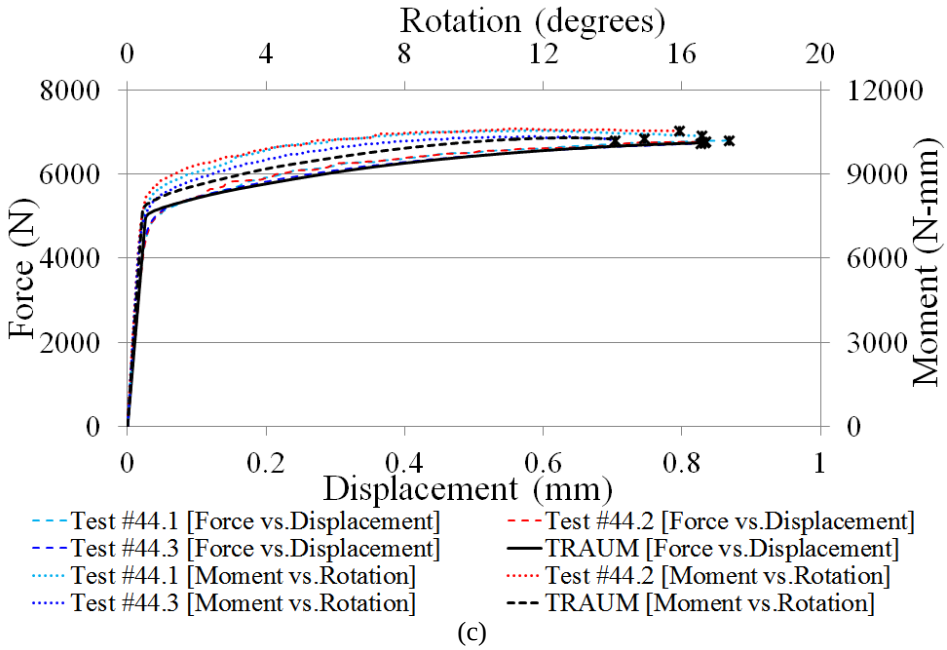

(c)

Figure 6-17: Quasi-static test results for Specimen #16; (a) DIC strain field measurement, (b) Test #44 surface strain prediction with TRAUM and (c) force vs. displacement comparison between Test #44 results and TRAUM predictions.

It should be noted that the ratios between the amount of torsion and tension for Specimen #16 and Specimen #17 are different and these specimens are specifically designed to match the Lode-angle-parameter of the two intermediate plane-stress specimens that are designed in Chapter 4 for 'bridging' purposes. Even though there can be changes in the initially designed stress-states; it is shown that tabulated construction of the failure surface with TRAUM can accurately predict the failure as the failure surface is built from designated specimens.

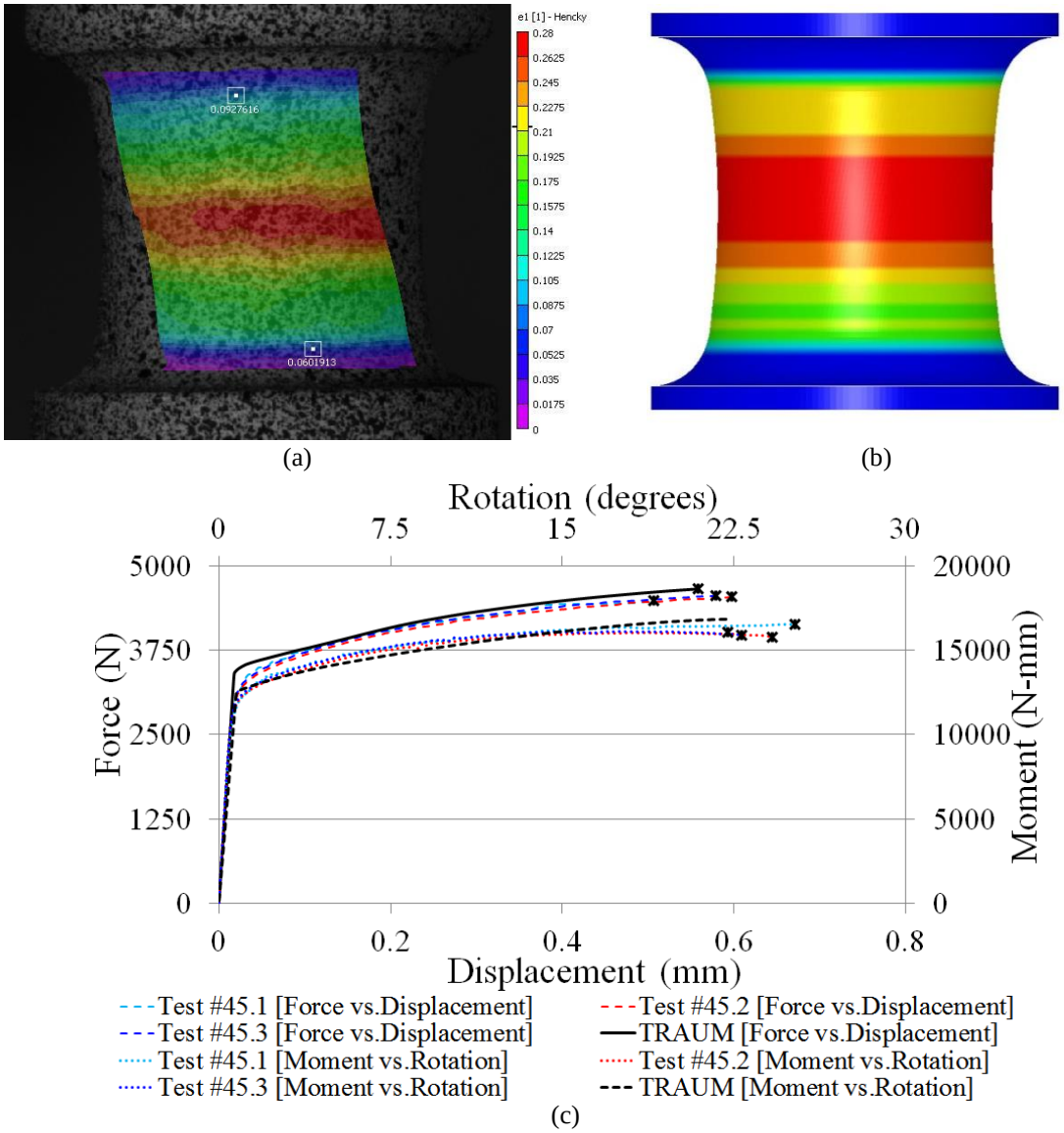

Figure 6-18: Quasi-static test results for Specimen #17; (a) DIC strain field measurement, (b) Test #45 surface strain prediction with TRAUM and (c) force vs. displacement comparison between Test #45 results and TRAUM predictions.

6.8 **Punch test specimens**

Punch test specimens are simulated by using the flow and failure curves that are characterized in Chapter 5. Figure 6-19(a), Figure 6-120(a) and Figure 6-21(a) illustrate the corresponding nose shapes and the specimen set-ups that are designed in Chapter 4 for specific stress-states at failure. These figures represent the simulation models when TRAUM is utilized with the characterized values of the material data. Figure 6-19(b), Figure 6-20(b) and Figure 6-21(b) represent the comparison of the force vs. displacement response between the test results and FE simulations.

It should be noted that Specimen #18 and Specimen #19 are designed to reach negative stress-triaxiality values around the biaxial-tension region, where Specimen #20 is designed to represent a stress-state around pure shear. It can be concluded that all punch test specimen results are accurately predicted.

(a)

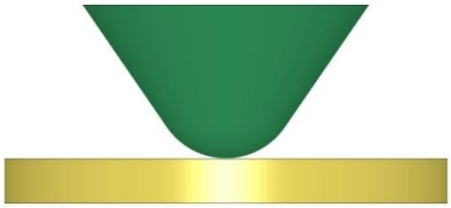

(b)

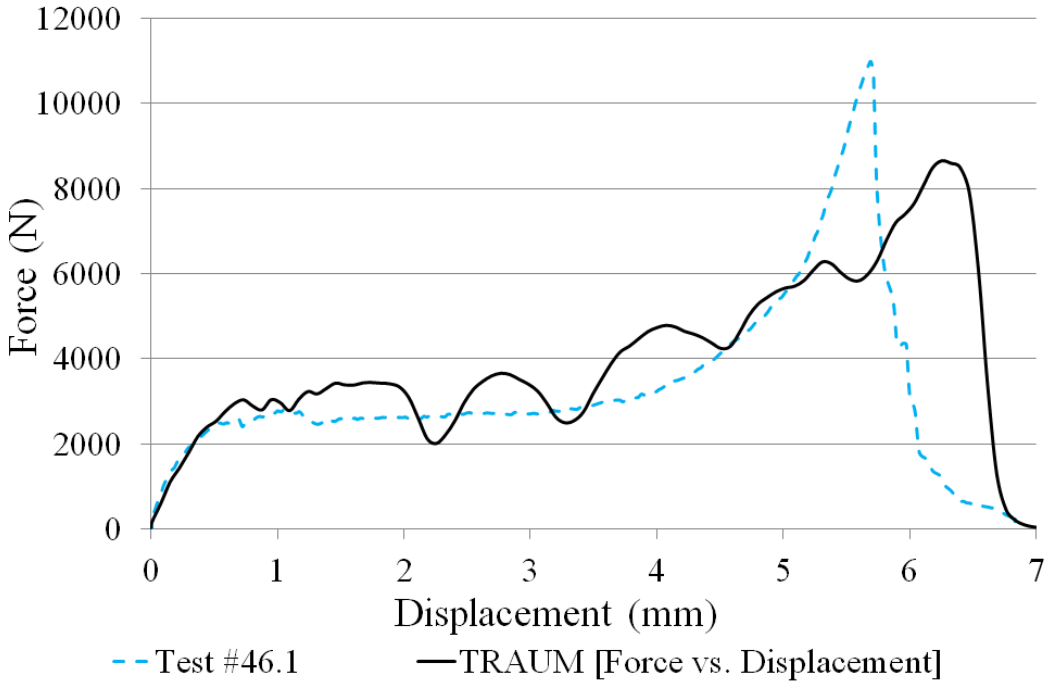

Figure 6-19: Quasi-static test results for Specimen #18; (a) corresponding punch nose shape and (b) force vs. displacement comparison between Test #46 results and TRAUM predictions.

(a)

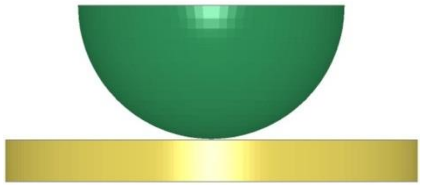

(b)

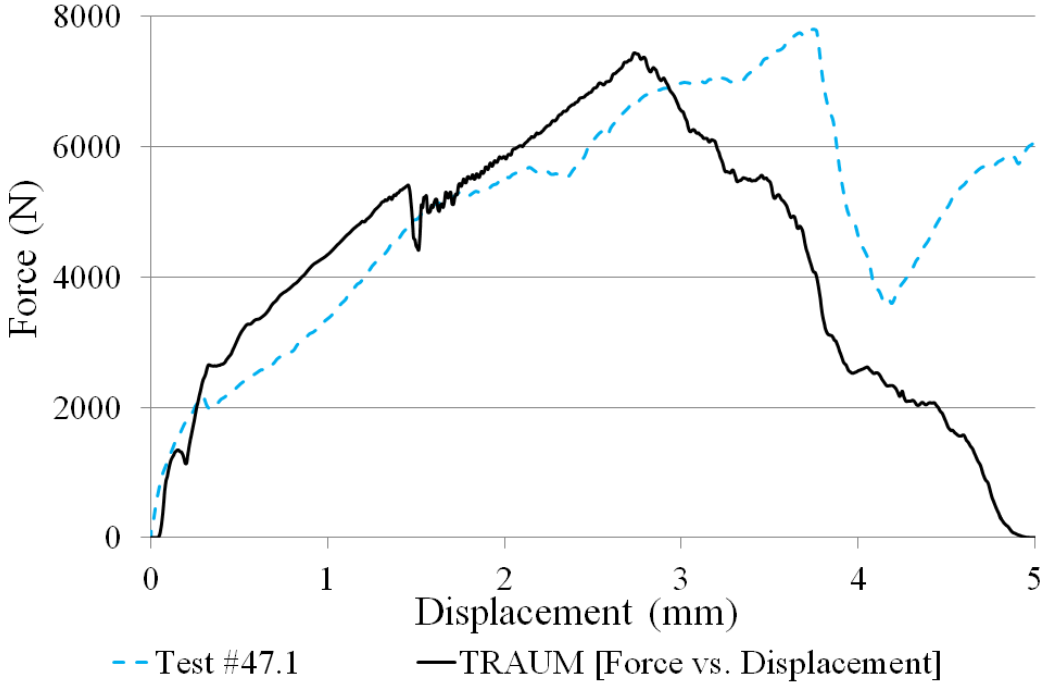

Figure 6-20: Quasi-static test results for Specimen #19; (a) corresponding punch nose shape and (b) force vs. displacement comparison between Test #47 results and TRAUM predictions.

6.9 **Summary and conclusions**

All specimens that are designed in Chapter 4 are validated at quasi-static conditions by using the new material model 'TRAUM' and newly characterized material properties from Chapter 5. Specimens with a very diverse range of states-of-stress and failure behavior are evaluated according to the force vs. displacement and moment vs. rotation measurements, which were attained by direct LVDT and DIC measurements. True strains at failure points are also compared, which were measured by DIC [108].

TRAUM can successfully predict the dynamic ductile deformation and failure behavior qualitatively and quantitatively considering the repeatability of the test results.

In the following chapter ballistic predictive performance of the new material model with newly characterized material data is evaluated.

(a)

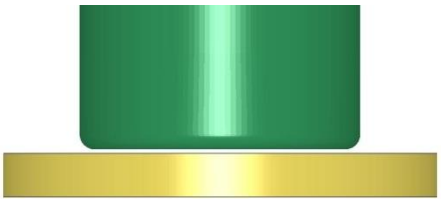

(b)

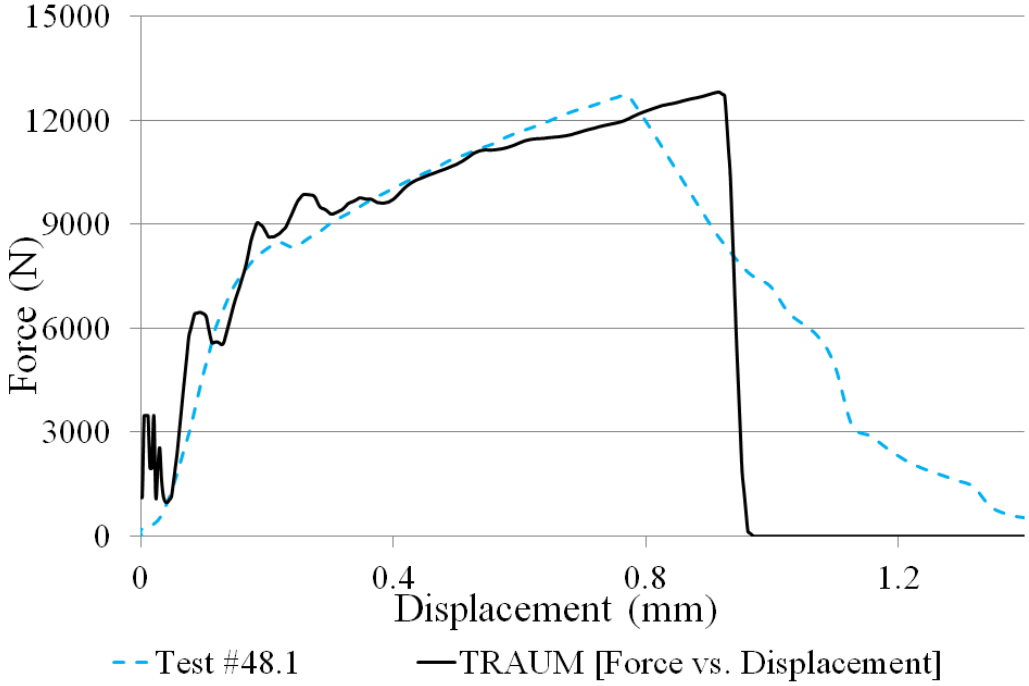

Figure 6-21: Quasi-static test results for Specimen #20; (a) corresponding punch nose shape and (b) force vs. displacement comparison between Test #48 results and TRAUM predictions.

CHAPTER 7 - **Impact loading applications**

7.1 **Introduction**

Thermo-elastic/viscoplastic material behavior is investigated in the previous chapters and a new material model is developed to address the challenges of the impact phenomenon that are described in detail by Chapter 3. The new material model and characterized material input is validated by a series of material tests at different loading regimes and boundary conditions.

In this chapter, the applications of the new material model are carried out by utilizing ballistic impact tests from Chapter 3 first. The justification for that is to compare the accuracy, robustness and performance of the new model and the newly characterized data set against J-C and the material data from literature. Therefore, TRAUM is employed with the characterized data set to simulate and compare the ballistic cases described in Chapter 3.

Additional ballistic impact test data is provided within the framework of this research, where the same lot of material that is characterized in Chapter 5 was used during the tests [388]. The test conditions comprise a cylindrical projectile with a large radius for the nose shape and use three different thicknesses of Al2024-T351.

7.2 **Ballistic impact with spherical projectiles**

Ballistic impact testing of aluminum targets was performed at three different thicknesses of 1.587, 3.175 and 6.35mm at different impact velocities [57]. A spherical projectile was used for the impacts. The ballistic limit for 1.5875mm plate was found about 122m/s, for 3.175mm it was about 213m/s and for 6.35mm it was about 411m/s.

It is shown by Figures 3-8, 3-10 and 3-12 that for a thin target, different set of material model parameters and different meshes can satisfactorily predict ballistic limit and failure mode. However, the results for successive thicker plates are not found to be satisfactory as the deformation and failure characteristics changes. This fact is further investigated in the proceeding chapters and a new material model is developed to address the failure criterion considering the state-of-stress and mesh size. The ballistic

experiments present a good comparison tool for the overall robustness of a new material model since the model is challenged against both qualitative and quantitative comparison.

Therefore, the ballistic impact simulations that were described in Chapter 3 are used by incorporating TRAUM as a material model and newly characterized Al2024-T351 material data set as an input. It should be noted that, after having seen in Figure 5-20 that a significant spread exist on the flow characteristics of the same material depending on different providers, some reservations naturally exist for a direct comparison. However, this application can still provide enough information about the mesh sensitivity and the performance of the regularization algorithm.

The corresponding results are plotted against some of the best results obtained from Chapter 3 for a comparison by the new material model. Figure 7-1 illustrates the ballistic limit prediction with the new material model. It is clearly seen that excellent correlation is obtained even though thin plates from a different lot of material was used. It is also remarkable to see that the mesh dependency is insignificant with the new model.

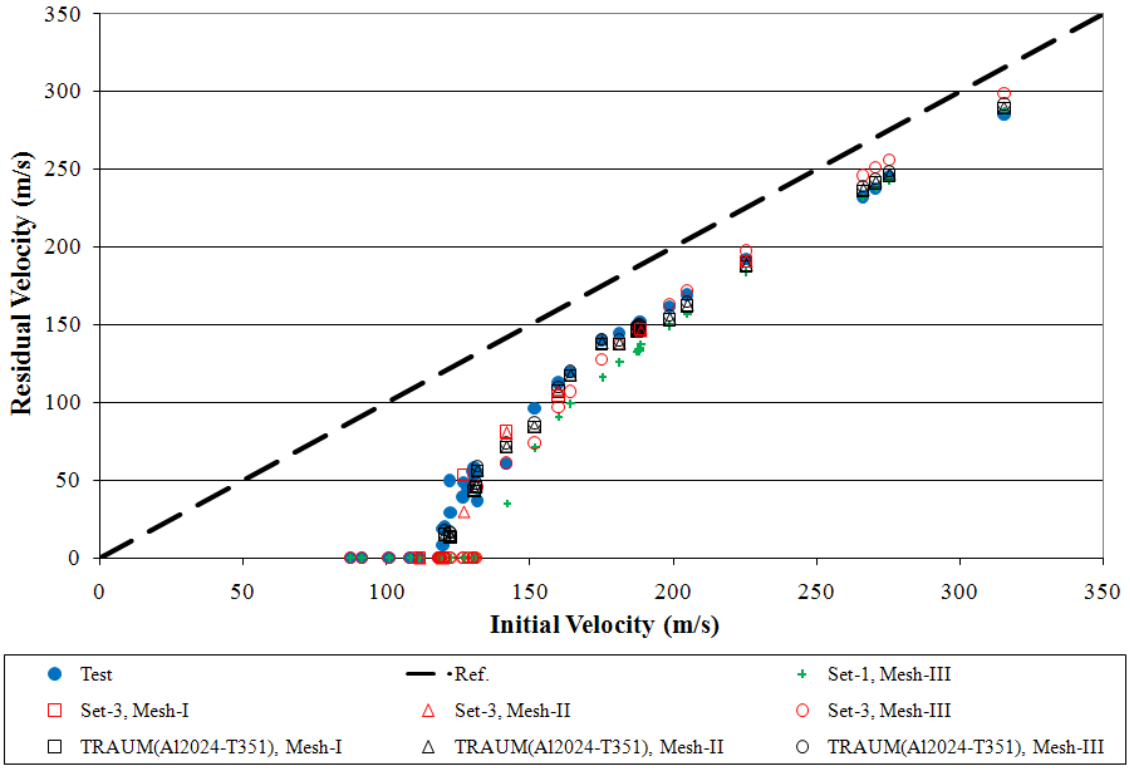

Figure 7-1: Ballistic limit predictions for 1.5875mm targets with TRAUM.

Figure 7-2 illustrates the failure modes and pattern for Mesh-III after petalling. Figure 7-2(a) illustrates only quarter of the full model for better illustration of the impact zone that is shown with the details of the mesh and the failure mode by Figure 7-2(b). The predicted failure mode can be compared with the test result that is illustrated by Figure 7-2(c) [57].

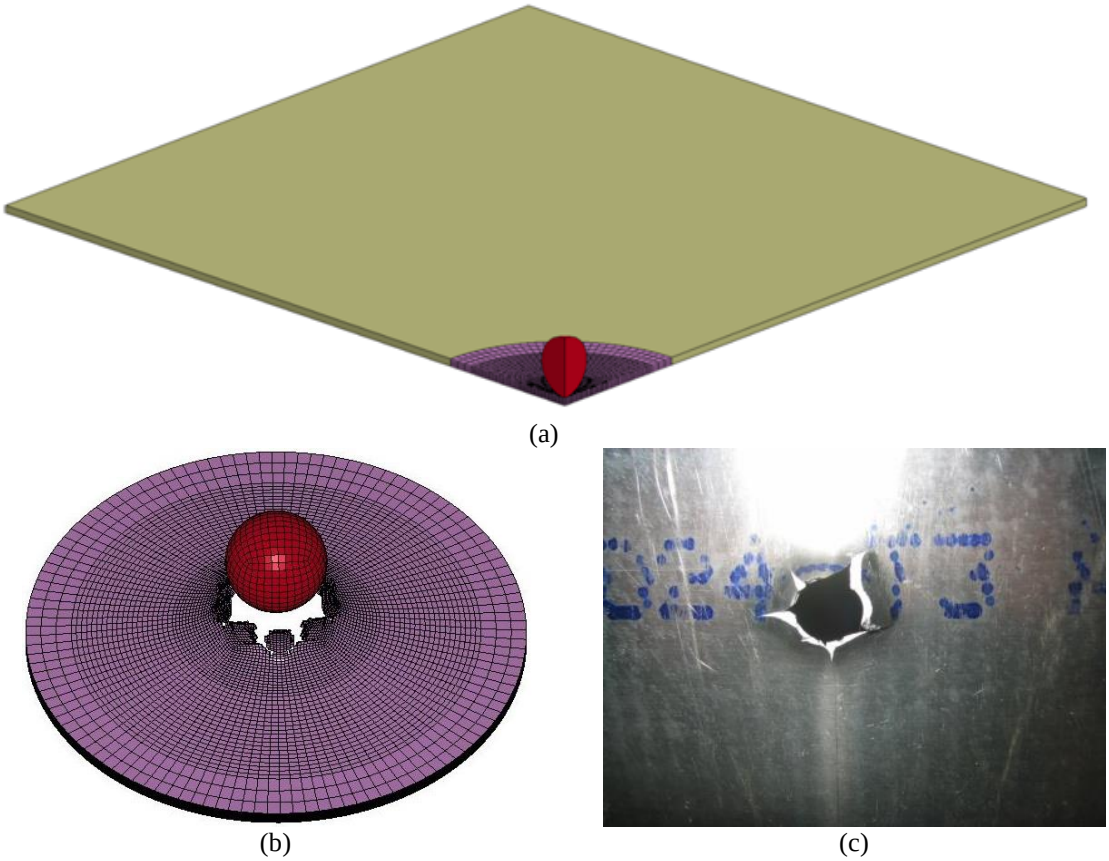

(a)

(b) (c)

Figure 7-2: Penetration through 1.5875mm target and petalling; (a) quarter of the full model, (b) simulation with TRAUM and (c) rear face of the test, after [57].

Similarly the analysis is carried out for 3.175mm thickness and it is observed that the prediction is comparable with J-C results. Figure 7-3 illustrates results with the new model for three different mesh lengths. The predictive performance of TRAUM can also

be observed when the failure mode changes from petalling to a hybrid form of both petalling and plugging.

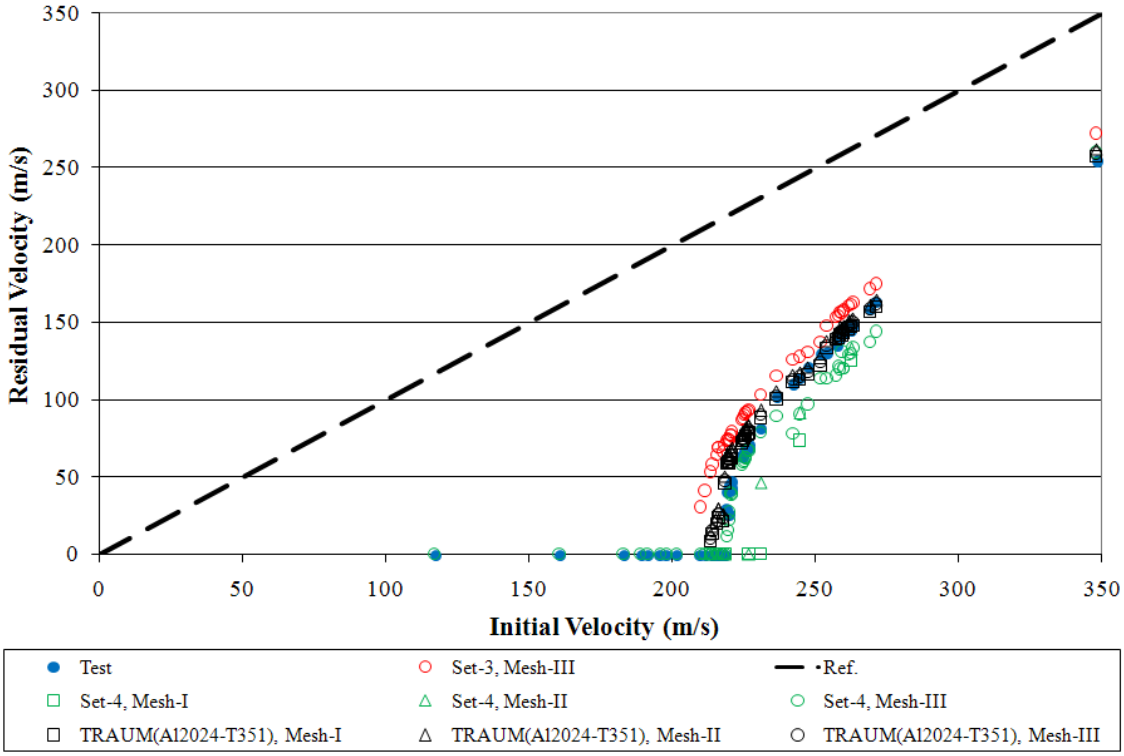

Figure 7-3: Ballistic limit predictions for 3.175mm targets with TRAUM.

It should be noted that the characterized material data set for TRAUM is from a different lot of material. Therefore, it is expected to have some differences on the plastic deformation and failure. However, ballistic limit, deformation and failure behavior are predicted accurately also for targets at 3.175mm thickness, where Figure 7-4 illustrates a transition in the failure mode with a plug and petals around the penetration cavity. Figure 7-4(b) illustrates the failure modes and pattern for Mesh-III after petalling, where Figure 7-4(a) illustrates quarter model for illustration. The predicted transition in the failure mode can be compared with the test result that is illustrated by Figure 7-4(c), where the plug is also shown on the target after impact [57].

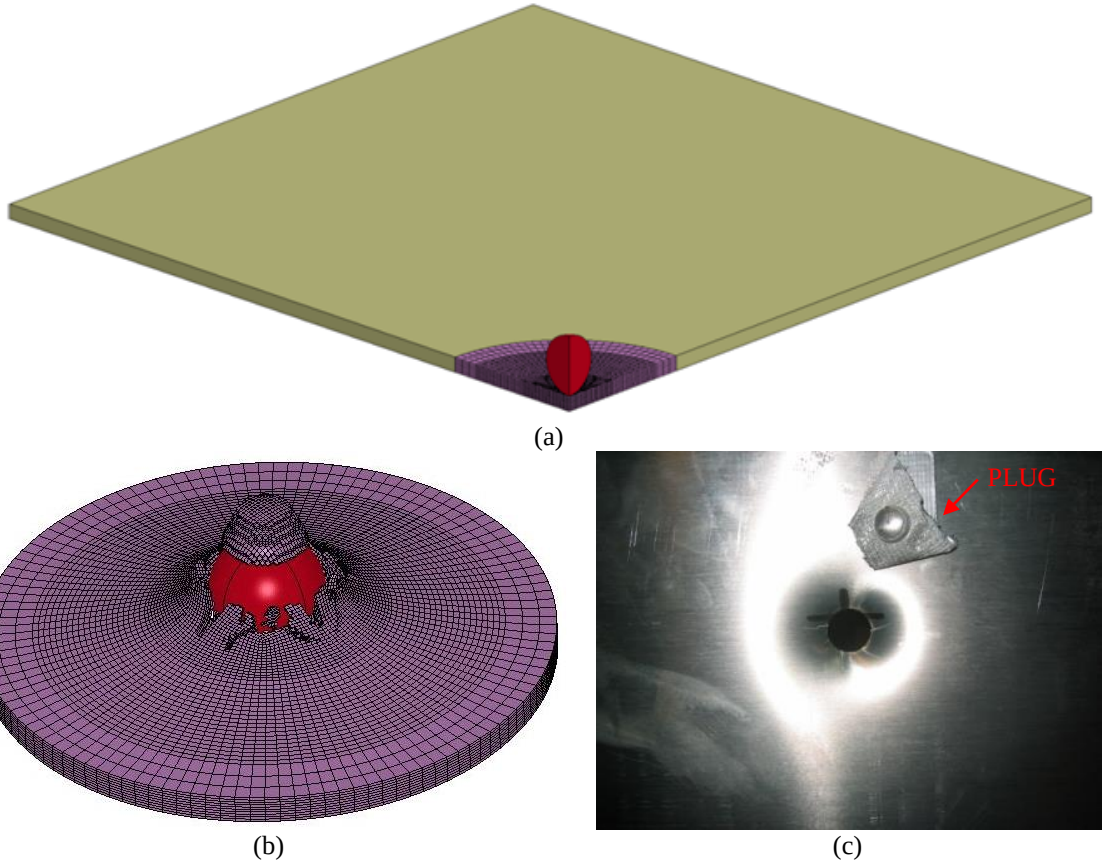

Figure 7-4: Penetration through 3.175mm target and mixed-mode failure formation; (a) quarter of the full model, (b) simulation with TRAUM and (c) front face of the test with the plug, after [57].

The thickest plate in that series was a 6.35mm thick target. The corresponding results predicted for the ballistic limit can be seen in Figure 7-5. The results suggest that the new model provides a dramatic improvement on the prediction of the ballistic limit also in that case. However, the ballistic limit is under-predicted with only 5.0ms^{-1} difference. This can be explained by the fact that the current model uses 0.9 as the Taylor–Quinney coefficient, which means 90% of the plastic work is converted into heat and the material softens according to the rise in the body temperature. However, Mason, et al. experimentally found a relation for the amount of plastic work converted by utilizing high speed infrared detectors and a Kolsky bar [316], where they have measured Taylor–Quinney coefficient with respect to the amount of plastic work. They have found that the coefficient is variable and a function of the plastic work. Especially at the beginning of

the plastic deformation, the amount of work converted into heat is lower than 90% for Al2024. It should also be noted that TRAUM is assuming a constant Taylor–Quinney coefficient. Therefore, under-predicting the ballistic limit can be expected if the material did not deform much, which is also expected for structures under shear loading. On the other hand, using a higher coefficient at the beginning of the deformation usually provides conservative predictions for the ballistic limit.

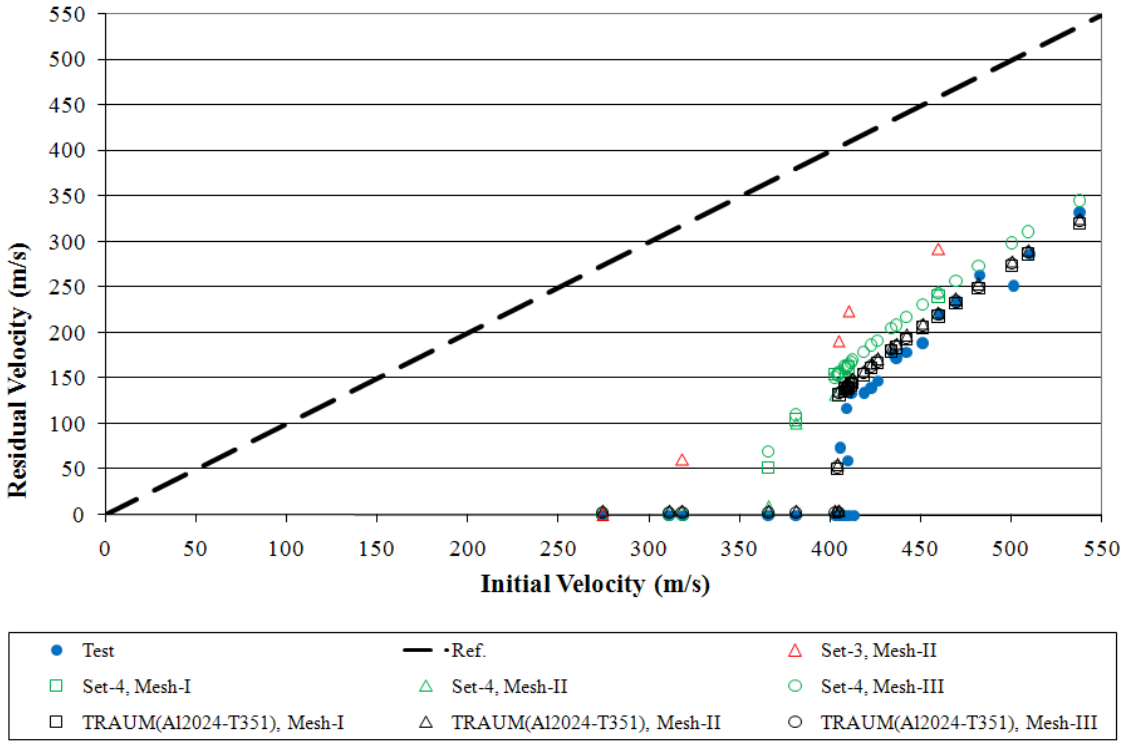

Figure 7-5: Ballistic limit predictions for 6.35 mm targets with TRAUM.

The failure mode in this thickness is observed as shear plugging. Figure 7-6 illustrates the plug formation during the simulation compared to the test result. Figure 7-6(a) illustrates quarter of the full model and the plugging failure mode for Mesh-III is shown in Figure 7-6(b). The predicted failure mode can be compared with the test result that is illustrated by Figure 7-6(c) [57].

It can be concluded that, even the material of interest was from a different lot of material stock, in all the cases, the new material model provides better and more

consistent results. As a result, impact behavior of aluminum Al2024-T351 can successfully be predicted by the new material model with the given characterization set.

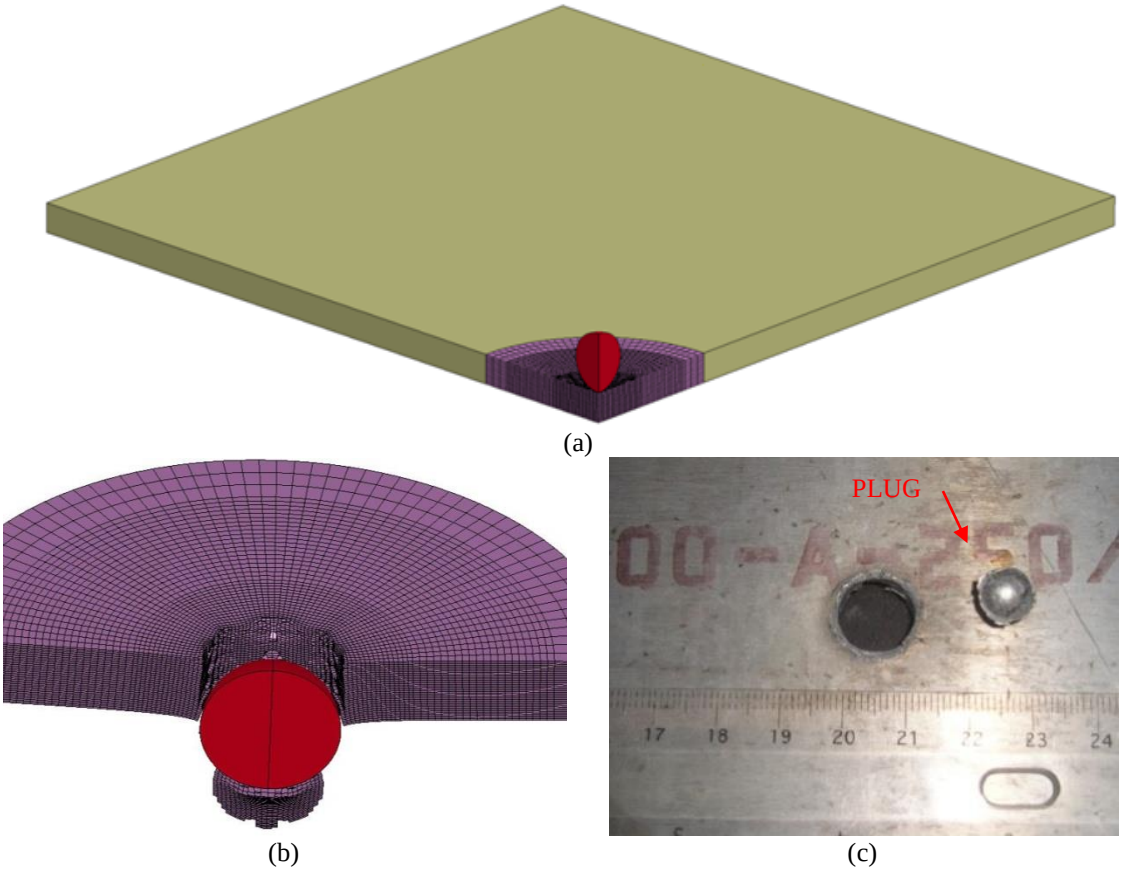

(a) (b) (c)

Figure 7-6: Penetration through 6.35mm target and plug formation; (a) quarter of the full model, (b) simulation with TRAUM and (c) front face of the test with the plug, after [57].

7.3 **Ballistic impact with cylindrical projectiles**

Cylindrical projectiles were used on targets, which were from the same lot of Al2024-T351 material with the specimens that are characterized in Chapter 5. Pereira, et al. has provided impact test results within the joint material research program [388]. The predictive performance of the new material model with the characterized material information is assessed under impact loading.

7.3.1 **Target geometries**

The target geometries were tested at three different thicknesses in the form of a square plate with 381mm edge length. Three different nominal target thicknesses at 3.175, 6.35 and 12.7mm were tested, where fifteen tests were performed for each thickness. The targets were rigidly constrained between a heavy steel fixture with a 254mm diameter circular aperture opening and 330mm fixture diameter as illustrated in Figure 7-7 [388].

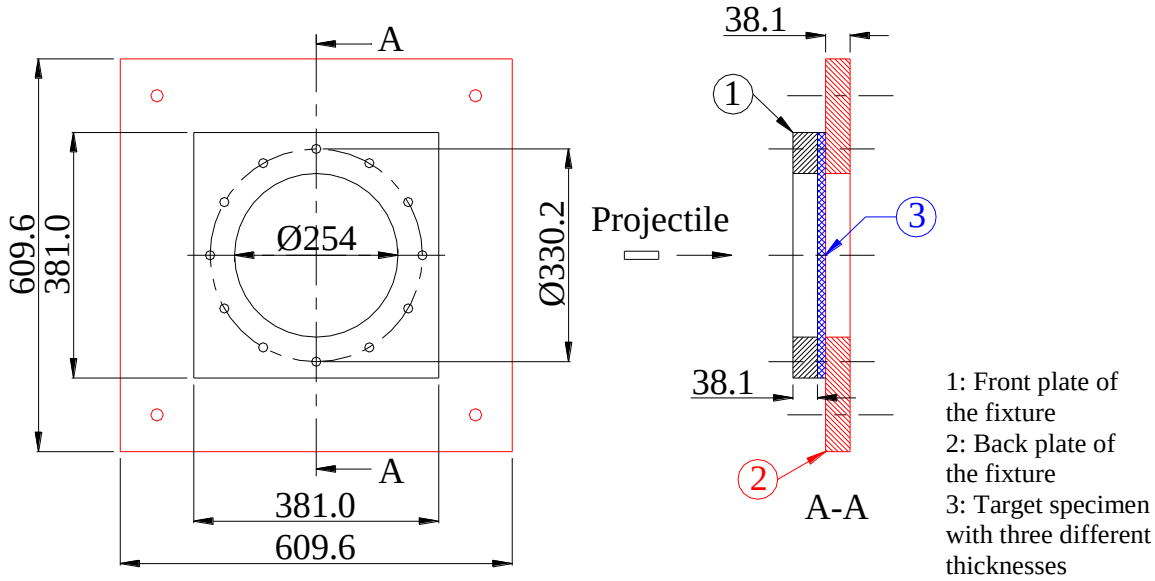

Figure 7-7: Specimen and fixture geometry that was used during the ballistic impact tests with three different target thicknesses, after [388].

7.3.2 **Projectile geometries**

Four different projectiles were used with different diameter to length aspect ratios and materials during the ballistic impact testing of Al2024 targets depending on the thickness of the specimen. It should be noted that the initial impact energy of the projectiles are selected to achieve a ballistic limit velocity of around 200ms^{-1} - 250ms^{-1}. Table 7-1 summarizes the nominal values of the projectile properties that were used during the testing [388]. The nose shapes of the specimens were also designed to avoid any complications due to misaligned or oblique impact. Therefore, a large radius was applied

to the front face and the edges were also ‘broken’ with a radius as illustrated in Figure 7-8 for the nominal dimensions that are listed in Table 7-1.

Table 7-1: Projectiles that were used during the ballistic testing of Al2024, after [388].

Projectile #	Target Thickness (mm)	Projectile Material	Projectile Diameter (mm)	Projectile Length (mm)	Projectile Mass (g)
1	3.175	Ti-6Al-4V	12.7	17.78	9.9
2	6.35	Ti-6Al-4V		22.86	12.8
3	12.7	A2 Tool Steel		38.1	37.5
4	12.7	A2 Tool Steel		28.575	28.0

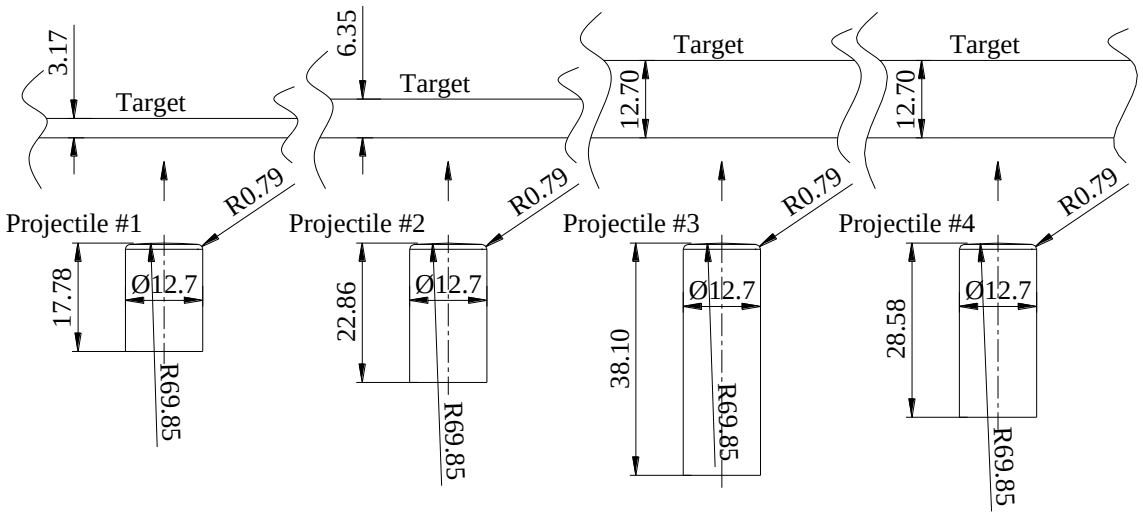

Figure 7-8: Cylindrical projectile with a round nose shape.

7.3.3 **Ballistic impact test apparatus**

A helium propelled gas gun with a vacuum chamber was utilized as the accelerator for the projectiles carried by appropriate sabot within a barrel that has a diameter of 50.8mm. The impact and residual velocities (i.e., if penetration occurs), the obliquity of the projectile and full field displacement measurements from the back side of the target were attained by using DIC and high speed cameras. The experimental set-up is shown in Figure 7-9 including the barrel and the vacuum chamber. More information about the testing apparatus and the ballistic experiments can be found from Pereira, et al. [388].



Figure 7-9: Ballistic impact apparatus, after [388].

7.3.4 **Ballistic impact test results**

The results of the ballistic impact tests can be summarized as illustrated in Figure 7-10. Clearly, the impact cases with residual velocities represent a penetration and the cases with no residual velocity may mean containment depending on the post impact analysis. A more detailed discussion about the test results can be found from Pereira, et al. [388].

It is seen that the impact tests with target thicknesses of 3.175 and 6.35mm have shown a trend and it was possible to identify a ballistic limit for the material depending on the initial impact energy. However, the 112.7mm thick targets have not shown a similar trend in the deformation and failure characteristics with a scatter independent of the test conditions, which was kept identical for the other thicknesses. These findings were discussed and it was suggested that the influence of friction due to the gauge thickness or the change in the failure mode could be the reason for the scatter [388]. Therefore, these ballistic tests are selected as a validation and benchmark problem to assess the accuracy of TRAUM with the stress-state dependent failure algorithm. Considering that these tests were also performed by using the same lot of material that

was also used to characterize the material flow and failure surfaces, it is expected that the new material model can demonstrate its predictive capability with this application.

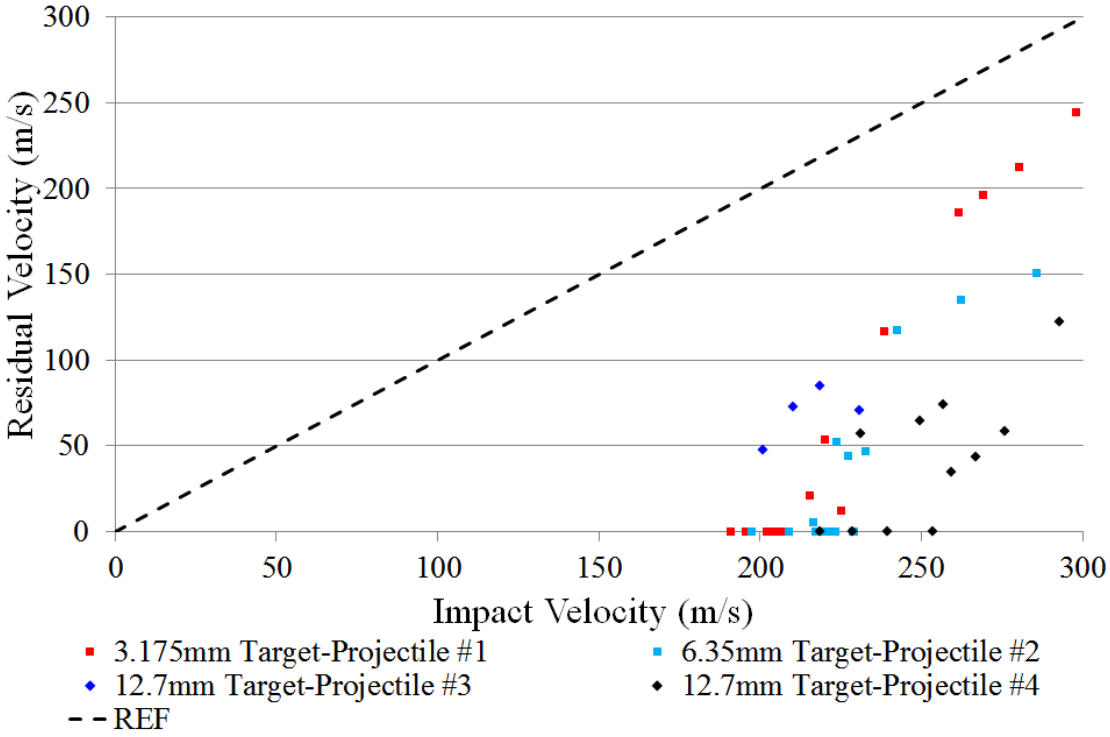

Figure 7-10: Ballistic impact test results, after [388].

7.3.5 **Numerical models of the ballistic impact with cylindrical projectiles**

Finite element models are developed to predict the ballistic impact performance of Al2024-T351 for the given impact conditions, where four different projectile models are developed according to the information in Table 7-1 and Figure 7-8. Each target material is modeled by using 8-noded solid elements with the characteristic element size that is used for the characterization of the material in Chapter 5. However, considering the overall dimensions of the target specimen and due to the concerns about the computational cost of the model mesh size is increased gradually towards the boundaries of the model, where a concentric mesh pattern is utilized to help wave propagation at the transition boundaries. It should be noted that since TRAUM utilizes a regularized failure algorithm, the plastic strains for the failure will automatically be calculated for the

corresponding elements. However, the characteristic element size should not exceed the limits that are defined during the construction of the regularization curve in order to predict localized necking. Figure 7-11(a) illustrates the FE model for 3.175mm thick target (i.e., in purple and green colors) considering that the specimen will be rigidly constrained around the circular aperture and Projectile #1 (i.e., in red color), where only a quarter of the model is shown for illustration purposes when the finite elements are hidden. A close up of the model can also be seen in Figure 7-11(b), where the impact zone is modeled in a more detailed fashion by using smaller elements.

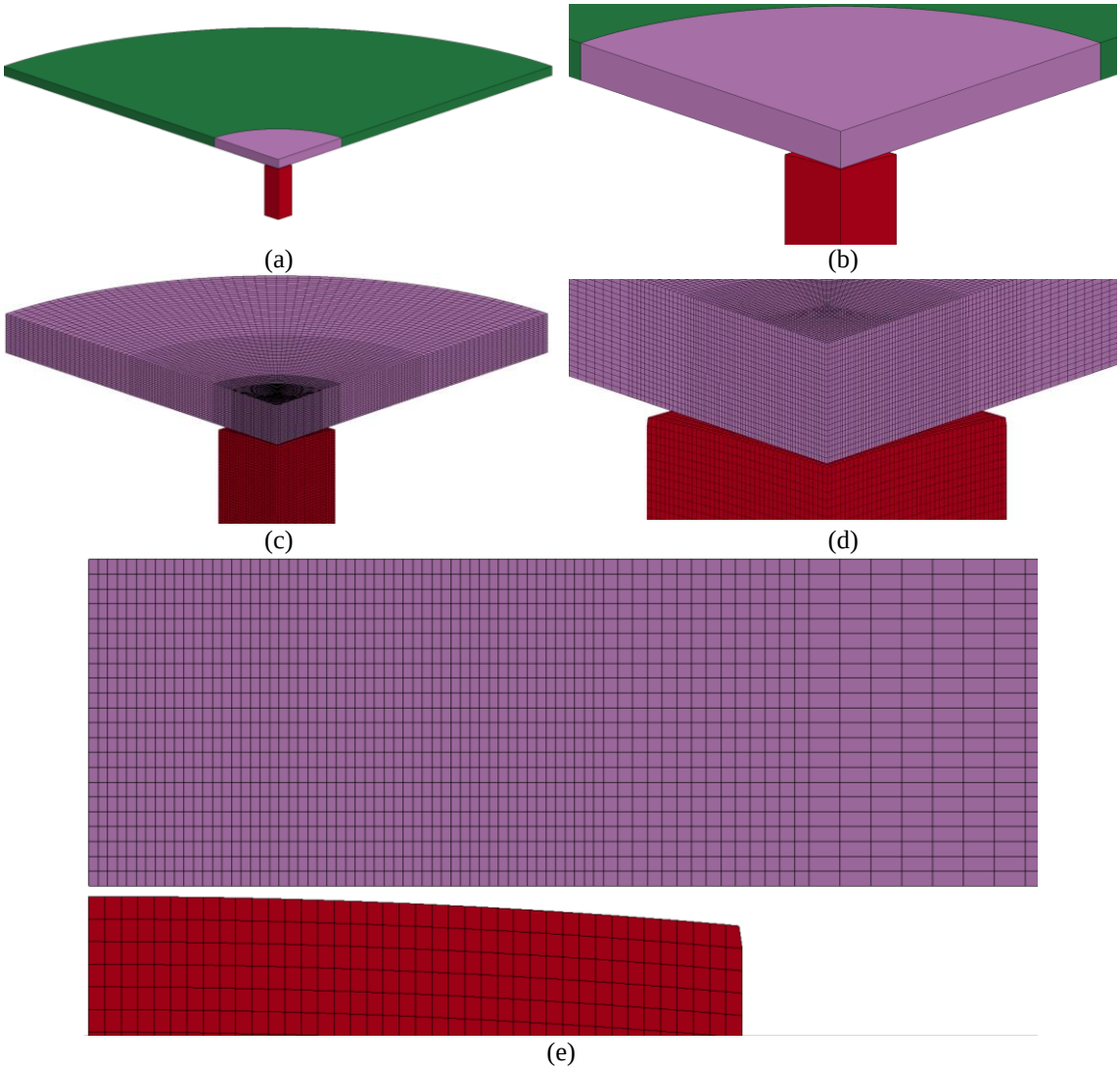

Figure 7-11: Quarter of the finite element model for 3.175mm thick targets with Projectile #1 showing; (a) quarter model, (b) close-up to the impact zone, (c) FE details of the concentric zoning, (d) FE details of the impact zone and (f) FE details of the cross-section of the projectile and the target for the quarter model.

Figure 7-11(c) illustrates the FE model when the element boundaries are visible and the concentric zoning is illustrated for the transition of the mesh boundaries between two successive characteristic element lengths. Figure 7-11(d) presents an even closer look-up into the impact zone. The curvature at the nose is clearly visible and modeled with high precision as illustrated in Figure 7-11(e) for the cross-section of the quarter model.

It should be noted that for 6.35 and 12.7mm targets, the same mesh size and pattern is preserved and the total number of elements are doubled each time when the thickness is doubled by using the same discretization through the thickness. The mesh details of the nose shape for the projectile FE model is also preserved for Projectiles #2, #3 and #4. The lengths of the projectiles are attained by adding the elements at the back side of the projectile to match the length and the required mass.

The target boundaries are constrained in the direction of motion of the projectile and it is assumed that the specimen can only be deformable within the opening defined by the size of the circular aperture.

The momentum transfer between the projectile and the target is attained by utilizing a contact impact algorithm, which is based on the penalty methodology and considers the newly forming target material surfaces as some of the elements within the impact zone are eliminated due to the element erosion algorithm when the plastic strain at failure is reached.

TRAUM utilizes the newly characterized material flow surface data with the features that incorporate stress-state dependent failure surface, adiabatic heating, mesh size regularization, strain-rate and temperature dependent failure strain scaling as illustrated in Figure 6-1.

Initial velocities, obliquity and small differences in the mass of the projectile at the time of impact can be found from Pereira, et al. [388]. These details are used to modify the models accordingly.

7.3.6 **TRAUM predictions for 3.175mm targets under ballistic impact with cylindrical projectiles**

Ballistic limit predictions for 3.175mm targets are illustrated in Figure 7-12. It is clearly shown that non-linear FE simulations are able to predict the ballistic limit accurately. The failure modes for the specimens are identified as predominantly shear due to the blunt nose shape of the projectile, which is in agreement with the experimental findings. It was reported that plug formation was observed after the ballistic limit. Figure 7-13 exhibits the formation of the plug during the incremental time-steps and eventually the separation of the plug from the target specimen is clearly observed. It should be noted that only the quarter of the target model and the projectile is shown to illustrate the formation of the shear-plugging better at the impact zone. It is predicted that as the plug separates from the target material, the projectile still has enough energy to push it forward for a free rigid body motion. Therefore, there are residual velocities after the penetration, which are in good agreement with the experimentally measured velocities.

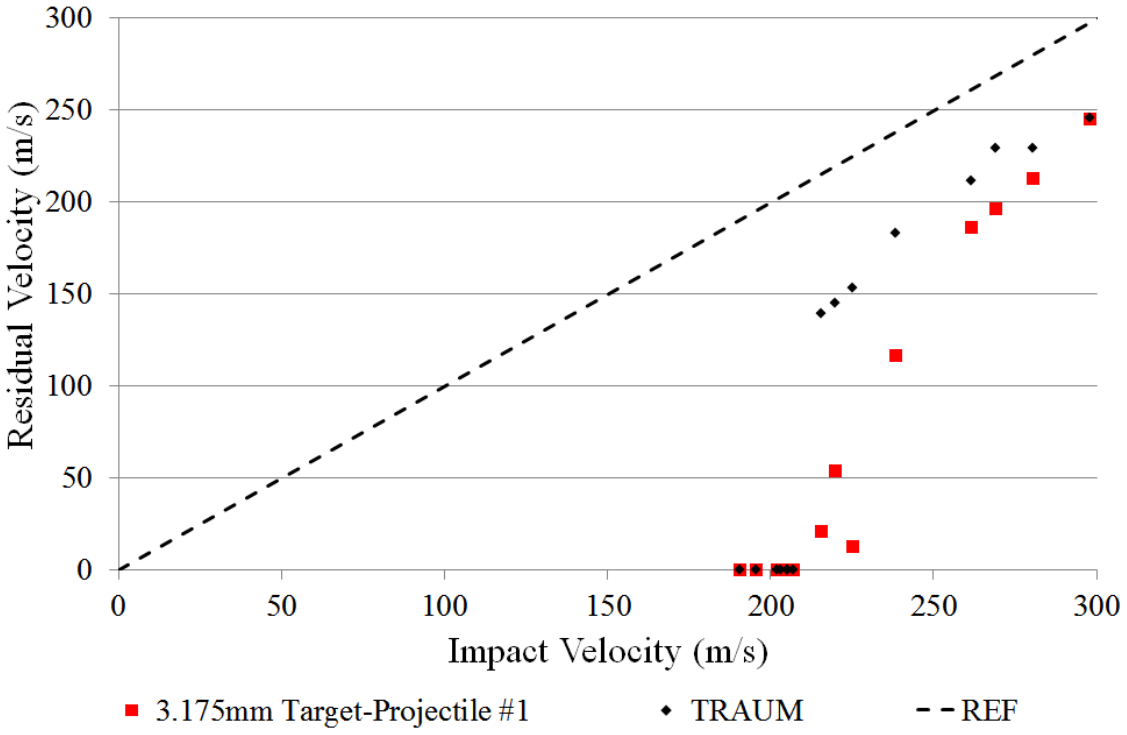

Figure 7-12: Ballistic limit predictions for 3.175mm targets with TRAUM.

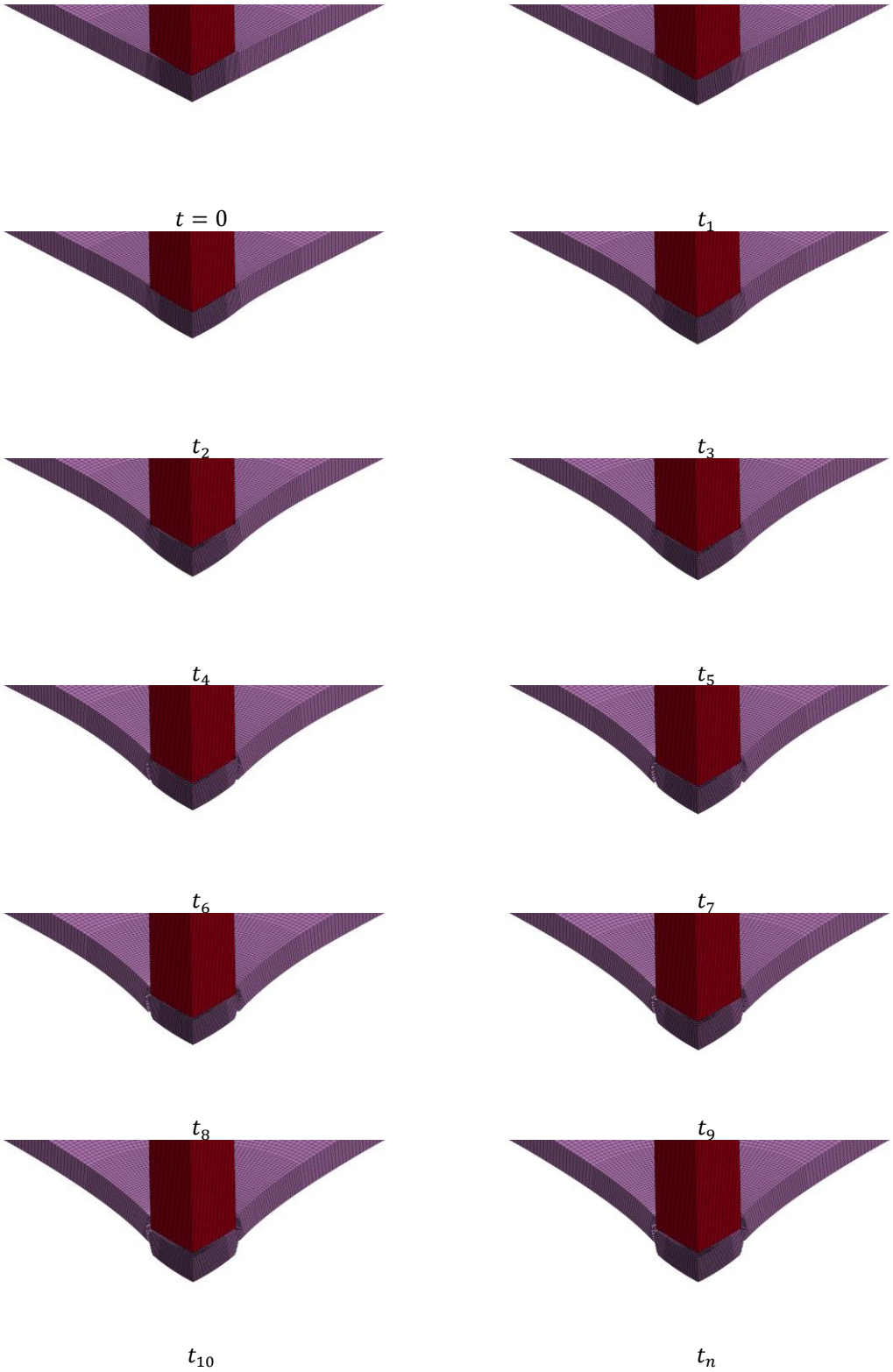

Figure 7-13: Incremental solution steps of the plug formation for 3.175mm target with TRAUM.

7.3.7 **TRAUM predictions for 6.35mm targets under ballistic impact with cylindrical projectiles**

Ballistic limit predictions for 6.35mm targets are illustrated in Figure 7-14. For this thickness, a 22.86 mm long projectile that is made of Ti-6Al-4V with a mass of 12.8g is used. It is shown that the ballistic limit is predicted with good accuracy and the residual velocities are also found to be consistent with an exception of the highest velocity. The reason for the over prediction is found to be the element erosion algorithm. It can clearly be seen in Figure 7-15 that as the elements reach their assigned failure strains and eroded from the simulation, the enlarging crater does not provide the necessary amount of sliding energy loss that should occur between the projectile and the surfaces of the enlarging punch hole. On the other hand, for lower velocities, it is successfully found that the projectile stuck in the hole as illustrated in Figure 7-16 even though the plug formation was completed.

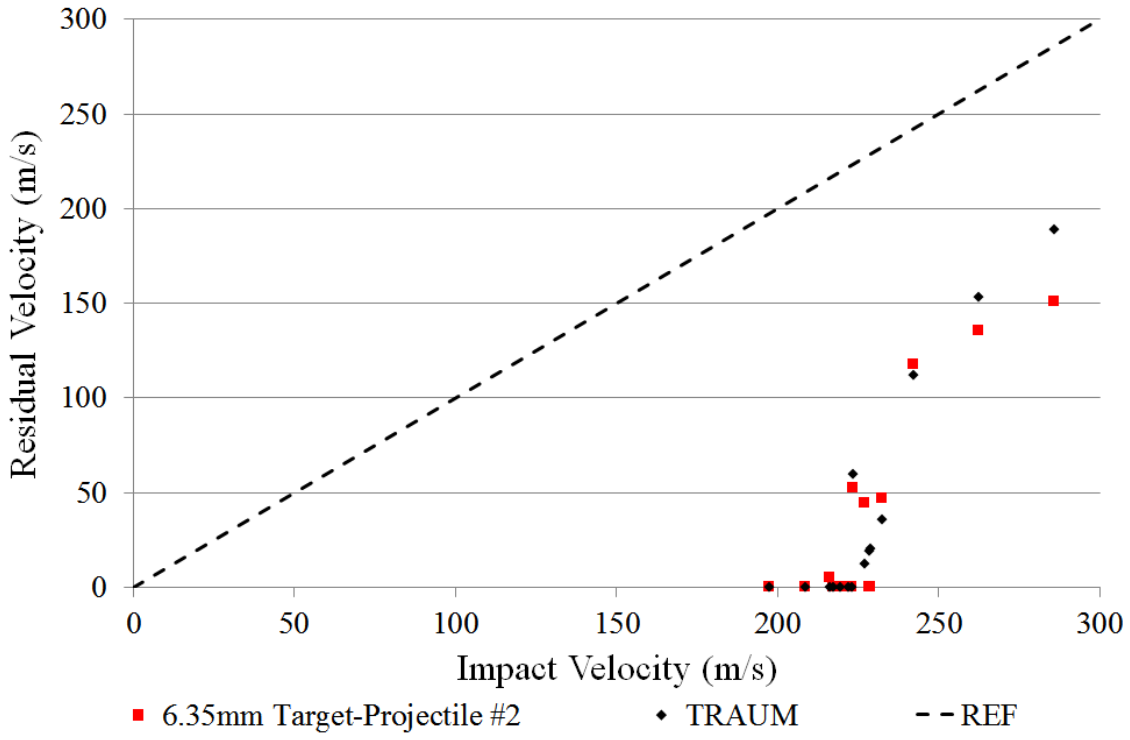

Figure 7-14: Ballistic limit predictions for 6.35mm targets with TRAUM.

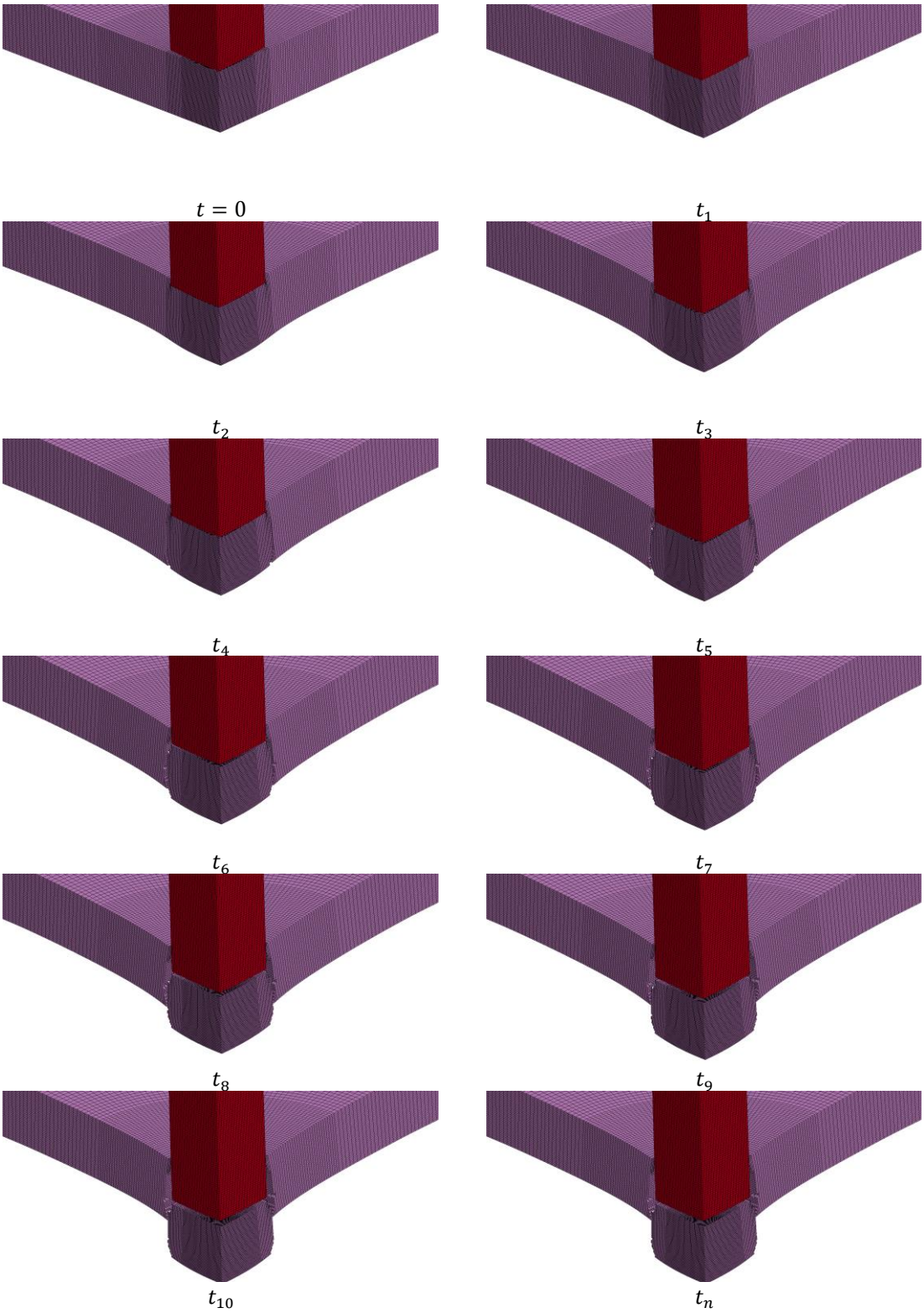

Figure 7-15: Incremental solution steps of the plug formation for 6.35mm target with TRAUM.

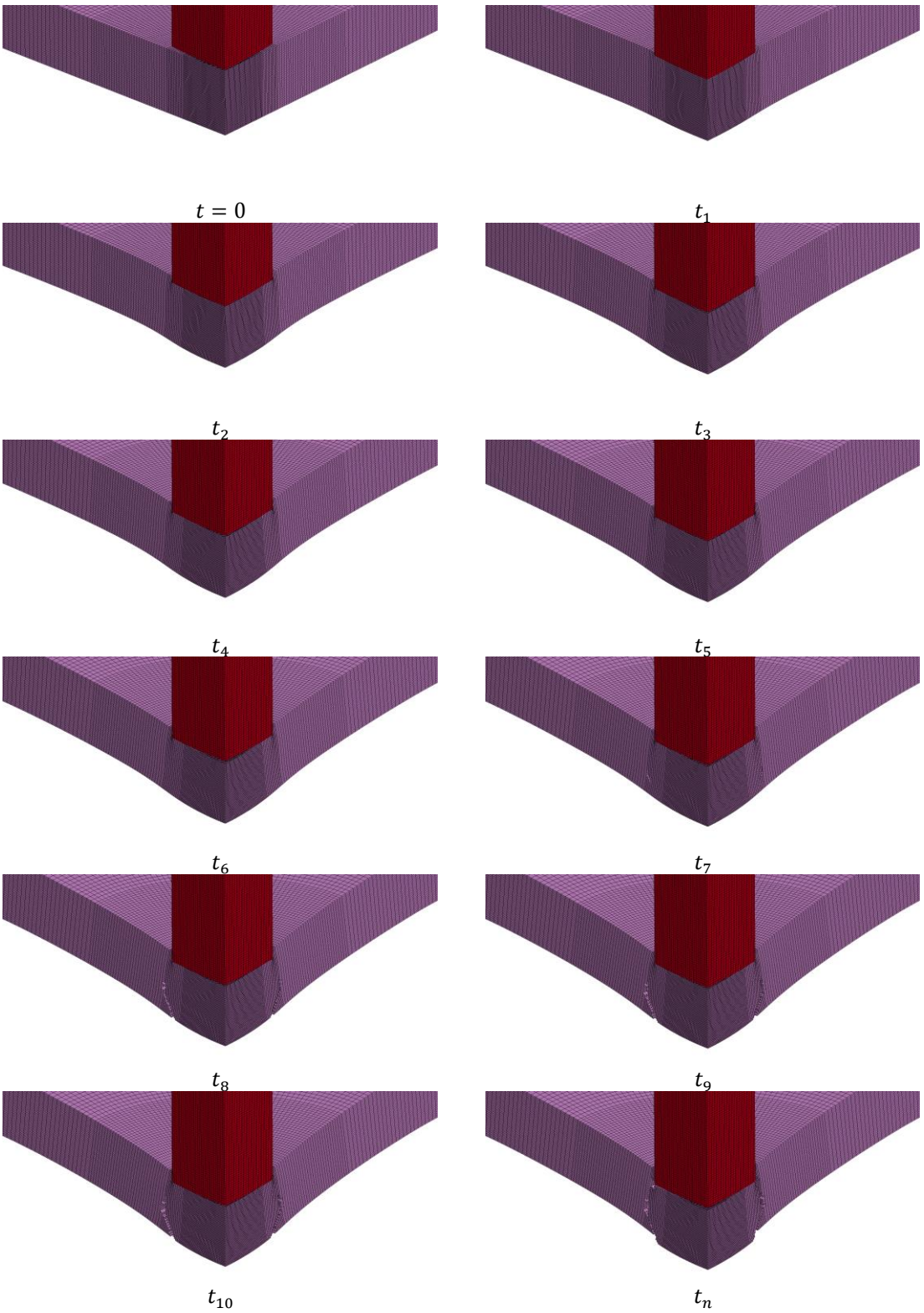

Figure 7-16: Incremental solution steps of the plug formation and projectile stuck for 6.35mm target with TRAUM.

7.3.8 **TRAUM predictions for 12.7mm targets under ballistic impact with cylindrical projectiles**

Ballistic limit predictions for 12.7mm targets are illustrated in Figure 7-17. For this thickness two different projectile lengths are used. The 'Projectile #4' is 28.575mm and the 'Projectile #3' is 38.1mm long. The projectiles are made of tool steel and the Projectile #4 is 28g, where the Projectile #3 is 37.5g, respectively. Since a ballistic limit around 200 ms^{-1} was desired, the mass of the projectiles were selected accordingly. However, it was found that all experiments with Projectile #3 provided a complete penetration for a thickness of 12.7mm. Therefore, the length of the projectile was reduced [388]. Both 3.175 and 6.35mm targets exhibited a similar ballistic response, where after a ballistic limit velocity the residual velocities increased as a function of the absorbed energy that provides a well-known ballistic performance characteristic curve. However, it is found with 12.7mm targets that the ballistic performance is providing a distributed response.

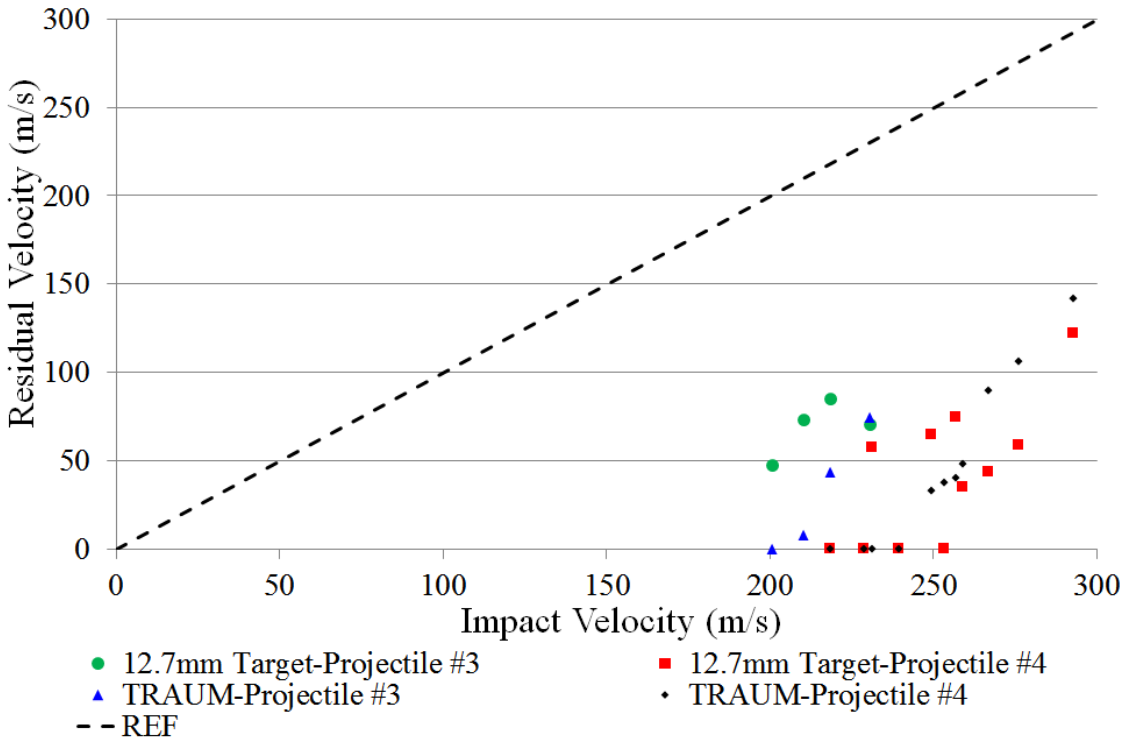

Figure 7-17: Ballistic limit predictions for 12.7mm targets with TRAUM.

It is shown with Figure 7-17 that TRAUM can still provide reasonable results for this problem, where it is suggested that the influence of friction should be considered more sensitively because the effects of stress-state dependent failure is fulfilled by utilizing TRAUM as the material model. Therefore, it is advisable to investigate the temperature and pressure dependent characteristics of friction for thick ballistic simulations, where it is clear that the effects of friction can be highly dependent on the localized temperature and pressure profiles.

Figure 7-18 illustrates a similar case for 12.7mm targets, where the projectile is stuck inside the punched hole. The interaction between the projectile and the inside surface of the enlarging hole is critical and needs to be investigated by incorporating nonlinear friction models. However, this is not within the scope of this dissertation and will be attained during the future research.

Therefore, it is concluded that, considering the repeatability of the ballistic impact tests, TRAUM can be used to predict the ballistic performance accurately. It can be utilized as a generic tool for dynamic ductile failure prediction under different states-of-stress, strain-rate and temperature.

7.4 **Summary**

An extensive effort is presented on the prediction of ductile failure for sheet metals under impact loading. In the first section, simulations of three different thicknesses with a spherical projectile impacting at varying speeds are carried out by using three different mesh patterns that are also used in Chapter 3. Promising results are obtained even though the material of interest was from a different stock. It is suggested that a fully tabulated input for a Taylor–Quinney coefficient as a function of plastic work may be desirable for the future work.

For the second section, ballistic performance predictions are attained for three different thicknesses for the same stock of material that was used for characterization. Good correlation is achieved between the predictions and the test results. It can be concluded that, TRAUM; as a thermo/elastic-viscoplastic material model with regularized stress-state dependent failure, can be used to predict dynamic failure behavior of ductile materials.

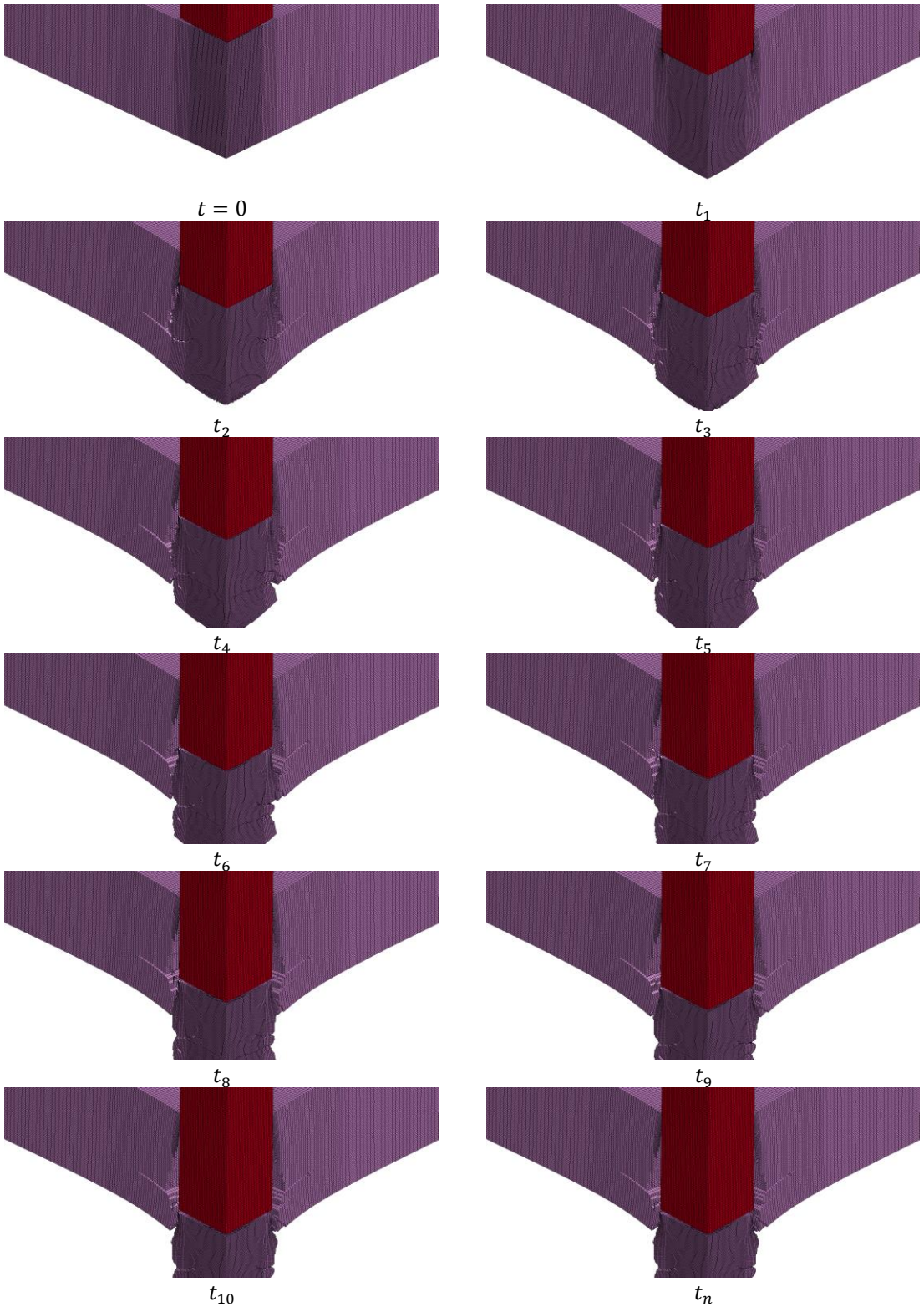

Figure 7-18: Incremental solution steps of the plug formation and projectile stuck for 12.7mm target with TRAUM.

CHAPTER 8 - **Summary, Conclusions and Recommendations**

8.1 **Summary and contributions**

Ductile deformation and failure of materials under impact loading is studied experimentally and numerically. Major contributions of the research within the course of the dissertation can be listed as:

Ballistic impact simulations are performed for aluminum plates by utilizing a phenomenological material model and it is found that these models may not necessarily be accurate enough to predict failure for a wide range of different modes. It is found and also verified with literature that one of the most significant factors effecting ductile failure is the state-of-stress.

A new elastic/viscoplastic material model with a regularized failure algorithm is developed and named as TRAUM. The failure criterion is formulated as a function of stress-triaxiality and Lode-angle-parameter. Product-triaxiality is used to identify the failure points during an impact event.

Several specimens with different geometries are designed to reflect different states-of-stress for specifically targeted stress-states by using an iterative procedure.

Material and failure characterization is performed to generate corresponding TRAUM inputs for Al2024-T351.

All material test cases for specifically designed specimens and ballistic impact tests are used during the validation of the new material model and characterized material information.

TRAUM uses a tabulated input format for any flow description independent of the shapes of the hardening curves for the corresponding strain-rates and temperatures. Therefore, can be applicable to fcc, bcc and hpc materials when the flow behavior is characterized adequately as described in Chapter 5.

8.2 **Conclusions**

Conclusion on the outlined summary of accomplishments can be further detailed as:

8.2.1 **Ballistic impact simulations on aluminum plates**

J-C is utilized to predict the ballistic limits and failure behavior of Al2024-T3/T351 aluminum alloy plates with three different thicknesses. 1.5875, 3.75 and 6.35mm plates are simulated with varying impact speeds and it is found that the failure mode changes drastically from petalling to plugging as the thickness and impact speed increases. J-C is found to satisfactorily predict the ballistic limit and failure mode for thinner plates. However, it is not as accurate for higher thicknesses and impact speeds. Four different material model sets that are found through the literature for J-C are benchmarked with three different mesh patterns to see the sensitivities of the current approach. It is concluded that the state-of-stress in the vicinity of failure changes drastically as the thickness and impact speed changes. It is confirmed through the literature that also nose shape, orientation and obliquity of the projectile has a significant role on the stress-states observed around the failure zone. On the other hand, J-C material sets are found to be calibrated and tuned for some specific test results and cannot be used generically for different impact scenarios especially if the stress-states and failure modes are changing. It is also concluded that a new material model was needed that can address these problems along with the mesh dependency of the phenomenon.

8.2.2 **Development of an elastic/viscoplastic material model with a regularized failure, TRAUM**

A new elastic/viscoplastic material model, with a regularized failure algorithm, TRAUM, is developed to address the needs that are identified by ballistic impact simulations. The new material model defines the flow surface as tabulated inputs of strain-rate and temperature dependent hardening curves and/or tables. Similarly, the model defines the failure surfaces as tabulated inputs of strain-rate and temperature dependent failure strain curves and/or tables. Considering that most metals under different loading conditions obey von Mises plasticity, a J_2 flow rule is considered for the

plasticity treatment. The accumulated failure algorithm is formulated by using stress-triaxiality and Lode-angle-parameter to include the effects of third deviatoric stress invariant on failure. Product-triaxiality, which is defined as a function of third stress invariant, is utilized as an alternative parameter to define a state-of-stress space to quantify failure. For ductile metals under impact loading, it is found that failure points accumulate around a certain location, which can be defined by stress-triaxiality and product-triaxiality on the space of state-of-stress. Identifying a certain area of the failure locus is significantly important for ductile failure, a bridging and an iterative specimen design algorithm is introduced to devise a test matrix with specifically designed specimens while constructing this failure locus. Several specimens with different geometries are designed to reflect different states-of-stress while testing such as; plane-stress, axi-symmetric tension, plane-strain, compression, shear and combined tension/shear. Targeted stress-states are calculated through an iterative procedure for these specimens. TRAUM is benchmarked against a commonly used material model, J-C by employing single element tests. It is concluded that the new material model can accurately predict strain-rate and temperature dependent deformation and failure.

8.2.3 **Material characterization for Al2024-T351**

Material characterization is performed on the specifically designed Al2024-T351 specimens to provide input data for TRAUM. While characterizing the hardening curve, a new methodology is introduced to generate the stress-strain curve after necking with fewer iterative FE simulations. Plane-stress specimen is selected for characterizing the quasi-static hardening curve at room temperature. It is found that this specimen fails after both diffuse and localized necking. It is also found that Al2024-T351 has negative strain-rate sensitivity, which is often referred as DSA and PLC effects are identified during the flow. Therefore, a more sophisticated automated material characterization algorithm is developed by utilizing SRSM and AOM. Adiabatic and iso-thermal flow surfaces are characterized by using the automated methodology for tension, compression and shear.

A complete failure locus is then characterized for Al2024-T351 based on the stress-triaxiality and Lode-angle-parameter. The failure surface is illustrated also as a function of stress-triaxiality and product-triaxiality. The scaling curves for accumulated failure law

are characterized through strain-rate and temperature dependent failure strain values. The failure criterion is regularized with respect to characteristic element size. A complete material input set is generated to be used for TRAUM during the validation phase.

8.2.4 **Validation and verification of material tests**

Quasi-static and dynamic material experiments are verified and validated with the complete data set prepared for TRAUM. It is concluded that the new material model can successfully validate a wide range of test conditions without any tuning or modifications on the input data.

8.2.5 **Validation and verification of impact tests**

New material model is utilized to validate ballistic impact tests with different initial and boundary conditions. Different projectiles and target orientations are validated. It is concluded that the overall predictive performance for TRAUM is promising for a wide range of impact applications.

8.3 **Recommendations for future research**

Due to the scope of this research, several other potential topics should be addressed in the future:

The failure locus is constructed through the most conspicuous points on the stress-state space. There is a need to enlarge the area of interest and design specimens for testing to cover the other areas of the state-of-stress diagram, especially towards the axi-symmetric compression meridian.

The current failure algorithm utilizes an element erosion technique, which may not necessarily be desirable for modeling failure in the form of crack initiation and propagation. Alternative implementations, especially along the line of meshfree or meshless techniques should be employed with the new material model to predict failure or crack without the need to delete elements but rather partitioning.

A variable Taylor–Quinney coefficient can be implemented in the model as a function of the plastic work, which will provide significant improvement on the prediction of the

heat generated due to the plastic work especially considering the small deformations lead to lower values of the coefficient.

The new material model should also be employed for different deformation and failure prediction of ductile structures under impact loading. A survey of different alternative has been given in Section 1.1. TRAUM is expected to be a generic tool for many different industrial applications especially in the crashworthiness and metal forming world.

The material model was limited to isotropic von Mises plasticity. Sheet metals may not necessarily obey these restrictions. Therefore, the plasticity algorithm should evolve to predict stress differential effects with higher order, anisotropic yield surfaces in a more generic way.

Although, the new material model was benchmarked against one of the most commonly used material models in the dissertation, there is a need to verify the performance by utilizing alternative models.

Validations of the impact tests were performed on relatively small scale; the performance of the new material model should be tested for even bigger scale models. Complete vehicle models for crashworthiness can be good alternatives for such benchmarks.

References

[1] Borvik T., Hopperstad O.S., and Berstad T., "On the influence of stress triaxiality and strain rate on the behavior of a structural steel. Part II. numerical study," *European Journal of Mechanics - A/Solids*, vol. 22, pp. 15-32, 2003.

[2] Curran D., Seaman L., and Shockey D., "Dynamic failure of solids," *Physics Reports (Review Section of Physics Letters)*, vol. 147, no. 5&6, pp. 253-388, 1987.

[3] Garrison W.M. and Moody Jr-N.R., "Ductile fracture," *Journal of Physics and Chemistry of Solids*, vol. 48, no. 11, pp. 1035-1047, 1987.

[4] Hertzberg W.R., *Deformation and fracture mechanics of engineering materials*, 4th ed.: John Wiley & Sons, 1996.

[5] Thomason P.F., *Ductile fracture of metals*.: Pergamon Press, 1990.

[6] Rosakis A.J. and Ravichandran G., "Dynamic failure mechanics," *International Journal of Solids and Structures*, vol. 37, pp. 331-348, 2000.

[7] Zukas J.A., *Introduction to hydrocodes*.: Elsevier Science, 2004.

[8] Bulson P.S., "Structures under shock and impact III," in *Proceedings of the Third International Conference*, Madrid, Spain, 1994, 1 - 3 June.

[9] Zukas J.A., *High velocity impact dynamics*.: John Wiley & Sons, 1990.

[10] Jonas G.H. and Zukas J.A., "Mechanics of penetration: analysis and experiment," *International Journal of Engineering Science*, vol. 16, pp. 879-904, 1978.

[11] Wilkins M.L., "Mechanics of penetration and perforation," *International Journal of Engineering Science*, vol. 16, pp. 793-807, 1978.

[12] Zukas J.A., *Impact dynamics*.: John Wiley & Sons, 1982.

[13] Zukas J.A., "Numerical simulation of high rate behavior," in *Computational Mechanics Publications - Shock and Impact on Structures*, Brebbia C.A. and Sanchez-Galvez V., Eds. Southampton , UK, 1994, pp. 1-26.

[14] Borvik T., Hopperstad O., Berstad T., and Langseth M., "Perforation of 12 mm thick steel plates by 20 mm diameter projectiles with flat, hemispherical and conical noses, part I: experimental study," *International Journal of Impact Engineering*, vol. 27, pp. 19-35, 2002.

[15] Belytschko T., Liu W.K., and Moran B., *Nonlinear finite elements for continua and structures*.: John Wiley & Sons, 2000.

[16] Alves M. and Jones N., "Influence of hydrostatic stress on failure of axisymmetric notched specimens," *Journal of the Mechanics and Physics of Solids*, vol. 47, pp. 643-667, 1999.

[17] "Aircraft accident report," National Transportation Safety Board, NTSB/AAR-90/06 1990.

[18] "Aircraft accident report," National Transportation Safety Board, NTSB/AAR-98/01 1998.

[19] "Part 25.903(d) (1) of Title 14 of the Code of Federal Regulations (14 CFR part 25.903, Engines)," US Government Printing Office, 2009.

[20] Frankenberger C.E., "Large engine uncontained debris analysis," Federal Aviation Administration, Report #DOT/FAA/AR-99/11, 1999.

[21] "Part 33.94 of Title 14 of the Code of Federal Regulations (14 CFR part 33.94, Blade Containment and Rotor Unbalance Tests)," US Government Printing Office, 2009.

[22] Corbett G.G., Reid S.R., and Johnson W., "Impact loading of plates and shells by free-flying projectiles: a review," *International Journal of Impact Engineering*, vol. 18, no. 2, pp. 141-230, 1996.

[23] Backman M.E. and Goldsmith W., "The mechanics of penetration of projectiles into targets," *International Journal of Engineering Science*, vol. 16, pp. 1-99, 1978.

[24] Pepin J., "Fiber reinforced structures for small turbine engine fragment containment (Phase 2)," Federal Aviation Administration, Report #DOT/FAA/AR-95/110 1995.

[25] Le D.D., "Evaluation of lightweight material concepts for aircraft turbine engine rotor failure prevention," Federal Aviation Administration, Report #DOT/FAA/AR-96/110 1996.

[26] Mathis J.A., "Design procedures and analysis of turbine rotor fragment hazard containment," Federal Aviation Administration, Report #DOT/FAA/AR-96/121 1996.

[27] Moussa N.A., Whale M.D., Groszmann D.E., and Zhang X.J., "The potential for fuel tank fire and hydrodynamic ram from uncontained aircraft engine debris," Federal Aviation Administration, Report #DOT/FAA/AR-96/95 1996.

[28] Shockey D.A. et al., "Advanced armor technology: application potential for engine fragment barriers for commercial aircraft," Federal Aviation Administration, Report #DOT/FAA/AR-97/53 1997.

[29] Presley K.L., "Assessment of an advanced containment system," Federal Aviation Administration, Report #DOT/FAA/AR-97/82 1997.

[30] Frankenberger C.E., "FAA T53-L-13L Turbine fragment containment test," Federal Aviation Administration, Report #DOT/FAA/AR-98/22 1998.

[31] Pepin J., "Fiber-reinforced structures for turbine engine rotor fragment containment," Federal Aviation Administration, Report #DOT/FAA/AR-99/6 1999.

[32] Frankenberger C.E., "Small-engine uncontained debris analysis," Federal Aviation Administration, Report #DOT/FAA/AR-99/7 1999.

[33] Shockey D.A., Simons J.W., and Elrich D.C., "Improved barriers to turbine engine fragments, interim report-I," Federal Aviation Administration, Report #DOT/FAA-99/8-I 1999.

[34] Shockey D.A., Simons J.W., and Elrich D.C., "Improved barriers to turbine engine fragments: interim report-II," Federal Aviation Administration, Report #DOT/FAA-99/8-II 1999.

[35] Shockey D.A., Elrich D.C., and Simons J.W., "Improved barriers to turbine engine fragments: interim report-III," Federal Aviation Administration, Report #DOT/FAA-99/8-III 1999.

[36] Shockey D.A., Elrich D.C., Simons J.W., and Shin H.S., "Improved barriers to turbine engine fragments: interim report-IV," Federal Aviation Administration, Report #DOT/FAA-99/8-IV 1999.

[37] Shockey D.A., Elrich D.C., and Simons J.W., "Improved barriers to turbine engine fragments: final annual report," Federal Aviation Administration, Report #DOT/FAA-99/8-V 1999.

[38] Manchor J. and Frankenberger C., "Engine debris penetration testing," Federal Aviation Administration, Report #DOT/FAA/AR-99/19 1999.

[39] Cobb A., "FAA debris mitigation impact test report," Federal Aviation Administration, Report #DOT/FAA/AR-99/54 1999.

[40] Shockey D.A., Elrich D.C., and Simons J.W., "Full-scale tests of lightweight fragment barriers on commercial aircraft," Federal Aviation Administration, Report #DOT/FAA/AR-99/71 1999.

[41] Lesuer D.R., "Experimental investigations of material models for Ti-6AI-4V Titanium and 2024-T3 Aluminum," Federal Aviation Administration, Report #DOT/FAA/AR-00/25 2000.

[42] Gogolowski R.P. and Morgan B.R., "Ballistic experiments with titanium and aluminum targets," Federal Aviation Administration, Report #DOT/FAA/AR-01/21 2001.

[43] Lundin S.J., "Engine debris fuselage penetration testing, phase I," Federal Aviation Administration, Report #DOT/FAA/AR-01/27-I 2001.

[44] Lundin S.J., "Engine debris fuselage penetration testing, phase II," Federal Aviation Administration, Report #DOT/FAA/AR-01/27-II 2001.

[45] Lundin S.J. and Mueller R.B., "Advanced aircraft materials, engine penetration testing," Federal Aviation Administration, Report #DOT/FAA/AR-03/37 2003.

[46] Kay G., "Failure Modeling of Titanium 6Al-4V and Aluminum 2024-T3 with the Johnson-Cook material model," Federal Aviation Administration, Report #DOT/FAA/AR-03/57 2003.

[47] Seng S., Manion J., and Frankenberger C., "Uncontained engine debris analysis using the uncontained engine debris damage assessment model," Federal Aviation Administration, Report #DOT/FAA/AR-04/16 2004.

[48] Seng S., "Turbine engine fan disk crack detection test report," Federal Aviation Administration,

Report #DOT/FAA/AR-04/28 2004.

[49] Rajan S.D. et al., "Explicit finite element modeling of multilayer composite fabric for gas turbine engine containment systems: Part 1: static tests and modeling," Federal Aviation Administration, Report #DOT/FAA/AR-04/40-P1 2004.

[50] Pereira J.M. and Revilock D.M., "Explicit finite element modeling of multilayer composite fabric for gas turbine engine containment systems: Part 2: ballistic impact testing," Federal Aviation Administration, Report #DOT/FAA/AR-04/40-P2 2004.

[51] Simmons J., Erlich D., and Shockey D., "Explicit finite element modeling of multilayer composite fabric for gas turbine engine containment systems: Part 3: model development and simulation of experiments," Federal Aviation Administration, Report #DOT/FAA/AR-04/40-P3 2004.

[52] Gomuc R., "Explicit finite element modeling of multilayer composite fabric for gas turbine engine containment systems: Part 4: model simulation for ballistic tests, engine fan blade-out, and generic engine," Federal Aviation Administration, Report #DOT/FAA/AR-04/40-P4 2004.

[53] Kwong K. and Goldsmith W., "Lightweight ballistic protection of flight-critical components on commercial aircraft: Part 1: ballistic characterization of Zylon," Federal Aviation Administration, Report #DOT/FAA/AR-04/45-P1 2004.

[54] Shockey D.A., Erlich D.C., and Simons J.W., "Lightweight ballistic protection of flight-critical components on commercial aircraft: Part 2: large-scale ballistic impact tests and computational simulations," Federal Aviation Administration, Report #DOT/FAA/AR-04/45-P2 2004.

[55] Verzemnieks J., "Lightweight ballistic protection of flight-critical components on commercial aircraft: Part 3: Zylon yarn tests," Federal Aviation Administration, Report #DOT/FAA/AR-04/45-P3 2004.

[56] Lundin S.J., Frankenberger C.E., and Mueller R.B., "Uncontained engine debris fire mitigation test-fuselage-mounted engines," Federal Aviation Administration, Report #DOT/FAA/AR-05/3 2005.

[57] Kelly S. and Johnson G., "Statistical testing of aircraft materials for transport- airplane rotor burst fragment shielding," Federal Aviation Administration, Report #DOT/FAA/AR-06/9 2006.

[58] Kay G., Goto D., and Couch R., "Statistical testing and material model characterization of aluminum and titanium for transport airplane rotor burst fragment shielding," Federal Aviation Administration, Report #DOT/FAA/AR-07/26 2007.

[59] May C.A., "Small-scale ballistic impact tests to optimize transport airplane rotor burst fragment fabric shielding designs," Federal Aviation Administration, Report #DOT/FAA/AR-07/43 2007.

[60] Buyuk M., Loikkanen M., and Kan C.D., "Explicit finite element analysis of 2024-T3/T351 aluminum material under impact loading for airplane engine containment and fragment shielding," Federal Aviation Administration, Report #DOT/FAA/AR-08/36 2008.

[61] Rajan S.D., Mobasher B., Sankaran S., Naik D., and Stahlecker Z., "Explicit finite element modeling of multilayer composite fabric for gas turbine engine containment systems, Phase II: Part 1: fabric material tests and modeling," Federal Aviation Administration, Report #DOT/FAA/AR-08/37-P1 2008.

[62] Revilock D.M. and Pereira J.M., "Explicit finite element modeling of multilayer composite fabric for gas turbine engine containment systems, Phase II, Part 2: ballistic impact testing," Federal Aviation Administration, Report #DOT/FAA/AR-08/37-P2 2008.

[63] Simons J., Erlich D., and Shockey D., "Explicit finite element modeling of multilayer composite fabric for gas turbine engine containment systems, Phase II, Part 3: material model development and simulation of experiments," Federal Aviation Administration, Report #DOT/FAA/AR-08/37-P3 2008.

[64] Vintilescu I.V., "Explicit finite element modeling of multilayer composite fabric for gas turbine engine containment systems, Phase II, Part 4: model simulation for ballistic tests, engine fan blade-out, and generic engine," Federal Aviation Administration, Report #DOT/FAA/AR-08/37-P4 2008.

[65] Powell D., Zohdi T., and Johnson G., "Multiscale modeling of structural fabric undergoing impact," Federal Aviation Administration, Report #DOT/FAA/AR-08/38 2008.

[66] Donovan K., Johnson G., and Zohdi T., "Impact tests of aircraft aluminums and composites for

uncontained engine fragment modeling," Federal Aviation Administration, Report #DOT/FAA/AR-08/46 2008.

[67] Powell D., Zohdi T., and Johnson G., "Impact and delamination failure characterization of BMS 8-212 composite aircraft material," Federal Aviation Administration, Report #DOT/FAA/AR-08/48 2008.

[68] Kay G.J., "Simulations of carbon fiber composite delamination tests," Federal Aviation Administration, Report #DOT/FAA/AR-09/39 2009.

[69] Kay G., Urabe D., Shields A., and DeTeresa S., "Characterization of BMS 8-212 for use in penetration simulations," Federal Aviation Administration, Report #DOT/FAA/AR-09/40 2009.

[70] Carney K.S., Lawrence C., and Carney D.V., "Aircraft engine blade-out dynamics," in *7th International LS-DYNA Users' Conference*, Detroit, 2002.

[71] Carney K., Pereira M., Revilock D., and Matheny P., "Jet engine fan blade containment using two alternate geometries," in *4th European LS-DYNA Users' Conference*, Ulm, Germany, 2003.

[72] Carney K., Pereira M., Revilock D., and Matheny P., "Jet engine fan blade containment using an alternate geometry," *International Journal of Impact Engineering*, vol. 36, pp. 720-728, 2009.

[73] Woodward R.L. and Cimpoeru S.J., "A study of the perforation of aluminium laminate targets," *International Journal of Impact Engineering*, vol. 21, no. 3, pp. 117–131, 1998.

[74] Rusinek A. et al., "Experimental and numerical study on the perforation process of mild steel sheets subjected to perpendicular impact by hemispherical projectiles," *International Journal of Impact Engineering*, vol. 36, pp. 565-587, 2009.

[75] Martinez J.A.R., Rusinek A., and Pesci R., "Experimental survey on the behavior of AISI 304 steel sheets subjected to perforation," *Thin-Walled Structures*, vol. 48, pp. 966-978, 2010.

[76] Backman M.E., "Terminal Ballistics," Naval Weapons Center, NWC TP 578 1976.

[77] Zukas J.A., "Impact dynamics: theory and experiment," U.S. Army Ballistic Research Laboratory, ARBRL-TR-02271 1980.

[78] Perzyna P., "Fundamental problems in viscoplasticity," *Advances in Applied Mechanics*, vol. 9, pp. 243–377, 1966.

[79] Chaboche J.L., "A review of some plasticity and viscoplasticity constitutive theories," *International Journal of Plasticity*, vol. 24, pp. 1642–1693, 2008.

[80] Krempl E., McMahon J.J., and Yao D., "Viscoplasticity based on overstress with a differential growth law for the equilibrium stress," *Mechanics of Materials*, vol. 5, pp. 35-48, 1986.

[81] Miller A.K., "The MATMOD equations," *Elsevier Applied Science Publishers*, pp. 139-219, 1987.

[82] Delobelle P., "Sur les lois de comportement viscoplastique a variables internes," *Revue de Physique Appliquee*, vol. 23, pp. 1–61, 1988.

[83] Bodner S.R., "Unified constitutive equations for plastic deformation and creep of engineering alloys," in *Unified Constitutive Equations for Creep and Plasticity*, Miller A.K., Ed.: Elsevier Applied Science, 1987, pp. 273-301.

[84] Johnson G.R. and Cook W.H., "A constitutive model and data for metals subjected to large strains, high strain rates and high temperatures," in *7th International Symposium on Ballistics*, Hague, Netherlands, 1983.

[85] Johnson G.R. and Cook W.H., "Fracture characteristics of three metals subjected to various strains, strain rates, temperatures and pressures," *Engineering Fracture Mechanics*, vol. 21, no. 1, pp. 31-48, 1985.

[86] Kocks U.F., "Laws for workhardening and low-temperature creep," *Journal of Engineering Materials and Technology*, vol. 98, pp. 76–85, 1976.

[87] Steinberg D.J., Cochran S.G., and Guinan M.W., "A constitutive model for metals applicable at high-strain rate," *Journal of Applied Physics*, vol. 51, pp. 1498-1504, 1980.

[88] Clifton R.J., "Dynamic plasticity," *Journal of Applied Mechanics*, vol. 50, pp. 941-952, 1983.

[89] Follansbee P.S., *High-strain-rate deformation of FCC metals and alloys, Metallurgical Applications of Shock-Wave and High-Strain-Rate Phenomena*. New York: Marcel Dekker, 1986.

[90] Zerilli F.J. and Armstrong R.W., "Dislocation-mechanics-based constitutive relations for material dynamics calculations," *Journal of Applied Physics*, vol. 61, pp. 1816–1825, 1987.

[91] Follansbee P.S. and Kocks U.F., "A constitutive description of the deformation of copper based on the use of the mechanical threshold stress as an internal state variable," *Acta Metallurgica*, vol. 36, no. 1, pp. 81-93, 1988.

[92] Kocks U.F., "Realistic constitutive relations for metal plasticity," *Materials Science and Engineering A*, vol. 317, pp. 181-187, 2001.

[93] Liang R. and Khan A.S., "A critical review of experimental results and constitutive models for BCC and FCC metals over a wide range of strain rates and temperatures," *International Journal of Plasticity*, vol. 15, pp. 963-980, 1999.

[94] Hill R., *The mathematical theory of plasticity*. Oxford: The University Press, 1950.

[95] Bridgman P.W., *Studies in large plastic flow and fracture*. NewYork: McGraw-Hill, 1952.

[96] Hallquist J.O., "LS-DYNA Theory Manual," Livermore Software Technology Corporation (LSTC) , 2006.

[97] Wierzbicki T., Bao Y., Lee Y.W., and Bai Y., "Calibration and evaluation of seven fracture models," *International Journal of Mechanical Sciences* , vol. 47, pp. 719-743, 2005.

[98] Teng X. and Wierzbicki T., "Evaluation of six fracture models in high velocity perforation," *Engineering Fracture Mechanics*, vol. 73, pp. 1653-1678, 2006.

[99] Bao Y., "Prediction of ductile crack formation in uncracked bodies," Massachusetts Institute of Technology, PhD Thesis 2003.

[100] Bao Y. and Wierzbicki T., "On fracture locus in the equivalent strain and stress triaxiality space," *International Journal of Mechanical Sciences*, vol. 46, pp. 81-98, 2004.

[101] Bao Y. and Wierzbicki T., "A comparative study on various ductile crack formation criteria," *ASME Journal of Engineering Materials and Technology*, vol. 126, no. 3, pp. 314-324, 2004.

[102] Barsoum I. and Faleskog J., "Rupture mechanisms in combined tension and shear -experiments," *International Journal of Solids and Structures*, vol. 44, no. 6, pp. 1768–1786, 2007.

[103] Xue L., "Ductile fracture modeling - theory, experimental investigation and numerical verification," Massachusetts Institute of Technology, PhD Thesis 2007.

[104] Bai Y., "Effect of loading history on necking and fracture," Massachusetts Institute of Technology, PhD Thesis 2008.

[105] Bai Y. and Wierzbicki T., "A new model of metal plasticity and fracture with pressure and Lode dependence," *International Journal of Plasticity*, vol. 24, pp. 1071-1096, 2008.

[106] Bao Y. and Wierzbicki T., "On the cut-off value of negative triaxiality for fracture," *Engineering Fracture Mechanics*, vol. 72, pp. 1049–1069, 2005.

[107] Carney K.S., Du Bois P.A., Buyuk M., and S. Kan, "Generalized, three-dimensional definition, description, and derived limits of the triaxial failure of metals," *Journal of Aerospace Engineering*, vol. 22, pp. 280-286, 2009.

[108] Seidt J.D., "Plastic deformation and ductile fracture of 2024-t351 aluminum under various loading conditions," The Ohio State University, PhD Thesis 2010.

[109] Lode von W., "Versuche uber den Einfluss der mittleren Hauptspannung auf das Fliessen der Metalle Eisen, Kupfer und Nickell," *Zeitschrift fur Physik*, vol. 36, pp. 913-939, 1926, In German.

[110] Taylor G.I. and Quinney H., "The plastic distortion of metals," *Philosophical Transactions of the Royal Society of London, Series A*, vol. 230, pp. 323-362, 1932.

[111] Lindholm U.S., *Techniques in metal research*, Bunshah R. F., Ed. New York: Interscience, 1971, vol. 5, ch. 1.

[112] Yu M.H., "Advances in strength theories for materials under complex stress state in the 20th Century," *ASME Applied Mechanics Reviews*, vol. 55, no. 3, pp. 169-218, 2002.

[113] Shimura M. and Saito S., "Progress in the development of failure maps; negative pressure - strain - temperature diagram," The Research Institute for Iron, Steel and Other Metals, The 1716th report of the Research Institute for Iron, Steel and Other Metals 1980.

[114] Atkins A.G., "Fracture Mechanics and Metalforming: Damage mechanics and the local approach of yesterday and today, Fracture Research in Retrospect, An Anniversary Volume in Honour of George R. Irwin's 90th Birthday," , 1997, pp. 327-350.

[115] McClintock F., "A criterion for ductile fracture by the growth of holes," *ASME Journal of Applied Mechanics*, vol. 35, no. 2, pp. 363-371, 1968.

[116] Cockcroft M.G. and Latham D.J., "Ductility and the workability of metals," *Journal of the Institute of Metals*, vol. 96, pp. 33-39, 1968.

[117] Rice J.R. and Tracey D.M., "On the ductile enlargement of voids in triaxial stress fields," *Journal of the Mechanics and Physics of Solids*, vol. 17, pp. 201-217, 1969.

[118] Brozzo P., Deluca B., and Rendina R., "A new method for the prediction of formability in metal sheet," in *7th Biennial Conference of the IDDRG*, vol. Sheet Metal Forming and Formability, 1972.

[119] Hancock J.W. and Mackenzie A. C., "On the mechanisms of ductile failure in high-strength steels subjected to multi-axial stress-states," *Journal of the Mechanics and Physics of Solids*, vol. 24, no. 2-3, pp. 147-160, June 1976.

[120] LeRoy G., Embury J.D., Edward G., and Ashby M.F., "A model of ductile fracture based on the nucleation and growth of voids," *Acta Metallurgica*, vol. 29, pp. 1509-1522, 1981.

[121] Oh S., Chen C.C., and Kobayashi S., "Ductile failure in axisymmetric extrusion and drawing Part 2-workability in extrusion and drawing," *Journal of Engineering for Industry*, vol. 101, 1979.

[122] Clift S.E., Hartley P., Sturgess C.E.N., and Rowe G.W., "Fracture prediction in plastic deformation processes," *International Journal of Mechanical Sciences*, vol. 32, no. 1, pp. 1-17, 1990.

[123] Gurson A.L., "Plastic flow and fracture behavior of ductile materials incorporating void nucleation, growth and interaction," Brown University, PhD Thesis 1975.

[124] Gurson A.L., "Continuum theory of ductile rupture by void nucleation and growth: Part I- Yield criteria and flow rules for porous ductile media," *ASME Journal of Engineering Materials and Technology*, vol. 99, pp. 2-15, 1977.

[125] Tvergaard V., "Influence of voids on shear band instabilities under plane strain conditions," *International Journal of Fracture*, vol. 18, pp. 237–252, 1981.

[126] Tvergaard V., "Ductile fracture by cavity nucleation between larger voids," *Journal of the Mechanics and Physics of Solids*, vol. 30, pp. 265-286, 1982.

[127] Tvergaard V., "On localization in ductile materials containing spherical voids," *International Journal of Fracture*, vol. 17, pp. 389–407, 1982.

[128] Needleman A. and Tvergaard V., "An analysis of ductile rupture in notched bars," *Journal of the Mechanics and Physics of Solids*, vol. 32, no. 6, pp. 461-490, 1984.

[129] Tvergaard V. and Needleman A., "Analysis of the cup-cone fracture in a round tensile bar," *Acta Metallurgica*, vol. 32, pp. 157–169, 1984.

[130] Tvergaard V. and Needleman A., "Effects of nonlocal damage in porous plastic solids," *International Journal of Solids and Structures*, vol. 32, pp. 1063-1077, 1995.

[131] Rousselier G., "Ductile fracture models and their potential in local approach of fracture," *Nuclear Engineering and Design*, vol. 105, pp. 97-111, 1987.

[132] Xia L., Shih C.F., and Hutchinson J.W., "A computational approach to ductile crack growth under large scale yielding conditions," *Journal of the Mechanics and Physics of Solids*, vol. 43, no. 3, pp. 389-413, 1995.

[133] Xi L. and Shih C.F., "Ductile crack growth-I. A numerical study using computational cells with microstructurally-based length scales," *Journal of the Mechanics and Physics of Solids*, vol. 43, no. 2, pp. 233-259, 1995.

[134] Xia L. and Shih C.F., "Ductile crack growth-II. Void nucleation and geometry effects on macroscopic fracture behavior," *Journal of the Mechanics and Physics of Solids*, vol. 43, no. 12, pp. 1953-1981, 1995.

[135] Xia L. and Shih C.F., "Ductile crack growth-III. Transition to cleavage fracture incorporating statistics," *Journal of the Mechanics and Physics of Solids*, vol. 44, no. 4, pp. 603-639, 1996.

[136] Faleskog J., Gao X., and Shih C.F., "Cell model for nonlinear fracture analysis-I. Micromechanics calibration," *International Journal of Fracture*, vol. 89, pp. 355-373, 1998.

[137] Gao X., Faleskog J., and Shih C.F., "Cell model for nonlinear fracture analysis-II.Fracture process calibration and verification," *International Journal of Fracture*, vol. 89, pp. 375-398, 1998.

[138] Jun S., "Effect of stress triaxiality on micro-mechanisms of void coalescence and micro-fracture ductility of materials," *Engineering Fracture Mechanics*, vol. 39, no. 5, pp. 799-805, 1991.

[139] Nahshon K., "Ductile shear failure," Harvard University, PhD Thesis 2007.

[140] Xue Z., Pontin M.G., Zok F.W., and Hutchinson J.W., "Calibration procedures for a computational model of ductile fracture," *Engineering Fracture Mechanics*, vol. 77, pp. 492–509, 2010.

[141] Kachanov L.M., "Time of the rupture process under creep conditions," *IZV Akad Nauk S.S.R., Otd. Tekhn. Nauk*, vol. 8, pp. 26-31, 1958.

[142] Lemaitre J., "A continuous damage mechanics model for ductile fracture," *Journal of engineering materials and technology*, vol. 107, pp. 83-89, 1985.

[143] Lemaitre J., "Local approach of fracture," *Engineering Fracture Mechanics*, vol. 25, pp. 523-537, 1986.

[144] Lemaitre J. and Difailly J., "Damage mechanics," *Engineering Fracture Mechanics*, vol. 28, pp. 643-661, 1987.

[145] Lemaitre J., *A course on damage mechanics*.: Springer, 1996.

[146] Wang T.J., "Unified CDM model and local criterion for ductile fracture-I. Unified CDM model for ductile fracture," *Engineering Fracture Mechanics*, vol. 42, no. 1, pp. 177-183, 1992.

[147] Wang T.J., "Further investigation of a new continuum damage mechanics criterion for ductile fracture: experimental verification and applications," *Engineering Fracture Mechanics*, vol. 48, no. 2, pp. 217-230, 1994.

[148] Horstemeyer M.F. and Revelli V., "Stress history dependent localization and failure using continuum damage mechanics concepts," in *Application of continuum damage mechanics to fatigue and fracture*.: American Society for Testing and Materials, 1997, vol. ASTM STP 1315, pp. 216-237.

[149] Dhar S.P.M.D. and Sethuraman R.A., "A continuum damage mechanics model for ductile fracture," *International Journal of Pressure Vessels and Piping*, vol. 77, pp. 335–344, 2000.

[150] La Rosa G., Mirone G., and Risitano A., "Effect of stress triaxiality corrected plastic flow on ductile damage evolution in the framework of continuum damage mechanics," *Engineering Fracture Mechanics*, vol. 68, pp. 417-434, 2001.

[151] Barenblatt G.I., "The mathematical theory of equilibrium cracks in brittle fracture," *Advances in Applied Mechanics*, vol. 7, pp. 55–129, 1962.

[152] Hillerborg A., Modeer M., and Petersson P.E., "Analysis of crack formation and crack growth in concrete by means of fracture mechanics and finite elements," *Cement and Concrete Research*, vol. 6, pp. 773-782, 1976.

[153] Needleman A., "An analysis of decohesion along an imperfect interface," *International Journal of Fracture*, vol. 42, pp. 21-40, 1990.

[154] Tvergaard V. and Hutchinson J.W., "Effect of strain-dependent cohesive zone model on predictions of crack growth resistance," *International Journal of Solids and Structures*, vol. 33, pp. 3297-3308, 1996.

[155] Que N.S. and Tin-Loi F., "Numerical evaluation of cohesive fracture parameters from a wedge splitting test," *Engineering Fracture Mechanics*, vol. 69, pp. 1269-1286, 2002.

[156] Elices M., Guinea G.V., Gomez J., and Planas J., "The cohesive zone model: advantages, limitations and challenges," *Engineering Fracture Mechanics*, vol. 69, pp. 137-163, 2002.

[157] Planas J. et al., "Generalizations and specializations of cohesive crack models," *Engineering Fracture Mechanics* , vol. 70, pp. 1759-1776, 2003.

[158] Tvergaard V., "Resistance curves for mixed more interface crack growth between dissimilar elastic-plastic solids," *Journal of the Mechanics and Physics of Solids*, vol. 49, no. 11, pp. 2689–2703,

2001.

[159] Tvergaard V., "Crack growth predictions by cohesive zone model for ductile fracture," *Journal of the Mechanics and Physics of Solids*, vol. 49, no. 9, pp. 2191-2207, 2001.

[160] Tvergaard V., "Predictions of mixed mode interface crack growth using a cohesive zone model for ductile fracture," *Journal of the Mechanics and Physics of Solids*, vol. 52, no. 4, pp. 925-940, 2004.

[161] Siegmund T. and Brocks W., "Prediction of the work of separation and implications to modeling," *International Journal of Fracture*, vol. 99, pp. 97–116, 1999.

[162] Bridgman P.W., "The stress distribution of the neck of a tensile specimen," *Trans ASM*, vol. 32, p. 553, 1944.

[163] Norris D.M., Reaugh J.E., Moran B., and Quinones D.F., "A plastic strain, mean-stress criterion for ductile fracture," *Journal of Engineering Materials and Technology*, vol. 100, pp. 279-286, 1978.

[164] Oyane M., Sato T., Okimoto K., and Shima S., "Criteria for ductile fracture and their applications," *Journal of Mechanical Work and Technology* , vol. 4, pp. 65-81, 1980.

[165] Atkins A.G., "Possible explanation for unexpected departures in hydrostatic tension-fracture strain relations," *Metal Science* , vol. 15, pp. 81-83, 1981.

[166] Wilkins M.L., Streit R.D., and Reaugh J.E., "Cumulative –strain damage model of ductile fracture: simulation and prediction of engineering fracture tests," Lawrence Livermore Laboratory, Livermore, California, UCRL-53058 1980.

[167] Mackenzie A., Hancock J., and Brown D., "On the influence of state of stress on ductile failure initiation in high strength steels," *Engineering Fracture Mechanics*, vol. 9, pp. 167-188, 1977.

[168] Johnson G.R. and Holmquist T.J., "Test data and computational strength and fracture model contants for 23 materials subjected to large strain, high strain rates, and high temperature," Los Alamos National Laboratory, LA-11463-MS 1989.

[169] Ganser H.P., Atkins A.G., Kolednik O., Fischer F.D., and Richard O., "Upsetting of cylinders: a comparison of two different damage indicators," *ASME Journal of Engineering Materials and Technology*, vol. 123, pp. 94–99, 2001.

[170] Borvik T., Hopperstad O., Berstad T., and Langseth M., "Perforation of 12 mm thick steel plates by 20 mm diameter projectiles with flat, hemispherical and conical noses, part II: numerical simulations," *International Journal of Impact Engineering*, vol. 27, pp. 37–64, 2002.

[171] Borvik T., "Ballistic penetration and perforation of steel plates," Norwegian University of Science and Technology, PhD Thesis 2000.

[172] Marciniak Z. and Kuczynski K., "Limit strains in the processes of stretch-forming sheet metal," *International Journal of Mechanical Sciences*, vol. 9, no. 9, pp. 609-612, 1967.

[173] Hooputra H., Gese H., Dell H., and Werner H., "A comprehensive failure model for crashworthiness simulation of aluminium extrusions," *International Journal of Crashworthiness*, vol. 9, pp. 449-464, 2004.

[174] Zadpoor A.A., Sinke J., and Benedictus R., "Formability prediction of high strength aluminum sheets," *International Journal of Plasticity*, vol. 25, no. 12, pp. 2269-2297, 2009.

[175] Xue L., "Damage accumulation and fracture initiation in uncracked ductile solids subject to triaxial loading," *International Journal of Solids and Structures*, vol. 44, no. 16, pp. 5163-5181, 2007.

[176] Huang H. and Xue L., "Prediction of slant ductile fracture using damage plasticity theory," *International Journal of Pressure Vessels and Piping*, vol. 86, pp. 319–328, 2009.

[177] Xue L., "Stress based fracture envelope for damage plastic solids," *Engineering Fracture Mechanics*, vol. 76, pp. 419–438, 2009.

[178] Hopperstad O.S., Borvik T., Langseth M., Labibes K., and Albertini C., "On the influence of stress triaxiality and strain rate on the behavior of a structural steel. Part I. experiments," *European Journal of Mechanics - A/Solids*, vol. 22, pp. 1-13, 2003.

[179] Borvik T., Hopperstad O. S., Berstad T., and Langseth M., "A computational model of viscoplasticity and ductile damage for impact and penetration," *European Journal of Mechanics - A/Solids*, vol. 20, pp. 685-712, 2001.

[180] Needleman A. and Tvergaard V., "Mesh effects in the analysis of dynamic ductile crack growth," *Engineering Fracture Mechanics*, vol. 47, no. 1, pp. 75-91, 1994.

[181] Skallerud B. and Zhang Z.L., "Effects of finite element mesh on numerical prediction of ductile tearing," in *Fatigue and Fracture Mechanics*.: ASTM STP 1332, 1999, vol. 29, pp. 201-214.

[182] Wilsius J., Imad A., Abdelaziz M.N., Mesmacque G., and Eripret C., "Void growth and damage models for predicting ductile fracture in welds," *Fatigue Fracture Engineering Materials and Structures*, vol. 23, pp. 105-112, 2000.

[183] Shin H. and Kim J.B., "A phenomenological constitutive equation to describe various flow stress behaviors of materials in wide strain rate and temperature regimes," *ASME Journal of Engineering Materials and Technology*, vol. 132, pp. 1-6, 2010.

[184] Meyers M.A., *Dynamic behavior of materials*. New York: Wiley, 1994.

[185] Ambur D.R., Jaunky N., Lawson R.E., and Knight N.F.-Jr., "Numerical simulations for high-energy impact of thin plates," *International Journal of Impact Engineering*, vol. 25, pp. 683-702, 2001.

[186] Corran R.S.J., Shadbolt P.J., and Ruiz C., "Impact loading of plates-and experimental investigation," *International Journal of Impact Engineering*, vol. 1, no. 1, pp. 3-22, 1983.

[187] Borvik T., Clausen A.H., Hopperstad O.S., and Langseth M., "Perforation of AA5083-H116 aluminium plates with conical-nose steel projectiles—experimental study," *International Journal of Impact Engineering*, vol. 30, pp. 367–384, 2004.

[188] Borvik T. et al., "Experimental and numerical study on the perforation of AA6005-T6 panels," *International Journal of Impact Engineering*, vol. 32, pp. 35–64, 2005.

[189] Gupta N.K., Iqbal M.A., and Sekhon G.S., "Experimental and numerical studies on the behavior of thin aluminum plates subjected to impact by blunt and hemispherical nosed projectiles," *International Journal of Impact Engineering*, vol. 32, pp. 1921-1944, 2006.

[190] Gupta N.K., Iqbal M.A., and Sekhon G.S., "Effect of projectile nose shape, impact velocity and target thickness on deformation behavior of aluminum plates," *International Journal of Solids and Structures*, vol. 44, pp. 3411-3439, 2007.

[191] Buyuk M., Kan S., and Loikkanen M.J., "Explicit finite-element analysis of 2024-T3/T351 Aluminum material under impact loading for airplane engine containment and fragment shielding," *Journal of Aerospace Engineering*, vol. 22, pp. 287-295, 2009.

[192] Hallquist J.O., "LS-DYNA Keyword User's Manual," Livermore Software Technology Corporation (LSTC), Volumes I and II 2009.

[193] Bathe K.J., *Finite element procedures*.: Prentice-Hall, 1996.

[194] Zienkiewicz O.C. and Taylor R.L., *The finite element method, Volume-2: Solid mechanics*.: Butterworth-Heinemann, 2000.

[195] Zukas J.A. and Scheffler D.R., "Practical aspects of numerical simulations of dynamic events: effects of meshing," *International Journal of Impact Engineering*, vol. 24, p. 925}945, 2000.

[196] Wisselink H.H. and Huetink J., "Modeling of ductile failure in metal forming," in *7th European LS-DYNA Users' Conference*, Salzburg, Austria, 2009, 14-15 May.

[197] Kurtaran H., Buyuk M., and Eskandarian A., "Ballistic impact simulation of GT model vehicle door using finite element method," *Theoretical and Applied Fracture Mechanics*, vol. 40, pp. 113–121, 2003.

[198] Kurtaran H., Buyuk M., and Eskandarian A., "Design automation of a laminated armor for best impact performance using approximate optimization method," *International Journal of Impact Engineering*, vol. 29, pp. 397-406, 2003.

[199] Rusinek A., Zaera R., and Klepaczko J.R., "Constitutive relations in 3-D for a wide range of strain rates and temperatures – application to mild steels," *International Journal of Solids and Structures*, vol. 44, pp. 5611-5634, 2007.

[200] Dhontdt G., *The finite element method for three-dimensional thermomechanical applications*.: John Wiley & Sons, 2004.

[201] Crisfield M.A., *Non-linear finite element analysis of solids and structures, Volume-1: Essentials*.:

John Wiley & Sons, 1991.

[202] Cook R.D., Malkus D.S., Plesha M.E., and Witt R.J., *Concepts and applications of finite element analysis*.: John Wiley & Sons, 2002.

[203] Berstad T., Hopperstad O.S., and Langseth M., "Elasto-viscoplastic constitutive models in the explicit finite element code LS-DYNA3D," in *2nd International LS-DYNA3D Conference*, St. Francis, 1994, 20-21 September.

[204] Jones N., "Dynamic inelastic failure of structures," *Transactions of the Japan Society of Mechanical Engineers A*, vol. 12, pp. 21-31, 1997.

[205] Wilkins M.L., "Calculation of elastic-plastic flow," in *Methods of computational physics*, Adler B. et al., Ed. New York: Academic Press, 1964, vol. 3, pp. 211-263.

[206] Hughes T.J.R., "Analysis of transient algorithms with particular reference to stability behavior," in *Computational methods for transient analysis*, Belytschko T. and Hughes T.J.R., Eds. Amsterdam: North-Holland, 1983.

[207] Truesdell C. and Toupin P.A., "The classical field theories," in *Handbuch der physik*, Flugge S., Ed. Berlin: Springer-Verlag, 1960, vol. III:I, pp. 226-258.

[208] Simo J.C. and Hughes T.J.R., *Computational Inelasticity*.: Springer-Verlag, 1998.

[209] Courant R., Friedrichs K., and Lewy H., "On the partial differential equations of mathematical physics," *IBM Journal*, pp. 215-234, March 1967, English translation and republication of the 1928 German original "Mathematische Annalen 100, 32-74 (1928)."

[210] Lemaitre J. and Chaboche J.L., *Mechanics of solid materials*.: Cambridge University Press, 1990.

[211] Neto E.A. de S., Peric D., and Owen D.R.J., *Computational methods for plasticity: theory and applications*.: John Wiley & Sons, 2008.

[212] Krieg R.D. and Krieg D.B., "Accuracies of numerical solution methods for the elastic-perfectly plastic model," *Journal of pressure vessel technology*, vol. 99, pp. 510-515, 1977.

[213] Zurek A.K., "Dynamic ductile evolution and tensile fracture:new experimental insights for models evaluation," in *Fundamental issues and applications of shock-wave and high-strain-rate phenomena*, K.P. Staudhammer, L.E. Murr, and M.A. Meyers, Eds.: Elsevier Science Ltd, 2001, ch. Chapter 16, pp. 126-134.

[214] Malvern L.E., *Introduction to the mechanics of a continuum medium*. Englewood Cliffs, New Jersey: Prentice-Hall, 1969.

[215] Keeler S.P. and Backofen W.A., "Plastic instability and fracture in sheet stretched over rigid punches," *Transactions of ASME*, vol. 56, pp. 25-48, 1963.

[216] Banadic D., Bunge H.J., Pohlandt K., and Tekkaya A.E., *Formability of metallic materials*.: Springer-Verlag, 2000.

[217] Lee Y.W., Woertz J.C., and Wierzbicki T., "International Journal of Mechanical Sciences," vol. 46, pp. 751-781, 2004.

[218] Ben-Dor G., Dubinsky A., and Elperin T., *Applied high-speed plate penetration dynamics*.: Springer, 2006.

[219] Roessig K.M. and Mason J.J., "Adiabatic shear localization in the dynamic punch test, part I: experimental investigation," *International Journal of Plasticity*, vol. 15, pp. 241-262, 1999.

[220] Walters C.L., "Development of a punching technique for ductile fracture testing over a wide range of stress states and strain rates," Massachusetts Institute of Technology, PhD Thesis 2009.

[221] Dabboussi W. and Nemes J.A., "Modeling of ductile fracture using the dynamic punch test," *International Journal of Mechanical Sciences*, vol. 47, pp. 1282–1299, 2005.

[222] Roessig K.M. and Mason J.J., "Adiabatic shear localization in the dynamic punch test, part II: numerical simulations," *International Journal of Plasticity*, vol. 15, pp. 263-283, 1999.

[223] Li Y., Luoa M., Gerlachb J., and Wierzbicki T., "Prediction of shear-induced fracture in sheet metal forming," *Journal of Materials Processing Technology*, vol. 210, pp. 1858-1869, 2010.

[224] Cverna F. et al., Eds., *Worldwide guide to equivalent nonferrous metals and alloys*, 4th ed.: ASM International, 2001.

[225] MIL-HDBK-5H, *Metallic materials and elements for aerospace vehicle structures*.: Department of Defense, 1998.

[226] Srivatsan T.S., Champlin J., Zakrajsek J., Lam P.C., and Manoharan M., "The impact fracture behavior of Aluminum alloy 2024-T351: influence of notch severity," *Journal of Materials Engineering and Performance*, vol. 10, pp. 362-370, 2001.

[227] Ives L.K. et al., "Processing/microstructure/property relationships in 2024 Aluminum alloy plates," U.S. Department of Commerce, National Bureau of Standards, Washington D.C., Technical Report NBSIR 83-2669, 1983.

[228] Hatch J.E., *Aluminum: properties and physical metallurgy*.: ASM American Society for Metals, 1984.

[229] MIL-HDBK-6088G, *Heat treatment of Aluminum alloys*.: Department of Defense, 1991.

[230] ANSI H35.1 / H35.1(M)-2009 Revision of H35.1 / H35.1(M)-2006, "American National Standard Alloy and Temper Designation System for Aluminum," Secretariat, The Aluminum Association Inc., Approved April7, 2009.

[231] Lee Y.W., "Fracture prediction in metal sheets," Massachusetts Institute of Technology, PhD Thesis 2005.

[232] Lagarde A., Ed., *IUTAM symposium on advanced optical methods and applications in solid mechanics*, Solid Mechanics and Its Applications ed. Dordrecht, The Netherlands: Springer, 2000, vol. 82.

[233] Sutton M., Orteu J.J., and Schreier H.W., *Image correlation for shape, motion and deformation measurements*.: Springer, 2009.

[234] Sutton M.A., Wolters W.J., Peters W.H., Ranson W.F., and McNeill S.R., "Determination of displacements using an improved digital correlation method," *Image and Vision Computing*, vol. 1, no. 3, pp. 133-139, 1983.

[235] Chu T., Ranson W., and Sutton M., "Applications of digital-image-correlation techniques to experimental mechanics," *Experimental Mechanics*, vol. 25, no. 3, pp. 232-244, 1985.

[236] Sutton M.A., Cheng M., Peters W.H., Chao Y.J., and McNeill S.R., "Application of an optimized digital correlation method to planar deformation analysis," *Image and Vision Computing*, vol. 4, no. 3, pp. 143-150, 1986.

[237] Helm J.D., McNeill S.R., and Sutton M.A., "Improved three-dimensional image correlation for surface displacement measurement," *Optical Engineering*, vol. 35, no. 7, pp. 1911-1920, 1996.

[238] Rastogi P.K., *Photo-mechanics*, Topics in Applied Physics ed.: Springer, 2000, vol. 77.

[239] Sutton M.A., McNeill S.R., Helm J.D., and Chao Y.J., "Advances in two-dimensional and three-dimensional computer vision," in *Photo-Mechanics*, Rastogi P.K., Ed.: Springer, 2000, pp. 323-372.

[240] Helm J.D., Sutton M.A., and McNeill S.R., "Deformations in wide, center-notched, thin panels, part I: three-dimensional shape and deformation measurements by computer vision," *Optical Engineering*, vol. 42, no. 5, pp. 1293-1305, 2003.

[241] Sutton M.A., Yan J., Deng X., Cheng C.S., and Zavattieri P., "Three-dimensional digital image correlation to quantify deformation and crack-opening displacement in ductile aluminum under mixed-mode I/III loading," *Optical Engineering*, vol. 46, no. 5, pp. 051003-051017, 2007.

[242] Hild F. and Roux S., "Digital image correlation: from displacement measurement to identification of elastic properties – a review," *Strain*, vol. 42, no. 2, pp. 69-80, 2006.

[243] Luo P., Chao Y., Sutton M., and Peters W., "Accurate measurement of three-dimensional deformations in deformable and rigid bodies using computer vision," *Experimental Mechanics*, vol. 33, no. 2, pp. 123-132, 1993.

[244] Luo P.F., Chao Y.J., and Sutton M.A., "Application of stereo vision to three-dimensional deformation analyses in fracture experiments," *Optical Engineering*, vol. 33, no. 3, pp. 981-990, 1994.

[245] Avril S. et al., "Overview of identification methods of mechanical parameters based on full-field measurements," *Experimental Mechanics*, vol. 48, pp. 381–402, 2008.

[246] Cooreman S., "Identification of the plastic material behavior through full-field displacement measurements and inverse methods," Vrije Universiteit , Brussel, PhD Thesis 2008.

[247] Kajberg J. and Wikman B., "Viscoplastic parameter estimation by high strain-rate experiments and inverse modelling speckle measurements and high-speed photography," *International Journal of Solids and Structures*, vol. 44, pp. 145-164, 2007.

[248] Orteu J.J., "3-D computer vision in experimental mechanics," *Optics and Lasers in Engineering*, vol. 47, pp. 282-291, 2009.

[249] Moon D.P. and J.E. Campbell, "Effects of moderately high strain rates on the tensile properties of metals," Defense Metals Information Center, Batelle Memorial Institute, Columbus, DMIC Memorandum 142, 1961.

[250] Dorward R.C. and Hasse K.R., "Strain rate effects on tensile deformation of 2024-O and 7075-O Aluminum ally sheet," *Journal of Materials Engineering and Performance*, vol. 4, pp. 216-220, 1995.

[251] Larour P., "Strain rate sensitivity of automotive sheet steels: influence of plastic strain, strain rate, temperature, microstructure, bake hardening and pre-strain," RWTH Aachen, PhD Thesis 2010.

[252] Portevin A. and Le Chatelier H., "Sur un phénomène observé lors de l'essai de traction Alliages d'en cours de transformation," *Comptes Rendus de l'Académie des Sciences*, vol. 176, pp. 507-510, 1923.

[253] Zaiser M. and Hahner P., "Oscillatory modes of plastic deformation: theoretical concepts, Review Article," *Physica Status Solidi (b)*, vol. 199, pp. 267-330, 1997.

[254] Bohlke T, Bondar G, Estrin Y, and Lebyodkin M.A., "Geometrically non-linear modeling of the Portevin–Le Chatelier effect," *Computational Materials Science*, vol. 44, pp. 1076–1088, 2009.

[255] McCormick P.G., "Theory of flow localisation due to dynamic strain ageing," *Acta Metallurgica*, vol. 36, no. 12, pp. 3061-3067, 1988.

[256] Kubin L.P. and Estrin Y., "The critical conditions for jerky flow," *Physica Status Solidi (b)*, vol. 172, no. 1, pp. 173-185, 1992.

[257] Rizzia E. and Hahner P., "On the Portevin–Le Chatelier effect: theoretical modeling and numerical results," *International Journal of Plasticity*, vol. 20, pp. 121-165, 2004.

[258] Klose F., "Experimental and numerical studies on the Portevin–Le Chatelier effect in Cu-Al and Al-Mg strain and stress controlled tensile tests," Technischen Universitat Carolo-Wilhelmina zu Braunschweig, PhD Thesis 2004.

[259] Benallal A. et al., "An experimental and numerical investigation of the behaviour of AA5083 aluminium alloy in presence of the Portevin–Le Chatelier effect," *International Journal of Plasticity* , vol. 24, pp. 1916-1945, 2008.

[260] Brindley B.J. and Worthington P.J., "Yield-point phenomena in substitutional alloys," *Metallurgical Reviews*, vol. 15, pp. 101-114, 1970.

[261] Bondar G., Bohlke T., and Estrin Y., "Three-dimensional continuum mechanical modeling of the Portevin-Le Chatelier effect," *Proceedings in Applied Mathematics and Mechanics*, vol. 7, pp. 4060035–4060036, 2007.

[262] Liang S., Chuan Z.Q., and Tao C.P., "Influence of solute cloud and precipitates on spatiotemporal characteristics of Portevin-Le Chatelier effect in A2024 aluminum alloys," *Chinese Physics B*, vol. 18, no. 8, pp. 3500-3508, 2009.

[263] Ling Y., "Uniaxial true stress-strain after necking," *AMP Journal of Technology*, vol. 5, pp. 37-48, 1996.

[264] Tvergaard V., "Necking in tensile bars with rectangular cross-section," *Computer Methods in Applied Mechanics and Engineering*, vol. 103, no. 1-2, pp. 273-290, 1993.

[265] Savitzky A. and Golay M.J.E., "Smoothing and Differentiation of Data by Simplified Least Squares Procedures," *Analytical Chemistry*, vol. 36, no. 8, pp. 1627–1639, 1964.

[266] Considère A.G., "Mémoire sur l'Emploi du Fer et de l'Acier dans les Constructions," *Annales des Ponts et Chausses*, vol. 9, no. 6, pp. 574–775, 1885.

[267] Havner K.S., "On the onset of necking in the tensile test," *International Journal of Plasticity*, vol.

20, pp. 965–978, 2004.

[268] Gromada M., Mishuris G., and A. Ochsner, *Correction formulae for the stress distribution in round tensile specimens at neck presence*. New York: Springer, 2011.

[269] Hollomon J.H., "Tensile Deformation," *Trans. Metall. Soc. AIME*, vol. 162, pp. 268-290, 1945.

[270] Hoffmann S., Bleck W., and Berme B., "In Situ Characterization of Deformation Behavior of Austenitic High Manganese Steels," *Steel research international*, vol. 83, no. 4, pp. 379-384, 2012.

[271] Aretz H., "Numerical analysis of diffuse and localized necking in orthotropic sheet metals," *International Journal of Plasticity* , vol. 23, pp. 798–840, 2007.

[272] Duan X., Jain M., Metzger D.R., and Wilkinson D.S., "A unified finite element approach for the study of postyielding deformation behavior of formable sheet materials," *Journal of Pressure Vessel Technology*, vol. 129, pp. 689-697, 2007.

[273] Bao Y., "Dependence of ductile crack formation in tensile tests on stress triaxiality, stress and strain ratios," *Engineering Fracture Mechanics*, vol. 72, pp. 505-522, 2005.

[274] La Rosa G., Mirone G., and Risitano A., "Post-necking elastoplastic characterization: degree of approximation in the Bridgman method and properties of the flow-stress/true-stress ratio," *Metallurgical and Materials Transactions A*, vol. 34A, pp. 615-624, 2003.

[275] Mirone G., "A new model for the elastoplastic characterization and the stress–strain determination on the necking section of a tensile specimen," *International Journal of Solids and Structures*, vol. 41, pp. 3545–3564, 2004.

[276] Mirone G., "Role of stress triaxiality in elastoplastic characterization and ductile failure prediction," *Engineering Fracture Mechanics*, vol. 74, pp. 1203–1221, 2007.

[277] Mirone G., "Elastoplastic characterization and damage predictions under evolving local triaxiality: axysimmetric and thick plate specimens," *Mechanics of Materials*, vol. 40, pp. 685–694, 2008.

[278] Zhang Z.L., Hauge M., Odegard J., and Thaulow C., "Determining material true stress-strain curve from tensile specimens with rectangular cross-section," *International Journal of Solids and Structures*, vol. 36, pp. 2386–2405, 1999.

[279] Zhang, J., Odegard Z.L., Sovik O.P., and Thaulow C., "A study on determining true stress–strain curve for anisotropic materials with rectangular tensile bars," *International Journal of Solids and Structures*, vol. 38, no. 26–27, pp. 4489-4505, 2001.

[280] Bacha A., Daniel D., and Klocker H., "On the determination of true stress triaxiality in sheet metal," *Journal of Materials Processing Technology* , vol. 184, pp. 272–287, 2007.

[281] Tao H., Zhang N., and Tong W., "An iterative procedure for determining effective stress–strain curves of sheet metals," *International Journal of Mechanics and Materials in Design*, vol. 5, pp. 13-27, 2009.

[282] Joun M.S., Eom J.G., and Lee M.C., "A new method for acquiring true stress–strain curves over a large range of strains using a tensile test and finite element method," *Mechanics of Materials* , vol. 40, pp. 586–593, 2008.

[283] Tarantola A., *Inverse problem theory and methods for model parameter estimation*. Philadelphia: Society for Industrial and Applied Mathematics (SIAM), 2005.

[284] Arora J.S., *Introduction to optimum design*. New York: McGraw-Hill, 1989.

[285] Haftka R.T. and Gurdal Z., *Elements of structural optimization*. Dordrecht: Kluwer, 1990.

[286] Bui H.D., *Inverse problems in the mechanics of materials, an introduction*. Boca Raton: CRC Press, 1994.

[287] Stander N., Craig K.J., Mullerschon H., and Reichert R., "Material identification in structural optimization using response surfaces," *Structural and Multidisciplinary Optimization*, vol. 29, pp. 93-102, 2005.

[288] Koc P. and Stok B., "Computer-aided identification of the yield curve of a sheet metal after onset of necking," *Computational Materials Science*, vol. 31, pp. 155–168, 2004.

[289] Springmann M. and Kuna M., "Identification of material parameters of the Gurson-Tvergaard-Needleman model by combined experimental and numerical techniques," *Computational Materials*

Science, vol. 32, pp. 544-552, 2005.

[290] Voce E., "The relationship between stress and strain for homogeneous deformation," *Journal of the Institute of Metals*, vol. 74, pp. 537–562, 1948.

[291] Scheider I., Brocks W., and Cornec A., "Procedure for the determination of true stress-strain curves from tensile tests with rectangular cross-section specimens," *ASME Journal of Engineering Materials and Technology*, vol. 126, pp. 70-76, 2004.

[292] Swift H.W., "Plastic instability under plane stress," *Journal of the Mechanics and Physics of Solids*, vol. 1, pp. 1–18, 1952.

[293] Teng X. and Wierzbicki T., "Effect of fracture criteria on high velocity perforation of thin beams," *International Journal of Computational Methods*, vol. 1, no. 1, pp. 171-200, 2004.

[294] Bai Y., Bao Y., and Wierzbicki T., "Fracture of prismatic aluminum tubes under reverse straining," *International Journal of Impact Engineering*, vol. 32, pp. 671-701, 2006.

[295] Mahmoud S. and Lease K., "Two-dimensional and three-dimensional finite element analysis of critical crack-tip-opening angle in 2024-T351 aluminum alloy at four thicknesses," *Engineering Fracture Mechanics*, vol. 71, pp. 1379-1391, 2004.

[296] Johnson W. and Mellor P.B., *Plasticity for Mechanical Engineers*. London: D.Van Nostrand Company LTD, 1962.

[297] Cook M. and Larke E.C., "Resistance of copper and copper alloys to homogeneous deformation in compression," *Journal of the Institute of Metals*, vol. 71, p. 371, 1945.

[298] Schey J.A., Venner T.R., and Takomana S.L., "The effect of friction on pressure in upsetting at low diameter-to-height ratios," *Journal of Mechanical Working Technology*, vol. 6, pp. 23-33, 1982.

[299] Li P., Siviour C.R., and Petrinic N., "The effect of strain rate, specimen geometry and lubrication on responses of Aluminum AA2024 in uniaxial compression experiments," *Experimental Mechanics*, vol. 49, pp. 587-593, 2009.

[300] Borvik T., Leinum J.R., J.K. Solberg, Hopperstad O.S., and Langseth M., "Observations on shear plug formation in Weldox 460 E steel plates impacted by blunt-nosed projectiles," *International Journal of Impact Engineering*, vol. 25, pp. 553-572, 2001.

[301] Borvik T., Hopperstad O.S., Langseth M., and Malo K.A., "Effect of target thickness in blunt projectile penetration of Weldox 460 E steel plates," *International Journal of Impact Engineering*, vol. 28, pp. 413-464, 2003.

[302] Kane A., Borvik T., Hopperstad O.S., and Langseth M., "Finite element analysis of plugging failure in steel plates struck by blunt projectiles," *Journal of Applied Mechanics*, vol. 76, no. 5, pp. 051302-11, 2009.

[303] Martinez J.A.R, "Advanced constitutive relations for modeling thermo-viscoplastic behaviour of metallic alloys subjected to impact loading," University Carlos III of Madrid, PhD Thesis 2010.

[304] Lipski A. and S. Mrozinski, "The effect of temperature on the strength properties of Aluminium alloy 2024-T3," *Acta Mechanica et Automatica*, vol. 6, no. 3, pp. 62-66, 2012.

[305] Gordon S.A., Simon R., and Achbach W.P., "Materials-property-design criteria for metals, Part 4: Elastic moduli: their determination and limits of application," Wright Air Development Center, Technical Report 55-150, Part 4. ASTIA Document No: AD 110475, 1956.

[306] Aluminum Kaiser. (2013, May) Kaiser Aluminum Sheet Coil & Plate Alloy 2024. [Online]. https://online.kaiseraluminum.com/depot/PublicProductInformation/Document/1012/Kaiser_Aluminum_2024_Sheet_Coil_and_Plate.pdf

[307] Vosteen L.F., "Effect of temperature on dynamic modulus of elasticity of some structural alloys," National Advisory Committee for Aeronautics, Technical Note: 4348. 1958.

[308] Hill W.H. and Shimmin K.D., "Elevated temperature dynamic elastic moduli of various metallic materials," Wright Air Development Division, Materials Central, Technical Report 60-438. 1961.

[309] Brammer J.A. and Percival C.M., "Elevated-temperature elastic moduli of 2024 Aluminum obtained by a laser-pulse tecnique," *Experimental Mechanics*, vol. 10, no. 6, pp. 245-250, 1970.

[310] Goldsmith A., Waterman T.E., and Hirschhorn H.J., *Handbook of thermophysical properties of*

solid materials. New York: The Macmillan Company, 1961, vol. 3.

[311] Charpentier P.L., Stone B.C., Ernst S.C, and Thomas, Jr. J.F., "Characterization and modeling of the temperature flow behavior of Aluminum alloy 2024," *Metallurgical Transactions A*, vol. 17A, pp. 2227-2237, 1986.

[312] Hodowany J., Ravichandran G., Rosakis A.J., and Rosakis P., "Partition of plastic work into heat and stored energy in metals," *Expetfmental Mechanics*, vol. 40, no. 2, pp. 113-123, 2000.

[313] Lee H.T. and Shaue G.H., "The thermomechanical behavior for aluminum alloy under uniaxial tensile testing," *Materials Science and Engineering A*, vol. 268, pp. 154-164, 1999.

[314] Bever M.B., Holt D.L., and Titchener A.L., "The stored energy of cold work," *Progress in Materials Science*, vol. 17, pp. 5-177, 1973.

[315] Rosakis P., Rosakis A.J., Ravichandran G., and Hodowany J., "A thermodynamic internal variable model for the partition of plastic work into heat and stored energy in metals," *Journal of the Mechanics and Physics of Solids*, vol. 48, pp. 581-607, 2000.

[316] Mason J.J., Rosakis A.J., and Ravichandran G., "On the strain and strain rate dependence of the fraction of plastic work converted to heat: an experimental study using high speed infrared detectors and the Kolsky bar," *Mehanics of Materials*, vol. 17, pp. 135-145, 1994.

[317] Zehnder A.Z., "A Model for the Heating Due to Plastic Work," *Mechanics Research Communications*, vol. 18, no. 1, pp. 23-28, 1991.

[318] Macdougall D., "Determination of the plastic work converted to heat using radiometry," *Experimental Mechanics*, vol. 40, no. 3, pp. 298-306, 2000.

[319] Vural M., Rittel D., and Ravichandran G., "Large strain mechanical behavior of 1018 cold-rolled steel over a wide range of strain rates," *Metallurgical and Materials Transactions A*, vol. 34A, pp. 2873-2885, 2003.

[320] Davis J.R., Ed., *Tensile testing*.: ASM International, 2004.

[321] Stander N. et al., *LS-OPT User's Manual*.: Livermore Software Technology Corporation, 2012.

[322] MATLAB and Curve Fitting Toolbox Release 2009b, The MathWorks, Inc., Natick, Massachusetts, United States.

[323] Kajberg J. and Lindkvist G., "Characterisation of materials subjected to large strains by inverse modelling based on in-plane displacement fields," *International Journal of Solids and Structures*, vol. 41, pp. 3439–3459, 2004.

[324] Ludwik P., *Elemente der technologischen Mechanik*. Berlin: Springer Verlag, 1909.

[325] Hockett J.E. and Sherby O.D., "Large strain deformation of polycrystalline metals at low homologous temperatures," *Journal of the Mechanics and Physics of Solids*, vol. 23, no. 2, pp. 87-98, 1975.

[326] Ghosh A.K., "Tensile instability and necking in materials with strain hardening and strain-rate hardening," *Acta Metallurgica*, vol. 25 , pp. 1413-1424, 1977.

[327] Witowski K., Feucht M., and Stander N., "An effective curve matching metric for parameter identification using partial mapping," in *8th European LS-DYNA Users' Conference*, Strasbourg, 2011, pp. 1-12.

[328] Alt H. and Godau M., "Computing the Fréchet distance between two polygonal curves," *International Journal of Computational Geometry & Applications*, vol. 5, no. 01n02, pp. 75-91, 1995.

[329] Witowski K. and Stander N., "Parameter identification of hysteretic models using partial curve mapping," in *Proceedings of the 12th AIAA Aviation Technology, Integration and Operations (ATIO) Conference and 14th AIAA/ISSMO Multidisciplinary Analysis and Optimization Conference*, Indianapolis, 2012.

[330] Myers R.H. and Montgomery D.C., *Response surface methodology process and product optimization using designed experiments*. New York: John Wiley and Sons, Inc., 1995.

[331] Stander N. and Craig K.J., "On the robustness of a simple domain reduction scheme for simulation-based optimization," *Engineering Computations*, vol. 19, no. 4, pp. 431-450, 2002.

[332] Chatterjee A., Murty K.L., Gayathri N., Mukherjee P., and Barat P., "Temperature dependence of the dynamics of Portevin-Le Chatelier effect in Al-2.5 Pct Mg alloy," *Metallurgical and Materials Transactions A*, vol. 42A, pp. 1184-1190, 2011.

[333] Quan G.-Z., "Characterization for dynamic recrystallization kinetics based on stress-strain curves," in *Recent developments in the study of recrystallization*, Wilson P., Ed.: InTech, 2013, ch. Chapter 2, pp. 61-88.

[334] Forest S. and Lorentz E., "Localization phenomena and regularization," in *Local approach to fracture*, Besson J., Ed.: Les Presses de l'École des Mines, 2004, ch. Chapter XI, pp. 311-371.

[335] Borvik T., Hopperstad O., Berstad T., and Langseth M., "Numerical simulation of plugging failure in ballistic penetration," *International Journal of Solids and Structures*, vol. 38, pp. 6241-6264, 2001.

[336] Johnson G.R., Hoegfeldt J.M., Linholm U.S., and Nagy A., "Response of various metals to large torsional strains over a large range of strain rates – part 2: less ductile metals," *Journal of Engineering Materials and Technology, Transactions of the ASME*, vol. 105, pp. 48-53, 1983.

[337] Panov V., "Modelling of behaviour of betals at high strain rates," Cranfield University, PhD Thesis 2006.

[338] Field J.E., Walley S.M., Proud W.G., Goldrein H.T., and Siviour C.R., "Review of experimental techniques for high rate deformation and shock studies," *International Journal of Impact Engineering*, vol. 30, pp. 725–775, 2004.

[339] Hopkinson B., "A method of measuring the pressure produced in the detonation of high explosives or by the impact of bullets," *Philosophical Transactions of the Royal Society (London) A*, vol. 213, pp. 437-456, 1914.

[340] Kolsky H., "An investigation of the mechanical properties of materials at very high rates of loading," *Proceedings of the Physical Society (London) B*, vol. 62, pp. 676-700, 1949.

[341] Kolsky H., *Stress waves in solids*.: Dover Publications, 1963.

[342] Lindholm U.S., "Some experiments with the split-Hopkinson pressure bar," *Journal of the Mechanics and Physics of Solids*, vol. 12, pp. 317-335, 1964.

[343] Lindholm U.S. and Yeakley L.M., "Dynamic deformation of single and polycrystalline Aluminum," *Journal of the Mechanics and Physics of Solids*, vol. 13, no. 1, pp. 41-53, 1965.

[344] Lindholm U.S. and Yeakley L.M., "High strain rate testing: tension and compression ," *Experimental Mechanics*, no. 8, pp. 1-9, 1968.

[345] Lindholm U.S., "High Strain Testing," in *Techniques of Metals Research*, R.F. Bunshah, Ed.: Wiley Interscience, 1971, vol. 5, ch. Part I: Measurement of Mechanical Properties, pp. 199-271.

[346] Follansbee P.S. and Gray G.T., "An analysis of the low temperature, low and high strain-rate deformation of Ti−6Al−4V," *Metallurgical Transactions*, vol. 20A, pp. 863-874, 1989.

[347] Bell J.F., *The experimental foundations of solid mechanics*.: Springer, 1973.

[348] Gray III G.T., "Classic split-Hopkinson pressure bar testing," in *ASM Handbook*.: ASM International, 2000, vol. 8 Mechanical Testing and Evaluation, pp. 462-476.

[349] Johnson W., *Impact strength of materials*. London: Edward Arnold, 1972.

[350] Chen W.W. and Song B., *Split Hopkinson (Kolsky) Bar Design, Testing and Applications*.: Springer, 2011.

[351] Staab G.H. and Gilat A., "A direct-tension split Hopkinson bar for high strain-rate testing," *Experimental Mechanics*, vol. 31, no. 3, pp. 232-235, 1991.

[352] Gilat A., "Torsional Kolsky bar testing," in *ASM handbook*, Kuhn H. and Medlin D., Eds.: ASM International, 2000, vol. 8, ch. Mechanical testing and evaluation, pp. 505-515.

[353] Follansbee P.S. and Frantz C., "Wave propagation in the split Hopkinson pressure bar," *Journal of Engineering Materials and Technology*, vol. 105, no. 1, pp. 61-66, 1983.

[354] Lindholm U.S., "Dynamic deformation of metals," in *Behavior of materials under dynamic loading*, N.J. Huffington, Ed.: ASME, 1965, pp. 42-61.

[355] Gama B.A. and Gillespie, Jr. J.W., "Numerical Hopkinson bar analysis: uni-axial stress and planar

bar-specimen interface conditions by design," Army Research Laboratory, ARL-CR-553, 2004.

[356] Dioh N.N., Ivankovic A., Leevers P.S., and Williams J.G., "Stress wave propagation effects in split Hopkinson pressure bar tests," *Proceedings of the Royal Society A: Mathematical, Physical and Engineering Sciences*, vol. 449, no. 1936, pp. 187-204, 1995.

[357] Follansbee P.S., "The Hopkinson bar, mechanical testing and evaluation," in *ASM Handbook*.: ASM International, 1995, vol. 8 Mechanical Testing and Evaluation, pp. 198–203.

[358] Malinowski J.Z. and Klepaczko J.R., "A unified analytic and numerical approach to specimen behaviour in the split-Hopkinson pressure bar," *International Journal of Mechanical Sciences*, vol. 28, no. 6, pp. 381–391, 1986.

[359] Davies E.D.H. and Hunter S.C., "Dynamic compression testing of solids by method of split Hopkinson pressure bar," *Journal of the Mechanics and Physics of Solids*, vol. 11, no. 3, pp. 155-179, 1963.

[360] Harding J., Wood E., and Campbell J., "Tensile testing of materials at impact rates of strain," *Journal of Mechanical Engineering Science*, vol. 2, pp. 88-96, 1960.

[361] Albertini C. and Montagnani M., "Testing techniques Based on the Split Hopkinson Bar," in *Mechanical properties at high rates of strain*, J. Harding, Ed. London: Institute of Physics, Conference Series No. 21, 1974, pp. 22-31.

[362] Nicholas T., "Tensile testing of materials at high rates of strain," *Experimental Mechanics*, vol. 21, pp. 177-185, 1981.

[363] Baker W.W. and Yew C.H., "Strain rate effects in the propagation of torsional plastic waves," *Journal of Applied Mechanics*, vol. 33, pp. 917-923, 1966.

[364] Frantz R.A. and Duffy J., "The dynamic stress-strain behavior in torsion of 1100-0 Aluminum subjected to a sharp increase in strain rate," *Journal of Applied Mechanics*, vol. 39, pp. 939-945, 1972.

[365] Lewis J.L. and Campbell J.D., "The development and use of a torsional Hopkinson bar apparatus ," *Experimental mechanics*, vol. 12, no. 11, pp. 520-524, 1972.

[366] Baker W.E. and Yew C.H., "Strain-rate effects in the propagation of torsional plastic waves," *Journal of Applied Mechanics, Transactions of ASME*, vol. 33, pp. 917–923, 1966.

[367] Hartley K.A., Duffy J., and Hawley R.H., "The torsional Kolsky (split-Hopkinson) bar," in *ASM Handbook*, Kuhn H. and Medlin D., Eds. Materials Park Ohio: ASM International, 2000, vol. 8, pp. 218–228.

[368] Ramesh K.T., "High rates and impact experiments," in *Springer Handbook of Experimental Solid Mechanics*, W.N. Jr. Sharpe, Ed.: Springer US, 2008, ch. 33, pp. 929-960.

[369] Marchand A. and Duffy J., "An experimental study of the formation process of adiabatic shear bands in a structural steel," *Journal of the Mechanics and Physics of Solids*, vol. 36, no. 3, pp. 251–283, 1988.

[370] Gilat A. and Cheng C.-S., "Torsional split Hopkinson bar tests at strain rates above 10000 1/s," *Experimental Mechanics*, vol. 40, no. 1, pp. 54-59, 2000.

[371] Seidt J.D. and Gilat A., "Development of a new metal material model in LSDYNA Part 3: Plastic deformation and ductile fracture of 2024 aluminum under various loading conditions," Federal Aviation Administration, Draft Report Submitted to FAA 2013.

[372] Meyers M.A., "Dynamic deformation and failure," in *Mechanics and materials: fundamentals and linkages*, M.A. Meyers, R.W. Armstrong, and H. Kirchner, Eds.: John Wiley & Sons, 1999, ch. 14, pp. 489-594.

[373] Armstrong R.W. and Walley S.M., "High strain rate properties of metals and alloys," *International Materials Reviews*, vol. 53, no. 3, pp. 105-128, 2008.

[374] Needleman A., "Material rate dependence and mesh sensitivity in localization problems," *Computer Methods in Applied Mechanics and Engineering*, vol. 67, pp. 69-85, 1988.

[375] Törnqvist R., "Design of crashworthy ship structures," Technical University of Denmark, PhD Thesis 2003.

[376] Du Bois P.A., "A note on regularization," Unpublished Technical presentation to Federal Aviation Administration, November, 2010.

[377] Hill R., "On Discontinuous plastic states, with special reference to localized necking in thin sheets," *Journal of the Mechanics and Physics of Solids*, vol. 1, pp. 19-30, 1952.

[378] Marciniak Z., Duncan J.L., and Hu S.J., *Mechanics of sheet metal forming*, 2nd ed.: Butterworth-Heinemann, 2002.

[379] Li Y., "Ductile fracture due to plastic flow, void growth and localization for 3D randomly voided materials," University of Michigan, PhD Thesis 2007.

[380] Seidt J.D. and Gilat A. (2013, March) Ohio State University, Dynamic Mechanics of Materials Laboratory. [Online]. http://www.mecheng.osu.edu/lab/dmm/sites/default/files/smooth-round-tension-e1.avi

[381] Zhang S., MCCormick P.G., and Estrin Y., "The morphology of Portevin–Le Chatelier bands: finite element simulation for Al–Mg–Si," *Acta Materialia*, vol. 49, pp. 1087–1094, 2001.

[382] Graff S. et al., "Strain localization phenomena associated with static and dynamic strain ageing in notched specimens: experiments and finite element simulations," *Materials Science and Engineering A*, vol. 387–389, pp. 181–185, 2004.

[383] Benallal A., Berstad T., Borvik T., Clausen A.H., and Hopperstad O.S., "Dynamic strain aging and related instabilities: experimental, theoretical and numerical aspects," *European Journal of Mechanics A/Solids*, vol. 25 , pp. 397–424, 2006.

[384] Seidt J.D. and Gilat A., "Low rate punch test status report," Ohio State University, Unpublished Technical presentation to Federal Aviation Administration, October, 2009.

[385] de Boor C., *A practical guide to splines*.: Springer, 2001, vol. 27, Applied Mathematical Sciences.

[386] de Boor C., *Spline toolbox, for use with MATLAB*.: The MathWorks, Inc., 2000.

[387] de Boor C., "Efficient computer manipulation of tensor products," *ACM Trans. Math. Software*, vol. 5, pp. 173–182, 1979.

[388] Pereira J.M., Revilock D.M., Lerch B.A., and Ruggeri C.M., "Impact testing of Aluminum 2024 and Titanium 6Al-4V for material model development," NASA Glenn Research Center, Technical Memorandum NASA/TM-2013-217869; DOT/FAA/TC-12/58, 2013.

Appendix - A: Preliminaries of the stress tensor and invariants

Considering the infinitesimally small rectangular parallelepiped that is shown in Figure A-1, the nine components of the second-order stress tensor (σ_{ij}) can be written as:

$$\sigma_{ij} = \begin{bmatrix} \sigma_x & \tau_{xy} & \tau_{xz} \\ \tau_{yx} & \sigma_y & \tau_{yz} \\ \tau_{zx} & \tau_{zy} & \sigma_z \end{bmatrix} = \begin{bmatrix} \sigma_{11} & \sigma_{12} & \sigma_{13} \\ \sigma_{21} & \sigma_{22} & \sigma_{23} \\ \sigma_{31} & \sigma_{32} & \sigma_{33} \end{bmatrix} \tag{A.1}$$

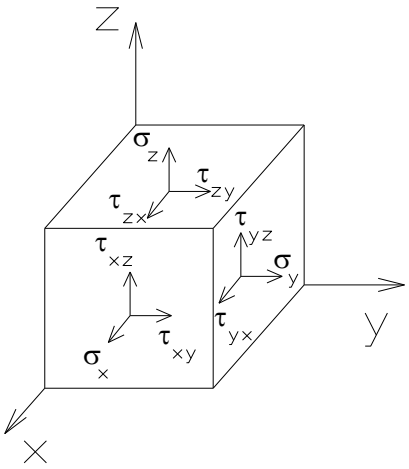

Figure A-1: Normal and shear stresses.

Three principle stresses can be calculated from the relation described in Equation (A.1) by finding the roots of the determinant as:

$$\left|\sigma_{ij} - \sigma\delta_{ij}\right| = 0 \Rightarrow \sigma^3 - I_1\sigma^2 + I_2\sigma - I_3 = 0 \tag{A.2}$$

where,

$$\begin{aligned} I_1 &= tr(\boldsymbol{\sigma}) = \sigma_{kk} = \sigma_{11} + \sigma_{22} + \sigma_{33} \\ &= \sigma_1 + \sigma_2 + \sigma_3 \end{aligned} \tag{A.3}$$

$$I_2 = \frac{1}{2}\left(\sigma_{ij}\sigma_{ij} - \sigma_{ii}\sigma_{jj}\right) = -(\sigma_{11}\sigma_{22} + \sigma_{22}\sigma_{33} + \sigma_{11}\sigma_{33}) + \sigma_{12}^2 + \sigma_{13}^2 + \sigma_{23}^2 \\ = -(\sigma_1\sigma_2 + \sigma_2\sigma_3 + \sigma_3\sigma_1) \quad \text{(A.4)}$$

$$I_3 = \frac{1}{3}\sigma_{ij}\sigma_{jk}\sigma_{ki} = \det\left[\sigma_{ij}\right] = \begin{vmatrix}\sigma_{11} & \sigma_{12} & \sigma_{13}\\ \sigma_{21} & \sigma_{22} & \sigma_{23}\\ \sigma_{31} & \sigma_{32} & \sigma_{33}\end{vmatrix} \\ = \sigma_1\sigma_2\sigma_3 \quad \text{(A.5)}$$

Principal stress invariants are arranged such that ($\sigma_1 \geq \sigma_2 \geq \sigma_3$). For each principle stress, an associated principle direction can be found and any stress tensor can be written in terms of the principle stresses. Therefore, if the principle stresses and their directions are known, the stress-state can be determined according to:

$$\begin{bmatrix}\sigma_{11} & \sigma_{12} & \sigma_{13}\\ \sigma_{21} & \sigma_{22} & \sigma_{23}\\ \sigma_{31} & \sigma_{32} & \sigma_{33}\end{bmatrix} = \left[R_{ij}\right]\begin{bmatrix}\sigma_1 & 0 & 0\\ 0 & \sigma_2 & 0\\ 0 & 0 & \sigma_3\end{bmatrix}\left[R_{ij}\right]^T \quad \text{(A.6)}$$

The mean of the three normal stresses (σ_m), which is also called as hydrostatic stress (σ_H) can be found as:

$$\sigma_m = \sigma_H = \frac{\sigma_{11} + \sigma_{22} + \sigma_{33}}{3} \text{ or } \sigma_m = \frac{1}{3}\sigma_{kk} = \frac{1}{3}I_1 \quad \text{(A.7)}$$

A deviatoric stress tensor can be defined as:

$$s_{ij} = \begin{bmatrix}s_{11} & s_{12} & s_{13}\\ s_{21} & s_{22} & s_{23}\\ s_{31} & s_{32} & s_{33}\end{bmatrix} = \begin{bmatrix}(\sigma_{11} - \sigma_H) & \sigma_{12} & \sigma_{13}\\ \sigma_{21} & (\sigma_{22} - \sigma_H) & \sigma_{23}\\ \sigma_{31} & \sigma_{32} & (\sigma_{33} - \sigma_H)\end{bmatrix} \quad \text{(A.8)}$$

Therefore, the deviatoric and hydrostatic stresses can be related as:

$$s_{ij} = \sigma_{ij} - \sigma_H\delta_{ij} = \sigma_{ij} - \frac{1}{3}\sigma_{kk}\delta_{ij} \quad \text{(A.9)}$$

where, (δ_{ij}) is the Kronecker delta.

Similarly, invariants of the deviatoric stress tensor can be found as:

$$\left|s_{ij} - s\delta_{ij}\right| = 0 \Rightarrow s^3 - J_1 s^2 + J_2 s - J_3 = 0 \tag{A.10}$$

where,

$$\begin{aligned} J_1 &= tr(\boldsymbol{s}) = s_{kk} = s_{11} + s_{22} + s_{33} \\ &= 0 \end{aligned} \tag{A.11}$$

$$\begin{aligned} J_2 &= \frac{1}{2}\left(s_{ij}s_{ij}\right) = \frac{1}{2}(s_1^2 + s_2^2 + s_3^2) \\ &= \frac{1}{2}((\sigma_1 - \sigma_m)^2 + (\sigma_2 - \sigma_m)^2 + (\sigma_3 - \sigma_m)^2) \\ &= \frac{1}{3}I_1^2 + I_2 \end{aligned} \tag{A.12}$$

$$\begin{aligned} J_3 &= \frac{1}{3}s_{ij}s_{jk}s_{ki} = \det\left[s_{ij}\right] = s_1 s_2 s_3 \\ &= \frac{1}{3}(\sigma_1 - \sigma_m)(\sigma_2 - \sigma_m)(\sigma_3 - \sigma_m) \\ &= \frac{2}{27}I_1^3 + \frac{1}{3}I_1 I_2 + I_3 \end{aligned} \tag{A.13}$$

The second invariant of the stress deviator tensor, (J_2) is directly related to the von Mises effective stress (σ_{vm}) by:

$$\sigma_{vm} = \sqrt{3J_2} \tag{A.14}$$

Stress-triaxiality is often defined as the ratio of mean or hydrostatic stress to effective stress. In this study, since a hydrocode is utilized to solve FE calculations and due to its convenience [7] [13] [96] to use directly pressure as an internal state variable, stress-triaxiality is defined as:

$$\sigma^* = \frac{p}{\sigma_{vm}} \tag{A.15}$$

where, ($p = -\sigma_H = -\sigma_m = -\frac{1}{3} I_1$).

Hence, the von Mises effective stress can also be written as:

$$\sigma_{vm} = \sqrt{\frac{3}{2}((\sigma_1 + p)^2 + (\sigma_2 + p)^2 + (\sigma_3 + p)^2)} \qquad \text{(A.16)}$$

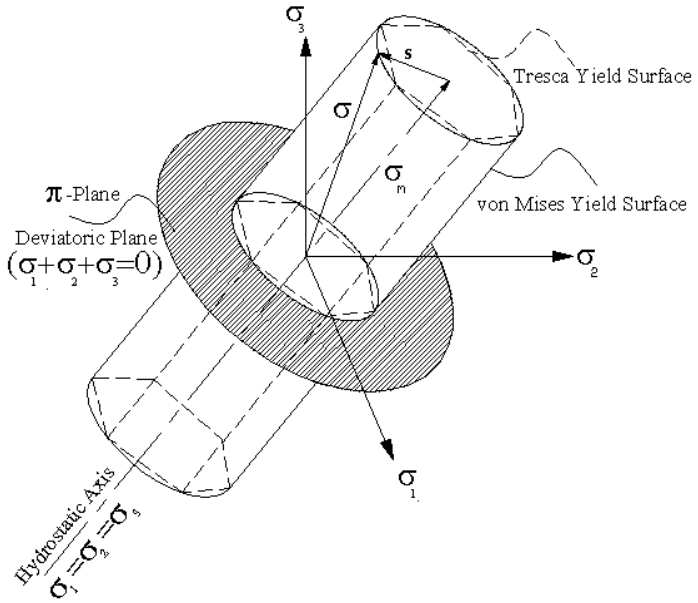

Figure A-2: Haigh–Westergaard space.

Appendix - B: Specimen geometries and FE models

Different specimens are designed in Chapter 4 for specific values of the stress-triaxiality, Lode-angle-parameter and product-triaxiality. Corresponding specimen geometries and FE models are then used in Chapter 5 for characterization of a tabulated flow and failure surface for TRAUM. Validation of the characterized TRAUM input data is carried out by utilizing the same specimens in Chapter 6. In this Appendix, major dimensions of the specimen geometries and corresponding FE models are illustrated by a color coded scheme that is followed throughout the dissertation based on the stress-state of the specimen. It should be noted that the same specimen geometry is used for pure shear and combined tension-torsion cases, where the required stress-states are achieved by different loading conditions. It should also be noted that the dimensions of the specimens represent a nominal value and the repeatability of the tests should be assessed based on the variations in the specimen dimensions that are listed in Appendix-C.

Table B-1: Specimen geometries and corresponding cross-references in the dissertation.

Specimen #	Reference Figure in Appendix-B
1	Figure B-1
2	Figure B-2
3	Figure B-3
4	Figure B-4
5	Figure B-5
6	Figure B-6
7	Figure B-7
8	Figure B-8
9	Figure B-9
10	Figure B-10
11	Figure B-11
12	Figure B-12
13	Figure B-13
14	Figure B-14
15	Figure B-15
16	Figure B-15
17	Figure B-15
18	Figure B-16
19	Figure B-17
20	Figure B-18
21	Figure B-19

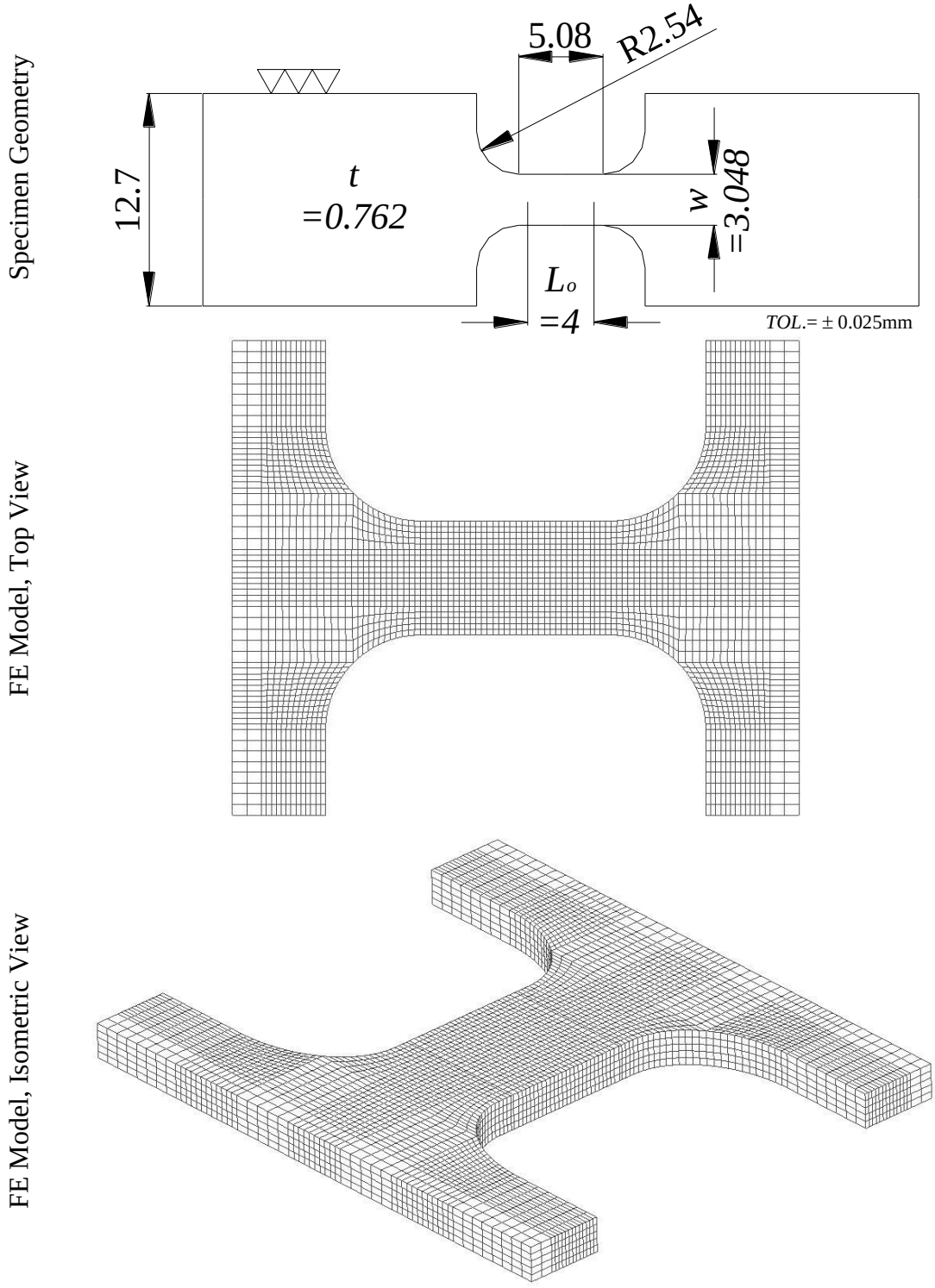

Figure B-1: Plane-stress smooth specimen, Specimen #1.

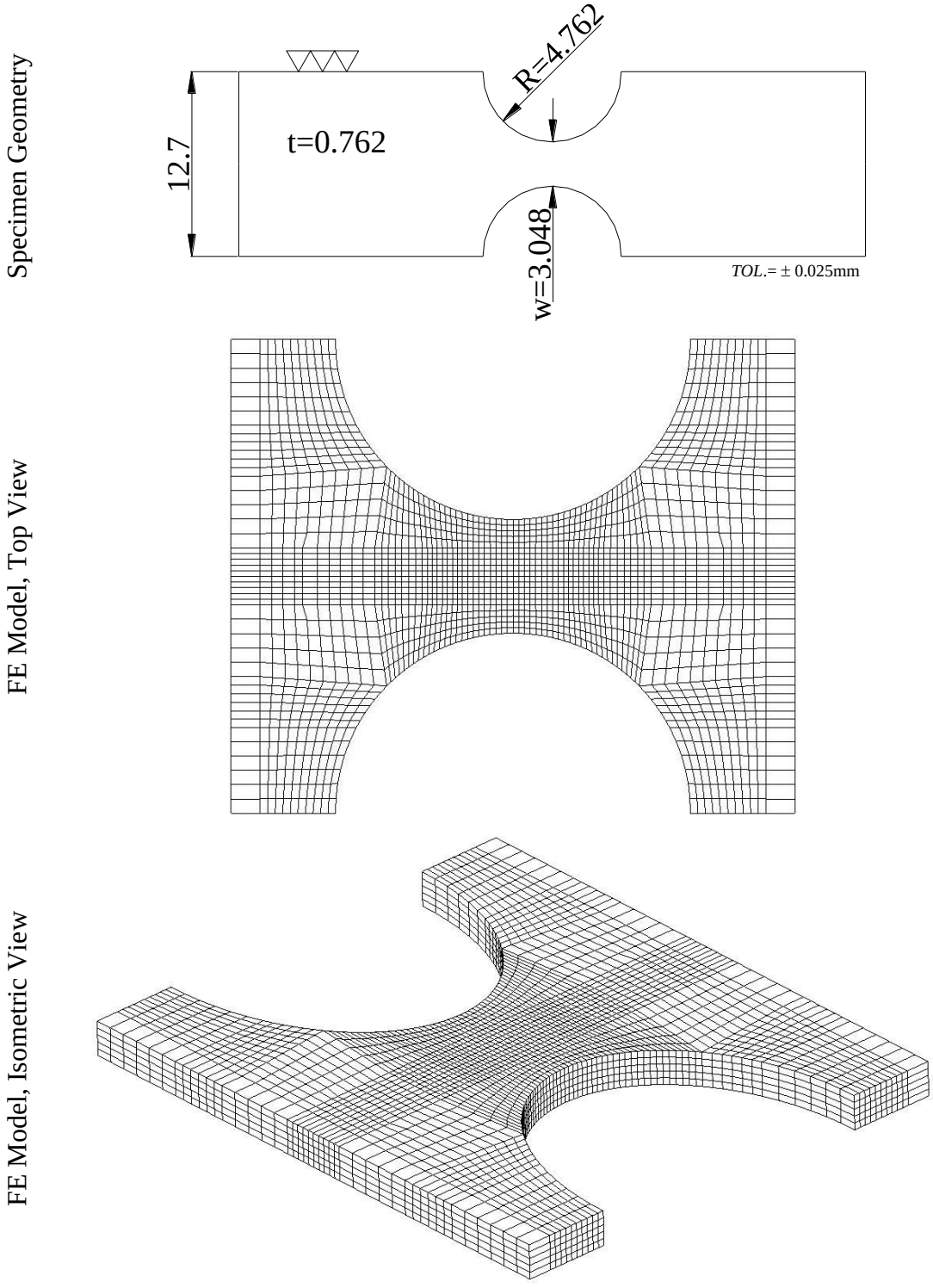

Figure B-2: Plane-stress notched, Specimen #2.

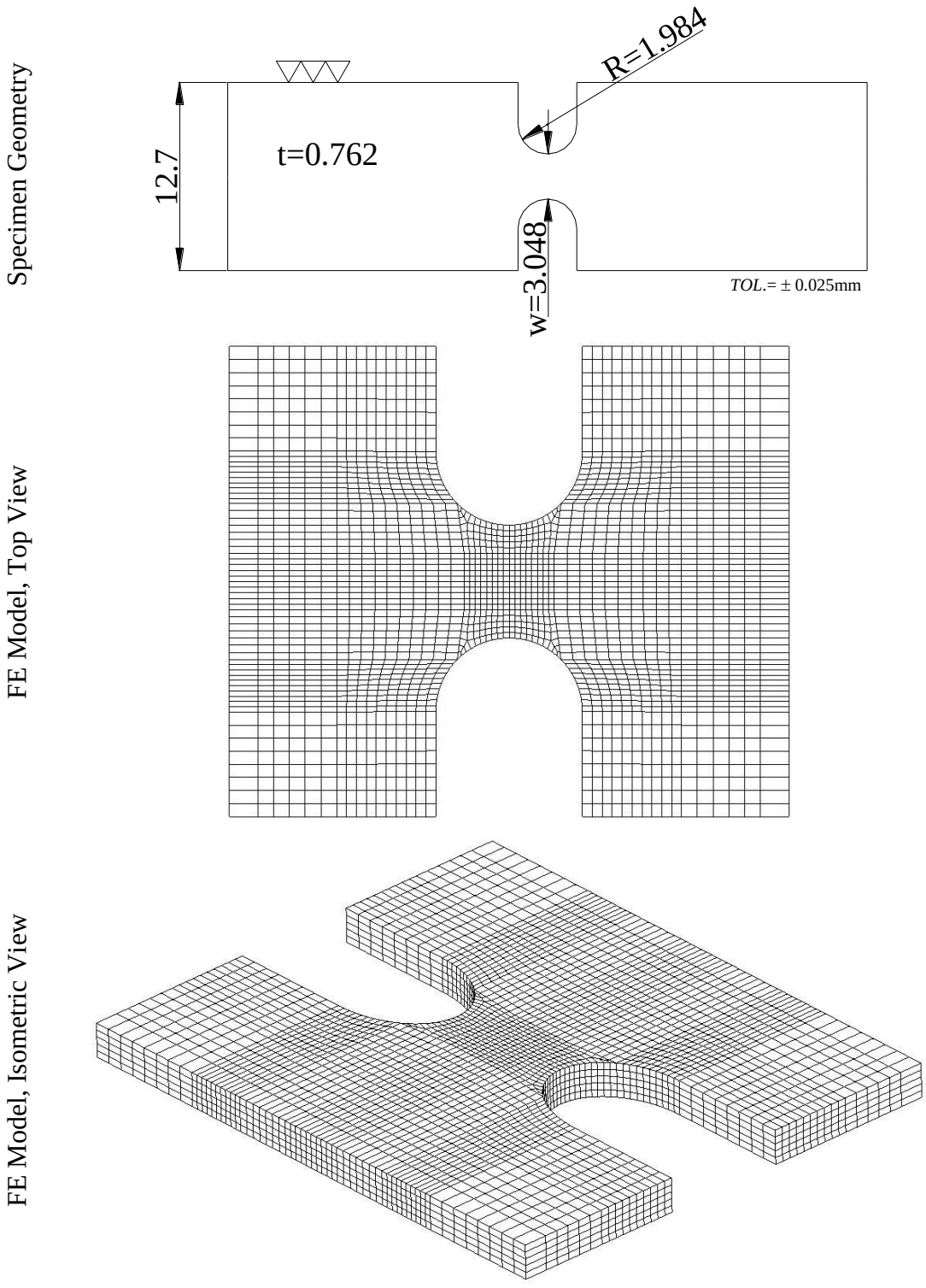

Figure B-3: Plane-stress notched, Specimen #3.

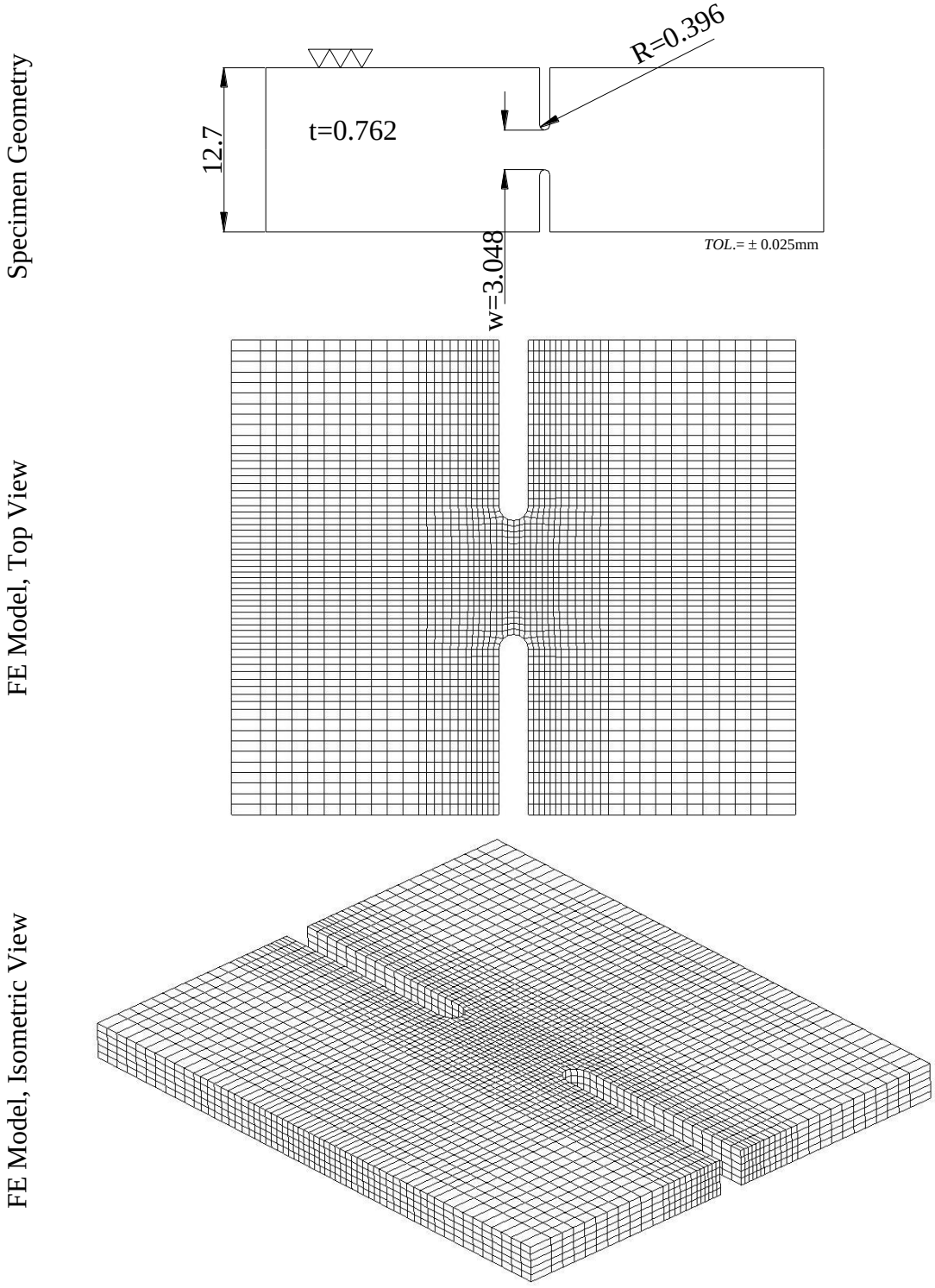

Figure B-4: Plane-stress notched, Specimen #4.

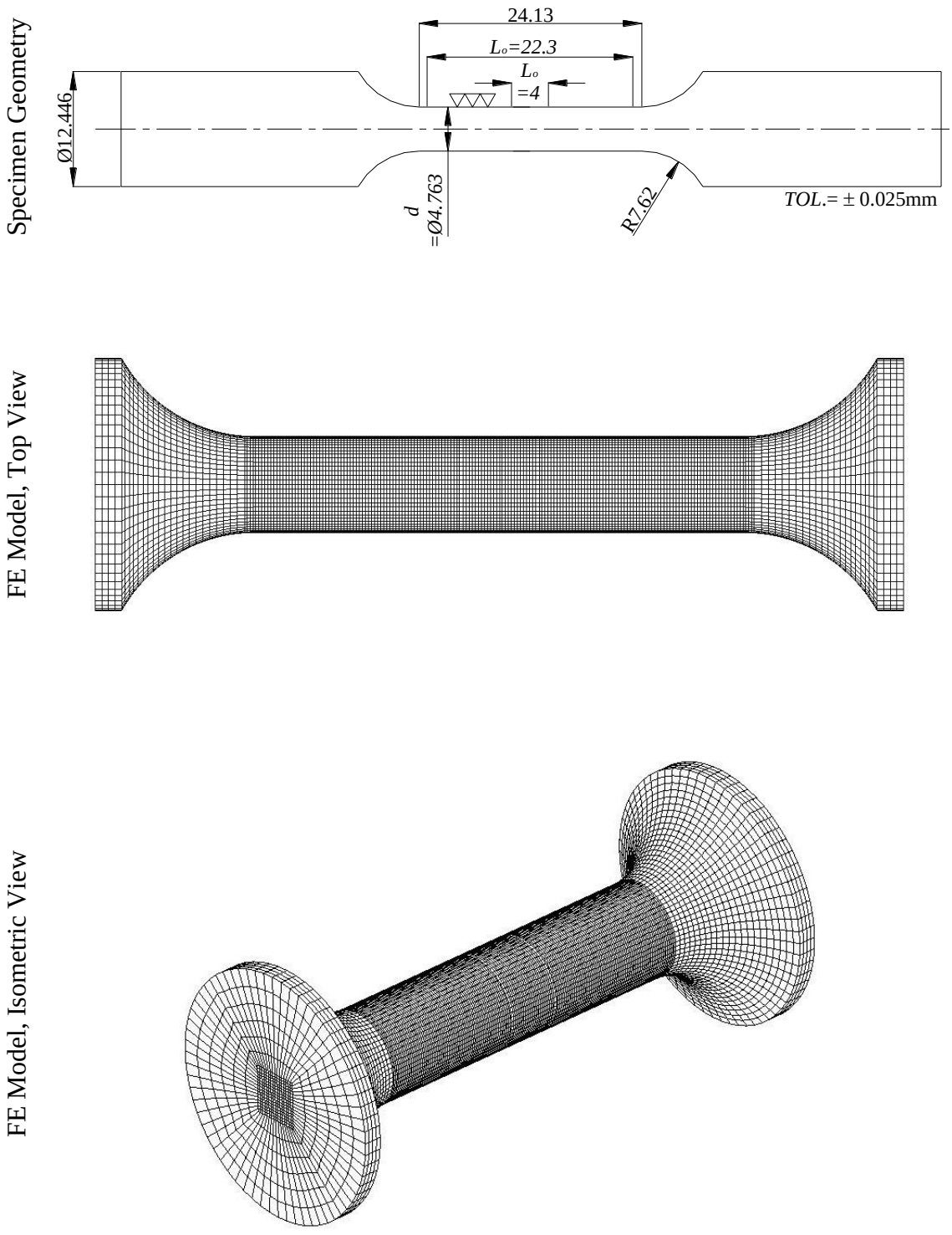

Figure B-5: Axisymmetric smooth specimen, Specimen #5.

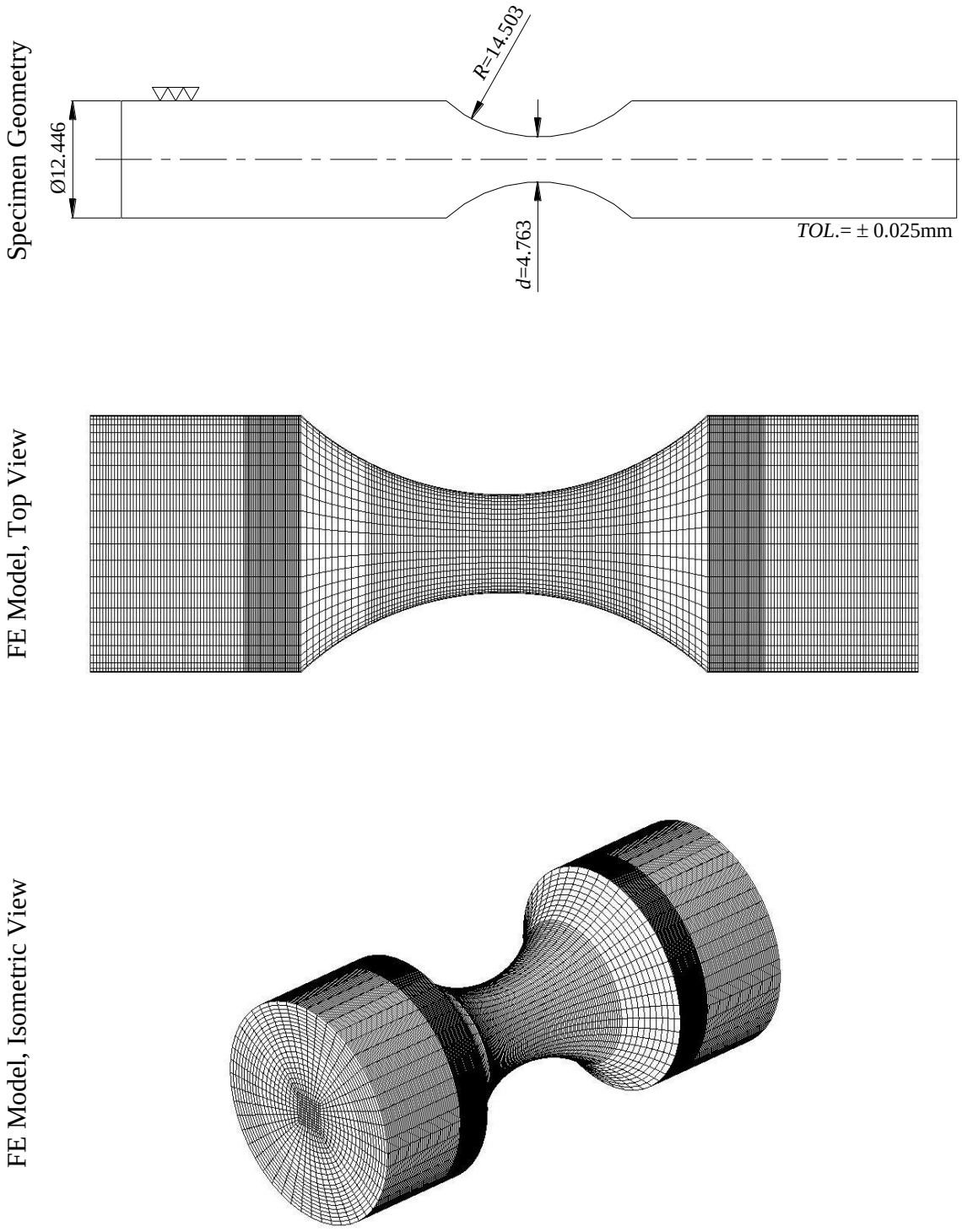

Figure B-6: Axisymmetric notched specimen, Specimen #6.

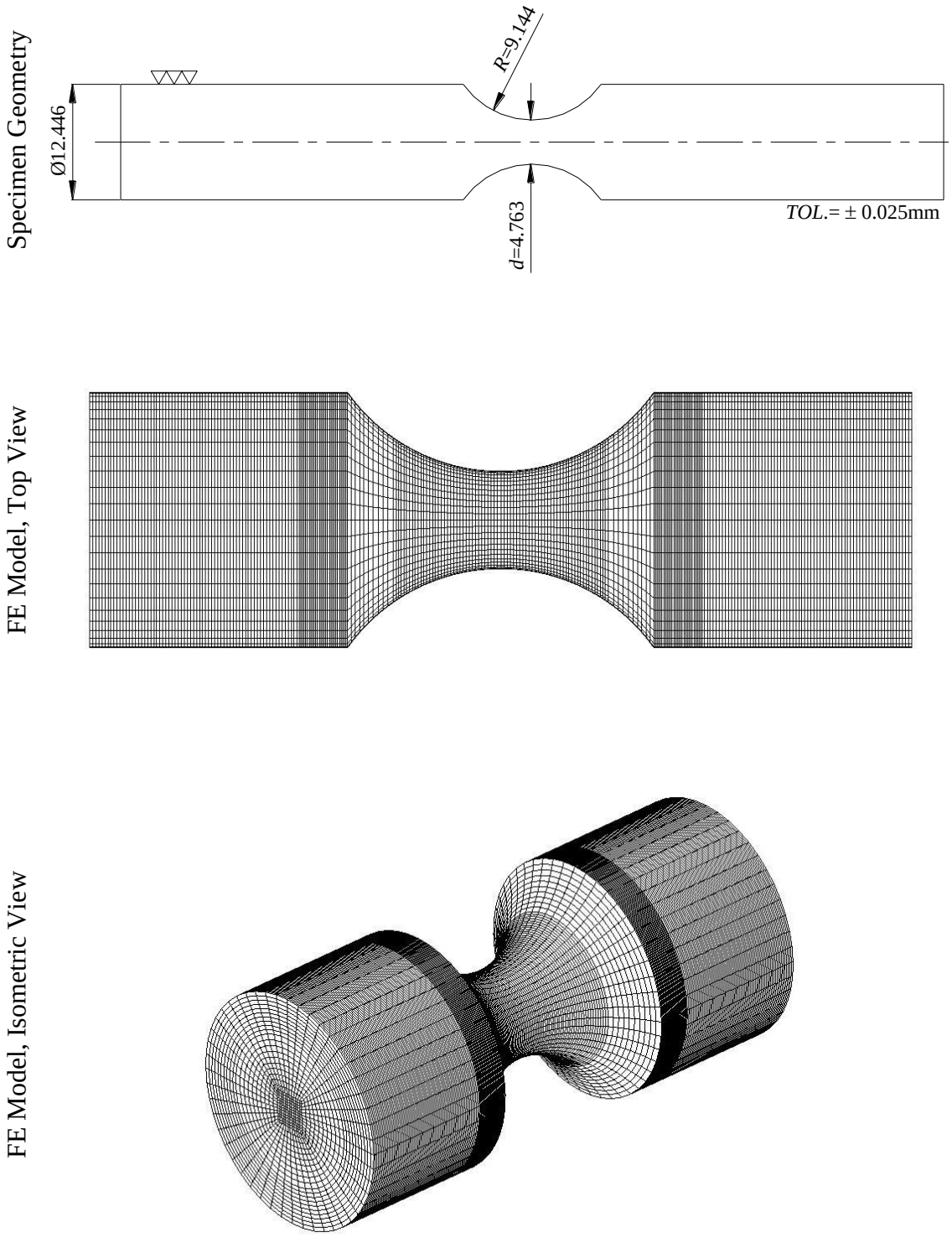

Figure B-7: Axisymmetric notched specimen, Specimen #7.

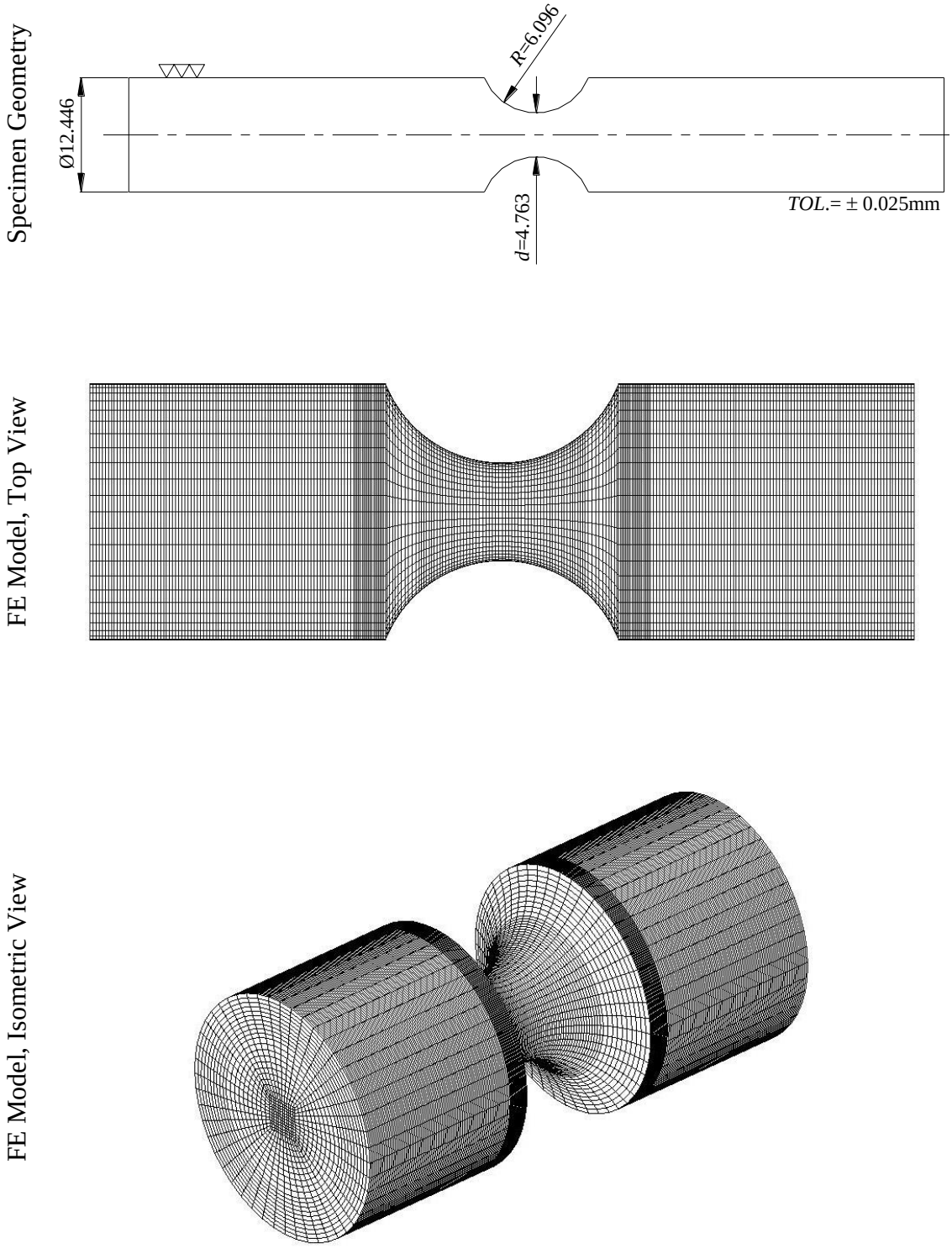

Figure B-8: Axisymmetric notched specimen, Specimen #8.

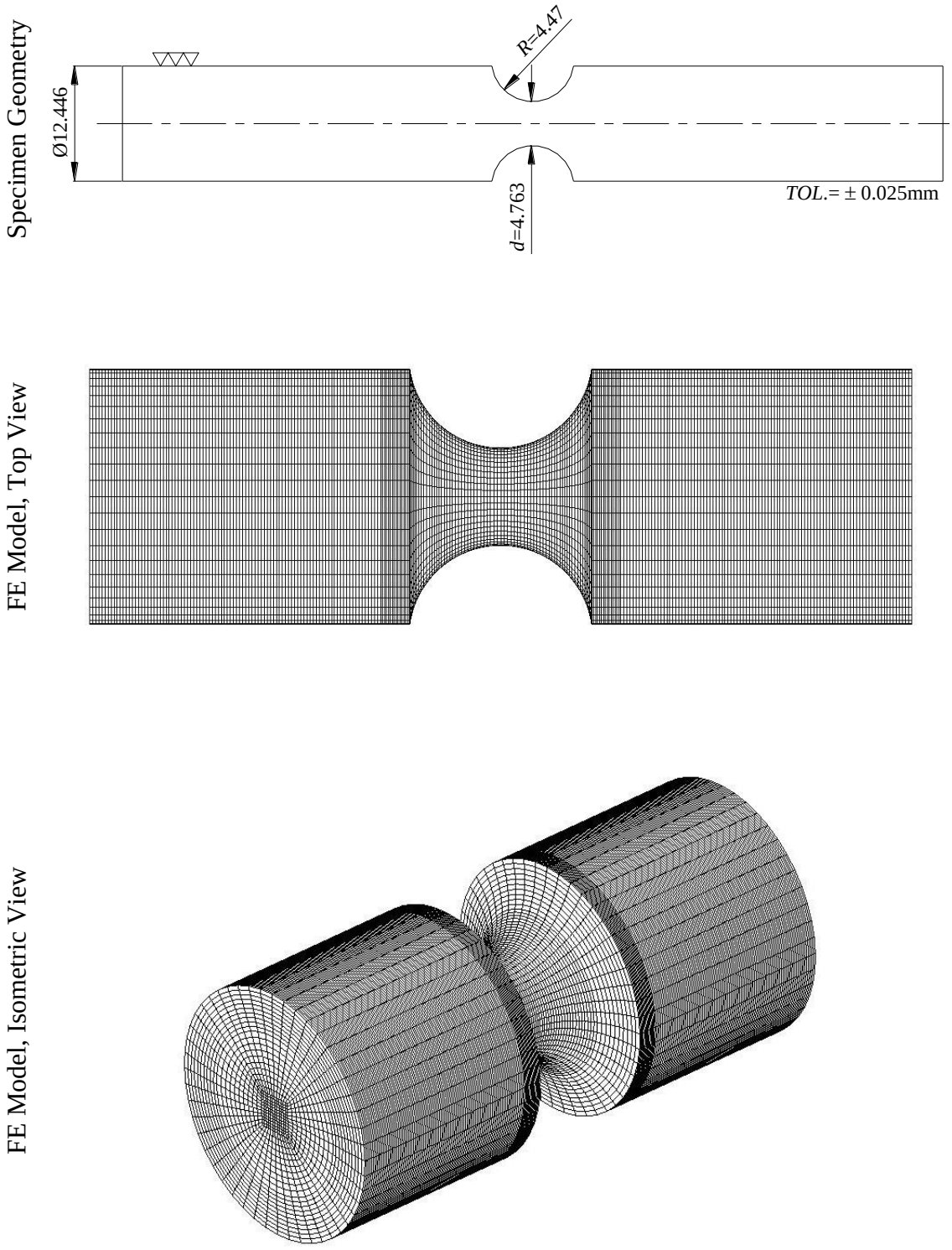

Figure B-9: Axisymmetric notched specimen, Specimen #9.

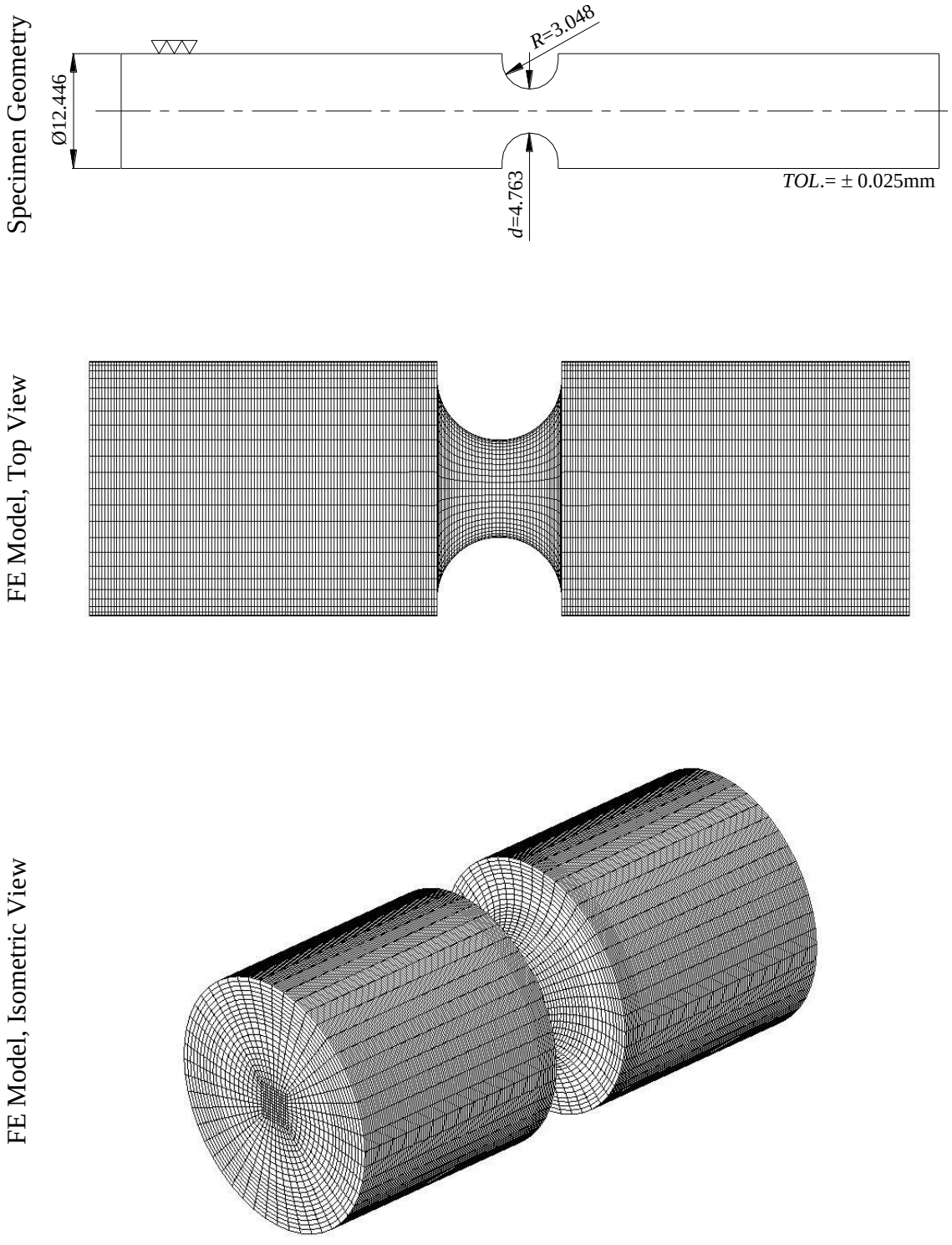

Figure B-10: Axisymmetric notched specimen, Specimen #10.

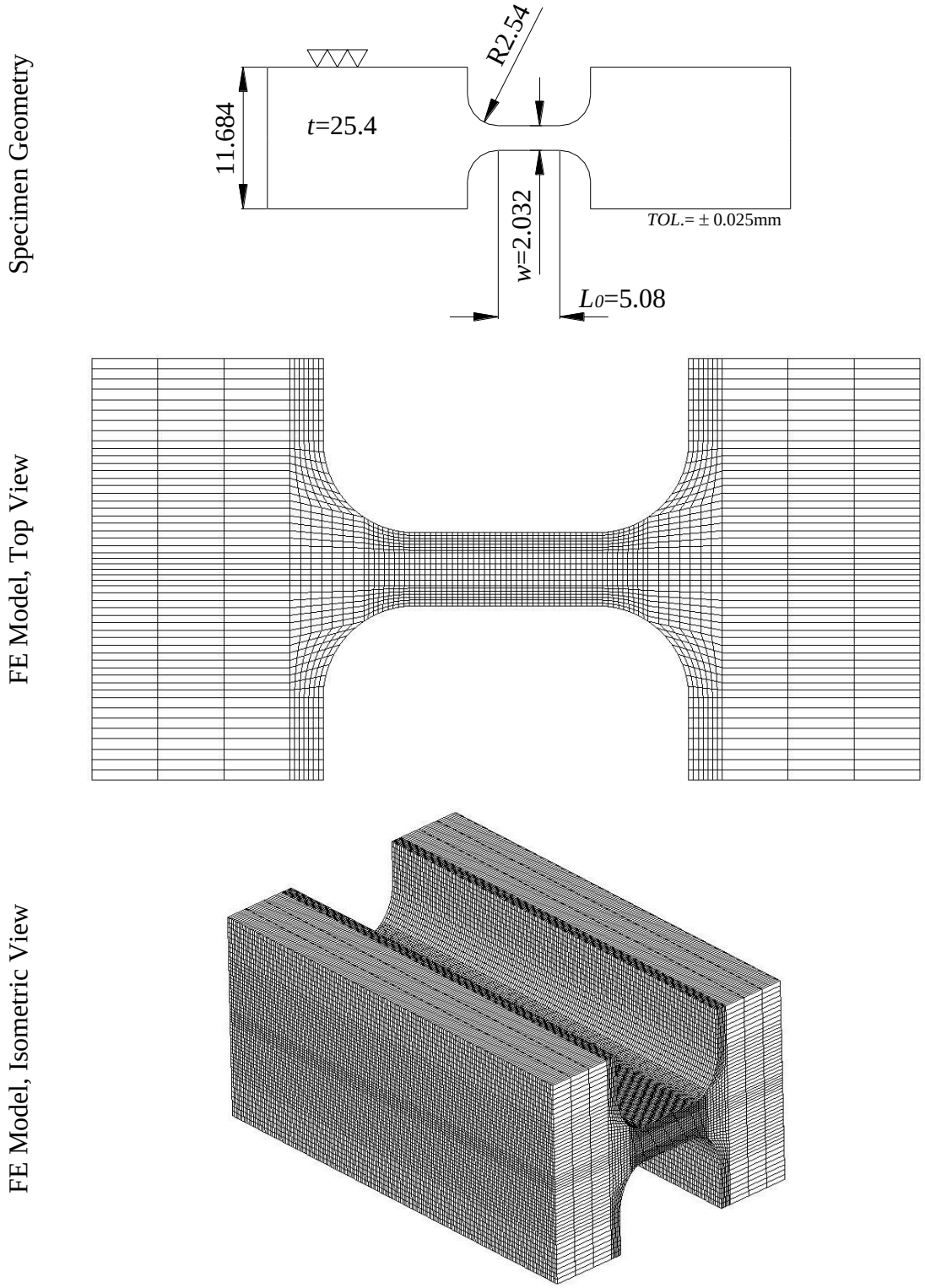

Figure B-11: Plane-strain smooth specimen, Specimen #11.

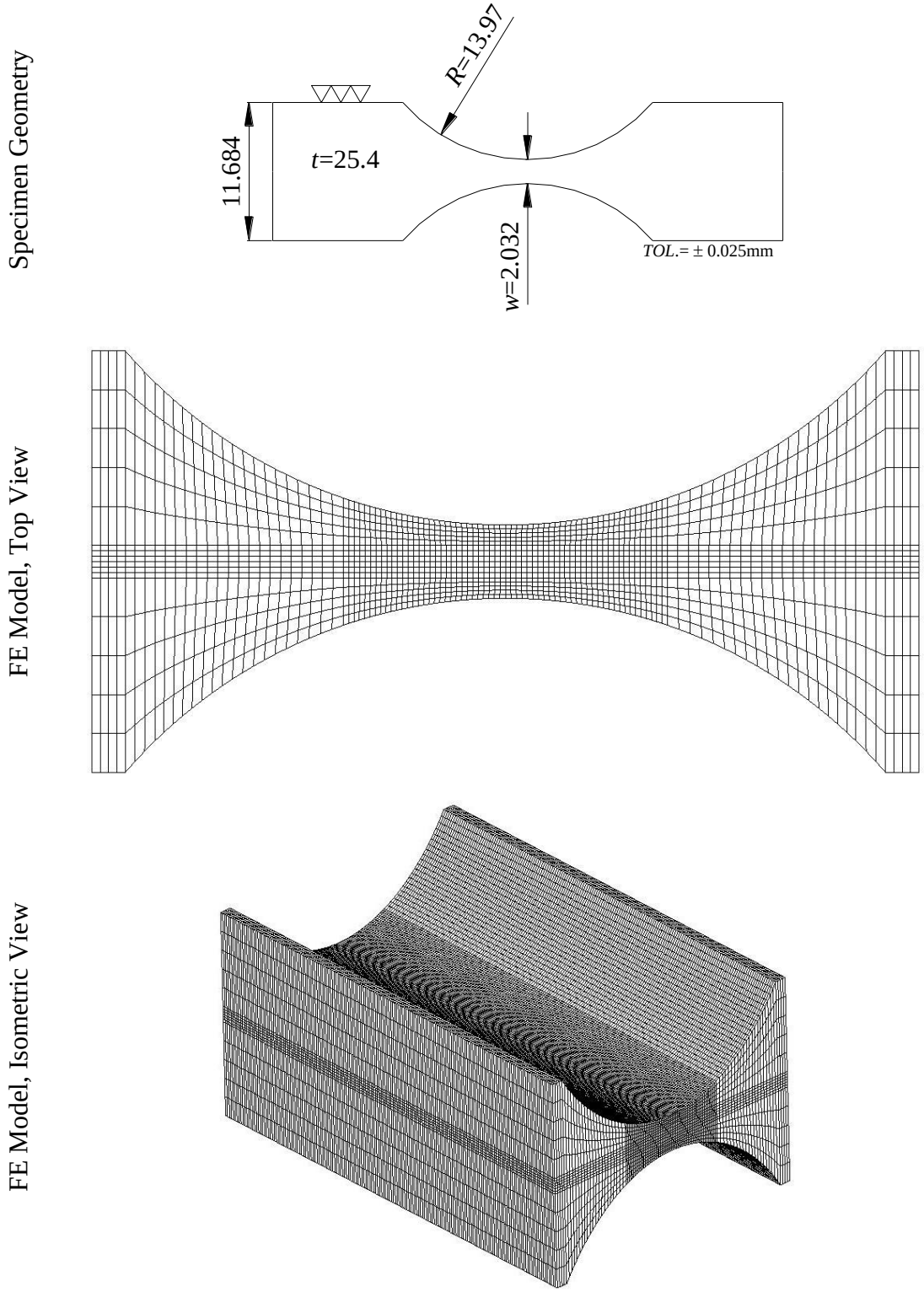

Figure B-12: Plane-strain notched specimen, Specimen #12.

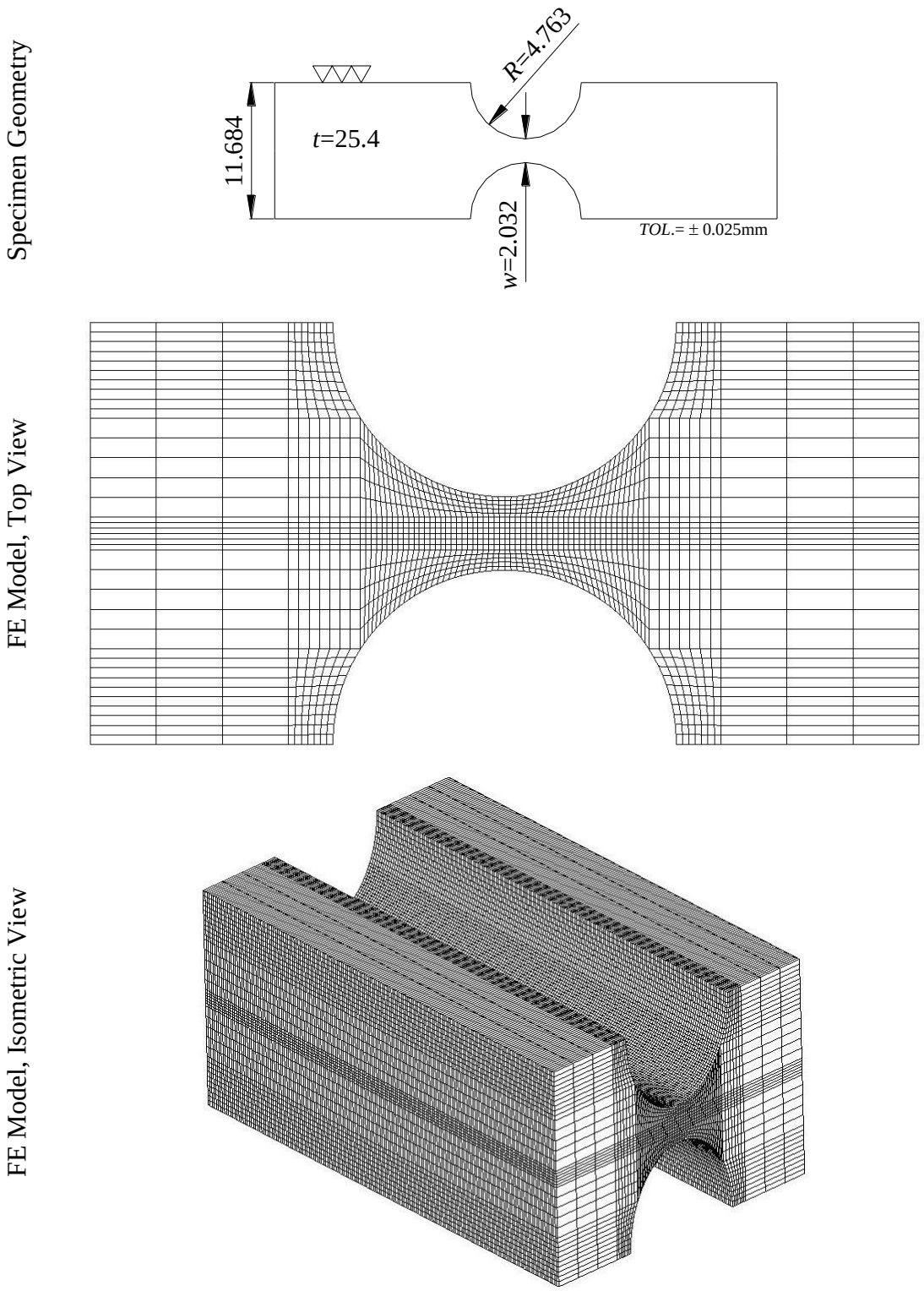

Figure B-13: Plane-strain notched specimen, Specimen #13.

Specimen Geometry

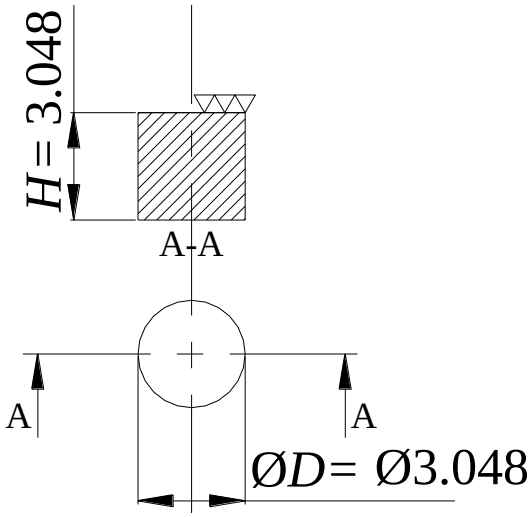

FE Model, Top View

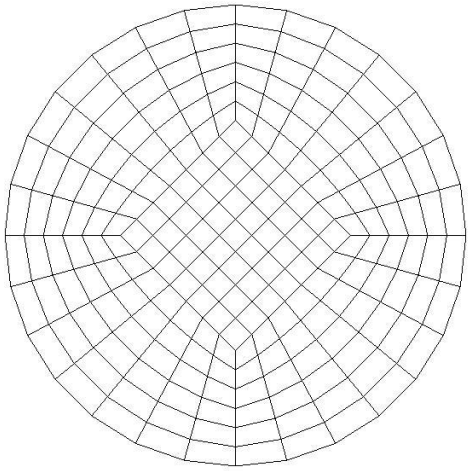

FE Model, Isometric View

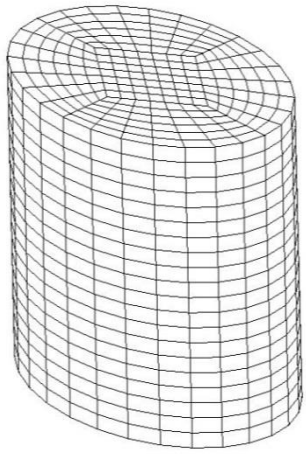

Figure B-14: Compression specimen, Specimen #14.

FE Model, Isometric View

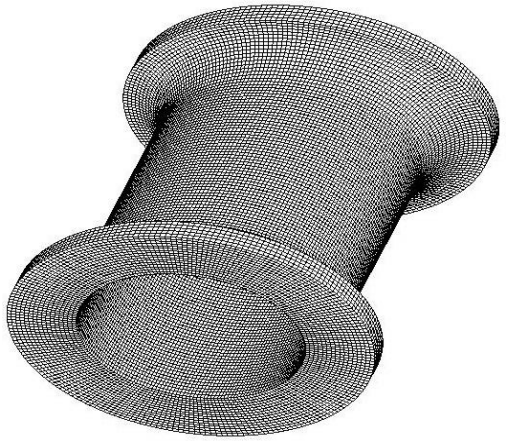

FE Model, Top View

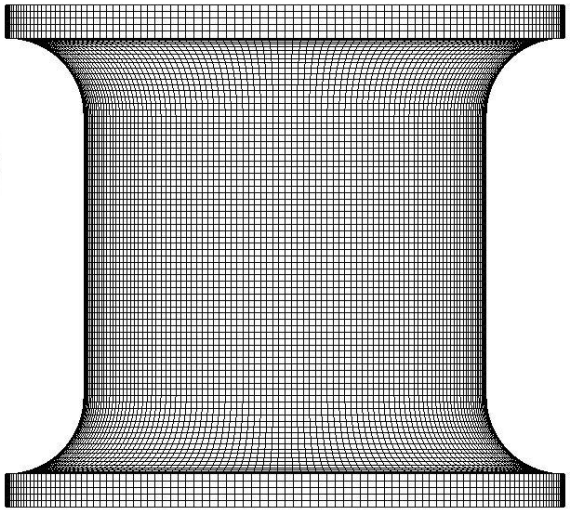

Specimen Geometry

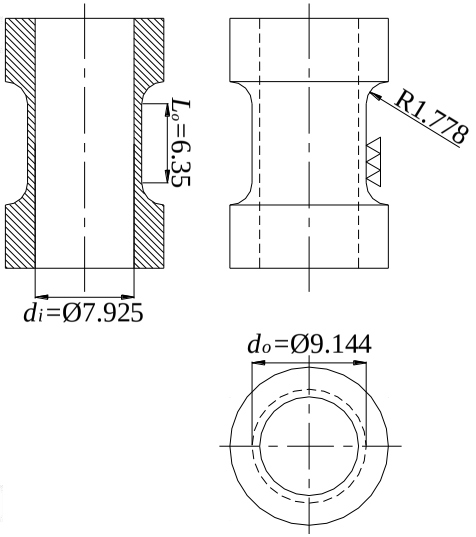

Figure B-15: Shear and combined tension-shear specimens, Specimen #15, Specimen #16 & Specimen #17.

Specimen Geometry

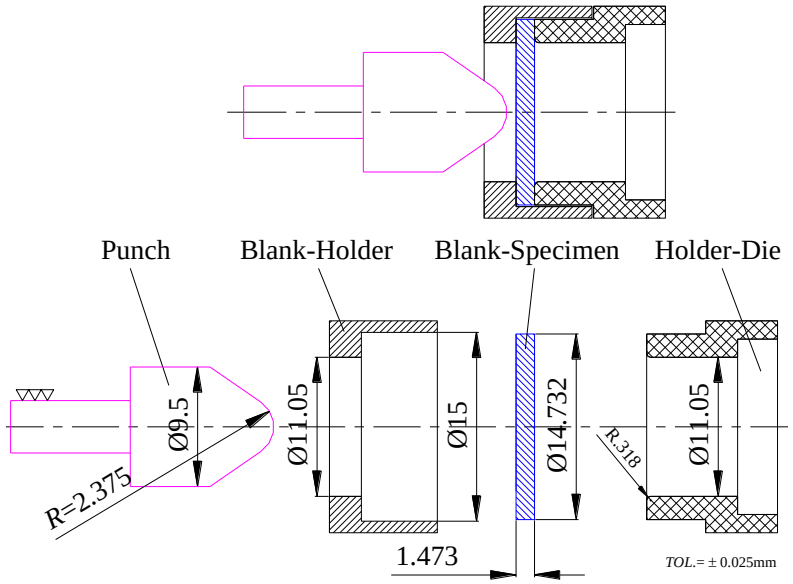

FE Model, Top View

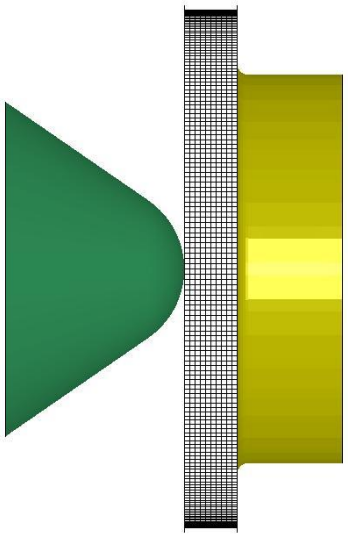

FE Model, Isometric View

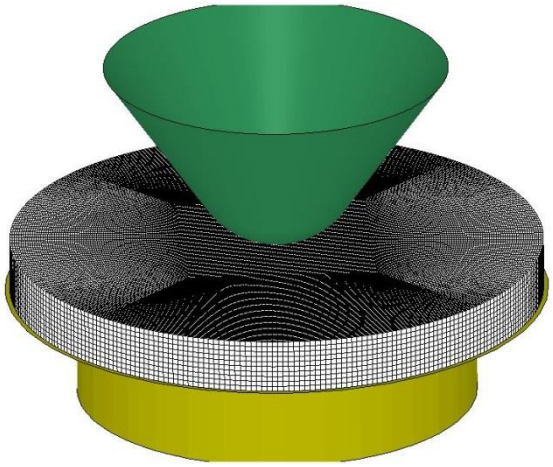

Figure B-16: Punch specimen, Specimen #18.

Specimen Geometry

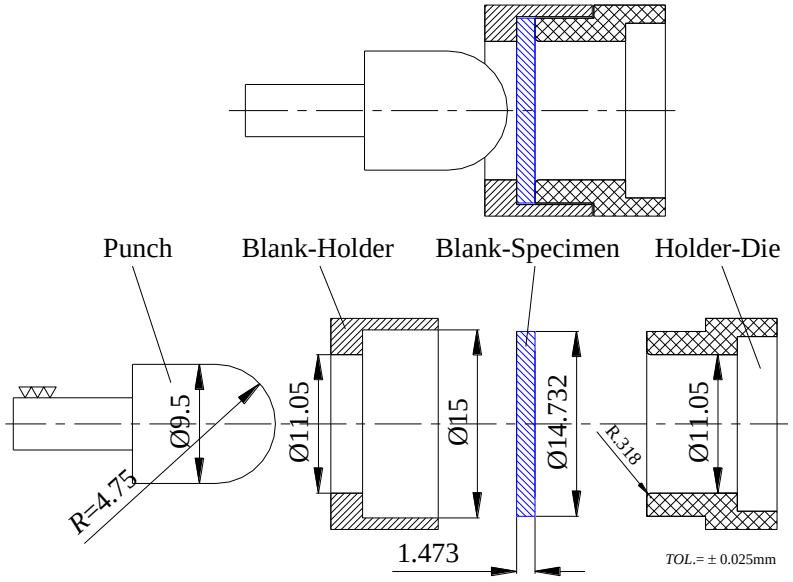

FE Model, Top View

FE Model, Isometric View

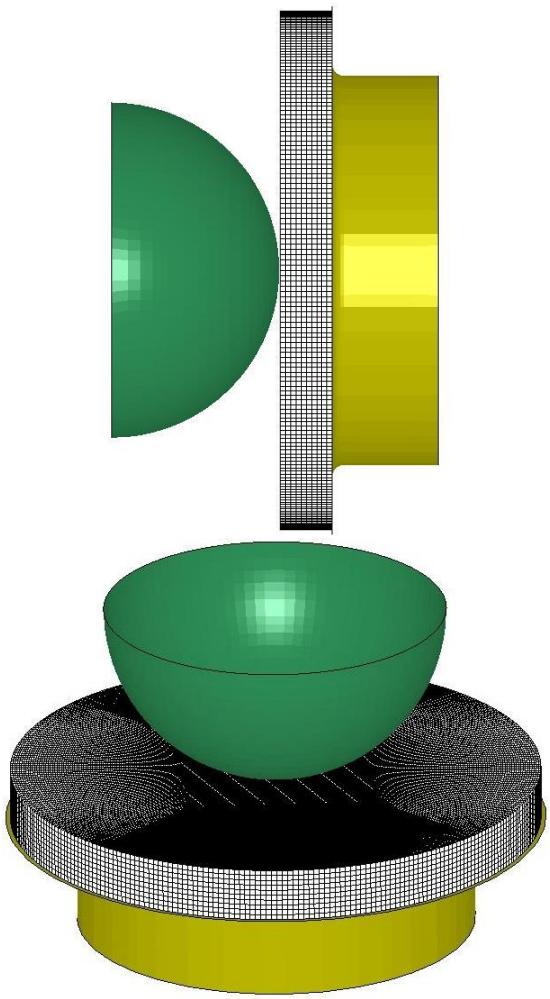

Figure B-17: Punch specimen, Specimen #19.

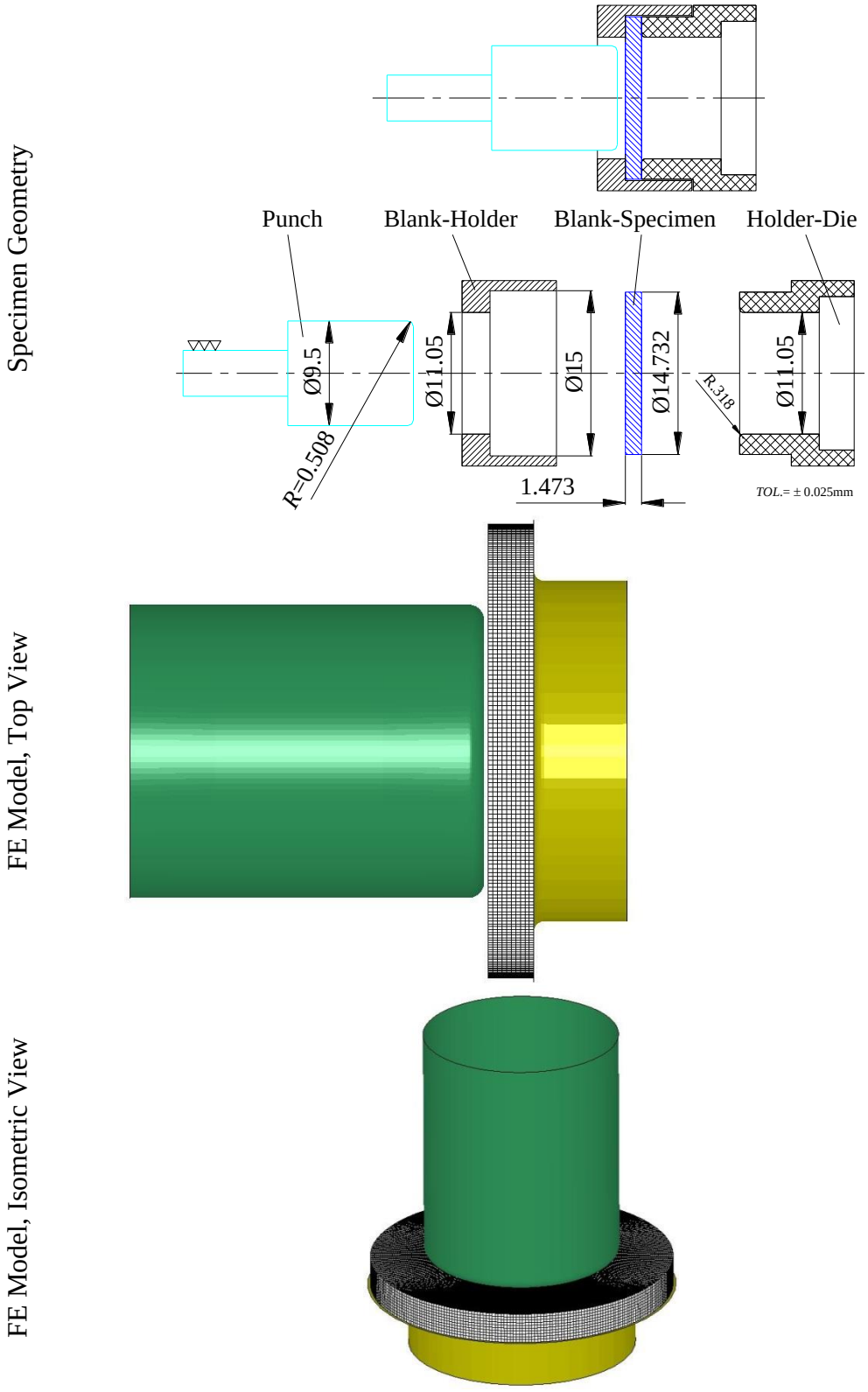

Figure B-18: Punch specimen, Specimen #20.

Specimen Geometry

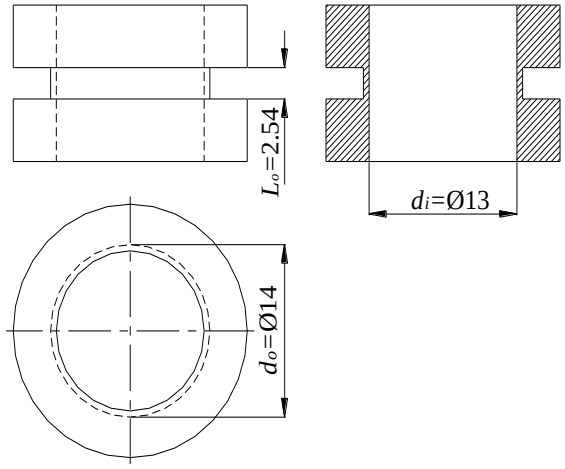

FE Model, Top View

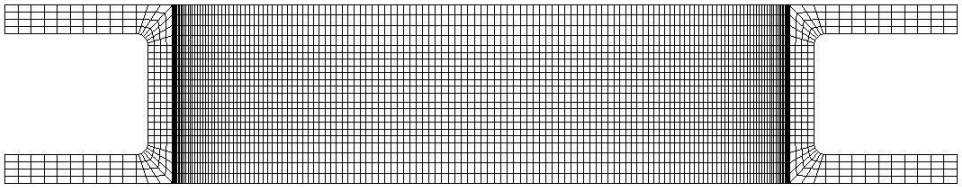

FE Model, Isometric View



Figure B-19: Torsion specimen, Specimen #21.

Appendix - C: Details of the test results that are used for the characterization of the material input data

Test results that are used to characterize and validate the material input data is presented in this Appendix. Characterization procedures are presented in Chapter 5. The repeatability of the test results are also demonstrated where each test was performed at least three times unless otherwise stated. Each test result is described by using a unique numbering scheme that is defined by two successive numbers as illustrated in Figure 5-7. The first number is specifically used to identify the major testing parameters and the successive number identifies the repeated test case with an expression to represent whether the measurement for the displacement field was obtained from an extensometer, or Digital Image Correlation (DIC). A suffix ‘e’ is added if the measurement is not from DIC. It should be noted that several different gauge lengths can be utilized with DIC technique. Therefore, unique test numbers are assigned that are corresponding to specific DIC gauge lengths.

It should be noted that the same specimen geometry can be utilized for the repeated tests with different characteristic lengths, which are illustrated in Appendix-B for nominal dimensions. Therefore, exact specimen geometries should be considered if the same results from the characterized material properties are expected.

It should also be noted that, especially with the high-strain rate data, the averaged strain rates should be considered as the rate-dependent flow surface is used for the analysis. Nominal or targeted strain-rates may be misleading due to the differences in achieving constant strain-rates.

Table C-1: Test #1 parameters for the characterization of the flow surface.

Test #	Specimen #1 Figure B-1‡			Test Apparatus	Loading	Equivalent Strain Rate [s^{-1}]		Temperature [K]
	t	w	L_0 **			Targeted	Measured	
1.1e†	0.74676	3.0734	4.0	SHLF*	Tension	1.0×10^{-4}	3.4041×10^{-5}	RT††
1.2e	0.7493	3.0226					8.3617×10^{-5}	
1.3e	0.75438	3.0353					9.0265×10^{-5}	

* Servo-Hydraulic Loading Frame (SHLF).
** Extensometer gauge length.
† Test stopped before failure.
†† Room Temperature (RT).
‡ Detailed geometries and corresponding FE models of the specimens are illustrated in Appendix-B.

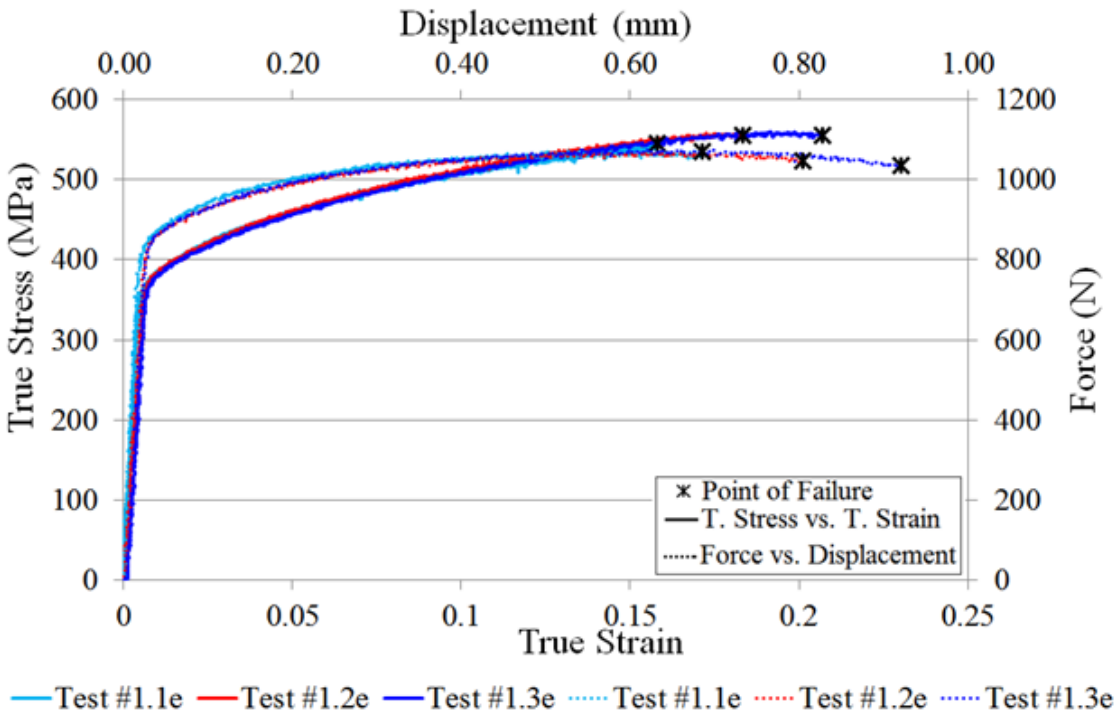

Figure C-1: Test #1 results and repeatability.

Table C-2: Test #2 parameters for the characterization of the flow surface.

Test #	Specimen #1 Figure B-1‡			Test Apparatus	Loading	Equivalent Strain Rate [s^{-1}]		Temperature [K]
	t	w	L_0 **			Targeted	Measured	
2.1e	0.75438	3.0734	4.0	SHLF*	Tension	1.0×10^{-2}	8.5948×10^{-3}	RT†
2.2e	0.75438	3.0353					9.1191×10^{-3}	
2.3	0.74168	2.9972					9.1327×10^{-3}	

* Servo-Hydraulic Loading Frame (SHLF).
** Extensometer gauge length.
† Room Temperature (RT).
‡ Detailed geometries and corresponding FE models of the specimens are illustrated in Appendix-B.

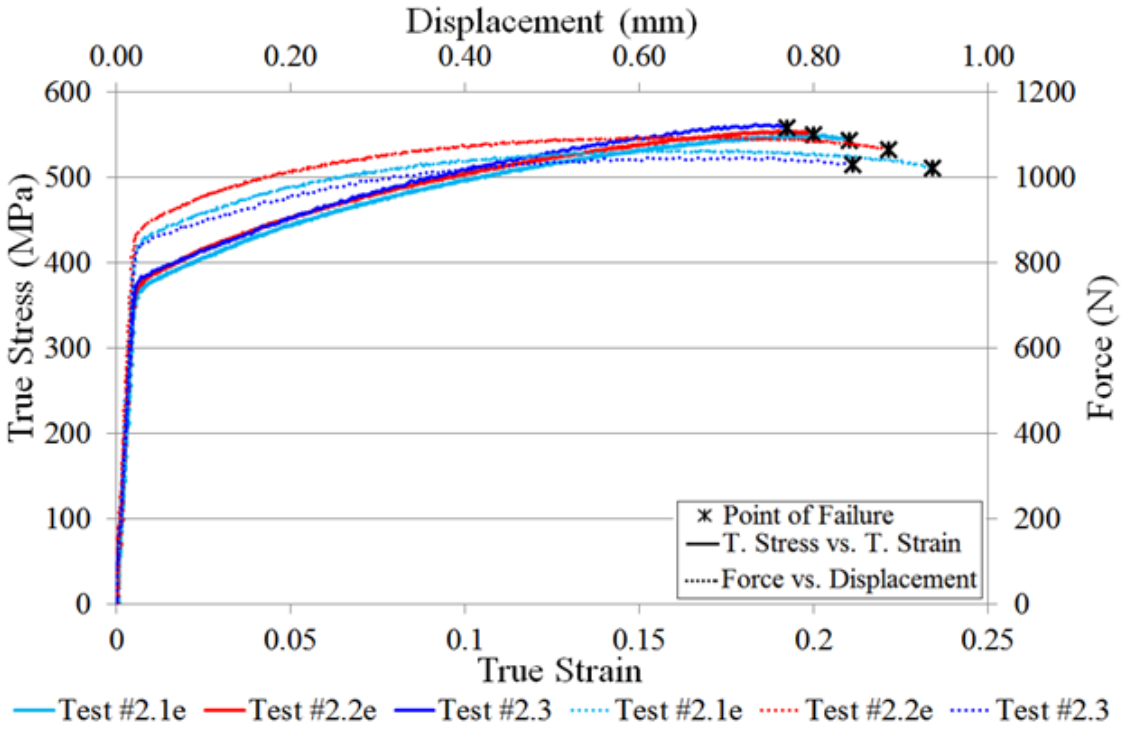

Figure C-2: Test #2 results and repeatability.

Table C-3: Test #3 parameters for the characterization of the flow surface.

Test #	Specimen #1 Figure B-1‡			Test Apparatus	Loading	Equivalent Strain Rate [s^{-1}]		Temperature [K]
	t	w	L_0 **			Targeted	Measured	
3.1	0.74168	3.048	4.0	SHLF*	Tension	1.0	1.105	RT†
3.2	0.77216	3.0226					1.052	
3.3	0.75184	3.048					1.003	

* Servo-Hydraulic Loading Frame (SHLF).
** Extensometer gauge length.
† Room Temperature (RT).
‡ Detailed geometries and corresponding FE models of the specimens are illustrated in Appendix-B.

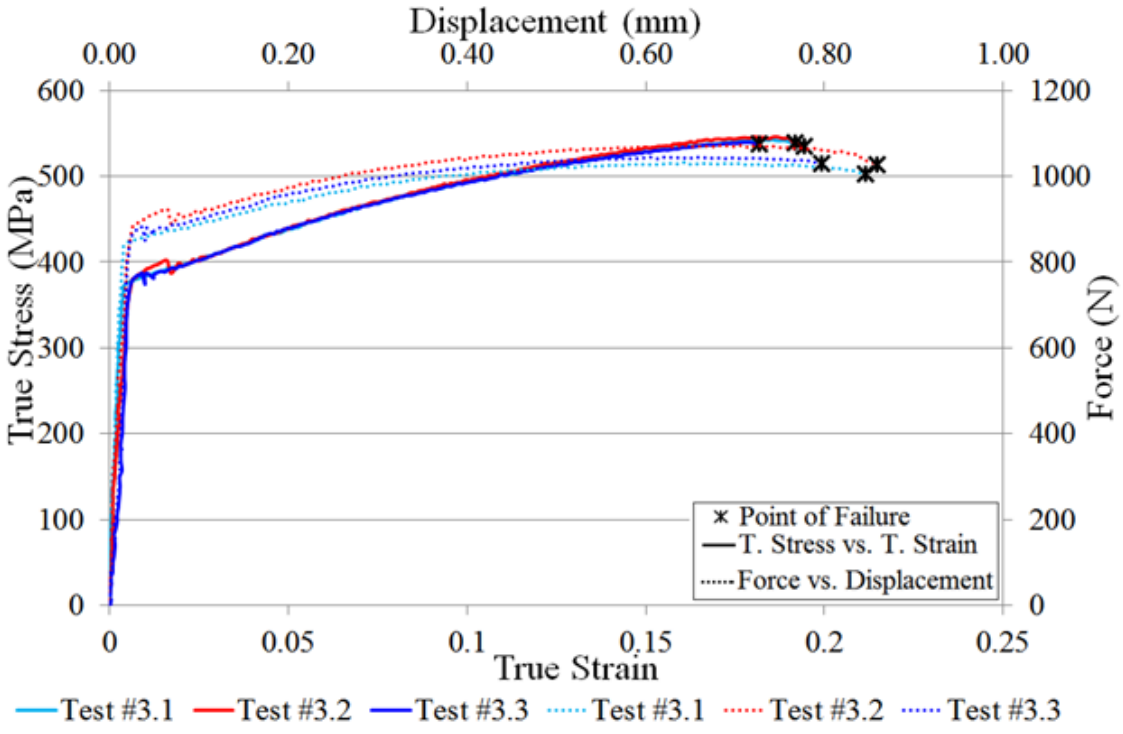

Figure C-3: Test #3 results and repeatability.

Table C-4: Test #4 parameters for the characterization of the flow surface.

Test #	Specimen #5 Figure B-5‡		Test Apparatus	Loading	Equivalent Strain Rate [s^{-1}]		Temperature [K]
	d	L_0 **			Targeted	Measured	
4.1	4.7498	22.3	SHLF*	Tension	1.0×10^{-2}	0.05	RT†
4.2	4.7498					0.01	
4.3	4.7244					0.01	
4.4	4.7498	4.0				0.05	
4.5	4.7498					0.01	
4.6	4.7244					0.01	

* Servo-Hydraulic Loading Frame (SHLF).
** Extensometer gauge length.
† Room Temperature (RT).
‡ Detailed geometries and corresponding FE models of the specimens are illustrated in Appendix-B.

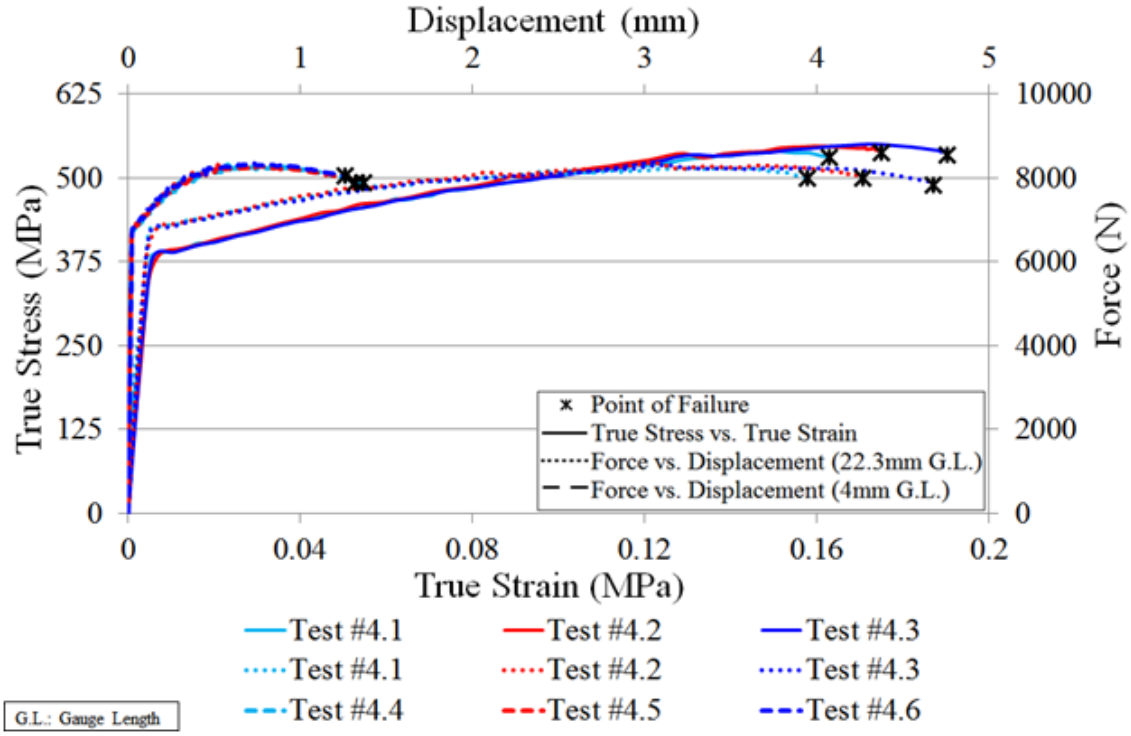

Figure C-4: Test #4 results and repeatability.

Table C-5: Test #5 parameters for the characterization of the flow surface.

Test #	Specimen #14 Figure B-14‡		Test Apparatus	Loading	Equivalent Strain Rate [s^{-1}]		Temperature [K]
	D	H^{**}			Targeted	Measured	
5.1e§	3.04292	3.048	SHLF*	Compression	1.0×10^{-4}	9.848×10^{-5}	RT†
5.2e	3.0353	3.01752				9.848×10^{-5}	
5.3e	3.04292	3.048				1.001×10^{-4}	

* Servo-Hydraulic Loading Frame (SHLF).
** Gauge length.
† Room Temperature (RT).
‡ Detailed geometries and corresponding FE models of the specimens are illustrated in Appendix-B.
§ Test is an outlier and excluded from further analysis.

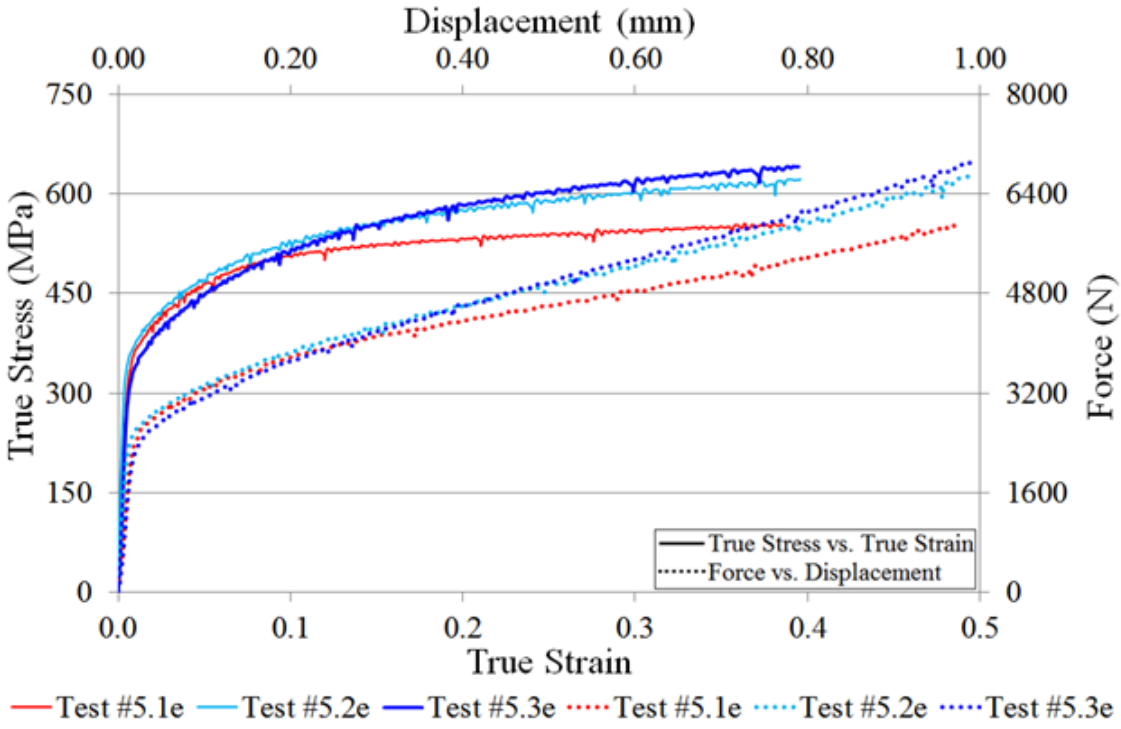

Figure C-5: Test #5 results and repeatability.

Table C-6: Test #6 parameters for the characterization of the flow surface.

Test #	Specimen #14 Figure B-14‡		Test Apparatus	Loading	Equivalent Strain Rate [s^{-1}]		Temperature [K]
	D	H^{**}			Targeted	Measured	
6.1e	3.048	3.03784	SHLF*	Compression	1.0×10^{-2}	9.173×10^{-3}	RT†
6.2e	3.02895	3.048				9.195×10^{-3}	
6.3e	3.048	3.05308				8.994×10^{-3}	

* Servo-Hydraulic Loading Frame (SHLF).
** Gauge length.
† Room Temperature (RT).
‡ Detailed geometries and corresponding FE models of the specimens are illustrated in Appendix-B.

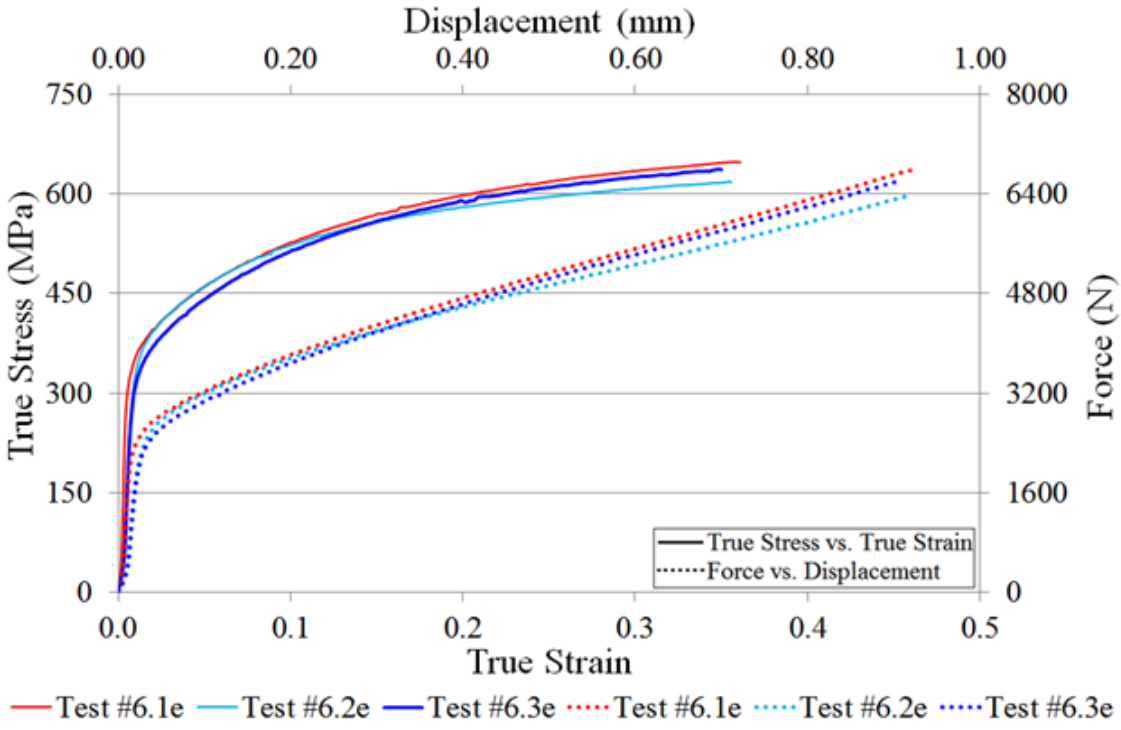

Figure C-6: Test #6 results and repeatability.

Table C-7: Test #7 parameters for the characterization of the flow surface.

Test #	Specimen #14 Figure B-14‡		Test Apparatus	Loading	Equivalent Strain Rate [s^{-1}]		Temperature [K]
	D	H^{**}			Targeted	Measured	
7.1e	3.04292	3.048	SHLF*	Compression	1.0	9.277×10^{-1}	RT†
7.2e	3.0353	3.0861				9.126×10^{-1}	
7.3e	3.048	2.9972				9.6087×10^{-1}	

* Servo-Hydraulic Loading Frame (SHLF).
** Gauge length.
† Room Temperature (RT).
‡ Detailed geometries and corresponding FE models of the specimens are illustrated in Appendix-B.

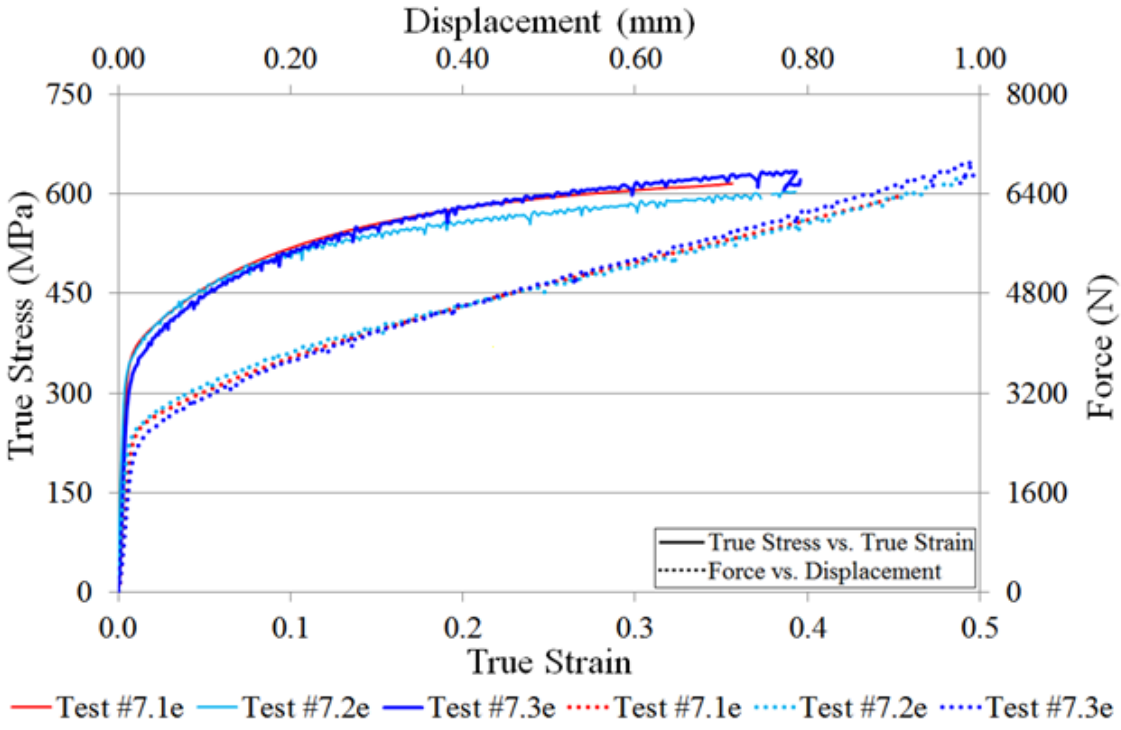

Figure C-7: Test #7 results and repeatability.

Table C-8: Test #8 parameters for the characterization of the flow surface.

Test #	Specimen #15 Figure B-15‡			Test Apparatus	Loading	Equivalent Strain Rate [s^{-1}]		Temperature [K]
	d_i	d_o	L_0 **			Targeted	Measured	
8.1	7.9629	9.1694	6.35	SHLF*	Torsion	1.0	0.972	RT†
8.2	7.9502	9.1694					1.073	
8.3	7.9629	9.144					1.155	

* Servo-Hydraulic Loading Frame (SHLF).
** Extensometer gauge length.
† Room Temperature (RT).
‡ Detailed geometries and corresponding FE models of the specimens are illustrated in Appendix-B.

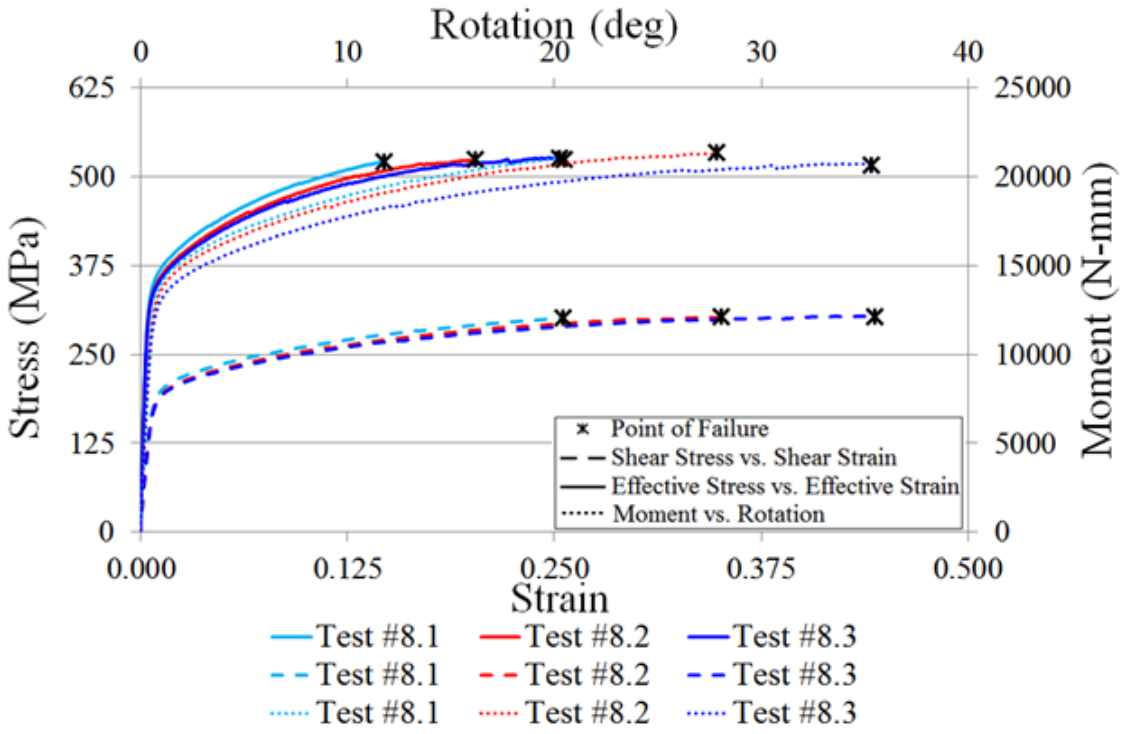

Figure C-8: Test #8 results and repeatability.

Table C-9: Test #9 parameters for the characterization of the flow surface.

Test #	Specimen #1 Figure B-1‡			Test Apparatus	Loading	Equivalent Strain Rate [s^{-1}]		Temperature [K]	
	t	w	L_0 **			Targeted	Measured	Targeted	Measured
9.1e	0.7493	3.0734	5.08	SHLF*	Tension	1.0	9.6169×10^{-1}	423	418.85
9.2e	0.7493	3.0734					9.8384×10^{-1}		421.45
9.3e	0.762	3.0607					9.6739×10^{-1}		420.15

* Servo-Hydraulic Loading Frame (SHLF).
** Extensometer gauge length.
‡ Detailed geometries and corresponding FE models of the specimens are illustrated in Appendix-B.

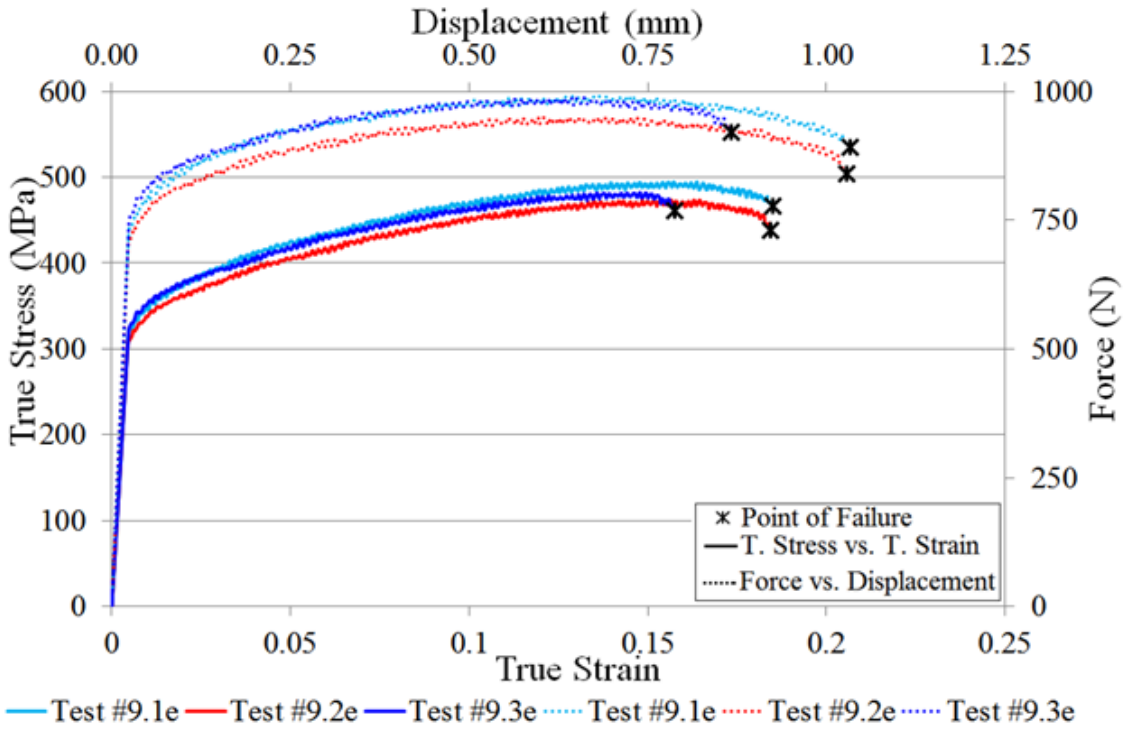

Figure C-9: Test #9 results and repeatability.

Table C-10: Test #10 parameters for the characterization of the flow surface.

Test #	Specimen #1 Figure B-1‡			Test Apparatus	Loading	Equivalent Strain Rate [s^{-1}]		Temperature [K]	
	t	w	L_0 **			Targeted	Measured	Targeted	Measured
10.1e	0.7747	3.048	5.08	SHLF*	Tension	1.0	8.942×10^{-1}	573	572.35
10.2e	0.77724	3.048					9.173×10^{-1}		573.85
10.3e	0.7747	3.048					9.277×10^{-1}		575.35

* Servo-Hydraulic Loading Frame (SHLF).
** Extensometer gauge length.
‡ Detailed geometries and corresponding FE models of the specimens are illustrated in Appendix-B.

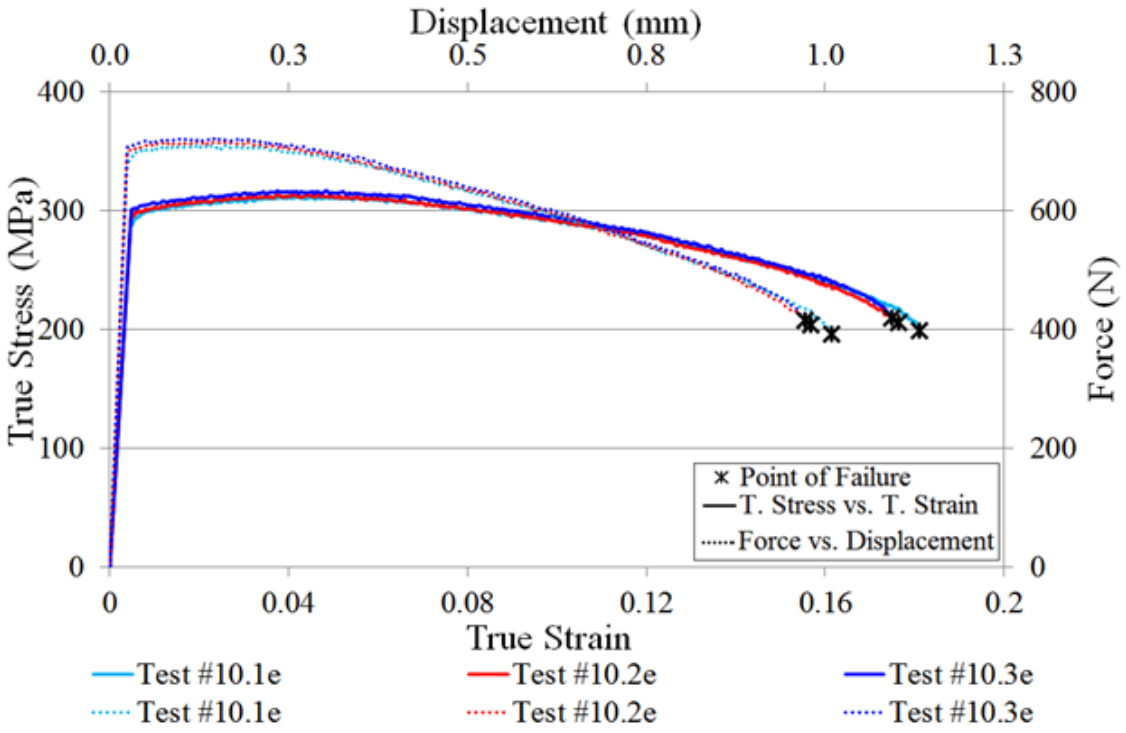

Figure C-10: Test #10 results and repeatability.

Table C-11: Test #11 parameters for the characterization of the flow surface.

Test #	Specimen #1 Figure B-1‡			Test Apparatus	Loading	Equivalent Strain Rate [s^{-1}]		Temperature [K]	
	t	w	L_0 **			Targeted	Measured	Targeted	Measured
11.1e	0.762	3.048	5.08	SHLF*	Tension	1.0	7.725×10^{-1}	723	726.85
11.2e	0.7747	3.048					7.423×10^{-1}		726.95
11.3e	0.7747	3.048					7.653×10^{-1}		723.05

* Servo-Hydraulic Loading Frame (SHLF).
** Extensometer gauge length..
‡ Detailed geometries and corresponding FE models of the specimens are illustrated in Appendix-B.

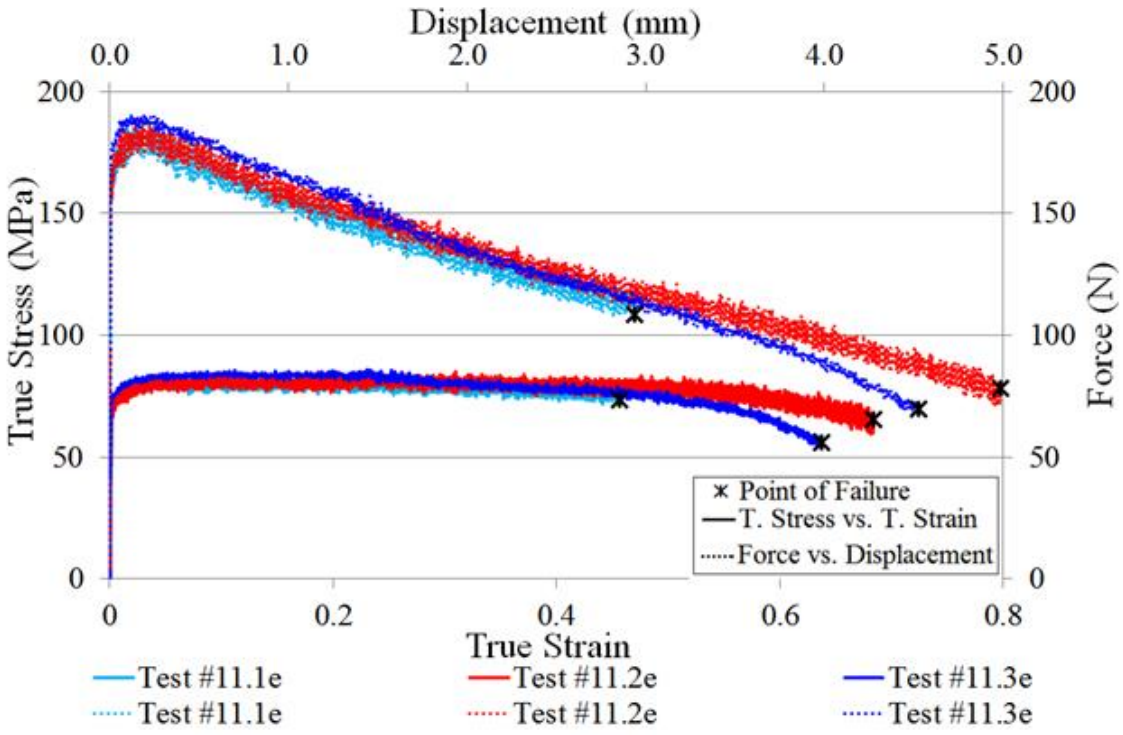

Figure C-11: Test #11 results and repeatability.

Table C-12: Test #12 parameters for the characterization of the flow surface.

Test #	Specimen #1 Figure B-1‡			Test Apparatus	Loading	Equivalent Strain Rate [s^{-1}]		Temperature [K]	
	t	w	L_0 **			Targeted	Measured	Targeted	Measured
12.1e	0.75438	3.0734	5.08	SHLF*	Tension	1.0	9.653×10^{-1}	223	223.15
12.2e	0.75438	3.0353					9.829×10^{-1}		222.15
12.3e	0.74168	2.9972					9.836×10^{-1}		222.15

* Servo-Hydraulic Loading Frame (SHLF).
** Extensometer gauge length.
‡ Detailed geometries and corresponding FE models of the specimens are illustrated in Appendix-B.

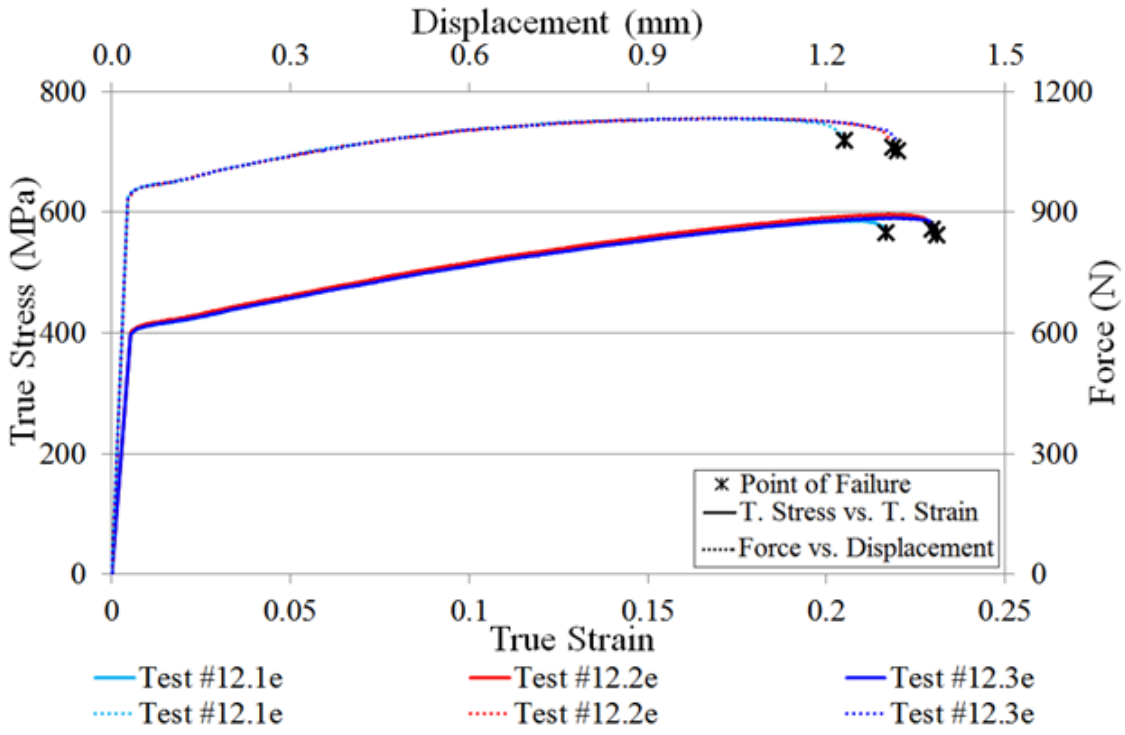

Figure C-12: Test #12 results and repeatability.

Table C-13: Test #13 parameters for the characterization of the flow surface.

Test #	Specimen #14 Figure B-14‡		Test Apparatus	Loading	Equivalent Strain Rate [s^{-1}]		Temperature [K]	
	D	H^{**}			Targeted	Measured	Targeted	Measured
13.1e	3.0353	3.048	SHLF*	Compression	1.0	1.01366	423	423
13.2e	3.02768	3.01625				1.02345		423
13.3e	3.04546	3.07086				1.01259		423

* Servo-Hydraulic Loading Frame (SHLF).
** Gauge length.
‡ Detailed geometries and corresponding FE models of the specimens are illustrated in Appendix-B.

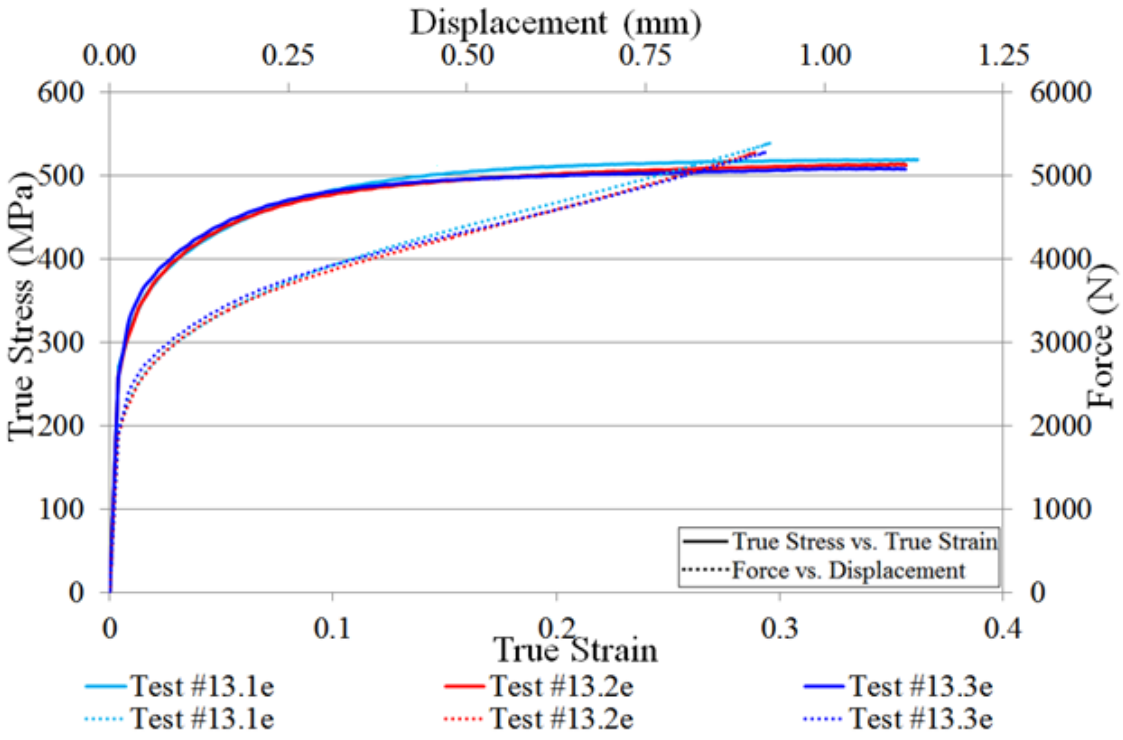

Figure C-13: Test #13 results and repeatability.

Table C-14: Test #14 parameters for the characterization of the flow surface.

Test #	Specimen #14 Figure B-14‡		Test Apparatus	Loading	Equivalent Strain Rate [s^{-1}]		Temperature [K]	
	D	H^{**}			Targeted	Measured	Targeted	Measured
14.1e	3.04292	3.07594	SHLF*	Compression	1.0	9.9617×10^{-1}	573	573
14.2e	3.048	3.0734				1.000015		573
14.3e	3.0607	3.0607				9.9894×10^{-1}		573

* Servo-Hydraulic Loading Frame (SHLF).
** Gauge length.
‡ Detailed geometries and corresponding FE models of the specimens are illustrated in Appendix-B.

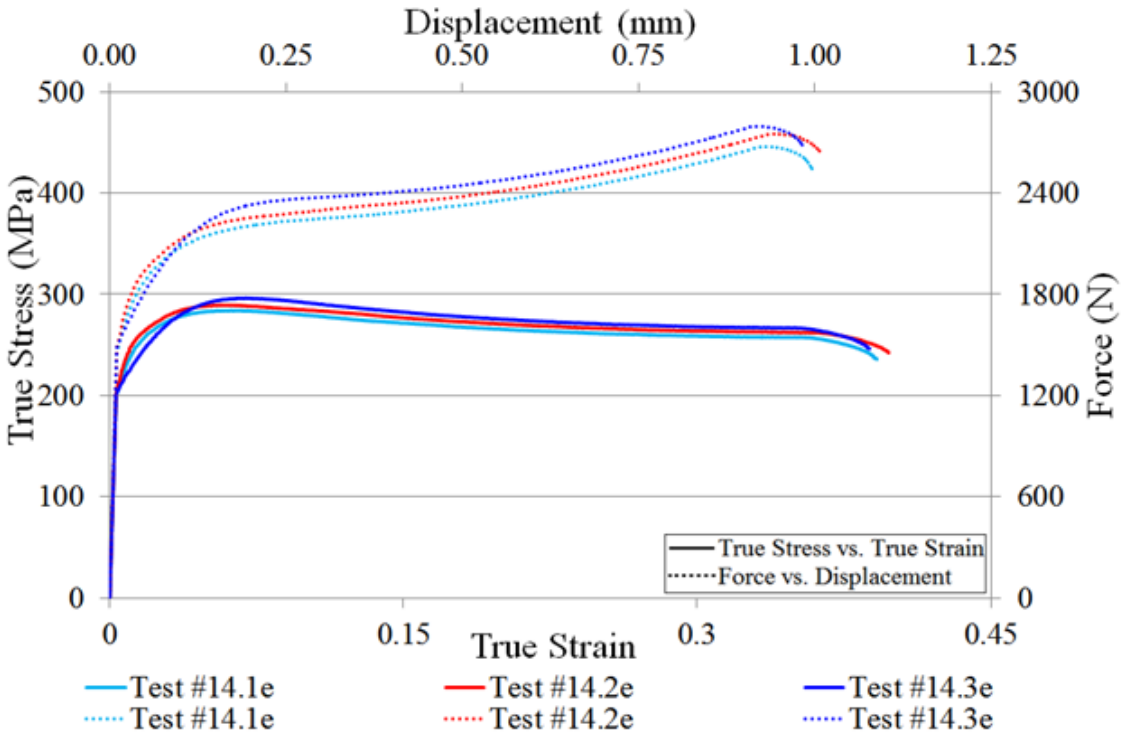

Figure C-14: Test #14 results and repeatability.

Table C-15: Test #15 parameters for the characterization of the flow surface.

Test #	Specimen #14 Figure B-14‡		Test Apparatus	Loading	Equivalent Strain Rate [s^{-1}]		Temperature [K]	
	D	H^{**}			Targeted	Measured	Targeted	Measured
15.1e	3.05562	3.0734	SHLF*	Compression	1.0	9.4351×10^{-1}	723	723
15.2e	3.02006	3.0734				9.5473×10^{-1}		723
15.3e	3.048	3.1242				9.4568×10^{-1}		723

* Servo-Hydraulic Loading Frame (SHLF).
** Gauge length.
‡ Detailed geometries and corresponding FE models of the specimens are illustrated in Appendix-B.

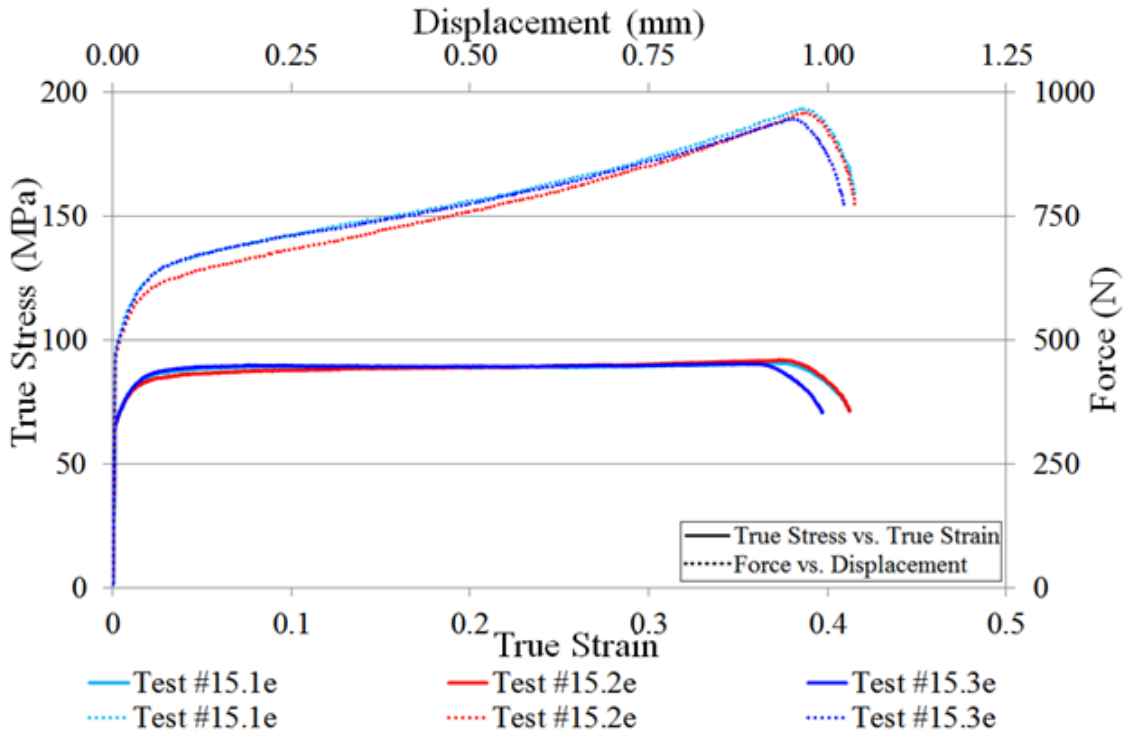

Figure C-15: Test #15 results and repeatability.

Table C-16: Test #16 parameters for the characterization of the flow surface.

Test #	Specimen #14 Figure B-14‡		Test Apparatus	Loading	Equivalent Strain Rate [s^{-1}]		Temperature [K]	
	D	H^{**}			Targeted	Measured	Targeted	Measured
16.1e	3.048	3.048	SHLF*	Compression	1.0	1.011268	223	223
16.2e	3.048	3.0353				1.016456		223
16.3e	3.04292	3.048				1.008921		223

* Servo-Hydraulic Loading Frame (SHLF).
** Gauge length.
‡ Detailed geometries and corresponding FE models of the specimens are illustrated in Appendix-B.

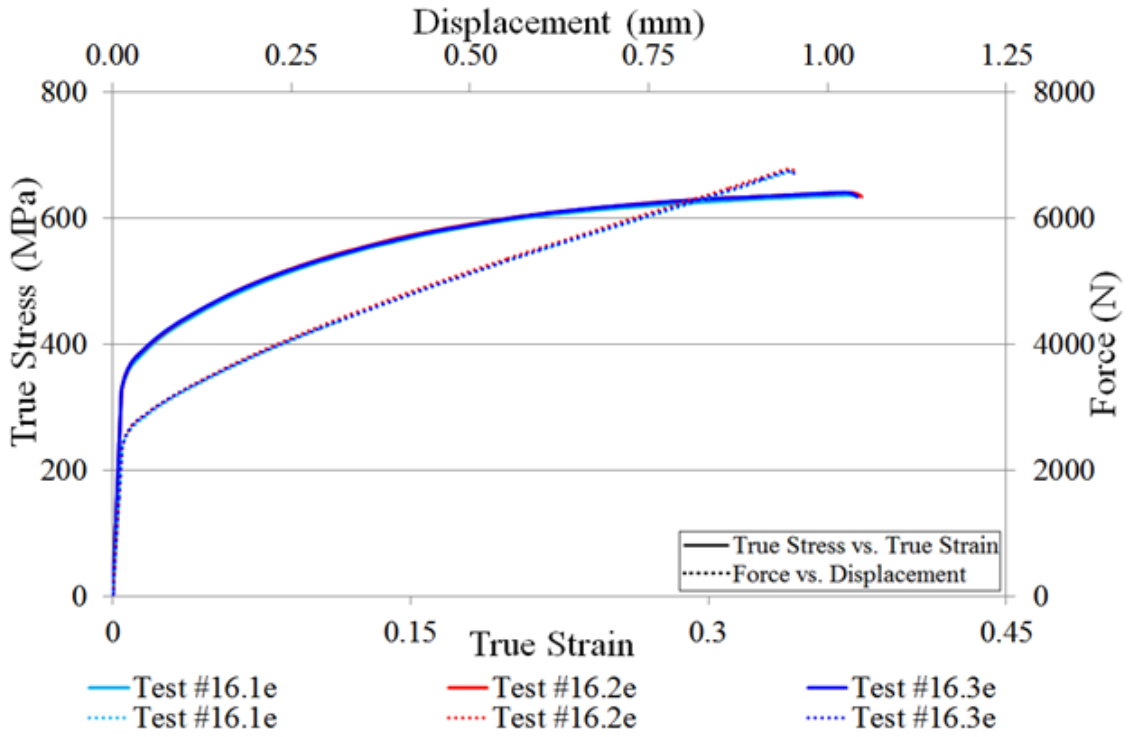

Figure C-16: Test #16 results and repeatability.

Table C-17: Test #17 parameters for the characterization of the flow surface.

Test #	Specimen #21 Figure B-19‡			Test Apparatus	Loading	Equivalent Strain Rate [s^{-1}]		Temperature [K]
	d_i	d_o	L_0 **			Targeted	Measured	
17.1e	12.954	13.9827	2.5654	SHLF*	Torsion	1.0×10^{-4}	1.9421×10^{-4}	RT†
17.2e	12.954	13.9954	2.54				1.9425×10^{-4}	
17.3e	12.954	13.9827	2.5654				1.9413×10^{-4}	

* Servo-Hydraulic Loading Frame (SHLF).
** Extensometer gauge length.
† Room Temperature (RT).
‡ Detailed geometries and corresponding FE models of the specimens are illustrated in Appendix-B.

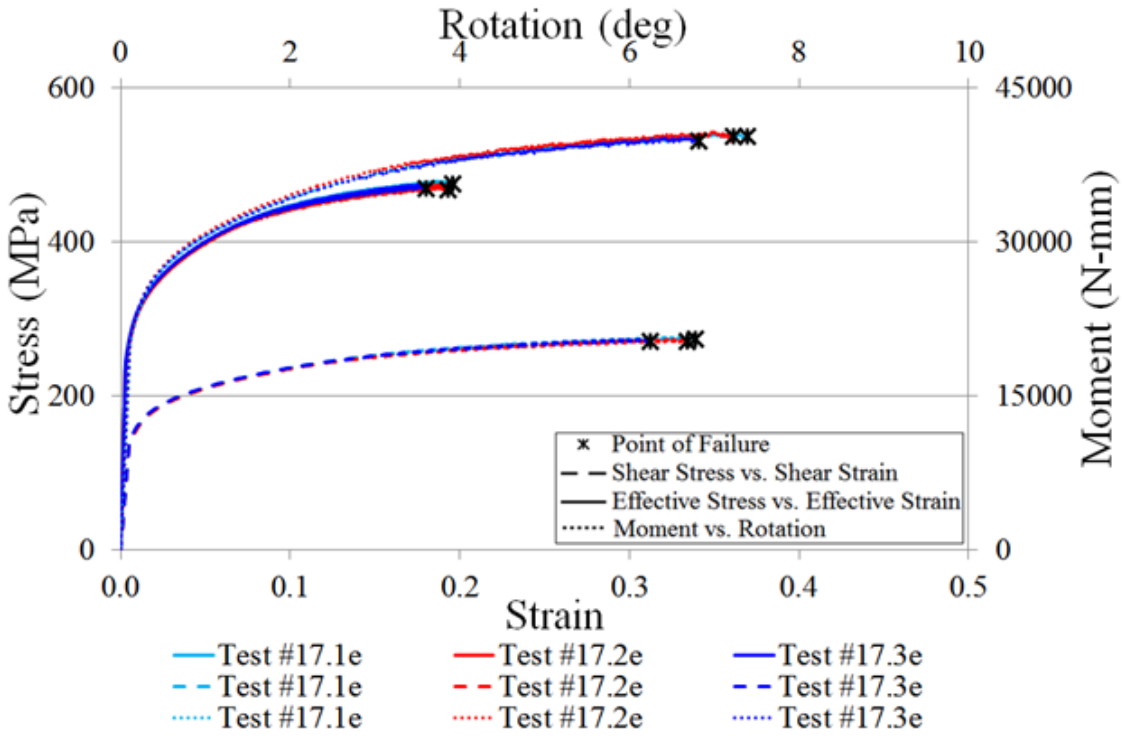

Figure C-17: Test #17 results and repeatability.

Table C-18: Test #18 parameters for the characterization of the flow surface.

Test #	Specimen #21 Figure B-19‡			Test Apparatus	Loading	Equivalent Strain Rate [s^{-1}]		Temperature [K]
	d_i	d_o	L_0 **			Targeted	Measured	
18.1e	12.954	14.0005	2.5654	SHLF*	Torsion	1.0×10^{-2}	1.9619×10^{-2}	RT†
18.2e	12.954	13.9954	2.54				1.9629×10^{-2}	
18.3e	12.954	13.9903	2.54				1.9642×10^{-2}	

* Servo-Hydraulic Loading Frame (SHLF).
** Extensometer gauge length.
† Room Temperature (RT).
‡ Detailed geometries and corresponding FE models of the specimens are illustrated in Appendix-B.

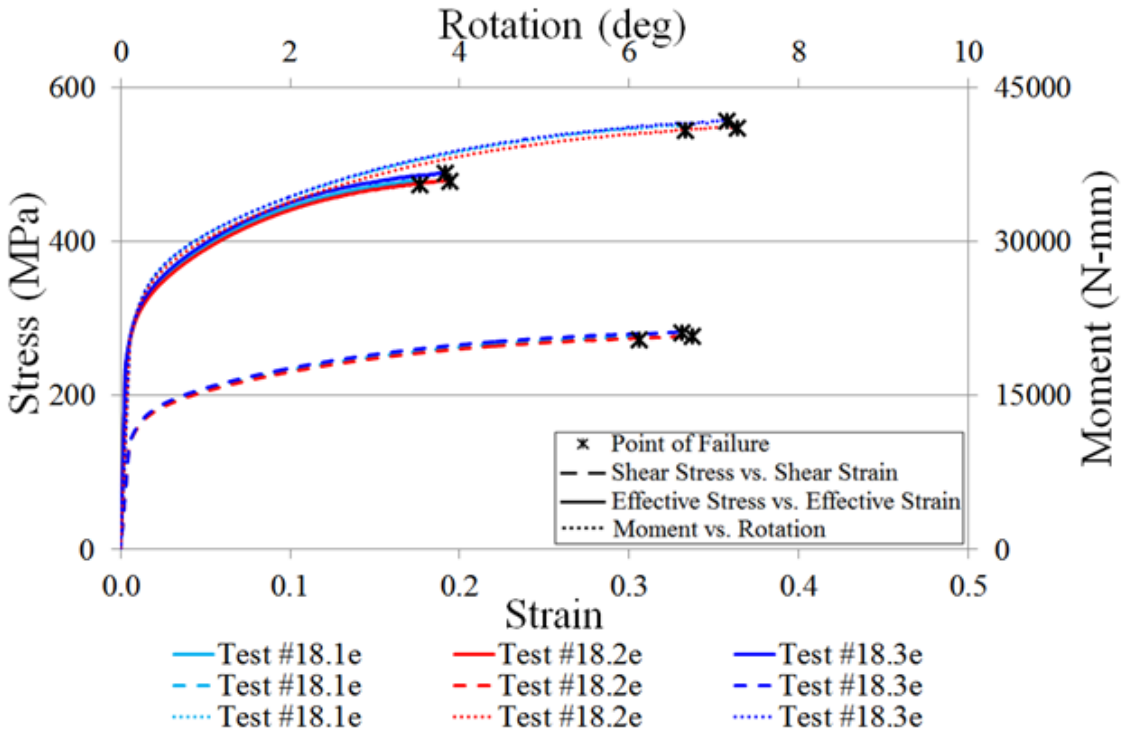

Figure C-18: Test #18 results and repeatability.

Table C-19: Test #19 parameters for the characterization of the flow surface.

Test #	Specimen #21 Figure B-19‡			Test Apparatus	Loading	Equivalent Strain Rate [s^{-1}]		Temperature [K]
	d_i	d_o	L_0 **			Targeted	Measured	
19.1e	12.954	13.9852	2.54	SHLF*	Torsion	1.0	1.7463	RT†
19.2e	12.954	13.9852	2.54				1.9243	
19.3e	12.954	13.9751	2.5654				1.9246	

* Servo-Hydraulic Loading Frame (SHLF).
** Extensometer gauge length.
† Room Temperature (RT).
‡ Detailed geometries and corresponding FE models of the specimens are illustrated in Appendix-B.

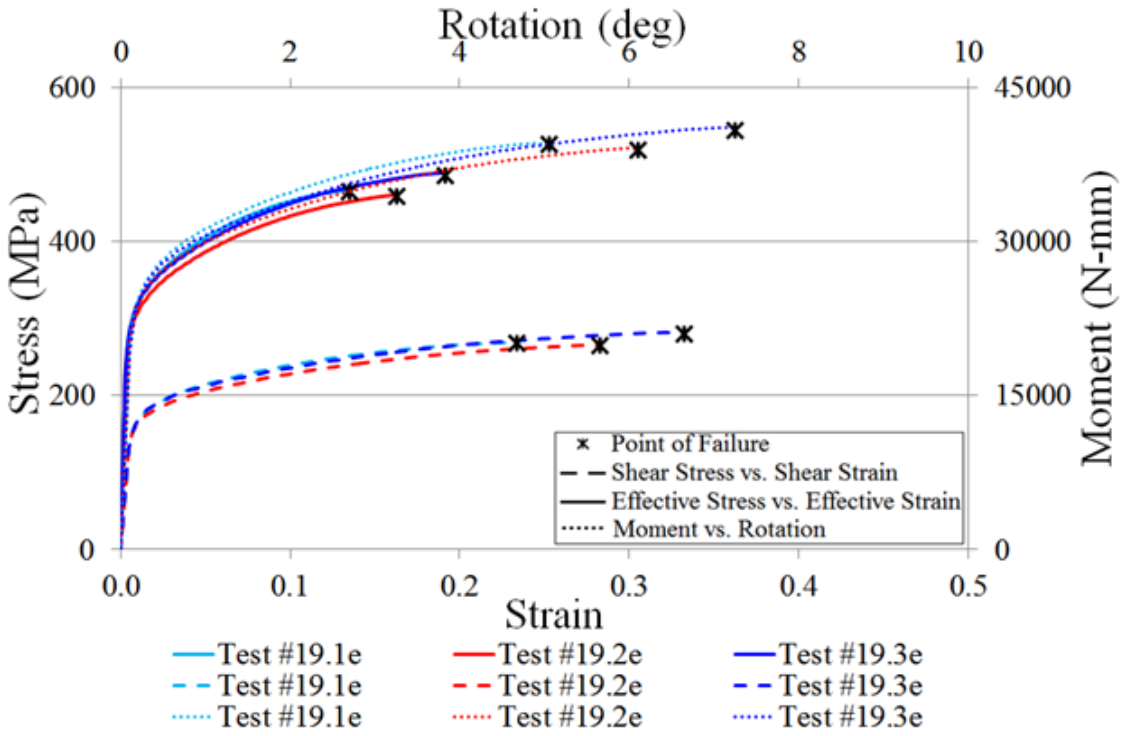

Figure C-19: Test #19 results and repeatability.

Table C-20: Test #20 parameters for the characterization of the flow surface.

Test #	Specimen #21 Figure B-19‡			Test Apparatus	Loading	Equivalent Strain Rate [s^{-1}]		Temperature [K]	
	d_i	d_o	L_0**			Targeted	Measured	Targeted	Measured
20.1e	12.9794	13.9954	2.54	SHLF*	Torsion	1.0	1.9465	423	423
20.2e	12.9794	14.0106	2.54				1.9475		423
20.3e	12.954	13.9954	2.54				1.9449		423

* Servo-Hydraulic Loading Frame (SHLF).
** Extensometer gauge length.
† Room Temperature (RT).
‡ Detailed geometries and corresponding FE models of the specimens are illustrated in Appendix-B.

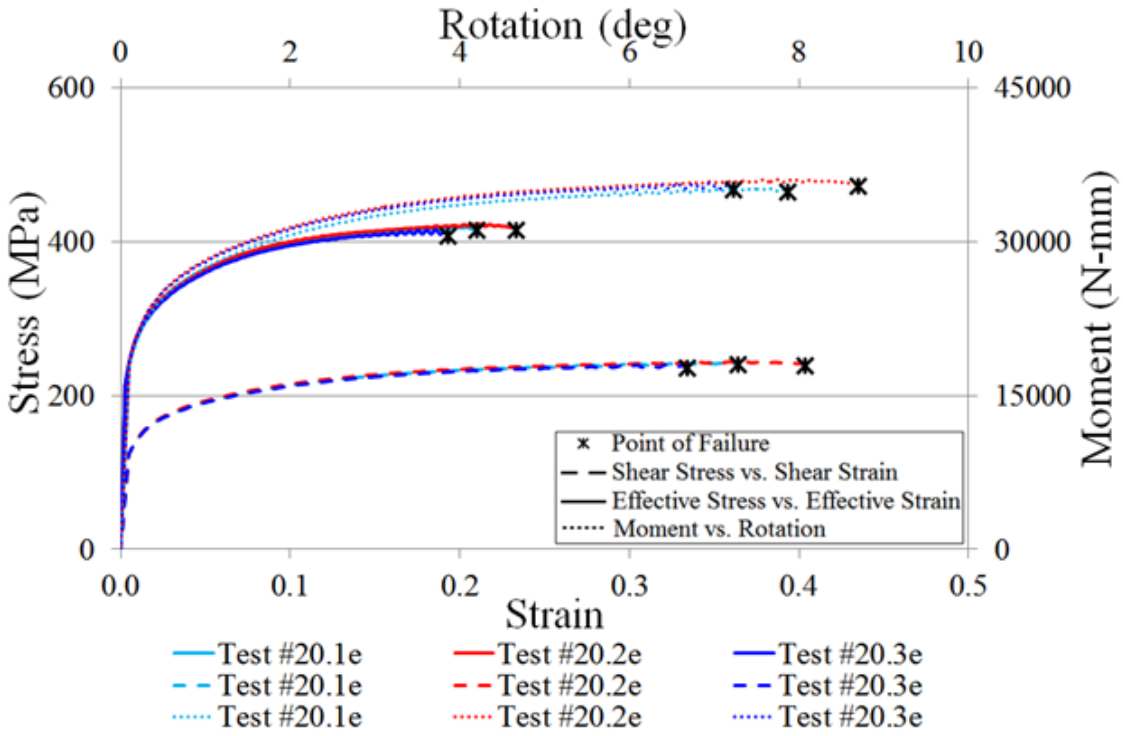

Figure C-20: Test #20 results and repeatability.

Table C-21: Test #21 parameters for the characterization of the flow surface.

Test #	Specimen #21 Figure B-19‡			Test Apparatus	Loading	Equivalent Strain Rate [s^{-1}]		Temperature [K]	
	d_i	d_o	L_0 **			Targeted	Measured	Targeted	Measured
21.1e	12.954	13.9954	2.54	SHLF*	Torsion	1.0	1.9465	573	573
21.2e	12.9794	13.9954	2.54				1.8313		573
21.3e	12.9794	14.0157	2.54				1.794		573

* Servo-Hydraulic Loading Frame (SHLF).
** Extensometer gauge length.
† Room Temperature (RT).
‡ Detailed geometries and corresponding FE models of the specimens are illustrated in Appendix-B.

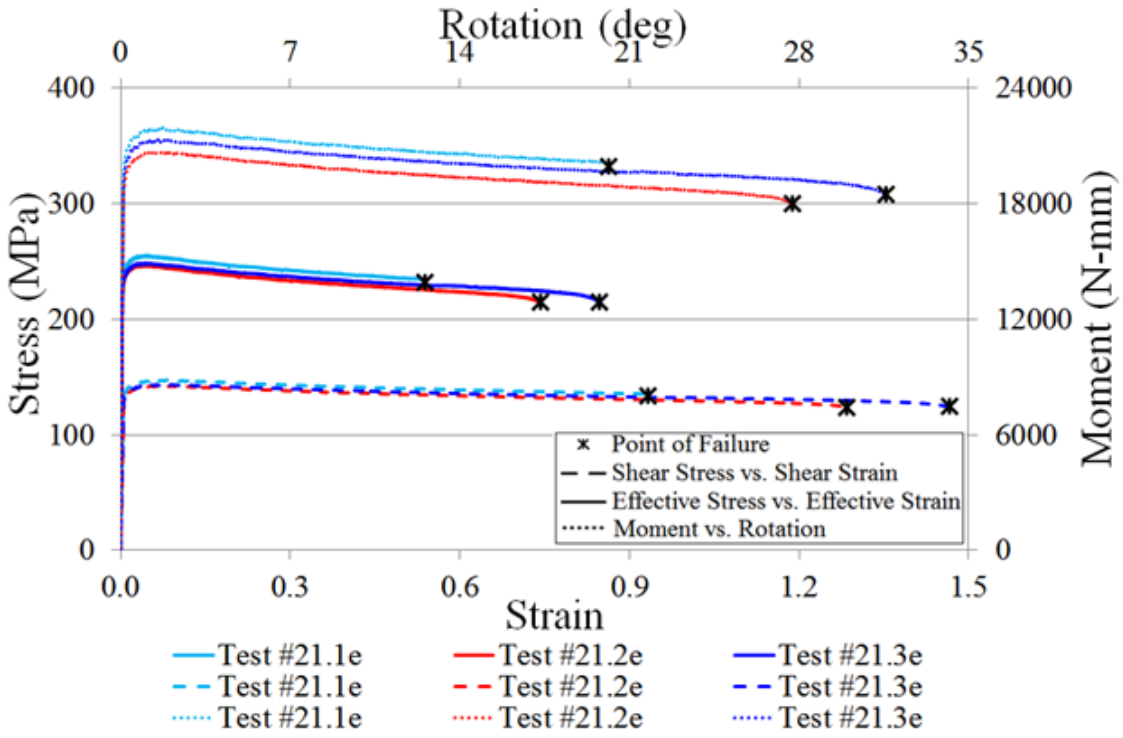

Figure C-21: Test #21 results and repeatability.

Table C-22: Test #22 parameters for the characterization of the flow surface.

Test #	Specimen #21 Figure B-19‡			Test Apparatus	Loading	Equivalent Strain Rate [s^{-1}]		Temperature [K]	
	d_i	d_o	L_0 **			Targeted	Measured	Targeted	Measured
22.1e	12.9794	13.9954	2.54	SHLF*	Torsion	1.0	1.2977	723	723
22.2e	12.9794	14.0208	2.5654				1.4641		723
22.3e	12.9794	14.0005	2.54				1.2382		723

* Servo-Hydraulic Loading Frame (SHLF).
** Extensometer gauge length.
† Room Temperature (RT).
‡ Detailed geometries and corresponding FE models of the specimens are illustrated in Appendix-B.

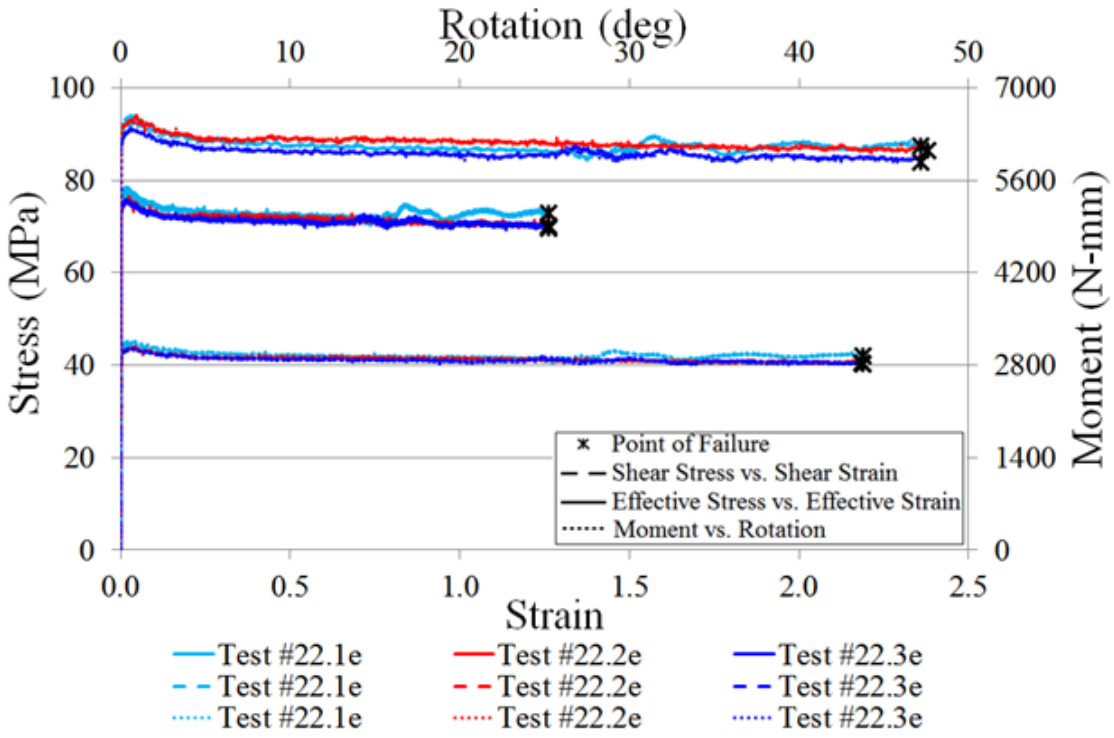

Figure C-22: Test #22 results and repeatability.

Table C-23: Test #23 parameters for the characterization of the flow surface.

Test #	Specimen #21 Figure B-19‡			Test Apparatus	Loading	Equivalent Strain Rate [s^{-1}]		Temperature [K]	
	d_i	d_o	L_0 **			Targeted	Measured	Targeted	Measured
23.1e	12.9794	14.0005	2.54	SHLF*	Torsion	1.0	1.9134	223	223
23.2e	12.9794	14.0005	2.54				1.9124		223
23.3e	12.9794	14.0056	2.54				1.918		223

* Servo-Hydraulic Loading Frame (SHLF).
** Extensometer gauge length.
† Room Temperature (RT).
‡ Detailed geometries and corresponding FE models of the specimens are illustrated in Appendix-B.

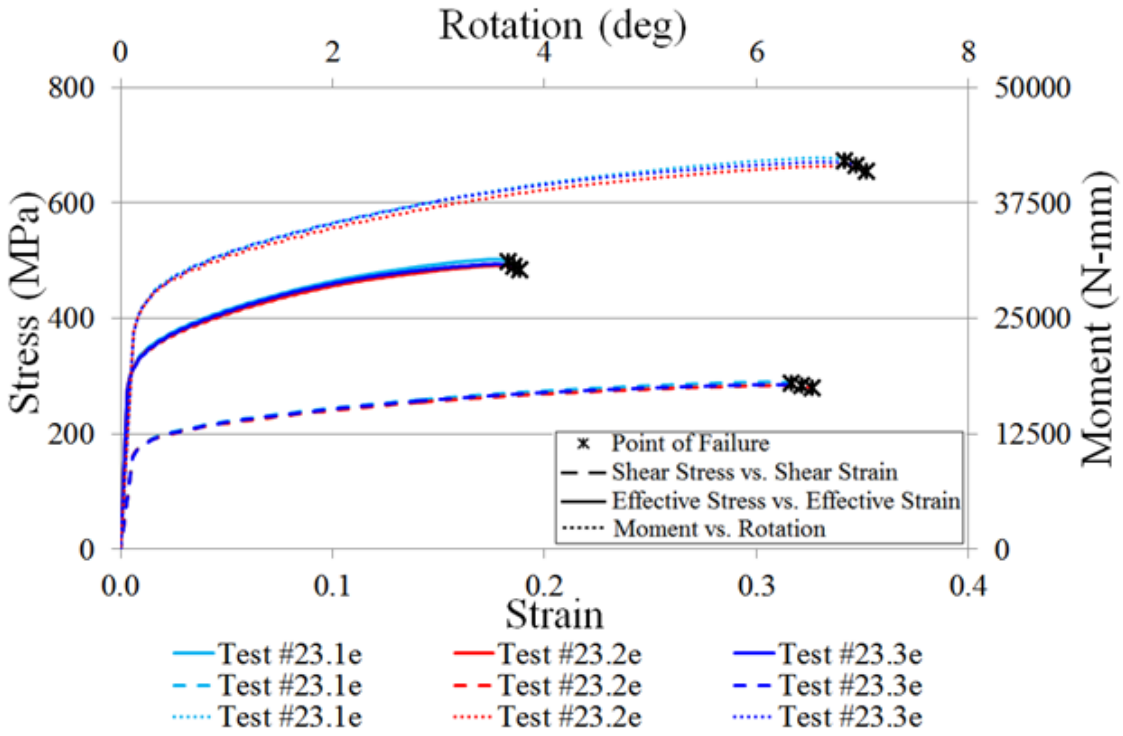

Figure C-23: Test #23 results and repeatability.

Table C-24: Test #24 parameters for the characterization of the flow surface.

Test #	Specimen #1 Figure B-1‡			Test Apparatus	Loading	Applied Force P [N]	Averaged Strain Rate [s^{-1}]		Temperature [K]
	t	w	L_0 **				Targeted	Measured	
24.1e	0.74676	3.048	5.08	TSHB *	Tension	6700	500	505.07	RT†
24.2e	0.7747	3.0226				6762		506.53	
24.3e	0.77724	3.0226				6769		507.29	

* Tension Split Hopkinson Bar (TSHB).
** Extensometer gauge length.
† Room Temperature (RT).
‡ Detailed geometries and corresponding FE models of the specimens are illustrated in Appendix-B.

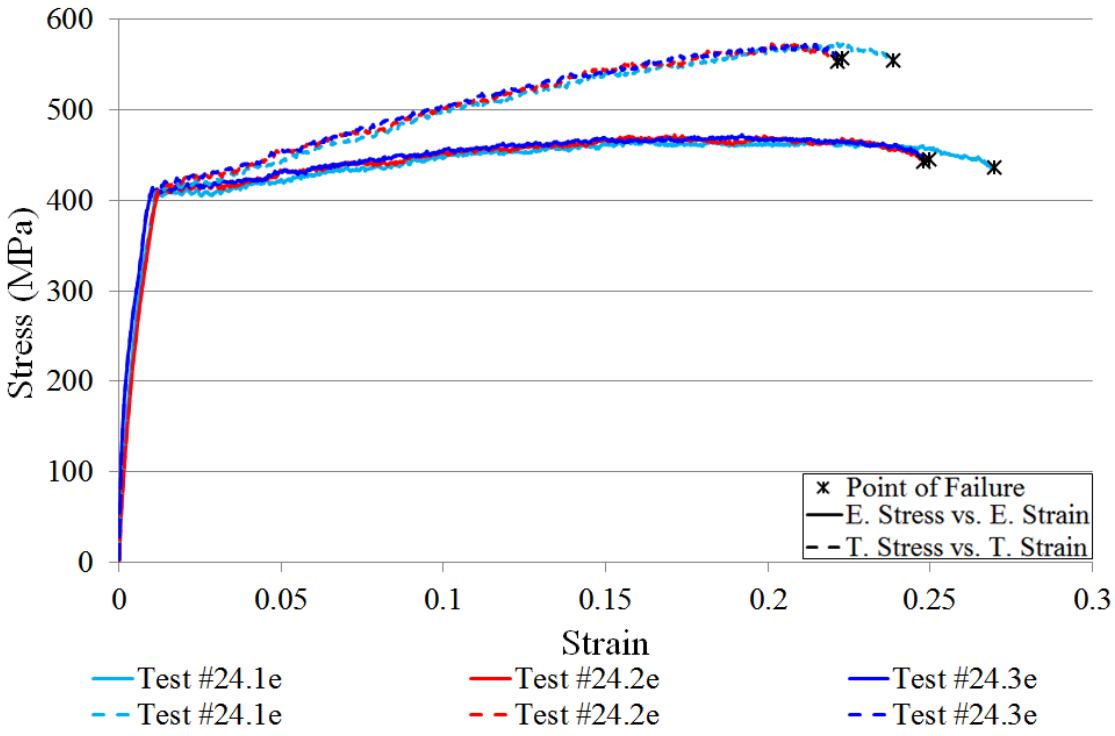

Figure C-24: Test #24 results and repeatability.

Table C-25: Test #25 parameters for the characterization of the flow surface.

Test #	Specimen #1 Figure B-1‡			Test Apparatus	Loading	Applied Force P [N]	Averaged Strain Rate [s^{-1}]		Temperature [K]
	t	w	L_0 **				Targeted	Measured	
25.1e	0.762	3.048	5.08	TSHB *	Tension	19710	1500	1862.17	RT†
25.2e	0.7747	3.06832				19762		1877.64	
25.3e	0.7493	3.048				19673		1857.79	

* Tension Split Hopkinson Bar (TSHB).
** Extensometer gauge length.
† Room Temperature (RT).
‡ Detailed geometries and corresponding FE models of the specimens are illustrated in Appendix-B.

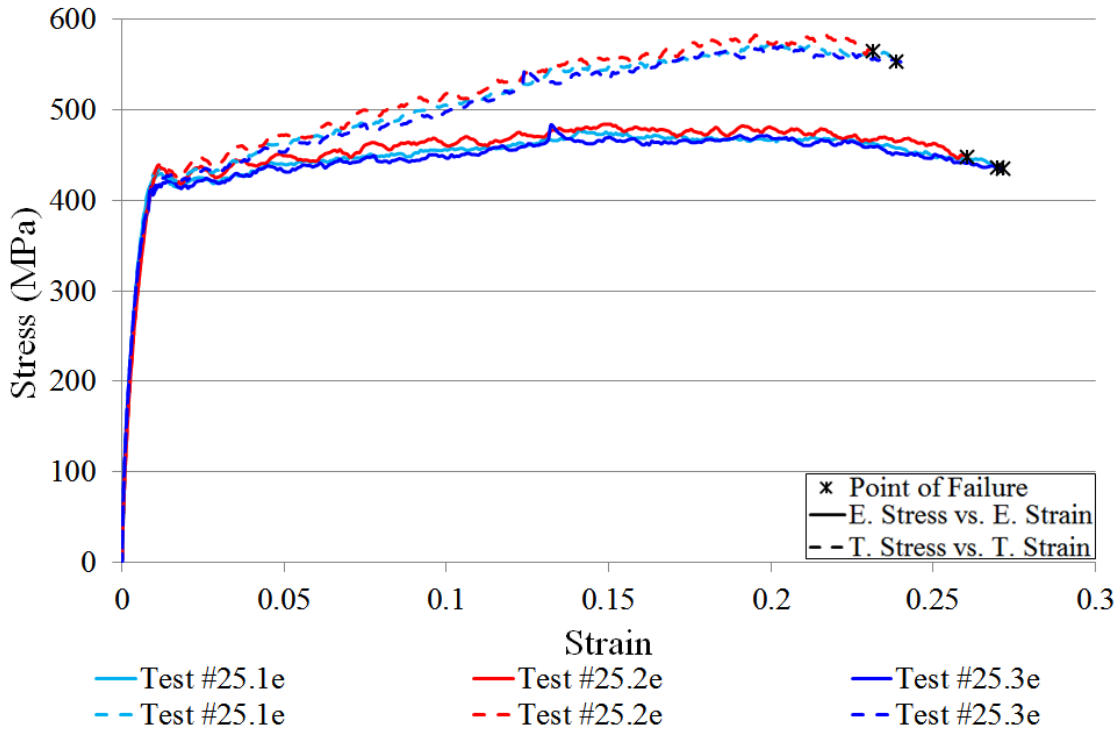

Figure C-25: Test #25 results and repeatability.

Table C-26: Test #26 parameters for the characterization of the flow surface.

Test #	Specimen #14 Figure B-14‡		Test Apparatus	Loading	Striker Velocity v [mm/s]	Equivalent Strain Rate [s^{-1}]		Temperature [K]
	D	H^{**}				Targeted	Measured	
26.1e	3.0734	3.0734	CSHB*	Compression	8593.4	2000	1389.95	RT†
26.2e	3.0861	3.0988			8664.5		1348.35	
26.3e	3.0734	3.0734			8593.4		1475.19	

* Compression Split Hopkinson Bar (CSHB).
** Gauge length.
† Room Temperature (RT).
‡ Detailed geometries and corresponding FE models of the specimens are illustrated in Appendix-B.

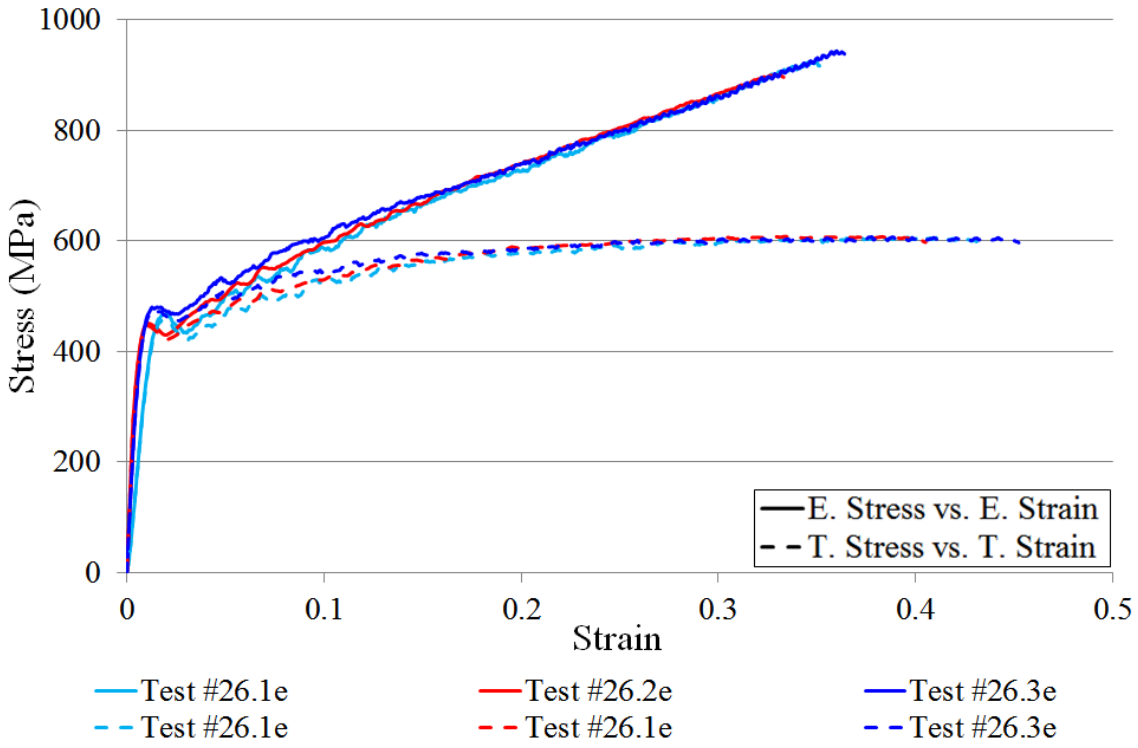

Figure C-26: Test #26 results and repeatability.

Table C-27: Test #27 parameters for the characterization of the flow surface.

Test #	Specimen #14 Figure B-14‡		Test Apparatus	Loading	Striker Velocity v [mm/s]	Equivalent Strain Rate [s^{-1}]		Temperature [K]
	D	H^{**}				Targeted	Measured	
27.1e	3.048	3.0734	CSHB*	Compression	19310.2	5500	4808.86	RT†
27.2e	3.048	3.0353			19100.5		4862.18	
27.3e	3.0353	3.0734			19290.1		5031.65	

* Compression Split Hopkinson Bar (CSHB).
** Gauge length.
† Room Temperature (RT).
‡ Detailed geometries and corresponding FE models of the specimens are illustrated in Appendix-B.

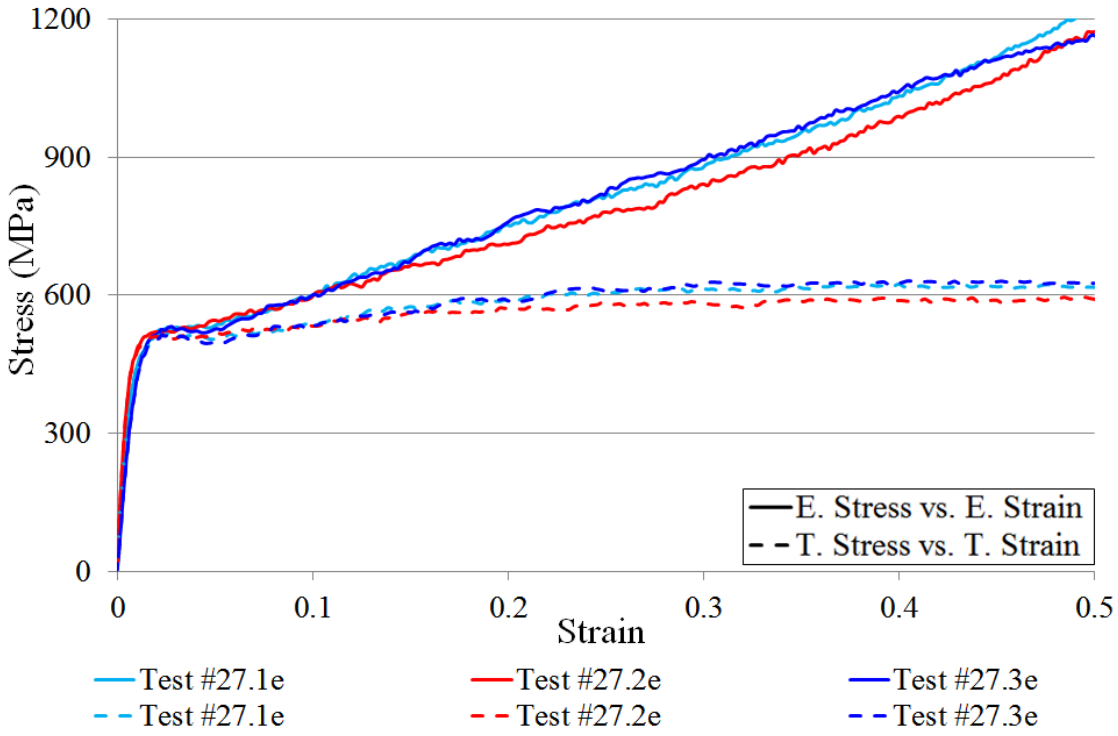

Figure C-27: Test #27 results and repeatability.

Table C-28: Test #28, #29 and #30 parameters for the characterization of the flow surface.

Test #	Specimen #14 Figure B-14‡		Test Apparatus	Loading	Striker Velocity v [mm/s]	Equivalent Strain Rate [s^{-1}]		Temperature [K]
	D	H^{**}				Targeted	Measured	
28.1e§	2.54	2.54	CSHB*	Compression	27410	9000	8113.06	RT†
29.1e§	2.54	2.54			32550	10000	9845.72	
30.1e§	2.54	2.54			36760	11000	10939.94	

* Compression Split Hopkinson Bar (CSHB).
** Gauge length.
† Room Temperature (RT).
‡ Detailed geometries and corresponding FE models of the specimens are illustrated in Appendix-B.
§ These tests were performed for only one case and were not repeated.

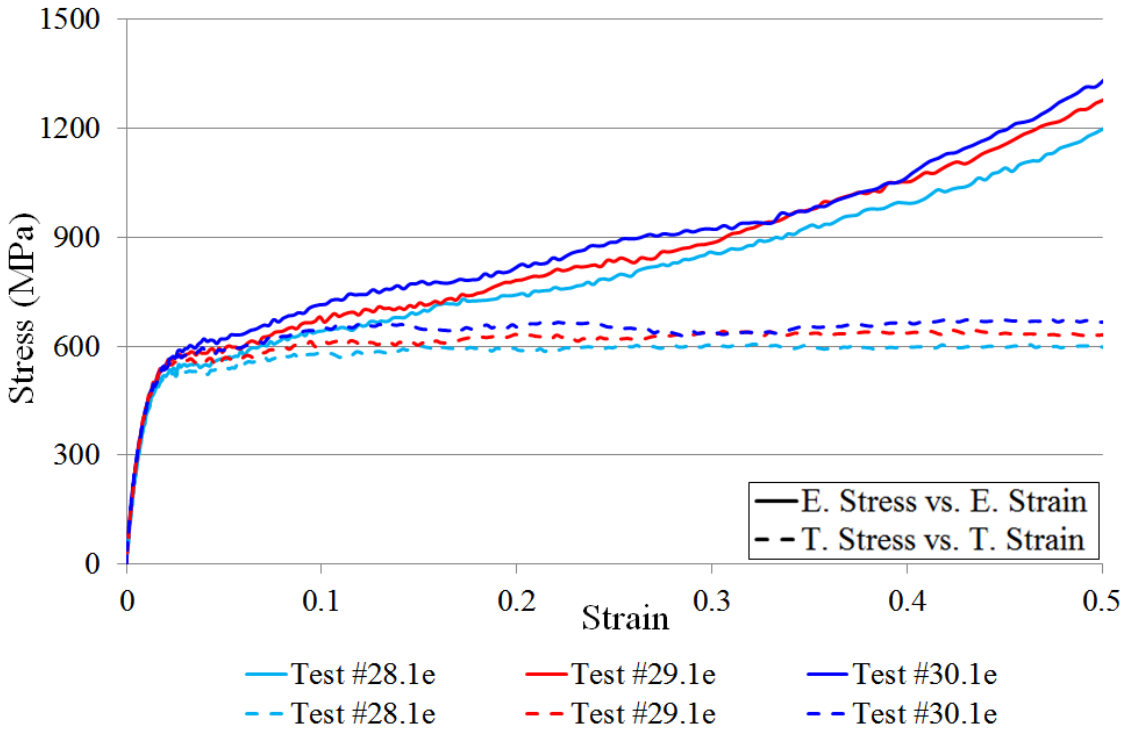

Figure C-28: Test #28, #29 and #30 results.

Table C-29: Test #31 parameters for the characterization of the flow surface.

Test #	Specimen #21 Figure B-19‡			Test Apparatus	Loading	Torque T [Nmm]	Shear Strain Rate [s^{-1}]		Temperature [K]
	d_i	d_o	L_0 **				Targeted	Measured	
31.1e	12.9794	13.76363	1.3462	SSHB*	Torsion	47917.3	866	900.84	RT†
31.2e	12.9794	13.74775	1.3462			47290.0		899.43	
31.3e	12.9794	13.75728	1.3462			47666.23		849.51	

* Shear Split Hopkinson Bar (SSHB).
** Extensometer gauge length.
† Room Temperature (RT).
‡ Detailed geometries and corresponding FE models of the specimens are illustrated in Appendix-B.

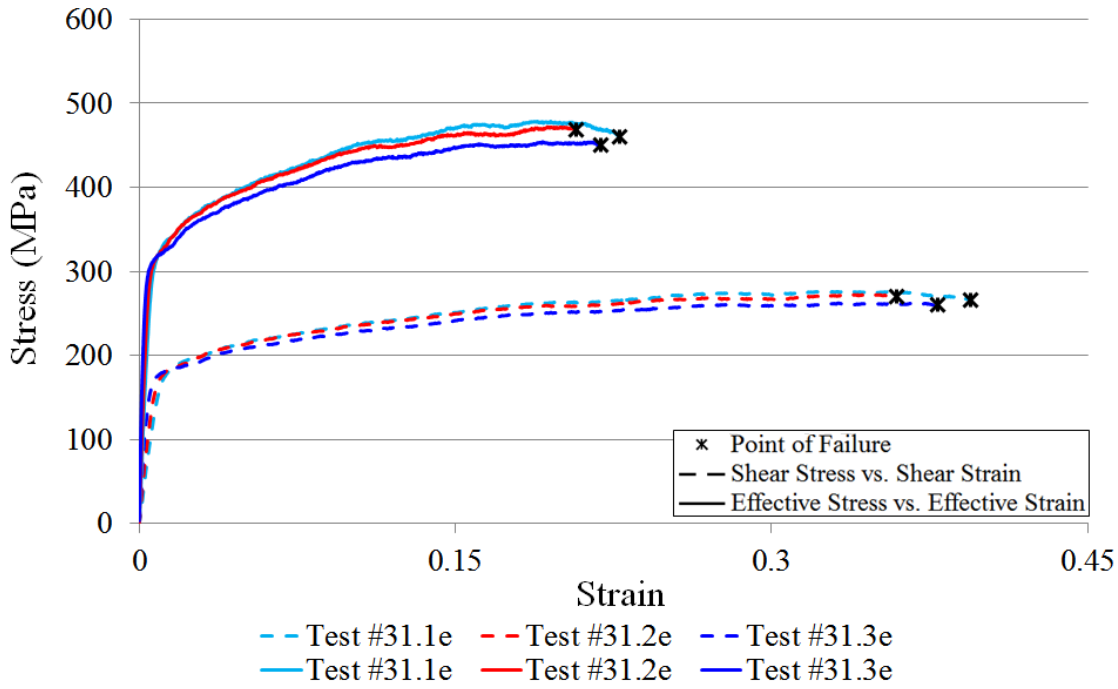

Figure C-29: Test #31 results and repeatability.

Table C-30: Test #32 parameters for the characterization of the flow surface.

Test #	Specimen #21 Figure B-19‡			Test Apparatus	Loading	Torque T [Nmm]	Shear Strain Rate [s^{-1}]		Temperature [K]
	d_i	d_o	L_0 **				Targeted	Measured	
32.1e	12.9794	13.77633	1.3716	SSHB*	Torsion	136787.3	5000	4667.97	RT†
32.2e	12.9794	13.7668	1.3462			134469.2		4639.23	
32.3e	12.9794	13.77633	1.3462			134815.7		4604.78	

* Shear Split Hopkinson Bar (SSHB).
** Extensometer gauge length.
† Room Temperature (RT).
‡ Detailed geometries and corresponding FE models of the specimens are illustrated in Appendix-B.

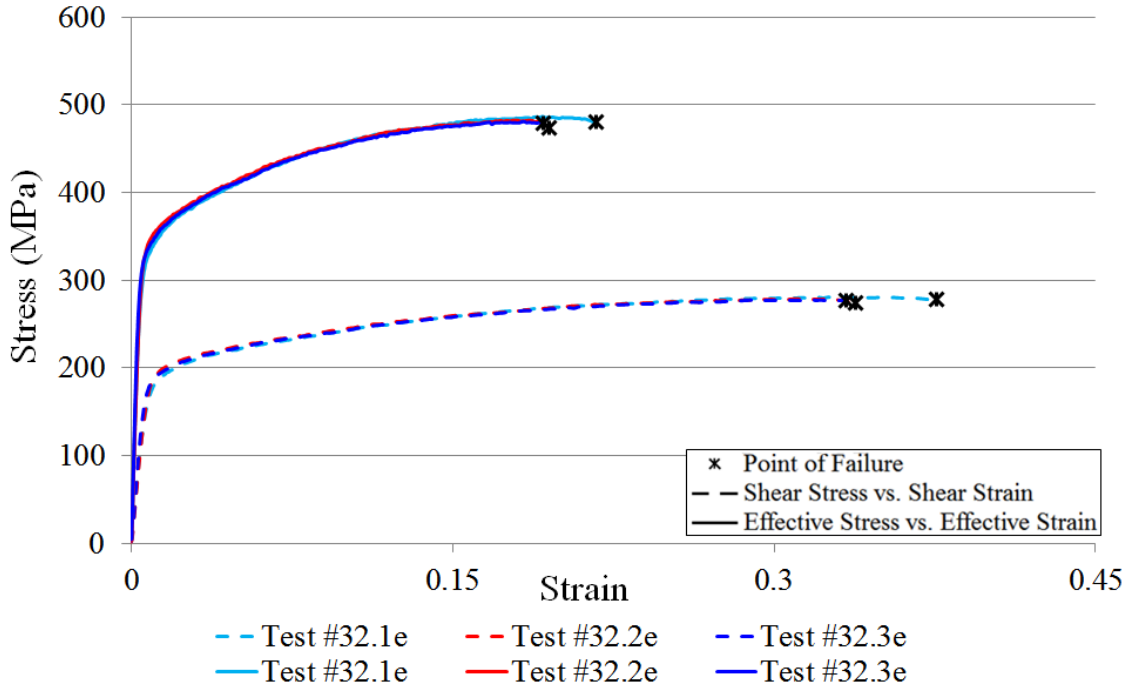

Figure C-30: Test #32 results and repeatability.

Table C-31: Test #2 and #3 parameters for the characterization of the failure surface.

Test #	Specimen #1 Figure B-1[§]			Test Apparatus	Loading	Initially Targeted				
						Stress-State Values			Strain Rate [s^{-1}]	Temperature [K]
	t	w	L_0 [**]			σ^*	σ_p^*	θ_L		
2.3 [Figure C-2][†] [Table C-2] [‡]	0.74168	2.9972	4.0	SHLF[*]	Tension	$-\frac{1}{3}$	0.0	1.0	1.0×10^{-2}	RT[††]
3.1 [Figure C-3][†] [Table C-3] [‡]	0.74168	3.0226							1.0	
3.3 [Figure C-3][†] [Table C-3] [‡]	0.75184	3.048								

* Servo-Hydraulic Loading Frame (SHLF).
† Test results for the corresponding specimen, strain-rate and temperature are illustrated in Appendix–C.
‡ Test results for the corresponding specimen, strain-rate and temperature are listed in Appendix–C.
§ Detailed geometries and corresponding FE models of the specimens are illustrated in Appendix–B.
** DIC Extensometer Gauge length.
†† Room temperature.

Table C-32: Test #33 parameters.

Test #	Specimen #2 Figure B-2§				Test Apparatus	Loading	Initially Targeted				
							Stress-State Values			Strain Rate	Temperature
	R	w	t	L_0 **			σ^*	σ_p^*	θ_L	[s^{-1}]	[K]
33.1	4.7625	3.048	0.7493	11.3	SHLF*	Tension	-0.41	0.0	0.9145	1.0	RT†
33.2	4.8006	3.00736	0.75692								
33.3	4.76504	3.06578	0.7747								

* Servo-Hydraulic Loading Frame (SHLF).
** DIC Extensometer Gauge length.
† Room Temperature (RT).
§ Detailed geometries and corresponding FE models of the specimens are illustrated in Appendix-B.

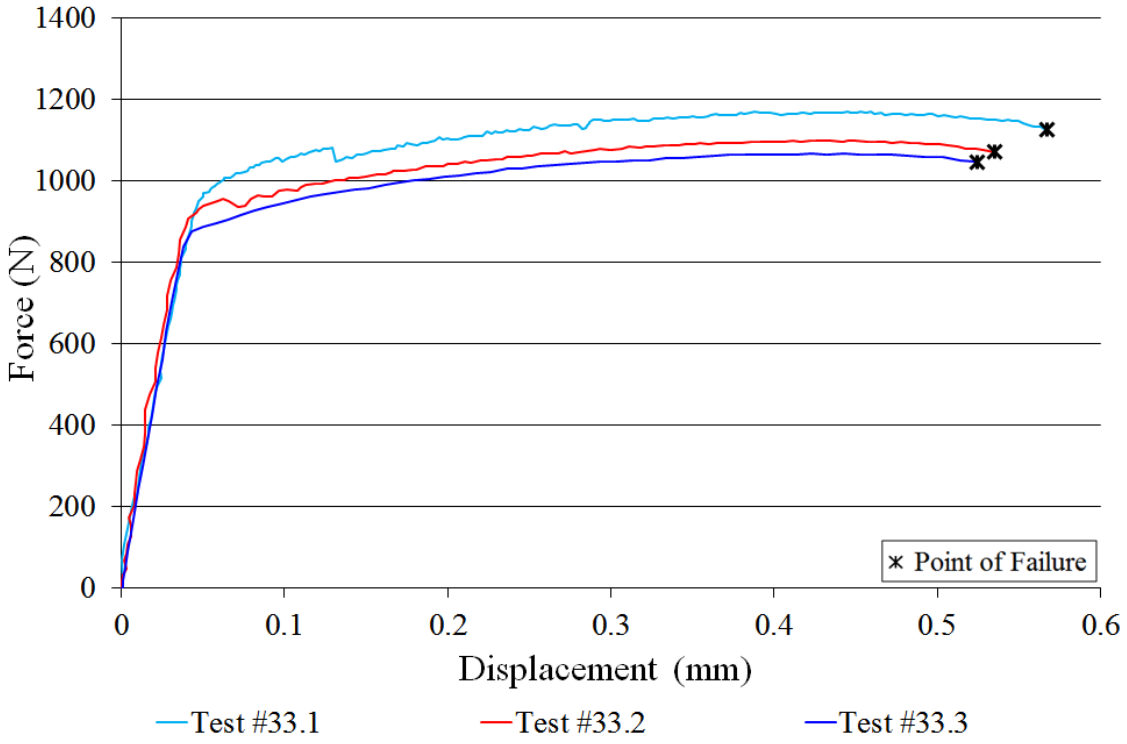

Figure C-31: Test #33 results and repeatability.

Table C-33: Test #34 parameters.

Test #	Specimen #3 Figure B-3§				Test Apparatus	Loading	Initially Targeted				
							Stress-State Values			Strain Rate	Temperature
	R	w	t	L_0 **			σ^*	σ_p^*	θ_L	[s^{-1}]	[K]
34.1	1.98057	3.13944	0.76962	6.6	SHLF*	Tension	-0.49	0.0	0.617	1.0	RT†
34.2	2.00025	3.08102	0.7874								
34.3	1.96215	3.0734	0.7874								

* Servo-Hydraulic Loading Frame (SHLF).
** DIC Extensometer Gauge length.
† Room Temperature (RT).
§ Detailed geometries and corresponding FE models of the specimens are illustrated in Appendix-B.

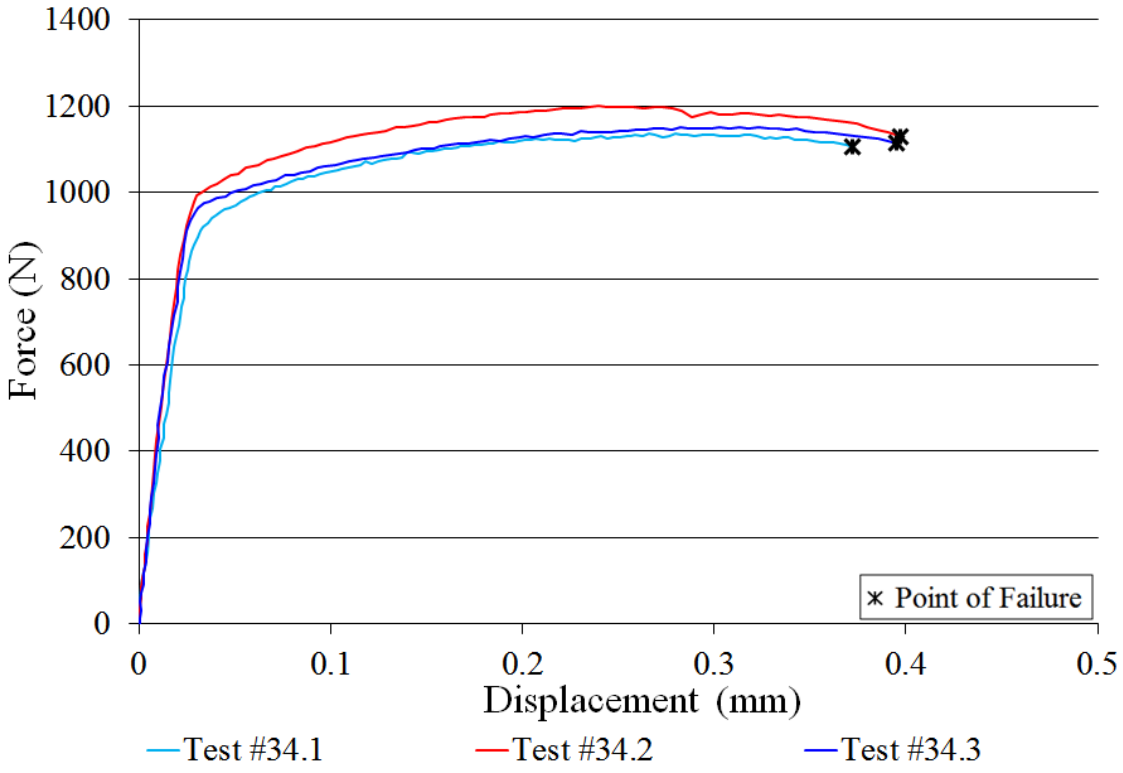

Figure C-32: Test #34 results and repeatability.

Table C-34: Test #35 parameters.

Test #	Specimen #4 Figure B-4§				Test Apparatus	Loading	Initially Targeted				
							Stress-State Values			Strain Rate	Temperature
	R	w	t	L_0 **			σ^*	σ_p^*	θ_L	[s^{-1}]	[K]
35.1	0.389255	3.1369	0.75184	3.8	SHLF*	Tension	-0.577	0.0	0.0	1.0	RT†
35.2	0.38989	3.13436	0.75184								
35.3	0.38227	3.21564	0.762								

* Servo-Hydraulic Loading Frame (SHLF).
** DIC Extensometer Gauge length.
† Room Temperature (RT).
§ Detailed geometries and corresponding FE models of the specimens are illustrated in Appendix-B.

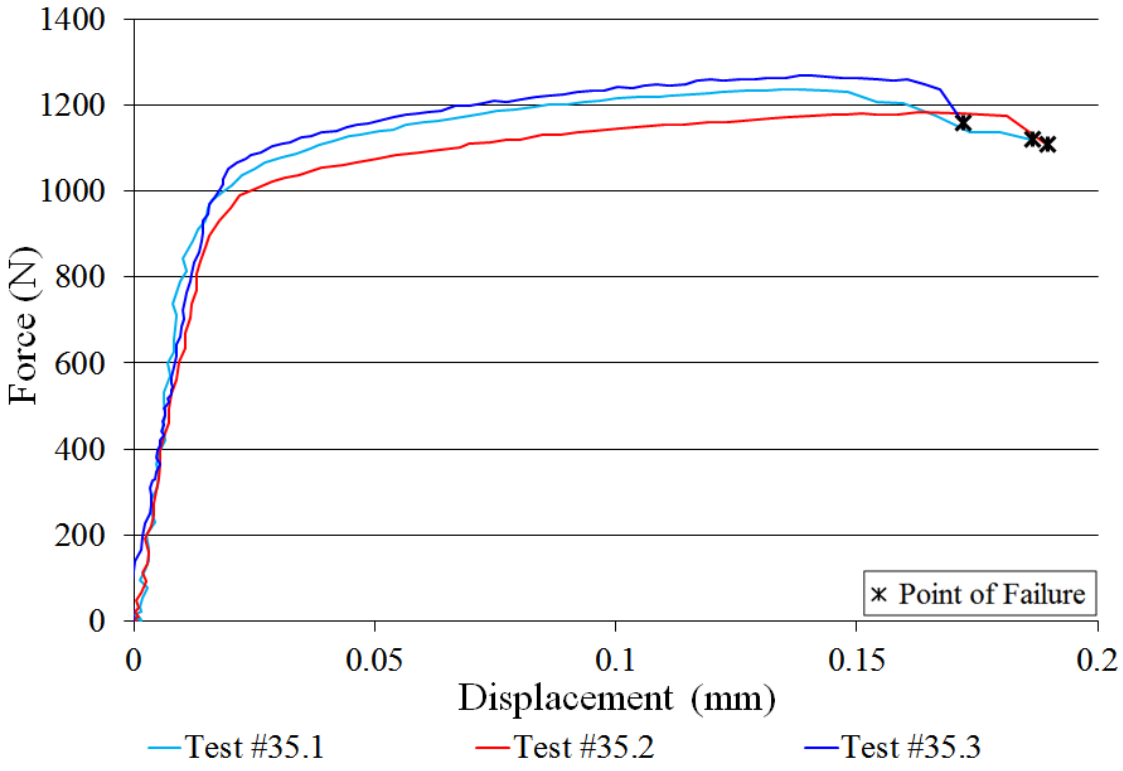

Figure C-33: Test #35 results and repeatability.

Table C-35: Test #4 parameters for the characterization of the failure surface.

Test #	Specimen #5 Figure B-5[§]		Test Apparatus	Loading	Initially Targeted				
					Stress-State Values			Strain Rate	Temperature
	d	L_0[**]			σ^*	σ_p^*	θ_L	[s^{-1}]	[K]
4.4 [Figure C-4][†] [Table C-4][‡]	4.7498	4.0	SHLF[*]	Tension	$-\frac{1}{3}$	0.0	1.0	1.0×10^{-2}	RT[††]
4.5 [Figure C-4][†] [Table C-4][‡]	4.7498								
4.6 [Figure C-4][†] [Table C-4][‡]	4.7244								

* Servo-Hydraulic Loading Frame (SHLF).
† Test results for the corresponding specimen, strain-rate and temperature are illustrated in Appendix–C.
‡ Test results for the corresponding specimen, strain-rate and temperature are listed in Appendix–C.
§ Detailed geometries and corresponding FE models of the specimens are illustrated in Appendix–B.
** DIC Extensometer Gauge length.
†† Room temperature.

Table C-36: Test #36 parameters.

Test #	Specimen #6 Figure B-6§			Test Apparatus	Loading	Initially Targeted				
						Stress-State Values			Strain Rate	Temperature
	R	d	L_0**			σ^*	σ_p^*	θ_L	[s^{-1}]	[K]
36.1	14.5034	4.7498	17.9	SHLF*	Tension	-0.41	0.006	1.0	1.0×10^{-2}	RT†
36.2	14.5034	4.7498								
36.3	14.5034	4.7498								

* Servo-Hydraulic Loading Frame (SHLF).
** DIC Extensometer Gauge length.
† Room Temperature (RT).
§ Detailed geometries and corresponding FE models of the specimens are illustrated in Appendix-B.

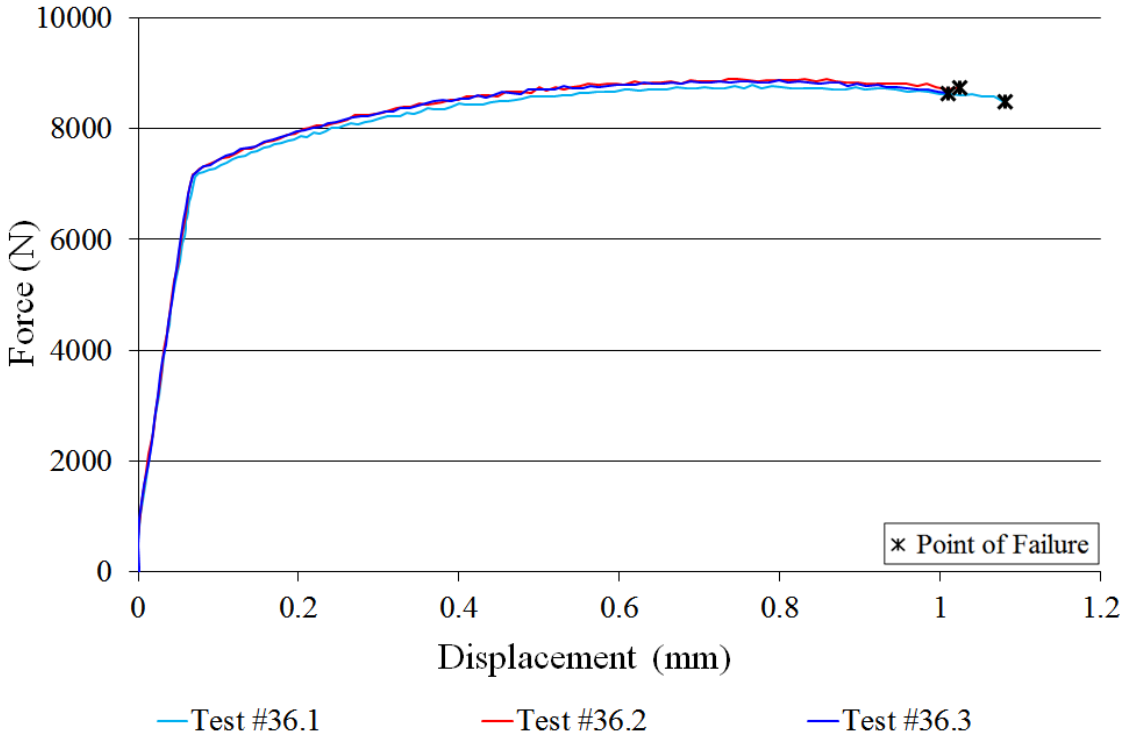

Figure C-34: Test #36 results and repeatability.

Table C-37: Test #37 parameters.

Test #	Specimen #7 Figure B-7§			Test Apparatus	Loading	Initially Targeted				
						Stress-State Values			Strain Rate	Temperature
	R	d	L_0 **			σ^*	σ_p^*	θ_L	[s^{-1}]	[K]
37.1	9.144	4.7498	13.5	SHLF*	Tension	-0.49	0.028	1.0	1.0×10^{-2}	RT†
37.2	9.144	4.7498								
37.3	9.144	4.7498								

* Servo-Hydraulic Loading Frame (SHLF).
** DIC Extensometer Gauge length.
† Room Temperature (RT).
§ Detailed geometries and corresponding FE models of the specimens are illustrated in Appendix-B.

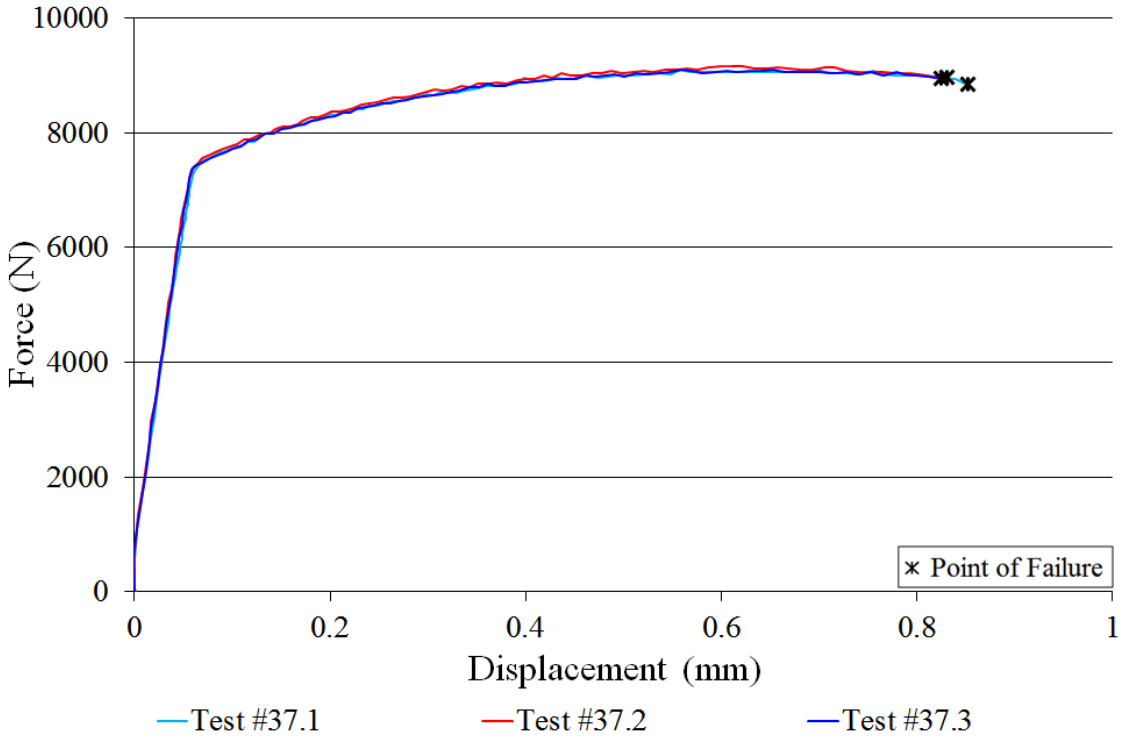

Figure C-35: Test #37 results and repeatability.

Table C-38: Test #38 parameters.

Test #	Specimen #8 Figure B-8§			Test Apparatus	Loading	Initially Targeted				
						Stress-State Values			Strain Rate [s^{-1}]	Temperature [K]
	R	d	L_0**			σ^*	σ_p^*	θ_L		
38.1	6.096	4.7498	10.2	SHLF*	Tension	-0.577	0.074	1.0	1.0×10^{-2}	RT†
38.2	6.096	4.7498								
38.3	6.096	4.7498								

* Servo-Hydraulic Loading Frame (SHLF).
** DIC Extensometer Gauge length.
† Room Temperature (RT).
§ Detailed geometries and corresponding FE models of the specimens are illustrated in Appendix-B.

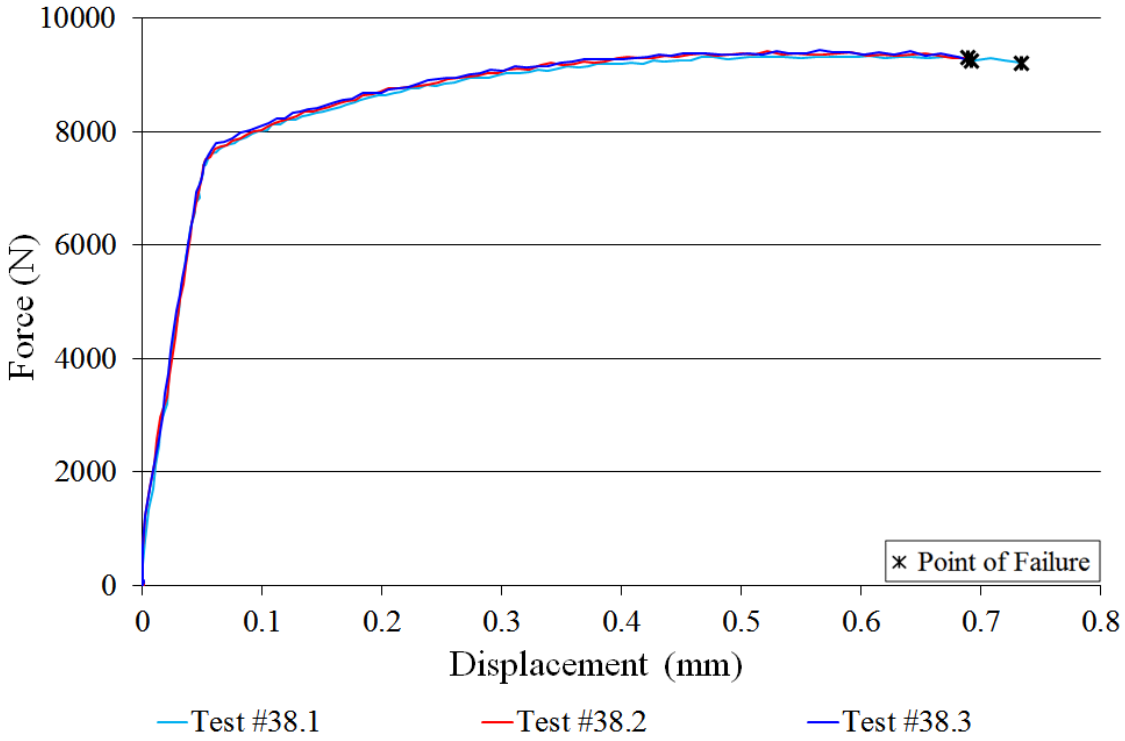

Figure C-36: Test #38 results and repeatability.

Table C-39: Test #39 parameters.

Test #	Specimen #9 Figure B-9[§]			Test Apparatus	Loading	Initially Targeted				
						Stress-State Values			Strain Rate [s^{-1}]	Temperature [K]
	R	d	L_0 **			σ^*	σ_p^*	θ_L		
39.1	4.4704	4.7625	7.7	SHLF*	Tension	-0.667	0.148	1.0	1.0×10^{-2}	RT†
39.2	4.4704	4.7625								
39.3	4.4704	4.7625								

* Servo-Hydraulic Loading Frame (SHLF).
** DIC Extensometer Gauge length.
† Room Temperature (RT).
§ Detailed geometries and corresponding FE models of the specimens are illustrated in Appendix-B.

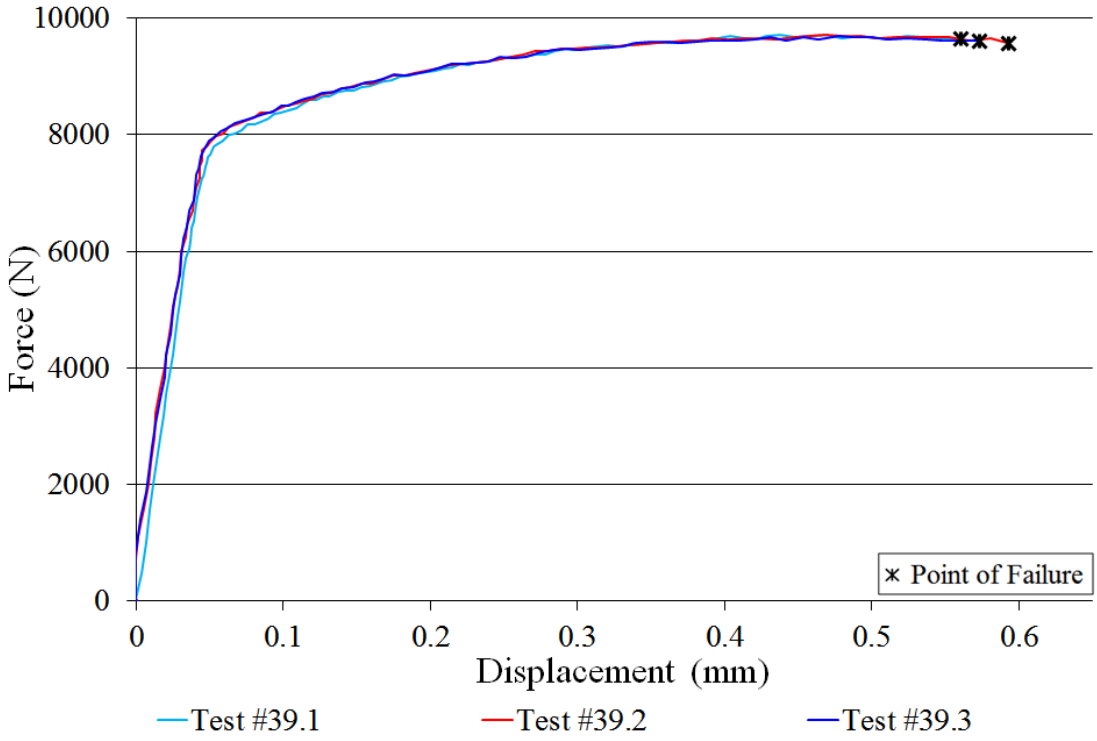

Figure C-37: Test #39 results and repeatability.

Table C-40: Test #40 parameters.

Test #	Specimen #10 Figure B-10§			Test Apparatus	Loading	Initially Targeted				
						Stress-State Values			Strain Rate	Temperature
	R	d	L_0 **			σ^*	σ_p^*	θ_L	[s^{-1}]	[K]
40.1	3.048	4.7625	5.0	SHLF*	Tension	-0.8	0.319	1.0	1.0×10^{-2}	RT†
40.2	3.048	4.7625								
40.3	3.048	4.7625								

* Servo-Hydraulic Loading Frame (SHLF).
** DIC Extensometer Gauge length.
† Room Temperature (RT).
§ Detailed geometries and corresponding FE models of the specimens are illustrated in Appendix-B.

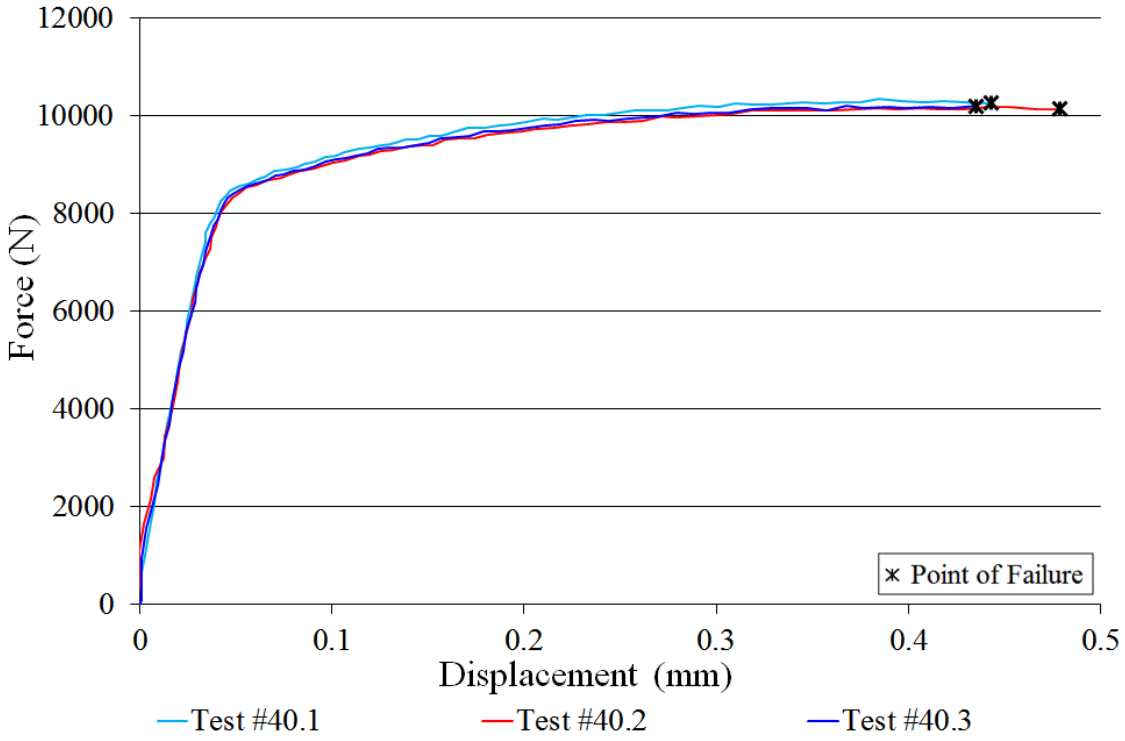

Figure C-38: Test #40 results and repeatability.

Table C-41: Test #41 parameters.

Test #	Specimen #11 Figure B-11§			Test Apparatus	Loading	Initially Targeted				
						Stress-State Values			Strain Rate	Temperature
	w	t	L_0**			σ^*	σ_p^*	θ_L	[s^{-1}]	[K]
41.1	2.0574	25.3746	5.08	SHLF*	Tension	-0.577	0.0	0.0	1.0×10^{-2}	RT†
41.2	2.032	25.3492								
41.3	2.0066	25.3238								

* Servo-Hydraulic Loading Frame (SHLF).
** DIC Extensometer Gauge length.
† Room Temperature (RT).
§ Detailed geometries and corresponding FE models of the specimens are illustrated in Appendix-B.

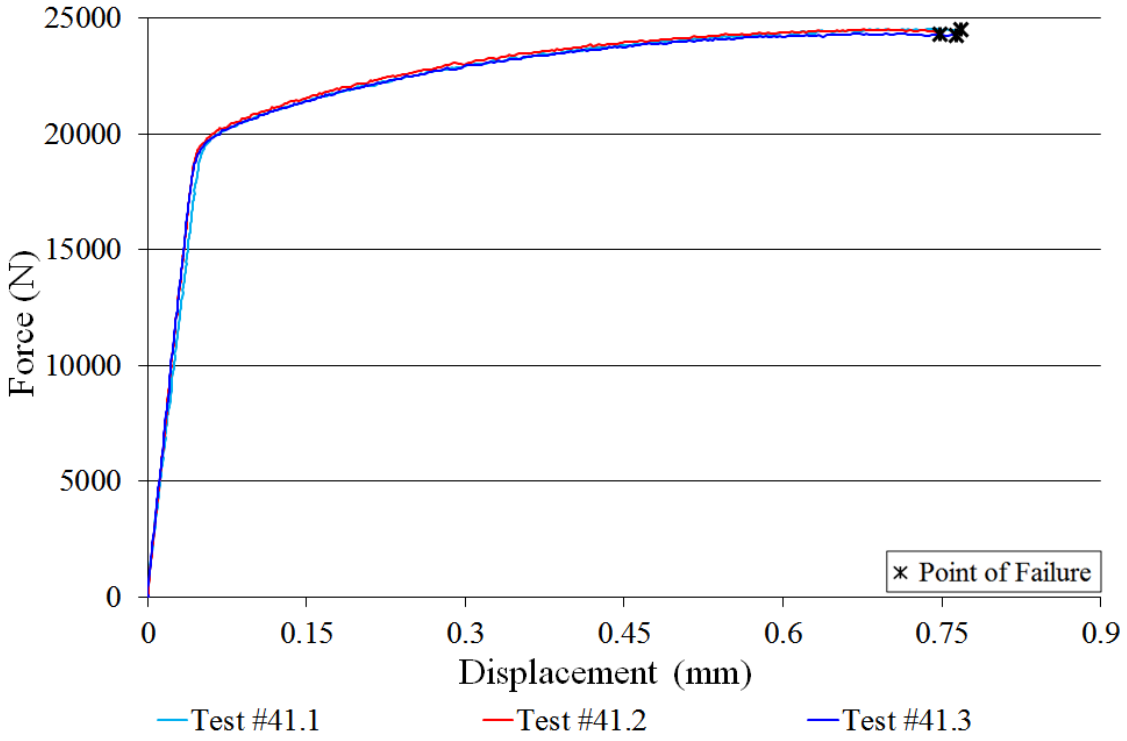

Figure C-39: Test #41 results and repeatability.

Table C-42: Test #42 parameters.

Test #	Specimen #12 Figure B-12§				Test Apparatus	Loading	Initially Targeted				
							Stress-State Values			Strain Rate	Temperature
	R	w	t	L_0 **			σ^*	σ_p^*	θ_L	[s^{-1}]	[K]
42.1	13.97	2.0574	25.3746	19.5	SHLF*	Tension	-0.666	0.074	0.0	1.0×10^{-2}	RT†
42.2	13.97	2.032	25.3492								
42.3	13.97	2.032	25.3492								

* Servo-Hydraulic Loading Frame (SHLF).
** DIC Extensometer Gauge length.
† Room Temperature (RT).
§ Detailed geometries and corresponding FE models of the specimens are illustrated in Appendix-B.

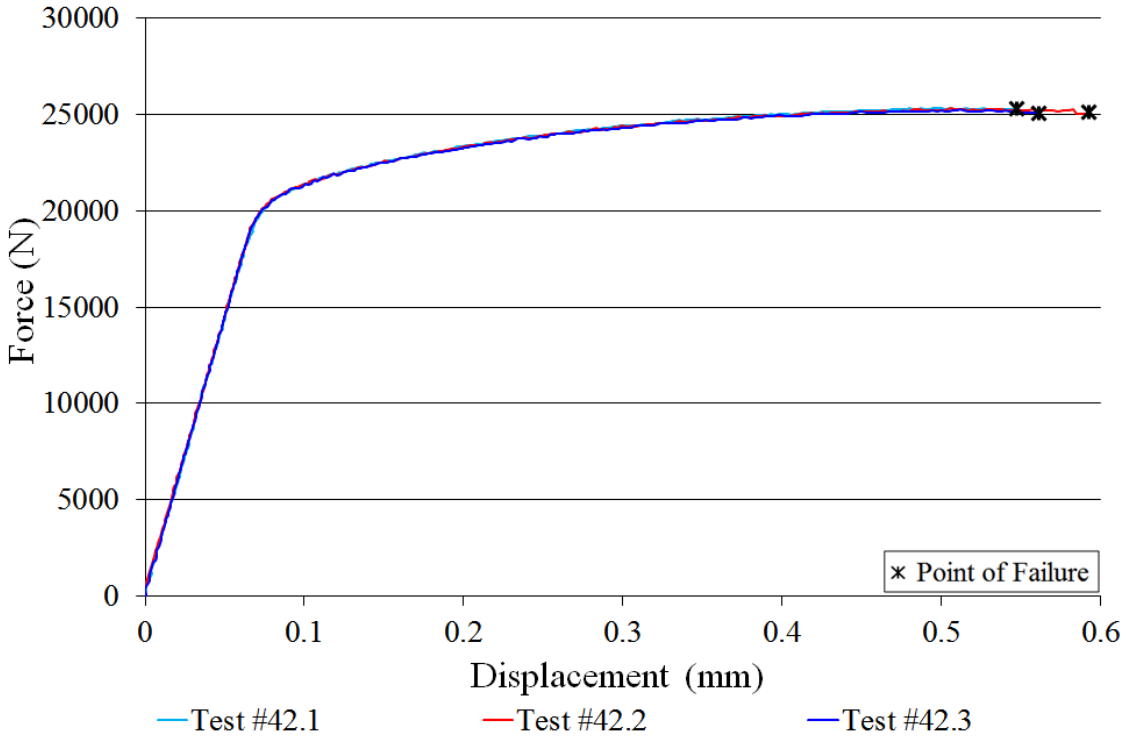

Figure C-40: Test #42 results and repeatability.

Table C-43: Test #43 parameters.

Test #	Specimen #13 Figure B-13§				Test Apparatus	Loading	Initially Targeted				
							Stress-State Values			Strain Rate	Temperature
	R	w	t	L_0 **			σ^*	σ_p^*	θ_L	[s^{-1}]	[K]
43.1	4.7625	2.0574	25.3746	8.0	SHLF*	Tension	-0.8	0.245	0.0	1.0×10^{-2}	RT†
43.2	4.7625	2.032	25.3492								
43.3	4.7625	2.0447	25.3492								

* Servo-Hydraulic Loading Frame (SHLF).
** DIC Extensometer Gauge length.
† Room Temperature (RT).
§ Detailed geometries and corresponding FE models of the specimens are illustrated in Appendix-B.

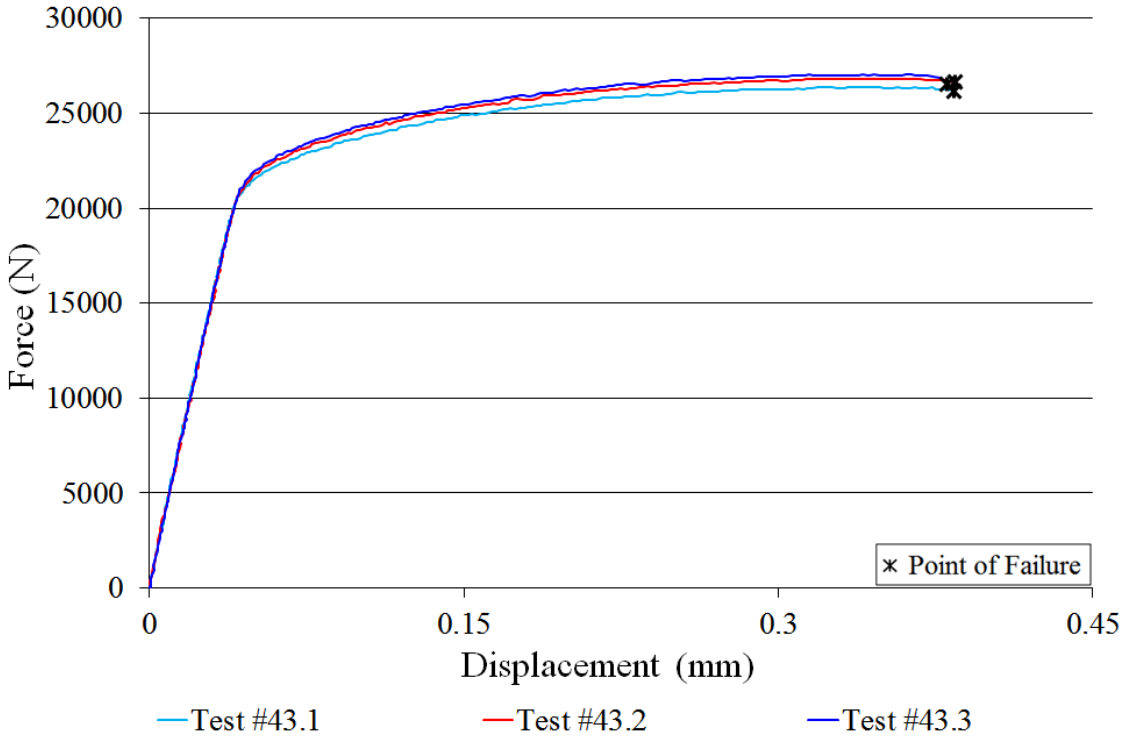

Figure C-41: Test #43 results and repeatability.

Table C-44: Test #6 parameters for the characterization of the failure surface.

Test #	Specimen #14 Figure B-14§		Test Apparatus	Loading	Initially Targeted				
					Stress-State Values			Strain Rate	Temperature
	D	L_0 **			σ^*	σ_p^*	θ_L	[s^{-1}]	[K]
6.1e [Figure C-4]† [Table C-4]‡	3.048	3.03784	SHLF*	Compression	$+\frac{1}{3}$	0.0	-1.0	1.0×10^{-2}	RT††
6.2e [Figure C-4]† [Table C-4]‡	3.02895	3.048							
6.3e [Figure C-4]† [Table C-4]‡	3.048	3.05308							

* Servo-Hydraulic Loading Frame (SHLF).
† Test results for the corresponding specimen, strain-rate and temperature are illustrated in Appendix–C.
‡ Test results for the corresponding specimen, strain-rate and temperature are listed in Appendix–C.
§ Detailed geometries and corresponding FE models of the specimens are illustrated in Appendix–B.
** Extensometer Gauge length.
†† Room temperature.

Table C-45: Test #8 parameters for the characterization of the failure surface.

Test #	Specimen #15 Figure B-15§			Test Apparatus	Loading	Initially Targeted				
						Stress-State Values			Strain Rate	Temperature
	d_i	d_o	L_0 **			σ^*	σ_p^*	θ_L	[s^{-1}]	[K]
8.1 [Figure C-8]† [Table C-8]‡	7.9629	9.1694	6.35	SHLF*	Torsion	0.0	0.0	0.0	1.0	RT††
8.2 [Figure C-8]† [Table C-8]‡	7.9502	9.1694								
8.3 [Figure C-8]† [Table C-8]‡	7.9629	9.144								

* Servo-Hydraulic Loading Frame (SHLF).
† Test results for the corresponding specimen, strain-rate and temperature are illustrated in Appendix–C.
‡ Test results for the corresponding specimen, strain-rate and temperature are listed in Appendix–C.
§ Detailed geometries and corresponding FE models of the specimens are illustrated in Appendix–B.
** DIC Extensometer Gauge length.
†† Room temperature.

Table C-46: Test #44 parameters for the characterization of the failure surface.

Test #	Specimen #16 Figure B-15§			Test Apparatus	Loading	Initially Targeted					
						Stress-State Values				Strain Rate	Temperature
	d_i	d_o	L_0 **			$\frac{\sigma_x}{\tau_{xy}}$	σ^*	σ_p^*	θ_L	[s^{-1}]	[K]
44.1	7.9248	9.1694	6.35	SHLF*	Combined Tension/ Torsion	1.973	-0.2505	0.0	0.915	1.0	RT†
44.2	7.9248	9.1694									
44.3	7.9629	9.1694									

* Servo-Hydraulic Loading Frame (SHLF).
** DIC Extensometer Gauge length.
† Room Temperature (RT).
§ Detailed geometries and corresponding FE models of the specimens are illustrated in Appendix-B.

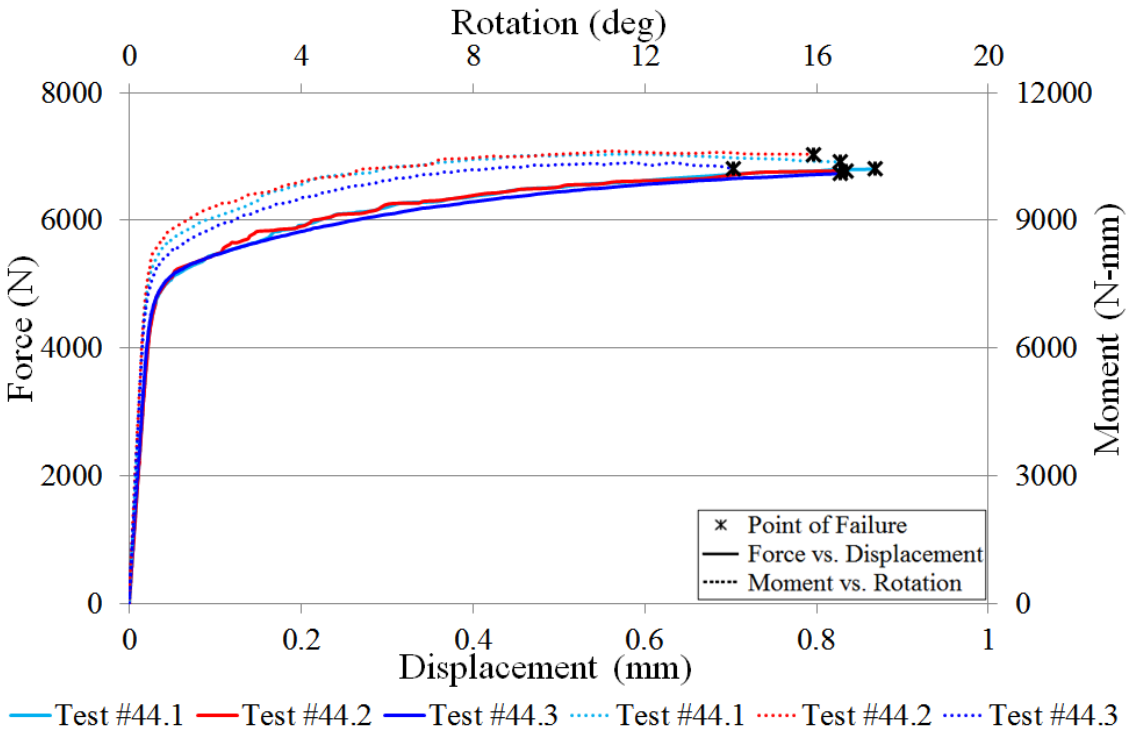

Figure C-42: Test #44 results and repeatability.

Table C-47: Test #45 parameters for the characterization of the failure surface.

Test #	Specimen #17 Figure B-15§			Test Apparatus	Loading	Initially Targeted					
						Stress-State Values				Strain Rate	Temperature
	d_i	d_o	L_0 **			$\frac{\sigma_x}{\tau_{xy}}$	σ^*	σ_p^*	θ_L	[s^{-1}]	[K]
45.1	7.9248	9.1694	6.35	SHLF*	Combined Tension/ Torsion	0.848	-0.1466	0.0	0.617	1.0	RT†
45.2	7.9756	9.1694									
45.3	7.9629	9.1694									

* Servo-Hydraulic Loading Frame (SHLF).
** DIC Extensometer Gauge length.
† Room Temperature (RT).
§ Detailed geometries and corresponding FE models of the specimens are illustrated in Appendix-B.

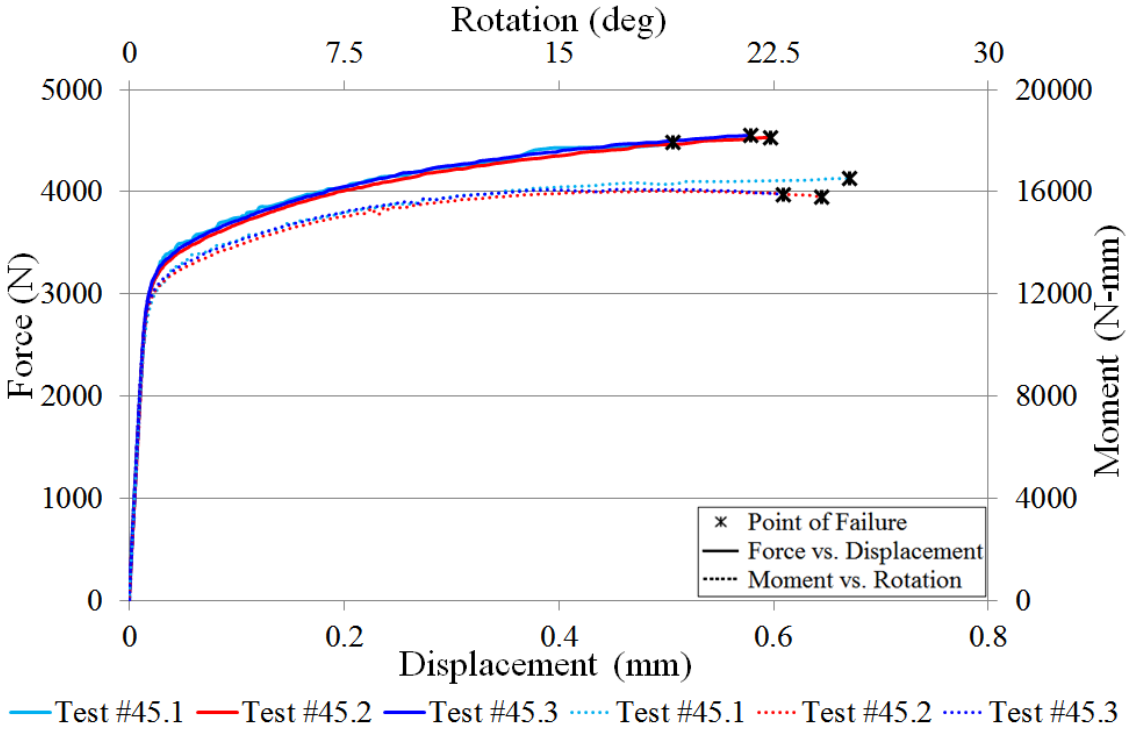

Figure C-43: Test #45 results and repeatability.

Table C-48: Test #46, #47 and #48 parameters for the characterization of the failure surface.

Test #	Specimen #	Test Apparatus	State-of-Stress and Loading	Initially Targeted				
				Stress-State Values			Temperature	Actuator Velocity
				σ^*	σ_p^*	θ_L	[K]	[mms^{-1}]
46.1§§	18 [Figure B-16]§ D = 9.5, R = 2.375	SHLF*	Plane-Strain Tension Punch	$-\frac{1}{\sqrt{3}}$	0.0741	-1.0	RT††	0.233
47.1§§	19 [Figure B-17]§ D = 9.5, R = 4.75		Equi-Biaxial Tension Punch	$-\frac{2}{3}$	0.0	-1.0		
48.1§§	20 [Figure B-18]§ D = 9.5, R = 0.508		Shear Punch	0.0	0.0	0.0		

* Servo-Hydraulic Loading Frame (SHLF).
† Test results for the corresponding specimen, strain-rate and temperature illustrated in Appendix–C.
‡ Test results for the corresponding specimen, strain-rate and temperature listed in Appendix–C.
§ Detailed geometries and corresponding FE models of the specimens are illustrated in Appendix–B.
†† Room Temperature (RT).
§§ These tests were performed for only once and were not repeated.

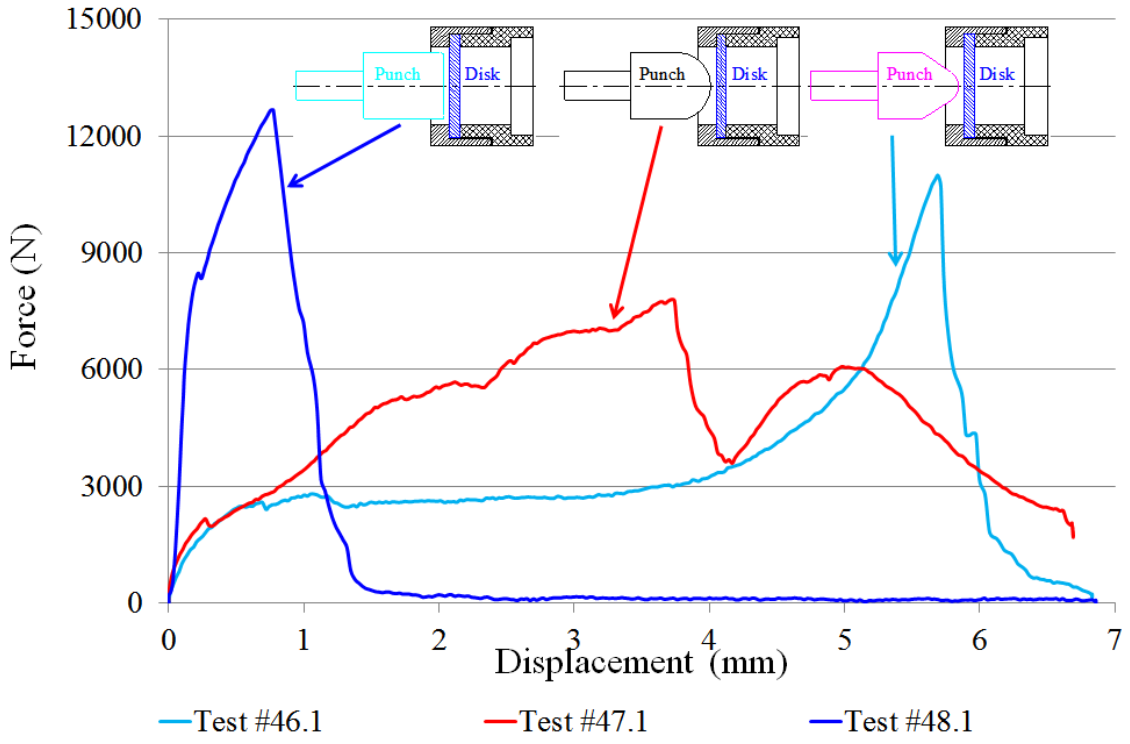

Figure C-44: Test #46, #47 and #48 results.

Appendix - D: List of tests for characterization of the input data for TRAUM

The lists of the material test data, which are used for the characterization of the flow and failure surfaces, can be found in Tables D-1 and D-2, respectively.

Table D-1: List of tests that are used to characterize the flow surface.

Test #	Specimen #	Test Apparatus	Loading	Targeted Equivalent Strain Rate‡‡ [s^{-1}]	Targeted Temperature [K]	Specimen Geometry§	Test Details†‡
1	1	SHLF*	Uni-axial Tension	1.0×10^{-4}	RT††	Figure B-1	Table C-1
2				1.0×10^{-2}			Table C-2
3				1.0			Table C-3
4	5			1.0×10^{-2}		Figure B-5	Table C-4
5	14		Uni-axial Compression	1.0×10^{-4}		Figure B-14	Table C-5
6				1.0×10^{-2}			Table C-6
7				1.0			Table C-7
8	15		Torsion			Figure B-15	Table C-8
9	1		Uni-axial Tension		423	Figure B-1	Table C-9
10					573		Table C-10
11					723		Table C-11
12					223		Table C-12
13	14		Uni-axial Compression		423	Figure B-14	Table C-13
14					573		Table C-14
15					723		Table C-15
16					223		Table C-16
17	21		Torsion	1.0×10^{-4}	RT††	Figure B-19	Table C-17
18				1.0×10^{-2}			Table C-18
19				1.0			Table C-19
20					423		Table C-20
21					573		Table C-21
22					723		Table C-22
23					223		Table C-23
24	1	TSHB**	Uni-axial Tension	5.0×10^{2}	RT††	Figure B-1	Table C-24
25				1.5×10^{3}			Table C-25
26	14	CSHB***	Uni-axial Compression	2.0×10^{3}		Figure B-14	Table C-26
27				5.5×10^{3}			Table C-27
28				9.0×10^{3}			Table C-28
29				1.0×10^{4}			Table C-28
30				1.1×10^{4}			Table C-28
31	21	SSHB****	Torsion	8.66×10^{2}		Figure B-19	Table C-29
32				5.0×10^{3}			Table C-30

* Servo-Hydraulic Loading Frame (SHLF).
** Tension Split Hopkinson Bar (TSHB).
*** Compression Split Hopkinson Bar (CSHB).
**** Shear Split Hopkinson Bar (SSHB).
† Test results for the corresponding specimen, strain-rate and temperature illustrated in Appendix–C.
†† Room Temperature (RT)
‡ Test results for the corresponding specimen, strain-rate and temperature listed in Appendix–C.
‡‡ Shear strain-rate for torsion.
§ Detailed geometries and corresponding FE models of the specimens are illustrated in Appendix–B.

Table D-2: List of tests that are used to characterize the failure surface.

Test #	Specimen #	Test Apparatus	State-of-Stress and Loading	Initially Targeted					Specimen Geometry[§]	Test Details[†‡]
				Stress-State Values			Strain Rate[‡‡] [s^{-1}]	Temp. [K]		
				σ^*	σ_p^*	θ_L				
$2^{R,SR}$	1	SHLF[**]	Plane-Stress in Tension	-0.333	0.0	1.0	1.0×10^{-2}	RT[††]	Figure B-1	Table C-2 Table C-31
$3^{SR,T}$							1.0			Table C-3 Table C-31
33	2			-0.41		0.9145			Figure B-2	Table C-32
34	3			-0.49		0.617			Figure B-3	Table C-33
35	4			-0.577		0.0			Figure B-4	Table C-34
4	5		Axi-symmetric in Tension	-0.333	0.0	1.0	1.0×10^{-2}		Figure B-5	Table C-4 Table C-35
36	6			-0.41	0.006				Figure B-6	Table C-36
37	7			-0.49	0.028				Figure B-7	Table C-37
38	8			-0.577	0.074				Figure B-8	Table C-38
39	9			-0.667	0.148				Figure B-9	Table C-39
40	10			-0.8	0.319				Figure B-10	Table C-40
41	11		Plane-Strain in Tension	-0.577	0.0	0.0			Figure B-11	Table C-41
42	12			-0.667	0.074				Figure B-12	Table C-42
43	13			-0.8	0.245				Figure B-13	Table C-43
6	14		Compression	0.333	0.0	-1.0			Figure B-14	Table C-44
8	15		Torsion	0.0	0.0	0.0	1.0		Figure B-15	Table C-45
44	16		Combined Tension/ Torsion	-0.251	0.0	0.915				Table C-46
45	17			-0.147	0.0	0.617				Table C-47
46	18		Plane-Strain Punch	-0.577	0.0741	-1.0	1.0×10^{-2}		Figure B-16	Table C-48
47	19		Bi-axial Tension Punch	-0.666	0.0	-1.0			Figure B-17	Table C-48
48	20		Shear Punch	0.0	0.0	0.0			Figure B-18	Table C-48
1^{SR}	1	TSHB[*]	Plane-Stress in Tension	-0.333	0.0	1.0	1.0×10^{-4}	423	Figure B-1	Table C-1
24^{SR}							500			Table C-24
25^{SR}							1800			Table C-25
9^{T}		SHLF[**]					1.0			Table C-9
10^{T}								573		Table C-10
11^{T}								723		Table C-11
12^{T}								223		Table C-12

[*] Tension Split Hopkinson Bar (TSHB).
[**] Servo-Hydraulic Loading Frame (SHLF).
[†] Test results for the corresponding specimen, strain-rate and temperature illustrated in Appendix–C.
[††] Room Temperature (RT)
[‡] Test results for the corresponding specimen, strain-rate and temperature listed in Appendix–C.
[‡‡] Shear strain-rate for torsion.
[§] Detailed geometries and corresponding FE models of the specimens are illustrated in Appendix–B.
[R] Test #2 is also used to characterize the regularization curve.
[SR] Tests #1, #2, #3, #24 and #25 are used to characterize the strain-rate dependent scaling curve for the failure surface.
[T] Tests #3, #9, #10, #11 and #12 are used to characterize the temperature dependent scaling curve for the failure surface.
It should be noted that the characterization is performed for a characteristic element size around 0.15mm.

Appendix - E: Mesh patterns that are used for regularization

TRAUM utilizes a regularized failure algorithm that is based on the regularization of the total elongation by the corresponding plastic strain at failure considering the characteristic element size. In this Appendix, seven different FE models are illustrated that are used to construct the regularization curve that is defined in Chapter 5.9. It should be noted that, although regularized failure algorithm of TRAUM is activated and used, element size of the [t/5] model is used as the baseline for the other FE models that are used to predict ductile failure throughout this dissertation for consistency unless otherwise stated.

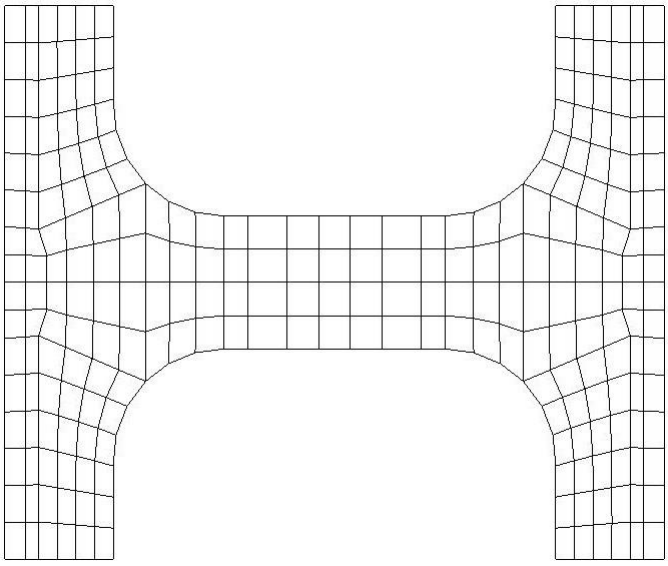

Figure E-1: Plane-stress specimen with smooth section (Specimen #1), 1 element through the thickness [t/1].

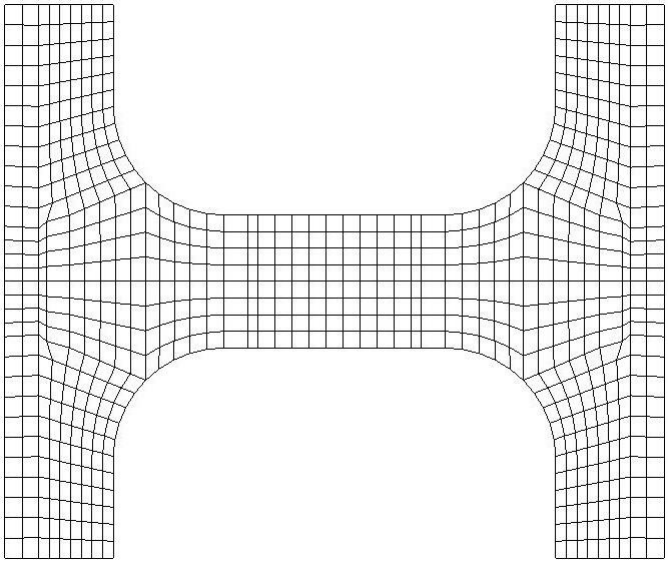

Figure E-2: Plane-stress specimen with smooth section (Specimen #1), 2 elements through the thickness [t/2].

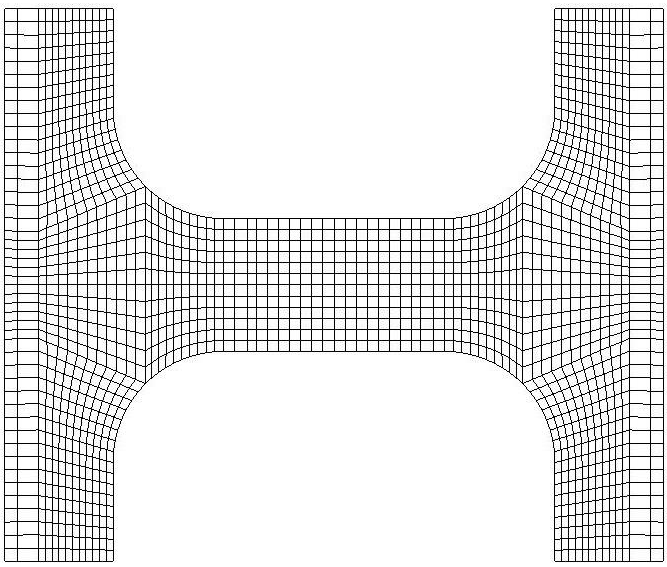

Figure E-3: Plane-stress specimen with smooth section (Specimen #1), 3 elements through the thickness [t/3].

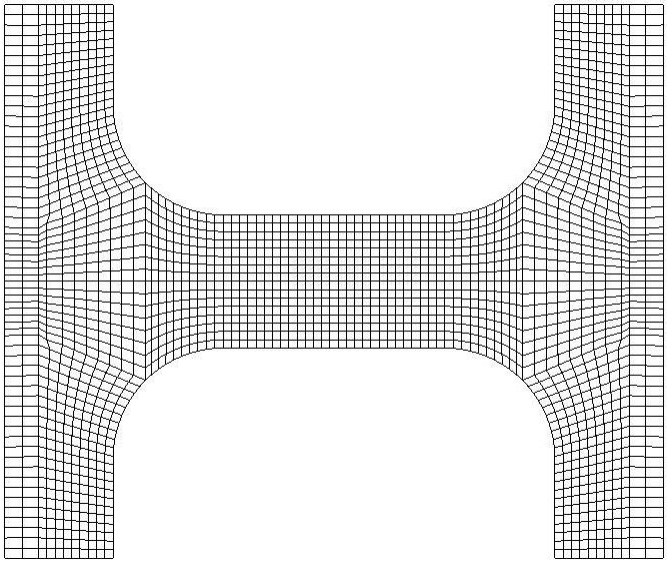

Figure E-4: Plane-stress specimen with smooth section (Specimen #1), 4 elements through the thickness [t/4].

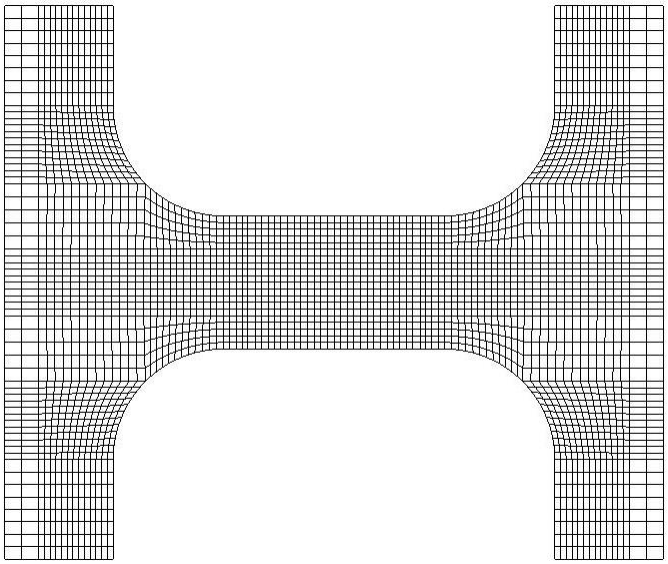

Figure E-5: Plane-stress specimen with smooth section (Specimen #1), 5 elements through the thickness [t/5].

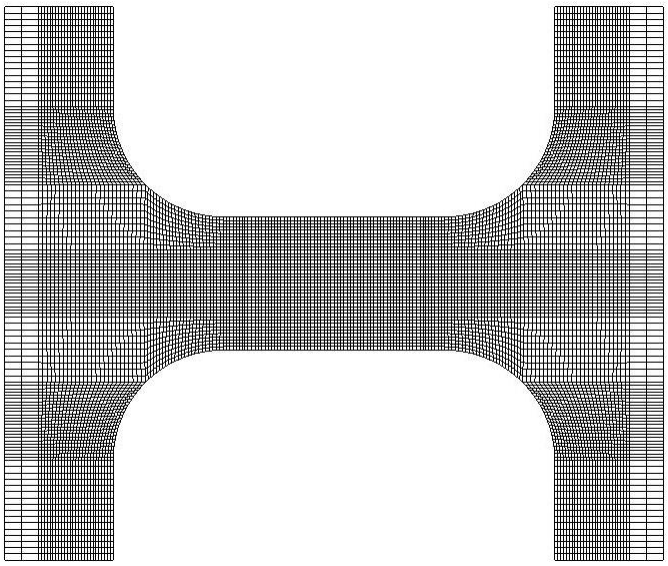

Figure E-6: Plane-stress specimen with smooth section (Specimen #1), 10 elements through the thickness [t/10].

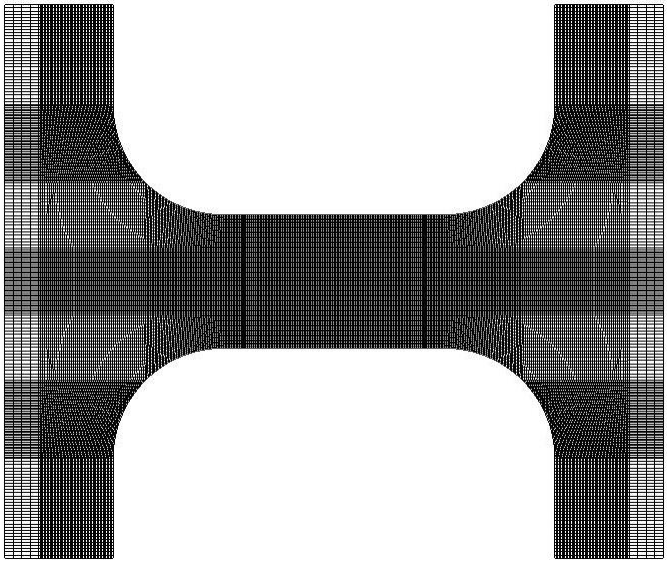

Figure E-7: Plane-stress specimen with smooth section (Specimen #1), 20 elements through the thickness [t/20].

Appendix - F: Verification of the input values for TRAUM simulations

In this Appendix, characterized input values for the strain-rate and temperature dependent flow surface for Al2024-T351 is verified by predicting the corresponding test results with TRAUM. It should be noted that a full validation is performed with TRAUM in Chapter 6 for the characterized values of the material including the stress-state dependent failure surface. General description of the characterization methodology can be found in Chapter 5.

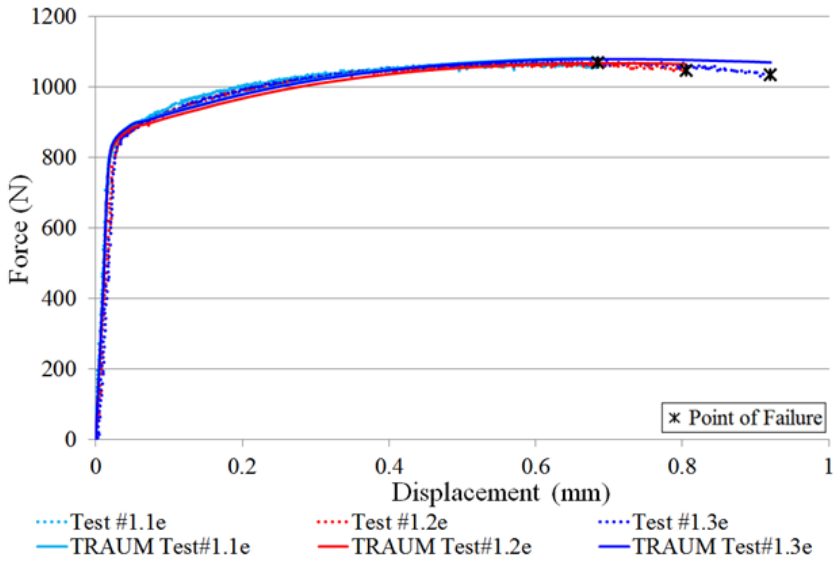

Figure F-1: Verification of the hardening curve for Test #1 at a strain-rate of $1.0x10^{-4}s^{-1}$ and RT.

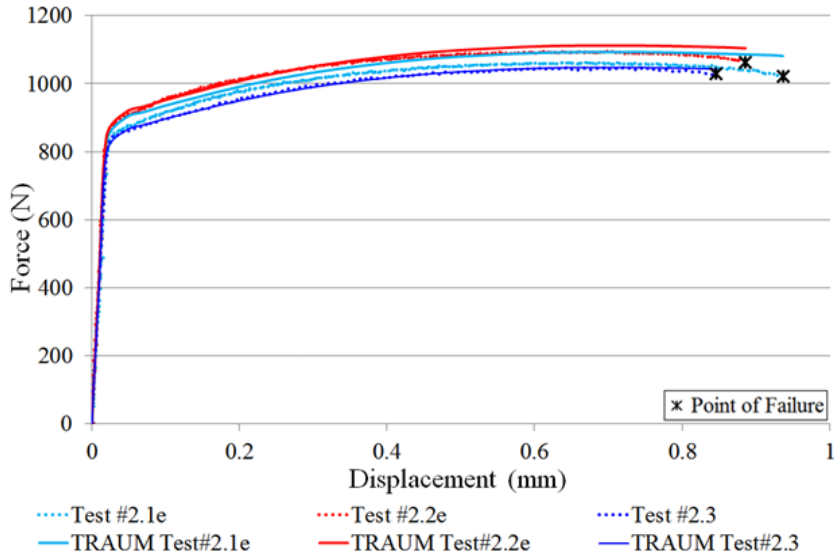

Figure F-2: Verification of the hardening curve for Test #2 at a strain-rate of $1.0x10^{-2}s^{-1}$ and RT.

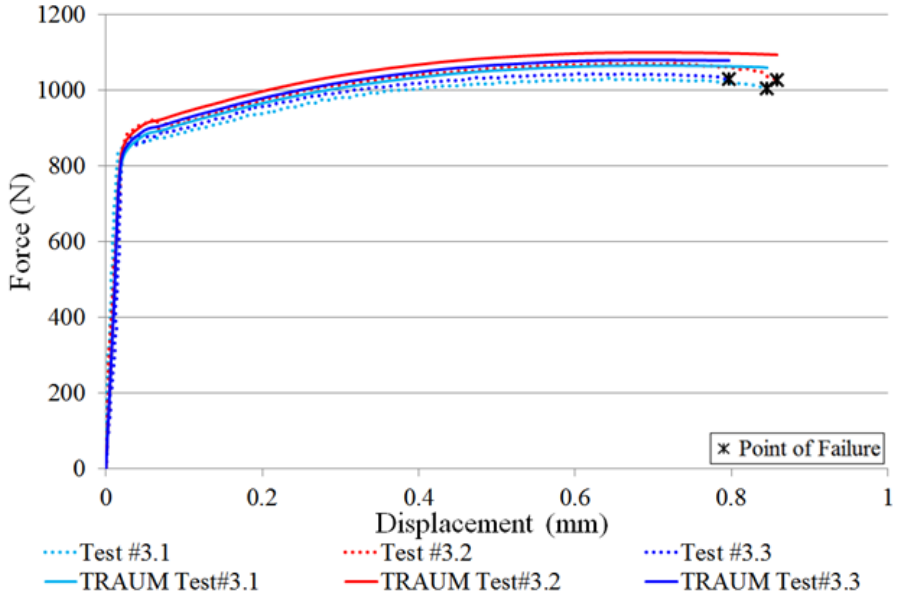

Figure F-3: Verification of the hardening curve for Test #3 at a strain-rate of $1.0s^{-1}$ and RT.

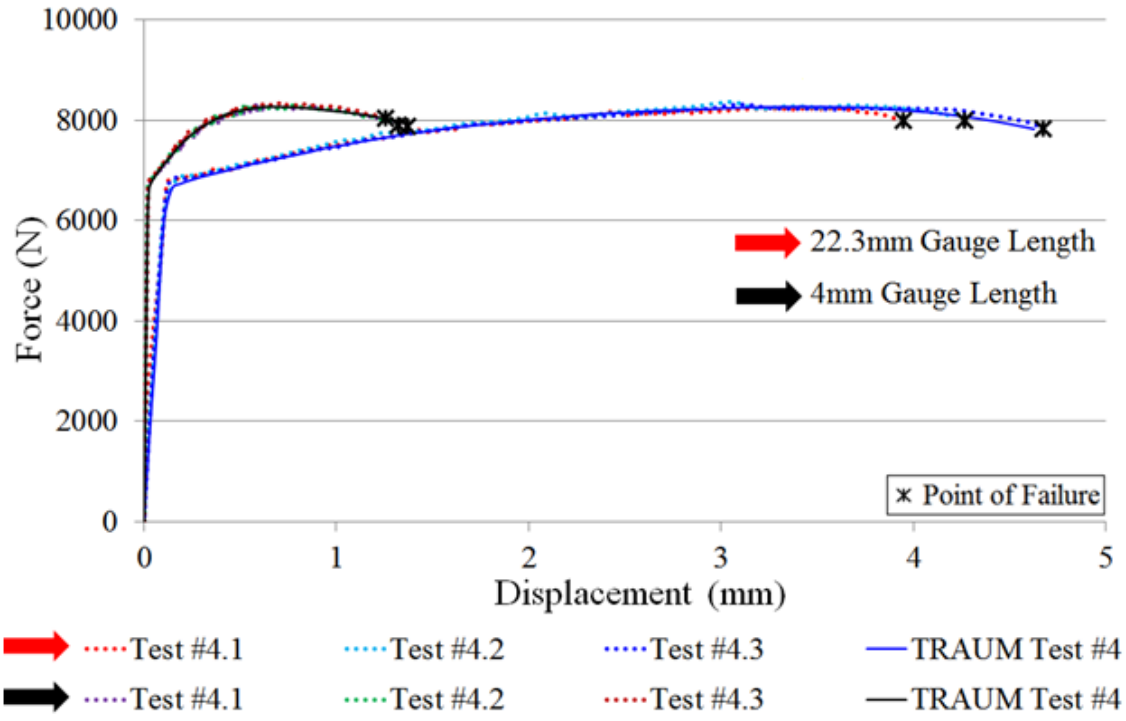

Figure F-4: Verification of the hardening curves for Test #4 at a strain-rate of $1.0x10^{-2}s^{-1}$ and RT.

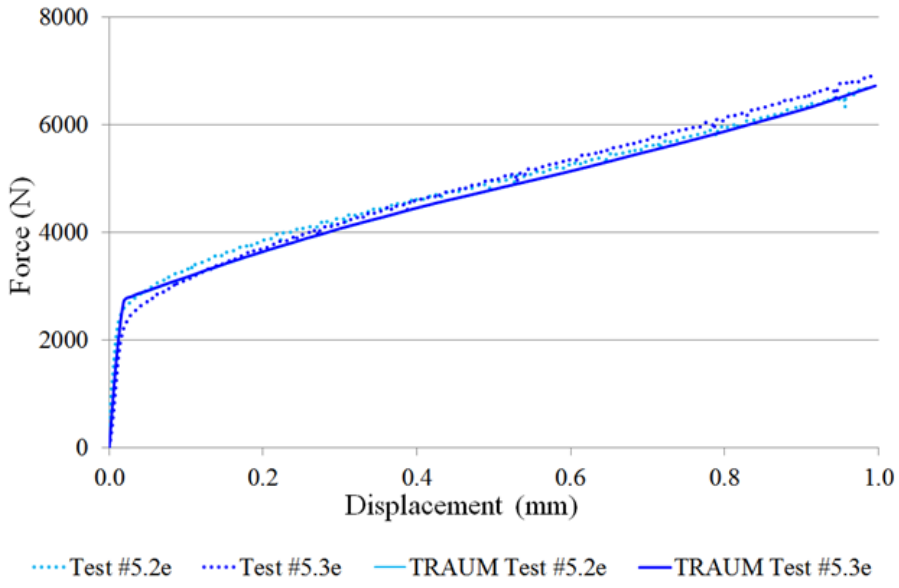

Figure F-5: Verification of the hardening curves for Test #5 at a strain-rate of $1.0x10^{-4}s^{-1}$ and RT.

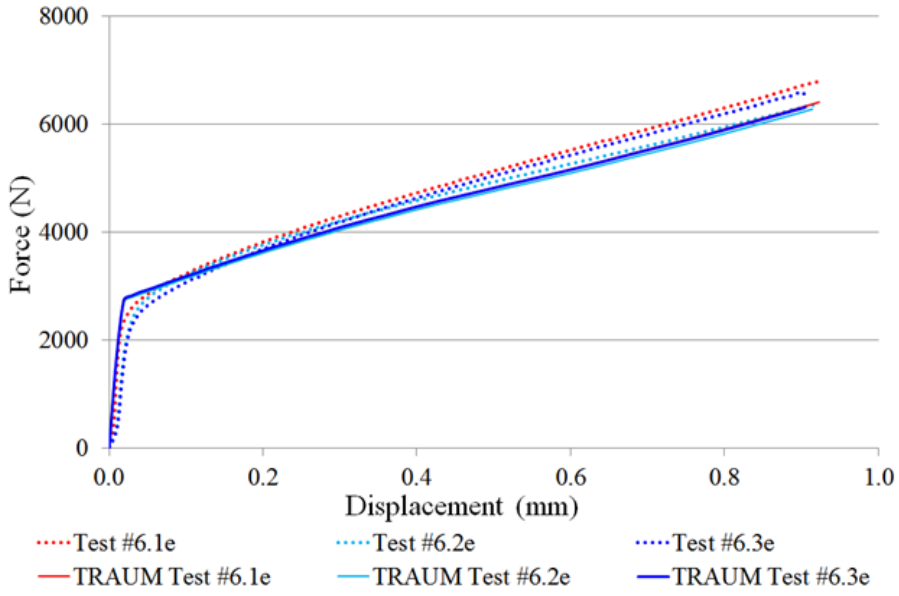

Figure F-6: Verification of the hardening curves for Test #6 at a strain-rate of $1.0x10^{-2}s^{-1}$ and RT.

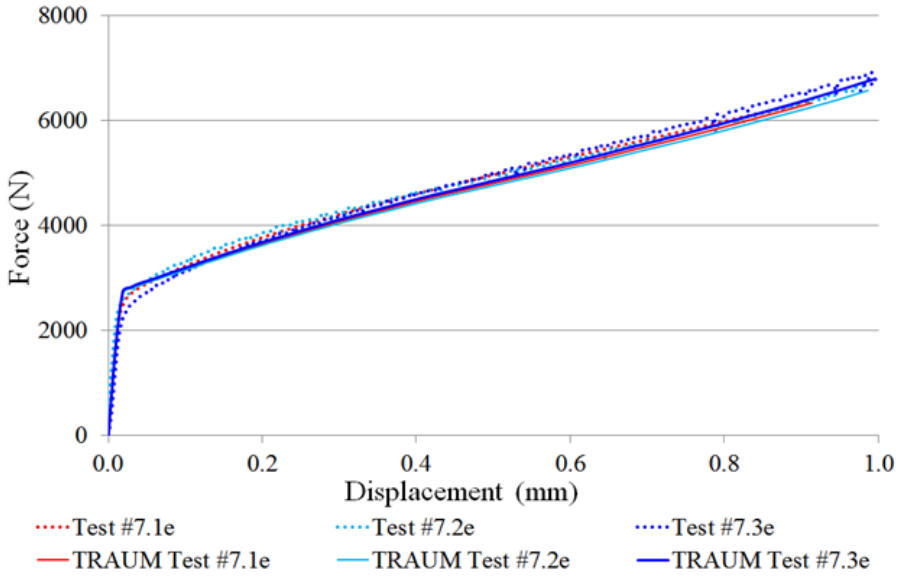

Figure F-7: Verification of the hardening curves for Test #7 at a strain-rate of 1.0s^{-1} and RT.

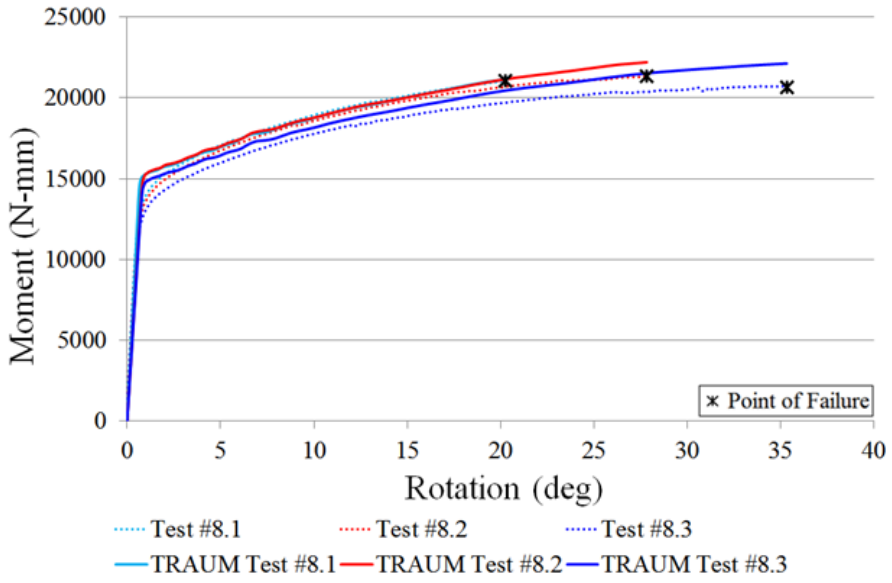

Figure F-8: Verification of the hardening curves for Test #8 at a strain-rate of 1.0s^{-1} and RT.

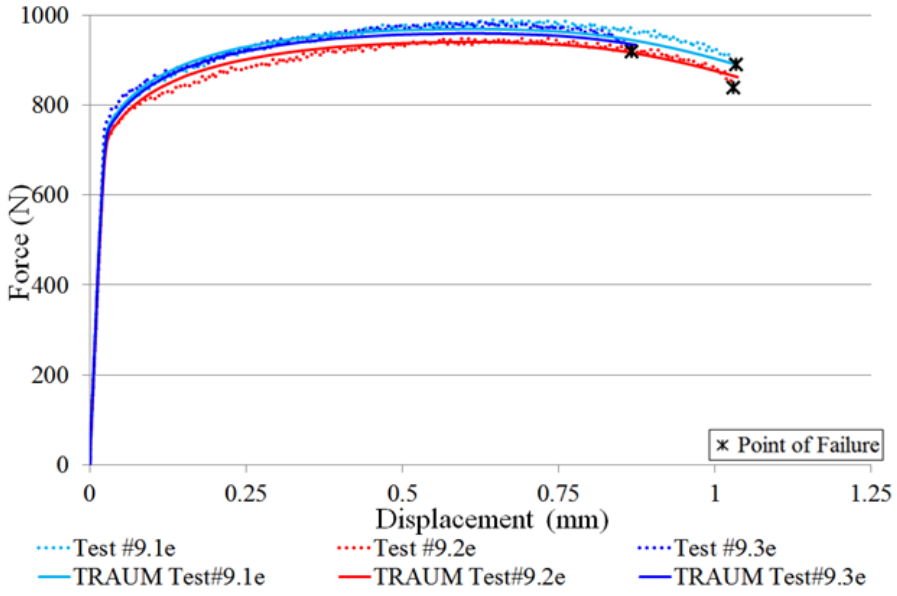

Figure F-9: Verification of the hardening curves for Test #9 at a strain-rate of 1.0s^{-1} and 443K.

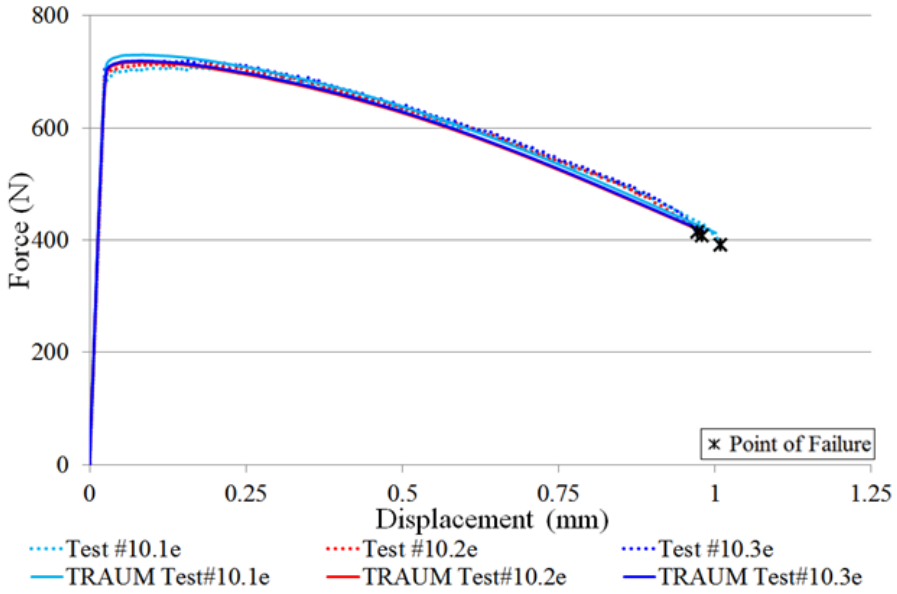

Figure F-10: Verification of the hardening curves for Test #10 at a strain-rate of 1.0s^{-1} and 573K.

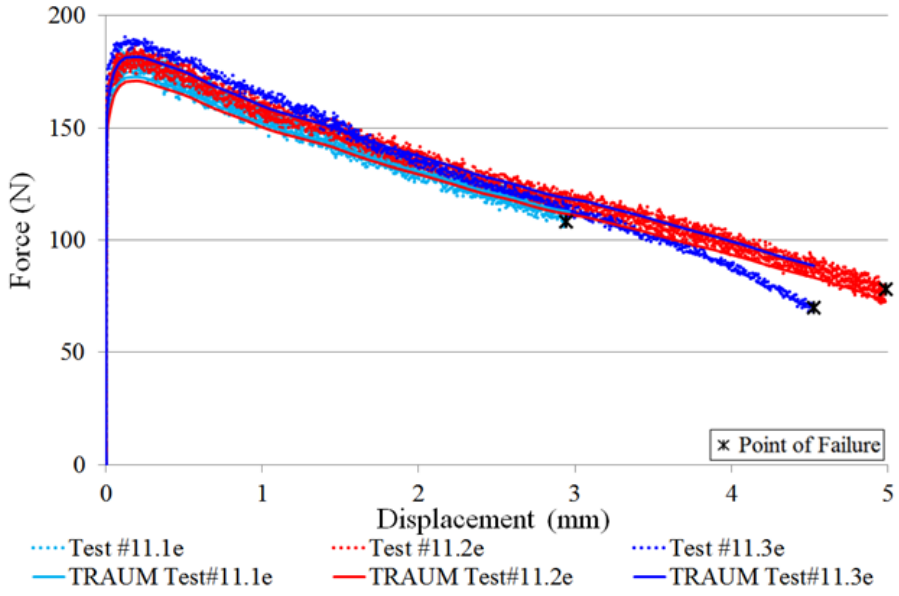

Figure F-11: Verification of the hardening curves for Test #11 at a strain-rate of 1.0s^{-1} and 723K.

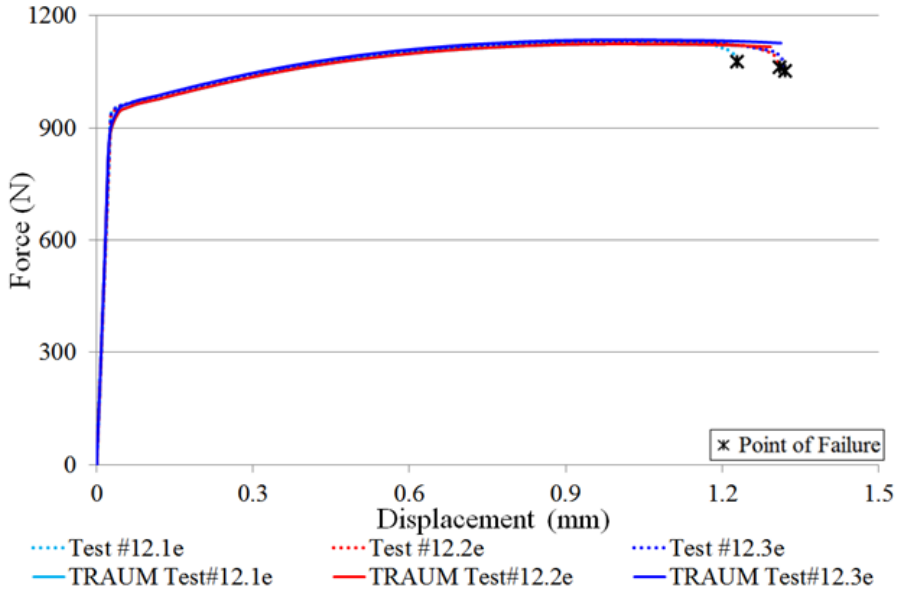

Figure F-12: Verification of the hardening curves for Test #12 at a strain-rate of 1.0s^{-1} and 223K.

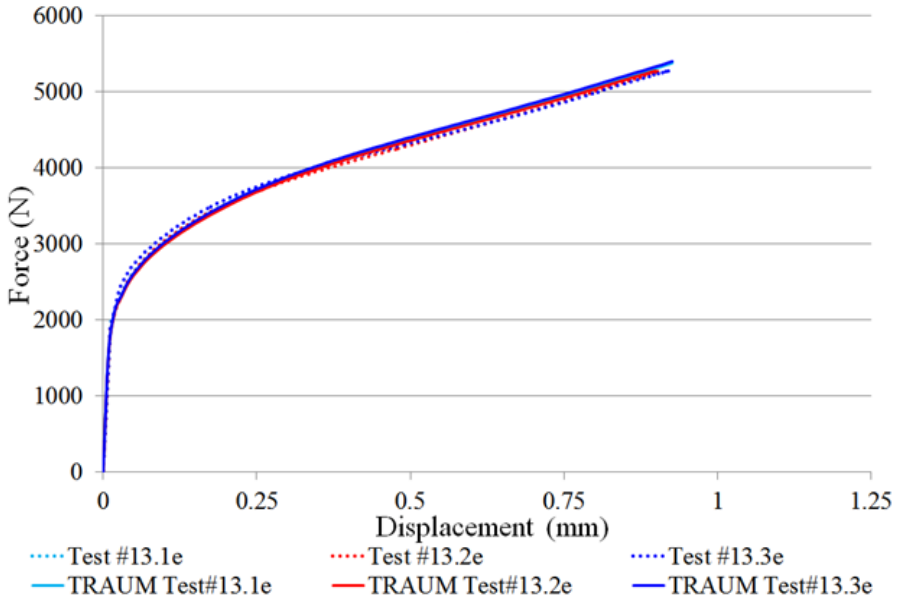

Figure F-13: Verification of the hardening curves for Test #13 at a strain-rate of 1.0s^{-1} and 423K.

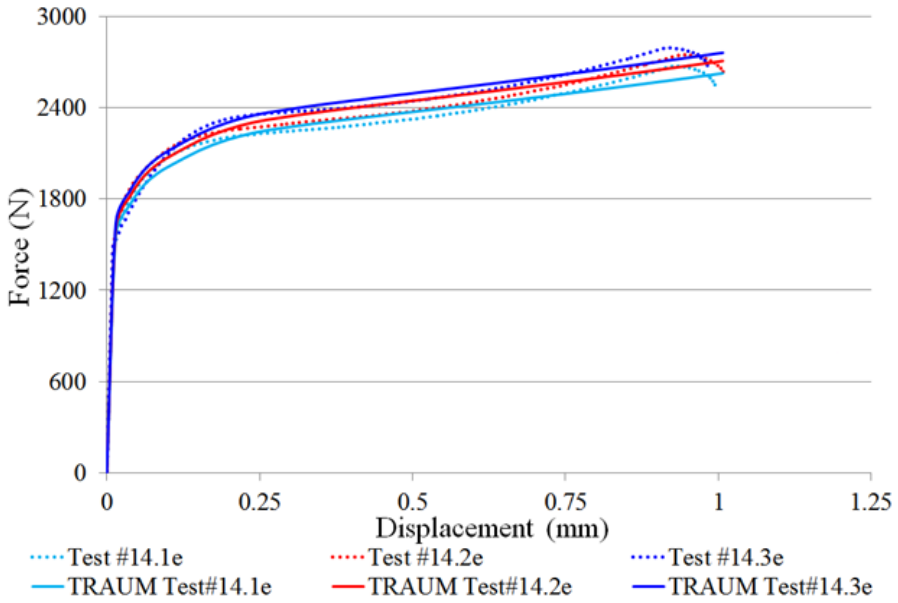

Figure F-14: Verification of the hardening curves for Test #14 at a strain-rate of 1.0s^{-1} and 573K.

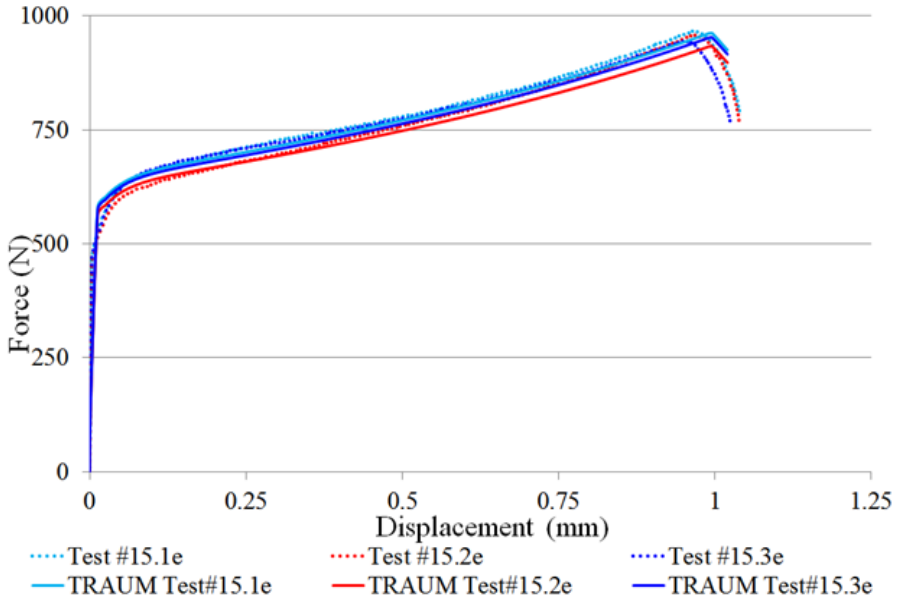

Figure F-15: Verification of the hardening curves for Test #15 at a strain-rate of 1.0s^{-1} and 723K.

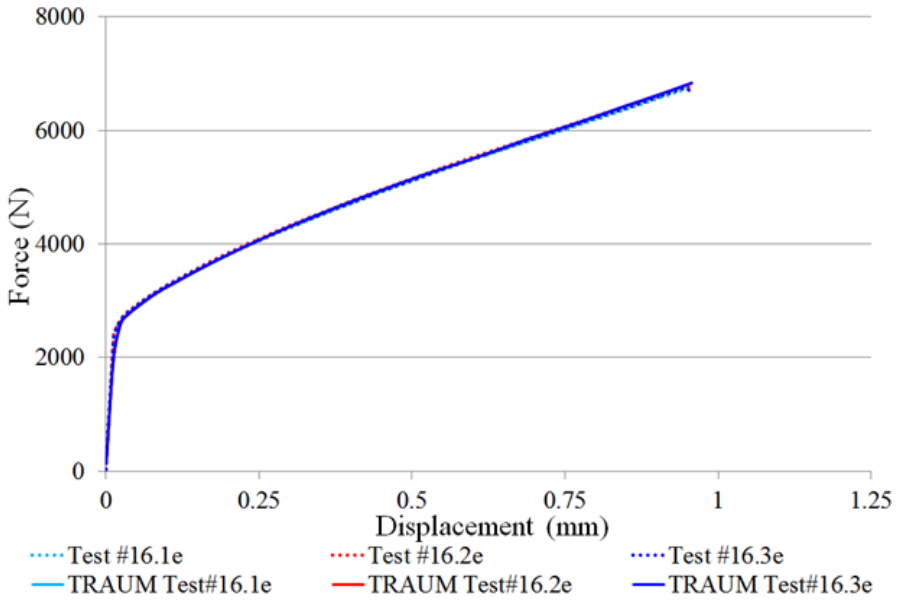

Figure F-16: Verification of the hardening curves for Test #16 at a strain-rate of 1.0s^{-1} and 223K.

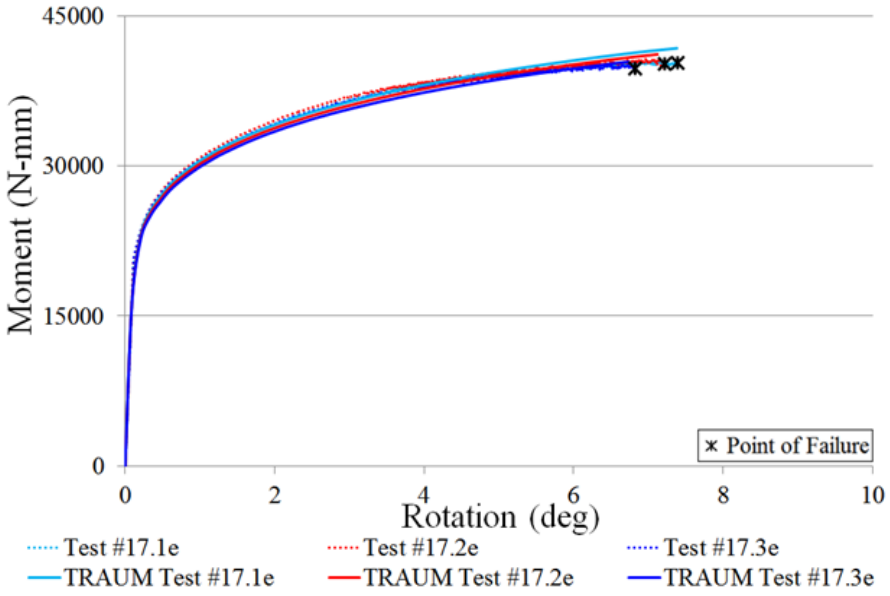

Figure F-17: Verification of the hardening curves for Test #17 at a strain-rate of $1.0x10^{-4}s^{-1}$ and RT.

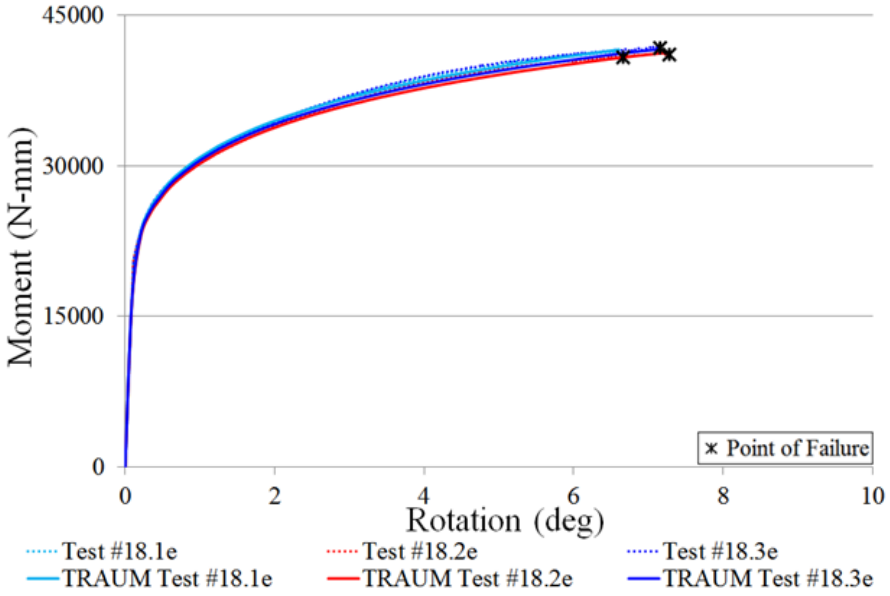

Figure F-18: Verification of the hardening curves for Test #18 at a strain-rate of $1.0x10^{-2}s^{-1}$ and RT.

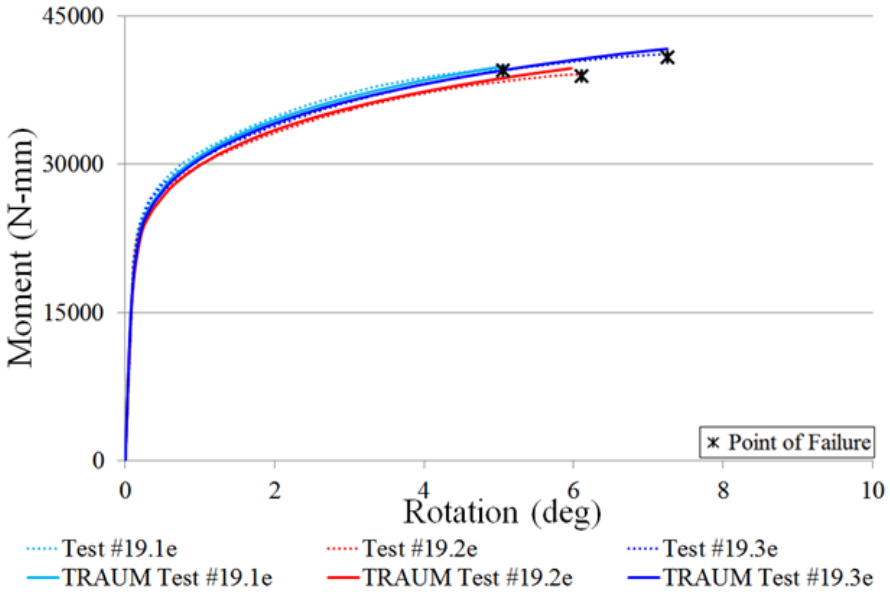

Figure F-19: Verification of the hardening curves for Test #19 at a strain-rate of 1.0s^{-1} and RT.

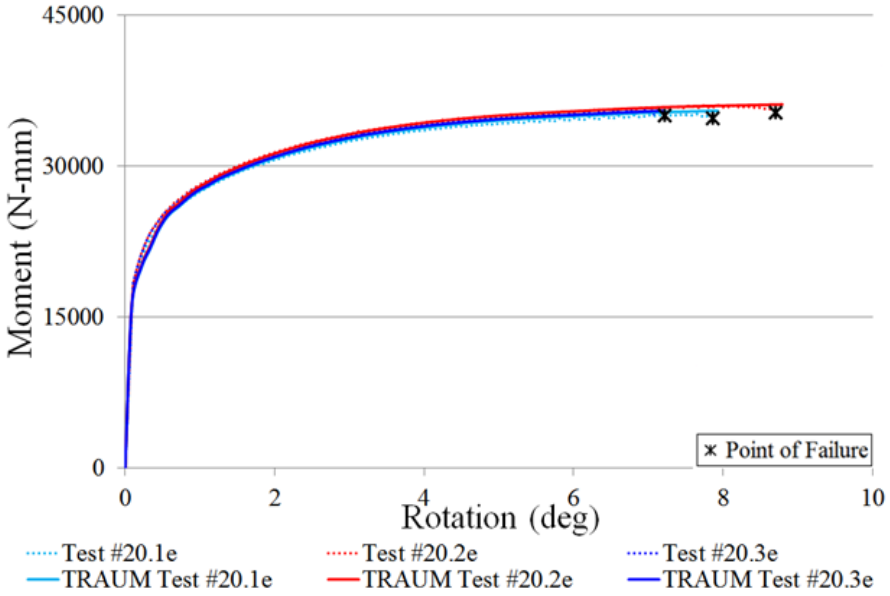

Figure F-20: Verification of the hardening curves for Test #20 at a strain-rate of 1.0s^{-1} and 423K.

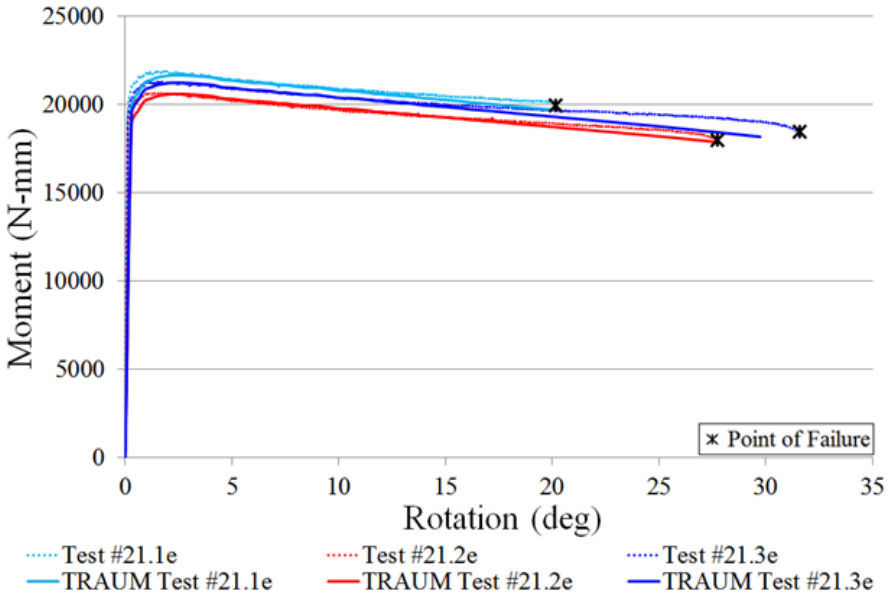

Figure F-21: Verification of the hardening curves for Test #21 at a strain-rate of 1.0s^{-1} and 573K.

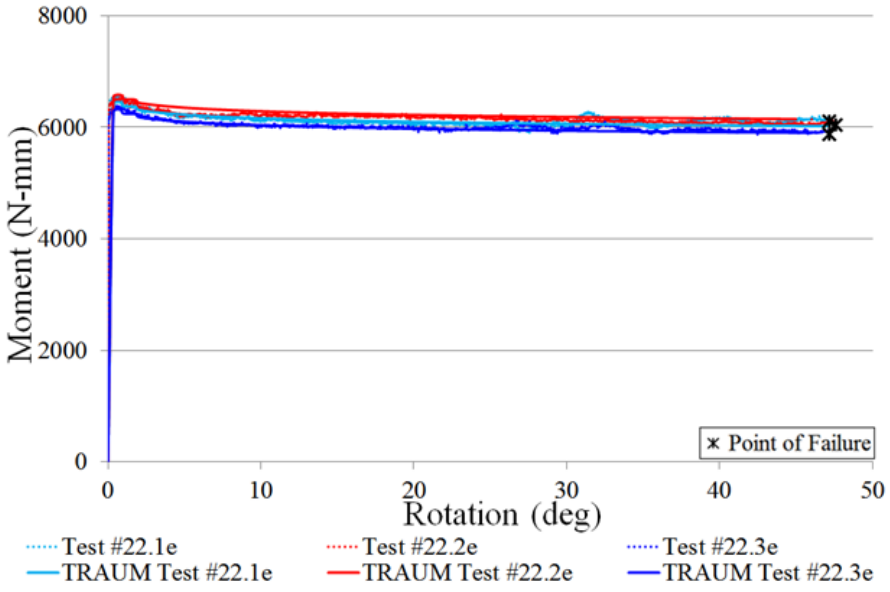

Figure F-22: Verification of the hardening curves for Test #22 at a strain-rate of 1.0s^{-1} and 723K.

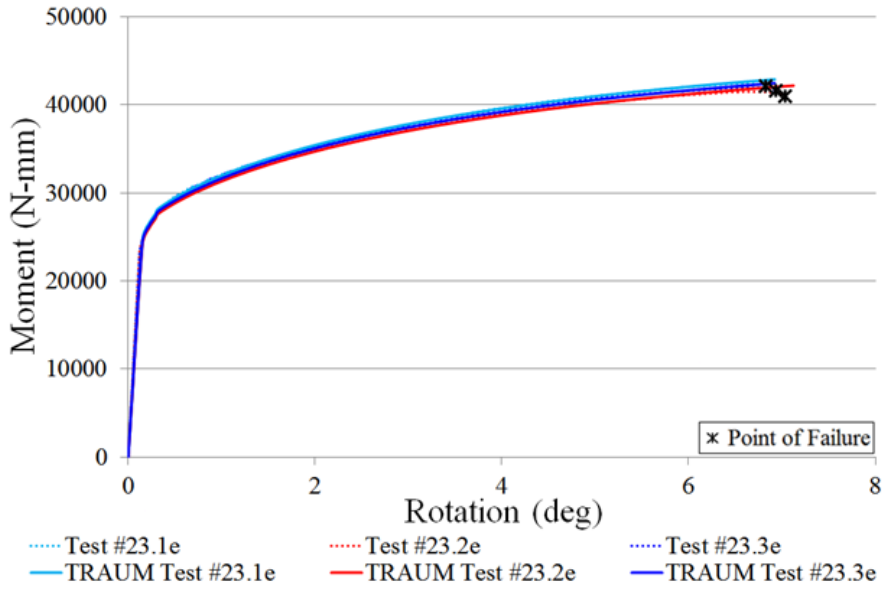

Figure F-23: Verification of the hardening curves for Test #23 at a strain-rate of 1.0s^{-1} and 223K.

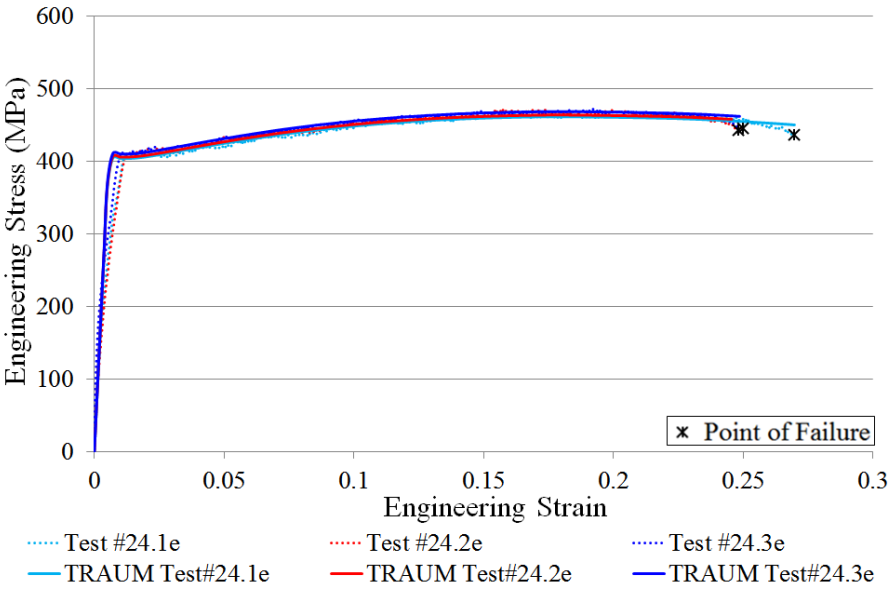

Figure F-24: Verification of the hardening curves for Test #24 at a strain-rate of 500s^{-1} and RT.

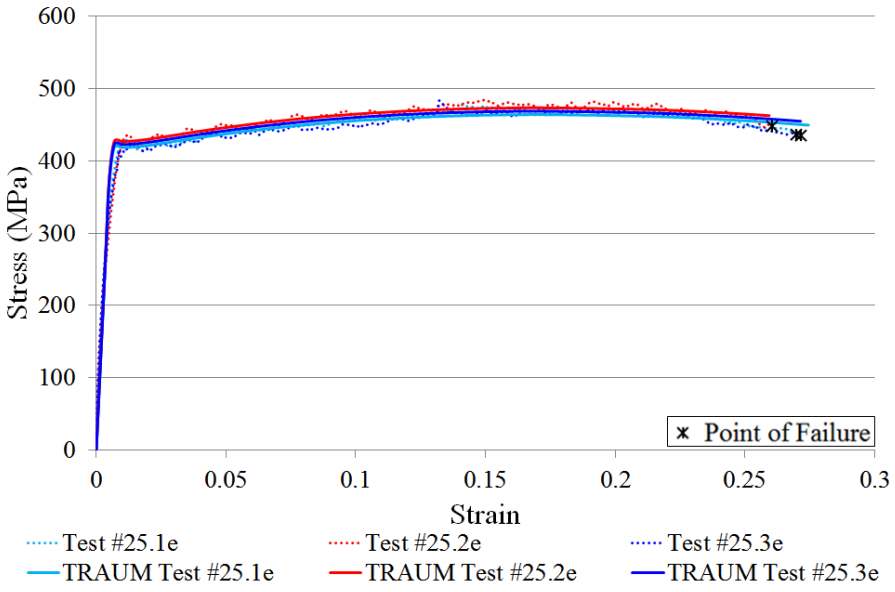

Figure F-25: Verification of the hardening curves for Test #25 at a strain-rate of 1800s^{-1} and RT.

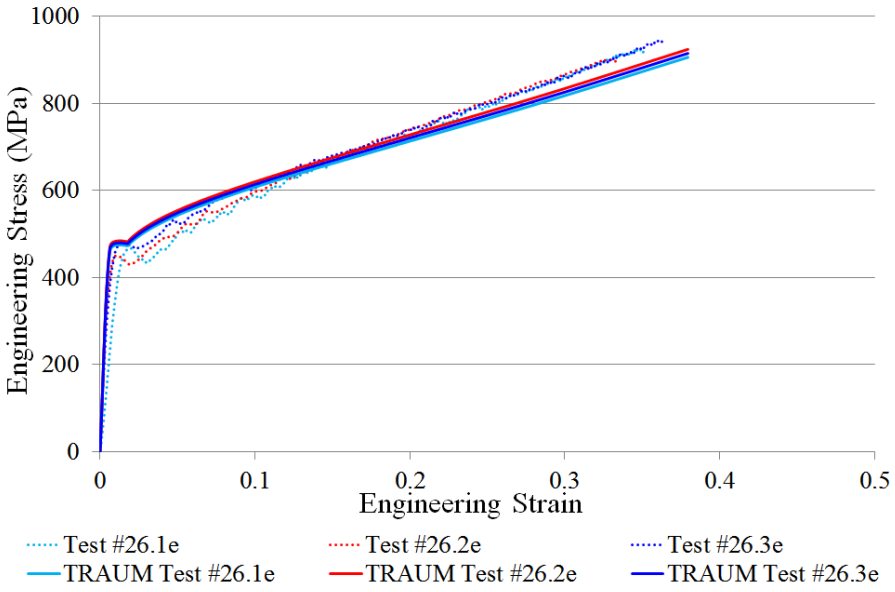

Figure F-26: Verification of the hardening curves for Test #26 at a strain-rate of 1400s^{-1} and RT.

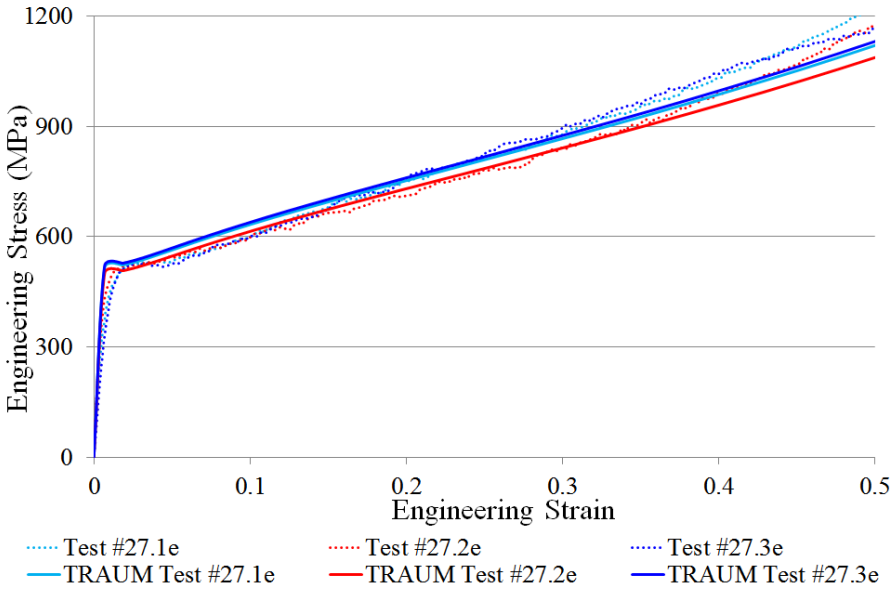

Figure F-27: Verification of the hardening curves for Test #27 at a strain-rate of 5000s^{-1} and RT.

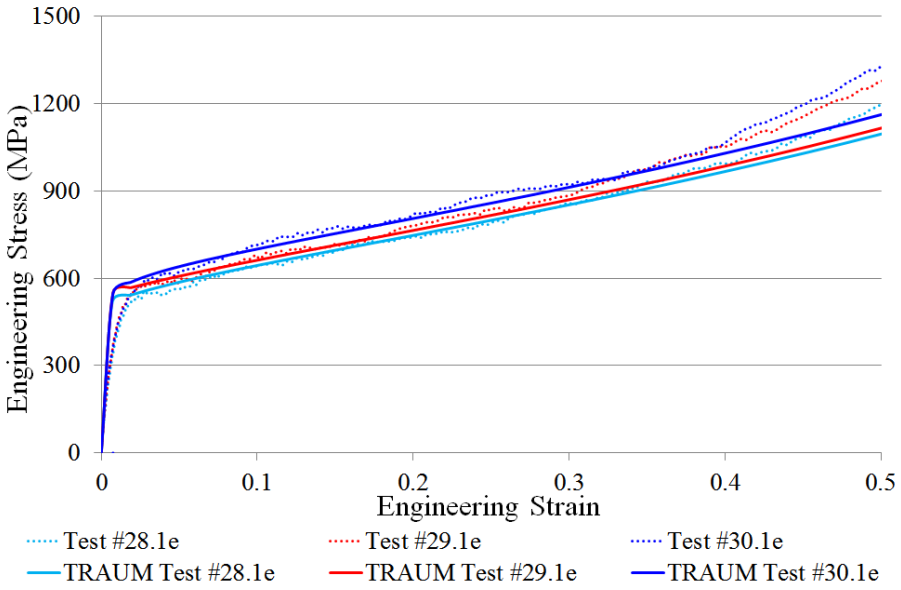

Figure F-28: Verification of the hardening curves for Tests #28, #29 and #30 at RT and strain-rates of 8100s^{-1}, 9800s^{-1} and 11000s^{-1}, respectively.

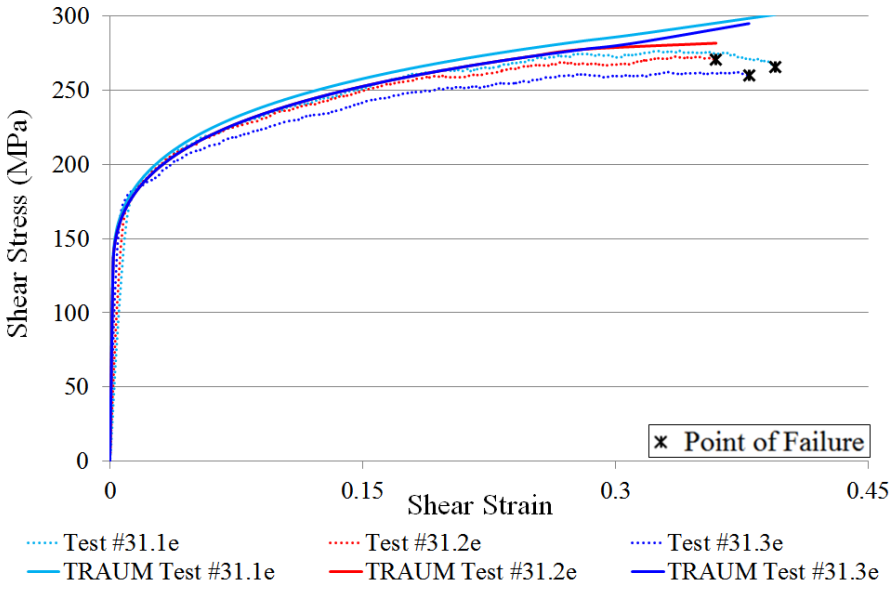

Figure F-29: Verification of the hardening curves for Test #31 at a shear strain-rate of 866s^{-1} and RT.

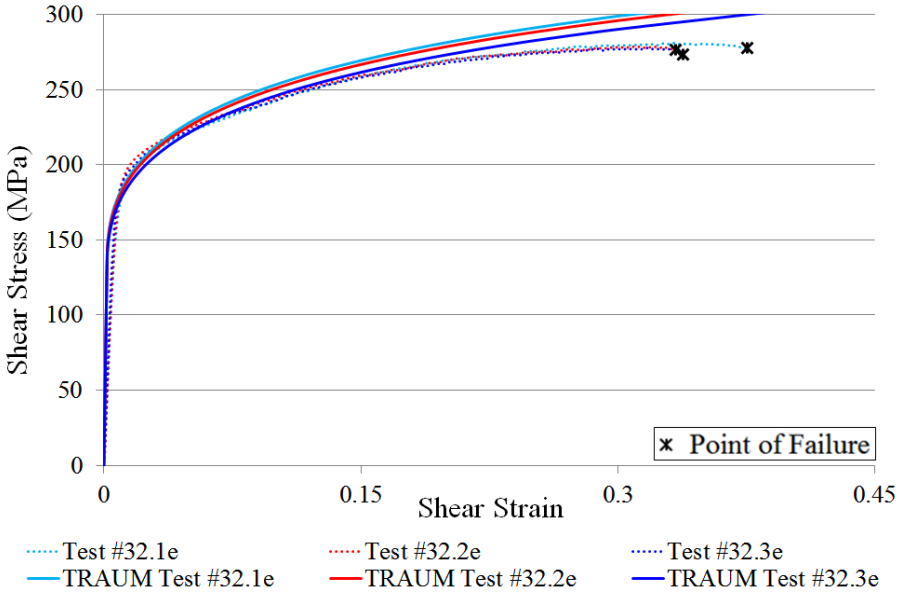

Figure F-30: Verification of the hardening curves for Test #32 at a shear strain-rate of 5000s^{-1} and RT.

Appendix - G: Mesh dependency of the prediction of localized necking

Predicting tensile instability is a mesh dependent procedure. It is shown in Chapter 5 that localized necking can only be predicted by using certain characteristic element lengths. Therefore, it is advisable to use element lengths that are verified by the regularization procedure that is also defined in Section 5.9.

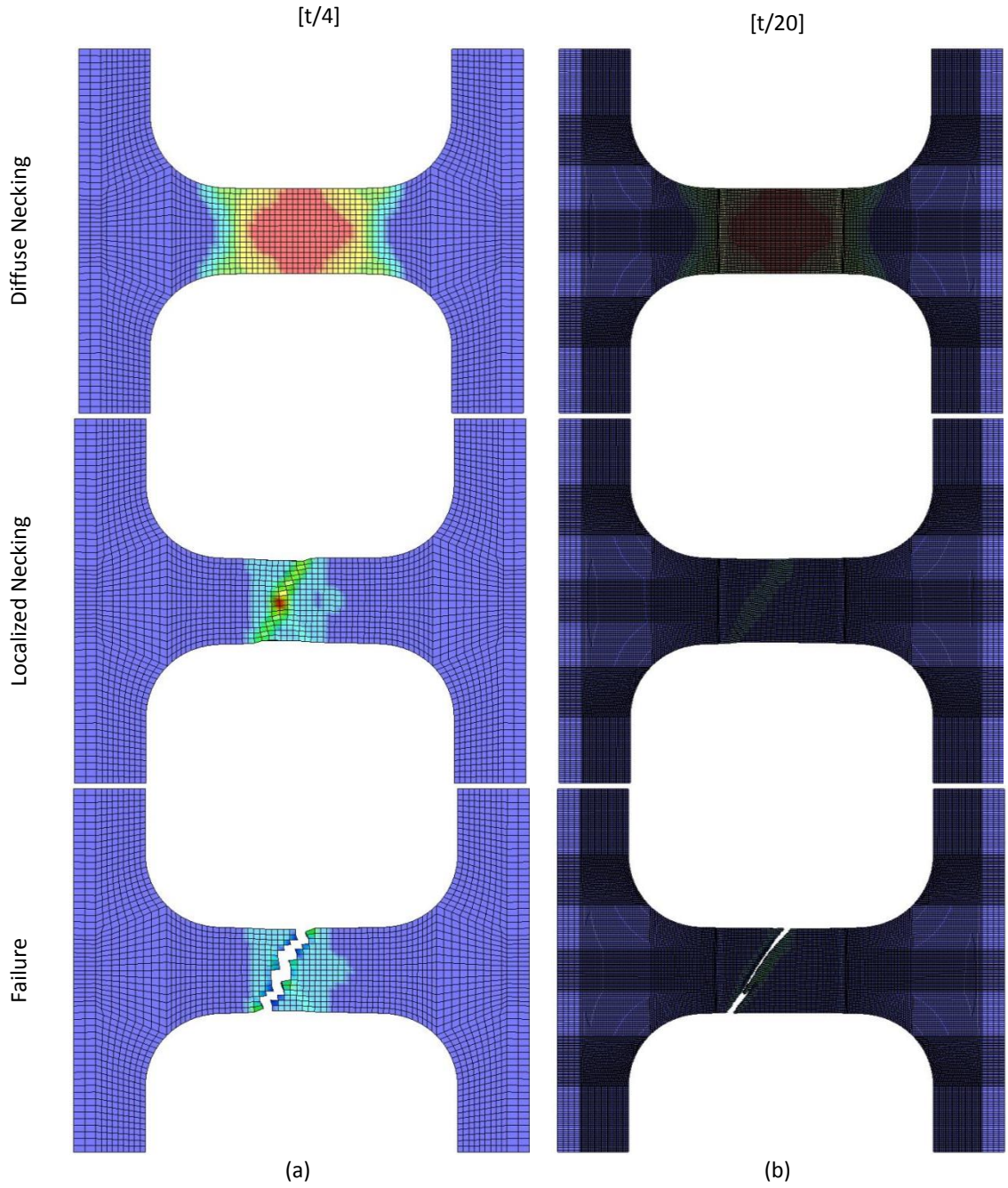

Figure G-1: Tensile instability and the effects of mesh size; (a) by using [t/4] model and (b) by using [t/20] model.

In this Appendix, predictive performance of localized necking is demonstrated with different element lengths even though regularized failure scheme is activated. It should be noted that all models are characterized to provide the same amount of elongation up to failure. However beginning with the [t/2] model, localized necking cannot be predicted as the element length is also outside the bifurcation zone that is illustrated in Section 5.9.

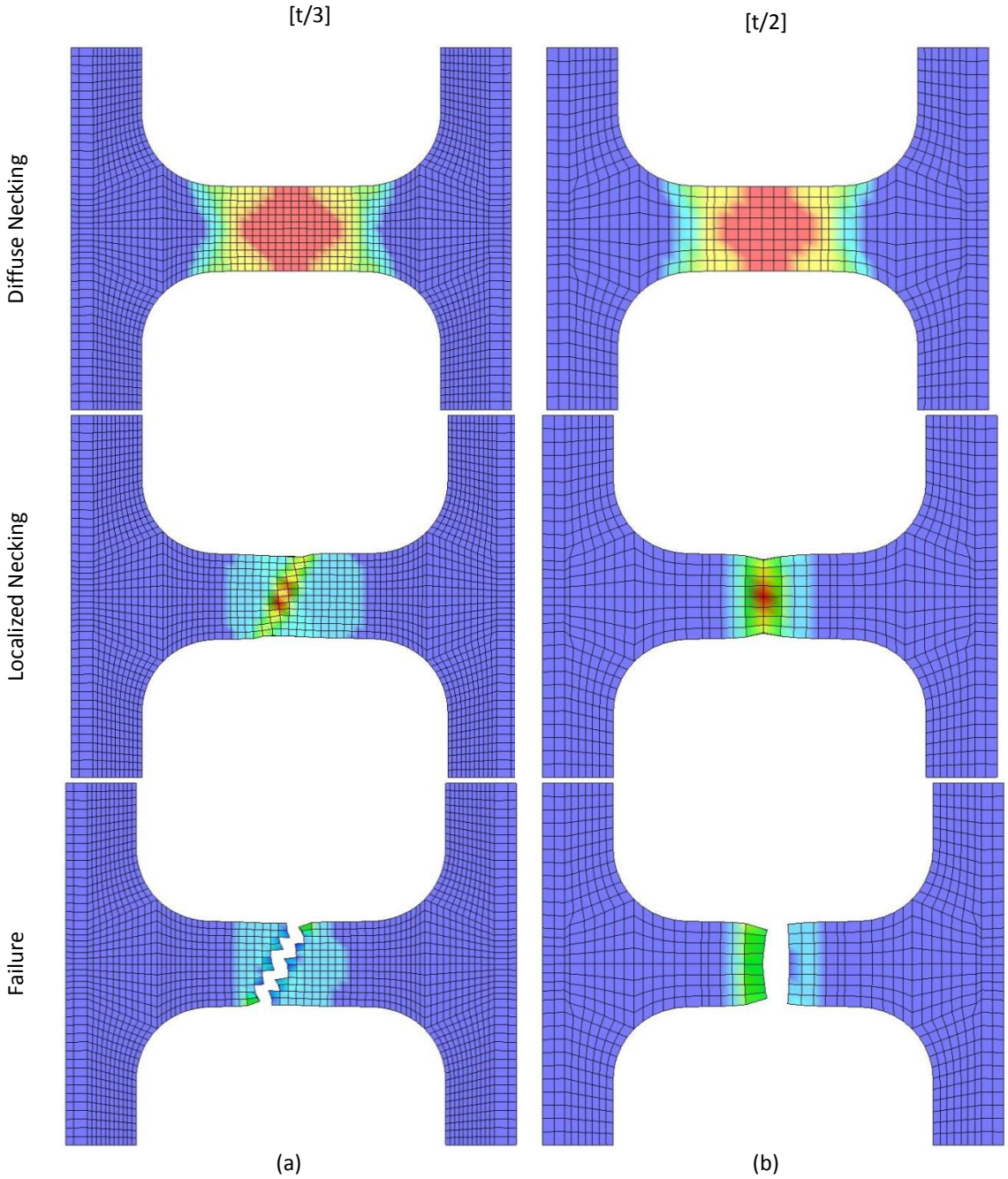

Figure G-2: Tensile instability and the effects of mesh size; (a) by using [t/3] model and (b) by using [t/2] model.

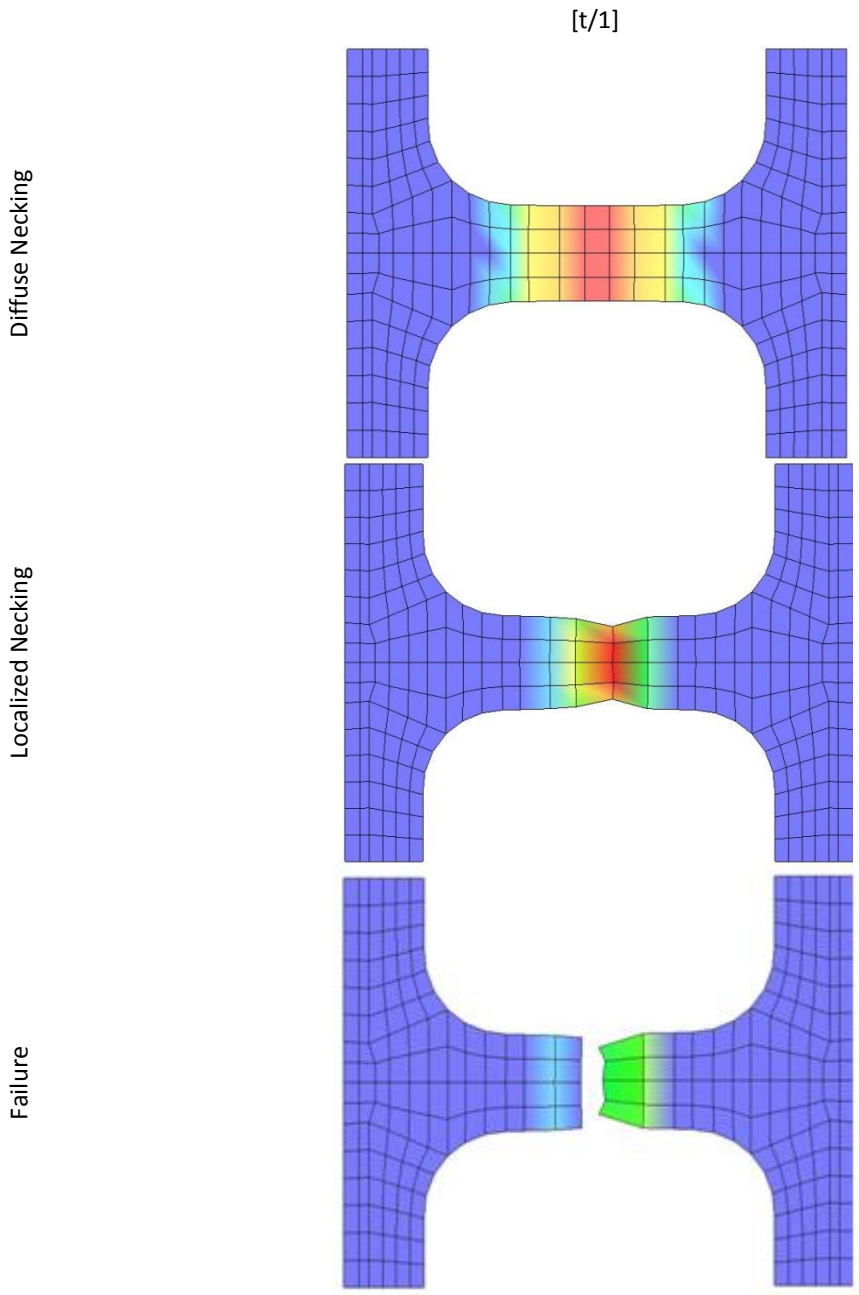

Figure G-3: Tensile instability and the effects of mesh size by using [t/1] model.

Appendix - H: Characterization of the ductile failure based on the state-of-stress for the corresponding tests and the specimens

Ductile failure is characterized by finding the plastic strain at failure and the corresponding states-of-stress as described in Chapter-5 for each specimen and repeated tests. The failure strains are then used to construct the failure surface as a function of the stress-states and are used to build the failure loci.

These figures should be interpreted as the iteratively found plastic strain at the point of failure by comparing the force vs. displacement curves per each test and reading the corresponding stress-state that the failure point will be associated with. Although each test is characterized separately, these figures illustrate only one case for brevity and the resultant findings are listed separately in Chapter-5 for the corresponding specimens. It should also be noted that the characterized strains are for the elements that are at the center of the gauge region.

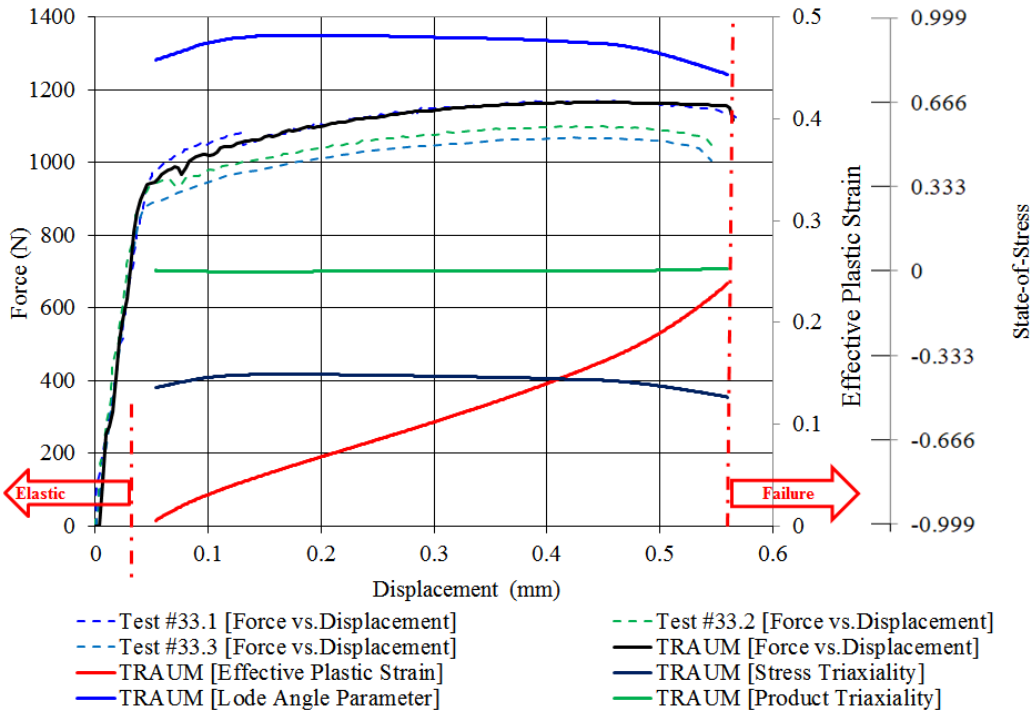

Figure H-1: Characterization of the stress-states and failure strain for Specimen #2.

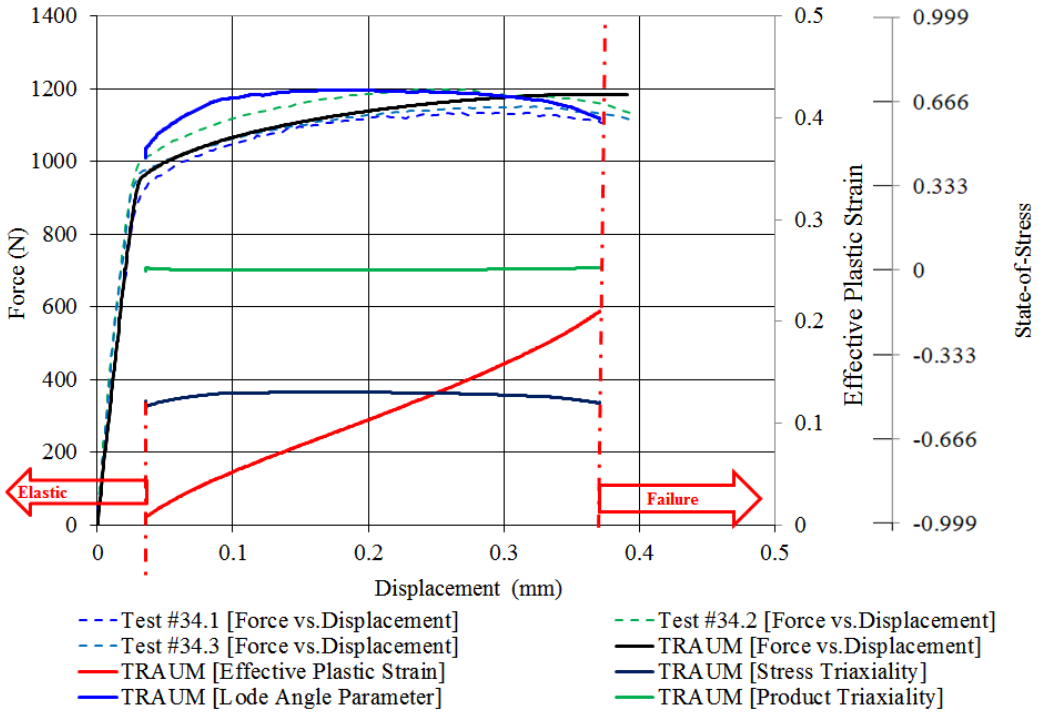

Figure H-2: Characterization of the stress-states and failure strain for Specimen #3.

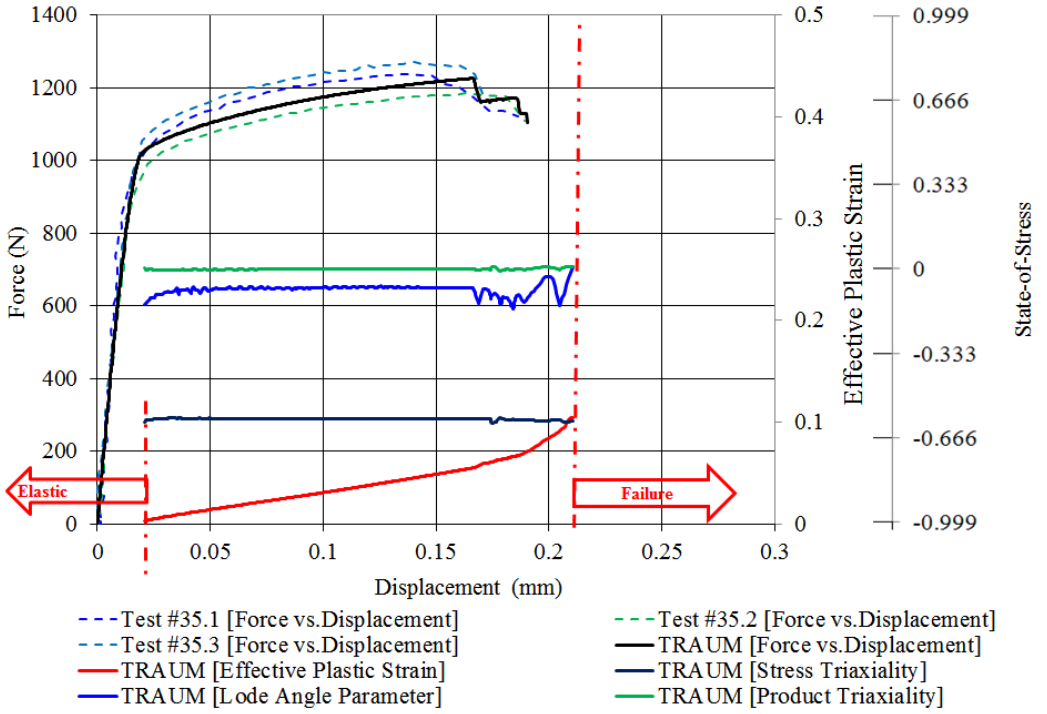

Figure H-3: Characterization of the stress-states and failure strain for Specimen #4.

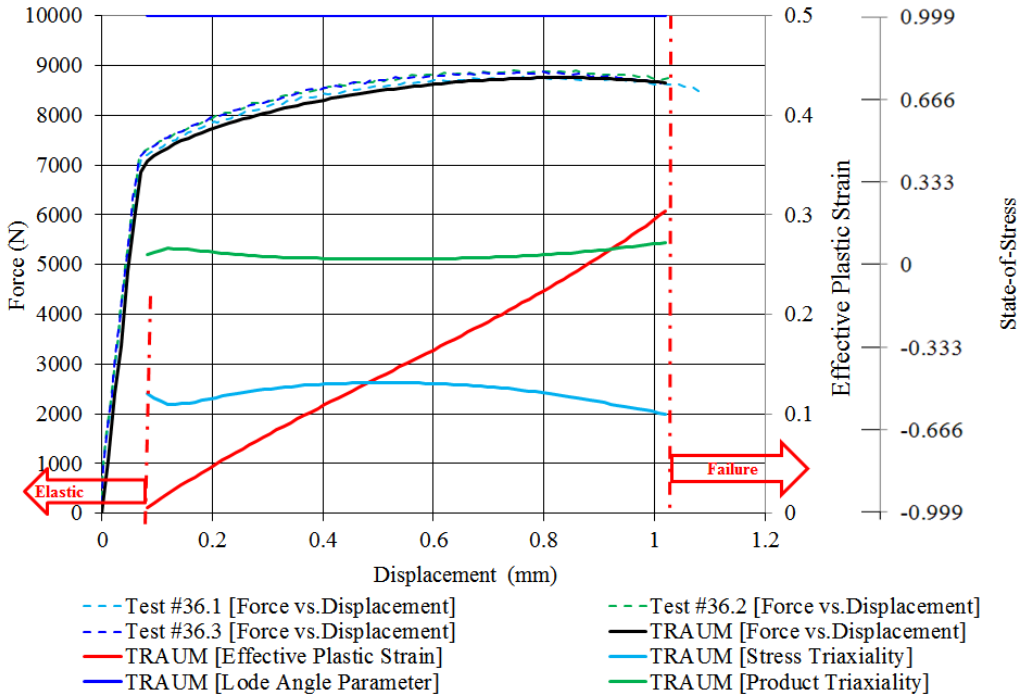

Figure H-4: Characterization of the stress-states and failure strain for Specimen #6.

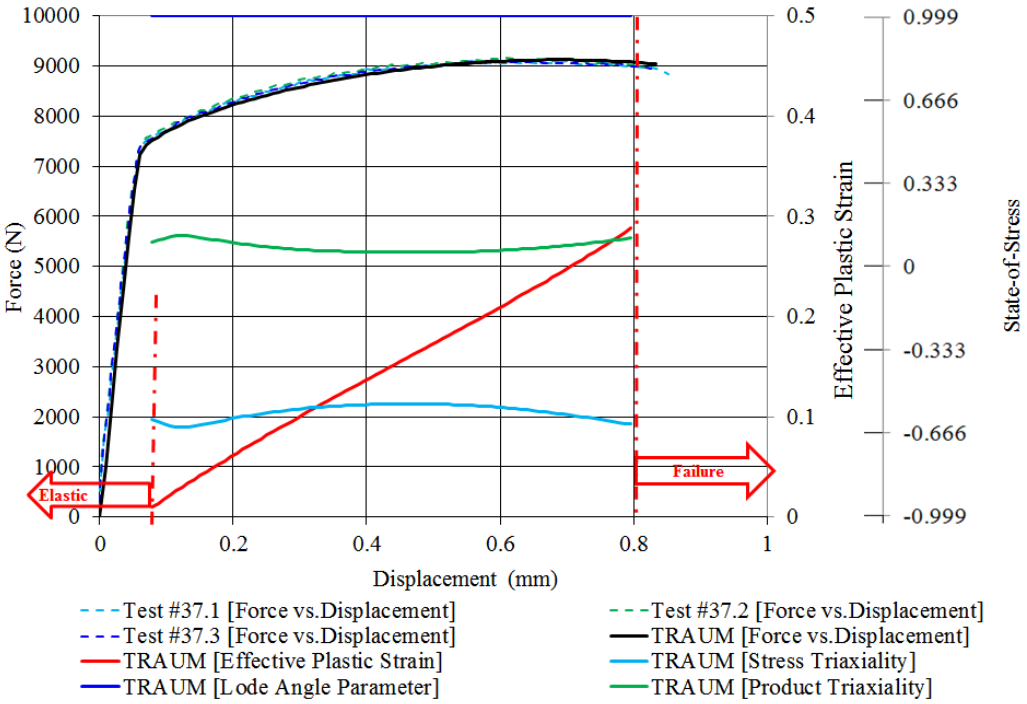

Figure H-5: Characterization of the stress-states and failure strain for Specimen #7.

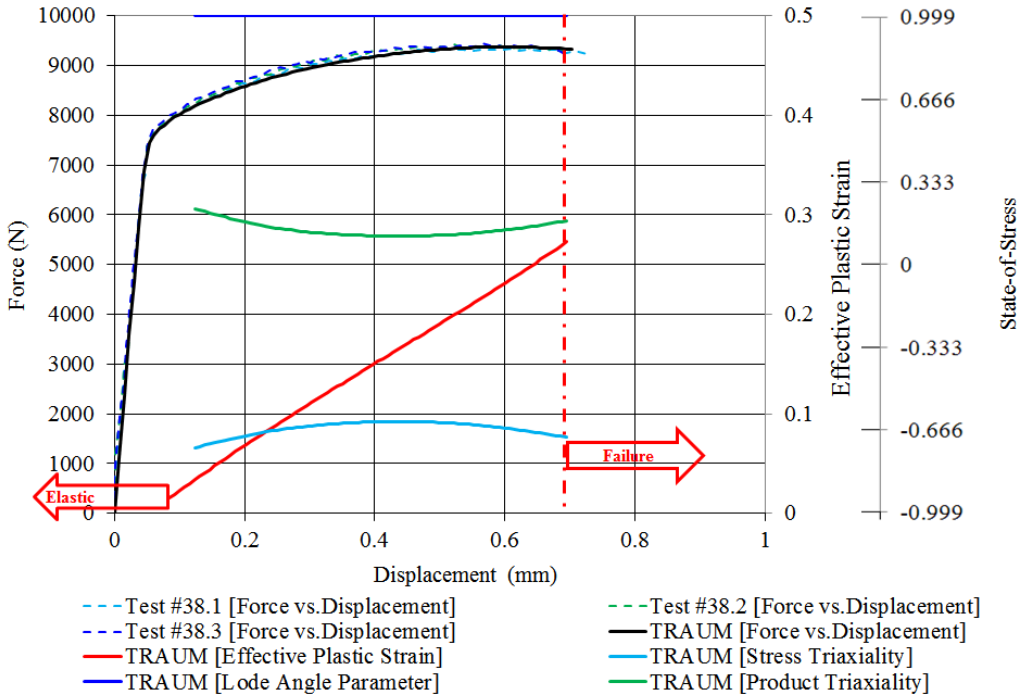

Figure H-6: Characterization of the stress-states and failure strain for Specimen #8.

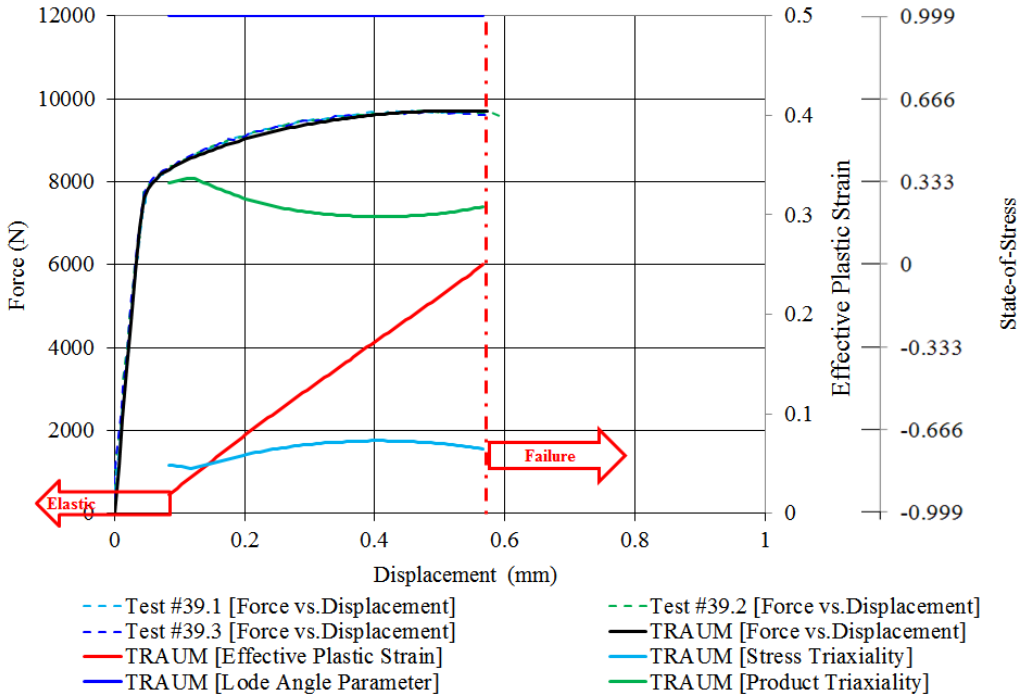

Figure H-7: Characterization of the stress-states and failure strain for Specimen #9.

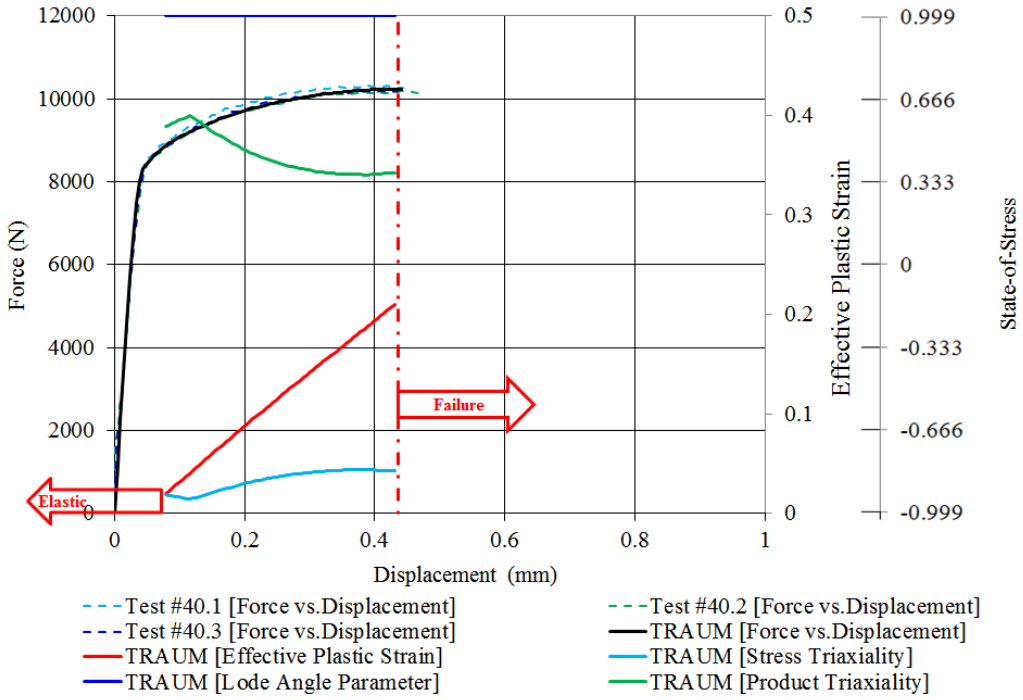

Figure H-8: Characterization of the stress-states and failure strain for Specimen #10.

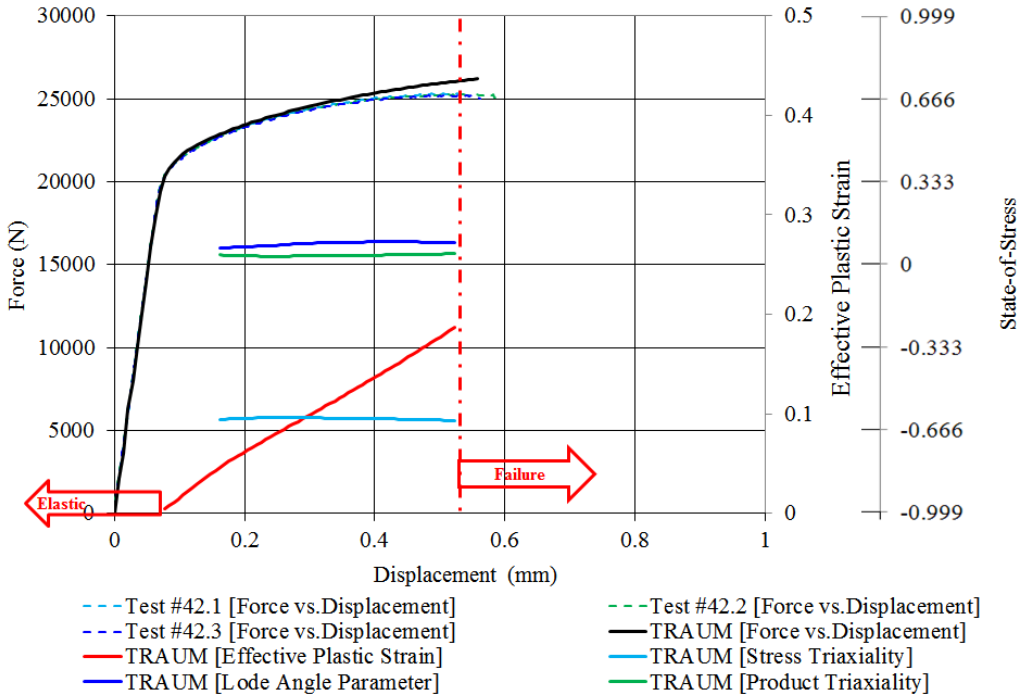

Figure H-9: Characterization of the stress-states and failure strain for Specimen #12.

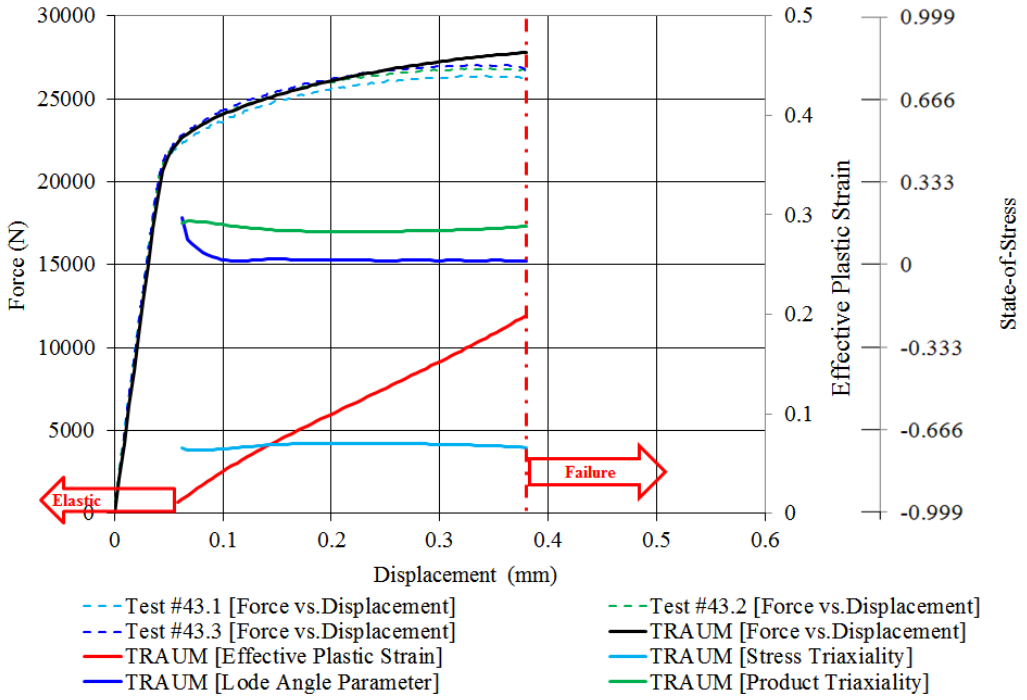

Figure H-10: Characterization of the stress-states and failure strain for Specimen #13.

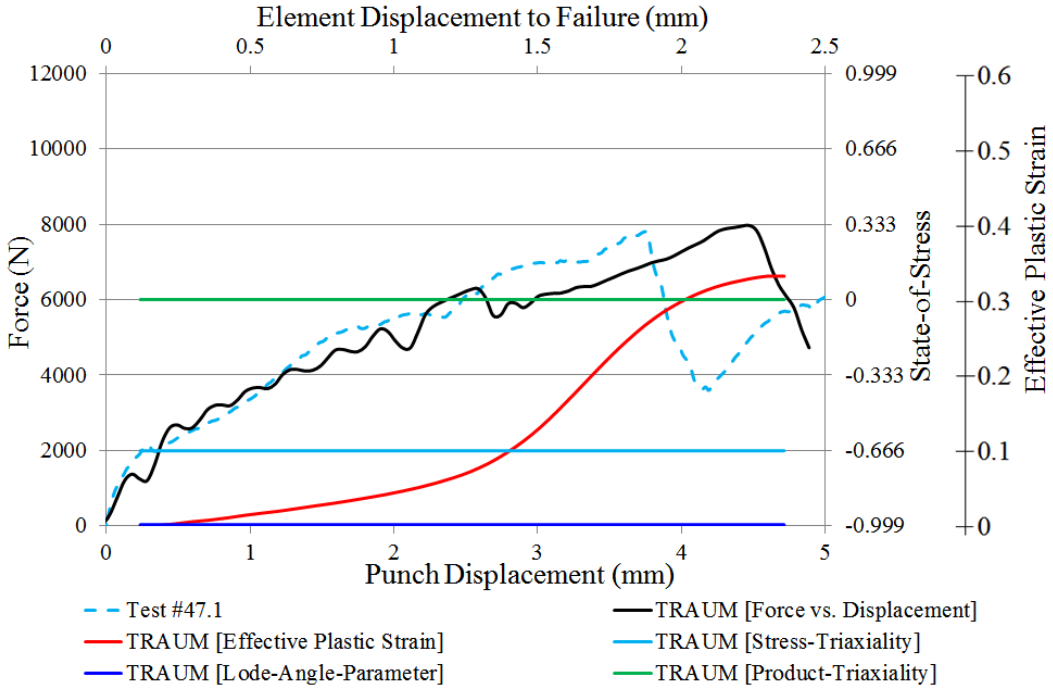

Figure H-11: Characterization of the stress-states and failure strain for Specimen #19.

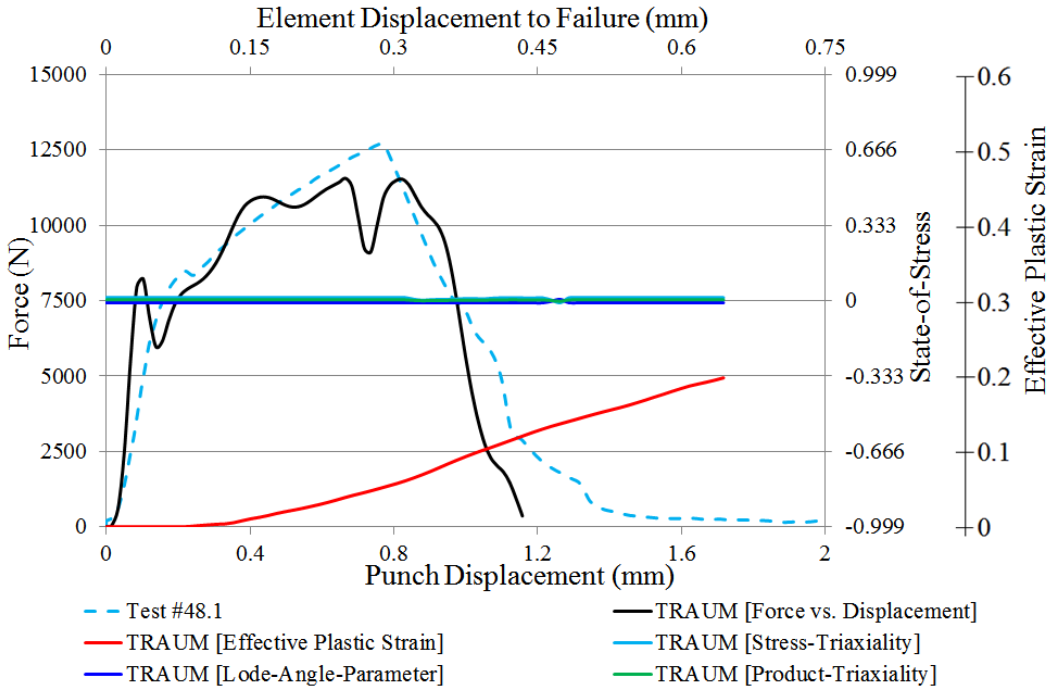

Figure H-12: Characterization of the stress-states and failure strain for Specimen #20.